

HANDBOOK OF THERMAL ANALYSIS AND CALORIMETRY

SERIES EDITOR: PATRICK K. GALLAGHER

VOLUME 2

APPLICATIONS TO INORGANIC AND MISCELLANEOUS MATERIALS

EDITORS

MICHAEL E. BROWN
PATRICK K. GALLAGHER

APPLICATIONS TO INORGANIC AND MISCELLANEOUS MATERIALS

HANDBOOK OF THERMAL ANALYSIS AND CALORIMETRY

SERIES EDITOR

PATRICK K. GALLAGHER

DEPARTMENT OF CHEMISTRY
OHIO STATE UNIVERSITY
USA



ELSEVIER

AMSTERDAM - BOSTON - HEIDELBERG - LONDON - NEW YORK - OXFORD
PARIS - SAN DIEGO - SAN FRANCISCO - SINGAPORE - SYDNEY - TOKYO

HANDBOOK OF THERMAL ANALYSIS AND CALORIMETRY

VOLUME 2

APPLICATIONS TO INORGANIC AND MISCELLANEOUS MATERIALS

EDITED BY

MICHAEL E. BROWN

DEPARTMENT OF CHEMISTRY
RHODES UNIVERSITY
GRAHAMSTOWN 6140
SOUTH AFRICA

PATRICK K. GALLAGHER

DEPARTMENT OF CHEMISTRY
OHIO STATE UNIVERSITY
USA

2003



ELSEVIER

AMSTERDAM - BOSTON - HEIDELBERG - LONDON - NEW YORK - OXFORD
PARIS - SAN DIEGO - SAN FRANCISCO - SINGAPORE - SYDNEY - TOKYO

ELSEVIER B.V.
Sara Burgerhartstraat 25
P.O.Box 211, 1000 AE
Amsterdam, The Netherlands

ELSEVIER Inc.
525 B Street, Suite 1900
San Diego, CA 92101-4495
USA

ELSEVIER Ltd
The Boulevard, Langford Lane
Kidlington, Oxford OX5 1GB
UK

ELSEVIER Ltd
84 Theobalds Road
London WC1X 8RR
UK

© 2003 Elsevier B.V. All rights reserved.

This work is protected under copyright by Elsevier B.V., and the following terms and conditions apply to its use:

Photocopying
Single photocopies of single chapters may be made for personal use as allowed by national copyright laws. Permission of the Publisher and payment of a fee is required for all other photocopying, including multiple or systematic copying, copying for advertising or promotional purposes, resale, and all forms of document delivery. Special rates are available for educational institutions that wish to make photocopies for non-profit educational classroom use.

Permissions may be sought directly from Elsevier's Rights Department in Oxford, UK: phone (+44) 1865 843830, fax (+44) 1865 853333, e-mail: permissions@elsevier.com. Requests may also be completed on-line via the Elsevier homepage (http://www.elsevier.com/locate/permissions).

In the USA, users may clear permissions and make payments through the Copyright Clearance Center, Inc., 222 Rosewood Drive, Danvers, MA 01923, USA; phone: (+1) (978) 7508400, fax: (+1) (978) 7504744, and in the UK through the Copyright Licensing Agency Rapid Clearance Service (CLARCS), 90 Tottenham Court Road, London W1P 0LP, UK; phone: (+44) 20 7631 5555; fax: (+44) 20 7631 5500. Other countries may have a local reprographic rights agency for payments.

Derivative Works
Tables of contents may be reproduced for internal circulation, but permission of the Publisher is required for external resale or distribution of such material. Permission of the Publisher is required for all other derivative works, including compilations and translations.

Electronic Storage or Usage
Permission of the Publisher is required to store or use electronically any material contained in this work, including any chapter or part of a chapter.

Except as outlined above, no part of this work may be reproduced, stored in a retrieval system or transmitted in any form or by any means, electronic, mechanical, photocopying, recording or otherwise, without prior written permission of the Publisher.
Address permissions requests to: Elsevier's Rights Department, at the fax and e-mail addresses noted above.

Notice
No responsibility is assumed by the Publisher for any injury and/or damage to persons or property as a matter of products liability, negligence or otherwise, or from any use or operation of any methods, products, instructions or ideas contained in the material herein. Because of rapid advances in the medical sciences, in particular, independent verification of diagnoses and drug dosages should be made.

First Edition 2003

Library of Congress Cataloging in Publication Data
A catalog record is available from the Library of Congress.

British Library Cataloguing in Publication Data
A catalogue record is available from the British Library.

ISBN: 0 444 82086 8

♾ The paper used in this publication meets the requirements of ANSI/NISO Z39.48-1992 (Permanence of Paper).
Printed in The Netherlands.

FOREWORD

The applications and interest in thermal analysis and calorimetry have grown enormously during the last half of the 20th century. The renaissance in these methods has been fuelled by several influences. Certainly the revolution in instrumentation brought on by the computer and automation has been a key factor. Our imaginations and outlooks have also expanded to recognize the tremendous versatility of these techniques. They have long been used to characterize materials, decompositions, and transitions. We now appreciate the fact that these techniques have greatly expanded their utility to studying many processes such as catalysis, hazards evaluation, etc. or to measuring important physical properties quickly, conveniently, and with markedly improved accuracy over that in the past.

Consequently, thermal analysis and calorimetry have grown in stature and more scientists and engineers have become, at least part time, practitioners. It is very desirable that these people new to the field can have a source of information describing the basic principles and current state of the art. Examples of the current applications of these methods are also essential to spur recognition of the potential for future uses. The application of these methods is highly interdisciplinary and any adequate description must encompass a range of topics well beyond the interests and capabilities of any single investigator. To this end, we have produced a convenient four volume compendium of such information (a handbook) prepared by recognized experts in various aspects of the topic.

Volume 1 describes the basic background information common to the broad subject in general. Thermodynamic and kinetic principles are discussed along with the instrumentation and methodology associated with thermoanalytical and calorimetric techniques. The purpose is to collect the discussion of these general principles and minimize redundancies in the subsequent volumes that are concerned with the applications of these principles and methods. More unique methods which pertain to specific processes or materials are covered in later volumes.

The three subsequent volumes primarily describe applications and are divided based on general categories of materials. Volume 2 concerns the wide range of inorganic materials, e.g., chemicals, ceramics, metals, etc. It covers the synthesis, characterization, and reactivity of such materials. Similarly, Volume 3 pertains to polymers and describes applications to these materials in an appropriate manner. Lastly the many important biological applications are described in Volume 4.

Each of these four volumes has an Editor, who has been active in the field for many years and is an established expert in the material covered by that specific volume. This team of Editors has chosen authors with great care in an effort to

produce a readable informative handbook on this broad topic. The chapters are not intended to be a comprehensive review of the specific subject. The intent is that they enable the reader to glean the essence of the subject and form the basis for further critical reading or actual involvement in the topic. Our goal is to spur your imaginations to recognize the potential application of these methods to your specific goals and efforts. In addition we hope to anticipate and answer your questions, to guide you in the selection of appropriate techniques, and to help you to perform them in a proper and meaningful manner.

PATRICK K. GALLAGHER
Series Editor

PREFACE TO VOLUME 2

This volume contains fifteen chapters on the applications of the techniques of thermal analysis and calorimetry to the study of mainly inorganic materials. Contributions were invited on the basis of the expertise of the authors in each particular area. Some overlap between chapters has been unavoidable, but the differences in points-of-view do add to the interest. In the absence of a better way of arranging the chapters they have been placed in alphabetical order to emphasize, at least, the vast range of materials - from adsorbents to superconductors - to which the techniques of thermal analysis and calorimetry have been successfully applied.

Production of the volume has been slow, for a variety of reasons, but it is hoped that the final result will be worth the long wait. Some of the contributors joined the project at an advanced stage after some of the original authors had withdrawn for various reasons. To those model authors who worked entirely to schedule and then had to wait for a long time for their work to appear, our sincere apologies.

MICHAEL E. BROWN
PATRICK K. GALLAGHER
Volume Editors

This Page Intentionally Left Blank

CONTENTS

Foreword - P.K. Gallagher v
Preface - M.E. Brown and P.K. Gallagher vii
Contributors xxi
Acknowledgements xxv

CHAPTER 1. APPLICATIONS OF THERMAL ANALYSIS AND CALORIMETRY IN ADSORPTION AND SURFACE CHEMISTRY
(Philip L. Llewellyn)

1. INTRODUCTION 1
2. IMMERSION CALORIMETRY 1
2.1. Introduction 1
2.2. Immersion calorimetry for the estimation of the surface area of a solid: the modified Harkins and Jura method 3
2.3. Immersion calorimetry for an evaluation of the chemical nature of the surface 6
2.4. Immersion calorimetry for the evaluation of microporosity 7
2.5. Intrusion of non-wetting fluids 10
3. THERMOPOROMETRY 11
4. SAMPLE CONTROLLED THERMAL ANALYSIS (SCTA) 14
5. ISOTHERMAL ADSORPTION MICROCALORIMETRY 22
5.1. Introduction 22
5.2. Adsorption calorimetry for the characterisation of heterogeneous adsorbents 30
5.3. Adsorption calorimetry for the characterisation of homogeneous adsorbents 35
5.4. Adsorption calorimetry for the detection of adsorbate phase transitions 37
5.5. Adsorption calorimetry to follow the various stages of micropore filling 40
5.6. Adsorption calorimetry in capillary condensation 42
REFERENCES 43

CHAPTER 2. THE APPLICATIONS OF THERMOANALYTICAL TECHNIQUES TO THE PRESERVATION OF ART AND ARCHAEOLOGICAL OBJECTS
(Marianne Odlyha)

1. INTRODUCTION 47
2. CHARACTERISATION OF ART AND ARCHAEOLOGICAL OBJECTS BY THERMAL ANALYSIS 51
2.1. General Considerations 51
2.2. Thermoanalytical Techniques 52
3. CASE STUDIES 55
3.1. Thermomicroscopy 55
3.2. Differential scanning calorimetry 56
3.3. Thermogravimetry 68
3.4. Thermomechanical analysis 78
3.5. Dynamic mechanical thermal analysis 80
3.6. Micro-thermal analysis 84
4. CONCLUSIONS 91
5. ACKNOWLEDGEMENTS 92
REFERENCES 92

CHAPTER 3. THE APPLICATION OF THERMAL ANALYSIS TO THE STUDY OF CARBONS
(Pauline Phang and the late David Dollimore)

1. INTRODUCTION 97
2. DIAMOND 98
3. GRAPHITE 99
4. THE FULLERENES AND ASSOCIATED CARBON MOLECULES 100
5. CARBON BLACK 101
6. CHARCOAL 105
7. ACTIVATED CARBON 106
8. CARBON FIBRES 110
9. THE INCORPORATION OF CARBON INTO POLYMER COMPOUNDS AND SIMILAR STUDIES 113
10. OTHER STUDIES 114
REFERENCES 115

CHAPTER 4. APPLICATIONS OF THERMAL ANALYSIS IN THE PREPARATION OF CATALYSTS AND IN CATALYSIS
(B. Pawelec and J.L.G. Fierro)

1. INTRODUCTION 119
2. THERMOGRAVIMETRY 120
2.1. Introduction 120
2.2. Transformation of catalyst precursors 120
2.3. Dehydration/dehydroxylation 126
2.4. Determination of the porous structure of catalysts 129
2.5. Thermogravimetry in the study of adsorption/desorption on catalysts 132
3. THERMOGRAVIMETRY IN REACTIVE ATMOSPHERES 142
3.1. Temperature-programmed reduction (TPR) 142
3.2. Determination of the stoichiometry of oxides 150
3.3. Kinetics studies on catalyst reduction 154
3.4. Determination of specific surface area/active phase dispersion 163
3.5. Kinetics and equilibrium of O_2 adsorption 167
3.6. Coke formation on pre-reduced catalysts 171
4. IDENTIFICATION OF THE NATURE OF ADSORPTION SITES BY THE TPD METHOD 174
4.1. Evolved gas analysis (EGA) 174
4.2. EGA – MS 174
4.3. EGA – FTIR 175
4.4. Temperature-programmed desorption of NH_3 176
5. DIFFERENTIAL THERMAL ANALYSIS (DTA) AND DIFFERENTIAL SCANNING CALORIMETRY (DSC) 177
6. CONCLUSION 184
REFERENCES 184

CHAPTER 5. CERAMICS, GLASS, AND ELECTRONIC MATERIALS
(Patrick K. Gallagher and John P. Sanders)

1. INTRODUCTION 191
1.1. Purpose and scope 191
1.2. Organization 192
2. PHASE EQUILIBRIA 192
2.1. Establishing a phase diagram 192
2.2. The nature of phase transformations 194

3. COMPOSITIONAL ANALYSIS 195
3.1. Methods based on changes in mass 195
3.2. Methods based on a transition temperature 205
3.3. X-Ray diffraction and spectroscopic methods 213
4. PHYSICAL PROPERTIES 215
4.1. Heat capacity 215
4.2. Thermal conductivity and diffusivity 216
4.3. Thermal expansion 218
4.4. Surface area and porosity 223
4.5. Electrical and magnetic properties 223
5. SOLID STATE REACTIVITY 225
5.1. Introduction 225
5.2. Heterogeneous reactions and mechanisms 225
5.3. Sintering phenomena 232
5.4. Thin films 239
5.5. Adsorbents 244
5.6. Cements and mortars 245
6. SYNTHESIS 248
6.1. Introduction 248
6.2. Conventional mix and heat 249
6.3. Decomposition of chemical precursors 250
7. CONCLUDING REMARKS 254
REFERENCES 254

CHAPTER 6. THERMAL ANALYSIS OF CLAYS
(Katherine S. Meyers and Robert F. Speyer)

1. INTRODUCTION 261
1.1. Clay products 261
1.2. The nature of clays 263
2. STRUCTURE-THERMAL PROPERTY RELATIONS 266
2.1. Kaolins 266
2.2. Montmorillonites 270
2.3. Illite and mica minerals 276
2.4. Chlorites and Vermiculites 282
3. INSTRUMENTAL EFFECTS 286

4. CLAY DEPOSITS 290
4.1. Introduction 290
4.2. China clays 292
4.3. Ball clays 293
4.4. Bentonites 295
4.5. Fire and brick clays 295
4.6. Thermal analysis of clays 296
4.7. Quantitative analysis 300
5. SUMMARY 300
REFERENCES 303

CHAPTER 7. ENERGY STORAGE
(Takeo Ozawa and Masayuki Kamimoto)

1. ENERGY STORAGE: NEEDS AND SCHEMES 307
2. THERMAL ENERGY STORAGE 310
3. LATENT THERMAL ENERGY STORAGE 312
3.1. Application systems with latent thermal storage units 312
3.2. Screening of latent thermal storage materials 313
3.3. Selection of appropriate heat exchangers 316
3.4. Heat transfer in latent thermal storage systems 318
3.5. The necessity for measurement of thermophysical properties 320
3.6. Example of a computer simulation for selection of a heat exchange method 321
3.7. A charge and discharge experiment and system evaluation with computer simulation 323
4. APPLICATIONS OF THERMAL ANALYSIS AND CALORIMETRY 326
4.1. Sensible thermal storage materials and heat-transfer fluids 326
4.2. Latent thermal storage materials 327
4.3 Chemical storage materials 344
4.4 Other applications 346
REFERENCES 346

CHAPTER 8. THE THERMAL STABILITY OF EXPLOSIVES
(Jimmie C. Oxley)

1. INTRODUCTION 349
2. THERMAL STABILITY TESTING 353
2.1. Introduction 353
2.2. Gas monitoring tests 355
2.3. Time-to-event tests 355

2.4. Thermoanalytical techniques 358
2.5. Kinetic aspects 359
2.6. Calorimetry 362
2.7. Checking kinetic data 364
2.8. Thermal runaway 364
3. CONCLUSION 366
REFERENCES 368

CHAPTER 9. FOSSIL FUELS - APPLICATION OF THERMAL ANALYSIS TECHNIQUES
(Mustafa Versan Kok)

1. INTRODUCTION 371
2. APPLICATION TO FOSSIL FUELS 371
2.1. DSC, TG/DTG, TG-MS-FTIR and DTA studies on coal samples 371
2.2. DSC, TG/DTG, DTA and TG-GC-FTIR studies on crude oil samples 381
2.3. DSC, TG/DTG, DTA and TG-GC-FTIR studies on oil shale samples 386
3. CONCLUSIONS 391
REFERENCES 391

CHAPTER 10. GENERAL INORGANIC CHEMICALS AND COORDINATION COMPOUNDS
(H.J. Seifert)

1. INTRODUCTION 397
2. CHEMICALS AND METHODS 397
2.1. Binary compounds 397
2.2. Complexes and double compounds 398
2.3. Properties and methods of measurement 398
3. THERMODYNAMIC PROPERTIES OF INORGANIC COMPOUNDS AND SYSTEMS 400
3.1. Thermodynamic data and their sources in the literature 400
3.2. Adiabatic calorimetry 402
3.3. Differential scanning calorimetry (DSC) 405
3.4. Drop calorimetry 408
3.5. Reaction calorimetry 411
3.6. Conclusions 417

4. PHASE DIAGRAMS 418
4.1. Introduction 418
4.2. Binary systems with accessible liquid phases 419
4.3. Galvanic cells for solid electrolytes 423
4.4. Three-component systems 426
4.5. Computation of phase diagrams 426
4.6. Systems with high-melting compounds 427
5. THERMOGRAVIMETRY 429
5.1. Introduction 429
5.2. Decomposition reactions 429
5.3. Precursors 437
5.4. Miscellaneous methods related to thermogravimetry 440
6. THERMOMECHANICAL ANALYSIS 441
6.1. Introduction 441
6.2. Thermal expansion 442
6.3. Experimental methods for measuring thermal expansion 443
6.4. High-temperature X-ray diffraction (HT-XRD) 443
REFERENCES 446

CHAPTER 11. APPLICATIONS OF THERMAL METHODS IN THE GEOSCIENCES
(Werner Smykatz-Kloss, Klaus Heide and Wolfgang Klinke)

1. INTRODUCTION 451
2. IDENTIFICATION AND DETERMINATION OF MINERALS 453
2.1. General: Effects, methods, calibration, standardisation 453
2.2. Dehydration and dehydroxylation 454
2.3. Decomposition 512
2.4. Phase transitions 521
2.5. Magnetic transitions 534
2.6. Exothermic effects, oxidation and pyrolysis 537
3. THERMODYNAMICS, KINETICS AND PHASE RELATIONS 539
3.1. Introduction 539
3.2. Phase relation studies - phase diagrams 540
3.3. Determination of thermodynamic properties in petrological systems 541
3.4. Kinetics 541

4. THE INFLUENCE OF STRUCTURAL DISORDER ON THERMAL EFFECTS 547
4.1. Hydrolysates and carbonates 547
4.2. Silica minerals 552
5. TECHNICAL AND APPLIED MINERALOGY 561
5.1. Quality control 561
5.2. Mineral processing and synthesis 562
5.3. Environmental studies 563
6. SPECIAL THERMAL METHODS AND INVESTIGATIONS 563
7. FUTURE ASPECTS 566
ACKNOWLEDGEMENTS 567
REFERENCES 567

CHAPTER 12. DEHYDRATION OF CRYSTALLINE HYDRATES
(Andrew K. Galwey)

1. INTRODUCTION 595
1.1. Crystalline hydrates 595
1.2. Hydrate structures and types 597
1.3. Theory of dehydrations 599
1.4. Dehydrations as endothermic and reversible reactions 606
1.5. The literature of dehydration reactions 609
1.6. The present review 614
1.7. Calorimetry 616
2. EXPERIMENTAL 616
2.1. General 616
2.2. Reaction stoichiometry 617
2.3. Reaction kinetics 617
2.4. Diffraction 619
2.5. Microscopy 619
2.6. Comment 620
3. DEHYDRATIONS OF CRYSTALLINE HYDRATES 621
3.1. General 621
3.2. Lithium sulfate monohydrate 622
3.3. Magnesium sulfate hydrates 624
3.4. Calcium sulfate dihydrate 624
3.5. Zirconium sulfate hydrate ($5.5H_2O$) 625
3.6. Copper sulfate hydrates 625
3.7. Nickel sulfate hexahydrate 627
3.8. Alums 629
3.9. Calcium sulfite hemihydrate 631

3.10. Sodium thiosulfate pentahydrate 631
3.11. Barium chloride dihydrate 632
3.12. Other hydrated halides 632
3.13. Sodium perchlorate monohydrate and magnesium perchlorate hexahydrate 633
3.14. Sodium carbonate monohydrate 634
3.15. Calcium nitrate tetrahydrate 634
3.16. Uranyl nitrate hexahydrate 634
3.17. Barium nitrite monohydrate 635
3.18. Some hydrated permanganates (Sr, Cd and Ca) 635
3.19. Sodium tungstate dihydrate 635
3.20. Some alkali and alkaline earth hydrated phosphates 635
3.21. Hydrated metal formates and acetates 636
3.22. Hydrated metal oxalates 638
3.23. Sodium citrate dihydrate 638
3.24. Lithium potassium tartrate hydrates 639
3.25. Coordination compounds containing H_2O and other ligands 639
3.26. Reproducibility of measured kinetic characteristics 641
4. OTHER DEHYDRATIONS 641
4.1. General 641
4.2. Metal hydroxides 641
4.3. Layer minerals containing hydroxide 642
5. SOME OTHER FEATURES OF DEHYDRATIONS 643
5.1. Explosive dehydrations 643
5.2. Glass formation and polymorphism 643
5.3. Topotaxy 644
5.4. Surface reactions 644
5.5. Reactant dehydration 645
6. COMMENTS AND CONCLUSIONS 646
ACKNOWLEDGEMENT 650
REFERENCES 650

CHAPTER 13. THERMAL ANALYSIS IN METALLURGY
(Shaheer A. Mikhail and A. Hubert Webster)

1. INTRODUCTION 657
2. EQUILIBRIUM PHASE DIAGRAMS 658
2.1. General 658
2.2. Phase transitions, eutectics and equilibrium lines and surfaces 658
2.3. Determination of phase diagrams 668
2.4. Verification and assessment of phase diagrams 674

3. TRANSFORMATIONS INVOLVING NON-EQUILIBRIUM PHASES 675
3.1. Introduction 675
3.2. Rapid diffusionless transformation - martensite 676
3.3. Common transformations in metals and alloys 679
3.4. Very rapidly cooled metals and alloys 686
3.5. Mechanically-milled alloys 698
4. OXIDATION AND CORROSION 707
4.1. Introduction 707
4.2. Kinetics of oxidation reactions 709
4.3. Oxidation of unalloyed metals 711
4.4. Oxidation of alloys 716
4.5. Oxidation by gases other than molecular oxygen 722
4.6. Oxidation and corrosion in aggressive atmospheres 723
4.7. Corrosion in the presence of salt deposits 726
4.8. Formation of sulfides in reducing atmospheres 730
4.9. Surface treatments to increase corrosion resistance 732
4.10. Non-isothermal studies 733
4.11. Investigations of corrosion of metals by liquids 734
5. EXTRACTIVE METALLURGY 735
5.1. General 735
5.2. Reduction 737
5.3. Roasting 741
5.4. Reactions of metal compounds 746
6. MISCELLANEOUS APPLICATIONS 753
6.1. Metal-matrix composites 753
6.2. Powder metallurgy 759
6.3. Thin films 762
REFERENCES 765

CHAPTER 14. PYROTECHNICS
(E.L Charsley, P.G. Laye and M.E. Brown)

1. INTRODUCTION 777
2. EXPERIMENTAL TECHNIQUES 779
3. SPECIALISED INSTRUMENTATION AND EXPERIMENTATION 781
3.1. Introduction 781
3.2. High-temperature DSC measurements 781
3.3. Thermal diffusivity measurements 783
3.4. Thermal conductivity measurements 785
3.5. Thermomicroscopy 785
3.6. Thermomagnetometry 785

3.7. Modulated-temperature DSC (MTDSC) 786
3.8. Temperature profile analysis 787
3.9. Combustion calorimetry 787
3.10. Microcalorimetry 788
4. SELECTED APPLICATIONS 788
4.1. Introduction 788
4.2. Thermal hazard evaluation, compatibility testing and life-time prediction 789
4.3. Reaction mechanisms 794
4.4. Ignition 802
4.5. Kinetics 805
5. CONCLUSIONS 807
REFERENCES 808

CHAPTER 15. THERMAL ANALYSIS IN STUDIES OF HIGH-T_c SUPERCONDUCTORS
(J. Valo and M. Leskelä)

1. INTRODUCTION 817
2. THERMOANALYTICAL TECHNIQUES 818
3. HIGH-T_c SUPERCONDUCTORS 820
4. THERMOANALYTICAL STUDIES ON PROPERTIES RELATED TO SUPERCONDUCTIVITY 824
4.1. Specific heat anomaly at T_c 824
4.2. Determination of T_c^{onset} 824
5. DETERMINATION OF SYNTHESIS CONDITIONS OF BULK HTSC 824
5.1. Introduction 824
5.2. Synthesis of Y $Ba_2Cu_3O_{7-\delta}$ by solid-state reactions 825
5.3. Synthesis of Y-123 and Y-124 by coprecipitation and sol-gel methods 826
5.4. Melt processing of RE-123 827
5.5. Growth of RE-123 single crystals 831
5.6. Formation of Bi,Pb-Sr-Ca-Cu-O superconductors 832
5.7. Synthesis of Bi,Pb-Sr-Ca-Cu-O superconductors by coprecipitation methods 835
5.8. Synthesis of Bi,Pb-Sr-Ca-Cu-O glass ceramics 836
5.9. Preparation of Tl-based superconductors 838
5.10. Preparation of Hg-based superconductors 839

6. THERMOANALYTICAL CHARACTERISATION OF BULK HTSC 840
6.1. Introduction 840
6.2. $La_{2-x}Sr_xCuO_{4-\delta}$ 840
6.3. $YBa_2Cu_3O_{7-\delta}$ 841
6.4. Thermal stability of $YBa_2Cu_4O_8$ 848
6.5. $Pb_2Sr_2(Y,Ca)Cu_3O_{8+\delta}$ 848
6.6. Bi-, Tl- and Hg-based superconductors 850
6.7. $RuSr_2GdCu_2O_{8-\delta}$ 853
6.8. $Nd_{2-x}Ce_xCuO_{4-\delta}$ 854
7. USE OF TG TO CONTROL THE AMOUNT OF OXYGEN 854
8. DETERMINATION OF ABSOLUTE OXYGEN CONTENT BY TG 856
8.1. TG reduction method 856
8.2. Oxygen content in $YBa_2Cu_3O_{7-\delta}$ and $YBa_2Cu_4O_{8-\delta}$ 856
8.3. Oxygen content in other cuprates 857
9. VOLATILE PRECURSORS FOR HTSC THIN FILM DEPOSITION 858
9.1. HTSC thin films 858
9.2. Chemical vapour deposition 859
9.3. TA studies of CVD β-diketonate precursors 859
9.4. CVD growth 866
10. SUMMARY 868
ACKNOWLEDGEMENTS 868
REFERENCES 869

INDEX 881

CONTRIBUTORS

Brown, M.E. Chemistry Dept, Rhodes University, Grahamstown, 6140 South Africa.

Charsley, E.L. Centre for Thermal Studies, School of Applied Sciences, University of Huddersfield, Huddersfield HD1 3DH, U.K.

Fierro, J.L.G. Consejo Superior de Investigaciones Cientificas, Instituto de Catálisis y Petroleoquímica, Camino de Valdelatas, s/n Campus Universidad Autónoma, Cantoblanco 28049, Madrid, Spain.

Gallagher, P.K. Emeritus Professor, Departments of Chemistry and Materials Science & Engineering, The Ohio State University, Columbus, OH, 43210, U.S.A.
Current address: 409 South Way Court, Salem, South Carolina 29676-4625, U.S.A.

Galwey, A.K. Retired from the School of Chemistry, Queen's Univerity, Belfast, Northern Ireland.
Current address:18 Viewfort Park, Dunmurry, Belfast, BT17 9JY, Northern Ireland.

Heide, Klaus Institute for Geosciences, University of Jena, Burgweg 11, D-07749, Jena, Germany.

Kamimoto, Masayuki National Institute of Advanced Industrial Science and Technology, 1-1-1 Higashi, Tsukuba, Ibaraki 305-8561, Japan.

Klinke, Wolfgang Institute for Mineralogy and Geochemistry, University of Karlsruhe, D-76128, Karlsruhe, Germany.

Kok, Mustafa V. Dept. of Petroleum and Natural Gas Engineering, Middle East Technical University (METU), 06531, Ankara, Turkey.

Laye, P.G. Centre for Thermal Studies, School of Applied Sciences, University of Huddersfield, Huddersfield HD1 3DH, U.K.

Leskelä, M. Laboratory of Inorganic Chemistry, Department of Chemistry, University of Helsinki, PO Box 55, Helsinki, Finland, FIN-00014.

Llewellyn, P. Materiaux Divises Revetements Electroceramiques (MADIREL UMR 6121), CNRS, Université de Provence, 26 rue du 141 R.I.A., 13003 Marseille, France.

Meyers, K.F. School of Materials Science and Engineering, Georgia Institute of Technology, Atlanta, Georgia, 30332, U.S.A.

Mikhail, S.A. Formerly: CANMET, Department of Natural Resources Canada, Ottawa, Ontario, Canada.
Current address: 14 Meadowbank Drive, Ottawa, Ontario K2G-0N9, Canada.

Odlyha, M. School of Biological and Chemical Sciences, Birkbeck College, University of London, Gordon House, 29 Gordon Square, London WC1H OPP, U.K.

Oxley, J. Chemistry Department, University of Rhode Island, Kingston, RI 02882, U.S.A.

Ozawa, Takeo 18-6 Josui shinmachi, 1-chome, Kodaira, Tokyo 187-0023, Japan.

Pawelec, B. Consejo Superior de Investigaciones Cientificas, Instituto de Catálisis y Petroleoquímica, Camino de Valdelatas, s/n Campus Universidad Autónoma, Cantoblanco 28049, Madrid, Spain.

Phang, P. 1104 East Main Street, Louisville, OH 44641, U.S.A.

Sanders, J.P. National Brick Research Center, Clemson University, 100 Clemson Research Park., Anderson, SC 29625, U.S.A.

Seifert, H-J. Auf der Hoh 7, D-35619, Braunfels, Germany.

Smykatz-Kloss, W. Institute for Mineralogy and Geochemistry, University of Karlsruhe, D-76128, Karlsruhe, Germany.

Speyer, R.F. School of Materials Science and Engineering, Georgia Institute of Technology, Atlanta, Georgia, 30332, U.S.A.

Valo, J. Laboratory of Inorganic Chemistry, Department of Chemistry, University of Helsinki, PO Box 55, Helsinki, Finland, FIN-00014.

Webster, A.H. Formerly: CANMET, Department of Natural Resources Canada, Ottawa, Ontario, Canada.
Current address: 1198 Checkers Road, Ottawa, Ontario K2C-2S7, Canada.

This Page Intentionally Left Blank

ACKNOWLEDGEMENTS

The Editors would like to acknowledge significant help given in solving some of the many problems encountered during the preparation of this volume by Dr David Maree, Mr Emmanuel Lamprecht and Mr Kevin Lobb.

Contributors are grateful to the publishers listed below for permission to reproduce material in this Volume.

Chapter 1

Figure 3 is reproduced from reference [2] with the permission of Elsevier.
Figure 4 is reproduced from reference [4] with the permission of Elsevier.
Figure 5 is reproduced from reference [5], with the permission of Wiley.
Figure 6 is reproduced from reference [6], with the permission of the American Chemical Society
Figure 8 is reproduced from reference [16], with the permission of American Chemical Society
Figure 13 is reproduced from reference [24], with the permission of Elsevier.
Figure 20 is reproduced from reference [44], with the permission of the Société Française de Chimie
Figure 22 is reproduced from reference [49], with the permission of IUPAC
Figure 23 is reproduced from reference [51], with the permission of the Engineering Foundation, NY.
Figure 24 is reproduced from reference [5 and 52], with the permission of Wiley and Elsevier.
Figure 26 is reproduced from reference [54], with the permission of the Mineralogical Society.
Figure 28 is reproduced from reference [57], with the permission of the American Chemical Society
Figure 29 is reproduced from reference [58], with the permission of the American Chemical Society
Figure 31 is reproduced from reference [61], with the permission of the American Chemical Society
Figure 32 is reproduced from reference [63], with the permission of Kodansha Ltd.
Figure 33 is reproduced from reference [66], with the permission of CNRS Editions.

Chapter 2

Figure 1 is reproduced from reference [33] with the permission of Kluwer Publishers.
Figure 4 is reproduced from reference [57] with the permission of Elsevier
Figures 5 and 13 are reproduced with the permission of the Tate picture library, London.
Figures 8,9,10 and 11 are reproduced with the permission of the Trustees of the British Museum, London.
Figure 12 is reproduced from reference [67] with the permission of the International Institute for Conservation of Historic and Artistic Works (IIC), London.
Figure 16 is reproduced with the permission of the School of Conservation, Copenhagen.
Figures 17 and 19 are reproduced from reference [25] with the permission of Archetype Publications,London
Figures 23 and 24 are reproduced from reference [85] with the permission of Kluwer Publishers.
Figure 26 is reproduced by courtesy of A. Haacke, University of Manchester Institute of Science and Technology (MODHT project).

Chapter 3

Figure 1 is reproduced from reference [1] with the permission of Elsevier.
Figure 2 is reproduced from [22] with the permission of Elsevier.
Figures 3, 4, 5 and 6 are reproduced from reference [28] with the permission of Kluwer Publishers.
Figure 7 is reproduced from reference [32] with the permission of Elsevier.
Figure 8 is reproduced from reference [29] with the permission of the Royal Society of Chemistry.
Figures 9 and 10 are reproduced from reference [55] with the permission of Elsevier.

Chapter 4

Figure 1 is reproduced from reference [10] with the permission of Elsevier.
Figure 2 is reproduced from reference [13] with the permission of Elsevier.
Figure 3 is reproduced from reference [14] with the permission of Elsevier.
Figure 4 is reproduced from reference [15] with the permission of Elsevier.
Figure 5 is reproduced from reference [16] with the permission of Elsevier.
Figure 6 is reproduced from reference [18] with the permission of Elsevier.

Figure 7 is reproduced from reference [27] with the permission of Elsevier.
Figures 8, 9 and 10 are reproduced from reference [32] with the permission of Elsevier.
Figure 11 is reproduced from reference [43] with the permission of Elsevier.
Figure 12 is reproduced from reference [50] with the permission of Kluwer Publishers.
Figure 13 is reproduced from reference [58] with the permission of Elsevier.
Figure 14 is reproduced from reference [64] with the permission of Elsevier.
Figure15a is reproduced from reference [52] with the permission of Elsevier
Figure15b is reproduced from reference [62] with the permission of Elsevier.
Figure15c is reproduced from reference [63] with the permission of the Royal Society of Chemistry.
Figure 16 is reproduced from reference [76] with the permission of the Chemical Society of Japan.
Figure 17 is reproduced from reference [78] with the permission of Elsevier.
Figure 19 is reproduced from reference [82] with the permission of Elsevier.
Figures 18, 20 and 21 are reproduced from reference [81] with the permission of Elsevier.
Figure 22 is reproduced from reference [52] with the permission of Elsevier.
Figure 24 is reproduced from reference [85] with the permission of Elsevier.
Figure 25 is reproduced from reference [87] with the permission of Elsevier.
Figures 23, 26,27 and 28 are reproduced from reference [62] with the permission of Elsevier.
Figure 29 is reproduced from reference [104] with the permission of the American Chemical Society.
Figure 30 is reproduced from reference [13] with the permission of Elsevier.
Figure 31 is reproduced from reference [122] with the permission of Elsevier.
Figure 32 is reproduced from reference [127] with the permission of Kluwer Publishers.
Figure 33 is reproduced from reference [132] with the permission of Elsevier.

Chapter 5

Figures 1 and 2 are reproduced from reference [1] with the permission of Wiley.
Figure 3 is reproduced from reference [2] with the permission of Butterworth-Heinemann.
Figure 4 is reproduced from reference [3] with the permission of Kluwer Publishers.
Figure 5 is reproduced from reference [9] with the permission of Elsevier
Figures 6 and 7 are reproduced from reference [11] with the permission of the American Ceramic Society.

Figure 8 is reproduced from reference [12] with the permission of Kluwer Publishers.
Figures 9 and 10 are reproduced from reference [17] with the permission of Elsevier.
Figure 11 is reproduced from reference [19] with the permission of the International Corrosion Council.
Figures 13 and 14 are reproduced from reference [22] with the permission of Elsevier.
Figure 15 is reproduced from reference [24] with the permission of the American Ceramic Society.
Figures 16 and 17 are reproduced from reference [25] with the permission of the American Ceramic Society.
Figures 18 and 19 are reproduced from reference [26] with the permission of Elsevier.
Figure 23 is reproduced from reference [30] with the permission of Kluwer Publishers
Figure 24 is reproduced from reference [31] with the permission of Kluwer Publishers
Figure 25 is reproduced from reference [33] with the permission of Elsevier.
Figures 26 and 67 are reproduced from reference [35] with the permission of Marcel Dekker Publishers.
Figure 27 is reproduced from reference [39] with the permission of the Royal Society of Chemistry, London.
Figure 28 is reproduced from reference [42] with the permission of Elsevier.
Figure 29 is reproduced from reference [46] with the permission of Wiley.
Figure 30 is reproduced from reference [44] with the permission of Elsevier.
Figure 33 is reproduced from reference [24] with the permission of the American Ceramic Society.
Figure 34 is reproduced from reference [51] with the permission of Elsevier.
Figure 35 is reproduced from reference [52] with the permission of Macmillan Publishers.
Figure 36 is reproduced from reference [54] with the permission of Wiley.
Figure 37 is reproduced from reference [32] with the permission of Kluwer Publishers.
Figure 38 is reproduced from reference [56] with the permission of Elsevier.
Figure 39 is reproduced from reference [65] with the permission of Kluwer Publishers.
Figure 40 is reproduced from reference [66] with the permission of Kluwer Publishers.
Figure 41 is reproduced from reference [67] with the permission of Kluwer Publishers.

Figures 42 and 43 are reproduced from reference [68] with the permission of Kluwer Publishers.
Figure 44 is reproduced from reference [70] with the permission of the TMS Society
Figure 45 is reproduced from reference [71] with the permission of Kluwer Publishers.
Figure 46 is reproduced from reference [72] with the permission of the American Chemical Society.
Figure 47 is reproduced from references [60] and [76] with the permission of Elsevier and the American Physical Society.
Figure 48 is reproduced from reference [79] with the permission of the American Ceramic Society.
Figures 49 and 50 are reproduced from reference [81] with the permission of the American Ceramic Society.
Figure 51 is reproduced from reference [85] with the permission of Elsevier.
Figures 52 and 53 are reproduced from reference [86] with the permission of the American Ceramic Society.
Figure 54 is reproduced from reference [87] with the permission of Gordon & Breach Publishers.
Figure 55 is reproduced from reference [88] with the permission of Elsevier.
Figure 56 is reproduced from reference [89] with the permission of Elsevier.
Figures 57 and 58 are reproduced from reference [92] with the permission of the American Chemical Society.
Figure 59 is reproduced from reference [93] with the permission of Elsevier.
Figure 60 is reproduced from reference [94] with the permission of the American Physical Society.
Figure 61 is reproduced from reference [95] with the permission of the Electrochemical Society.
Figure 62 is reproduced from reference [97] with the permission of Elsevier.
Figure 63 is reproduced from reference [100] with the permission of the National Brick Institute.
Figure 64 is reproduced from reference [103] with the permission of Kluwer Publishers.
Figure 65 is reproduced from reference [104] with the permission of Elsevier.
Figure 66 is reproduced from reference [107] with the permission of Wiley.
Figure 68 is reproduced from reference [110] with the permission of the American Ceramic Society.
Figure 69 is reproduced from reference [111] with the permission of the American Ceramic Society.
Figure 70 is reproduced from reference [116] with the permission of the Materials Research Society.

Figure 71 is reproduced from reference [117] with the permission of the Materials Research Society

Chapter 6

Figure 16 is reproduced from reference [15] with the permission of Simon and Schuster Inc., New York (Addison-Wesley).

Chapter 7

Figures 5,8 and Table 2 are reproduced from reference [7] with the permission of the American Chemical Society.
Figures 7 and 14 are reproduced from reference [13] with the permission of the Japan Society of Thermophysical Properties.
Figure 9 is reproduced from reference [16] with the permission of the American Society of Mechanical Engineers.
Figure 10 is reproduced from reference [12] with the permission of the American Society of Mechanical Engineers.
Figures 11,12 and 13 are reproduced from reference [3] with the permission of the American Society of Mechanical Engineers.
Figures 15,16 and 17 are reproduced from reference [19] with the permission of Elsevier.
Figure 18 is reproduced from reference [10] with the permission of Elsevier.
Figures 19,20 and 21 are reproduced from reference [8] with the permission of Elsevier.
Figure 22 is reproduced from reference [21] with the permission of Elsevier.
Figure 23 is reproduced from reference [29] with the permission of The Chemical Society of Japan.
Figures 24 and 25 are reproduced from reference [28] with the permission of Elsevier.
Figures 26,27 and 28, as well as Tables 5 and 6, are reproduced from reference [11] with the permission of Elsevier.
Table 7 is reproduced from reference [31] with the permission of the Japan Society of Refrigerating and Air-conditioning Engineers.

Chapter 9

Figures 1-4 are reproduced from a Ph.D. thesis with the acknowledgement of Middle East Technical University.
Figures 5 and 6 are reproduced from a M.Sc. thesis with the acknowledgement of Middle East Technical University

Chapter 10

Table 1. Thermodynamic properties for $BaCO_3$ is reproduced from I. Barin, "Thermochemical Data of Pure Substances", 1989, with the permission of VCH-Verlag, Weinheim.
Table 2 is reproduced from reference [1] with the permission of Elsevier.
Figure 5 is reproduced from reference [55b] with the permission of Elsevier.
Figure 6 is reproduced from reference [55c] with the permission of Elsevier.
Figure 7 is reproduced from reference [55a]with the permission of Kluwer Publishers.
Figure 8 is reproduced from reference [62] with the permission of Elsevier.
Figure 10 is reproduced from F. Paulik, Special Trends in Thermal Analysis, Wiley, New York, 1995, with permission.
Figure 11 is reproduced from G. Liptay, 'Atlas ofThermoanalytical Curves, Vol. 1-5, Akad. Kiado, Budapest, 1975.
Figure 12 is reproduced from reference [73] with the permission of Elsevier.
Figure 13 is reproduced from reference [95] with the permission of Kluwer publishers.
Figure 14 is reproduced from reference [100] with the permission of Chemical Reviews.
Figures 15a and b are reproduced from reference [107] with acknowledgement to Archiwum Hutnictwa.
Figure 16 is reproduced from reference [111] with the permission of Kluwer Publishers.

Chapter 11

All the DTA-curves and PA-curves are reproduced with the permission of Springer Company from the book of W. Smykatz-Kloss, "DIFFERENTIAL THERMAL ANALYSIS- APPLICATION AND RESULTS IN MINERALOGY", published in 1974 as Volume 11 of "MINERALS AND ROCKS".
Figure 50 is reproduced from reference [330] H.G. Wiedemann and W. Smykatz-Kloss, Thermochim. Acta, 50 (1981) 17-29, with the permission of Elsevier.

Chapter 12

Figure 1 is reproduced from reference [1] with the permission of Elsevier.
The diagrams WET 1 to WET 5 are reproduced from A.K. Galwey, Thermochim. Acta, 355 (2000) 181-238 with the permission of Elsevier.

Chapter 13

Figure 1 is reproduced from reference [10] with the permission of The Minerals, Metals & Materials Society.
Figure 2 is reproduced from reference [12] with the permission of ASM International.
Figures 3,4 are reproduced from reference [16] with the permission of The Minerals, Metals & Materials Society.
Figure 5 is reproduced from reference [17] with the permission of The Institute of Metals.
Figure 6 is reproduced from reference [19] with the permission of ASM International.
Figure 7 is reproduced from reference [20] with the permission of Elsevier.
Figure 8 is reproduced from reference [23] with the permission of ASM International.
Figure 9 is reproduced from reference [25] with the permission of Elsevier.
Figures 10,11 are reproduced from reference [30] with the permission of Elsevier.
Figures 12,13 are reproduced from reference [33] with the permission of Elsevier.
Figure 14 is reproduced from reference [52] with acknowledgement to Societe Francaise de Physique.
Figure 15 is reproduced from reference [53] with the permission of The Minerals, Metals & Materials Society.
Figure 16 is reproduced from reference [54] with the permission of the Kluwer Academic Publishing.
Figure 17 is reproduced from reference [56] with the permission of The Minerals, Metals & Materials Society.
Figure 18 is reproduced from reference [59] with the permission of The Casting Development Centre.
Figure 19 is reproduced from reference [68] with the permission of Elsevier.
Figure 20 is reproduced from reference [71] with the permission of R. Olderbourg Verlag.
Figure 21 is reproduced from reference [72] with the permission of the author, T. Yamasaki.
Figure 22 is reproduced from reference [73] with the permission of Philosophical Magazine.
Figure 23 is reproduced from reference [75] with the permission of Elsevier.
Figures 24,25 are reproduced from reference [79] with the permission of Elsevier.
Figure 26 is reproduced from reference [86] with the permission of Elsevier.

Figure 27 is reproduced from reference [88] with the permission of Elsevier.
Figure 28 is reproduced from reference [90] with the permission of Elsevier.
Figure 29 is reproduced from reference [92] with the permission of ASM International.
Figure 30 is reproduced from reference [93] with the permission of Elsevier.
Figure 31 is reproduced from reference [95] with the permission of ISIJ.
Figure 32 is reproduced from reference [98] with the permission of Materials Science Forum.
Figure 33 is reproduced from reference [112] with the permission of the Plenum Publishing Corporation.
Figure 34 is reproduced from reference [120] with the permission of the Plenum Publishing Corporation.
Figure 35 is reproduced from reference [126] with the permission of the Plenum Publishing Corporation.
Figure 36 is reproduced from reference [131] with the permission of the Plenum Publishing Corporation.
Figure 37 is reproduced from reference [102] with the permission of Elsevier.
Figure 38 is reproduced from reference [100] with the permission of Elsevier.
Figure 39 is reproduced from reference [146] with the permission of Elsevier.
Figure 40 is reproduced from reference [148] with the permission of The Electrochemical Society Inc.
Figure 41 is reproduced from reference [150] with the permission of The Minerals, Metals & Materials Society.
Figures 42,43 are reproduced from reference [174] with acknowledgement to The Canadian Institute of Mining and Metallurgy.
Figure 44 is reproduced from reference [181] with the permission of Elsevier.
Figure 45 is reproduced from reference [183] with the permission of The Metallurgical Society of AIME.
Figure 46 is reproduced from reference [187] with the permission of Elsevier.
Figure 47 is reproduced from reference [194] with the permission of Elsevier.
Figures 48,49 are reproduced from reference [197] with the permission of Elsevier.
Figure 50 is reproduced from reference [203] with the permission of John Wiley and Sons Limited.
Figure 51 is reproduced from reference [206] with the permission of Kluer Academic / Plenum Publishers.
Figure 52 is reproduced from reference [211] with the permission of John Wiley and Sons Limited.
Figure 53 is reproduced from reference [212] with the permission of the Ceram Forum International.

Figure 54 is reproduced from reference [215] with the permission of The Minerals, Metals & Materials Society.
Figure 55 is reproduced from reference [217] with the permission of the American Institute of Physics.
Figure 56 is reproduced from reference [220] with the permission of the American Institute of Physics.

Chapter 14 Pyrotechnics

Figures 1 and 2 are reproduced from reference [12] with acknowledgement to the Fraunhofer-Institut für Chemische Technologie, Karlsruhe, Germany.
Figure 3 is reproduced from reference [15] with the permission of Elsevier.
Figure 4 is reproduced from reference [16] with the permission of the International Pyrotechnic Society.
Figure 5 is reproduced from reference [3] with the permission of the International Pyrotechnic Society.
Figure 6 is reproduced from reference [57] with acknowledgement to the Sektionen för Detonik och Förbränning, Sweden.
Figure 7 is reproduced from reference [64] with acknowledgement to Propellants Explosives, Pyrotechnics.
Figure 8 is reproduced from reference [70] with the permission ofthe International Pyrotechnic Society.
Figure 9 is reproduced from reference [77] with the permission of Kluwer Publishers.
Figure 10 is reproduced from reference [87] with acknowledgement to Propellants Explosives, Pyrotechnics.
Figure 11 is reproduced from reference [90] with the permission of Elsevier.
Figure 12 is reproduced from reference [94] with the permission of the Journal of Pyrotechnics.
Figure 13 is reproduced from reference [36] with the permission of Elsevier.

Chapter 15

Figure 1A is reproduced from reference [37] with permission from the Japanese Journal of Applied Physics.
Figure 1A is reproduced from reference [38], Figure 8B from reference [96], Figure 10 from reference [136], Figure 14B from reference [152], Figure 15 from reference [171], Figure 17 from reference [188], and Figure 20 from reference [236], with the permission of Elsevier.
Figure 1B is reproduced from reference [39] with permission from the World Scientific Publishing Co.

Figures 2A and B are reproduced from reference [40] with permission from the Agne Gijutsu Center, Tokyo, Japan.
Figures 2ÇF, ḤM are reproduced from reference [24], Figure 6 from reference [78], Figure 16 from reference [109] and Figure 18A from reference [196], with permission from the Institute of Physics Publishing, Bristol, United Kingdom.
Figures 4 and 5 are reproduced from reference [59] with permission from Current Topics in Crystal Growth Research, Trivandrum, India.
Figure 7 is reproduced from reference [91] with permission from John Wiley & Sons Ltd, Chichester, United Kingdom.
Figure 9 is reproduced from reference [127] with permission from Academic Press, Inc., Orlando, Florida, USA.
Figures 11ẠC are reproduced from reference [121], Figure 14A from reference [162], Figure 19A from reference [238] and Figure 19B from reference [213], with permission from the American Chemical Society.
Figure 12 is reproduced from reference [15] with permission from the American Ceramic Society.

This Page Intentionally Left Blank

Handbook of Thermal Analysis and Calorimetry. Vol. 2: Applications to Inorganic and Miscellaneous Materials
M.E. Brown and P.K. Gallagher, editors
© 2003 Elsevier B.V. All right reserved.

Chapter 1

APPLICATIONS OF THERMAL ANALYSIS AND CALORIMETRY IN ADSORPTION AND SURFACE CHEMISTRY

Philip L. Llewellyn

MADIREL Laboratory, CNRS-Université de Provence, Marseille, France

1. INTRODUCTION

Several thermoanalytical and calorimetric methods can be used for the characterisation of adsorbent surfaces and of adsorption phenomena. The texture of solids, that is to say the extent of surface area and pore size distribution, can be characterised by controlled rate thermodesorption, thermoporometry and immersion calorimetry. An advantage of the calorimetric approach over more standard methods lies in the possibility to characterise a more realistic surface area in the case of microporous solids. The probing of the chemical nature of surface can also be attained by controlled rate thermodesorption and immersion calorimetry, as well as by adsorption calorimetry

The following paragraphs will briefly describe these methods and will highlight several results that have been obtained.

2. IMMERSION CALORIMETRY

2.1. Introduction

Immersion calorimetry is a simple method which can lead to information about the surface area as well as the surface chemistry of a solid. The surface area of a solid can be obtained by the immersion of the solid into a non-porous liquid or by using the modified Harkins and Jura method [1,2]. In this method, the solid is pre-recovered with a film of liquid prior to immersion into the same liquid.

An estimation of a micropore size distribution can be obtained by the immersion into liquids of different molecular dimensions. Finally, the surface chemistry of a solid can be followed by the immersion into various polar liquids.

The experimental procedure is relatively straightforward. The sample cell is blown from glass with a brittle point added to the bottom of the bulb and the top open. After the sample is placed into the cell, it can be outgassed under vacuum

in a standard manner or by using SCTA. The top of the cell is then closed and is attached to a glass rod which is found inside the immersion cane. The immersion fluid is added to a tube at the bottom of this cane. This tube can then be screwed on to complete the immersion cane. The whole system is placed into the calorimeter. After thermal equilibrium is attained, the glass rod is pressed down so that the brittle point on the sample cell is broken. This allows the intrusion of the immersion liquid to the sample and a heat effect is measured (Figure 1).

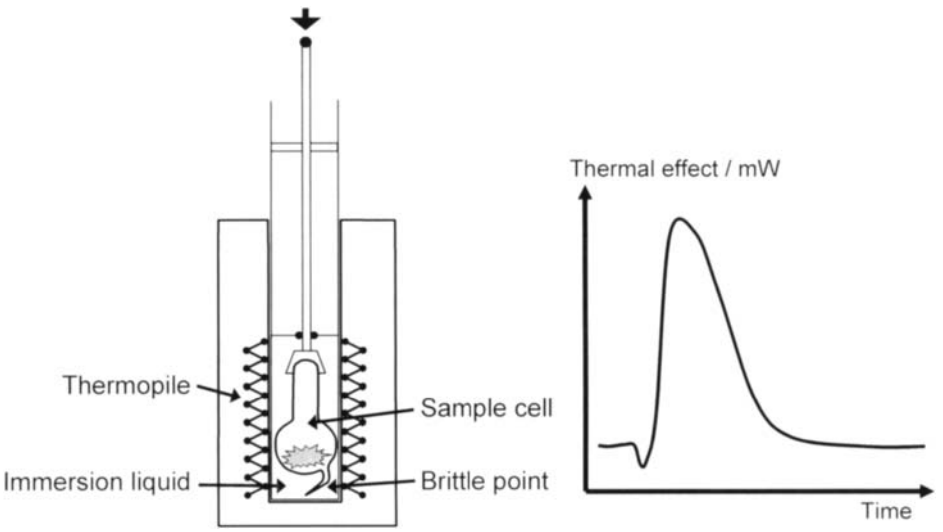


Figure 1. Schematic diagram of the set-up used for immersion calorimetry (left) and the thermal effect measured during an immersion experiment (right).

This heat effect, schematised in Figure 1, shows an initial dip before the peak. This endothermic dip corresponds to the initial vaporisation of the immersion liquid as it enters the cell. The exothermic peak then corresponds to the wetting of the sample, as well as to effects due to the breaking of the brittle point and the compression – depression of the immersion fluid inside and outside the cell. These different effects can be summarised by the following terms [2]:

$$Q_{exp} = \Delta_{imm}U + W_b + \int_0^{V-v} p\,dv + \frac{\Delta_{liq}h}{RT}\left[(p-p^\circ)V + p^\circ v\right]$$

Energy of immersion	Breaking of brittle point	Compression of vapour in bulb *(v)*	Liquefaction of liquid in bulb *(v)* and vaporisation of liquid outside bulb *(V)*

An estimation of the terms other than the energy of immersion can be obtained by a series of blank experiments with sample cells of various sizes. A plot of the heat effect measured as a function of the volume of the sample cell should then give a slope which is proportional to the heat of vaporisation of the immersion liquid.

The heat of immersion that is measured depends on several factors :

- The *surface area of the solid.* For solids of identical surface chemical nature, the immersion energy is proportional to the surface area. A means to overcome the problem of comparing solids with different surface chemistries is to use the modified Harkins and Jura method which is described below.
- The *chemical nature of the surface*. For a given liquid, the immersion energy depends of the chemical nature of the surface. For example, if the liquid is polar, the immersion energy increases with the polarity of the surface chemical functions. An application of such a study is to follow the influence of a treatment (thermal treatment, grafting ...) on the nature and density of surface functions.
- The *chemical nature of the liquid* : for a given non-porous surface, the immersion enthalpy depends on the chemical nature of the immersion liquid. Here, an application can be the evaluation of the average dipolar moment of surface sites by immersion of the solid in liquids of increasing polarity. This leads to an analysis of the hydrophilic or hydrophobic character of a surface.
- The *porosity*. If the solid is microporous, the molecules of the liquid may be too large to penetrate into all the pores. In this case it is interesting to carry out a series of immersion experiments with molecules of different size but similar in chemical nature. In this case a micropore size distribution can be obtained and in some cases, it is possible to follow the kinetics of wetting or pore filling.

2.2. Immersion calorimetry for the estimation of the surface area of a solid: the modified Harkins and Jura method

As mentioned above, the surface area of a solid is proportional to the immersion energy that is released on wetting. In many cases it is possible immerge the solid into a non-polar liquid such as hexane. The heat effect measured can then be compared with that obtained with that of a reference solid.

In some cases though, the surface chemistry of the solid can still play a role on the heat effects measured. One procedure to overcome this problem is known as the modified Harkins and Jura method [2] which is schematised in Figure 2.

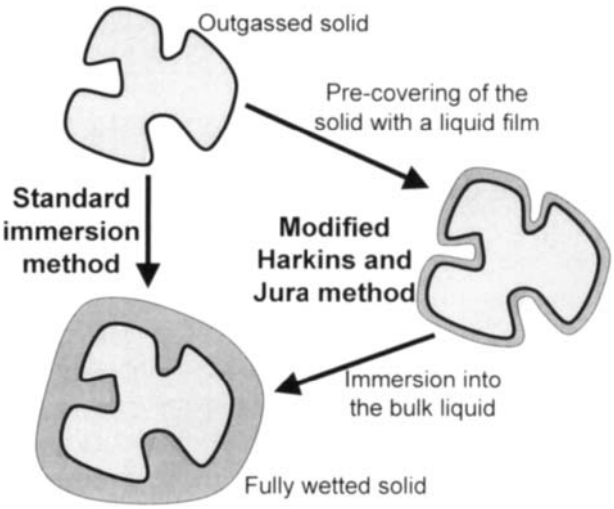


Figure 2. Schematic diagram comparing the standard immersion method with the modified Harkins and Jura method.

In this method, after outgassing, the sample is equilibrated at a given relative pressure of the immersion liquid. The surface is thus pre-covered with a liquid film prior to the immersion experiment proper. Thus the heat effect that is measured is simply related to the disappearance of the liquid-vapour interface and is given by the expression [3]:

$$\Delta_{imm}H = A\left(\gamma_{lv} - T\left\{\frac{\partial\gamma_{lv}}{\partial T}\right\}_A\right)$$

where $\Delta_{imm}H$ is the immersion enthalpy, A the area of solid, γ_{lv} the liquid-vapour surface tension of the wetting liquid and T the temperature.

The question arises as to the thickness of the pre-covered film that should be used. If too thick, there is a risk of pore filling and that the film surface is not representative of the solid covered. Partyka *et al.* [2] studied this problem in the case of the immersion of a silica sample into water. The sample was pre-covered with water at various relative pressures before immersion experiments. The results thus obtained were then compared with the water adsorption isotherm (Figure 3).

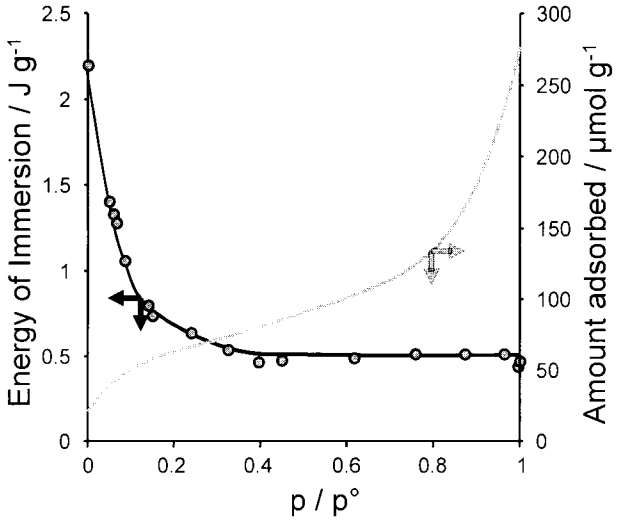


Figure 3 . Immersion energy of water on a silica sample pre-covered with water a various relative pressures and corresponding water adsorption isotherm [2].

Figure 3 shows that the immersion energy decreases for samples pre-covered at low relative pressures. From a relative pressure of around 0.4, however, the immersion energy remains constant. This relative pressure corresponds to the formation of two layers of water on the surface of the silica. This study thus implies that if pore filling occurs before the formation of two adsorbed layers, then the Harkins and Jura method will not give valid results. This is typically the case for microporous samples.

Table 1.
Comparison of specific surface areas obtained from adsorption experiments (a_{BET}) and from immersion calorimetry ($a_{Harkins\text{-}Jura}$) (from [2]).

Sample	a_{BET} / m^2 g^{-1}	$a_{Harkins\text{-}Jura}$ / m^2 g^{-1}
Quartz	4.2	4.2
Silica	129	140
Alumina	81	100
Titania	57	63
Gibbsite	24	27
Kaolinite	19.3	19.4
Zinc oxide	2.9	3.1
Gallium hydroxide	21	21.3

The comparison of the results obtained with the Harkins and Jura method with those obtained using the BET method from adsorption experiments is given in Table 1. It can be seen that, in many cases, the agreement is good between the two methods.

An advantage of the Harkins and Jura method is that there is no assumption about the size of the wetting molecule as there is with the BET method. Such experiments require that the solid in question should be fully wetted. However, as noted above, the method is limited to samples which are essentially non-porous. It should be noted that, experimentally, the Harkins and Jura method is quite painstaking.

2.3. Immersion calorimetry for an evaluation of the chemical nature of the surface

An evaluation of the surface chemistry of samples can be carried out by comparing results with a sample containing few surface chemical sites. This is highlighted in Figure 4 in which the immersion energy of titania is compared with that obtained for a graphon sample as a function of the dipole moment of the immersion liquid used [4].

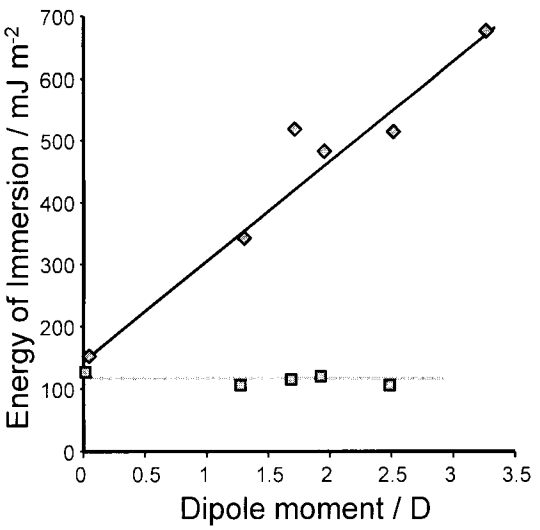


Figure 4. Immersion energy of titania (diamonds) and graphon (squares) as a function of the dipole moment of the immersion liquid (drawn from data in [4]).

For a sample which has few surface chemical sites, such as the graphon sample, a change in the polarity of the immersion liquid shows little variation in the energy of immersion. On the other hand, it can be seen that the interaction of the increasing dipole moment of the immersion liquid with the titania leads to a slope which is a function of the surface chemistry of the solid.

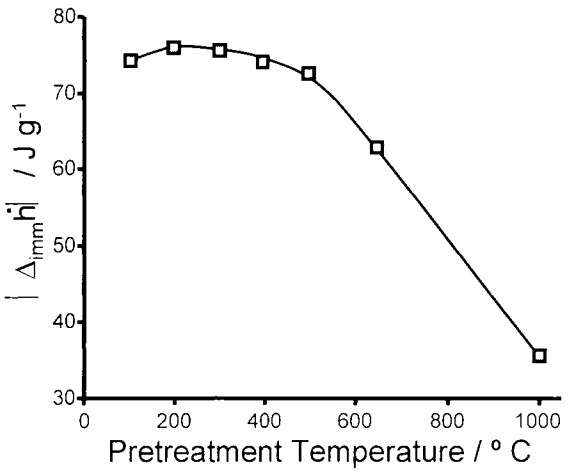


Figure 5. Variation of immersion energy for a precipitated silica as a function of its pre-treatment temperature [5].

Immersion calorimetry can be used to follow the variation of surface chemistry as a function of various thermal treatments. Figure 5 shows the variation of immersion energy as a function of the thermal pre-treatment temperature in the case of a silica sample [5]. It can be seen that there is little variation in immersion energy for temperatures below 500°C, however the thermal treatment of silica samples above 500°C lead to a progressive dehydroxylation which results in a decrease in immersion energy.

2.4. Immersion calorimetry for the evaluation of microporosity

It is possible to estimate the micropore size distribution of heterogeneous samples such as carbons via the use of different immersion liquids of different size and similar chemical nature. This is demonstrated in several studies such as those in references [6-8].

Figure 6 shows the surface area of a series of carbon samples as a function of the pore width [6]. This pore width is calculated from the molecular dimensions of the various immersion liquids used. It can be seen that a distinct cut-off point is observed for sample C4 just before 0.5 nm which indicates that the narrow

pore size distribution for this sample. C3 however, seems to show a rather large pore size distribution in the micropore range whereas the other two samples seem to consist of pores of larger dimensions.

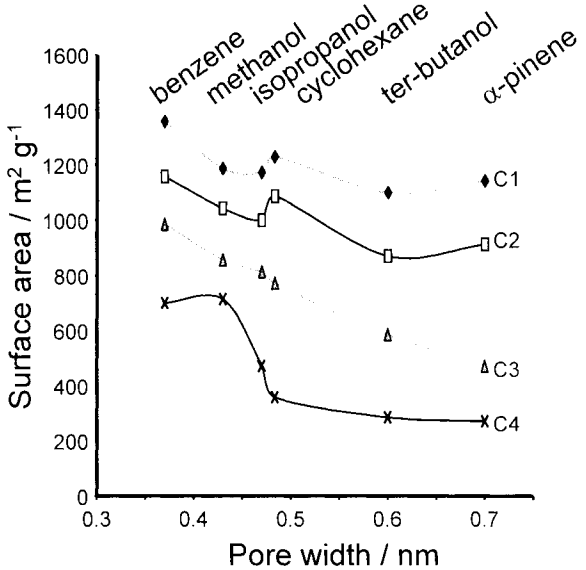


Figure 6. Accessible surface area of a series of charcoal samples as a function of pore width calculated from the molecular dimensions of different immersion liquids [6].

An advantage of the use a calorimetric method for the estimation of micropore surface areas lies in the fact that the energy released on immersion is directly proportional to the interacting surface [9]. This is an advantage with respect to the BET method which considers the molecular cross-section as is schematised in Figure 7. Figure 7 shows that the BET method, in which the number of molecules which form a statistical monolayer is multiplied by the cross-sectional area of the molecules, can lead to an underestimation and overestimation of ultramicropore and supermicropore surface areas respectively. This is not the case for immersion calorimetry in which the immersion energy is proportional to the area of interaction with the surface. Thus, for example, the immersion energy of a molecule inside a cylindrical ultramicropore is 3.6 times greater than on an open surface.

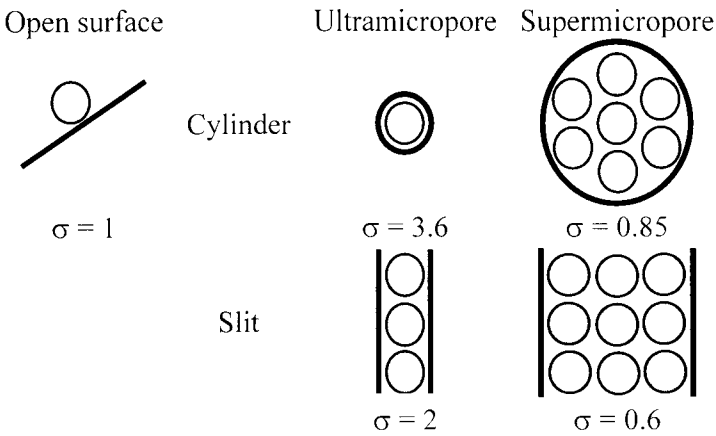


Figure 7. Diagram highlighting the problems that can be encountered when one considers the molecular cross-section 'σ' in the estimation of ultra- and super-micropore surface areas. The cases shown are for cylindrical and slit-shaped pores.

To access the micropores, relatively small molecules should be used. This leads to limits for studies at room temperature where mostly alkanes are used. In such cases, the use of immersion into liquid argon would seem to be advantageous [10-12]. This can be attained using the low temperature calorimeter described below (Figure 17) and the use of a non-polar liquid such as argon. In such studies an estimation of the surface areas of microporous carbon and silica samples allows one to go one step further in the determination of the internal surface area of micropores. Liquid nitrogen and liquid argon provide a very similar areal enthalpy of immersion for carbons : for instance, 165 and 160 mJ m^{-2} in nitrogen and argon, respectively, if the surface area of the reference material is measured by the BET method with nitrogen at 77 K [12]. The enthalpies of immersion obtained with silica samples into liquid nitrogen is systematically higher than into liquid argon but this should not influence the derivation of the "immersion surface area" provided the reference sample is correctly selected. Such results rule out a simplifying asumption initially made by the pioneers of the method, Chessick et al [10] and Taylor [11] that the areal enthalpy of immersion is somewhat independent from the chemical nature of the adsorbent. This means that a calibration with a non-porous sample is needed for each type of surface. This is not too much of a problem since the duration of a complete calorimetric experiment (after preliminary weighing and outgassing of the sample) is approximately 2 hours.

2.5. Intrusion of non-wetting fluids

In the case of non-wetting systems, pressure is required for intrusion of the fluid into the pore to occur. This is the case for mercury porosimetry for example. There is growing interest in highly hydrophobic systems in which water intrusion occurs under pressure. Such systems can be used for shock absorbers or for storing energy. There have been several studies of water intrusion into hydrophobic systems such as pure silica zeolites and grafted mesoporous silicas [13-15].

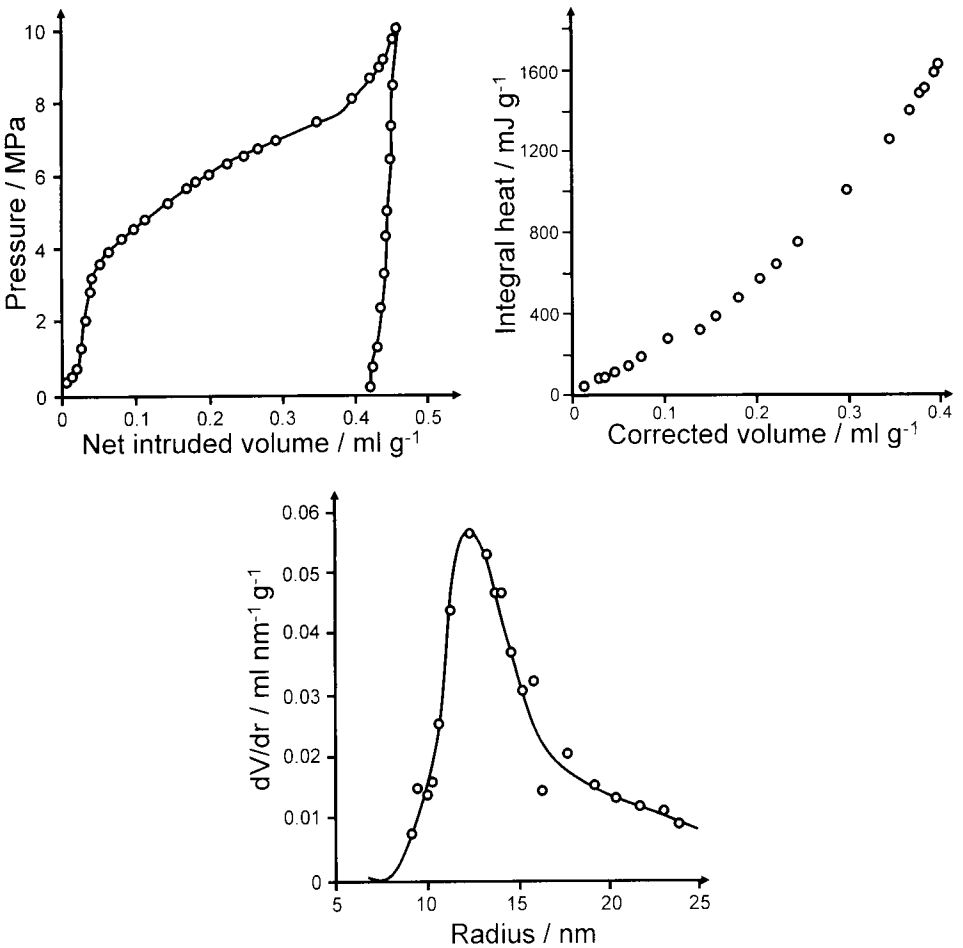


Figure 8. Results obtained for the intrusion of water into a polymer grafted silica [16] : upper left pressure / volume curve, upper right heat / volume curve, lower curve : differential pore size distribution calculated from the upper curves.

In such systems the increase in pressure is accompanied by a decrease in volume of the system corresponding to the intrusion of water into the porosity. In this case, the pore size is calculated via the Washburn equation :

$$p = -\frac{2\gamma_{lg}}{r}\cos\theta$$

where p is the pressure, γ_{lg} the interfacial tension, r the radius of curvature and θ the contact angle. An estimation of the contact angle thus has to be made.An advantage of combining such a system with a simultaneous calorimetric reading is that the contact angle can be calculated by a combination of the above Washburn equation and the following expression [16] :

$$dU = \left(T\frac{\partial(\gamma_{lv}\cos\theta)}{\partial T} - \gamma_{lv}\cos\theta \right) dA$$

where U is the internal energy, T the temperature, and A the surface area.

An example of the results that can be obtained for the intrusion of water into porous silica is given in Figure 8. From the upper curves and applying the relevant formulas, it is possible to obtain the pore size distribution in the lower curve. The contact angle calculated during this experiment was 126 ± 5 °.

3. THERMOPOROMETRY

Thermoporometry is a simple method to obtain the pore size distribution of mesoporous solids. It is based on the phenomenon that liquids will freeze at lower temperatures in confined media than in the bulk.

Experimentally, this phase transition can be followed by DSC. A typical experimental protocol (Figure 9) begins with the immersion of the solid with a slight excess of liquid before being placed into the DSC. A temperature programme starts with a quench to low temperature (typically -80 °C for water) before gradual heating (0.5 to 1 °C min^{-1}) to just below the bulk melting temperature. In this part of the procedure, the fluid is initially frozen both inside and outside the pores. On heating to just below the bulk melting temperature, only the fluid inside the pores melts leaving solid outside the pores. The temperature is then lowered again at the same rate on heating to re-solidify the fluid inside the pores. Such a procedure avoids any large deviation from equilibrium and avoids undercooling of the liquid. In some cases the temperatures of liquefaction and solidification differ. This has been ascribed to pore shape, as well as to differences in mechanisms on heating and cooling.

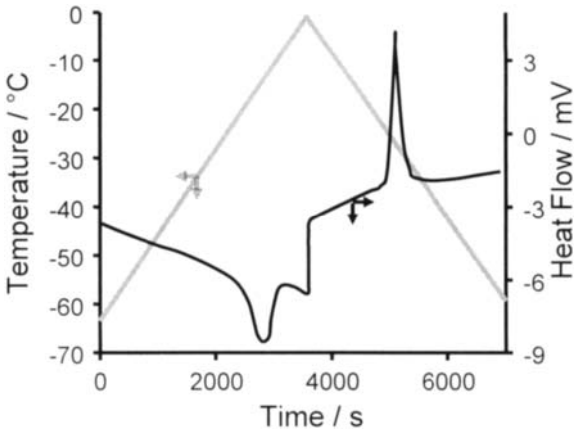


Figure 9. Heating programme and heat flow observed during a thermoporometry experiment.

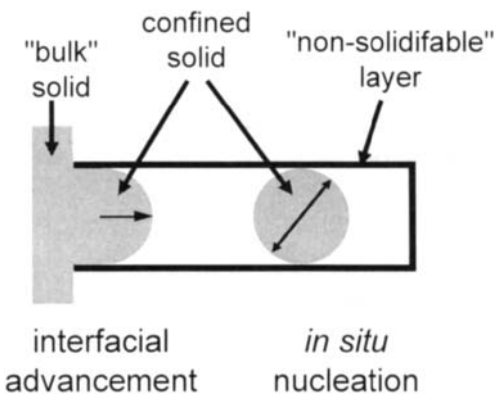


Figure 10. Diagram showing the different mechanisms of solidification inside a pore. Left : the penetration of a solid interface from the bulk solid outside the pore. Right : nucleation of solid inside the pore.

From a phenomenological point of view, there is still discussion as to the mechanism of solidification inside the pores. This is schematised in Figure 10 in which the mechanisms of interfacial advancement and *in situ* nucleation are shown. The interfacial advancement mechanism was first described by Everett as the plastic ice model [17]. A further point that can be seen in the figure is that a layer of fluid remains on the pore walls which does not freeze on cooling. It is generally accepted that this non-freezable film consists of two molecular layers.

The depression in freezing point is described by the equation put forward by Kubelka [18]:

$$\Delta T = T - T_0 = \frac{2\gamma_{sl} M T_0}{R \rho_l \Delta H_s}$$

where T and T_0 are the temperature of freezing in the pore and in the bulk respectively. γ_{sl} is the surface tension, M the molar mass, R the radius of curvature, ρ_l the liquid density and ΔH_s the enthalpy of solidification. Of these parameters, γ_{sl}, ρ_l, and ΔH_s all vary with temperature.
The heat flow on solidification can be given by [19] :

$$Q = T_e \left\{ \Delta S_{s0} + \int_{T_0}^{T} \frac{Cp_l - Cp_s}{T} dT + 2 \frac{v_l}{R_p - t} \frac{d\gamma_{ls}}{dT} + \left(\frac{\partial v_l}{\partial T} \right)_p \cdot (P_l - P_0) + \left(\frac{\partial v_s}{\partial T} \right)_p \cdot (P_0 - P_s) \right\}$$

where T_e is the equilibrium temperature, S_{s0} is the entropy of solidification, Cp_l and Cp_s are the specific heats at constant pressure of the liquid and solid respectively, v_l and v_s are the volumes of liquid and solid, t is the thickness of the non-freezable layer and the terms P_0, P_l and P_s are the initial pressure and pressures within the liquid and solid phases. This expression can be used to calculate the volume of the pores.

More simple however, is the calculation of the pore size. However, for this, the above variation in the parameters with temperature as well as the thickness of the non-freezable layer. For characterisation purposes, Quinson and Brun developed simple formulae which model the different variations in temperature and integrate the non-freezable film thickness [19]. For water the pore radius R_p is given by the following expression :

$$R_p = \frac{-64.67}{\Delta T} + 0.57$$

Whereas for benzene the expression used is :

$$R_p = \frac{-131.6}{\Delta T} + 0.54$$

For two MCM-41 samples, Figure 11 shows the results that can be obtained using thermoporometry. These results compare well with those obtained via other methods.

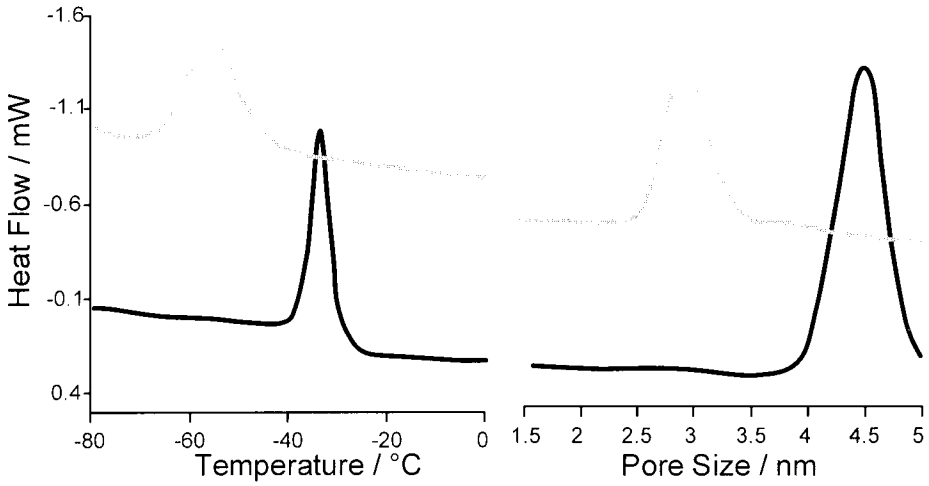


Figure 11. Thermoporometry on water : Experimental cooling curves (left) and pore size calculation (right) obtained with two MCM-41 samples.

There are several advantages of using thermoporometry with respect ot adsorption-desorption experiments. Firstly, the experiment is relatively rapid compared to a full adsorption-desorption isotherm. Furthermore, it is possible to analyse relatively fragile samples such as polymers which can undergo degradation on outgassing or at liquid nitrogen temperature. Finally, it is possible to analyse samples in their application media if used in the liquid phase.

4. SAMPLE CONTROLLED THERMAL ANALYSIS (SCTA)

The characterisation of adsorbents can be carried out using sample controlled methods. Indeed, in the same way that it is possible to characterise the surface chemistry of catalysts via the desorption of chemisorbed species, it is also possible to characterise adsorbents via the thermodesorption of physisorbed molecules. In such cases, one can glean information about surface area and pore size.

Two main approaches have been taken to characterise adsorbents using Sample Controlled Thermal Analysis or SCTA [20]. On one hand, the adsorbent, saturated with liquid, is equilibrated with its saturated vapour. Thus, on heating, a curve is obtained which relates the loss of liquid with respect to the saturated vapour pressures on a flat liquid surface and the liquid inside the pores [21]. This approach has been taken by several authors who have used a Sample Controlled Thermogravimetric approach, namely the Pauliks' Derivatograph, and is currently known as Quasi-isothermal thermodesorption. Whilst a direct

measurement of the mass loss is obtained, the estimation of the actual water vapour pressures is not straightforward. Another approach that is based on Controlled Rate Evolved Gas Detection in which the pressure above the sample (directly related to the rate of desorption) is continuously measured and kept constant with time. Whilst the pressure is kept constant, the saturated vapour pressure varies with temperature [22]. In each case, the thermodesorption curves are interpreted via the Kelvin equation to give pore size distributions. A further description of the two approaches and selected results is given in the following sections.

The quasi-isothermal heating mode proposed by the Paulik brothers, which is used here for the thermodesorption of liquids, is one way to increase the resolution of traditional TPD experiments [23]. The Derivatograph was used in all of the quasi-isothermal studies presented in this particular section. The quasi-isothermal heating mode starts here with a linear temperature rise (*e.g.* 3 K min^{-1}). The differential mass loss is calculated with time and when this increases above a certain pre-set value (*e.g.* 0.5 mg min^{-1}), an isothermal plateau is maintained. When the differential mass loss with time descends below this pre-set value, a linear increase in temperature again takes over. The mass loss is thus recorded as a function of temperature.

In thermodesorption experiments, it is important that the vapour pressure above the sample be known. Using the derivatograph, the partial water vapour pressure above the sample is not directly measured. In such cases however, a special "labyrinth" sample cell was developed in which the cell, including sample and excess liquid, is covered with an overfitting lid. Such a cell insures that a self-generated atmosphere is maintained above the sample during the experiment and is therefore equal to the atmospheric pressure [33]. During the experiment an increase in temperature leads to an evaporation / boiling of the excess liquid which expels the excess air. The overfitting lid and labyrinth sample cell ensures a relatively long diffusion path of vapour from the sample and avoids any retrodiffusion of air.

Thus, during the experiment, it is expected that the water vapour pressure p is maintained constant at the atmospheric pressure and a variation in saturation vapour pressure p° occurs with temperature T. Schematically, a curve is obtained of the form shown in Figure 12. The first half of the curve is due to the loss of the excess liquid and has nothing to do with the sample. It can be used to calibrate the instrument temperature. The next part of the curve is due to the emptying of the various classes of pores. An increase in temperature leads to the progressive emptying of pores of ever decreasing widths.

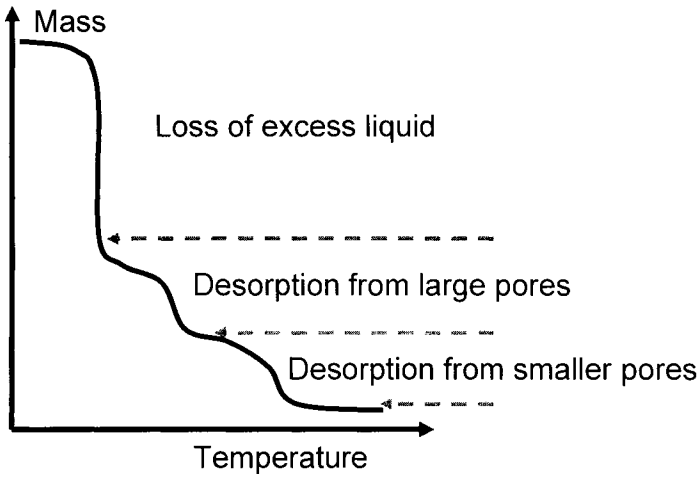


Figure 12. Schematic representation of a curve obtained from a quasi-isothermal gravimetric experiment with a solid with a bimodal pore size distribution.

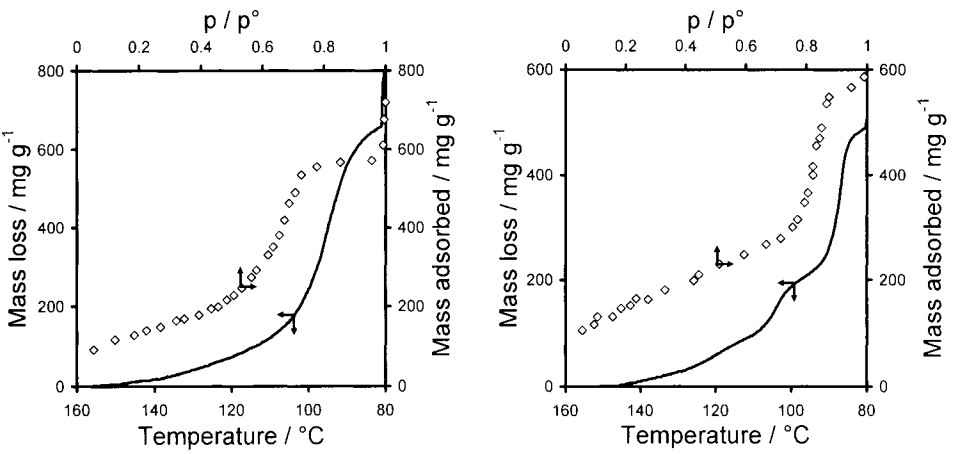


Figure 13. Comparison of desorption curves of benzene (full line) obtained from quasi-isothermal thermogravimetry, and nitrogen (points) obtained via physisorption : (a) silica gel, (b) mixture of two silica gels of different pore sizes (adapted from [24]).

An analogy can thus be made between the results obtained by use of this method and those obtained from physisorption measurements. This is

highlighted in Figure 13 in which the co-ordinates of the two graphs are adjusted such that the forms of the curves are similar.

One can thus appreciate how it is possible to calculate the pore volume and even the pore size distribution in analogy with adsorption calculations. Thus, the mass loss observed for each step can be related to the pore volume and the temperature range in which the mass loss occurs can be related to the pore width via the Kelvin equation. Supposing perfect wetting, the equation takes the form :

$$r = \frac{2\gamma V_M}{RT \ln(p/p^\circ)}$$

Here, in addition to p, p° and T mentioned above, one has to take into account the surface tension of the liquid γ, the molar volume V_m, both of which also vary with temperature. The radius r obtained via this expression is a *core radius* and one has to additionally take into account a surface layer which is not desorbed.

This layer is dependent on the type of surface, the size of pore and on the pre-adsorbed species used. Indeed, as in adsorption, the thickness of the surface layer increases with pore size. In several cases, the relationship put forward for adsorption experiments can be used in thermodesorption. This is the case, for example, for water-silica system [25]. In other cases, the difference in pore size distribution compared with that obtained for nitrogen has been used [26].

The surface under investigation can lead to differences in the thickness of the adsorbed layer. When grafted solids are under investigation, one can also observe the case where the preadsorbed species would seem to migrate between the chains of the organic grafts, leading to discrepancies. This was shown for adsorption of benzene on a C18 chain grafted silica [26]. There are many examples, however, where good agreement has been obtained in measurements of pore volume and pore size distribution by quasi-isothermal gravimetry and by nitrogen physisorption.

The choice of liquid used for the characterisation via thermodesorption is important. The liquid has to wet the solid sufficiently and specific interactions with the surface have to be avoided. A number of different wetting liquids have been used as can be seen in the table above. Most of the studies have given satisfactory results, suggesting good wetting. Nevertheless, it has been noted that for silica, water is unsuitable because it forms a stable surface film [27]. However, in other studies, water has been found to be quite satisfactory [21, 28].

The SCTA curves obtained via quasi-isothermal gravimetry can be treated to yield desorption energy profiles. The theoretical treatment for heterogeneous surfaces is detailed in reference [21].

One advantage of using a saturated system for thermodesorption is that it is possibile to characterise the sample in the wet state in the actual liquid used in

the application itself. A second advantage can be for the characterisation of fragile solids, such as organic films [29] and porous polymers [30], which shrink in vacuum and are brittle at low temperature making nitrogen physisorption experiments meaningless. The results obtained with quasi-isothermal gravimetry thus can be compared with those obtained using thermoporometry.

Whilst the quasi-isothermal method is quite a satisfactory method for the characterisation of most porous solids, some discrepancies are observed with respect to other methods such as nitrogen physisorption or mercury porosimetry. This may sometimes be due to phenomena such as adsorbent swelling or migration between organic chains, as mentioned above. However, it would seem that this method has difficulty in detecting small amounts of porosity [31] which may simply be due to the experimental conditions chosen, which may lead to too rapid desorption of the wetting liquid and too low a vapour pressure in the surrounding atmosphere. Furthermore, difficulties also arise in the characterisation of micropore volumes [32]. This has been explained by the difficulty in the observation of the end of pore emptying. This may be due to a difference in the pressure above the sample with respect to the assumed saturation vapour pressure. This variation in vapour pressure above the sample at the end of the experiment may be due to the special form of sample cell used and difficulty in the actual measurement of the vapour pressure above the sample.

Although a special "labyrinth" sample cell can be used, the partial pressure is not measured and more importantly, not controlled. Finally, the experiments always require an excess of liquid to be used. This allows pore volumes and pore size distributions to be calculated, but estimations of surface area are not possible.

The above mentioned points suggest that some improvements can be made with respect to quasi-isothermal thermogravimetric measurements. One possibility is to use evolved gas analysis instead of thermogravimetry. This can be done using the apparatus developed by Rouquerol [33]. For such experiments, the sample is firstly outgassed via SCTA under vacuum to clean the surface and pores of impurities. The cell is then attached to an apparatus for the pre-adsorption. The sample and pure liquid are placed at different temperatures to induce the required relative pressure above the sample. Thus for calculation of the surface area, a relative pressure corresponding to monolayer coverage is used. For information on the total pore volume and pore size distribution, a relative pressure around 0.95 is required.

After pre-adsorption, the sample cell is isolated and transferred to the SCTA apparatus adapted for evolved gas analysis [33]. Such experiments have been carried out under constant reduced pressures in the range from 10^{-3} to 5 mbar. This is in contrast to the quasi-isothermal thermogravimetric experiments

carried out under atmospheric pressure. Here, once again, the pressure p is maintained constant and the saturated vapour pressure $p°$ varies with temperature T. The Kelvin equation can be used to calculate pore size distributions as described above. One therefore relates the desorption *temperature* to the pore size via the Kelvin equation, instead of relating the pore size to the desorption *pressure*, as is usually done in the isothermal Barrett, Joyner and Halenda method [34].

The other experimental conditions are adjusted to give a constant mass loss of around 0.14 to 0.5 mg h^{-1} which is much slower than those used in quasi-isothermal thermogravimetric measurements (30 mg min^{-1}). This rate of mass loss is calculated in a separate experiment. This much lower rate leads to an increased resolution, allowing small amounts of porosity to be investigated. This resolution has been used in a study where the small amount of porosity created during the surface corrosion of metallic alloys needed to be followed [35]. An interesting point is that the fluid used to characterise this porosity is the same as that involved in the ageing process.

Such experiments have also been used for the study of thermodesorption of water from various zeolites [36], as well as from heterogeneous surfaces [37,38]. Here a residual pressure above the sample of the order of 10^{-2} mbar was used, which is sufficient to estimate the micropore volume, as well as to highlight the influence of cation sites on the thermodesorption curves [36]. Even though the temperature at which the experiments were started was around –30 °C, this is not sufficient to retain physisorbed water within mesopores. Two solutions are possible : the first is to drastically increase the residual pressure above the sample as above; the second is to decrease the initial temperature at which the experiments start.

Whilst the former solution is very well exploited by the quasi-isothermal method, the latter solution has been adopted for experiments carried out under reduced pressure. A schematic diagram of the furnace is shown in Figure 14 [22] which is placed onto a liquid nitrogen dewar. Inside the dewar, an electrical resistance maintains constant boiling of the liquid nitrogen. The vapour thus produced passes through a spiral tube within the furnace assuring constant cooling down to a minimum temperature of 163 K. The furnace resistance is connected to a PID regulator, whilst the sample temperature is measured *via* a 100 Ω platinum probe. This apparatus permits a temperature interval from 163 to 473 K to be explored. The maximum time taken for an experiment depends on the amount of liquid nitrogen in the dewar. A 50 L reservoir allows experiments to be carried out for up to 48 h.

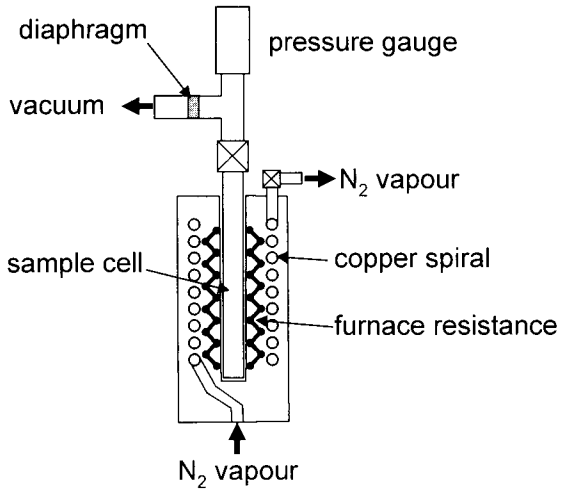


Figure 14. Schematic diagram of the furnace developed for thermodesorption studies starting at low temperature.

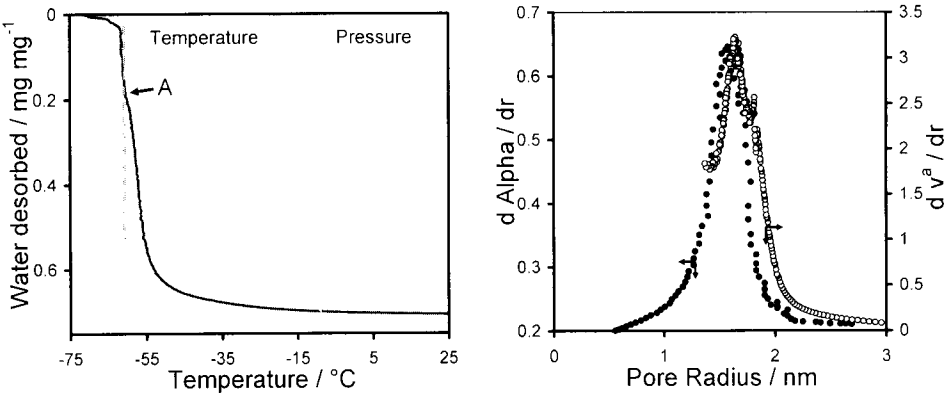


Figure 15. Constant Rate Evolved Gas Detection (CR-EGD) curve obtained for the thermodesorption of water from MCM-41 (left). Pore size distributions for MCM-41 from SCTA (dark circles) and from water desorption at 25°C (light circles) (right).

The water desorption curve for the mesoporous sample MCM41 is shown in Figure 15. The initial temperature of –80°C was low enough under the conditions of residual pressure (10^{-3} mbar) to avoid vapour loss prior to heating. This curve can be treated as described in reference [22], in an analogous manner

to that described above for quasi-isothermal measurements, to give the pore size distribution in Figure 15 (dark circles). This compares well with the pore size distribution obtained from the BJH treatment of the desorption branch of the physisorption isotherm at 25°C (light circles).

The SCTA curve shown in Figure 16 is obtained for the thermodesorption of water from the aluminophosphate $AlPO_4$-5. Logically, this microporous sample (pore diameter 0.73 nm) desorbs water at a higher temperature than MCM-41. Nevertheless, this desorption occurs well below room temperature, highlighting the interest in using the set-up shown in Figure 14.

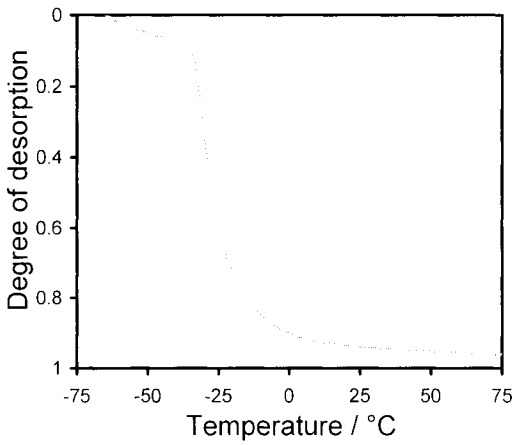


Figure 16. Constant Rate Evolved Gas Detection (CR-EGD) curve obtained for the thermodesorption of water from $AlPO_4$-5.

It is also possible to pre-adsorb at a partial pressure in which a monolayer is adsorbed, before desorbing under SCTA conditions to calculate the amount desorbed and thus the specific surface area. This can be of interest when the surface area under investigation is low or the amount of sample that can be studied is limited, for example where a thin, porous oxide layer is formed during the corrosion of metals. The resolution of 2 cm^2 that can be attained using this approach is of great interest [22, 35].

The thermodesorption of liquids other than water can be used in studying zeolites to characterise the chemical nature of the surface active sites. One suggestion has been the use of isopropylamine which would seem to desorb in two regimes from HY and NaY zeolites [39]. The rate jump method was used to characterise these two regimes. The first regime corresponds to the physisorbed species, whereas the second regime corresponds to the species chemisorbed on

Brønsted acid sites. Interestingly, the 20% difference in apparent activation energies obtained from CRTA and linear heating experiments was explained by diffusion effects that occur in the latter measurements.

Controlled rate thermodesorption under reduced pressure has been applied to the characterisation of active carbons [40]. Phenol was used as the desorption fluid. In contrast with traditional linear heating TPD experiments [41,42], the SCTA experiments showed that no cracking of phenol occurred and, for the carbon studied, three domains were identified and characterised with the aid of high resolution argon physisorption experiments.

Finally, it is possible to further exploit the SCTA thermodesorption curves obtained with heterogeneous solids using statistical rate theory of interfacial transport [38]. The theoretical basis is detailed in reference [38], in which two different approaches are given for SCTA experiments. Each approach leads to a different condensation energy distribution, calculated assuming equilibrium or mixed equilibrium/non-equilibrium conditions. An example of water desorption from hydroxyapatite is given in which physisorbed and chemisorbed species are highlighted.

5. ISOTHERMAL ADSORPTION MICROCALORIMETRY

5.1. Introduction

Different calorimetric methods are available for the study of adsorption phenomena. Whilst *adiabatic* calorimetry is more suitable for the determination of heat capacity, both *isoperibol* and *diathermal* calorimetry have been used to follow adsorption phenomena. Isoperibol calorimetry, where no special connection is made between the sample temperature and that of the surroundings, was the first to be applied to adsorption. The experimental set-ups and the experiments themselves are complicated and comparison of results obtained using this methodology with those obtained by standard, isothermal measurements is difficult. Diathermal calorimeters, where the sample temperature follows that of the surroundings, are most suited to follow gas adsorption phenomena. The isothermal conditions of adsorption manometry can be reproduced so that the thermal events that occur during adsorption can be measured. The examples given below were obtained under these diathermal or *quasi-isothermal* conditions.

For the characterisation of adsorbents, low temperature measurements, in the range of 77 K are generally used. However, data obtained in the temperature region from 25 to 100°C can often be of interest, for example in studies related to gas storage and gas separation. Specific instruments are required for each of these temperature domains.

An example of a diathermal calorimeter [43] used for low temperature adsorption studies is given in Figure 17. This apparatus is formed of three main parts : the dosing apparatus, the sample cell and the calorimeter. The calorimeter is a Tian-Calvet apparatus where two thermopiles are mounted in electrical opposition. The calorimeter is placed upside down, like a diving bell in the cryogenic fluid. Each thermopile houses around 1000 thermocouples that provide an overall sensitivity of around 5 mJ. The electrical resistance is housed in the reference thermopile, allowing calibration via the Joule effect. The calorimeter is maintained in a liquid nitrogen (or argon) cryostat containing around 1000 L of cryogenic fluid. A small flow of helium is maintained through the thermopiles. This helium flow maintains the calorimeter under isothermal conditions, as well as allowing a good thermal contact between the sample and the thermopile.

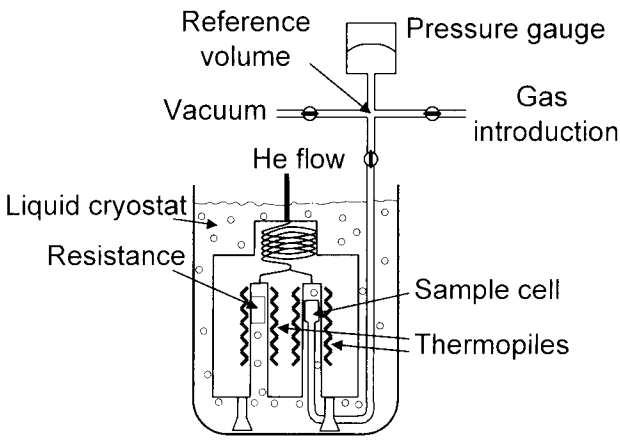


Figure 17. Schematic representation of a calorimetric set-up used for adsorption experiments.

There are, however, two different methods of adsorbate introduction. The first, and most common, is to inject discrete quantities of adsorbtive to the adsorbent. Each introduction of adsorbate to the sample is accompanied by an exothermic thermal effect, until equilibrium is attained. This peak in the curve of energy with time has to be integrated to give an integral (or pseudo-differential) molar enthalpy of adsorption for each dose.

The calorimetric cell (including the relevant amounts of adsorbent and gas phase) is considered as an open system. In this procedure, as well as in the quasi-equilibrium procedure of gas introduction (following section) it is important to consider that the gas is introduced reversibly. However, to calculate

the differential enthalpy of adsorption via the discontinuous procedure, one must introduce quantities dn small enough for a given pressure increase dp.

Under these conditions it is possible to determine the differential enthalpy of adsorption $\Delta_{ads}\dot{h}$, via the following expression :

$$\Delta_{ads}\dot{h} = \left(\frac{dQ_{rev}}{dn^a}\right)_T + V_c\left(\frac{dp}{dn^a}\right)_T$$

Here, dQ_{rev} is the heat reversibly exchanged with the surroundings at temperature T, as measured by the calorimeter. δn^a is the amount adsorbed after introduction of the gas dose, dp is the increase in pressure and V_c is the dead space volume of the sample cell within the calorimeter itself (thermopile).

For the observation of subtle adsorption phenomena, such as adsorbate phase changes, an increased resolution in both the isotherm and differential enthalpy curves is required. It would be possible to introduce very small doses of gas to increase the number of points taken. This is both time consuming and may lead to the summation of a number of errors. However, a continuous introduction of gas leads to an infinite resolution in both curves.

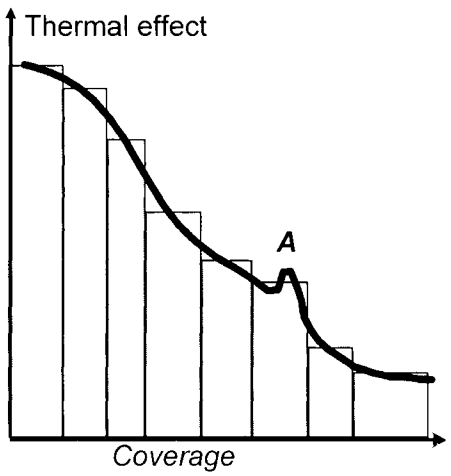


Figure 18. Comparison of the results obtained using either the discontinuous (bars) or continuous (full line) procedure of gas introduction. The peak, A, corresponds to an adsorbate phase change which is overlooked when using the discontinuous procedure of adsorbtive introduction.

Figure 18 highlights how this resolution can be interesting. The peak, A, in the full line would be indicative of an adsorbate phase change which would go unnoticed using the discontinuous procedure of gas introduction.

In what has been termed the "continuous flow" procedure, the adsorbate is introduced to the system at a defined rate, slow enough that the adsorbate – adsorbent system can be considered to be essentially at equilibrium at all times [44,45]. To verify this equilibrium it is possible to stop the adsorbate flow and verify that the heat signal stops (Figure 19).

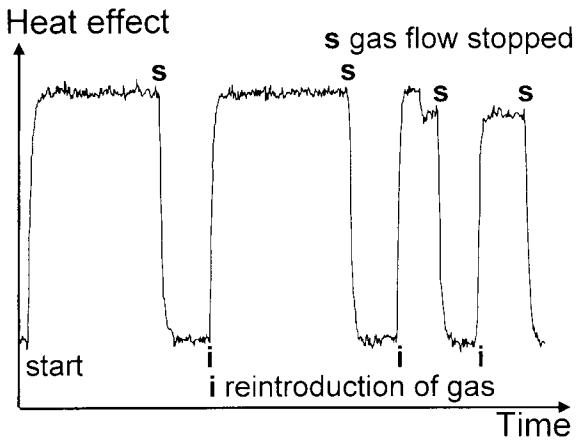


Figure 19. Adsorption of krypton on silicalite-1. The flow of gas to the sample is stopped periodically to verify the adsorbate-adsorbent equilibrium.

In this "quasi-equilibrium" state, the quantity of adsorbate admitted to the system Δn can be replaced in adsorption calculations by the rate of gas flow dn/dt. The calorimeter under these conditions measures a heat flow, ϕ.

The use of a sonic nozzle allows the gas flow to the sample, $f = dn/dt$ to be kept constant. A rate of adsorption, f^a, can therefore be calculated using the following expression :

$$f^a = \frac{dn^a}{dt} = f - \frac{1}{R}\left(\frac{V_d}{T_d} - \frac{V_c}{T_c}\right)\frac{dp}{dt}$$

Here, V_d and V_c are the volumes of the dosing system and that "accessible" to the calorimeter at temperatures T_d and T_c. The corresponding heat flow, ϕ, can be given by :

$$\phi = \frac{dQ_{rev}}{dt} = \frac{dQ_{rev}}{dn^a} \cdot \frac{dna}{dt} = f^a \left(\frac{dQ_{rev}}{dn^a} \right)_T$$

Combining the last two expressions leads to :

$$\Delta_{ads}\dot{h} = \left(\frac{dQ_{rev}}{dn^a} \right) + V_c \left(\frac{dp}{dn^a} \right) = \frac{\phi}{f^\sigma} + V_c \frac{dp}{dt} \frac{dt}{dn^a}$$

$$\Delta_{ads}\dot{h} = \frac{1}{f^a} \left(\phi + V_c \frac{dp}{dt} \right)$$

Blank experiments can lead to an estimation of $V_c(\mathrm{d}p/\mathrm{d}t)$. This term is large during horizontal parts of the isotherm. The error in the estimation of the differential enthalpy thus becomes large. However, in these regions of multilayer adsorption, an estimation of the enthalpy is less interesting and can be readily obtained using the isosteric method.

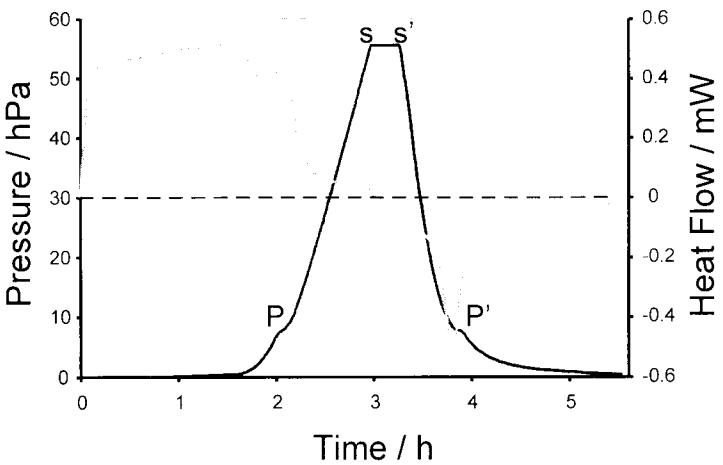


Figure 20. Plot of the signals of heat flow and pressure obtained during the adsorption of nitrogen on graphite at 77.4 K. (adapted from [45]).

For micropore filling, or during capillary condensation, the term $V_c(\mathrm{d}p/\mathrm{d}t)$ is minimal. Effectively, during such phenomena, the increase in pressure with time

is small. Furthermore, almost all of the flow of gas to the sample is adsorbed making $f \approx f^a$. In such cases, the last equation can be simplified to:

$$\Delta_{ads}\dot{h} \approx \frac{\phi}{f}$$

Thus if the rate of gas flow, f, is constant, a direct measurement of $\Delta_{ads}\dot{h}$ with the amount adsorbed is recorded [43].

An example of the results that can be obtained using combined adsorption manometry / calorimetry is given in Figure 20. This figure represents the direct signals of pressure and heat flow as a function of time, recorded during the adsorption of nitrogen onto a well-organised graphite sample [45,46].

This diagram highlights several points relative to the measurement of differential enthalpies of adsorption using the continuous procedure of gas introduction. It can be seen that the initial introduction of gas, up to 1.5 hours, leads to only a slight increase in the pressure signal. This corresponds to a relatively strong signal in the heat flow curve that is the result of monolayer adsorption on a highly organised homogeneous surface. The point "P" corresponds to a small step in the pressure signal and a large peak in the heat flow signal. This phase transition corresponds to the completion of the monolayer in epitaxy with the highly organised substrate [45,46]. At point "s" however, the flow of gas is stopped in order to check equilibrium. It can be seen that the pressure signal does not change and the heat flow signal decreases to the baseline within the response time of the calorimeter. These two points allow the conclusion of a quasi-equilibrium state. At point "s'", the vacuum line is opened to desorb the nitrogen and check the reversibility of the system. Note that this is one of the requirements for the above-mentioned calculations. It can be seen that at "P'", an effect similar to that produced on adsorption occurs. This and the fact that the two hatched areas are equivalent show the reversibility of this system.

As shown above, the differential enthalpy curves obtained using such adsorption microcalorimetric experiments is a global effect that includes both adsorbate – adsorbent as well as adsorbate – adsorbate interactions. Various adsorbate filling mechanisms and phase transitions can be highlighted, as well as any structural changes of the adsorbent.

In general though, the calorimetric curve highlights three different types of behaviour as schematised in Figure 21. In each system, an increase in the amount of gas adsorbed on a sample leads to an increase in the interactions between the adsorbate molecules. Concerning the adsorbate – adsorbent interactions, the interaction of an adsorbate molecule with an energetically homogeneous surface will give rise to a constant signal.

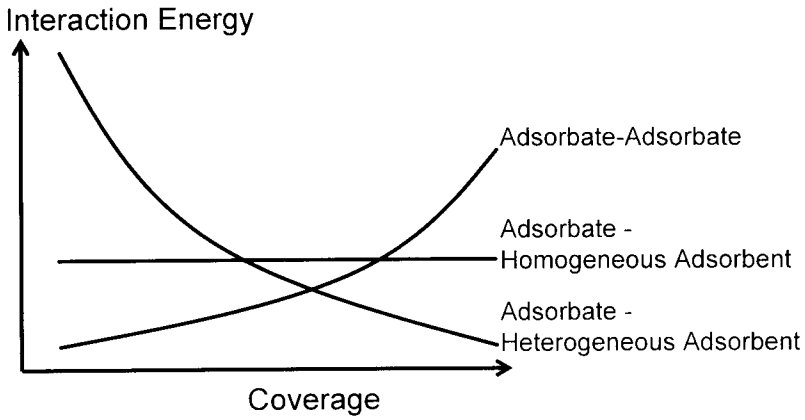


Figure 21. Hypothetical breakdown of calorimetric curves due to various interactions in play during the adsorption of simple gases at low temperature.

Finally, in most cases, the adsorbent is energetically heterogeneous due to a pore size distribution and/or a varying surface chemistry (defects, cations ..). Initially, one would expect relatively strong interactions between the adsorbing molecules and the surface. The extent of these interactions will then decrease as these specific sites are occupied. Thus, for energetically heterogeneous adsorbents, a gradual decrease in the calorimetric signal is observed. However, each differential enthalpy curve varies and is a composite of varying percentages of each type of interaction.

Both Kiselev [47] and Sing [48] have put forward classifications of differential enthalpy curves. Figure 22 shows hypothetical differential enthalpy of adsorption curves which would correspond to the IUPAC [49] classification of adsorption isotherms.

For non-porous and macrporous ($d_p > 50$ nm) solids which give rise to Type II isotherms, the differential enthalpy curve invariably decreases rapidly to the enthalpy of vaporisation ($\Delta_{vap}H$) of the gas. In several cases where there exist many specific sites on these materials, this decrease in the curve is less marked. These differences would seem to correspond to different C values derived from the BET equation.

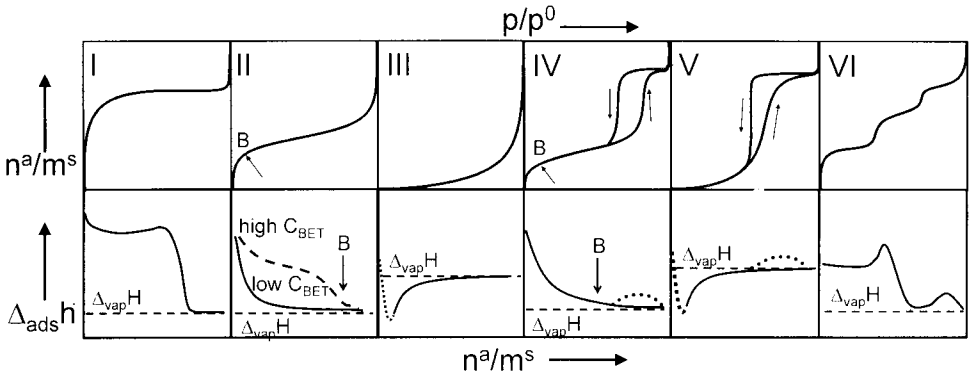


Figure 22. Six IUPAC classified isotherms (upper row) and corresponding hypothetical differential enthalpy of adsorption curves (lower row).

Mesoporous materials ($2 < d_p < 50$ nm) which normally give rise to Type IV isotherms also give rise to differential enthalpy curves which decrease to the enthalpy of vaporisation ($\Delta_{vap}H$) of the gas under investigation. For solids with a very narrow pore size distribution (MCM-41 type materials, for example) a slight increase in calorimetric signal of around 0.5-1 kJ·mol^{-1} is observed during the capillary condensation step [50].

Systems that give rise to Type III or Type IV isotherms are indicative of very weak adsorbate – adsorbent interactions. For these systems, the differential enthalpy of adsorption is initially below that of the enthalpy of vaporisation of the gas. In such cases, it would seem that entropy effects drive the adsorption process.

Type VI isotherms are typical for very homogeneous two-dimensional solids such as graphite. Each step corresponds to the edification of a different adsorbate layer. The differential enthalpy curve is relatively constant for the initial monolayer coverage. The completion of this monolayer results in a distinct peak in the differential enthalpy curve which corresponds to the formation of an epitaxal layer of adsorbate (see above, Figure 20). It is noteworthy that this 2-dimensional disorder – order transition was first observed by microcalorimetry [46] before being characterised by neutron diffraction methods.

Finally, the filling of micropores ($d_p < 2$ nm) is characterised by Type I isotherms. The initial uptake is characterised by a very small increase in pressure and is the result of enhanced interactions. Such cases are ideal for microcalorimetric studies as the technique is at its most sensitive. The differential enthalpy of adsorption curves are typically elevated throughout the pore filling process.

5.2. Adsorption calorimetry for the characterisation of heterogeneous adsorbents

Most adsorbents that are encountered can be considered energetically heterogeneous, whether this be from a textural point of view (pore size distribution ...) or from the point of view of their surface chemistry.

A typical example is that of porous silica gel. The pore size distribution is relatively large and the surface contains hydroxyl groups of different energy. Figure 23 shows the isotherms and differential enthalpy curves for the adsorption argon and nitrogen on a microporous silica gel. Both the differential enthalpy curves obtained with argon and nitrogen decrease continually with relative coverage. This is characteristic of large electrical homogeneity and is due to both the surface chemistry and the pore size distribution.

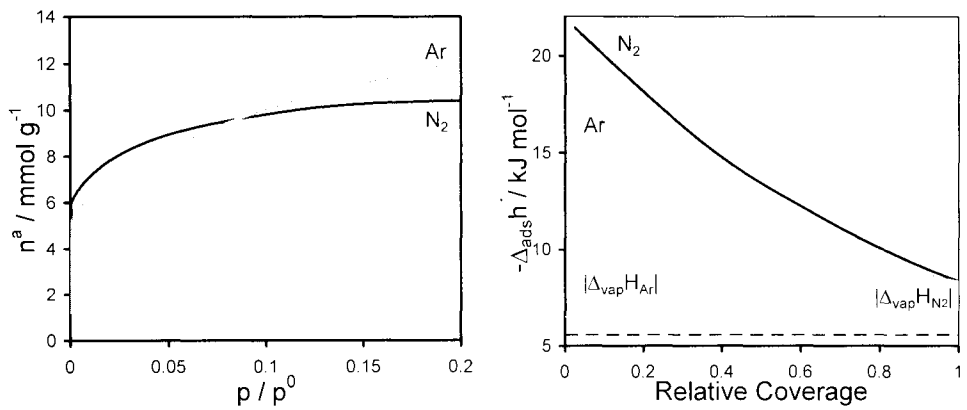


Figure 23. Isotherms (left) and corresponding differential enthalpies (right) at 77.4 K for nitrogen and argon adsorbed onto a microporous silica gel [51].

Often the comparison between the results obtained with argon and nitrogen can give an idea of the relative importance of the inhomogeneity due to the pore size distribution and surface chemistry. Indeed, argon being a spherical and non-polar molecule interacts only very weakly with surface chemical species such as hydroxyl groups. The behaviour thus observed is essentially due to the textural properties (pore geometry, pore size distribution ...). Nitrogen however, has a permanent quadrupole which is able to interact with any specific surface groups. The behaviour thus observed corresponds to any specific interactions with the surface as well as any interaction due to the textural nature of the sample.

The difference in the differential enthalpies of argon and nitrogen can be taken as an indication of the extent of the interactions due to the surface chemistry of the adsorbent under investigation.

An example of the information that can be obtained from the difference in energy of adsorption of argon and nitrogen can be seen in Figure 24. Here the difference in energy at zero coverage is plotted for a series of silica samples that had been pre-treated to different temperatures. This plot gives an insight into the hydroxyl content on the surface of the silica under investigation. It can be seen that the surface hydroxyl groups start to be transformed into siloxane bridges from around 300°C for the precipitated silica, whereas these groups would seem to be more stable on pyrogenic and Stöber silica's. [52]

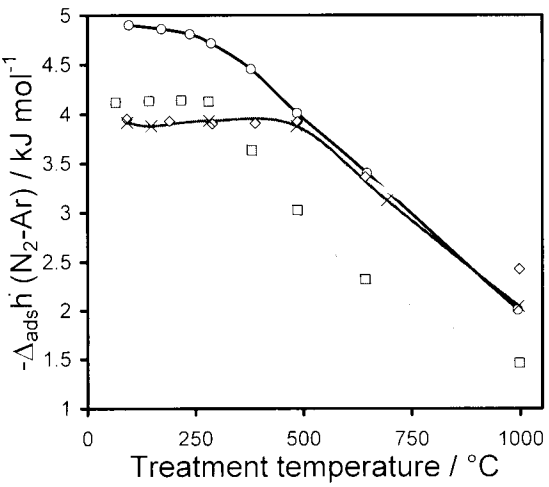


Figure 24. The difference in the enthalpy of adsorption at zero coverage of argon and nitrogen for different silica samples (A pyrogenic silica, G silica gel, P precipitated silica, S Stöber silica) as a function of thermal treatment [5,52].

Porous carbons often have a rather large pore size distribution and as such the differential enthalpy of adsorption curves also suggest energetic heterogeneity. However, these curves often have more features than those for silicas. The adsorption of simple gases onto microporous active carbons generally lead to calorimetric curves containing three different regions during the filling of the micropores. An example is given in Figure 25 for the adsorption of nitrogen and argon onto an activated carbon at 77.4 K. The three regions are clearly shown : the first region, AB, decreases before a second, more horizontal region, BC. The

third region, CD, again shows a marked decrease towards the enthalpy of liquefaction of the gas under consideration.

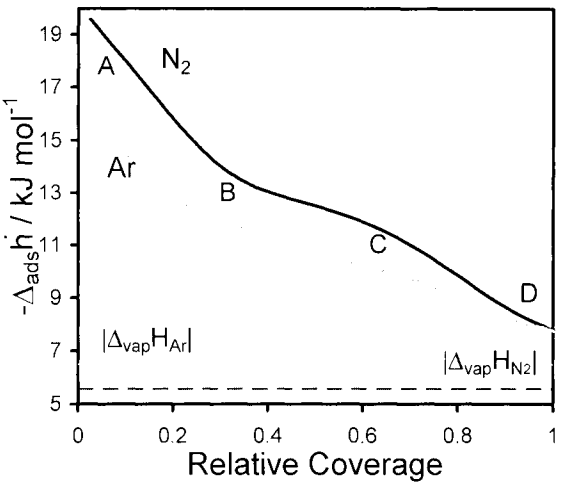


Figure 25. Differential enthalpies at 77.4 K for nitrogen and argon adsorbed onto an activated carbon.

A number of authors have noted and discussed such phenomena with varying interpretations [34,53]. It would seem that the following conclusions are generally given :

• Region AB is characteristic of interactions between the adsorbate and an energetically heterogeneous adsorbent (Figure 25). If one considers that the 2-dimensional graphite surface is energetically homogeneous, an explanation of the observed heterogeneity has to be found. Such heterogeneity can arise from defects or impurities, as well as from a distribution in micropore size. Although the first two possibilities can be eliminated in some cases, the nature of the preparation and activation of such materials makes a certain pore size distribution inevitable. One can therefore assume that the smallest micropores (or ultramicropores) are filled in this initial region AB.

• Region BC however, corresponds to a more homogeneous phenomenon and to an enthalpy of adsorption not far from that for the adsorption on a perfect 2-dimensional surface ($\approx$ 14 kJ mol^{-1}). Furthermore, simulation studies [53] have shown that for the adsorption of nitrogen in larger micropores (or supermicropores), above 0.7 nm in diameter, a two-step process may occur. The first step would seem to correspond to the coverage of the pore walls, whereas the second step is the filling of the void space. It would thus seem possible that the region BC corresponds to the coverage of the pore walls. The fact that this

step is not completely horizontal, in comparison to the adsorption on a 2-dimensional graphite surface, may be due to curvature effects within the micropores.

• Taking into account the above-mentioned hypothesis, it would seem that the region CD corresponds to the completion of the filling of the larger micropores.

Clay samples in general can also be considered relatively heterogeneous. However, often the differential energy curves indicate both heterogeneous and relatively homogeneous regions. One example is that of kaolinite which has a 1:1 sheet structure with a layer repeat distance of 0.72 nm. This is approximately the distance of the sheets themselves, which means that there is insufficient space to accommodate intercalated molecules such as water. The isotherms obtained for such materials are of Type-II which are typical for non-porous or macroporous materials.

The differential enthalpy curves for argon and nitrogen (Figure 26) [54] show two main regions. The first, AB, corresponds to the adsorption on defect sites and the adsorption on lateral facets of the materials. These high energy domains provoke an enhanced interaction with the nitrogen quadrupole. The second region, CD, corresponds to the adsorption on more energetically homogeneous basal planes. Such calorimetric measurements are thus a simple means to estimate the proportion of lateral and basal planes of such materials as well as the effect of grinding.

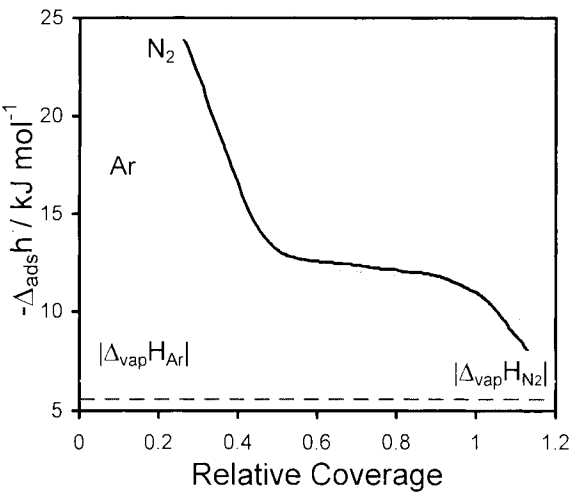


Figure 26. Enthalpies of adsorption with respect to relative coverage at 77.4 K for nitrogen and argon on kaolinite (after [54]).

The palygorskites are fibrous clay minerals. Attapulgite and sepiolite are two members of this family which both contain structural micropores. Their structures comprise of talc-like layers arranged quincuncially, forming microporous channels of rectangular cross-section parallel to the longitudinal axis of the crystals [55]. Whilst attapulgite has a pore section of 0.37 x 0.64 nm^2, the section of sepiolite is of 0.67 x 1.34 nm^2. The pores contain $Mg(OH_2)_2$ groups situated in the structural micropore walls.

The differential enthalpy curves obtained for the adsorption of nitrogen on sepiolite and attapulgite at 77.4 K are shown in Figure 27 [55,56]. Two separate domains can be observed for each of these curves. The first, domain, AB (Figure 27), is quasi-horizontal which is characteristic of adsorption in highly homogeneous regions. This would seem to correspond to the adsorption within the intrafibrous micropores containing the $Mg(OH_2)_2$ groups.

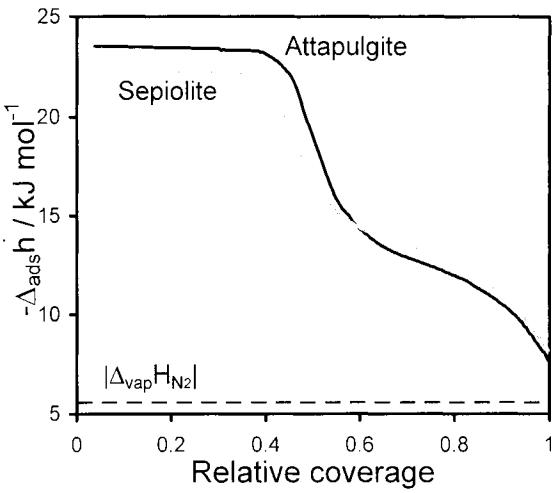


Figure 27. Enthalpies of adsorption with respect to relative coverage at 77.4 K for nitrogen on attapulgite (a) and sepiolite (b).

The second domain corresponds to the end of any micropore filling in the adsorption isotherms. The differential enthalpy curves in this region, CD (Figure 27), correspond to a decrease towards the enthalpy of liquefaction. This is characteristic of more energetically heterogeneous regions. It would seem that such regions are found between the fibres. Thus this would seem to correspond to adsorption in these interfibrous micropores.

5.3. Adsorption calorimetry for the characterisation of homogeneous adsorbents

As has been seen above for the case of attapulgite and sepiolite clays, the presence of energetically homogeneous regions within an adsorbent material will often lead to a near horizontal region in the differential energies of adsorption vs. coverage curves. A typical homogeneous non-porous solid is graphite. Indeed the hexagonally ordered carbon of graphite can be considered as a model surface. For the adsorption of nitrogen on graphite, the coverage of the surface is accompanied by a slight increase in differential energy of adsorption (compare Figure 20) which would translate into the addition of homogeneous gas-solid interactions and increasing gas-gas interactions.

Fullerene nanotubes can be considered as a homogeneous porous carbon material. An example of adsorption measurements is given in Figure 28 [57]. Here, two main regions can be distinguished. It is well known that such nanotubes are closed at each end, hence blocking any inherent microporosity. Moreover, these nanotubes arrange themselves into bundles with a porosity of around 0.3 nm between the fibres. This latter porosity should thus be inaccessible.

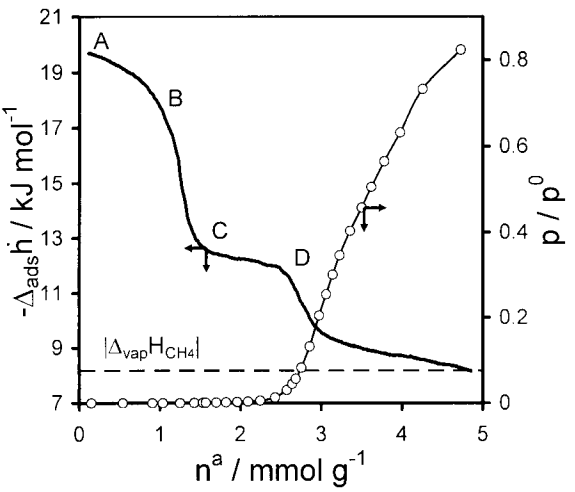


Figure 28. Enthalpies of adsorption and relative pressures as a function of quantity adsorbed at 77.4 K for methane on carbon nanotubes [57].

The first step (AB, Figure 28) may be explained by the filling of a small percentage of *unblocked* nanotubes. According to the preparation mode, the quantity of unblocked pores can be in the region of 20%. The second region,

BC, would thus seem to be the formation of a monolayer on the external surface of these nanotubes.

From the applications point of view, zeolites and related materials (aluminophosphates, gallophosphates ...) are interesting materials. The synthesis of such materials can be adjusted to give a wide range of crystal structures and an almost infinite variety of chemical compositions make it possibile to tailor-make samples for specific applications.

From a fundamental point of view, the regular pore systems can be indexed by X-ray diffraction and the structure can be elucidated using Riedvield refinement-type methods for example. The zeolite family of materials are thus ideal for the understanding of adsorption phenomena. It is the knowledge gained by such studies, using thermodynamic methods (manometry, calorimetry ...), complemented by structural methods (neutron diffraction, X-ray scattering ...), which permits, by analogy, the interpretation of adsorption phenomena in more disordered systems. Simulation studies are essential to complete the fundamental understanding.

However, the regularity of the channel systems can lead to distinct adsorption phenomena due to the confinement in such homogeneous systems. Nevertheless, a fine example of the adsorption in an energetically homogeneous solid is given in Figure 29.

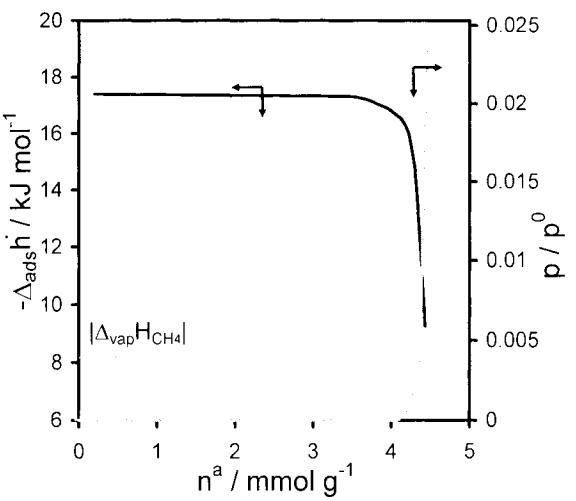


Figure 29. Enthalpies of adsorption and relative pressure as a function of quantity adsorbed at 77.4 K for methane on silicalite-I [58].

The behaviour shown during the adsorption of methane on silicalite at 77.4 K (Figure 29) can be considered almost model. The quasi-horizontal calorimetric signal, corresponding to the entire micropore filling region, would seem to be the result of adsorbent – adsorbate interactions only. One would expect a certain contribution due to adsorbate – adsorbate interactions, however this would seem to be minimal due to the reduced possibility of such interactions taking place in such a quasi-1D pore system.

The chemistry of such systems can also be probed by adsorption calorimetry and the adsorption enthalpies at zero coverage can be compared as shown in Figure 30.

The adsorption of various simple gases was studied on a series of hydrogen-exchanged ZSM-5 zeolites with different Si/Al ratios. The enthalpies at zero coverage are plotted as a function of the Si/Al ratio in Figure 30. It can be seen that for non-specific gases, such as methane, argon and krypton, there is little change in adsorption energy. For nitrogen (quadrupole) and carbon monoxide (dipole) with a permanent electric moment, a distinct variation in interaction energy is observed. Indeed, an increase in Si/Al ratio results in a decrease in the content of the compensation cation (H^+). The cations within the structure can be considered specific adsorption sites.

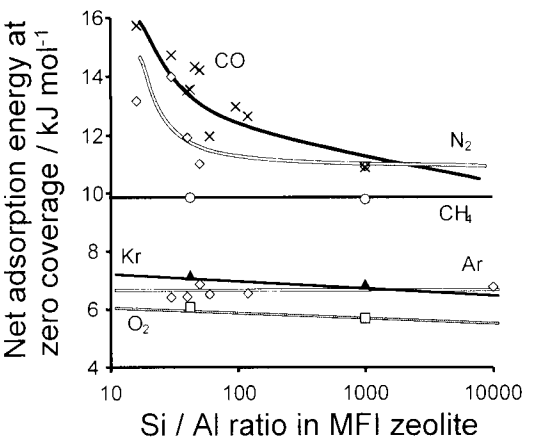


Figure 30. Adsorption energies for different probe molecules as a function of the Si/Al ratio for various HZSM-5 zeolites.

5.4. Adsorption calorimetry for the detection of adsorbate phase transitions

The adsorbed gas can sometimes be highly influenced by the homogeneity of the surface with which it is in contact, for example for nitrogen adsorption on graphite (Figure 20) in which the nitrogen forms an epitaxial film on completion

of the surface monolayer. Even more surprising phenomena can occur during adsorption on some zeolites and aluminophosphates, for example silicalite and $AlPO_4$-5.

Figure 31 highlights the rather interesting adsorption behaviour that can be observed for the adsorption of nitrogen on silicalite at 77 K. The adsorption isotherm exhibits two substeps, α and β. The initial pore filling, however, results in a differential curve which is not completely horizontal. An initial decrease would seem to indicate an enhanced interaction, possibly with defect sites. This curve then increases again which seems to be characteristic of increasing adsorbate – adsorbate interactions.

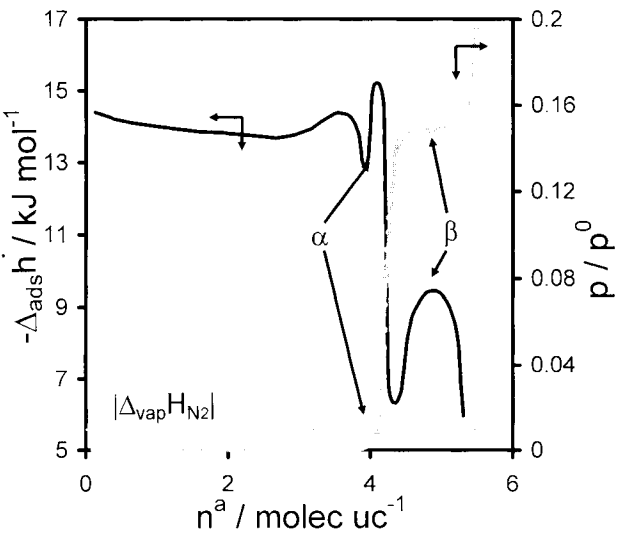


Figure 31. Differential enthalpies of adsorption and relative pressure as a function of quantity adsorbed at 77.4 K for nitrogen on silicalite [61].

The substeps in the isotherm correspond to marked differences in the differential enthalpy curves. Although this second substep, β, was observed in the isotherm prior to any microcalorimetic measurements [59,60], the first substep, α, was initially observed in the calorimetric curve [61]. A complementary study by neutron diffraction was carried out on this system [61]. The first substep, α, was concluded to be due to an ordering of the adsorbate from a fluid phase to a network fluid. The second substep, β, would seem to correspond to an adsorbate phase transition similar to that previously observed

for argon [58], characterised by a network fluid to a "solid-like" adsorbate phase.

Much research has been done into the synthesis of zeolite-like materials with framework species other than silica and alumina. The first family of materials that resulted from this research were the aluminophosphate molecular sieves. Thus $AlPO_4$-5 5 [62] has a unidirectional pore system consisting of parallel circular channels of 0.73 nm in diameter. $AlPO_4$-5 has a framework which, like silicalite-I, is theoretically globally electrically neutral, although the pore openings are slightly larger than those of the MFI-type zeolites. These characteristics make $AlPO_4$-5 an excellent structure for fundamental adsorption studies.

For $AlPO_4$-5, the adsorption isotherms of argon and nitrogen traced up to a relative pressure of 0.2 are indistinguishable (Figure 32). Methane adsorbs significantly less, suggesting a different pore filling mechanism.

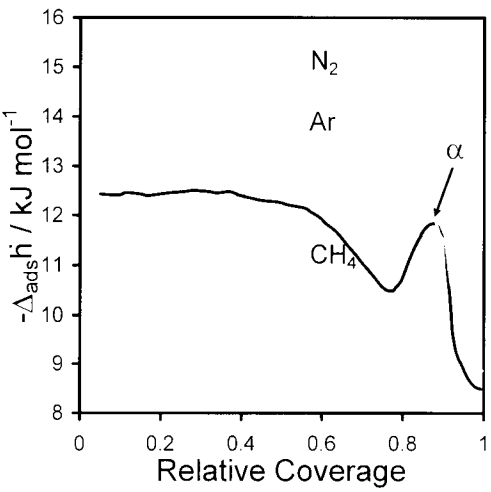


Figure 32. Differential enthalpies at 77.4 K for nitrogen, argon and methane adsorbed on $AlPO_4$-5 [63].

For the adsorption of methane, an exothermic peak (noted α in Figure 32) is observed in the differential enthalpy curve, which would seem to correspond to an energetic term ≈ RT. This could indicate both a variation of mobility and a variation of the adsorbed methane phase. A complementary neutron diffraction study [64] indicated that the behaviour of the methane adsorbed phase is unusual. The methane appears to undergo a transition between two solid-like phases. The first "solid-like" phase corresponds to the adsorption of 4 molecules

per unit cell, whilst the second phase corresponds to an increase in the amount adsorbed to 6 molecules per unit cell.

This could be a result of a favourable dimensional compatibility between the methane molecule and $AlPO_4$-5 micropore, permitting, from a spatial point-of-view, the appearance of two relatively dense phases. This hypothesis is supported by simulation studies [65].

5.5. Adsorption calorimetry to follow the various stages of micropore filling

For some systems, the different stages of micropore filling can be followed by adsorption calorimetry, for example for large-pore zeolites a two-step filling process can be observed.

The 5A zeolites consist of regularly spaced spherical cages of 1.14 nm in diameter. These cages are linked to each other by six circular windows of about 0.42 nm in diameter. The negatively charged silico-aluminate framework requires compensation cations. For zeolite 5A, these exchangeable cations are generally a mixture of calcium and sodium.

The 13X zeolite, or faujasite, has very similar primary building blocks to the 5A zeolites. For 13X however, the spherical cages are 1.4 nm in diameter and they are linked to each other by four circular windows of about 0.74 nm in diameter. The exchangeable cations are generally sodium (NaX).

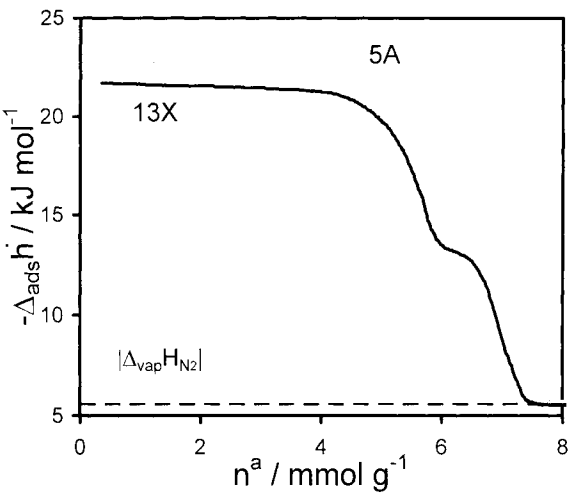


Figure 33. Differential enthalpies of adsorption and relative pressure as a function of quantity adsorbed at 77.4 K for nitrogen on 5A and 13X zeolites [66].

A study of the adsorption of nitrogen at 77 K on 5A and 13X zeolites using quasi-equilibrium, isothermal, adsorption microcalorimetry experiments at 77K [66] detected a step in the differential enthalpies of adsorption, towards the end of micropore filling (Figure 33). At the time, this was interpreted as a consequence of specific adsorbate - adsorbate interactions. Recently, however, in the light of other microcalorimetry studies, this change in signal has been interpreted as a possible phase change within the cavities [66]. This latter study detected the same phenomenon for a number of other probe molecules, including argon, methane and carbon monoxide. A second explanation is could simply be that the cages are filled in two steps : near the walls, prior to complete filling.

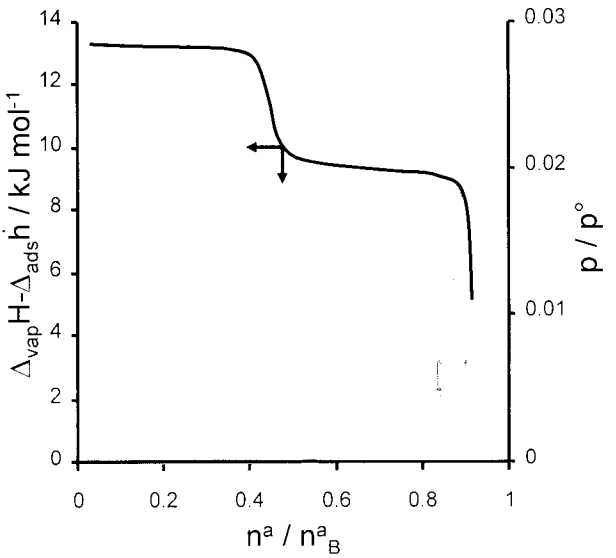


Figure 34. Differential enthalpy (black) and isotherm (grey) for the adsorption of carbon monoxide on $AlPO_4$-11 at 77 K.

For adsorption on $AlPO_4$-11 an unusual pore filling mechanism can be observed using adsorption calorimetry. $AlPO_4$-11 has a rectilinear pore system similar to that of $AlPO_4$-5. However the cross-section of the pores is elliptical (0.39 x 0.63 nm^2). The adsorption of a number of probe molecules occurs in two distinct steps as is indicated in Figure 34 [67,68]. From the form of the differential enthalpy curve, each step would seem to correspond to a relatively homogeneous filling process. Complementary neutron diffraction experiments showed that the coefficient of diffusion for the first step is around $1/10^{th}$ of that

in the second step [67,68]. This is contrary to the expected behaviour where the coefficient of diffusion decreases with increasing adsorbate loading.

In this example, however, the adsorbate is initially situated in the most curved part of the elliptical pore. The curvature acts as a very strong adsorption site, but about 50% of the porosity remains unfilled. In the second adsorption step, the initial adsorbate molecules have to be dislodged to allow the complete filling of the micropores.

5.6. Adsorption calorimetry in capillary condensation

As seen above, adsorption calorimetry is of value for examining specific interactions with a surface, or for microporous samples. In general, capillary condensation in mesoporous samples is associated with the enthalpy of liquefaction of the adsorbate fluid. For very well-ordered mesoporous samples, such as MCM-41, a small increase in the enthalpy of adsorption is observed during capillary condensation with respect to the liquefaction energy [69,70].

This is shown in Figure 35 for methane adsorption on an MCM-41 sample of 4 nm pore diameter. The initial adsorption leads to an enthalpy curve typical for silica (compare with Figure 23). The capillary condensation within the mesopores is accompanied by a slight increase of around 0.5 to 1 kJ mol^{-1}.

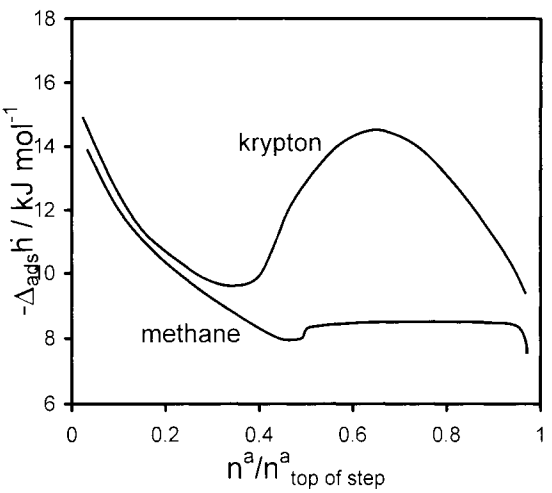


Figure 35. Differential enthalpy of adsorption as a function of coverage for methane and krypton on MCM-41 at 77 K.

Krypton adsorption on MCM-41 at 77 K shows a similar behaviour to that of methane. However, the mesopore filling process is accompanied by a

surprisingly strong heat effect [69,70]. Complementary experiments suggest that the krypton is adsorbed within the mesopores in a solid-like state. Indeed for samples of such pore size, krypton within the mesopores undergoes a liquid-solid transition at around 83 K [71].

REFERENCES

1. W. D. Harkins, G. Jura, J. Am. Chem. Soc., 66 (1944) 1362.
2. S. Partyka, F. Rouquerol and J. Rouquerol, J. Coll. Interf. Sci., 68 (1979) 21.
3. W. D. Harkins, The Physical Chemistry of Surface Films, Reinhold, New York, 1952, p.275.
4. J. J. Chessick and A. C. Zettlemoyer, Adv. Catal., 11 (1959) 263.
5. Y. Grillet and P. L. Llewellyn, in "The surface chemistry of silica", (Ed. A .P. Legrand), Wiley, Chichester, 1998, Ch.2, p.23.
6. R. Denoyel, J. Fernandez-Collinas, Y. Grillet and J. Rouquerol, Langmuir, 9 (1993) 515.
7. H. F. Stoeckli, P. Rubstein and L. Ballerini, Carbon, 28 (1990) 907.
8. C.G. de Salazar, A. Sepùlveda-Escribano and F. Rodrìguez-Reinoso, Stud. Surf. Sci., Catal., 128 (2000) 303.
9. D. H. Everett and J. C. Powl, J. Chem. Soc. Faraday Trans. 1, 72(3) (1976) 619.
10. J. J. Chessick, G. J. Young and A. C. Zettlemoyer, Trans. Faraday Soc., 50 (1954) 587.
11. J. A. G. Taylor, Chem. Ind., (1965) 2003.
12. J. Rouquerol, P. Llewellyn, R. Navarrete, F. Rouquerol and R. Denoyel, Stud. Surf. Sci. Catal., 144 (2002) 171.
13. A. Y. Fadeev and V. Eroshenko, J. Coll. Interf. Sci., 187 (1997) 275.
14. V. Eroshenko, R. C. Regis, M. Soulard and J. Patarin, J. Am. Chem. Soc., 123 (2001) 8129.
15. V. Eroshenko, R. C. Regis, M. Soulard and J. Patarin, Comptes Rendus Physique, 3 (2002) 111.
16. F. Gomez, R. Denoyel and J. Rouquerol, Langmuir, 16 (2000) 4374.
17. D. H. Everett, Trans. Faraday Soc., 57 (1961) 1541.
18. P. Kubelka, Z. Elekt. Ang. Phys. Chem., 38 (1932) 611.
19. M. Brun, A. Lallemand, J. F. Quinson and C. Eyraud, Thermochim. Acta, 21 (1977) 59.
20. J. Rouquerol, Thermochim. Acta, 144 (1989) 209.
21. V. I. Bogillo and P. Staszczuk, J. Thermal Anal. Cal., 55 (1999) 493.
22. V. Chevrot, P. L. Llewellyn, F. Rouquerol, J. Godlewski and J. Rouquerol, Thermochim. Acta, 360 (2000) 77.

23. J. Goworek, W. Stefaniak and A. Dąbrowski, Thermochim. Acta, 259 (1995) 87.
24. J. Goworek and W. Stefaniak, Colloids Surfaces A, 134 (1998) 343.
25. H. Naono and M. Hakuman, J. Coll. Interf. Sci., 145 (1991) 405.
26. J. Goworek and W. Stefaniak, Colloids Surfaces A, 80 (1993) 251.
27. J. Goworek, W. Stefaniak and M. Prudaczuk, Thermochim. Acta, 379 (2001) 117.
28. P. Staszczuk, J. Thermal Anal., 53 (1998) 597.
29. J. Goworek and W. Stefaniak, Colloids Surfaces A, 82 (1994) 71.
30. Z. Hubicki, J. Goworek and W. Stefaniak, Bull. Pol. Acad. Sci. Chem., 42 (1997) 169.
31. J. Goworek and W. Stefaniak, Thermochim. Acta, 286 (1996) 199.
32. J. Goworek and W. Stefaniak, Ads. Sci. Technol., 14(1) (1996) 39.
33. J. Rouquerol, S. Bordère and F. Rouquerol in Thermal Analysis in the Geosciences, (Eds W. Smykatz-Kloss and S. St. J. Warne), Springer-Verlag, Berlin, 1991, p.134.
34. F. Rouquerol, J. Rouquerol and K.S.W. Sing, Adsorption by powders and porous solids: principles, methodology and applications, Academic Press, London, New-York (1999).
35. J. Godlewski, A. Giordano, V. Chevrot, P. Llewellyn, F. Rouquerol and J. Rouquerol, CEA Technical Note N° DEC/SECA/LCG/98.003, June 1998.
36. M. J. Torralvo, Y. Grillet, F. Rouquerol and J. Rouquerol, J. Thermal Anal., 41 (1994) 1529.
37. P. A. Barnes, G. M. B. Parkes, D. R. Brown and E. L. Charsley, Thermochim. Acta, 269/270 (1995) 665.
38. F. Villiéras, L. J. Michot, G. Gérard, J. M. Cases and W. Rudzinski, J. Thermal Anal. Cal., 55 (1999) 511.
39. E. A. Fesenko, P. A. Barnes, G. M. B. Parkes, D. R. Brown and M. Naderi, J. Phys. Chem. B, 105 (2001) 6178.
40. L. J. Michot, F. Didier, F. Villiéras and J. M. Cases, Pol. J. Chem., (1997) 665.
41. J. Rivera-Utrilla, M. A. Ferro-Garcia, C. Moreno-Castilla, I. Baautista-Toledo and J. P. Joly, J. Chem. Soc. Farad. Trans., 91 (1995) 3213.
42. M. A. Ferro-Garcia, J. P. Joly, J. Rivera-Utrilla and C. Moreno-Castilla, Langmuir, 11 (1995) 2648.
43. J. Rouquerol in Thermochimie, Colloques Internationaux du CNRS, No.201, CNRS Ed., Paris 1972, p.537.
44. C. Letoquart, F. Rouquerol and J. Rouquerol, J. Chim. Phys., 70 (1973) 559.

45. Y. Grillet, F. Rouquerol and Jean Rouquerol, J. Chim. Phys., 7-8 (1977) 778.
46. J. Rouquerol, S. Partyka and F. Rouquerol, J. Chem. Soc. Faraday Trans. 1, 73 (1977) 306.
47. A. V. Kiselev, Doklady Nauk USSR, 233 (1977) 1122.
48. K. S. W. Sing, In Thermochimie, Colloques Internationaux du CNRS, No.201, CNRS Ed., Paris 1972, p.537.
49. K. S. W. Sing, D. H. Everett, R. A. W. Haul, L. Moscou, R. A. Pierotti, J. Rouquerol and T. Siemieniewska, Pure Appl. Chem., 57 (1985) 603.
50. P. L. Llewellyn, Y. Grillet, J. Rouquerol, C. Martin and J-P. Coulomb, Surf. Sci., 352-354 (1996) 468.
51. D. Atkinson, P. J. M. Carrott, Y. Grillet, J. Rouquerol and K. S. W. Sing in Proc. 2nd Int. Conf. on Fundamentals of Adsorption (Ed. A. I. Liapis), Eng. Foundation, New York, 1987, p.89.
52. A. P. Legrand, H. Hommel, A. Tuel, A. Vidal, H. Balard, E. Papirer, P. Levitz, M. Czerichowski, R. Erre, H. Van Damme, J. P. Gallas, J. F. Hemidy, J. C. Lavalley, O. Barres, A. Burneau and Y. Grillet, Adv. Coll. Interf. Sci., 33 (1990) 91.
53. M. Salameh, Ph.D. Thesis, Université d'Aix-Marseille I, 1978.
54. P. Brauer, H. R. Poosch, M. V. Szombathely, M. Heuchel, and M. Jarioniec in Proc. 4th Int. Conf. On Fundamentals of Adsorption (Ed. M. Suzuki), Kodansha, Tokyo, 1993, p.67.
55. J. M. Cases, P. Cunin, Y. Grillet, C. Poinsignon and J. Yvon, Clay Minerals, 21 (1986) 55.
56. Y. Grillet, J. M. Cases, M. François, J. Rouquerol and J. E. Poirier, Clays and Clay Minerals, 36 (1988) 233.
57. J. M. Cases, Y. Grillet, M. François, L. Michot, F. Villieras and J. Yvon, Clays and Clay Minerals, 39 (1991) 191.
58. M. Muris, N. Dufau, M. Bienfait, N. Dupont-Pavlovsky, Y. Grillet and J. P. Palmary, Langmuir, 16 (2000) 7019.
59. P. L. Llewellyn, J.-P. Coulomb, Y. Grillet, J. Patarin, H. Lauter, H. Reichert and J. Rouquerol, Langmuir, 9 (1993) 1846.
60. P. J. M. Carrott and K. S. W. Sing, Chem. Ind., (1986) 786.
61. U. Müller and K. K. Unger, Fortschr. Mineral., 64 (1986) 128.
62. P. L. Llewellyn, J.-P. Coulomb, Y. Grillet, J. Patarin, G. André and J. Rouquerol, Langmuir, 9 (1993) 1852.
63. S. T. Wilson, B. M. Lok, C. A. Messina, T. R. Cannan and E. M. Flanigen, J. Am. Chem. Soc., 104 (1982) 1146.
64. Y. Grillet, P. L. Llewellyn, N. Tosi-Pellenq and J. Rouquerol in Proc. 4th Int. Conf. On Fundamentals of Adsorption, (Ed. M. Suzuki), Kodansha, Tokyo, 1993, p.235.

65. C. Martin, N. Tosi-Pellenq, J. Patarin, J. P. Coulomb, Langmuir, 14 (1998) 1774.
66. V. Lachet, A. Boutin, R. J. M. Pellenq, D. Nicholson and A. H. Fuchs, J. Phys. Chem., 100 (1996) 9006.
67. F. Rouquérol, S. Partyka and J. Rouquérol in "Thermochimie", CNRS Ed., Paris (1972) p.547.
68. N. Dufau, P. L. Llewellyn, C. Martin, J.-P. Coulomb and Y. Grillet in Proceedings of Fundamentals of Adsorption VI, (Ed. F. Meunier), Elsevier, Paris, 1999, p.63.
69. N. Dufau, N. Floquet, J.-P. Coulomb, P. Llewellyn and J. Rouquerol, Stud. Surf. Sci. Catal., 135 (2001) 2824.
70. P. L. Llewellyn, C. Sauerland, C. Martin, Y. Grillet, J.-P. Coulomb, F. Rouquerol and J. Rouquerol in Proceedings of Characterisation of Porous Solids IV, Royal Society of Chemistry, Cambridge, 1997, p.111.
71. P. L. Llewellyn, Y. Grillet, J. Rouquerol, C. Martin and J.-P. Coulomb, Surf. Sci., 352-354 (1996) 468.
72. J.-P. Coulomb, Y. Grillet, P. L. Llewellyn, C. Martin and G. André in Proceedings of Fundamentals of Adsorption VI, (Ed. F. Meunier), Elsevier, Paris, 1999, p.147.

Handbook of Thermal Analysis and Calorimetry. Vol. 2: Applications to Inorganic and Miscellaneous Materials
M.E. Brown and P.K. Gallagher, editors
© 2003 Elsevier B.V. All right reserved.

Chapter 2

THE APPLICATIONS OF THERMOANALYTICAL TECHNIQUES TO THE PRESERVATION OF ART AND ARCHAEOLOGICAL OBJECTS

Marianne Odlyha

Birkbeck College, University of London, Gordon House, 29 Gordon Square, London WC1H 0PP

1. INTRODUCTION

This chapter describes the contribution of thermoanalytical techniques to the preservation of art and archaeological objects, and focuses on the work performed within the research area "Research for Protection, Conservation and Enhancement of Cultural heritage" which is supported by the European Commission Environment and Climate Programme. Part of this work was reported in a recent special edition of Thermochimica Acta on the Preservation of Cultural Heritage [1]. As the name of the research area suggests, the work focuses on the preservation of art objects that are housed in museums and galleries. To ensure their preservation, environmental conditions surrounding the objects are monitored and attempts made to estimate the overall damage that can occur to the objects through the synergistic action of light, fluctuations in relative humidity and temperature, and pollutant gases. At the same time attention is also directed to the condition of the object. To understand the degradation processes which are occurring, it is essential to characterise the materials of which the object is composed and any of the alteration products. These activities are part of a research area referred to as conservation science.

Before a description of the work is given, some attention is directed to how conservation science evolved. Concern for the appearance of the objects has led in the past to treatment of the objects to improve their appearance. In the conservation of paintings in the mid 19th century, public concern about the appearance of paintings in the collection at Schloss Schleissheim in Bavaria provided an opportunity for an interaction between scientists and curators. Professor Pettenkofer found a solution to the bloom or blanching that occurred on the paintings by placing them into containers over alcoholic vapours to

regenerate them. This appeared to improve the appearance of the paintings but in recent times concern has been expressed over the long-term effects on the layer structure of the paintings [2]. Towards the end of the 19th century, the Rathgen laboratory in Berlin was established for the characterisation of art and archeological objects. In this chapter a brief description of how conservation science evolved in the British Museum and the Tate will be presented, because the author has collaborated on some projects with the Conservation Departments in these institutions. The British Museum has employed scientists to investigate the deterioration and conservation of the collection since 1919 and, in 1922, a research laboratory was established at the museum [3]. The breadth of work undertaken gave rise to one of the first comprehensive texts on conservation [4]. This text illustrated that, in order to understand the processes of deterioration, it was necessary to know what the objects were made of and the nature of the alteration products. The conservator has to deal with objects which have already deteriorated and objects where previous conservation treatment, such as with adhesives or consolidants, has started to fail.

In the 1970s there was considerable interest in new materials amongst the conservators and schemes were developed by conservation scientists in the Conservation Department of the British Museum for systematic evaluation of conservation materials involving accelerated ageing regimes. A comparison of naturally aged samples with artificially aged samples has provided useful information on the stability of cellulose nitrate adhesive [5]. Through the introduction of this approach it is possible to ensure that materials used on the objects are long lasting and will not damage the object [3]. Attention is also directed to preventive conservation strategies where the aim is to optimise the microclimate, i.e environmental conditions surrounding the object, with a view to retarding the extent of deterioration and thus prolonging the lifetime of the objects. A standard procedure was developed for monitoring collections in showcases [6] and this is in place in the British Museum for screening their collections [7].

At the Tate, by comparison, conservation science is a recent addition to their activities [8]. The majority of the collection consists of paintings and sculpture from the 19th and 20th century. Studies have been performed on the canvas supports used in paintings [9], which included accelerated ageing tests and also a study of the response of mechanical properties of canvas to environmental conditions [10]. Characterisation of artists' materials of the 19th century, in particular those of Turner [11], and then later 20th century media [12], have formed the basis of two important projects. The Tate Conservation Department is also in the unique situation that they have the opportunity of preventing damage to newly created and acquired works. In addition to research and

analysis, handling, packing and transport, glazing and framing, and display are also areas where conservation science plays a part [8].

The training of conservators takes place at institutions such as the Courtauld Institute of Art in London [13]. This was established in the 1930's and a three year postgraduate Diploma in the Conservation of Easel Paintings is offered in which students, under supervision, undertake historical and scientific investigations of paintings, which influence their decisions about their subsequent conservation treatment and display. Another location for the training of conservators is the School of Conservation in Copenhagen. It was established in 1973 when the parliament in Denmark decided that the preservation of national cultural heritage should take place on a scientific basis [14]. It provides training of conservators in a wide range of activities, which includes the preservation of historic collageneous materials. These two institutes are mentioned because the author has previously collaborated in projects and, in the latter case, still continues with the project on Improved Damage Asssessment of Parchment (IDAP) supported by the European Commission.

So what is conservation science, also referred to as conservation-restoration science? It can be defined as the art and science of prevention and treatment of the decay of objects of cultural heritage, where the word 'art' refers to practical skill [14]. The very complex nature of the field of conservation of objects is described by Feller [15]. The object, with all its complexity of material constituents, is the basis of conservation-restoration science. On display or in storage it is subject to a complicated mixture of deteriorative physical and chemical processes The path and type of the deterioration is determined by the nature and combination of the materials which make up the object and the type and degree of environmental action on them. It is recognised that the development of conservation and restoration methods and materials should be based on scientifically acquired knowledge of these factors. Furthermore, proper diagnoses should be made, based on the results of analysis to determine the nature and extent of deterioration, and from this the appropriate methods and materials for conservation and restoration should be selected and developed.

The objectives are to improve methods of conservation-restoration and in doing this to improve access to cultural heritage and its information.

What is then the role of thermoanalytical techniques in this complex area of investigation? If we consider that natural and synthetic polymers constitute a large proportion of materials used in objects and their conservation, then it is evident that thermoanalytical techniques can contribute to this area of activity. The following aspects of thermal analysis in polymer science appear to be relevant: the measurement of thermal properties including thermo-oxidative stabilities of polymers and polymer-composite materials, which can be used for their characterisation, also for the evaluation of age-related and environmental

changes [16], and the measurement of glass-transition temperatures (T_g) and predictions of how these values vary with natural ageing and environmental factors. With respect to the latter, the significance of the glass-transition temperature in conservation has been discussed with reference to the profound effect it has on the many physical properties of polymeric conservation materials [17]. Later it was also demonstrated that the effect on T_g of conservation treatment and variations in relative humidity could be measured using thermomechanical and dielectric techniques [18]. In recent times the introduction of micro-thermal analysis [19,20] opens the path for non-invasive investigation of (a) the topography, which could be used to detect changes in the surface of objects during cleaning and this can include laser cleaning of objects, a technique which is being widely explored on a range of objects including parchment, (b) individual layers of a sample from an object mounted in cross-section and where there is interest in the softening temperatures of the individual layers. Some preliminary studies will be included in the final section of this chapter. Though emphasis has been placed on thermal analysis and polymer science and the transfer of this to conservation science, it needs to be mentioned that metallic and ceramic objects are not excluded and some examples will be discussed in this chapter. This chapter then advocates, on the basis of case studies described, integrating the area of thermal analysis within conservation science research.

The person who pioneered the application of thermoanalytical techniques to cultural heritage has been Professor Hans G. Wiedemann and he has demonstrated that these techniques can provide information on a wide range of artefacts and on the ancient technologies which produced them [21,22]. In one of his publications [23], amongst other things, he describes the use of thermogravimetry (TG) for the synthesis of the pigment, Egyptian blue $CaCu(Si_4O_{10})$, from the raw materials malachite, calcite, silica and borax. He was then able to compare the synthesised material with the blue pigment from the bust of Nefertiti to prove that the blue pigment of the bust was indeed the crystalline compound $CaCu(Si_4O_{10})$ and not a blue glassy frit as previously assumed. Egyptian blue is one of the first synthetic pigments It was invented and used in ancient Egypt a thousand years BC. In this way Wiedemann demonstrated that TG could be used to reproduce ancient technology and assist in characterising the historical pigment. He has also used differential scanning calorimetry (DSC) and thermomechanical analysis (TMA) to characterise samples from various ancient papyri, and Egyptian bronzes (Late Period, 700 BC). The nature of transitions observed is related to the age and the nature of the materials used. He also demonstrated that DSC could distinguish between ancient silk fabrics which had been discovered some 300 years earlier in tombs

(475-221 BC). Differences between these curves were considered to be due to environmental effects which had altered the composition of the silk fabrics.

2. CHARACTERISATION OF ART AND ARCHAEOLOGICAL OBJECTS BY THERMAL ANALYSIS

2.1. General considerations

Thermoanalytical techniques provide a convenient method for characterising materials and for monitoring their response to temperature, stress and environmental factors and the examples in this chapter demonstrate their application to the area of historical materials. Sample size is one of the major problems when working with historical materials because it is obviously limited. Sampling also relies on the fact that the conservation history of the object is known and that sampling is avoided from areas which may have traces of materials used in the previous conservation treatment of the object.

Due to limited sample size it is frequently not possible to make more than one measurement on the actual sample. For this reason, it is generally useful to have readily available un-aged samples of similar composition to the material being tested, which can be used to optimise instrument and sample response before measuring the historical samples. The heating rate, sample size, and atmosphere will have major effects on the resulting thermal curves. Some archival material from previous conservation treatment has been made available for research purposes. In a study of canvas-supported paintings, 19th century loose linings, which were removed from previous conservation treatment, were made available to the author's laboratory and this enabled measurements to be made using dynamic mechanical thermal analysis (DMTA), discussed in Section 3.4.1.

In addition, it is frequently important to know the response of materials to relative humidity variations. This testing was performed by exposing samples to selected relative humidity environments for set periods of time and then removing them for measurement by DMTA [24]. Sample transfer was made rapidly to minimise loss in moisture content and the sample was usually enclosed in a protective oil coating to retain its moisture content At a later stage, the DMTA instrument was modified to allow direct immersion of objects in a selected environment during measurement [25]. Recently a DMTA instrument has been further modified to take a custom-built RH/temperature control system. [26]. This system is currently being used to measure the response of naturally aged parchments (EC project IDAP "Improved Damage Assessment of Parchment") and wool and silk fibres from historical tapestries (EC project Monitoring of Damage to Historical Tapestries). Some of the data are discussed in Section 3.5.3.

Complementary to studies on archival material, un-aged samples of similar composition and prepared according to known historical recipes are also analysed to improve the understanding of the mechanisms of degradation processes. This has the advantage that sample size is not limited and that samples can be subjected to accelerated ageing, involving enhanced levels of light, pollutant levels, and varying levels of relative humidity and temperature. This approach has become part of preventive conservation studies, in particular in the context of recent projects supported by the European Commission. The aim of one of these projects (MIMIC Microclimate Indoor Monitoring in Cultural Heritage Preservation, http://iaq.dk/mimic) is to develop damage dosimeters for testing the microclimate of objects. The rationale for this project is based on the outcome of an earlier one "Environmental Research for Art Conservation "(ERA) where the idea was to prepare paint-based dosimeters according to known historical recipes and to use the physicochemical changes measured in these dosimeters to assess the quality of indoor environments in museums and galleries [27].

2.2. Thermoanalytical techniques

The techniques which have been used in the analysis of historical objects include the following:

2.2.1. Thermomicroscopy

Thermomicroscopy allows the observation of changes in the sample to be monitored at selected magnifications using an optical microscope during controlled heating of the sample [28]. For historical objects, thermomicroscopy has been used by the Tate Conservation Department (Section 3.1.1) for the characterisation of binding media in microscopic-sized samples taken from paintings and by the School of Conservation in Copenhagen (Section 3.1.2) for determining the denaturation temperatures of samples from leather objects and parchments.

2.2.2. Differential thermal analysis (DTA)

DTA is a technique in which the difference in temperature between the sample and reference pan is monitored against time or temperature while the temperature, in a specified atmosphere, is programmed. The first use of DTA (Mettler 2000B) on samples from actual paintings was made by Preusser [29] at the Doerner Institute, Munich, and included a study of Ruben's "Meleager e Atalante", where it was necessary to determine whether part of the painting was a later addition [30]. His overall conclusion was that DTA could be used to date oil-based paintings that were not more than 100 years old. The ratio of peak heights of exothermic peaks in the region of 300 and 400 °C was used as the

ageing index. Further work revealed the effect of additives on the exothermic effects observed and indicated that DTA could be used to characterise the binding media of paintings [31].

2.2.3. Differential scanning calorimetry (DSC)

DSC is a technique in which the difference in heat flow (power) to a sample and reference pan is monitored against time or temperature while the temperature, in a specified atmosphere, is programmed. In studies of ancient papyri, Wiedemann showed that the shape of the DSC curves was dependent on the age of the papyrus sheets and on the different treatments to which the papyrus had been subjected [23]. In samples from paintings, as was shown for DTA, age-related effects [32] could be observed and DSC could be used for the characterisation of media [33,34]. Differences in the nature of the drying oils used could also be detected in prepared samples of lead-white and oil-based paint [35].

*2.2.4. Thermogravimetry (*TG)

TG measures the mass loss during the decomposition of the sample as it is being heated, or if the sample is held at a selected temperature. In conservation science one of the applications of TG has involved the detection of calcium carbonate in ground layers of artworks [36,37], described in Section 3.3.3, and in cuneiform tablets [38], described in Sections 3.2.6 and 3.3.1. This information can also be used to provide information on the ancient techniques used. Apparently the protecting layers of mummy coffins (2575 BC-395 AD) from the Egyptology collection in Berne contain calcium carbonate [22]. TG has also been used to characterise historical parchments on the basis of their degradation characteristics [25], and is discussed in Section 3.3.5. With respect to conservation treatment of parchment, it has been used to quantify moisture loss and monitor rehydration processes in fire-damaged and desiccated parchments [39]. It has also been used to characterise the degradation of archival canvas support used in paintings [40], and the lime wood supports of old paintings [41], to monitor moisture sorption at selected relative humidity values in samples of old silk [21] and to determine the moisture sorption characteristics in paint films [42].

2.2.5. Thermomechanical analysis (TMA)

TMA is a technique in which the deformation of a substance is measured under a static or oscillatory load as a function of temperature, or at a selected temperature. TMA has been used to determine the thermal characteristics of terracotta sculptures from the Qin dynasty [21] and of cuneiform tablets [38]. In paintings conservation it has been used in compression mode to measure the

glass-transition temperature of prepared paint films, before and after treatment with aqueous and non-aqueous cleaning agents, to simulate the cleaning of paintings [43] and in studies of the effect of humidification on samples from paintings [44]. TMA under isothermal conditions has been used to determine the amount of swelling caused on wetting of papyrus [23].

2.2.6. Dynamic mechanical thermal analysis (DMTA or DMA).

In DMTA a sinusoidal force is applied at a particular frequency on a sample under a selected strain. The resulting measurement is of the complex mechanical modulus (E^*). This is then resolved into two components: E', the storage modulus, which corresponds to the energy stored in the material undergoing deformation and which derives its value from the elastic or stiffer components of the sample, and E'', the loss modulus, which corresponds to the energy dissipated during the deformation and which derives its value from the viscous or rubbery component of the sample.

The calculated ratio of these moduli, expressed as (E''/E'), is known as *tan* δ. This is frequently used as a measure of the glass-transition temperature, T_g, of the material. The technique was introduced into conservation science research with the aim of measuring the glass-transition temperature of prepared paint films and to assess the effect on the glass-transition temperature of paint films subjected to cleaning agents to simulate the cleaning of paintings [45]. The technique has also been used to characterise water-dispersed polymers used for conservation and restoration of cultural objects [46], and historical parchments (Section 3.5.2) [25].

2.2.7 Micro-thermal analysis (μ-TA)

Micro-TA combines the technique of atomic force microscopy (AFM) with thermal analysis to provide spatially resolved information on parameters such as the glass-transition temperature or softening temperature [19,20]. In the simplest form of conventional AFM, a sharp tip, located at the end of a *cantilever*, is scanned in the near field of a surface to produce high-resolution topographic images. Scanning is achieved by means of an array of piezo-electric crystals (the *scanner*). AFM probes are typically made of silicon or silicon nitride (Si_3N_4) and may have a tip radius of the order of 10 nm and a cantilever 100-500 μm long. As the tip is scanned across the surface, variations in the sample topography cause deflections (bending) in the cantilever. Usually, an optical detection system is used to magnify and measure these changes; a laser beam is reflected off the back of the cantilever and any changes in its position are recorded by a photodetector. This enables the forces acting between tip and sample to be monitored. The most common probe used for micro-TA is the Wollaston resistive thermal probe, which is capable of acting both as a temperature sensor

and as a heater This enables variations in local thermal conductivity (as well as topography) to be imaged in a lateral spatial resolution at the μm scale (scanning thermal microscopy – SThM) and localised thermal analysis (L-TA) to be carried out, typically on a few μm^3 of material. By monitoring the power required to maintain a temperature scan, a signal analogous to DSC is obtained (L-DSC or micro-DSC). Simultaneously, by monitoring the height of the cantilever, a signal analogous to TMA (L-TMA, micro-TMA), is acquired. Some preliminary measurements are described in Sections 3.6.1, 3.6.2 and 3.6.3 on historical parchments, tapestries and paint media.

3. CASE STUDIES

3.1. Thermomicroscopy

3.1.1. Paint media

Thermomicroscopy has been used by J.H.Townsend of the Tate Conservation Department for studying the thermal behaviour of artists' paint media from the late 18th and 19th centuries which include samples from paintings by Sir Joshua Reynolds (1723-1792), J.A.M. Whistler (1834-1903), and J.M.W. Turner (1775-1851) [47]. In the case of J.M.W Turner's "The Opening of the Wallhalla,1842", a low melting-point component was detected. This was later identified by Direct Temperature Resolved Mass Spectrometry (DTMS) as spermaceti wax. [48]. On the basis of knowledge of artists' palettes and materials available at the time, it is likely to be the original material used [47]. Turner's use of oil and resin mixtures, referred to as "megilp", are, however, not distinguishable by thermomicroscopy alone from oil paint with lead driers or oil with some resin added, though the groups are distinguishable from unmodified oil medium. Resin-rich lead acetate megilps have been found by DTMS in yellow glazes in "The Opening of the Wallhalla, 1842" [48]. The medium of these samples has darkened to brown, they tend to soften or melt in one or two stages between about 90 and 120 °C, and they darken when heated to 130-140 °C [46]. Low melting-point components were also present in samples from Whistler and Reynolds, but these were identified as alteration products which also had a low melting-point. Where there is no clear evidence of melting, the onset temperatures of the charring of media are used to characterise the paint media. Townsend has made an extensive study on samples from paintings and from existing artists' palettes [49].

Knowledge of the behaviour of paint media at temperatures up to 90 °C, where melting processes may occur (e.g of wax additives) and which may reveal sensitivity to temperature, is invaluable for assisting conservators in knowing

which temperature range they can safely use during conservation treatment of paintings. This is further discussed in section 3.4.1.

3.1.2. Historical collagen-based materials

R.Larsen, of the School of Conservation, Copenhagen, has used thermomicroscopy to measure the hydrothermal stability of vegetable-tanned leathers [50] and of parchment [51]. The method has shown that data correlate well with DSC studies [52]. The School of Conservation in Copenhagen introduced this approach and now it is routinely used to assess the condition of leather and parchment objects prior to conservation treatment. Samples (fibres 0.3 mg) from the corium (flesh side) of the parchment are wetted with demineralized water for 10 minutes on a microscope slide with a cavity. If oils, fats or waxes are present, these are removed by washing the fibre sample in acetone. Fibres are covered completely with distilled water and then heated on the hot stage (Mettler FP82) at 2 $^{\circ}$C/min. Shrinkage can be described in three temperature intervals : distinct shrinkage in individual fibres, shrinkage activity in one or more fibres which is followed by shrinkage in another fibre, and then where at least two fibres show shrinkage activity simultaneously and continuously The starting temperature of this main interval of shrinkage is the shrinkage temperature.

The rationale for measurement of shrinkage temperature is the concern for the state of collagen in parchment and its degree of gelatinisation. Earlier studies on the Dead Sea scroll parchments [53] showed that they had transformed into gelatin. This differs from the behaviour of vegetable-tanned leathers where powdering of fibres occurs. The fact that spontaneous shrinkage and gelatinisation may take place as a result of humid storage or water-based cleaning and conservation treatment makes thermomicroscopy particularly important as an early warning system to prevent irreversible fatal damage to cultural heritage objects.

3.2. Differential scanning calorimetry (DSC)

3.2.1. Paint media

As mentioned in Section 2.2.2, Preusser studied the thermal behaviour of samples from oil paintings in the late seventies at the Doerner Institute (Munich, Germany). This led to further work by the author, also using DTA, initially in collaboration with Burmester (Doerner Institute) [31]. Investigations confirmed that, in samples from oil based paintings, there was an age-related effect on the DTA curves for paintings up to 100 years old. The presence of mixed media affected the shape of the curves, as did certain pigments. The shape of thermal analysis curves from egg tempera paintings also differed considerably from

those of oil-based paintings [33] and work continued in collaboration with the Opificio Pietre Dure Florence, the Courtauld Institute of Art, London, and Tate Britain.

Samples were obtained from the 13th century painting "Madonna del Popolo" by Coppo di Marcovaldo (The Brancacci Chapel, Church of S.Maria del Carmine, Florence) during conservation treatment, in which egg tempera was identified in the presence of lead white (basic lead carbonate) pigment [33]. In a later 16th century painting by Francesco di Giorgio Martini, both egg tempera and a drying oil were identified in two different locations on the painting [33]. Figure 1 shows the DSC curves for these samples and the differences between the oil-based medium, used in the painting of a figure, where the dominant exothermic peak is in the region of 400°C, and the egg tempera based medium, used in the painting of the background, and where the dominant exothermic peak is in the region of
280 °C.

Samples from wall paintings of 16th century artists Federico Zuccari and Giorgio Vasari were also obtained during the restoration of Brunelleschi's dome of the Cathedral Santa Maria del Fiore, Florence. The resulting DSC curves (Figure 2) were complex to interpret, due to the presence of overlapping features from both the organic and inorganic components, and required additional techniques for their further characterisation [54]. The two lower curves are from the artist Vasari (red and pink pigmented areas) and the upper two curves are from the artist Zuccari (red and white pigmented areas). There is an indication of differences in the curves of the materials of the two artists.

The last exothermic peak occurs at higher temperatures for the Vasari samples (Figure 2), indicating that a more thermally stable material is present, which agrees with observations that the Vasari-painted areas were in a better state of preservation than some of the Zuccari-painted areas at the time of their restoration.

In Figure 2 the first peak (endothermic) in nearly all the curves consists of overlapping features and indicates that gypsum is present with calcium oxalate monohydrate. Dei has performed DTA studies on samples from the wall painting (Andrea da Firenze, X1V century) from the eastern wall of the Spanish Chapel in the Green Cloister of Santa Maria Novella in Florence [55]. In this paper he describes the quantification of gypsum in the presence of oxalate.

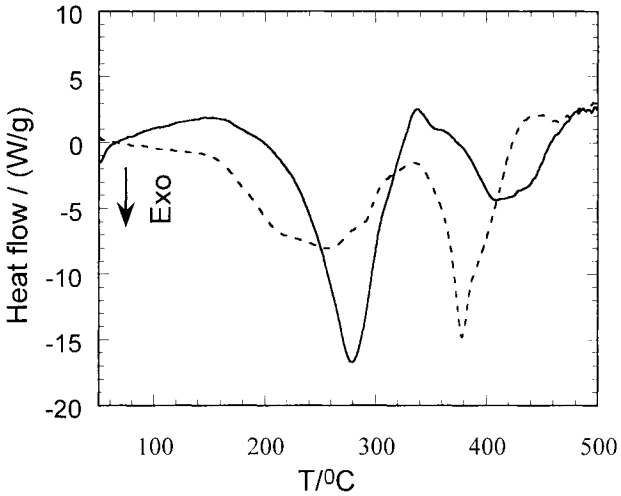


Figure 1. DSC oxidative degradation curves from two locations on the 16th century painting by F. di Giorgio Martini, egg tempera based medium (—) and oil-based medium (--) [33].

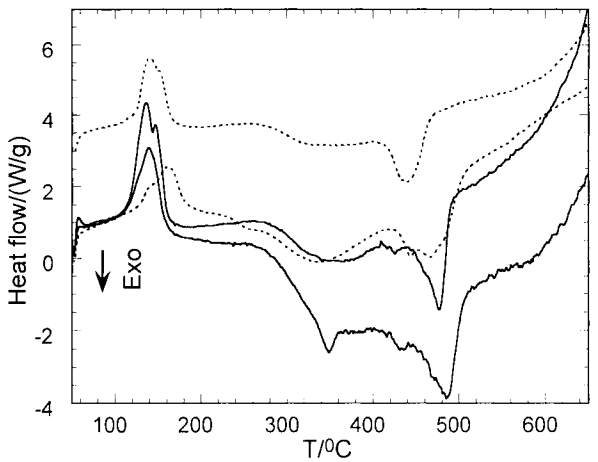


Figure 2. DSC oxidative degradation curves of samples from wall paintings (Brunelleschi's dome, Cathedral Santa Maria del Fiore, Florence), lower two Vasari (—) and upper two Zuccari (....).

In collaboration with the Technology Department of the Courtauld Institute of Art, samples were taken from paintings from various art historical periods during their conservation treatment and a database of DSC curves was established in the author's laboratory. These included mainly oil-based paintings on canvas and panel supports. DSC studies were performed on the paint media of Giovanni Bellini's "The Assassination of St.Peter Martyr" (16th cent. oil on panel, Lee bequest, Courtauld Institute Galleries [33]. Figure 3 shows the DSC curves resulting from white-pigmented areas from different locations of the painting.

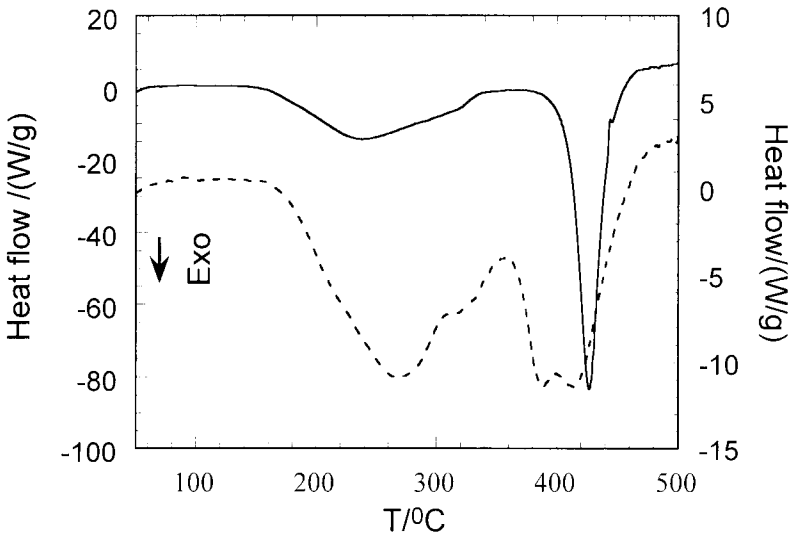


Figure 3. DSC oxidative degradation curves of samples from" The Assassination of St.Peter Martyr" G. Bellini (Venice c1430-1516) (Lee bequest, Courtauld Institute Galleries, London).

In the lower DSC curve of Figure 3, peaks are of smaller intensity and of a similar size; in the upper curve there is a very strong exothermic peak in the region of 400 °C. This indicates that DSC is a useful technique and is sensitive to differences in paint media.

Studies were also performed of the paint media in selected paintings by Stanley Spencer on display in Sandham Memorial Chapel, Hampshire, England. This is the property of the National Trust, England, Northern Ireland and Wales. The

aim was to characterise the materials used by Stanley Spencer with the view that this knowledge would contribute to an understanding of the cause of surface deterioration and whitish appearance which recurred in these paintings [56].

A study with the Tate Conservation Department involved Turner's "The Opening of the Wallhalla, 1842", on display together with other works by Turner in the Clore Gallery at Tate Britain, also discussed in Section 3.4.2. During its conservation treatment in the 90's samples were taken from nine locations during [57]. There was interest in understanding the materials used by Turner as his paintings suffer from wrinkled and cracked paint and discoloured glazes. DSC and mass spectrometric measurements were made on the samples [48]. DSC curves showed shapes inconsistent with those previously observed for oil as the major component of the paint media. Figure 4 shows the curve obtained from a yellow glaze taken close to the bottom edge of the painting, Figure 5. It is shown together with a sample prepared by the Tate Conservation Department containing one part oil to two parts resin mastic in oil of turpentine with lead acetate drier (megilp). There is close similarity between the curves, which indicates similarity in chemical composition. Further mention of this type of paint medium is made in Sections 3.4.2 and 3.6.3. Additional curve fitting and resolution of peaks in some of the other curves, together with known thermal stabilities of possible additions, e.g wax, resin and protein, allowed characterisation of the medium as being predominantly a drying oil with beeswax, resin and protein [57]. The pigment volume concentration also differed from what was expected for a drying oil and lead white. DTMS confirmed the presence of additives and identified the specific nature of the additives, such as spermaceti wax [48]. Thermomicroscopy also confirmed the presence of low melting-point components as mentioned in Section 3.1.1.

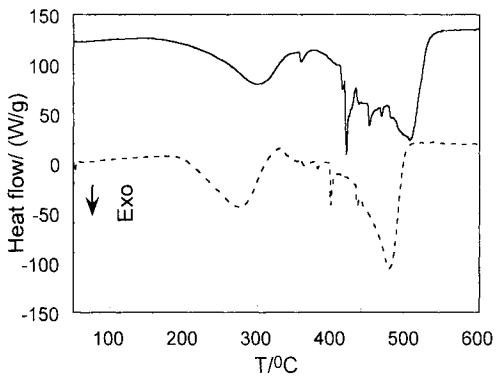


Figure 4. DSC oxidative degradation curves of yellow glaze from Turner's "Opening of Wallhalla,1842" (--) and from a prepared megilp sample (1:2 resin mastic in oil of turpentine with lead acetate drier. (—) [57].



Figure 5. Turner's "Opening of Wallhalla,1842" (with permission from the Tate, London).

DSC measurements were made using a Perkin Elmer DSC7 analyser. Sample mass varied between 0.10 and 0.5 mg, and for wall painting samples up to about 1.5 mg. Heating at a rate of 40 °C/min was performed in oxygen (60 cm^3/min). The mass loss and colour change were recorded after the experiment. Custom-made Pt micro-crucibles were used (5 mm ID). Samples were always taken from painted surfaces during conservation treatment and from areas of existing damage, if present. The upper layer of varnish was physically removed so that it did not contribute to the DSC curve. The majority of studies performed by the author have been made on lead white (basic lead carbonate) pigmented samples. The latter was chosen since it has been used over the centuries in combination with other pigments. Pigment type and pigment volume concentration have a significant influence on the resulting curve [58]. The formation of lead salts is of particular interest since recent studies of paint cross-sections, using imaging FTIR and ancillary methods, have identified "protrusions" which consist of lead soaps [59]. Their presence has been linked to the disturbance of the paint surface which causes paint loss.

3.2.2. Canvas support

DSC studies have been made on the canvas support used in paintings. The main constituent is cellulose, which is a linear polymer of anhydroglucopyranose units linked by β-1,4-glucosidic bonds. The molecule is an essentially rigid straight chain, where the arrangement is stabilised by hydrogen bonding between the hydroxyl groups on the chains of glucopyranose rings. To determine the effects of ageing, samples were heated in open aluminium crucibles from room temperature to 500 °C at 10 °C/min in a Shimadzu DSC-50. After the first heating from ambient to 150 °C, samples were allowed to cool and then re-heated from ambient to 500 °C. Degradation of new and artificially aged linen was found to be similar. Archival samples showed a depressed T_g and a lower degradation temperature, suggesting that chain scission had occurred by natural ageing [40].

3.2.3. "Mock" paintings for use as damage dosimeters

The task was to test the potential of an early warning system or risk assessment tool for paintings. The system used was a small test tempera painting. The main objective was to evaluate the extent of damage incurred by this test painting on exposure to various environmental conditions [27]. Samples of paint films were prepared and subjected to accelerated ageing. Prepared paint films were also exposed at different locations and then the effects of natural ageing were compared with those of accelerated ageing. Accelerated ageing involved exposure to enhanced intensities of light in the Tate Conservation Department light ageing box for selected periods of time (18,000 lux for periods of 2-64

days). Partial area measurements were made on the resulting DSC curves of lead white and smalt tempera (cobalt oxide) pigmented paint films. The amount reacted at selected temperatures was calculated for the differently aged samples and showed a systematic change in chemical composition with increasing levels of light exposure [60]. The resulting calibration graph allowed the degree of natural ageing to be expressed in terms of equivalents of light ageing. It was found that the effects of natural ageing after nine months' exposure in selected locations at the Rijksmuseum, El Alcázar, Segovia, Spain, and Sandham Memorial Chapel exceeded that of accelerated light ageing, even though periods of exposure for 64 days were calculated to be equivalent to 12 years at the recommended levels of museum exposure of 200 lux. Thus it was concluded that other factors, in addition to light, such as fluctuations in relative humidity, temperature and pollutant gases, contributed to the ageing process. In a current project "Microclimate Indoor Monitoring in Cultural Heritage Preservation" (MIMIC http://iaq.dk/mimic) the effect of exposure to pollutant gases is being examined. The kinetics of degradation of a prepared lead white tempera sample have been studied and parameters calculated. Using a computational method (AKTS-TA software) for solid-state kinetic analysis [61], the progress of the solid-state reaction was calculated under temperature conditions different from those at which the experiments were performed

The limitations of DSC are that it is not able to provide specific information at the molecular level. For the study of paintings, the use of additional spectroscopic and mass spectrometric techniques is required. Nevertheless DSC remains a technique which on very small sample size (0.1 mg) can provide information on the broad category of medium used (e.g oil or egg), the binder/pigment ratio (lean or medium rich) and, in some cases, information on the pigment type (e.g. lead white).

3.2.4. Historical parchment and leather

DSC has been used in the study of parchment and leather degradation [61] and the development of effective restoration treatment of fire-damaged parchment [39]. Degradation studies involved the measurement of denaturation temperatures *(T_d)* and corresponding enthalpies *(ΔH)*. The work is described elsewhere [61] but a brief description of the procedure used and the results and conclusions will be presented here. The denaturation temperature is defined as the temperature at which the transition from the triple helix in collagen to a randomly coiled form occurs, the process taking place in the domains between the cross-links. Measurements were made on samples that had been previously immersed in water for several hours, then hermetically sealed in aluminium crucibles. It was found that for leather, values of T_d were more significant than those of ΔH, whereas for parchment both parameters had to be looked at

carefully for an evaluation of the state of the material. An unchanged T_d value, if considered alone, can result in a false evaluation because, in certain cases, an accompanying decrease in ΔH denotes a re-arrangement of molecular structure, which is correlated with loss in mechanical strength. Crosslinking is probably responsible for this phenomenon, as it is for the hydrothermal behaviour of certain historical parchments, where high T_d values are associated with low ΔH, values. In studies of aged parchments by other authors [39], the main endotherm was attributed to the denaturation of less tightly cross-linked triple helices, while denaturation of the most cross-linked collagen triple helices produced the shoulder of the DSC signal at higher temperatures. Recently, to assist in understanding the ageing process, complementary studies have been made using small-angle X-ray scattering (micro-SAXS) and DMTA. A correlation was found between denaturation temperature and degree of crystallinity [62]. This is discussed in the dynamic mechanical thermal analysis section (Section 3.5.2).

3.2.5. Historical tapestries

Previous thermoanalytical studies on natural fibres [16] provide a useful background for current studies on naturally aged wool and silk fibres taken from historical tapestries. Samples from tapestries from collections of various Musea in Brussels, Bruges and Tournai, and the Royal Palace in Madrid are being analysed as part of the project "Monitoring Damage in Historical Tapestries" (MODHT). The aim is to assess the extent of alteration or damage to the physicochemical properties of wool and silk with ageing, and to define markers for assessment of damage in other tapestries. Previous studies using DSC, together with wide-angle X-ray diffraction, on wool fibres suggested that the change in the 230°C endothermic peak observed in wool fibres is due to the disappearance of the α-form of wool keratin on heating [64]. Recent DSC thermal degradation data of un-aged and light-aged (150,000 lux, 4 and 64 h) samples of wool in N_2 are shown in Figure 6. With light ageing the intensity of the peak at 230°C decreases. Preliminary measurements on one of the historic wool samples by micro-TA are reported in Section 3.6.2.

With respect to silk fibres, the intensity of the main DSC peak decreases with age. Figure 7 shows the decrease in intensity of the main peak from control sample to the light-aged sample and then the sample of historic yellow silk from the tapestry "Jupiter and Ganimedes" (1545) from the collection of the Royal Palace in Madrid. There are also appreciable differences between natural silk and other fibres from the tapestry which proved to be synthetic from a previous restoration (Figure 6).

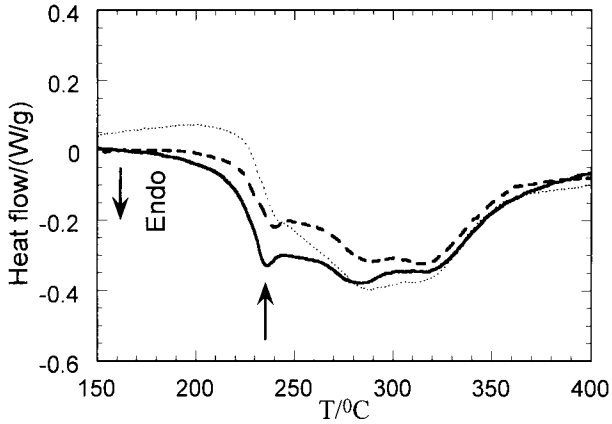


Figure 6. DSC thermal degradation endotherms (in N_2) of unaged (—) and light aged 4 hrs (--) and 64 hrs (....) samples of wool thread in N_2. With light ageing the intensity of the peak at 230 °C decreases.

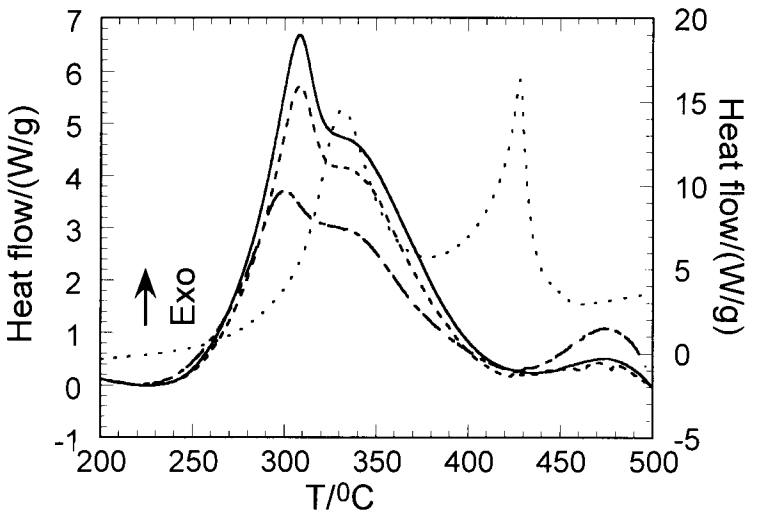


Figure 7. DSC oxidative degradation curves of control(—), light aged 64 hrs (--) and historical 16th century silk fibres, "Jupiter and Ganimedes" (Brussels 1545) collection Royal Palace in Madrid (— --), and synthetic fibre (...).

3.2.6. Cuneiform tablets

A collaborative project with the British Museum involved a study on cuneiform tablets. The British Museum holds a collection in excess of 120 000 of these tablets, which originated from 22 major sites [38]. They provide an unparalleled resource for scholars of the ancient Mesopotamian civilisation. Tablets were originally made by incising script and then drying in the sun. so the vast majority of the tablets do not have the robust properties associated with well-fired ceramic bodies. Also the soils of Mesopotamia (present day Iraq, northeast Syria and southeast Turkey) can contain very high concentrations of soluble salts and these have impregnated many of the tablets. The action of the salts contributes to the tablets' fragility. Scholars need to handle the tablets to decipher the text and, without conservation, the tablets' fragility precludes their study. Figure 8 shows an example of a cuneiform tablet from the collection where the script is clearly incised, and Figure 9 shows the problems in deciphering script in a low-fired fragment of cuneiform tablet. The latter originates from neo-Babylonian Mesopotamia, Iraq (South).

Conservation treatment at the British Museum has used the following firing schedule: heat from room temperature to 150 °C at 19 °C/h, hold at 150 °C for 48 h, heat from 150 °C to 740 °C at 50 °C/h, hold for 2 h, cool from 740 to 30 °C by switching the kiln off, and this takes 26 h. Firing can be followed by desalination. The aim of the present study was to re-examine the firing process. A simulation of the firing treatment was made using TG (Section 3.3.1). DSC was used to determine whether there were differences between clay types from the different sites. Multiple sets were sampled by drilling into broken surfaces and the samples were analysed. Multiple tablets from two sites, Sippar and Ur, were also analysed to determine the variation within the sites.Various known clay components were also studied, e.g. palygorskite, amphibole. The first group (Sippar) was characterised by an exotherm at 370°C (strong) followed by endotherms at 450°C (weak) and 520°C (strong). The Ur tablets, the second group, showed a weaker exothermic process and also a lower iron oxide content, and endotherms at 450 °C (weak) and 520 °C (strong). The Kanesh and Ninevah tablets, which formed the third group, were similar to Group 1 but showed a weaker exotherm at 370 °C followed by a strong endotherm at 450 °C. The final group of tablets, Larsa and Kutha, did not show any features below 520 °C, which probably indicates that these tablets had previously undergone some form of heating. Figure 10 shows how some tablets were also fired at the actual excavation sites before acquisition by the Museum.



Figure 8. Cuneiform tablet (copyright Trustees of the British Museum).



Figure 9. Low-fired fragment of Cuneiform tablet, neo-Babylonian from Mesopotamia,Iraq (South) (copyright Trustees of the British Museum).



Figure 10. Kiln used to fire cuneiform tablets at the actual excavation sites (copyright Trustees of the British Museum).

On the basis of the data it appears that the tablets have been made from a palygorskite-based silt with inclusions of calcite, quartz and amphibole. The thermal behaviour of the tablets could be placed into 2 major groups, since groups 1 to 3 were similar, and these were as follows: tablets that had undergone some heating, those from northern sites, and those from southern sites and those which had not. It was decided that differences detected between groups 1 to 3 were not significant as far as the conservation treatment was concerned and that they could be accommodated by a single well-designed firing schedule.

3.3. Thermogravimetry

3.3.1. Cuneiform tablets

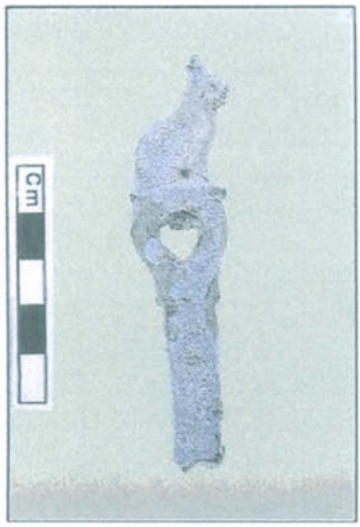
A number of tablet fragments with no text, and hence of no academic value, were supplied by the Department of Western Asiatic Antiquities of the British Museum for an initial trial. A typical TG curve of a cuneiform tablet in N_2 showed two distinct stages of mass loss before 150 °C and this was followed by small gradual mass loss until 650 °C, at which temperature the decomposition of

the calcium carbonate occurred [65]. The tablet from Kanesh, however, was unusual in that it did not have any calcite present. The site of Kanesh was a trading post established by Assyrian traders shortly after 2000 BC in Anatolia, and is the only site investigated that was not in Mesopotamia. A separate TG experiment was also performed to simulate the firing schedule used in the kiln. Because the firing schedule included a maximum temperature of 740 °C, it was felt that the large amount of carbon dioxide emitted rapidly in the late stages of the present firing schedule would certainly induce stress in the tablets and could well be the cause of the surface disruption observed during some firings. Trial firings have shown that lowering the firing temperature to 630 °C causes a small but acceptable decrease in physical properties of the fired tablets. The strength and surface hardness of the tablets are decreased by approximately 10% when the firing temperature is lowered. Tablet firings have confirmed a decreased amount of damage from the modified schedule. The new firing schedule has been used successfully in the British Museum since 2000 [66].

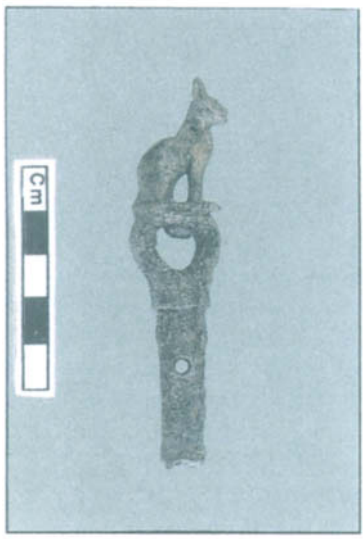
It was appropriate to use TG for this study because Wiedemann has characterised and analysed a range of historical materials: ancient tree stubs, ancient Egyptian pigments, Nabataic pottery [23], Egyptian Mummy caskets and calcium carbonate containing materials [21]. The Conservation Department of the British Museum has also previously used thermogravimetry to study busts by Roubiliac which were undergoing repair and cleaning [65]. Analysis identifed that several of the busts undergoing cleaning treatment were formed from kaolinite and illite. The degree of firing of the clays was of vital importance because unfired clays would react adversely to water-based cleaning methods. Results indicated that low-temperature firing had been used and so non-aqueous cleaning methods were employed.

3.3.2. Egyptian copper alloys

Recently TG has assisted in characterising a novel pale blue corrosion product affecting Egyptian copper alloy statuary and tools [67]. During a conservation survey of a collection of 2840 Egyptian copper alloy objects, a pale blue corrosion product was observed on 184 artefacts. Figure 11 shows the upper section of a bronze staff, with the top in the form of a cat seated on a plinth with an aperture, the shaft is of rectangular section. It originates from lower Egypt, Memphis or Saquarra. The collection contains a wide range of artefact types including statuary, vases, tools and weapons, which are made predominantly of copper, arsenical copper, tin bronze and leaded tin bronze. The collection is housed in well-buffered wooden cupboards with relative humidity (RH) in the range 35-45%. The moisture content of the wood of the cupboards and shelves was measured using a Protimeter moisture meter and found to be stable during a four-year monitoring period. The environment in the cupboards contains



(a)



(b)

Figure 11. Egyptian copper alloy upper section of a bronze staff with the top in the form of a cat seated on a plinth with an aperture, the shaft is of rectangular section. It originates from lower Egypt, Memphis or Saquarra. (a) Before conservation treatment and (b) after treatment (copyright Trustees of the British Museum).

significant levels of acetic acid of between 1071 and 2880 $\mu g/m^3$ and very low concentrations of other carbonyl pollutants. These concentrations were found to be relatively constant within any given cupboard over the four-year monitoring period.

TG assisted in the characterisation of a previously unreported compound, sodium copper acetate carbonate in the corrosion products. The aim was to verify the presence of carbonate in this novel corrosion product and to characterise the acetate-to-carbonate ratio. Figure 12 shows the decomposition of the corrosion product, together with that of a standard mixture with the suspected stoichiometry. The mass increase observed in the TG curve from 357 °C is probably due to re-carbonation of the compound from reaction with the carbon dioxide atmosphere. Measurement was made in an atmosphere of carbon dioxide to retard the carbonate decomposition to higher temperature and thus separate the acetate and carbonate decomposition. The standard mixture was prepared by grinding together malachite, copper acetate, sodium acetate and sodium carbonate. Analysis of the corrosion product did not match any standards, thus adding to evidence that this was a new corrosion product and not a physical mixture of already known materials. TG allowed determination of the acetate-to-carbonate ratio and the stoichiometry of the corrosion product.

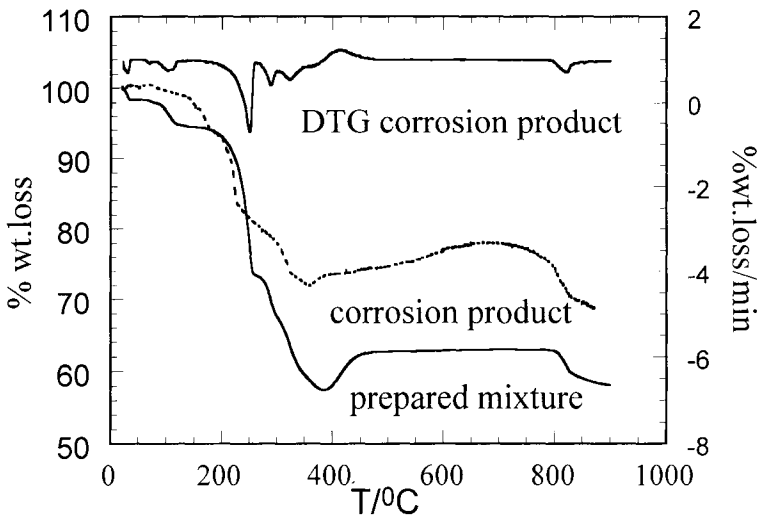


Figure 12. TG curve for the corrosion product (----) from an Egyptian copper alloy (Figure 10), together with that of a standard mixture (—) of the suspected stoichiometry and its DTG curve (—) [67].

An unusual crystalline efflorescence was characterised on an Egyptian limestone relief stored in a wooden cabinet at the Burrell collection, Glasgow, Scotland [68]. A sample of the efflorescence salt was heated in a thermogravimetric analyser and the volatile compounds released during the decomposition were identified by coupling an infrared spectrophotometer to the analyser. Sample residues were also collected after each decomposition stage, extracted in distilled water, and the aqueous extracts were analysed by ion chromatography. The salt consisted of mainly calcium, acetate, chloride and nitrate ions. This is a new crystalline salt which occurs solely as an effloresence compound on museum collections. Its composition indicates that it may occur on specimens which consist of, or include, calcium carbonate and that, not only chloride and nitrate salt contamination, but also acetic acid pollution, which occurs from wooden storage cabinets, are prerequisites for its formation. The authors advocate that this efflorescence is called thecotrichite, which translates as a " hairy mineral from a storage cabinet" [68].

3.3.3. Ground layers of paintings

The ground layers of paintings have also been studied by TG. Typical ground layers in early European panel paintings consist of gesso or gypsum (calcium sulphate dihydrate) or the hemihydrate form mixed with rabbit-skin glue and applied to the wooden support. The presence of hydrated gypsum has been confirmed by DSC on a sample from Meliore's painting "Madonna col Bambino", and the hemihydrate form has been identified by X-ray diffraction in the painting of Tintoretto's "Assumption of the Virgin in Bamberg [69]. In Northern European 16th century paintings the use of calcium carbonate grounds is recorded. This type of ground used can be readily characterised by TG. A recently published paper [37] is part of a study of grounds used in sculpture and altarpieces from the Balearic Islands during the 15-18th centuries. It included a number of commercially available calcite and gypsum-based grounds and two samples from a sculpture and a Gothic Predella from Mallorca (15th and 17th centuries).

A traditional canvas support for a painting normally consists of a stretched linen fabric, onto which is brushed an aqueous size of rabbit-skin glue. An oil-based (or more recently, acrylic) layer of paint, or what is commonly referred to as the ground, preparation layer or primed layer, is then applied onto the sized canvas. The presence of ground and the additional paint films constitutes an element of protection for the canvas. The ground layer of a 19th century loose lining removed from the reverse side of Landseer's "Study of a Lion" (Figure 13) during restoration was investigated [18]. The first stage of decomposition involved basic lead carbonate, the drying oil (linseed) and glue, and the final stage involved the decomposition of calcium carbonate. This sample on the



Figure 13. Landseer's "Study of a Lion" (with permission from the Tate, London, UK).

canvas support was later used in thermomechanical studies (Section 3.4.1) and dielectric analysis reported elsewhere [70].

3.3.4. Wall paintings

Combined TG-DTA techniques were found to be most reliable and practical techniques for identification of the salt, calcium nitrate tetrahydrate, both as a pure compound and in mixtures with other materials in wall paintings. Identification is possible with these techniques because of the presence of the melting endotherm of calcium nitrate tetrahydrate at 43 °C. Calcium nitrate, a deliquescent salt commonly found in wall paintings, was selected for this study to clarify the role played by very hygroscopic salts in the deterioration of wall paintings. It was found to deliquesce easily and recrystallise under environmental conditions typically prevailing for wall paintings [55]. Soluble salts are among the main causes of deterioration in wall paintings and so their characterisation is of practical importance.

Samples from Brunelleschi's dome of the Cathedral S.Maria del Fiore, Florence, (Section 3.2.1) were also studied by thermogravimetry [71]. To facilitate in the interpretation of results, samples were prepared accorded to traditional recipes used for wall paintings and TG curves were recorded. The blue sample taken from the painted area of the sky, level eight of the cathedral dome, painted by Vasari, showed that it was different to the blue sample taken from an area painted by Zuccari on the second level. The blue pigmented sample (containing cobalt oxide, as identifed by X-ray Fluorescence Analysis) of Vasari could be compared to the degradation of a standard sample of smalt pigment and casein, whereas the blue of Zuccari showed a similarity to a standard sample of smalt and animal glue or mixtures of animal glue with egg or casein. This would support observations that regions painted by Zuccari are sensitive to moisture and there is evidence of moisture damage, whereas those painted by Vasari are well preserved. Gas chromatographic and mass spectrometric analyses of these samples have also been performed [54].

3.3.5. Historical tapestries

As mentioned in Section 3.2.5, samples from historical tapestries have been analysed by DSC and the state of degradation of their fibres (wool and silk) assessed. Where sample size permits, thermogravimetry is also used. The first derivative thermogravimetric (DTG) curves for un-aged, light-aged and historical undyed wool thread (Raphael and Tobias, Brussels 1550) are shown in Figure 14. The DTG curves reveal a shift to lower temperatures, particularly in the final decomposition stage of the historical sample. The rate at which degradation occurs at each of the stages is lower for the historical than for the un-aged and light aged samples. The difference with ageing of wool fibres can

also be seen by scanning electron microscopy, which shows that the surface structure present in the un-aged sample is no longer evident in the historical sample (Figure 15).

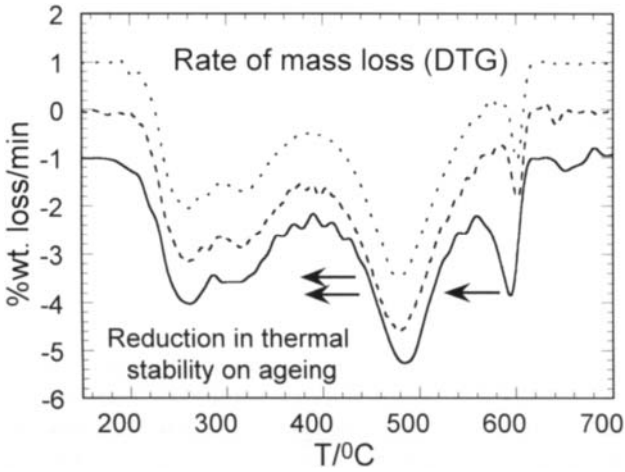
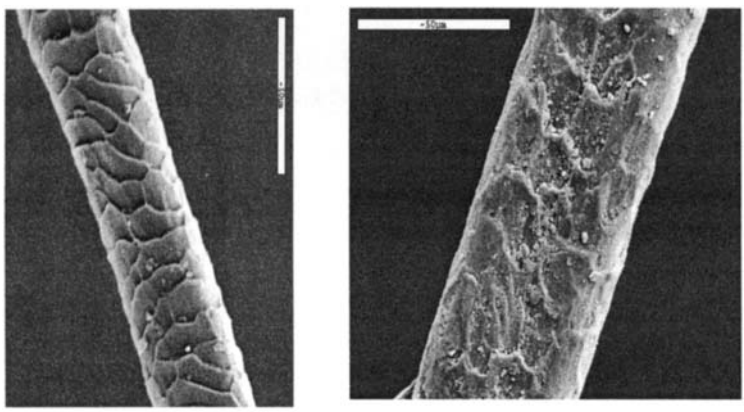


Figure 14. DTG curves for the control (...), 64 h light-aged (---) and historical wool thread (—), Raphael and Tobias, Brussels 1550, Royal Palace Madrid.



(a) **(b)**

Figure 15. The difference on ageing of wool fibres can be seen by scanning electron microscopy (x1000) ; structure in the (a) un-aged sample (a) is no longer evident in (b) the historical sample.

3.3.6. Parchment and leather

A major project, Microanalysis of Parchment (MAP), with the School of Conservation, Copenhagen, involved a study of historical parchments mainly from bookbindings [25]. Parchment (calf) from Z.H. de Groot (Rotterdam, The Netherlands) was used as the control sample. Twelve historical parchments, some dated, 17th century, and most undated, included samples from parts of bookbindings and manuscripts from the Royal Library,Denmark. Thermooxidative degradation studies were made between room temperature and 750 °C [25]. Parchment samples for TG were obtained either by scraping with a scalpel or by using small pieces (4 mm^2). Following the moisture loss, two major degradation steps were reported and, in some cases, a third step was observed. The latter corresponded to the decomposition of calcium carbonate. When parchment is used as a writing material the grain layer is often removed, polished with pumice stone and smoothed with chalk. Figure 16 shows an example of historical parchment (School of Conservation, Copenhagen). Due to this method of preparation, calcium carbonate is usually found in various amounts. Figure 17 illustrates the shift to lower temperatures of the second degradation stage for historical samples. To obtain a more complete picture of the variation across the temperature range, principal component analysis was performed This revealed that historical parchments could be readily distinguished from the control sample and that there were differences within the historical parchments [25]. The clustering was consistent with data from HPLC amino acid analysis where the ratio of basic to amino acids was taken as a marker for ageing.

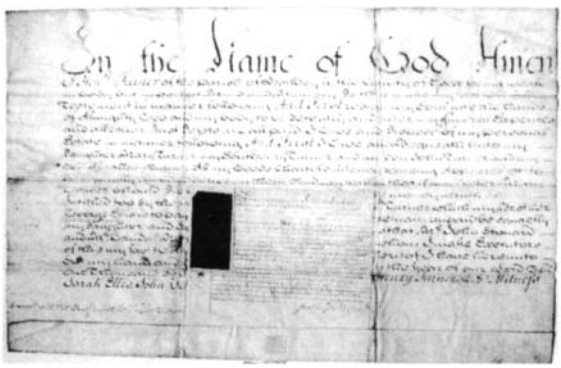


Figure 16. An example of historical parchment (courtesy of the School of Conservation, Copenhagen).

TG studies have also been made on leathers that are supports of cultural or historical objects. These include leather from book covers (17-19th centuries), leather from an Austrian belt from the Franz Josef period and Cordoba leather (17th century). Results suggest that the thermal behaviour of degraded leather tends to that of parchment or collagen, which are not tanned materials. Investigations were performed using a Q-15000D Derivatograph (MOM, Hungary) [72]. The Derivatograph was also used for studies on the effect of leather and gelatin of poly(hexamethyleneguanidine), proposed as an alternative to traditional chrome tanning and dyeing processes used for treating shoe leather [73]. On the basis of the thermoanalytical results gelatin was considered to be a suitable model for studying leather properties.

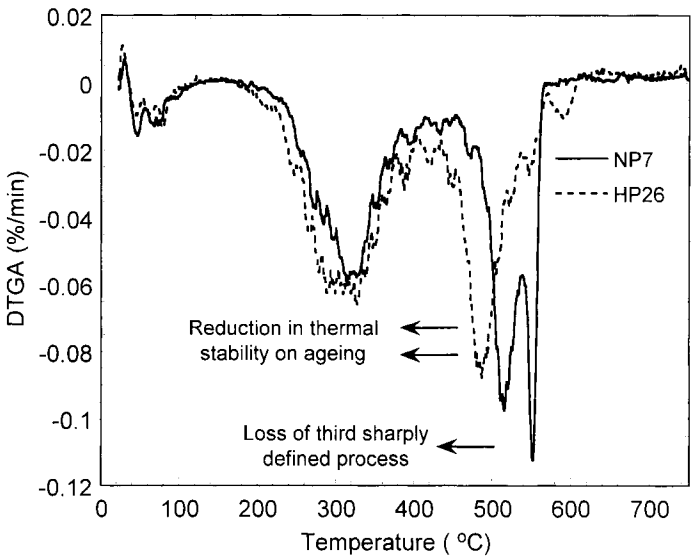


Figure 17. Shift to lower temperatures of DTG curve for historical parchment (HP26) compared to DTG curve of new parchment (NP7), MAP project [25].

3.3.6. Paper

Thermoanalytical techniques have been used to study the composition of paper and paper-like materials for a few decades. This has included studies involving the accelerated ageing of paper for conservation research purposes [74,75], the effect of conservation treatment on 17th century archival paper [76], and also the ability to distinguish between original and forged lithographs [77].

A study of lithographs was performed by Wiedemann using the Mettler Toedo Thermosystem TA8000 (TG850). He was able to distinguish between Japanese Mitsumata paper (1952) and paper from the Japanese artist Kunisada (1846) on

the basis of differences in paper composition, in particular for hemicellulose and cellulose [78]. He also tested black and white lithographs of Picasso and Chagall and demonstrated that papers from a similar age and quality give similar TG traces.

Studies of conservation treatment included the measurement of thermal stability of letters from the 17th century archive, prior to and after de-acidification treatment involving calcium and magnesium carbonates [76]. Samples from the edges of less-important items in the archive were selected for testing. After conservation treatment, it was observed that, in addition to the main characteristic peak which corresponds to cellulose degradation, smaller peaks at higher temperatures in the vicinity of 500-550 °C and then 750-800 °C were also present, indicative of the decomposition of magnesium and calcium carbonates formed in the de-acidification process. This was considered beneficial for the paper because it provided an alkaline buffer. The presence of carbonate was further confirmed by X-ray photoelectron spectroscopy.

3.4. Thermomechanical analysis (TMA)

3.4.1. Paintings conservation

Several projects with the Courtauld Institute of Art, Department of Conservation and Technology, London, involved the first use of thermomechanical techniques applied to problems associated with paintings conservation. Two major areas were addressed : the cleaning of paintings and the effect of structural treatment involving humidification processes. Prepared paint films were subjected to various cleaning agents (non-aqueous and aqueous based) and measurements of the softening temperatures of the paint films were made. Paint films were also subjected to different levels of relative humidity. In the study of the cleaning the aim was to determine whether the action of solvents on paint films would remove portions of the oil media, and in the study of humidification there is interest in knowing how long it takes to soften paint. The conservator's task of manipulating highly fragile brittle flakes of paint back into place is frustrating and can be made simpler if the paint becomes soft and compressible. In the structural treatment of paintings the practice of using a combination of heat, moisture, aqueous glues and minimal pressure for the relaxation, regeneration and consolidation of paintings on canvas preceded any basic physical data on the painting undergoing treatment [43] and so now there is a requirement to quantify these processes. Research into the interaction of moisture with oil paintings on canvas was pioneered at the Courtauld Institute of Art and the effect of moisture-based treatments on paint films was investigated [43]. As part of this research both TMA and DMTA (Section 3.5.1) have been used.

The TMA work included measurements on medium lean basic lead carbonate pigmented oil films and medium rich ochre (iron oxide) pigmented oil paint films. The former were found to have a high softening-temperature or glass-transition temperature in the region of 90 °C, and the latter were found to have an initial softening below room temperature with another transition at higher temperatures in the region of 60 °C. This transition was found to be affected by the use of cleaning agents, such as acetone, and further analysis indicated loss of long-chain fatty acids, which act as internal plasticisers in the paint [43]. The data, however, were obtained on prepared paint films that were about 12 years old. Recent work on archival samples using GC/MS indicates that, in aged materials, this does not occur [79].

Humidification studies were performed on a 19th century primed canvas which had been previously removed from the back of Landseer's "Study of a Lion" (c.1862) [18] (Section 3.3.3, Figure 13). The Tate Conservation Department provided this sample of primed canvas, which came originally from double stretchings prepared by artists' suppliers in the 19th century. These preparations were made so that there were two identical primed supports at the front and rear. During conservation treatment some of the rear primed supports had been removed and retained. The primed canvas samples were all on closely woven linen and were primed with lean mixtures of lead white and calcium carbonate. Studies of the cross sections showed evidence of at least two applications of ground and a size layer [43]. Samples were placed in open tubes in glass vessels containing saturated solutions to provide RH conditions from 54% to 97%. for periods of at least one week. The overall softening-temperature was seen to decrease with increasing levels of humidification, from about 40 °C at 54% to 20 °C at 85% [69]. Preliminary work on moisture gradients demonstrated that greater softening of the composite occurred when it was humidified from below, which underlines the importance of the role of the size layer and the fact that it may assist in plasticising the adjacent ground layer [44]. With samples humidified at 97% RH, TMA curves showed an anomaly that was reproducible in the region of −10 to 0 °C, which could be explained in terms of the collapse of the size layer as it sinks into the canvas [44].

3.4.2. 19th century paint media (Megilps)

As discussed in Section 3.1.1, 18th and 19th century British artists made use of oil and resin mixtures, referred to as "megilp". Prior to 1850, the ratio of drying oil to varnish was given most often as 2:1 with 1:1 as a second choice. After 1850, the ratio was consistently reported to be 1:1 [80]. It was understood that megilp would not gel unless the oil had been treated with a lead compound and the presence of mastic resin in preference to other natural resins was required. The presence of megilps has been identified in paintings of Turner "Opening of

the Wallhalla", Figure 5. In the early 1990's the Tate Conservation Department initiated a study where they prepared and made available oil resin films, unpigmented and pigmented, for studies by TMA. In oil–rich megilps two distinct stages of softening were observed at –10 °C and 60 °C. As resin content increased to 1:1, a single transition was observed at about 20 °C, which then increased in temperature with increasing resin content. At 1:3 the value for this transition was in the region of 40 °C. The change at 1:1 composition from two transitions to one confirms differences observed in the infared spectra. The value of 1:1 corresponds to a threshold concentration beyond which there is total miscibility or formation of a new polymeric phase. Below this ratio there is segregation of phases [81]. This could explain the artists' preference for the 1:1 composition. A further example of a study on this paint media is given in Section 4.1.3.

3.4.3. Humidification of Dead Sea scrolls

Humidification of the sample *in situ* using TMA has been performed at the Getty Conservation Institute in a study of the effects of changes in RH on Dead Sea scrolls parchment samples [82]. Results of this study revealed that RH-step jump thermomechanical analysis can provide useful information on the dimensional response of modern and ancient parchments to changes in relative humidity. Fragments from selected Dead Sea scrolls were found to respond more slowly to RH fluctuations, and undergo smaller dimensional changes, than modern parchment under the same conditions. The expansion coefficient data indicate that parchment fragments (Dead Sea scrolls) behave more like degraded modern parchment and gelatin than un-degraded modern parchment. It was found that, because the absolute response time is relatively rapid, care should be taken not to subject aged brittle parchment to rapid dehumidification, particularly if the parchment is restrained.

3.5. Dynamic mechanical thermal analysis (DMTA or DMA)

3.5.1. Painting conservation - oil-primed canvases

DMTA (Polymer Labs Mark 2) was first used in paintings conservation in one of the projects with the Courtauld Institute of Art, Section 3.4.1. The aim was to measure the softening temperature of paint films subjected to various cleaning tests to simulate the procedure used with paintings. Measurements were rather limited because they relied on having a free paint film which could be clamped. Due to the general unavailability of such samples, primed canvas supports (Section 3.3.3) were then used. These were well suited for use in the DMTA (Polymer Labs Mark 2) and the Rheometric Mark 3 DMTA analyser in bending mode. The modulus and tan delta curves for the sample from the Landseer

primed canvas are shown in Figure 18. The modulus decreases on heating from −160 °C and at about 70 °C its value starts to fall rapidly, and continues until 150 °C. The maximum in tan delta occurs in the region of 90-100 °C. This measurement was then compared to un-aged and artificially aged primed canvases [18]. Accelerated ageing was performed at the Tate Conservation Department (17 and 34 days of heat (70 °C) and light ageing at 18 000 lux). In the un-aged sample, a broad tan delta peak is measured which occurs over the temperature range −30 °C to 100 °C with a maximum at about −10 °C and shoulder peak at 50 °C. On ageing there is a small decrease in intensity of the main peak, followed by a shift of the peak temperature to about 70 °C. This demonstrates that DMTA can be used to monitor accelerated ageing procedures to determine whether the ageing will induce changes observed from natural ageing alone.

In collaboration with the Tate, a series of tests using DMTA were also made to determine the effect of de-acidification treatment on painting canvases [18]. These were conducted on both primed and unprimed canvases. The unprimed canvases were tested in the tensile mode of the DMTA analyser. It was found that differences could be measured on testing the response of canvases to changes in RH before and after de-acidification treatment. The treatment caused a lower response to RH, measured in terms of the amount of displacement of the sample. This is a positive result of the treatment because it implies that less movement of the canvas support would occur and this would minimise the possibility of small cracks forming in the painting.

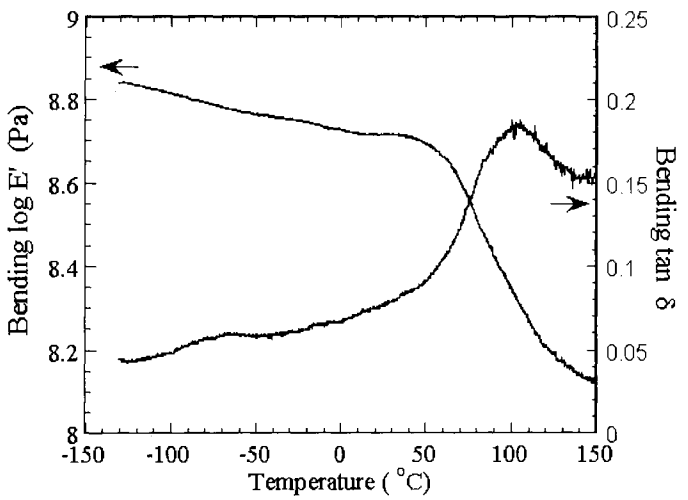


Figure 18. The modulus and tan delta curves, Landseer's primed canvas, "Study of a Lion" [18].

3.5.2. Parchment

Parchment is based on collagen, where the primary structure is defined as the sequence of amino acid residues in its polypeptide chains. This is considered as a block coploymer containing imino acids (proline and hydroxyproline) with glycine at every third position, i.e –(Gly-A-B)-(Gly-Pro-HyPro)- . The presence and size of the imino acid residues will have some effect on the mechanical properties because they will restrict rotation and lead to a certain rigidity in blocks containing them. The structure can thus be considered in terms of soft and hard blocks, depending on whether glycine or proline occurs at every third position [83]. Figure 19 shows the DMTA response of un-aged parchment. In aged parchments, the transitions occur at higher temperatures in the region of 90°C and 150°C similar to those in gelatin (Figure 17). Shrinkage temperatures of these parchments were also measured and are described in Section 3.5.3 [84].

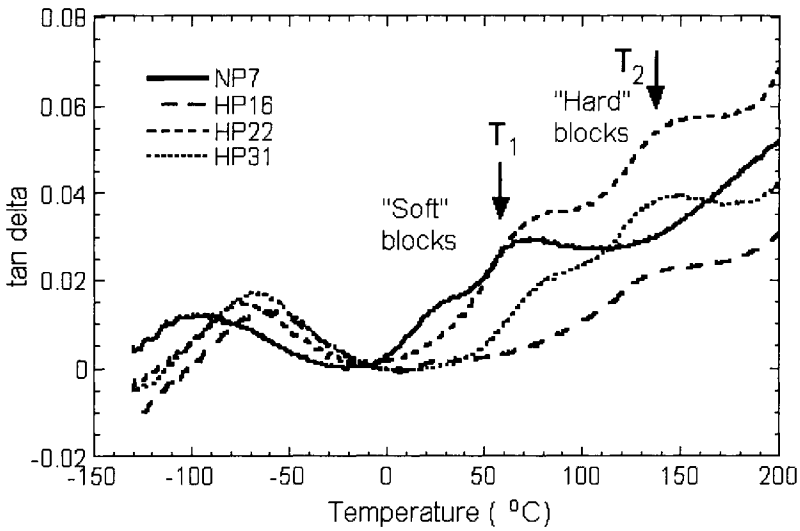


Figure 19. DMTA curves for un-aged (NP7) and historical parchments (HP16,HP22, HP31) (MAP project) [25] with transitions at 90 °C and 150 °C.

Recent DMTA measurements on archival samples, together with X-ray diffraction studies, have demonstrated that the measured tan delta values (or degree of viscoelastic response) of the parchment are correlated with the degree of crystallinity as measured by XRD. In samples of low crystallinity, tan delta

peaks of higher intensity were obtained than in samples with higher levels of crystallinity where tan delta values were barely measurable. Measurements have been performed on historic bookbindings where sufficient material is available for measurement. Where historic books of parchment and manuscripts are concerned it will be necessary to use micro-TA (Section 4.1.1).

3.5.3. Reverse configuration DMTA

Measurement of the effect of immersion of samples in water and the effect of varying levels of relative humidity led to the adaptation of the DMTA to its use in reverse configuration. The Rheometric Mark 3 analyser was literally inverted and placed on a special stand. The clamps for supporting the sample were extended. The sample was then either immersed in a beaker of water supported in a controlled temperature water bath, or the sampling area was protected by a glass vessel and the relative humidity of the air flow was manually controlled from dry and wet (Dreschel bottle with distilled water to produce 100% relative humidity). This has been superseded by a computer-controlled humidification system [26], and is currently measuring the response of historical parchment, model tapestries that have been light aged, and individual silk and woollen fibres from historical tapestries. Figure 20 shows the change in displacement which occurs on humidification of un-aged, light aged and historical parchment when samples were subjected to varying RH values between 20% and 80%.

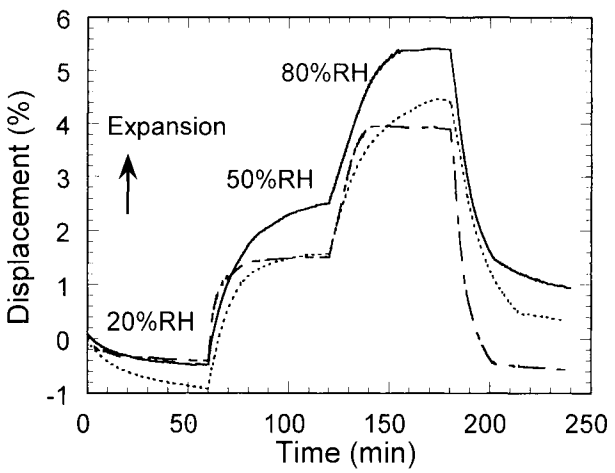


Figure 20. Displacement (%) vs time (mins) for un-aged (—), 64 h light-aged (---) and historical parchment (...), when samples were subjected to varying relative humidity.

Immersion tests were initially made using canvas to determine the effect of wetting and then drying under different loads. This was performed both on un-aged samples and samples from archival linen [18]. Figure 21 shows that, as the load is increased, canvas takes longer to dry. This is of interest to conservators because canvas undergoes treatment with moisture as it is stretched onto the support frame and a load is applied. For parchment samples immersion in water followed by heating provided another means for determining the denaturation temperature of the parchment and also to quantify the amount of shrinkage that occurred [84].

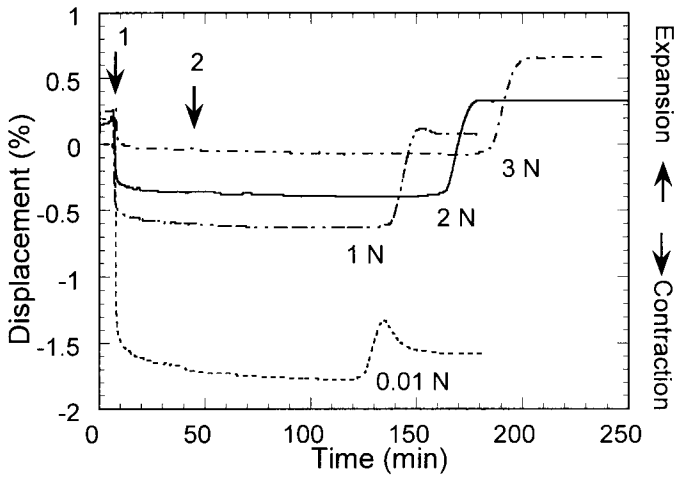


Figure 21. Drying of canvas under various loads, after immersion in water. As the load is increased (lowest 0.01 N at bottom, 1 N, 2 N, and 3 N at the top) the canvas takes longer to dry [18].

3.6. Micro-thermal analysis

The examples given in the above sections demonstrate the advantages and the limitations of thermoanalytical techniques. One main limitation is the restriction of sample size that historical samples impose and the added complication that historical samples represent complex degraded composite materials. A technique which will be beneficial for future work is the state-of-the-art micro-thermal analysis technique, and this has been described in Section 2.2.7. Some recent examples of measurements on archival material are given below to demonstrate the potential of the technique. In each case, the Wollaston probe was used to heat the sample at 5 °C/s and 25 °C/s. As the material under the probe heats, it expands and, in the absence of any transition that causes the material to soften,

deflects the probe upwards. However, if the material softens, for example at a glass or melting transition, the tip will be pushed into the sample surface by the spring-like action of the bent cantilever.

3.6.1. Parchment

Transitions have been measured using DMTA (Section 3.5.2) on historical parchments (c 17th cent) and un-aged parchments and, from these measurements, it was possible to distinguish between them. The conclusions from DMTA were supported by values of denaturation temperatures from thermomicroscopy and DSC, amino acid analysis (HPLC) and solid-state NMR. Selected samples that had been studied in this way were then examined by micro-TA. Preliminary observations were made on collagen-containing prepared thin films of rabbit-skin glue. These were selected because the films had a smooth surface and would, in the first instance, be more accessible to this technique than the parchment surface. The images obtained from these samples are shown in Figure 22 as a "matrix" of high thermal conductivity (lighter area) and domains with lower thermal conductivity (darker areas). Because the effects of topography dominate the conductivity image, it is not possible to say whether

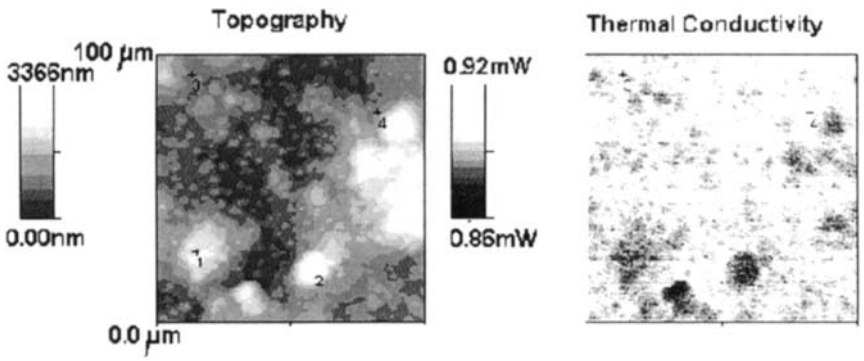


Figure 22. Rabbit-skin glue film ; on the right a "matrix" of high thermal conductivity (light) and domains with lower thermal conductivity (dark). The effects of topography (on the left) dominate the conductivity image. The micro-TMA signal showed some distinct features; relative thermal expansion was lower at the lower thermal conductivity locations than at the higher ones.

the domains with different thermal conductivity are due to different phases. Local thermal analysis was subsequently performed on two locations with lower conductivity and two locations with higher thermal conductivity. The micro-TMA signal showed some distinct features. The relative thermal expansion was measured and an indication of a small increase in expansion occurred in the temperature region which corresponds to the denaturation of unaged collagen

(50-70 °C). The relative thermal expansion also appeared to be lower at the lower thermal conductivity locations than at the higher thermal conductivity ones. This indicated that differences could be measured in what appeared to be homogeneous clear films of un-aged collagen. For comparison, films of gelatin were also measured and these showed a change in relative thermal expansion at higher temperatures in the region of 120 and 180 °C. The presence of higher-temperature transitions has been taken as an indication of the presence of gelatin in the collagen of historical collagen-based material. Collagen reverts to gelatin when it loses its triple helix configuration (Sections 3.1.2 and 3.2.4).

Samples of parchments in the as-received state were also tested on their smoother "flesh" side, as opposed to the reverse or "grainy" side. For un-aged parchment transitions, characterised in terms of the temperature at which change in thermal expansion occurs, differences were observed in the region 30-60 °C, whereas, in the historical samples, transitions occurred at 90 °C and 150 °C. Images were not recorded because smoother surfaces were required. Sample preparation involved removal of a small sample and setting it in polyester resin and microtoming thin sections from the sample. Re-examination enabled images to be obtained from the historical sample (HP28, MAP project) (Figure 23). The figure on the left-hand side reveals the topography of the surface. Figure 25 provides the results of micro-mechanical measurements on selected locations of the sample area. At location 1, two transitions around 90 and 140 °C were detected in an area of low thermal conductivity. Figure 23, on the left-hand side, is the topographical image of the surface and Figure 23, on right-hand side, is the conductivity image. (Areas that are lighter are more conducting than those that are darker.)

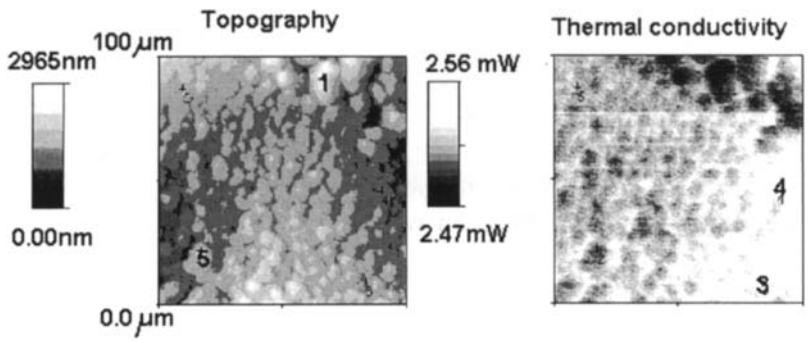


Figure 23. Historical parchment sample (HP28); the left-hand side is the topography of the image; the right-hand side is the conductivity image. Lighter areas are more conducting than those that are darker. Locations 1& 5 (topography) 3 & 4 (conductivity) refer to locations of micro-TMA (Figure 24) [85].

3.6.2. Historical tapestries

Preliminary measurements have also been made on samples from historical tapestries. A sample of a green wool fibre removed from a tapestry (Dedalo e Icaro, Brussels, 1545, Royal Palace Madrid) was prepared for micro-TA as a thin section. The imaging still revealed imperfections in the sample preparation technique. Localised TMA measurements, however, provided information on

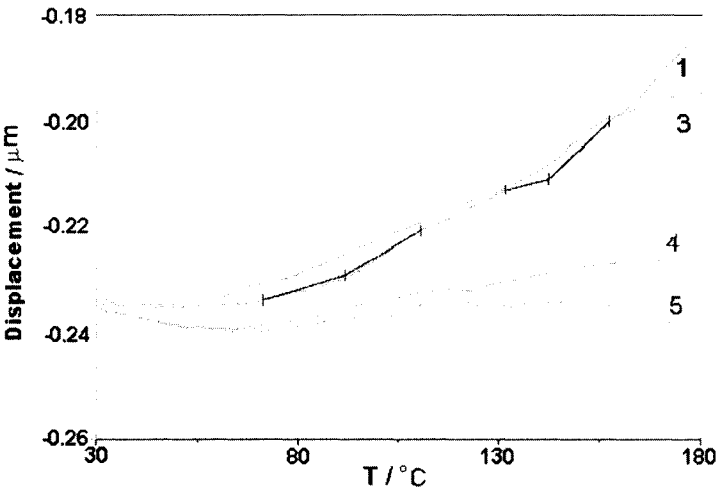


Figure 24. Micro-mechanical measurements on selected locations of the sample area shown in Figure 23. At location 1 two transitions around 90 and 140 °C are detected in an area of low thermal conductivity [85].

the thermal behaviour of different locations on the sample surface. The initial softening at 70 °C, which is common to the locations studied, may be due to the fact that the sample was mounted on carbon-based adhesive tape because no transition at this temperature is expected. One of the curves shows an expansion at higher temperatures near 200 °C, followed by a rapid softening (Figure 25). This is of particular interest because in wool fibres this temperature has been assigned to the disappearance of the α-form of wool keratin (Section 3.2.5).

Tapestries frequently have woven metallic threads (Ag or Au). Samples from a tapestry located in one of the museums in Brussels of "Christ before Pilate" (c1520, Brussels) were taken and the metallic threads examined. Figure 26 is a photomicrograph showing silver threads from a tapestry and the silk core within.

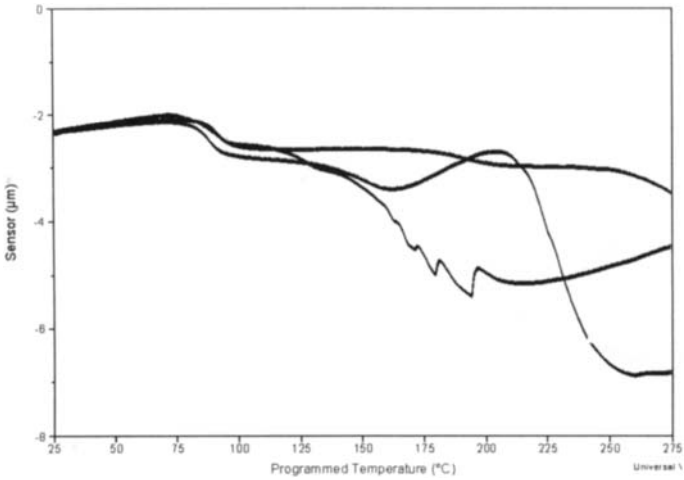


Figure 25. Spatially resolved micro-TMA of thin section of an historical wool fibre. Expansion occurs in one of the curves at higher temperatures near 200 °C followed by a rapid softening.

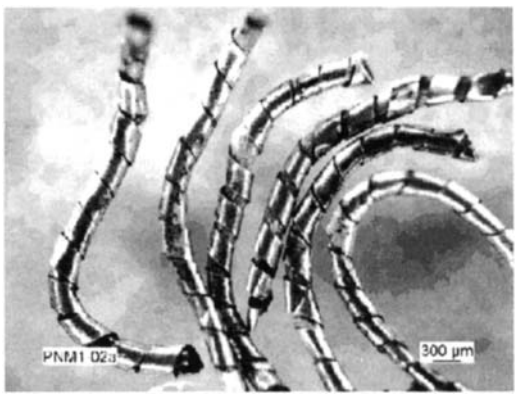


Figure 26. Photomicrograph showing silver threads from a tapestry and the silk core within. (Courtesy of A. Haacke, MODHT project.)

Micro-TMA curves on one of the samples from this tapestry reveal that three of the locations (Figure 27, curves 2,3,4) tested are similar and that curve 1 is quite different because it has a softening temperature at about 225 °C. The common low-temperature transition may be due to sample positioning on the adhesive carbon tape. Curves 2,3,4 show no transitions, as expected for metallic silver. Curve 1 indicates that deterioration of the silver threads may have

softening temperature. Another sample, taken from a different area in the tapestry, shows that expansion occurs for curves 2 and 4 (Figure 28). Conservators suspect that this is an area of recent restoration and the difference in thermal behaviour supports this. The uncorroded metal shows strong expansion on heating and differs from the previous example.

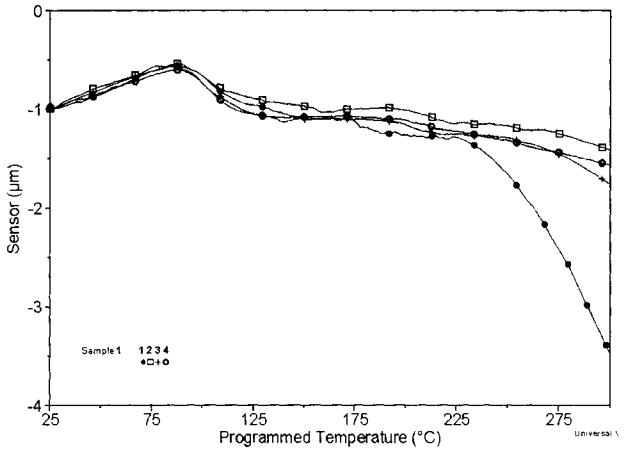


Figure 27. Micro -TMA curves on one of the silver threads from a historical tapestry; 3 locations tested are similar with a softening temperature at about 225°C.

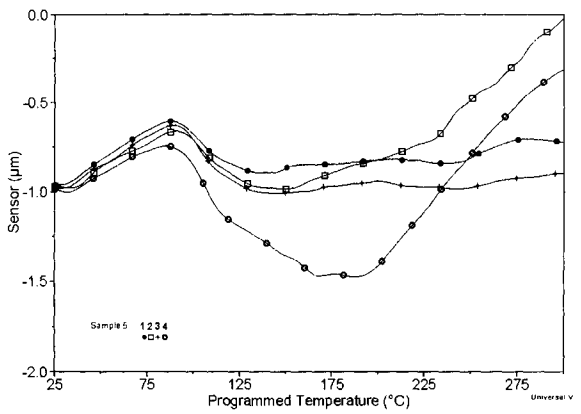


Figure 28. Another sample taken from a different area in the tapestry shows that expansion occurs for curves 2 & 4. Conservators suspect that this is an area of recent restoration and the difference in thermal behaviour supports this.

3.6.3. Paint media

Figure 29 shows measurements on samples of paint media prepared according to 19th century recipes for oil/resin mixtures and set as a single layer in cross-section. The observed difference in softening temperature is due to different ageing conditions and the use of different lead driers (label am1cs1 refers to natural ageing of basic lead white oil resin paint (1:1) containing lead acetate drier, lm1cs2 refers to artificially light-aged lead white oil resin paint (1:1) containing litharge drier). The next stage will be to include the examination of multi-layered paint cross-sections.

Preliminary results are encouraging because it is possible to obtain information which can be interpreted on the state of historical collagen in parchment, the state of keratin in historical wool fibres, and some indications of differences in the silver threads. Further work is in progress with particular reference to optimising sample preparation. The possibility of *in situ* measurements made directly on the object, where it is not possible to remove a sample, is being considered. In addition, paint samples in cross-section have been examined and softening temperatures have been measured.

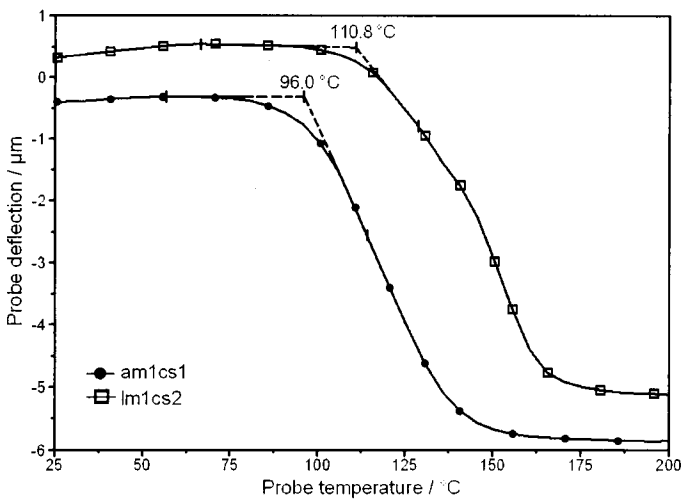


Figure 29. Micro-TMA curves on samples of paint media (oil/resin mixtures) set as a single layer in cross-section. Differences in softening temperatures are due to different ageing conditions, different lead driers [am1cs1; lead white in oil resin paint (1:1) lead acetate drier, lm1cs2 artificially light aged lead white oil resin paint (1:1) and litharge drier].

4. CONCLUSIONS

The many examples given in this chapter clearly establish that thermal analysis techniques (DTA, DSC, TG, DTG, TMA, and DMA) are broadly applicable to the characterisation of art and archeological objects. The emphasis has been on objects in indoor environments, either on display or in storage in museums and art galleries, and it is during their conservation treatment that samples were taken for analysis. As demonstrated clearly by Wiedemann, thermal analysis together with ancillary spectroscopic and mass spectrometric techniques provides an understanding of early technologies. Examples of the application to paintings and wall paintings further confirm this, in particular the paint media by Turner in "The Opening of the Wallhalla", and the differences in the materials and techniques of Zuccari and Vasari. Both were discussed in terms of the conservation problems which have occurred partly as a result of the materials used by the artists and then the synergistic effects of environmental factors.

In addition to the characterisation of materials and of art objects, attention has been directed to the application of thermoanalytical techniques to the evaluation of the effects of conservation treatment on objects, in particular canvas-supported paintings, where cleaning of the paint surfaces involves the use of aqueous and non-aqueous based systems, and structural treatment involves humidification. This is where thermomechanical techniques have been shown to make a contribution (Section 3.4.1), and this includes the recent development of automated relative humidity control for DMA in reverse configuration, which allows the testing of the response of materials to variations in RH which is also of vital importance to parchments (Section 3.5.3). As mentioned in the chapter, the general progress of the deterioration of parchment collagen from a fibrous state into a gelatin-like state is not detectable in the dry state at the macroscopic level. This transformation is detected by observation of the parchment fibres in water under a microscope (Section 3.1.2) and unless measured may lead to irreversible damage of historical parchment manuscripts and objects if conservation treatment or storage involves humid conditions.

In samples prepared according to traditional recipes (Section 3.2.3), this has led to the development of paint dosimeters for evaluation of damage imposed by synergistic effects of indoor environmental factors, light, relative humidity, and indoor pollutant gases, which include levels of NO_2 and NO_x which come from outdoors and those generated from indoor conditions such as carbonyl pollutants. Examples given in this chapter refer to the study of corrosion products (Section 3.3.2). There are also many examples of the applications of thermal analysis to outdoor cultural heritage known to the author and which have not been covered in this chapter because this merits a separate section and includes buildings and monuments.

The examples mentioned in this chapter demonstrate also the opportunity for future basic research into artists' materials using the techniques described. With the measurements made so far, it has been clearly shown that the important parameter for monitoring conservation treatment, i.e the softening or glass-transition temperature, can be measured. In this way the chapter has demonstrated how knowledge and techniques from polymer science, and in the future the state-of-the-art thermal analysis technique (micro-TA), can be successfully transferred and applied to evaluate effects of treatment. In this way it has established a basis for future research into the material science approach to conservation science research.

5. ACKNOWLEDGEMENTS

The author acknowledges the support of the European Commission, the Directorate General X11 for Science, Research and Development within the research programme "Science and Technology in Environmental Protection", research area "Protection and Conservation of the European Cultural Heritage" in the projects mentioned in the chapter. As with any undertaking, this chapter has benefited from and been strengthened by the contributions from many sources. In particular the author would like to acknowledge the contribution of David Thickett, conservation scientist, formerly of the British Museum, and now at English Heritage, Dr.Joyce Townsend, conservation scientist at Tate Britain, and Dr.René Larsen, Rector of the School of Conservation, Copenhagen. I would also like to thank Dr.D.Grandy for the micro-TA measurements, Nancy Wade, paintings conservator and graduate of the Courtauld Institute of Art, for critical reading of the manuscript and Dr.Quanyu Wang and Dorte V. Poulsen for help with some of the figures. The author would especially like to thank Professor M. Brown for his assistance and encouragement.

REFERENCES

1. M. Odlyha, Preface, Special Issue "Preservation of Cultural Heritage. The Application of Thermal Analysis and other Advanced Techniques to Cultural Objects", Thermochim. Acta, 365 (2000) ix-x.
2. S. Schmidt, IIC Preprints, Cleaning, Retouching and Coatings, Brussels, (1990) 81.
3. S.Bradley, British Museum Occasional Papers, Occasional Paper No.116 (1997) 1-8.

4. H.J. Plenderleith, The Conservation of Antiquities and Works of Art, Oxford University Press, London, 1956.
5. Y. Shashoua, S.M. Bradley, and V.D. Daniels, Studies in Conservation, 37 (1992) 113.
6. W.A. Oddy, Museum Journal, 56 (1957) 265.
7. S. Bradley, ICOM International Council for Museums Committee for Conservation, Preprints, 11th Triennial Meeting, Edinburgh, September Vol. 1 (1996) 8.
8. S. Hackney, British Museum Occasional Papers, Occasional Paper No.116 (1997) 9.
9. G. Hedley and S. Hackney in Measured Opinions (Ed. C. Villers), United Kingdom Institute for Conservation, London, 1993, p70. ISBN 1 871656 21.
10. G. Hedley, in Measured Opinions (Ed. C. Villers), United Kingdom Institute for Conservation, London, 1993, p86. ISBN 1 871656 21.
11. J.H. Townsend, Turner's Painting Technique, 2nd ed., Tate Publications, London, 1995.
12. T. Learner in Resins Ancient and Modern (Eds M.W. Wright and J.H. Townsend), SSCR, (1995) 76.
13. A. Burnstock, British Museum Occasional Papers, Occasional Paper No.116 (1997) 47.
14. R. Larsen, The School of Conservation the Jubilee Symposium Preprints, Copenhagen,1998. p77. ISBN: 87-89730-25-9.
15. R. Feller in Training in Conservation, Institute of Fine Arts, New York University, 1983, p17. ISBN 0-9623175-0-0.
16. E.A. Turi, Thermal Characterisation of Polymeric Materials, Academic Press, New York, 1997.
17. M. Schilling, Studies in Conservation, 34 (1989) 110.
18. M. Odlyha, "Characterisation of Cultural Materials by Measurement of their Physicochemical Properties", Ph.D thesis, University of London, 1988.
19. H.M. Pollock and A. Hammiche, J. Phys. D: Appl. Phys., 34 (2001) R23.
20. D.M. Price, M. Reading, A. Hammiche, H.M. Pollock and M.G. Branch, Thermochim. Acta, 332 (1999) 143.
21. H.G. Wiedemann , Thermochim. Acta, 200 (1992) 215.
22. H.G. Wiedemann, J. Therm. Anal., 52 (1998) 93.
23. H.G. Wiedemann, Thermochim. Acta, 100 (1986)283.
24. M. Odlyha, T.Y.A. Chan and O. Pages, Thermochim. Acta, 263 (1995) 7.
25. M. Odlyha, N.S. Cohen, G.M. Foster and R. Campana in Microanalysis of Parchment, (Ed. R. Larsen), Archetype London Publications, 2002, p73.

26. G.M. Foster, S. Ritchie and C. Lowe, J. Therm. Anal. Calorim., 71 (2003) 1.
27. M. Odlyha, N.S. Cohen, R. Campana and G.M. Foster, J. Therm. Anal. Calorim., 56 (1999) 1219.
28. H.G.Wiedemann and S. Felder-Casagrande in Handbook of Thermal Analysis and Calorimetry, (ed. M.E. Brown), Vol.1, Elsevier, Amsterdam, 1998, Ch.10.
29. F. Preusser, Maltechnik Restauro, 85 (1979) 54.
30. H. Von Sonnenburg and F. Preusser, Maltechnik Restauro, 85 (1979) 101.
31. M. Odlyha and A. Burmester, J. Therm. Anal., 33 (1988) 1041.
32. M. Odlyha, C.D. Flint and C.F. Simpson, Anal. Proc., 26 (1989) 52.
33. M. Odlyha, J. Therm. Anal., 37 (1991) 1431.
34. A. Burmester, Studies in Conservation, 37 (1992) 73.
35. M. Odlyha, Thermochim. Acta, 134 (1988) 85.
36. M. Odlyha, D.Q.M.Craig and R.M.Hill, J.Therm.Anal.39 (1993)1181.
37. C. Genestar and J. Cifre, Thermochim. Acta, 385 (2002) 117.
38. D. Thickett and M. Odlyha in Reprints of the 12th Triennial Meeting of ICOM-CC, Lyon, James and James, London, 1999, p809.
39. D. Fessas, A. Schiraldi, R. Tenni, L. Vitellaro Zuccarello, A. Bairati and A. Facchini, Thermochim. Acta, 348 (2000) 129.
40. D.J. Carr, M. Odlyha, N.S. Cohen, A. Phenix and R.D. Hibberd, J. Therm. Anal. Calorim., in press.
41. I.C.A. Sandu, M. Brebu, C. Luca, I. Sandu and C. Vasile, Polym. Degrad. Stab., 80 (2003) 83.
42. T.Y.A. Chan and M. Odlyha, Thermochim. Acta, 269/270 (1995) 755.
43. G. Hedley and M. Odlyha in Measured Opinions, (Ed. C.Villers), United Kingdom Institute for Conservation, London, 1993, p99. ISBN 1 871656 21 4.
44. R. MacBeth, M. Odlyha, A. Burnstock, C.Villers and R. Bruce-Gardner in ICOM Committee for Conservation, 10th Triennial meeting Preprints, 1 (1993) 150.
45. G. Hedley, M. Odlyha, A. Burstock, J. Tillinghast and C. Husband in Cleaning, Retouching and Coatings, Preprints of the IIC Congress, Brussels (1990).
46. L. D'Orazio, G. Gentile, C. Mancarella, E. Martuscelli and V. Massa, Polymer Testing, 20 (2001) 227.
47. J.H. Townsend, Thermochim. Acta, 365 (2000) 79.
48. J.J. Boon, J. Pureveen, D,Rainford and J.H. Townsend in Turner's ` Painting Techniques in Context, United Kingdom Institute for Conservation, London, 1995, p35. ISBN 1 871656 23 0.

49. J.H.Townsend, The Materials and Techniques of J.M.W. Turner, RA 1775- 1851, Ph.D Thesis, University of London.
50. R. Larsen, M. Vest and K. Nielsen, J. Soc. Leather Technol. Chem., 77 (1993) 151.
51. R. Larsen, D.V. Poulsen and M. Vest in Microanalysis of Parchment, (Ed. R. Larsen, Archetype Publications, London, 2002, p55.
52. R. Larsen The Determination of Hydrothermal Stability (shrinkage temperature), STEP Leather project , European Commission DG X11 Research Report No.6, The Royal Danish Academy of Fine Arts, School of Conservation, Copenhagen, 1994, p145. ISBN 87 89730 07 0.
53. S.Z. Weiner, Z. Kustanovich, E. Gil-Av and W. Raub, Nature (London), 287 (1980) 820.
54. P.M. Colombini, F. Modugno and A. Giacomelli, J. Chromatogr. A, 846 (1999) 101.
55. L. Dei, M. Mauro and G. Bitossi, Thermochim. Acta, 317 (1998) 133.
56. A. Burnstock, M. Caldwell and M. Odlyha in ICOM Committee for Conservation, 10th Triennial meeting Preprints, 1 (1993) 231.
57. M. Odlyha, Thermochim. Acta, 269/270 (1995) 705.
58. S. Felder-Casagrande and M. Odlyha, J. Therm. Anal., 49 (1997) 1585.
59. J. Van der Weerd, J.J. Boon, M. Geldof, R.M.A. Heeren and P. Noble, Zeitschrift für Kunsttechnologie und Konservierung, 16 (2002) 35.
60. M. Odlyha in Modern Analytical Methods in Art & Archaeology, (Ed. E. Ciliberto and G. Spoto), J.Wiley & Sons, Inc, New York, 2000, Ch. 11.
61. B. Roduit, Thermochim. Acta, 388 (2002) 377.
62. C. Chahine, Thermochim. Acta, 365 (2000) 101.
63. C. Kennedy, J. Hiller, M. Odlyha, K. Nielsen, M. Drakopoulos and T.J.Wess, Papier Restaurierung, 3 (2002) 23.
64. A. Konda, M. Tsukada and S. Yamakawa, J. Polym. Sci., Polym. Lett., 11 (1973) 247.
65. D. Thickett and M. Odlyha, Thermochim. Acta, 365 (2000) 167.
66. D. Thickett, M. Odlyha and D. Ling, Studies in Conservation, 47 (2002) 1.
67. D. Thickett and M. Odlyha, Studies in Conservation, 45 (2000) 63.
68. L.T. Gibson, B.G. Cooksey, D. Littlejohn and N.H. Tennent, Anal. Chim. Acta, 337 (1997) 151.
69. A. Burmester in The Bamberg Assumption of the Virgin by J.Tintoretto, 42 Bayerische Landesamt fur Denkmalpflege, 1988, p113. ISBN 3-87490-911-5.
70. M. Odlyha, D.Q.M. Craig and R.M. Hill, J. Therm. Anal., 39 (1991) 1181.

71. M. Odlyha, Internal Report Opificio Pietre Dure, Florence, 1995.
72. P. Budrugeac, L. Miu, V. Bocu and C. Popescu, J. Therm. Anal. Calorim., in press.
73. V. Logvinenko, O. Kosheleva and E. Popova, J. Therm. Anal. Calorim., 66 (2001) 567.
74. R.D.Cardwell and P.Luner, in Preservation of Paper and textiles of historic and Artistic Value, ed, J.C. Williams Advances in Chemistry Series 164, American Chemical Society (1977), Ch.22 & 24.
75. E. Franceschi, D. Palazzi and E. Pedemonte, J. Therm. Anal. Calorim., 66 (2001) 349.
76. M. Odlyha, Preprints of the IIC Contributions to the Madrid Congress, September, 1992, p.104-111.
77. C. Marcolli and H.G. Wiedemann, J. Therm. Anal. Calorim., 64 (2001) 987.
78. H.G. Wiedemann, Chemie in Unserer Zeit, 35 (2001) 368.
79. R. White and A. Roy, Studies in Conservation, 43 (1998) 159.
80. J.H. Townsend, L. Carlyle, A. Burnstck, M. Odlyha and J.J. Boon in Painting Techniques, History, Materials and Studio Practice, IIC Preprints, Dublin, 1998, p205.
81. O. Pages, B. Legendre, M. Odlyha and D. Craig, Thermochim. Acta, 287 (1996) 53.
82. M.J. Schilling and W.S. Ginell in ICOM Committee for Conservation, 10th Triennial meeting Preprints, 1 (1993) 50.
83. A.N. Fraga and R.J.J. Williams, Polymer, 26 (1985) 113.
84. N.S. Cohen, M. Odlyha and G.M. Foster, Thermochim. Acta, 365 (2000) 111.
85. M.Odlyha, N.S. Cohen, G.M. Foster, A.Aliev,E.Verdonck,and D.Grandy, J.Therm.Anal., 71(2003) 939.

Handbook of Thermal Analysis and Calorimetry. Vol. 2: Applications to Inorganic and Miscellaneous Materials
M.E. Brown and P.K. Gallagher, editors
© 2003 Elsevier B.V. All right reserved.

Chapter 3

THE APPLICATION OF THERMAL ANALYSIS TO THE STUDY OF CARBONS

Pauline Phang and the late David Dollimore

University of Toledo, Toledo, Ohio, USA

1. INTRODUCTION

Carbon is known to exist in various forms. Some of these forms have been known since prehistoric times and others are of recent origin. A characteristic feature of all of these forms is the combustion to carbon monoxide and carbon dioxide in air or oxygen:

$$2C\ (s) + O_2\ (g) \rightarrow 2CO\ (g)$$

or

$$C\ (s) + O_2\ (g) \rightarrow CO_2\ (g)$$

Total combustion to carbon dioxide very rarely occurs and the proportions of CO and CO_2 vary according to the environment in which combustion occurs.

Carbon in its free form exists in the earth's crust to the extent of 0.027%. It occurs in four allotropic forms: (i) diamond, (ii) graphite, (iii) fullerenes, and (iv) amorphous carbon. The last is a supposedly non-crystalline form of carbon, capable of occurring in many morphological forms. Each form is described more fully under separate headings and their chemical reactivities, as revealed by thermal analysis, are outlined. Included in this survey are carbon black, activated carbon, decolorizing carbon, coal, lamp black, etc. Coal should also be treated under this heading, but there are many hetero atoms associated with the basic carbon skeleton. The applications of thermal analysis to the study of coals and other fossil fuels are described in Chapter 9 of this Volume. The various forms are best regarded as quasi-graphite forms of carbon where the crystallite

sizes of the graphitic plates are small, and the alignment of the plates is characterized by different degrees of randomness. This kind of structure can lead to some forms of material that are non-porous and other forms which are porous. A selection of examples of amorphous forms would include:

- animal charcoal - obtained by charring bones, meat, blood, etc.
- carbon black - various forms available, e.g. furnace black, channel black, etc. obtained by incomplete combustion of natural gas.
- lamp black - obtained by burning various fats, oils, resins, etc.
- charcoal and activated carbon - Carbomix, Carboraffin, Opocarbyl, Ultracarbon, Medicoal, and Norit - obtained from wood and other vegetable matter.

In these hetero-graphite structures, there are ample sites for attachment of hetero-atoms and groups. Thus, the Food and Drug Administration (FDA) has banned channel black (also known as gas black) for use in foods, drugs, and cosmetics because of the carcinogenic properties associated with its hetero-atoms.

2. DIAMOND

Diamond is a crystalline form of carbon which exists naturally but can be synthesized from lignin at high temperatures and pressures. It has a face-centred cubic crystal lattice.

The oxidation rates for natural diamond have been studied by Dallek et al. [1]. [111] faces convert at very small burn off to the [100] face. Oxidation of the [100] face (see Figure 1) is initiated at defect sites and proceeds laterally along the surface rather than into the bulk. The researchers used the Flynn and Wall kinetic method of analysis for studying oxidation at the [100] face. At the [111] and [110] surfaces, the activation energy was found to be approximately 96 to 184 kJ mol^{-1} and for the [100] face about 230 kJ mol^{-1}. The mechanism for oxidation of synthetic diamond powders, on the other hand, was found to be multistage, depending on the reaction medium composition and impurity content [2]. The oxidation characteristics of diamond films thus depend on the orientation of the faces of the diamond exposed in the film. The preparation of such films is best achieved by chemical vapour deposition processes.

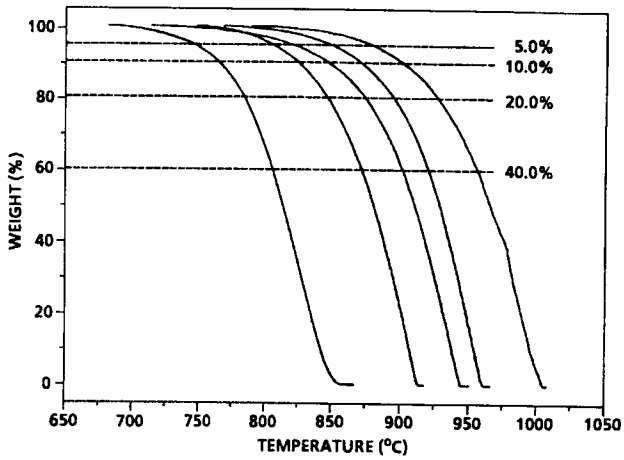


Figure 1. TG curves for the oxidation of natural diamond specimens with polished [100] faces in pure oxygen at heating rates of 0.18, 0.45, 0.89, 1.81 and 3.64 K min^{-1} [1].

3. GRAPHITE

Graphite is another crystalline form of carbon. In an ideal case, graphite consists of plates of fused hexagonal layers held 335 pm apart by weak van der Waals forces. The distance between layers can be greater than 335 pm if adsorption occurs between these layers.

The thermal oxidation of graphite might be expected to follow zero-order kinetics, with preferential oxidation occurring either at the edge atoms or the basal planes of the graphite structure. Most studies, however, seem to favour first-order kinetics, but the decision would seem to be marginal. Grade A graphite, used in atomic piles, has been studied extensively. Knibbs and Morris considered that the oxidation rates determined from thermogravimetry were higher than expected [3]. They attributed this to the porous nature of the graphite blocks. Their interpretation of the kinetics was based on a zero-order mechanism. Hawtin and Gibson [4] found an even higher activation energy. Sampath et al. found a significant decrease in the decomposition temperature and the activation energy for oxidation due to the presence of the oxides, U_3O_8, CeO_2, ThO_2, and alumina [5]. Similar effects were observed by Dollimore and Jones on spheron which had been similarly impregnated [6]. The effect of oxides on the oxidation of activated carbons and carbon blacks is discussed further below.

McKee, Spino and Lamby found that the impregnation of graphite with organic phosphorus compounds caused an increased resistance to air oxidation at elevated temperatures [7]. They argued that the thermal decomposition of these phosphorus compounds at 200 to 600 °C resulted in a hydrophilic residue, which was strongly adsorbed on the graphite surface at active sites where oxidation normally takes place.

4. THE FULLERENES AND ASSOCIATED CARBON MOLECULES

This crystalline form of carbon takes on the structural shape of a ball. Each of these 'balls' has a C_{60} structure. The C_{60} structure is known as Buckminsterfullerene (or commonly as the "buckyball"). It is only one of a number of cage carbon structures known as fullerenes. A comprehensive review of the various methods used to prepare Buckminsterfullerene has been published [8]. The most easily repeatable synthesis is that of Kratschmer et al. who produced soot containing C_{60} and higher fullerenes by evaporating graphite electrodes in an atmosphere of either argon or helium [9, 10]. The isolation of C_{60} and C_{70} molecules is readily achieved by using solvents such as benzene, toluene or methylene chloride, followed by simple Soxhlet extraction [11-14]. Further purification may be achieved by column chromatography, using various materials as the stationary phases [15-17]. The preparation of fullerenes has also led to the synthesis of tube-like carbon structures known as buckytubes or nanotubes [18-21].

Typical preparative routes lead to gram quantities of C_{60} and C_{70} fullerenes, but milligram quantities of the other varieties. Thermal analysis has been useful for the detection of these small amounts in the prepared materials. DSC has been used to measure the specific heat capacity of a C_{60} single crystal. Yang et al. established, by this method, the existence of a delta transition around 250 K and a lamda transition around 310 K [22]. Figure 2 illustrates the data obtained for the delta and lamda transitions. The bottom line in the plot of specific heat capacity versus temperature indicates the change in specific heat capacity after the intra-molecular contribution has been accounted for.

Wiedemann and Bayer [23] confirmed the existence of a sharp endothermic phase transition in the region 200 to 270 K. They also measured the vapor pressure of their material by the Knudsen method. Saxby et al. [24] showed that chemisorption of oxygen was very small, and was followed by a loss in mass due to the production of carbon monoxide and carbon dioxide. The small change in mass was confirmed by Gallagher and Zhong [25].

It has also been shown [26] that the phase change at 250 K is strongly affected by absorption of carbon dioxide, due to the very strong interaction between carbon dioxide and C_{60}.

DSC was also used to establish that the differences in thermal behaviour of the C_{60} fullerene in toluene and in other solvents may be attributed to the formation of solid solvates [27]. Although C_{60} has received the most attention, many other kinds of fullerenes have also been identified.

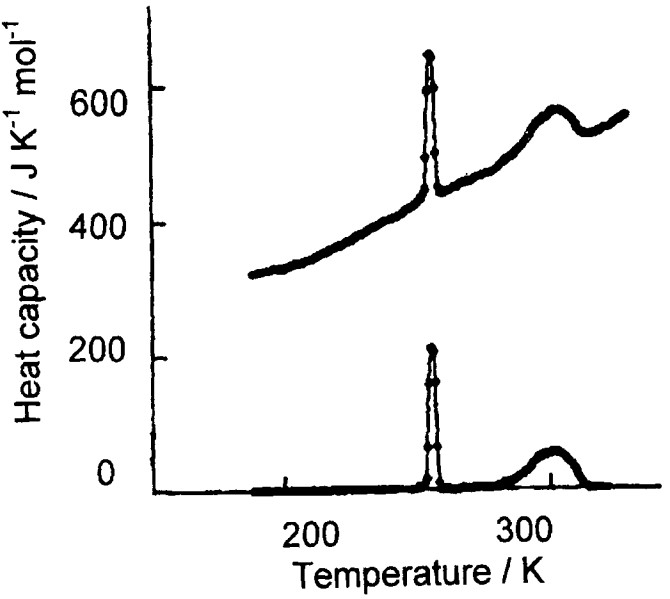


Figure 2. The delta and lamda transitions of a C_{60} single crystal [22].

5. CARBON BLACK

Carbon blacks are prepared by heat treatment of natural gas in the absence of air. Such materials find immense use in the manufacture of tyres.

The oxidation of carbon blacks in air has been studied by Azizi et al. [28]. From their investigation, a relationship between the surface and textural properties of carbon blacks and the gasification process induced thermally in air was noted. A temperature jump method was used to follow the gasification in air and to establish the relevant Arrhenius parameters. A typical graph of mass loss versus time is shown in Figure 3. Upon close inspection of the curve, it can be seen to be made up of a series of straight lines. The rates can be considered to be zero order, and hence the rate of the reaction can be calculated from the percent mass loss over a given time period. To make this calculation easier, graphs of mass loss versus temperature were constructed. A typical plot of this kind is represented in Figure 4.

All the data for each carbon black examined gave good Arrhenius plots. Overall, the data collected in this manner showed a typical compensation plot (Figure 5). The activation energy values ranged from 125 to 195 kJ mol^{-1}. These values agree with earlier work done on α and β resins extracted from coal [29]. These authors conclude that the reaction of carbon with oxygen produces surface oxygen complexes, which decompose to form gaseous products. It appears that there are at least two components to the carbon surface. One of these components is called the active surface, associated with the oxidation and gasification process while the other components are relatively inactive.

A comparison of the oxidation rates of carbon blacks was done at three different temperatures [28]. It was found to be more informative to transform the specific reaction rate to specific reaction rate per unit area and, for the purposes of comparison, to refer this rate per unit area to the oxidation rate of N774 (this carbon black was chosen as a point of reference due to its low surface area). Figure 6 shows a plot of the specific reaction rate per unit area against the total surface area for the oxidation of carbon blacks at 773 K. Similar data were obtained at 793 K and 819 K. The choice between active sites (for the gasification by oxygen) and the inactive sites would be the edge carbon atoms at the surface and the basal carbon atoms. According to Grisdale [30] and Smith and Polley [31], the rate of oxidation of carbon crystallites is about 17 times faster in the direction parallel to the basal planes (along their edge atoms) than perpendicular to them. Low surface-area carbon blacks tended to have faster rates per unit area of surface than the higher surface-area carbons (see Figure 6). In other words, the lower surface-area carbon blacks are more reactive towards oxygen than the higher surface-area carbons. The conclusion from these results must be that the lower surface-area carbon blacks have a greater proportion of their surface consisting of edge carbon atoms, whilst the higher surface-area carbon blacks expose a larger proportion of the relatively inactive basal plane carbon atoms.

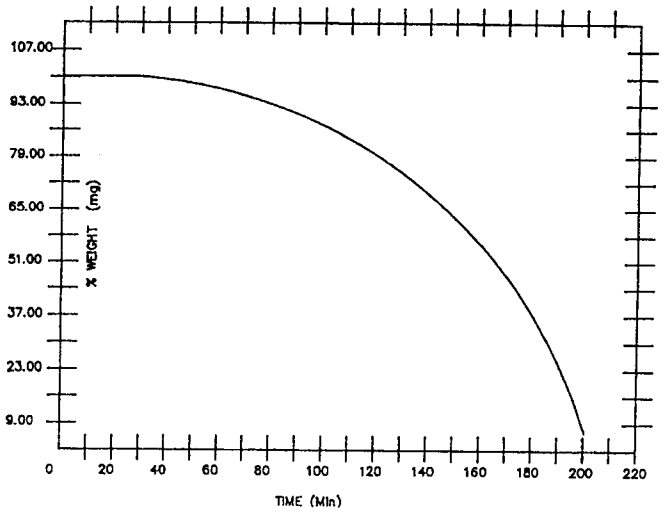


Figure 3. A typical graph of mass loss versus time for the oxidation of carbon black in air [28].

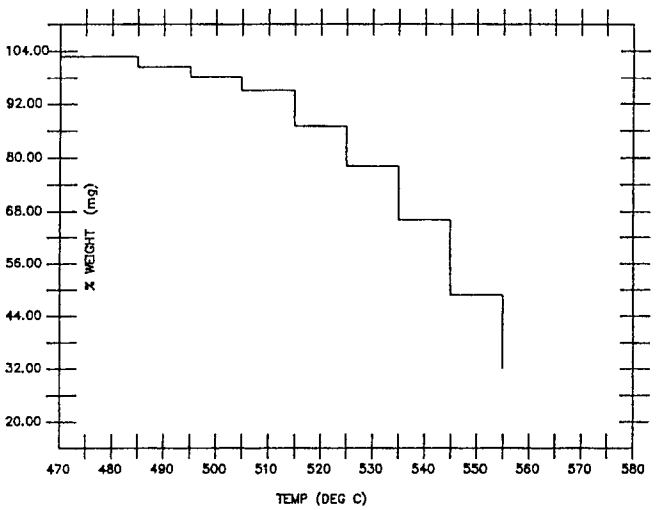


Figure 4. A graph of mass loss versus temperature for the oxidation of carbon black in air [28].

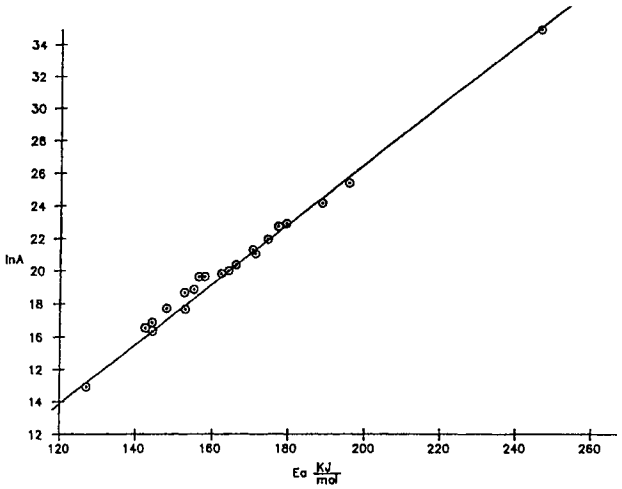


Figure 5. A compensation plot for the oxidation of carbon black in air [28].

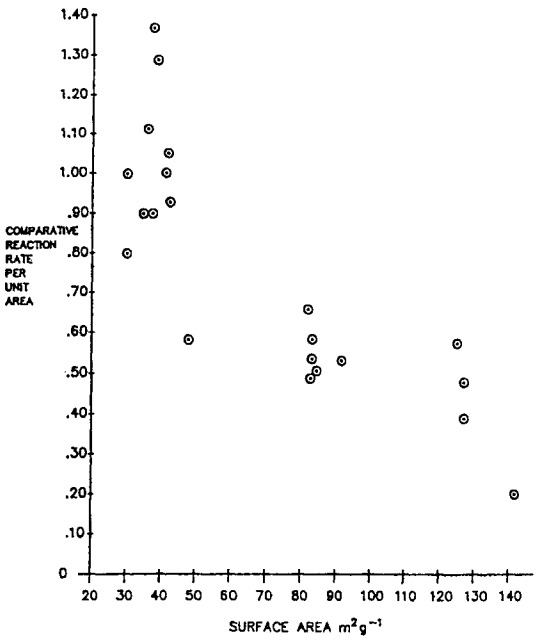


Figure 6. A plot of the specific reaction rate per unit area against the total surface area for the oxidation of carbon blacks at 773 K [28].

6. CHARCOAL

Charcoals are prepared by heating materials such as wood in the absence of air. In the laboratory, this process may be imitated by heating cellulose, and other polymeric materials in nitrogen. In practice, the production of charcoal dates back to pre-historic times where the charcoal was used as a source of fuel. In commerce, two products may be distinguished - one in which degradation to a carbon proceeds from a liquid state (commonly called cokes), while the word 'charcoal' is best reserved for degradation that proceeds from the solid state. A typical TG-DTG plot for the one-step degradation to carbon in nitrogen of pharmaceutical grade microcrystalline cellulose [32] is shown in Figure 7.

Many synthetic polymers have also been shown to degrade to carbon in nitrogen and involved in such a process must be a mechanism of chain stripping to leave a carbon residue [33].

The thermal degradation of wood in nitrogen is a multi-stage process that eventually produces carbon [34]. The complex nature of these processes is discussed in detail by Wiedemann and Lamprecht in Chapter 14 of Volume 4 of this Handbook.

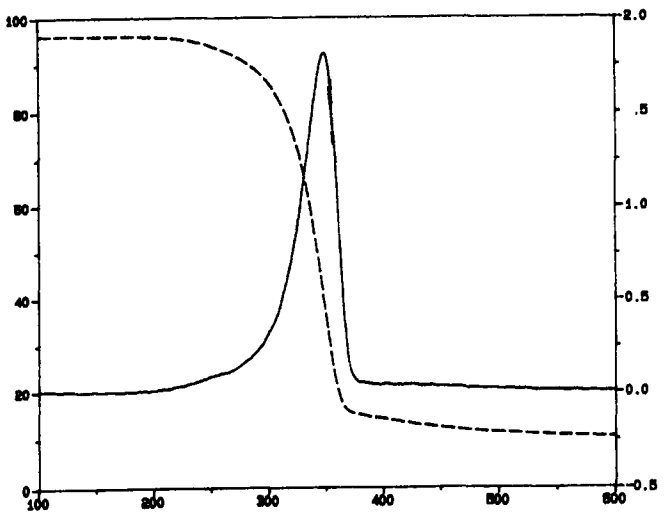


Figure 7. The degradation of pharmaceutical grade microcrystalline cellulose to carbon in a nitrogen atmosphere [32].

7. ACTIVATED CARBON

The charcoals described in the previous section may be activated to develop an extensive surface area and adsorptive capacity, usually by controlled burning in air. This process is called activation, although chemical activation to develop the adsorptive capacity is also practiced.

The basic structure of activated carbon is that of small, disoriented graphite platelets. The edges of the layers have a different electron density to that of the faces of the layer structure. These edges act as sites for organic functional groups that may be acidic or basic. These hetero groups show up in reactions or on FTIR studies and may be identified as carboxyl, phenolic, quinone, or lactone structures. The disordered structure of the graphite platelets leads to a porous structure where adsorptive studies establish the appearance of macropores (diameters of 50 to 2000 nm), mesopores (diameters of 10 to 50 nm) and micropores (diameters of 0.8 to 10 nm). Many adsorptive carbons have an apparent pore size of micropores, but an extremely high adsorptive capacity. This discrepancy may be due to the technique used for estimating the pore size distribution. Adsorption isotherms may give an analysis based on the pore size entrance, whereas behind the entrance is a very large volume - the analogy of a mailbox has been used to describe this situation.

Carbons may be activated (i.e. their surface area may be increased) by acid and alkaline washing. A comparative method that is used to prove that the reactivity has been enhanced, but avoids the more complicated use of measured Arrhenius parameters, is to record TG plots for the oxidation of these treated and untreated carbons in air and to use the oxidation of a selected carbon sample as a reference [6].

The activation of carbon by solvent extraction may be demonstrated by reference to the solvent extraction of coal, followed by heat treatment in oxygen. In the solvent extraction of coals and pitches, the magnitude and reproducibility of the results depend very largely on the experimental technique employed - particularly the concentration of solvent, temperature, and time of extraction. Thus, the results obtained are not absolute for the particular solvents used. Dollimore and Turner [29] selected solvents such as quinoline, toluene, and petroleum ether (80 to 100 °C fraction) for their work, and the procedure adopted was similar to that of Morgan, Schlag, and Wilt [35]. 100 g of sample was crushed and ground to pass a B.S.S. 60 mesh sieve and used immediately. It was added slowly with stirring to 250 mL of warm quinoline and kept below the boiling point for two hours. The mixture was then filtered, and the insoluble material collected was washed with additional warm quinoline. The quinoline - insoluble material (α-resin) was then dried in a vacuum oven at 100 to 110 °C for two hours. By progressively increasing the polarity of the solvent with

toluene, a brown precipitate was produced. Figure 8 shows the typical isothermal oxidation rates of these resins. The activation of the carbon product can be judged in terms of the surface area developed as the resin is gasified.

Dollimore and Campion prepared carbons from synthetic polymers and then followed the oxidation characteristics on a TG balance [36]. The samples of carbon were heated to 700 °C in a nitrogen atmosphere and graphitized at 2000 °C and 2700 °C. Further treatment of these samples included oxidation processing in air and in oxygen, as indicated in Table 1. The specific reaction rate was calculated on the basis of a first-order expression:

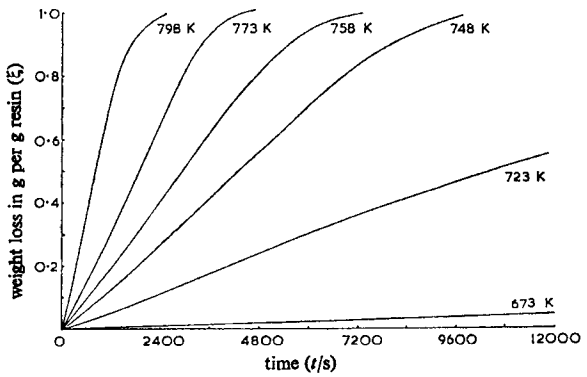


Figure 8. Typical isothermal oxidation rates of pitch α-resins at various temperatures [29].

$$k = (d\alpha/dt)\,(1 - \alpha)^{-1}$$

On the basis that the oxidation rate per unit area of reaction interface is constant, the explanation must reside in the oxidation causing an increase in available surface area. These results are presented in Table 2.

The oxidation of carbons in oxygen and in air can easily be followed by TG experiments. It is well known that most metal oxides serve as efficient catalysts in the oxidation of carbon surfaces by air or by oxygen [37 - 41]. Quantitative data on the effect of impurities are often difficult to interpret since they depend greatly on the location in, and the extent of interaction with, the carbon matrix. Long and Sykes [42] suggested that impurities interact with π-electrons of the basal planes in carbon, thus altering the bond order of surface carbon atoms with a consequent change in their ease of removal. An alternative mechanism proposes an oxidation-reduction cycle in which carbon is oxidized by the metal

oxide, which is itself reduced to a lower oxide, or the free metal [43 - 46]. Re-oxidation to the higher oxidation state is effected by the main air stream.

For spheron impregnated with manganese oxide (Mn_2O_3) and uranium oxide (U_4O_9) at different loadings, the application of the Arrhenius equation gave a two-stage plot with two distinct temperature zones [6]. The higher temperature zone was ascribed to diffusion control as the rate-determining process, while the lower temperature zone is governed by the chemical reactivity of the sample.

Table 1.
Comparative oxidation rates in air and oxygen [36]

Values of specific reaction rate: $d\alpha/[(1 - \alpha)\, dt]$

	AIR				OXYGEN	
Heat Treatment Temperature	2000°C		2700°C		2000°C	2700°C
Oxidation Temperature	500°C	550°C	550°C	600°C	2000°C	550°C
	Values at α = 0.1					
Order of Decreasing Reactivity (i)	Lactose 23.0×10^{3}	Lactose 83.2×10^{-3}	PVA 22.0×10^{-3}		Lactose 177×10^{-3}	PPF 12.2×10^{-3}
	PVA 20.0×10^{-3}	PVA 70.0×10^{-3}	PPF 12.0×10^{-3}	PPF 60.0×10^{-3}	PVA 22×10^{-3}	Lactose 12.1×10^{-3}
	PPF 5.3×10^{-3}	PPF 20.0×10^{-3}	Lactose 12.0×10^{-3}	Lactose 55.0×10^{-3}	PPF 5.5×10^{-3}	PFA 10.0×10^{-3}
	PFA 2.0×10^{-3}	PFA 10.0×10^{-3}	PFA 10.0×10^{-3}	PFA 27×10^{-3}	PVC 5.0×10^{-3}	PVC 5.6×10^{-3}
	PVC 1.7×10^{-3}	PVC 9.0 x 10-3	PVC 6×10^{-3}	PVC 23×10^{-3}	PFA 4.0×10^{-3}	

Notes: Abbreviations are:
PVC – Polyvinyl chloride carbon;
PVA – Polyvinyl alcohol carbon;
PFA – Polyfurfuryl alcohol carbon;
PPF – Polyphenol-formaldehyde carbon;
Lactose – Lactose carbon

Various models exist to describe the kinetic mechanisms of oxidation of carbons. According to Wicke [47] and Walker et al. [48], the carbon-oxygen reaction can be classified into three zones:

- Zone 1 (Low temperatures): The oxygen concentration is uniform throughout the sample and the rate of oxidation is governed by the chemical reactivity of the sample.
- Zone 2 (Intermediate temperatures): The oxygen concentration falls to zero in the interior of the sample and the rate is controlled by diffusion of oxygen into the interior of the sample (porous carbons).
- Zone 3 (High temperatures): Oxygen penetrates only a little way into the sample and the rate is controlled by diffusion across a relatively stagnant layer of gas.

Table 2.
Experimental oxidation rates ($d\alpha/dt$) of carbons [36]

Specimen	Temperature of Oxidation			
	Number of Carbon Atoms Gasified per cm^2 per s		Number of Carbon Atoms Gasified per cm per s	
	500°C	550°C	550°C	600°C
PVC carbon	1.9×10^{12}	7.3×10^{12}	2.1×10^{12}	1.1×10^{13}
PFA carbon	2.5×10^{12}	1.0×10^{13}	6.2×10^{12}	2.1×10^{13}
Lactose carbon	2.5×10^{13}	1.1×10^{14}	4.9×10^{12}	3.1×10^{13}
PPF carbon	1.0×10^{13}	2.5×10^{13}	1.0×10^{13}	4.4×10^{13}
PVA carbon	1.8×10^{13}	8.0×10^{13}	2.3×10^{14}	-
Predicted Rate from Polanyi-Wigner Equation	1.2×10^{17}	5.6×10^{17}	1.2×10^{17}	5.6×10^{17}

Sample prepared at 2000°C Sample prepared at 27°C

Variations in flow rates and sample sizes had negligible effects on rates of oxidation in the low temperature zone, showing that the mass transport of reactant gas was not a rate-controlling factor. Oxidation rates in the higher temperature zone were increased when the sample sizes were decreased, or when the flow rates were increased. This indicated a diffusion-controlled

reaction. For the low temperature zone, the values of activation energy compared favourably with results obtained by other workers [49 - 51] for graphite reacting under zone-1 conditions. Similarly, the low activation energy values in the higher temperature zone were indicative of diffusion-controlled reaction [49].

In studies where the rate-determining step is the actual reaction between surface carbon layers and oxygen, the Arrhenius equation has been used in the form of the Polanyi - Wigner expression [52], where the number of molecules decomposing per second per cm^2:

$$-dz/dt = N_o\, v \exp(-E/RT)$$

where N_o = number of molecules per $cm^2 = (r\, \rho\, N_A)/M$

v = frequency of activation = frequency of vibration of the atoms in the solid lattice (10^{13} s^{-1})

r = distance between atoms of carbon

M = atomic mass

ρ = density of carbon

N_A = Avogadro's constant

E = energy of activation

T = temperature in Kelvin

R = gas constant

Inserting the appropriate vaues for these terms gives:

$$\log_{10}(-dz/dt) = -(E/2.303RT) + \log_{10}[(2)(3)(10^{28})].$$

Campion and Dollimore [36] found that, for their samples, the oxidation activation energies were of the order of 170 kJ mol^{-1}, but there was a wide range of variation.

These theoretical rates are seen to be too high by factors between 10^4 and 10^5. The reason for the elevated numbers obtained for the theoretical rates, is due to the fact that the Polanyi-Wigner expression does not take into account factors such as variations in reactivity caused by previous heat treatment, the pore geometry or the stacking or disorientation of graphite layers.

8. CARBON FIBRES

Carbon fibres are prepared from polymer fibres. These fibres may be carbonized under tension, i.e. as they are drawn, or carbonized without the application of tension. Under tension there is a marked tendency to orient the structure and, in order to impart strength to the fibre, they may undergo

graphitization. Fibres prepared by carbonization without the application of tension tend to have a large surface area. Typical precursors are polyacrylonitrile (PAN), saran, and pitch. In the degradation of PAN fibres to carbon fibres, HCN is a by-product [53]. The carbon fibres so produced may be present as oxidized fibres or unoxidized fibres [54]. The term refers to the oxidation treatment of the PAN fibres prior to or during carbonization. The pre-oxidation of the PAN fibre secures stability during carbonization up to 1000 °C. Graphitization temperatures are commonly around 2000 °C.

DSC curves obtained on heating PAN fibres in oxygen, air and argon [55] are shown in Figure 9. At least two exothermic peaks below 400 °C can be seen in which oxidative stabilization is occurring, accompanied by shrinkage. Oxidative stabilization is thought to be due to intermolecular cross-linking. Exothermic behaviour close to 450 °C is due to oxidative gasification of the carbon residue, leading to complete mass loss at 600 °C. A broad peak below 400 °C is indicative of oxygen diffusing into the core of the fibre [55]. The authors proposed the scheme shown in Figure 10 for the processes involved.

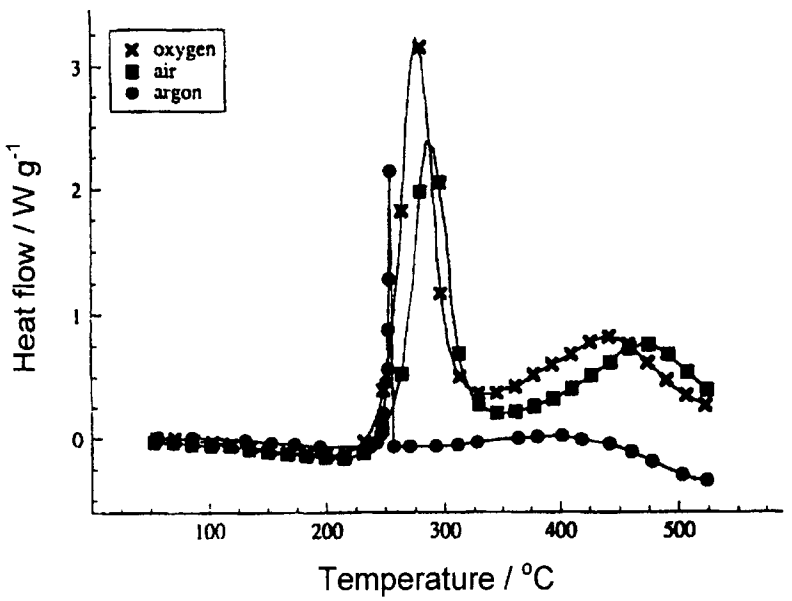


Figure 9. DSC curves for PAN fibres heated at 1 °C min^{-1} in oxygen, air and argon [55].

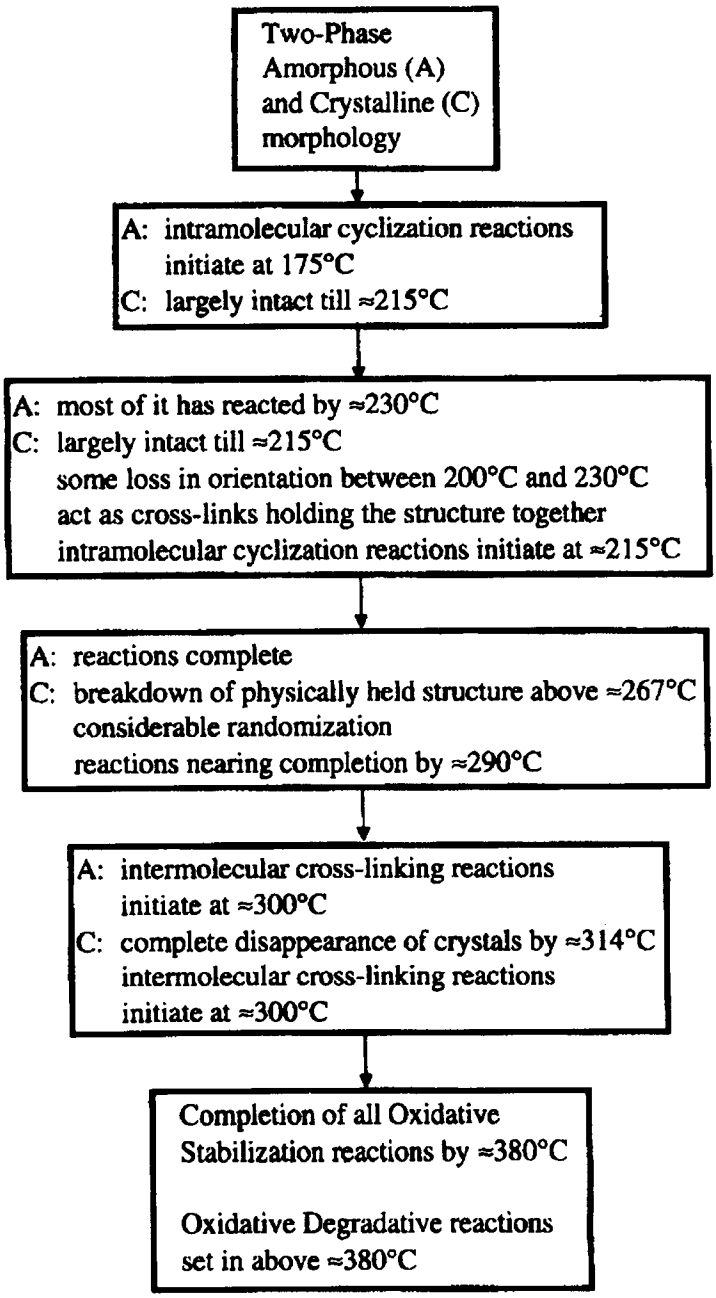


Figure 10. Scheme proposed for the oxidation of PAN fibres [55].

9. THE INCORPORATION OF CARBON INTO POLYMER COMPOUNDS AND SIMILAR STUDIES

It is commonly quoted, and supported by TG experiments in nitrogen, that carbon blacks incorporated into elastomer systems (as in commercial tyres) show evaporation of plasticizer and other organic volatiles, followed by gasification of the elastomer, leaving the carbon black behind. If, at this point, the atmosphere is changed to air, then the carbon black is oxidized to CO and CO_2, leaving behind any organic ash residues [56]. This provides analytical data on the amounts of plasticizer, elastomer, carbon black, and inorganic constituents.

Studies involving known mixtures of carbon and elastomer have shown that this traditional method of assessing carbon content may be subject to some error. This is due to interaction between the carbon and the polymer during the degradation in nitrogen, preceding the oxidation of the carbon [57]. Table 3 provides typical data on this topic. The reactivity of the carbon blacks is unaltered (see previous section). The TG data reveal that the percentage of carbon determined from the TG experiment is greater than that of the actual carbon content, and that the difference in values is highest for the carbons with the highest surface area. This suggests that the degradation of the elastomer to carbon is local and confined to the interface between the carbon and the polymer.

The observations on the relative rate of oxidation of carbon blacks, presented in Section 5 above, help in indicating the reinforcing action noted when carbon blacks are incorporated in elastomer systems. Lower surface-area carbon blacks act mainly as fillers in carbon black-elastomer systems while reinforcement is clearly seen in carbon black-elastomer systems with carbon blacks of high external surface-areas. This would suggest that the interaction between the elastomer and the basal carbon atoms is the feature that imparts reinforcing action in the carbon-elastomer composite. It is therefore suggested that this kind of oxidation study might be a useful criterion in selecting suitable carbon fillers which would have a reinforcing action in carbon-elastomer composites. Further observations are that carbon blacks recovered from elastomer composite blends retain their original reactivity. This reinforces the idea that higher rates of oxidation are associated with the presence of edge carbon atoms compared to the slower rates of adsorption of the basal carbon atoms.

Table 3.
Carbon sample reactivity to oxygen [56].

Carbon	Activation energy before incorporation in polymer system /kJ mol^{-1}	Activation energy after incorporation in polymer system /kJ mol^{-1}
N110	190.5	183.0
N234	128.8	115.5
N326	140.4	67.2
N330	125.4	102.6
N550	188.9	83.2
N650	152.5	113.9
N660	158.9	72.7
N774	182.2	92.8

It is known that high surface-area carbons expose a larger portion of the basal plane carbon atoms. Although the actual order of the oxidation reactivity is changed, the same trends in reactivity are apparent in the carbons separated from the elastomer system as in the carbons before inclusion into the polymer complex. It is known that smaller surface-area carbon blacks act mainly as fillers in elastomer formulations, while the higher area carbon blacks actually have a reinforcing action [58]. It is therefore a reasonable speculation that bonding between the carbon blacks and the elastomer concerns the basal plane atoms of the carbon black graphite structures and not the edge atoms.

10. OTHER STUDIES

Carbon, in the form of coke and pre-cursor polymer blends, is used industrially in a coupled reaction. If we consider the general oxide dissociation reaction:

$$MO\,(s) \rightarrow M\,(s) + \tfrac{1}{2}O_2\,(g)$$

then, at high temperatures, ΔG is negative and the reaction may proceed. At lower temperatures the reverse reaction will proceed:

$$M\,(s) + \tfrac{1}{2}O_2\,(g) \rightarrow MO\,(s)$$

and in this temperature region, ΔG is negative for the reaction as written. In other words, the metal oxide, MO, will not dissociate at these lower temperatures.

For the reaction:

$$C\ (s) + \tfrac{1}{2}O_2\ (g) \rightarrow CO\ (g)$$

ΔG becomes more negative as the temperature is increased.

If these two reactions are coupled, then dissociation of the oxide is possible at a much lower temperature than for the oxide alone:

$$MO\ (s) + C\ (s) \rightarrow M\ (s) + CO\ (g).$$

In other words, ΔG for the coupled reaction becomes negative at a lower temperature than for the oxide dissociation by itself. This is the basis for many metal extraction processes, and can be shown in thermal analysis experiments.

The reactions involved are not always as simply stated as this because other carbon reactions should be taken into account. For example:

$$C\ (s) + \tfrac{1}{2}O_2\ (g) \rightarrow CO\ (g)$$

and

$$CO\ (g) + \tfrac{1}{2}O_2\ (g) \rightarrow CO_2\ (g)$$

Nevertheless, these applications of carbon in the metal extraction process have found their way into thermal analysis studies, particularly thermogravimetry. Other thermal analysis studies involve investigations of gas desorption, the desorption of materials already adsorbed and regeneration studies.

REFERENCES

1. S. Dallek, L. Kabacoff, and M. Norr, Thermochim. Acta, 192 (1991) 321.
2. J.E. Butler and H. Windeschmann, MRS Bulletin, 23 (1998) 22.
3. R.H. Knibbs and J.B. Morris, Third Conference on Industrial Carbons and Graphite, Editor: J.G. Gregory, Soc. Chem. Ind., (1971) 297.
4. P. Hawtin and J.A. Gibson, Third Conference on Industrial Carbons and Graphite, Editor: J.G. Gregory, Soc. Chem. Ind., (1971) 309.
5. S. Sampath, N.K. Kulkarni and D.M. Chackraburtty, Thermochim. Acta, 86 (1985) 7.
6. D. Dollimore and W. Jones, J. Thermal Anal., 46 (1996) 15.

7. D.W. McKee, C.L. Spino and E.J. Lamby, Carbon, 22 (1984) 285.
8. G.S. Hammond and V.J., Kuck, ACS Symposium Series, 481 (1992) 1.
9. W. Kratschmer, K. Fostiropoulos and D.R. Huffman, Chem. Phys. Lett., 170 (1990) 167.
10. W. Kratschmer, L. Lamb and F. Fostiropoulos and D.R. Huffman, Nature (London), 347 (1990) 354.
11. A. Koch, K.C. Khemani and F. Wudl, J. Org. Chem., 56 (1991) 4543.
12. K.C. Khemani, M. Prato and F. Wudl, J. Org. Chem., 57 (1992) 3254.
13. P.-M. Allemand, Science, 253 (1991) 301.
14. T. Suzuki, Science, 254 (1991) 1186.
15. F. Diederich and R.L. Whetten, Acc. Chem. Res., 25 (1992) 119.
16. F. Diederich, Science, 252 (1991) 548.
17. W.A. Scrivens, P.V. Bedworth and J.M. Tour, J. Am. Chem. Soc., 114 (1992) 7917.
18. S. Iijima, Nature (London), 354 (1991) 56.
19. S. Iijima, T. Ichihashi and Y. Ando, Nature (London), 356 (1992) 776.
20. T.W. Ebbesen and P.M. Ajayan, Nature (London), 358 (1992) 220.
21. P.M. Ajayan and S. Iijima, Nature (London), 361 (1993) 333.
22. H. Yang, P. Zheng, Z. Chen, P. He, Y. Xu. C. Yu and W. Li, Solid State Commun., 89 (1994) 735.
23. H.G. Wiedemann and G. Bayer, Thermochim. Acta, 214 (1993) 214.
24. J.D. Saxby, S.P. Chatfield, A.J. Palmisano, A.M. Vassallo, M.A. Wilson and L.S.K. Pang, J. Phys. Chem., 96 (1992) 17.
25. P.K. Gallagher and Z. Zhong, J. Thermal Anal., 28 (1992) 2247.
26. Y. Nagano, T. Kiyobayashi and T. Nitta, Chem. Phys. Lett., 217 (1994) 186.
27. N. V. Avramenko, A.L. Mirakyan and M. V. Korobov, Thermochim. Acta, 299 (1997) 141.
28. J.A. Azizi, D. Dollimore, P.J. Dollimore, G.R. Heal, P. Manley, W.A. Kneller, W.J. Yang, J. Thermal Anal., 40 (1983) 831.
29. D. Dollimore and A .Turner, Trans. Farad. Soc., 66 (1970) 2655.
30. R.O. Grisdale, J. Appl. Phys., 24 (1953) 1288.
31. W.R. Smith and M.H. Polley, J. Phys. Chem., 60 (1956) 689.
32. S. Lerdkanchanaporn and D. Dollimore, Thermochim. Acta, 324 (1998) 25.
33. D. Dollimore and G.R. Heal, Carbon, 5 (1967) 65.
34. Y. Wu and D. Dollimore, Thermochim. Acta, 324 (1998) 49.
35. M.S. Morgan, W.H. Schlag and M.H. Wilt, J. Chem. Eng., 5 (1960) 91.

36. P. Campion and D. Dollimore, Thermal Analysis, Proc. 7th ICTA, 2 (1982) 1111.
37. E.A. Heintz and W.E. Parker, Carbon, 4 (1966) 473.
38. J.F. Rakszawski and W.E. Parker, Carbon , 2 (1964) 53.
39. H. Sato and H. Akamatu, Fuel, 33 (1954) 195.
40. J.E. Day, Ind. Eng. Chem., 28 (1936) 234.
41. G.J. Nebel and P.L. Cramer, Ind. Eng. Chem., 47 (1955) 2393.
42. F.J. Long and K.W. Sykes, J. Chim. Phys., 47 (1950) 361.
43. P.L. Walker, Jr., M. Shelef and R.A. Anderson, Chemistry and Physics of Carbon, Marcel Dekker, New York, 1968.
44. F.J. Vastola and P.L. Walker, Jr., J. Chim. Phys., 58 (1961) 20.
45. H. Amariglio and X. Duval, Carbon, 4 (1966) 323.
46. D.W. McKee, Carbon, 8 (1970) 131.
47. E. Wicke, Fifth Symposium on Combustion, Reinhold, New York, 1955.
48. P.L. Walker, Jr., F. Rusinko, Jr., and L.G. Austin, Advances in Catalysis, Academic Press, New York, 1959.
49. E.A. Gulbrausen, K.F. Andrew and F.A. Brassart, J. Electrochem. Soc., 110 (1963) 476.
50. S.J. Gregg and R.F.S. Tyson, Carbon, 3 (1965) 39.
51. G. Blyholder and H. Eyring, J. Phys. Chem., 61 (1957) 682.
52. M. Polanyi and E. Wigner, Z. Phys. Chem. Abt. A, 139 (1928) 439.
53. W. Watt, Third Conf. on Industrial Carbon and Graphite, Soc. Chem. Ind., Editor: J.G. Gregory, 1971, 431.
54. J. W. Johnson, P. G. Rose and G. Scott, Third Conf. on Industrial Carbon and Graphite, Soc.Chem. Ind., Editor: J.G. Gregory, 1971, 443.
55. A. Gupta and I.R. Harrison, Carbon, 34 (1996) 1427.
56. N.V. Schwartz and D.W. Brazier, Thermochim. Acta, 26 (1978) 349.
57. D. Dollimore, G.R. Heal and P.E. Manley, Proc. Nineteenth North American Thermal Analysis Society Conference, Editor: I.R. Harrison, 1990,438.
58. M. Morton, Rubber Technology, Van Nostrand Reinhold Co., 1987.

This Page Intentionally Left Blank

Handbook of Thermal Analysis and Calorimetry. Vol. 2: Applications to Inorganic and Miscellaneous Materials
M.E. Brown and P.K. Gallagher, editors
© 2003 Elsevier B.V. All right reserved.

Chapter 4

APPLICATIONS OF THERMAL ANALYSIS IN THE PREPARATION OF CATALYSTS AND IN CATALYSIS

B. Pawelec and J.L.G. Fierro

Instituto de Catálisis y Petroleoquimica, CSIC, Campus UAM, Cantoblanco, 28049 Madrid, Spain

1. INTRODUCTION

Catalysis is one of the few general fields of science that has had a great impact on modern chemical technology. In general, all commercial catalysts do not consist of homogeneous surfaces, either chemically in the strict sense of extremely high purity, or geometrically in the crystallographic (or topographic) sense. Since catalytic processes necessarily involve adsorption of molecules on the topmost layer, the characterization of this surface region is essential for achieving the predictive power needed to design new catalysts [1,2].

Catalysis and chemical engineering have made great strides in elucidating the fundamental steps involved in catalytic reactions [3]. As is well known, a catalytic reaction at a solid surface implies the following elementary steps: (i) transport of reactants to the desired surface sites, (ii) adsorption of reactants onto these sites, (iii) reaction to form the desired product either directly or through some intermediate, (iv) desorption of the products, and (v) transport of the products from the surface to the gas stream. Optimum performance of a given catalyst depends on a precise knowledge of each of these five individual steps. Modern microgravimetric techniques, working with sensitivity in the order of 10^{-6}-10^{-7} g, permit the thermodynamics, kinetics, equilibrium and mechanisms involved in each step to be evaluated.

This chapter deals mainly with the use of one of the oldest measuring tools [4,5], the electronic microbalance with all its refinements, to study and evaluate the chemical processes taking place in the bulk and surface of heterogeneous catalysts. Examples are reported to elucidate the chemical processes involved during the genesis of the catalytic material. The solid catalysts are usually contained in a chemical reactor in a rigid array such that the maximum amount of catalyst is available for reaction mixture and is not entrained in the products. To this end the catalyst is prepared either as bulk material or dispersed on a substrate

as pellets, extrudates, honeycombs, wall-supported, membranes, or other geometric configurations, depending on various reactor engineering factors such as the temperature, space velocity of the gas feed, pressure, etc., involved in the specific process. Thermal analyses are often used as a tool for investigating changes of surface and bulk reactivity of these geometries toward the environment, as a result of variations in composition, preparation method and pretreatment. Murray and White [6], and Sewell [7] were the first to derive activation energies of heterogeneous reactions from thermoanalytical data. An extensive review relating the use of thermoanalytical methods for the study of the kinetics of heterogeneous reactions has been published by Sestak et al. [8] and another on temperature-programmed methods in heterogeneous catalysis by Lemaitre [9].

For the sake of simplicity, this chapter is divided into four main sections: (i) thermogravimetry (TG), including precursor transformations, studies of dehydration/ dehydroxylation, porous structure of catalysts by means of water and n-hexane adsorption, and adsorption/desorption properties of selected gases (CO, CO_2, O_2, H_2); (ii) thermogravimetry in reactive environments, including temperature-programmed reduction (TPR), reduction/oxidation cycles, determination of stoichiometry of oxides, kinetics of reduction, measurement of active area and phase dispersion, and coking reactions; (iii), identification of surface sites by temperature programmed desorption (TPD) of adsorbed probe molecules and/or evolved gas analysis (EGA), and (iv) the information available in support of TG measurements through use of other thermoanalytical techniques, such as differential thermal analysis (DTA) and/or differential scanning calorimetry (DSC).

2. THERMOGRAVIMETRY

2.1. Introduction

The basic principles, the equipment used and the variety of techniques possible in thermogravimetry (TG) (also referred to as thermogravimetric analysis (TGA)) are described in detail in Chapter 3 of Volume 1 of this Handbook. In this section, emphasis will be placed on precursor transformations, studies of dehydration/ dehydroxylation, determination of the porous structure of catalysts by adsorption measurements and studies of the adsorption/desorption properties of gases frequently used in heterogeneous catalytic processes.

2.2. Transformation of catalyst precursors

2.2.1. Silica-supported vanadia catalysts

The formation of vanadium oxide on a silica support can easily be monitored by TG of the corresponding vanadium precursors [10]. Figure 1(b) shows the TG

curve of the vanadyl acetate silica-impregnated precursor. For comparison, the TG curve of the massive $H_2[VO(C_2O_4)_2]\cdot H_2O$ complex is also given in Figure 1(a). For this precursor, the initial 3.54 % mass loss that occurs between room temperature and 403 K is due to molecular water present as crystallization water in the complex. True vanadyl oxalate decomposition takes place at temperatures between 523 and 623 K. In this region the DTG curve shows two main peaks (exotherms) at 563 and 593 K, respectively. The first stage amounts to 47.2 % and can be attributed to the reaction:

$$H_2[VO(C_2O_4)_2] \rightarrow [VO(CO_3)] + H_2O + 2CO + CO_2$$

for which the theoretical mass loss is 48.18 %. The second stage results in the formation of V_2O_4 (permanganometric titration of V^{4+} indicated that the concentration of V^{4+} is 98.7 % of the total vanadium content). Water was only detected in the outlet of the thermoanalyzer in the first step of the thermal decomposition. Wenda [11] has shown that the decomposition of ammonium dioxovanadium (V) dioxalate occurs in two steps: the first is accompanied by an endothermic effect at 487 K to give ammonium oxovanadium (IV) trioxalate, and the second by an exothermic effect at 585 K (and another smaller one at 623 K) in which V_2O_4 is formed.

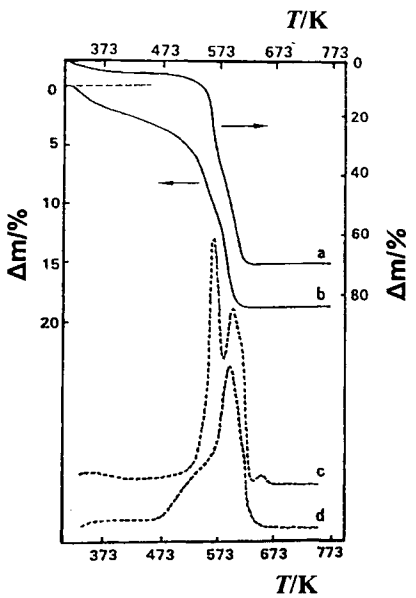


Figure 1. (a) TG of $H_2[VO(C_2O_4)_2]\cdot H_2O$ at 277 K min^{-1} in dry N_2; (b) TG of the precursor under the same experimental conditions; (c) time-temperature derivative of TG curve (a); (d) time-temperature derivative of TG curve (b).

After thermal treatment up to 873 K, the massive complex exhibited a dark colour, which became yellow upon re-oxidation with water-free oxygen at 453 K. The slight increase of mass in this process might be due to re-oxidation (to V_2O_5) of V_2O_4 and some suboxides such as V_6O_{13} and V_5O_{11}. This hypothesis is strengthened by a mass loss of the V_2O_5 (produced by oxidation at 453 K) at temperatures higher than 493 K. A similar behaviour has been observed by Roozeboom et al. [12] who found a very small mass loss at temperatures higher than 583 K for completely reoxidized vanadia on ZrO_2. The catalyst precursor (with 7.8 mass % V) shows a behaviour similar to that of $H_2[VO(C_2O_4)_2]\cdot H_2O$, although the mass loss percentages are markedly lower. An interesting point to consider here is the very large derivative TG peak that appears at temperatures slightly above 473 K for the supported vanadyl complex. This may be explained by the heterogeneity of support on the anchored complex that should be in a very high degree of dispersion on the surface.

2.2.2. Mixed oxide catalysts

TG and derivative TG (DTG) analyses have been used to reveal the chemical steps involved in the genesis of Mo-Pr-Bi-O catalysts [13]. The preparation of these mixed oxides basically involved aqueous solutions of nitric acid at pH = 2 of $(NH_4)_6Mo_7O_{24}\cdot 4H_2O$, $Pr(NO_3)_3\cdot 5H_2O$ and $Bi(NO_3)_2\cdot 5H_2O$ salts, followed by evaporation at 333 K with continuous stirring till dryness. The solid precursors so obtained were heated in an oven at 383 K for 12 h and TG analysis was then performed. The TG and DTG curves of the precursors of an Mo-Pr-Bi-O sample with a ratio Bi:Mo = 0.125 are given in Figure 2. Three decomposition steps at 400-500 K, 500-530 K and above 530 K were detected. These correspond, presumably, to the decomposition of the three compounds present in the precursors. Although separate TG analyses were also performed for ammonium molybdate and praseodymium nitrate, it was not possible to identify unequivocally each decomposition step without a more detailed study of these materials. In all cases a constant mass was observed at 823 K. Therefore, for sample preparation, the precursors underwent a final heat treatment in a forced air flow for 16 h at 823 K, raising the temperature at 15 K min^{-1}. The reagent concentrations were conveniently chosen to yield a constant Pr:Mo atomic ratio (0.125) and a variable Bi:Mo atomic ratio, ranging from 0 to 0.125 in the final samples. The analysis of these may then be formulated as $Mo_4Pr_{0.5}Bi_xO_y$.

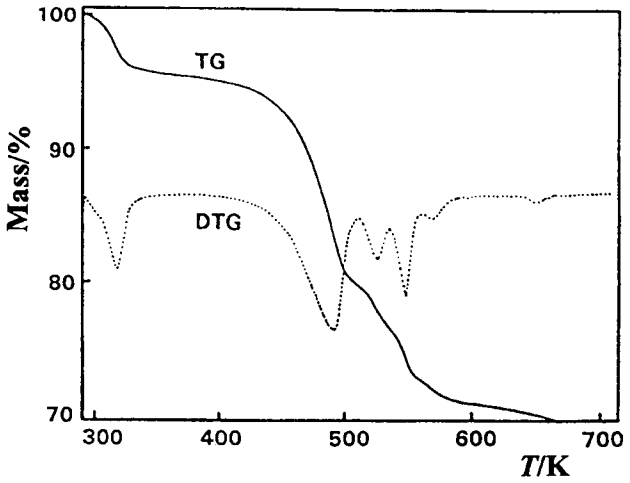


Figure 2. TG (solid line) and DTG (dashed line) curves of the precursor of an Mo-Pr-Bi-O sample with an atomic ratio Bi:Mo = 0.125 (heating rate, 1 K min^{-1}).

2.2.3. Potassium-doped CaO catalysts

Calcium oxide is very sensitive to the ambient atmosphere, which makes the composition of its surface strongly dependent on the history of the sample, as demonstrated by microgravimetric experiments [14]. Mass losses of the catalysts upon heating at a constant rate of 4 K min^{-1} in an oxygen stream are compiled in Figure 3(A). These TG curves show two well-defined mass-loss steps: one between 593 and 673 K, and an other between 723 and 973 K, which can be reasonably ascribed to the thermal decomposition of $Ca(OH)_2$ and $CaCO_3$, respectively. On the basis of the overall mass loss, quantitative calculations revealed that, besides calcium hydroxide and carbonate, a fraction of calcium was present initially as CaO. Accordingly, it must be noted that the extent of these phenomena could well hide any possible mass loss related to the presence of alkali metal. For a given catalyst composition, the ratio of the extent of these two steps depended strongly on the history of catalyst sample (specifically on the time of exposure to environment). From Figure 3(A) the TG curves of the 1.8 % K/CaO catalyst subjected to different pretreatments can be compared. Curve (a) in this figure was obtained when the dried catalyst precursor was calcined inside the microbalance in a CO_2-free oxygen stream and kept protected from the atmosphere. As can be seen, the catalyst samples became partially hydroxylated and carbonated even during the preparation and drying steps. On prolonged storage of the calcined samples in air, the high-temperature mass-loss clearly increased, while that of the first step decreased slightly (curves (b) and (c)). It was

also observed that the change in carrier atmosphere did not modify the extent of the two steps, although an oxidant atmosphere tends to shift them to higher temperatures.

Figure 3(B) compares the TG curves of K/CaO catalysts with different K contents when subjected to similar pretreatments. The total mass-loss was similar for all samples, irrespective of K content. The more pronounced differences were found in the rate of mass loss for the second step, viz., the slope at the inflection point of the high-temperature mass-losses was found to decrease when the K content increased. Also the mass loss for the 16.6 % K/CaO catalyst sample was much slower since a stable mass was only attained after prolonged isothermal treatment at the maximum temperature studied.

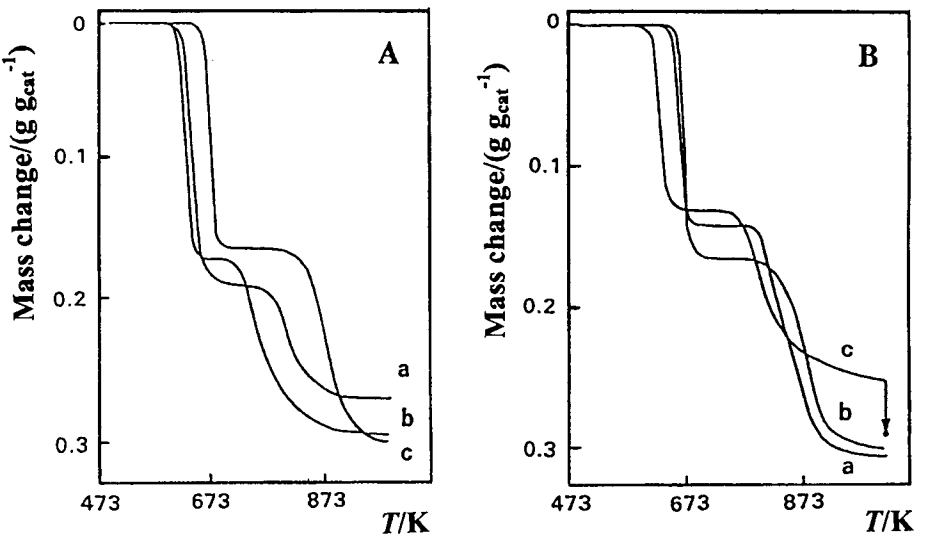


Figure 3. (A), TG curves of the 1.8 % K/CaO sample subjected to different pretreatments: (a) precalcinated in situ at 1023 K; (b) fresh sample under He atmosphere; (c) fresh sample under O_2 atmosphere. (B), TG curves of the *x*K/CaO samples with variable K amounts when subjected to the same experimental conditions: (a), CaO; (b), 1.8 % K/CaO; (c), 16.6 % K/CaO.

These results indicate that, even during the preparation of catalyst precursors at room temperature, part of the surface was carbonated by atmospheric carbon dioxide. Nevertheless, TG experiments in a CO_2-free gaseous stream indicate that our standard procedure to initiate the catalytic runs permits the catalyst surface to regenerate, thus avoiding the possible influence of the history of the sample on its catalytic performance. The modification of the chemical nature of the catalyst

during the initial step of the reaction appears to be related to the carbonation of the catalytic surface which involves mainly CaO. It is worth noting that the alkali-metal carbonates are more stable than that of calcium. Furthermore, the amount of alkali in the samples could not account for the magnitude of the mass changes observed in microgravimetric analysis. Thus, one would expect that the same phenomena should take place in the initial steps of the catalytic run over every sample, regardless of its alkali content. Therefore an initial carbonation of the catalyst during the run should take place in every case, although this has only been observed in samples with high alkali loading. In fact, when the alkali content increases, a longer period is required to complete the process, in order to observe it from the analysis of the reaction products.

2.2.4. Magnesium-nickel oxide catalyst

The magnesium-nickel mixed oxide catalyst is very active and stable for the oxidative coupling of methane ($CH_4 + O_2 \rightarrow C_2H_6 + C_2H_4 + H_2O$). The catalyst $Ni_{0.1}Mg_{0.9}O$ has been prepared following thermal decomposition of the carbonate precursor $[Mg_5(CO_3)_4(OH)_2{\cdot}4H_2O]$ method at a heating rate of 4 K min^{-1} from room temperature up to 1073 K [15]. The precursor decomposition monitored by thermogravimetry shows distinct steps (Figure 4). Up to 423 K, the desorption of

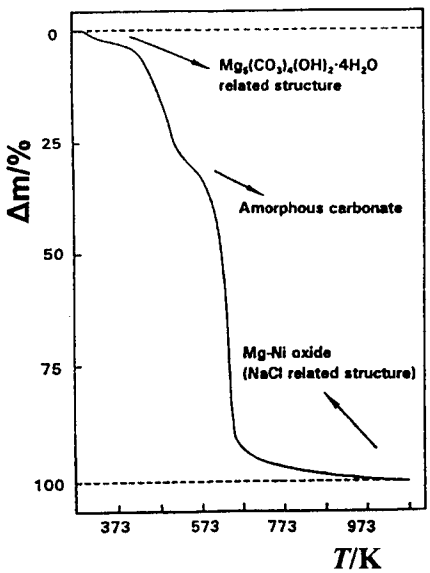


Figure 4. TG curve of the decomposition at a heating rate 4 K min^{-1} of the carbonate precursor $[Mg_5(CO_3)_4(OH)_2{\cdot}4H_2O]$ in the formation of a Mg-Ni oxide catalyst. The total mass loss is shown on the ordinate scale.

a large amount of adsorbed, coordination and lattice water occurs. Most of the water was lost between 423 and 493 K, resulting in a break-down of the structure to yield an amorphous carbonate. Between 423 and 523 K, the sample loses 25 % of the total mass loss. Finally, from 623 to 1023 K, the carbonate structure decomposes and the Mg-Ni oxide was obtained. From the TG profiles, together with XRD and FTIR experiments, it was concluded that the precursor prepared was a carbonate hydroxide of magnesium and nickel with a reasonable dispersion of both metals.

2.3. Dehydration/dehydroxylation

2.3.1. The role of water

Bulk and supported metal oxide catalysts usually contain variable amounts of water. Quantitative determination by TG methods under controlled atmospheres becomes imperative because several surface characteristics of the catalysts depend to a great extent on the population of molecular water and hydroxyl groups retained by the oxides. Although the literature on the subject is abundant, we select here only a few systems in order to emphasize the ability of TG methods to reveal the chemical processes taking place during water removal on solid surfaces.

2.3.2. Cerium oxide

CeO_2 with a large surface area was obtained by slow thermal decomposition, under constant and very low water vapor pressure [16]. A thermogravimetric curve and its time derivative of the cerium oxide precursor are shown in Figure 5. Two well-defined processes with maximum rate of mass loss at 350 and 800 K can be observed. The first mass loss, which represents 3.65 %, is attributed to loss of water coming from the surface of the precursor, either as molecular water or as both remaining hydroxyl groups and molecular water. The large tail of this first stage, extending down to about 700 K, can be ascribed to elimination of surface OH groups heterogeneously distributed on the surface. Taking into account this mass loss, the composition of the precursor was determined to be $CeO_2 \cdot 0.6\ H_2O$. The second 0.77 % mass loss, which occurs between 720 and 900 K, is attributed to decomposition of carbonate structures formed on the surface as a result of the interaction of basic surface sites with the CO_2 molecules during preparation and handling. A similar behaviour was found by Rosynek and Magnuson for La_2O_3 [17] and by Fierro et al. [18] for Sc_2O_3, although various researchers have ascribed this high-temperature mass-loss to a multi-step decomposition of oxyhydroxide intermediates.

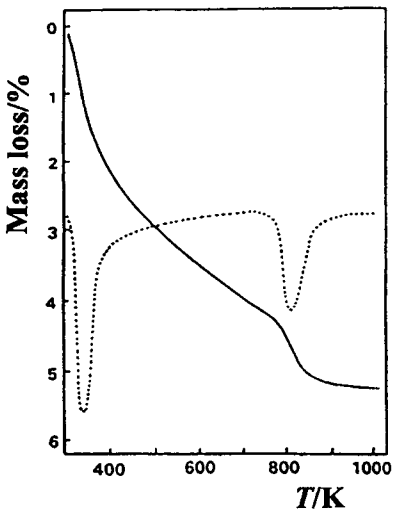


Figure 5. TG (full line) and DTG (dashed line) of a cerium hydroxide precursor decomposed at a heating rate of 4 K min^{-1} in dry nitrogen.

2.3.3. Lanthanide sesquioxides

Lanthanide oxides show a rich variety of behaviours and solid state properties which make them interesting subjects for catalytic investigations [19]. Available high-purity lanthanide oxides can be used for such a purpose, however the starting materials have a very small surface area due to the high thermal treatment required for their purification. For this reason, the preferred method of preparation converts the starting oxides into compounds that may be decomposed to give the same oxides in more porous forms. Although carbonates, oxalates, nitrates and hydroxides have been used, dehydration of the latter precursors has been favored because of the relatively low temperatures at which the decomposition occurs.

The thermal dehydration behaviours of the lanthanide sexquioxide (Ln_2O_3) precursors have been studied by TG and DTA techniques. Thermal analyses show that, in most cases, dehydroxylation takes place through an intermediate oxyhydroxide, LnO(OH) that decomposes to the respective oxide at around 670 K. The TG curve for $Yb(OH)_3$, obtained at a heating rate of 10 K min^{-1} in air [20], revealed an initial mass loss from 300 to 473 K, due to removal of crystallization water an/or physically adsorbed water on the hydroxide. The true stage of $Yb(OH)_3$ decomposition occurs in the temperature range 483 to 633 K and results in the formation of a well-defined YbO(OH) intermediate (endothermic peak). Subsequent dehydration of the hydroxide to Yb_2O_3 takes place at 633-703 K

(another endothermic peak). Strongly bound carbonates, present on the oxide surface, were difficult to remove due to the interaction of the basic trihydroxide precursor with atmospheric CO_2 during its preparation and handling. It was necessary to raise the outgassing temperature to 970 K to achieve carbonate decomposition. At temperatures around 770 K these oxides are well-crystallized and have moderate specific surface areas (10-40 $m^2 g^{-1}$).

Similar behaviour was observed for a $Sc(OH)_3$ xerogel [18]. A typical TG curve obtained for of this xerogel, at a heating rate of 5 K min^{-1} in nitrogen atmosphere, is shown in Figure 6. The initial 7.4 % mass loss that occurs between room temperature and 433 K [21,22] is due to loss of molecular water, either H-bonded bridge or crystallization water. True $Sc(OH)_3$ decomposition occurs at 423-573 K [22,23] and results in the formation of a ScO(OH) intermediate at the inflexion of the curve (point 3). Dehydration of the oxyhydroxide to give Sc_2O_3 takes place at 573-703 K [23,24]. A broad tail up to 1023 K [24,25] is due to the decomposition of carbonate structures that were formed on the surface as a result of the interaction of the strongly basic Sc_2O_3 precursor with CO_2.

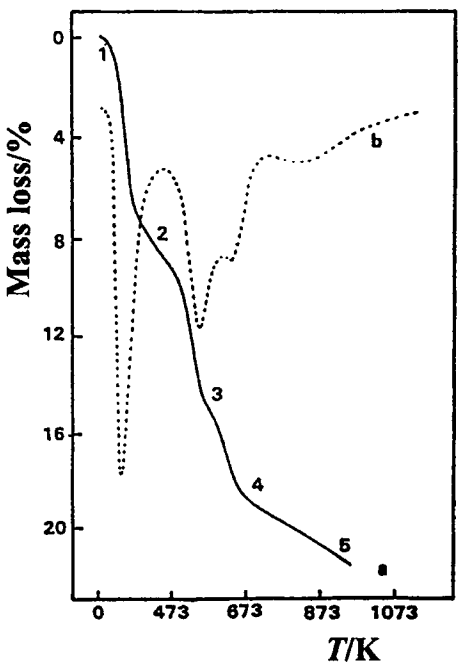


Figure 6. (a) TG curve of $Sc(OH)_3$ xerogel decomposition in dry nitrogen at a heating rate of 5 K min^{-1}. (b) Time-temperature derivative of TG curve (b).

2.4. Determination of the porous structure of catalysts

2.4.1. Techniques

Adsorption-equilibrium experiments using polar (water) and non-polar (hydrocarbons) adsorbates have been conducted by Fierro et al. [26-28] in order to evaluate the changes in porous structure of supported catalysts when subjected to thermal treatments under reactive environments. The polar character of water involves specific interactions between water molecules and hydrophilic centers, which are silanol groups or compensating cations. These experiments were carried out microgravimetrically using a Cahn 2000 microbalance connected to a vacuum line and gas-handling system, which provide either high-vacuum or controlled working atmospheres. Selected examples of the application of microgravimetric adsorption are described below.

2.4.2. Water and n-hexane adsorption on MoNaY zeolites

Molybdenum containing Y-type zeolites (10 % mass) have been prepared by thermal decomposition of molybdate-impregnated samples according to a nonconventional procedure which uses a constant-rate decomposition at very low water vapor pressure (0.10 torr) [26]. The adsorption capacities at 297 K of n-hexane (nonpolar) and water (polar) were obtained for both Mo/Y and reference NaY zeolite, previously thoroughly outgassed at 623 K. These isotherms in the entire range of relative pressures for the Mo sample decomposed at 793 K and the parent NaY zeolite samples in all cases revealed a lower adsorption capacity for n-hexane than for water. The n-hexane isotherm is type I behaviour while the water isotherm is a combination of types I and II, with an important increase of the adsorbed amount at P/P^0 above 0.8. In parallel to these measurements, the N_2 adsorption isotherms at 77 K were obtained, and the surface areas were calculated from the apparent monolayer point. These isotherms could not be fitted to the usual two-parameter BET equation, showing instead type I behaviour. From the sorption capacity measurements, one can conclude that the zeolite structure was largely retained when the impregnated material was activated at temperatures below 623 K. Above this temperature, the relative adsorption capacities of both adsorbates (at $P/P^0 = 0.4$), with respect to the parent NaY zeolite, decreased with increasing calcination temperature [26], indicating that crystallinity, and therefore pore structure, becomes partially destroyed.

2.4.3. Water adsorption on NiHY zeolites

The changes in porosity brought about by nickel incorporation into HY zeolites was revealed from the adsorption isotherms of water by Pawelec et al. [27]. The water sorption isotherms were determined for various calcined xNi (x = 1.4, 5.0 and 9.0 % mass) samples at 298 K at relative pressures P/P_0 between 0 and 1. For all catalysts, the water isotherms exhibit a rapid increase in water adsorption at

P/P^0 below 0.2, which increases slowly up to P/P^0 close to 0.8. By comparing the amounts of water condensed at $P/P^0 = 0.4$ (Table 1), it is apparent that the Ni-free zeolite shows the maximum sorption capacity. A very small decrease in sorption capacity is observed for the 1.4 Ni and 5.0 Ni zeolites and slightly larger for the 9.0 Ni homologue. This is expected because the micropore volume of the zeolite decreases with increasing Ni percentage. The maximum volume (W_o) accessible to water was calculated from the Dubinin-Raduschkevitch (DR) equation [29-31]. In the linear form, the DR isotherm is:

$$\log W = f[T \log(P^0/P)] \quad (1)$$

The ordinate at the origin of the line defines W_o. The linear transforms of the DR equation for the isotherms are shown in Figure 7, and the W_o values are compared in Table 1 with the results of N_2 isotherms at $P/P^0 = 0.2$. The maximum W_o and N_2 adsorption capacities are observed for the USY zeolite, but they decrease for xNi samples. The strongest decrease is observed at the highest Ni content. Accordingly, both the N_2 sorption capacity and the maximum micropore volume of the zeolite accessible to water provide information about the distribution of Ni within the zeolite pores.

Table 1.
Water adsorption at 298 K (P/P^0=0.4) and N_2 adsorption at 78 K (P/P^0=0.2) for xNi/HY zeolites

Zeolite	Ni (mass %)	W_o (cm^3/g_{zeo})[a]	V_{N2}(cm^3/g_{zeo})
1.4 Ni[b]	1.4	0.35	176
5.0 Ni[c]	5.0	0.34	165
9.0 Ni[c]	9.0	0.28	164
USY	-	0.37	185

[a] W_o is the maximum volume of the zeolite accessible to water.
[b] The catalyst prepared by ion exchange.
[c] The catalyst prepared by ion exchange followed by impregnation.

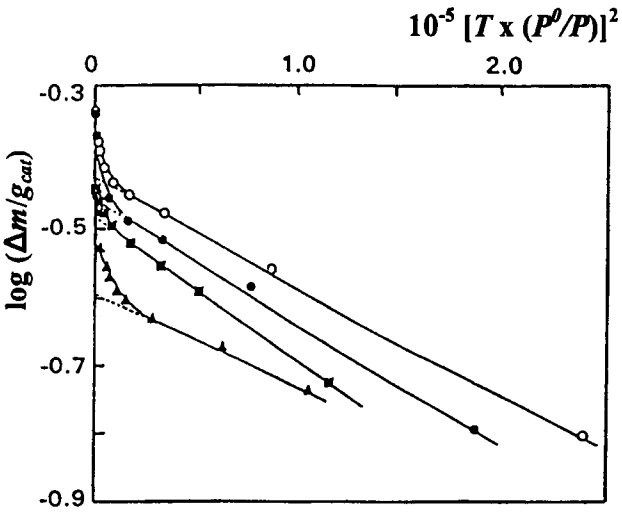


Figure 7. Dubinin-Raduschkevitch (DR) [29-31] transforms (see equation (1)) for the adsorption isotherms of water at 295 K on unsulfided *x*Ni/USY zeolites: (○), HY; (●), 1.4 Ni; (■), 5.0 Ni; (▲), 9.0 Ni.

As expected from the low ion-exchange capacity of HY zeolite the extent of Ni-exchange in this zeolite was rather small but sufficient to exchange essentially all the Ni in the 1.4 Ni zeolite. However, incorporation of larger amounts of Ni by ion-exchange and impregnation procedures (samples 5.0 and 9.0) leads to a poorly dispersed NiO phase. As the Ni content increases in the 5.0 and 9.0 Ni zeolites, it can be assumed that the proportion of exchanged nickel does not change substantially but the fraction of nickel deposited on the inner or outer surface of the zeolite crystals increases. As confirmed by all the characterization data the two different preparation methods and the severe calcination conditions led to a different Ni distribution in macro- and mesopores of the zeolite and result in the formation of some NiO on the outer surface. Water and N_2 adsorption indicate a small change in volume for the three *x*Ni zeolites, and the volumes indicate that the porous structure of the zeolite is not blocked by the NiO precursor. This finding suggests that for the *x*Ni zeolites with highest Ni content (5.0 and 9.0 Ni) an important fraction is located on the outer surface of the zeolite crystals.

2.5. Thermogravimetry in the study of adsorption/desorption on catalysts

2.5.1. Introduction

In this section, the adsorption properties of simple molecules on the surface of metal oxides or mixed oxides are reviewed. Important parameters derived from these studies, such as kinetics of adsorption, monolayer coverage, activation energies and isosteresis in heats of adsorption, provide useful information to describe chemical processes taking place at the catalyst surface. Attention is focused in the next section on CO, O_2 and CO_2 molecules since these are all involved in CO oxidation.

2.5.2. CO adsorption on mixed oxides

The kinetics of CO adsorption on the perovskite-type oxide, $LaCrO_3$, at various pressures (3 to 120 torr) and constant temperature (523 K), and variable temperature (273 to 724 K) and constant pressure (50 torr) has been studied by Fierro and Tejuca [32] using a vacuum microbalance. The adsorption isobar showed a sharp maximum at ~ 500 K. The experimental data fit satisfactorily the integral Elovich's equation (see equation (2), below). The existence of a precursor state previous to the adsorption process itself has been shown by means of analysis of t vs $Z(t)$ (reciprocal of the adsorption rate) curves. The ascending branch of the isobar (between room temperature and 500 K) corresponds to the activated adsorption of the CO molecule. From the Arrhenius plot of r_m (maximum adsorption rate at zero time) versus $1/T$, an activation energy of 9.7 kJ mol^{-1} was calculated. From plots of r_m vs P, a specific rate constant of 0.69 ±0.03 torr-1 was obtained.

Effect of temperature: The integral kinetic data (q vs t) at a constant pressure (50 torr), in the range 273-724 K are plotted in Figure 8. At each temperature, the adsorbed amount (q) at equilibrium ($t = \infty$) was also recorded. The CO isobar showed an ascending branch between 273 and 500 K, and a descending one above 520 K. The adsorption behaviour of O_2 on the $LaCrO_3$ system was somewhat different: it showed a slight decrease in the adsorbed amount in the temperature range 273-370 K and then an important increase between 370 and 670 K (at 670 K, q_{O2} becomes larger than that at 370 K by a factor of 6). Finally, above 670 K, a very sharp decrease in q_{O2} was observed. The maxima of q_{CO} (at 520 K) and q_{O2} (at 670 K) were 60.0 and 44.5 μg m^{-2}, respectively, i.e., q_{O2} (max) is 74 % of q_{CO} (max). However, at 400 K, where the catalytic reaction CO + 1/2 $O_2 \rightarrow CO_2$ on $LaCrO_3$ begins, q_{O2} only amounted to 18 % of q_{CO}.

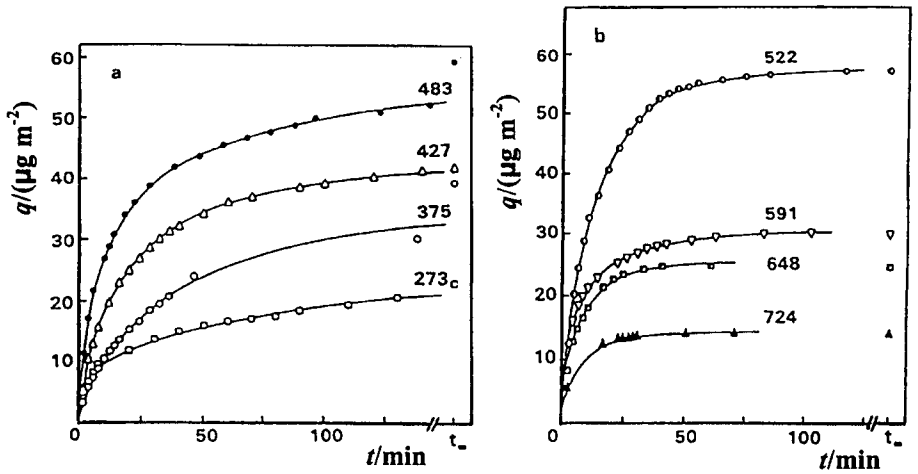


Figure 8. Integral kinetic data for CO adsorption on $LaCrO_3$ at constant pressure (50 torr) and different adsorption temperatures (K). q is the amount adsorbed at time t.

Effect of pressure: Figure 9 displays the integral kinetic data (q vs t) for adsorption of CO on $LaCrO_3$ at 523 K and pressures between 3 and 120 torr. At short adsorption times (less than 3 min) the isothermal curves overlap, but at larger times a clear separation between them appears. Although there is some controversy about whether differential or integral data should be employed in the analysis of the experimental results [33], we considered here only the integral data due to their smaller uncertainty, especially in the first seconds after the admission of gas to the microbalance bottle. Disturbances caused by convection streams (peak-to-peak signal of 10 μg), and reactor geometry make it difficult to determine the maximum adsorption rate (at t = 0, i.e., at the time of gas admission).

In this work, these problems were obviated by means of analytical differentiation of the polynomial function which fitted the experimental results best. The maximum adsorption rates (r_m) at t = 0 were calculated following this analytical method. Values of these rates at 523 K, as a function of the adsorbate pressure, are plotted in Figure 10. An approximately linear dependence of r_m on P was found and the nearly straight line (which does not pass through the origin) has only a small slope. Extrapolation to zero pressure yields a value of 7.3 μg CO m^{-2} min^{-1} for the adsorption rate. This (instantaneous) rate is not dependent on the pressure and its direct measurement would be difficult because mass transfer [34] and thermomolecular effects [35,36] may influence the adsorption process.

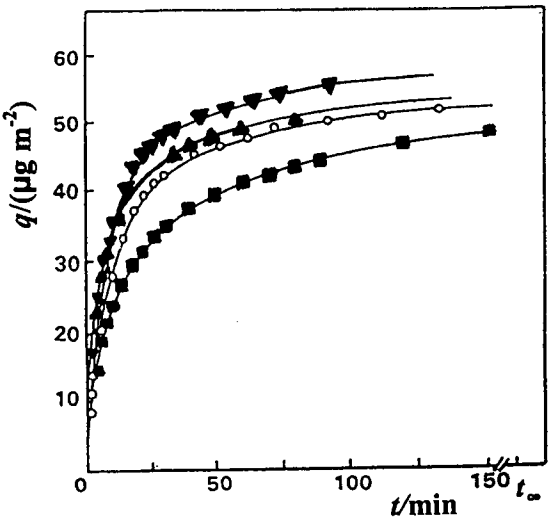


Figure 9. Integral kinetic data for CO adsorption on $LaCrO_3$ at 523 K and different pressures. (■), 3.6; (○), 8.5; (▲), 20; (▼), 117 torr. q is the amount adsorbed at time t.

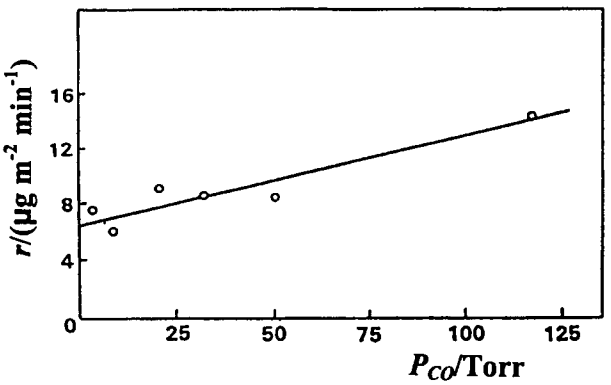


Figure 10. Effect of pressure on the initial adsorption rate, r_m, for CO adsorption on $LaCrO_3$ at 523 K.

Precursor adsorption state: In the first seconds after contacting the adsorbate with the adsorbent surface, the adsorption process is fast. After this, adsorption occurs at a considerably lower rate. An interpretation of this phenomenon, on the basis of a precursor state through which the adsorption occurs, was given by Gundry and Tompkins [37]. The presence of this precursor state can be

demonstrated by analysis of the experimental results with Elovich's equation modified by simple transformations.

Elovich's equation in its integral form is:

$$q = (1/b) \ln (ab) + (1/b) \ln (t + t_0) \quad (2)$$

where a, b and t_0 are constants which depend on the experimental conditions, and q is the amount adsorbed at time t. If it is assumed that equation (2) is obeyed from the start of the adsorption process, then $q = 0$ at $t = 0$, therefore:

$$t_0 = 1/(ab) \quad (3)$$

Aharoni and Ungarish [38] devised a very simple method for the evaluation of t_0 from experimental results without introducing any hypothesis on the existence of pre-Elovichian adsorption. Equation (3) can be expressed as:

$$t + t_0 = Z(t)/b \quad (4)$$

where $Z(t)$ is the reciprocal of the adsorption rate which, of course, is a function of time. A plot of t vs $Z(t)$ should be linear in the Elovichian range and its extrapolation at $Z(t) = 0$ directly gives t_0.

Following this method, the integral kinetic curves for a constant pressure of 45 torr and temperatures between 273 and 724 K were plotted according to equation (4). Curves of t vs $Z(t)$, corresponding to the ascending (a) and descending (b) branches of the CO isobar, were of a sigmoidal type, particularly those in the interval 273-500 K, from which a value of t_0 was obtained by means of a graphic method (extrapolating the linear segments to $Z(t) = 0$, Table 2). For the system $CO/LaCrO_3$, the sigmoidal shape of the plots t vs $Z(t)$, in the first minutes of the adsorption process and for temperatures in the ascending branch of the isobar, clearly shows the presence of an (activated) precursor state prior to the proper adsorption of CO.

Assuming that a small difference exists in q_0 values [39] for the instantaneous process in the ascending and descending branches of the isobar, any difference in t_0 for these two regions will proceed from differences in b. As is well known, the ascending branch of an adsorption isobar is associated with the activated process, whereas the adsorption rate is controlled by the rate at which the CO molecules overcome the energy barrier. In this case, the adsorption rate increases with the temperature up to 520 K (maximum of the isobar). At higher temperatures, in the descending branch (higher kT), the desorption rate becomes important, and also the concentration of species weakly bound to the adsorbent surface decreases, so that the net rate of adsorption becomes lower. This is the reason for the drastic

change in b values (Table 2) observed at temperatures higher than the isobar maximum.

Effect of temperature: Activation energy: The interpretation of the kinetics of adsorption on solids had been made, in many cases, with idealized models in which a homogeneous surface of the adsorbent was assumed. On this basis, a single kinetic equation which satisfactorily describes the integral data over a wide range of temperatures and pressures has been developed, although it is well established that the adsorption energy is a function of coverage.

For the system $CO/LaCrO_3$, the kinetic data were fitted to the integral equation (2), although the differential equation was also used for the calculation of kinetic constants of adsorption. Elovich's plots (q vs ln $(t+t_0)$) for a CO pressure of 45 torr and temperatures between 273 and 740 K were obtained and the parameters a, b and $1/ab$ for several temperatures are summarized in Table 2. As can be observed, a and b values do not follow a monotonous trend throughout the studied temperature interval. Reexamining published experimental results, Low [40] found a very simple relation between the exponential parameter b of Elovich's equation and the temperature: $b = \alpha - \beta/T$ (α and β are constants). However, it should be emphasized that these types of relations are obeyed only within specific intervals of the adsorption isobar (the ascending or descending branch). This is perhaps the most important impediment for comparisons of the kinetic and equilibrium data that have appeared in the scientific literature over the years.

Shereshefsky and Russell [41] and Leibowitz et al. [42] have calculated activation energies derived from r_m as given by the equation $r_a = 1/(bt)$, where b is the exponential parameter of Elovich's equation and r_m is the adsorption rate at time t. In our view, the determination of the maximum adsorption rate (r_m) at zero time is the best method for the calculation of E_a (it should be pointed out here that E_a should be calculated only in those temperature zones where the adsorption isobar shows an ascending branch). In the system under study, the plot of ln r_m vs $1/T$ in the interval 273-520 K is a straight line. From its slope a value of 9.7 kJ mol^{-1} for the activation energy of CO adsorption on $LaCrO_3$ was calculated.

Table 2.
Kinetic parameters of equation (2) for isobaric experiments on the system $CO/LaCrO_3$

T (K)	a	b	ab (min)	t_0^a (min)	r_m (g m^{-2} min^{-1})
273	16.7	0.216	3.6	3.6	2.29
375	45.4	0.098	4.5	4.2	2.42
427	28.9	0.086	2.5	2.8	3.13
482	37.1	0.068	2.5	2.7	7.46
522	56.3	0.053	2.9	2.9	8.50
591	5.9	0.170	1.0	1.1	14.73
648	6.5	0.156	1.0	1.4	7.38
724	11.2	0.216	2.4	1.8	5.75

[a] Calculated from $t + t_0 = Z(t)/b$

2.5.3. Interaction of cumene on a silica-alumina surface

The chemical interaction of cumene with the OH groups of silica-alumina has been microgravimetrically studied by Corma et al. [43]. It has been found that the surface of the silica-alumina is heterogeneous for the adsorption of cumene, and the Freundlich model fits the experimental results reasonably well.

The catalyst samples were always degassed at 10^{-6} torr before the isotherms were recorded. After each isotherm was obtained and the vapor desorbed, a very small amount of coke remained on the catalyst surface, so a fresh sample was used in each run. The system was considered to have achieved the adsorption-desorption equilibrium when the change in mass of the sample was less than 5 μg h^{-1}. Measurements of the uptake rate were performed in the pressure interval 0.4 to 10 torr at temperatures between 424 and 497 K. The vapor pressure of hydrocarbon in the microbalance chamber was large compared to the amount adsorbed. The specific adsorption rate (calculated according to reference [44] was independent of sample mass, indicating that the mass transfer effects within the powder were not limiting the rates. For example, at a constant pressure of hydrocarbon (0.4 torr) and 435 K, the experimental rates of 5.69 ± 0.17 and 5.81 ± 0.17 mg cumene g^{-1} min^{-1} obtained on 43 and 15 μm particle-size samples, respectively, were recorded. The close agreement in both experiments must be considered conclusive.

Cumene adsorption isotherms were measured at 453, 473 and 493 K, in the range of 0-5 torr of cumene partial pressure, and the results are given in Figure 11(A), showing that the isotherm exhibited Brunauer type-I behaviour [45], the surface coverage of the monolayer being 1.65 mmol of cumene per gram of sample. The heats of adsorption, and their dependence on cumene coverage, have

been calculated by application of the Clausius-Clapeyron equation to the family of isotherms. This equation is:

$$[d(\ln P)/d(1/T)] = - Q_{iso}/R \qquad (5)$$

where P is equilibrium pressure at temperature T, Q_{iso} is the isosteric adsorption heat and R is the gas constant. The heats of adsorption at different coverages are plotted in Figure 11(B). These results fit an adsorption model fairly well in which the number of sites of a given adsorption heat decreases exponentially with increasing adsorption heat. At lower coverages, the cumene molecules are adsorbed predominantly on the stronger acid sites, while they also adsorb on the sites of medium and low acid-strength at higher coverages. It is clear that if a wide range of coverages is considered, these adsorption data cannot be fitted by a Langmuir adsorption model. However, in most kinetic studies of cumene cracking, a Langmuir-type adsorption is assumed [46,47] and good fits with the overall kinetic models are obtained. To rationalize these results with the heterogeneity of the surface of cumene adsorption, one may assume that, although cumene can be adsorbed on acid sites within a wide range of acid strengths, not all of the adsorbed species can evolve to form a carbonium ion and, consequently, only the cumene molecules adsorbed on acid sites of a short range of strengths evolve in the reaction coordinate. The question that now arises is which range of acidities can give "active" adsorbed species.

For the range of coverages studied here, the Freundlich equation:

$$q_A = c \cdot P^{1/n} \qquad (6)$$

has been found to fit the experimental results, as can be seen from the plots of ln q_A vs ln$P$ for each temperature. Straight lines with correlation coefficients higher than 0.99 are obtained at the low surface coverages where this equation is expected to apply. Values of n (and therefore of $-H_m$) and c calculated by extrapolation to an equilibrium pressure of 1 torr and from the slopes of these straight lines, respectively, are summarized in Table 3.

Extrapolation of the set of isotherms to an intersection point gives the amount of cumene required for one monolayer, 0.68 mmol/g, at an equilibrium pressure near 200 torr. This value is lower than that found in physical adsorption (1.65 mmol/g), for which a close packing of cumene molecules was assumed.

Table 3.
Parameters of Freundlich's equation

$1/n$	T (K)	nT (K)	nRT (J mol^{-1})	c (mmol g^{-1}) [a]
0.5577	453	812.3	6790	4.7×10^{-2}
0.6734	473	702.4	5872	3.1×10^{-2}
0.7527	493	655.0	5476	2.0×10^{-2}
			H_{max} = 6046	

[a] Calculated for an equilibrium pressure equal to 1.0 torr

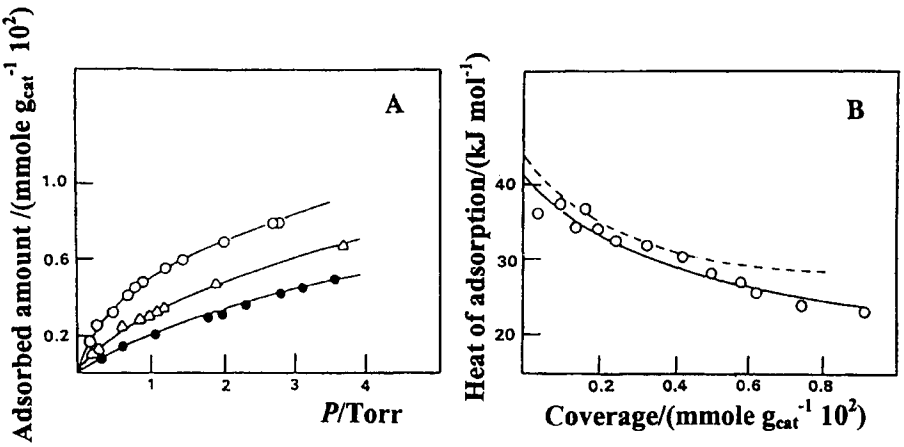


Figure 11. (A) Adsorption isotherms of cumene: (○) 453 K, (Δ) 473 K, (●) 493; (B) Heat of adsorption: (○) experimental results, (- - -) results computed from equation $Q_{iso}(\theta) = -6.05 \ln\theta$.

2.5.4. H_2 and CO_2 adsorption on scandium oxide

Scandium oxide has been selected as a model catalyst because it is a typical insulator oxide with a relatively stable and easy to reproduce surface. This property has been considered and exploited to validate the application of models which describe both the kinetics and equilibrium of adsorption of simple molecules. Following this philosophy, Pajares et al. investigated the kinetic and equilibrium adsorption of CO_2 [48,49] and H_2 [44] on Sc_2O_3. The integral chemisorption kinetics of hydrogen on scandium oxide fitted the integrated Elovich equation (equation 2) well, but this kinetic law was not obeyed for CO_2 chemisorption. For H_2 chemisorption, t_0 values from $Z(t)$ curves (Aharoni and

Ungarish's method) agreed with those obtained from q vs $\ln(t + t_0)$ plots. For CO_2 chemisorption. The data fitted an integrated kinetic law:

$$\ln [q_e/(q_e - q)] = kPt \quad (7)$$

based on a Langmuirian treatment. The quantity q_e is the amount adsorbed in the equilibrium isotherm, and the fraction of clean surface is given by $(q_e - q_0)$, which is an experimentally measurable quantity. In plots of the integrated equation, $\ln [q_e/(q_e - q)]$ vs t, the intercepts give information about q_0, the quantity chemisorbed very rapidly at "zero time". The value of q_0 is related to the gas pressure and to the state of surface dehydroxylation.

The adsorbed equilibrium amounts of H_2 and CO_2 on Sc_2O_3, at a constant pressure of 30 torr, as a function of OH coverage are given in Table 4. The plot of equilibrium adsorption *vs* OH coverage is nearly a straight line with a negative slope which points to competition between OH and H_2 (or CO_2) for available surface sites. From this, it is clear that the state of the surface has a strong influence on the amount of chemisorbed H_2 or CO_2 and on the rate of adsorpton, which both increase as the number of hydroxyls on the surface are decreased.

Table 4.
Amounts of H_2 and CO_2 adsorbed on Sc_2O_3 for different outgassing temperatures

T/K	n/(OH/nm^2)	q_{H2} (μg g^{-1})	q_{CO2} (μg g^{-1})
373	6.2	47	460
423	4.3	78	805
473	2.7	105	1040
573	2.0	120	1150
673	1.4	125	1200
773	0.9	128	1250

Both systems show similar behaviour, with a marked decrease of H_2 adsorption for outgassing temperatures lower than 429 K, where OH coverage is greater than 2 OH per nm^2. This points to a competitive adsorption of H_2 and CO_2 with the OH groups on the surface [44,48,49].

The study of the effect of CO_2 pressure on the highest recorded rate of adsorption, r_{max} has been limited to a restricted range, 1-20 torr, where problems introduced by gas dynamics are reduced to a minimum. Above 1.5 torr, the rate of adsorption depended linearly on the pressure of CO_2. Extrapolation to zero pressure indicated a significant initial rate of adsorption, because the straight lines do not cross the ordinate axis at the zero point. At pressures below 1.5 torr, the

plot dq/dt vs P bends toward the origin. Mathematical analysis is complicated because account must be taken of the intervention of the thermomolecular effect and limitations in the mass transport to the gas/solid interphase.

The sample behaviour was found to depend strongly on the outgassing temperature. When the sample was well hydroxylated, by desgasification at low temperatures, good fits to equation (7) were not found; adsorption constants were low and values for $(q_e - q_0)$ were very small. If the Sc_2O_3 sample underwent a stronger pumping treatment, good kinetic fits were found, with large $(q_e - q_0)$ values, which reflect the degree of surface dehydroxylation. The calculated q_0 for samples pumped out at 623 and 798 K have equal values.

The basis of equation (7) is the introduction of a driving force, $(q_e - q)$, as the factor related to the clean surface fraction. The factor $(q_e - q)$ is obviously proportional to the available fraction of adsorption centers, and it can be experimentally measured. This method eliminates indeterminate variables in the calculations of such a factor. For example, those related to the use of the BET monolayer or the value deduced from the Freundlich isotherms cross-point when both do not reach the same values; or those derived from numerous systems with a pseudo-Langmuirian behaviour, where the isotherms fit a Langmuir equation at each temperature, but the value for the monolayer progressively decreases at increasing temperatures. In summary, it was found that the $(q_e - q_0)$ values are very important and that they are clearly associated with the extent of surface dehydroxylation, given in the last column of Table 5.

Table 5.
Effect of the state of surface hydroxylation of Sc_2O_3: Parameters from fitting to equation $\ln[q_e/(q_e - q)] = kPt$[a]

T_{des} (K)	$k \cdot 10^2$ (torr^{-1}·sec^{-1})	$q_e - q_0$ (μg of CO_2 g^{-1})	q_0 (μg of CO_2 g^{-1})	OH/100Å^2
252	0.61	164	531	Total
458	0.57	220	583	12
623	1.41	643	232	4
798	1.37	936	204	1.5

[a] $T = 298$ K; $P = 4.6$ torr

3. THERMOGRAVIMETRY IN REACTIVE ATMOSPHERES

3.1. Temperature-programmed reduction (TPR)

3.1.1. Reduction of oxides

Thermogravimetry (TG) combined with temperature-programmed reduction (TPR) is a widely used technique for the characterization of reducible catalysts. The reduction of solid materials such as metal oxides, sulfides or halides, has been studied extensively with microbalances to determine the effect of temperature, pressure and gas composition on the extent and rate of reduction. In general, the mechanism of reduction is sought from the mass loss as well as from other supplementary data. The reaction of many transition metal oxides with H_2 or CO has been investigated, and the gravimetric data have been supplemented with measurements of surface area (to investigate sintering of the metal phases), X-ray diffraction, IR spectroscopy of the products and magnetic susceptibility. Sample size, impurity additions, the influence of a carrier substrate and the effect of static or flowing gas mixtures have also been studied. In this section, some examples of integral mass changes as a function of the reduction temperature are reported.

$PrCoO_3$ catalysts: Small cobalt particles deposited on the surface of lanthanide oxides constitute a class of important catalysts for a large variety of technologically important reactions, such as CO hydrogenation, methane reforming and selective hydrogenations. These metal catalysts are usually obtained by reduction of cobalt oxide precursors under H_2 atmosphere and controlled temperature. The first example selected here is a mixed oxide, $CoPrO_3$, in which the formal oxidation of both Pr and Co is +3, and the crystal structure is a cubic perovskite [50]. The TPR diagram of $PrCoO_3$ expressed as electrons per molecule ($1e^-$ per molecule would correspond to reduction of Co^{3+} to Co^{2+}) against temperature is given in Figure 12.

Two reduction steps are observed: the first step, of $1e^-$ per molecule, takes place between 475 and 635 K, and the second step, corresponding to $3e^-$ per molecule, occurs between 725 and 815 K. Similar reduction steps were found for $LaCoO_3$ [51] and $LaNiO_3$ [52]. However, Crespin et al. [53] and Levitz et al. [54] identified divalent (Ni^{2+}) and monovalent (Ni^+) nickel phases in reduced $LaNiO_3$. By measuring the H_2 consumption as a function of the reduction temperature, Futai et al. [55] observed two reduction steps for $PrCoO_3$, although at higher temperatures (maxima for the rate of mass loss at 650 and 860 K) than those measured in this work. This may be due to the rather different experimental conditions used by these authors (heating rate 9 K min^{-1} and a flow of 25 cm^3 min^{-1} of a mixture of 10 % H_2 in N_2). The temperature for reduction levels of $1e^-$ and $3e^-$ per molecule in $PrCoO_3$ (Figure 12) are lower than those needed for reduction of $LaCoO_3$ (720 and 890 K, respectively). This also indicates that

lanthanum perovskite is more stable in H_2 atmosphere than praseodymium perovskite.

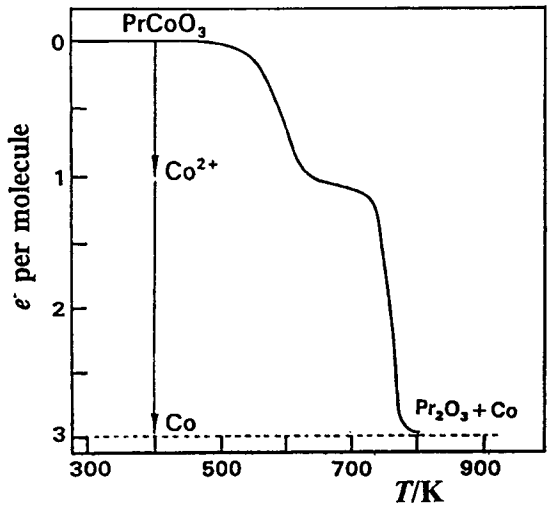


Figure 12. Microgravimetric TPR of $PrCoO_3$ in H_2. A flow rate of 90 cm^3 min^{-1} and a heating rate of 4 K min^{-1} were used.

Mo/Al_2O_3 catalysts: Mo catalysts play an important role in a wide range of reactions. Bulk MoO_3 and several molybdates are used in selective oxidations, while Al_2O_3- and SiO_2-supported MoO_3 catalysts are applied for various purposes, such as hydrodesulfurization, hydrogenation and alkene metathesis. The study of the reducibility of Mo catalysts is useful in characterizing the oxidic structure and in simulating activation procedures needed for creation of active sites for hydrogenation and alkene metathesis. Although MoO_3 reducibility has often been studied by means of isothermal reduction, TPR has proved to be a technique with its own merit.

The TPR patterns of Mo/Al_2O_3 catalysts in their unextracted and extracted forms (extraction of Mo by solubilization was carried out by treating samples with ammonia solution for 0.5 h) have been recorded by microgravimetry [56]. The starting reduction temperatures, as well as the temperatures at which the TPR maxima occur for different molybdenum contents, are summarized in Table 6. It can be seen from these data that the reducibility of Mo/Al_2O_3 catalysts is connected with the Mo loading. The starting reduction temperature decreases with increasing Mo loading and this effect is much smaller for the Mo-extracted preparations. For example, the 8.9 % Mo/Al_2O_3 catalyst started to be reduced at 589 K, whereas the parent Mo-extracted catalyst with 5.5 % Mo started at 668 K. Notice also that, for both unextracted and extracted catalysts with almost the same

Mo loading, the starting reduction temperature follows the same trend. This indicates not only that the interaction between the Mo species and the support is stronger with lower Mo loading, but also that the degree of aggregation increases with increasing Mo content, i.e., decreasing dispersion. The higher reduction temperatures indicate a stronger interaction of Mo at the alumina surface.

Table 6.
TPR parameters of Mo/Al_2O_3 catalysts[a]

	Mo %	T_{st} (K)	T_1 (K)	T_2 (K)
Impregnated	1.8	653	863	1043
	8.9	589	839	1025
	25.6	575	788	1013
Extracted	1.1	693	870	1073
	5.5	668	843	1047
	9.7	653	836	1033

[a] T_1 and T_2 are the temperatures at which the rate of mass loss is maximum

Complementary information is obtained from the two maxima (T_1 and T_2) observed on each TPR pattern. Although such maxima could be ascribed to the reduction of two well-defined Mo species of different reducibility [57], it is more probably due to two separate steps in the reduction of Mo ions. It is well known that the reduction of Mo^{6+} ions by H_2 at temperatures about 773 K preferentially gives Mo^{4+}; however, further reduction of such ions at temperatures above 923 K may progress to metallic Mo. Thus, the T_1 peak could arise from the first reduction step, whereas the T_2 peak could then be ascribed to a further reduction of the ionic Mo sites to metallic Mo. In addition, because both TPR peaks are very broad, it can be inferred that the heterogeneity of the surface is important.

Li-Mn/MgO catalysts: The genesis of lithium-doped Mn/MgO catalysts has been investigated in detail considering their relevance in the oxidative coupling of methane which yields C_2 hydrocarbons [58]. Integral mass changes as a function of the reduction temperature for the manganese-containing catalysts are summarized in Figure 13(A). The two lithium-free Mg_6MnO_8 (14.5 % Mn atom) and Mn-MgO (5.53 % Mn atom) catalysts display two well-resolved reduction steps, the high temperature step being the larger. These profiles change markedly for the two lithium-containing catalysts. The 1Li-Mn-MgO ([Li]/[Mn] at. ratio = 0.66) shows a single reduction step, while two poorly-resolved steps can be discerned for the parent 2Li-Mn-MgO ([Li]/[Mn] at. ratio = 2.21) catalyst. In

order to define more accurately the temperatures at which the maximum mass changes occur, the integral data were differentiated. These derivative curves are displayed in Figure 13(B).

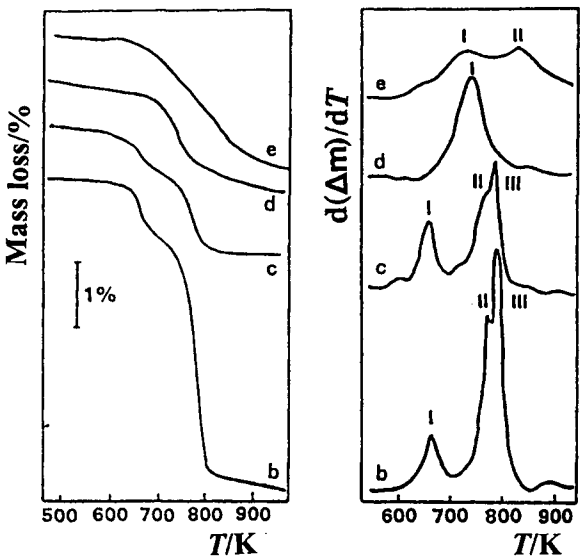


Figure 13. (A) Integral mass changes (%) as a function of the temperature of reduction of manganese-containing catalysts: (b), Mg_6MnO_8; (c), Mn-MgO; (d), 1Li-Mn-MgO; (e), 2Li-Mn-MgO. (B) Derivative curves of the TPR profiles.

Three peaks can be distinguished for Mg_6MnO_8 and Mn-MgO catalysts: there is one well-resolved low-temperature peak at 668 K and two other overlapping peaks located at temperatures above 770 K. The intensity of the low-temperature peak is substantially lower than that of the high-temperature peak. These TPR profiles were dramatically changed upon incorporation of lithium into the Mn-MgO base catalyst. For the 1Li-Mn-MgO catalyst a single asymmetric peak at 741 K with a long tail extending to the lower temperature side is observed, whereas two broader peaks at about 723 and 823 K can be discerned for the 2Li-Mn-MgO homologue. These results compare rather well with TPR data of Bradshaw et al. [59] and Baronetti et al. [60] on K-doping in MgO_2-based catalysts. TPR showed a broad doublet at 673-773 K on the profile of pure MnO_2 and also a decrease of this doublet and its shift to higher temperatures (973-1073 K) upon addition of KCl to the MnO_2 catalyst. The experimental mass losses were found to be slightly higher than those calculated assuming complete reduction of Mn^{4+} to Mn^{2+}.

3.1.2. Reduction/oxidation cycles

Considering the importance of dispersed metals in heterogeneous catalysis, the reduction-oxidation cycles of catalysts in controlled conditions play a central role in the preparation of highly active catalysts. Moreover, as previously demonstrated, re-oxidation of reduced phases in supported metal catalysts is a simple and efficient way to redisperse metallic phases.

Catalysts may undergo reversible reduction-oxidation cycles when these are carried out at temperatures where sintering of the oxidized or reduced species does not occur. For instance, re-oxidation at 673 K of $LaCoO_3$ reduced to $3e^-$ per molecule fully restores the perovskite structure. However, reduction to $3e^-$ per molecule, followed by heating in He at 1073 K and re-oxidation as above, did not produce a perovskite phase but instead, Co_3O_4 appeared [51]. This irreversibility in the redox cycle is caused mainly by the drastic increase that the particle size of the metal undergoes in the sintering process. The formation of simple oxides may be avoided by carrying out the re-oxidation at a slower rate, using diluted oxygen in an inert gas or air as an oxidizing agent. Reversible reduction-oxidation processes were reported, for example, for $LaRhO_3$ [61] and $PrCoO_3$ [50]. In these cases the particle sizes of the regenerated perovskites were found to be smaller than those of the starting samples. Some examples of reversible reduction-oxidation processes over perovskite-type oxides are presented below. The observed mass loss was taken as a measure of the reduction degree in terms of electrons (e^-) per molecule (for example, $1e^-$ per molecule in case of Ni^{3+} reduction to Ni^{2+} and $3e^-$ per molecule in cases of reduction of Mn^{3+} and Fe^{3+} to Mn^0 and Fe^0, respectively) [52,62,63].

CuO/kieselguhr catalyst: Although copper-based catalysts are useful in many reactions, such as low-temperature methanol synthesis, water-gas-shift and oxidation of hydrocarbons, we selected here another interesting application, namely the hydration of acrylonitrile to acrylamide in the liquid phase at low temperature. Reduction and re-oxidation cycles of kieselguhr-supported copper oxide catalysts have been investigated by microgravimetry [64] with the aim of defining the activation protocol and the pathway to regenerate the deactivated catalysts. For copper oxide, the kinetics of reduction were followed in a microbalance connected to a high vacuum system. Hydrogen (300 Torr) was used for reduction and a liquid N_2 trap was placed near to the sample in order to remove water from the gas phase. Both reduction and re-oxidation in a 1% O_2/N_2 mixture were carefully conducted to avoid sintering of Cu metal particles which results in immediate that activity losses. This is a consequence of the rather low melting point of copper which favors copper mobility at temperatures as low as 550-600 K. Reduction in H_2 at 573 K of a fresh CuO/kieselguhr sample, followed

by oxidation at the same temperature and by a second reduction, shows: (i) The water content in the outgassed sample is nearly 2.6 mass %. (ii) The oxidation rate of the reduced catalyst is considerably higher than that of the reduction of CuO to Cu metal. (iii) For each oxidation-reduction cycle the CuO or Cu content calculated on basis of a dry substrate, coincided fairly well with the chemical analysis (within 1 %).

Typical reduction kinetics curves at temperatures between 450 and 484 K are shown in Figure 14(A). Gravimetric reduction data are presented as mass loss of the catalyst upon reduction ($CuO \rightarrow Cu^0$) against time. S-shaped curves appeared in all cases, i.e. there is an induction period. Both this period and the time required to achieve a quantitative reduction of CuO become shorter at increasingly high reduction temperatures. Obviously, in the primary outgassing a small concentration of domains of Cu_2O could appear on CuO crystallites, which should define a fast progress of the reaction interface [65]. From the slope of the quasi-straight line of these curves and/or the reciprocal time required to attain a definite reduction degree, an apparent activation energy (E_a) has been calculated.

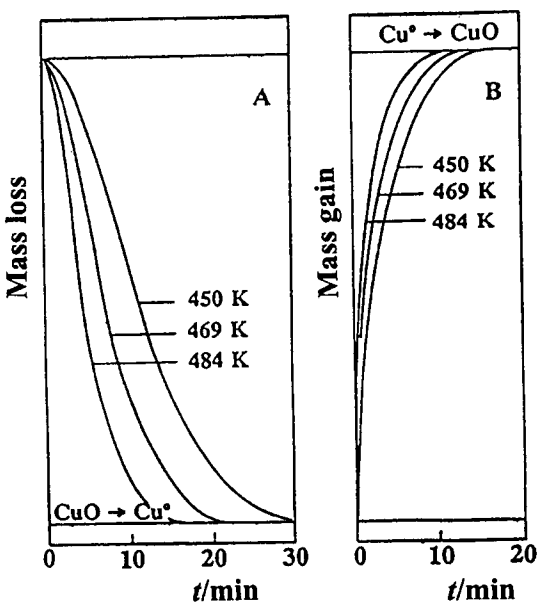


Figure 14. Kinetic curves for reduction at 300 Torr H_2 pressure (A) and re-oxidation in a $1\%O_2/N_2$ mixture (B) of CuO/kieselguhr.

Its value, $E_a = 82.1 \pm 4.2$ kJ mol^{-1}, agrees satisfactorily with that reported by Puchot et al. [66] and Schoepp and Hajal [67] who studied this reduction on powdered bulk CuO. However, discrepancies emerge when compared with E_a

values calculated from data obtained in the absence of some Cu_2O domains preformed on CuO crystallites [68]. Figure 14(B) shows kinetic re-oxidation curves of the catalysts which were quantitatively reduced to metallic Cu. Re-oxidation is a faster process than the reduction itself and no sigmoidal behaviour is observed at short oxidation times. Moreover, the time required to complete oxidation (Cu $\rightarrow$ CuO) is about one half of that needed to fulfill complete reduction.

$LaMO_3$ (M=Ni,Mn,Fe) oxides: TPR results of $LaNiO_3$, $LaMnO_3$ and $LaFeO_3$ mixed oxides are given in Figures 15(a-c), respectively. As can be observed in Figure 15(a), the reduction of $LaNiO_3$ takes place in two well-defined steps [52]. The first step (a) of $1e^-$ per molecule occurs between 425 and 675 K and the second step (b) of $3e^-$ per molecule occurs between this last temperature and 900 K. Temperatures for reduction levels of 1 and $3e^-$ per molecule found in this work are between those reported by Wachowski et al. [69] and Crespin et al. [70]. In addition, Crespin et al. [70] found a stable intermediate reduction level of $2e^-$ per molecule.

In reduction step (a), a distorted $LaNiO_3$ (because of the presence of anion vacancies) was identified by X-ray diffraction (results not shown here). After sintering in He at 1073 K, the perovskite structure was destroyed and La_2NiO_4 and NiO were formed. In reduction step (b), La_2O_3 and Ni were formed and these species were better crystallized after sintering at 1173 K. The fact that, in step (b), full reduction ($3e^-$ per molecule) was not reached, points to the presence of anion vacancies and, therefore, to a non-stoichiometric starting sample of formula $LaNiO_{3-\alpha}$. Thus, it was concluded that reduction in step (a) takes place according to the contracting-sphere model, while reduction in step (b) is controlled by formation and growth of reduction nuclei. In this study, steps (a) and (b), in the non-sintered samples (both described in details in section 3.4), were reversible, i.e., after oxidation at 973 K the perovskite structure was newly formed [70]. Crespin et al. [53] presented evidence that the reduction products (up to $1e^-$ and $2e^-$ per molecule of $LaNiO_3$ ($La_2Ni_2O_5$ and $LaNiO_2$) were fully re-oxidized in O_2 at 453 K. Vidyasagar et al. [71] reported a somewhat higher re-oxidation temperature of 598 K for $La_2Ni_2O_5$. In the re-oxidation at 453 K of the fully reduced ($3e^-$ per molecule) $LaNiO_3$, a strongly exothermic reaction was observed and a mixture of La_2NiO_4 and NiO was obtained [53].

TPR results for $LaMnO_3$ perovskite (heating rate 4 K min^{-1}) between 295 K and 1173 K are represented in Figure 15(b) [62]. The reduction can be observed to start at 755 K. From this temperature up to 950 K, the reduction rate is low because of the slowness of nuclei formation and growth. Once reduced nuclei are formed, the reduction process occurs at a higher rate (950-1050 K). Above 1050 K the reduction curve levels off and a stable reduced-state of about $1e^-$ per

molecule is reached. By re-oxidation at 873 K in purified air (1 h) the initial mass was practically regained (Figure 15(b)).

Results of the temperature-programmed reduction of $LaFeO_3$, mass loss (left-hand axis) or degree of reduction in terms of electrons per molecule (right-hand axis) against temperature, are given in Figure 15(c) [63]. The curve presents two reduction steps which occur in the temperature zones 600-850 and 850-1250 K. The total mass loss observed (7.67 mg) was higher than that expected for full reduction of Fe^{3+} to metallic Fe (6.93 mg for a 70.1 mg starting sample). This suggests that the lanthanum iron oxide exhibits oxidative non-stoichiometry, as was also observed in this perovskite by Voorhoeve et al. [72] and by Wachowski et al. [69]. Its formula would be $LaFeO_{3.18}$ (with Fe^{4+} to balance the oxygen excess [72]), because the final reduction step corresponds to the formation of La_2O_3 and metallic Fe. The first plateau, at about 2 % mass loss, could thus be associated with reduction of the starting sample to a nearly stoichiometric oxide. Following oxidation at 1073 K in air, the reduced material at 1273 K did not regain its initial mass, but only that corresponding to the oxidation of metallic Fe to Fe^{3+}, i.e. to the formation of stoichiometric $LaFeO_3$ together with unreacted α-Fe_2O_3 and La_2O_3 (Figure 15(c)). The excess of oxygen, δ, (in $LaFeO_{3+\delta}$) decreases with increasing calcination temperature [72] (note that the calcination temperature during sample preparation was 923 K). On the other hand, the defects present in the as-prepared lanthanum iron oxide may not be formed in the perovskite structure after the reduction-oxidation process. This effect was not observed in $LaMnO_3$ [62] or $LaNiO_3$ [52], where following oxidation of the reduced samples the initial mass was regained. After reduction of a fresh sample in 300 torr H_2 at 1273 K, oxidation in 300 torr O_2 at 1073 K and a second temperature-programmed reduction, no plateau was observed for mass losses between 0 and 5 %. The total mass loss (6.38 mg) indicated that the second reduction was not complete. This may be because, in this case, the starting material was a mixture of the perovskite and simple oxides. Also, some sintering of these oxides probably occurs in the previous reduction and oxidation treatments as deduced from X-ray diffraction measurements (results not shown here). The above results show that the reducibility of $LaFeO_3$ comes between those of $LaCoO_3$ [51] and $LaNiO_3$ [52], and that of $LaCrO_3$ [73]. This is in agreement with the findings of Nakamura et al. [74] on the stability to reduction of $LaMO_3$ oxides.

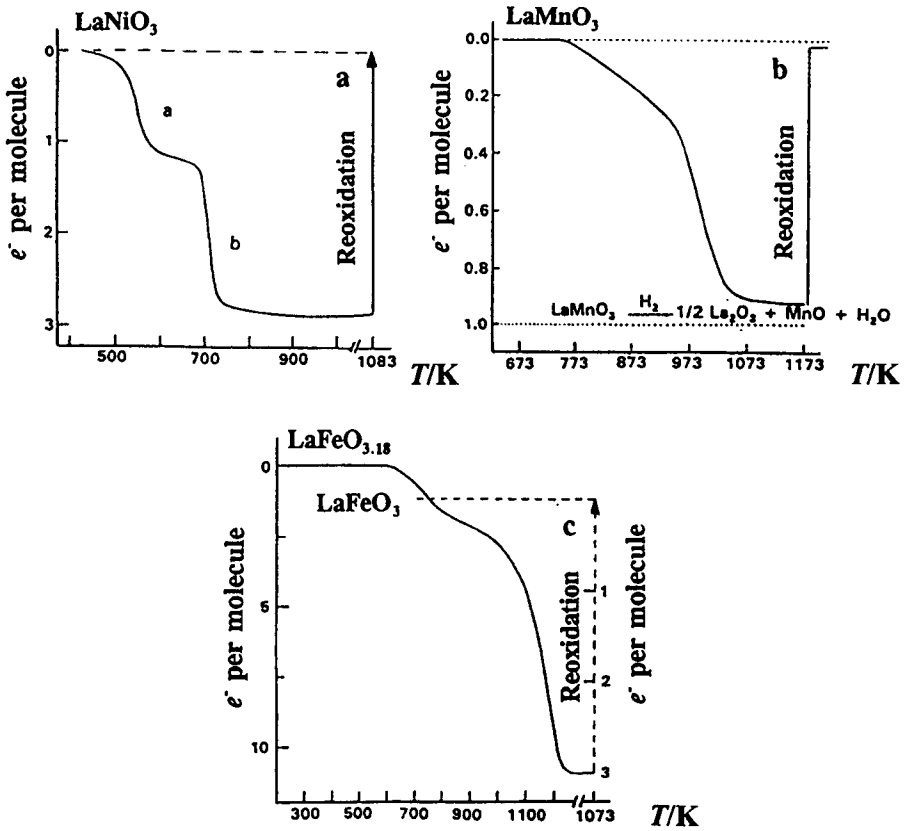


Figure 15. TPR curves for $LaNiO_3$ (a), $LaMnO_3$ (b) and $LaFeO_3$ (c) in 300 torr H_2 (heating rate, 4 K min^{-1}).

3.2. Determination of the stoichiometry of oxides

Many oxides used in catalytic oxidations and combustion reactions display deviations from the stoichiometry. Whatever the non-stoichiometry (oxidative or reductive), its implications in catalytic reactions have been perceived and used to design oxidation catalysts for specific purposes. The degree of non-stoichiometry depends on the preparation variables, mainly the oxygen partial pressure of the surrounding atmosphere and the final calcination temperature, so that higher P_{O2} and lower calcination temperatures tend to increase λ in $LaMnO_{3+\lambda}$. Deviations from the stoichiometry of metal oxides have frequently been revealed by thermogravimetry. By means of TG, Patil et al. [75] showed that substituted

oxides $Ba_xLn_{1-x}CoO_3$ (Ln = La, Nd) lose lattice oxygen easily, yielding oxygen-deficient compounds. The oxygen loss in air is higher than in an O_2 atmosphere and increases with increasing x values and with temperature. This is shown in Figure 16, where the percent mass loss is plotted as a function of the heating temperature for several values of x. The reductive non-stoichiometry is, therefore, dependent on the surrounding oxygen partial pressure, the Ba content and the temperature. In agreement with these results, Yamazoe et al. [76] found that desorbed oxygen from $Sr_xLa_{1-x}CoO_{3-\lambda}$ samples and λ both increased with Sr^{2+} content. According to Jonker and van Santen [77], in this mixed oxide, Co^{4+} is formed without the appearance of oxygen vacancies for $x < 0.4$. However, oxygen vacancies, besides Co^{4+}, are formed for $x > 0.4$. This is due to the instability of Co^{4+}, which tends to be reduced by a simultaneous release of oxygen. The reductive non stoichiometry, which increases with increasing x, was found to have a remarkable effect on the reducibility of these oxides and in their catalytic activity for the oxidation of CO and hydrocarbons.

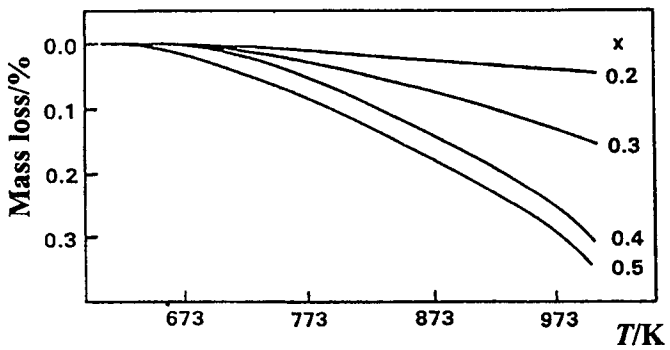


Figure 16. Percentage mass loss as a function of temperature for the $Ba_xLa_{1-x}CoO_3$ compositions. (Reprinted by permission from reference [76]).

Substituted mixed oxides $LaTi_{1-x}Cu_xO_3$ [78] exhibited deviations from stoichiometry. TPR profiles of the $LaTi_{1-x}Cu_xO_3$ perovskites, as example, and the reference CuO oxide are given in Figure 17. For the temperature-programmed reduction measurements, a 20 mg sample was first heated in a He flow at a rate of 4 K min^{-1} up to 673 K and then cooled to 373 K under He flow. Then the temperature was increased at the same rate up to 1023 K while passing H_2 through the sample. The overall reduction process of $LaTi_{1-x}Cu_xO_3$ oxides can be represented by the equation:

$$2LaTi_{1-x}Cu_xO_3 + (4x - 1)H_2 \rightarrow La_2O_3 + 2xCu + 2(1 - x)TiO_2 + (4x - 1)H_2O$$

Reduction of the unsubstituted $LaTiO_3$ compound led to a very small mass-loss corresponding to about 0.4 % at temperatures above 850 K. For substitutions $0.2 \leq x \leq 0.8$, the TPR profiles show, however, two different reduction steps. The first step at 440-570 K is very fast, and closely corresponds to the reduction of CuO to metallic Cu^0 (Figure 17, dashed line), while the second step occurs at higher temperatures at a much slower rate. The extent of the reduction of both steps increases, in general, with substitution. H_2-reduction of copper ions in the perovskite structure is observed to be reached at substantially higher temperatures than in CuO, which indicates the increased stability of Cu^{2+} ions in the perovskite structure.

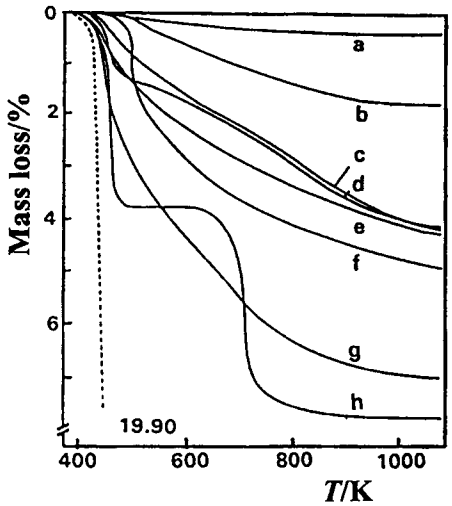


Figure 17. TPR profiles for H_2 reduction at a rate of 4 K min^{-1} of $LaTi_{1-x}Cu_xO_3$ samples with different degrees of substitution (x): (a) 0.0; (b) 0.2; (c) 0.3; (d) 0.4; (e) 0.5; (f) 0.6; (g) 0.8; (h) 1.0. The dashed line corresponds to the bulk CuO reference.

The fully substituted (x = 1.0) sample shows, however, two well-differentiated steps, the first below 500 K and the second above 600 K. The low temperature TPR peak is due to CuO reduction, while the high temperature TPR peak is due to the reduction of the more stable La_2CuO_4 oxide. This assignment is confirmed, not only by the XRD diagram (not shown here), but also by the approximately equal mass-losses in both high- and low-temperature TPR steps, which implies the distribution of copper over both phases, viz. CuO and La_2CuO_4. Therefore, the reduction process for the fully substituted (x = 1.0) sample can be formulated according to the equation:

$CuO + La_2CuO_4 + 2H_2 \rightarrow 2Cu + La_2O_3 + 2H_2O$

This result is a little surprising when compared with literature findings. For instance, the mixed $LaCuO_3$ perovskite and La_2CuO_4 and CuO phases have been found by Gallagher et al. [79] in the preparation of copper-rich $LaMn_{1-x}Cu_xO_3$ ($0.7 \leq x \leq 1.0$) compounds. In the light of these results, we can infer that our preparations, with nominal compositions $LaCuO_{2.5}$ (or $LaCu_2O_5$), are not stable under the experimental conditions.

Values of the nonstoichiometry factor (λ) of the resulting $TiO_{2-\lambda}$ oxide, formed upon H_2 reduction of $LaTi_{1-x}Cu_xO_3$ perovskites (assuming reduction of Cu^{2+} to Cu^0 and oxidation of Ti^{3+} to Ti^{4+}) are summarized in Table 7. A very small deviation from the stoichiometry is found only in the substitution range $0.3 \leq x \leq 0.6$. However, these results contrast with the major crystalline titanium oxide ($TiO_{1.90}$) phase revealed by XRD. It must be noted that the molecular water, the product of H_2 reduction, reacts at once with La_2O_3 to form a very stable LaO(OH) phase or can even form $La(OH)_3$ after long exposure to moisture (Table 7). The small mass increase, which also accompanies the reduction of perovskites, is the result of two concurrent processes, viz. oxidation of Ti^{3+} and formation of LaO(OH) by the water produced during the reduction. Therefore, considering the above interpretation, values derived from TPR measurements can only be taken as an estimate of the non-stoichiometry of the titanium oxide.

Table 7.
Characteristics of the reduced $LaTi_{1-x}Cu_xO_3$ mixed oxides

Substitution	Crystalline phase	$TiO_{2-\lambda}$[a]
$x = 0.0$	La_2O_3, $La_2O_3{\cdot}3TiO_{1.9}$	-
0.2	La_2O_3, $La_2O_3{\cdot}3TiO_{1.9}$	-
0.3	La_2O_3, $La_2O_3{\cdot}3TiO_{1.9}$, Cu	$TiO_{1.98}$
0.4	$La_2O_3{\cdot}3TiO_{1.9}$, Cu	$TiO_{1.96}$
0.5	La_2O_3, $La_2O_3{\cdot}3TiO_{1.9}$, Cu	$TiO_{1.98}$
0.6	$La_2O_3{\cdot}3TiO_{1.9}$, Cu	$TiO_{1.97}$
0.8	$La(OH)_3$, Cu	$TiO_{2.00}$
1.0	La_2O_3, $La(OH)_3$, Cu	$TiO_{2.00}$
1.0	La_2O_3, $La(OH)_3$, Cu	-

[a] λ is the nonstoichiometry degree

3.3. Kinetic studies on catalyst reduction

3.3.1. Introduction

Different TPR steps, discussed above in Section 3.1, correspond to different reduction mechanisms. These can be studied by kinetic experiments of reduction under isothermal conditions [80]. As an illustration, the reduction kinetics of some catalysts is discussed below.

3.3.2. Pr_6O_{11} and Mo-Pr-O catalysts

The structural conversion of Pr_6O_{11} [81] and Mo-Pr-O [82] during reduction was investigated gravimetrically by measurement of the kinetics of reduction. Isothermal reduction curves (ΔW vs t) of Pr_6O_{11} for temperatures in the range 518-681 K are plotted in Figure 18. For the Mo-Pr-O catalyst, the mass changes were taken as a measure of the extent of reduction (α), determined as the ratio between the experimental and the theoretical mass loss expected for a quantitative reduction of MoO_3 to MoO_2 and of Pr_6O_{11} to Pr_2O_3 [82]. Initial reduction rates were calculated by analytical differentiation at time zero of the integral data fitted to a mathematical equation (Figure 19).

As can be seen for Pr_6O_{11}, both the extent of reduction and the initial reduction rate r_o depend strongly on the reduction temperature (Figure 18). The steady increase of both parameters with temperature is convincing proof of activated reduction. Another interesting feature of these kinetic curves is that, in the temperature range studied, they reach an almost constant level of reduction, α, much faster as the reduction temperature increases. The kinetic curves at 518 and 565 K showed that reduction did not reach equilibrium.

On the other hand, the shape of the kinetics curves in Figure 19 depends on the atomic ratio Mo/(Mo+Pr). While for the Mo-Pr-O catalysts with a high Pr content (a, b) the reduction rate decreases continuously with time, the catalysts with high Mo content (d, f, h, i) present sigmoidal reduction curves. This suggests that reduction takes place through two different mechanisms. Reduction of the Pr-rich catalysts (Mo/(Mo+Pr) < 0.27) takes place according to the contracting- sphere model [80], where the process starts with very fast nucleation which results in a total coverage of the catalyst grains (Pr_6O_{11}) by a thin layer of the reduced phase (Pr_2O_3). This causes a continuous decrease in the reaction rate in the interface, Pr_6O_{11}-Pr_2O_3, as the grains of the starting oxide are consumed in the reaction. Reduction of the catalysts with high Mo content (Mo/(Mo+Pr) $\geq$ 0.43) takes place according to the nucleation model: First, the reduction rate increases because of the slow growth of nuclei already formed and the appearance of new ones. At the inflection point, the reduced nuclei overlap and the reduction starts advancing from the surface to the bulk. From this point on, the interface of oxidized-reduced phases starts decreasing and so does the reduction rate.

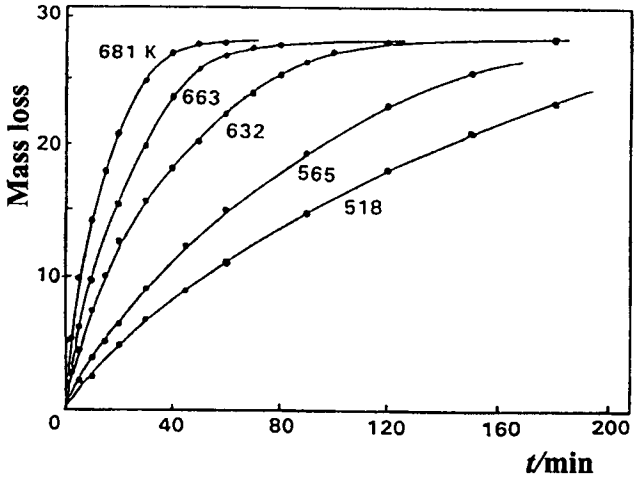


Figure 18. Kinetic reduction curves of Pr_6O_{11} in an 8.5 vol. % H_2 - Ar stream (7.2 $dm^3\ h^{-1}$).

The reduction curve yielded by the catalyst with a ratio of Mo/(Mo+Pr) = 0.27 (c) is a combination of the characteristic curves produced by the contracting-sphere model (reduction of Pr_6O_{11}) and the nucleation model (reduction of MoO_3). These reduction processes are described, respectively, by the contracting-cube equation, $1 - (1 - \alpha)^{1/n} = kt$, and by the Avrami-Erofeev equation [83]:

$$1 - \alpha = \exp(-kt^n) \qquad (8)$$

where α is the degree of reduction of the catalyst at time t, and k and n are functions of temperature but not of time. The latter equation is of interest in the quantitative description of the reduction process of metal oxides [62] in which the reduction implies (i) the formation of nuclei at the interface and (ii) further growth of these initial nuclei by the inward reduction of the crystals (polycrystalline powdered oxides), as in the case of Pr_6O_{11}.

Taking logarithms in equation (8):

$$\ln [- \ln (1 - \alpha)] = \ln k + n \ln t \qquad (9)$$

According to equation (9), a plot of $\ln [-\ln (1 - \alpha)]$ *versus* $\ln t$ must give a family of straight lines. This type of representation is shown in Figure 20 for all of the kinetic curves of Pr_6O_{11} given in Figure 18. As can be seen in this figure, the experimental data satisfactorily fit equation (9). The k and n values were

calculated from the slope and intercept of these lines. They are summarized in Table 8. The parameter k varies with temperature (one order of magnitude in the temperature range studied), as is expected for an activated reduction process, while n varies only slightly.

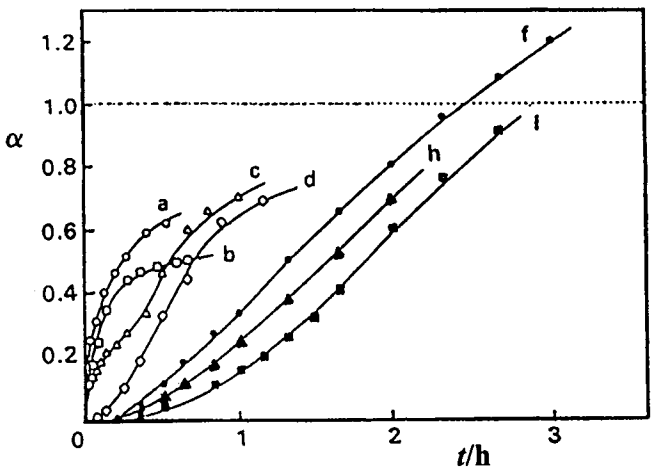


Figure 19. Kinetics of reduction of Mo-Pr-O catalysts: (Mo/(Mo+Pr) = 0.0, (a); 0.09, (b); 0.27, (c); 0.43, (d); 0.80, (e); 0.88, (f); 0.91, (g); 0.95, (h); 1.0, (i)) in a flow of 50 cm^3 min^{-1} H_2 at 773 K.

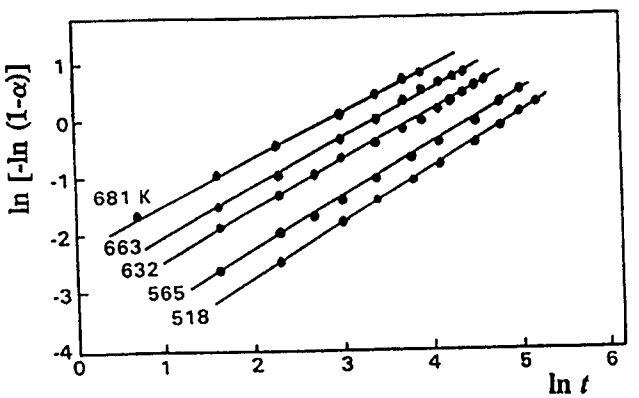


Figure 20. Linear transforms of the Avrami-Erofeev equation according to the linear plot ln [-ln (1 - α)] = ln k + n ln t for the kinetic reduction curves given in Figure 18.

Table 8.
Kinetic parameters for the reduction of Pr_6O_{11}

T(K)	r_0(mg·g^{-1} min^{-1})	n	ln k	k
518	0.283	0.97	-4.73	8.83×10^{-3}
565	0.602	0.94	-4.02	1.79×10^{-2}
632	1.751	0.90	-3.22	4.01×10^{-2}
663	2.420	0.89	-2.87	5.69×10^{-2}
681	2.823	0.84	-2.64	7.11×10^{-2}

The apparent activation energy, E_a, for the reduction process of the Pr_6O_{11} catalyst can be determined either from the k values, calculated using the model analysis of the kinetic reduction curves, or from the initial reduction rates, r_0. Figure 21 is a graphical representation of both ln k and ln r_0 as a function of the reciprocal of the reduction temperature. Values of E_a of 36.5 kJ mol^{-1} and 43.4 kJ mol^{-1}, respectively, were obtained from the slopes of the straight lines. The slightly higher value of E_a calculated from r_0 is expected, because various surface phenomena which take place, i.e. activation of hydrogen molecules and the effect of the reduction nuclei on the non-reduced surface, are excluded at zero time. These phenomena, which are present at considerably longer reduction times, are accounted for in the k values, which average all intervals for each kinetic curve.

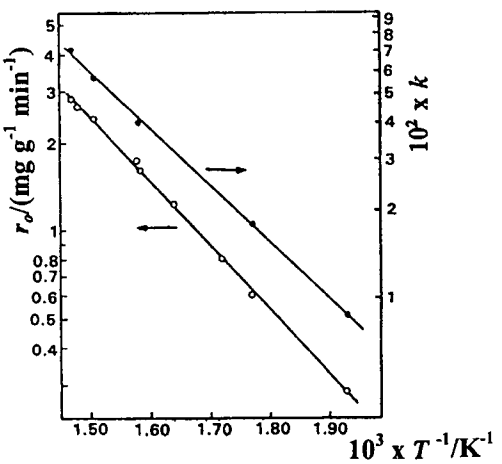


Figure 21. Dependence of the reciprocal temperature on both the initial reduction rate r_0 (O) and the k parameter (●) of the Avrami-Erofeev equation -ln (1-α) = kt^n for the kinetic reduction curves given in Figure 18.

3.3.2 . $LaNiO_3$ and $LaMnO_3$ catalysts

The kinetics of reduction of $LaNiO_3$ and $LaMnO_3$ perovskites in H_2 were studied by Tejuca et al. [52,62]. The kinetics of $LaNiO_3$ reduction in H_2 was studied at temperatures (510-570 and 670-730 K) within the regions where the two well-defined reduction steps occur ($1e^-$ and $3e^-$ per molecule, respectively, see Section 3.1.2 and Figure 15(a)). The kinetic curves plotted in Figures 22(a) and 22(b) point to reduction levels of 1 and 2.68e^- per molecule, respectively.

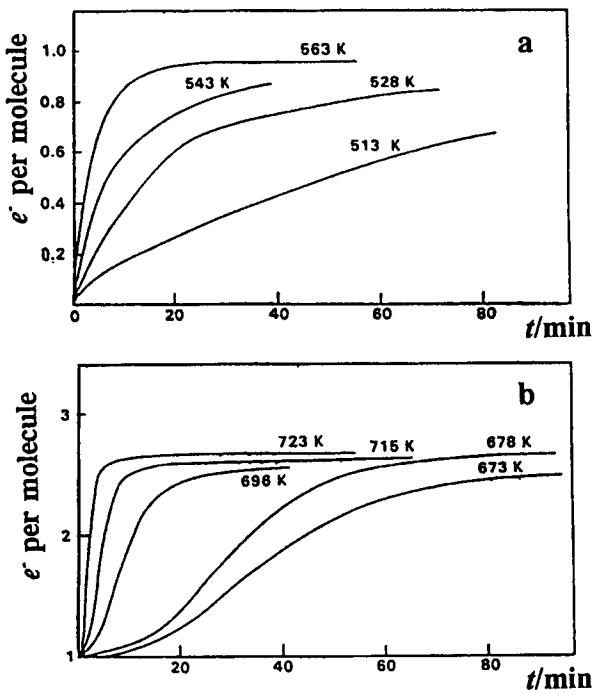


Figure 22. Kinetics of reduction of $LaNiO_3$ under 300 torr H_2 at (a) lower and (b) higher temperatures.

The kinetic curves in Figure 22(b) start with a very fast (immeasurable) reduction after which a slower reduction took place. The fast process was estimated to amount to $1e^-$ per molecule and this was considered as the starting point of reduction. The increase in the initial reduction rate with temperature shows that both processes of reduction are activated. While in the first step ($1e^-$ per molecule) the reduction rate continuously decreased with t (Figure 22(a)), in the second step ($3e^-$ per molecule), sigmoidal curves were found (Figure 22(b). This suggests that the reduction takes place through two different mechanisms.

On one hand, the low temperature reduction (510-570 K; $1e^-$ per molecule) can be interpreted by means of the contracting-sphere model, assuming that this process starts with a very fast nucleation which results in a total coverage of the $LaNiO_3$ grains by a thin layer of the reduced phase [80]. This causes a continuous decrease in the rate of the interfacial reaction as the grains of the starting oxide are consumed in the reaction. On the other hand, the high temperature reduction (670-730 K; $3e^-$ per molecule) is controlled by the formation and slow growth of reduction nuclei (metallic Ni) on the surface of the phases reduced at lower temperature (La_2NiO_4 and NiO). Initially, the reduction rate increases because of the growth of nuclei already formed and the appearance of new ones. The inflection point (Figure 22(b)) indicates when the reduction nuclei start overlapping. From this point on, the interface of the oxidized and reduced phases and the reduction rate both start decreasing. Sigmoidal reduction curves were observed in unsupported NiO, V_2O_5, and Co_3O_4, while MnO_2 and supported NiO exhibited curves characteristic of the contracting-sphere model [80,84]. The distinction between the two mechanisms of reduction described is somewhat arbitrary because the contracting-sphere model starts with very fast nucleation and the nucleation mechanism ends according to a contracting-sphere model. (Note that reduction in the region after the inflection point of both curves is similar for both reduction steps).

The plots e^- per molecule vs t (Figure 23) for the kinetic reduction isotherms of $LaMnO_3$ perovskite in 300 torr H_2 at temperatures of 873 tp 1013 K, present a sigmoidal form typical of a reduction process controlled by formation and growth of reduction nuclei on the surface, followed by reduction in the bulk [62]. The time corresponding to the inflection of the curves indicates the point where these nuclei start advancing from the surface to the bulk. These plots point to a common reduction degree of about $0.93e^-$ per molecule. The time required for attaining this reduction level drastically decreased with increasing temperature. On the other hand, the increase in the initial reduction rate with temperature shows that this is an activated process.

The kinetic data given in Figure 22(b) (full reduction) and in Figure 23 were analyzed according to the Avrami-Erofeev equation (equation 9) in a similar manner to that presented above for Pr_6O_{11}. For $LaNiO_3$, the apparent activation energy of reduction (E_{red}) at low temperature (partial reduction) was calculated from ln $r_{0.red}$ vs $1/T$ plots ($r_{0.red}$, initial reduction rate determined analytically by fitting the kinetic data to a polynomial function and differentiation to time zero). E_{red}, in step (b) was calculated from ln k vs $1/T$ plots (k, is the constant of the Avrami-Erofeev equation). For $LaNiO_3$ the mean values of E_{red} were 108 and 221 kJ mol^{-1} for 1 and $3e^-$ per molecule, respectively. These values are lower than the activation energy for reduction of $1e^-$ per molecule in $LaMnO_3$ (247 kJ mol^{-1}), showing that the latter oxide is more difficult to reduce than $LaNiO_3$.

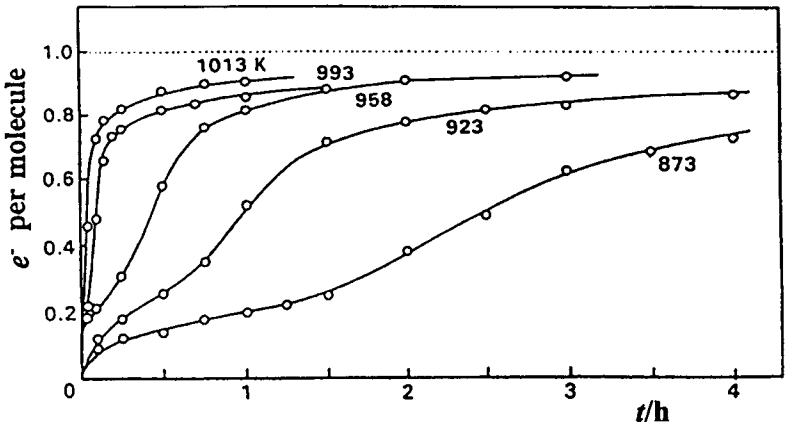


Figure 23. Kinetic reduction isotherms of $LaMnO_3$ under 300 torr H_2.

3.3.3. Cerium oxide

The mass changes of CeO_2 samples were explored by Fierro et al. [85,86] after contacting with H_2 in the 195-773 K range on a sample previously outgassed at 773 K. The microgravimetric results indicated that H_2 interacts with CeO_2 according to two well-differentiated processes. Firstly, H_2 is incorporated at low temperatures (195-500 K), giving a value of $CeO_2H_{0.17}$ at 500 K and, secondly, a slow mass-loss takes place, becoming more significant with increasing temperature, T_r, due to ceria reduction (Figure 24). As can be observed, the average reduction degree reached at 773 K ($CeO_{1.89}$) is smaller than that corresponding to stoichiometric bulk cerous oxide ($CeO_{1.50}$). By assuming a reasonable surface density of Ce^{4+} ions of 3.8 x 10^{14} cm^{-2}, the theoretical surface reduction corresponds on average to $CeO_{1.97}$, which is about one-third of the experimental value found at 773 K, hence the reduction process of CeO_2 must not be confined only to the ceria surface but extended to the subsurface layers.

These observations may be explained by the following reactions:

Chemisorption: $CeO_2 + x/2\ H_2 \rightarrow CeO_2H_x$

Reduction: $CeO_2H_x \rightarrow CeO_{2-x/2} + x/2\ H_2O$

or $CeO_2H_x + x/2\ H_2 \rightarrow CeO_{2-x} + x\ H_2O$

The chemisorption process describes the mass gain of ceria samples after H_2 treatments up to about 500 K, whereas reduction reactions account for the mass loss due to the lattice oxygen removal at $T_R > 500$ K.

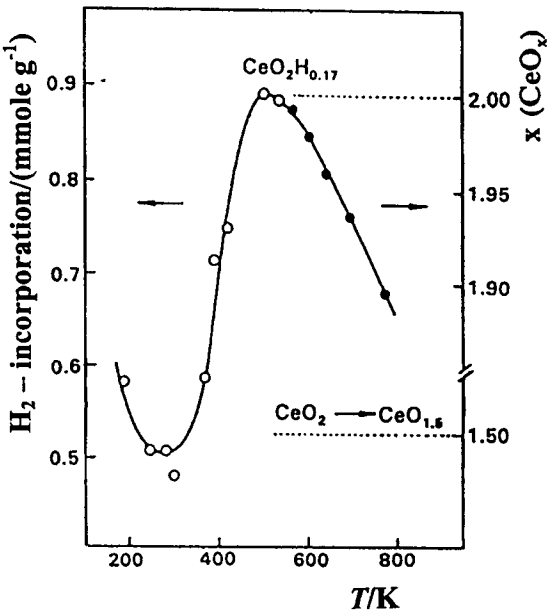


Figure 24. Mass changes of a CeO_2 sample subjected to H_2 treatments, (O) H_2 incorporation at constant H_2 pressure (70 torr); (●), average degree of reduction given by the O/Ce ratio (CeO_x).

3.3.4. V_2O_5/SiO_2 and MoO_3/SiO_2 catalysts

It was found that V_2O_5/SiO_2 catalyst reducibility, calculated from the kinetic reduction isotherms, is very sensitive to the reduction temperature [87,88]. The higher temperature results in both faster and more extensive reduction. For all loadings, reduction at 643 K is slow and non-stoichiometric. Even for the lowest loading (0.3 V nm^{-2}), the extent of reduction only approaches a plateau of about 0.6 oxygen atoms removed per vanadium atom. Reduction at 823 K, in contrast, results in almost stoichiometric reduction of V^{5+} to V^{3+} for loadings of 0.3 and 0.7 V atoms nm^{-2}. Oxygen removal is about 0.89 oxygen atom per vanadium atom for the 0.3 V nm^{-2} loading, and 0.95 for the 0.7 V nm^{-2} loading catalysts; this is accomplished in the relatively short time of 2 h. Bulk V_2O_5 species show a lower reducibility than surface dispersed vanadium oxide species.

MoO_3/SiO_2 catalysts of low loading (0.3-0.9 Mo nm^{-2}) show the same mass loss pattern as the V_2O_5/SiO_2 catalysts [87]. The higher-loaded (1.3-3.5 Mo nm^{-2}) MoO_3/SiO_2 catalysts exhibited two distinct reduction stages: an initial rapid mass-loss during the first few minutes (equivalent to that of the low-loaded samples) and then a slow process which reached equilibrium after approximately 3.5 h at

823 K. The appearance of the second reduction stage is associated with a decrease in the dispersion of molybdenum oxide species on silica. Kinetic limitation is responsible for the two-stage reduction observed in pure H_2, because no difference can be observed between dispersed and aggregated molybdenum oxide species in diluted hydrogen.

An increase in the reducibility of the higher-loaded SiO_2-supported molybdenum oxide catalysts is observed (Figure 25(a)), with respect to the lowest loaded sample, in the loading range characterized by dispersed surface molybdenum oxide species. Aggregation of the molybdenum oxide results in a significant increase in the overall degree of reduction of the silica-supported molybdenum oxide (Figure 25(a)), implying that the dispersed surface molybdenum oxide species are less reducible than the bulk ones. Highly dispersed particles cannot be fully reduced because a minimum particle size is required for stabilization. Additionally, silanol groups are reported to oxidize isolated metal particles [89].

For both series, an increase in the metal loading results in an increase in the initial reduction rate, r_0 (Figure 25b). For the MoO_3/SiO_2 series, the sharp increase of the initial reduction rate (r_0) in the low-molybdenum loading region corresponds to the presence of incipient surface polymerization of molybdenum oxide species. With a further increase in size, the crystalline orthorhombic MoO_3 phase appears and a significant decrease in r_0 takes place. For V_2O_5/SiO_2 loadings above 1 V nm^{-2}, a less-dramatic increase in r_0 with increased loading is observed when compared with lower-loaded catalysts. At higher vanadium-loadings (3.0 V nm^{-2}), the initial reduction-rate declined significantly. On the other hand, for supported vanadia catalysts, the change in slope observed between 0.8 V and 1.8 V corresponds with the formation of microcrystalline vanadium oxide, whereas the sharp decrease in r_0 above 2 V per nm^2 corresponds with the onset of formation of larger vanadium oxide crystallites.

The reduction of molybdenum oxide species has been shown to be highly dependent on their dispersion [90] and the initial rate of reduction for V_2O_5 crystals is sensitive to the crystal thickness, according to the lattice parameter c [91]. The reduction isotherms show that reduction occurs in two stages for the xMo series at concentrations above those showing a maximum in r_0. This reduction behaviour is characteristic of the bulk crystalline oxide [92]. At 1.3 Mo nm^{-2}, molybdate species are formed, while at higher loadings the formation of crystalline orthorhombic α-MoO_3 occurs. For the xV series, the initial deviation of r_0 is associated with the onset of formation of microcrystalline V_2O_5 species and the sharp decrease in r_0 corresponds with the onset of formation of crystalline vanadium oxide.

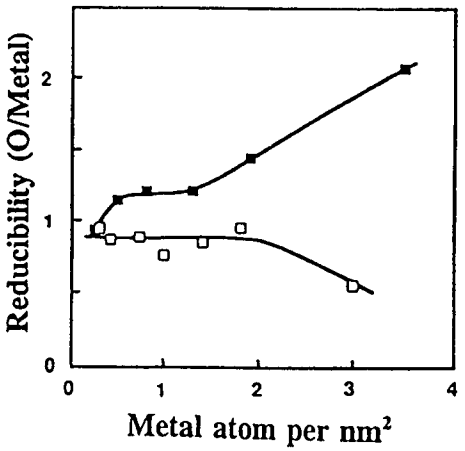


Figure 25. (a), Reducibility of the silica-supported metal oxide catalysts (■), *x*Mo and (□), *x*V. (b), Initial reduction rates (r_0) for *x*Mo (■) and *x*V (□) series.

3.4. Determination of the specific surface area/active phase dispersion

3.4.1. Low-temperature oxygen chemisorption (LTOC)

In general, knowledge of the apparent surface-area of a transition metal oxide (TMO) in a supported catalyst, measured by chemisorption of oxygen, has proved useful for several systems [93]. As originally developed, the method based on oxygen chemisorption involves a preliminary reduction in hydrogen at elevated temperatures, followed by oxygen chemisorption at an appropriately low temperature. This procedure, referred to as "LTOC" (low-temperature oxygen chemisorption), has been employed with chromia catalysts for about 40 years, and with molybdena catalysts for about 15 years. For instance, oxygen chemisorption at low temperature on reduced alumina-supported molybdena catalysts proved to be a useful method for the determination of specific molybdena areas and, consequently, Mo dispersion [94]. A review summarizes the LTOC for chromia and molybdena up to 1983 [93].

The philosophy underlying the LTOC methodology is as follows: (i) Because the higher valence TMO's do not chemisorb oxygen in a stoichiometric manner, hydrogen pre-reduction is conducted under conditions such that the metal ion ends up in a reproducible and well-defined lower-valence state. Standardized conditions (temperature, time) for this reduction should be chosen only after the extent of reduction has been quantitatively monitored in preliminary studies on the system of interest. Bulk reduction, as well as reduction of surface ions, of TMO's may occur in this step and should be known. (ii) Although bulk reduction may have occurred, the purpose of oxygen chemisorption is to measure only the

transition metal ions on the surface. The chemisorption temperature recommended for a standardized LTOC test procedure is chosen, therefore, to be low enough to preclude re-oxidation of the bulk phase material. Because the standardized test conditions are arbitrary, one reasonable demand is that the measured chemisorption value should be relatively insensitive to small variations in adsorption temperature.

In our laboratory, oxygen chemisorption has been used successfully for determination of the specific-metal area in silica-supported vanadia catalysts [10] and in a series of MoO_3 (4.8-13.0 mass %)/SiO_2 [95,96], Mo/α-Al_2O_3 [94,96] and CoMo/α -Al_2O_3 [94], NiMo/α -Al_2O_3 [94,97] catalysts. The experiments were carried out gravimetrically with samples quantitatively reduced to MoO_2. MoO_2 samples with a high specific area (50-80 $m^2\ g^{-1}$) were used to determine a factor for relating oxygen chemisorption to an equivalent molybdena area [95]. The application of the LTOC method to a series of α -alumina-supported catalysts (6.9-14.3 mass % MoO_3), prepared by a "wet" impregnation procedure, showed that Mo was highly dispersed on the alumina surface, within the MoO_3 loading range studied [94]. A linear relationship between molybdena loading, up to about 15 mass % MoO_3, and an equivalent molybdena area was found. Most of the Mo was present as a monolayer, but a very small fraction was probably present as multi-layers or bulk-like microcrystals. On the contrary, the equivalent molybdena areas in the silica-supported molybdenum samples corresponded to relatively low coverages of the silica surface. The particle size deduced from oxygen chemisorption for reduced MoO_3(13.0 %)/SiO_2 was 6.9 nm, higher than that of 2.5 nm for a reduced MoO_3(15 %)/SiO_2 catalyst, in agreement with the weaker interaction with silica. In the range 77-195 K, temperature had no effect on the amount of chemisorbed oxygen on both unsupported and silica-supported molybdena catalysts [95]. On the other hand, the extent of O_2 chemisorption at low temperatures on partially-reduced molybdena-silica catalysts demonstrated that, in these catalysts, mainly the Mo^{5+} species were responsible for O_2 chemisorption in the experimental conditions used [98].

In summary, results of oxygen chemisorption determined gravimetrically at 77, 141 and 195 K on both series of 5-15 mass % MoO_3/SiO_2 and MoO_3/Al_2O_3 catalysts showed that molybdena dispersion increases with the active phase loading [96]. Details of the experimental method used have been published elsewhere [94,95-98] and a short discussion of results is presented below.

3.4.2. Unsupported MoO_3 catalysts

The reduction to MoO_2 of the high-area MoO_3-MoO_2-Mo mixture was carried out in the microbalance in two stages: (a) treatment in hydrogen, at 165 torr and 150 K, for 2 h, and (b) removal of the hydrogen atmosphere and a second treatment with H_2 at 300 K, for 6 h, at a pressure of 60 torr [95]. Successive

oxygen adsorption isotherms were determined at different temperatures, with MoO_2 samples of 150-500 mg. After the first isotherm at 77 K, corresponding to the physically adsorbed plus the chemisorbed oxygen, had been measured, the physically adsorbed gas was desorbed by pumping for 1 h at 195 K, and then a second isotherm at 77 K was determined. When the adsorption was carried out at 142 or 195 K, the pumping was conducted at the working temperature, also for 1 h. The O_2 chemisorption values, Δm (mg O_2 g^{-1}), were calculated from the difference between the first and second isotherms at each adsorption temperature.

In Table 9, values are collected for Δm obtained for a single sample (443 mg) of MoO_2, for which adsorption experiments were carried out at each temperature. Between experiments at different temperatures, a standard reduction treatment was always carried out at 60 torr H_2 for 16 h at 300 K. Also included in Table 9 are values of the BET area, carried out after the second isotherm at each temperature, and the calculated "factor" (m^2/mg O_2) for subsequent use with MoO_2/SiO_2 for conversion of O_2 adsorption to equivalent molybdena area. The average value of this (gravimetric) factor, determined at the three temperatures, is 8.80 m^2/mg O_2. This value is equivalent to a (volumetric) factor of 12.6 m^2/ml(STP)O_2 chemisorbed, which is rather close to the factor 13.6 m^2/ml(STP)O_2 deduced by Parekh and Weller [99] for samples of reduced molybdena prepared by quite a different method (precipitation from ammonium molybdate solution and H_2 reduction). The present average value is believed to be more accurate, because the unsupported molybdena samples, studied by Parekh and Weller [99], were considerably lower in surface area than the samples used here. Chemisorption at 273 K resulted in a slow, progressive mass increase, indicating that bulk oxidation was already occurring at that temperature. Our attempts to experiment with MoO_3 samples prepared by high-temperature re-oxidation of the high-area MoO_2, MoO_3 material were unsuccessful; the re-oxidation was accompanied by severe loss of specific surface area.

Table 9.
O_2 chemisorption on unsupported MoO_2

T (K)		Ämᵃ	S_{BET}	Factor
Adsorption	Pumping	(mg O_2 g^{-1})	(m^2 g^{-1})	(m^2/mg O_2)
142	142	6.6	56.7	8.59
195	195	5.8	54.9	9.47
77	195	6.1	50.8	8.33
			Average:	8.80

[a] Mass of O_2 chemisorbed per gram of MoO_2

3.4.3. MoO_2/SiO_2 catalysts

Two oxygen adsorption isotherms, with intermediate pumping, were run at each adsorption temperature (77, 142, and 195 K) for each of the MoO_2/SiO_2 samples (4.8, 9.1 and 13.0 % MoO_3) [95]. When adsorption was at 77 or 195 K, pumping was at the working temperature for 1 h. The BET surface area was generally determined after measurement of the second isotherm at a given temperature. Table 10 summarizes the results, for the three MoO_3/SiO_2 samples, for oxygen chemisorption (Δm) and BET surface area (S_{BET}). The "equivalent molybdena area" (EMA) in Table 10 was calculated by multiplying Δm by the factor 8.80 m^2/mg O_2 (see Table 9). The apparent fractional coverage of the silica by the (reduced) molybdena, θ, in Table 10 was calculated as θ (%) = EMA/S_{BET} x 100. The apparent dispersion, D, also in Table 10, was calculated as D = (number of chemisorbed oxygen atoms)/(number of Mo atoms in sample).

The surface areas of the MoO_3/SiO_2 catalysts were relatively constant (105-107 m^2/g catalyst) and lower than that of the SiO_2 support (131 m^2/g SiO_2). Even on a SiO_2-only basis, the area of the 13.0 % MoO_3 sample was calculated to be only 107/0.870 = 123 m^2/g SiO_2. In all cases the total surface areas were less than the area that should have been contributed by the amount of SiO_2 support present in the sample. The pore volumes also decreased: 1.34 cm^3 g^{-1} for the SiO_2 support, and 1.03, 0.86, and 0.75 cm^3 g^{-1} catalyst for the catalysts containing 4.8, 8.1 and 13.0 % MoO_3, respectively. These results, suggest that the molybdena mainly blocks pores in the SiO_2. The coverages θ indicated in Table 10 are quite low. The average values of EMA plotted as a function of the molybdena loading (% MoO_3 in the samples before reduction) (figure not presented here) showed approximately a straight line through the origin, implying that the MoO_2 crystallites obtained on reduction of the MoO_3/SiO_2 samples have about the same average size for the range of 4.8 to 13.0 mass % loading of MoO_3.

Table 10.
O_2 chemisorption on MoO_3/SiO_2

Catalyst	T (K)	Äm[a] (mg O_2/g)	EMA ($m^2\ g^{-1}$)	S_{BET} ($m^2\ g^{-1}$)	θ (%)	D
MoO_3/SiO_2 4.8 %	77	0.83	7.3	105	6.9	0.16
	142	0.74	6.5	-	6.2	0.14
	195	0.80	7.0	101	7.0	0.15
MoO_3/SiO_2 9.1 %	77	1.20	10.6	105	10.1	0.12
	142	1.19	10.5	-	10.1	0.12
	195	1.12	9.9	103	9.6	0.11
MoO_3/SiO_2 13.0 %	77	1.70	15.0	107	14.0	0.12
	142	1.85	16.3	-	15.2	0.13
	195	1.67	14.7	107	13.7	0.12

[a] Mass of O_2 chemisorption per gram of sample before reduction
[b] Mass percentage of MoO_3 in catalyst before reduction

3.5. Kinetics and equilibrium of O_2 adsorption

The kinetics and equilibrium of adsorption of oxygen have been studied on a wide range of examples of perovskite-type catalysts ($LaNiO_3$, $LaMnO_3$, $LaFeO_3$, $LaCrO_3$ and $LaCoO_3$) by Tejuca et al. [52,62,63,73,100]. Detailed discussion of experimental procedure for $LaMnO_3$ is presented below.

Two series of kinetics experiments of O_2 adsorption on $LaMnO_3$ perovskite (heating rate 4 K min^{-1}) were carried out [62]. In the first series, the effect of temperature on both the initial adsorption rate, r_0, at zero time, and the extent of O_2 adsorption (isobaric experiments) were studied. The mass changes were recorded for 2 h and also after the system $O_2/LaMnO_3$ reached equilibrium. In the second series, the effect of pressure on the initial adsorption rate (isothermal experiments) was studied. Kinetic curves were recorded for 20 min. From these, initial adsorption rates, r_0, were calculated by fitting the data to a polynomial function and differentiation to $t = 0$. The integral kinetic data q vs t at 25 torr and temperatures of 303 to 685 K are given in Figure 26(a). The adsorption recorded at equilibrium (q_e, at t_∞) is also given. Both r_0 and q_e increase with temperature showing the existence of an activated process.

Adsorption data at equilibrium (at 25 torr) as a function of temperature are given in Figure 27. In this plot, the adsorption at 195 K was also included. In the range 195 to 350 K, q_e decreases with increasing temperature, indicating an adsorption which occurs with no activation energy. Between 350 and 525 K (first ascending branch), activated adsorption occurs. At 573 K, an adsorption lower than that at 525 K was observed, which was confirmed in a duplicate experiment. Above 600 K, q_e increases sharply with temperature (second ascending branch). These results

suggest the appearance at higher temperatures of a process with an activation energy higher than that of the process which takes place at 350-525 K.

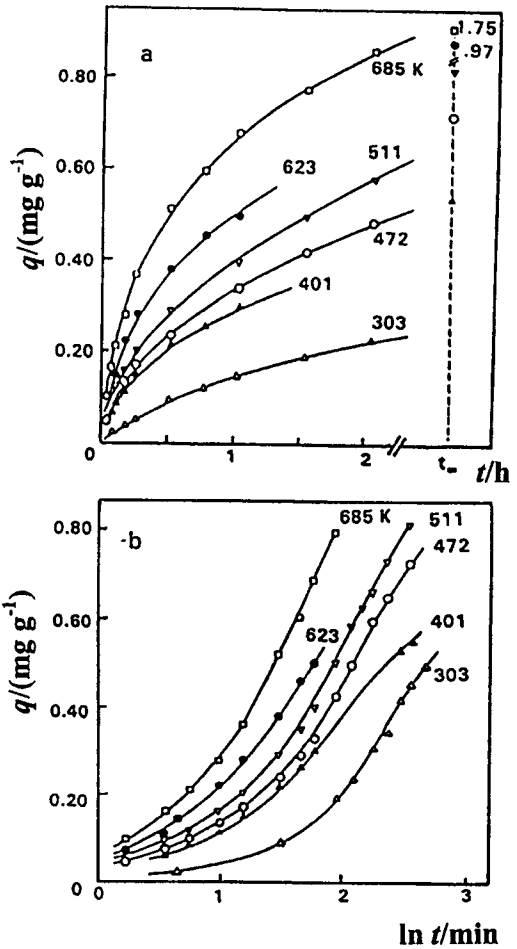


Figure 26. Plots of q vs t (a) and q vs ln t (b) of integral kinetics data of adsorption of O_2 (25 torr) on $LaMnO_3$ at different temperatures.

The kinetic curves of O_2 adsorption in the interval 303-685 K (Figure 27(a)), represented in coordinates q vs ln t (Figure 26(b)), had a sigmoidal shape which is typical of a kinetic process of activated adsorption. In the region of maximum slope (around the inflection point) the plots are frequently linear and, in this part, Elovichian kinetics of adsorption are obeyed. This region is preceded by a concave part and followed by convex parts which correspond to pre-Elovichian and post-Elovichian regions, respectively. Aharoni and Ungarish [38] deduced

the existence of these regions from the sigmoidal form of t vs $(dq/dt)^{-1}$ curves. These regions are also clearly shown when kinetic data are represented as $dq/d\ln t$ vs t plots. As an illustration, kinetic data at 472 and 511 K represented in these coordinates (figure not shown here) showed volcano plots with the ascending and descending branches which correspond to the pre-Elovichian and post-Elovichian parts. The rather sharp maxima observed indicate that, in this case, the Elovichian region is not predominant [62].

The kinetic data were described quantitatively using a model of adsorption on a heterogeneous surface [101]. The model assumes that the adsorbent surface is comprised of a large number of homogeneous patches characterized by a given value of the energy of adsorption, H, constant for a given patch and varying from patch to patch. Taking into account that the activation energy of adsorption, E_a, in a patch is given by the equation:

$$E_a - \alpha H = RT \ln (\beta \theta + \gamma) \qquad (10)$$

(θ, coverage, α, β and γ constants) and assuming that desorption is negligible, the following integrated equation is derived:

$$-\ln (1 - \theta) - \theta = (t/\tau) \exp(-\alpha H) \qquad (11)$$

(τ, constant inversely proportional to the adsorption constant).

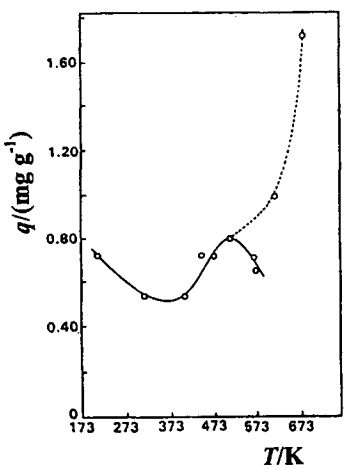


Figure 27. Isobar of adsorption of O_2 on $LaMnO_3$ at 25 torr.

The kinetic data for isobaric runs given in Figure 26 were represented, according to equation (10), in Figure 28. All the linear transformations pass through the origin. For temperatures of 303 K to 511 K, the experimental results fit equation (11) satisfactorily. (At higher temperatures and longer times the experimental points scatter somewhat from the straight line). This is in agreement with previous results which showed that the surface of $LaMnO_3$ perovskite-type oxides is highly heterogeneous [102]. From a plot of ln r_0 vs $1/T$, an activation energy of adsorption of 16 kJ mol^{-1}, equal to that calculated for the system $O_2/LaCrO_3$ [73], was found.

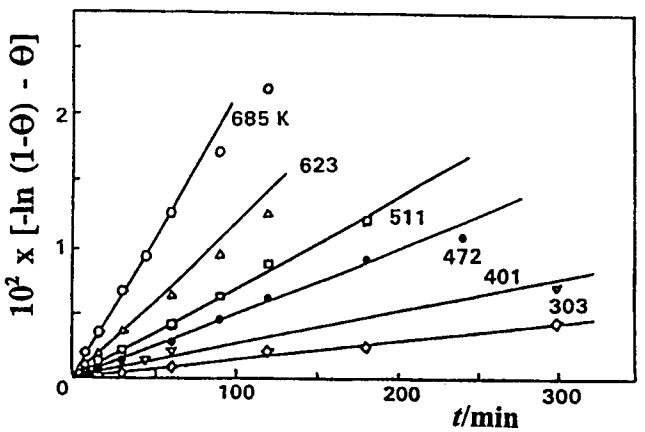


Figure 28. Plots of integral kinetic data in Figure 26, for the adsorption of O_2 (25 torr) on $LaMnO_3$ at different temperatures, according to equation (11) (see text).

Values of oxygen coverage at 25 torr on $LaCoO_3$ [100], $LaCrO_3$ [73] and $LaMnO_3$ [62] in the temperature range 300-700 K are given in Table 11. These can be observed to decrease from $LaCoO_3$ to $LaCrO_3$. On the other hand, the adsorption of O_2 on these oxides, as well as their reducibility, follow the same sequence as the catalytic activity found for CO oxidation: $LaCoO_3$ > $LaMnO_3$ > $LaCrO_3$. These differences in adsorption and catalytic properties must be related to the transition metal cation (La^{3+} is a poor adsorbent of O_2). The outgassing treatment undergone by the samples (15 h at 773 K) prior to an adsorption experiment produces a higher concentration of oxygen vacancies on the adsorbent surface and this causes the O_2 adsorption to be higher on most reducible oxides.

Coverage of adsorbed oxygen on $LaMnO_3$ (taking 0.141 nm^2 as the cross-section area of O_2 molecule) [103] in the first ascending branch of the isobar ranges from 0.12 (300 K) to 0.20 (600 K) (Table 11). However, the adsorption at 685 K amounts to a coverage of 0.38. This, together with the form of isobar

(Figure 27, two ascending branches separated by an inflection), strongly suggest that, in the temperature range 350-700 K, two very different chemical processes occur. Taking into account that at 400 K, $LaMnO_3$ becomes catalytically active for CO oxidation, the activation undergone by the O_2 molecule at 350-525 K should be related to oxygen chemisorption as O^- through O_2^-, as observed in the system $O_2/LaCoO_3$ [100]. The high coverage obtained above 600 K must be related to incorporation of oxygen into the oxide lattice. The adsorption of oxygen on $LaCoO_3$ (an easily reducible oxide) also presented an isobar with a second ascending branch above 600 K, although not as pronounced as that found in the system $O_2/LaMnO_3$. On the contrary, in the adsorption of O_2 on $LaCrO_3$ (an oxide difficult to reduce) this behaviour was not observed [100].

Table 11.
Coverage of O_2 on $LaMeO_3$ oxides[a]

	T (K)				
	300	400	500	600	700
$LaCoO_3$	0.10	0.36	0.34	0.23	0.24
$LaMnO_3$	0.12	0.12	0.17	0.20	-
$LaCrO_3$	0.01	0.03	0.11	0.17	0.13

[a] Cross-sectional area of O_2 molecule, 0.141 nm^2

In summary, the trends observed for oxygen adsorption on the series of $LaMeO_3$ oxides is: $LaCoO_3 \approx LaMnO_3 > LaNiO_3 >> LaCrO_3 > LaFeO_3$. Thus, within the $LaMeO_3$ series, the more easily reducible oxides ($LaNiO_3$, $LaCoO_3$, $LaMnO_3$) were found to be better adsorbents of oxygen than the less reducible one ($LaCrO_3$).

3.6. Coke formation on pre-reduced catalysts

An example of the application of microgravimetry to monitoring chemical reactions is the reaction of propane dehydrogenation and coke formation on CO-pre-reduced alumina-supported chromia catalysts with different chromia contents [104]. In these experiments, samples were placed in the microbalance and heated at 4 K min^{-1} up to the reduction temperature in a He flow. Reduction was done with a mixture of CO in He, at a total flow of 36 cm^3 min^{-1}, until constant mass was attained. After catalyst reduction, the system was purged to remove CO, and the study of coke formation was started by feeding a gaseous mixture of hydrocarbon (propane or propene) in He at a total flow of 44 cm^3(STP) min^{-1}.

In the study of the influence of chromia content on the reduction of catalysts by CO it was found that the maximum extent of reduction was highest for the catalyst with the lowest chromia content (1.5 % Cr_2O_3), and it decreased as the chromia content increased.

The kinetic curves of coke formation on chromia-alumina catalysts for a feed of propane and propene are displayed in Figs. 29(a) and 29(b), respectively. The initial rate of coke formation was calculated from the slope of the curves at zero time. The extent of coke formation was taken from the "equilibrium" values measured at very long times. Both parameters are recorded in Table 12. The initial rate of coke formation, as well as the total amount of coke deposited for both propane and propene, varied depending on the chromia content of catalysts.

In general, as the chromia content increased, the initial rate of coke formation increased, but conversely the extent of coke deposited per unit mass of catalyst decreased. However, when the final coke loading was related to the specific surface area of the catalysts, this was an almost constant value irrespective of the chromium oxide content of the catalysts. Table 12 also demonstrates that initial rates of coke formation were much higher for propene than for propane. This can be interpreted as meaning that the alkene or surface species originating from it are the precursors of coke, as suggested by König and Tétényi [105] in their study of ethane dehydrogenation on unsupported Cr_2O_3. Note also that the initial coking rate with propene on the bare support surface (0 % Cr_2O_3) was one order of magnitude higher than with propane, and of the same order as those observed in the lower chromia content catalyst samples (1.5 % Cr_2O_3 and 3.0 % Cr_2O_3) with propene. Although one would expect that initial rates should be determined by the conversion level of propane to propene, it is also clear that chromia content plays a role, because a variation is even observed when the propene concentration is kept constant in the feed, especially on the samples with lower Cr_2O_3 content.

The participation of the alumina carrier (0 % Cr_2O_3) in coking rates and extent of coke formation is not surprising. This originates in the acid sites present on its surface which induced a faster dehydrogenation for propene than for propane. To avoid this side reaction, such as the poisoning of the acid sites of alumina with potassium, it was a common practice to replace the alumina carrier by another less-acid support, such as zirconia [106,107].

The study of the effect of coke deposition on catalyst structure confirmed that coke formation influences both the specific area and the pore distribution. Coke deposition had a marked effect on the surface areas even at very low loadings. The effect was even more marked for samples with low chromia content which possessed the highest initial surface area. Moreover, it was found that the main effect of coke deposition was to reduce the pore volume of pores with a lower radii. The influence of the oxidation state of chromium on coke formation has

also been examined. Microgravimetric study of coke deposition on an unreduced 15.0 % Cr_2O_3 catalyst and its CO-pre-reduced homologue showed that coke formed immediately on contact of the propene with the reduced sample, but this formation was not observed on the unreduced sample until a certain time had elapsed. In this time lapse, comparable to that observed in the reduction experiments with CO, a clear inhibition of coke formation was observed. After this initial period, the rate of coke formation attained values similar to those observed for the pre-reduced sample.

In general, the catalytic behaviour of samples pre-reduced by CO was found to depend on the chromia content. The increase of conversion with increasing chromia content up to a 6 % was observed. Coke formation onto pre-reduced catalysts was immediate and was related to the level and stability of the conversion of the olefin product.

Table 12.
Coke formation on chromia-alumina catalysts at 873 K

% Cr_2O_3	r_i [10^4 g/(g_{cat}·min)]		max coke loading [10^3 g/m^2 of catalyst]	
	propane	propene	propane	propene
0	2.0	12.3	-	2.13(309)
1.5	11.0	48.5	0.80(110)	2.12(290)
3.0	14.0	63	0.75(104)	2.12(293)
6.0	32.1	76	0.73(102)	2.01(281)
9.0	32.9	99	0.83(105)	2.13(268)
12.0	41.3	105	0.78(85)	2.25(245)
15.0	48.0	120	0.84(81)	2.05(197)

[a] Values in parentheses are expressed in mg/(g of catalyst)

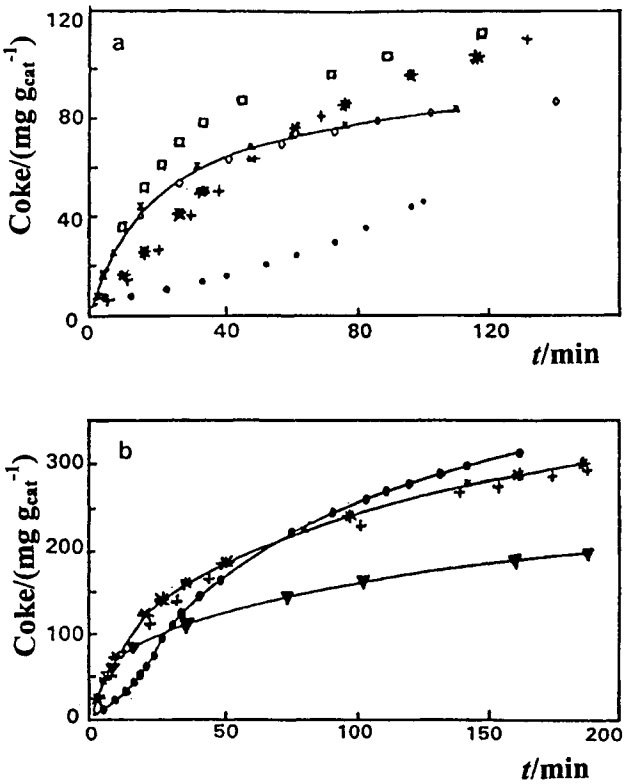


Figure 29. Coke deposition from propane (a) and propene (b) onto Cr_2O_3 catalysts pre-reduced by CO: (●), 0.0 %; (+), 1.5 %; (★), 3.0; (□), 6.0; (◊), 12.0; (▼) 15.0 % of Cr_2O_3.

4. IDENTIFICATION OF THE NATURE OF ADSORPTION SITES BY THE TPD METHOD

4.1. Evolved gas analysis (EGA)

To investigate desorption process from adsorbents, it is recommended that evolved gas analysis (EGA), using gas chromatography (EGA-GC) and/or mass spectroscopy (EGA-MS) and/or Fourier transform infrared spectroscopy (EGA-FTIR) [108-110], be used in addition to the gravimetric techniques described above. The details of evolved gas analysis are described in Chapter 12 of Volume 1 of this Handbook. Some examples of the use of this method in catalysis are presented below.

4.2. EGA-MS

This technique was employed by Viswanathan and Wilson [111] with the aim of determining the effect of cerium oxide as a support in stabilising various chemical and molecular states of chromia. Combined TGA, DTA, EGA-FTIR and EGA-MS methods have been efficiently used in our laboratory for the study of the thermal decomposition of a hydrotalcite-containing Cu-Zn-Al precursors [112]. The samples were placed in a quartz flow micro-reactor connected to a quadrupole mass spectrometer. A mixture of 21 vol% O_2 in Ar was introduced at a rate of 50 mL min^{-1} and the temperature was increased by 10 K min^{-1} while the composition of the evolved gas was continuously monitored. The H_2O and CO_2 evolution was monitored by detection of fragments at m/z = 18 and 44. A good agreement between TG analysis and the peaks detected by MS was obtained. The precursor underwent four mass-loss processes upon heating in a flow of air. The first mass-loss was due to the removal of the crystallisation water present in the Cu-Zn hydrotalcite-like structure. A second process (the broad peak at 570 K) was due to H_2O and CO_2 co-evolution during decomposition of the hydrotalcite and rosasite phases. The evolution of H_2O was due to elimination of structural hydroxyl groups from both phases, whereas the evolution of CO_2 was only due to the decomposition of the rosasite. Finally, the two mass-loss processes, which occur in the range of 700-900 K, were due to decomposition of the hydrotalcite carbonate CO_3^{2-} groups. The assignment of those TG peaks was based on the TGA/EGA-MS study of the reference Cu-Zn hydrotalcite-like compound. This analysis showed H_2O evolution at 440 K (dehydration) and 550 K (dehydroxylation), followed by CO_2 formation resulting from carbonate decomposition upon heating at 750-900 K.

4.3. EGA-FTIR

This method was employed by Melian-Cabrera et al. [112] in a study of the dehydration, dehydroxylation and decarbonation of the Cu-Zn hydrotalcite phase. In this study, the diffuse-reflectance infrared spectra (DRIFTS) were collected on an FT-IR spectrometer over the air-treated sample (heating from room temperature to 673 K at 5 K min^{-1}). The first large change in the IR spectrum upon heating of the Cu-Zn hydrotalcite phase was observed at 393 K. A slight decrease in the intensity of the band at 3500 cm^{-1} and disappearance of the band at 1651 cm^{-1} were ascribed to the loss of physisorbed water at the surface. Following heating at 373-423 K, it was observed that the carbonate v_3 band splits into two separate bands at 1528 and 1370 cm^{-1}. This rearrangement of the carbonate groups was associated with the loss of interlayer water. The former band was assigned to the CO vibration in interaction with the hydroxyl groups of the octahedral brucite-like layers, whereas the second band was assigned to the C=O vibration. Partial removal of structural hydroxyl groups

was observed during heating at 423-533 K. A further increase of temperature from 533 to 573-623 K resulted in complete dehydroxylation of the Cu-Zn hydrotalcite phase.

4.4. Temperature-programmed desorption of NH_3

To evaluate temperature-programmed desorption (TPD) curves, it is necessary to know the basic process, which may be controlled either by desorption or diffusion. Although the microgravimetric technique has been frequently used to quantify the number of acid (or basic) sites in heterogeneous catalysts, we select here, as an example, the mixed Mo-Pr-Bi oxides to illustrate the capability of the technique.

Mo-Pr-Bi mixed oxide, used in the selective oxidation of propylene, was evaluated after NH_3 adsorption. After NH_3 adsorption at 298 K on Mo-Pr-Bi-O catalysts, the total desorption was measured by TPD experiments [13]. Ammonia desorption experiments were carried out microgravimetrically under dynamic conditions. First, a flow of 50 cm^3 min^{-1} nitrogen was passed through the sample for 1 h at 413 K. The adsorption step was carried out by passing a flow of 50 cm^3 min^{-1} nitrogen with 10 cm^3 min^{-1} NH_3 at 298 K, allowing sufficient time (2 h) for saturation. Then, the adsorption line was purged with nitrogen (50 cm^3 min^{-1}) for 1 h (at 298 K) and the oven temperature was raised to 823 K at a heating rate of 5 K min^{-1}.

The total amounts of NH_3 desorbed from the different samples are given in Figure 30. NH_3 desorbs in two steps: at 370-420 K and at 420-580 K. The amount of NH_3 desorbed in the first step is significantly larger than the desorption in the second step. This curve shows a maximum for the catalyst sample with an atomic ratio Bi:Mo of 0.075. The surface acidity exhibited a maximum at the same Bi:Mo atomic ratio which yielded the maximum catalytic activity in propene oxidation. An increase in acidity after adding a basic component such as Bi_2O_3 to the Mo-Bi-P-O systems was reported by Ai and Ikawa [113]. These authors found acidity maxima for atomic ratios Bi:Mo $\approx$ 0.1.

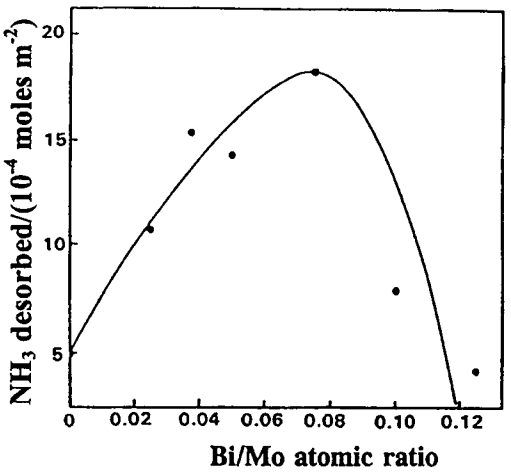


Figure 30. NH_3 desorbed from Mo-Pr-Bi mixed oxide samples.

5. DIFFERENTIAL THERMAL ANALYSIS (DTA) AND DIFFERENTIAL SCANNING CALORIMETRY (DSC)

In addition to the use of thermogravimetric methods in catalysis, information available from other quantitative thermoanalytical methods, such as differential thermal analysis (DTA) or differential scanning calorimetry (DSC), as well as for simultaneous analysis of volatile products by evolved gas analysis (EGA) (see above) is very useful. It is emphasized that the final evaluation and interpretation of thermoanalytical data has to be supported by information provided by independent methods such as X-ray diffraction, as well as light and electron microscopy [114]. DTA and DSC are described in detail in Chapter 5 of Volume 1 of this Handbook.

Non-isothermal or isothermal DTA/DSC methods are used frequently in heterogeneous catalysis in several areas: (i), preparation of catalysts; (ii), rapid screening of potential catalysts in model reactions; (iii), study of the effects of variables such as catalyst composition, temperature and gas flow rates on reaction rates; (iv), evaluation of the effects of various pretreatments; (v), study of catalyst deactivation and poisoning; (vi), study of oscillatory behaviour of different reactions over catalysts; and (vii), study of the different kinetic events taking place in a given system. Thermodynamic features of catalysts, kinetic factors and stoichiometry of a catalyst during DTA/DSC application have been extensively reviewed, for example, by Dollimore [115] and Wendlandt [116].

Briefly, in the mechanism of a heterogeneously catalyzed reaction it is assumed that two (or more) reactants must be adsorbed adjacent to each other on the catalyst surface to form the adsorbed activated complex, which subsequently undergoes chemical transformation and then is desorbed as a different species. Thus, the catalyst modifies the kinetics of the process by increasing the rate and decreasing the activation energy. Because the sum of the heats produced by all of the elementary steps of the reaction is equal to the enthalpy change of the reaction, DTA and DSC data enable activation energies and other features of the reaction kinetics, such as the rate constant (k), the pre-exponential factor (A) and the reaction order (n) to be evaluated. In a qualitative estimation, the position, shape and number of DTA/DSC peaks are considered, while in a semi-quantitative estimation, the thermochemistry and the kinetics of the processes occurring are related to the areas and shapes of the observed exothermic or endothermic peaks [116]. The shape of the peaks and also the peak maximum (ΔT_{max}) and peak minimum temperatures (ΔT_{min}), are controlled basically by the reaction kinetics, whereas the area of the peak is determined by the enthalpy change.

Because of the large number of the DTA/DSC applications, only a few examples have been selected from the literature, in which the applications of DTA/DSC in catalysis appear particularly justified.

DSC analysis was employed by Sharma and Kaushik [117] with the aim to optimize the preparation of zinc and cadmium titanyl oxalate catalyst precursors. The influence of synthesis parameters and activation procedures on the one-step sol-gel synthesis of sulfated-zirconia catalysts was followed by TG-DSC technique by Armendariz et al. [118]. It was concluded that the H_2O/Zr^{IV} molar ratio in the sol-gel synthesis medium influences the crystallization temperature into the tetragonal phase, which gives a first exothermic peak in DSC profiles with a concurrent water evolution around 680-700 K observed in TG profiles. The crystallization is therefore delayed when the water/metal molar ratio increases. This parameter influences also the stability of the sulfates and their decomposition rate. It was found that an endothermic decomposition of sulfate species occurs at the beginning of the tetragonal to monoclinic transition at 800 K and sulfate hinders the sintering of the crystals. A kinetic analysis of the thermal decomposition of lithium sulphate monohydrate ($Li_2SO_4 \cdot H_2O$), derived from non-isothermal and an unconventional isothermal TG/DSC method is another example of DSC use in catalyst preparation [119]. Both the thermal stabilities and the structural changes of sodium- and hydrogen-type modified pentasil zeolites with different aluminum and iron contents were investigated by DTA analysis by Kim and Ahn [120]. The DTA curves of the Na-ZSM-5 zeolites showed exotherms in the range 623-823 K which were due to the decomposition of tetrapropylammonium (TPA) used in the catalyst preparation. Moreover, from the

shift of the exothermic peaks to higher temperature on the DTA curves, corresponding to the collapse of the crystal structure, it was concluded that pentasil zeolites with high silica-contents resulted in enhanced thermal stability.

Milburn et al. [121] used DTA to study the impact of a variety of promoters in the preparation of iron oxide Fischer-Tropsch catalysts, considering the mass loss, thermal events and the extent of heat liberated in the thermal events. They found that the impact of added promoters upon the temperature at which an exothermic event (crystallization) occurred depended upon the ionic radius of the promoter. Thus, the exotherm temperature decreases with increasing ionic radius. However, the heat liberated during this exothermic event does not appear to be related to the ionic size. These changes should occur during catalyst calcination and/or activation, and because promoters impact on catalyst performance, the changes may be important in scale-up for commercial catalyst production.

DTA was used by Sohn et al. [122] to examine the thermal properties of precursors of $NiO\text{-}ZrO_2$ catalysts modified with H_2SO_4 for ethylene dimerization. As can be seen in Figure 31, for pure ZrO_2, the DTA curve shows an endotherm in the range 303-453 K due to water elimination and a sharp exotherm at 703-743 K due to the ZrO_2 crystallization. For this system, sulfate ions influence the phase transitions of ZrO_2 from amorphous to tetragonal (note that the exothermic peak due to this phase transition appears at about 723 K for pure ZrO_2, while for samples modified with H_2SO_4 it is shifted to a higher temperature of about 913 K). The incorporation of nickel oxide also influences the phase transition of ZrO_2. For the sample 25 % $NiO\text{-}ZrO_2$, the exothermic peak due to the phase transition appears to be shifted to 823 K and this shift increases, and the shape of the peak becomes broadened, with increasing NiO content. For the $NiO\text{-}ZrO_2$ sample, an additional endotherm is observed at 503-603 K due to the decomposition of $Ni(OH)_2$. Finally, the samples modified with H_2SO_4 exhibit an endotherm at 1073-1113 K resulting from the evolution of SO_3 arising from the decomposition of sulfate ion bonded to catalyst surface. Therefore, it becomes apparent that the strong interaction between nickel oxide (or sulfate ion) and zirconia delays the transition ZrO_2 from amorphous to tetragonal.

By use of DSC, Dooley et al. [123] presented additional evidence for the role of gallium reduction in the preparation of active Ga/ZSM-5 catalysts for alkane aromatization. It was confirmed that the reduced catalyst undergoes rapid re-oxidation at 823 K. However this re-oxidation does not regenerate the $\beta\text{-}Ga_2O_3$ phase, but rather a higher energy, dispersed Ga^{3+} which appears to be optimal for production of aromatics from ethane. This form of Ga^{3+} is stable under reaction conditions typical of ethane dehydrogenation, but can be reduced by hydrogen.

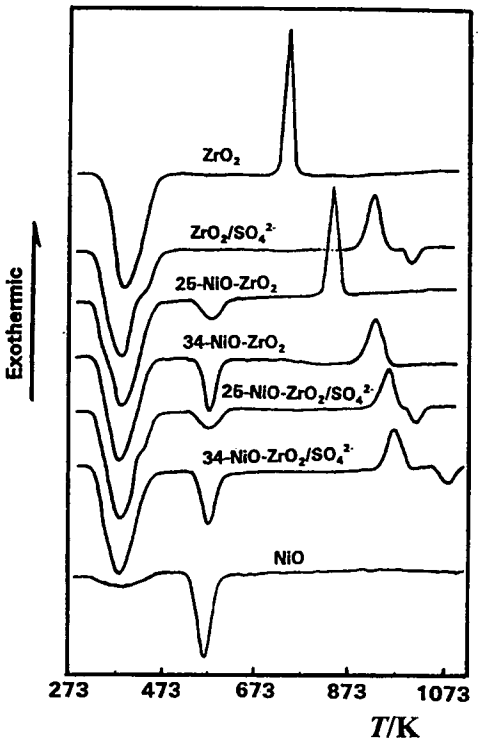


Figure 31. DTA curves of $NiO-ZrO_2$ catalyst precursors (adapted from reference [122]). DTA conditions: air atmosphere, heating rate 10 K min^{-1}; sample mass 10-15 mg.

The re-oxidation of hydrogen-treated Mn_3O_4 was monitored by DTA [124] because the re-oxidation step is closely associated with the selective reduction activity of Mn_3O_4. The sample which was hydrogen treated (at 473 K) shows a DTA profile which is more or less akin to that of the untreated one. However, the sample which was hydrogen treated at temperatures above 573 K shows a completely different DTA profile from that of the untreated one. Accordingly, DTA can be used to judge whether the structure cleavage of Mn_3O_4 caused by hydrogen treatment has occurred.

DTA was used by Kovacheva et al. [125] to elucidate the possible changes in the X-zeolite after ion exchange with lithium and cesium. The DTA profiles showed endotherms with a plateau between 333 and 473 K, ascribed to the loss of water. The lower mass loss observed for CsX samples suggests a lower adsorption capacity and hence a lower surface-area. Unlike the CsX samples, three sharp exotherms in the range 983-1178 K were observed on the curves for

the LiX zeolites. The first two exotherms were assigned together to phase transformations with participation of lithium, accompanied by structural changes in the LiX zeolites, whereas the last exotherm was assigned to zeolite recrystallization. In contrast, the absence of exotherms for CsX zeolites was related to structure stabilization. The higher C_2-selectivity of CsX zeolites observed in the oxidative conversion of methane was interpreted in terms of their lower surface-area (lower mass-loss during TG) and the stabilization of the zeolite structure (no exotherms) compared to the LiX zeolites.

The DTA technique was exploited by Gallagher et al. [126] for the rapid screening of potential catalysts. These authors presented evidence of a close correlation between DTA results and more conventional reactor studies. DTA screening of unsupported $La_{1-x}M_xMnO_3$ catalysts, where M is a divalent ion partially substituted for lanthanum in the perovskite lattice, was performed for the oxidation of hexane and carbon monoxide. The DTA results showed that, even in the crude DTA experiments, the differential signal is a sensitive technique for determining the onset of the reaction. It closely parallels the course of the reaction up to 40 % conversion over the whole temperature range and does much better at lower temperatures. The close correspondence indicates that the DTA should be quite suitable for catalyst screening in such highly exothermic reactions. Because of its simplicity and rapidity, DTA was also chosen to study the possible effects of SO_2 upon the catalytic activity of some polycrystalline $La_{1-x}M_xMnO_3$ (M = Sr,Pb) perovskites. DTA results for the series of Pt-doped $La_{0.5}Pb_{0.5}MnO_3$ oxidation catalysts are summarized in Figure 32 [127]. Solid curves correspond to the equilibrium heating curve and dashed lines represent steady state curves with SO_2 in the gas stream. In the absence of SO_2, the activity of Pt-doped $La_{0.5}Pb_{0.5}MnO_3$ catalysts did not significantly increase with increasing Pt loading. Although the catalytic activity of these perovskites was greatly reduced in the presence of SO_2 poison, experiments with Pt-doped (0-1000 ppm of Pt) demonstrated that these catalysts can be made resistant to SO_2 poisoning by doping with as little as 200 ppm of Pt.

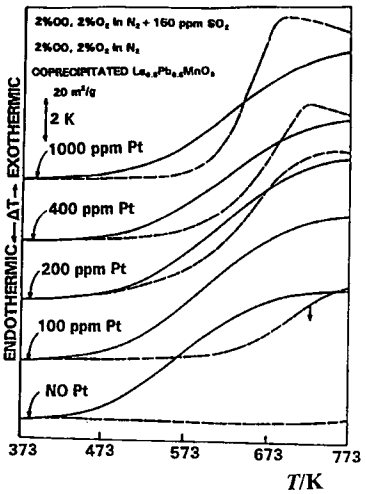


Figure 32. Effect of Pt additions and exposure to SO_2 on the equilibrium DTA curves of a polycrystalline series of Pt-doped $La_{0.5}Pb_{0.5}MnO_3$ oxidation catalysts (adapted from reference [127]).

Heterogeneous catalytic reactions exhibiting oscillatory behaviour have been studied by thermoanalytical methods. Very often when these reactions oscillate, oscillations are also observed in the temperature of the catalyst surface. Using DTA, Gallagher and Johnson [128] observed certain oscillatory phenomena which involve rapid changes in the rate of CO oxidation with O_2 on a $La_{0.7}Pb_{0.3}MnO_3$ catalyst containing Pt in significant amount (> 2400 ppm). By feeding a mixture of 2 % CO, 2 % O_2, 96 % N_2, with or without 150 ppm of SO_2, they concluded that a significant amount of the observed activity, particularly in the presence of SO_2, was due to Pt [129,130]. Danchot and Cakenberghe [131] attributed these oscillations to the applicability of the Langmuir-Hinselwood mechanism in which the reaction takes place between CO and O_2 molecules adsorbed upon the surface of the Pt. The exothermicity of the reaction markedly raises the temperature of the catalyst and the CO_2 product is desorbed. At higher temperatures, however, O_2 is preferentially adsorbed and the sample must cool in order to adsorb enough CO before reacting again. This gives rise to cycles whose period and amplitude depend upon the thermal transport, concentration in the gas phase, etc.

TG has been used by Ozkan et al. [132] to study the self-sustained oscillatory behaviour of NO + CH_4 reaction in the presence of O_2 over titania-supported Pd catalysts. These authors observed that there was a sudden mass loss when the temperature of the catalyst reached around 1150 K. The mass loss corresponded

to the theoretical amount of oxygen associated with Pd oxide in the catalyst. During the isothermal region of the temperature programme, the mass of the catalyst oscillated as shown in Figure 33. The amplitude of these oscillations corresponded to 1.5 % of Pd being re-oxidized to PdO. When the temperature variation of the catalyst was examined, similar oscillations were observed with amplitudes approaching 40 K. The maxima in the temperature oscillations corresponded to the minima in the mass oscillations. During the cooling phase, when the temperature of 1100 K was reached, the catalyst started gaining mass. By the end of the experiment, when the catalyst was cooled to room temperature, it had recovered 53 % of the mass it had lost during the heating, pointing to a hysteresis effect. These results, which were reproduced in both NO + CH_4 + O_2 and CH_4 + O_2 systems, suggested that the oscillations were due to cyclic phase transformation of palladium between the metallic and the oxidic phases. These cyclic phase transformations, in turn, were the result of temperature variations that were caused by the varying levels of exothermicity of the two major reactions, namely NO reduction and CH_4 combustion that were favored by the metallic and the oxidic sites, respectively.

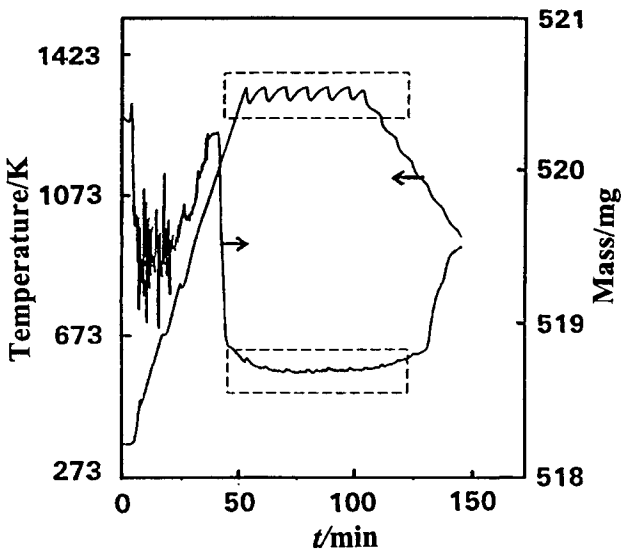


Figure 33. Temperature and mass oscillations in the TG and DTA curves of Pd/TiO_2 (adapted from reference [132]).

6. CONCLUSION

Microgravimetric studies of catalysts and catalytic processes require a detailed knowledge of every aspect of microweighing. The challenge of catalyst studies is broad and multifaceted, requiring a rather detailed understanding of virtually every phase of surface chemistry and physics. Catalytic processes involve specific surface reactions as their critical steps in conjunction with the diffusional processes. A detailed knowledge of the thermodynamics, mechanisms and kinetics is required to optimize the performance of a catalyst with respect to its activity and/or selectivity. Most of this chapter has dealt with use of the microbalance system alone, but the benefits of simultaneous and/or supporting information are obvious, for the more information one can obtain, more will be understood of the complexities involved. Thus, we can see that the microbalance system is an excellent device to bridge the gap between the work on ultraclean perfect crystal surfaces and the real world of polycrystalline catalysts.

The applications considered in this chapter were chosen on the basis of the commonest problems encountered by authors with the vacuum microbalance. The physical and chemical adsorption of gases, with respect to both kinetics and equilibrium, the chemical transformation of catalysts in reactive environments and the determination of surface properties such as the surface area of the active ingredient or the number or surface sites by chemisorption of suitable probe molecules cover the vast body of current applications of microgravimetry in catalysis. Perhaps one of the greatest unexplored areas of gas-solid interactions is to determine the nature of adsorbed molecules on solid surfaces. For this, a combined study of adsorption-surface reaction-desorption could be carried out by simultaneously employing a microbalance, surface analysis techniques and evolved gas analysis. Similarly, in the area of solid-state science, the simultaneous measurement of mass changes with physical properties of the solid catalyst will provide correlations of the deviations from stoichiometry and carrier concentrations and the impact of its performance. Therefore, microgravimetry either alone or combined with other surface analysis techniques, is a relatively simple and valuable tool to obtain relevant structural and chemical information to design heterogeneous catalysts.

REFERENCES

1. J.L.G. Fierro (ed.), Spectroscopic Characterization of Heterogeneous Catalysts. Part B. Methods of Surface Analysis. Studies of Surface Science and Catalysis, Vol. 57A, Elsevier Science, Amsterdam, 1990, p. 1.
2. B. Gates, Catalytic Chemistry, John Wiley & Sons, New York, 1992.

3. J.M. Thomas and W.J. Thomas, Principles of Heterogeneous Catalysis, Academic Press, New York, 1997.
4. G.D. Patterson, Jr., in I.M. Koltoff, P.J. Elving and E.B. Sandell (eds), General Concepts of Instrumentation for Chemical Analyses. Treatise on Analytical Chemistry, Vol. 10, Wiley Interscience, 1972.
5. E.L. Fuller, Jr., H.F. Holmes, R.B. Gammage and C.H. Secoy, in Th. Gast and E. Robens (eds), Progress in Vacuum Microbalance Techniques, Vol. 1, Heyden, London, 1972.
6. P. Murray and J. White, Trans. Br. Ceram. Soc., 54 (1955) 204.
7. E.C. Sewell, Clay Miner. Bull., 2 (1955) 233.
8. J. Sestak, V. Satava and W.W. Wendlandt, Thermochim. Acta, 7 (1973) 333.
9. J.L. Lemaitre, in F. Delannay (ed.), Characterization of Heterogeneous Catalysts, Marcel Dekker, New York, 1984, p. 29.
10. J.L.G. Fierro, L.A. Gambaro, T.A. Cooper and G. Kremenic, Appl. Catal., 6 (1983) 363.
11. E. Wenda, J. Therm. Anal., 20 (1981) 153.
12. F. Roozeboom, A.J. van Dillen, J.W. Geus and P. Gellings, Ind. Eng. Chem. Prod. Res. Dev., 20 (1981) 304.
13. G. Kremenic, J.M. López Nieto, J.L.G. Fierro and L.G. Tejuca, J. Less-Common Metals, 135 (1987) 95.
14. G.T. Baronetti, C. Padró, O.A. Scelza, A.A. , V. Cortés Corberán and J.L.G. Fierro, Appl. Catal. A: General, 101 (1993) 167.
15. F. Gómez-Garcia, L.P. Gómez, L.M. Jiménez-Mateos, S. Vic, J.L.G. Fierro, M.A. Peña and P. Terreros, Solid State Ionics, 63-65 (1993) 325.
16. J.L.G. Fierro, S. Mendioroz and A.M. Olivan, J. Colloid Interface Sci., 107 (1985) 60.
17. M.P. Rosynek and D.T. Magnuson, J. Catal., 46 (1977) 402.
18. J.L.G. Fierro, S. Mendioroz and J. Sanz, J. Colloid Interface Sci., 93 (1983) 487.
19. L. González Tejuca, J.L.G. Fierro and J.M.D. Tascon, Adv. Catal., 36 (1989) 237.
20. J.L.G. Fierro, S. Mendioroz and A.M. Olivan, J. Colloid Interface Sci., 100 (1984) 303.
21. R.C. Vickery, The Chemistry of Yttrium and Scandium, Pergamon, Oxford, 1960.
22. G.V. Samsonov, The Oxide Handbook, Plenum, New York, 1973.
23. C.T. Horovitz, K.A. Gschneidner Jr., G.A. Meison, D.H. Youngblood and H.H. Schock, Scandium, Academic Press, New York/London, 1975.
24. K.W. Browall and R.H. Doremus, J. Amer. Chem. Soc., 60 (1973) 262.
25. E. Cremer, Z. Phys. Chem. A, 144 (1929) 231.

26. J.L.G. Fierro, J.C. Conesa and A. Lopez Agudo, J. Catal., 108 (1987) 334.
27. B. Pawelec, J.L.G. Fierro, J.F. Cambra, P.L. Arias, J.A. Legarreta, G. Vorbeck, J.W. de Haan, V.H.J. de Beer and R.A. van Santen, Zeolites, 18 (1997) 250.
28. J.A. Anderson, B. Pawelec and J.L.G. Fierro, Appl. Catal., A: General, 99 (1993) 37.
29. M.H. Simonot-Grange, A. Elm'Chaouri, G. Weber, P. Dufresne, F. Raatz and J.F. Joly, Zeolites, 12 (1992) 155.
30. C.Y. Li and L.V.C. Rees, Zeolites, 6 (1986) 217.
31. K.E. Wisniewski and R. Wojsz, Zeolites, 12 (1992) 37.
32. J.L.G. Fierro and L. González Tejuca, J. Colloid and Interface Sci., 96(1) (1983) 107.
33. I.S. McLintock, Nature, (London), 216 (1967) 1204.
34. C.N. Satterfield, Mass Transfer in Heterogeneous Catalysts, MIT Press, Cambridge, Mass., 1970.
35. J.L.G. Fierro and A.M. Alvarez, Vacuum, 31 (1981) 79.
36. S.K. Loyalka, J. Chem. Phys., 66 (1977) 4935.
37. P.M. Gundry and F.C. Tompkins, Trans. Faraday Soc., 52 (1956) 1609.
38. C. Aharoni and M. Ungarish, J. Chem. Soc., Faraday Trans. I, 72 (1976) 400; 73 (1977) 456, 1943.
39. C. Aharoni and F.C. Tompkins, Adv. Catal., 31 (1970) 1.
40. M.J.D. Low, Chem. Rev., 60 (1960) 267.
41. J.L. Shereshefsky and E.R. Russell, J. Phys. Chem., 60 (1956) 1164.
42. L. Leibowitz, M.J.D. Low and H.A. Taylor, J. Phys. Chem., 62 (1958) 471.
43. A. Corma, J.L.G. Fierro, R. Montañana and F. Thomas, J. Mol. Catal., 30 (1985) 361.
44. J.L.G. Fierro and J.A. Pajares, J. Catal., 66 (1980) 222.
45. S. Brunauer, The Adsorption of Gases and Vapours, Clarendon Press, Oxford, 1945.
46. E.V. Bezre, B.V. Romanovski, K.V. Topchieva and K.S. Tkonang, Kinet. Katal., 9 (1968) 931.
47. P.A. Jacobs, H.E. Leeman and J.B. Uytterhoeven, J. Catal., 33 (1974) 17.
48. J.A. Pajares, J.L.G. Fierro and S.W. Weller, J. Catal., 52 (1978) 521.
49. J.A. Pajares, J.E. González de Prado, J.L.G. Fierro, L. González Tejuca and S.W. Weller, J. Catal., 44 (1976) 421.
50. J.L.G. Fierro, M.A. Peña and L. González Tejuca, J. Mater. Sci., 23 (1988) 1018.
51. M. Crespin and W.K. Hall, J. Catal., 69 (1981) 359.
52. J.L.G. Fierro, J.M.D. Tascón and L. González Tejuca, J. Catal., 93 (1985) 83.

53. M. Crespin, P. Levitz and L. Gatineau, J. Chem. Soc., Faraday Trans. 2, 79 (1983) 1181.
54. P. Levitz, M. Crespin and L. Gatineau, J. Chem. Soc., Faraday Trans. 2, 79 (1983) 1195.
55. M. Futai, C. Yonghua and Llhui, React. Kinet. Catal. Lett., 31 (1986) 47.
56. C.V. Caceres, J.L.G. Fierro, A. Lopez Agudo, M.N. Blanco and H.J. Thomas, J. Catal., 95 (1985) 501.
57. R. Thomas, E.M. van Oers, V.H.J. de Beer, J. Medema and J.A. Moulijn, J. Catal., 76 (1982) 241.
58. R. Mariscal, J. Soria, M.A. Peña and J.L.G. Fierro, J. Catal., 147 (1994) 535.
59. D.I. Bradshaw, P.T. Coolen, R.W. Judd and C. Komodromos, Catal. Today, 6 (1990) 427.
60. G.T. Baronetti, O.A. Scelza, A.A. , V. Cortés Corberán and J.L.G. Fierro, Appl. Catal., 61 (1990) 311.
61. J.M.D. Tascón, A.M.O. Oliván, L.G. Tejuca and A.T. Bell. J. Phys. Chem., 90 (1986) 791.
62. J.L.G. Fierro, J.M.D. Tascón and L. González Tejuca, J. Catal., 89 (1984) 209.
63. J.M.D. Tascón, J.L.G. Fierro and L.G. Tejuca, J.Chem. Soc., Faraday Trans. I, 81 (1985) 2399.
64. E. Niño, A. Lapeña, J. Martinez, J.M. Gutierrez, S. Mendioroz, J.L.G. Fierro and J.A. Pajares, in G. Poncelet, P. Grange and P.A. Jacobs (eds), Preparation of Catalysts III, Elsevier, Amsterdam, 1983, p. 747.
65. W. Verhoeven and B. Delmon, Bull. Soc. Chim. France, (1966) 3065.
66. M.T. Puchot, W. Verhoeven and B. Delmon, Bull. Soc. Chim. France, (1966) 911.
67. R. Schorpp and I. Hajal, Bull. Soc. Chim. France, (1975) 1965.
68. W.D. Bond, J. Phys. Chem., 66 (1962) 1573.
69. L. Wachowski, S. Zielinski and A. Budrewicz, Acta Chim. Acad. Sci. Hung., 106 (1981) 217.
70. M. Crespin, L. Gatineau, J. Fripiat, H. Nijs, J. Marcos and E. Lombardo, Nouv. J. Chim., 7 (1983) 477.
71. K. Vidyasagar, A. Reller, J. Gapalakrishnan and C.N.R. Rao, Chem. Commun., (1985) 7.
72. R.J.H. Voorhoeve, J.P. Remeika and L.E. Trimble, Ann N.Y. Acad. Sci., 272 (1976) 3.
73. J.L.G. Fierro and L. González Tejuca, J. Catal., 87 (1984) 126.
74. T. Nakamura, G. Petzow and L.J. Gauckler, Mater. Res. Bull., 14 (1979) 649.

75. S.B. Patil, A. Bandyopadhyay, D.K. Chakrabarty and H.V. Keer, Thermochim. Acta, 61 (1983) 269.
76. N. Yamazone, Y. Teraoka and T. Seiyama, Chem. Lett., (1981) p. 1767.
77. G.H. Jonker and J.H. van Santen, Physica (Amsterdam), 19 (1953) 120.
78. M.L. Rojas and J.L.G. Fierro, J. Solid State Chem., 89 (1990) 299.
79. P.K. Gallagher, D.W. Johnson, Jr., and E.M. Vogel, J. Amer. Ceram. Soc., 60 (1977) 28; E.M. Vogel, D.W. Johnson, Jr., and P.K. Gallagher, J. Amer. Ceram. Soc., 60 (1977) 31.
80. N.W. Hurst, S.J. Gentry and A. Jones, Catal. Rev. Sci. Eng., 24 (1982) 233.
81. J.L.G. Fierro and A.M. Olivan, J. Less-Common Metals, 107 (1985) 331.
82. J.M. López Nieto, J.L.G. Fierro, L. González Tejuca and G. Kremenic, J. Catal., 107 (1987) 325.
83. C.J. Keattch and D. Dollimore, An Introduction to Thermogravimetry, Heyden, London, 2nd edn., 1975, Chap. 5, and references cited therein.
84. A. Roman and B. Delmon, Compt. Rend., C 273 (1971) 1310.
85. J.M. Rojo, J. Sanz, J.A. Soria and J.L.G. Fierro, Z. Physikalische Chemie Neue Folge, 152 (1987) 407.
86. J.L.G. Fierro, J. Soria, J. Sanz and J.M. Rojo, J. Solid State Chem., 66 (1987) 154.
87. M. Faraldos, M.A. Bañares, J.A. Anderson, Hu Hangchun, I.E. Wachs and J.L.G. Fierro, J. Catal., 160 (1996) 214.
88. M. Faraldos, M.A. Bañares, J.A. Anderson and J.L.G. Fierro, in M.M. Bhasin and D.W. Slocum (eds), Methane and Alkane Conversion Chemistry, Plenum Press, New York, 1995, p. 241.
89. R.F. Howe, in Y. Iwasawa (ed.), Tailored Metal Catalysts, Reidel, Dordrecht, 1986.
90. J.R. Regalbuto and J.-W. Ha, Catal. Lett., 29 (1994) 189.
91. R.J. Tilley and B.G. Hyde, J. Phys. Chem. Solids, 31 (1970) 613.
92. J. Valyon, M. Henker and K.-P. Wendandt, React. Kinet. Catal. Lett., 38 (1989) 265.
93. S.W. Weller, Acc. Chem. Res., 16 (1983) 101.
94. A. López Agudo, F.J. Gil Llambias, P. Reyes and J.L.G. Fierro, Appl. Catal., 1 (1981) 59.
95. J.L.G. Fierro, S. Mendioroz, J.A. Pajares and S.W. Weller, J. Catal., 65 (1980) 263.
96. J.L.G. Fierro and J.A. Pajares, in J. Rouquerol and K.S.W. Sing (eds), Adsorption at the Gas-Solid and Liquid-Solid Interface, Elsevier, Amsterdam, 1982, p. 367.
97. J.L.G. Fierro, J. Soria and A. López Agudo, Appl. Catal., 3 (1982) 117.
98. L.A. Gambaro and J.L.G. Fierro, React. Kinet. Catal. Lett., 18(3-4) (1981) 495.

99. B.S. Parekh and S.W. Weller, J. Catal., 47 (1977) 100.
100. M.D. Tascón and L. González Tejuca, Phys. Chem. Neue Folge, 121 (1980) 79.
101. M. Ungarish and C. Aharoni, J. Chem. Soc., Faraday Trans. I, 79 (1983) 119.
102. L. González Tejuca, C.H. Rochester, J.L.G. Fierro and J.M.D. Tascón, J. Chem. Soc. Faraday Trans. I, 80 (1984) 1089.
103. P.H. Emmett, in Catalysis, Vol.1, Chap. 2, Reinhold, New York, 1954.
104. O. Gorriz, V. Cortes and J.L.G. Fierro, Ind. Eng. Chem. Res., 31 (1992), 2670.
105. P. König and P. Tétényi, Acta Chim. Acad. Sci. Hung., 89 (1976a) 123; 89 (1976b) 137.
106. K. Tanabe, Mater. Chem. Phys., 13 (1985) 347.
107. S. de Rossi, G. Ferrati, S. Fremiotti, A. Cimino, V. Indovina, Appl. Catal., 81 (1992) 113.
108. R. Sh. Mikhail and E. Robens (eds), Microstructure and Thermal Analysis of Solid Surfaces, John Wiley & Sons, Chichester, 1983, p.294.
109. W. Xie and W.-P. Pan, J. Thermal Anal. Calor., 65(3) (2001) 669.
110. J. Rouquerol, Thermochim. Acta, 300 (1997) 247.
111. R.P. Viswanathan and P. Wilson, Appl. Catal. A: General, 201(1) (2000) 23.
112. I. Melian-Cabrera, M. López Granados and J.L.G. Fierro, Phys. Chem. Chem. Phys., 4(13) (2002) 3122.
113. M. Ai and T. Ikawa, J. Catal., 40 (1975) 203.
114. H.R. Oswald and A. Reller, Thermochim. Acta, 95 (1985) 311.
115. D. Dollimore, Thermal Analysis, Spec. Publ.-R. Soc. Chem., 117 (1992) 238.
116. W. W. Wendlandt, Thermal Analysis, (John Wiley & Sons, New York, Vol. 19 (1986) p. 216.
117. A.K. Sharma and N. K. Kaushik, Thermochim. Acta, 49 (1981) 385.
118. A. Armendariz, B. Coq, D. Tichit, R. Dutartre, and F. Figuéras, J. Catal., 173 (1998) 345.
119. M.E. Brown, A.K. Galwey and A. Li Wan Po, Thermochim. Acta, 220 (1993) 131.
120. G.J. Kim and Wha S. Ahn, Appl. Catal., 71 (1991) 55.
121. D.R. Milburn, K.V.R. Chary, R.J. O'Brien, and B.H. Davis, Appl. Catal. A: General, 144 (1996) 133.
122. J.R. Sohn, Hae Won Kim, Man Y. Park, Eun Hee Park, J.T. Kim, and S. Eun Park, Appl. Catal. A: General, 128 (1995) 127.
123. K.M. Dooley, C. Chang and G. L. Price, Appl. Catal. A: General, 84 (1992) 17.

124. Y. Yongnian, H. Ruili, C. Lin, and Z. Jiayu, Appl. Catal. A: General, 101 (1993) 233.
125. P. Kovacheva, K. Arishtirova, and N. Davidova, Appl. Catal. A: General, 149 (1997) 277.
126. P.K. Gallagher, D.W. Johnson, Jr., and E.M. Vogel, pp. 113-36 in Catalysis in Organic Syntheses 1976, Edited by P.N. Rylander and H. Greenfield, Academic Press, New York, 1976,
127. D.W. Johnson Jr., P.K. Gallagher, E.M. Vogel and F. Schrey, pp. 181-91 in Thermal Analysis, Vol. 3, Edited by I. Buzas, Akademiai Kiado, Budapest, 1975.
128. P.K. Gallagher and D.W. Johnson, Jr., Thermochim. Acta, 15 (1976) 238.
129. P.K. Gallagher, D.W. Johnson, Jr., J.P. Remeike, F. Schrey, L.E. Trimble, E.M. Vogel and R.J.H. Voorhoeve, Mater. Res. Bull., 10 (1975) 529.
130. P.K. Gallagher, D.W. Johnson and E.M. Vogel, Mater. Res. Bull., 10 (1975) 623.
131. J.P. Danchot and J. Van Cakenberghe, Nature, Phys. Sci., 246 (1973) 61.
132. U.S. Ozkan, M.W. Kumthekar, and G. Karakas, J. Catal., 171 (1997) 67.

Handbook of Thermal Analysis and Calorimetry. Vol. 2: Applications to Inorganic and Miscellaneous Materials
M.E. Brown and P.K. Gallagher, editors
© 2003 Elsevier B.V. All right reserved.

Chapter 5

CERAMICS, GLASS, AND ELECTRONIC MATERIALS

[a]Patrick K. Gallagher and [b]John P. Sanders

[a]Departments of Chemistry and Materials Science & Engineering, The Ohio State University, Columbus, OH, 43210, U.S.A.; Departments of Chemistry and Ceramic & Materials Engineering, Clemson Univ. Clemson, SC, 29632, U.S.A.

[b]National Brick Research Center, Clemson University, 100 Clemson Research Park., Anderson, SC 29625, U.S.A.

1. INTRODUCTION

1.1. Purpose and Scope

Thermoanalytical and calorimetric methods play an important role in the characterization of virtually all materials and their processes. This is particularly true for ceramics, glass, and inorganic electronic materials because the synthesis and applications of these materials generally involve such a wide range of temperature. Hence, the evaluation of their composition, properties, and reactivity as a function of temperature and time is of vital importance.

The basic scientific principles, instrumentation, and general methodology involved are extensively described in Volume 1 of this Handbook. Modifications and extensions of these descriptions are provided as needed for the specific applications described herein. The contributions and insights provided by thermoanaltytical or calorimetric investigations are highly complementary to those obtained from a variety of other techniques and complete understanding is generally achieved through an interactive combination of methods.

Analysis in the context of "thermal analysis" is used in its broadest sense. Besides the conventional chemical or compositional analysis, it entails following the course of a wide range of physiochemical processes, illustrated by the diversity of chapters within this and other volumes of the Handbook. Topics of particular interest in this chapter are those associated with the synthesis, phase equilibria, solid-state reactivity, and physical properties of the relevant materials. These include both their bulk behavior and in a finely divided state as particles or thin films.

The treatment is not intended as an exhaustive review, but has more of a tutorial nature, with numerous examples selected to illustrate the great potential of these methods to address an enormous range of scientific and technological problems.

1.2. Organization

This chapter covers a particularly wide range of technologically very important materials. It is therefore especially necessary that the treatment be carefully organized to enable the reader to peruse the content easily while avoiding significant redundancies. The primary element of organization is by the type of application, as opposed to an instrumental technique or class of material. Five broad topics are established. They are compositional analysis (both qualitative and quantitative), physical properties, phase equilibria, solid-state reactivity, and synthesis. Each of these major categories is then sub-divided into more specific classes of material or techniques when appropriate. The order of these five topics is arranged in a sequence that the authors feel will be most productive and meaningful.

2. PHASE EQUILIBRIA

2.1. Establishing a phase diagram

The applications portion of the chapter is started with the discussion of phase equilibria because an appreciation of this aspect is essential for the following sections. Thermoanalytical methods play an important role in the determining of phase diagrams and in the detailed study of phase transformations.

DTA or DSC is frequently used to establish the temperatures associated with the solid-state and liquid-solid transitions in phase equilibria. Judd and Pope provide a particularly good introduction to the usefulness of DTA [1]. Figure 1 is the hypothetical phase diagram is for a simple binary system. A point, W, is selected in the liquid-phase field and the resulting cooling (time-temperature) curve and DTA pattern are presented.

In reporting the equilibrium temperatures for the diagram, problems associated with supercooling and other metastabilities must be kept in mind. Consequently, both heating and cooling curves should be determined to establish the degree of equilibrium that has been attained. Compromises need to be made that generally lead to a series of experiments involving different sample sizes of the same composition and variations in the heating or cooling rates. Large sample sizes and faster heating rates enhance the sensitivity of the techniques to events having a small change in enthalpy. On the other hand, smaller samples and slower rates allow for a closer approach to the equilibrium temperature and better resolution of overlapping events.

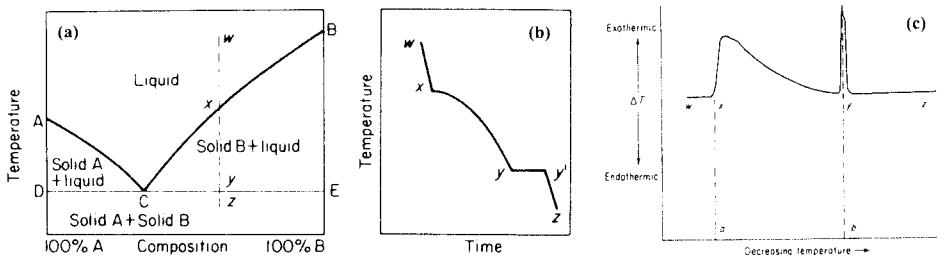


Figure 1. (a) Hypothetical phase diagram for a simple binary system. (b) Cooling curve of the indicated section. (c) DTA curve of the indicated section [1].

This concept is extended to the more complex diagram shown in Figure 2, using a hypothetical binary system with multiple eutectic and peritectic points, as well as congruently and incongruently melting compounds. The transitions in these examples are first-order thermodynamic transitions and the possible effects of gas-solid reactions have been ignored.

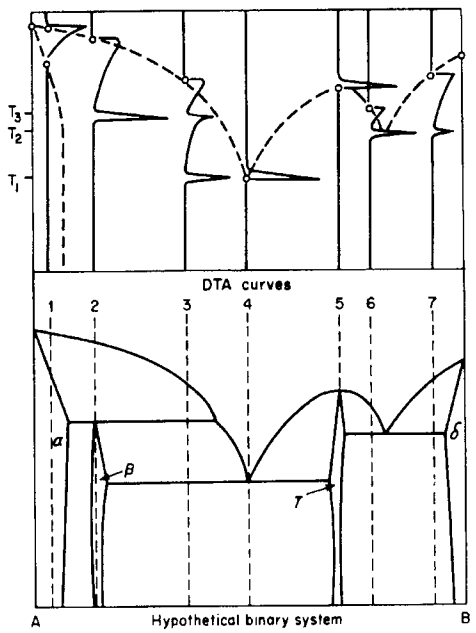


Figure 2. A hypothetical phase diagram for a binary system with multiple eutectic and peritectic points, showing several DTA curves obtained at different portions of the diagram [1].

2.2. The nature of phase transformations

Higher-order phase transformations can also occur, particularly where only small atomic movements are required. For example, had the cooling from the liquid phase in Figures 1 or 2 involved the formation of a glassy phase, the resulting DTA curve upon reheating might have resembled that in Figure 3 for a glass forming composition [2]. In this case, the higher-order glass-transition involves only a change in heat capacity, ΔC_p, instead of an enthalpy change, ΔH, and thus a step rather than a peak occurs in the DTA curve at the glass-transition temperature, T_g. This is followed by the exothermic crystallization of two solid phases and the subsequent endotherms associated with the melting of these newly-formed crystalline phases.

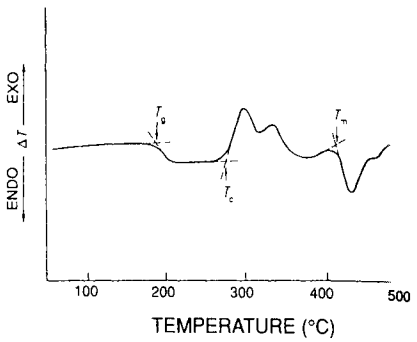


Figure 3. The DTA curve for the glass, $0.5BeF_2$-0.3KF-$0.1CaF_2$-$0.1AlF_3$, heated in flowing N_2 at 20 °C min^{-1} [2].

The inability of a system to nucleate the product phases is what leads to metastability. The critical interplay between thermodynamics and kinetics is the essence of solid-state reactivity. Arguably the most important ferroelectric material, $BaTiO_3$, also displays intriguing irregularities in its nucleation processes [3]. The differences in the nucleation processes associated with the tetragonal to cubic transformation in $BaTiO_3$ are revealed in the careful simultaneous TD-DSC studies by Tozaki et al. [3]. Figure 4 shows simultaneous TD and DSC curves for the transformation on both heating and cooling. The process on heating, going from the tetragonal to the cubic phase, takes place as a single sharp transition, displaying no tendency toward metastability, as indicated in Figure 4(a). In contrast, Figure 4(b) shows the multiple steps that occur during nucleation of the tetragonal structure in the cooling process. There are many examples of the metastable cubic phase for $BaTiO_3$ persisting at room temperature.

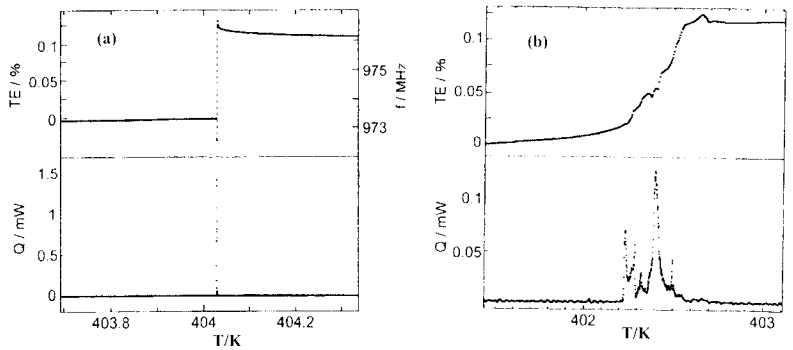


Figure 4. Curves for the simultaneous TD-DSC of single crystal $BaTiO_3$ along the <100> axis. (a) Heating at 10 μK s^{-1}. (b) Cooling at 0.2 μK s^{-1}. [3]

Although DTA or DSC remains the most common method of establishing the relevant temperatures associated with phase transformations, other thermoanalytical methods based on thermal expansion, mechanical properties, electrical properties, etc., are also useful. When nonstoichiometry is a factor, TG is often used to establish phase boundaries for varying atmospheres. An example of this is presented in the following section.

Besides the establishing of equilibrium phase diagrams, examples will be given of the use of these methods to determine chemical composition and to study solid-state reactivity.

3. COMPOSITIONAL ANALYSIS

3.1. Methods based on changes in mass

3.1.1. Introduction

There are several techniques that are based on actual or apparent changes in the mass of material or of the system under investigation. Direct changes in mass are followed by thermogravimetry, TG. Thermomagnetometry, TM, includes not only the changes in actual mass, but also those based on the magnetic properties of the sample and the strength of the magnetic field gradient at the sample position [4]. Compositional analysis of the sample based on these techniques requires knowledge that allows the conversion of the above indirect information into meaningful analytical results. For example, such knowledge might be that the only mass loss in the particular sample is due to the loss of CO_2 from $CaCO_3$, or that the only magnetic attraction in the sample is that of Fe metal.

Alternatively, one can measure the amount and/or nature of the volatile species that are lost from the sample. This can be done in real time as the products are

evolved, or by collecting the products and analyzing them subsequently. Analysis of these products is referred to as evolved gas analysis, EGA, and may be achieved through the use of many analytical techniques [5]. Quantitative information is sufficient by itself, but even qualitative information may be adequate to achieve quantitative determinations, if the specific product evolved over a particular temperature range can be adequately coupled with the TG results.

3.1.2. Thermogravimetry

Nonstoichiometry plays a vital role in determining the properties of most materials and in controlling their reactivity. Generally the range of nonstoichiometry is small. However, when the cations involved can readily adopt multiple valencies then nonstoichiometry may be achieved over a wide range of compositions. Clearly, these variations in stoichiometry frequently involve changes in the mass of the sample associated with the loss or gain of a constituent, e.g., chalcogenides or halides. TG and EGA are viable and convenient methods to follow such changes quantitatively.

Perovskite or perovskite-like materials are good examples of systems that can exist as single-phase material over a wide range of stoichiometry. The cuprate-based high-temperature superconducting systems offer a particularly good example of the wide range of stoichiometry, see for example Chapter 15 in this volume [6], a special issue of Thermochimica Acta devoted to that topic [7], or a book devoted to the applications of perovskites [8].

Using TG, the exact degree of nonstoichiometry can be determined as a function of temperature and partial pressure of the active component, by following the change in mass from a point of established stoichiometry. Two examples are described, which illustrate both large and small departures from stoichiometry.

The first example comes from a study of catalysis [9]. The value of x in the compound $BaPtO_{3-x}$ was determined by heating the material in H_2 to form the point of known stoichiometry, namely $Ba(OH)_2$ and Pt, as indicated by equation 1. Figure 5 illustrates such a typical heating curve. The mass loss at the plateau around 400 °C corresponds to the water vapour lost in accordance with equation 1 and allows calculation of the value for x in the initial sample.

$$BaPtO_{3-x\,(s)} + (2 - x)\,H_{2\,(g)} \leftrightarrow Ba(OH)_{2\,(s)} + Pt_{(s)} + (1 - x)\,H_2O_{(g)} \qquad (1)$$

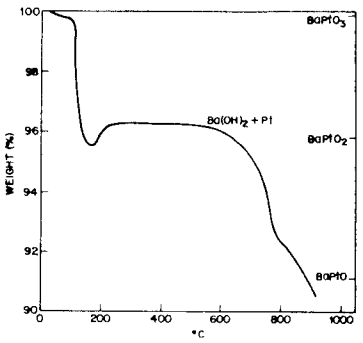


Figure 5. A TG curve for $BaPtO_3$, formed at high oxygen pressure, heated in H_2 at 10 °C min^{-1} [9].

Table 1 summarizes the results for a conventionally prepared sample at high oxygen pressure with those obtained from the decomposition of the precursor, $BaPt(OH)_6$, decomposed under the indicated conditions. A similar approach has been used to determine the oxygen content in cuprate semiconductors [10].

Table 1.
Oxygen stoichiometry of various $BaPtO_X$ materials. [9]

Sample	Formula
High Pressure	$BaPtO_{3.02}$
$BaPt(OH)_2$, 500 °C, Q[a]	$BaPtO_{2.99}$
$BaPt(OH)_2$, 600 °C, Q	$BaPtO_{2.99}$
$BaPt(OH)_2$, 700 °C, Q	$BaPtO_{2.95}$
$BaPt(OH)_2$, 800 °C, Q	$BaPtO_{2.84}$
$BaPt(OH)_2$, 900 °C, Q	$BaPtO_{2.72}$
$BaPt(OH)_2$, 1000 °C, Q	$BaPtO_{2.38}$
$BaPt(OH)_2$, 1000 °C, SC	$BaPtO_{2.60}$

[a] Temperature to which the material had been heated for 30 min in O_2 and either quenched (Q) or allowed to cool slowly with the furnace (SC).

The second example represents a much more difficult determination, where the amount of nonstoichiometry is small and the conditions require high temperatures and carefully controlled atmospheres. The magnetic and electrical properties of commercial ferrites are highly dependent on the departure of stoichiometry from the ideal spinel phase, M_3O_4 or $(MO{\cdot}M_2O_3)$. The specific example selected is for a technologically relevant material, nickel zinc ferrite, represented by the generic formula $Ni_XZn_yFe_{(1-x-y)}Fe_2O_{4+\gamma}$ [11]. The value of γ

determines the amount of Fe^{2+} that is oxidized beyond the stoichiometric value of $1 - x - y$. The equilibrium amount of such oxidation that can be tolerated before a second phase of hematite, α-Fe_2O_3, exsolves is quite limited. The maximum temperature in the processing is determined by the sintering conditions and may approach 1400 °C. The value of γ is established at that point and the cooling program, including the partial pressure of oxygen, p_{O2}, is controlled to maintain the desired value of γ. This necessitates detailed knowledge of both the equilibrium and metastable values of γ as a function of temperature and p_{O2}. There are several serious complications imposed on such an analytical study due to the high temperatures and small mass losses involved. These are:

- Significant losses of Zn from the sample, particularly at low p_{O2}.
- Significant losses of Pt from the support, particularly at high p_{O2}.
- Distinguishing between metastability and equilibrium.
- Accurately correcting the small mass losses for buoyancy effects.

Figure 6 presents the corrected values of mass and γ as observed by isothermal TG at the indicated points. The metastability is determined by the direction from which equilibrium is approached. Metastability occurs due to the difficulty associated with nucleating and precipitating the second phase. There is not a comparable difficulty in the dissolution process. Consequently, equilibrium is reached within the experimental times when coming from the two-phase direction, the higher p_{O2} and lower temperature side, in this case (Zone II). Under those conditions there is an obvious change in slope at the phase boundary, indicated by the dashed curve.

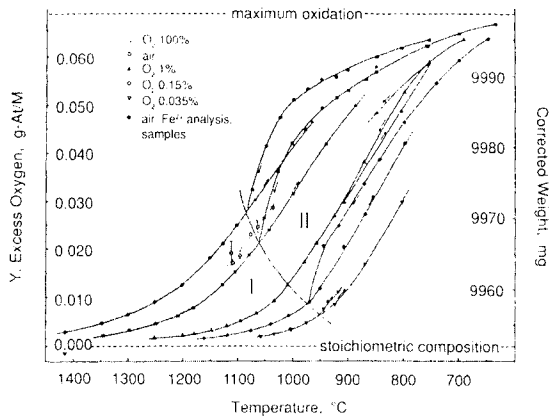


Figure 6. Changes in mass for $Ni_{0.685}Zn_{0.177}Fe_{2.138}O_{4+\gamma}$ as a function of temperature and partial pressure of oxygen [11].

The results from such a study are more readily appreciated and utilized in the form of isocompositional plots as presented in Figure 7. The results for metastable samples continue as straight lines as they cross the phase boundary, while the equilibrium values for the two-phase material exhibit a change in slope. Plant engineers can utilize such plots to establish the desired degree of nonstoichiometry associated with the intended magnetic and electrical properties.

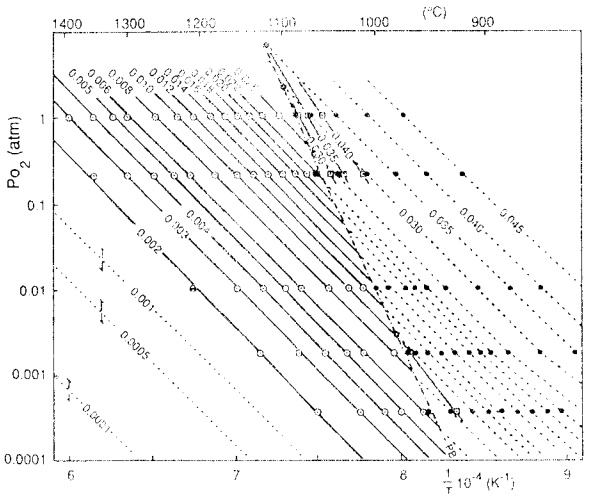


Figure 7. Isocompositional phase diagram constructed with interpolated values from Figure 6. The oxygen-excess coefficient is indicated on each isocompositional line; open and filled circles are from zones I and II, respectively, in Figure 6. Star symbols belong to the phase boundary limit; isocompositional lines for $\gamma = 0.001$, 0.0005, and 0.0001 are extrapolated [11].

The use of thermoanalytical methods for the chemical analysis of thin films is severely hampered by the diminution of the signal-to-noise aspects caused by the large amount of irrelevant substrate material present. The thickness of the protective carbon film on a fused silica fibre optic, however, has been successfully determined using TG [12]. Burning off the carbon film in O_2 yields the mass percent of the coating, from which the thickness can be calculated based on the known diameter and density of the fibre. Success requires very accurate correction for the effects of buoyancy. Fortunately, the sample can be immediately reheated, untouched, under identical conditions and the second curve subtracted from the original one to yield an essentially perfect correction for buoyancy. Figure 8 is an example of such an analysis. The approximately

30 mg sample consisted of many short sections, approximately 3 mm each. The results indicate that the mass loss of only 100 μg can be measured as a function of temperature in a meaningful manner. Even the resulting differential curve is relatively smooth.

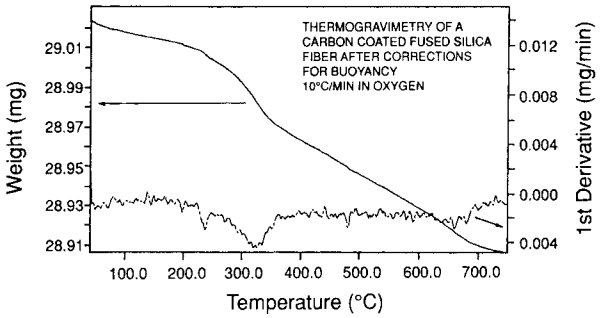


Figure 8. TG and DTG curves, after buoyancy correction, for a carbon-coated fused-silica fibre heated at 10 °C min^{-1} in oxygen [12].

The analysis of clays and shales by TG alone is complicated by the presence of impurities or accessory minerals that give conflicting or overlapping mass losses. Guggenhiem and Koster van Groos have discussed this uncertainty in the analysis of reference clay raw materials for the Clay Minerals Society's Source Clay Project [13]. For well-known single-phase materials, the identification of thermal events by TG is relatively straightforward, but with natural multi-phase materials, thermal events cannot be directly identified with absolute certainty. To identify mass losses observed by TG for unknown multiphase samples, it is necessary to refer to tables of decomposition data for minerals [14, 15]. In most cases, the characteristic temperatures reported in the literature are derived from DTA data. To provide more definitive results, it is common to resort to some other analytical technique, such as DSC or X-ray diffraction, to complement TG measurements and provide for a less ambiguous analysis [16].

3.1.3. Evolved gas analysis

Recently, the coupling of evolved gas analysis (EGA) with TG has greatly enhanced the analytical capability of TG measurements for clays and shales [17]. The EGA signal provides additional information that makes the identification of thermal events in the TG signal much more definitive. An example of a coupled TG/EGA (FTIR) analysis of a brick-making raw material is given in Figure 9. For this material, three overlapping thermal events are

apparent in the EGA signals that TG alone could not identify due to overlapping decompositions. In this case, the evolved gas signals are integrated traces from a Fourier transform infrared (FTIR) spectrometer that is coupled to a large-sample TG as described by Kaisersberger and Post [17]. With the EGA signals, the pyrite oxidation (SO_2 trace) and oxidation of organic impurities (CO_2 trace) can be distinguished from the expected H_2O emission due to the dehydroxylation of the clay mineral. Although the EGA data is qualitative in this example, it provides valuable information about the firing process of this brick raw material.

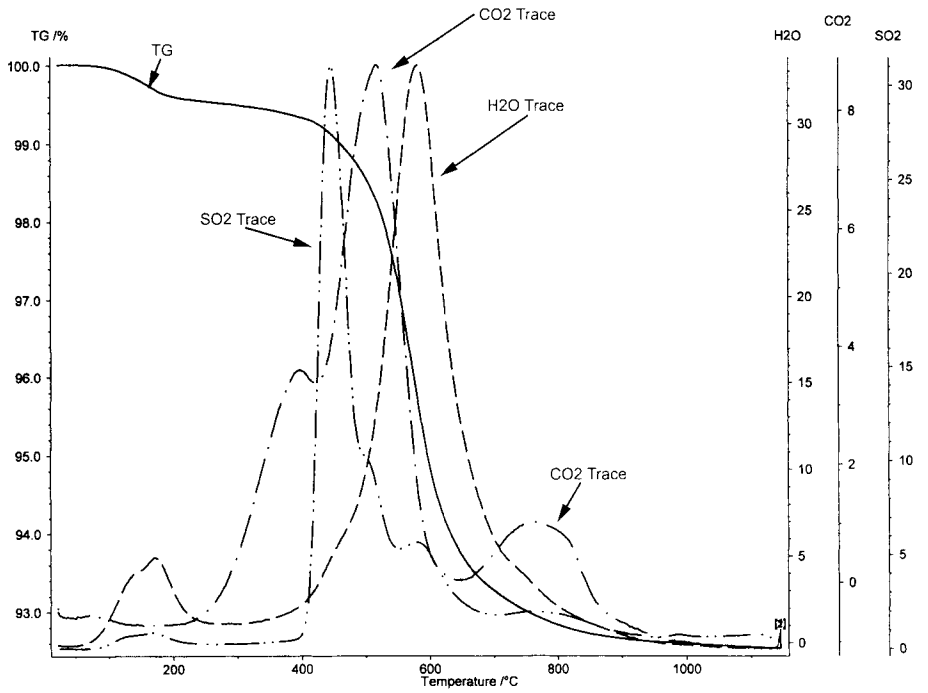


Figure 9. Combined TG and EGA (FTIR) for shale with pyrite, carbon burnout, and dehydroxylation heated in flowing N_2 with 20% O_2 (by volume) at 10 °C min^{-1} [17].

Combined TG-EGA data can also be used to detect impurities in very minute quantities [17]. In many cases, evolved gas analysis is more sensitive than TG. Figure 10 is an example where trace emissions of HF were detected from a raw material, where TG detected no mass loss. This type of analysis could be used to select raw materials based on their potential environmental impact. Sanders

and Brosnan discuss several similar applications for combined TG-EGA to study the air-pollution potential of raw materials for traditional ceramic products [18].

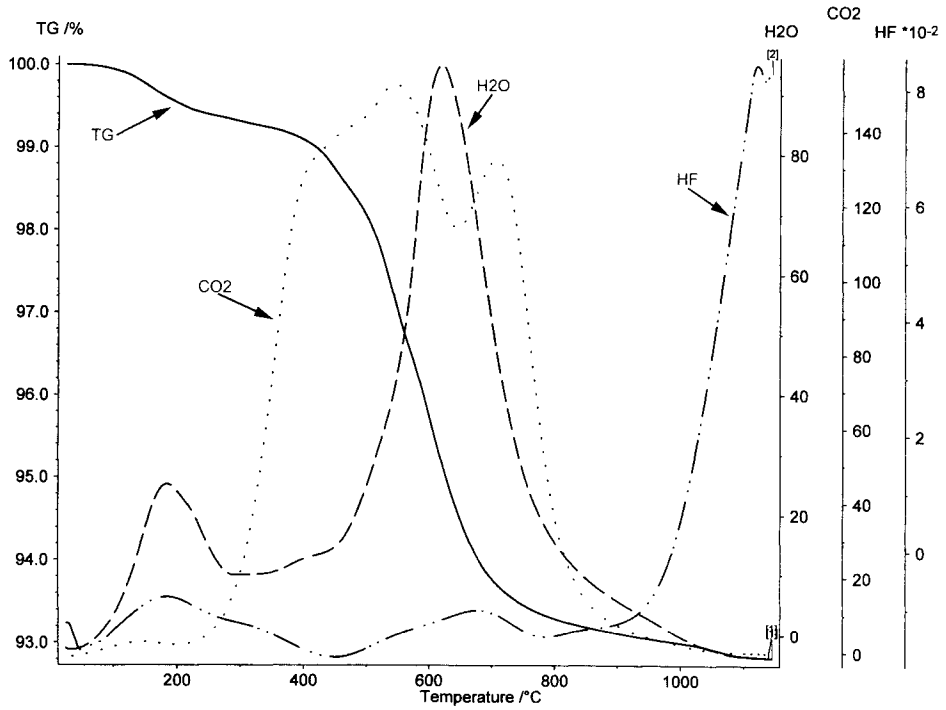


Figure 10. Combined TG and EGA (FTIR) for shale with HF emission heated in flowing N_2 with 20% O_2 (by volume) at 10 °C min^{-1} [17].

The investigation of the corrosion products on copper is a good example of the use of EGA for qualitative analysis. Frequently these corrosion products are not well formed, or the X-ray diffraction patterns of the multiple products overlap too much for clear interpretation. Figure 11 shows the results of a mass spectrographic scan of a corroded copper specimen heated to about 530 °C [19]. Clearly the specimen contains sulfates, carbonates, hydroxides, and chlorides, which decompose in this temperature range. Scans made at other temperatures revealed other components.

Evolved gas analysis signals typically provide qualitative information that complements and enhances the quantitative information provided by some other technique, such as TG or DSC, as described in the previous examples. Pulse thermal analysis, however, is a means of calibrating the evolved gas analysis signal to get quantitative data [20,21]. The EGA signal is calibrated by sending

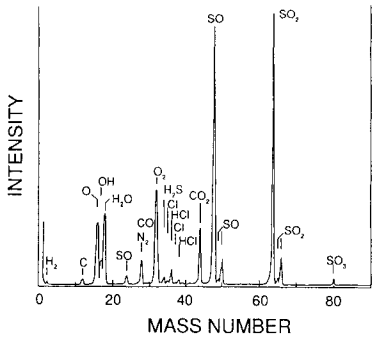


Figure 11. MS-EGA scan, centered at 530 °C, of a corroded specimen of copper [19].

a pulse of a known volume of reagent gas to the evolved gas analyzer. The peak area from the gas pulse can then be quantified and used as a reference to quantify the peak area of sample decompositions. This method was originally developed for the calibration of coupled mass spectrometers (MS), but has also been successfully applied to Fourier transform infrared spectroscopy (FTIR) [20,21]. An example of pulse thermal analysis is given in Figure 12, where pulses of SO_2 are used to determine the quantities of SO_2 evolved by the oxidation of pyrite and the decomposition of sulfates from naturally-occurring shale.

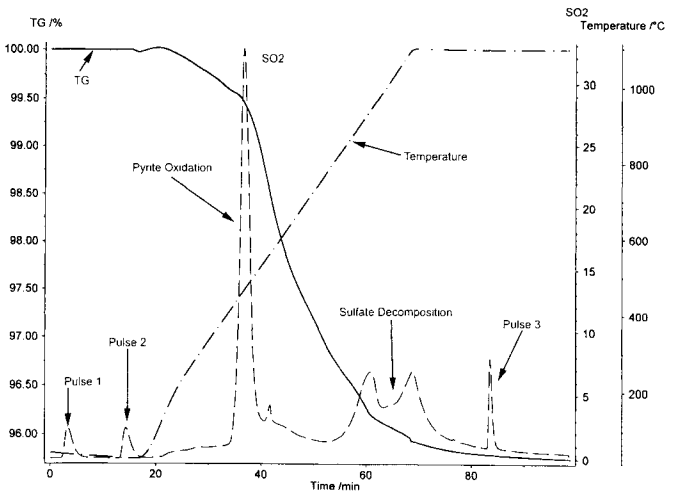


Figure 12. Pulse thermal analysis of shale heated in flowing N_2 and O_2 atmosphere (50% O_2 by volume) at 12 °C min^{-1} with a 30 minute dwell at 1150°C.

3.1.4 Thermomagnetometry

The proximate analysis of coal, including its iron content, has been successfully achieved by a combination of TG and TM in controlled atmospheres [22]. Figure 13 shows how the mass percentages of moisture, volatiles, fixed carbon, ash, and iron (presumed to be pyrite) is measured through a method that is relatively simple and fast compared to alternative methods.

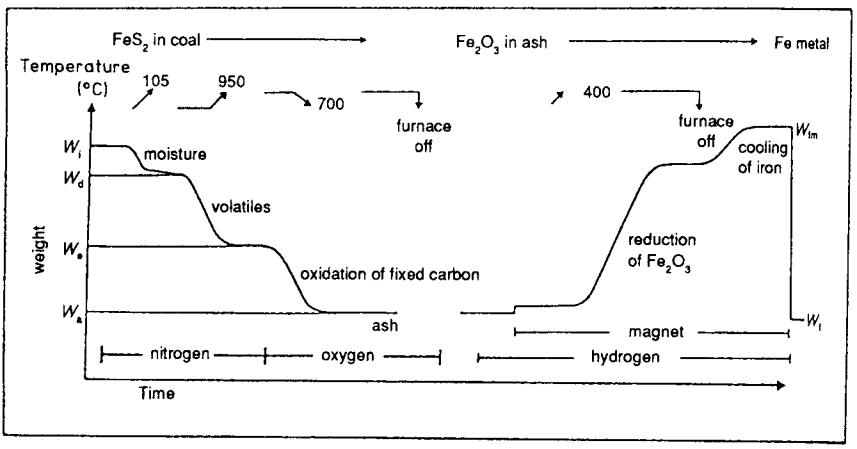


Figure 13. Proximate analysis of coals and lignites using TG and TM in controlled atmospheres [22]. See the text for details.

The temperature and atmosphere control programs are established to initially evaporate the moisture content by rapidly heating to 105 °C in N_2. After about 10 minutes the temperature is rapidly raised to 950 °C in flowing N_2 to determine the amount of volatiles. When constant weight is achieved the sample is cooled to 700 °C and the atmosphere switched to O_2 to burn off the fixed carbon. The remaining mass at that point is the ash content. The original pyrite content of the coal, which has now been converted to Fe_2O_3, is then measured by TM. The magnet is applied and the atmosphere is changed to H_2. The ash is heated to 400 °C, which reduces the Fe_2O_3 in the ash to Fe. The furnace is allowed to cool to room temperature while still in a flow of H_2 to prevent oxidation and the amount of Fe is determined from the amount magnetic attraction.

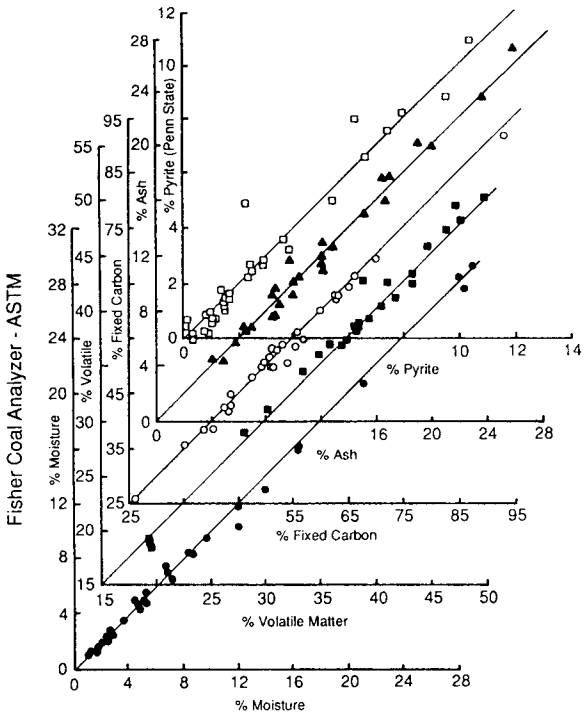


Figure 14. Comparison of the proximate analysis of coals based on TG-TM with that derived from the ASTM-Fisher method [22].

3.2. Methods based on a transition temperature

3.2.1 Differential thermal Analysis and differential scanning calorimetry

Large single crystals of lithium niobate are grown from the melt, because of the material's useful electro-optical properties. Such applications require that crystals be of essentially perfect optical quality and hence very homogeneous. The material has a fairly wide range of Li nonstoichiometry and is represented as $Li_{1-x}NbO_{3-0.5x}$. To ensure that the crystal's composition does not vary during growth, it is crucial that the starting melt be exactly at the congruent composition. An accurate analytical method was needed to determine the precise Li content at the congruent composition and for use as a subsequent tool in quality control. The material has a perovskite structure and, fortunately, there is a high-order ferroelectric phase-transformation in the nonstoichiometric material that has a strong dependence composition [23]. This higher-order phase-transformation leads to a small change in heat capacity, ΔC_p, at the transition temperature which can be detected by careful DTA, DSC, or dilatometric experiments [24]. A series of standards of known composition

were prepared and measured by DTA. Figure 15 shows DTA curves for two samples of the same composition, to indicate the nature, sensitivity, and reproducibility of the measurements. The transition temperature, T_c, shows little hysteresis in temperature, even at a heating and cooling rate of 20 °C min^{-1}. The resulting calibration curve is presented in Figure 16 [25]. The least-squares fit to the data points for a second-order equation yields Equation 2, where C is the Li_2O content in mole %.

$$T_c = 9095.2 - 360.05\ C + 4.228\ C^2 \qquad (2)$$

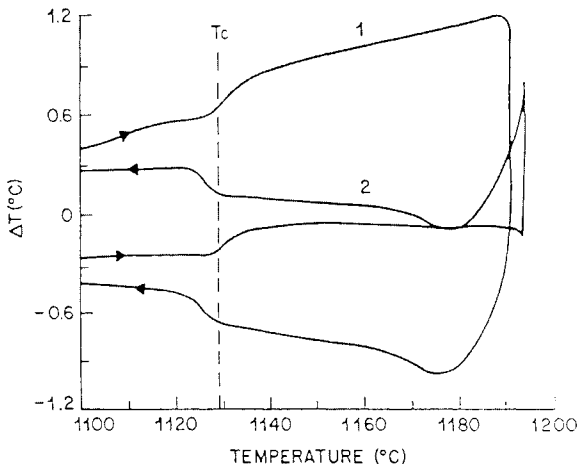


Figure 15. DTA curves for two samples of $Li_{0.969}NbO_{2.985}$ heated at 20 °C min^{-1} in N_2; (1) 164 mg (2) 149 mg [24].

The precise congruent composition was then determined by pulling crystals from melts whose compositions encompassed the congruent value. Values of T_c for samples taken from the initial and final melts, along with those from the top and bottom of the crystals, were determined and the distribution coefficients for Li between the phases determined. The results are plotted in Figure 17. The stoichiometry of the congruent composition corresponds to that at a distribution coefficient of unity, or 48.45 mole % of Li_2O. The value of T_c for the incoming cullet supplied for crystal growth is then specified and monitored for incoming quality control.

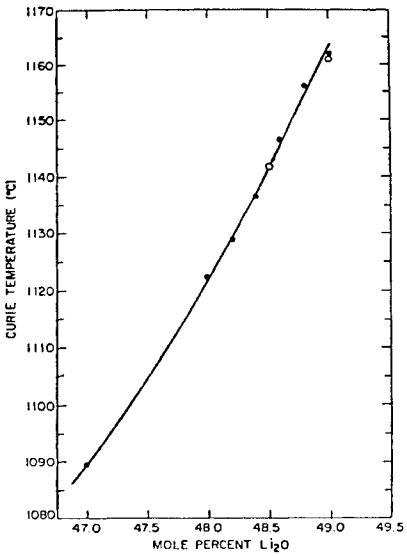


Figure 16. Curie temperature versus mole % Li_2O in $Li_{1-x}NbO_{3-0.5x}$ [25].

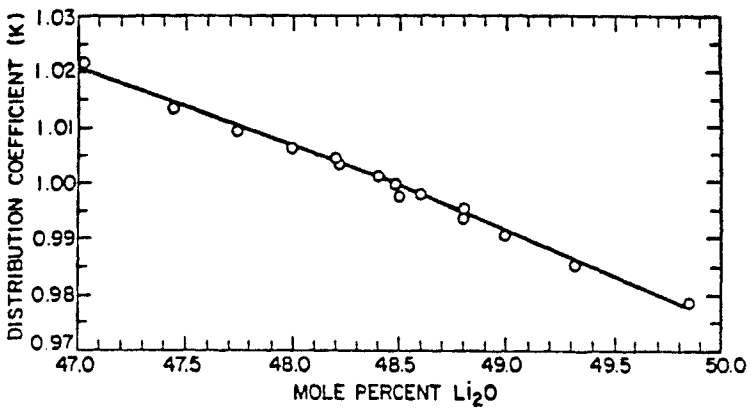


Figure 17 - Distribution coefficient versus Li_2O mol % in the melt [25].

Interconnect technology between devices on printed-circuit boards is an important aspect of reliability. One of the methods frequently utilized depends on the electro-deposition of a lead and tin-based solder having a well controlled melting temperature for subsequent processing. DTA or DSC is a sensitive and rapid method capable of measuring the melting points of relatively small areas of the deposit. This enables trouble-shooting of problems associated with

current density, inhomogenieties, and other variables involved in the deposition [26]. The phase diagram determined by DTA is shown in Figure 18. The liquidus curves show a strong dependence on composition and enough information has to be available to determine on which side of the eutectic composition the sample composition lies.

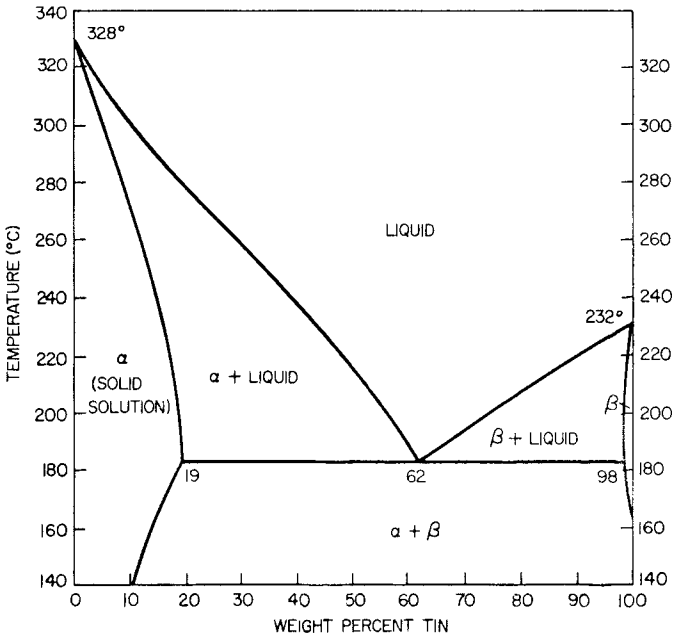


Figure 18. Phase diagram for the tin - lead system [26].

Figure 19 shows representative DTA curves for alloys from different regions of the phase diagram. The eutectic composition, of course, yields a single melting point, while the other three curves reveal the liquidus as they return to the base line at higher temperatures. These extrapolated end points on heating are used to define the tin/lead ratio in the samples accurately. Kuck's study gave a reproducibility of ±0.4°C. For a hypoeutectic alloy this translates to about ±0.2 mass % according to Figure 18. More recent and detailed studies have addressed the problem associated with potential under-cooling of the melts [27].

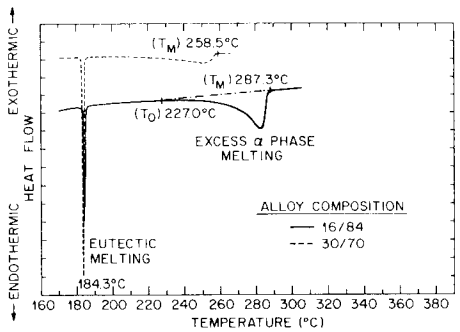


Figure 19. DTA curves for samples of Sn/Pb solder from various areas of Figure 18 [26].

Many types of traditional ceramics, from porcelain to brick, contain crystalline silica as an impurity or an intentional constituent. Crystalline silica refers to the portion of silica that is not combined in the silicate matrix. The most common form of crystalline silica is α-quartz. Quartz undergoes a reversible crystalline inversion from the α to β form at approximately 573 °C, which is accompanied by an expansion on heating and a contraction on cooling. An example of the dimensional change (TD or dilatometric analysis) associated with the quartz inversion, for a fired brick body on heating and cooling, is given in Figure 20. If

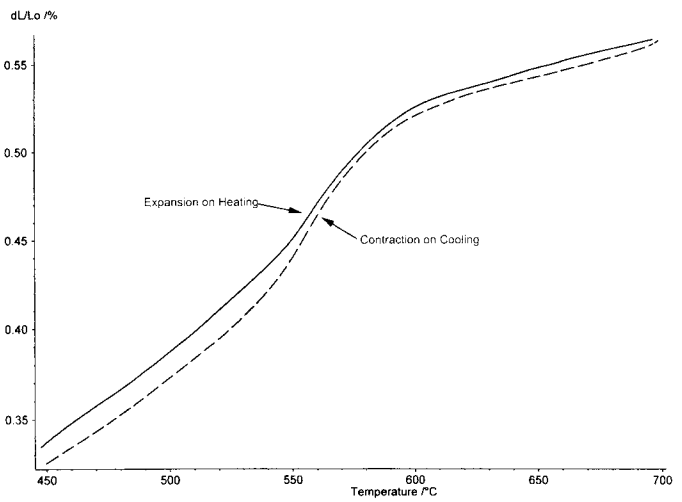


Figure 20. Thermodilatometric (TD) curve showing the quartz inversion on heating and cooling in flowing air at 5°C/min.

the ware is not cooled isothermally, the differential stresses involved in this inversion on cooling can result in the development of cracks in the ceramic ware. This is a common problem for large, dense ceramic units where the outside of the unit, which is exposed to the kiln atmosphere, cools at a different rate from the interior of the unit. For this reason it is critical to control the quartz content of the raw materials and body compositions carefully so that a heating schedule can be developed for the particular body, to minimize the stresses caused by the quartz inversion.

The most common means of measuring the crystalline silica content of ceramics is X-ray diffraction, but there is a practical lower detection limit of about 1% [28]. When lower detection limits are required, the heat associated with the quartz inversion can also be measured calorimetrically and related to the amount of quartz in a raw-material sample. The quartz inversion is endothermic on heating and exothermic on cooling. The DSC curve in Figure 21 displays the endotherm on heating. Because the areas of the DSC peaks are proportional to the amounts of quartz in ceramics, it is possible to develop a calibration curve to determine the quantity of quartz in an unknown sample. By measuring a series of calibration standards with known quartz contents, a linear calibration curve like the one in Figure 22 can be constructed which relates peak area to known quartz content. With proper calibration, the quartz content of unknown samples can be measured by comparing the peak area of the unknown to the calibration curve. To measure very low quartz contents, fast heating rates help to define the DSC peaks for the quartz inversion

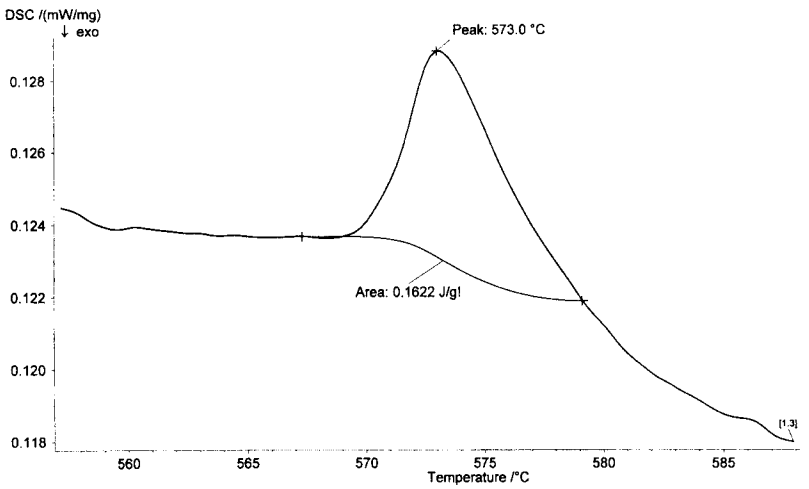


Figure 21. DSC curve of quartz inversion on heating in flowing N_2 with 20% O_2 (by volume) at 20 °C min^{-1}.

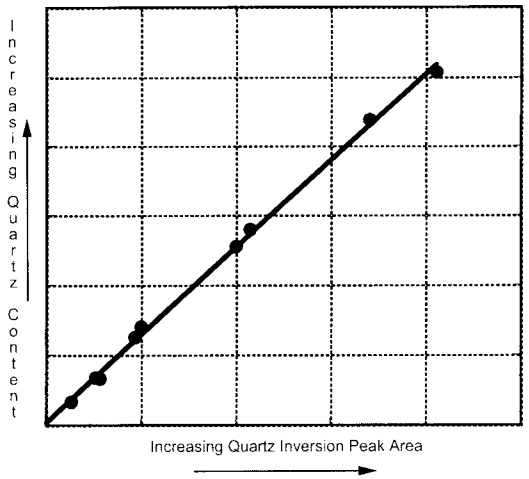


Figure 22. Quartz calibration curve.

The Orton Foundation has produced a specialized calorimeter for measurement of the quartz content of ceramic raw-materials [28]. This instrument uses a single sensor or thermopile. The single sensor purportedly gives less baseline drift than a traditional DSC. Calibration using known quartz standards is still required to determine the quartz concentration in unknown samples.

3.2.3 Thermomagnetometry

Magnetic transition temperatures can vary in a smooth monotonic function of composition. Thermomagnetometry, TM, can be used to measure the Curie temperature, T_c, which, combined with a calibration curve, will provide a quantitative compositional analysis of the magnetic phase. A good example of this is described by Haglund in his review article on TM [29]. Finely divided tungsten carbide dispersed in cobalt is used for machining because of its hardness. Some WC dissolves in the small amount of Co binder phase and alters the value of T_c for that phase. The substantial decrease in T_c with WC content is shown in Figure 23 [30]. The results measured by TM compare well with those determined by microprobe analysis, as indicated in Figure 24 [31]. Similarly the value of T_c can be used to determine the composition of Co-Ni alloys [32].

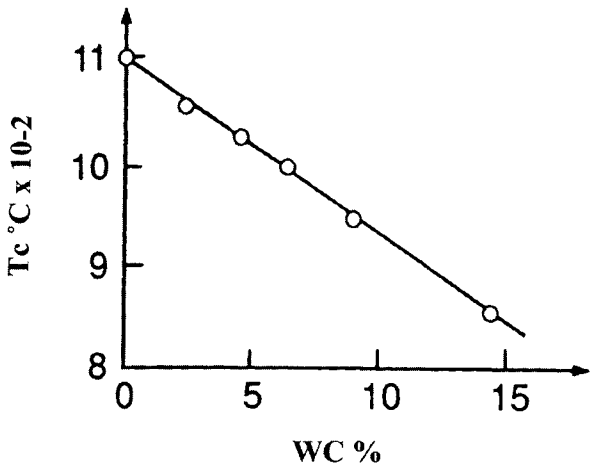


Figure 23. T_c of solid solutions of the cobalt binder phase in WC-Co alloys [30].

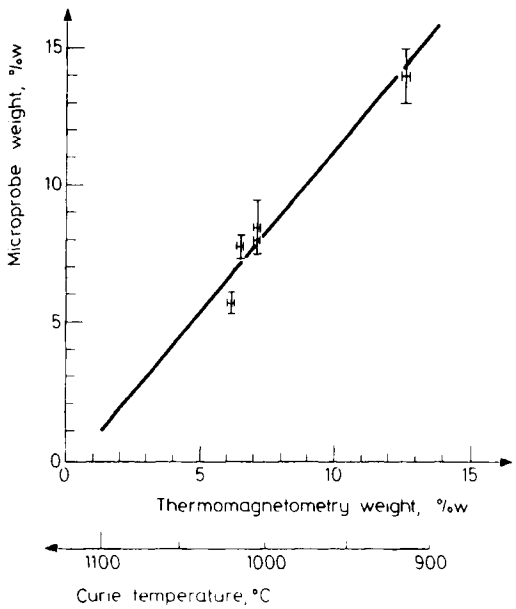


Figure 24. Correlation of the tungsten content of the binder phase in WC-Co alloys determined by TM with that determined by microprobe analysis [31].

3.2.3 Thermosonimetry

Thermosonimetry (TS) is a technique which measures acoustical emissions from a material as it is heated [33]. For traditional ceramics, thermosonimetry can be used to monitor crystalline inversions such as the quartz or cristobalite inversion, decompositions, or the crystallization of glasses. Lønvik described a study where the relative amounts of quartz and cristobalite in a silicate ceramic were determined by comparing the magnitude of the sonic emissions during the cristobalite inversion (220 °C) and the quartz inversion (573 °C). An example of this type of evaluation is given in Figure 25.

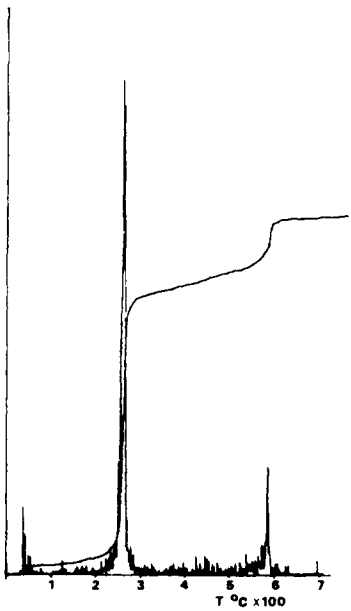


Figure 25. Example thermosonimetric curves collected from a silicate ceramic with a heating rate of 20 °C min^{-1} [33].

3.3. X-ray diffraction and spectroscopic methods

Thermomicroscopy could also be included in this section, however, the topic and its applications have been thoroughly covered by Wiedemann and Felder-Casagrande in Volume 1 of this series [34].

It is usually more convenient experimentally to record spectra of materials at room temperature, so this type of data is generally obtained on cooled, perhaps quenched, samples that have been heated and held at pre-determined temperatures. This, however, may not provide a completely accurate indication

of what the situation was at the elevated temperatures, or of the dynamic response of the system. Consequently, most spectroscopic methods have been adapted to thermoanalytical instruments.

The use of X-ray diffraction and most spectroscopic techniques usually involves scanning a range of the energy spectrum and, hence, requires significant time. Consequently, a continuous trace, as a function of time or temperature, is usually not obtained, but rather, data at each specific energy are taken at generally equally-spaced increments of time or temperature. Alternatively, one can scan only a pre-selected value of the energy to obtain a continuous trace.

Figure 26 shows an example of a limited 2Θ range of the X-ray diffraction pattern of a soda-lime-silica glass scanned repeatedly as the temperature is increased. [35] The three-dimensional plot summarizes how the various phases form and disappear as a function of temperature. At 1000 °C crystalline phases still remain and the final homogeneous liquid phase has not yet been achieved.

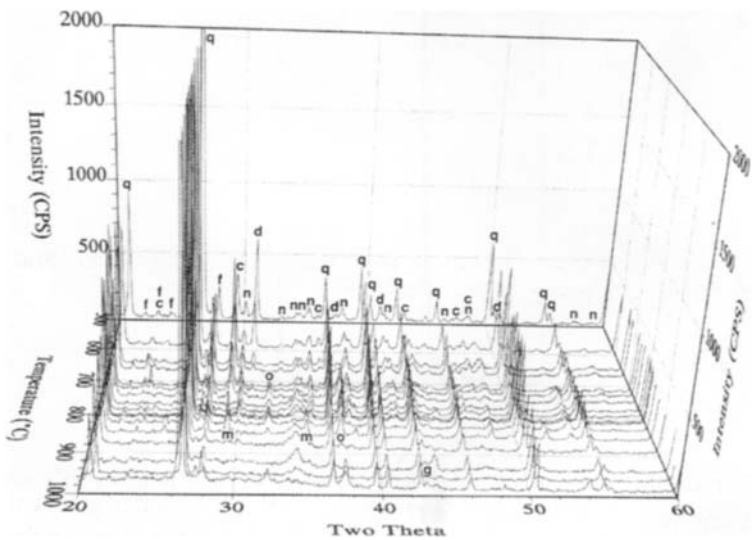


Figure 26. X-ray diffraction scans during the formation of soda-lime-silica glass [35]. c=calcite, d=dolomite, g=magnesium oxide, m=sodium metasilicate, n=soda ash, o=calcium oxide, q=quartz.

Wendlandt has utilized a wide range of optical spectroscopies to study many inorganic materials [36,37]. Mössbauer spectroscopy has found success for systems involving suitable isotopes, most prominently iron, tin, and europium (see the review by Gallagher [38]). The vast majority of applications involve

sampling at room temperature or at isothermal steps. A rare instance of the use of Mössbauer spectroscopy in a dynamic manner was for the determination of the Néel temperature for $LaFeO_3$ [39]. A comparison of the results using DTA at 10 °C min^{-1} with very slow heating and cooling in a Mössbauer spectrometer is presented in Figure 27. The correspondence of the curves for heating and cooling indicates equilibrium conditions. The radioactive count-rate changes abruptly as the internal magnetic field collapses above the Néel temperature around 750 K. This value is in good agreement with the DTA results.

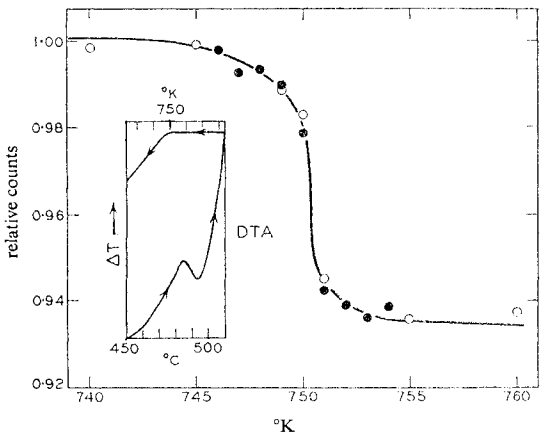


Figure 27. The Mössbauer spectrum at zero velocity for $LaFeO_3$ and the DTA curve at 10 ° C min^{-1} (insert) [39].

4. PHYSICAL PROPERTIES

4.1. Heat capacity

The heat capacity (C_p) of ceramic materials is a critical design-parameter for many applications. For structural ceramics, the heat capacity of the ceramic components is used to calculate the heat flow through structural members while, for refractories, heat capacity is used to determine thermal loss through a furnace wall. Heat capacity is also used to evaluate thermal transport from nuclear fuel materials. Heat capacity is a fundamental thermodynamic property of materials [40] and is used to estimate both enthalpy and entropy changes [40]. DSC measurements can be used to measure heat capacity by heating a sample and measuring the resultant heat flow. When a sample is introduced into the DSC, there is an endothermic shift in the baseline that is related to the heat capacity of the material [40]. A sapphire disk is usually used to calibrate heat

capacity measurements and, according to Rudtsch, the chief limitation of these type of measurements is the temperature lag in the calorimeter and the quality of the data associated with the calibration standard [41]. An example of this type of analysis is given in Figure 28 for UO_2 fuel pellets [42] In this analysis, the spike in heat capacity around 2600 °C and the accompanying baseline shift is due to a suspected phase transition that takes place in this material.

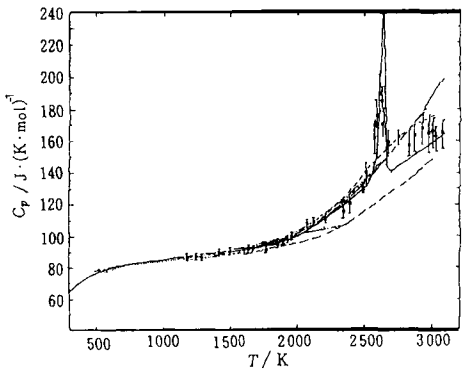


Figure 28. Heat capacity measurements on UO_2 at high temperature [42].

4.2. Thermal conductivity and diffusivity

Like heat capacity, thermal conductivity (λ) and thermal diffusivity (D) data are used to determine the performance of a material when subjected to heat. Thermal conductivity and thermal diffusivity are related as follows:

$$D = \lambda / (\rho C_p) \tag{3}$$

where ρ is the sample density and C_p is the heat capacity at constant pressure [40]. Thermal conductivity can be measured by traditional DSC, or by use of more specialized instruments, such as hot-wire measurements or modulated temperature DSC, while thermal diffusivity is commonly measured by the laser-flash technique [40, 43, 44].

For structural and refractory ceramics, low thermal conductivities are desirable to minimize heat loss while, for electronic ceramics, the rate at which heat can be removed or dissipated is important. Olorunyolemi et al. have described a method of evaluating the microstructure development of sintered ZnO compacts resulting from a variety of fabrication techniques, using thermal conductivity measurements [45]. In this study the authors found that, based on the thermal conductivity during sintering, the neck growth between ZnO particles occurred

at a lower temperature than predicted by most sintering models. Thermal conductivity can also be used to compare the performance of fibrous ceramic insulating materials [46]. In this analysis the effect of fibre density on thermal conductivity was compared. An example of this analysis is given in Figure 29. Collin and Rowcliffe have also described the use of thermal conductivity in the estimation of the thermal-shock resistance of ceramic composites [47].

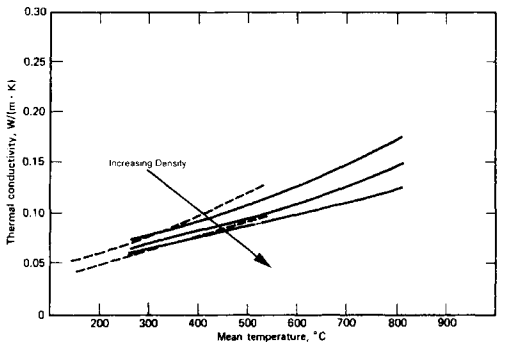


Figure 29. Thermal conductivity versus temperature for ceramic fibres with different densities. [46]

Albers et al. have studied the thermal diffusivity of a variety of ceramic materials using the laser-flash method [44]. An example of this type of measurement is given in Figure 30. In this example, the duration of the laser pulse was varied with no apparent effect on the measured thermal diffusivity. In their study of the effect of varying experimental conditions on the measurement of thermal diffusivity, Albers et al. found the method to be quite robust.

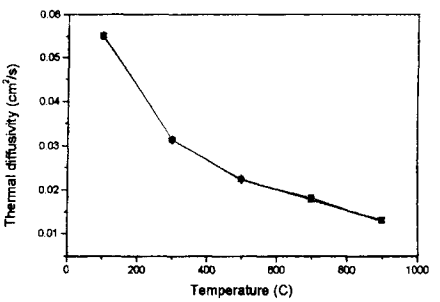


Figure 30. Thermal diffusivity versus temperature measurements for alumina under different laser-flash excitation conditions. [44].

4.3. Thermal expansion

Nearly all materials expand on heating due to increased atomic vibrations. For ceramics, the magnitude of this expansion is related to the phases present and the pore-size distribution of the ceramic. Thermal expansion is typically measured using a thermodilatometer (TD). The thermal expansion of refractory ceramics is related to the potential thermal-shock resistance [48]. For structural ceramics, thermal expansion is a critical design parameter for the design of expansion joints. Thermal expansion is commonly reported as the coefficient of linear thermal expansion (α) which is the slope of the thermal expansion curve. The linear coefficient of thermal expansion is calculated as :

$$\alpha = (L_2 - L_1)/\{ L_0 (T_2 - T_1)\} = \Delta L/(L_0 \Delta T) \quad (4)$$

where L_0 is the original length, L_2 is the length at temperature T_2 and L_1 is the length at temperature T_1 [49]. The units of α are thus K^{-1} or $°C^{-1}$. A typical thermal expansion curve for a fired ceramic is given in Figure 31. The coefficient of thermal expansion calculated over the range of 40 to 60 °C is indicated on the plot.

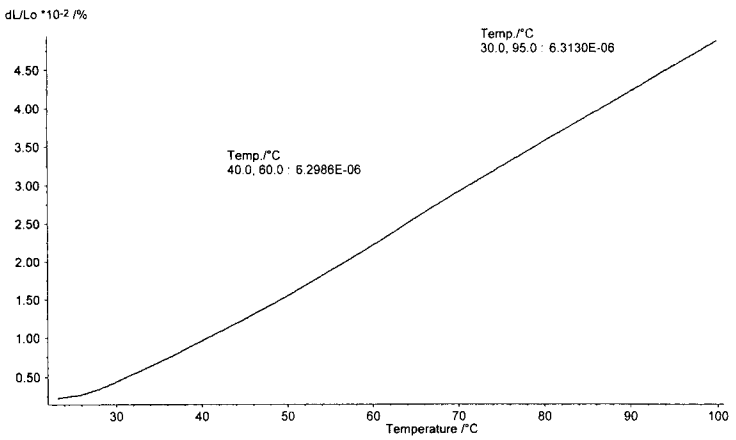


Figure 31. A typical thermal expansion plot for a fired ceramic over the range of 40 to 60 °C with heating at 5 °C min^{-1} in flowing air.

The TD curve given in Figure 31 illustrates a linear thermal expansion but, for many traditional silicate-based ceramics, this is not the case. For silicates the presence of crystalline silica (SiO_2) phases results in a discontinuous thermal expansion, due to the reversible phase changes associated with silica's

crystalline inversions. The most common phase change is the α- to β-quartz inversion on heating or cooling at about 573 °C, but in some silicate ceramics that have been fired to temperatures above 1300 °C, some of the quartz begins to convert to cristobalite. The cristobalite phase also goes through an α to β phase change at about 220 °C. Both the cristobalite and quartz inversions result in abrupt expansions on heating and abrupt contractions on cooling. A thermodilatometric (TD) curve of a fired silicate, exhibiting inversions for both cristobalite and quartz on heating, is given in Figure 32. The magnitude of the dimensional change is also proportional to the amount of quartz or cristobalite in the ceramic. These abrupt dimensional changes result in differential stresses that can result in the development of cracks in the microstructure.

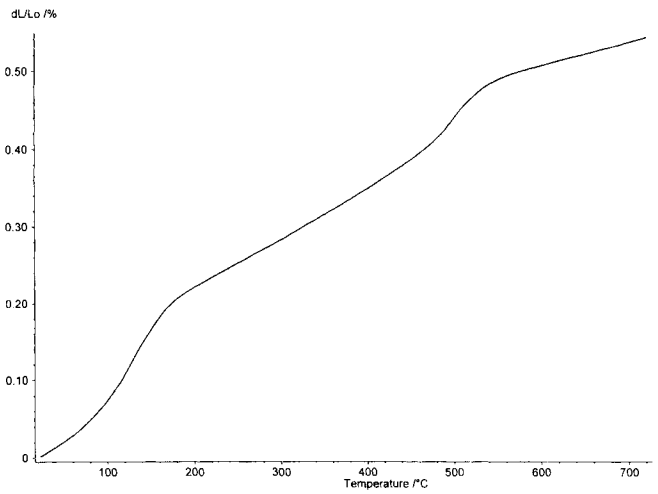


Figure 32. Expansion curve for a fired silicate, exhibiting inversions for both cristobalite and quartz on heating in flowing air at 5 °C min^{-1}.

Dilatometric analysis can be used as a tool to compare the relative quantity of crystalline silica phases in refractories. Silicate ceramics, such as refractories for kiln furniture, that contain quartz or cristobalite are especially subject to premature failure during cyclical heating and cooling due to the dimensional changes associated with these inversions.

In the field of optical communications it is frequently necessary to maintain the critical alignment of various components in a variety of environments and under different temperatures. The latter aspect requires knowledge of the coefficients of thermal expansion of the materials and their supports. This is particularly true for electro-optic devices mating with fibre optics.

Complicating this concern is the fact that the thermal expansion of crystals may vary along different axes depending upon the crystal structure. Therefore characterization of single crystals by TD must be performed on carefully oriented specimens.

Lithium niobate shows a wide range of nonstoichiometry as discussed earlier. Single crystals must be grown at the congruent composition in order to achieve large homogeneous crystals. The thermal expansion has been accurately determined for this important material over a wide range of temperatures for both the stoichiometric composition and the lithium-deficient congruent composition, $Li_{0.969}NbO_{2.9825}$ [24]. Figure 33 shows the strong dependence of thermal expansion on crystallographic orientation. Expansion parallel to the c-axis is quite small and actually goes through a maximum. The dependence on concentration is more obvious along the c-axis because of the approximately ten times greater coefficient of thermal expansion.

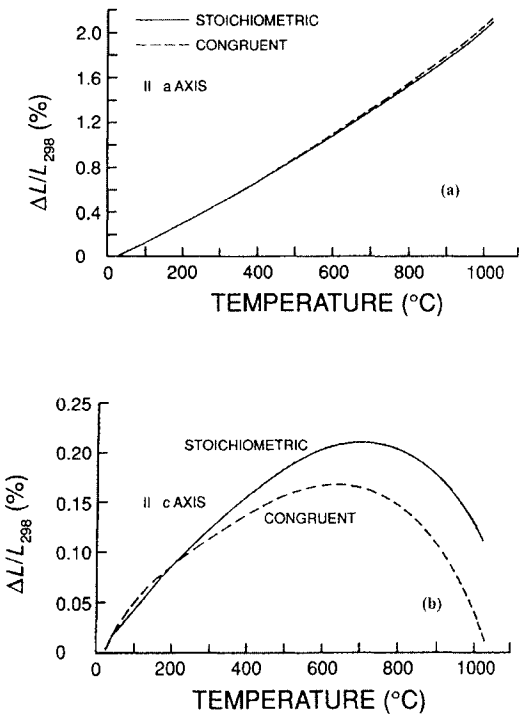


Figure 33. Thermal expansion of stoichiometric (----) and congruent (—) single crystal lithium niobates. (A) parallel to the a-axis and (B) parallel to the c-axis [24].

The order of the crystallographic transition determines the nature of the resulting irregularity in the thermal expansion. Figure 34(a) shows examples of a first-order transformation in a single crystal of $LaGaO_3$, parallel and orthogonal to the <111> crystallographic axis [50]. The abrupt discontinuity at the transition is evident. In contrast, Figure 34(b) shows the thermal expansion along the c-axis for a single crystal of $KTiOAsO_4$ [51]. The higher-order phase transformation near 900 °C appears as a simple change in slope rather than a discontinuity. Glass-transition temperatures are another example of higher-order transformations, however, the range of temperature is broader and varies with the specific thermal history of the composition.

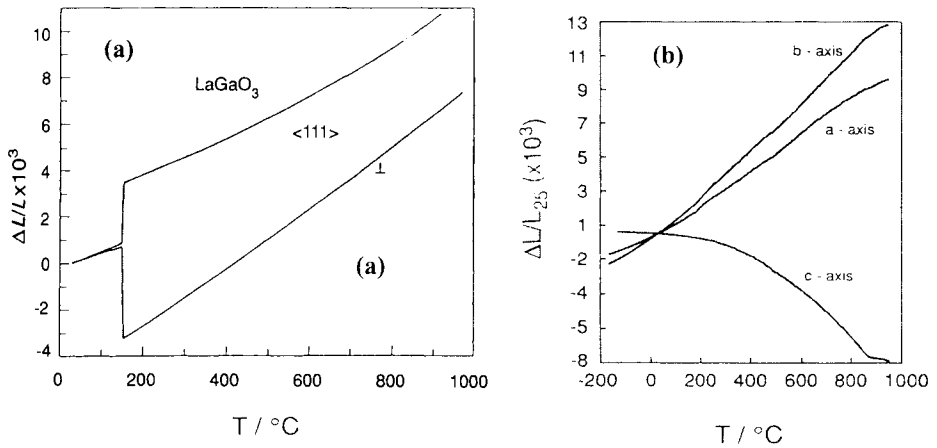


Figure 34 - Thermal expansion of single crystals through a phase transformation. (a) $LaGaO_3$ parallel and orthogonal to the 111- axis [50] (b) along the c-axis for $KTiOAsO_4$ [51].

It is common practice to represent thermal expansion data in the form of a simple power-series expansion. As an example, Table 2 describes the coefficients for the fit to the curves in Figure 34(b). Besides adequately representing the data, the power expansion is readily differentiated to yield the coefficient of thermal expansion at any temperature in the range of the equation. A crystallographic transition causes an irregularity in the thermal expansion curve and so data may be fitted to different temperature ranges in order to accommodate any breaks in the expansion curve.

Table 2.
A fit to the thermal expansion of $KTiOAsO_4$, over the range from –170 to 800 °C.
$\Delta L/L_{298} = a + bT + cT^2 + dT^3$, where T is the temperature in Kelvin [51].

Axis	a	b	c	d
|| a	-1.5420×10^{-3}	2.20972×10^{-6}	1.12511×10^{-8}	-4.6042×10^{-12}
|| b	-2.5298×10^{-3}	5.98544×10^{-6}	9.66804×10^{-9}	-3.6037×10^{-12}
|| c	-4.0622×10^{-4}	3.51577×10^{-6}	-5.8902×10^{-9}	-2.1710×10^{-12}

During thermal expansion of polycrystalline ceramics the grains or crystallites are generally assumed to be randomly oriented so that the resulting curve represents an average expansion. Figure 35 is an example selected from one of the major compilations of thermophysical data [52]. It is for a synthetically prepared beryllium silicate, $2BeO \bullet SiO_2$, which has been given several heat treatments. Those samples heated at 1560 °C and above have undergone a partial decomposition into the individual oxides, which is clearly reflected in the change in thermal expansion.

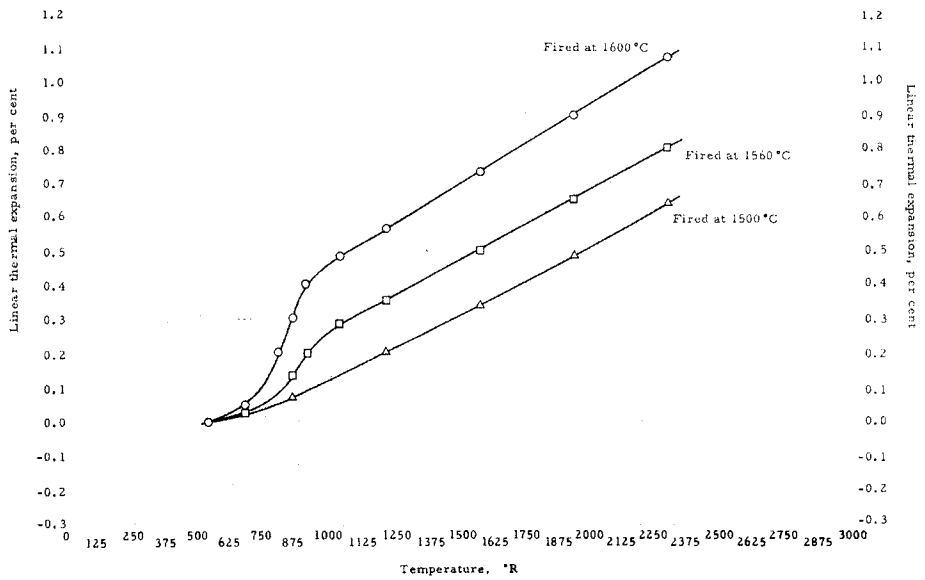


Figure 35. Thermal expansion of polycrystalline beryllium silicate heated to the indicated temperatures [52].

4.4. Surface area and porosity

The surface area of powders and porous materials is an important characteristic of many ceramic materials. Determination of adsorption and desorption isotherms provides valuable insights into the nature of the pore structure and use of the BET-based methods allows for the determination of the total surface area. Details of this analysis can be seen, for example, in the text of Gregg and Sing [53]. Figure 36 illustrates how gravimetric data may be used to determine such isotherms [54]. Stage A represents the outgassing of the sample on the microbalance under vacuum at several temperatures. The selected gas, generally N_2, is then bled into the system, which is thermostatted at the boiling point of the gas, in controlled steps and the mass of the adsorbed gas measured after reaching equilibrium for each step. This stage B corresponds to the adsorption stage. Stage C represents the desorption process as the gas is pumped out in a stepwise manner, while the mass loss is measured after equilibration at each step. Büchner and Robens calculated the resulting isotherms and illustrated three methods of numerical analysis for determining the surface area per gram of the sample.

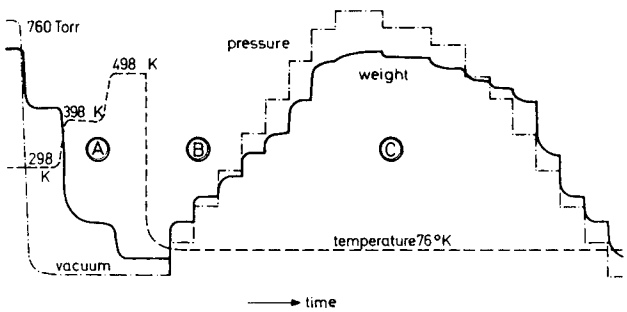


Figure 36. Schematic representation of gravimetric adsorption/desorption measurements [54].

4.5. Electrical and magnetic properties

The simple classical measurements of magnetic susceptibility and electrical conductivity as a function of temperature are not normally considered as being in the domain of thermal analysis. When their purpose is to determine transformations and reactivity, however, then they rightfully are considered to be thermoanalytical techniques.

A good example is the use of TM to determine the Curie or Neel temperature (T_c) for magnetic materials. Simultaneous TM with DTA or DSC offers the opportunity to measure T_c very accurately, by comparing the observed loss of

magnetic attraction with the melting points of the primary standards that determine the International Temperature Scale [55]. Figure 37 shows such a set of simultaneous measurements in which the melting points of Pb and Zn were used to correct the observed value of T_c for Ni. [32] A simple linear correction curve was calculated from differences between the observed melting points and their standard values. The appropriate correction was then applied at the observed value of T_c to produce the true value of T_c. The values of T_c can then be used for identification, see Figure 38 [56], or for quantitative analyses as described earlier in section 3.1.4.

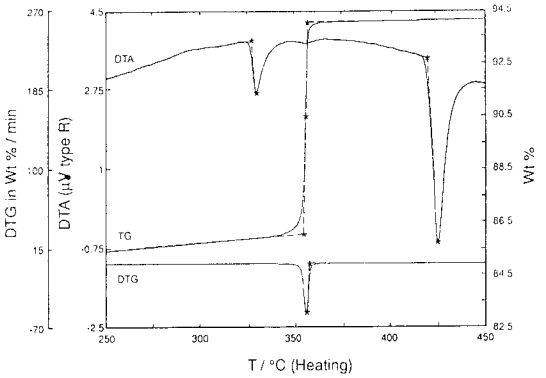


Figure 37. Simultaneous TM-DTA curves for Pb, Zn, and Ni [32].

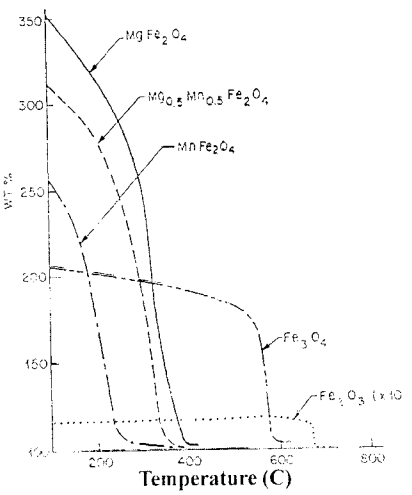


Figure 38. TM curves for some selected compounds of iron [56].

5. SOLID-STATE REACTIVITY

5.1. Introduction

The topic of solid-state reactivity is of immense technological importance and has been the subject of many books and conferences, see for example [57, 58,59,60,61,62] Its many complexities and controversies are well known and a general discussion of such a subject is outside the scope of this chapter. However, because of the vital role that thermoanalytical and calorimetric techniques play in this field, it is essential to provide a selection of representative examples demonstrating their applicability to study many facets of this topic. The chapters in Volume 1 of this Handbook on the thermodynamic [63] and kinetic [64] backgrounds of these methods are particularly relevant.

5.2. Heterogeneous reactions and mechanisms

The reduction of various oxides using H_2 is of both practical and theoretical importance. Thermoanalytical methods are valuable both in determining the conditions required and in understanding the mechanisms involved. Caution, however, must be exercised in such studies because of the highly flammable and potentially explosive nature of the gas. An interesting recent study has been made using EGA to follow both the consumption of H_2 and the appearance of the product, H_2O [65]. Manganese ferrite, $MnFe_2O_4$ was reduced using H_2 in the gas stream and with or without mixed carbon in the solid phase. A Ta_2O_5 detector, based on electrical conductivity, was constructed for moisture analysis and a thermal conductivity detector measured the changes in concentration of H_2. Figure 39 presents the EGA curves during the course of the reduction in the absence of carbon. Clearly the reduction takes place in two steps. The initial step, around 260 °C, involves the reduction of the trivalent iron to divalent iron and the second stage, beginning around 430 °C, is the reduction to elemental Fe. Other experiments were performed with a solid mixture including carbon and results with and without carbothermic-assisted reduction were compared.

Dweck et al. have shown the usefulness of TG for comparing the reactivity of AlN from various sources towards oxidation to α-Al_2O_3 [66]. Three examples were used of different sources of AlN. Sample A was an uncoated (unprotected) commercial specimen, sample B was a water-resistant version (protected) commercial specimen, and sample C was a partially hydrated specimen. TG curves for the materials heated in air are shown in Figure 40. Both samples A and B showed essentially the theoretical mass gain associated with the oxidation at high temperature. The protected sample, however, requires a higher temperature or a longer time to acquire the full mass gain. Sample C shows a large mass loss associated with the decomposition of a substantial amount of

$Al(OH)_3$. The amount of hydroxide was calculated, from the mass gain after the final oxidation, to be 47.5% .

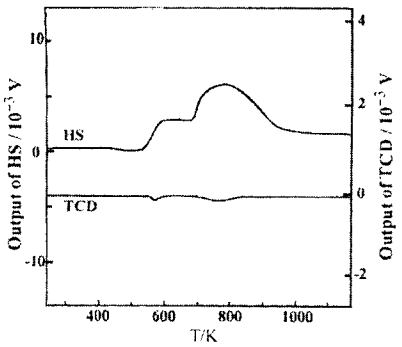


Figure 39. EGA curves for moisture and H_2 concentrations during the reduction of $MnFe_2O_4$ in a gas stream of H_2 in He [65].

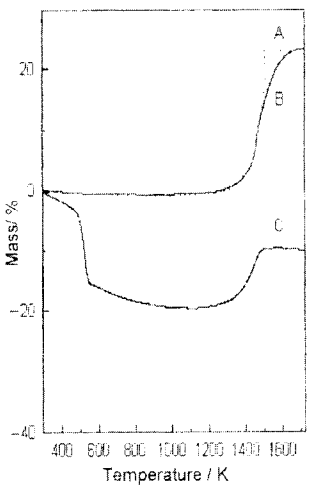


Figure 40. TG curves for samples of AlN heated in air [66].

Actual diffusion coefficients for the diffusion of oxygen in the product layer or in a nonstoichiometric compound can be estimated from a detailed study of the rate of mass change during such processes. As an example, Mickkelsen and Skou used TG to determine the chemical diffusion coefficient of oxygen in the $La_{1-x}Sr_xMnO_{3+\delta}$ system [67]. A typical plot of the isothermal mass change

following a rapid decrease in the partial pressure of O_2 is presented in Figure 41. The line shows the fit to their oxygen-vacancy equation. From such data at different temperatures, the activation energy for the diffusion process was determined and observed to change only marginally with strontium substitutions up to 12%. Knowledge of the diffusion rates and activation energies are important for the use of these materials as conductors in fuel-cell applications.

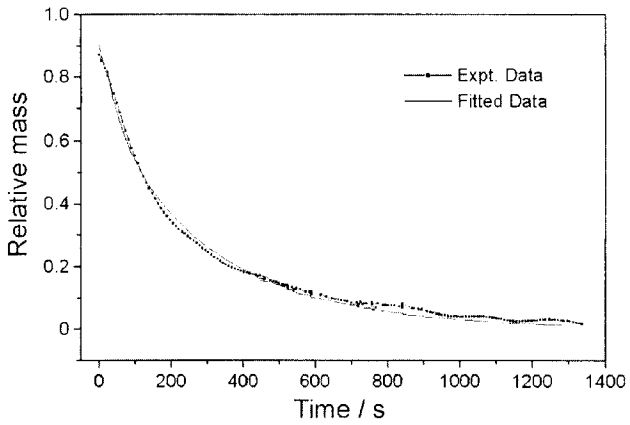


Figure 41. Isothermal TG curve after a change in the partial pressure of O_2 for a sample in the system, $La_{1-x}Sr_xMnO_{3+\delta}$ [67].

Thermally toughened glass panels used in the construction of office buildings contain metastable α-NiS inclusions incorporated into the glass during forming at higher temperatures. Failure of the glass has been closely linked to fracture induced by the increase in volume by 4% associated with the conversion of the metastable α-NiS to the room temperature stable β-NiS. Detailed DSC and isothermal DSC studies of the recrystallization process led to predictions of the time to failure, which corresponded well with observations of failure in existing office buildings. Figure 42 shows a series of DSC curves for metastable α-NiS. Induction periods as a function of temperature were determined from the onsets of reaction as a function of heating rate and compared in Figure 43 with induction times derived from isothermal DSC at different temperatures. The results were extrapolated to the ambient temperatures for several cities and found to agree well with the observed times to failure.

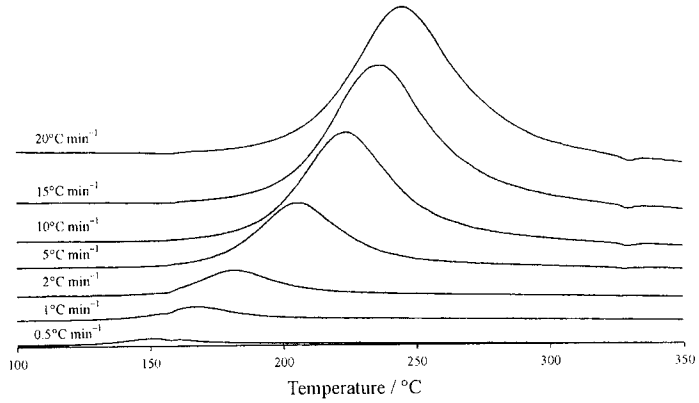


Figure 42. Dynamic DSC curves for the metastable conversion of α- to β-NiS [68]

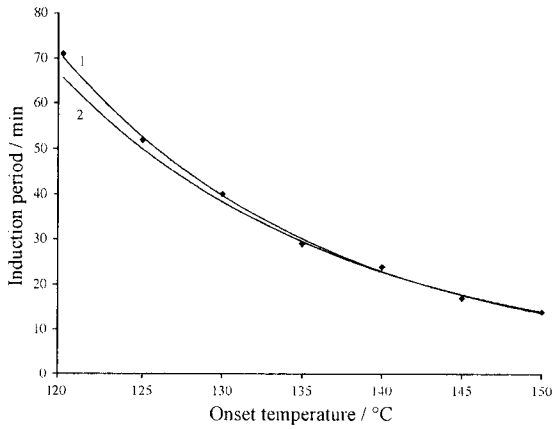


Figure 43. Induction time as a function of temperature for the conversion of α- to β-NiS. Curve 1 is based on isothermal DSC measurements and curve 2 is based on dynamic DSC measurements [68].

One of the earliest and most extensive uses of TG has been to study the corrosion or oxidation of materials in a wide variety of atmospheres [69]. Charles, however, developed a very clever modification of TM to study corrosion in the liquid phase [70]. Figure 44(a) shows how a sealed quartz vial containing the magnetic sample in the liquid corrosive media was suspended in a magnetic field gradient. As the magnetic sample was consumed (dissolved) the apparent weight changed although all the material was still contained in the

quartz tube reactor. Analysis of the resulting curves of apparent weight loss versus time, see Figure 44(b), allowed for determination of the kinetic parameters.

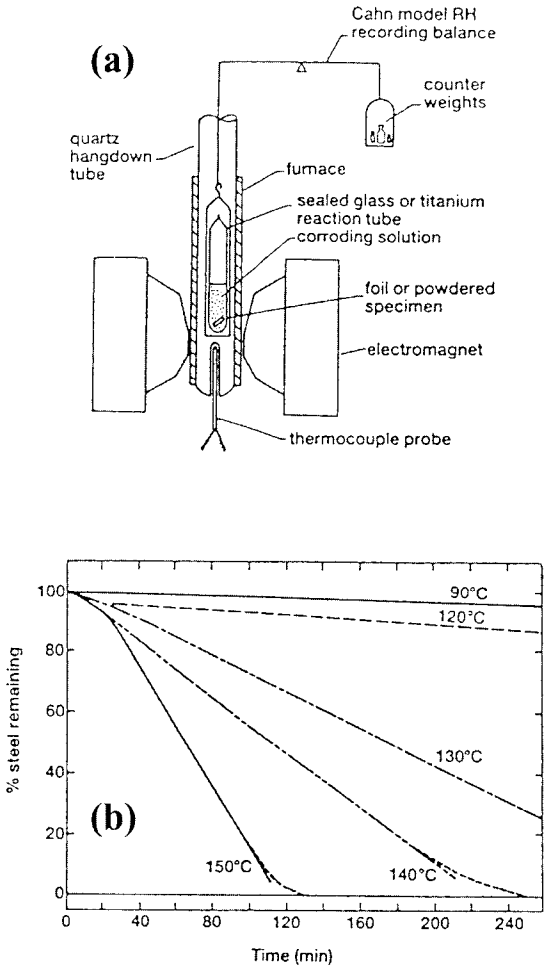


Figure 44. TM analysis of the liquid-phase corrosion of steel. (a) Apparatus, (b) resulting TM curves [70].

Hot-stage X-ray diffraction is very useful in studies of oxidation. Figure 45 illustrates the development of various oxide products of corrosion during the oxidation of iron [71]. Magnetite initially appears in the scan at 390 °C. While FeO might be the intuitive initial product, it is thermodynamically unstable with respect to disproportionation into magnetite and iron metal. Fe_2O_3 will not

appear until all the metal has been consumed, or until the film has lost contact with the underlying metal.

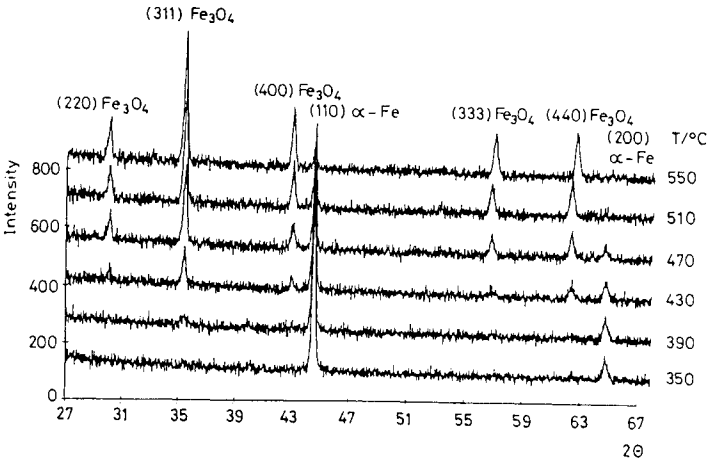


Figure 45. X-ray diffraction scans of the film forming on iron during oxidation [71].

Besides the more conventional studies of heterogeneous kinetics involving the rates as a function of temperature, atmosphere, and intrinsic defects, thermoanalytical techniques lend themselves to the study of less-familiar influences such as phase transformations and external irradiation or electrical or magnetic fields. Herley and Spencer performed an interesting study on the effects of UV irradiation superimposed on the isothermal decomposition of AlH_3 [72]. The effects of exposing the sample to UV radiation during the course of the isothermal decomposition are presented in Figure 46. Upon exposure, the rate of decomposition accelerated dramatically and immediately.

Hedvall, in his seminal review of solid-state reactivity, discussed the potential influence of solid-state transformations on the rate of ongoing chemical reactions [73]. Irregularities caused in the rate have come to be known as the "Hedvall Effect". During the time of a phase transformation, bonds are undergoing changes and atoms are more mobile, so the substance should be more vulnerable toward reactions with other materials and diffusion rates should be enhanced in that time frame. This remains a controversial topic, see for instance the conflicting papers concerning such an effect during thermal decomposition in the system $Na_2CO_3 - CaCO_3$ [74, 75]. Two examples of the effect are given in Figure 47. The classic example is the enhancement in the rate of reduction observed at the phase transformation during the reduction of NiO with H_2 [60]. Figure 47(b) shows an anomaly in the oxidation rate of Fe_3O_4 that

occurs at the magnetic transition, T_c [76]. The two lines are for the Arrhenius plots derived from the best-fitting kinetic models. There is obviously more involved in this latter example than a simple Hedvall Effect.

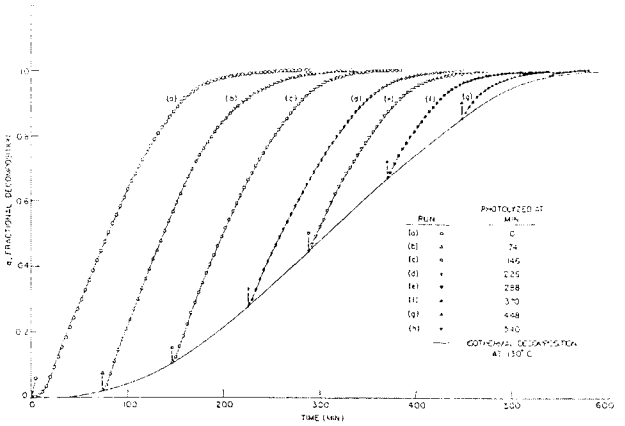


Figure 46. Isothermal TG curves for the decomposition of AlH_3 showing the effects of UV radiation on the rate of reaction [72].

The anomaly in Figure 47(b) suggests that, perhaps, an external magnetic field might influence the rates of reaction for some materials. This has provided a number of controversial publications, see for example Rowe et al. and references therein [77]. Because TG will be influenced by superimposing an external magnetic field gradient on the sample, EGA is the preferred technique for such studies.

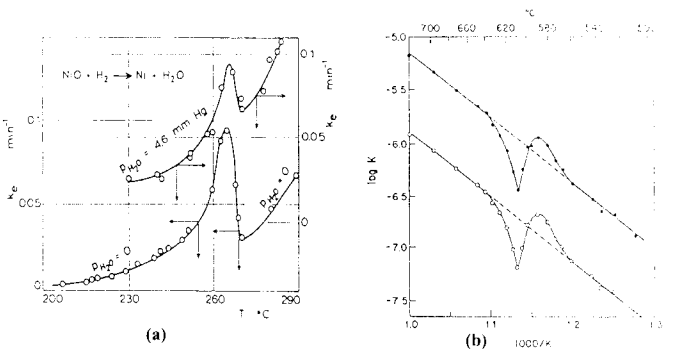


Figure 47. Examples of the Hedvall Effect. (a) Rate of reduction of NiO by H_2 [60]. (b) Arrhenius plots for the oxidation of Fe_3O_4 by O_2 [76].

5.3. Sintering phenomena

For ceramic products that are not clay based, organic binders are generally required for forming processes. Thermal analysis is widely used to understand how binders decompose in the firing process. The analysis can be as simple as a comparison lot-to-lot of the amount of binder, by measuring the mass lost on firing to a specific temperature, to much more sophisticated analysis of the decomposition products under different atmospheric and heating conditions, or kinetic analysis of the decomposition process under a specific set of conditions.

In the simplest case, binder oxidation is usually studied by TG. Binder removal can take place either by oxidation or pyrolysis (absence of oxidation), both of which can be studied by TG with proper atmosphere control [78]. For this type of analysis a ceramic powder, or part of a ceramic component, can be used, depending on the configuration of the TG. The sample is heated at a controlled rate in a controlled atmosphere and the resulting mass loss is observed. From this type of analysis, it is possible to determine the quantity of binder added to a formulation, which can be used to compare batch-to-batch consistency. The onset of oxidation, or decomposition, or the steps of oxidation or decomposition can also be determined, which is useful for designing furnace cycles for binder removal. A simple example of oxidation of a poly(vinyl butyral) binder from a multilayer capacitor is given in Figure 48 [79]. In this example, the influence of heating rate on the binder decomposition is studied. Increasing the heating rate clearly retards the onset of decomposition and delays the completion of the burnout. The effect of atmosphere on the rate of removal of binder can also be studied [80]. Liau et al. have described a similar study where the effect of the ceramic capacitor material and the metallic electrode on the onset of binder decomposition was observed [81]. An example of this study is given in Figure 49. From this study it is clear that the ceramic and metal electrode lower the apparent decomposition temperature of the binder system. This illustrates the importance of studying the binder decomposition behavior of the complete system when using thermal analysis data to develop or improve manufacturing processes. A study of the decomposition of the binder alone would have resulted in an overestimation of the onset of binder decomposition. This type of information provides quantitative information for the development of binder removal cycles.

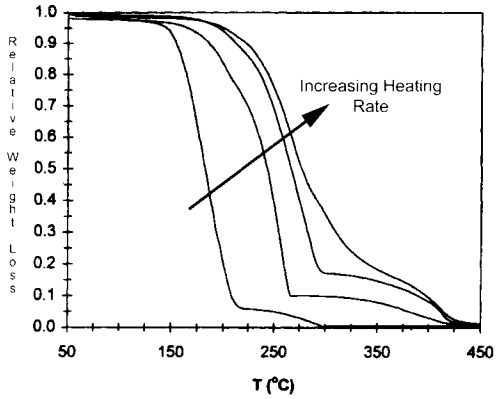


Figure 48. TG analysis of binder decomposition in flowing air [79].

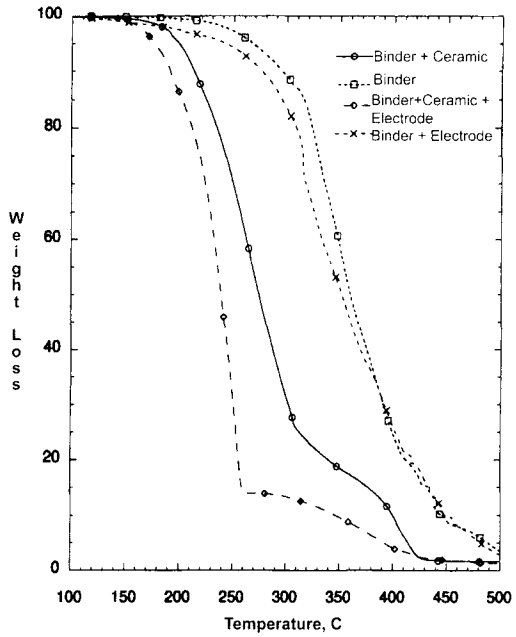


Figure 49. TG analysis of binder decomposition with heating at 10 °C min^{-1} in flowing air [81].

The binder decomposition products can also be studied by TG/EGA [82]. Liau et al. describe the distribution of decomposition products for a poly(vinyl butyral) binder with and with out the presence of ceramic capacitor material and

the metal electrode [81]. An example of this type of comparison is given in Figure 50. The addition of the electrode material to the ceramic binder system dramatically changes the nature or distribution of the binder decomposition products and the rates at which they are evolved.

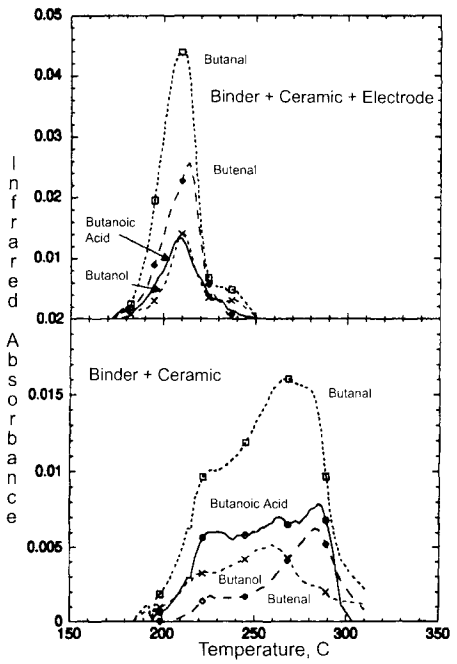


Figure 50. The nature and distribution of binder decomposition products with heating at 10 °C min^{-1} in flowing air [81].

For evolved gas analysis of some decomposition products, there is some concern that high boiling-point compounds do not move through coupling systems at the same rate as lower boiling-point compounds. Jackson and Rager have described a modification of the traditional TG/FTIR coupling system to improve the detection of high boiling-point compounds [83]. Instead of the typical flow-through system, where the gas is passed through the TG and then carried to the gas cell of the FTIR by a heated transfer line, the system described operates at reduced pressure and pulls gas from the TG sample chamber to the FTIR for analysis. The pressure reduction decreases the boiling point of high boiling-point compounds and improves flow characteristics through the gas-transfer line.

The oxidation of carbonaceous binder phases from carbon-bonded refractories can also be studied by thermal analysis. Carbon-bonded alumina or magnesia

refractories are used in a variety of applications in steel making processes, from pouring tubes to ladle bricks. The carbon phase provides thermal shock resistance to the refractories, but is subject to oxidation during preheating or during service. The oxidation of the binder phase decreases the thermal-shock resistance and allows for increased slag penetration. Several additives, such as Si metal or B_4C, are used to retard the oxidation of the carbon phase [84]. The oxidation rate of carbon-bonded refractory products can also be studied by TG. Typically bulk samples are studied to simulate the mass-transport effects of bricks in service. An example of a typical analysis is given in Figure 51 which shows that increasing the temperature increases the rate of oxidation.

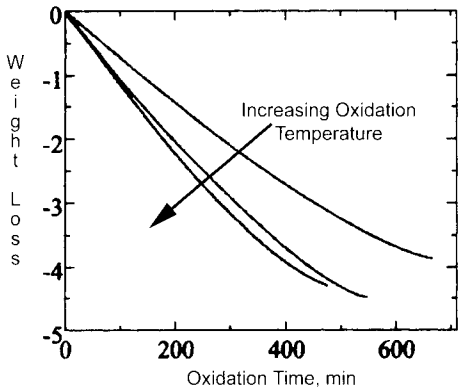


Figure 51. Oxidation of the carbonaceous binder-phase in a MgO-C refractory brick [85].

The successful sintering of a green ceramic body is often dependent on the temporary existence of liquid phases and the viscous flow properties that result during rapid heating. DTA and DSC are useful in establishing the phase equilibria, but thermal dilatometry, TD, is more valuable in establishing the optimum sintering program. Because relatively large sample sizes are used in TD, quite slow heating rates are needed to achieve a homogeneous temperature throughout the sample. Thus, when equilibrium conditions or properties are desired, maximum heating rates of a few degrees per minute are required. To simulate rapid firing of ceramic bodies, however, rates of 50 °C min^{-1} may be used. An example of such a rapid process in glass ceramic frits is the recent work of Paganelli [86]. In the initial TD study shown in Figure 52 the ceramic body was heated at 50 °C min^{-1} and both the shrinkage and the shrinkage rate were measured. Besides achieving a strong dense ceramic product, the optimum sintering programme should minimize the time and temperature as a cost saving.

Inspection of Figure 52 indicates that the maximum sintering rate occurs at about 1230 °C and a period of undesired bloating sets in at about 1280 °C, as seen by the upturn in the shrinkage curve. Up to about 900 °C the curve exhibits simple thermal expansion. At that point the glass-phase additive reacts with clay and some early shrinkage occurs prior to the main sintering step starting at about 1100 °C.

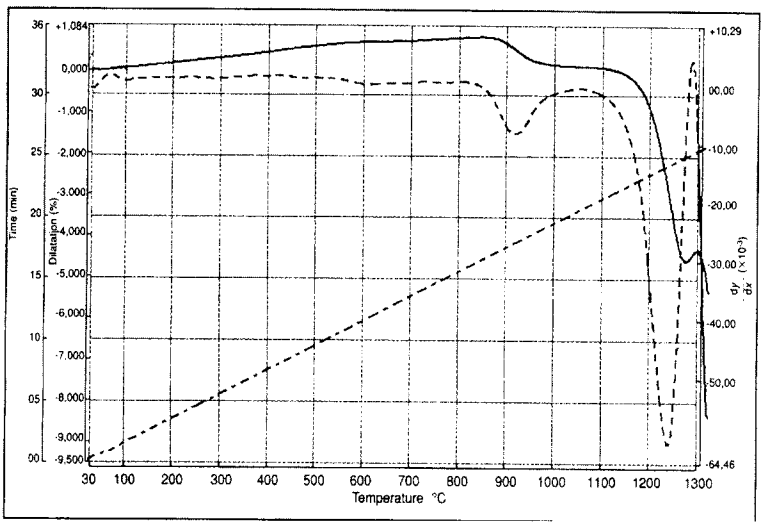


Figure 52. TD curves for a fast-fired, glass-ceramic frit [86].

The next step in the study was to heat identical samples at the same rate to various holding temperatures approaching the temperature for the maximum rate of sintering, 1230 °C. Maximum shrinkage in a reasonably short time, six minutes, was desired. The rate of shrinkage should approach zero at the end of this time. Figure 53 shows the results for an experiment at 1220 °C, which achieved a stable body in six minutes and had a total shrinkage of slightly more than 6%. Such studies were made with various compositions to achieve a sintered product with optimum properties while requiring a minimum firing time and temperature.

Besides using rapid-firing schedules to save energy and costs, the use of feedback control has proven to be a highly effective method for achieving, not only lower costs, but also better-sintered products. This process of "rate controlled sintering", RCS, was initially demonstrated by Palmour and Johnson for the preparation of high-density and fine-grained alumina [87]. The general principle and result are illustrated in Figure 54. A traditional linear sintering profile is indicated in part (a) and part (b) presents the resulting densification

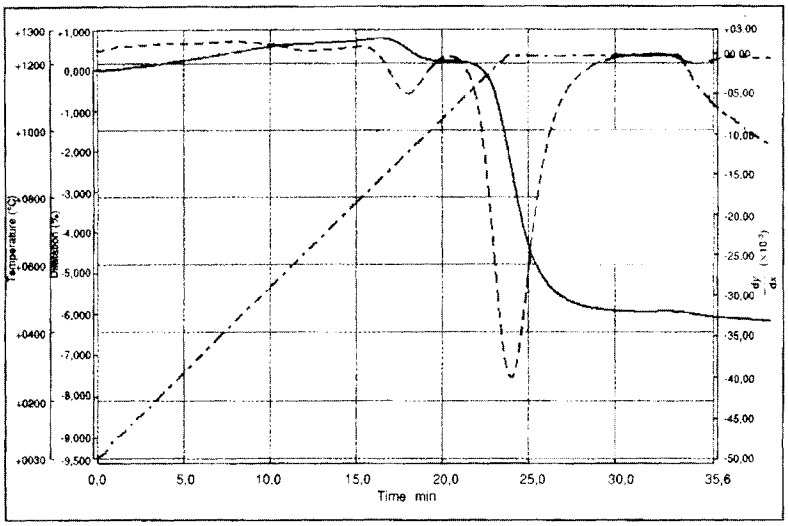


Figure 53. TD curves for the near optimum fast-firing of the glass ceramic frit in Figure 51 [86].

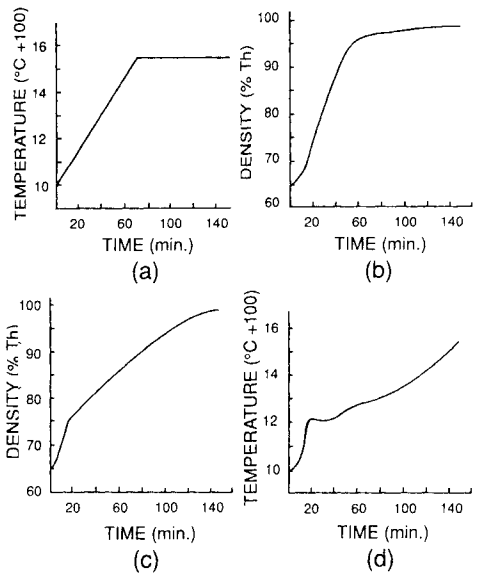


Figure 54. The rate controlled sintering process for doped Al_2O_3: (a) traditional sintering programme, (b) resulting shrinkage curve, (c) optimum shrinkage curve, (d) resulting shrinkage programme through controlled feedback [87].

profile for a sample of doped Al_2O_3. The initially rapid densification closes the pore structure and the trapped pores then have to be eliminated by much slower volume diffusion at higher temperatures. However, if feedback from the TD measurement is used to control the densification process, this initial process can be slowed so that a much greater portion of the porosity can be removed while the pore structure remains open. Part (c) of Figure 54 shows the predetermined shrinkage curve for near optimum conditions. The resulting temperature programme is presented in part (d). Integration of the area under the curves in (a) and (d) represents the energy consumed. Clearly the RCS process involves a significant energy saving and also results in a finer-grained superior product.

The shrinkage of oxide silica gel preforms is an important aspect in the preparation of some fibre-optic cables. TD of gel samples produced by alkoxide hydrolysis frequently shows that severe bloating occurs during the consolidation process. TD curves for specimens that were prepared using different catalysts in the hydrolysis process are compared in Figure 55 [88]. The host glass softens

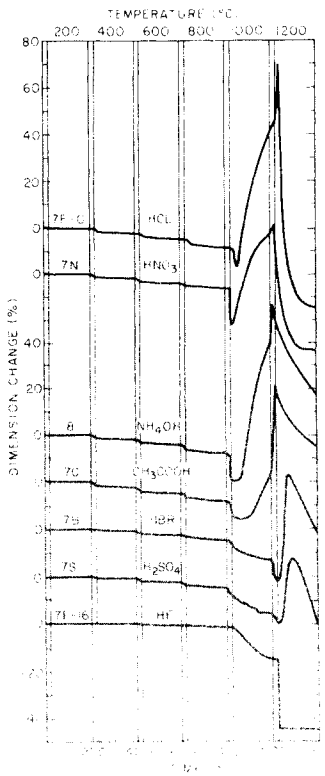


Figure 55. TD curves of silica gels prepared by hydrolysis of alkoxide using the catalysts indicated [88].

around 800 °C and the water evolved from the decomposition of the OH^- bonds above that temperature leads to a destructive expansion of the preform. The TD study clearly indicates that fluoride ions, having a similar size and charge, can replace the OH^- ions and have a highly beneficial effect in the suppression of the bloating.

Emanation thermal analysis, ETA, can also be used to provide valuable complementary information regarding silica gels [89]. The rate of release of radioactive gas from samples of silica gel depends upon diffusion in the pores and volume diffusion from the sintered sample when the pores become closed off. Figure 56 shows curves for the release of ^{220}Rn from two samples of silica gel that have been doped with the parent nuclide ^{228}Th [90]. Sample 1 has twice the initial surface area of sample 2. In the temperature region below about 350 °C, the effusion results from diffusion through the open network of micropores and thus the higher surface-area material has a greater effusion rate. In sample 2, the higher OH content above this temperature leads to an enhanced open porous network and a markedly increased rate of effusion for the radioactive gas. As shown in Figure 55, the silica gel softens above 800 °C and the open networks collapse, forcing the rate of effusion to depend upon the slower volume diffusion for the escape of the radioactive nuclide. Similar studies have been made related to the sintering of polycrystalline materials [89].

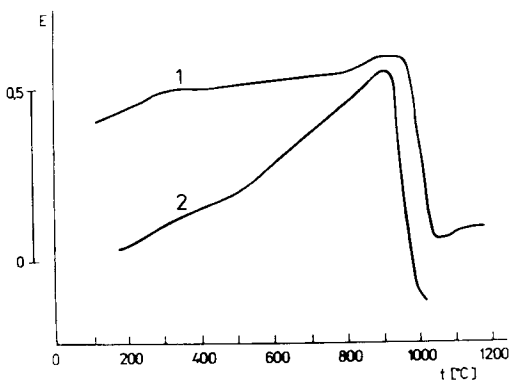


Figure 56. Emanation thermal analysis (ETA) curves for two silica gels [89].

5.4. Thin films

Thin films present substantial challenges in thermal analysis because of the minute amounts of relevant sample and the frequently large amounts of diluent, i.e., the substrate [91]. The processing and properties of thin films are especially

important with reference to semiconductor materials. The stability of III-V type semiconductors is frequently a problem. Studies of the thermal decompositions of bulk-size samples of such materials are commonplace, however, the very initial stages of decomposition are critical in dealing with thin films. Because of the high sensitivity of mass spectrometry, MS-EGA has proven very valuable in such studies [92]. The evolution of P_4 from a single crystal of InP as it is heated at 10 °C min^{-1} in vacuum is shown in Figure 57. The data are shown at several decades of sensitivity so that the kinetics of the decomposition can be determined at numerous stages of the decomposition, including at the fraction of a percent level. The mass of P_2 was measured because it is the strongest peak in the MS cracking pattern for P_4 vapor.

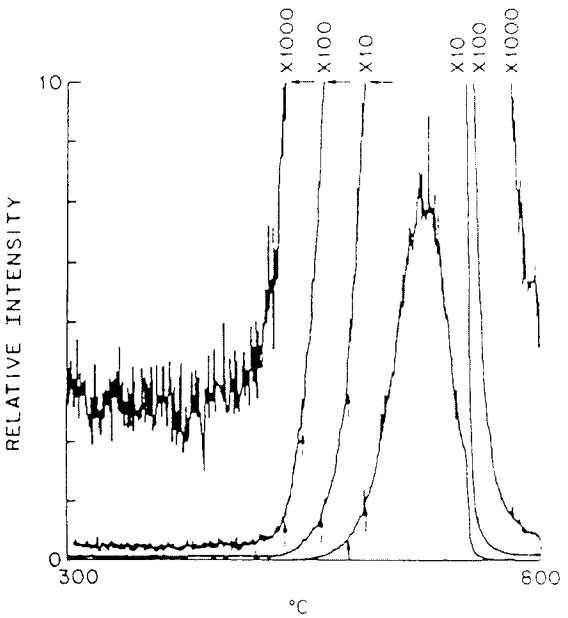


Figure 57. MS-EGA curves, at several levels of sensitivity, depicting the evolution of P_4 from InP heated at 10°C min^{-1} in vacuum. [92]

The Arrhenius parameters determined from this kinetic study were used to make plots of the fraction decomposed as a function of time over the appropriate temperature range, see Figure 58. The processing engineer can then determine the maximum time, at a given temperature, that the material can withstand for the assigned level of tolerance.

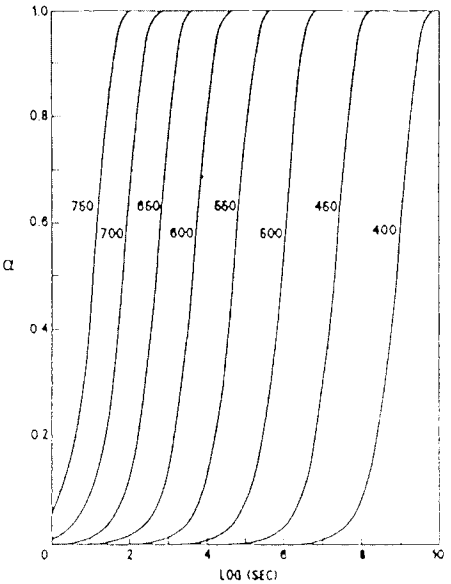


Figure 58. Plots of the fraction of single crystalline InP decomposed as a function of time at the indicated temperatures [92].

In the application of thin films, it is essential that stable low-resistance electrical contacts be readily made. Gold is frequently the electrode of choice. Early studies, however, indicated that these contacts were unstable at temperatures well below the stability of the underlying GaAs-based semiconductors. Experiments using MS-EGA indicated that As was being evolved at remarkably low temperatures, around 200 °C compared to the initial decomposition temperature of about 620 °C for pure GaAs [93]. The amount of As evolved was shown to be proportional to the thickness of the Au contact, see Figure 59. This suggested that the Ga was alloying with the Au at low temperatures releasing elemental As, which vaporized. This was substantiated by microscopic and analytical results.

Conventional processing of Si-based semiconductors also relies heavily on thin-film technology. Masks made of BN are used in X-ray lithography. These films are quite opaque to light, facilitating alignment, but relatively transparent to X-rays because they are composed of very light elements. Initially the masks of BN prepared by chemical vapour deposition (CVD) processes were highly strained and severely distorted (bowed) relative to the underlying Si wafers. Through the use of MS-EGA these strains were shown to originate from the trapped or occluded H_2 in the BN [94]. The evolution of H_2 is shown in Figure

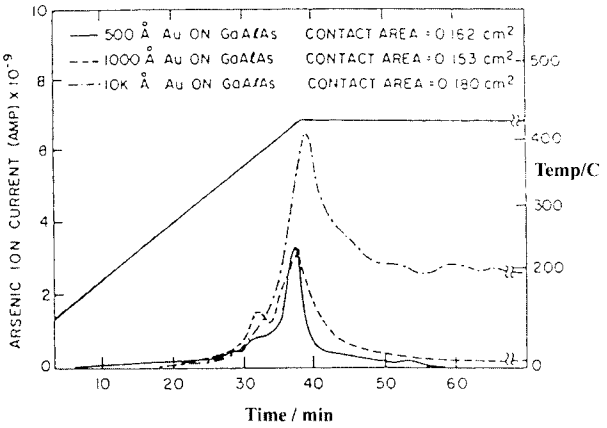


Figure 59. Evolution of As from $Ga_{0.7}Al_{0.3}As$ samples having the Au electrodes indicated [93].

60(a) for a typical mask. There are a variety of bonding sites for the H_2 that is incorporated in the films. Annealing at 500 °C is shown in Figure 60(b) to be capable of removing the less-strongly bonded H_2. Fortunately, this allows the wafers to relax to their original flat shape and to serve the intended purpose.

The incorporation of a product gas during the preparation of these films by CVD processes is not surprising. Less obvious occlusions occur, however, during sputtering processes. Sputtered $TaSi_2$ films are conducting and occasionally used as contacts to Si circuitry. When the resulting device is encapsulated in a protective glass layer at about 1000 °C, a blistering of the glass occurs and the $TaSi_2$ contact loses adherence. The identification of the gas evolved at this stage was made by MS-EGA [95]. Figure 61 reveals that the unexpected culprit is Ar gas that is occluded during the sputtering process. This has been demonstrated in other sputtered films [96].

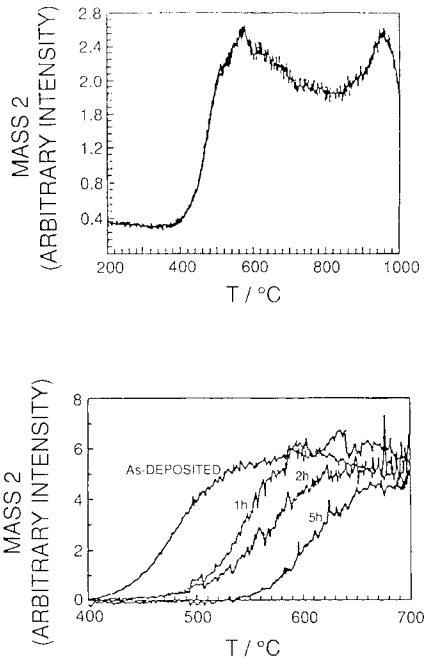


Figure 60. Evolution of H_2 from BN masks indicated by MS-EGA: (a) heated at 20 °C min^{-1} in vacuum, (b) similar masks after annealing at 500°C for the indicated times [94].

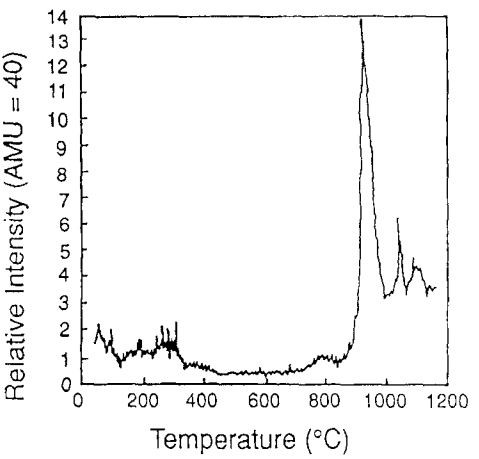


Figure 61. MS-EGA curve for Ar released from sputtered thin films of $TaSi_2$ [95].

If the thin film involves a magnetic material, it may be possible to use TM in order to enhance the sensitivity. Oxidation and reduction of Co containing thin films have been studied in this manner [97]. Figure 62 shows an apparent weight loss gradient when a 75 nm film of Co on a sapphire substrate was heated in O_2 in the presence of a modest magnetic field gradient. The weight gain associated with the formation of the non-magnetic oxide is overwhelmed by the loss of magnetic attraction as the strongly magnetic Co is consumed. When the sample was cooled and reheated in H_2, the dashed curve in Figure 62 was obtained. The magnetic Co film is regenerated and the curve returns to the original apparent weight in the magnetic field gradient.

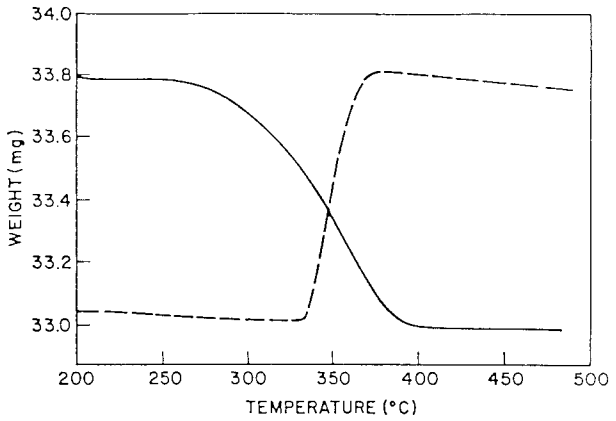


Figure 62. TM curves for a 75 nm film of Co on sapphire. The solid curve is is the result from initial heating in O_2. The dashed curve was obtained on reheating the oxidized sample in H_2 [97].

5.5. Adsorbents

Many traditional ceramic processes require some sort of flue-gas cleaning system to capture trace quantities of acid gases released from the raw material during the firing process. Adsorbent materials can be evaluated and compared using pulse thermal analysis [98]. Pulse thermal analysis is primarily a means of calibrating evolved gas analysis signals, but can also be adapted to investigate gas-solid reactions [99]. A known volume of reagent gas is injected into the thermal analyzer and the resultant signal from the coupled gas analyzer is observed. Because precisely known quantities of gas are injected, the resulting peak areas can be quantitatively related to the amount of unreacted gas. To evaluate an adsorbent material, a pulse of reagent gas is sent across a sample of the adsorbent. The peak area from the EGA signal can then be compared to the

peak area obtained with an empty cell to determine how much gas was adsorbed by the adsorbent. The mass change (TG) of the adsorbent can also be used to determine the quantity of gas adsorbed. The interpretation of the TG data can be complicated if the reagent gas must displace a portion of the adsorbent to be adsorbed. For example, when calcium hydroxide adsorbs SO_2, H_2O must be displaced according to the following reaction:

$$Ca(OH)_2 + SO_2(g) + \frac{1}{2} O_2(g) \rightarrow CaSO_4 + H_2O(g)$$

Additionally, the pulse causes some turbulence as it passes through the gas cell which results in some further perturbation of the TG signal. An example of the isothermal adsorption of SO_2 by a granular calcium hydroxide reagent at 150 °C is given in Figure 63.

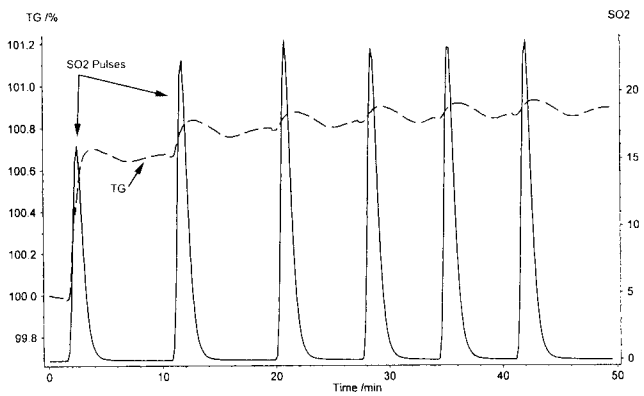


Figure 63. Pulse thermal analysis for isothermal adsorption of SO_2 by a granular calcium hydroxide reagent at 150 °C.

A series of pulses can be sent across the adsorbent to determine how much reagent gas can be adsorbed by the adsorbent [100]. As the adsorbent approaches saturation, the peak area of the sample pulse approaches that obtained for a pulse through an empty cell. At saturation, the amount of reagent gas adsorbed can be summed from each pulse to determine the total quantity of gas adsorbed by the adsorbent. This information can be used to compare adsorbents with different chemistries or surface properties.

5.6. Cements and mortars

Thermal analysis is commonly used in the study of cements and mortars. It can be used to study the formation of the cementation phases, the hydration process and in the forensic identification of existing or historic cements and

mortars. In the production of cements, calcareous (containing calcium carbonate) and argillaceous (clay containing) raw materials are heated together in a rotary kiln in the range of 1300-1500 °C [101]. In this process, called clinkering, a series of dehydrations (dehydroxylation of the clay mineral), decarbonation (decomposition of the calcium carbonate phase), formation of new calcium silicate and calcium aluminate phases and sintering take place [102]. Thermal analysis can be used to study the processes involved in clinkering. Additives and impurities play a significant role in the rate of sintering and the formation of new phases. Chen described the use of DTA and TG to study the formation of an undesirable phase in a rotary kiln [102]. Perakki et al. described the use of DSC to study the effect of sintering aids [103]. An example of the use of DSC in the study the formation cement phases during firing is given in Figure 64 which is a comparison of the formation and sintering of a reference composition and a composition with 2% of a sintering aid [103]. DSC analysis of the manufacturing process usually involves an endotherm due to clay dehdryoxylation in the range of 400 to 600 °C, a large endotherm due to the decomposition of the carbonate phase around 800 °C, exothermic reactions in the range 1200 to 1350 °C associated with the formation of belite phase, $(CaO)_2SiO_2$, and a final endotherm above 1300 °C associated with the formation of a liquid phase [103]. In this example (Figure 64), the addition of the sintering aid lowered the onset of liquid formation and presumably enhanced the degree of sintering. DSC can also be used to determine the relative reactivity of cement raw formulations [101]. Kakali used DSC to study the effect of particle size and the chemistry of the raw materials on the formation of new phases and the sintering of clinker.

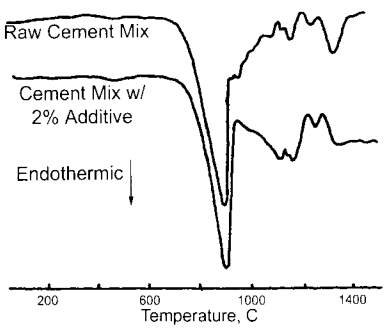


Figure 64. DSC comparison of the sintering of cement clinker with various additives with heating at 15 °C min^{-1} in flowing nitrogen [103].

Studies of the rate of hydration of cement formulations are also commonly studied by thermal analysis. In the past DTA was the preferred method for studying hydration reactions, but this yielded only qualitative information. Currently TG is thought to be a more quantitative tool [104]. An example of a TG/DTG hydration study for a portland cement mixed with calcium carbonate is given in Figure 65. Three mass losses and DTG peaks are observed [104]. The first DTG peak corresponds to the dehydration of a calcium silicate hydrate phase known as tobermorite. The second DTG peak corresponds to the dehydration of portlandite (calcium hydroxide) and the final DTG peak corresponds to the decomposition of the admixed calcium carbonate phase. As the hydration continues, the mass losses due to the dehydration of the tobermorite phase and the portlandite phase increase.

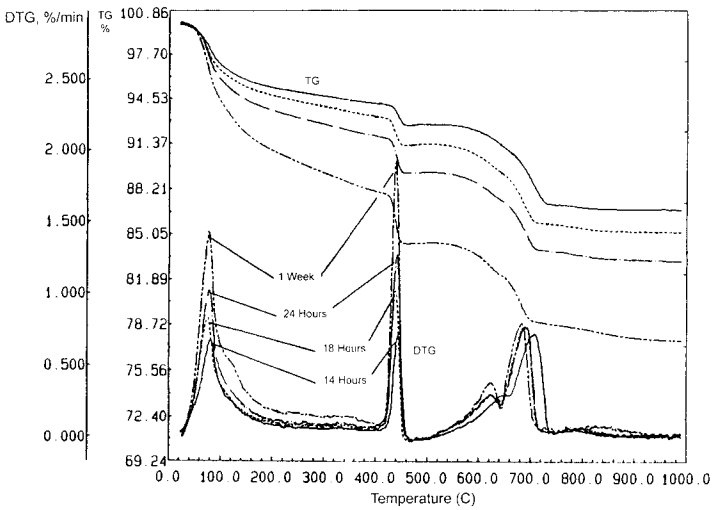


Figure 65. TG/DTG study of the rate of hydration of cement with heating at 15 °C min^{-1} in flowing air [104].

Several studies describe the use of TG to determine the amount of portlandite and carbonate phases in cements [105,106]. Tsivilis et al. described the use of TG to study the hydration process of Portland cement mixed with limestone [106]. In this study the degree of mass loss due to the dehydration of the portlandite ($Ca(OH)_2$) phase was used to determine the overall degree of hydration [106]. The effect of additives can also be studied by TG [107]. An example of this type of study is given in Figure 66, where the mass loss due to the dehydration of portlandite was used to determine the degree of hydration [107]. The amount of portlandite was measured at fixed intervals to determine

the rate of hydration as seen in Figure 66. TG is the preferred method for studying the hydration of cements due to the quantitative nature of the data obtained.

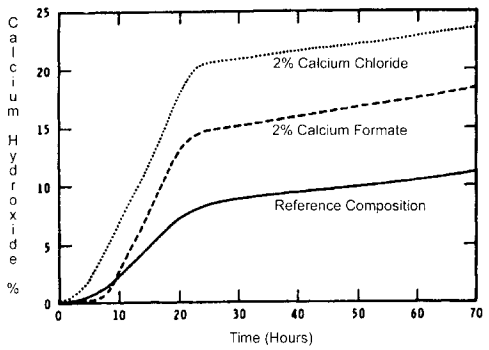


Figure 66. The effect of additives on the formation of the $Ca(OH)_2$ phase in a hydrated $(CaO)_3SiO_2$ phase [107].

In addition to the study of the manufacturing and hydration of cement phases, the composition of existing cement phases can be evaluated using thermal analysis. This is especially a concern in the area of antiquities. TG/DTG, along with chemical and mineralogical analysis (XRD), can be used to determine the composition and origin of historic mortars [108,109]. Addition of evolved gas analysis allows for more precise understanding of mass loss steps observed by TG [108].

6. SYNTHESIS

6.1. Introduction

All of the preceding sections bear on the problems that are also associated with the synthesis of inorganic materials with desired compositions and structures. Traditional methods of ceramic processing have relied on repeated mixing and grinding of the starting components, combined with firing at relatively high temperatures. The last fifty years or so has introduced approaches that start from more intimately mixed components in solution or perhaps even on an atomic scale in the form of a single precursor compound. Combining the decomposition of these precursors with an almost simultaneous reaction of the initial decomposition products often yields the final product at much lower temperatures and/or after shorter periods of time. This not only conserves energy, but also allows for a wider range of properties, e.g., particle size and

reactivity, for subsequent processing such as sintering. It also allows greater latitude for the synthesis of metastable phases where desired.

Thermoanalytical methods play a major role in evaluating these more modern methods of synthesis and in determining the optimum processing parameters. Several examples are chosen to illustrate both the preparation of active starting materials for conventional ceramic technology and the use of precursor compounds derived from solutions.

6.2. Conventional mix and heat

A good example of the power of thermoanalytical techniques applied to traditional ceramic processing is the detailed case associated with the production of commercial soda-lime-silica glass study in Speyer's monograph [35]. DTA, TG and X-ray diffraction were used to study the sequence of reactions and their dependence upon the particle size of the reactants. Figure 67 is a summary of the results for two different particle sizes. The X-ray data are for peak heights derived from Figure 26 described earlier in Section 3.4. Phase transformation peaks, such as the α to β transformation in quartz, do not have an associated peak in the DTG curve. Endotherms due to carbonate decompositions, however, have corresponding peaks in the DTG curves. Stresses induced in grinding and the resulting better particle-to-particle contact affect the reactions. A detailed interpretation of the results is given in [35].

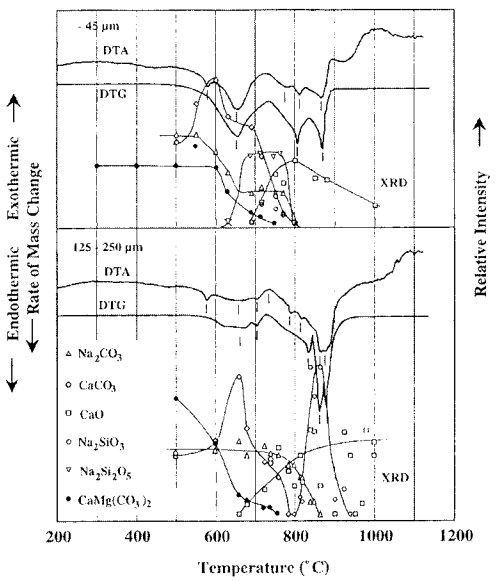


Figure 67. Thermoanalytical study on the formation of soda-lime-silicate glass. Points on the XRD curves are peak heights from Figure 26 [35].

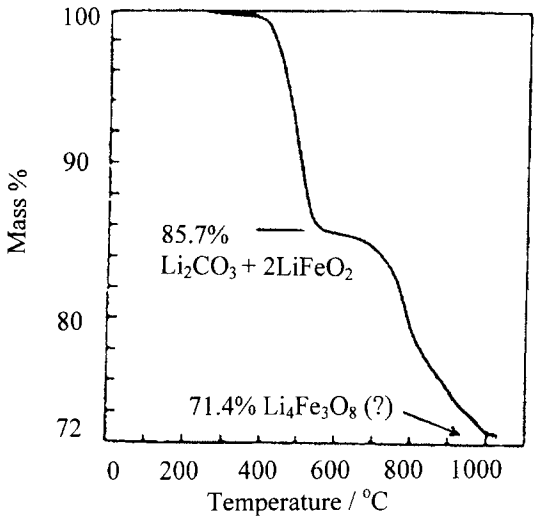
The reactivity of the starting Fe_2O_3 is a major factor in the successful preparation of ferrites by conventional methods. The Fe_2O_3 is mixed and reacted with other oxides or carbonates to form the desired composition. The reactivity of the Fe_2O_3 can vary over an enormous range. In addition, the reactivity must be carefully defined to relate to the temperature regime where it is most relevant, i. e., where it reacts with the desired components [110]. The conversion of various salts of iron to Fe_2O_3 was followed by TG. The product oxide was subsequently prepared at the minimum temperature, based on those TG curves.

The relevant reactivity was then determined by measuring the reaction of the oxides with excess Li_2CO_3 to form $LiFeO_2$. Figure 68 shows a typical TG curve and summarizes the results of the study. The temperatures at which the mass loss corresponded to 85%, along with the temperatures used to prepare the samples of Fe_2O_3 are tabulated. Clearly, the reactivity varies dramatically among the various oxides. All of them, however, facilitate the decomposition of Li_2CO_3 as indicated by the bottom line in Figure 68.

6.3. Decomposition of chemical precursors

$BaTiO_3$ and $LiNbO_3$ have been used as examples in this chapter because of their great technological importance. The preparation of these compounds, starting from aqueous solution, and the importance of thermal methods in these syntheses, are now considered. The complex compound $BaTiO(C_2O_4)_2 \cdot 4H_2O$ has the desired Ba/Ti ratio and precipitates readily from an aqueous solution. The TG curve in Figure 69 indicates that the complex oxalate decomposes in multiple steps to a constant mass around 800 °C [111]. The mass loss at that temperature corresponds to the formation of $BaTiO_3$ and the formation of the compound was confirmed by X-ray diffraction. The product is very finely divided and the desired particle size can be controlled by subsequent calcinations.

The mass loss at the earlier plateau around 600 °C corresponds to that expected for the formation of $BaCO_3$ and TiO_2 and this was also confirmed by X-ray diffraction. The reaction that follows at 800 °C is taking place about 400 °C below that of the mixed bulk components, demonstrating the value of this synthetic approach.



Decomposition Temperatures of Iron-Lithium Mixtures

Iron salt	°C Calcined iron salt	°C 85% Decomp. Li_2CO_3
Iron (III) sulfate	700	535
Ammonium iron (III) sulfate	660	495
Iron (II) sulfate	720	580
Ammonium iron (II) sulfate	660	490
Iron (III) nitrate	390	570
Ammonium hexacyanoferrate (III)	670	600
Ammonium hexacyanoferrate (II)	480	840
Iron (III) oxalate	325	560
Ammonium trisoxalatoferrate (III)	500	560
Ammonium iron (III) citrate	580	800
Magnetite + ethylenediaminetetraacetic acid	525	615
Commercial iron (III) oxide		670
Lithium carbonate		950

Figure 68. The reactivities of samples of Fe_2O_3 from various sources with excess Li_2CO_3 [110].

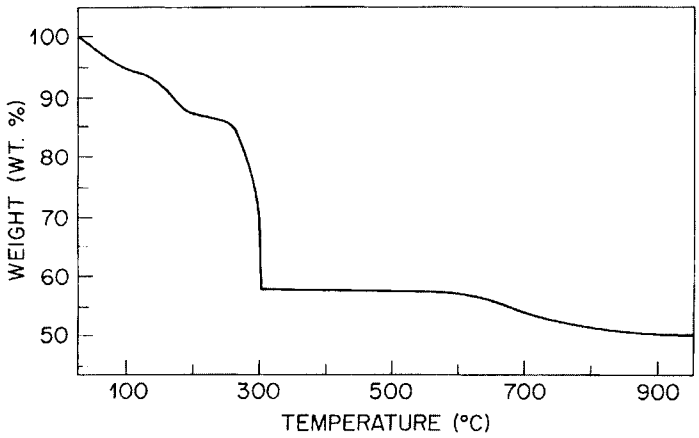


Figure 69. A TG curve for the decomposition of $BaTiO(C_2O_4)_2 \cdot 4H_2O$ in air [111].

Similarly, TG, EGA, and DTA were used to follow the reactions associated with the conversion of freeze-dried aqueous mixtures of the complex oxalates of NH_4^+ and Nb or Ta with $Li_2C_2O_4$ to produce $LiNbO_3$ or $LiTaO_3$ [112]. The decompositions of cyanide precursors such as $M_I[M_{II}(CN)_6] \cdot XH_2O$, where M_I is a rare earth and M_{II} is Fe, Co, or Mn, are more complex and involve hydrolytic decomposition which produces HCN [113,114,115].

Sol-gel processing was discussed earlier in conjunction with the thermal expansion of preforms for optical wave-guides, but has become a major method for the synthesis of many ceramic materials. Doped TiO_2 photo-anodes have been prepared in this manner because they have advantages of improved control of the doping, stabilization of the anatase phase, and better control over the final shape of the anode [116]. Titanium butoxide is doped with the desired metal (Cr and Al) organics and the resulting material is hydrolyzed with acetic acid. Some thermoanalytical curves for the resulting xerogel are presented in Figure 70. The DTA curve in air shows exotherms attributed to the stepwise combustion of the evolved organic gases. In an inert atmosphere, however, these are combined into a singe endotherm. The final exotherm was shown by X-ray diffraction methods to correspond to the crystallization of the anatase phase from the amorphous or microcrystalline decomposition product. Further confirmation of the mechanisms was obtained using FTIR spectroscopy and ESR spectroscopy.

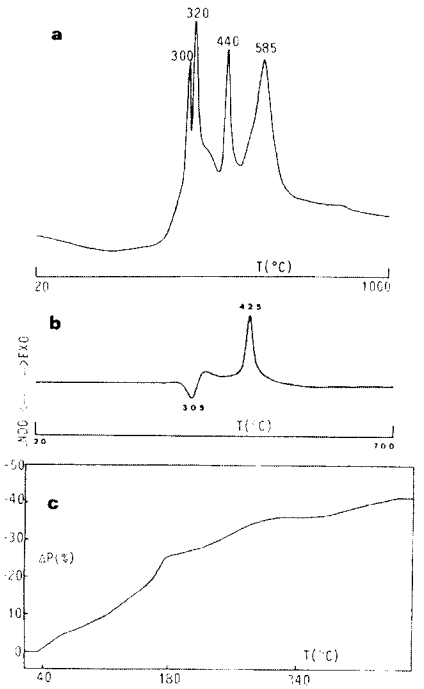


Figure 70. Thermoanalytical curves associated with the decomposition of a titania xerogel doped with Cr^{3+} and Al^{3+} [116].

Thick films are often prepared by repeated dippings of the substrate into a solution of the appropriate precursor compounds with a drying step in between each. The final step involves heating the combination to a temperature suitable to convert it to the intended compound and to sinter the film to the desired density. The TG and DTG curves in Figure 71 show that the dried nitrate precursor films for $PbZr_{.62}Ti_{.38}O_3$ and $NiFe_2O_4$ decompose around 300 °C and can be fired to higher temperatures without indication of reaction with the substrate [117].

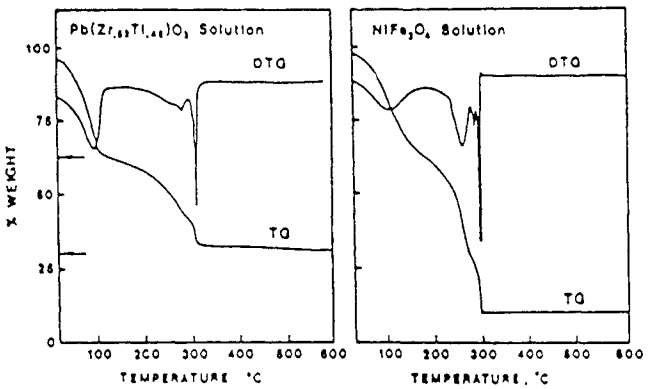


Figure 71. TG and DTG curves for the decompositions of thick films of two dried nitrate precursor combinations [117].

7. CONCLUDING REMARKS

This chapter has only revealed the tip of the iceberg of the potential applications of thermal analysis and calorimetry to the study of inorganic materials. The examples have been described in a brief manner but the original sources of further information have been given. The authors hope that some of these examples may have provided insights and possible guides to the solution of a range of technological problems.

Although these techniques have tremendous possibilities, they can also be misleading if the investigator does not focus on the specific property being monitored. In most cases assumptions must be made in relating the apparent mass change, heat absorbed or evolved, dimensional change, etc. to some event at the atomic/molecular level. Complementary studies using more direct techniques, such as X-ray diffraction, microscopy, and various forms of spectroscopy, are frequently necessary. Particular care is required when interpreting observed evolution or absorption of heat, because physical processes, e.g., amorphous to crystalline transformations and sintering, may accompany chemical reactions.

REFERENCES

1. M.I. Pope and M.D. Judd, Differential Thermal Analysis, Heyden & Sons, London, 1977, Chap. 6.
2. P.K. Gallagher, Characterization of Ceramics, (Ed. R.E. Loehman), Butterworth-Heinemann, Boston, 1993, Chap. 8.

3. K. Tozaki, R. Masuda, S. Matsuda, C. Tokitomo, H. Hayashi, H. Iniba, Y. Yoshimura, and T. Kimura, J. Therm. Anal. Cal., 64 (2001) 331.
4. P.K. Gallagher, Handbook of Thermal Analysis and Calorimetry, Vol. 1 Principles and Practice, (Ed. M.E. Brown), Elsevier, Amsterdam, 1998, Chap. 4.
5. J. Mullens, Handbook of Thermal Analysis and Calorimetry, Vol. 1 Principles and Practice, (Ed. M.E. Brown), Elsevier, Amsterdam, 1998, Chap. 12.
6. J. Valo and M. Leskelä, Handbook of Thermal Analysis and Calorimetry, Vol. 2 Applications to Inorganic Materials (Eds M.E. Brown and P.K. Gallagher), Elsevier, Amsterdam, 2003, Chap. 15.
7. High-Temperature Superconductors, (Eds P.K. Gallagher, T. Ozawa, and J. Sestak) Thermochim. Acta. 174 (1991).
8. B. Raveau, C. Michel, and M. Hervieu, Properties and Applications of Perovskite-Type Oxides, (Eds. L.G.Tejuca and J.L.G. Fierro), Marcel Dekker, New York, 1993, Chap. 4.
9. P.K. Gallagher, D.W. Johnson, Jr., E.M. Vogel, G.K. Wertheim, and F.J. Schnettler, J. Solid State Chem., 21 (1977) 277.
10. P.K. Gallagher, Thermochim. Acta, 174 (1991) 85.
11. P. Bracconi and P.K. Gallagher, J. Am Ceram. Soc., 62 (1979) 171.
12. P.K. Gallagher, J. Therm. Anal., 38 (1992) 17.
13. S. Guggenheim and A. Koster van Groos, Clays and Clay Minerals, 49 (2001) 433.
14. A. Blažek, Thermal Analysis, Van Nostrand Reinhold Company, London, 1973, p.176.
15. R. Grimshaw, The Chemistry and Physics of Clays, reprinted by Techbooks, Fairfax, VA, 1971, p.967.
16. D. Bish and C. Duffy, (Eds J. Stucki, D. Bish, and F. Mumpton), CMS Workshop Lecture Series, Vol. 3, Thermal Analysis in Clay Science, The Clay Minerals Society, Boulder, CO, 1990, p.96.
17. E. Kaisersberger and E. Post, Thermochim. Acta, 295 (1997) 73.
18. D. Brosnan and J. Sanders, 2002 Annual - Ziegelindustrie International, Bauverlag, GmBH, Weisbaden, 2002, p.123.
19. K. Nassau, P.K. Gallagher, A.E. Miller, and T.E. Graedel, Corrosion Sci., 27 (1987) 669.
20. M. Maciejewski, and A. Baiker, Thermochim. Acta, 295 (1997) 95.
21. K. Marsanich, F. Barontini, V. Cozzani, and L. Petarca, Thermochim. Acta, 390 (2002) 153.
22. D. Alymer and M.W. Rowe, Thermochim. Acta, 78 (1984) 81.
23. L.O. Svaasand, M. Eriksrud, G.N. Kenode, and A.P. Grande, J. Cryst. Growth, 72 (1974) 230.

24. P.K. Gallagher and H.M. O'Bryan, J. Am. Ceram. Soc., 68 (1985) 147.
25. P.K. Gallagher, H.M. O'Bryan, and C.D. Brandle , J. Am. Ceram. Soc., 68 (1985) 493.
26. V. Kuck, Thermochim. Acta, 99 (1986) 233.
27. A.S. Pedersen, N. Pryds, S. Linderoth, P.H. Larsen, and J. Kjøller, J. Therm. Anal. Cal., 64 (2001) 887.
28. G. Sheffield and J. Schorr, Ceramic Eng. Sci. Proc., 18 (1997) 374.
29. B. Haglund, J. Therm. Anal., 25 (1982) 21.
30. T. Fukatsu, J. Japan Soc. Powder Metallurgy, 8 (1961) 183.
31. U. Oscarson and T. Luks, Sandvik Internal Technical Memo, ALF 41971, (1981).
32. ICTAC Task Group, J. Therm. Anal. Cal., (2003)
33. K. Lønvik, Thermochim. Acta, 110 (1987) 253
34. H.G. Wiedemann and S. Felder-Casagrande, Handbook of Thermal Analysis and Calorimetry, Vol. 1 Principles and Practice, (Ed. M.E. Brown), Elsevier,Amsterdam, 1998, Chap. 10.
35. R.F, Speyer, Thermal Analysis of Materials, Marcel Dekker, New York, 1994, Chap. 5.3.
36. W.W. Wendlandt and H.G. Hecht, Reflectance Spectroscopy, Intersience, New York, 1966.
37. W.W. Wendlandt, Thermal Analysis, 3rd Edn, Wiley & Sons, New York, 1985, Chap. 9.
38. P.K. Gallagher, Applications of Mössbauer Spectroscopy, Vol. 1, (Ed. R.L. Cohen), Academic Press, New York, 1976, Chap. 7.
39. P.K. Gallagher and J.B. MacChesney, Symp. Faraday Soc., 1 (1967) 40.
40. M.E. Brown, Introduction to Thermal Analysis, Chapman Hall, London, 1988, p.35.
41. S. Rudtsch, Thermochim. Acta, 382 (2002) 17.
42. T. Matsui, Y. Arita, and K. Watanabe, Thermochim. Acta, 352-353 (2000) 285.
43. M. Merzlyakov and C. Schick, Thermochim. Acta, 377 (2001) 183.
44. A. Albers, T. Restivo, L. Pagano, and J. Baldo, Thermochim. Acta, 370 (2001) 111.
45. T. Olorunyolemi, A. Birnboim, Y. Carmel, O. Wilson, I. Lloyd, S. Smith and R. Campbell, J. Am. Ceram. Soc., 85 (2002) 1249.
46. W. Miller, Kirk-Othmer Encyclopedia of Chemical Technology, 3rd edition, Vol. 20, John Wiley and Sons, New York, 1982, p.65.
47. M. Collin and D. Rowcliffe, J. Am. Ceram. Soc., 84 (2001) 1334.
48. D. Hasselman, J. Am. Ceram. Soc., 52 (1969) 600.

49. ASTM C372-94, Standard Test Method for Linear Thermal Expansion of Porcelain Enamel and Glaze Frits and Fired Ceramic Whiteware Products by the Dilatometer Method (2001).
50. H.M. O'Bryan, P.K. Gallagher, G.W. Berkstresser, and C.D. Brandle, J. Mater. Res., 5 (1990) 183.
51. Z. Zhong, P.K. Gallagher, D.L. Loicano, and G.M. Loicano, Thermochim. Acta, 234 (1994) 255.
52. A. Goldsmith, T.E. Waterman, and H.J. Hirshhorn, Handbook of Thermophysical Properties of Solid Materials, Vol. III: Ceramics, Macmillan Co., New York, 1961, p.469.
53. S.J. Gregg and K.S.W. Sing, Adsorption, Surface Area and Porosity, Academic Press, NY, 1967.
54. M. Büchner and E. Robens, Prog. Vacuum Microbalance Techniques, Vol. 1, (Eds T. Gast and E. Robens), Heyden & Sons, London, 1972, p.333.
55. T.J. Quinn, Temperature, 2nd Ed., Academic Press, New York, 1990.
56. P.K. Gallagher, K.W. West and S.St.J. Warne, Thermochim. Acta, 50 (1981) 41.
57. Treatise on Solid State Chemistry: Volume 4 Reactivity of Solids, (Ed. N.B. Hannay), Plenum Press, New York, 1976.
58. H. Schmalzreid, Solid State Reactions, Verlag Chemie, Basel, 1981.
59. H. Schmalzreid, Chemical Kinetics of Solids, VCH Publishers, New York, 1995.
60. V.V. Boldyerev, M. Bulens, and B. Delmon, The Control of the Reactivity of Solids, Elsevier, Amsterdam, 1979.
61. Reactivity of Solids: Past, Present, and Future, (Ed. V.V. Boldyrev), IUPAC, Oxford, 1996.
62. A.K. Galwey and M.E. Brown, Thermal Decomposition of Ionic Solids, Elsevier, Amsterdam, 1999.
63. P.J. van Ekeren, Handbook of Thermal Analysis and Calorimetry, Vol. 1 Principles and Practice, (Ed. M.E. Brown), Elsevier, Amsterdam, 1998, Chap. 2.
64. A.K. Galwey and M.E. Brown, Handbook of Thermal Analysis and Calorimetry, Vol. 1 Principles and Practice, (Ed. M.E. Brown), Elsevier, Amsterdam, 1998, Chap. 3.
65. T. Hasizume, K. Terayama, T. Shimazaki, H. Itoh, Y. Okuno, J. Therm. Anal. Cal., 693 (2002) 1045.
66. J. Dweck, R.S. Aderne, and D.J. Shanefield, J. Therm. Anal. Cal., 64 (2001) 1163.
67. L. Mikkelsen and E Skou, J. Therm. Anal. Cal., 64 (2001) 873.

68. D.W. Bishop, P.S. Thomas, A.S. Ray and P. Simon, J. Therm. Anal. Cal., 64 (2001) 201.
69. U.R. Evans, The Corrosion and oxidation of Metals: Scientific Principles and Practical Applications, St. Martin's Press, New York, 1960.
70. R.G. Charles, Thermal Analysis in Metallurgy, (Eds R.D. Schull and A. Joshi) TMS, Warrendale, Pa, 1992, p.27.
71. V. Kolarik, M. Juez-Lorenzo, N. Eisenreich, and W. Engle, J. Therm. Anal. Cal., 38 (1992) 649.
72. P. Herley and D. Spencer, J. Phys. Chem., 83 (1979) 1701.
73. J.A. Hedvall, Chem. Rev., 15 (1934) 139.
74. P.K. Gallagher and D.W. Johnson, Jr., J. Phys. Chem., 86 (1982) 295.
75. P.D. Garn and T.S. Habash, J. Phys. Chem., 83 (1979) 229.
76. P.K. Gallagher, E.M. Gyorgy and H.E. Bair, J. Chem. Phys., 71 (1979) 830.
77. M.W. Rowe, P.K. Gallagher and E.M. Gyorgy, J. Chem. Phys., 79 (1983) 3534.
78. J. Lewis, Ann. Rev. Mater. Sci., 27 (1997) 147.
79. R. Shende, and S. Lombardo, J. Am. Ceram. Soc., 854 (2002) 780.
80. A. Das, G. Madras, N. Dasgupta, and A. Umarji, J. Euro. Ceram. Soc., 23 (2003) 1013.
81. L. Liau, B. Peters, D. Krueger, A. Gordon, S. Viswanath, and S. Lombardo, J. Am. Ceram. Soc., 83 (2000) 2645.
82. E. Post, S. Rahner, H. Möhler, and A. Rager, Thermochim. Acta, 263 (1995) 1.
83. R. Jackson and A. Rager, Thermochim. Acta, 367-368 (2000) 415.
84. C-F. Chan, B. Argent and W. Lee, J. Am. Ceram. Soc., 81 (1988) 3177.
85. M. Faghihi-Sani, and A. Yamaguchi, Ceram. Int., 28 (2002) 835.
86. M. Paganelli, Am. Ceram. Soc. Bull., 81 (2002) 25.
87. H. Palmour and P.P. Johnson, Sintering and Related Phenomena, (Eds G.C. Kuczynski, N.A. Hooten, and C.F. Gibbon), Gordon & Breach, New York, 1967, p.779.
88. K. Nassau, E.M. Rabinovich, A.E. Miller, and P.K. Gallagher, J. Noncryst. Solids, 82 (1986) 78.
89. V. Balek and M.E. Brown, Handbook of Thermal Analysis and Calorimetry, Vol. 1 Principles and Practice, (Ed. M.E. Brown), Elsevier, Amsterdam, 1998, Chap. 9.
90. V. Balek and I.N. Beckman, Thermochim. Acta, 85 (1985) 15.
91. P.K. Gallagher, J. Therm. Anal., 38 (1992) 17.
92. P.K. Gallagher and S.N.G. Chu, J. Phys. Chem., 86 (1982) 3246.

93. E. Kinsbron, P.K. Gallagher, and A.T. English, Solid-State Electronics, 22 (1979) 517.
94. T.M. Duncan, R.A. Levy, P.K. Gallagher, and M.W. Walsh, J. Appl. Phys., 64 (1988) 2990.
95. R.A. Levy and P.K. Gallagher, J. Electrochem. Soc., 132 (1985) 1986.
96. M. Hong, E.M. Gyorgy, P.K. Gallagher, S. Nakahara and L.C. Feldman, Appl. Phys. Lett., 48 (1986) 730.
97. P.K. Gallagher, E.M. Gyorgy, F. Schrey, and F. Hellman, Thermochim. Acta, 121 (1987) 231.
98. F. Eigenmann, M. Maciejewski, A. Baiker, Thermochim. Acta, 359 (2000) 131.
99. M. Maciejewski, C. Müller, W. D. Emmerich, and A. Baiker, Thermochim. Acta, 295 (1997) 167.
100. J. Sanders and D. Brosnan, 2003 Annual - Ziegelindustrie International, Bauverlag, GmBH, Weisbaden, 2003, p.47.
101. G. Kakali, E. Chaniotakis, S. Tsivilis, and E. Danassis, J. Therm. Anal., 52 (1998) 871.
102. H. Chen, Thermal Analysis, Proceedings of the Seventh International Conference on Thermal Analysis – Volume II, (Ed. Bernard Miller), John Wiley and Sons, New York, 1982, p.1303.
103. M Perraki, T. Perraki, K. Kolovos, S. Tsivilis, and G. Kakali, J. Therm. Anal. Cal., 70 (2002) 143.
104. J. Dweck, P Mauricio Buchler, A.C. Vieira Coelho, F. Cartledge, Thermochim. Acta, 346 (2000) 105.
105. J. Bhatty, K. Ried, D. Dollimore, G. Gamlen, R. Mangabhai, P. Rogers and T. Shah, Compositional Analysis by Thermogravimetry, ASTM STP 997, (Ed. C. Earnest), American Society for Testing and Materials, Philadelphia, 1998, p.204.
106. S. Tsivilis, G. Kakali, E. Chaniotakis, and A. Souvaridou, J. Therm. Anal., 52 (1998) 863.
107. V. Ramachandran, Thermal Analysis, Proceedings of the Seventh International Conference on Thermal Analysis – Volume II, (Ed. Bernard Miller), John Wiley and Sons, New York, 1982, p.1296.
108. I. Paama, I Pitkänen, H. Rönkkömäki, and P. Perämäki, Thermochim. Acta, 320 (1998) 127.
109. I. Paama, I Pitkänen, and P. Perämäki, Talanta, 51 (2000) 349.
110. P.K. Gallagher, D.W. Johnson, Jr., F. Schrey and D.J. Nitti, Am. Cer. Soc. Bull., 52 (1973) 842.
111. P.K. Gallagher and J. Thomson, Jr., J. Am. Ceram. Soc., 48 (1965) 644.
112. P.K. Gallagher and F. Schrey, Thermochim. Acta, 1 (1970) 465.

113. P.K. Gallagher and F. Schrey, Thermal Analysis, Vol. 2, (Eds R.F. Schwenker, Jr. and P.D. Garn), Academic Press, New York, 1969, p.969.
114. P.K. Gallagher & B. Prescott, Inorg. Chem., 9 (1970) 2510.
115. Y. Masuda, Y. Seto, X. Wang, and Y. Tuchiya, J. Therm. Anal. Cal., 64 (2001) 1045.
116. S. Doeuff, M. Henry, and C. Sanchez, Better Ceramics Through Chemistry II, (Eds. C.J. Brinker, D.E. Clark, and D.R. Ulrich), MRS, Pittsburgh, 1986, p.653.
117. W.W. Davison, S.G. Shyu, R.D. Roseman, and R.C. Buchanan, Mat. Res. Soc. Symp. 121 (1988) 797.

Handbook of Thermal Analysis and Calorimetry. Vol. 2: Applications to Inorganic and Miscellaneous Materials
M.E. Brown and P.K. Gallagher, editors
© 2003 Elsevier B.V. All right reserved.

Chapter 6

THERMAL ANALYSIS OF CLAYS

Katherine S. Meyers and Robert F. Speyer

School of Materials Science and Engineering, Georgia Institute of Technology, Atlanta, Georgia, 30332-0245

1. INTRODUCTION

The phase transformations which occur upon heating are signatures of many natural minerals, especially the clay minerals. Cooperatively, DTA, TG, and dilatometry are cost effective means of identifying individual ceramic raw materials, identifying the minerals comprising complex mixtures, and characterizing the reactions among the constituents of these mixtures during heating. In this chapter, the thermal behavior of clay and related minerals will be discussed and correlated to changes in their atomic structure.

1.1. Clay products

The invaluable characteristic of unfired clay minerals is that they are plastic; ceramic bodies containing them can be shaped via throwing (hand shaping while spinning) pressing, extrusion or slip casting (discussed shortly), and these shapes are retained during subsequent handling, drying and firing. Crude clay deposits (containing organic constituents, as well as accessory and impurity minerals, along with the clay minerals) are used for structural clay products such as bricks and tiles, while clay deposits of higher purity (containing, or purified to contain, primarily clay minerals) are used for ceramic whitewares (i.e. become white after firing), examples of which are various types of porcelain, such as dinnerware, sanitary ware, electrical insulators, and dental porcelains. Clays are also essential ingredients in cement and some refractories. They function as a coating and filler for paper, to increase surface shine and opacity, and are added to rubber to increase wear resistance. Clay is added to soil for building dams to decrease water

permeability. Certain clays function as water softeners, in which sodium ions in the clay exchange with calcium and magnesium ions in the water.

Porcelains typically consist of triaxial mixtures of clay (e.g. kaolinite: $Al_2Si_2O_5(OH)_4$), feldspar (e.g. albite: $NaAlSi_3O_8$) and quartz (SiO_2). During heating, the water contained within the clay becomes a decomposition product. At higher temperatures, the alkali/alkaline earth elements in the feldspar minerals cause a small amount of liquid phase to form (for that reason, feldspars are often referred to as "fluxes"). The liquid phase fills the interstices between solid particles by capillary action, and the body densifies via liquid-phase sintering. At peak firing temperatures (~1250 °C), reactions among the constituents result in the growth of mullite ($Al_6Si_2O_{13}$) with a needle-like crystal habit. During cooling, the liquid phase is retained as a silicate glass. Thus, the fired porcelain generally consists of a glassy phase binding mullite and residual quartz crystals, forming a translucent body. As firing temperatures are increased, more liquid forms, but it is increasingly silica rich (quartz and clay particles become more soluble in the liquid phase) and correspondingly more viscous. Thus, triaxial porcelains avoid slumping despite wide variations in composition and firing temperature. Higher clay content, relative to feldspar, results in the presence of less alkali, and hence less glassy phase, whereby porosity may be retained in the fired product, unfavorably affecting mechanical and dielectric properties. Excessive feldspar content, on the other hand, results in a glassy phase with a high concentration of alkali. This narrows the firing range and forms a glassy phase with a high coefficient of thermal expansion, resulting in a porcelain with diminished thermal shock resistance. Typical porcelain formulations are shown in Table 1.

Table 1.
Typical compositions of porcelain bodies. Flint is a form of microcrystalline or amorphous SiO_2. 1.5 wt% of alkaline earth carbonates are added to hotel china [1].

Type of ware	Kaolin (wt%)	Ball clay (wt%)	Flint (wt%)	Feldspar (wt%)
Semivitreous ware	28	25	36	11
Hotel china	37	8	35	20
Hard porcelain	46	-	34	20
Sanitary ware	30	10	28	32
Floor tile	32	-	10	58
High-tension inulators	15	30	20	35
Low-tension insulators	20	25	20	35
Dental porcelain	5	-	14	81
Parian porcelain	35	-	-	65

1.2. The nature of clays

The main classes of clay minerals, categorized by similarity in crystal structure, are the kaolins, montmorillonites, and illites (Table 2). Although not strictly considered clay minerals, chlorites, vermiculites, and micas have sheet-structures akin to those of the clay minerals and are often composed of elements similar to those in clay minerals as well, and are thus considered accessory minerals.

Table 2.
Clay minerals, accessory minerals, as well as inorganic and organic impurities found in clay deposits.

Clay Minerals	**Accessory Minerals**	**Impurities**
Kaolins	*Micas*	*Inorganic*
Kaolinite, Nacrite, Dickite	Muscovite	Quartz
$Al_2Si_2O_5(OH)_4$	$KAl_3Si_3O_{10}(OH)_2$	SiO_2
Halloysite	Paragonite	Feldspar
$Al_2Si_2O_5(OH)_4{\cdot}2H_2O$	$NaAl_3Si_3O_{10}(OH)_2$	Orthoclase
Montmorillonites	Margarite	$KAlSi_3O_8$
Montmorillonite	$CaAl_4Si_2O_{10}(OH)_2$	Albite
$(Al_{1.67}Mg_{0.33})Si_4O_{10}(OH)_2{\cdot}nH_2O$	Phlogopite	$NaAlSi_3O_8$
$\uparrow\!\!\rightarrow Na_{0.33}$	$KMg_3AlSi_3O_{10}(OH)_2$	Anorthite
Nontronite	Lepidolite	$CaAl_2Si_2O_8$
$Fe_{2.22}AlSi_3O_{10}(OH)_2{\cdot}nH_2O$—	$KLi_2AlSi_4O_{10}(OH)_2$	Iron Minerals
$Fe_{1.67}Mg_{0.33}Si_4O_{10}(OH)_2{\cdot}nH_2O$	Biotite	Limonite
Beidellite	$K(Mg, Fe, Mn)_3Si_3AlO_{10}(OH)_2$	$Fe_2O_3{\cdot}nH_2O$
$Al_{2.22}(AlSi_3)O_{10}(OH)_2{\cdot}nH_2O$	Zinnwaldite	Siderite
$\uparrow\!\!\rightarrow Na_{0.33}$	$K(Li, Fe, Al)_3(Si, Al)_4O_{10}(OH)_2$	$FeCO_3$
Hectorite	*Chlorites*	Calcite
$(Li_{0.33}Mg_{2.67})Si_4O_{10}(OH)_2{\cdot}nH_2O$	Chlorite	$CaCO_3$
$\uparrow\!\!\rightarrow Na_{0.33}$	$Mg_5Al_2Si_3O_{10}(OH)_8$	Dolomite
Saponite	Penninite	$Ca,Mg(CO_3)_2$
$Mg_3(Al_{0.33}Si_{3.67})O_{10}(OH)_2{\cdot}nH_2O$	$Mg_5(Al,Fe)(Al,Si)_4O_{10}(OH)_8$	Gypsum
$\uparrow\!\!\rightarrow Na_{0.33}$	*Vermiculites*	$CaSO_4{\cdot}2H_2O$
Illites	$(Mg,Fe)_3(Al,Si)_4O_9(OH)_8{\cdot}3.5H_2O$	Titania
Hydromuscovite		TiO_2
$KAl_3Si_3O_{10}(OH)_2$		*Organic*
$\uparrow\!\!\rightarrow H_3O^+$		Lignite
Amersooite		Waxes
$K(Mg, Fe, Mn)_3Si_3AlO_{10}(OH)_2$		Carbonaceous matter
$\uparrow\!\!\rightarrow H_3O^+$		Humic acid
Brammalite		Derivatives
Glauconite		

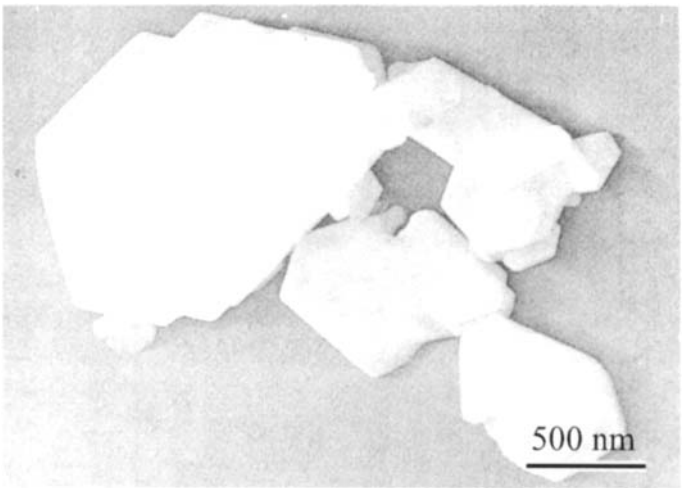


Figure 1. Electron micrograph of clay particles [1].

Additional impurity minerals commonly found in clay deposits include quartz, feldspars, dolomite ($(Ca,Mg)CO_3$), and iron minerals (e.g. limonite $Fe_2O_3 \cdot nH_2O$). Clay deposits also contain organic matter to varying extents, such as lignite (an immature brown coal formed from fossilized wood [2]), waxes, resins, and humic acid derivatives.

The composition, crystal structure, particle size, shapes and surface charge of clay deposits dominate their rheological and thermal properties. The crystal structure of clay minerals can be described as being based on the stacking of layers containing sheets of specific chemical constituents. Since different elements reside within different layers, the stacking of the layers requires some accommodation, and atomic-level stresses build up in the direction perpendicular to the layers. Over many layers, these stresses cannot be accommodated and as a result, clays exist as fine plate-like particles (Figure 1) with narrow particle-size distributions.

Atoms on the surface of a particle suffer from unsatisfied bonds, rendering a surface charge to the particle. Water, being a polar molecule, forms a contiguous film on clay particles, acting to shield its surface charge. These water films permit the easy sliding of particles which results in the plastic behavior of clay, allowing it to be molded or pressed into a shape. A significant fraction of clay particles have an average diameter of less than 1 μm; particles of this size are referred to as colloidal particles. In water, colloidal clay particles become suspended, i.e. they do not (or do not quickly) settle to the bottom of the container as the forces of

Brownian (random) motion of the fluid dominate over the gravitational forces on the particles (chemicals called deflocculants, such as sodium silicate, are often added to facilitate mutual repulsion of the particles so that they do not flock together and settle). Clay-based articles are slip cast when a clay suspension is poured into a porous plaster mold; the water between particles near the mold wall is extracted into the mold, compacting the clay particles to conform to the mold shape. This shape is maintained after the mold is pulled away.

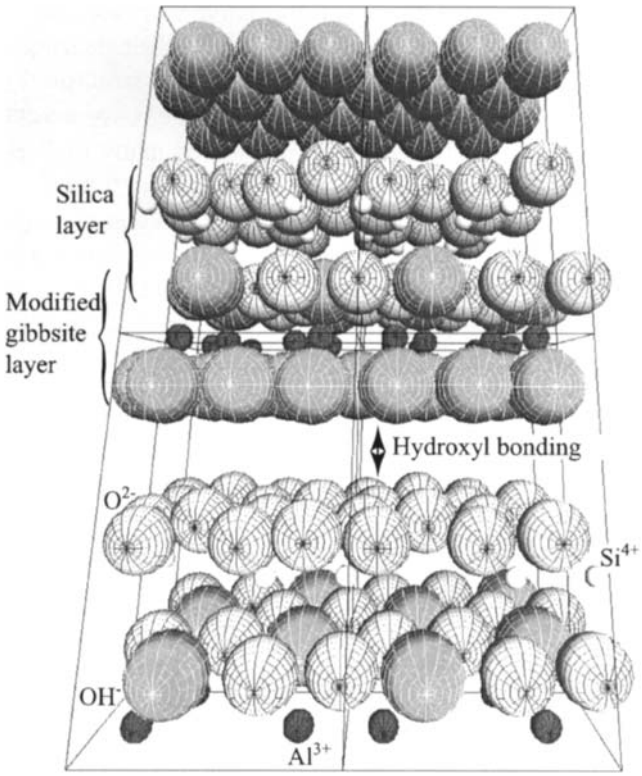


Figure 2. The structure of kaolinite, a kaolin mineral. Hydroxyl (OH^-) groups are crystallographically represented by a single sphere, due to the small size of hydrogen relative to all other atoms present. Eight triclinic unit cells are shown. The *c*-axis (vertical axis) is expanded by 2× for visual clarity. Data for this and all other crystal structure drawings are from Wyckoff [3].

2. STRUCTURE-THERMAL PROPERTY RELATIONS

2.1. Kaolins

2.1.1. Structure of the kaolin minerals

Figure 2 depicts the triclinic structure of kaolinite ($Al_2Si_2O_5(OH)_4$), the most abundant of the kaolin minerals, and of all clay minerals. Alternating silica layers, with repeat unit $Si_2O_5^{2-}$, and modified gibbsite layers*, with repeat unit $Al(OH)_2^+$, comprise the kaolin mineral structure. The missing hydroxyls (OH^-) in the modified gibbsite layer are replaced by oxygen anions associated with the silica layer. Silicon atoms are tetrahedrally coordinated with oxygen while aluminum ions are octahedrally coordinated with hydroxyls. Silicate rings containing six silicon atoms are similar in size to the modified gibbsite-structured rings containing six aluminum atoms, allowing superposition of the two layers with a slight distortion. Kaolin mineral platelets are composed of many of these double-layers (~100)—the double-layers are henceforth referred to as "units". These units are held together by hydroxyl bonding forces between oxygen and hydroxyl ions; the hydrogen components of hydroxyl ion layer are thought to alternate association with hydroxyl ions and oxygen ions in the adjacent layer. This bonding is considerably weaker than that within the units, and cleavage readily occurs between these units.

The two-layer unit structure distinguishes the kaolin clay minerals; the individual minerals of this group are delineated by how the silica and modified gibbsite layers are positioned. In nacrite, oxygen atoms are lined up in the stacking of each silica layer, resulting in a cell that is monoclinic (but nearly orthorhombic), and requires six of the kaolinite units to define a unit cell. Dickite is described by a monoclinic unit cell in which the oxygen ions are buckled slightly from perfect alignment along a sheet (Figure 3), and requires two of the kaolinite units to define a unit cell. Offsets of the oxygen atoms associated with adjacent silica layers in halloysite are partially random. This contributes to its tendency to exist in the hydrated form $Al_2Si_2O_5(OH)_4 \cdot 2H_2O$, with layers of water molecules lodging between the haphazardly-stacked units. The presence of the water layers prevents normal hydroxyl bonding between adjacent units, and the stress associated with the resulting distortion is manifested as curvature into tube-like particles [4]. The size of halloysite crystals is comparable to that of kaolinite, while the lower atomic strains associated with the stacking of nacrite and dickite permit them to occur as larger particles [5].

---

* Removing one hydroxyl group from each gibbsite ($Al(OH)_3$) unit forms modified gibbsite units $Al(OH)_2^+$.

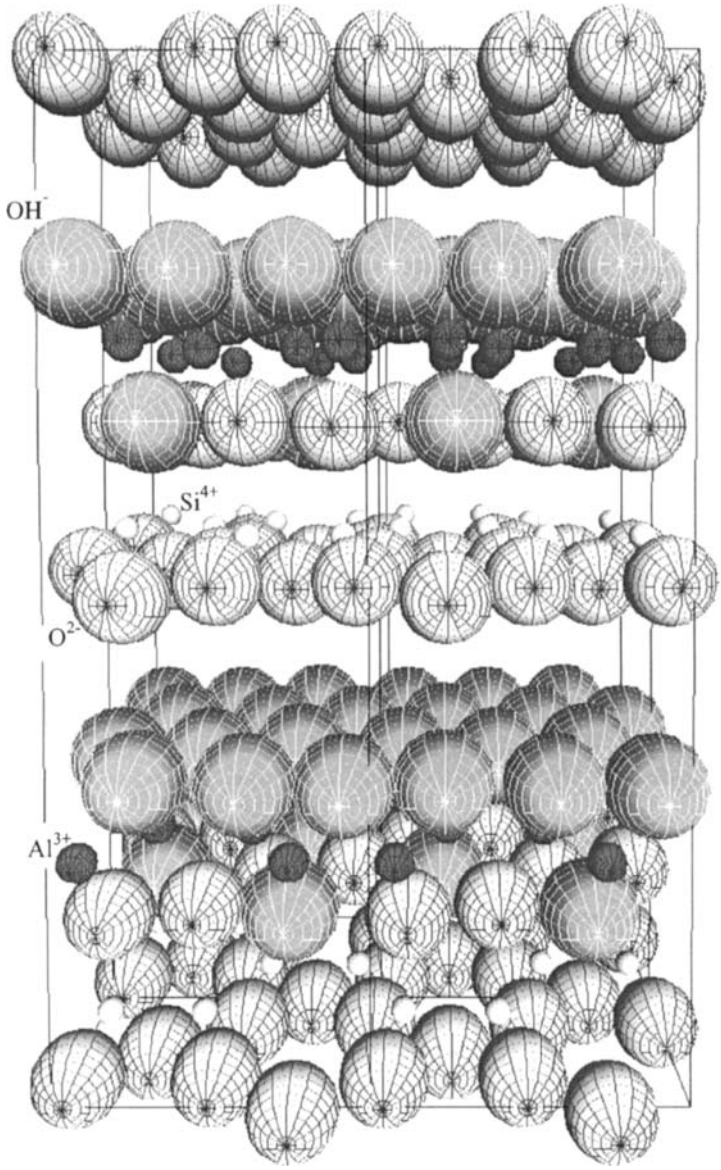


Figure 3. The structure of dickite, a kaolin mineral. Four monoclinic unit cells are shown. The *c*-axis (vertical axis) is expanded by 2× for visual clarity.

The kaolin minerals have a very low base-exchange capacity—their maximum capacity to adsorb cations on the unit surface. Cations are adsorbed between unit surfaces of a particular mineral in response to a charge deficiency in the units, in turn caused by substitutions of ions for lattice ions with difference valences. As kaolin minerals allow very little lattice substitution, they have very low base-exchange capacity. The small amount of cation absorption observed in kaolinite has been attributed to broken bonds at the edges of the particles (termination edges of the silica and modified gibbsite layers). Higher base-exchange capacities have been measured for kaolinite with decreasing particle size since there is a corresponding increase in total particle edge area [1].

A final type of kaolin mineral is known as disordered kaolinite, or livesite, with a structure similar to that of kaolinite, but containing some randomness in layer stacking. This structure possesses a higher base-exchange capacity than the aforementioned kaolin minerals, because Mg^{2+} cations may substitute for some of the Al^{3+} cations, yielding a charge deficiency.

2.1.2. Thermal analysis of the kaolin minerals

Upon heating, kaolinite undergoes dehydroxylation, starting at temperatures of about 450-500 °C, losing its structural water, i.e. the hydroxyl groups in the modified gibbsite layers, forming meta-kaolin ($Al_2O_3 \cdot 2SiO_2$). This dehydroxylation reaction, indicated as a sharp mass loss and DTA endotherm in Figure 4, has a latent heat (heat absorption) ranging from 42 to 250 kJ mol^{-1}, but typically around 150 kJ mol^{-1} [7]. Meta-kaolin is structurally similar to kaolinite, but with the lattice broken up so that no long-term atom periodicity exists at the resolution of X-ray diffraction. Prior to dehydroxylation, clays containing these kaolin minerals are sensitive to the action of water (clay masses can be shaped with the addition of water), while this is not the case afterwards. The exotherm onset at ~925 °C with maximum at ~980 °C represents the rapid crystallization of meta-kaolin to a spinel crystal structure ($2Al_2O_3 \cdot 3SiO_2$) rejecting silica in the process. This metastable spinel transforms into pseudo-mullite ($Al_2O_3 \cdot SiO_2$) and then into mullite ($3Al_2O_3 \cdot 2SiO_2$) through additional diffusional rejection of silica, resulting in a microstructure of mullite needle-like crystals in a silicate glass. All transformations after dehydroxylation are solid-state, and are thus devoid of corresponding mass changes. When pure, well-crystallized kaolinite is the original structure, the small exotherm with a peak at 1250 °C indicates a surge in the formation of mullite (i.e. the secondary mullite exotherm). For disordered kaolinite as the original mineral, this exotherm represents the crystallization of the glassy silica phase to form cristobalite [7]. The dilatometry trace in Figure 4 shows small

contraction surges associated with dehydroxylation and spinel formation. The most rapid dimensional change starts at ~1100 °C, as grains sinter together and porosity decreases, aided by the formation of a liquid phase which fills voids and draws solid particles together through capillary forces.

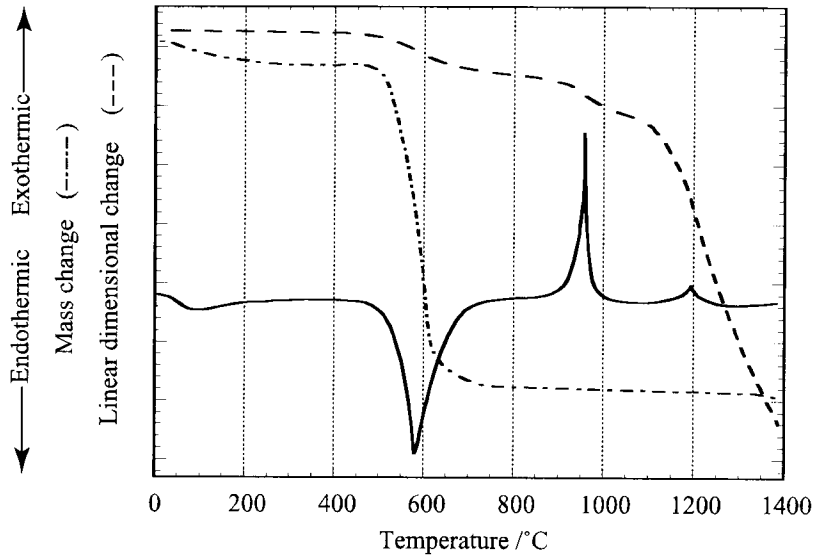


Figure 4. DTA, TG, and dilatometry curves for a kaolinite specimen [6]. Thermodilatometry is discussed in Chapter 6 of Volume 1 of this Handbook.

The extent of structural order of a kaolinite specimen may be gleaned from the dehydroxylation endotherm. For less stable, disordered kaolinite, the endotherm peak temperature appears at 580 °C, slightly lower than the position for ordered kaolinite at 600 °C. The endotherm is also less intense and broader. Bonding between silica and modified gibbsite layers is weakened by greater ion separation distances imposed by impurity cations substituting for aluminum ions [8], thus less thermal energy is required in severing the structure (i.e. lower temperature dehydroxylation). A small endotherm may be seen at 100 °C for some kaolinite samples, corresponding to the evolution of adsorbed water. For most kaolinite specimens, this endotherm is usually so small as to be undetected, but is larger for more disordered kaolinites, which have greater base-exchange capacities and hence greater concentrations of adsorbed water.

Nacrite and dickite display a similar behavior in response to temperature changes as kaolinite (Figure 5). However, the temperature of the dehydroxylation endotherm for dickite tends to be higher than that of kaolinite and nacrite, with an endotherm peak temperature at ~650 °C and a correspondingly higher-temperature TG mass loss onset. The DTA trace for halloysite also resembles that of kaolinite, but always contains an endotherm with an onset at ~50 °C and a peak at ~150 °C. This endotherm, of significant magnitude, denotes the evolution of the random, inter-unit water characteristic of halloysite, and the concurrent formation of meta-halloysite, which adopts the same structure and chemical formula as kaolinite. Significant mass loss and shrinkage are associated with the evolution of this interlayer water. Subsequent to this low temperature water removal, the thermal behavior (DTA, TG and dilatometry) of halloysite is identical to that of kaolinite.

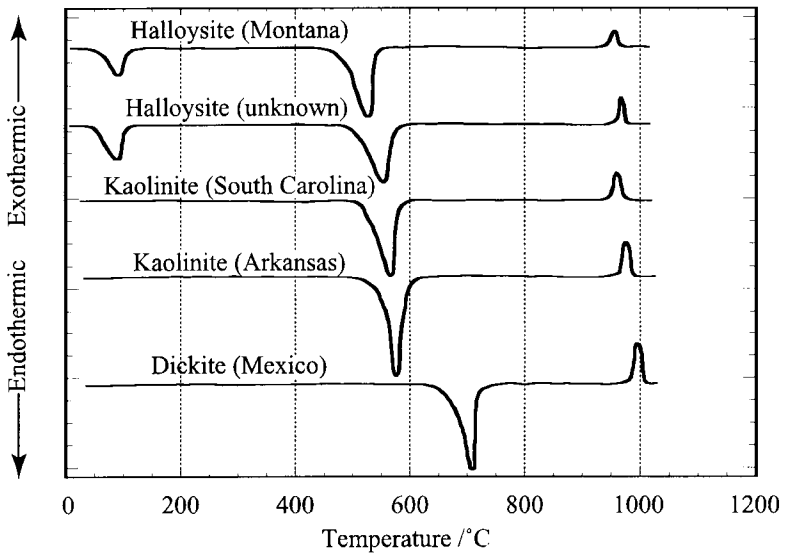


Figure 5. DTA curves for various kaolin clay mineral specimens [9].

2.2. Montmorillonites

2.2.1. Structure of the montmorillonite minerals

The structure of the montmorillonite minerals, also hydrous aluminosilicates, differs from that of the kaolin minerals in unit constitution. A modified gibbsite layer is sandwiched between two silica layers, yielding triple-layer units with the general formula $Al_2Si_4O_{10}(OH)_2$. This is the formula for pyrophyllite (Figure 6),

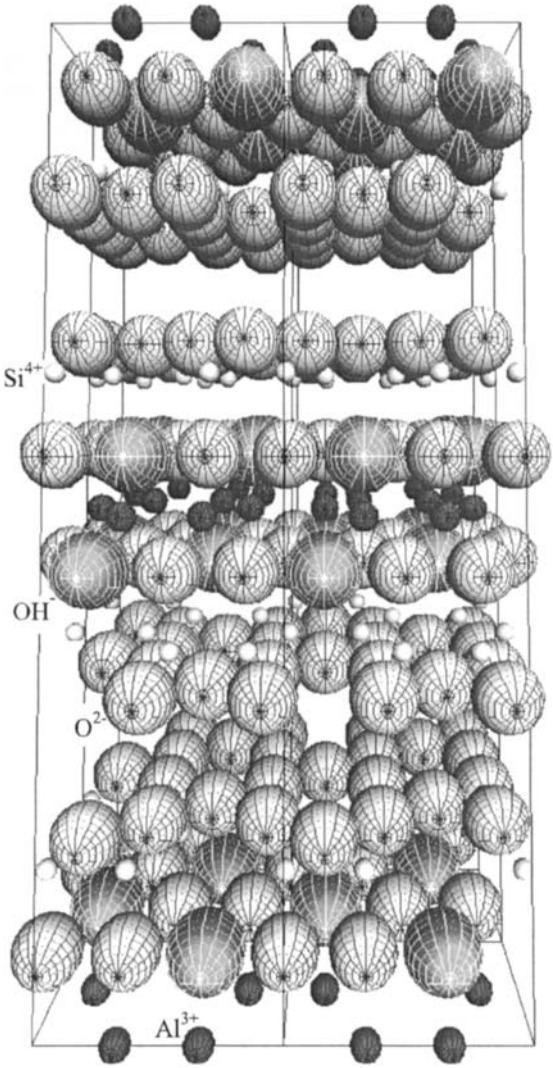


Figure 6. The structure of pyrophyllite. Montmorillonite clay minerals are based on the structure of pyrophyllite with cation substitutions for Al^{3+} and Si^{4+}.

which is not a clay mineral (it is often mined for its use as a fluxing material). Montmorillonite mineral structures are derived from this pyrophyllite structure through lattice substitutions for aluminum and silicon ions, producing triple-layer units that are not electrically neutral. With a preference for maintaining similar (cation / anion) radius ratios, some of the Al^{3+} ions in the modified gibbsite layers may be replaced with cations such as Mg^{2+}, Fe^{2+}/Fe^{3+}, or Li^{+}, and some Si^{4+} atoms in the silica layers may be replaced by Al^{3+}. When a magnesium ion substitutes for one of the aluminum ions in the aluminum ring of the modified gibbsite layer of the pyrophyllite structure, the mineral montmorillonite, with chemical formula $Mg_{0.33}Al_{1.67}Si_4O_{10}(OH)_2$, results. Different lattice substitutions in the pyrophyllite structure produce the other montmorillonite minerals: nontronite is a montmorillonite in which Fe^{3+} substitutes for some Al^{3+} (solid solution range $Fe_{2.22}AlSi_3O_{10}(OH)_2$ to $Fe_{1.67}Mg_{0.33}Si_4O_{10}(OH)_2$), and beidellite is a high-alumina montmorillonite $Al_{2.22}AlSi_3O_{10}(OH)_2$) [5].

Montmorillonite minerals with similar properties may also form from cation substitutions in the structure of talc—another fluxing mineral with chemical formula $Mg_3Si_4O_{10}(OH)_2$ (Figure 7). The talc structure closely resembles the pyrophyllite structure, except that a hydrated magnesia, i.e. brucite, layer with formula $Mg(OH)_2$, rather than a gibbsite layer, joins with two silica layers to form the triple-layer unit. Montmorillonite minerals derived from this talc structure show a complete range of solid solution from hectorite ($(Li_{0.33}Mg_{2.67})Si_4O_{10}(OH)_2$) to saponite ($Mg_3(Al_{0.33}Si_{3.67})O_{10}(OH)_2$) [5].

To achieve electrical neutrality in montmorillonites, cation absorption occurs between adjacent silica layers (i.e. between units). These adsorbed cations are referred to as exchangeable cations. These inter-unit cations in turn tend to hydrate, drawing water molecules to positions between the units. The most common exchangeable cation for the montmorillonite minerals is Na^{+}, but the exchangeable cation may also be Li^{+}, K^{+}, Ca^{2+} or Mg^{2+}. When sodium acts as the exchangeable cation in montmorillonite, the mineral is referred to as a Na-montmorillonite, with the chemical formula $Na_{0.33}$ $(Al_{1.67}Mg_{0.33})Si_4O_{10}(OH)_2$. Because exchangeable cations are weakly bonded to the mineral, they may diffuse out from between the units when exposed to water, allowing the water molecules to assume the inter-unit positions. Thus, montmorillonite minerals, also known as smectites, tend to inflate, or swell, in the presence of water. Montmorillonites are known for their great stickiness, plasticity, and unfired ("green") strength.

Montmorillonite minerals are distinguished from kaolins by their weaker inter-unit bonding forces. In montmorillonites, adjacent triple-layer units are each terminated by silica layers, so no hydroxyl bonding like that in the kaolin minerals

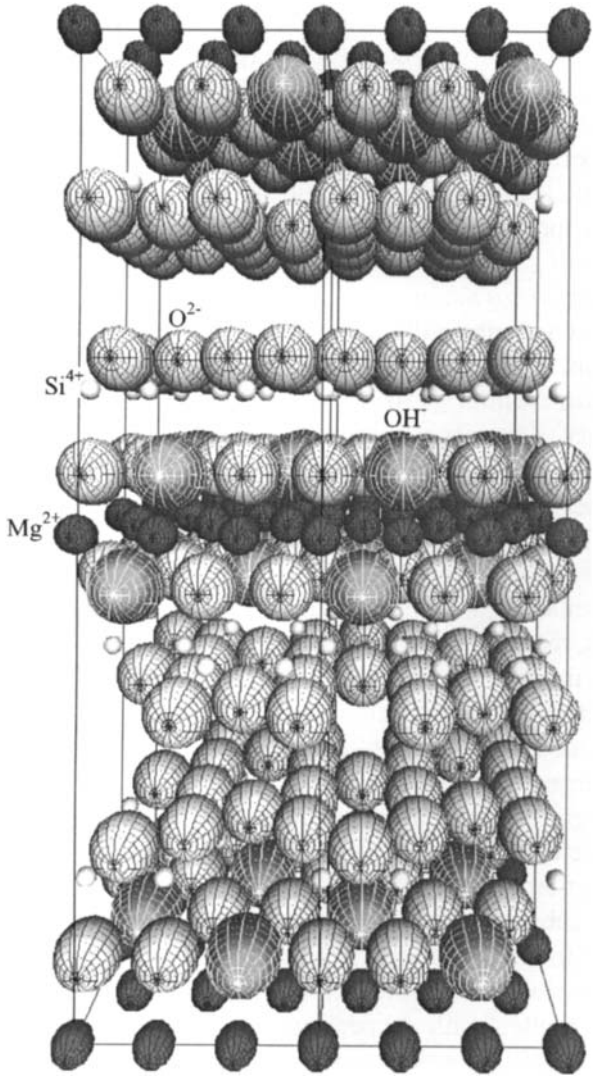


Figure 7. The structure of talc. Talc has a similar structure to pyrophyllite, in which Mg^{2+} replaces Al^{3+}, and additional Mg^{2+} ions are placed in the Mg^{2+} sheets to maintain space charge neutrality.

occurs, and units are held together solely by relatively weak van der Waals forces. Water molecules may easily force these weakly-bonded layers apart, causing the swelling phenomenon observed in montmorillonite minerals upon exposure to water. Weak bonding also results in the ready cleavage of these layers, accounting for their "soapy" texture. Macroscopically, montmorillonite minerals occur as very fine, plate-like particles, typically less than 50 nm in diameter with thicknesses of about 2 nm, which approaches the unit cell dimension in that direction [7,8].

2.2.2. Thermal analysis of the montmorillonite minerals

DTA traces of two montmorillonite minerals are shown in Figure 8. Due to the appreciable amount of water that montmorillonite minerals can adsorb, the endotherm with maximum at ~150 °C, indicating the loss of adsorbed water, has a relatively large area. The loss of adsorbed water in montmorillonite minerals may often take the form of a double endotherm (montmorillonite I in Figure 8): one endotherm indicates the loss of surface-adsorbed water and the other denotes the loss of water from hydrated exchangable cations [7]. An endothermic dehydroxylation reaction then occurs at ~600 °C, producing an amorphous mass containing oxides of silica, alumina, and the substitutional cations. Much less heat (~2.1 kJ mol^{-1}) is required for the removal of structural hydroxyl groups from montmorillonite than that required for kaolinite (~150 kJ mol^{-1}) [7], which is manifested as smaller dehydroxylation endotherm areas for montmorillonite. The exotherm with onset at ~900 °C is of low intensity relative to the intensities of water-loss endotherms. It represents the transformation of the amorphous material to a spinel structure. With increasing temperature, this phase subsequently converts to mullite and rejected silica glass, after which the glass phase may crystallize to cristobalite at higher temperatures, as in the kaolin minerals.

Different cation substitutions in the formation of montmorillonite minerals result in much diversity in their thermal behavior. For beidellite, a montmorillonite mineral with a high aluminum content, the dehydroxylation endotherm is similar to that of montmorillonite, with a peak temperature of ~550-600 °C, but the crystallization exotherm is not detectable [11,12] (Figure 8). The presence of iron in nontronite strains the lattice due to the larger size of Fe^{3+} relative to Al^{3+}, substantially lowering the dehydroxylation endotherm peak temperature relative to that of montmorillonite (Figure 8), to the temperature range of ~400-500 °C.

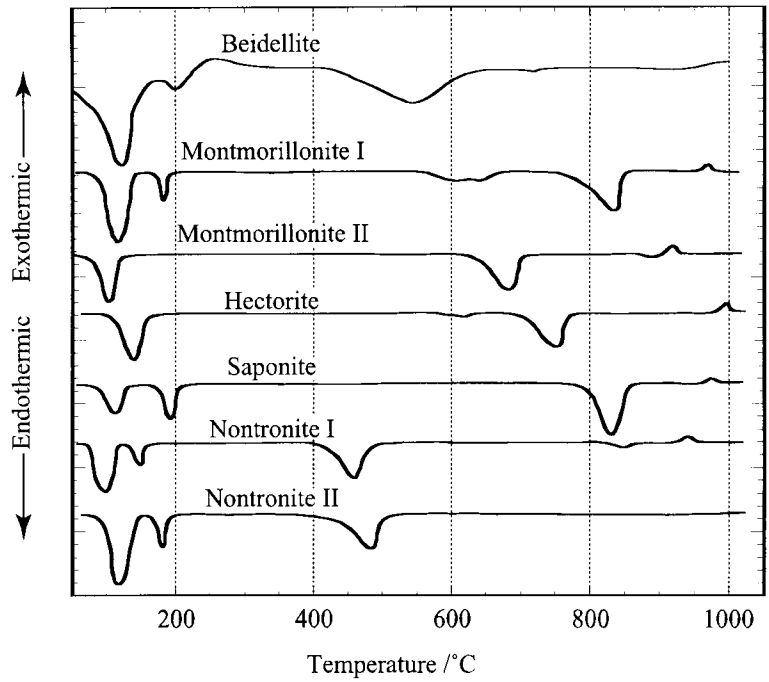


Figure 8. DTA curves of montmorillonite specimens. Montmorillonite I originates from Otay, California; montmorillonite II from Upton, Wyoming; hectorite from Hector, California; saponite from Fichtelgeb, Germany; nontronite I from Harz, Germany; and nontronite II from Garfield, Washington [9]. The beidellite trace is from a different source [11,12].

Nontronite can also display an additional, small exotherm with onset at ~370 °C corresponding to oxygen uptake as Fe^{2+} converts to Fe^{3+}. The rare montmorillonite minerals, saponite and hectorite, dehydroxylate at higher temperatures than nontronite (Figure 8). Shifts in the exothermic crystallization peak positions may be attributed to the types and amounts of the substitutional cation. For example, the introduction of magnesium cations into the pyrophyllite structure may result in the crystallization of cordierite ($Mg_2Al_3(AlSi_5O_{18})$) solid solution and periclase (MgO), along with the expected mullite and cristobalite.

The alkali base-exchange cations affect the thermal behavior of montmorillonite minerals, as shown by the TG traces in Figure 9. Exchangeable cations, absorbed between units, hydrate (attract water molecules) to varying extents. Decreasing alkali cation sizes (e.g. $K^+ > Na^+ > Li^+$) result in greater binding forces, in turn

facilitating greater concentrations of inter-unit water and correspondingly larger associated mass losses. A sample with an alkaline earth (2+ charge) exchangeable cation such as Mg^{2+}, results in a larger and more prolonged mass loss, to the point in which it encroaches on the temperature range of dehydroxylation.

2.3. Illite and mica minerals

2.3.1. Structure of the illite and mica minerals

The mica minerals are accessory minerals frequently found in clay deposits. Similar to the montmorillonites, micas are formed by cation substitutions for the aluminum and silicon atoms in pyrophyllite or talc, producing charged triple-layer unit structures.

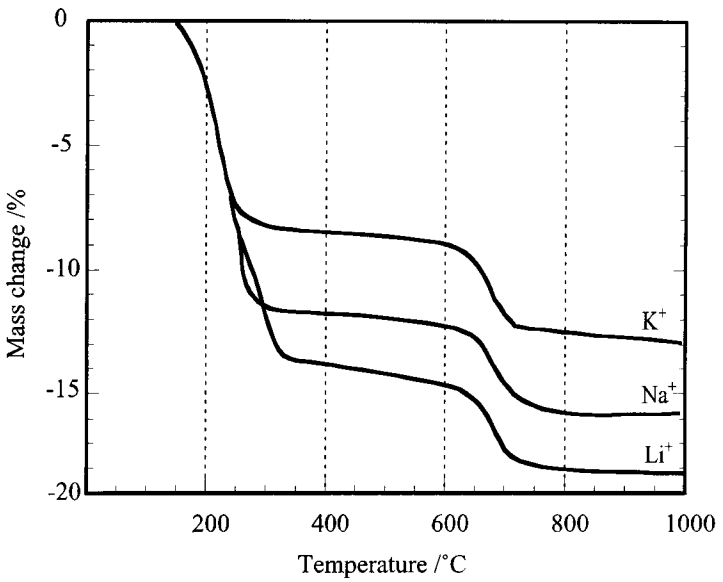


Figure 9. TG curves for potassium, sodium, and lithium montmorillonites [10].

Muscovite ($KAl_3Si_3O_{10}(OH)_2$, Figure 10), also called potash mica, the most common mica structure, forms with an aluminum atom substituting for one of every four silicon atoms in the pyrophyllite unit, giving the unit a negative charge. This charge is balanced by the addition of non-exchangeable potassium ions which reside between, and chemically bond to, oxygens in the two adjacent silica layers. These potassium ions hold the triple-layer units together with ionic bonding forces,

instead of the weaker van der Waals forces responsible for binding the units in montmorillonite mineral structures.

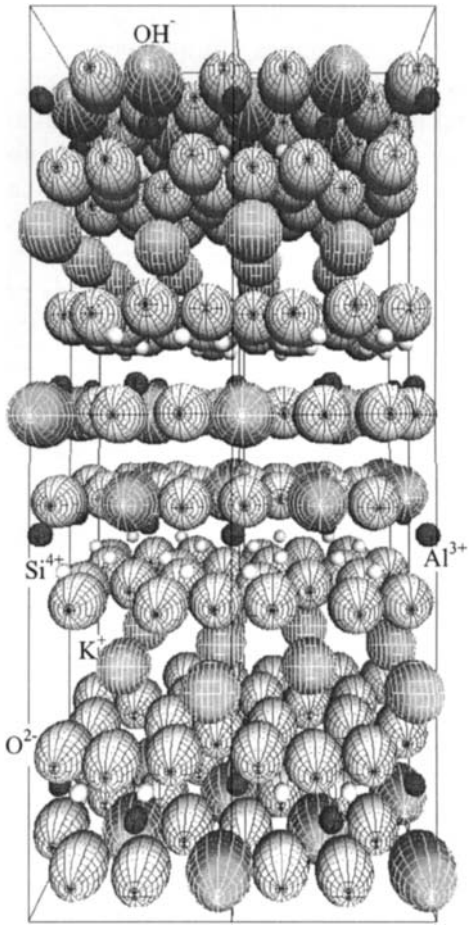


Figure 10. Crystal structure of muscovite: $KAl_3Si_3O_{10}(OH)_2$, a mica mineral.

With sodium acting as the charge-balancing cation in place of potassium, the mica mineral becomes paragonite, with chemical formula $NaAl_3Si_3O_{10}(OH)_2$. When one of every two silicon atoms in the pyrophyllite structure is replaced by an aluminum atom, and the doubly-charged calcium cation bonds silica layers together, the mica mineral, margarite, forms with formula $CaAl_4Si_2O_{10}(OH)_2$. Micas derived from the pyrophyllite structure are known as dioctahedral micas. Similar substitutions and interlayer bonding of charge-balancing cations in the talc ($(Mg_3Si_4O_{10}(OH)_2$) structure result in the formation of other mica minerals with fluxing properties, known as trioctahedral micas—examples of which are phlogopite ($KMg_3(Si_3Al)O_{10}(OH)_2$), lepidolite ($KAlLi_2Si_4O_{10}$ $(OH)_2$), biotite ($K(Mg, Fe, Mn)_3Si_3AlO_{10}(OH)_2$), and zinnwaldite ($K(Li, Fe, Al)_3(Si, Al)_4O_{10}(OH)_2$). Although the interlayer chemical bonds provided by the charge-balancing cations are stronger than van der Waals forces, they are still weaker than the bonding within the units, explaining the easy cleavage of micas, and their typical occurrence as large, thin flakes. In clay deposits, however, mica particle diameters tend to be smaller, about 0.5 μm [2]. Micas have very low plasticity and a low base-exchange capacity, resulting in practically no water adsorption or swelling.

The illite minerals comprise the third class of clay minerals. Illite mineral structures are formed from the mica mineral structures through the replacement of some of the inter-unit cations (potassium, sodium, or calcium) by hydronium ions (OH_3^+). Illite minerals, also known as sericites, sedimentary micas, or hydrous micas, include hydromuscovite, an illite similar to muscovite, and amersooite, an illite similar to biotite, with structural differences due to hydronium ions substituting for some of the potassium ions, assuming the charge-balancing role. Other illitic minerals include brammalite, an illite containing sodium, and glauconite, an illite containing iron. These are found, with particle diameters as large as 36 μm, and as small as 0.1 μm [8]. They possess little plasticity, and both illites and micas cause fired clays to have a low refractoriness, because of their high alkali content, producing an appreciable volume percentage of glassy phase in the fired body.

2.3.2. Thermal analysis of the illite and mica minerals

Figure 11 shows the DTA traces of three mica minerals. Micas typically dehydroxylate, at comparatively high temperatures (in the range of 850-920 °C). The activation energy for muscovite dehydroxylation is about 226 kJ mol^{-1} [5], larger than that for both kaolinite and montmorillonite. A small endotherm may be present at ~100 °C, indicating the loss of a small amount of adsorbed water. Micas

that contain iron, such as biotite and zinnwaldite, show an exotherm between 300-500 °C, corresponding to the oxidation of Fe^{2+}. This exotherm is less intense for zinnwaldite, which contains substantially less divalent iron.

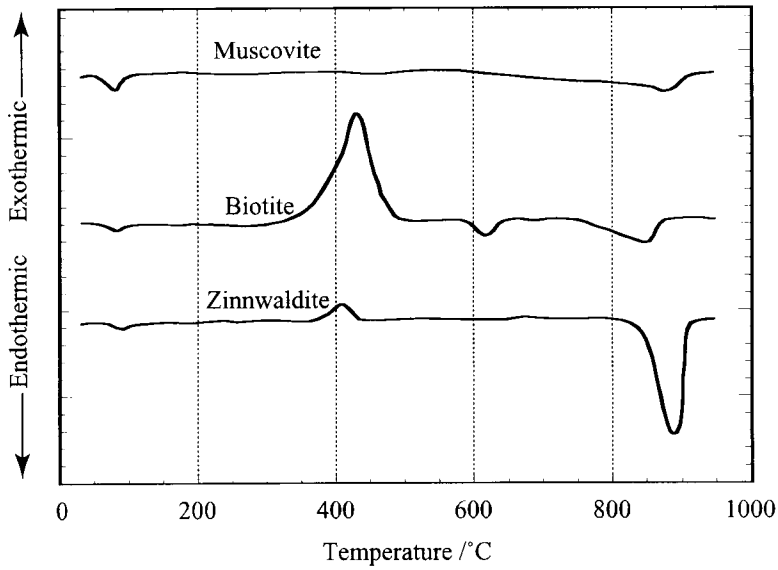


Figure 11. DTA traces of three micas [9].

Illites generate a more intense endotherm for the loss of adsorbed water at 100-300 °C, as the typical DTA trace for a dioctahedral illite in Figure 12 shows. This endotherm includes the loss of absorbed water loosely bound on particle sufaces and between the units. Illites have lower peak temperatures than those of mica minerals for the first endotherm, indicating that dehydroxylation (500-650 °C), and the loss of structural water in illite minerals, occurs over a wide temperature range, typically indicated by two or more distinct endotherms. Illites evolve more water than micas upon heating (as they possess inter-unit water), though they still possess much less total (absorbed and structural) water than do the kaolin minerals, as exemplified by the TG curves of Figure 13. Illites undergo a final dehydroxylation, represented by an endotherm at approximately the same temperatures as those in mica minerals, between 850 and 940 °C. A crystallization exotherm generally directly follows the decomposition, forming the *s*-shaped endothermic-exothermic characteristic at ~900 °C (Figure 12). High temperature structural changes (not shown) appear as small endotherms following the dehydroxylation and

decomposition endotherm in DTA traces for the mica minerals. These indicate the transformation of spinel compositions to phases which may include mullite, corundum (Al_2O_3), leucite ($KAlSi_2O_6$), and silicate glass [5][16].

Figure 14 shows the thermal behaviors of illites of varying compositions. DTA trace *A* represents the most typical thermal behavior of a dioctahedral illite, like that in Figure 12. Curves *B* and *C* exemplify changes in dioctahedral illite thermal behavior that may be induced by differences in chemical composition. Curve *D* illustrates the thermal behavior of a typical trioctahedral illite, which has a larger fraction of dehydroxylation occurring at higher temperatures than dioctahedral illites. This effect may be predicted since the dehydroxylation onset temperature of the pyrophyllite structure, on which the dioctahedral illite structures are based, is lower (by ~300 °C) than that of talc, the structure on which the trioctahedral illites are based (Figure 15).

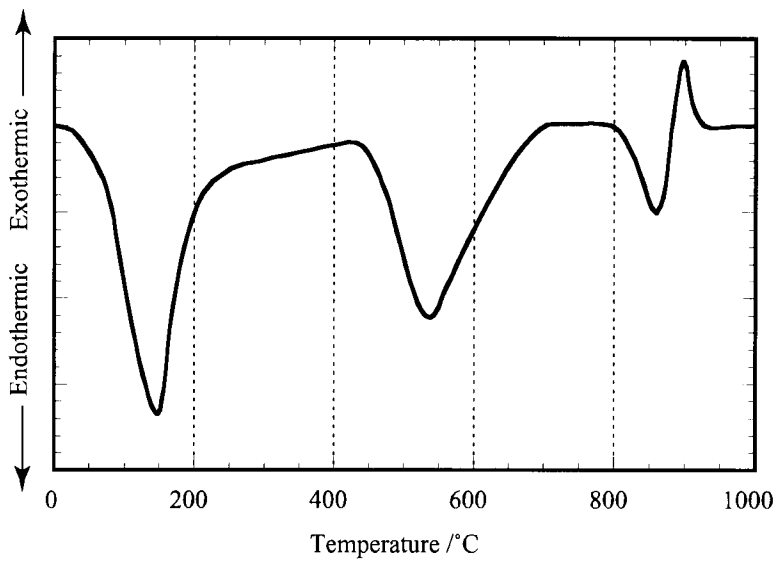


Figure 12. DTA trace for a dioctahedral illite specimen [5].

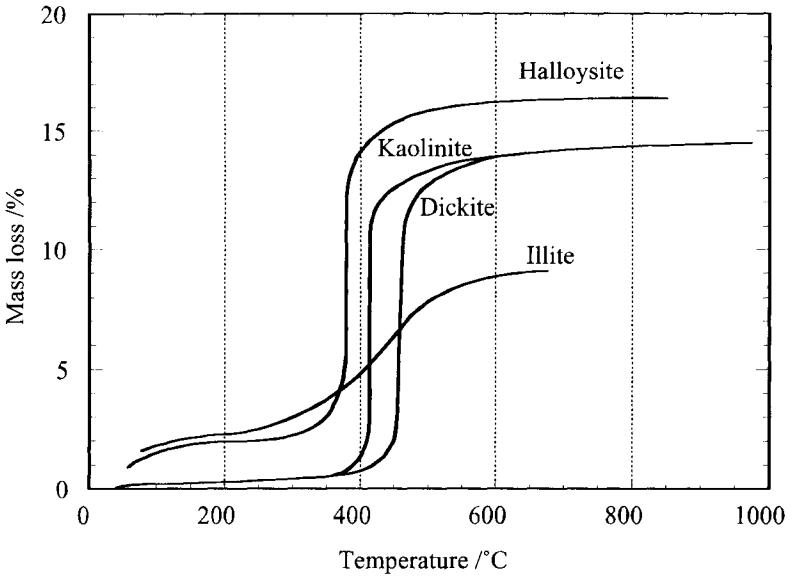


Figure 13. TG traces for three kaolin minerals and an illite mineral [13].

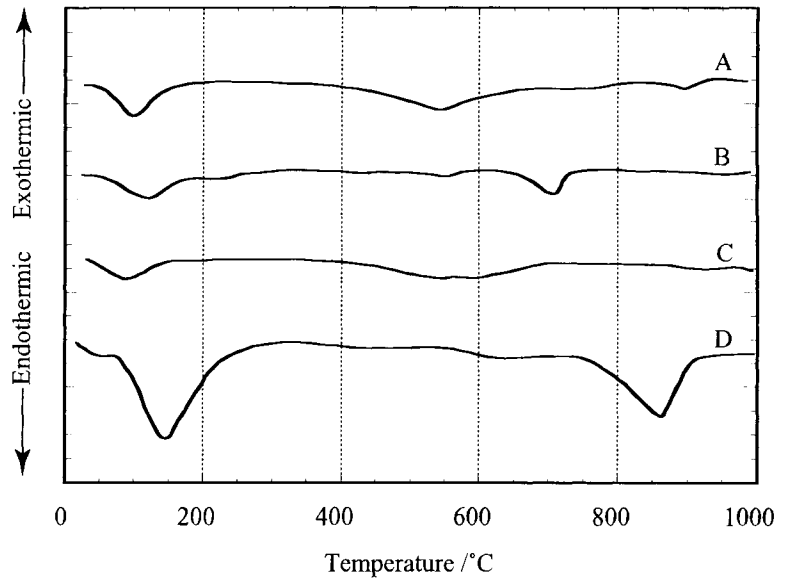


Figure 14. DTA traces of three dioctahedral illites (A, B, and C) and a trioctahedral illite (D) [12].

2.4. Chlorites and vermiculites

2.4.1. Structure of the chlorite and vermiculite minerals

Although considered accessory (e.g. mica) rather than clay (e.g. kaolin, montmorillonite, and illitic) minerals, chlorites and vermiculites are sheet-silicate structures commonly found in clays deposits. Like some montmorillonites, micas, and illites; most chlorite minerals are derived from the talc structure, with lattice substitutions producing a negative charge, such as an aluminum ion replacing one of every four silicons in a layer. Rather than achieving charge neutrality through the presence of base-exchange cations, as in the montmorillonite mineral structures, or through forming chemical ionic bonds between cations and silica layers in adjacent units, as in the mica and illite mineral structures, the chlorites obtain charge neutrality through the insertion of a layer of $Mg_2Al(OH)_6^+$. This layer is a modification of a brucite structure ($Mg(OH)_2$) with one third of the magnesium ions replaced by aluminum ions. The structure of such chlorites consists of laminations of the modified talc units and modified brucite layers, yielding a general formula for the chlorites of $Mg_5Al_2Si_3O_{10}(OH)_8$. With additional cation substitutions, such as aluminum for silicon and iron for magnesium, different chlorite minerals are formed. Substitution of iron ions for aluminum forms the most abundant chlorite, penninite ($Mg_5(Al,Fe)(Al,Si)_4O_{10}(OH)_8$).

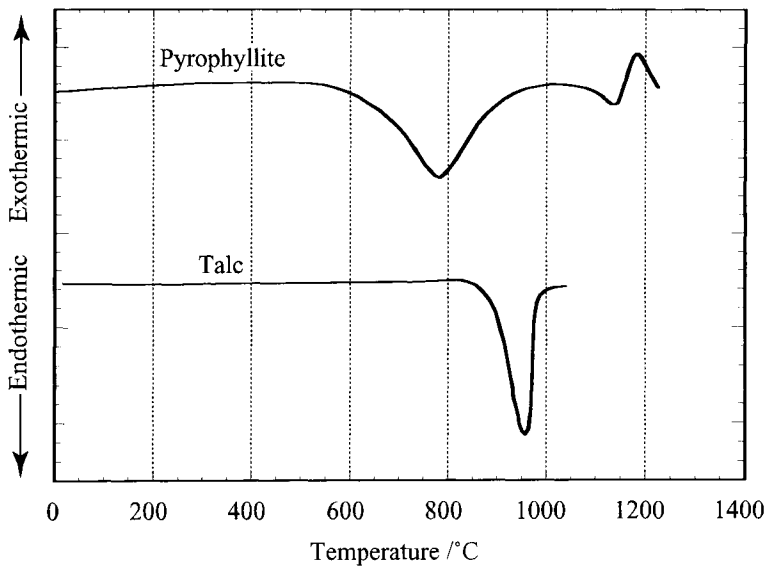


Figure 15. DTA traces of pyrophyllite and talc [12].

Vermiculite structures resemble those of the chlorite minerals, except that hydrated magnesium cations, rather than modified brucite layers, provide charge balance for the negatively-charged modified talc units, yielding the chemical formula $(Mg,Fe)_3$ (Al,Si_4) $O_9(OH)_8 \cdot 3.5H_2O$ [5]. The region between modified talc units may be envisioned as upper and lower layers of water molecules adjacent to modified talc unit surfaces, with exchangeable Mg^{2+} (or other) cations located between these layers [14]. Vermiculite structures have some substitution of Fe^{2+} for Mg^{2+}, and Al^{3+} for Si^{4+}. The vermiculite structure sustains a great deal of inter-unit water, causing swelling, but to a lesser extent than the montmorillonites. Exfoliation is a unique property of the vermiculites, in which during rapid heating, structural layers rupture from the sudden release of large amounts of contained water. This results in volume expansions by amounts of 18-25 times the original volume [15] (Figure 16), giving vermiculites value as thermal insulation [5]. Both chlorites and vermiculites occur as plate-like flakes that are softer than mica, and occur as particles whose sizes tend to be large relative to those of the kaolin and montmorillonite minerals.

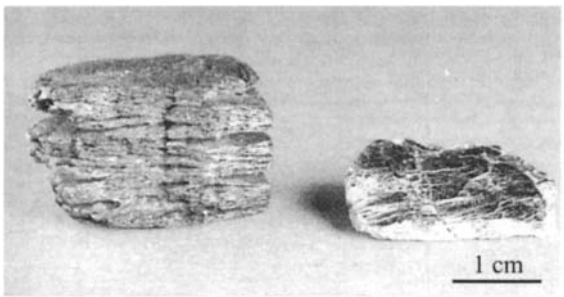


Figure 16. Expanded (left) and natural (right) vermiculite [15].

Chlorite crystals are of a green tint (from which the name chlorite is based). Vermiculites tend to be of a darker color (brown, red, or black), than the buff-colored montmorillonites and white-colored kaolin minerals. Illites and micas are found in a wide range of light and dark colors.

2.4.2. Thermal analysis of the vermiculite and chlorite minerals

The wide range of compositions of chlorite minerals result in a correspondingly wide range of thermal characteristics (Figure 17). Typically, chlorites produce two endotherms, the first attributed to the liberation of hydroxyl groups associated with

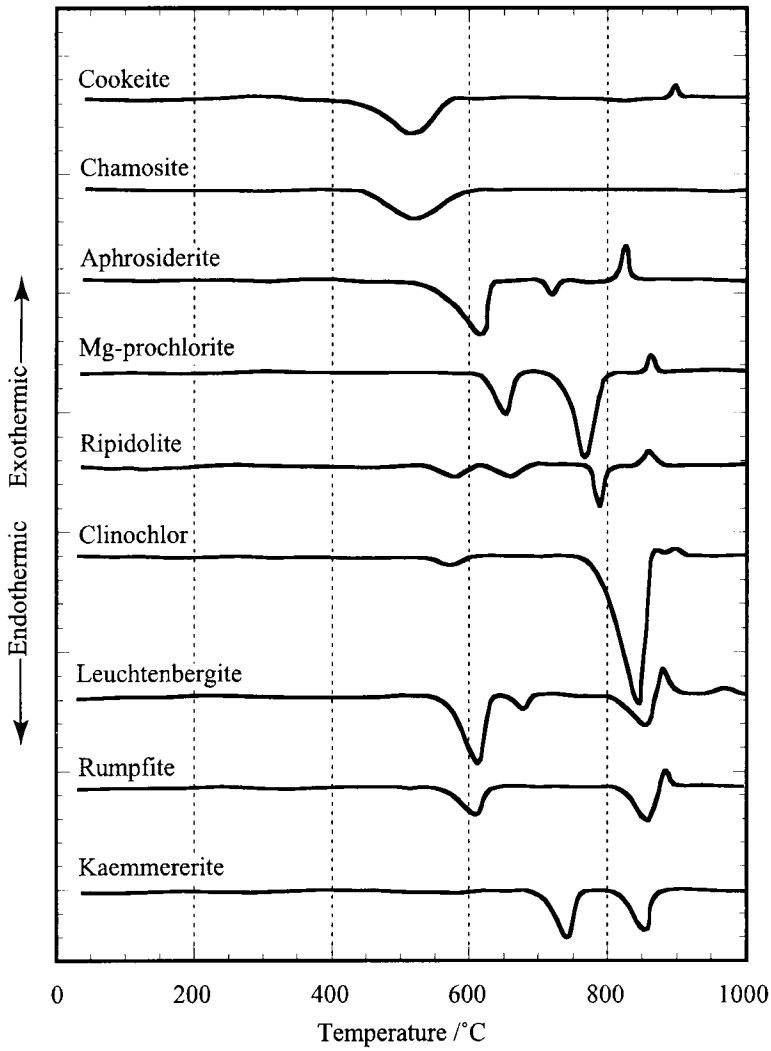


Figure 17. DTA traces of various chlorite minerals [9].

the modified brucite layers between 500 and 700 °C, and the second produced by the liberation of hydroxyl groups from the modified talc layers at ~800 °C. An exotherm at ~900 °C follows this second endotherm, indicating crystallization to products such as spinel (e.g. $MgAl_2O_4$) and olivine (e.g. forsterite Mg_2SiO_4). A low temperature endotherm for the loss of adsorbed water is not observed in

chlorites, unless sufficiently ground (see following section), creating weakly bound, adsorbed water groups that are released to form an endotherm at ~110 °C. Increased iron contents result in decreased dehydroxylation temperatures, as do increased amounts of aluminum substitution for magnesium in the modified brucite layer. Extensive aluminum and iron substitutions cause the two dehydroxylation endotherms to merge into one.

DTA traces of vermiculites, as shown in Figure 18, display a series of endotherms at low temperatures (0-350 °C) indicating the loss of adsorbed water, as well as multiple higher-temperature dehydroxylation endotherms. Loss of

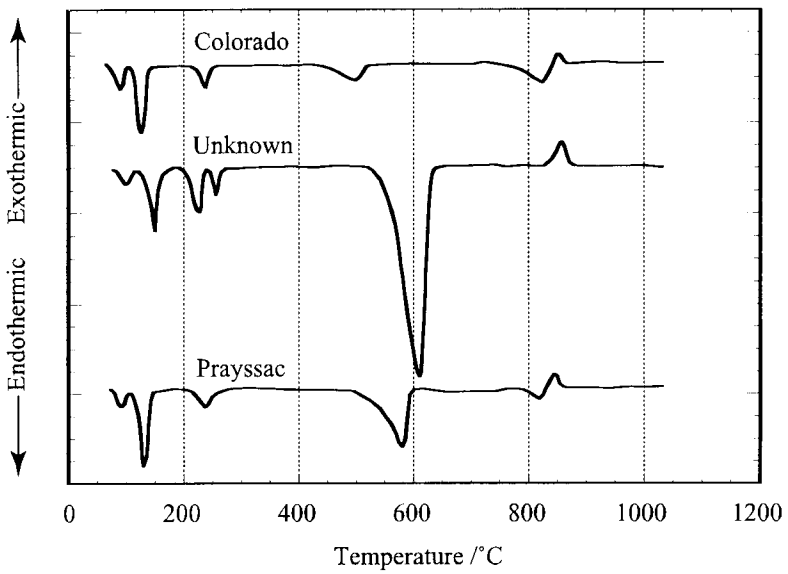


Figure 18. DTA traces of three vermiculite specimens from deposits in Prayssac, France, an unknown location, and Colorado [9].

adsorbed water occurs in several steps due to the laminated form of the minerals and the large amount of inter-unit water [16]. At high temperatures, DTA traces of vermiculites exhibit an *s*-shaped endotherm/exotherm in the temperature range 800-900 °C, indicating a final surge of dehydroxylation, followed by crystallization to products such as enstatite ($MgSiO_3$). Some vermiculite samples may produce additional endotherms at even higher temperatures, indicating loss of additional structurally bound water [16]. The wide variations in vermiculite compositions yield many differences in dehydroxylation endotherm shapes and onset

temperatures; for example, the presence of more trivalent iron cations causes the dehydroxylation temperatures to decrease.

Exchangeable cation types also have a significant influence on the thermal behavior of vermiculite minerals, as seen in Figure 19, as with the montmorillonite minerals. When Mg^{2+} is the exchangeable cation, adsorbed water loss usually occurs in three steps, producing three endotherms, although these may often be superimposed rather than distinct. Ca^{2+}, Sr^{2+}, Ba^{2+}, Li^{+} and Na^{+} cations also produce a series of superimposed dehydration effects. With large monovalent cations, K^{+}, Rb^{+}, and Cs^{+}, absorbed water-extraction endotherms are of comparatively low intensity.

3. INSTRUMENTAL EFFECTS

Hampering more useful cataloging of thermal analysis data of minerals are variations in traces caused by different instrument designs, heating rates, thermocouple placement, etc., from one investigator to the next. Discussed presently are the marked effects on the thermal signatures of clay and accessory minerals imposed by variations in specimen preparation, size, and environment.

As shown in Figure 20, with increased time of dry grinding (via dry ball milling), the dehydroxylation onset temperatures of dickite decrease along with the endotherm intensities. Abrasion during ball milling strains, i.e. amorphizes, atom lattice positions near particle surfaces. This higher-energy structural state more readily undergoes dehydroxylation, resulting in its occurrence at lower temperatures. At first (2 h), some of the particles (partially) amorphize while others remain unchanged, producing the overlapping endotherms, corresponding to the structural water removal of the amorphous (strained) and unstrained materials. Smaller particle sizes also contribute to the lowering of the dehydroxylation temperature, since smaller sizes result in less bulk material through which the structural water must escape. Eventually, only the lower temperature dehydroxylation endotherm is apparent (6 h). With grinding in excess of 15 h, the concentration of strained regions continues to increase and particle size decreases until the dehydroxylation endotherm disappears altogether, implying that dehydroxylation had essentially occurred during grinding.

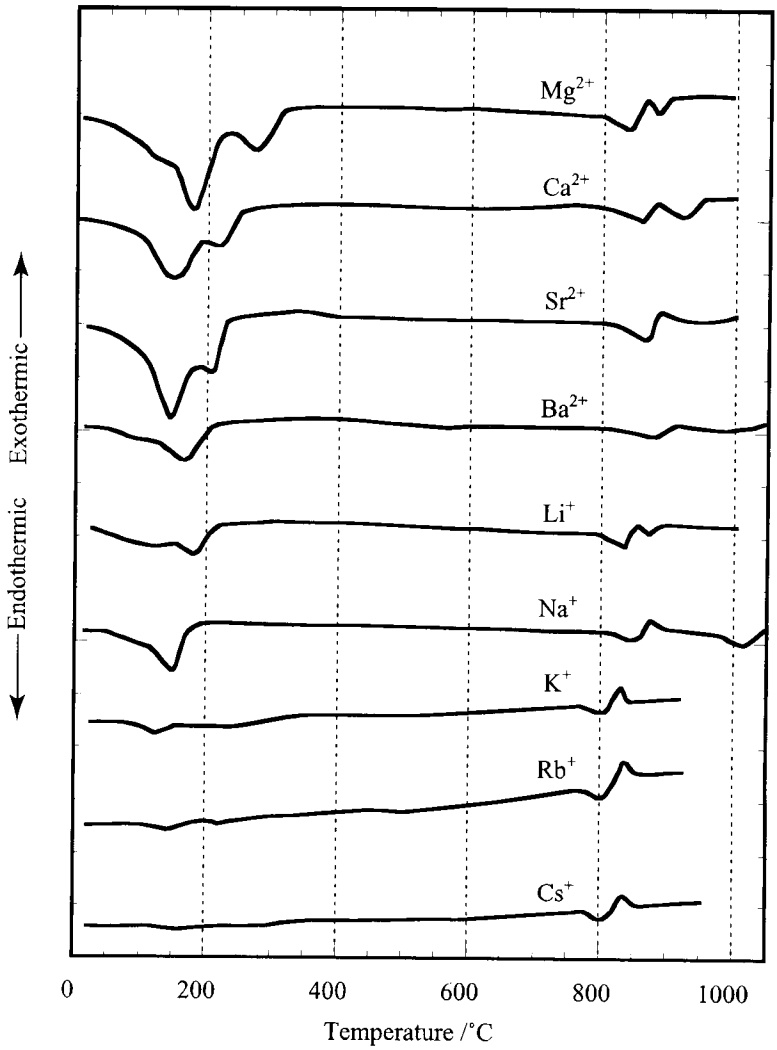


Figure 19. DTA traces of vermiculites saturated with the indicated exchangeable cations. Mg^{2+}, Ca^{2+}, Sr^{2+}, Ba^{2+}, Li^{+}, Na^{+} vermiculite samples are from a West Chester, PA deposit, while K^{+}, Rb^{+}, and Cs^{+} samples are from a Macon County, North Carolina deposit [17].

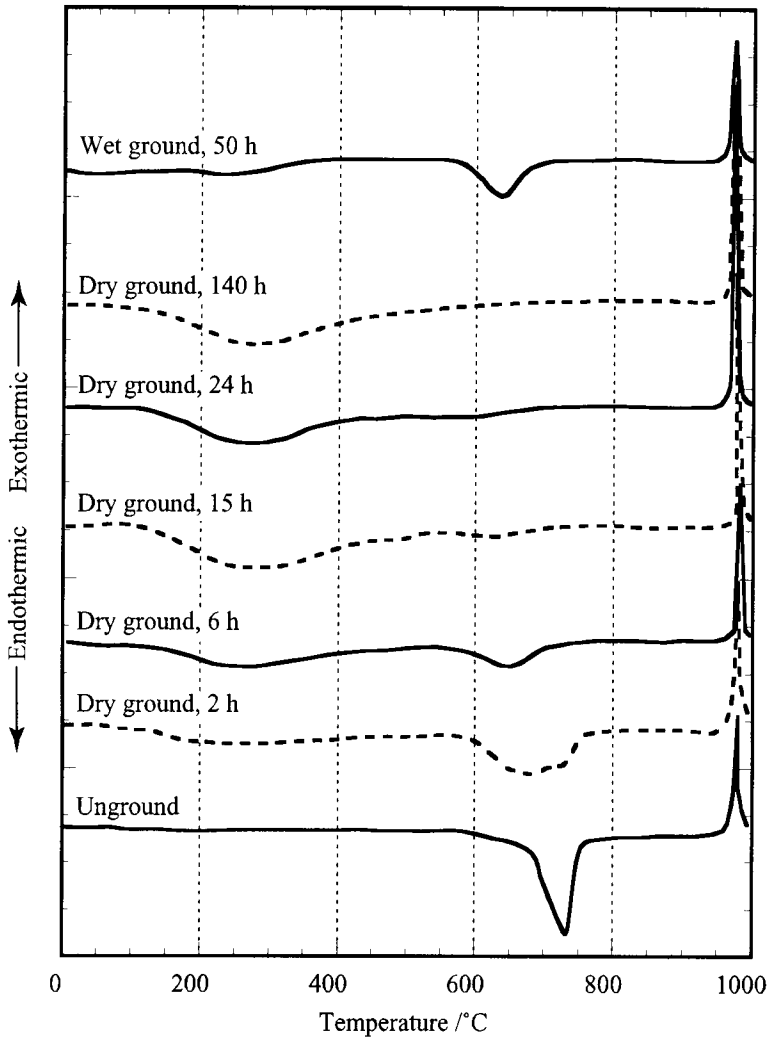


Figure 20. DTA traces for dickite specimens subjected to grinding to different extents [18].

The gradual disappearance of the dehydroxylation endotherm with increased grinding time occurs concurrently with the formation and growth of a broad endotherm in the 100 to 400 °C range, the temperature range in which adsorbed surface water is removed. The increase in intensity of this endotherm with grinding time corresponds in part to the increased surface area of smaller particles, as well as the release of increasing concentrations of water located between units (having taken those positions to shield the net charge developed in the deformed units). The broad range of bond strengths with which this water is attached to particle surfaces and unit interfaces, due to local distortions, is responsible for the wide breadth of these endotherms. With increased grinding time, the spinel-formation exotherm at ~980 °C also increases in intensity, due to the greater extent of disorder of the dehydroxylized amorphized particles (facilitating more energy release as these regions crystallize). Wet grinding, which results in particle size reduction without amorphization, also produces a small broad endotherm at ~120 °C, due to increases in water adsorption by the increased surface area of smaller particles. The dehydroxylation endotherm also shifts to lower temperatures with wet grinding, since smaller particle sizes ease the escape of structural water. This endotherm also broadens due to the greater range of particle sizes produced by the grinding process. Because the structure of the wet ground dickite remains the same as that of the un-ground material, the exotherm at 980 °C is of similar intensity to the un-ground mineral.

Figure 21 shows the effect of vapor pressure on the dehydroxylation endotherm for halloysite. Water vapor can more easily diffuse away from an uncovered container, forcing water vapor to be more rapidly evolved from the halloysite in effort to maintain the equilibrium vapor pressure for a given temperature. Thus, dehydroxylation reaches completion earlier, resulting in a lower endotherm peak temperature than that from using a covered sample. Figure 22 demonstrates the effect of sample mass on the dehydroxylation endotherm and spinel crystallization exotherm in kaolinite. More massive samples result in endotherms and exotherms of larger areas. Broadening of dehydroxylation endotherms occurs with increasing sample mass, since a distribution of times are required for the diffusion of water vapor out of various depths of the sample. The constriction to the diffusion of water vapor away from the clay particles with increasing sample mass imposes an increased water vapor partial pressure, which suppresses dehydroxylation in interior regions of the sample to higher temperatures. This correspondingly causes the dehydroxylation endotherm peakss to shift to higher temperatures. Crystallization exotherms narrow with increasing sample mass as specimens self-heat, accelerating the crystallization process.

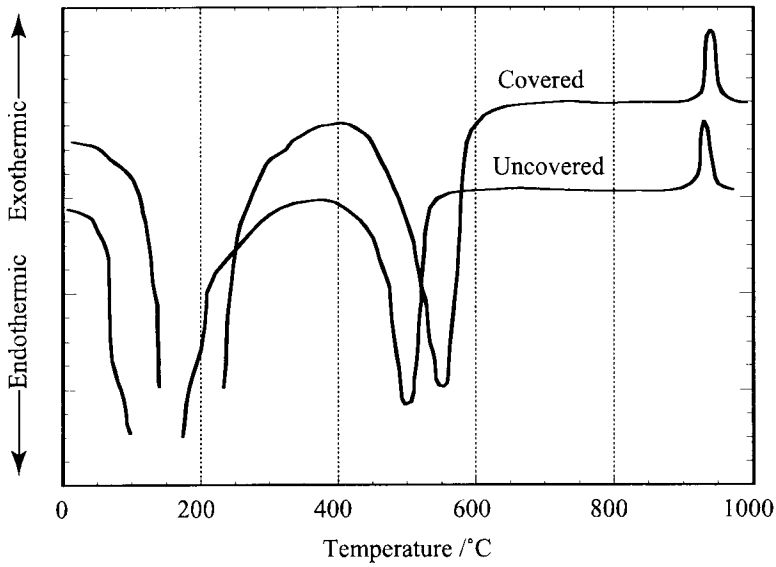


Figure 21. DTA traces of halloysite with covered and uncovered sample chambers [19].

4. CLAY DEPOSITS

4.1. Introduction

During the earth's long evolution, igneous rock solidified from the molten magma and was forced to the surface. On land masses, these rocks are primarily granite (mostly feldspar, e.g. orthoclase: $KAlSi_3O_8$ and anorthite: $CaAl_2Si_2O_8$, with some quartz and mica), while under the oceans these rocks are primarily basalt (mostly iron-bearing minerals from magma originating more from the center of the earth (pyroxene: $(Mg,Fe)SiO_3$, olivine: $(Mg,Fe)_2SiO_4$, and hornblende: $(Ca,Na,K)_{2-3}(Mg,Fe,Al)_5Si_6 \cdot (Al,Si)_2O_{22}(OH,F)_2$, with a small concentration of feldspar). Clay minerals were formed through the hydrothermal decomposition of igneous rock. For example, kaolinite formed through hydrolysis ($KAlSi_3O_8 + H_2O \rightarrow HAlSi_3O_8 + KOH$), desilication ($HAlSi_3O_8 \rightarrow HAlSiO_4 + 2SiO_2$), and hydration ($2HAlSiO_4 + H_2O \rightarrow Al_2Si_2O_5(OH)_4$) of potassium feldspar, leaving residual potash (K_2CO_3) and silica, without alteration of the surrounding quartz and mica. The specific clay minerals which formed by decomposition were largely dependent on atmospheric conditions; for example, warm humid conditions favored the formation of kaolin

minerals, while montmorillonite minerals tended to form in cooler, drier environments.

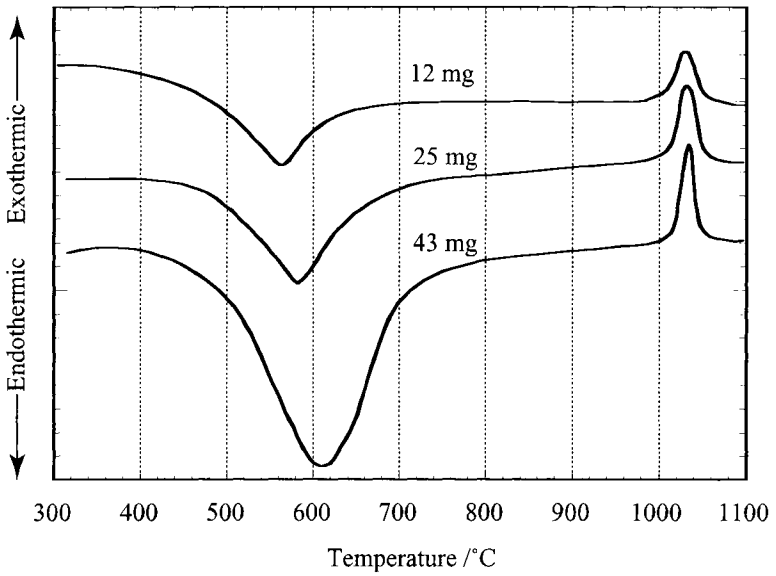


Figure 22. DTA traces for kaolinite specimens of different masses [20].

Residual clays consist of clay minerals deposited at the location of their formation, and are usually present as a mixture with undecomposed parent rock. Sedimentary clay deposits were created from clay minerals which became suspended in water, and accumulated a large concentration of impurity and accessory minerals, as well as organic materials, during their transport to settling points as stratified layers at the bottoms of lakes and rivers. Because their formation required suspension in and transport through water, sedimentary clays tend to consist of finer particles than residual clays. Typically, the impurities in such a deposit are of a significantly larger particle size than that of kaolinite, and may easily be removed during processing.

Clay minerals may constitute less than 35% of a clay deposit, with the balance consisting of accessory minerals such as those described above, as well as quartz, feldspars, iron minerals (e.g. limonite $Fe_2O_3 \cdot nH_2O$), calcite ($CaCO_3$), dolomite ($CaMg(CO_3)_2$ solid solution), gypsum ($CaSO_4 \cdot 2H_2O$), titania, and organic matter (e.g. lignite, waxes, carbonaceous matter, and humic acid derivatives). The types and amounts of these components that are present determine the composition and

properties of the clay deposit. The thermal properties of each component material contribute to create the composite thermal behavior of the clay deposit.

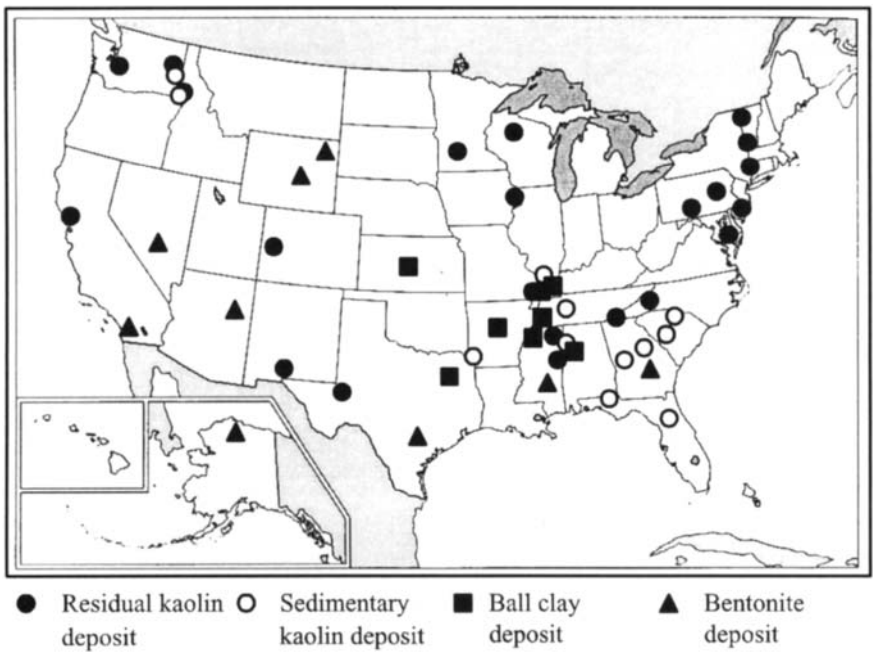


Figure 23. U. S. deposits of china clays, ball clays, and bentonites [1,22].

Clay deposits, henceforth referred to simply as "clays," are typically categorized based on the period in earth's history in which they were formed. Important types of clays for traditional ceramic applications include china clays, ball clays, bentonites, fireclays, and brick clays. Figure 23 depicts the main locations of china clay, ball clay, and bentonite deposits in the United States. A smaller percentage of clay deposits are residual clays (generally china clays); most are sedimentary clays.

4.2. China clays

China clays (interchangeably referred to as kaolins) are predominantly residual clays; they can be extracted and processed to a very pure form (i.e. consist largely of clay minerals). Residual kaolins are most commonly mined by impinging high-

power water or steam jets on natural deposits, causing clay particles and accessory minerals to be carried by a water stream to the bottom of a pit, where pumps transfer the material to settling tanks. After coarse clay and impurity minerals settle out, the remaining suspension of fine clay and impurity mineral particles are separated according to size by a hydrocyclone or centrifuge. This produces material masses with particle sizes typically under 30 μm, and clay minerals comprising 80-90% or more of the mineral mixture, with main contaminants being quartz and fine-grained micas [23]. This high purity clay usually fires to a very white color. Water removal from the clay is performed through evaporation or filter pressing. The comparatively coarse particle size (relative to sedimentary kaolins) and narrow particle size distribution confers a low plasticity and green (unfired) strength to china clay, relative to clays containing finer clay mineral particles, but also results in less drying shrinkage.

Sedimentary kaolins, characterized by finer particle sizes, tend to be more plastic than residual kaolins, and contain more organic matter from vegetation encountered during transport. Since the kaolinite constituent in kaolins has a low base-exchange capacity, kaolins are easily deflocculated (particles are dispersed in water by additives which substitute ions in solution near particle surfaces, causing electrically repulsive forces to form between particles, preventing their close approach). China clays, because of their low inorganic mineral impurity content, have a high firing shrinkage (6-17% at 1300 °C), and thus are rarely used alone in the fabrication of ceramic parts [7]—quartz and feldspar are added as discussed previously. Kaolin deposits in addition to those in Figure 23 are found in various South American countries, England, France, Germany, Czechoslovakia, China, and Japan.

4.3. Ball clays

Ball clays are always sedimentary clays, with finer particle sizes than those of kaolins, and contain a significant concentration of organic material. Their composition varies widely, so that they are distinguished on the basis of their location and the geological age of the deposit. Ball clays contain kaolinite as the main clay mineral, but the finer kaolinite mineral particles found in ball clays tend to be of the disordered kaolinite variety, rather than the well-ordered kaolinite particles found in china clays. Additionally, ball clays may contain small amounts of other clay minerals such as montmorillonite and illite, along with substantial amounts of fine-grained impurities. Typical impurities residing in ball clays include quartz, mica, titania (anatase), and iron sulfide (pyrite, marcasite). The finer particle size and greater impurity contents of ball clays, relative to kaolins,

provide the advantages of higher plasticity (more particle surfaces for water absorption, facilitating particle sliding) and thus enhanced workability, and higher green strength (finer particles become more intertwined), but induce high drying shrinkages (up to 15% [24]) and can be very difficult to dry without cracking of the ware. Also, due to the impurity content of ball clays, they usually do not fire to the very white color of kaolins, but to a less translucent white or cream color. However, the impurity constituents iron oxide and titania improve firing properties by providing a longer vitrifying range (temperature range over which a liquid phase forms without slumping), while the organic impurities improve casting properties by lowering the viscosity of casting slips. Ball clays contain more soluble salts (such as calcium sulfate) than china clays, and have higher base-exchange capacities, due to the disordered form of the kaolinite, and to the presence of organic matter, which contributes to the base-exchange capacity of the clay. However, ball clays rarely contain the feldspar minerals commonly found in kaolins.

Ball clays display a large variation in impurity clay mineral content, which yields a wide range of compositions and properties. The organic constituents in ball clays, which range from 3-10% and consist mainly of lignite, also impact clay properties, as higher organic matter concentrations yield higher plasticity, green strength, and drying shrinkage. Organic matter, which forms organic anions in alkaline conditions, also aids in the deflocculation of clays (polyanions, complex anions comprised of several atoms, adsorb on the surface of clay particles and increase the charge density) [2][23]. Ball clays are readily deflocculated, as long as soluble salts are not present in sufficient amounts to interfere with deflocculation (soluble salts exert a "crowding effect," causing clay to flocculate and rendering the addition of deflocculants ineffective) [24].

Ball clays are either mined from open pits, as kaolins are, or extracted from underground mining tunnels. The particle sizes of ball clays present a difficulty, since particles are so fine that they may not be filtered to remove impurities after washing in water. Thus, ball clays are either supplied in the as-extracted form, after being left to weather for a time (weathering, or drying under natural conditions, breaks up hard clay, makes the clay more plastic, and promotes chemical processes such as the removal of soluble salts), or after processing through a rotary disintegrator*, producing air-floated clay. Also, ball clay particles do not tend to disperse in water, and the water penetration of densely-packed clumps (i.e. balls) of ball clay that is necessary for the application must be carried

* In a rotary disintegrator, finer particles are gathered and dehydrated through being swept up by a flow of hot air [23].

out with substantial agitation. Ball clays possess less refractoriness than do kaolins, owing to their higher flux content.

Ball clays are not used alone in whitewares, but are typically mixed with other clays and nonplastics (Table 1). The addition of ball clays provides the ceramic body with greater plasticity and green strength, but decreases the whiteness and translucency.

4.4. Bentonites

Clays containing montmorillonite minerals as the primary clay mineral (composed of a minimum of 75% montmorillonite minerals) are known as bentonites. Due to the great interlayer water adsorption (swelling) tendencies of the montmorillonite minerals, bentonites correspondingly tend to swell substantially in response to water. This property is exploited to stop leakage in soil, rocks, and dams [14]. Also owing to the behavior of montmorillonite, bentonites have a very high base-exchange capacity, with sodium acting as the main exchangeable cation. Due to the fine size of montmorillonite minerals, bentonites are very plastic and possess a high green strength, but suffer a very high drying shrinkage. Some common accessory minerals in bentonites include quartz, calcite, iron oxide, lime, magnesia, and feldspars. Bentonite clays are formed through extensive weathering of volcanic glass or volcanic ash.

Because of their large shrinkage, bentonites are typically added to whiteware compositions in very small amounts of about 1-2%, to increase the plasticity/workability and green and fired strength of the less plastic clays that are the primary constituents of the body. Excessive bentonite additions cause cracks to develop in a ceramic body from excessive drying shrinkage. Small amounts of bentonite (2-5%) may also be added to nonplastic materials, such as titania used in the fabrication of electroceramics and alumina for the manufacture of refractories, to induce plasticity for forming, without greatly affecting the dielectric constant or refractoriness, respectively, of the primary materials. Mined in England, Fuller's Earth constitutes another montmorillonite-based clay, which has a high impurity content and calcium as the main exchangeable cation. Like ball clays, montmorillonite-based clays are acquired through both open pit and underground mining methods.

4.5. Fire and brick clays

Brick clays are sedimentary clays whose major constituents are kaolinite and chlorite, along with illite, quartz, and organic matter; most brick clays are distinguished by having high concentrations of iron oxide and calcite. The iron

oxide content of brick clays cause them to fire to a dark red/brown color (firing range: 950-1200 °C). Other such non-white-burning clays are referred to as stoneware clays, used in ceramic tiles in which an esthetically pleasing colored glaze (glass containing crystalline pigment particles) is applied over the exposed surface. Brick clays contain fluxing agents which do not make them suitable for refractory applications.

Fireclays, as well as other clays, correspond to deposits formed during a specific period in earth's history (in this case, the Carboniferous Period [8]). In contrast to the implications of the name, a large proportion of fireclays are not very refractory, and are used in making sanitary fixtures, buff tiles, and building bricks. They are chiefly composed of poorly crystallized kaolinite, mica, and quartz. As with brick clays, their iron oxide content does not make them suitable for use in whitewares. Fireclays, which are used for refractory firebricks, have a high alumina content (up to 40 mass%) and a low concentration of fluxes. Grog (pre-fired material) and quartz are often added to fireclays to minimize firing shrinkage of fireclays. Such refractories will maintain their mechanical integrity up to ~1600°C.

4.6. Thermal analysis of clays

The thermal behavior of clay deposits is a composite of the thermal behaviors of the individual clay, accessory, and impurity minerals, as well as the organic constituents in the clays (DTA traces of some of these minerals, overlaid with selected clay minerals, are shown in Figure 24), in addition to the reactions occurring between them. The organic matter in clays (usually lignite), undergoes extensive exothermic oxidation reactions, causing intense and broad exotherms in DTA traces. Figure 25 shows DTA traces of a ball clay before and after removal of carbonaceous material. These oxidation exotherms may completely disguise the other thermal signatures of the clay below 700 °C; thus, organic matter is often removed from clays containing substantial organic material before thermal analysis, through treatment with hydrogen peroxide.

Figure 26 shows differences in the thermal behavior of typical china clays, ball clays, and bentonites. Due to their low organic content, kaolins and bentonites also do not contain the broad, low temperature exotherm of many ball clays, associated with the loss of carbonaceous matter. The thermal behavior of china clays during heating mainly resemble that of kaolinite, which comprises most of the clay deposit. Because kaolins contain very little adsorbed water, the adsorbed water-loss endotherm observed from ball clays and bentonites is absent in the kaolin DTA trace. This endotherm has the greatest magnitude in the bentonite trace, due to the surface-adsorbed and inter-unit water associated with the considerable

concentration of montmorillonite minerals in the deposit. The plasticity (ability to deform without cracking) of the clay increases with increasing area under the

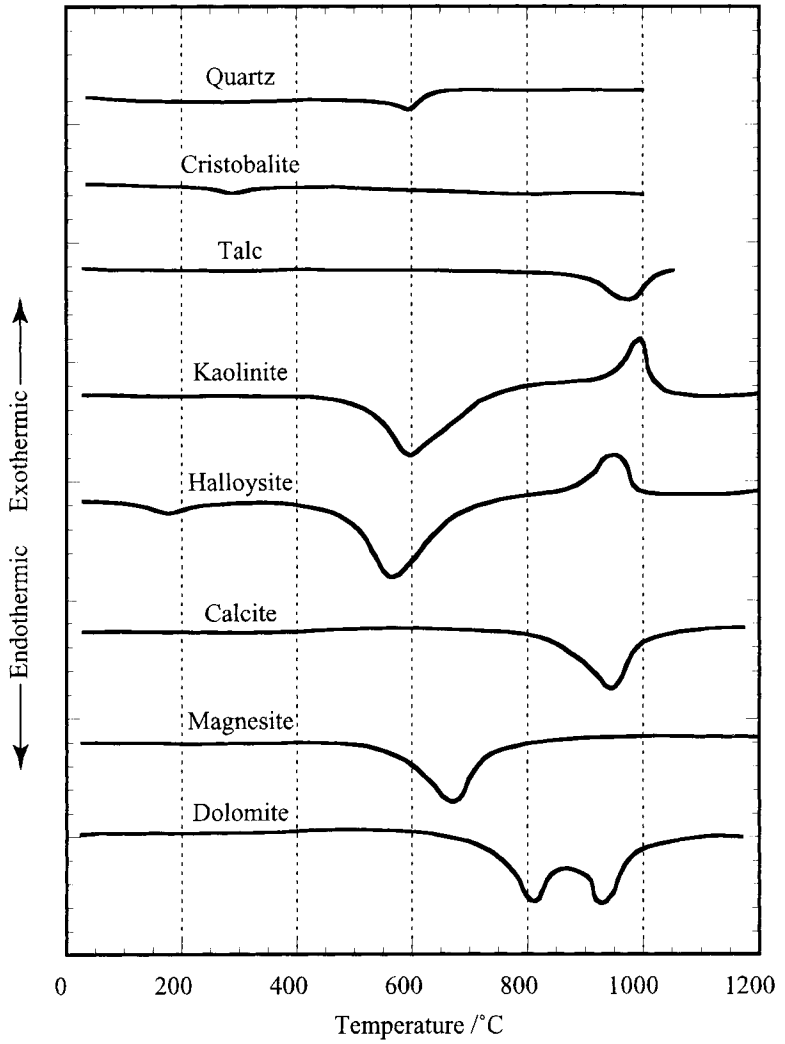


Figure 24. DTA traces of common clay minerals, as well as other minerals often found in clay deposits [25].

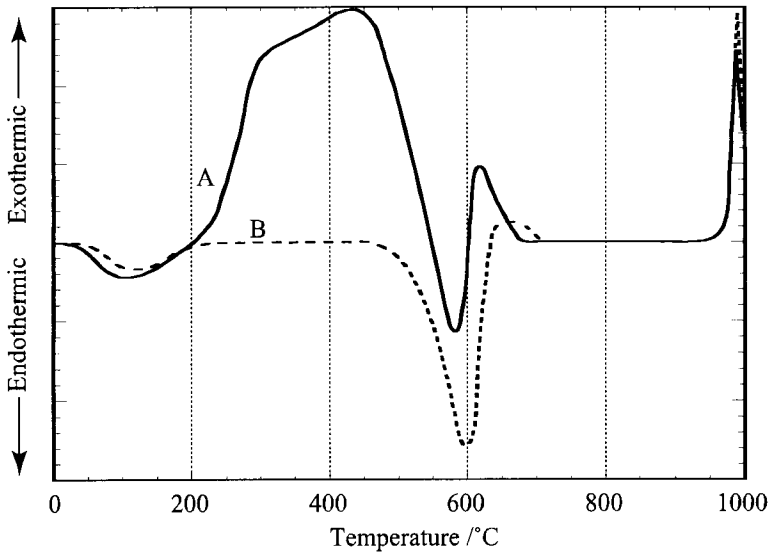


Figure 25. DTA traces of A) a black ball clay and B) the same black ball clay after the removal of carbonaceous material [26].

absorbed water endotherm. Kaolin has a sharper crystallization exotherm than the others, which corresponds to the concentration and/or heats of crystallization of the dehydroxylized minerals in this sample being higher. The montmorillonite mineral content of bentonite causes the dehydroxylation endotherm for this clay to appear at a higher temperature. It should be noted that the thermal behavior among clay deposits of the same type can vary, due to the specific clay and accessory minerals that are present in the sampling, and their relative concentrations.

All clays, when heated to a high temperature, begin to form a viscous liquid, which consists mainly of silica and fluxing oxides of sodium, potassium, calcium, and magnesium. For ball clays, the shrinkages resulting from the formation of this eutectic liquid are observed as sharp contractions beginning at ~950 °C, as shown in Figure 27. The figure also shows that the sample with the highest proportion of quartz has a much lower rate of contraction in the temperature range in which the liquid phase forms. With a large concentration of quartz, there are fewer contact points between quartz, clay, and fluxing materials, which lessens the amount of

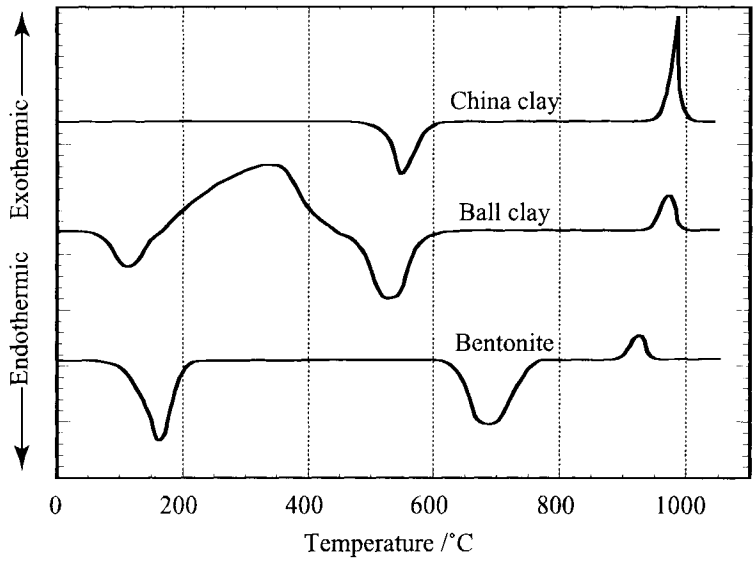


Figure 26. DTA traces for kaolin, ball clay, and bentonite specimens [23].

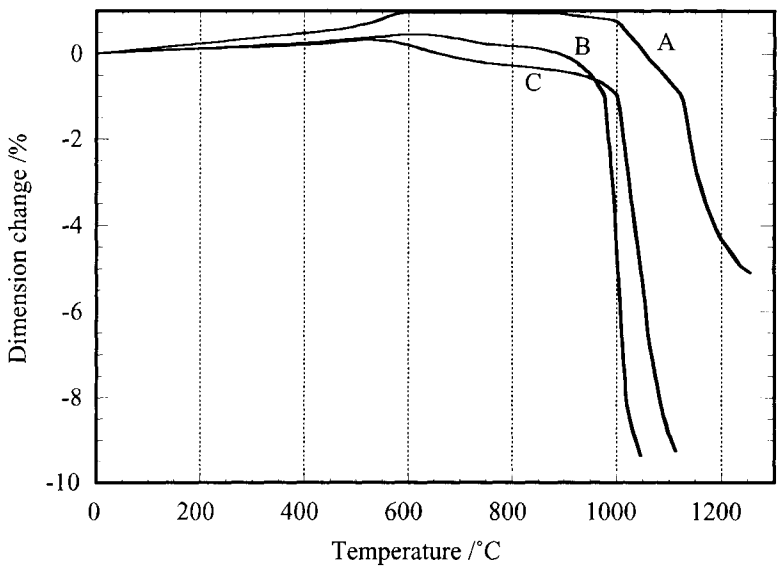


Figure 27. Dilatometric traces of ball clays with A) 31% kaolin mineral, 48% quartz, and 17% mica; B) 57% kaolin mineral, 10% quartz, and 25% mica; C) 76% kaolin mineral, 6% quartz, and 14% mica [5].

eutectic liquid phase. Quartz undergoes a displacive expansion* ($\alpha \rightarrow \beta$ quartz) at 573°C, as apparent in Figure 27. The amount of quartz in such a mixture may be gleaned from the extent of expansion measured in this temperature range. Impure quartz sluggishly undergoes an expansive transformation to tridymite above 867 °C (superimposed upon the rapid sintering contraction in the figure). The ball clay sample with high mica content shows a rapid contraction in the region of liquid formation, as most fluxing alkalis present in ball clays come from micas. The principal products of such clays after firing to these high temperatures include mullite, glass, cristobalite, and quartz.

4.7. Quantitative analysis

The correlation between endotherm/exotherm area and amount of material is often exploited to determine the percentage of a particular mineral present in a mixture. Figure 28 shows the linear relationship between the amount of kaolinite present in a constant total volume mixture with alumina (a thermally inert material) and dehydroxylation endotherm areas. Phase concentration analysis in clay samples by DTA is considered semi-quantitative. Affecting resolution are interfering thermal absorption effects from other constituents, difficulty in construction of the precise position of the baseline for determination of endotherm area, and convolution of endotherms/exotherms from superimposed thermal effects from different minerals [21]. Fairly accurate quantitative results have been successfully obtained, however, from samples in which each mineral produced at least one distinct endotherm unaffected by other mineral components, and when a standardization process was performed using different mixtures of the pure minerals present in the unknown composition [5].

Figure 29 demonstrates that dehydroxylation endotherm peak temperature may be correlated to the amount of a clay mineral present in a mixture. An approximately logarithmic relationship exists between the amount of a particular montmorillonite mineral and this temperature.

5. SUMMARY

The plastic nature of clays makes them an invaluable component of triaxial porcelains, permitting porcelains to retain a shape before firing. Plasticity arises from the very fine particle size of clay minerals, which form (hydrated) platelike particles owing to atomic-level stresses and periodic hydroxyl / van der Waals

* After heating, a displacive polymorphic transformation is one which is easily reversed upon cooling.

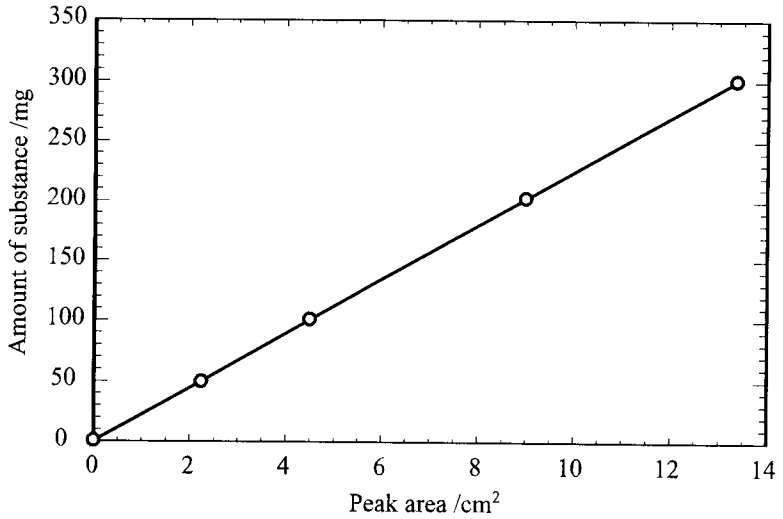


Figure 28. Relationship between dehydroxylation endotherm area and sample mass for kaolinite [29].

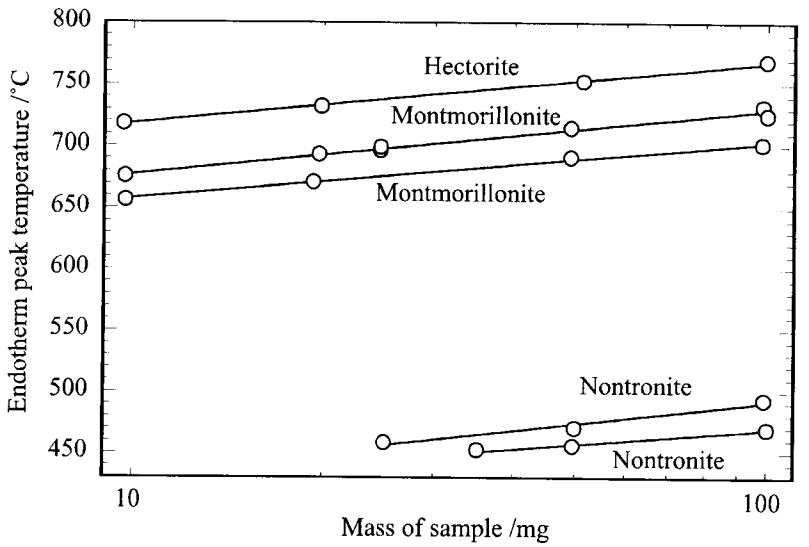


Figure 29. Relationship between sample mass and endotherm maximum temperature for various montmorillonite minerals from different locales [9].

bonding in the stacking of structural layers. The quartz component of a porcelain functions as a filler material, while the feldspar is a flux which permits the formation of eutectic liquid phase, in turn facilitating densification during heat treatment.

The kaolins, montmorillonites, and the illites are classes of clay minerals distinguished by similarities in crystal structure. Kaolins are composed of superimposed layers of silica and modified gibbsite; these two-layer units are bound to similar units by hydroxyl forces. Montmorillonites are composed of three-layer units, based on either pyrophyllite or talc structures, with modified gibbsite layers sandwiched between silica layers, in which lattice cation substitution occurs (e.g. Mg^{2+} for Al^{3+}), impressing a negative charge on the units. To achieve space charge neutrality, alkali and alkaline earth cations are absorbed at locations between units. These exchangeable cations may be hydrated, or may be exchanged for water, facilitating a high concentration of inter-unit absorbed water. In mica (accessory) minerals, monovalent cations such as K^+ position between units to form ionic bonds. In illite clays, some of these inter-unit cations are replaced by H_3O^+ ions. Chlorite accessory minerals are based on modified talc units separated by modified brucite layers, and vermiculite accessory minerals are based on modified talc units separated by hydrated magnesium ions.

Kaolin minerals undergo endothermic dehydroxylation (loss of structural water) at 500-700 °C, forming amorphous meta-kaolin, which then exothermically crystallizes to a spinel structure at 900-1000 °C. This phase transforms with increasing temperature to mullite with concurrent rejection of silica. The kaolin minerals generally do not show an absorbed water extraction endotherm at 50-150 °C unless they are in a highly disordered form. Montmorillonite minerals display an absorbed water extraction endotherm of significant intensity, corresponding to water held on particle surfaces and between the units. Dehydroxylation endotherms vary substantially in temperature range, and are of lower intensity than in kaolins. The temperatures of the crystallization exotherms also vary, depending on the phases which form from the presence of a particular exchangeable cation.

Dry grinding causes regions of a clay mineral sample to amorphize. This diminishes the intensity and lowers the temperature of dehydroxylation, and increases the intensity of a broad absorbed-water endotherm. This absorbed water originates both from increased absorption on particles of reduced size, as well as insertion of inter-unit water to shield charge imbalances fostered by amorphization. A covered sample container shifts dehydroxylation endotherms to higher temperature, caused by an increase in water vapor pressure. Increasing sample size also shifts dehydroxylation endotherms to higher temperatures because of increases

in water vapor pressure at locations more immersed in the specimen; crystallization exotherms narrow and increase in intensity with increasing sample size as the transformation is accelerated due to self-heating.

Clay deposits are classified based on their period of formation. China clays are composed mainly of kaolinite as the clay mineral and are both residual (deposit formed at the location of formation) and sedimentary clays (deposit formed remote from formation); they function as the plastic component of triaxial porcelains (whitewares). Ball clays have disordered kaolinite as their main clay mineral, and retain a comparatively higher impurity content than china clays. They are often added to porcelain compositions in small amounts to improve plasticity and strength of the unfired body. Their comparatively high iron impurity content and firing shrinkage prohibits them from being the dominant clay ingredient. Bentonite clays have montmorillonites as the dominant clay mineral. For the same reasons as ball clays, they are used as minority clay additives in whiteware compositions. Brick clays are impure clays, whose major constituents are kaolinite and chlorite. Their high flux and iron contents make them suitable for neither refractory nor whiteware applications. Fireclays which contain high concentrations of alumina and low concentrations of flux are used for refractories, which maintain their structural integrity up to ~1600 °C.

DTA thermal signatures of clay minerals in deposits with high organic content (e.g. ball clays) are often masked by broad exotherms corresponding to combustion of these constituents. Dilatometry traces of clay deposits and additives distinguish the concentration of fluxes relative to quartz. Fluxes encourage lower temperature and rapid densification via liquid-phase sintering. A high content of quartz shifts sintering to higher temperatures and lessens the firing shrinkage, owing to less formation of a liquid phase. The amount of clay in a deposit can be semi-quantitatively determined based on the area of the DTA dehydroxylation endotherm or the shift in the dehydroxylation peak temperature.

REFERENCES

1. F. H. Norton, Elements of Ceramics, Addison-Wesley, Reading, MA, 1974.
2. W. E. Worrall, Clays: Their Nature, Origin, and General Properties, Transatlantic Arts, New York, 1968.
3. R. W. G. Wyckoff, Crystal Structures, 2nd Ed., Volume 4, John Wiley and Sons, New York, 1968.

4. T. F. Bates, The American Mineralogist, 23 (1938) 863, cited in R. W. Grimshaw, The Chemistry and Physics of Clays and Allied Ceramic Materials, Ernest Benn Limited, London, 1971.
5. R. W. Grimshaw, The Chemistry and Physics of Clays and Allied Ceramic Materials, Ernest Benn Limited, London, 1971.
6. J. Hlavac, The Technology of Glass and Ceramics: An Introduction, Elsevier Science, New York, 1983.
7. F. H. Norton, Fine Ceramics: Technology and Applications, McGraw-Hill, New York, 1970.
8. W. E. Worrall, Clays and Ceramic Raw Materials, John Wiley and Sons, New York, 1975.
9. W. Smykatz-Kloss, Differential Thermal Analysis: Applications and Results in Mineralogy, Springer-Verlag, New York, 1974.
10. R. C. Mielenz, N. C. Schieltz, and M. E. King, "Effect of Exchangeable Cation on X-Ray Diffraction Patterns and Thermal Behavior of a Montmorillonite Clay," pp. 146-173 in Clays and Clay Minerals, Edited by W. O. Milligan, National Academy of Sciences, Washington, D. C., 1955, cited in R. K. Ware "Thermal Analysis," pp. 273-305 in Characterization of Ceramics, Edited by L. L. Hench and R. W. Gould, Marcel Dekker Inc., New York, 1971.
11. A. H. Weir and R. Greene-Kelly, The American Mineralogist, 47 (1962) , 137-146, cited in R. C. MacKenzie "Simple Phyllosilicates Based on Gibbsite- and Brucite-like Sheets," pp. 497-537 in Differential Thermal Analysis. Volume 1: Fundamental Aspects, Edited by R. C. Mackenzie, Academic Press Inc., New York, 1972.
12. R. C. Mackenzie "Simple Phyllosilicates Based on Gibbsite- and Brucite-like Sheets," pp. 497-537 in Differential Thermal Analysis. Volume 1: Fundamental Aspects, Edited by R. C. Mackenzie, Academic Press Inc., New York, 1972.
13. P.G. Nutting, "Some Standard Thermal Dehydration Curves of Minerals," U. S. Geological Survey Professional Papers, 197E, 1943, cited in F. H. Norton, Fine Ceramics: Technology and Applications, McGraw-Hill, New York, 1970.
14. C. S. Hurlbut, Jr., and C. Klein, Manual of Mineralogy, 19th Ed., John Wiley and Sons, New York, 1977.
15. A. Mottana, R. Crespi, and G. Liborio, Simon and Schusters Guide to Rocks and Minerals, Simon and Schuster Inc., New York, 1978.

16. A. Blazek, Thermal Analysis, Van Nostrand Reinhold Company, New York, 1973.
17. G. F. Walker and W. F. Cole, pp. 191-206 in The Differential Thermal Investigation of Clays, Edited by R. C. Mackenzie, Mineralogical Society, London, 1957, cited in R. C. MacKenzie "Simple Phyllosilicates Based on Gibbsite- and Brucite-like Sheets," pp. 497-537 in Differential Thermal Analysis. Volume 1: Fundamental Aspects, Edited by R. C. Mackenzie, Academic Press Inc., New York, 1972.
18. R. J. W. McLaughlin, "Effects of Grinding on Dickite," Clay Minerals Bulletin, 2, (1955) 309-317, cited in P. D. Garn, Thermoanalytical Methods of Investigation, Academic Press Inc., New York, 1965.
19. P. L. Arens, "A Study of the Differential Thermal Analysis of Clays and Clay Minerals," Excelsiors Foto-Offsets, 1951, cited in P. D. Garn, Thermoanalytical Methods of Investigation, Academic Press, New York, 1965.
20. A. M. Langer and P. F. Kerr, Du Pont Thermogram, 3 [1] (1966), cited in T. Daniels, Thermal Analysis, John Wiley and Sons, New York, 1973.
21. W. W. Wendlandt, Thermal Methods of Analysis, John Wiley and Sons, New York, 1974.
22. R. E. Grim and N. Guven, Bentonites: Geology, Mineralogy, Properties, and Uses, Elsevier Scientific, 1978.
23. W. Ryan and C. Radford, Whitewares Production, Testing, and Quality Control, Pergamon Press, Oxford, 1987.
24. W. E. Worrall, Ceramic Raw Materials, Pergamon Press, Oxford, 1982.
25. V. P. Ivanova et al., Thermal Analysis of Minerals and Rocks, Leningrad, 1974, cited in J. Hlavac, The Technology of Glass and Ceramics: An Introduction, Elsevier Science, New York, 1983.
26. D. G. Beech and D. A. Holdridge, "Testing Clays for the Pottery Industry," Transactions of the British Ceramic Society, 53 (1954) 103-133, cited in P. D. Garn, Thermoanalytical Methods of Investigation, Academic Press Inc., New York, 1965.
27. P. S. Keeling, "The Common Clay Minerals as a Continuous Series," in Science of Ceramics, Academic Press, Inc., New York, 1962, cited in P. D. Garn, Thermoanalytical Methods of Investigation, Academic Press Inc., New York, 1965.

28. P. S. Keeling, "The Common Clay Minerals as a Continuous Series," in Science of Ceramics, Academic Press, Inc., New York, 1962, cited in P. D. Garn, Thermoanalytical Methods of Investigation, Academic Press Inc., New York, 1965.
29. G. Rosenthal, "A Study of the Plasticity of Mono-ionic Clays," Science of Ceramics, Academic Press, Inc., New York, 1962, cited in P. D. Garn, Thermoanalytical Methods of Investigation, Academic Press Inc., New York, 1965.
30. I. Barshad, "Temperature and Heat of Reaction Calibration of the Differential Thermal Analysis Apparatus," American Mineralogist, 37 (1952) 667-694, cited in P. D. Garn, Thermoanalytical Methods of Investigation, Academic Press Inc., New York, 1965.

Handbook of Thermal Analysis and Calorimetry. Vol. 2: Applications to Inorganic and Miscellaneous Materials
M.E. Brown and P.K. Gallagher, editors
© 2003 Elsevier B.V. All right reserved.

Chapter 7

ENERGY STORAGE

Takeo Ozawa[a] and Masayuki Kamimoto[b]

[a] 18-6 Josui shinmachi, 1-chome, Kodaira, Tokyo 187-0023, Japan

[b] National Institute of Advanced Industrial Science and Technology, 1-1-1 Higashi, Tsukuba, Ibaraki 305-8561, Japan

1. ENERGY STORAGE: NEEDS AND SCHEMES

In a certain sense, energy storage is not a new technology but a very old technology. Thousands of years ago flywheels were used for managing rotational power in Mesopotamia. However, advanced energy storage technologies are becoming very important for future human life because of the following situations.

Generally energy production and supply take place simultaneously with energy consumption. Conventional electric power supply is a typical example. In this system, the power generation is precisely controlled in accordance with consumption to maintain high quality of the power supply, namely constant voltage, constant frequency and high reliability in avoiding power failure. This high-quality power supply is essential for modern electronic equipment, electrical appliances etc. Energy production from fossil fuels can be easily controlled. However, this is not the case for natural renewable energy utilization, such as solar energy and wind energy, and also for waste energy recovery for energy conservation. Needs for energy storage stem from situations of mismatch between supply and consumption, though energy loss occurs inevitably during charge, discharge and storage. One clear example is regenerative braking. In fuel-cell vehicles and hybrid vehicles, energy recovered during braking with a motor-generator is stored in a double-layer capacitor and is used for starting and acceleration. In an electric railway, a flywheel has also been used for regenerative braking as a demonstration of this technology. Thus, energy storage technologies are essential for conservation of good global environment and

energy resources, and they are among the key technologies for sustainable development of mankind.

Energy storage technology is also useful in another application, that is in a steam accumulator, in which high-pressure steam is stored in a large cylinder. Steam accumulators have been used for supplying heat in the night, for instance in hospitals, without attendance of boiler operators. Thus, they are useful for labour- and cost-saving. They are also used for supplying high power in a short time to meet high power needs with a relatively small boiler to reduce the installation cost.

Because different forms of energy have to be stored for specific needs, various schemes have been investigated and they are listed in Table 1. Among them, pumped hydroelectric systems are now used on a large scale. Surplus electricity, mainly from nuclear power plants, is transmitted during the night to hydroelectric plants in mountainous area for pumping water from a lower dam to

Table 1.
Various schemes of energy storage

Scheme	Input/Output	Form of Stored Energy
Sensible thermal storage	Heat / Heat	Sensible heat
Steam accumulator	Heat / Heat	Sensible heat[5)]
Latent thermal storage	Heat / Heat	Latent heat
Thermochemical storage	Heat / Heat	Chemical energy
Electrochemical battery	Elec/ Elec	Chemical energy
Regenerative fuel cell	Elec/ Elec	Chemical energy
Water electrolysis & hydrogen fuel-cell[1)]	Elec/ Elec	Chemical energy
Double layer capacitor[2)]	Elec/ Elec	Capacitive energy
Superconducting magnetic energy storage (SMES)	Elec/ Elec	Electromagnetic energy (permanent current)
Flywheel[3)]	Mech/ Mech (Elec/ Elec)	Rotational energy
Compressed-air energy storage (CAES)[4)]	Air/ Air	High pressure (Compressional energy)
Pumped hydro storage	Elec/ Elec	Potential energy

Elec: Electricity, Mech: Mechanical energy

1) Still low efficiency, 2) Short time storage, 3) Short time storage, 4) Underground cavity.

5) Although condensation and evaporation occur during charge and discharge, thermal energy is stored in the form of sensible heat: temperature increase of pressurized water.

a higher dam so that the electrical energy is stored in the form of the potential energy of the water. This potential energy is converted back to electricity during the day to cope with peak demand. The overall efficiency, that is the ratio of the regenerated energy to the input energy, is usually 70% or higher. Some decades earlier, lead-acid batteries were used for the same purpose, but nowadays pumped hydroelectric plants are the main facilities because of the rather high cost of lead-acid batteries. However, sites for pumped hydroelectric plants are limited and research and development for alternative schemes of similar efficiency are ongoing.

For instance, three schemes have been investigated for more than two decades. They are new advanced secondary batteries, such as the sodium-sulfur battery, regenerative fuel cells (electrochemical cells in which reactants, e.g., redox ions, are regenerated by electricity and they are stored in outside tanks) and superconducting magnets. The former two are now in the stage of commercialization. The secondary batteries can be used for daily operation, while pumped hydroelectric plants and regenerative fuel cells can be used in a daily cycle and also for longer term storage. On the other hand, a double-layer capacitor and a flywheel are both suitable for high power charge and discharge but over a short time, so that they are used for regenerative braking and similar applications. Superconducting magnetic energy storage (SMES) is theoretically suitable both for short and long term storage, but a strong magnetic field requires quite a high strength of the magnet and its support, resulting in high cost. It seems that large-scale use in a daily cycle will be a future target of the technology. On the other hand, micro SMES for stabilization of an electric grid is almost in a commercialization stage in the USA.

Thermal energy forms a large part of total energy consumption, so that thermal energy storage is also important among various energy storage technologies. The most important role seems to be its use in cogeneration. The efficiency of electric power generation is less than 50%, even for the most advanced combined cycle of a gas turbine and a steam turbine, and more than half of the input energy is being cooled to about 30°C for increasing the efficiency (as is seen from the Carnot cycle). Finally heat is released into the environment. However, in fuel cells, any enthalpy change unconverted to electricity is heat around the operating temperature, so that the exhausted heat, including the entropy change of electrochemical reaction, can be used efficiently, for instance for air-conditioning, and an estimation claims an overall efficiency of up to about 80% with electric power efficiency over 40%. For conventional power generation, the overall efficiency can be improved by increasing the temperature of the exhausted heat with a sacrifice of electric power efficiency. In both cases thermal energy storage

is needed for efficient utilization, and thus it also contributes to decreasing carbon dioxide emission and to maintaining the global environment.

As seen in the above applications, there are many requirements for newly developed energy storage technologies. High efficiency, high reliability, low cost and low environmental impact are essential and common requirements, together with high energy-density and high power-density, which are regenerated energy and power per unit mass or unit volume of a storage equipment, respectively.

2. THERMAL ENERGY STORAGE

Three varieties of thermal energy storage are now in practical use or under research and development; sensible thermal storage, latent thermal storage and thermochemical storage. In these three, thermal energy is stored in the forms of sensible heat by temperature increase, latent heat in molten and/or high temperature crystalline states, and chemical energy, respectively. Thermochemical storage, using a reversible chemical reaction, has a unique feature in that it can be operated as a chemical heat pump, because the equilibrium temperature is easily controlled by the pressure. Beside these three schemes, storage in the form of a concentrated solution, for instance sulfuric acid, has been studied, but the temperature of the output heat is low and working materials are generally corrosive.

Sensible thermal storage is well established and has been used for many years, for instance in refractory furnaces for steel production, and it is still used for various applications, such as electric heating appliances and hot water suppliers, in both of which low-cost midnight electricity is used to heat thermal energy storage materials, such as bricks, rocks and water. This technology is also useful in passive solar energy utilization for heating, and annual thermal storage using an underground aquifer or soil for air conditioning is also in this category.

The technology required for sensible thermal storage is an established technology, but its performance is not as satisfactory as the others. One of drawbacks of sensible thermal storage is the temperature decrease during discharge. Because low-temperature thermal energy is not as useful as high-temperature thermal energy, as easily seen from the Carnot efficiency, temperature constancy is one of the most important characteristics for thermal energy output, so that the output thermal energy from sensible thermal storage is of rather low quality. For this reason, this technology is mainly used in heating. Another drawback is its low energy-density.

For designing heat-storage equipment, heat capacity is the most important quantity. Conventional calorimetry is precise and accurate, but it needs experience and skill, otherwise it tends to lead to unreliable results. DSC is the most suitable technique for this purpose, because it needs less skill and provides reliable data of sufficient accuracy.

Latent thermal storage has advantages over sensible thermal storage. Its high energy-density and constant-temperature heat recovery are remarkable. A typical commercialized application of this technology is energy storage using ice. Ice is produced by using low-cost midnight electricity and is then used for air conditioning in the daytime. The low cost and large heat of fusion of water are essential points for the commercialization. As clearly shown in this example, realization of latent thermal storage is based on cheap working materials, which undergo fusion and/or transition at desirable temperatures, with large heats of fusion and/or transition. For selecting the materials, characteristics such as temperatures and heats of fusion or transition, their reversibility in discharge (e.g., supercooling), thermal conductivity, thermal stability and compatibility with container material, need to be examined. Thermal analysis, especially DSC and TG, are powerful tools for this purpose, and examples are described later in this chapter. Heat transfer within the equipment is another essential factor. In most cases, power density and cost are dependent on this factor. Some device to enhance heat transfer (or active heat exchange) is needed, instead of conventional passive heat exchange, to achieve wide application of this technology. These points are illustrated in the next section in detail.

An application of this technology that appears to making full use of these advantages is the advanced utilization of solar energy and waste heat for air conditioning, power generation etc. One particular scheme is load levelling for nuclear power plants, in which thermal output is stored during the night and recovered for electricity generation in the daytime to cope with peak demand.

Higher energy-density can be expected for thermochemical storage. Examples for this scheme are reversible reactions of benzene with hydrogen to form cyclohexane and of alloys with hydrogen to form metal hydrides. The most important aspect of such a scheme is the reversibility of the reactions. If more than 50% of the energy capacity is expected to remain after 1000 cycles of charge and discharge, more than 99.93% of the working material should be recovered after one cycle of charge and discharge. Both a high reaction rate and high heat conduction in the storage materials are needed, particularly for solid-gas reactions, in order to achieve the theoretically expected high storage density. Control of the reaction with a catalyst is another aspect to be studied for control

of discharge. When such desirable performances can be achieved, the technology can also be applied to large-scale long distance thermal energy transmission by transporting the working material with pipe lines.

3. LATENT THERMAL ENERGY STORAGE

3.1. Application systems with latent thermal storage units

Latent thermal storage has a great advantage such as high storage-density. This advantage can be realized by using latent thermal storage materials with melting or transition temperatures appropriate to the temperature needed for each application system. Melting and transition temperatures of latent thermal storage materials should lie between the temperature determined by a heat source and that required by the demand side. Air-conditioning with ice storage has been widely used for load levelling in Japan. Although most of the other application systems are still in the R&D stage, they are good examples to show how important thermal analysis, calorimetry, and the measurement of thermal properties are in researching and developing latent thermal energy storage. The application systems shown hereafter are as follows:

1. solar energy and waste heat utilization systems for air-conditioning and process heat production [1],
2. molten salt latent thermal storage for peak coverage of pressurized water reactor (PWR) nuclear power plants [2] and for molten carbonate fuel cell (MCFC) cogeneration systems [3],
3. solar dynamic power generation systems for low earth-orbit satellites [4].

Conventional solar systems for heating and hot water supply require around 30 °C, whereas the temperature needed for air conditioning is 120 °C and more. High performance solar collectors of non-tracking and non-concentration type, such as a reverse-flat-plate collector, can produce heat at 140 °C with a reasonable efficiency, and those of tracking and low-concentration type, such as a segmented-mirror solar collector, can produce heat at 200 °C which can generate high-pressure steam.

Latent thermal storage is one of the options for peak coverage of PWR operated at a constant output power for cost and safety reasons. Steam extraction in the off-peak period is performed from the outlet of the reactor at about 270 °C, and the stored heat as latent heat is used to operate a peak-turbine in the on-peak period during the day. The temperature range is also attractive for the cogeneration system of MCFC.

A conventional power system of a low earth-orbit satellite is a photovoltaic system with large photovoltaic panels which cause reduction in altitude of the satellite due to air drag force. Solar dynamic power generation using a Brayton

cycle (gas turbine using He-Xe gas at 900 °C) has a conversion efficiency of 30% or more, which is much higher than solar photovoltaic systems. Therefore, the solar dynamic power generation system needs a smaller area of mirrors and the air drag force can be decreased. Key technology for its R&D is thermal storage under micro-gravity, because the power generation system requires thermal energy storage for about 30 min of eclipse when the satellite moves around the earth in 90 min.

3.2. Screening of latent thermal storage materials

Latent thermal storage materials were first screened from the points-of-view of their temperatures of transition or fusion, latent heats and material costs. Figure 1 shows the relation between the performance of thermal energy storage systems and the characteristics of the latent thermal storage materials. Some important performances of the latent thermal storage system are primarily dependent on the characteristics of the latent thermal storage materials, and other performances are dependent on the design of the system as well as the materials. In the figure, the

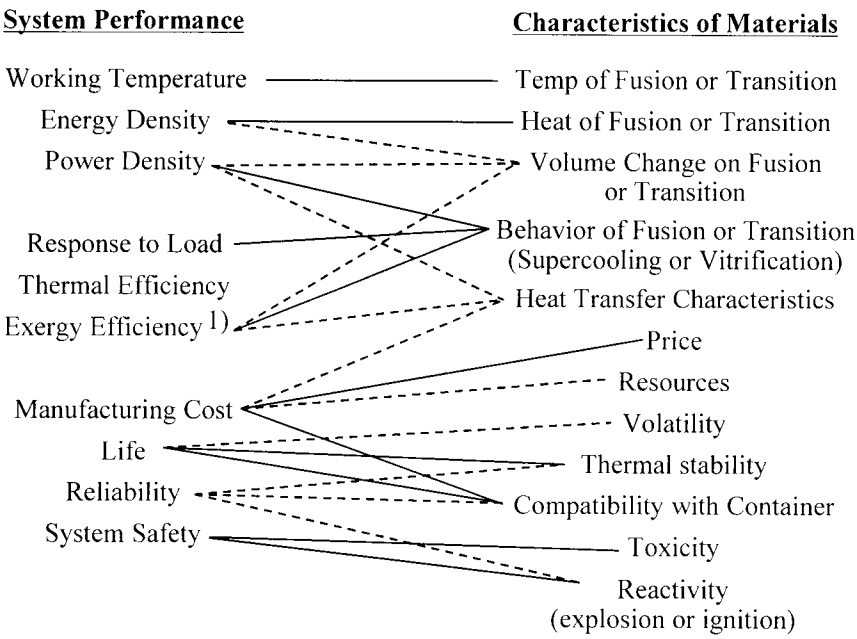


Figure 1. Relation between the performance of thermal energy storage systems and the characteristics of latent thermal storage materials [5].

1) To express the usefulness of heat, the term "exergy" is used. It is the product of thermal energy and Carnot efficiency and is equal to the maximum available work.

solid lines represent relations in which the performance are strictly limited by the characteristics connected with the solid lines, and the limit cannot be overcome by changing the design of the system. For instance, the energy density of the system cannot by any means be increased beyond the limit of the latent heat of the latent thermal storage materials, and the operating temperature of the system is defined by the temperature of transition or fusion. On the other hand, the broken lines express relations where the performances can be improved by the modifying the design of the system, even if the characteristics of the latent thermal storage materials are poor. Examples are the response to load and the power density. These performances are dependent not only on the thermal conductivity of the latent thermal storage materials but also on the heat transfer techniques and surface area for the heat transfer between the latent thermal storage materials and the heat transfer fluid.

Screening of latent thermal storage materials from the viewpoints of cost and latent heat is therefore reasonable, and the candidate materials were thus selected [5]. Values of the latent heat are usually available from handbooks or the literature for most single-component materials and for some multi-component-materials. When the data for multi-component materials are not available, they can be estimated based on the assumption of additivity of entropy of transition and/or fusion, although it is a zero-order approximation. The results of the screening are shown in Figure 2. Most of the candidate latent thermal storage materials for high-temperature use are inorganic materials and only polyethylene, pentaerythritol and their related materials are organic materials.

Figure 3 shows the results of screening materials above 600 °C for space use [6]. In this screening, the cost of the material was not considered because high storage-density is a primary concern, and cost is less critical an issue, in comparison with the applications on the ground.

From the figures and thermoanalytical observations (see Section 4 of this Chapter), we can select the following candidate latent thermal storage materials for the application systems listed in 3.1:

1. High-density polyethylene (T_m=135 °C), eutectic salts of alkali metal hydroxides such as NaOH-KOH (T_m=171 °C), and pentaerythritol ($C(CH_2OH)_4$) (T_c=188 °C) for solar energy and waste heat utilization systems for air-conditioning and process heat production,
2. Eutectics and compounds, $NaOH$-$NaNO_3$ and $NaOH$-$NaNO_2$, for molten salt latent thermal storage for peak coverage of PWR nuclear power plants and for MCFC cogeneration systems,
3. LiF and its mixtures with alkali and alkaline earth fluorides for solar dynamic power generation systems for low earth-orbit satellites.

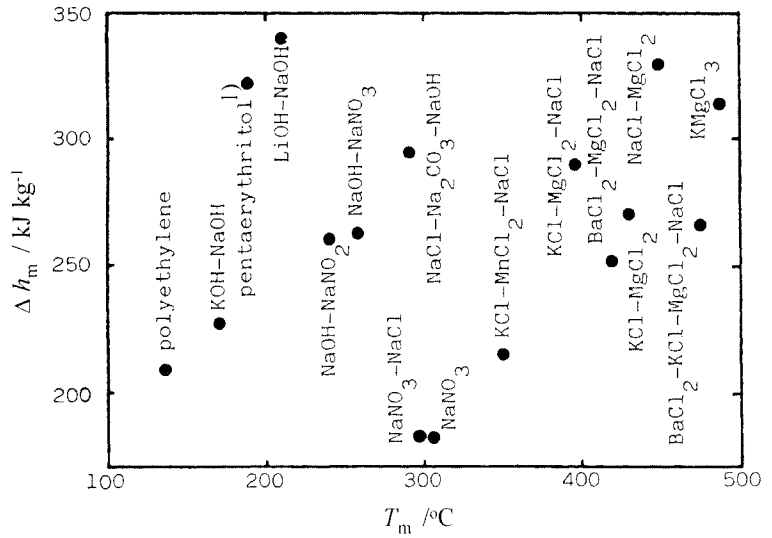


Figure 2. Temperatures of phase changes and latent heats of promising latent thermal storage materials between 100 °C and 500 °C [5].

1) The phase changes are mostly fusion except for pentaerythritol (solid-solid phase transition).

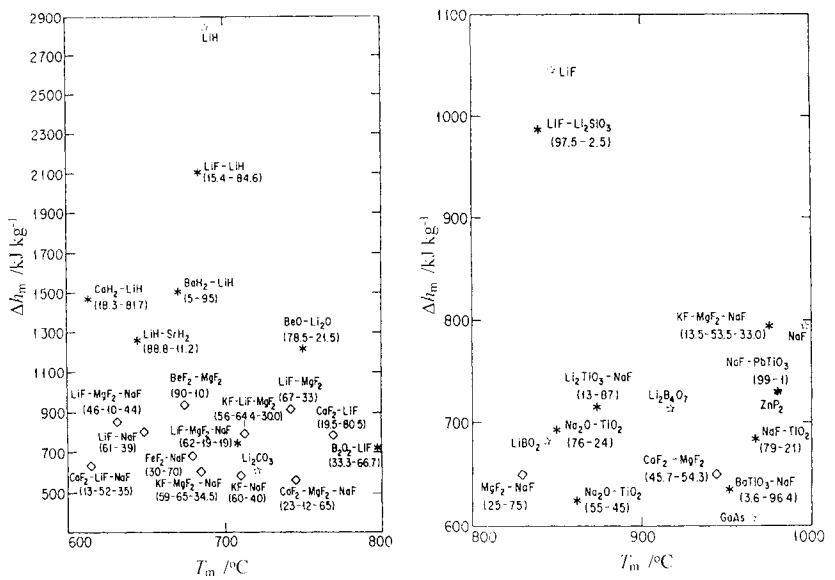


Figure 3. Temperatures of fusion and latent heats of promising latent thermal storage materials above 600 °C [6].

3.3. Selection of appropriate heat exchangers

In order to make effective use of each latent thermal storage material, an appropriate heat exchange method should be selected. Conventional passive heat exchangers for latent thermal storage are the shell & tube and the encapsulated-type shown in Figure 4. Latent thermal storage material is put in the shell and the charge and discharge are done by heat transfer fluid flowing in the tube of the shell & tube-type heat exchanger. For the encapsulated-type, latent thermal storage material is encapsulated in the capsules and heat transfer fluid flows through the shell. To promote heat exchange drastically, various active heat exchange methods have been proposed.

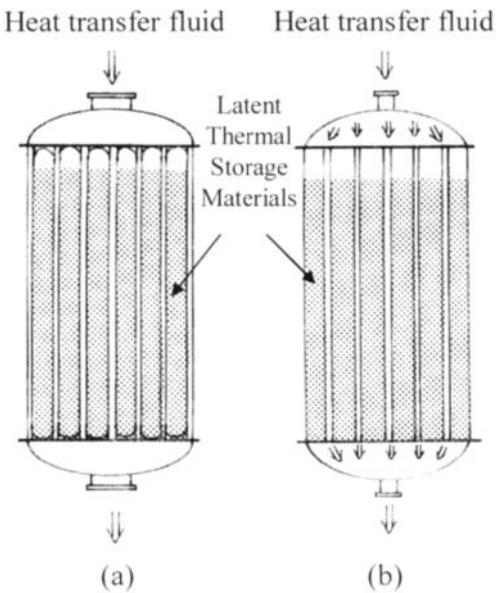


Figure 4. Cross-sectional views of conventional passive heat exchangers for latent thermal storage: (a) encapsulated type and (b) shell & tube type

For pentaerythritol, Kamimoto et al. [7] proposed an encapsulated-type (passive) storage device and two active-heat-exchange thermal storage devices. These were selected from many candidate devices based on the construction cost of the storage systems and the heat transfer characteristics in the storage units obtained from a computer simulation. Because pentaerythritol is confirmed by TG to sublime above the transition point [8], it should be used in closed systems. The computer simulation method and its results are described in Sections 3.4, 3.6, and 3.7. It is well known that heat extraction from a conventional latent thermal

storage unit, such as an encapsulated-type, strongly depends on heat conduction in the storage material. Pentaerythritol is usually supplied as a powder which has a low thermal conductivity. By filling spaces within the powder with heat transfer oil (by making the powder a slurry), the apparent thermal conductivity is expected to be improved. The oil also fills the voids formed due to the volume change accompanying the solid-phase transition. For these reasons, a slurry of pentaerythritol was used for the encapsulated-type storage unit.

The other two storage systems are active-heat-exchange latent thermal storage systems. Their cross-sectional views are shown in Figure 5. The shell & coil storage system with agitation of the slurry was proposed by Abe et al. [9]. Heat transfer in the storage medium is actively improved by agitation of the slurry. Heat exchange between the slurry and heat transfer oil is performed through the heat transfer coil. The slurry circulation system consists of a storage column and a plate-type heat exchanger. In the storage column, the slurry is stirred by a screw or by a forced flow of the slurry. Heat exchange between the storage medium and the heat transfer oil is conducted at the plate-type heat exchanger separated from the storage column.

Latent thermal storage materials are sometimes modified to improve their performance or cost; for example slurry formation in the case of pentaerythritol [7, 9] as already described. For the shell & coil storage system with agitation of the slurry mentioned above, alkyl diphenylethane was used to make the slurry of pentaerythritol. The maximum concentration is limited by the viscosity of the slurry. This is especially true above the transition temperature, because the high-temperature phase is a plastic crystal. Fifty mass percent seems to be the maximum concentration. On the other hand, the optimum concentration for the encapsulated-type should be different from that for the active-heat-exchange storage units, because the purpose of the slurry is different. The heat transfer oil is used to fill the spaces within pentaerythritol particles in this static system. The concentration of the slurry should be as high as possible to increase the storage density. However, too high a concentration cannot achieve the purpose of filling the spaces within pentaerythritol. From the volume change of pentaerythritol and alkyldiphenylethane with temperature, the optimum concentration was decided to be 75 mass percent of pentaerythritol.

Various cross-linking methods have been applied to modify high-density polyethylene. Cross-linking enables direct-contact heat exchange between the latent thermal storage material (high-density polyethylene) and the heat transfer fluid, because the cross-linked polyethylene does not flow or stick together, even above its melting temperature [10]. Cross-linking should be restricted to the surface so as not to decrease the latent heat of the original material.

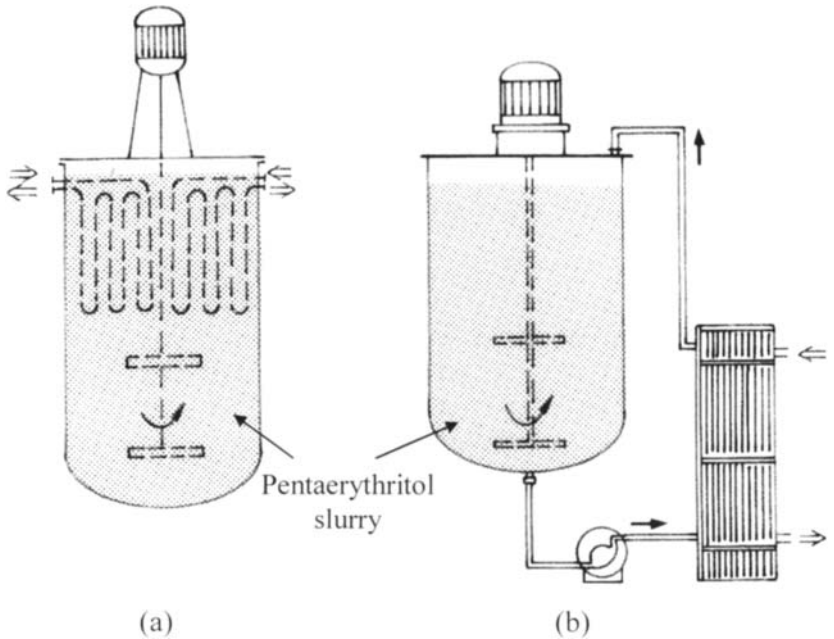


Figure 5. Cross-sectional views of the active heat-exchange storage units selected for pentaerythritol [7]: (a) shell & coil storage system with agitation of the slurry, (b) slurry circulation system.

LiF and its eutectics are candidate latent thermal storage materials for solar dynamic power generation system for low earth-orbit satellites and they are used under micro-gravity conditions. Composite materials of LiF with porous SiC or carbon [11] have been proposed in order to decrease the specific mass of the storage unit and the mechanical stress on the container, arising from the volume change on fusion, and also to enhance thermal conduction within the storage materials. A shell & tube type exchanger is most appropriate for mixtures of NaOH with $NaNO_3$ or $NaNO_2$ because the higher steam pressure, due to the high temperature, requires thicker outer containers of the encapsulated-type, resulting in higher cost.

3.4. Heat transfer in latent thermal storage systems [7, 12]

In order to design thermal energy storage systems and to evaluate their performance, computer simulation is used. For example, heat transfer equations can be derived based on the simplified model shown in Figure 6 for an encapsulated-type or a shell & tube type latent thermal storage unit.

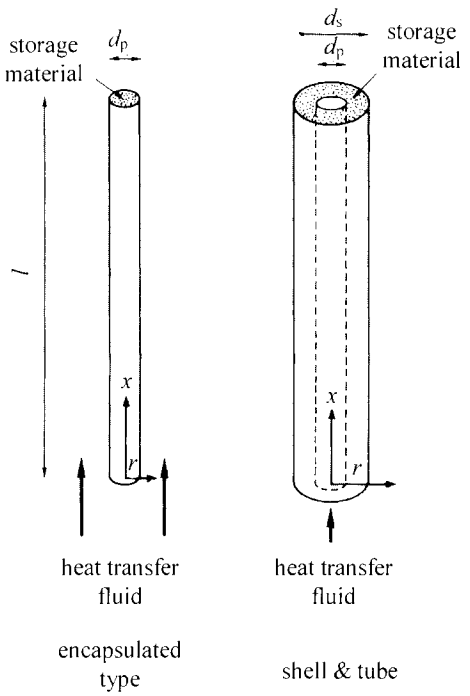


Figure 6. Models for computer simulation of heat transfer in encapsulated-type and shell & tube type storage units.

Temperature histories of the heat transfer fluid and those of the thermal storage material at various points can be calculated from the equations which require values of the following important properties:

(1) the specific heat capacity, density and thermal conductivity of the thermal storage material,
(2) the volume fraction and heat transfer area of the latent thermal storage material,
(3) the diameter of the latent thermal storage material (see Figure 6),
(4) the specific heat capacity, density and velocity of the heat transfer fluid,
(5) the heat transfer coefficient between the heat transfer fluid and the thermal storage material.

The calculation can be done with explicit finite-difference equations. The latent heat of latent thermal storage materials is usually included in the heat capacity within a narrow temperature interval near the phase-change temperature.

3.5. The necessity for measurement of thermophysical properties

The thermophysical properties of latent thermal storage materials need to be known from a very early stage of R&D of latent thermal storage. Performance of the storage unit can be roughly evaluated using the data available from handbooks, databases, original papers, etc. When such data are not available, these properties can be estimated on various assumptions. In order to establish the latent thermal storage technology, however, the storage unit has to be designed and the performance of the whole system has to be evaluated. For this purpose, computer simulation has to be accurate enough to describe the performance of the actual storage unit.

Values of thermophysical and/or thermochemical properties available from handbooks etc. are usually those for purified reagent-grade materials. For multi-component materials, such as eutectics, values of heat capacities, latent heats and, particularly, thermal conductivities are much more difficult to obtain. Simple and reliable methods of measurement of these properties are therefore highly desirable. DSC is a most powerful tool for research on latent thermal storage materials, because it is commercially available and the reliability and accuracy of the DSC measurements are adequate. Many examples of DSC measurements are introduced in the following section.

Another example described here is measurement of the thermal conductivity of a pentaerythritol slurry. The heat capacity and the latent heat of a slurry are usually calculated as the sum of those properties of the component materials, but the thermal conductivity of the slurry is difficult to estimate accurately from the values of the components. The thermal conductivity of a pentaerythritol slurry was measured by the transient hot-wire method. The transient hot-wire apparatus consists of a vertical thin metallic wire immersed in a liquid sample (slurry in this case) where the wire acts both as an electric heating element and a resistance thermometer. Initially a step voltage is applied, and the transient temperature rise of the wire is measured. Ideally the thermal conductivity k can be determined by $k = (q/4\pi) \ln (d\Delta T/ d \ln t)$, where, q is the heat generation per unit length of the wire, ΔT is the transient temperature rise, and t is time. The results of such measurements are shown in Figure 7 [13]. An interesting stepwise change in the thermal conductivity is seen at the transition.

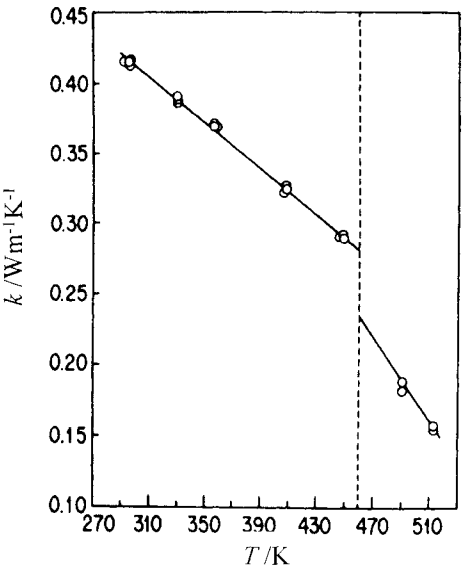


Figure 7. Temperature dependence of the thermal conductivity of a slurry of pentaerythritol with alkyldephenylethane [13].

3.6. Example of a computer simulation for selection of a heat exchange method

The outlet temperatures of a heat transfer fluid during discharge mode were calculated for the encapsulated-type and shell & tube type storage units using pentaerythritol, with the specifications listed in Table 2.

As Figure 8 shows, the heat extraction from the shell & tube storage unit is very slow [7]. The poor discharge characteristics can be improved if the volume fraction of the slurry is decreased by a reduction of the pitch of the tubes. A decrease of the volume fraction of the slurry is, however, not desirable because of the cost increase due to an increase in heat transfer surface area and a reduction of storage density. From the results, the encapsulated-type exchanger was selected for pentaerythritol rather than the shell & tube type. This is not always true for other cases, such as NaOH-$NaNO_3$ (T_m is around 250 °C) [2]. In this case, the shell & tube type is superior to the encapsulated-type, because the higher steam pressure due to the high temperature requires thicker outer containers of the encapsulated-type, resulting in higher cost.

Table 2.
Specifications of the pentaerythritol storage units for computer simulation [7].

	encapsulated	shell & tube
Storage capacity	2 000 kWh	1 000 kWh x 2 units
Diameter of the storage column	2.44 m	1.89 m
Height of the storage column	6.72 m	5.67 m
Mass of the slurry	24.4 ton	12.2 ton x 2
Volume fraction of the slurry	0.90	0.75
Diameter of tubes	19.1 mm	19.1 mm
Number of tubes	12 387	2 448
Pitch of tubes	19.2	36.5
Heat transfer surface area	4 497 m^2	749 m^2 x 2
Flow rate of HTF	27.3 ton/h	14.7 ton/h x 2
Construction cost (M$)*	0.25445	0.24995

* Specifications were determined under the condition of almost equal construction costs for the two types of heat exchangers. One dollar was 200 yen in the literature [7].

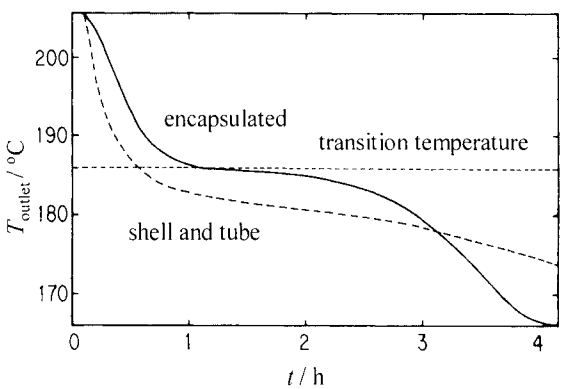


Figure 8. Calculated outlet temperatures of the heat-transfer fluid during discharge mode for the encapsulated-type and the shell & tube type storage units, using pentaerythritol slurry [7].

3.7. A charge and discharge experiment and system evaluation with computer simulation

Although the computer simulation model shown in Figure 6 is quite simple, charge and discharge experiments agreed well with the calculated heat transfer characteristics in the storage units using high-density polyethylene [12], $NaOH\text{-}NaNO_3$ [14] and LiF composites [15]. The calculations were done using explicit finite-difference equations.

The temperature histories of the heat transfer fluid, ethylene glycol, were calculated and compared with the experimental data for the prototype latent thermal storage unit using high-density polyethylene. The storage column is shown in Figure 9. Many form-stable high-density polyethylene rods, 4 mm in diameter and 450 mm in length, are vertically arranged in the storage column with an aluminum honeycomb. Ethylene glycol, the heat transfer fluid, flows into the column from the top during charge, and from the bottom during discharge.

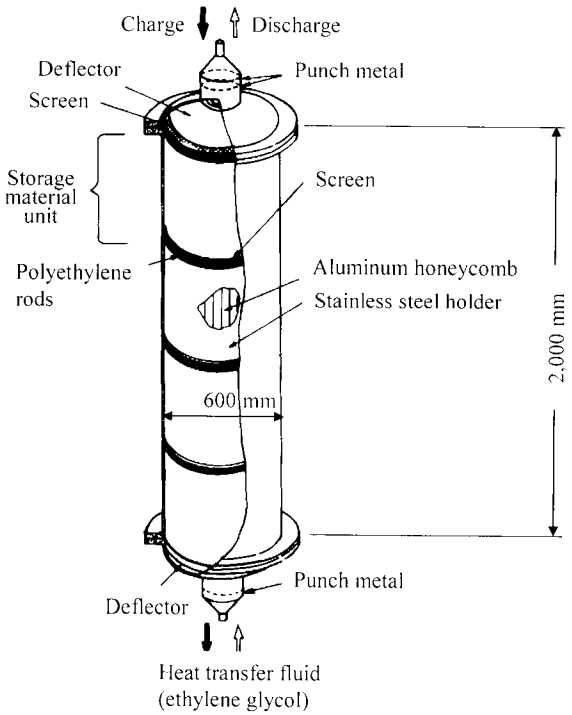


Figure 9. Storage column of the prototype latent thermal storage unit using form-stable high-density polyethylene [16].

In the discharge process, the latent heat of high-density polyethylene was included in the heat capacity between 126 °C and 127 °C. In the charge process, on the other hand, the apparent heat capacity data obtained at every 1 K from DSC measurement were used because the melting occurs over rather a wide temperature range. In Figure 10, the temperature histories of ethylene glycol at the inlet, at the middle, and at the outlet of the storage column are plotted for the charge and discharge processes, under a constant flow rate of 600 l/h.

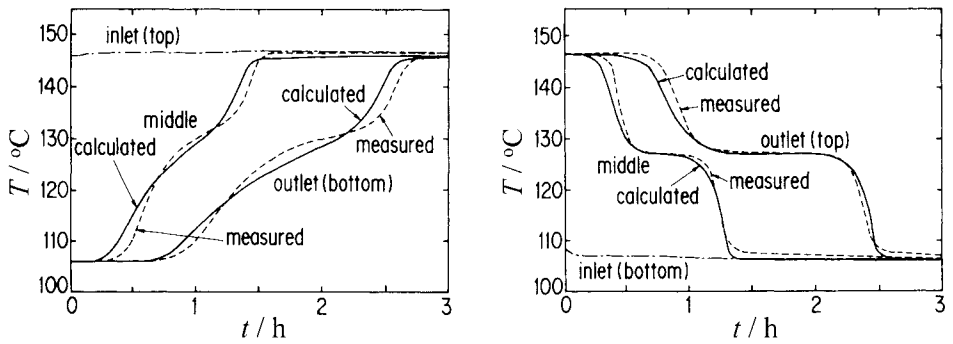


Figure 10. Comparison between the calculated and measured temperature histories of ethylene glycol (the heat-transfer fluid) in the prototype latent thermal storage unit, using form-stable high-density polyethylene [12].

Because the validity of the model and the assumptions for the computer simulation were confirmed for all the storage units mentioned above, the computer simulation was applied to simulation of various thermal application systems with latent thermal storage units, such as the MCFC cogeneration system with molten salt latent thermal storage for hotels shown in Figure 11. The reject gas from the cathode of the MCFC heats up a boiler and an oil heat exchanger and the oil is used to charge and discharge the molten salt latent thermal energy storage unit. A typical example of the peak (summer) hourly demands for electricity and heat for a 5 000 m^2 floor-area hotel is shown in Figure 12. The operation of MCFC systems is controlled so that the electricity demand can be met and the resultant thermal energy from the cells is also shown in the figure with the actual heat demand. The excess heat produced between 9 am and 4 pm is stored in the molten salt storage system and the stored heat is discharged to cover the insufficient heat supply between 4 pm and 8 pm.

The simulation results for the designed storage unit are shown in Figure 13. In this simulation, the flow rate of the heat transfer fluid was calculated from the

required thermal output and the difference between the inlet and outlet temperatures of the storage unit so that the calculated thermal output could be fitted to the required one. The performance of the designed storage unit seems to satisfy both the required outlet temperature and the thermal output.

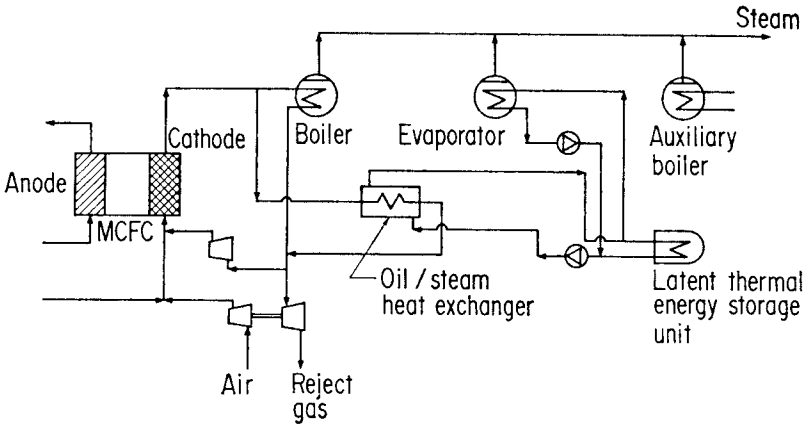


Figure 11. MCFC cogeneration systems with molten salt latent thermal storage for hotels [3].

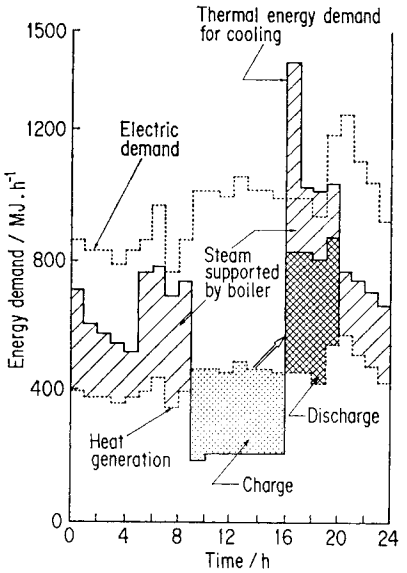


Figure 12. Hourly demands for electricity and heat for a 5 000 m^2- floor area hotel [3].

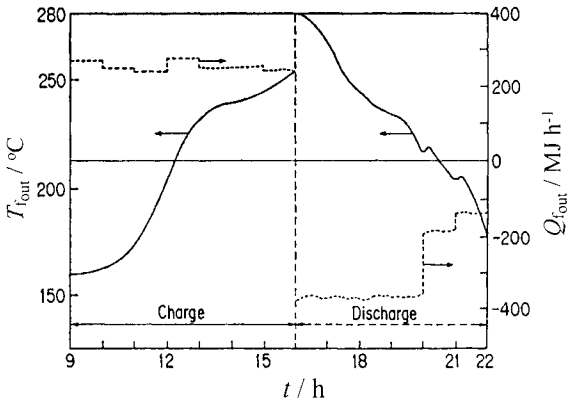


Figure 13. Results of a computer simulation for the performance of the MCFC cogeneration system for hotels [3]. T_{fout} : Outlet temperature of the heat transfer fluid, Q_{fout} : Thermal output from the storage unit.

4. APPLICATIONS OF THERMAL ANALYSIS AND CALORIMETRY

4.1. Sensible thermal storage materials and heat-transfer fluids

In order to design sensible thermal storage equipment, the heat capacities of the materials used in the equipment are the basic data needed and this is also the case for other methods of thermal energy storage. DSC is the most suitable tool for such heat capacity measurements. An example is illustrated in Figure 14

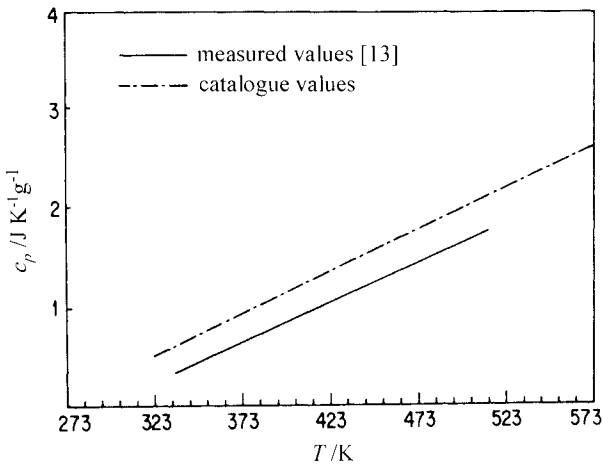


Figure 14. The specific heat capacity of alkyldiphenylethane (a heat-transfer fluid) [13].

[13], where the specific heat capacity, c_p, of alkyldiphenylethane (a heat-transfer fluid) measured by DSC is compared with that in the catalogue, which was obtained not by actual measurement but by theoretical estimation. A discrepancy of about 10% was found. This example clearly shows the need for measurements of the properties of the materials actually used and similar examples are given later.

4.2. Latent thermal storage materials

For air-conditioning applications, water is the most desirable working material, as mentioned before, but its working temperature is limited at 0°C. In the temperature range below 100 °C, some organic compounds, gas clathrate compounds and inorganic salt hydrates were investigated. They are listed in Table 3, together with the temperatures and heats of fusion, T_m and Δh_m, respectively [17]. For the salt hydrates the heat of fusion is roughly proportional to the amount of crystalline water [18].

As described above, candidate working materials in the temperature range from 100 °C to 1000 °C were screened by using their thermodynamic data and material prices as chemical commodities [5]. However, further characterization is needed for materials actually used, because the data in the literature are generally those for purified samples. The necessary data are, for instance, temperatures and heats of transition and/or fusion, reversibility, effects of moisture and/or impurities on their thermal behaviours, stabilities and compatibilities with container materials. Thermal analysis techniques, such as DSC and TG, are very powerful tools, and DSC is especially essential, because it measures fundamental characteristics of the candidate materials. Characteristic applications to several of these candidate materials are shown below, together with other applications of thermal analysis. The description begins with a low-temperature material, i.e. urea, and continues to higher temperature materials, i.e. lithium fluoride.

4.2.1. Urea

Among the thermodynamically-selected candidate materials in the working temperature range from 100 °C to 150 °C, urea provides a unique example for which negative results were obtained [19], in spite of a large heat of fusion and a low cost. The thermal behaviour during repeated melting and crystallization by DSC showed a strong tendency for supercooling as seen in Figure 15. This is not desirable because of the decrease in the usefulness of the recovered heat. The heat of fusion also decreased during the cycles and this indicates low thermal stability of this material.

Table 3.
Organic compounds, gas clathrate compounds and inorganic salt hydrates investigated for their suitability as latent thermal storage materials in the low-temperature range.

Compounds		T_m/°C	Δh_m/kJ kg^{-1}
Organic compound	C_{14}-C_{16} paraffin	2-7	152
	C_{15}-C_{16} paraffin	4-10	153
	1-Decanol	5-7	206
	C_{14} paraffin	2-5	165
	C_{16} paraffin	14-18	201
Gas clathrate	$SO_2 \cdot 6H_2O$	7	247
	$C_4H_8O \cdot 17H_2O$	4.4	255
	$(CH_3)_3N \cdot 10.25H_2O$	5.9	239
	$(C_4H_9)_4NCH_2 \cdot 32H_2O$	12.5	184
	$(C_4H_9)_4NCH_3CO_2 \cdot 32H_2O$	15.1	201
Inorganic salt hydrate	$Na_2SO_4 \cdot 10H_2O/NaCl/NH_4Cl$	13	180
	$CaCl_2 \cdot 6H_2O$	29	180
	$Na_2SO_4 \cdot 10H_2O$	32.4	251
	$Na_2CO_3 \cdot 10H_2O$	32.0	247
	$Na_2HPO_4 \cdot 12H_2O$	36	280
	$Ca(NO_3)_2 \cdot 24H_2O$	43	142
	$Na_2S_2O_3 \cdot 5H_2O$	48.5	200
	$NaCH_3COO \cdot 3H_2O$	58	251
	$Ba(OH)_2 \cdot 8H_2O$	78	293
	$Sr(OH)_2 \cdot 8H_2O$	88	352
	$Mg(NO_3)_2 \cdot 6H_2O$	89	160
	$KAl(SO_4)_2 \cdot 12H_2O$	91	232
	$NH_4Al(SO_4)_2 \cdot 12H_2O$	94	251

T_m: Temperature of fusion, Δh_m: Specific heat of fusion

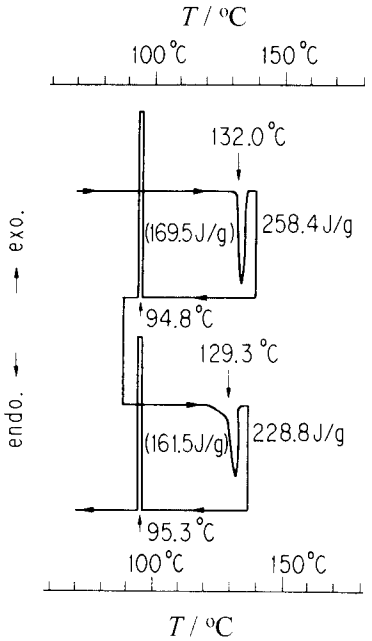


Figure 15. Typical DSC curves for urea during repeated heating and cooling [19].

TG was then used to examine the thermal stability of urea in a nitrogen atmosphere. The mass-loss behaviour observed at different heating rates was kinetically analyzed. Ozawa-Flynn-Wall plots were applied to estimate the activation energy [20], as reproduced in Figure 16. Parallel lines were obtained at different extents of conversion and this is evidence that the activation energy does not change with increasing conversion and, hence, that the thermal decomposition reaction is a simple reaction in which a single elementary process is involved. The activation energy was estimated as 85.0 kJ/mol. Further kinetic analysis, using the concept of reduced-time [20], led to the conclusion that the reaction is a first-order reaction, as seen in Figure 17. From the reduced-time, the real times were calculated at two different temperatures (Figure 17) to predict the actual life during the practical use of this material. For instance, 80% of this material would be decomposed after about 6 h at 413 K or after about 40 h at 383 K and these times are too short for practical use.

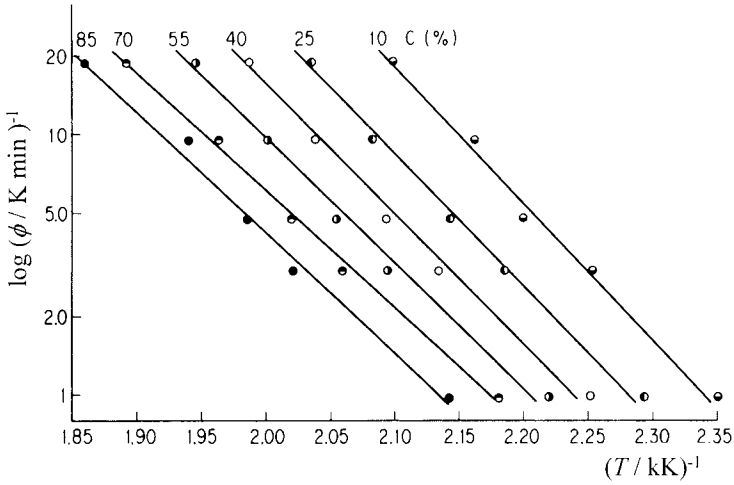


Figure 16. Ozawa-Flynn-Wall plot to determine the activation energy for the thermal decomposition of urea [19]. C : conversion, ϕ: heating rate.

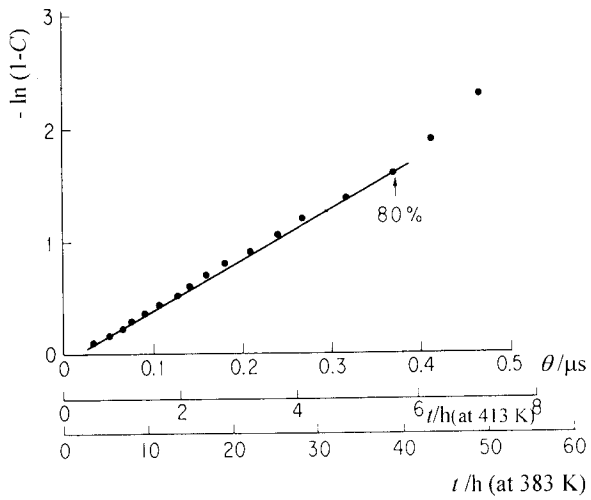


Figure 17. Experimental master curve for the thermal decomposition of urea [19]. θ : reduced-time.

To overcome the drawbacks of urea, mixtures of urea with some other materials was tried. Addition of *n*-hexadecane, *n*-hexadecane-1-ol or stearic acid to form clathrate compounds does not show any effect on the supercooling tendency. Eutectic mixtures with potassium carbonate and sodium nitrate

increase the supercooling tendency and the mixtures do not crystallize even at the room temperature. Improvement in this tendency was found for eutectic mixtures with ammonium chloride (17 mol%) or potassium chloride (9 mol%) and also for the clathrate compound with sebacic acid (36 mol%), but with a decrease in the heat of fusion. Kinetic analysis of the TG results for these mixtures was not successful because of the complexity of the reactions, but the TG curves shifted to a lower temperature range, suggesting low thermal stability of these mixtures. Thus, positive results were not obtained [19]. In conclusion, urea is not suitable for latent thermal storage.

4.2.2. Form-stable polyethylene

As an alternative to urea, high-density linear polyethylene of high crystallinity was investigated, because of its large heat of fusion and low cost. Although urea is preferable on both of these grounds, polyethylene is the second choice. The main fundamental drawbacks of polyethylene and other organic materials are their low thermal conductivity and low thermal diffusivity, which result in a low power-density and a decrease in the quality of the recovered heat. For polymeric materials, a high melt-viscosity enhances this drawback by diminishing convection. A large interface for heat exchange between the storage material and the heat-transfer fluid is thus needed and this brings high cost. To overcome this drawback, the concept of form-stable polyethylene was devised [10]. A surface layer of thin polyethylene rods is crosslinked by argon plasma bombardment. Thus the form of the polyethylene can be retained even in molten state. Surface crosslinking can also be achieved by covering the surface with modified polyethylene, which is polyethylene copolymerized with siloxane, and this surface layer is crosslinked later by introducing moisture. By flowing heat-transfer fluid through bundles of the form-stable polyethylene rods, direct heat exchange between the polyethylene and the fluid can be realized. Heat exchange is thus active and costs are reduced and the power density is increased.

Compatibility of various heat-transfer fluids with the surface crosslinked polyethylene was investigated by DSC. The heat-transfer fluids tested were ethylene glycol, silicone oil, alkyldiphenyl, alkyldiphenylethane and Caloria HT-43 (Exxon Corp.) Samples of the polyethylene and a selected heat-transfer fluid were packed together into a DSC sample cell and sealed in an atmosphere of nitrogen. The cell was then kept for hundreds of hours in the molten state at 150 ^{o}C and changes in the heats of fusion and crystallization were observed, together with their extrapolated onset temperatures. The results are reproduced in Figure 18. Surface crosslinking was found to cause no appreciable changes in the

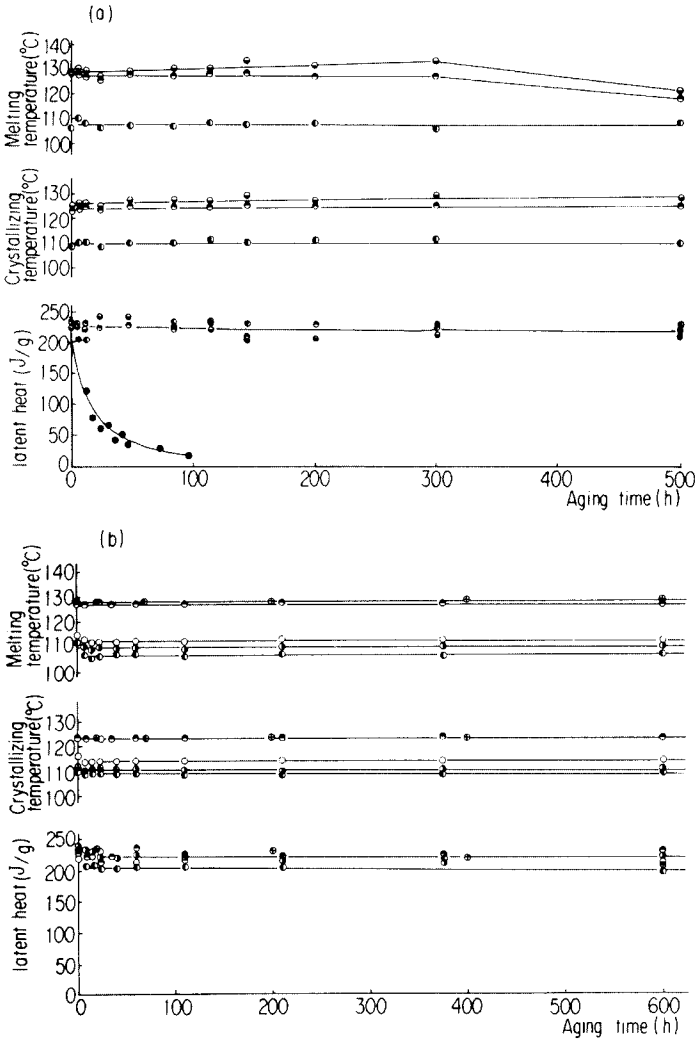


Figure 18. Degradation test of polyethylene with heat transfer fluid [10].
(a) original polyethylene and (b) surface-cross-linked polyethylene.
◒, polyethylene without heat-transfer fluid;
◓, polyethylene with silicone oil;
◐ ,polyethylene with alkyldiphenyl;
◑ ,polyethylene with alkyldiphenylethane;
○, polyethylene with Caloria HT;
⊕, polyethylene with ethylene glycol;
●, polyethylene without heat transfer fluid.
All but the last sample were aged in a sealed pan.

temperatures and the latent heats. Good thermal stability was also clearly observed for the polyethylenes and the mixtures with heat-transfer fluid, especially in the values measured for the latent heat, except for untreated polyethylene in open pan which was used as a control.

Decreases in the melting and crystallization temperatures were found for polyethylene with alkyldiphenyl, alkyldiphenylethane and Caloria HT, although sharp and reversible DSC peaks were observed. Microscopic observation of these heat-transfer fluids, after compatibility tests for long times at 150 °C, revealed spherulite formation in the fluids. Thus, it is clear that polyethylene swells and dissolves in these fluids and this causes decreases in the temperatures but without detectable changes in the latent heat. In contrast with these fluids, no appreciable change was found for ethylene glycol and silicone oil. It was also found that shape of the surface-crosslinked polyethylene was retained in this compatibility test, but melt down was found for polyethylene without the surface crosslinking. Thus, good compatibility and good thermal stability were clearly shown [10] for the surface-crosslinked polyethylene with ethylene glycol or silicone oil. Use of these combinations in inert atmospheres is recommended.

The other unique feature of this material is its wide temperature range of fusion and crystallization; this is a characteristic of polymeric material. Instead of the heats of fusion and crystallization, the enthalpy change as a function of temperature was measured from the DSC results by the method described elsewhere [21, 22] and the results were used for successful simulation of the storage equipment with the polyethylene [12] (see Figure 10).

4.2.3. Pentaerythritol

Pentaerythritol was selected as a candidate material in the temperature range below 200°C. It is a material with several interesting features. Its heat of crystalline transition is as large as the heat of fusion of ice and it is not costly, because it is produced on a relatively large scale as a chemical commodity. Above the transition temperature, the spherical molecule of this material rotates around its crystalline site by dissociating intermolecular hydrogen bonds, but it does not migrate in the crystal, so that it changes to a plastic crystal above the transition temperature. This solid-solid transition is a unique feature of this material.

The transition behaviour was observed by DSC. When a few small grains of the sample (less than 2 mg) were used, the results reproduced in Figure 19 were obtained [8]. The supercooling seen in these DSC curves suggests that nucleation controls the transition. This transition behaviour was then observed at different cooling rates for fine powder samples. The results are shown in Figure 20.

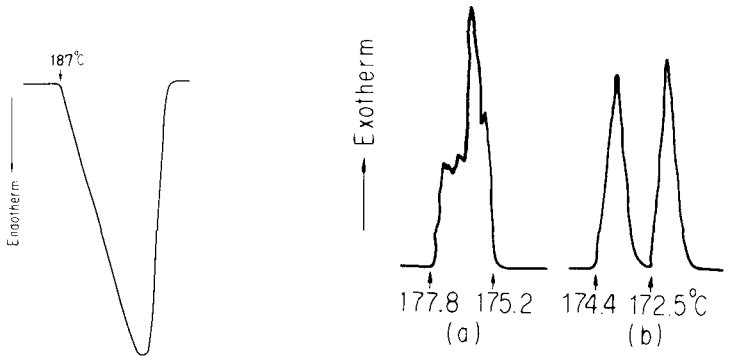


Figure 19. Typical DSC curves for the transition of pentaerythritol [8]. The heating rate is 1.25 °C/min, and the cooling rates are (a) 0.625 °C/min and (b) 1.25 °C/min.

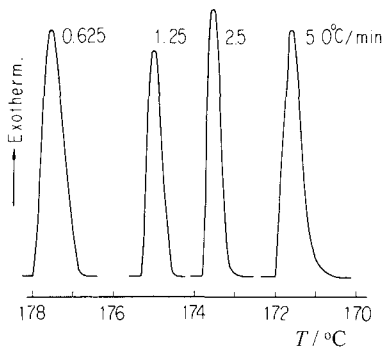


Figure 20. Dependence of the pentaerythritol transition on the cooling rate [8]. The cooling rates are indicated.

Because no overlapping occurs in these curves, a method for kinetic analysis of the transition [23] cannot be applied, but the extent of supercooling was estimated to be less than 10 °C in the practical discharging mode.

In the literature [24], a large influence of moisture on the heat of transition has been described. The temperature and heat of transition measured by high-accuracy calorimetry in a precisely controlled atmosphere were reported to be 188 °C and 322 kJ/kg, respectively. Because our purpose was to use commercially available materials without purification, we measured the temperatures and heats of transition for several commercial products as received. They were 186~187 °C and 287~298 kJ/kg, respectively [8]. These data for the

sample of pentaerythritol actually used were used in the simulation, together with the supercooling tendency as described in the previous section, and again the necessity for measuring the properties of the materials used in actual practice is stressed. DSC is very useful here because it provides reliable data of sufficient accuracy.

The next problem concerning this material is the possibility of thermal decomposition. TG was carried out in a nitrogen atmosphere with a shallow open sample pan. The results are reproduced in Figure 21 and mass loss occurs even in the plastic crystal state. At the melting temperature a discontinuity is not seen in the mass-loss rate. These results were kinetically analyzed in the same way as urea [19]. Parallel lines were obtained in Ozawa-Flynn-Wall plots showing a constant activation energy of 104.4 kJ/mol and a linear plot, similar to that in Figure 16, was obtained up to 80% mass loss, but for a zero-order reaction mechanism. Thus it was clear that the mass loss is sublimation, so that this material should be used in sealed containers.

As pointed out before, improvement of the heat transfer for this organic powder material is needed for practical use. The compatibility of pentaerythritol with the heat-transfer fluids tested for polyethylene was examined. Pentaerythritol samples were packed with fluid into glass containers suitable for DSC and sealed in a nitrogen atmosphere. Similarly to polyethylene, the mixtures were kept at above the transition temperature 195~200 °C for 1 000 h. Good compatibility was found for alkyldiphenyl, alkyldipenylethane and Caloria HT, with which pentaerythritol does not show any change in the temperature and heat of transition.

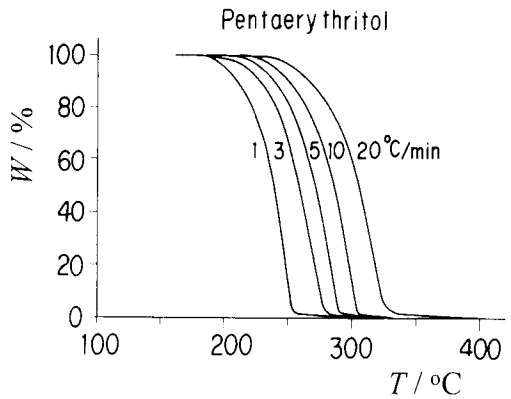


Figure 21. TG curves of pentaerythritol heated in nitrogen in shallow open sample pans at the indicated heating rates [8]. W : Residual mass %.

4.2.4. Alkali hydroxides and their eutectic mixtures

In the temperature range around 200°C, eutectic mixtures of alkali hydroxides were selected as candidate materials [5]. In this selection [5], the heats of fusion of the mixtures were calculated by assuming additivity of the entropies of fusion of the components, because the heats of fusion of eutectic mixtures are generally not available but only the eutectic temperatures [25, 26]. When the transition temperature of a component was higher than the eutectic temperature, the entropy change of the transition was added to the calculated entropy change of the eutectic mixture [5]. The calculated heats are listed in Table 4, together with the DSC results which were obtained later [27, 28]. Fairly good agreement is seen in this table. Among the three mixtures, the NaOH – KOH mixture is the most feasible because lithium compounds are costly.

Table 4.
Compounds and eutectic mixtures of alkali hydroxides, sodium nitrate and sodium nitrite.

Mixture	Composition (mol %)	T_m /°C (obs)	Δh_m /kJ kg^{-1} (obs)	Δh_m /kJ kg^{-1} (calc)
LiOH-NaOH	30 – 70	215	290+58(transition)	339
LiOH-KOH	29 – 71	227	184	285
NaOH-KOH	50 – 50	171	213	230
$NaNO_3$•NaOH		271	265	214 ~ 251
$NaNO_3$•2NaOH		270	295	222 ~ 267
NaOH-$NaNO_3$	81.5 – 18.5	257	292	225 ~ 278
NaOH-$NaNO_3$	59 – 41	266	278	216 ~ 257
NaOH-$NaNO_3$	28 – 72	247	237	197 ~ 226
$NaNO_2$•NaOH		265	313	226 ~ 251
NaOH-$NaNO_2$	73 – 27	237	294	220 ~ 261
NaOH-$NaNO_2$	20 – 80	232	252	205 ~ 214

T_m: Temperature of fusion, Δh_m: Specific heat of fusion

The most serious problems in handling these mixtures are their low surface-tensions and their corrosiveness. When they are put in a metallic cell for thermoanalytical measurements and kept in the molten state, they creep up the wall of the cell and flow out. The answer to this very serious problem is a sample cell made of polytetrafluoroethylene (PTFE) because of its low wettability, high

thermal stability and resistance to corrosion. A PTFE block was machined into a cell of the same dimensions as the usual metallic cells. Because the thermal conductivity of PTFE is very low, DSC peaks becomes broad, but it was shown that this effect had no influence on the calorimetric precision, as seen in Figure 22 [21], so that it can be used for measurements of heat capacity and heat of fusion, but the temperature is limited to use below 300 °C by the temperature of fusion of PTFE.

Another problem of using alkali hydroxides is the large effect of water on transitions and fusions [29]. One example is shown in Figure 23, where TG-DTA results for KOH are shown. KOH was used as received and, by repeated heating and cooling, contaminating water was volatilized as seen in the TG curves and also by the endotherms around 100 °C in the DTA curves. Volatilization of the water results in the shape of the endotherm at the transition of KOH (231°C) becoming sharp and a similar change was observed for the fusion. Heine et al [30] reported earlier that a eutectic mixture of NaOH and KOH shows no appreciable peak. According to the above results it might be the effect of moisture. Therefore, adequate dehydration is recommended before loading these materials into heat-storage equipment.

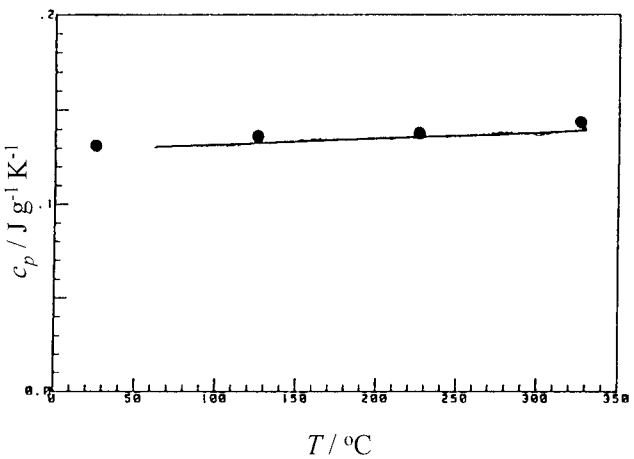


Figure 22. The specific heat capacity of platinum (continuous line) measured by DSC with the PTFE sample pan [21]. Literature data are shown as points.

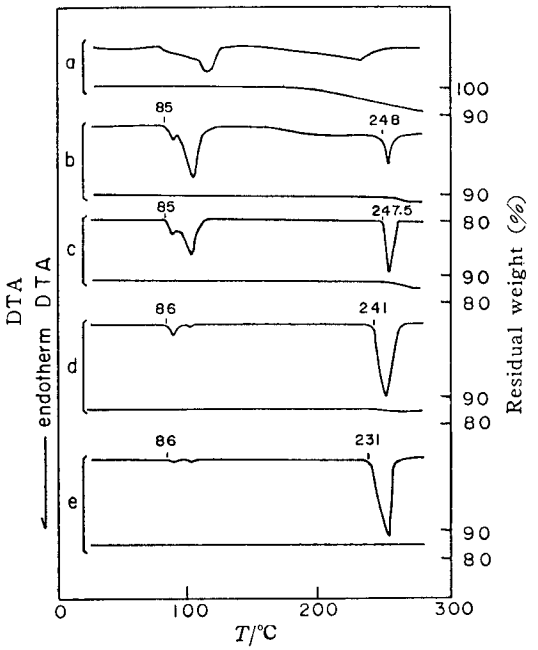


Figure 23. TG-DTA curves of repeated heating and cooling of KOH contaminated with traces of water [29].

4.2.5. Compounds and eutectic mixtures of NaOH with $NaNO_3$ or $NaNO_2$

In the temperature range from 230 °C to 300 °C, compounds and eutectic mixtures of NaOH with $NaNO_3$ or $NaNO_2$ were chosen [5]. The selection was done using the calculated heats of fusion (see Table 4). According to the literature [25, 26], there are two compounds in the system of NaOH and $NaNO_3$, namely $NaNO_3$·NaOH and $NaNO_3$·2NaOH, and therefore three eutectic mixtures exist. They are: $NaNO_3$ 72 mol% - NaOH 28 mol%; $NaNO_3$ 41 mol% - NaOH 59 mol% and $NaNO_3$ 18.5 mol% - NaOH 81.5 mol%. An equimolar compound between $NaNO_2$ and NaOH is reported and hence two eutectic mixtures exist: i.e., $NaNO_2$ 27 mol% - NaOH 73 mol% and $NaNO_2$ 80 mol% - NaOH 20 mol% [25, 26]. These materials are very important, because their melting temperatures are suitable for storing heat in commercial nuclear power plants, such as a PWR.

DSC scans for these compounds and mixtures were obtained with the above-mentioned PTFE sample cell [27, 28]. Most of the samples show a strong tendency to supercool. A typical result is reproduced in Figure 24, where a sharp exothermic peak due to crystallization is observed in the DSC cooling curve for $NaNO_3$·2NaOH. For all compounds and mixtures, the melting temperatures

(extrapolated onset temperatures) are listed in Table 4, together with the heats of fusion. Values of the heat capacity were also obtained for all of the samples [22, 27, 28]. An example is shown in Figure 25 and a small endotherm with peak at 154 °C is visible, which was assigned to the transition of the compound $NaNO_3$•NaOH.

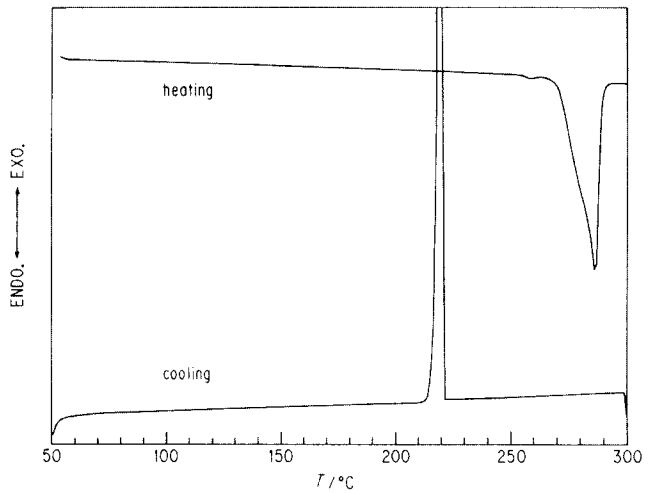


Figure 24. DSC curves for $NaNO_3$•2NaOH [28].

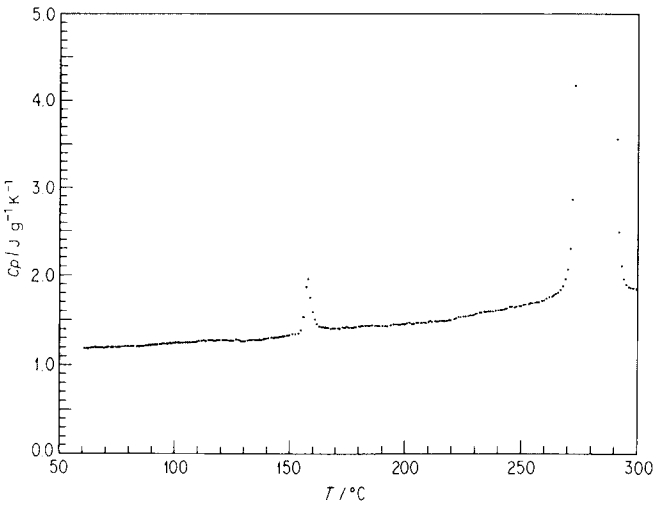


Figure 25. The heat capacity of $NaNO_3$•NaOH [28].

All the compounds have a strong tendency to supercool and some of the eutectic mixtures also show the same tendency. However, there is one promising material because of its low supercooling tendency and large heat of fusion, i.e., $NaNO_3$ 18.5 mol% - NaOH 81.5 mol%. For the same reason, $NaNO_2$ 27 mol% - NaOH 73 mol% was selected as the second promising material. In the practical applications of the above materials, for instance for a nuclear power plant, industrial-grade materials are used. Suppose that such a storage unit is to be introduced to a power plant of 200 MW rated electrical output and that thermal storage of 4.2 GW h is needed for 8 h duration, then about 60 kt of the above material will be used. It is interesting to point out that these quantities are about 6 x 10^{12} times the amount used in a DSC experiment.

The mercury electrode process for producing NaOH was prohibited in Japan because of its potential environmental pollution. Instead the asbestos separator process was operated and later the ion-exchange membrane process was introduced. Therefore, three varieties of commercial-grade NaOH are available and their purities are different, for instance they contain different amounts of NaCl as contaminant. To observe the effects of impurities, mixtures of $NaNO_3$ 18.5 mol% - NaOH 81.5 mol% were made from the different varieties of NaOH and tested in steel tubes (as in a practical unit) through 1000 cycles of heating and cooling [30]. The time that the sample was kept above its melting temperature was, on average, over 3000 h. The initial temperatures and heats of fusion were scattered in a range of 245 to 257 °C and 253 to 292 kJ/kg, respectively, and, in their DSC curves, additional small shoulders and peaks, presumably due to ternary eutectic mixture formation, were detected. Samples were taken during this cyclic heating and cooling and, in the DSC curves of the samples, differences were found compared to the original DSC curves. One difference is thought to be due to contamination from the steel tubes. Another difference was caused by a zone-refining effect, because the fusion proceeds from top to bottom and the crystallization proceeds in the opposite direction. However, although the other varieties of NaOH showed impurity effects, little change was detected for the sample of NaOH made by the ion-exchange membrane process and this result was also confirmed by a 1000 cycle bench-scale test [30].

4.2.6. LiF and its eutectic mixtures [11]

Brayton-cycle and Stirling-cycle solar dynamic power generation systems require storage materials with melting temperatures around 1000 K. LiF and its eutectic mixtures with CaF_2 and MgF_2 were selected for candidate materials in this temperature range. Because the solar dynamic power generation systems are operated in a low earth-orbit, the storage unit will be used under micro-gravity

conditions. In order to decrease the specific mass of the storage unit and the mechanical stress on the container arising from the volume change on fusion, and also to enhance thermal conduction within the storage materials, composite storage materials of fluoride salts with SiC or carbon have been proposed [11].

Heat-flux DSC was used to measure the latent heats of the fluorides and their composites. Because the fluoride salts readily creep up in a sample pan at high temperatures, a sealed gold pan and an open graphite pan were successfully used. Fluorides with high melting points and high vapour pressures, such as LiF, were sealed in a gold sample pan, specially made to fit inside the alumina liner as shown in Figure 26.

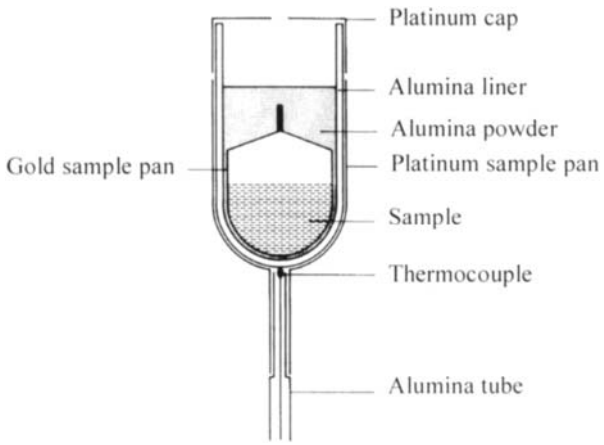


Figure 26. The sealed gold sample pan and the arrangement around the sample pan in the DSC [11].

The gold sample pan was covered with fine alumina powder to make the radiation heat flux from the sample uniform. A platinum cap was made to cover the platinum sample cup. The use of the platinum cap was confirmed to be quite effective in making the radiation heat-flux uniform and in obtaining reproducible measurements. The proportionality constant of the apparatus with this arrangement (but using an alumina sample pan) was almost temperature independent, at least between 400 and 1200 °C, as shown in Figure 27.

The melting and solidification temperatures and heats of fusion of samples with different purities are listed in Table 5. Although the melting temperatures are almost the same, the heats of fusion show a slight difference. This is another example showing the necessity of measurement of the latent heat of the actual sample used in the storage unit.

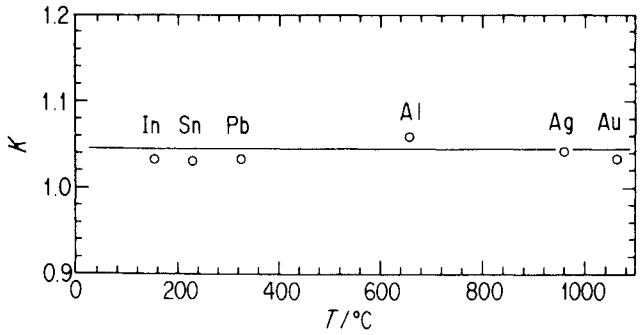


Figure 27. Proportionality constant of the heat-flux DSC [11].

From the DSC results obtained under repeated melting and crystallization, it was confirmed that the melting and crystallization temperatures and heat of fusion are almost unchanged, both for LiF and its composite with porous SiC. Figure 28 illustrates the results for the latter.

Table 5.
Melting temperatures and heats of fusion of different LiF specimens [11]

Material	T_m /°C	Δh_m /kJ kg^{-1}
LiF(99.99%), Aldrich	844.8	1015
LiF(99.9 %), Rare Metallic	844.4	991
LiF(99.9 %), Soekawa	843.5	956

Heats of fusion of the candidate fluorides are listed in Table 6, together with the literature values and values estimated on the assumption of the additivity of the entropies of fusion. The melting temperatures are also listed in the table. LiF and LiF-CaF_2 and their composites showed reasonably high heats of fusion. The heat of fusion of LiF-MgF_2 was, however, so low that it should be excluded from the candidate latent thermal storage materials for space use.

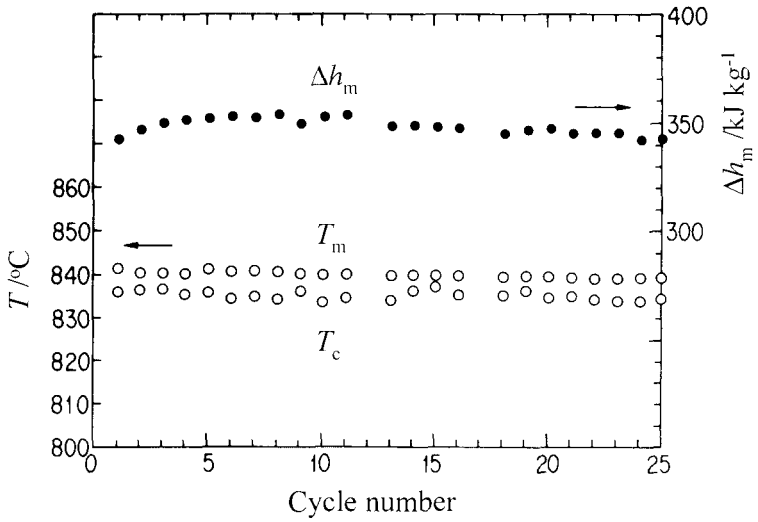


Figure 28. Changes in heats of fusion and melting and solidification temperatures of a LiF/SiC composite after increasing numbers of cycles of heating and cooling [11].

Table 6
Melting temperatures, T_m, solidification temperatures, T_c and specific heats of fusion, Δh_m, of LiF, LiF-CaF_2, LiF-MgF_2 and their composites with porous SiC [11].

Material (mol %)	T_m /°C		T_c /°C	Δh_m / kJ kg^{-1}		
	measured	literature	measured	measured	literature	calculated
LiF(99.99% purity)	845	848	841	1015	1037	
LiF/SiC	844		837	335		
LiF-CaF_2(80.5-19.5)	763	765	774	757	820	656
LiF-CaF_2(80.5-19.5)/SiC	762		758	174		
LiF-MgF_2(67-33)	730	742	726	490	917	761
LiF-MgF_2(70-30)	728	728	735	516	520	770

4.3 Chemical storage materials

Examples of chemical reactions for thermal energy storage are listed in Table 7, together with adsorption reactions. The turning temperature, T^*, is the temperature where the standard Gibbs energy change is 0 and it can serve as one of the criteria for screening chemical reactions for thermal energy storage. The enthalpy of formation, ΔH_f, is another criterion. The equilibrium temperature of a reversible chemical reaction can be controlled by pressure, so that the temperature of the heat extracted after storage can be changed easily. In other words, the chemical reaction can be operated as a heat pump.

Table 7.
Examples of chemical reactions suitable for chemical storage [31]

Working Fluid	Reaction	ΔH^o kJ / (mol working fluid)	T^* K
H_2O	Zeolite 13X	79.4	
	Silica gel	46.8	
	$MgCl_2 \cdot 4H_2O \rightarrow MgCl_2 \cdot 2H_2O + 2H_2O$	68.0	462.0
	$CaCl_2 \cdot 2H_2O \rightarrow CaCl_2 + 2H_2O$	62.0	490.0
	$Mg(OH)_2 \rightarrow MgO + H_2O$	81.0	531.0
	$Ca(OH)_2 \rightarrow CaO + H_2O$	109.0	752.0
NH_3	$NiCl_2 \cdot 6NH_3 \rightarrow NiCl_2 \cdot 2NH_3 + 4NH_3$	60.0	441.0
	$CaCl_2 \cdot 8NH_3 \rightarrow CaCl_2 \cdot 4NH_3 + 4NH_3$	42.0	303.0
	$CaCl_2 \cdot 4NH_3 \rightarrow CaCl_2 \cdot 2NH_3 + 2NH_3$	46.0	315.0
	$MnCl_2 \cdot 6NH_3 \rightarrow MnCl_2 \cdot 2NH_3 + 4NH_3$	50.0	365.0
	$FeCl_2 \cdot 6NH_3 \rightarrow FeCl_2 \cdot 2NH_3 + 4NH_3$	51.0	388.0
	$NH_4Cl \cdot 3NH_3 \rightarrow NH_4Cl + 3NH_3$	28.0	276.0
H_2	$MgH_2 \rightarrow Mg + H_2$	76.0	560.0
	$MgNiH_4 \rightarrow MgNi + 2H_2$	64.0	530.0
	$LaNi_5H_6 \rightarrow LaNi_5 + 3H_2$	30.0	273.0
	$TiH_2 \rightarrow Ti + H_2$	144.0	1100.0
CO_2	$MgCO_3 \rightarrow MgO + CO_2$	117.0	670.0
	$CaCO_3 \rightarrow CaO + CO_2$	178.0	1110.0
Others	$CH_3CH(OH)CH_3 \rightarrow CH_3CO\,CH_3 + H_2$	54.3	475.0
	$CaCl_3 \cdot 2\,CH_3OH \rightarrow CaCl_3 + 2\,CH_3OH$	51.9	410.0
	$C_6H_{12} \rightarrow C_6H_6 + 3H_2$	207(C_6H_6)	568.0

The reactions from left to right are endothermic and used for charging.
ΔH^o: Standard enthalpy of reaction per mole of working fluid, T^*: Turning temperature where the standard Gibbs energy change is 0.

Figure 29 shows the principle of upgrading to using two reaction equilibria, such as metal hydrides with different vapour pressures. A plot of equilibrium decomposition pressure against temperature is shown for various metal hydrides in Figure 30 [32]. Enthalpies of formation can be estimated using the thermodynamic relation $\ln p = \Delta G^{\circ}/RT = \Delta H^{\circ}/RT - \Delta S^{\circ}/R$, where p is pressure, T is temperature, ΔG° is standard Gibbs energy change, ΔH° is standard enthalpy change, ΔS° is standard entropy change, and R is the gas constant. For a desiccant air-conditioning system using silica-gel, zeolite, etc., an adsorption-temperature diagram is essential. Vapour pressure and adsorption measurements, and calorimetry are powerful tools for the R & D of chemical storage.

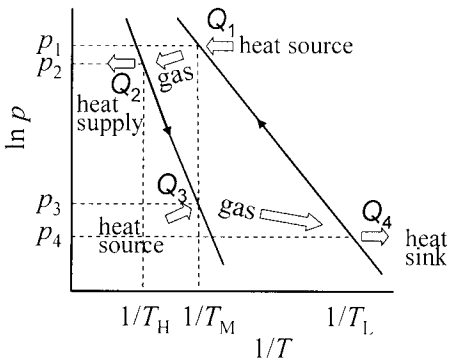


Figure 29. Principle of adsorption upgrading

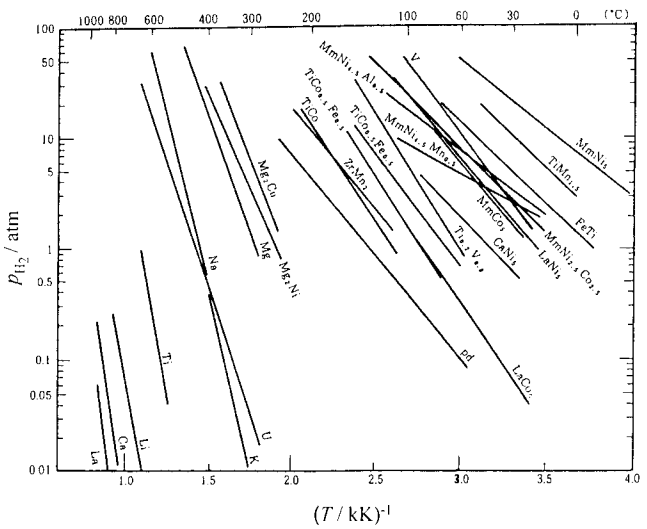


Figure 30. Dependence of dissociation pressures on temperature for various metal hydrides [32].

4.4 Other applications

Thermal analysis and calorimetry have proved useful in studies of batteries and their component materials [33]. As the energy and power densities of batteries increase, thermal management becomes more important. Various measurements on Li-ion batteries have recently been reported. DSC has been used to study the thermal decomposition of electrolytes [34], the reactions of electrolytes with cathode materials [35], the thermal behaviour due to phase transitions of cathode materials such as Li_xCoO_2 [36] and so forth. Calorimetric studies on Li-ion batteries during charge and discharge have also been reported [37]. Thermal analysis and thermal property measurements will continue to be used as convenient and powerful tools for R&D of energy storage technology.

The authors are grateful for permission to reproduce tables and figures granted by Elsevier, the Chemical Society of Japan, the Japan Society of Refrigerating and Air Conditioning Engineers, the Japan Society of Thermophysical Properties, the American Society of Mechanical Engineers, and the American Chemical Society.

REFERENCES

1. M. Kamimoto, Y. Abe, S. Sawata, T. Tani, T. Ozawa , J. Chem. Eng Japan, 19 (1986) 287.
2. Y. Abe, M. Kamimoto, Y. Takahashi, R. Sakamoto, K. Kanari, T. Ozawa, Proc. 19th Intersoc. Energy Conv. Eng. Conf., (1984) 1114.
3. Y. Abe, K. Kanari, M. Kamimoto, Proc. 23rd Intersoc. Energy Conv. Eng. Conf., (1988) 165.
4. Y.Abe, K.Tanaka, O.Nomura, K.Kanari, Y.Takahashi, M.Kamimoto, Proc. 23rd Intersoc. Energy Conv. Eng. Conf., Vol.3 (1991) 63.
5. T. Ozawa, M. Kamimoto, R. Sakamoto, Y. Takahashi, K. Kanari, Bull. Electrotech. Lab. (Densoken Iho), 43 (1979) 289.
6. Y. Takahasshi, R. Sakamoto, Y. Abe, K. Tanaka, M. Kamimoto, Proc. 2nd Asian Thermophys. Properties Conf., (1989) 567.
7. M. Kamimoto, Y. Abe, K. Kanari, S.Sawata, T.Tani, T. Ozawa, Proc. 21st Intersoc. Energy Conv. Eng. Conf., (1986) 730.
8. R. Sakamoto, M. Kamimoto, Y. Takahashi, Y. Abe, K. Kanari, T. Ozawa, Thermochim. Acta, 77 (1984) 241.
9. Y. Abe, R. Sakamoto, Y. Takahashi, M. Kamimoto, K. Kanari, T. Ozawa, Proc. 19th Intersoc. Energy Conv. Eng. Conf., Vol.2 (1984) 1120.
10. Y. Takahashi, R. Sakamoto, M. Kamimoto, K. Kanari, T. Ozawa , Thermochim. Acta, 50 (1981) 31.

11. Y.Takahashi, A.Negishi, Y.Abe, K.Tanaka, M.Kamimoto, Thermochim. Acta, 183 (1991) 299.
12. M. Kamimoto, Y. Abe, K. Kanari, Y. Takahashi, T. Tani and T. Ozawa, Trans. ASME J. Solar Energy Eng., 108 (1986) 290.
13. Y. Takahashi, M. Kamimoto, Y. Abe, Y. Nagasaka, A. Nagashima , Netsu Bussei(J. Thermophys. Prop. Jpn.), 2 (1988) 53.
14. K. Kanari, Y. Abe, K. Tanaka, Y. Takahashi, R. Sakamoto, M. Kamimoto, T. Ozawa, Kagaku Kogaku Ronbunshu, 17 (1991) 15.
15. O.Nomura, K.Tanaka, Y.Abe, Y.Takahashi, K.Kanari, M.Kamimoto, Space Power, 12 (1993) 229.
16. M. Kamimoto, Y. Abe, S. Sawata, T. Tani, T. Ozawa , Trans. ASME J. Solar Energy Eng., 108 (1986) 282.
17. K. Narita and J. Kai, J. Inst. Electr. Eng., Jpn. (Denki-gakkai Shi), 101 (1981) 15.
18. K. Narita, J. Kai, H. Kimura and M. Ikeda, 15th Jpn. Conf. on Calorimetry and Thermal Analysis (Kanazawa, 1979).
19. M. Kamimoto, R. Sakamoto, Y. Takahashi, K. Kanari and T. Ozawa, Thermochim. Acta, 74 (1984) 281.
20. T. Ozawa, Bull. Chem. Soc. Jpn., 38 (1965) 1881.
21. Y. Takahashi, Thermochim. Acta, 88 (1985) 199.
22. M. Kamimoto, J. Thermophys., 11 (1990) 305.
23. T. Ozawa, Polymer, 12 (1971) 150.
24. I. Nitta, S. Seki and M. Momotani, Proc. Jpn. Acad., 26 (1950) 25; I. Nitta, S. Seki, M. Momotani and S. Nakagawa, Proc. Jpn. Acad., 26 (1950) 11; I. Nitta, T. Watanabe, S. Seki and M. Momotani, Proc. Jpn. Acad., 26 (1950) 19; I. Nitta, S. Seki and K. Suzuki, Bull. Chem. Soc. Jpn., 24 (1951) 63
25. E. M. Levin, C. R. Robins and H. F. McMurdie, Phase Diagrams for Ceramists, 3rd Edn, American Ceramic Society, Columbus, OH, 1974.
26. G. J. Janz and R. P. T. Tomkins, Physical Properties Data Complilations Relevant to Energy Storage, IV, Molten Salts: Data on Additional Single and Multi-Component Salt Systems (NSRDS-NBS 61, Part IV), Natl. Bur. Stand., Washington, DC, 1981.
27. Y. Takahashi, M. Kamimoto, Y. Abe, R. Sakamoto, K. Kanari and T. Ozawa, Thermochim. Acta, 121 (1987) 193.
28. Y. Takahashi, M. Kamimoto, Y. Abe, R. Sakamoto, K. Kanari and T. Ozawa, Thermochim. Acta, 123 (1988) 233.
29. Y. Takahashi, M. Kamimoto, R. Sakamoto, K. Kanari and T. Ozawa, J. Chem. Soc. Jpn., Chem. and Ind. Chem. (Nippon Kagaku Kaishi), [6] (1982) 1049.

30. D. Heine, F. Heess nd M. Groll, Proc. 14th Intersoc. Energy Conv. Eng. Conf., (1984) 1120.
31. H. Kameyama, Reito (Refrigeration) 71 (1996) 476.
32. S. Ono, Y. Ohsumi, Ceramics, 14 (1979) 339.
33. Special Issue – Calorimetry and Thermal Analysis in Battery Technology, Netsu Sokutei (Calorimetry and Thermal Analysis), 30 (2003) 2.
34. M. A. Gee, F. C. Laman, J. Electrochem. Soc., 140 (1993) L53; T. Kawamura, A. Kimura, M. Egashira, S. Okada, J. Yamaki, J. Power Sources, 104 (2002) 260.
35. Y. Baba, S. Okada, J.Yamaki, Solid State Ionics, 148 (2002) 311.
36. Y. Saito, K. Takano, K. Kanari, A. Negishi, K. Nozaki, K. Kato, J. Power Sources, 97-98 (2001) 688.
37. K. Takano, Y. Saito, K. Kanari, K. Nozaki, K. Kato, A. Negishi, T. Kato, J. Appl. Electrochem., 32 (2002) 251.

Handbook of Thermal Analysis and Calorimetry. Vol. 2: Applications to Inorganic and Miscellaneous Materials
M.E. Brown and P.K. Gallagher, editors
© 2003 Elsevier B.V. All right reserved.

Chapter 8

THE THERMAL STABILITY OF EXPLOSIVES

Jimmie C. Oxley

Chemistry Department, University of Rhode Island, Kingston, RI 02882, USA

1. INTRODUCTION

Military explosives tend to be extremely thermally stable materials. They have to be. The military wants to be able to store them for decades without incident; yet, when they are used, they must perform at full strength. Military explosives are typically organic chemicals, containing only carbon (C), hydrogen (H), oxygen, (O), and nitrogen (N). The reason for this is found in the performance of these materials. With proper initiation, chemical explosives (as opposed to mechanical or atomic explosives) undergo violent decomposition to produce much heat, gas, and rapid expansion of matter. A detonation is a special type of explosion. A detonation is initiated by the heat accompanying shock compression; it liberates sufficient energy, before any expansion occurs, to sustain the shock wave. The shock wave propagates into the unreacted material at supersonic speed (1500 to 9000 m/s). To maximize the volume change, gas formation, and heat release, chemical explosives are designed to be dense and have high oxygen content and positive heats of formation. A good explosive must react *quickly* to release *energy* and to form products that take up a much larger volume than the original material, i.e. *gases*.

Detonation is distinguished from combustion by its rapidity. The energy in calories or joules, released by an explosive is not dramatic; burning fuel generally generates more energy than an explosive. More important, in terms of functioning as an explosive, is the rate of energy release (joules/seconds = watts) and the volume of the working fluid (gases). Some typical examples of energy release are given in Table 1.

Detonation is so rapid that external oxygen (e.g. in the air) does not contribute to the initial heat-producing reaction. The oxidation reaction can be sufficiently rapid to support the detonation wave only if the explosive has internal oxygen readily available. This is usually achieved in military explosives by having

oxygen available in the form of the $-NO_2$ group (Figure 1). That functionality may be attached to oxygen ($O-NO_2$) as in the nitrate esters, nitroglycerin, nitrocellulose, and pentaerythritol tetranitrate (PETN); or to carbon ($C-NO_2$), saturated carbons in nitroalkanes like nitromethane or unsaturated carbon as in trinitrotoluene (TNT) and picric acid; or to nitrogen ($N-NO_2$) as in nitramines like RDX and HMX ($C_3H_6N_6O_6$ and $C_4H_8N_8O_8$, respectively).

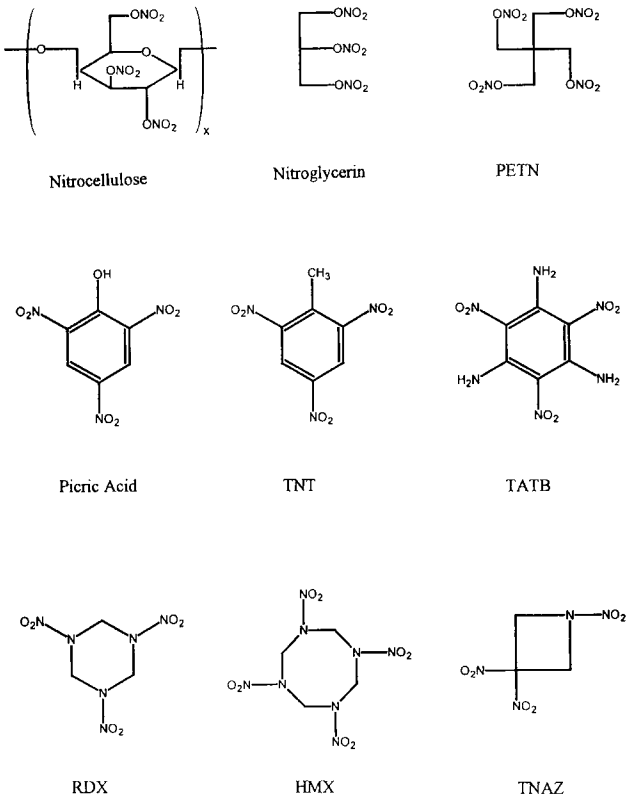


Figure 1. Typical military explosives

Optimally, the mono-molecular explosive would have sufficient oxygen to convert every H to H_2O and every C to CO or CO_2, e.g. RDX and HMX. However, many explosives are oxygen deficient; for example, TNT ($C_7H_5N_3O_6$). Though not as "powerful" an explosive as RDX and HMX, TNT is a perfectly good explosive, even though it is oxygen deficient.

RDX $C_3H_6N_6O_6 \rightarrow 3\ N_2 + 3\ H_2O + 3\ CO$

TNT $C_7H_5N_3O_6 \rightarrow 1.5\ N_2 + 2.5\ H_2O + 3.5\ CO + 3.5\ C$

Commercial explosives are generally mixtures of oxidizer and fuel. Ammonium nitrate (AN) is the usual oxidizer. These mixtures do not have the high detonation velocities exhibited by military materials, but they do detonate. The key to their functioning is an intimate mix of the oxidizer (AN) and fuel, such as in the formulation ANFO (ammonium nitrate/fuel oil), where the fuel is allowed to soak into the AN.

Table 1.
Some examples of the energy outputs of common fuels and explosives

	kJ/g
Burning petroleum	50
Burning coal	33
Burning wood	17
Detonating Dynamite	5.4
	W/cm^3 ($J\ s^{-1}\ cm^{-3}$)
Burning acetylene	10^3
Deflagrating propellant	10^6
Detonating high explosive	10^{10}

The NO_2 functionality is typically found in monomolecular explosives because the nitrogen can convert to nitrogen gas, while the oxygen aids the gasification of carbon and hydrogen. Of equal importance with the fact NO_2 carries oxygen but does not require it, is the fact that breaking the X-NO_2 bond is not too energetically unfavorable. Generally, the X-NO_2 bond provides a "trigger" linkage to start the reaction. However, other functionalities can served as trigger linkages. Peroxides are an obvious example. The oxygen-to-oxygen (O-O) bond offers a potential trigger linkage. In fact, that bond is weaker than carbon-to-nitrogen or nitrogen-to-nitrogen bonds (Table 2); thus, it functions as the weak link that permits low-energy degradation of peroxide molecules. The relative ease of peroxide decomposition is exploited in a variety of chemical syntheses. However, it should be remembered that the O-O bond is a source of oxygen available for potentially rapid self-oxidation and explosion. The peroxides in common industrial use contain only one O-O functionality per molecule, which leaves them with insufficient oxygen to gasify the majority of

the C and H atoms in the molecule. These peroxides are not usually considered explosives, even though some, such as di-t-butyl peroxide (C_4H_9-O-O-C_4H_9), are reported to have "TNT equivalence" of 30%. TATP and HMTD exhibit the peroxide characteristic of easy decomposition, but they also contain three peroxide linkages per molecule. As a result, their explosive output is higher than the peroxides typically used in commercial manufacture: TATP is listed as having 88% TNT equivalence, and HMTD, 60%. The unusual danger in these peroxides is not their blast strength; it is their ease of initiation (due to the peroxide linkage) and the easy with which terrorists have acquired and used the materials for their synthesis (e.g. Richard Reid the would-be shoe bomber, Dec. 2001).

Table 2. Some bond and activation energies

Compound	Trigger linkage	Bond energy/kcal mol^{-1}	E_a/kcal mol^{-1}
nitroarene	C-NO_2	73	70
nitramine	N-NO_2	39	47
nitrate ester	O-NO_2	53	40
peroxide	CO-OC	34	35

In discussing TNT equivalence there are several points to consider. (1) If a material is low-energy, such as di-t-butyl peroxide, it may be stored or shipped in large quantities. Five thousand tons of a material with a TNT equivalence of 20% could still affect a blast on the order of one kiloton TNT. (2) "TNT equivalence" is evaluated by a variety of tests, and the results from different tests are not necessarily parallel. In fact, many explosive designers never use the term "TNT equivalence." Evaluation of explosive performance depends on the end objective. The Department of Defense and Department of Energy generally want to fragment or shatter metal. For that application the pressure jump associated with the shock front is important; performance is measured in terms of detonation pressure or velocity. For the mining industry, the objective is to move mountains; heaving action is important (Table 3). For that purpose, the work produced by expansion of the hot detonation gases must be maximized. The explosives used for this purpose may have slower detonation velocities than military explosives. Composite explosives—intimate mixtures of fuel and oxidizer (e.g. ANFO)—are adequate if gas and temperature output are high, creating lots of $P\Delta V$ (expansion) work.

The thermal stability of an explosive determines its shelf-life, critical dimensions, and critical temperature. The first-step in evaluating the stability of a newly synthesized explosive is laboratory-scale analysis. Since this analysis should be performed prior to any scale-up, only limited amounts of the material will be available. Furthermore, since the material is supposed to be an explosive, working with a small amount is a wise precaution. A common safety check with a compound of uncharacterized stability is to put a bit (5 mg) on the end of a spatula and place it in a flame; a similar amount is impacted between an anvil and a two-pound hammer. Violent response is a severe warning, but the ability to recognize unusual violence comes with experience with other explosives. These tests correspond to a "back-of-the-envelope" calculation. Herein a number of more characterized analytical techniques are discussed. Since each method has its own failings, results should be confirmed by another method; further, it is imperative laboratory-scale results be corroborated by large-scale tests.

Table 3.
Two Types of Explosive Performance

application	Military	Mining
Task	shatter demolish	heave, displace move rock knock down walls
Name	brisance	power (incorrect) strength, blast
Factors	detonation velocity detonation pressure	heat of detonation gas volume/weight
Assessment metric	crusher tests compression of Cu detonation velocity	ballistic motor Trauzl or lead block underwater explosion cylinder test
Control	rate of release cannot be predicted	adjustment of CHNO can predict heat & gas release

2. THERMAL STABILITY TESTING

2.1. Introduction

Thermal stability assessment testing can be categorized in a number of ways: (a) by sample size, (b) by the quantitativeness of the outcome, and (c) by the assessment mode. (a) Laboratory-scale thermal hazards testing can be divided into micro-, small-, and mid-scale test techniques. Micro-scale testing involves

less than 5 mg of sample and includes techniques such as DSC (differential scanning calorimetry), DTA (differential thermal analysis), TG (thermogravimetry), and a number of classical isothermal heating and analytical techniques. Small-scale tests involve between 40 mg to 5 g of sample. Henkin [1], ODTX (one-dimensional time-to-explosion test) [2], vacuum stability [3], CRT (chemical reactivity tests) [4], ARC (accelerating rate calorimetry), RSST (FAI) and RC1 (Mettler) are tests that fall in this category. The Koenen test [5], SCB (small-scale cook-off bomb) [5], 1-litre cook-off and various sealed cook-off tests are mid-scale tests (30 to 1000 g sample). (b) Many of these tests are useful only in comparing the relative stability of like materials, e.g. two different batches of nitrocellulose. Such tests usually lack sufficient information to extrapolate results to different conditions. Examples of tests which are usually used in a comparative mode are the Abel, Taliani, "65.5°C, vacuum stability, CRT, and all the cook-off tests. Tests, which are often used in a quantitative fashion, include DSC, DTA, TG, and Henkin. When these tests are used to quantify thermal stability (i.e. determine Arrhenius parameters), the results can be extrapolated to regimes of temperature beyond that explicitly studied. (c) The tests can be classified in terms of the mode of stability assessment. Let us consider the decomposition of ammonium nitrate (AN) as an example of the exothermic decomposition of any explosive [6]:

$$NH_4NO_3 \rightarrow N_2O + N_2 + 2\,H_2O + 300 \text{ cal/g.}$$

There are a number of ways to assess the stability of AN. One can monitor the production of heat, or observe the time or temperature needed to produce a catastrophic event, such as vessel failure. While monitoring time-to-catastrophic event does take advantage of the buildup of decomposition products, it, generally, does not lend itself to quantification. On the other hand, there are several commercial instruments that monitor heat released (DSC, DTA, calorimeters), but they do so in real time (cal/s). Since one necessarily heats a small amount of an explosive, it requires sensitive instruments, the more sensitive, the more expensive and, generally, the more demanding of the operator. If one monitors formation of the decomposition products, one can make up for the small amounts formed by analyzing the cumulative formation. The rate of gas formation can be quantified by infrared spectroscopy (nitrous oxide only, nitrogen being IR inactive), or by gas manometry (measuring the total volume of all gases). Over the temperature range of 200 to 400°C, the relative ratios of nitrous oxide and nitrogen produced by AN vary, but the total amount of gas evolved remains about one mole per mole of ammonium nitrate [6]. The change in product production must be determined before kinetics can

be quantified. Alternatively, the most straightforward way of determining the thermal stability of AN is by measuring its disappearance as a function of time and temperature. This can be done by monitoring nitrate or ammonium concentrations by ion chromatography. As might be expected, the last method gives the most reliable determination of thermal stability and yields data that can be extrapolated to other regimes. However, it is often the most cumbersome to perform.

2.2. Gas monitoring tests

The *Abel test* (1875) was developed to evaluate the thermal stability of nitrate esters: nitrocellulose, nitroglycerin, and nitroglycol. The test exploits the fact that nitrate esters release NO_2 upon decomposition. As a 1 g sample is heated at 180°F, the time required to change starch/iodide paper from white to blue is noted. The test is only useful in comparing explosives that evolve nitrogen dioxide during decomposition, and it should only be used to compare like materials, e.g. the relative thermal stability of two batches of nitrocellulose. No extrapolation of the results is possible. Since the Abel test, a number of comparative tests have been devised to observe the formation of decomposition gas: the *Taliani test* (1904) [7], the vacuum stability test, and the gun propellant surveillance program *(65.5 °C test)*. Both the Taliani and the "65.5°C" tests use constant volume test containers and observe build up of pressure. The *vacuum stability test* [7] involves heating 5 g samples for 40 hours at 90°C for double-base propellants, at 100°C for single-base propellants, or at 200°C for high explosives, with the sample tube directly attached to a mercury manometer for real-time measurements. The *chemical reactivity test* is a modern version of these tests; a sample is heated at 120°C for 22 hours in a sealed metal tube, and evolved gases are identified and quantified using gas chromatography. With any of these tests it is important that the user realizes that they are only valid in comparing like samples. Table 4 illustrates the wide variation in amount of decomposition gas that may be produced upon decomposition [8]. For example, after 22 hours at 220°C, ammonium dinitramide (ADN) produced two moles of gas per mole ADN and 1,3,5,7-tetranitro-1,3,5,7-tetrazocine (HMX) produced four moles of gas per mole of HMX. ADN is, however, not the more stable compound; its rate constant at 240°C was measured as 0.4 s^{-1} while that of HMX was 7×10^{5} $s.^{-1}$

2.3. Time-to-event tests

Ray Rogers of Los Alamos National Laboratory (LANL) pioneered many of the techniques for assessing the thermal stability of energetic materials. He modified the Henkin/McGill time-to-explosion test [1] and correlated the results

with critical temperatures predicted from activation parameters determined by differential scanning calorimetry (DSC) [9]. The modified *Henkin test* uses a 40 mg sample loosely sealed in an aluminum tube (an empty commercial blasting cap). The seal on the sample is loose enough to allow a slow build up of gas to escape; the depth of the sample under the seal is recorded. However, if the sample evolves gas too quickly as it is heated in a Wood's metal bath, the cap ruptures. The time-to-rupture (usually detected by ear) is measured, and critical temperature is bracketed by "Go/No Go" runs at varying temperatures. Using Rogers's Arrhenius values to calculate rate constants [9], it can be seen that the typical explosive exhibits "GO" Henkin results when its rate of decomposition is on the order of 10^{-2} to 10^{-3} s^{-1}.

Scientists at Lawrence Livermore National Laboratory developed the ODTX [2] test to determine thermal stability and kinetics of decomposition. A spherical charge (1.27 cm dia.) of explosive (~2.2 g) is confined between O-ring-sealed, heated anvils at pressures of 1500 atm; and time-to-confinement failure is measured at various temperatures. Kinetic parameters can be derived from this technique. Various cook-off tests have been designed to satisfy safety testing criteria; some might be modified to produce kinetic data. The United Nations "Orange" book [5] lists two cook-off tests in the Series 1 test plan: the Koenen and the SCB tests. In the *Koenen test,* a steel cylinder (24.2 mm i.d.) is filled to a height of 60 mm with explosive. The tube is sealed with the exception of an orifice; the diameter of the orifice is varied from 20 mm down to 1 mm during the test sequence. The tube is heated using four propane burners and the time from the start of heating until a reaction is evidenced is noted. In subsequent tests the orifice size is decreased until the reaction to heating is an explosion, which is defined by the number of pieces into which the tube fragments. Any more than two fragments is considered explosive reaction, and any explosive reaction with a diameter 1 mm or more is considered indicative of an explosive compound. This test is used primarily for classification of materials for transport purposes. The *Small-Scale Cook-off Bomb (SCB) test* examines stability under slow heating [5]. An explosive is loaded into a small steel cylinder (e.g. 400 cm^3), and the ends of the cylinder are capped with witness plates. Thermocouples in the walls of the vessel allow detection of self-heating as the sample is heated at a controlled rate (e.g. from 25°C to 400°C at a rate of 3°C per minute). Poor performance is one where the cylinder ruptures or fragments or the witness plate is punctured or deformed.

Table 4. Moles of gas formed per mole of compound at various temperatures and times [5].

Temp °C	120				220				320				#	m.p.	DSC	rate constant (1/s)		Eact kcal/	log A /sec
Hours	22	72	hours*	561	22	72	Hours*	550	22	72	hours*	>416	NO_2	°C	°C	240 °C	320 °C	mole	
NG	2.54	3.2			3.55	3.50			3.96	4			3	13					
EGDN	0	2.17			2.3	2.3			2.74	2.75			2	-23					
PETN	0	0	120		5.04	5.19			6.32	6.3			4	143	210	2.0E-01	3.68E+01	39.4	16.1
NC	0	0	360		0	0	360		0.001	0.001	360			none	220				
AND	1.25	1.45		2.53	2.13	2.2	46		2.4	2.3			2	94	189	3.7E-01	5.2E+01	37.3	15.5
AN	0	0			0.88	0.9	46		0.89	0.9		0.96	1	169	328	3.E-05	5.71E-03	30.4	9.04
AP	0	0			0.87	0.9	47		1.25	1.25				**	340	2.00E-05	1.6E-03	20.5	4.68
RDX	0	0	240		2.92	3.9			3.84	3.9		4.8	3	204	285	1.70E-02	2.3E+00	37.8	14.3
HMX	0	0	240		4.33	4.3			4.24	5.4		8.39	4	280	244	7.13E-05	7.8E-02	52.8	18.4
TNAZ	0	0			3.01	3			3.46	3.77		4:44	3	101	278	4.60E-03	1.4E+00	43.7	16.3
DMN	0	0	560		0.57	0.57		0.8				1	1	57	292	1.00E-03	1.7E-01	38.0	13.2
NTO	0	0			2.13	2.2			2.4	2.3	48	2.42	1	none	267	1.00E-04	2.7E+00	78.5	29.4
PA	0	0	120		3.47	3.64			3.89	4.09		4.62	3	124	332	1.E-05	7.3E-02	44.3	15.2
TNT	0	0	120		1.83	2.18			2.68	3.23		3.27	3	80	328	2.3E-05	2.55E-03	38.1	11.6
TNX	0	0	120		1.01	1.66			2.13	2.22		2.45	3	187	351	8.1E-06	1.31E-03	41.5	12.6
TNM	0	0	170		0	0			1.77	1.92		2.16	3	240	368	4.8E-06	4.63E-04	36.6	10.3
TNA	0	0			0.25	0.50		3.03	3.21	3.41			3	192	387	1.8E-06	8.48E-04	48.0	14.7
DATB	0	0			0.24	0.24		1.3	3.19	3.45		3.98	3	286	360	3.40E-06	2.73E-03	47.9	15.3
TATB	0	0	170		0	0			3.23	3.40		3.84	3	449	397	1.6E-07	1.06E-04	46.8	13.1

Hours* Denotes longest time for which this sample was heated with no results differing from the previous column.

** the AP does not melt; an endothermic phase change occurs at 240 °C

DSC heating rate 20 °C per minute

Time-to-explosion can be used to calculate kinetic parameters. The time is defined as the length of time an explosive can be exposed to temperatures above critical before it causes a catastrophic event. Time-to-explosion is sometimes computed (albeit not very accurately) from the adiabatic model:

$$t = (CRT^2 / AQE) \exp(E/RT)$$

where t is the time, E is activation energy, A is the pre-exponential factor, C is the heat capacity, Q is heat of reaction and T is temperature in kelvin.[10,11]. With this equation and experimentally measured induction times (t), E values are sometimes computed. However, because this time-to-explosion model is based on zero-order kinetics, which does not allow for depletion of the energetic material, it predicts times that are too short. The prediction is particularly inaccurate if the decomposition process involves an induction time, such as a material that melts with decomposition or decomposes auto-catalytically. Time-to-explosion may be dependent on geometry (see discussion below) if the temperature is low enough for runaway reaction to develop in the center of the sample. In that case, the explosive warms throughout, and the hottest region prior to the explosion is the center where explosion develops. However, at high temperatures, a runaway reaction may quickly develop at the surface, while the interior is still cool [10], and, in that case, geometry is unimportant.

2.4. Thermoanalytical techniques

There are many types of instruments which measure heat release: an insulated thermos flask with a thermometer would be the simplest; a calorimeter the most complex. Three types of thermal analyzers are routinely employed in laboratories examining explosives:

TGA Thermogravimetric Analyzer
DTA Differential Thermal Analyzer
DSC Differential Scanning Calorimetry

These instruments can be used to heat a sample at constant temperature (isothermally) or with constantly increasing temperature. The latter method is called "programmed" heating since the temperature is raised at a constant rate. (The techniques are described in detail in Volume 1 of this Handbook.) In a simple comparative stability study, if two samples are heated at the same rate, the sample with the mass loss (TGA) or the exotherm (DTA or DSC) at the lowest temperature is the least thermally stable. Mass losses are usually due to evolution of decomposition gases, but they may also be due to loss of water or

sublimation of the sample. TGA can be made more quantitative by combination with evolved gas analysis (Volume 1 of this Handbook).

Differential thermal instruments, DTA and DSC, are used to examine heat flow differences between a sample and a reference as they are heated. Heat flow (positive or negative) accompanies melting, crystal-phase transition, and chemical reaction. There is often little apparent difference between the results of DSC and DTA experiments (the differences in principle are described in detail in Volume 1 of this Handbook). DTA measures the temperature difference between the reference and the sample and the calculated heat flow is shown; DSC measures the actual heat flow difference and temperature is calculated. DTA can be constructed to go to high temperature, but explosives rarely survive temperatures over 400°C so this is not an issue. Both DSC and DTA can operate in either programmed or isothermal mode. The programmed mode, most commonly used, raises the temperature of the sample and reference at a pre-set rate. An exothermic reaction is indicated by a deviation in the baseline trace, either up or down, as set by the manufacturer or user. The position of the exothermic maximum moves to lower temperatures as the programmed heating rate, β, decreases; this fact means that for the response curves to be comparable they must be run at the same programmed heating rate. This fact is also used in a number of variable heating-rate methods for obtaining activation energies.

2.5. Kinetic aspects

The *ASTM (American Society for Testing and Materials) E698-79* method [12] for DSC and the *Kissinger* method [13] rest on the assumption that though the temperature of the exothermic maximum varies with rate, the fraction of material decomposed at the peak maximum remains the same regardless of scan rate. In the ASTM method, heating rate, log β, is plotted against $1/T$, resulting in a line with slope equal to $-E/(2.19R)$, where T is the temperature in kelvin, E the Arrhenius activation energy (Joules/mol), R the gas constant (8.32 J/mol deg), and the value 2.19 makes the conversion from "$\log_{10}$" to "ln" as well as applies a small correction factor. Calculation of the pre-exponential factor (A) involves evaluation of the complex term $[\beta^* E^* e^{E/RT}]/RT^2$. Commercial software is available for these calculations. In the Kissinger method, ln β/T^2 is plotted versus $1/T$; the slope is $-E/R$.

Two methods have often been used based on data from a single programmed scan. They use similar assumptions that the rate of decomposition is equal to the rate at which heat is evolved and the area under the DSC curve is proportional to the total heat evolved. For the *Borchardt and Daniels* [14] method a number of values of the rate constant (k) at various temperatures are calculated along the

DSC curve as the ratio of the deflection from the baseline to the area under the curve representing the undecomposed material. These k values at various temperatures are used in a typical Arrhenius analysis. The *Rogers* and *Morris* [15] method simply plots ln(deflection from baseline) versus the inverse of T at that point. The slope is $-E/R$. The methods do not necessarily give the same activation energies, but E and A values tend to be paired in a compensation effect (high E with high A) (see Table 5) [16].

Table 5. Decomposition of Azidotriphenylmethane [17]

	E/ kcal mol^{-1}	A/s^{-1}
ASTM E698-79	37.1	14.3
Kissinger	37.3	14.3
Borchardt/Daniels	40.7	17.1
Rogers/Morris	37.4	14.3

There are many problems associated with single-scan methods (more details of kinetic aspects of thermal analysis are given in Chapter 3 of Volume 1 of this Handbook). The assumption of zero-order reaction, which is often made, is generally unrealistic. Furthermore, unlike endothermic peaks, the exotherms produced by decomposing explosive, tend to vary widely in terms of the amount of heat released (area under the curve). This may be due to the fact that the rapidity of the heat release is difficult for the instrument to follow. In a DSC examination (20°C/min) of twenty-five sample of ammonium nitrate (AN) ranging from 0.38 to 0.70 mg, we found the variability in heat release (350 cal/g) was 13%, while the variability in peak maximum (318°C) was 7%; similar observations were made among twenty-eight AN emulsion samples—heat release variability 13% (737 g/mol) and peak maximum variability 2 to 1% (297 and 384°C) [17]. Decompositions that follow more than one pathway are, of course, poorly analyzed by programmed scans. This is the case with ammonium nitrate even though AN exhibits only a single exotherm in the DSC curve.

Ray Rogers (LANL) was one of the first to extensively use DSC analysis to study explosive stability (e.g. references 9,11,15,18,19). He recommended none of the programmed methods, including the one that bears his name. He published a paper illustrating the problem with the variable scan-rate methods, showing that the assumption that the fraction of decomposition at the peak maximum is

constant was false [18]. He preferred to determine the kinetics of decomposition using isothermal DSC scans. The isothermal method brings the sample and reference to a pre-determined temperature and holds them there. As soon as the sample reaches temperature, it begins to decompose and evolve heat. For most decompositions, the rate of decomposition is a function of the concentration of unreacted sample present (x); thus, the highest decomposition rate occurs at the beginning of the reaction, when the most sample is present. The rate decreases as the decomposition proceeds because less reactant is available. The rate of decomposition, the decrease in reactant concentration with time ($-dx/dt$), is equal to the rate constant, k, multiplied by the concentration of reactant remaining (x) to the nth power, where n is the order of the reaction.

$$-dx/dt = kx^n$$

$$\ln(-dx/dt) = n(\ln x) + \ln k$$

For a first-order reaction:

$$\ln x = -kt - C \quad (C \text{ is a constant})$$

Since in first-order reactions rate ($-dx/dt$) is proportional to the fraction remaining x, the equation becomes

$$\ln(-dx/dt) = -kt - C$$

The natural logarithm of the decomposition rate, assumed to be proportional to the signal deflection from the baseline on the DSC curve can thus be plotted versus time, producing a line of slope $-k$. Isothermal determinations of the activation energy (E) require that the rate constant (k) be determined at a number of temperatures.

For first and second-order decompositions, the reaction initiates at maximum rate (maximum concentration) and slows with time as the reactant is depleted. However, there are many instances where no simple order of reaction is recognized, or the decomposition is autocatalytic. An autocatalytic reaction does not begin at maximum rate; rather there is an induction period in which the rate increases to a maximum followed by the normal decay of the reaction rate. It is assumed that, during the induction period, decomposition products form which catalyze further decomposition. Isothermal DSC scans which show increases to maximum decomposition rates are observed not only in autocatalytic reactions but also for solids held near their melting point. If the

latter is the case, the apparent induction period will disappear as the temperature examined is raised 20 to 30°C above the sample melting point.

There are several difficulties in practicing isothermal DSC. The first is bringing the sample up to a constant, elevated temperature without decomposition occurring on the way. It does. The initial part of the DSC curve must be ignored since the entire system is far from equilibrium, and there is a huge starting transient. The operator must try to minimize this region. Secondly, the technique requires that the operator know where the true baseline is so that the deflection from the baseline can be measured. Allowance must also be made for any shift in baseline due to the change in heat capacity of the reactant(s) and product(s). In addition to this, there is the slow return to baseline as the reaction approaches completion. It is difficult to know when the reaction is complete and the true final baseline has been reached. Errors in this assessment result in fairly substantial errors in the calculated Arrhenius parameters. Roger published a correction to a set of Arrhenius parameters for RDX when he realized that concurrent sublimation was giving a false baseline [19].

2.6. Calorimetry

In recent years, the ARC (accelerating rate calorimeter) has become widely used in laboratories for examining samples prone to thermal runaway. The ARC is intended "to maintain a sample in an adiabatic state and permit it to undergo thermal decomposition due to self-heating while recording the time-temperature-pressure relationship of the runaway process" [20]. However, in practice, true adiabatic conditions cannot be maintained with solid samples, and analysis of data is somewhat complex. Researchers use this instrument to derive kinetic parameters, as well as to do comparative thermal stability tests. The drawbacks with this technique are that it requires relatively large samples (1-5 g), and determination of kinetic values is not straightforward [20].

While DSC, DTA, and ARC are commonly used, the measurement of heat production is not restricted to the instruments discussed in the above section. Calorimeters of varying degrees of sophistication can be employed; the more sensitive the instrument, the lower temperature at which the exothermic response associated with decomposition can be detected. (Generally, price is also proportional to sensitivity.) Table 6, modeled after one in reference [20], compares the temperatures at which exothermic decomposition (E = 20 kcal/mol or 82 kJ/mol; $Z = 10^{-8}$ s^{-1}; zero-order) of an energetic material can be detected by various calorimeters or by a "GO" in Henkin tests, or in 1-litre cook-offs. DTA, DSC, and Henkin are the least sensitive techniques [20]. An exothermic event will not be detected until the rate of decomposition is quite

fast, between 10^{-2} and 10^{-3} s^{-1}. ARC and C-80 (Setaram) are more sophisticated and expensive calorimeters; they will detect thermal decomposition of the order of 10^{-4} and 10^{-5} s^{-1}, respectively. As the sample size is increased (see discussion below) or the calorimeter becomes more heat sensitive, even lower rates of reaction (i.e. decomposition at lower temperatures) can be observed.

In addition to the heat-sensing limitations of a given instrument, most calorimetric results are complicated by the thermal constants of the sample and instrument and by multiple heat-change events. Furthermore, many of the thermal analysis techniques are used in a dynamic heating mode (temperature is constantly raised). Although dynamic heating saves operator time, it makes results difficult, and sometimes impossible, to extrapolate to real situations. The temperature over which a calculated activation energy is valid is completely unknown. All these complications can be circumvented by isothermal heating in an oven or constant temperature bath (water, oil, or metal). The bath is pre-warmed, and the sample is quickly immersed. Rate constants must be measured at several temperatures, over as broad a temperature range as possible. At a given temperature (isothermally), the reaction progress is monitored as a function of time by observing either the formation of products or the depletion of reactants. Since the composition of the products may change over a wide temperature range, monitoring reactant depletion is generally more straightforward. Analyses must be tailored for the compound. Discussion of conditions for gas or liquid chromatographic analyses of common explosives can be found in references 21, 22, and 23.

Table 6.
Rate constants and temperatures required for instrumental detection of decomposition, assuming zero-order kinetics, $E = 82$ kJ/mol, $A=10^8$ s^{-1}.

Instrument	rate constant k/s^{-1}	$T/^{\circ}C$
DTA	8×10^{-3}	160
Henkin	6×10^{-3}	155
DSC	3×10^{-3}	140
ARC	2×10^{-4}	100
C80	7×10^{-6}	60
1-Litre	2×10^{-6}	46
microcalorimeter	1×10^{-7}	20

2.7. Checking kinetic data

Several concerns arise when using kinetics values derived from small-scale testing to predict the thermal stability of bulk material storage. First, Arrhenius plots are not usually straight over large temperature ranges; and, thus, the kinetics at high temperature may not be applicable at normal storage temperatures. Furthermore, the micro-samples may not be representative of the overall material. Kinetic parameters determined from small-scale tests ***must*** be used with caution in predicting the behavior of larger-scale systems. In order to determine if there is a problem with scaling, the kinetic parameters determined from small-scale experiments must be tested against modest size samples. Good agreement confirms the validity of the micro-scale kinetics.

2.8. Thermal runaway

Thermal stability depends on whether a balance can be maintained between the heat generated by decomposition reactions and the dissipation of heat to the surroundings. A self-sustained (runaway) reaction can occur when the rate of self-heating, resulting from decomposition, exceeds the rate at which heat can be dissipated. The "critical temperature" is defined as the lowest constant surface temperature at which a specific material of a specific size and shape will self-heat catastrophically. If an energetic material is maintained below its critical temperature, no runaway self-heating will occur. (That is not to say no decomposition will occur; it does.) Thermal safety of an energetic sample depends on whether a balance can be maintained between the heat generated by decomposition reactions and the dissipation of heat to the surroundings. This heat flow in and out of the energetic material depends on the thermal conductivity of the material, the reaction rates (kinetics) of heat producing reactions, the size and shape of the sample, its heat capacity, phase transition energies, if any, and reaction energies. Since the critical temperature depends on how fast heat escapes the explosive, the surface-to-volume ratio of a sample is important. A small surface-to-volume ratio means that generated heat cannot easily escape from the sample; therefore the critical temperature (T_c) is low. Yet, when a sample of small surface-to-volume ratio is initially subjected to external heat, it takes longer to heat through; thus, a small surface-to-volume ratio means a long time-to-event. As the size of an explosive sample increases, its surface-to-volume ratio decreases. Therefore, the critical temperature decreases as the size of the sample increases, while the time-to-explosion increases with increasing sample size. In addition to size (amount), the geometry of a sample affects its surface-to-volume ratio (Table 7). For geometric shapes with the same radius, an infinite slab has the smallest surface-to-volume ratio; a sphere

has the largest; and an infinite cylinder is intermediate. Accordingly, the infinite slab has the lowest critical temperature and the sphere the highest. All these heat flow considerations are generally modelled according to one of two formulas.

Table 7.
Geometrical parameters

Shape	Volume(V)	Surface Area(S)	S/V ratio	T_c	time-to-event
sphere	$4 \pi r^3/3$	$4 \pi r^2$	3/r	high	short
cylinder	$d \pi r^2$	$2 d \pi r$	2/r	medium	medium
slab	$2 d^2 r$	$2 d^2 + 4d r$	1/r *	low	long

r = radius or half smallest dimension; cylinder & slab are infinite, i.e. d is very large * 2/d + 1/r ~ 1/r since d is very large

The Frank-Kamenetskii equation models conductive heat transfer within a sample [24]. The material is assumed to be unstirred and too viscous for convection to dissipate heat:

$$E/T_c = R \ln (r^2 \rho Q A E)/(T_c^2 \kappa s R) \quad (1)$$

where r is the radius (cm), s is a unitless shape factor (0.88 for an infinite slab, 2.00 for an infinite cylinder, 3.32 for a sphere), R is the gas constant (cal*mol^{-1} deg^{-1}), ρ is the density (g/cm^3), κ is thermal conductivity (cal*cm^{-1}s^{-1}deg^{-1}) Q is the heat of decomposition (cal/g), E is the activation energy (cal/mol), A is the pre-exponential factor (s^{-1}), and T_c is the critical temperature in degrees kelvin. Because the Frank-Kamenetskii model allows for only one mode of heat removal, conduction, it predicts the worst case. The Semenov [25] equation performs a similar calculation (where V is the volume, S is the surface area, and a is the heat flow coefficent for sample) but allows for stirring of the sample, as well as conduction, to remove heat.

$$E/T_c = R \ln (V \rho Q A E)/(T_c^2 S a R) \quad (2)$$

In both equations (1) and (2), T_c appears on both sides of the equation and, thus, must be solved iteratively. Simple mathematical analysis shows that because the activation energy is outside of the logarithm term, it has the most dramatic effect on the critical temperature. Typical activation energy values, obtained by any of the quantitative methods discussed above, are between 20 and 40 kcal/mol, while pre-exponential factors are of the order of 10^{13} to 10^{16} s^{-1}.

One-litre of explosive is a reasonable size to check the scale-up of laboratory-determined kinetics. A 1-litre, glass, round-bottom flask gives a spherical configuration for easy modeling. If the flask is immersed in a transparent bath, such as low-viscosity silicon oil held in a battery jar, the reaction can be monitored visually. While this has many advantages, it means that the vessel cannot be tightly sealed; a small vent must be provided to ensure that the event observed is thermal runaway and not pressure rupture. Unfortunately, under these conditions, volatile samples will boil away rather than decompose. Such samples must be sealed in containers that maintain pressure. Such vessels do not permit visual monitoring. In any case, the bath and sample are monitored by thermocouples; and, when possible there should be at least two thermocouples in the sample - one in the center and one at the edge. If viewing is not possible, the height of the sample can also be monitored by properly placed thermocouples. The sample is heated isothermally until a runaway occurs; the time-to-event is measured; and the critical temperature is bracketed by "Go/No Go" runs at two temperatures. If the test results confirm the predicted critical temperature, the kinetics determined on the milligram scale and at higher temperatures can be used with some confidence to predict the safety of large charges at storage temperatures. Examples of such experiments are given in Table 8.

3. CONCLUSION

A number of laboratory thermal analysis tests have been devised specifically for energetic materials. Many are only useful to compare relative thermal stability among similar compounds. Most are based upon monitoring product formation - gas formation (a cumulative event), or heat production (a real time event). Among the gas-monitoring techniques are vacuum stability, Abel, Koenen, CRT, Henkin, ODTX, SCB, and TGA. Many of these could be used to obtained kinetic rate constants at a fixed temperature, but that is not their common application; in fact, most are used in a dynamic heating mode. As new thermal analytical techniques are developed, it is reasonable to expect they will be applied to energetic materials. The only limitation is the requirement for ultra-small sample size.

Table 8. Experimental rate constants, Arrhenius parameters and predicted and observed critical temperatures.

	Exotherm maximum (20°/min)	average DSC Exo Heat (cal/g)	Ea kcal/mol	A s^{-1}	Temp range °C	calc k (s-1) at 240C	obs. k (s-1) at 240C	mol gas/ mol HE	Pred. Tc	Obs Tc	Size of Test
NG	211	500						4.0			
PETN	215	800	39.4	1.3E+16		2.1E-01	2.0E-01	6.3			
RDX	253	900	37.8	2.0E+14	200-250	1.6E-02	1.7E-02	3.9			
TNAZ	275	750	46.6	3.6E+17	160-260	5.0E-03	4.6E-03	3.8			
NTO	267	500	78.5	2.5E+29	220-280	9.1E-05	9.4E-05	2.3			
HMX	277	1000	52.9	2.5E+18	230-270	7.1E-05	7.1E-05	5.4			
TNT	320	600	41.5	2.6E+13	240-280	5.4E-05 200C	1.1E-05 200C	3.2			
NH_4NO_2	107	700	27.2	1.2E+14	54-120	3.1E+01			36	30-35	20g
ADN, $NH_4N(NO_2)_2$	189	430	37.3	2.8E+15	140-200	1.6E-02	1.7E-02	2.5			
HAN, NH_3OHNO_3	214	600	38.8	3.6E+17	88-125	4.4E-01		1.3	114	110	25 g
HAN, LP XM46	214	600	38.8	3.6E+17	88-125	4.4E-01		1.3	80	75	3.5 L
HA , NH_2OH	233	900	33.2	2.4E+14	45-85	1.1E-01			91	110-113	0.5L
nitrocellulose	217	670	42.7	5.9E+17	140-200	1.1E-02	1.3E-02				
TATP, triacetone triperoxide	229	800	36.3	3.8E+13	150-225	6.3E-04	4.7E-04				
RDX	257	900	37.8	2.0E+14	200-250	6.8E-04	7.5E-04	3.9			
TNAZ	275	750	46.6	3.6E+17	160-260	1.0E-04	1.3E-04	3.8			
AN, NH_4NO_3	328	350	26.8	1.6E+07	200-290	6.6E-06	9.3E-06	1.0			
AP, NH_4C1O_4	360	450	21.2	3.4E+04	215-385	5.5E-06		1.2			
AN emulsion	321/364	800	49.2	9.1E+15	210-370	1.7E-07		1.0	202	190-207	1 L

Tc = critical temperature; Exo = exothermic

REFERENCES

1. H. Henkin and R. McGill, Ind. Eng. Chem., 44 (1952) 1391.
2. E. Catalano, R. McGuire, E. Lee, E. Wrenn, D. Ornellas and J. Walton, Sixth Int. Symposium on Detonation, Aug. 1976, pp 214-222.
3. MIL-STD-286B, Method 403.1.3, 1975.
4. D.W. Prokosch and F. Garcia, DoD Explosives Safety Seminar, Miami, USA, August 16-18, 1994.
5. Recommendations on the Transport of Dangerous Goods Tests and Criteria, 1st edn, United Nations, New York, 1986.
6. K.R. Brower, J.C. Oxley, M.P. Tewari, J. Phys. Chem., 93 (1989) 4029.
7. MIL-STD-286B, method 406.1.2.
8. J.C. Oxley, J.L. Smith, E. Rogers and X. Dong, J. Energetic Materials, 18 (2000) 97.
9. R.N. Rogers, Thermochim. Acta, 11 (1975) 131.
10. C.L. Mader, Numerical Modeling of Detonation, U. Calif. Press, Berkeley, 1979, 145.
11. J. Zinn and R.N. Rogers, J. Phys. Chem., 66 (1962) 2646.
12. ASTM Method E 698-79 (re-approved 1993) Standard Test Method for Arrhenius Kinetic Constants for Thermally Unstable Materials, 1995 Annual Book of ASTM Standards, Vol. 14.02, Philadelphia, USA, 1995.
13. H.E. Kissinger, J. Res. Nat. Bur. Standards, 57 (1956) 217; Anal. Chem., 29 (1957) 1702.
14. H.J. Borchardt, J. Inorg. Nucl. Chem., 12 (1960) 252; H.J. Borchardt and F. Daniels, J. Am. Chem. Soc., 79 (1957) 41.
15. R.N. Rogers and E.D. Morris, Jr., Anal. Chem., 38 (1966) 412.
16. T.B. Brill, P.E. Gongwer, G.K. Williams, J. Phys. Chem., 98 (1994) 2242.
17. J.C. Oxley, RCEM Semi-annual Technical Report, Dec. 1986; Apr.1990.
18. R.N. Rogers and L.C. Smith, Thermochim. Acta, 1 (1970) 1.
19. R.N. Rogers, Thermochim. Acta, 9 (1974) 444.
20. T.C. Hofelich and R.C. Thomas, The Use/Misuse of the 100 Degree Rule in the Interpretation of Thermal Hazard Tests; T.C. Hofelich, The Use of Calorimetry for Studying the Early Part of Potential Thermal Runaway Reactions, Int. Symp.on Runaway Reactions, Center for Chem. Process Safety of Am. Inst. Chem. Eng., Boston, Mar. 7-9, 1989.
21. J. Yinon and S. Zitrin, The Analysis of Explosives, Pergamon, Oxford, 1981.
22. B. McCord and E.C. Bender in Chromatography of Explosives, (Ed. A. Beveridge), Taylor & Francis, Gunpowder Square, London, 1998.
23. J.C. Oxley, J.L. Smith, E. Resende, E. Pearce, and T. Chamberlain, J. Forensic Sci., 48 (2003) 1.

24. F. Frank-Kamenetskii, Diffusion and Heat Transfer in Chemical Kinetics, Plenum Press, New York, 1969.
25. N.N. Semenov, Chemical Kinetics and Chain Reactions, Oxford University Press, London, 1935.

This Page Intentionally Left Blank

Handbook of Thermal Analysis and Calorimetry. Vol. 2: Applications to Inorganic and Miscellaneous Materials
M.E. Brown and P.K. Gallagher, editors
© 2003 Elsevier B.V. All right reserved.

Chapter 9

FOSSIL FUELS - APPLICATION OF THERMAL ANALYSIS TECHNIQUES

Mustafa Versan Kok

Department of Petroleum and Natural Gas Engineering, Middle East Technical University, 06531, Ankara-Turkey

1. INTRODUCTION

In recent years the application of thermal analysis techniques to the study of the pyrolysis-combustion behaviour and kinetics of fossil fuels has gained a wide acceptance among research workers, which is of outstanding significance for industry and for the economy. Thermal analysis methods have been extensively used in the general areas of fossil fuel evaluation, such as washability assessments, utilization, waste and final product investigations, petrochemical aspects, as well as environmental studies concerning spontaneous combustion. Thus, fossil fuel research has become one of the modern fields of application of thermal analysis and, over the last three decades, thermal analysis has passed through phases of full recognition and consolidation to rapid expansion owing to advances in several directions. New methods and techniques have been evolved and several techniques have been employed together for the determination of several parameters under identical conditions. The purpose of this chapter is to provide a survey of thermal analysis applications and how these techniques can play a key role in the technology of fossil fuels.

2. APPLICATION TO FOSSIL FUELS

2.1. DSC, TG/DTG, TG-MS-FTIR and DTA Studies on Coal Samples

Many hydrocarbon compounds undergo permanent change when subjected to extreme heat. The extent of this change depends on the molecular structure and the reaction environment. Pyrolysis is a fundamental process in the combustion, carbonization and gasification of coal. In the initial stages of pyrolysis, distillation of the low molecular weight species occurs, but as the temperature is raised, in addition to the increased rate of volatilization due to the progressive evaporation of larger molecules, cracking of the compounds may also occur to

produce volatile fragments. The study of pyrolysis kinetics is essential for the understanding of the mechanisms and mathematical modelling of the process. The related kinetic parameters derived from thermal analysis applications can also be used for coal characterization.

On the other hand, combustion of fuel can be initiated whenever oxygen comes in contact with fuel. The temperature, composition of the fuel and oxygen supply dictate the nature of this reaction. Although the combustion profiles of coals possess a number of common features, such as loss of moisture and volatiles, oxidation of fixed carbon and evolution of heat, the differences in detail result in the characteristic combustion profiles. In the temperature range of 200 °C to 350 °C, all coals start to lose small amounts of pyrolysis water from decomposing phenolic structures, and oxides of carbon from carboxylic and carbonyl groups. At around 350 °C, primary carbonization starts initially with the release of carbon dioxide and hydrogen. Methane and other lower aliphatics are evolved together with hydrogen, carbon monoxide and alkyl aromatics as the temperature increases [1]. The thermogravimetric curves [2] both in nitrogen and in air of *Beypazarı* lignite are shown in Figures 1 and 2.

Historically, differential thermal analysis (DTA) was the first thermo-analytical tool used in studying coal samples. Much of the work on thermal analysis of coal samples was directed towards correlation between thermal behaviour and rank or towards characterisation of various stages in the carbonisation process. Rai and Tran [3] conducted a kinetic study on non-catalysed and catalysed coal. In their kinetic model, the apparent activation energy was found to be a rectilinear function of the extent of pyrolysis of the coal. For the hydro-gasification of char, the apparent activation energy was found to vary as a second-degree polynomial with respect to conversion. The order of reaction was found to be about 0.3 for the pyrolysis step and 0.67 for the hydro-gasification step. Mahajan and Tomita [4] reported differential scanning calorimetry (DSC) curves for 12 coals of various ranks in a helium atmosphere at 5.6 MPa and at temperatures up to 580 °C. They concluded that the thermal effects during the pyrolysis of coals, ranging in rank from anthracite to bituminous coals, were endothermic. Exothermic effects were observed only in the case of sub-bituminous coals or lignites. The net thermal effects were found to be strongly rank-dependent. Ciuryla and Weimar [5] performed thermal characterization (TG/DTG) of four different coals and their chars to obtain fundamental information on the pyrolysis and coal and char reactivity of these materials. Mass loss as a function of temperature was systematically determined for each coal, heated in helium at 40 and 160 °C/min under various experimental conditions, and for its derived char heated in air over a temperature range of 20-1000 °C. The results indicated that the temperature of the maximum rate of devolatilization increases with heating rate for all coals.

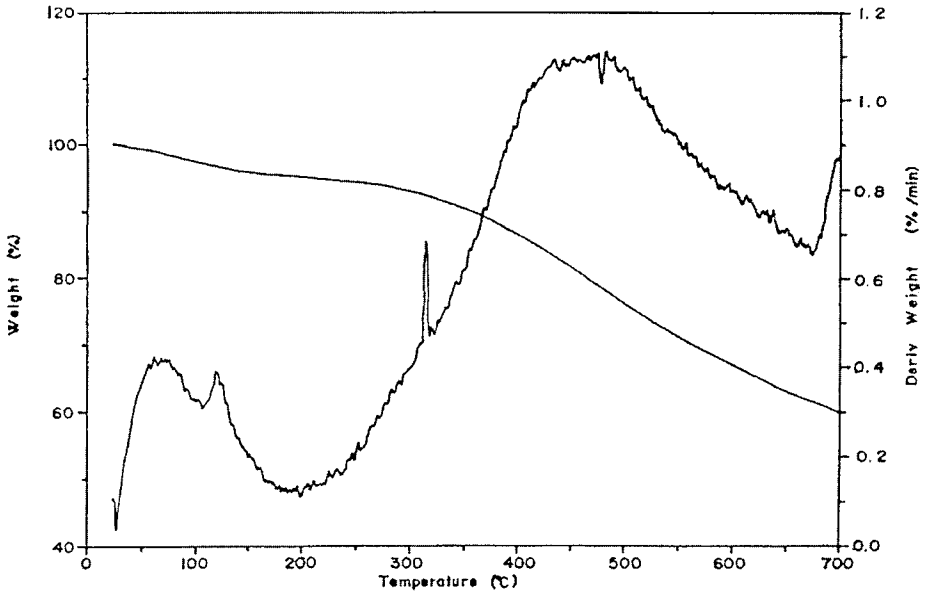


Figure 1. TG/DTG curves for Beypazarı lignite in nitrogen at a heating rate of 10^0C/min.

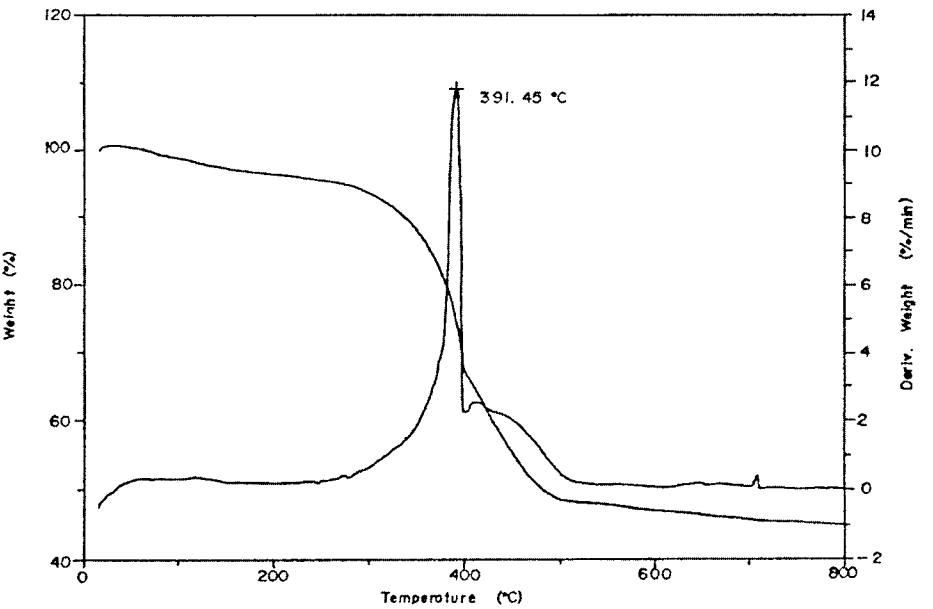


Figure 2. TG/DTG curves for Beypazarı lignite in air at a heating rate of 10^0C/min.

Collett and Rund [6] studied the mass losses (TG/DTG) accompanying the pyrolysis of four pitches over two ranges of linear heating rates. The data for all the samples were analysed by multiple heating rate methods and the apparent activation energies increased with the value of the heating rate. Ratcliffe and Pap [7] investigated the reactivity of lignite and different ranks of coal samples. In all of the coal samples studied, the reaction occurred in two distinct stages. A rapid initial stage was controlled primarily by the devolatilization rate of the coal. The second stage limited the overall rate and was controlled by the surface properties of coal. Gold [8] demonstrated the occurrence of exothermic processes associated with the production of volatile matter in or near the plastic region of the coal samples studied (TG/DTG). He observed that the temperature and magnitude of the exothermic peak were strongly affected by the heating rate, sample mass and particle size.

Cumming [9] developed a method for describing the reactivity or combustibility of solid fuels, such as lignite, bituminous coals and petroleum coke, in terms of a weighted mean apparent activation energy, derived from simultaneous TG/DTG experiments heated at a constant rate in flowing air. He proposed that the mean activation energy method be the established method, which involves recording overall temperatures on the burning profile curve. Smith and Neavel [10] carried out coal combustion experiments in the temperature range 25-900 °C using air at atmospheric pressure in a TG/DTG system. Sixty-six coals high in vitrinite and low in inorganic were examined as part of a coal characterisation programme. Arrhenius plots for the rate data were showed four distinct regions of combustion. Calculated apparent activation energies were of the correct orders of magnitude to describe combustion regions corresponding to chemical-reaction-controlled as well as diffusion-controlled processes. Smith et al. [11] investigated the burning process of different coal samples (TG/DTG), from lignite to black coal, and found that the burning temperature for half of these coal types is linearly dependent on their concentration. Cumming and Mclaughlin [12] applied TG and DTG to a range of samples and obtained proximate analysis results for a total of 14 coal samples of widely different properties. They also established burning and volatile-release profile tests. They suggested that the volatile-release profile test might find application in the fields of coking and gasification rather than in combustion, and that it could be the basis of a system for fingerprinting coals.

Rosenvald and Dubow [13] analysed the pyrolysis of 21 bituminous coal samples by DSC. They have distinguished three regions of endothermic activity in the DSC curves. The first peak (25-150 °C) corresponds to a loss of moisture: the second, very broad endothermic peak in the range 400-450 °C, corresponds to the devolatilization of organic matter and, above 550 °C, probably corresponds to cracking and coking processes subsequent to the pyrolysis step.

Butler and Soulard [14] investigated the specific heats (C_p) of bituminous and sub-bituminous coals in the temperature range 25-325 °C by DSC. Good agreement was obtained with the values for the specific heats of glass and graphite in the literature, and it was established that the specific heats were not dependent on the degree of diminution of these materials. Specific heats of coal samples were found to depend upon the mesh size, temperature, rank, moisture content and whether the coal powder was wet- or dry-screened.

Elder [15] developed a procedure for the automatic proximate analysis (TG/DTG) of solid fossil fuels and related matter. The procedure was tested with coals of varying rank, biomass samples and Devonian oil shales. The simplicity of the technique suggests that it may supplement the classical ASTM method and could be used when this latter procedure cannot be employed.

Richardson [16] measured the specific heats of a range of coals, cokes and ashes using DSC. He observed a rapid increase of specific heat with content of volatile matter in the region 0-10 mass%, followed by only mild increases at high concentrations. Elder and Harris [17] investigated the thermal characteristics of Kentucky bituminous coals undergoing pyrolysis in an inert atmosphere at three different heating rates and determined the specific heats of the coals by DSC. The specific heats of the dry coals lay in the range 1.21-1.47 J g^{-1} K^{-1}. The exothermic heat flow from 300 to 550 °C, where the major mass loss occurred, was associated with the primary carbonisation process and the development of the plastic state, and the onset of secondary gasification, which is responsible for coke formation, was established.

Seragaldin and Pan [18] developed a linear relationship between activation energy and heat of reaction (TG/DTG). The effects of alkali metal salts on the decomposition of coal under three different atmospheres (nitrogen, CO_2 and air) were also investigated. The effect of the catalysts on coal conversion and CH_4, CO_2 and CO emissions are related to observed changes in the activation energy. Morgan and Robertson [19] determined coal-burning profiles by TG/DTG. They claimed that kinetic parameters from Arrhenius plots of the profiles cannot readily be related to any specific stage of combustion. However, some features of the profiles are clearly related to coal properties and a correlation exists between unburned carbon loss, as predicted from high-temperature oxidation rates, and a characteristic temperature of the thermogravimetric profile. This suggested that burning profiles could provide a valuable, rapid laboratory method of ranking coals in terms of their burnout performance.

Patel et al. [20] measured the rate of combustion of lignite char using TG/DTG over a range of oxygen concentrations (5-20 %) and at temperatures between 325 and 650 °C. The activation energy in the chemical rate-controlled zone was 120 kJ mol^{-1} and the transition to film-diffusion control occurred at 430 °C. The Arrhenius plots indicated no region of pore-diffusion control. The pyrolysis

conditions were found to have a notable influence on the activation energy. Janikowski et al. [21] analysed ten different coals (four lignite, four sub-bituminous and two bituminous) in argon and hydrogen atmospheres using TG/DTG. Upon heating the coals in an inert atmosphere up to 500 °C, 30.8 - 43.7 % mass loss occurs. They distinguished two temperature regions of increased chemical reactivity: one at 75-118 °C and the second at 375-415 °C. Morris [22] carried out pyrolysis runs on a low-ash coal and correlated yields of hydrogen and methane as a function of particle size and final temperature, and yields of CO and CO_2 as a function of particle size at a final temperature before decomposition of the carbonates in the mineral matter. Alula et al. [23] used Tg and DSC to characterise low- and high-temperature coal tar and petroleum pitches and their fractions. The temperature at which the maximum rate of mass loss occurred was determined, and its variation with the specific heat and glass transition temperatures was discussed.

Starzewski and Zielenkiewich [24] investigated the influence of the inert gases helium and argon on the thermal properties of coal using DSC. The coals studied were high-volatiles bituminous coal and anthracite. The heat capacity of the coal was strongly influenced by helium. This phenomenon is especially noticeable for high-volatiles bituminous coal.

Crelling et al. [25] determined the combustion properties of separated single coal maceral fractions from a rank series of coals and then tried to predict the combustion behaviour of various whole coals on the basis of their maceral composition and rank (DTA). The results of this study indicated that most of the reactivity and combustion profile parameters varied significantly with coal rank. Alonso et al. [26] studied the pyrolysis of a number of coal tar and petroleum pitches by means of thermal methods. Acenzathylene was used as a model compound to interpret the results of thermal methods. DTA exothermic and endothermic peaks were assigned to different types of phenomena such as devolatilization, polymerisation, condensation and cracking. Endothermic phenomena were found to be prevalent for binder coal tar pitches.

Coil et al. [27] developed a dynamic pyrolysis model, which takes into account three different groups of thermal decomposition reactions of coals (TG/DTG). A simple procedure was proposed for determining the kinetic parameters using a differential method and experimental data obtained at low heating rates. This method also allowed the determination of the lowest value of the heating rate at which a single peak will be obtained.

Haykiri et al. [28] investigated the behaviour of some fossil fuels during thermal treatment. DTA and TG were applied to peat, lignite, bituminous coal, anthracite, oil shale and asphaltite samples under a nitrogen atmosphere and the results were discussed. They concluded that an increase in the ratio of the volatile matter content to the active matter content of coal causes a decrease in

the temperature at which the mass loss rate is a maximum. Morris [29] carried out pyrolysis runs (TG/DTG) in the temperature range ambient to 900 °C and the particle size +38 –2360 μm on a low-ash coal. Empirical correlations were established for the evolution rates of hydrogen, carbon monoxide and methane as a function of particle size and temperature. The observations suggest that tar deposition is rate determining. The observations for the rate of evolution suggest that it is governed by several complex reactions, of which methanation and secondary cracking of tar are possibilities.

Mianowski and Radko [30] developed a method for the evaluation of the kinetic parameters of coal pyrolysis using TG/DTG. For twelve coal samples of different rank, it was shown that pyrolysis in the temperature range 280 - 580 °C is a first-order process with apparent activation energy of 78-151 kJ mol^{-1}. An isokinetic effect was also observed for the coal samples investigated.

Solomon and Serai [31] used the most popular technique (solvent swelling ratio) for cross-linking reactions in coal and char, to determine cross-link density changes during pyrolysis and liquefaction. The results from pyrolysis studies at heating rates between 0.5 and 100 °C/min. showed that cross-linking is rank-dependent, occurring in lignites at lower temperatures than in bituminous coals

Richardson [32] measured the specific heats of a range of coals, cokes and ashes from 25 to 750 °C using DSC under pyrolysis conditions. A rapid increase of specific heat with the content of volatile matter in the region 0-10 mass% was followed by only slight increases at higher concentrations. A general equation was given expressing the heat capacity of a coal in terms of proximate composition and temperature, providing a simple and accurate method of assessing enthalpy changes up to 325 °C.

Warne [33] discussed the application of thermal analysis in the earth sciences, particularly for the assessment of coal, its constituents and products. A growing number of TA methods have been used, including thermomagnetometry (TM), high temperature differential scanning calorimetry and the wide ranging new method of proton magnetic resonance thermal analysis (PMRTA). In addition to the routine techniques of TA, "simultaneous thermal analysis" and "variable atmosphere thermal analysis" (where the furnace atmosphere conditions may be pre-selected, controlled and ultimately even changed repeatedly during individual TA runs) have proved particularly valuable.

Nosyrev et al. [34] used TG to study the influence on thermal behaviour of the structural modifications caused to a bituminous coal by several chemical treatments. The results were discussed in relation to the structural information already obtained by infrared spectroscopy and the rheological properties characterised by thermomechanical analysis.

Kok [35] investigated the thermal behaviour of lignite using TG/DTG, high-pressure thermogravimetry (HPTG) and combustion cell experiments. Different

models were used to obtain kinetic parameters and the results were discussed. Kok et al. [36,37] carried out TG/DTG experiments from ambient to 900 °C in air to study the effect of particle size on the combustion properties of a coal sample. Twelve different size fractions were used and the data were analysed using an Arrhenius-type reaction model assuming a first-order reaction. Kinetic parameters of the samples were determined and the results were discussed.

Huang et al. [38] investigated a wide range of coal ranks from lignite to anthracite using TG/DTG. The DTG maximum for volatile matter evolution showed a strong correlation with vitrinite reflectance, thereby providing a convenient measure of degree of coalification (coal rank) without requiring the equipment of more time-consuming petrographic analysis. T-max by the rock evaluation method also shows a positive correlation with vitrinite reflectance. TG also reproduces the components of the proximate analysis of coal.

Liu et al. [39] investigated the combustion behaviour of coal dust by means of TG/DTG. The reaction fraction, alpha, was obtained from isothermal data. The mechanism of nucleation and nuclei growth was determined to be the controlling step of the coal dust combustion reaction. The kinetic equation of the coal dust combustion reaction was established. Pranda et al. [40] performed combustion experiments in air using TG/DTA, which served for determination of the ignition temperature and the kinetics data. Fly-ash carbon was also treated with carbonates and hydroxides. The ignition temperature decreased with the alkali metal salt concentration of the treated samples. The apparent activation energy for combustion of the impregnated samples decreased.

Kok [41] studied the effect of particle size on the oxidation mechanisms of lignites using TG/DTG) for twelve different size fractions. Data were converted into dimensionless size vs. dimensionless time to show the progress of oxidation. The lignites showed linear behaviour at elevated temperatures, which justifies the assumption that chemical reaction is the controlling step.

Boiko [42] discussed the methods for the complex thermal analysis of solid fuels. The following processes were studied: moisture evaporation, emission of volatile products, and reaction of non-volatile fuel residue with the oxygen in air. The results of the work can be used in mathematical simulation of processes for coal processing.

Benfell et al. [43] used TG/DTG for characterising the effects of rank and maceral variations on coal combustion behaviour. These coals showed an increase in char burnout temperature with rank for both dull, inertinite-rich and bright, vitrinite-rich coals. The maximum rates of combustion for dull coals were lower than their bright counterparts, with the difference between the two varying with rank.

Ceylan et al. [44] investigated the kinetics of non-isothermal pyrolysis of raw, de-mineralised or oxidised lignites by TG, DTA and DSC experiments in inert

and air atmospheres. The mass loss data indicated that the pyrolysis characteristics of the lignites and the prevailing kinetic mechanisms varied depending on temperature. The mass loss rates showed essentially two regimes and the major mass loss occurred in the range of 300-650 °C. DTA and DSC data gave similar values for the overall reaction order and activation energy.

Zoller et al. [45] studied the volatile matter evolved during pyrolysis of different rank coals by TG and photoionization mass spectrometry (TG-PI-MS). The composition of the TG effluent revealed several significant trends with coal rank. The raw coal, extracted material and coal residue remaining after solvent extraction produced very similar mass spectra. The results from these analyses suggest that the volatile matter, like coal itself, consist of compounds with a range of molecular weights, but with similar molecular structures. Pitkanen et al. [46] studied various fuels, such as coal, peat, wood chips and bark with FTIR spectrometry combined with TG. The gases evolved in a TG analyser were transferred to the FTIR via a heated teflon line. The spectra and TG curves indicated that the major gases evolved were carbon dioxide and water, while there were many minor gases, e.g. carbon monoxide, methane, ethane, methanol, ethanol, formic acid, acetic acid and formaldehyde.

Takanohashi et al. [47] applied DSC to study the extraction residues of coals giving different extraction yields. For the residues with extraction yields lower than 30 mass%, an endothermic peak similar to that given by the raw coal was observed around 300 °C. This endothermic peak disappeared on the second and third scans, indicating that the peak was due to irreversible structural changes in coal. The reason for these endothermic peaks was discussed from the relationships among the extraction, swelling, and structural changes of coals.

Garcia et al. [48] measured the non-isothermal oxidation enthalpies for three coals, which had been weathered under ambient conditions. Although the total oxidation enthalpies decreased with increasing oxidation, the decrease was not systematic. The onset temperature of oxidation increased with oxidation in a more systematic way and also increased with increasing coal rank. The onset temperatures were thus proposed to be a better indicator of the propensity of the coals to oxidation.

Ozbas et al. [49] reported on the combustion characteristics of lignite before and after the cleaning process. TG/DTG experiments were carried out for four different size fractions and the curves revealed three reaction regions: evaporation of moisture in the coal, the primary reaction region and decomposition of mineral matter in the lignite. Guldogan et al. [50] determined the pyrolysis kinetics of lignite at different heating rates by TG/DTG. Although some differences were obtained at different heating rates, the same volatile matter yield of 40.7 % of the total mass of the sample was calculated. Lower activation energies (~24.8 kJ/mol) were calculated at higher heating rates.

Mayoral et al. [51] reported the experimental optimisation by the simplex method of the proximate analysis of coal and biomass by TG/DTG. The heating rate, final temperature, holding time, gas flow rate and sample size were the control variables. The relative accuracy of the method was demonstrated by determination of the volatile matter contents of a number of coals.

Kok [52] analysed the combustion curves of seventeen lignite samples using TG/DTG. The relationships between peak temperature, burnout temperature, moisture content, ash, volatile matter, fixed carbon and calorific values of the samples were examined. Iordanidis et al. [53] carried out TG/DTA experiments for seven lignite samples. The samples were chosen to represent the vertical distribution of the lignite beds in the entire deposit. The burning profiles of the samples studied, combined with proximate analysis and calorimetric results, contributed to a clearer identification of lignite structure and a better understanding of the coalification process. Seven thermal effects were distinguished and a good correlation between the results of proximate and calorimetry analyses and the DTA and TG data was noticed. Alonso et al. [54] investigated the pyrolysis and combustion behaviour of a set of eleven coals with different ranks and maceral composition by TG/DTG. Results showed that the pyrolysis curves of the coals did not match at all with any specific feature of the corresponding combustion profiles, and that the temperatures of initiation of both processes were very different at the low-rank end and became similar only for coal ranks of similar vitrinite reflectance and above.

Varhegyi et al. [55] discussed several techniques for the handling of the non-statistical errors during the least-squares evaluation of kinetic data. The methods were illustrated by the evaluation of oxidative thermogravimetric experiments on a lignite.

Xie and Pan [56] reviewed the thermal characterisation of materials using evolved gas analysis. TG/FTIR, TG/MS and pyrolysis/GC-MS systems and their applications in the study of several materials were discussed, including the analysis of the degradation mechanisms of originally modified clays, polymers and coal blends.

Avid et al. [57] determined the influence of temperature, heating rates (10-50 ^{o}C/min.) and purge gas (N_2 and CO_2) employed on the thermal degradation of coal samples pyrolysed non-isothermally in a thermogravimetric analyser. The coal was also investigated in a fixed-bed reactor to determine the influence of temperature and heating rate of the pyrolysis on the yield of products and composition of gases evolved. The main gases produced were H_2, CH_4, C_2H_2, C_2H_4, C_2H_6, C_3H_6 and C_3H_8 and also minor concentrations of other gases.

Altun et al. [58] investigated the effect of particle size and heating rate on the combustion properties of asphaltites. TG/DTG experiments were carried out at three different size fractions and five different heating rates. Weighted mean

activation energies of the samples were around 47.5 kJ/mol. As the particle size was decreased and the heating rate was increased, the activation energies of combustion of the samples also increased.

Lizella and de las Hears [59] derived kinetic parameters of low-rank coals from many TG curves recorded with different heating rates (5, 15, and 25 K/min) using the maximum temperature of oil generation (T_{max}). These results were contrasted with those obtained by a nonlinear least-squares algorithm used to derive kinetic parameters near T_{max} from a single TG curve. Finally, a method to compare the kinetic parameters at different heating rates was applied near the maximum temperature of oil generation (T_{max}) and yielded similar kinetic values. The method applied was thus concluded to be correct for these selected coals.

Altun et al. [60] studied the effect of particle size and heating rate on the pyrolysis of asphaltites using two different kinetic models. The liability of asphaltite to crack into products and the efficiency of the reactions were observed to be favoured by low heating rates and coarse fractions during the primary devolatilization and secondary gasification of pyrolysis.

2.2. DSC, TG/DTG, DTA and TG-GC-FTIR studies on crude oil samples

In the pyrolysis of crude oils, two different mechanisms causing loss of mass are critical. In general, the first mechanism, between ambient temperatures and around 400 °C, is distillation. A second mechanism around 400-600 °C corresponds to vis-breaking and thermal cracking. On the other hand, in combustion, a reaction up to around 350 °C is due to low temperature oxidation (LTO). This low temperature oxidation reaction produces small quantities of carbon dioxide and presumably acids, aldehydes, ketones and peroxides as primary products. Depending on the crude oil type and origin, a second reaction takes place around 350-475 °C, where major production of carbon dioxide starts and this stage is called fuel deposition (FD). The final reaction of crude oil inferred from the curves takes place between 475-600 °C. This reaction contributes most of the exothermic heat of reaction when the crude oil is heated in an oxidizing environment and is called high temperature oxidation (HTO) [61]. The thermogravimetric curves [2] both in nitrogen and in air of *B.Raman* crude oil are shown in Figures 3 and 4.

DTA was the first thermo-analytical tool used in crude oil characterisation. Much of the work on thermal analysis of crude oils was directed towards correlation between the thermal behaviour of the samples and kinetic studies. Effects of different metallic additives on the combustion properties of crude oils have also been studied. Burger and Sahuquet [62] used DTA to illustrate the catalytic effect of some metallic derivatives and to investigate how the properties of both the oil and the porous media influence crude oil combustion.

Three successive oxidation regions were observed in the DTA curves, namely low-temperature partial oxidation, combustion of crude oil fractions and finally, coke combustion. Bae [63] investigated the thermo-oxidative behaviour and fuel-forming properties of various crude oils using TG/DTG. The results indicated that oils can be classified according to their oxidation characteristics. No complete correlation could be established between viscosity, composition or density of the crude with the thermo-oxidative characteristics of the oil. Drici and Vossoughi [64] applied DSC and TG/DTG to studying crude oil combustion in the presence and absence of metal oxides. Vanadium, nickel and ferric oxides behaved similarly in enhancing the endothermic reactions. In the presence of a large surface area, such as on silica, the surface reactions are predominant and unaffected by the small amount of metal oxide present. Vossoughi [65] has used TG/DTG and DSC techniques to study the effect of clay and surface area on the combustion of selected oil samples. The results indicate that there was a significant decrease in the activation energy of the combustion reaction regardless of the chemical composition of additives. Moreover, the low-temperature oxidation of the oil and probably the coke deposition were strongly affected by the specific surface area of the solid matrix. Yoshiki and Philips [66] examined the thermo-oxidative and thermal cracking reactions of Athabasca bitumen qualitatively and quantitatively using DTA. Reaction kinetics of low-temperature oxidation and high-temperature cracking were determined. The effects of atmosphere, pressure, heating rate and support material on the thermal reactions of bitumen were studied. They found that low heating rates (2.8 °C min^{-1}) favoured low-temperature oxidative addition and fission reactions. Verkocy and Kamal [67] performed thermogravimetric and pressurised differential scanning calorimetric (PDSC) investigations on Saskatchewan heavy oils collected from wells under primary, steam flood and fire-flood production, and on cores. They estimated kinetic and thermochemical data for thermolysis, low-temperature oxidation and combustion, which were non-linearly dependent on the heating rate. Kamal and Verkocy [68] used TG/DTG and DSC on two Lloydminster regions, heavy-oil cores, and extracted oils and mineral matter. TG/DTG and DSC curves, obtained in helium and air atmospheres, for the two Lloydminster region cores and the extracted oils demonstrated at least three groups of chemical reactions occurring in three temperature regimes. Reactions in zone 1 were attributed to evaporation, distillation, thermolysis, and low-temperature oxidation (LTO), in zone 2 to distillation and thermal alteration of minerals, LTO, and combustion, and in zone 3 and/or 4 to pyrolysis, coking, polymerisation, mineral matter decomposition and combustion.

Ranjar and Pusch [69] studied the effect of the oil composition, based on their light hydrocarbon, resin and asphaltene contents, on the pyrolysis kinetics of the

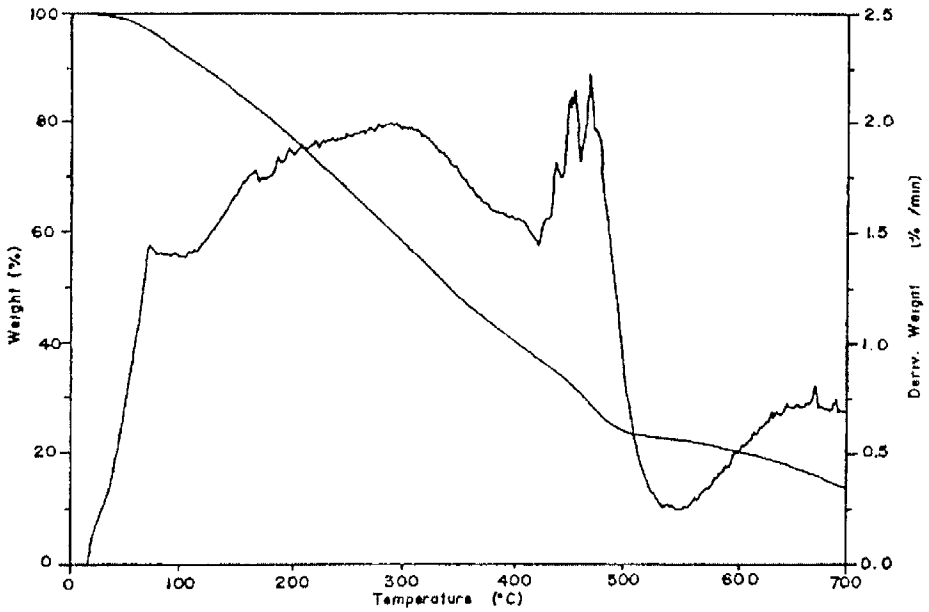


Figure 3. TG/DTG curves for Raman crude oil in nitrogen at a heating rate of 10^0C/min.

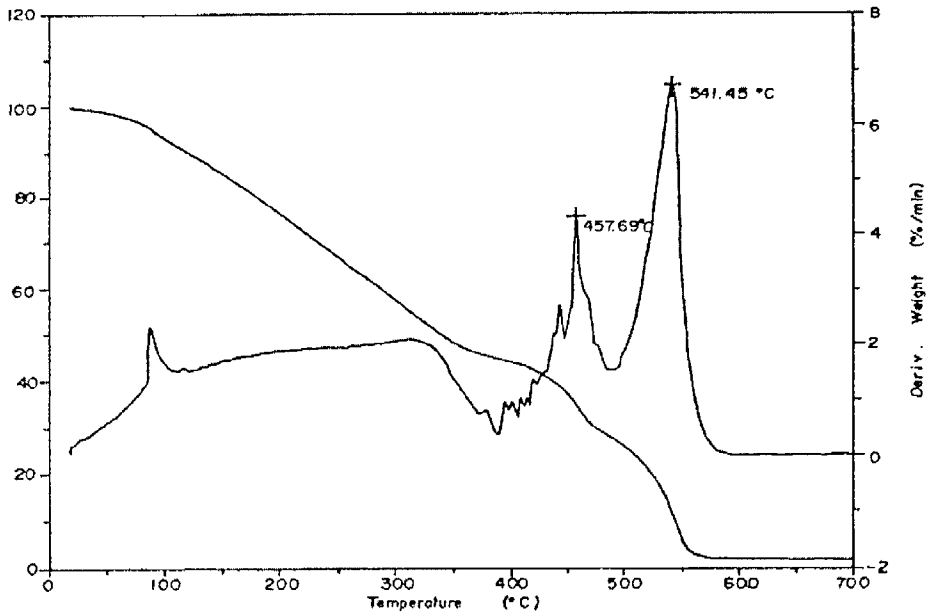


Figure 4. TG/DTG curves for Raman crude oil in air at a heating rate of 10^0C/min.

oil and the combustion kinetics of the fuel, using TG/DTG and DSC. The colloidal composition of oil, as well as the transferability and heat transfer characteristics of the pyrolysis medium, had a pronounced influence on the fuel formation and composition. Ali and Saleem [70] investigated the asphaltenes precipitated from Arabian crude oils by thermogravimetry and pyrolysis-GC analysis at 350 and 520 °C. Under severe pyrolysis conditions (520 °C), 98 – 100 % of asphaltenes are converted to the products. The evolution of methane and other normal alkanes from all the asphaltenes under mild pyrolysis conditions indicates that these asphaltenes contain thermally labile alkyl groups on the periphery. The loss of nitrogen from the asphaltenes during pyrolysis remained low (1-6 mass%), whereas the losses of oxygen and sulphur ranged from 58 to 74 mass% and 10 to 29 mass%, respectively.

Ranjbar [71] investigated the influence of reservoir rock composition on the pyrolysis and combustion behaviour of crude oils in porous media. Pyrolysis and combustion tests were performed to examine how clays affect the amount of fuel and its reactivity. He concluded that clay minerals present in the matrix enhance fuel deposition during the pyrolysis process and also catalyse the oxidation of fuel. Kok and Okandan [72] analysed the combustion properties of crude oil-lignite mixtures by DSC. The effect of heating rate was also studied and higher reaction temperatures and heat flow rates were observed with increasing heating rate. The specific heats of samples were measured in the temperature range 20 – 660 °C and were found to increase continuously with increasing temperature until the decomposition temperature was reached. Calculated activation energies were found to vary between 66-131 kJ $rnol^{-1}$.

Kok [73] characterized the pyrolysis and combustion properties of two heavy crude oils. On combustion in air, the three different reaction regions associated with low-temperature oxidation, fuel deposition and high-temperature oxidation, were identified. DSC-TG/DTG curves were also used to determine the heat values and reaction parameters of the crude oil. Kinetic data were obtained from the high-temperature oxidation region from the DSC and DTG curves. Higher activation energy values were found as the API gravity of the crude oil decreased.

Kopsch [74] determined the glass transition temperatures of petroleum asphaltenes using DSC. From these temperatures, a hypothetical melting temperature of the asphaltenes could be calculated as falling within the range of pyrolysis temperatures of the asphaltenes. The glass transition in polymers is a kinetically controlled process with an associated activation energy. They also found a relationship between the glass transition temperatures and the melting temperatures of the petroleum asphaltenes studied.

Lukyaa et al. [75] used pressurised differential scanning calorimetry (PDSC) to study the effects of sand particle-size, pressure and oxygen partial pressure on

the heat evolution during the combustion of North Sea crude-sand mixtures. Decreasing the particle size of the sand and increasing the pressure increased the onset temperature for low-temperature oxidation and thus favoured fuel storage.

Kok et al. [76] used PDSC to obtain information on the combustion characteristics of crude oils and their mixtures in two chemically different matrix materials, sand and limestone. Crude oil and sand/limestone mixtures were prepared to give a composition of 10 mass% crude oil in matrix. The PDSC curve clearly demonstrates two distinct transitional stages, namely combustion of liquid hydrocarbons and combustion of coke. The kinetic part of this research was concerned with only the coke combustion. Two different kinetic models were used to analyse the kinetic data and the results are discussed. Kok and Karacan [77] also presented the results of an experimental study on the determination of the pyrolysis behaviour and kinetics of six crude oils using DSC and TG/DTG. Two main temperature ranges accompanied by loss of mass were observed during pyrolysis. The first region, between ambient and 400 °C, was distillation. The second region, between 400 °C and 600 °C, was vis-breaking and thermal breaking. As the crude oil becomes denser, the activation energy of cracking increases. The activation energy of cracking also shows a general trend with asphaltene content.

Di Lala and Kosinski [78] developed a new methodology using TG-FTIR to study the low temperature treatment of waste lubricating oils. The major part of the process, in terms of mass loss and gas-phase evolution, was over by 650 °C, and thus the remainder of the sample heating was carried out at 5 °C/min. The information gathered was used to understand and explain the conversion of the waste oil from an initial liquid state to a final solid ash state. Laux et al. [79] investigated an atmospheric residue, a vacuum residue, a vis-breaking residue, the maltene fractions of the residues, a mixture of the atmospheric residue with the vacuum residue and the residue from the supercritical extraction of the vacuum residue, as well as the residues mixed with dispersing agents, by TG at three different heating rates. The content of colloid disperse phase and its stability had a significant influence on the properties of the residues, especially on the evaporation enthalpy. The stabilities of the residues were investigated by the determination of flocculation points. TG proves to be an effective method for the determination of the important parameters for processing of crude oil residues, when the influence of the colloidal character of these complex mixtures is considered. Goncalves et al. [80] investigated the thermal behaviour of asphaltenes from crude oil using TG-DTA/GC/MS. The approach involved kinetic studies of the thermal decomposition of asphaltenes under controlled conditions by TG/DTG, characterization of volatile fractions by TG and DTA-GC/MS and by GC/MS of the volatiles recovered. The coke formed was also studied after being decomposed into smaller molecules using selective

oxidation.

Kok and Iscan [81] applied DSC to the study of crude oil combustion in the presence and absence of metal chlorides. In the presence of small ratios of metallic additives, the surface reactions were predominant and the catalyst did not affect the reactions much. Three different reaction regions were identified as low temperature oxidation, fuel deposition and high temperature oxidation in all the samples studied. Kok and Keskin [82] also investigated the combustion characteristics and kinetics of three crude oils in air using TG/DTG. Again the three distinct reaction regions were identified in all crude oil samples studied. A computer program was developed for automatically processing the data to estimate the reaction parameters.

2.3. DSC, TG/DTG, DTA and TG-GC-FTIR studies on oil shale samples

When oil shales are heated in an inert atmosphere, two different mechanisms causing loss of mass are critical. The first mechanism is distillation and the second is vis-breaking and thermal cracking. The onset temperatures of pyrolysis of rich grade oil shales are lower than those of poor grade. Thermogravimetry in air results in distinctly different mechanisms due to the differences in organic matter type and organic matter maturity in oil shales. The thermogravimetric curves [2] both in nitrogen and in air of *Mengen* oil shale are shown in Figures 5 and 6.

TG/DTG of oil shale samples has been extensively used as a means of determining the characteristics and kinetics of devolatilization. A number of researchers have reported the influences of heating rate and final pyrolysis temperature on oil shale decomposition. Shih and Sohn [83] used TG with a variety of heating rates to determine the kinetics parameters for the pyrolysis of Green River oil shale. Four different methods were employed for kinetics analysis and the results appear to be in fair agreement. The same group has used TG for studying the oxidation kinetics of oil shale char under conditions in which diffusion and mass transfer effects were claimed to be unimportant. Rejashwar [84] has studied the pyrolysis kinetics of the thermal decomposition of Green River oil shale kerogen by TG. He critically reviewed the factors influencing kinetic data, such as sample geometry, heating rate and atmosphere. He analysed the mass-loss data by direct Arrhenius, Coats-Redfern and Freeman-Carroll techniques.

Sweeney [85] obtained DTA curves for selected micaceous soil/clays from the Eastern Caribbean over the temperature range 25-1150 °C. The curves run under N_2 were used to identify the clay minerals present. Supporting evidence on the clay minerals present was found from X-ray crystallographic techniques. A marked similarity between the DTA curves of the virgin soils analysed under nitrogen gas and the clays from which the organic constituents had been

analytically degraded was observed. Earnest [86] analysed the thermal behaviour of Green River oil shale in a dynamic nitrogen atmosphere with TG and DTG and compared it with that in retorting processes. Using the results of this study, the pyrolysis onset temperatures and the temperatures at the maximum pyrolysis rate were related to the type of organic maceral components of the oil shale specimen. Thakur and Nuttall [87] studied the pyrolysis kinetics of the thermal decomposition of Moroccan oil shale by isothermal and non-isothermal TG and showed that decomposition involves two consecutive reactions with bitumen as an intermediate. Both reactions follow first-order kinetics. Among the three models used, the Anthony-Howard model [88] yields lower deviations and thus provides a better fit of the data. Skala et al. [89] have investigated the pyrolysis kinetics of oil shales under non-isothermal conditions using thermal methods. The results obtained were incorporated into a multi-step kinetic model which was adjusted according to the specific properties of the particular oil shale samples and tested by comparison of the experimental and simulated TG, DTG and DSC curves. The modelling procedure developed was found to be useful in modelling the pyrolysis of other oil shales of the same kerogen type.

Skala and Sokic [90] developed a kinetic expression commonly used in the thermal analysis of oil shale pyrolysis. This was derived on the basis of a simple first-order kinetic equation of kerogen decomposition. The results obtained showed that the largest values of activation energies were obtained by using isothermal TG data, while combined data from non-isothermal and isothermal TG gave the smallest values. In all of the samples examined and TG analyses performed, there was an increase in the activation energy with increased content of paraffinic structures in the oil shale. Burnham [91] showed how chemical kinetics influences the design and operation of different processes for different types of oil shales. Kinetic methods for organic pyrolysis are presented. He also briefly reviewed pyrolysis results with the intention of drawing comparisons between open, high-pressure and hydrous pyrolysis. Empirically, the degree of severity of pyrolysis required to form volatile products in open pyrolysis is similar to that required to form an expelled oil phase in hydrous pyrolysis.

Lillack and Schwochau [92] performed ion-isothermal pyrolysis experiments on an immature oil shale sample. Evaluation of the experimental evolution profiles with a kinetic model yielded more kinetic parameters. Fainberg and Hetsroni [93] studied secondary pyrolysis of products of Israeli oil shale processing in a two-stage bench-scale unit. The gas and oil vapours generated from the primary pyrolysis were sent to the converter for the secondary pyrolysis at temperatures of 650 - 820 ^{o}C. The oil yield based on kerogen decreased from 35.3 % at the pyrolysis temperature of 500 ^{o}C to 15.4 % at 820 ^{o}C. The gas yield increased in the same temperature range from 10.7 to 25.5 %.

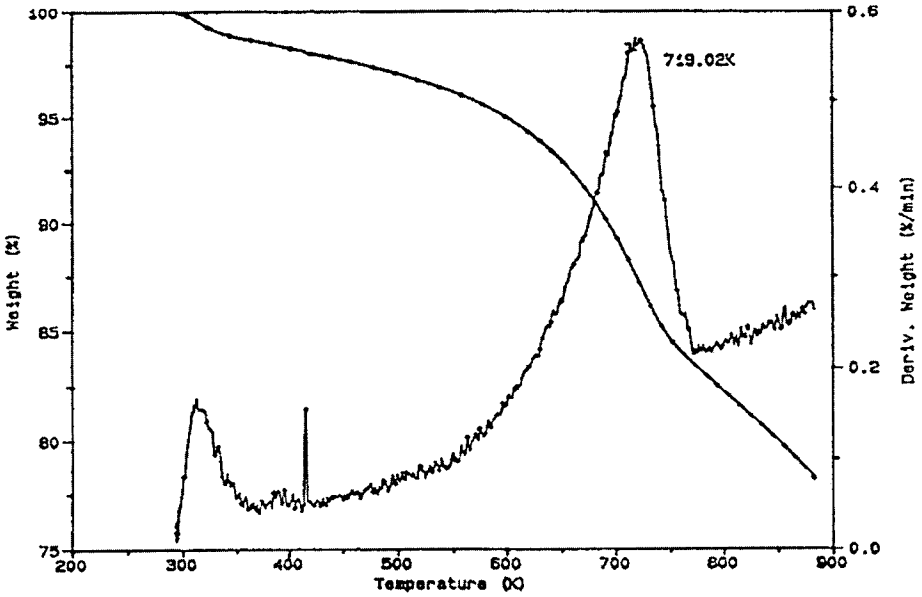


Figure 5. TG/DTG curves of Mengen oil shale in nitrogen at a heating rate of 10^0C/min.

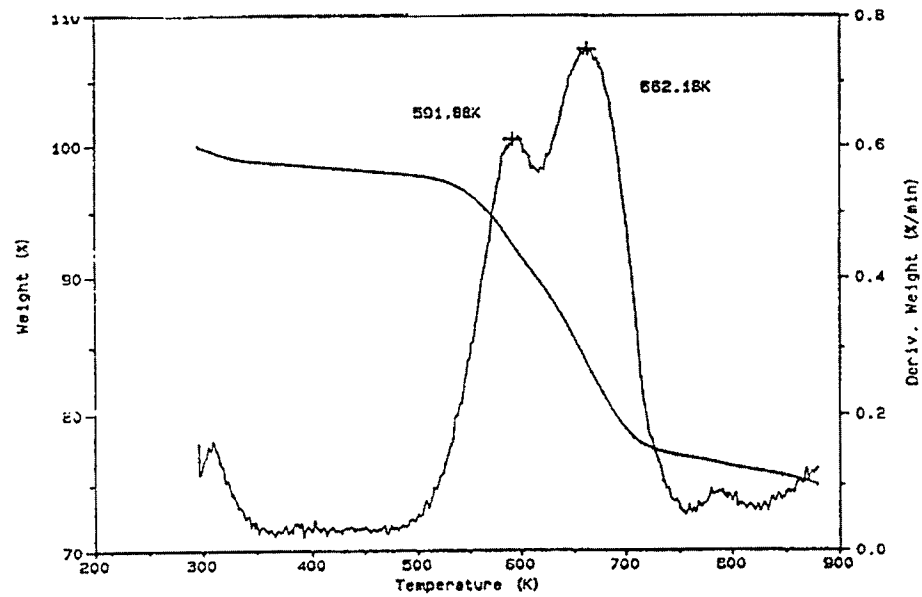


Figure 6. TG/DTG curves for Mengen oil shale in air at a heating rate of 10^0C/min.

The yields of hydrogen, methane, ethylene, and carbon monoxide increased with temperature, whereas yields of alkanes decreased. The secondary pyrolysis enabled the composition of the primary shale oil to be us to simplify substantially simplified.

Kok and Pamir [94] used DSC to determine the combustion kinetics of oil shale samples by the ASTM method. Higher heating rates resulted in higher reaction temperatures and higher heat of reactions. Distinctive peaks shifted to higher temperatures with an increase in heating rate. Activation energy values were found to be in the range of 132 - 185 kJ/mol. Lisboa and Watkinson [95] used TG for the study of the kinetics of pyrolysis and combustion of oil shale. This study investigated the effects of key parameters on the observed reaction rates, such as: the gas flow rate, the gas purity, the gas nature, the particle sizes and sample sizes. Jaber and Probert [96,97] studied two oil shale samples using TG. The controlling parameters studied were the final temperature and influence of particle size as well as the heating rate employed during the process of thermal degradation of the oil shale sample. An integral method was used in the analysis of mass loss data to determine the pyrolysis and gasification kinetics. Gasification and pyrolysis of the investigated shales complied with first-order kinetics. The activation energy decreased slightly as the shale-particle size decreased.

Kok et al. [98] used pressurized differential scanning calorimeter (PDSC) to obtain information on the pyrolysis and combustion characteristics of oil shales at different pressures (100-400 psi). Two distinct peaks were identified in combustion experiments known as low temperature oxidation (LTO) and high temperature oxidation (HTO) reaction regions. The pyrolysis of all oil shale samples showed one exothermic effect at each total pressure studied. Kinetic data were analysed and the results were discussed.

Karabakan and Yurum [99] investigated the effect of the mineral matrix of oil shales and air diffusion on the conversion of organic material in oxidation reactions. The overall reaction orders from the kinetic analysis were found to be pseudo first-order. The magnitude of the activation energies of oxidation reactions at equal heating rates changed. The rate of reaction depended on the rate of transport of the gas into the zone of reaction by diffusion. The diffusion of oxygen into the organic matrix was proposed to be the major resistance controlling the rate of oxidation reactions.

Gersten et al. [100] investigated the thermal decomposition behaviour of polypropylene, oil shale and a 1:3 mixture of the two in a TG/DTG reaction system in an argon atmosphere. Experiments were conducted at three heating rates in the temperature range of 30-900 ^{o}C. The results indicated that the characteristics of the process depend on the heating rate, and the polypropylene acts as a catalyst in the degradation of oil shale in the mixture.

Berkovich et al. [101] presented a novel technique for the thermal characterization of oil shale. This approach involves the separation of the unique components of oil shale, the kerogen and the clay minerals, using chemical and physical techniques. The heat capacity and enthalpy changes for the kerogen and clay minerals were measured using modulated temperature DSC from 25 to 500 °C. Enthalpy data for the dehydration and pyrolysis of kerogen were also determined.

Williams and Ahmad [102] pyrolysed oil shale samples in a thermogravimetric analyser using non-isothermal and isothermal analysis. The main region of mass loss corresponding to hydrocarbon oil and gas release was between 200-620 °C and at higher temperatures significant mass loss was attributed to carbonate decomposition. For the oil shale samples analysed, increasing the heating rate shifted the reaction to higher temperatures. The kinetic data were analysed using the Coats and Redfern method. There was no clear relationship between activation energy and heating rate. Kok and Pamir [103] developed a general computer program for determining the kinetic parameters of pyrolysis and of combustion of oil shale samples by TG/DTG. Activation energies were determined by five different methods and the methods were compared with regard to their accuracy and the ease of interpretation.

Williams and Ahmad [104] investigated the pyrolysis behaviour of two oil shales in a thermogravimetric analyser and in a fixed-bed reactor to determine the influence of temperature and heating rate on the thermal degradation of the samples. For the oil shale samples analysed in TG/DTG, increasing the heating rate shifted the reactions to higher temperatures. The main region of mass loss, corresponding to hydrocarbon oil and gas release, was between 20-620 °C and, at higher temperatures, significant mass loss was attributed to carbonate decomposition.

Torrente and Galan [105] studied the kinetics of thermal decomposition of oil shale using TG/DTG. The rate of thermal decomposition of oil shale could be suitably described by overall first-order kinetics. No mass and heat transfer resistance was observed for the different particle sizes studied.

Jaber and Mohsen [106] investigated the drying kinetics of two oil shales from different deposits over a temperature range of 70-150 °C using TG/DTG. The drying rate decreases at a critical temperature (120 °C) and approaches zero beyond this temperature.

Li et al. [107] investigated the pyrolysis of oil shale kerogen using TG/DTG. An overall first-order reaction model was successfully used to simulate mass loss data. The activation energies measured for most of the oil shales studied ranged from 160 kJ/mol to 170 kJ/mol. Khraisha and Shabib [108] used TG/DTG and DSC for investigation of oil shale. The mass loss data show that the pyrolysis of shale oils takes place in one regime, and that the major mass

loss occurs in the range of 175-450 °C. The DSC data reveal the endothermic behaviour of the decomposed samples. The results could be described by a first-order reaction and the measured activation energies varied from 21 to 30 kJ mol^{-1}. Barkia et al. [109] examined the organic matter evolved and the kinetics of combustion of oil shales using TG and DTA. Both techniques showed that combustion of organic matter occurs in two steps. Experimental results gave activation energies of the same magnitude for the first step of both oil shales 103 kJ mol^{-1}, whereas for the second step values were in the range of 118 - 148 kJ mol^{-1}. Li and Yue [110] carried out pyrolysis experiments on oil shale samples with the aid of thermogravimetry at a constant heating rate of 5 °C /min. The relationships between the kinetic parameters were further investigated and the correlation equations were obtained. These relationship equations can provide important information to understand the pyrolysis mechanism and to investigate the chemical structure of oil shale kerogen.

3. CONCLUSIONS

A survey of this chapter reveals that thermal methods are finding increasing application in the study of fossil fuels, and that thermal analysis techniques have been applied very successfully to studies of the interaction of these fossil fuels with nitrogen and with other gases such as air and oxygen. Use of these techniques has considerable significance in terms of the determination of the changes in properties such as pyrolysis, combustion, decomposition characteristics, calorific effects, kinetics, proximate analysis, utilization and value of these fuels [111].

REFERENCES

1. K. Rajeshwar, Thermochim. Acta, 63 (1983) 97.
2. M.V.Kok, Ph.D.Thesis, Dept. of Petroleum Eng., Middle East Tech. Univ. (1990) 49.
3. C. Rai and D.Q. Tran, Fuel, 58 (1977) 603.
4. O.P. Mahajan and A. Tomita. Fuel, 56 (1977) 33.
5. V.T. Ciuryla and R.F. Welmer, Fuel, 58 (1979) 748.
6. G.W. Collett and B. Rund. Thermochim. Acta, 41 (1980) 153.
7. C.T. Ratcliffe and G. Pap, Fuel, 59 (1980) 244.
8. P.I. Gold, Thermochim. Acta, 42 (1980) 135.
9. J.W. Cumming, Fuel, 63 (1980) 1436.
10. E.S. Smith and C.R. Neavel, Fuel, 60 (1981) 458.
11. S.E. Smith, R.C. Neavel and E.J. Hippo, Fuel, 60 (1981) 458.
12. J.W. Cumming and J. Mclaughlin, Thermochim. Acta, 57 (1982) 253.

13. R.J.Rosenvold and J.B.Dubow, Thermochim. Acta, 53 (1982) 321.
14. E.I. Butler and M.R. Soulard, Fuel, 61 (1982) 437.
15. J.P. Elder, Fuel, 62 (1983) 580.
16. M.J. Richardson, Fuel, 72 (1983) 1047.
17. J.P. Elder and M.B. Harris, Fuel, 63 (1984) 262.
18. M.A. Seragaldin and W. Pan, Thermochim. Acta, 76 (1984) 145.
19. P.A. Morgan and S.D. Robertson, Fuel, 65 (1986) 1546.
20. M.M. Patel, D.T. Grow and B.C. Young, Fuel, 67 (1988) 165.
21. S.K. Janikowski and V.I. Stenberg, Fuel, 68 (1989) 95.
22. R.M. Morris, Fuel, 69 (1990) 776.
23. M. Alula, D. Cagniant and J.C. Laver, Fuel, 65 (1990) 177.
24. P. Starzewski and W. Zielenkiewic, Thermochim. Acta, 160 (1990) 215.
25. J.C. Crelling, E.J. Hippo, A. Woerner and D.P. West, Fuel, 71 (1992) 151.
26. A.M. Alonso, J. Bermego, M.Gruda and M.D. Tason, Fuel, 71 (1992) 611.
27. T. Coil, J.F. Perale and J. Arnaldos, Thermochim. Acta, 196 (1992) 53.
28. H. Haykiri, S. Kucukbayrak and G. Okten, Fuel Sci. Tech. Int., 11 (1993) 1611.
29. R.M. Morris, J. Anal. Appl. Pyrolysis, 27 (1993) 97.
30. A. Mianowski and T. Radko, Fuel, 72 (1993) 1537.
31. P.R. Solomon and M.A. Serai, Fuel, 72 (1993) 589.
32. M.J. Richardson, Fuel, 72 (1993) 1047.
33. S.St.J. Warne, Thermochim. Acta, 272 (1996) 1.
34. I.E. Nosyrey, D. Cagniant, D.Gruber and B.Fixari, Analusis, 25 (1997) 313.
35. M.V.Kok, J. Therm. Anal., 49 (1997) 617.
36. M.V.Kok, E.Ozbas, C.Hicyilmaz and O.Karacan, Thermochim. Acta, 302 (1997) 125.
37. M.V.Kok, E.Ozbas, O.Karacan and C.Hicyilmaz, J. Anal. Appl. Pyrolysis, 45 (1998) 103.
38. H.Huang, S.J.Wang, K.Y. Wang, M.T. Klein, W.H. Calkins and A.Davis, Energy and Fuels, 13, (1999) 396.
39. J.Liu, D.He, L.Xu, H.Yang and Q.Wang, J. Therm. Anal. Cal., 58 (1999) 447.
40. P.Pranda, K.Prandova and V.Hlavacek, Fuel Processing Technology, 61 (1999) 211.
41. M.V.Kok, Thermochim. Acta, 336 (1999) 121.
42. E.A.Boiko, Thermochim. Acta, 348 (1-2), (1999) 97.
43. K.E.Benfell, B.B.Beamish, P.J.Crosdela and K.A.Rodgers, Fuel Processing Technology, 60 (1999) 1.
44. K.Ceylan, H. Karaca and Y. Onal, Fuel, 78 (1999) 1109.

45. D.L.Zoller, M.V. Johnston, J. Tomic, X.G. Wang and W.H. Calkins, Energy and Fuels, 13, (1999) 1097.
46. I.Pitkenan, J.Huttunen, H. Halttunen and R.Vesterien, J. Therm. Anal. Cal., 56 : (3) (1999) 1253.
47. T.Takanohashi, Y.Terao, M.Iino, Y.S.Yun and E.M.Suuberg, Energy and Fuels, 13 (2), (1999) 506.
48. P.Garcia, P.J.Hall and F.Mondragon, Thermochim. Acta, 336 (1999) 41.
49. K.E.Ozbas, C.Hicyilmaz and M.V.Kok, Fuel Processing Technology, 64 (2000) 211.
50. Y.Guldogan, T.O.Bozdemir and T.Durusoy, Energy Sources, 22 (2002) 305
51. M.C.Mayoral, M.T. Izquierdo, J.M.Andreas and B. Rubio, Thermochim. Acta, 370 (2001) 91.
52. M.V.Kok, J. Therm. Anal. Cal., 64 (2001) 1319.
53. A.Iordanidis, A.Georgakopoulos, K.Markova, A.Filippidis and A. Fournaraki, Thermochim. Acta, 371 (2001) 137.
54. M.J.G.Alonso, A.G.Borrego, D.Alvarez, W.Kalkreuth and R.Menendez, Fuel, 80 (3) (2001) 1857.
55. G.Varhegyi, P.Szabo, E.Jakab and F.Till, J. Anal. Appl. Pyrolysis, 57 (2001) 203.
56. W.Xie and W.P.Pan, J. Therm. Anal. Cal., 65 (2001) 669.
57. B.Avid, B.Purevsuren, M. Born, J.Dugarjav, Y. Davaajav, A. Tuvshinjargal, J. Therm. Anal. Cal., 68 (2002) 877.
58. N.E.Altun, M.V.Kok and C. Hicyilmaz, Energy & Fuels, 16 (2002) 785.
59. M.A. Lizella and F.X.C. de lass Hears, Energy & Fuels 16 (2002) 1444.
60. N.E.Altun, C. Hicyilmaz and M.V.Kok, J. Anal. Appl. Pyrolysis, 67 (2003) 378.
61. S. Vossoughi and G. W. Bartlett, Soc. Pet. Eng. AIME, 11073 (1982) 1.
62. J.C. Burger and B.C. Sahuquet, Soc. Pet. Eng. AIME, (1972) 410.
63. J.H. Bae. Soc. Pet. Eng. AIME, (1977) 211.
64. D. Drici and S. Vossoughi, SPE Reservoir Eng., (1977) 591.
65. S. Vossoughi. J. Therm. Anal., 27 (1983) 17.
66. K.S. Yoshiki and C.R. Phillips, Fuel, 64 (1985) 1591.
67. J. Verkocy and N.J. Kamal, J. Can. Pet. Technol., (1986) 47.
68. N.J. Kamal and J. Verkocy, SPE Reservoir Eng., (1986) 329.
69. M. Ranjbar and G. Pusch, J. Anal. Appl. Pyrolysis, 20 (1991) 185.
70. M.F. Ahmed and M. Saleem, Fuel Sci. Tech. Int., 9 (1991) 461.
71. M. Ranjbar, J. Anal. Appl. Pyrolysis 27 (1993) 87.
72. M.V. Kok and E. Okandan, Fuel, 71 (1992) 1499.
73. M.V. Kok, Thermochim. Acta, 214 (1993) 315.

74. H. Kopsch, Thermochim. Acta, 235 (1994) 271.
75. A.B.A. Lukyaa, R. Hughes, A. Millington and D. Price, Trans. Inst. Chem. Eng., 72 (1994) 163.
76. M.V.Kok, J.Sztatisz and G.Pokol, Energy and Fuels, 11, (1997) 1137.
77. M.V.Kok and O.Karacan, J. Therm. Anal. Cal., 52 (1998) 781.
78. S.Di Lalla and J.A.Kosinski, J. Air & Waste Management Assoc., 49 (1999) 925.
79. H.Laux, T.Butz and I.Rahimian, Oil and Gas Science and Tech., 55 (2000) 315.
80. M.L.A. Goncalves, M.A.G.Teixeira, R.C.L. Pereira, R.L.P. Mercury and J.R. Matos, J. Therm. Anal. Cal., 64 (2001) 697.
81. M.V.Kok and A.G.Iscan, J. Therm. Anal. Cal., 64 (2001) 1311.
82. M.V.Kok and C.Keskin, Thermochim. Acta, 369 (2001) 143.
83. S.M. Shih and H.Y. Sohn, Ind. Eng. Chem. Process Des. Dev., 19 (1980) 420.
84. K. Rejashwar, Thermochim. Acta, 45 (1981) 253.
85. M. Sweeney, Thermochim. Acta, 48 (1981) 295.
86. C.M. Earnest, Thermochim. Acta, 58 (1982) 271.
87. D.S. Thakur and H.E. Nuttall, Ind. Eng. Chem. Res., 26 (1987) 1351.
88. A.A. Zabaniotou, A.A. Lappas and N. Kousidis, J. Anal. Appl. Pyrolysis, 21-3 (1991) 293.
89. D. Skala, H. Kopsch, M. Sokik, H.I. Neum and A. Boucnovic, Fuel, 65 (1990) 490.
90. D. Skala and M. Sokic, J. Therm. Anal. Cal., 38 (1992) 729.
91. A. Burnham, in C. Snape (Ed.), NATO ASI Composition, Geochemistry and Conversion of Oil Shale, Akcay, Turkey, 1993. URCL-IC-1 14129.
92. H. Lillack and K. Schwochau, J. Anal. Appl. Pyrolysis, 28 (1994) 121.
93. V.G. Fainberg and G.Hetsroni, Energy & Fuels, 11 (1997) 915.
94. M.V.Kok and M.R.Pamir, J. Therm. Anal. Cal., 53 (1998) 567.
95. A.C.L. Lisboa and A.P. Watkinson, Powder Technology, 101 (1999) 151.
96. J.O.Jaber and S.D.Probert, Applied Energy, 63 (1999) 269.
97. J.O.Jaber and S.D.Probert, Fuel Processing Technology, 63 (2000) 57.
98. M.V.Kok, J.Sztatisz and G.Pokol, J. Therm. Anal. Cal., 56 (1999) 939.
99. A.Karabakan and Y.Yurum, Fuel, 79 (2000) 785.
100. J.Gersten, V.Fainberg, G.Hetsroni and Y.Shindler, Fuel, 79 (2000) 1679.
101. A.J.Berkovich, J.H.Levy, S.J.Schmidt and B.R.Young, Thermochim. Acta, 57 (2000) 4.
102. P.T.Williams and N.Ahmad, Applied Energy, 66 (2000) 113.
103. M.V.Kok and M.R.Pamir, J. Anal. Appl. Pyrolysis, 55 (2000) 185.
104. P.T.Williams and N.Ahmad, Fuel, 78 (2000) 653.

105. M.C.Torrento and M.A.Galan, Fuel, 80 (2001) 327.
106. J.O.Jabber and M.S.Mohsen, Oil Shale, 18 (2001) 47.
107. S.Y.Li, Z. You, J.L. Quan and S.H. Guo, Oil Shale, 18 (2001) 307.
108. Y.H. Khraisha and I.M. Shabib, Enery Conversion and Management, 43 (2002) 229.
109. H.Barkia, L.Belkbir and S.A.A.Jayaweera, J. Therm. Anal. Cal., 71 (2003) 97.
110. S.Y. Li and C.T. Yue, Fuel, 82 (2003) 337.
111. M.V. Kok, J. Therm. Anal. Cal., 68 (2002) 1061.

This Page Intentionally Left Blank

Handbook of Thermal Analysis and Calorimetry. Vol. 2: Applications to Inorganic and Miscellaneous Materials
M.E. Brown and P.K. Gallagher, editors
© 2003 Elsevier B.V. All right reserved.

Chapter 10

GENERAL INORGANIC CHEMICALS AND COORDINATION COMPOUNDS

Hans-Joachim Seifert

Auf der Höh 7, D-35619, Braunfels, Germany.

1. INTRODUCTION

This chapter deals with the applications of Thermal Analysis (TA) in the study of inorganic chemicals and coordination compounds. Calorimetry is included in so far as it complements results from TA measurements. The main objects of such investigations are solids. Some few examples of studies of fluids are known, while gases are beyond the field of thermal analysis. To illustrate the application of the methods in question, examples are taken mainly from the author's own researches on the halides of transition metals and rare earth elements.

2. CHEMICALS AND METHODS

2.1. Binary compounds

Binary compounds consist of two elements: $A_\alpha B_\beta$. If they are solids, A is mostly a metal or semi-metal and B = halides, oxygen; sulfur etc., nitride, phosphide etc., carbide. Their properties are given by the bond character, determined by the difference Δ in electronegativities between A and B. If Δ is large, salts such as halides or salt-like compounds such as oxides are formed. Their melts consist of ions. For a medium value of Δ, the bond character is between ionic-covalent-metallic, examples are sulfides, carbides etc. with often high melting temperatures. For a small Δ, the compounds are: a) molecular systems (gases, liquids or low-melting solids, such as CO_2, CS_2, $SbCl_3$); b) polymers (e.g. P-S-compounds); c) intermetallic phases (e.g. Zintl-phases) This group of compounds is not treated in this Chapter.

2.2. Complexes and double compounds

Complexes are defined entities $[BC_z]^n$ with B = the central particle (or particles in multi-centre-complexes); C = monodentate ligands; z is the coordination number (CN) of the central particle. If C is an ion, in general an anion, and B a cation, then n is the difference of the charges. Counterions, A, compensate the complex charge, n. For anionic complexes, counterions are often alkali-metal ions, A^+, or onium-ions, specially ammonium ions. If the complex entities are extremely stable, then their formation reactions:

$$BX_m + zC \rightarrow [BC_z]\, X_m$$

(cationic complexes with C= molecule) or:

$$BC_m + nAC \rightarrow [BC_{m+c}]A_n$$

(anionic complexes with C = monocharged anion) are not equilibrium reactions. In this case it is reasonable to treat the compounds as pseudo-binary; examples are the salts of oxo-acids, like sulfates, nitrates, carbonates, acetates, etc.

Double compounds (double oxides, double halides, etc.) exist only in crystal lattices. In a skeleton of anions, which often forms close packings, interstices are occupied by two different cations, A^{m+} and B^{n+}. An example of a double salt is $NaMnCl_3$, where, in a closest packed arrangement of Cl^- ions, 1/3 of the octahedral holes are occupied by Na^+ ions, 1/3 by Mn^{2+} ions and 1/3 are empty. Thus electroneutrality is achieved. The formation reaction is:

$$NaCl + MnCl_2 \rightarrow NaMnCl_3$$

An important question is, how many compounds Na_xMnCl_{x+2} exist in the pseudo-binary system $NaCl/MnCl_2$? Thus, the elucidating of phase diagrams is closely connected with the field of ternary compounds.

2.3. Properties and methods of measurement

Detailed descriptions of the methods of thermal analysis and calorimetry are given in Volumes 1 and 4 of this Handbook. Here only a short discussion is given, so that the reason why a specific method is applied to solve a special problem for a particular compound or system can be understood.

Enthalpy-functions ($\Delta H_T - \Delta H_o$) and heat-capacities c_p are the main thermodynamic properties measured with calorimetry and/or DSC (DSC will be used here to include quantitative DTA). Among the calorimetric methods,

adiabatic and drop calorimetry are nearly exclusively used for such measurements. In a rough approximation, one can say that DSC is used in the temperature range from 0 to 600 - 800°C, depending on the DSC-equipment, adiabatic calorimetry below 0 °C and at moderate temperatures, and drop calorimetry at moderate and high temperatures. The advantages of DSC are: a) the short time of measurement; b) the continuous temperature change, and c) the small amount of substance needed (mg against g). However, the accuracy of calorimetrically determined c_p values is, in general, ten times higher than that of c_p values obtained from DSC. Additionally, reaction calorimetry as combustion calorimetry in oxygen or fluorine, and solution calorimetry are of importance for determining the formation enthalpies of compounds.

A further field for the application of DTA is in the determination of phase diagrams. If one considers pure compounds as one-component systems, solid-solid and solid-liquid transitions can occur. Solid-liquid transitions lead to the determination of melting and solidification temperatures. Solid-solid transitions can be a change of crystal modification or a solid reaction, a decomposition or a formation reaction. The kind of reaction has nearly always got to be confirmed by high-temperature X-ray diffraction (HT -XRD). With DSC or calorimetric measurements, the dependence on temperature of transition enthalpies can also be obtained. According to $H/T = S$, transition entropies may also be calculated.

To determine the phase diagram of a binary system, A/B, one has to measure the dependence of enthalpies on $c_{mol}(A) = 1 - c_{mol}(B)$. In addition to considering the reactions in one-component systems, liquidus lines, eutectic and peritectic temperatures and compositions and, if necessary, mixed crystal regions must be determined.

The specific heat capacity, i.e. heat capacity per unit mass, usually shortened to 'specific heat', is the amount of heat that must be supplied to a unit mass of material to raise its temperature by an infinitesimal amount, divided by that increase in temperature. It can be defined as the amount of heat supplied per unit mass, per unit resultant temperature change.

The heat capacity at constant pressure, $c_p = (\delta H/\delta T)_p$. The heat -capacity becomes extremely large when first-order transitions such as melting or reconstructive crystal structure changes occur. These transformations are considered to take place abruptly, at a fixed temperature. It is not possible to perform experiments in which the temperature rise is infinitesimal, so all measurements of c_p are actually measurements of the average heat capacity over a temperature interval. The average c_p, by definition, is the enthalpy increment $H_{T2} - H_{T1}$ divided by the temperature change. The enthalpy function between two temperatures T_1 and T_2 is given by:

$$H_{T2} - H_{T1} = {}_{T1}\int^{T2} c_p \, dT + \Sigma \Delta_{tr} H$$

where $\Delta_{tr} H$ are the enthalpies of any transitions in the temperature range T_1 to T_2. To get the correlated entropy change ($S_{T2} - S_{T1}$) one must replace $\Delta_{tr} H$ by $\Delta_{tr} H / T$ and c_p by c_p/T. Because the entropy usually approaches zero as the temperature approaches absolute zero, measurements of the absolute entropy can be made by calorimetry.

3. THERMODYNAMIC PROPERTIES OF INORGANIC COMPOUNDS AND SYSTEMS

3.1. Thermodynamic data and their sources in the literature

The two-volume compilation of thermochemical data by Barin ("Thermochemical Data of Pure Substances", 1989, VCH-Verlag Weinheim (ISBN 3-527-27812-5) and VCH Publishers, New York (ISBN 0-89573-866-X)) contains the most comprehensive tables of the thermodynamic properties of 2372 pure substances as a function of temperature at 100 °C intervals. The substances, mainly inorganic, also include about 100 organic compounds, 91 elements (and the gaseous electron e^- !). Barin has relied heavily on critically evaluated data (CODATA and JANAF) where such values are available. For other substances he has drawn on a wide variety of sources, including the US Bureau of Mines Bulletin, the NBS Tables of Wagman et al. and the Landold-Börnstein compilations (all together more than a hundred references). To give an impression of the variety of compounds covered, those of barium will be used as an example. 42 species are treated, of which ten are gases (e.g. BaCl, $BaCl_2$). Binary compounds include the halides, BaO, BaO_2, BaS, BaTe, BaH_2, BaC_2, Ba_3N_2, Ba_2Sn, then $Ba(OH)_2$, Ba-nitrate, -sulfate, -chromate, -molybdate, -carbonate, -arsenate; some silicates and double oxides with Al, Ti, Zr, Hf and U.

As an example, the data for $BaCO_3$ are given in Table 1. There are two crystalline phases with a transition temperature of 1079 K and the liquid phase (m.p.=1241 K).

The basic experimental property needed to determine the T - dependence of thermochemical functions is the heat capacity. For condensed phases it is determined by calorimetric measurements. The results are usually described by a temperature function of the form:

$$c_p(T) = a + bT + cT^2 + dT^3 + eT^{-2} + fT^{-3}$$

Discontinuities exist at phase transitions. For λ-transitions the temperature ranges for the validity of such polynomials must be limited drastically.

Table 1. Thermodynamic properties for $BaCO_3$ (from I. Barin, "Thermochemical Data of Pure Substances", 1989, VCH-Verlag, Weinheim.)

197.336 BARIUM CARBONATE **BaCO3**

Phase	T	Cp	S	-(G-H298)/T	H	H-H298	G	ΔH_f	ΔG_f	log K_f
	[K]	[----------J/(K mol)----------]			[----------kJ/mol----------]					[-]
SOL-A	298.15	85.353	112.131	112.131	-1216.289	0.000	-1249.721	-1216.289	-1137.653	199.312
	300.00	85.687	112.660	112.133	-1216.131	0.158	-1249.929	-1216.280	-1137.165	197.998
	400.00	98.409	139.246	115.672	-1206.859	9.430	-1262.558	-1215.489	-1110.904	145.069
	500.00	106.577	162.125	122.729	-1196.591	19.698	-1277.654	-1214.947	-1084.834	113.332
	600.00	113.341	182.166	130.999	-1185.589	30.700	-1294.888	-1215091	-1058.799	92.177
	700.00	119.558	200.109	139.612	-1173.941	42.348	-1314.017	-1213.920	-1032.847	77.072
	800.00	125.526	216.465	148.210	-1161.685	54.604	-1334.857	-1212.808	-1007.052	65.754
	900.00	131.369	231.588	156.645	-1148.840	67.449	-1357.269	-1211.195	-981.423	56.960
	1000.00	137.143	245.729	164.853	-1135.414	80.875	-1381.142	-1209.148	-956.000	49.936
	1079.00	141.675	256.327	171.166	-1124.400	91.889	-1400.977	-1215.133	-935.471	45.286
			16.274		17.560					
SOL-B	1079.00	154.808	272.601	171.166	-1106.840	109.449	-1400.977	-1197.573	-935.471	45.286
	1100.00	154.808	275.585	173.131	-1103.589	112.700	-1406.733	-1196.781	-930.377	44.180
	1200.00	154.808	289.055	162.238	-1088.108	128.181	-1434.974	-1193.013	-906.325	39.451
	1241.00	154.808	294.256	185.853	-1081.761	134.528	-1446.933	-1191.476	-896.556	37,737
			2.522		3.130					
SOL-C	1241.00	158.992	296,778	185.853	-1078.631	137.658	-1446.933	-1188.346	-896.556	37.737
	1300.00	158.992	304.163	191.056	-1069.251	147.038	-1464.662	-1185.897	-882.741	35.469
	1400.00	158.992	315.945	199.561	-1053.351	162.938	-1495.675	-1181.805	-859.576	32.071

Because the absolute value of the enthalpy cannot be determined, the concept of the standard formation reaction is employed. $\Delta_f H^\circ$ (298.15) is the enthalpy of formation from the elements in their standard states at 298.15 K (and standard pressure). For this condition, the formation enthalpies of the elements are set as zero. The enthalpy function then is:

$$H(T) = \Delta_f H^\circ (298.15) + {}_{298.15}\int^{T} c_p \, dT$$

When there are phase transitions, the temperature ranges must be divided and the enthalpies of transition added. The entropies are given by:

$$S(T) = S^\circ(298.15) + {}_{298.15}\int^{T} (c_p/T) \, dT + \Sigma (\Delta_{tr} H/T)$$

The standard entropy is:

$$S^\circ(298.15) = S^\circ(T=0) + {}_{0}\int^{298.15} (c_p/T) \, dT$$

The Third Law of thermodynamics gives $S^\circ(0) = 0$ for perfect crystals.

Using the Gibbs-Helmholtz equation: $G = H - TS$, the Gibbs energy $G(T)$ can be calculated. The Gibbs energy function, $[G - H(298.15)]/T$, and the enthalpy function, $[H - H(298.15)]$, useful for thermochemical calculations, can be calculated directly from the three basic functions. The last three columns in the tables as illustrated in Table 1, namely ΔH_f, ΔG_f and log K_f, relate to the formation of the compound from the elements at the temperature T.

Note that these tables do not indicate the accuracy of the data and values for $c_p(T)$ and $H(T)$ below 298.15 K, particularly in the region of absolute zero, are not listed. For such data, standard works like the JANAF tables or the original literature must be used.

3.2. Adiabatic calorimetry

In the adiabatic method the sample is isolated, as far as possible, from heat exchange with its environment, and the remaining heat exchange is made as reproducible as possible. Measured amounts of heat are then supplied to the sample and the resulting temperature changes are measured. The heat is usually supplied by electrical means.

The sample being studied is usually sealed into a container (the calorimeter proper). The heat capacity of the sample is then determined as the difference between the heat capacity of the filled container and that of the empty container. All errors that are the same in the two measurements will cancel out. At higher temperatures, radiation shields outside the calorimeter are used. Usually, adiabatic heat capacity calorimeters are heated intermittently giving average c_p-

values over small ranges of temperature. However, they also can be heated continuously giving curves of c_p against T. Classic examples are the investigations of Sommers and Westrum in 1976/77 of the heat capacities and Schottky anomalies of lanthanide chlorides, $LnCl_3$ [1]. The calorimeter of gold-plated copper had an internal volume of 92 cm^3 and a mass of 61 g. It was loaded with about 80 g of sample and sealed with a He-atmosphere. The temperature was measured with a Pt-resistance thermometer, calibrated with NBS-standards. For $LaCl_3$, for example, four series of T - c_p values were measured. From these values, separately determined values for the empty calorimeter were subtracted. With these values (Table 2a), a curve-fitting regression process was performed, giving a power series which was integrated to derive thermodynamic functions at rounded temperature intervals (Table 2b for 5 to 100 K). In Figure 1, c_p vs T curves for $LaCl_3$, $PrCl_3$ and $NdCl_3$ are given.

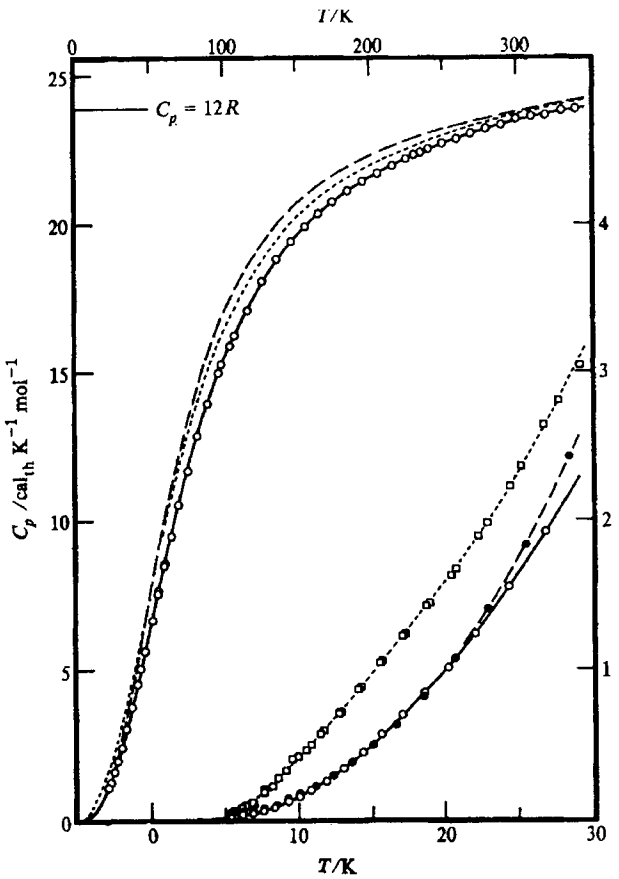


Figure 1. Experimental c_p vs T curves for $LaCl_3$, $PrCl_3$ and $NdCl_3$.

Table 2.
Experimental heat capacities of $LaCl_3$ (2a) and derived thermodynamic functions (2b) [1].

T/K	C_p/cal$_{th}$ K^{-1} mol^{-1}	T/K	C_p/cal$_{th}$ K^{-1} mol^{-1}	T/K	C_p/cal$_{th}$ K^{-1} mol^{-1}	T/K	C_p/cal$_{th}$ K^{-1} mol^{-1}
Lanthanum trichloride							
Series I		Series II		63.18	9.450	13.03	0.332
98.56	15.26	230.42	22.30	68.63	10.53	14.30	0.440
107.11	16.23	240.21	22.51	74.68	11.64	15.63	0.565
116.22	17.14	249.92	22.68	81.31	12.82	17.06	0.692
126.18	18.02	259.73	22.83	88.50	13.98	18.58	0.839
136.44	18.78	269.64	23.01	96.28	14.98	20.16	1.008
146.34	19.39	279.71	23.20	104.09	15.89	22.03	1.232
155.96	19.90	289.95	23.29			24.36	1.550
165.35	20.34	300.11	23.48	Series IV		26.85	1.920
174.96	20.74	310.21	23.58	5.63	0.017	29.64	2.379
185.09	21.10	320.28	23.61	6.18	0.024	33.10	3.005
195.38	21.41	330.29	23.76	6.87	0.039	36.78	3.723
205.53	21.68	340.28	23.81	7.53	0.054	40.44	4.486
215.56	21.95	347.26	23.79[a]	8.30	0.083	42.74	4.978
225.49	22.19			9.24	0.064[b]	45.54	5.589
235.33	22.39	Series III		10.05	0.153	50.18	6.611
		54.64	7.602	10.78	0.193	54.38	7.530
		58.56	8.458	11.83	0.248	58.96	8.541

T/K	C_p/cal$_{th}$ K^{-1} mol^{-1}	$S°(T) - S°(0)$/cal$_{th}$ K^{-1} mol^{-1}	$H°(T) - H°(0)$/cal$_{th}$ mol^{-1}	$-\{G°(T) - H°(0)\}/T$/cal$_{th}$ K^{-1} mol^{-1}
Lanthanum trichloride				
5	0.011	(0.005)	(0.017)	(0.001)
10	0.150	0.042	0.326	0.010
15	0.496	0.163	1.866	0.038
20	0.996	0.370	5.538	0.094
25	1.640	0.659	12.066	0.177
30	2.438	1.026	22.199	0.286
35	3.371	1.471	36.675	0.423
40	4.395	1.987	56.06	0.586
45	5.469	2.566	80.71	0.773
50	6.571	3.199	110.80	0.984
60	8.767	4.593	187.57	1.467
70	10.795	6.100	285.57	2.020
80	12.584	7.661	402.67	2.627
90	14.123	9.234	536.4	3.274
100	15.43	10.792	684.4	3.948

In 1993, Westrum et al. [2] measured the heat capacity and thermodynamic properties of $CaSn_2F_6$ from 6 to 310 K. Hysteresis was experienced, but reproducible heat capacities were obtained after cooling the sample twice to $T <$ 150 K. With the same method a first-order phase transition was detected by Bartolomé et al. [3] for the compound NH_4MgF_3 at 107.5 ± 1.0 K, characterized by XRD. In the range of the anomaly a heating curve was recorded with the adiabatic shield held warmer than the sample holder.

A very careful investigation, on a substance with several phase transitions of different types, was performed in 1983 on Rb_2ZnCl_4, in the range 4 - 350 K, by the group of Atake and Chihara[4].

3.3. Differential scanning calorimetry (DSC)

DSC has been generally regarded by most classical calorimetrists as an untrustworthy means of acquiring accurate thermodynamic data. This view is critically discussed by Mraw [5] in a basic investigation of the accuracy of heat capacities measured by DSC. The sample was pyrite in the temperature range 100 – 800 K. The apparatus used was a DSC-2 of Perkin-Elmer, coupled with a computer. Closable gold pans were used both for the sample and reference. Three series were measured in a single day: empty - empty for the baseline, with sapphire - empty for calibration, and with pyrite - empty for the desired c_p-values. To keep the uncertainty in the baseline as low as possible, temperature intervals of 10 K were scanned in 4 minutes. A series of 10 - 15 runs, covering an interval of 100 - 150 K, was done before opening the calorimeter to change to the next pan. Masses of the samples were about 40 mg, with an accuracy of 0.01 mg. Below 270 K, liquid nitrogen was used as coolant and (0.1 He + 0.9 N_2) as purge gas. From 250 to 470 K the purge gas was N_2, and above 460 K, Ar.

For the treatment of the results, two methods were used: the 'scanning method' and the 'enthalpy method'.

Scanning-method: One after another, a series of scans with the empty pan, pan + sapphire, pan + pyrite are measured, always in 10 K steps. For each step the DSC signal line, S, is calculated by interpolating between the averaged values for the initial and final temperatures and the differences:

D_s = S(sapphire) - S(empty) and D_p= S(pyrite) - S(empty)

are determined. Then:

$c_p(\text{pyrite})/c_p(\text{sapphire}) = (m_s D_p) /(m_p D_s)$

where m_p and m_s are the masses of pyrite and sapphire, respectively.

Enthalpy method: The procedure of the measurement is the same. For each step the area between the actual scan and the hypothetical baseline is numerically integrated to determine the enthalpy, ΔH, involved in heating the sample over the temperature step, ΔT. Then, in this temperature range: $c_p = \Delta H/\Delta T$. Thus the methods of classical calorimetry are more nearly duplicated.

For both methods the resulting c_p vs T curves are smoothed graphically to determine the best values for c_p. The mean percentage deviation between

experimental and smoothed values is ± 0.8% for the scanning method and ± 0.6% for the enthalpy method. The deviations from c_p-values measured by Grønvold and Westrum [6] with adiabatic calorimetry were ± 1.0% and ± 0.7%. Taking into account the absolute values of c_p, the accuracy by either method was approximately 1% over most of the temperature range and generally within 2% at the very lowest and highest temperatures. However, the enthalpy method is to be preferred, because it eliminates lack of equilibrium and sample temperature lags during a scan.

The quality of such measurements depends upon a good calibration, both of temperature and enthalpy or heat capacity [7]. Recommendations are given by a GEFTA/ICTAC working group [8]. Again measurements on lanthanide-chlorides will be taken as an example. Gaune-Escard et al. [9] determined c_p values for $LnCl_3$ (Ln = La-Nd, Gd and Dy) in the temperature range 300 K to the melting temperatures of the compounds. They used a variation of the enthalpy-method. Two correlated experiments were carried out: the first with two empty containers, the second with the same containers, one filled with the sample. For both runs, the heat flux between the two containers was recorded as a function of temperature. The area between two curves is proportional to the heat necessary for the increase of the temperature. The heating steps were 5 K, the heating rate was 1.5 K min^{-1}. To achieve equilibrium an isothermal delay of 400 s followed each step. Linear regression of the resulting values for $LaCl_3$ gave:

$$c_p/\text{J mol}^{-1}\,\text{K}^{-1} = 82.51 + 3.816 \times 10^{-2}\, T/\text{K}$$

with an standard error of 2.01. The values found are in generally good agreement with experimental results of other scientists.

DSC-measurements are a continuous scanning method, so they are very suitable for determining temperatures and enthalpies of *phase transitions*. Blachnik [10] studied the phase transitions of alkylammonium-tetrachlorozincates in the range 173-500 K, at a heating rate of 5 K min^{-1} and a sample size of about 50 mg. For example, $[(C_2H_5)NH_3]_2ZnCl_2$ exhibits two transitions at 239 and 257 K with enthalpies of 2.75 and 1.18 kJ mol^{-1}. The accuracy in the transition temperatures was ± 2 K and in the transition enthalpies ± 5%. The enthalpy of melting of Na_3FSO_4 [11] was measured in a HT-scanning calorimeter of SETARAM (heating rate 2 K min^{-1}) and evaluated using a procedure by Guttman and Flynn [12] generally applicable for reaction enthalpies. The reference substance was NaCl and its melting enthalpy was used for calibration. The result was $\Delta_{fus}H°(Na_3FSO_4) = 69 \pm 4$ kJ mol^{-1} at T = 1060 K.

A second advantage of the DSC-method is that only small amounts of the sample are needed. Two examples: 1) $TlCdF_3$ and $RbCaF_3$ undergo phase transitions at 187 and 198 K, respectively. The heat capacities of single crystals as a function of T were measured in the range 150 to 240 K [13]. 2) The heat capacity of a single crystal of Rb_2CoCl_4 (m= 44.33 mg), grown with the Bridgman-method, was measured in the range 240 - 360 K. At 293 K a pronounced peak was found on the c_p vs T curves, with a long tail on the low-temperature side, indicating a second-order phase transition, so a definite enthalpy value could be given [14].

The limit for low temperature DSC-measurements is at about 150 K, while with normal adiabatic calorimeters measurements down to about 5 K are possible. To obtain a complete set of thermodynamic data from 5 to 1100 K, an extensive number of investigations has to be performed, applying both methods. An example is an investigation by the group of Bartolome [15] on $CsCrCl_3$ and $RbCrCl_3$. They measured heat capacities of large (about 27 g) samples with an adiabatic calorimeter between 6 and 340 K. The estimated precision was better than 4% at $T < 30$ K and better than 0.2% at $T > 30$ K. The molar heat capacities at 298 K are: c_p/R ($CsCrCl_3$) = 15.38; c_p/R($RbCrCl_3$) = 15.76. For both substances, first-order transitions were detected at 171.1 and 193.3 K, respectively. In this region, in addition to the heat pulse measurements. continuously measured scans in heating and in cooling mode were recorded. The DSC measurements from 300 to 500 K had a precision of 3%. In Figure 2, c_p vs T-curves are shown from 200 to 500 K. A second-order transition occurs at about 400 K. The crystallographic arrangements of the different phases are known.

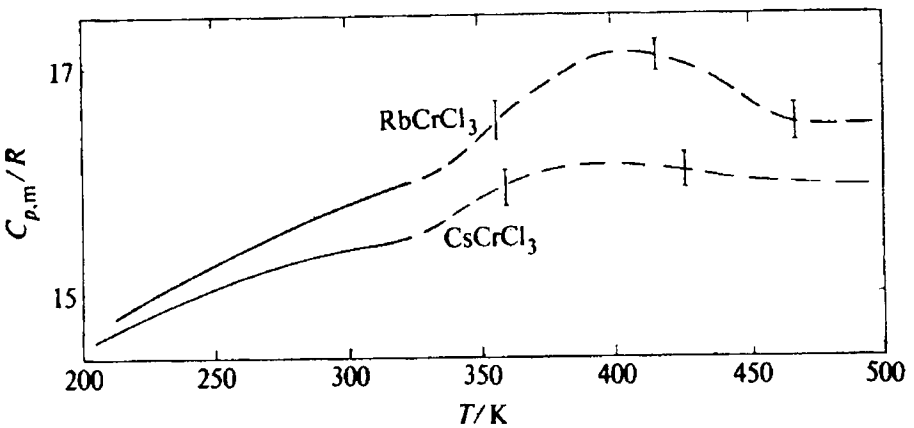


Figure 2. c_p vs T curves for $CsCrCl_3$ and $RbCrCl_3$

3.4. Drop calorimetry

A third method of measuring heat capacities and enthalpies, profitably applied to high temperatures, is drop calorimetry. In drop calorimetry, the sample is heated to the desired temperature T in a furnace and then dropped into a calorimeter of known heat capacity at a temperature T_0 near room temperature. The resulting heat effect measured in the calorimeter gives the average heat capacity (or enthalpy increment) of the sample between the calorimeter temperature and the original sample temperature. From these values (H_T - H_{To}) the c_p-values were obtained by integration of H vs T.

Drop calorimetry is somewhat more readily adaptable to extremely high temperatures where adiabatic calorimetry becomes impractical. Its main disadvantages are: a) the heat capacities are found from the differences between large enthalpy increments, and b) the sample may not come to equilibrium as it cools very rapidly through large temperature differences.

The main method in drop calorimetry is copper-block-calorimetry. In contrast to isothermal-drop-calorimetry, which uses the volume changes during the melting of ice or diphenyl-ether, copper-block-calorimetry is not completely isothermal. Here the average heat capacity of the sample is determined from the rise in temperature of the receiving-well in the block. A prototype of a drop-calorimeter for high temperatures was described in 1941 by Southard [16], who measured the heat content of silica, wollastonite ($CaSiO_3$) and ThO_2 between ambient temperature and 1500 °C. The measured enthalpy differences (H_T - $H_{298.1}$) were fitted to polynomials of the form:

$$(H_T - H_{To}) = aT + bT^2 + c/T - d$$

The deviations of the fitting curves from the measured values were 0.4%, 0.25% and 0.5% for silica, wollastonite and ThO_2, respectively. The accuracy of the drop-temperatures was estimated as better than 1 K. A copper-block calorimeter built in 1958 by Margrave and Grimly [17] with improvements was used to measure the heat contents of NBS-Al_2O_3 and $NaFeO_2$ up to 1400 K. With electrical calibration, deviations of 0.42% for alumina and 0.3% for sodium ferrite were found.

Dworkin and Bredig [18] used this method for measuring the heat of fusion of halides of the alkali, alkaline-earth and rare-earth metals. The method entailed the measurement of heat content over a sufficient temperature range above and below the melting point of the salt to allow extrapolation to the melting point. The difference between the lines for the solid and the liquid at the melting point was taken as the temperature rise of the copper block due to the heat of fusion of the salt. From that, $\Delta_{fus}H^\circ$ was calculated. The heat equivalent of the calorimeter was determined with 20 g samples of Al_2O_3 over a temperature range 400 -

800°C. Nine determinations gave a range of error of 0.22%. The accuracy of the $\Delta_{fus}H^{o}$ values was approximately 1%. Special care must be taken for solid-state phase transitions. For instance, for $SrBr_2$ there is a transition at 918 K (645 °C) and 5 points were measured in the range 570 – 645 °C and above the melting point of 657 °C.

Flengas et al. [19] described an aluminium-block twin-calorimeter for measuring heat contents, transition and fusion enthalpies up to 1000°C. The temperature rise was measured using a thermopile and calibration was done with sapphire. The measured enthalpy contents were fitted by simple polynomials: $(H_T - H_{298}) = a_o + a_1T + a_2T^2$ and hence $c_p = a_1 + 2a_2T$. For example, for KCl eight points were measured below the melting point (25 - 770 °C) and ten values from 790 - 1030°C for liquid KCl with an accuracy of approximately 0.5%. The fusion enthalpy is 26.15 ± 0.46 kJ mol^{-1} (Dworkin and Bredig [18] found 26.53 ± 0.50 kJ mol^{-1}). For Ag_2S altogether 31 values were measured. The fusion enthalpy is 7.87 ± 0.59 kJ mol^{-1}. The enthalpy for an α-β-transition at 176 °C is 3.9 ± 2.1 kJ mol^{-1}. It must be pointed out that literature values for $\Delta_{fus}H^{o}(Ag_2S)$ range from 3.8 to 15.1 kJ mol^{-1}.

Holm et al. [20] have measured the heat contents and enthalpies of fusion for some ternary magnesium chlorides. The samples were lifted into a silver calorimeter above the furnace for equilibrating. The calorimeter was surrounded by a silver shield, electrically heated to maintain quasi-adiabatic conditions with temperatures between 30 and 50 °C. They, however, disregarded solid-state transitions for two compounds: $KMgCl_3$ at 297 °C and Rb_2MgCl_4 at 415 °C and, as a consequence, they found a non-linear temperature dependence of the enthalpy function for Rb_2MgCl_4 between 380 °C and the melting temperature 467 °C.

Mochinaga et al. [21] measured fusion enthalpies of $KMgCl_3$ (33 kJ mol^{-1}) and K_2MgCl_4 (37 kJ mol^{-1}) by DSC. These values differ significantly from those of Holm (43.10 and 44.98 kJ mol^{-1}).

Generally it is recommended that several methods should be used for one substance. For example, Kleykamp [22] determined the thermodynamic data for Li_2SO_4, a compound with two solid-state transitions. The enthalpy values were obtained between 363 and 1300 K using isothermal drop calorimetry. Samples of about 100 mg were dropped from 25°C into the preheated working cell of a high-temperature calorimeter. By such a 'reverse dropping' procedure, errors from kinetic hindrance of the existing second-order phase transitions could be prevented. The transition temperatures and the integrals of the excess heat capacities were determined by heating the samples at a rate of 2 K min^{-1} from room temperature up to about 800 °C. The enthalpy of fusion was measured with a 250 mg sample in the cooling mode of the calorimeter at a rate of 0.5 K min^{-1}. The results were: $(H^{o}_T - H^{o}_{298})$/J mol^{-1} = 17156 + 73.694 T + 0.103210 T^2

- 4163.115 T^{-1}; $c_{p,298}$/J K^{-1} mol^{-1} = 182.1 ± 5.4; and $\Delta_{fus}H^{o}$ (1531 K)/kJ mol^{-1} = 53 ± 4. The critical temperatures of the second-order phase transitions were: 938 K and 996 K. The shifts of the (H_T - H_{298}) vs T -curves were 0.90 and 0.63 kJ mol^{-1}.

A very extensive investigation was performed by Gmelin et al. [23] on the polyphosphides $(Ag_6M_4P_{12})Ge_6$ with M = Ge, Sn. In the temperature range 2 K ≤ T ≤ 100 K, the specific heat capacities were determined with an automated adiabatic calorimeter. Temperatures were measured with a germanium resistor and the calibration substance was copper. More than 550 experimental data points for each substance, were measured. The total error of the smoothed c_p data was less than 0.8%. From 100 K to 310 K, samples of 3 - 4 g were measured in a DSC calorimeter against a sapphire standard. The error in c_p was less than 1.5%. DTA measurements in closed quartz ampoules (100 mg samples, heating rate 10 K min^{-1}) indicated congruent melting for M = P at 1026 ± 10 K and decomposition of the Sn-compound at about 823 K. In a vacuum thermobalance the P-compound started to decompose at 723 K. Measurements of thermal decomposition under Knudsen conditions were done using the thermobalance combined with a mass spectrometer. The nature of the solid decomposition products was confirmed by X-ray diffraction measurements. For the interpretation of the powder diagrams, the structures of the starting cluster compounds were determined with single crystals. The paper is an excellent example of a multi-method investigation.

The alkali-metal-tetrafluoroborates have been studied by several research groups. Marano and Shuster [24] studied the phase transitions of the compounds, ABF_4 (A = Li to Cs) by using DTA. The transition temperatures were: $LiBF_4$ = 111 ± 4 °C; $NaBF_4$ = 243 ± 3 °C; KBF_4 = 279 ± 1 °C; $RbBF_4$ = 249 ± 2 °C; $CsBF_4$ = 168 ± 2 °C. Dworkin and Bredig [25] measured enthalpy functions for the compounds with A = Na to Cs, in the temperature range 298 to 1000 K by drop calorimetry. From the (H_T - H_{To}) vs T -curves they derived the enthalpies and entropies of transition. For $LiBF_4$, Dworkin [26] found no phase transition at 111 °C (384 K) in agreement with the results of the measurements of the dependence of density on temperature by Cantor et al. [27]. By heat capacity measurements with adiabatic calorimetry in the low temperature range (10-340 K) Gavrichev et al. [28] found an anomaly of heat capacity in the form of a sharp peak at 301 K (28 °C) with a transition enthalpy of 3.01 ± 0.05 kJ mol^{-1}. These findings are supported by the temperature dependence of the F^{19} second moment measured by NMR [29]. Later they [30] used DSC in the range 283 - 423 K to study the behaviour of $LiBF_4$ and its mono- and trihydrate. They found that the effect observed at 380 K must be associated with the melting of $LiBF_4.H_2O$. Dworkin [26] had suspected that the monohydrate must have been formed when grinding the strongly hygroscopic $LiBF_4$ in the open air during

preparation for the DTA-measurements described above. The correct crystal structure of $LiBF_4$ is not yet known. Gavrichev et al. also performed low-temperature measurements for the other alkali fluoroborates [31] and DSC-measurements for KBF_4 [30]. The value of these papers lies in the discussion of sources for errors not only from the instruments, but also from the chemistry of the compounds.

3.5. Reaction calorimetry

3.5.1. Enthalpy of formation

The specific heat or heat capacity per unit mass is in general a quantity characteristic of a single compound or a one-component system (for practical purposes, heat capacities of mixtures may be measured). Another important thermodynamic quantity is the enthalpy of formation, $\Delta_f H^o$, which is the enthalpy for the reaction of the elements to the compound, all in standard states. Two types of calorimetry are mainly used for determining $\Delta_f H^o$: combustion calorimetry and solution calorimetry.

3.5.2. Combustion calorimetry

The development of combustion calorimetry has been spurred primarily by the need to measure the heat of combustion of fuels and by the need to acquire precise and accurate values of the heat of formation of compounds. Measurements can be made with high precision (0.1%) and precisions better than 0.01 % are not unknown.

There are two methods: oxygen bomb calorimetry and fluorine bomb calorimetry. Oxygen bomb calorimetry is the well-known classical method for determining the heats of formation of organic material. The calibration standard is benzoic acid. Many inorganic substances have also been investigated by oxidation with O_2. As an example, the measurement of $\Delta_f H^o$ for Mo_6S_{8-y} ($7.8 \leq (8-y) < 8.0$) in flowing oxygen using a Calvet-type twin calorimeter [32] will be described. The combustion of the Chevrel-phase related clusters of Mo_6S_{8-y} gives $6MoO_3$ and a mixture of gaseous SO_2 and SO_3. The ratio of SO_2 to $SO_3$was determined by quantitative analysis of SO_2 and this allowed to the reaction equations to be derived for which the combustion enthalpies were measured. The purities of the reactant sample and of the MoO_3 produced were monitored by X-ray diffraction patterns. The sample mass was 20 ± 0.01 mg. Before starting, the optimal experimental conditions for the combustion experiments were determined by TG-DTA from 630 to 873 K. These were: 773 K, flow rate of reaction gas 2 $\mu L\ s^{-1}$, time of measurement 1 h. At lower temperatures, unreacted sulfide was found by XRD; at higher temperatures (in argon atmosphere) MoS_2 was formed. For calibration, the oxidation of Nb to Nb_2O_5 was adopted. The precision of four measurements for each composition

y = 0 to 0.2 was 0.4 to 1.2%. The formation enthalpies from Mo(s) and $S_2(g)$ were calculated with $\Delta_f H^\circ$-values for MoO_3, SO_2 and SO_3 at 773 K taken from the thermodynamic data base MALT-2. The standard formation enthalpies were determined by measuring the heat contents for clusters with various compositions in the temperature range from 298 to 773 K by drop-calorimetry with the same instrument. The final result was that $-\Delta_f H^\circ$ /kJ mol^{-1} goes from 1254 for $Mo_6S_{7.8}$ and 404 for $Mo_6S_{7.9}$ to 973 for Mo_6S_8. The minimum is at $Mo_6S_{7.91}$ which corresponds with a maximum of the heat of combustion. A source for errors in oxygen combustion is the fact that the oxidation may be incomplete (for instance, the oxidation of metal pieces may lead to a product which envelopes a core of unreacted metal) or the stoichiometry of the reaction products may not be well defined, as for many transition metal oxides, and especially for many metallic hydrides, borides and silicides. Here fluorine combustion calorimetry is advantageous, because fluorides of elements in higher oxidation states are often volatile and therefore strongly stochiometric. The precision of such measurements is often 0.01 % or better. Thus, the heat of combustion for quartz was found to be - 911.07 ± 1.4 kJ mol^{-1}.

Constant volume reaction cells are either made of pyrex glass or, for raised temperatures, of nickel or monel metal. O'Hare and Hope [33] determined the formation enthalpy of WTe_2 by measuring the combustion enthalpy according to the equation:

$$WTe_2(s) + 9F_2(g) = WF_6(g) + 2TeF_6(g)$$

They also measured the combustion of Te(s) to $TeF_6(g)$ and used the earlier determined value for $WF_6(g)$. They used a stainless-steel set-up for high-pressure fluorine. Because WTe_2 on its own did not react to completion in fluorine, a tungsten saucer in conjunction with a sulfur fuse were used as combustion aids. The calorimetric system was calibrated by combustion of benzoic acid in oxygen. The molar combustion enthalpy, corrected for the additives of tungsten and sulfur, was found to be $\Delta_c H^\circ (WTe_2) = -4445 \pm 1.1$ kJ mol^{-1}. The final value for the formation of crystalline WTe_2 from W and 2Te at 298.15 K was calculated to – 38 ± 5 kJ mol^{-1}.

3.5.3. Solution calorimetry

In solution calorimetry, the heat of reaction when dissolving a sample in an appropriate solvent is measured. This solution enthalpy $\Delta_{sol} H^\circ$ is evolved in exothermic processes. For endothermic reactions, electrical energy is added to the calorimeter to maintain a rising temperature overall. Most solution calorimeters are relatively simple in design. Thermal and chemical equilibrium are generally achieved through stirring. It is important that the design of the

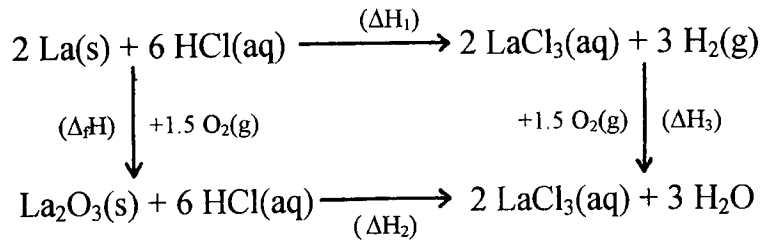
stirrer produces a constant quantity of heat per unit time. The calibration is done electrically. Test reactions for aqueous solutions are the dissolution of KCl or the neutralisation of trishydroxymethyl-aminomethane with hydrochloric acid or with sodium hydroxide solutions. The quantities measured in solution calorimetry are generally much smaller than those of combustion calorimetry, such that the uncertainty is about 0.1%.

The simplest calorimeters are based on glass Dewar-vessels, immersed in a water thermostat. To reach thermal equilibrium between the calorimeter and the surroundings in a shorter time, thin-walled metal cans can be used as calorimeters with an evacuated outer metal can instead of a glass Dewar. Solution calorimeters of the adiabatic type can have a precision of ± 0.01 % under optimum conditions. Their jacket temperature is controlled to remain equal to that of the calorimeter itself. In the more common isoperibolic devices, the jacket temperature is constant; that is, they behave as an adiabatic calorimeter with a heat leak.

The main features of the measurement of solution enthalpies in aqueous systems are illustrated for the lanthanide chlorides. Fitzgibbon and Holley in the USA and Wadsö in Sweden independently conducted measurements on La and La_2O_3 in isoperibolic solution calorimeters and published their results in [34]. The volume of the reaction chamber was about 450 mL. The temperature of the environment was kept constant to ± 0.001 K; the mass of the sample (about 10^{-2} mg) was chosen to give a temperature change of about 1 K with an accuracy of ± 10^{-4} K. The average time, from the breaking of the sample bulb until equilibrium was reached in the post-period, was 10 min. The measured heat of solution was corrected according to the analytically determined purity of the sample (98.810% for La; 99.882% for La_2O_3). The solvent was 1.0 m hydrochloric acid, saturated with H_2. A correction was applied for the evaporation of H_2O by the escaping H_2.

The formation enthalpy $\Delta_f H°(La_2O_3)$ can be calculated by the cycle shown in Table 3 in which ΔH_3 is the formation enthalpy of water ($3H_2(g) + 1.5O_2(g) = 3H_2O(l)$) taken from the literature. The results for ΔH_1 and ΔH_2 obtained in the two studies mentioned above [34] were in remarkable agreement: ΔH_1 = - 1441.0 ± 2.7 kJ mol^{-1} and ΔH_2 = - 474.0 ± 0.4 kJ mol^{-1}.

Table 3.
Thermodynamic cycle for the formation enthalpy of La_2O_3



Hence $\Delta_f H°(La_2O_3) = \Delta H_1 + \Delta H_3 - \Delta H_2 = -1794 \pm 3$ kJ mol^{-1}. This value agrees well with the combustion value of -1793 ± 1 kJ mol^{-1}, obtained by Huber and Holley [35].

Using the solution enthalpy of $LaCl_3$ in 1.006 m hydrochloric acid, determined by Cordfunke et al. [36] as $\Delta_{sol}H°(LaCl_3) = -126.39 \pm 0.52$ kJ mol^{-1} and the formation enthalpy of HCl in water (1 m), the formation enthalpy of $LaCl_3$ can be calculated using a cycle analogous to that for La_2O_3, to be $\Delta_f H°(LaCl_3) = -1072.22 \pm 1.44$ kJ mol^{-1}. Analogous measurements were conducted by Oppermann et al. [37]. They found the formation enthalpy to be $\Delta_f H°(LaCl_3) = -1081.6 \pm 3.3$ kJ mol^{-1}. The difference between values obtained for LaI_3 is greater, namely 25 kJ. These discrepancies may be related to the fact that Cordfunke worked in 1 m HCl, and Oppermann in 4 m HCl, however, their values for $\Delta_{sol}H°(La_2O_3)$ were nearly the same, -474 and -473 kJ mol^{-1}.

The solution enthalpy of $LaCl_3$,- 137.8 kJ mol^{-1} in pure water, decreases with increasing concentration of HCl. The reason is that mixed complexes $[La(H_2O)_xCl_y]^{(y-3)-}$ are formed. If one wants to deal with pure aqueous complexes, for instance for the assessment of enthalpy increments for hydrated cations and anions, one has to use salts with non-complexing anions, like ClO_4^-. But there is still a further uncertainty concerning the state of aqueous $LnCl_3$ solutions. According to Spedding et al. [38], the coordination number of the Ln^{3+} ions with H_2O in aqueous solutions is 9 for La^{3+} to Nd^{3+} and 8 for Gd^{3+} to Er^{3+}. Between these groups a 'displacement equilibrium' exists for Pm^{3+}, Sm^{3+} and Eu^{3+}. They derived their findings from partial molar volume data, calculated from specific gravity measurements of $LnCl_3$ solutions.

For the determination of formation enthalpies, as shown for $LaCl_3$, it is not necessary to know the structure of the hydrated ions, they must only be the same at given conditions, such as concentration and additional ingredients like HCl. Sometimes this condition is not met, for instance with samples that are strongly reducing or oxidizing agents.

Solutions of V^{3+} are readily oxidized to V^{4+}, so Vasilkova and Perfilova [39] used KOH with H_2O_2 as oxidizing solvents for M_3VCl_6 and $M_3V_2Cl_9$ (M = Na, K, Rb). Together with the solution enthalpies of MCl and VCl_3 in the same medium they obtained the formation enthalpies of the ternary chlorides, from MCl and VCl_3. $FeCl_3$ solutions are often used as an oxidizing medium, for example, for compounds $M_xTiCl_{(2+x)}$ with divalent titanium [40].

Solution enthalpies for numerous ternary chlorides of divalent and tervalent metals have been measured, for example, K_2PrCl_5 [41]. As the cycle in Figure 3 shows, the $\Delta_f H°$ value for the reaction: $2KCl(s) + PrCl_3(s) = K_2PrCl_5(s)$ is given by the equation:

$$\Delta_f H°(K_2PrCl_5) = 2\,\Delta_{sol}H°(KCl) + \Delta_{sol}H°(PrCl_3) - \Delta_{sol}H°(K_2PrCl_5)$$

The result is - 34.0 kJ mol^{-1}. As the second cycle demonstrates, this value is also the difference between the lattice enthalpies of the ternary chloride and the binary parent compound. 34.0 kJ is a very small value compared with the lattice enthalpies of KCl (-702 kJ mol^{-1}) and $PrCl_3$ (- 4340 kJ mol^{-1}).

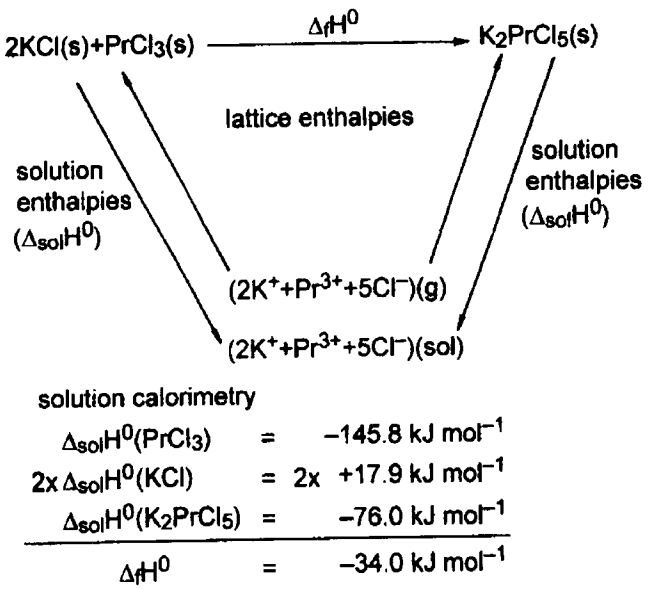


Figure 3. Thermodynamic cycle for the formation of $K_2PrCl_5(s)$.

In general the solution enthalpies of the anhydrous chlorides of di- and trivalent metals and of the ternary chlorides are relatively strongly exothermic, compared with the desired formation enthalpies, that is, the formation values are the differences of two big quantities. To avoid this, Papatheodorou [42] used a LiCl-KCl eutectic at 455 °C as solvent. For instance, the molar solution enthalpy of CsCl is 6.11 kJ mol^{-1}, for $MnCl_2$ it is 11.5 kJ $mol^{-1}$and for $CsMnCl_3$ = - 58.9 kJ mol^{-1}. That gives a value of $\Delta_f H°(CsMnCl_3)$ = - 41.2(8) kJ mol^{-1}. In each experiment, about 6 g eutectic and about 0.3 millimol of sample salt were used.

3.5.3. Reaction calorimetry by reverse dropping

Kleppa [43] has described a twin high-temperature reaction calorimeter, which permits detection of heat effects of 0.04 J. It consists of two nearly identical calorimetric units. In each of these units, a temperature difference between the calorimeter itself and the surrounding heavy aluminium jacket gives rise to an emf in a 96 couple thermopile. The two thermopiles are connected in series, backed against each other. The one unit was used as reaction chamber, the other serving as a 'reference dummy'. If a reaction occurs in the one unit, the released or absorbed heat gives rise to an emf. The resulting emf vs time curve was integrated to obtain the corresponding ΔH of the reaction. Calibration was done either electrically or by 'reverse dropping' of gold from 25 to 450 °C. As a test, the mixing heats of liquid sodium-potassium nitrates at 346 and 448°C were measured.

Papatheodorou and Kleppa [44] used this calorimeter for measuring the decomposition enthalpy of $Cs_3NiCl_5(s) \rightarrow CsNiCl_3(s) + 2CsCl(s)$. Cs_3NiCl_5 is stable only above 417 °C, so they dropped a mixture of ($2CsCl + CsNiCl_3$) from room temperature to 445 °C, obtaining the sum of the heat contents of the three compounds involved and the formation enthalpy of Cs_3NiCl_5 from 2CsCl and $CsNiCl_3$. Then, the heat contents of each of CsCl, $CsNiCl_3$ and metastable Cs_3NiCl_5, yielded by quenching, were determined. As result, a decomposition enthalpy $\Delta_{dec}H°(Cs_3NiCl_5)$ = - 33 kJ mol^{-1} at 445 °C was found.

Cristol et at. [45] determined partial molar excess enthalpies for {(1 - x) ($CdCl_2$ + xKCl)} melts over the whole composition range at 857 K by reverse dropping, and measured the reaction enthalpy for $KCl(s) + CdCl_2(s) = KCdCl_3(s)$ by dropping a) the three constituent compounds and b) an exact 1: 1 mixture (KCl + $CdCl_2$) to KCl/$CdCl_2$ melts.

Kleppa and Guo [46] used a single unit differential microcalorimeter for measuring the reaction enthalpies: $MO(s, 298 K) + WO_3(s, 298 K) = MWO_4(s, 1473 K)$ (M = Mg, Ca, Sr, Ba) by reverse dropping of the constituent compounds and stoichiometric mixtures of ($MO + WO_3$) in the form of pressed pellets. Thus, they found for $MgWO_4$ a molar formation enthalpy of - 1518.3 ± 4.8 kJ mol^{-1} compared with the NBS value of - 1532.6 kJ mol^{-1}.

3.6. Conclusions

Three essential trends in the development of calorimetry can be noticed:

1. Measurements of c_p near T = 0 K by adiabatic calorimetry; e.g., c_p-measurements below 1 K on perovskites, $NdMO_3$, are described by Bartholomé [47].
2. Measurement of enthalpy increments at temperatures > 1300 K by drop-calorimetry; reviewed generally by Navrotsky [48].
3. The improvement of devices in all calorimetric branches by application of modern electronics and computerization; e.g., Blachnik [49] describes an improved isoperibol drop-calorimeter.

Outstanding developments in DSC have been reported by Wunderlich's group. They reconstructed a commercial DSC in such a way that a third crucible with a sapphire sample could be added to the measuring cell containing the reference and the sample crucibles. Thus, all necessary values could be obtained in a single run [50].

Even more important has been the development of temperature modulated differential scanning calorimetry (TMDSC). The domain for its application are polymers and glasses, where equilibrium and non-equilibrium processes need to be considered. The future will show if there is also an improvement for c_p measurements on inorganic solids, such as metal oxides and salts. A considerable improvement is expected in quasi-isothermal measurements where the underlying heating rate is set to zero and the only temperature changes are caused by the modulation.

Using calorimetry, enthalpies, ΔH, heat capacities d ΔH /dT and entropies $\Delta S = \int c_p \, d\ln T$ can be measured. Gibbs energies ΔG can be obtained by the Second Law ($\Delta G = \Delta H - T\,\Delta S$). Direct measurements of ΔG can be obtained by pressure measurements and emf measurements.

An example of the pressure measurement method is the determination of $\Delta_r G^\circ$ for the reaction: $CsCl(s) + CaCl_2(s) = CsCaCl_3(s)$ [51]. The pressure of CsCl is much greater than that of $CaCl_2$ and $CsCaCl_3$ and was measured in a Knudsen cell from 600 to 900 °C, where the system is in the solid state. $\Delta G^\circ = - RT \ln a(CsCl)$ with $a(CsCl) = p(CsCl)/p^\circ(CsCl)$, where $p^\circ(CsCl)$ is the equilibrium pressure for the reaction: $CsCl(s) = CsCl(g)$. Because the dependence of ln a on $1/T$ proved to be linear, regression gave ΔH and ΔS directly. The range of error for the derived values is, however, ten times greater than that of calorimetric measurements.

An example of the use of solid electrolyte galvanic cells is the measurement by Karkhanavala et al. [52] of values of ΔG for the metal difluorides, NiF_2, FeF_2 and CoF_2. Cells of the type Pt/Fe, $FeF_2/CaF_2/NiF_2$, Ni/Pt, where single crystals of CaF_2 acted as a F^- - conducting solid electrolyte were used in Ar-atmosphere

in the temperature range 850-1050 K. ΔG° values for the reaction: $Fe + NiF_2 \rightarrow Ni + FeF_2$ were obtained from the measured emf values, which were linearly dependent on T. Combination of these results with $\Delta_f G^{\circ}(NiF_2)$ from the literature enabled the Gibbs energies of formation for the other fluorides to be calculated.

Other methods for obtaining thermodynamic functions for chemical reactions, such as thermometric and enthalpimetric titrations, are beyond the scope of this chapter.

4. PHASE DIAGRAMS

4.1. Introduction

Phase diagrams of binary systems at constant pressure are representations of one- and two-phase regions with their phase boundaries being functions of the temperature and concentration. Assuming chemical equilibrium, the phase regions are zones of minimum Gibbs energy and the coexistence of phases is governed by the Gibbs phase rule. To generate a phase diagram means to detect all phase boundaries. In general, this is not done by measuring the dependence of ΔG on T (or c), but by measuring heating and cooling curves by DTA. Thus, the enthalpy of phase reactions is utilized, which is related to the Gibbs energy, ΔG, by the heat capacity.

Unfortunately, the enthalpy, ΔH, tells us nothing about the kind of reaction by which it is generated. Therefore, it is usual to support DTA by additional methods. The most effective one is X-ray crystallography. Generally, one compares the powder patterns of quenched or normally cooled samples with those of pure compounds. New, additional reflections indicate new compounds. A better procedure, however, is to try to solve the structure of the new compound by indexing each reflection. This is not possible in all cases. A further development is the application of high-temperature X-ray techniques. Other methods occasionally applied are high temperature microscopy, the measurement of electrical properties or of the micro-hardness, and metallographic methods in the case of alloys.

The phase diagram of a single compound is one-dimensional – a temperature scale on which solid-solid phase transitions and the melting temperature are singular points. However, if a compound AB is not stable at each temperature, a binary system is generated. If the compound is unstable at high temperature, decomposition: $AB_n \rightarrow A + nB$, takes phase in a heating mode; if it is unstable at low temperatures, a formation reaction: $A + nB \rightarrow AB_n$ occurs. At one dimension higher, a change from a binary system into a ternary system may occur.

The problems of determining phase diagrams are illustrated using systems of alkali metal chlorides/ lanthanide(III)-chlorides which were investigated by the group of the author. They all are systems where equilibration is achieved in homogenous melts. In a second section, systems are treated, in which compounds with very high melting points exist, so that equilibration must be achieved by annealing. Finally, some remarks are given for ternary systems.

4.2. Binary systems with accessible liquid phases

4.2.1. Solid-liquid transitions

In Figure 4, all solid-liquid transitions in a binary system, except those of mixed crystal formation, are displayed, together with the correlated ΔT traces.

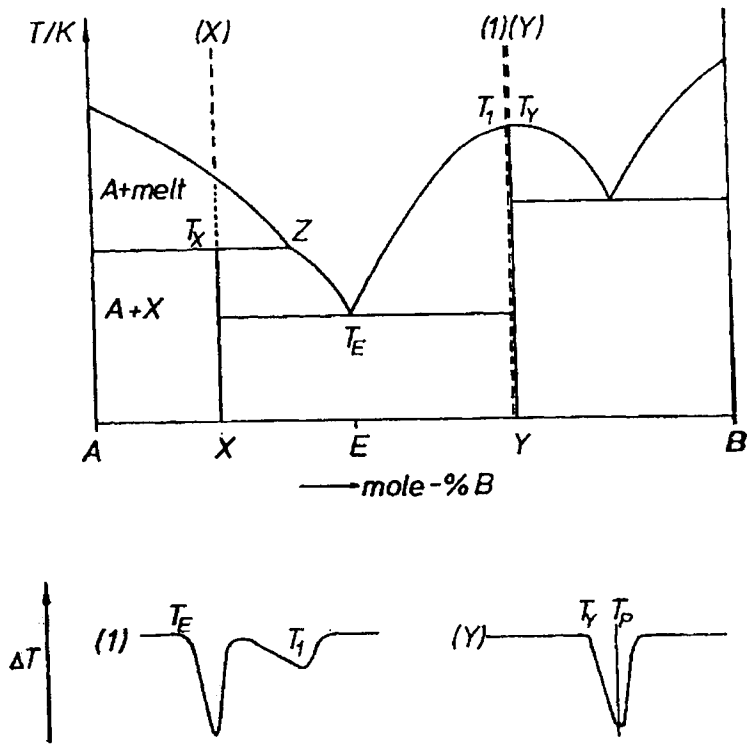


Figure 4. Solid-liquid transitions in a binary system, except those of mixed crystal formation, together with the correlated ΔT traces.

To avoid undercooling, the values for the liquidus curves (Table 4) are generally taken from heating experiments and T_l is the 'peak temperature' of the melting process. However, for the compound, the correct melting temperature, T_y, is taken from the 'extrapolated onset'. Thus, one is abruptly changing the kind of evaluation and the result is a sinusodial curve. In other words, the liquid temperatures near a congruently melting compound are too high! One can avoid this error by taking the onset-temperatures from cooling curves, using a sufficiently large sample to prevent errors by undercooling.

Table 4.
Liquidus temperatures from heating curves near the composition KSr_2Br_5 [54].

mol% $SrBr_2$	60.0	63.2	66.6	70.2	73.2
			(584°C) (T_P)		
		582°C			
	580°C			581°C	
					580°C
			(576°C) (T_Y)		
			KSr_2Br_5		

T_P = fusion temperature from peak maximum; T_Y = onset temperature.

Another source of errors can arise in the case of incongruently-melting compounds: during the freezing of the melt, X, sedimentation of the solid formed can occur. The rest of the melt becomes richer in B and the 'wrong' eutectic will be found at T_E. One can avoid this mistake, which leads to a wrong composition of the compound, by quenching the melt, with subsequent short annealing below T_X.

4.2.2. Solid-solid transitions

In the pseudo-binary systems, $RbCl/LaCl_3$ [54] and $CsCl/NdCl_3$ [55] (Figure 5), all features of the hypothetical system discussed are shown. Additionally, one finds all types of solid reactions: transitions between crystallographic modifications (CsCl, $RbLa_2Cl_7$, Cs_3NdCl_6), formation of high-temperature compounds (Rb_3LaCl_6, $RbLa_2Cl_7$) and decomposition of a compound by heating (Cs_2NdCl_5).

From a structural point of view, solid-state reactions can be classified as reconstructive or non-reconstructive (displacive, order-disorder-transitions). In the second category, the topology of the ions in a lattice is maintained: the ions are only a little shifted from their original sites. The activation energy is expected to be rather small. The same holds for the hysteresis between heating

and cooling curves. Reconstructive means that the topology is drastically changed: the ions have to migrate to different sites and the activation energy is anticipated to be high.

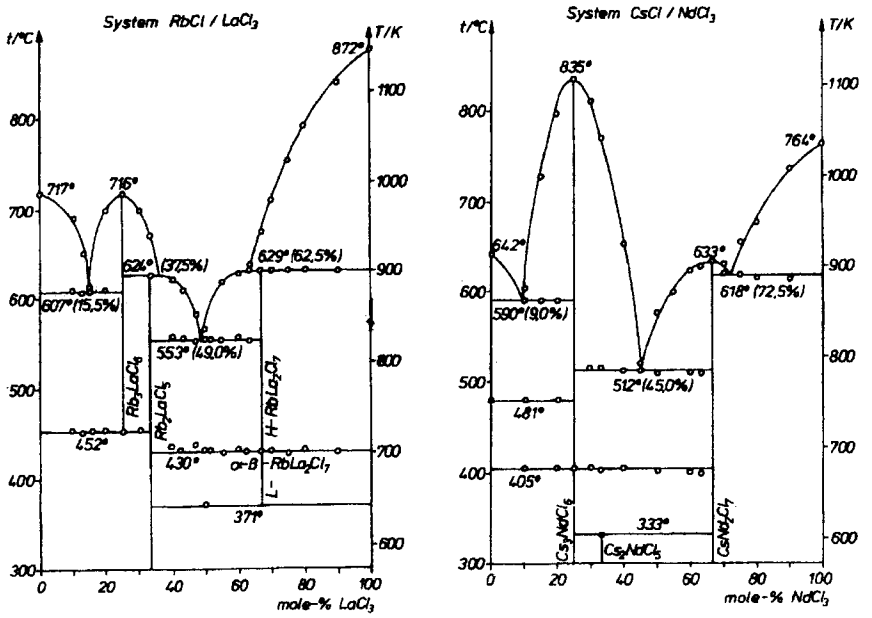


Figure 5. The pseudo-binary systems: $RbCl/LaCl_3$ [55a]and $CsCl/NdCl_3$ [55b].

Solid-state reactions, such as the formation or decomposition of compounds in the solid state, can be considered as a special kind of reconstructive transition. An example is the compound Rb_3LaCl_6, which is stable at temperatures higher than 444 °C. As Figure 6 indicates, the reaction temperature taken from heating curves is too high, and too low from cooling curves. Hysteresis still exists when results are extrapolated to zero heating rate.

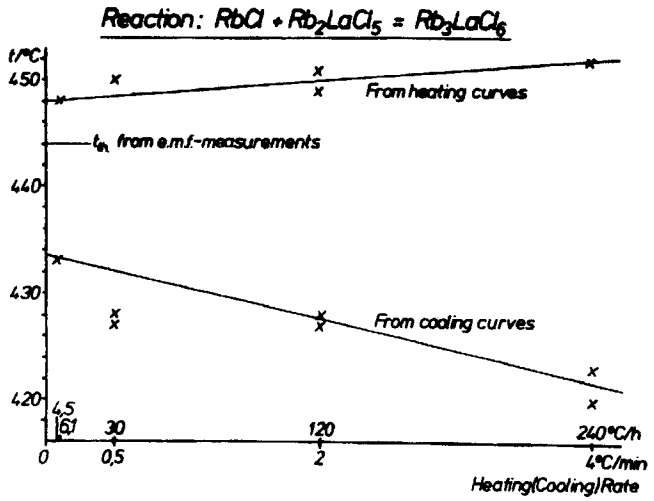


Figure 6. Hysteresis for the formation/decomposition temperature of Rb_3LaCl_6 [55c].

DTA (and DSC) signals are influenced by the finite transfer of heat. The magnitude of the error, produced by this, depends on the heating rate, on apparatus details and the mass, geometry and thermal conductivity of the sample and can be corrected for by theoretical calculations (see textbooks of thermal analysis). Taking into account these corrections, one should expect that the temperatures taken from heating and from cooling experiments would be the same. The hysteresis, $\Delta T = T_{heat} - T_{cool}$, should be zero. This is observed in many cases, but there are reactions with considerable hysteresis. Large hysteresis effects originate in kinetic hindrance and it is often possible to obtain the high-temperature phase in a metastable state at ambient temperature by quenching. Heating such metastable systems results in exothermic effects at temperatures sufficiently high to generate enough activation energy for the system to convert to 'thermodynamic legality'. This takes place for metastable Rb_3LaCl_6 at about 260 °C and the compound decomposes to ($RbCl + Rb_2LaCl_5$). At lower temperatures, kinetic hindrance can become so strong that the reaction does not occur at all on the time-scale of a DTA measurement. One can often ensure this by annealing for days, weeks, or sometimes months. Using a heating curve, the reaction temperature can be measured only once. A repeat measurement is only possible after a second annealing procedure. For example, in the system $CsCl/NdCl_3$ the compound Cs_2NdCl_5 is stable at temperatures below about 300 °C and was not formed even after annealing a quenched melt of the correct composition at 250 °C for two months. After a catalytic amount of water had been added, the reaction took place during two days. DTA heating

measurements and X-ray diffraction patterns showed that the decomposition occurred at 333°C.

The worst situation is when annealing does not help at all. For example, $KMnCl_3$ crystallizes at high temperature with the cubic perovskite structure. At 386 and 300 °C displacive phase transitions occur and, at room temperature, the $GdFeO_3$-type structure is found with slightly deformed octahedra. Horowitz et al. [56] reported that the stable room-temperature modification crystallizes with the NH_4CdCl_3-structure. A quotation from their paper states that "X-ray examination of these materials after storage in evacuated and sealed glass ampoules for 3-4 years revealed partial transformation of these materials to the new phase." (A much better way to prepare the room temperature phase is the dehydration of the hydrate, $KMnCl_3.2H_2O$, at 90 °C). This phase reveals a thermal effect in a heating curve at 267 °C, with a transition enthalpy of 4.60 kJ mol^{-1} measured by DSC.

4.3. Galvanic cells for solid electrolytes

All difficulties with retardations are generated by the obvious fact that a reaction must occur, if the reaction enthalpy is to be measured. Methods that do not require the adjusting of equilibrium would not be disturbed by any kinetic hindrance. This condition is realized in galvanic cells: the system is far from equilibrium and the measured emf, E, is related by the equation $\Delta G = - n F E$ (n = transported charge, F = Faraday constant) to the chemical power ΔG, the Gibbs energy of reaction, which would be released if the reaction did occur (measurement in the currentless state). There are two further advantages with such measurements: 1) ΔG is the real thermodynamic function determining the stability of a compound, not the enthalpy ΔH, and 2) the emf is an intensive quantity, independent of the sample mass. Galvanic cells for solid state reactions of the type: $nACl + MCl_x = A_nMCl_{(n+x)}$ have been developed [57]. They consist of chlorine electrodes and alkali-metal ion conducting diaphragms of sintered glass. The set-up of a cell for the reaction: $RbCl + Rb_2LaCl_5 = Rb_3LaCl_6$ (Figure 7a) is:

$$(C + Cl_2)/RbCl(s)/Rb^+\text{- conducting diaphragm}/Rb_2LaCl_5(+ Rb_3LaCl_6)/(C + Cl_2)$$

The anode and cathode are graphite discs in a chlorine atmosphere, the electrolytes are pressed pellets of RbCl and Rb_2LaCl_5 (mixed with some Rb_3LaCl_6 to give a reversible cell). The temperature dependence of the emf is measured stepwise in several temperature cycles. It proved to be linear down to about 300 °C, so the collected emf vs T-values could be subjected to linear regression analysis, yielding an equation, which after multiplication with ($- n F$) is identical with the Gibbs-Helmholtz equation: $\Delta G = \Delta H - T \Delta S$.

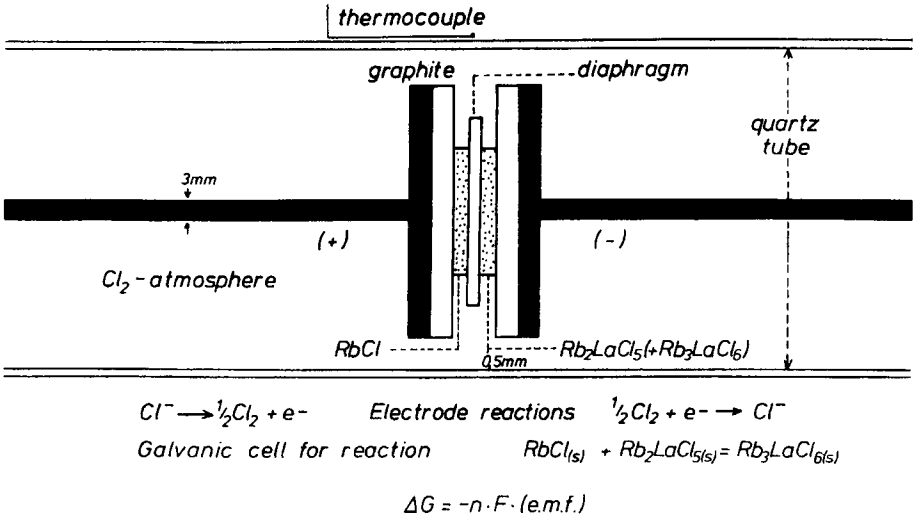


Figure 7a. Galvanic cell for the reaction: $RbCl + Rb_2LaCl_5 = Rb_3LaCl_6$ [55a].

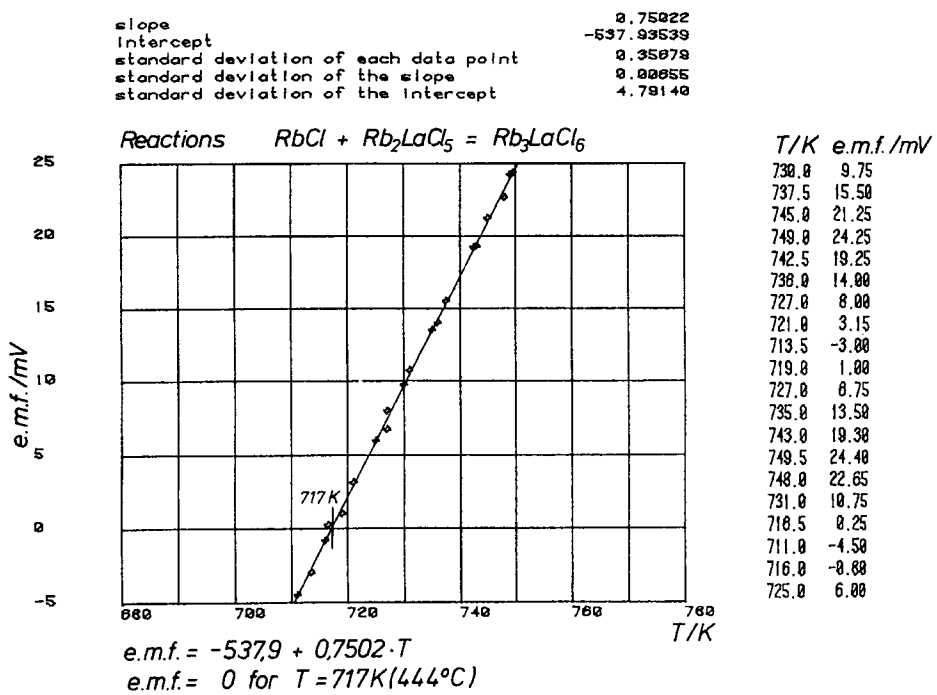


Figure 7b. Emf vs T curve for Rb_3LaCl_6 [55a].

The condition for a phase transition: A → B is $\Delta G_A = \Delta G_B$. This condition is found from the intersection of the emf vs T lines. Generally, a compound is stable relative to the two adjacent compounds in the phase diagram if the Gibbs energies for the synthesis reactions from these compounds, $\Delta_{syn}G^o$, is negative. At the temperature of formation (or decomposition) $\Delta_{syn}G^o$ must be zero. As Figure 7b demonstrates, Rb_3LaCl_6 will not decompose immediately when cooled to temperatures < 444 °C, but will remain metastable as indicated by a negative emf, what corresponds to a positive ΔG. Thus, metastable states can also be detected by such emf measurements.

The following programme for elucidating phase diagrams is suggested:

(i) Use differential thermal analysis (DTA) to determine the phase diagrams of the pseudo-binary systems AX/MX_n → ternary compounds, together with their composition.

(ii) Use X-ray diffraction to determine the crystal structures of the compounds.

(iii) Use solution calorimetry to determine the enthalpies of formation of the binary compounds ($\Delta_f H^o$) and the enthalpies of the synthesis reactions ($\Delta_{syn}H^o$) from the compounds adjacent in the phase diagram.

(iv) Use measurements of emf as f(T) to determine Gibbs energies ($\Delta_r G^o$)and entropies ($\Delta_r S^o$) of reactions.

As an illustration, investigations on the system $RbCl/LaCl_3$ [55a] are discussed in more detail. To avoid separation effects in the case of the incongruently-melting compounds Rb_2LaCl_5 and $RbLa_2Cl_7$, quenched melts over the composition range 25 to 33.3 and 66.6 to 100 mol % $LaCl_3$ had to be annealed at about 600 °C. This procedure prevented the appearance of 'wrong' eutectic effects at 553 °C and misleading X-ray patterns of the two compounds. Annealing was also necessary at about 440 °C for Rb_3LaCl_6 and at about 350 °C for $RbLa_2Cl_7$ to prove that these compounds are not stable at this (and ambient) temperature. After quenching, X-ray patterns for these compounds in a metastable state were obtained. The X -ray patterns of all the compounds could be indexed according to the known structure families and the unit cell parameters obtained. Solution enthalpies could be measured only for Rb_2LaCl_5 and (quenched) $RbLa_2Cl_7$. Samples of quenched Rb_3LaCl_6 contained some RbCl and Rb_2LaCl_5 from initial decomposition. Emf measurements were performed for all the compounds in the temperature range 350 to 400 °C, and for the compound poorest in $LaCl_3$ up to 450 °C. $\Delta_r G^o = \Delta_r H^o - T\,\Delta_r S^o$ relationships were obtained for the formation from RbCl and the occasionally $LaCl_3$-richer compounds in the system. By manipulating these results, the Gibbs-Helmholtz relations for $\Delta_f G^o$ were obtained and hence the $\Delta_{syn}G^o$ relations. For Rb_3LaCl_6, $\Delta_r G^o = \Delta_{syn}G^o$ (reaction $RbCl + Rb_2LaCl_5 = Rb_3LaCl_6$). The result is $\Delta_{syn}G^o$ /kJ mol^{-1} = 50.4 - 0.0703 T/K. The formation temperature 717 K (444 °C) is

obtained by setting $\Delta_{syn}G^{o} = 0$. The strongly endothermic reaction (+ 50.4 kJ mol^{-1}) indicates a decrease of lattice enthalpy by the synthesis-reaction from RbCl and Rb_2LaCl_5. It is compensated at 717 K by a sufficiently large gain in entropy ($\Delta_{syn}S^{o} = 70.3$ J K^{-1} mol^{-1}).

If mixed crystals are formed or solid solutions exist, the measurements become more difficult, because between the liquidus and solidus curves, reactions between the solid excretion and rest of the melt must take place continuously. Complete formation of mixed crystals results in diagrams similar to those well known from the evaporation curves for liquid mixtures like liquid air. If the solutions are not ideal, maxima or minima exist. Such systems are very common for alloys. For inorganic compounds, an example is the system KCl/RbCl where the ionic radii $r(K^{+})$ and $r(Rb^{+})$ are not very different. The unit cell parameter of the cubic cell varies linearly with composition (Vegard's line). In a similar way, Al_2O_3 and Cr_2O_3 are miscible above about 950 °C, but have a broad miscibility gap at lower temperatures.

4.4. Three-component systems

Triangular diagrams ABC are used to represent the composition; on the three sides the constituent binary systems AB, AC and BC are localized. If no ternary compounds are formed, only ternary eutectics and peritectics can exist. With ternary compounds, $A_aB_bC_c$, the situation becomes more difficult. An example is the system CsCl-NaCl-$LaCl_3$ with the ternary compound $Cs_2NaLaCl_6$ [58]. The-first step was the subdivision of the complete triangle into smaller 'compatibility triangles' with the help of X-ray photos of quenched and, if necessary, annealed samples, lying on the sides of the smaller triangles. Thus, one can find out the phase composition of such points. DTA measurements were then performed on samples taken along reasonably selected cuts. Assume that in a system ABC one binary compound BC exists. The connection, A-BC, is pseudo-binary and any composition on this line can be represented completely by positive quantities of A and BC alone. The whole system is then subdivided into two systems AB (BC) and A (BC) C.

4.5. Computation of phase diagrams

For the calculation of equilibrium lines, one has to consider that these are lines separating phases of minimal Gibbs energy. Using reasonable approximations, one can perform such calculations using experimentally determined enthalpies of fusion and mixing. Numerous applications of this procedure for simple binary systems have been described (see [59] and the journal CALPHAD/Computer Coupling of Phase Diagrams and Thermochemistry, Elsevier).

4.6. Systems with high-melting compounds

If the melting points of the constituent compounds are too high for the instrumental parameters, or if the compounds decompose before melting, the equilibration of the samples for DTA and the other mentioned techniques must be achieved by annealing. The typical procedure is to mix the weighed compounds and to grind them thoroughly in an agate mortar or in a ball mill. The material is then compressed into pellets and exposed to an appropriate heating programme. The annealed pellets are ground again and reheated up to the completion of the reaction. X-ray diffraction patterns are recorded each time, to enable the progress of the reaction to be followed. If desired, the material can be quenched after the last annealing. This procedure is often called a 'ceramic synthesis'. The reaction temperatures of the solid-solid reactions can be determined from DTA heating curves or by using high-temperature XRD. Dynamic methods give a somewhat higher initiation temperature than static (isothermal) methods because of the temperature gradients in the specimen. An example is given by Pillai and Ravindran [60] for the formation of $PbTiO_3$ from PbO and TiO_2. The exothermic reaction was observed in the temperature range 848-1020 K at a heating rate of 10 K min^{-1}. At 5 K min^{-1}, a smaller DTA peak was found from 833-983 K. In subsequent cooling curves, the ferroelectric transition temperature of $PbTiO_3$ was found at 783 K. The similar reaction of PbO and MoO_3 must be performed in closed containers because MoO_3 is strongly volatile at about 700 °C. By use of PbO_2 instead of PbO, it was possible to prepare $PbMoO_4$ and Pb_2MoO_5 at 405 and 430 °C, respectively, instead of 650 and 760 °C. This decrease depends on the intermediate formation of Pb_3O_4 at 370 °C. Eissa et al. [61] have found this by constructing the phase diagram for the ternary system PbO_2-Pb-MO_3, from dissociation curves of selected compositions by thermogravimetry.

The next step for the preparation of ternary compounds is the utilisation of 'precursors'. As an example, if it is possible to prepare the double carbonate, $M_1M_2(CO_3)_2.xH_2O$ from aqueous solution, these compounds can be thermally decomposed to the double oxide, $M_1M_2O_2$. Again the reaction parameters can be found by DTA. The further treatment of the now homogenous samples depends on the purpose in view of the investigators. By heating in a DTA/DSC device, existing solid-solid or solid-liquid reactions can be detected. By measuring samples of different compositions, the phase diagram of the system up to the attainable temperature can be constructed. The compounds formed can be identified from their X-ray patterns. An example is the construction of the phase diagram of the binary system Sc_2O_3/ScF_3 in the temperature region 1400-1822 K (Figure 8 [62]).

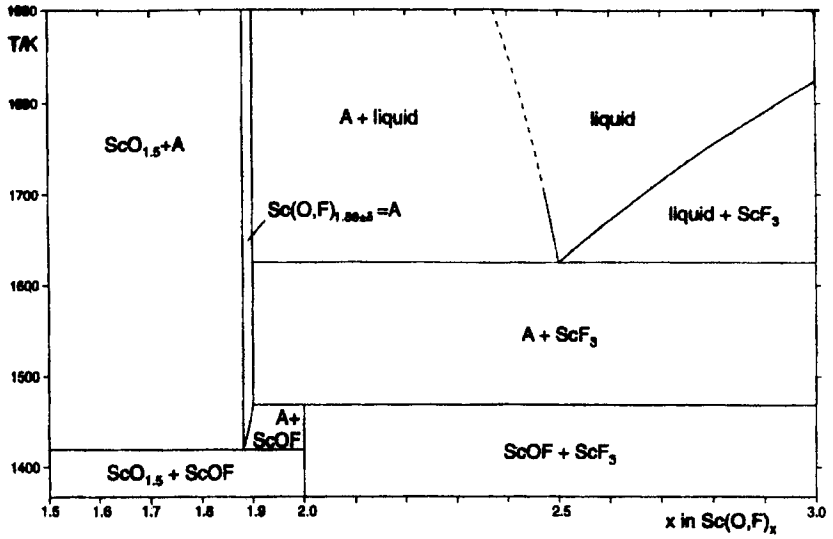


Figure 8. Tentative phase diagram of the binary system Sc_2O_3/ScF_3 in the temperature range 1400-1822 K [62].

Carefully homogenized Sc_2O_3-ScF_3 mixtures, weighing approx. 100 mg were enclosed in sealed Pt-capsules. For equilibrium purposes, each enclosed mixture was annealed at 1800 K for 3 h and then run through heating/cooling cycles at 8 K min^{-1}. The well-known compounds Sc_2O_3, ScOF and ScF_3 were identified by their X-ray patterns. A slightly non-stoichiometric high-temperature phase, $ScO_{1.12}F_{0.76}$ was formed at 1419 ± 3 K. ScOF decomposes at 1460 ± 3 K to this non-quenchable phase and ScF_3. The eutectic with ScF_3 lies at 1627 ± 3 K. Pure ScF_3 melts at 1822 ± 3 K and does not have any solid phase transition. Researchers with preponderantly structural interests usually measure only compositions for which they expect the existence of compounds.

As already mentioned, equilibrium systems are those with areas of minimal Gibbs energy, ΔG. This Gibbs energy of formation can be measured with galvanic cells for solid electrolytes. Weppner [63] used such a cell for emf measurements at constant temperature, but also changed the composition of the sample by transporting appropriate ions from a source electrode through an ion-conducting diaphragm into the sample (coulometric titration) . They employed this technique for investigating the region Cu-CuO-GeO_2 in the ternary system Cu/Ge/O.

Measurement of the equilibrium pressure about the reaction system can also be used, provided that the pressure is high enough for the gauge used. Good results

are obtained when the total pressure is predominantly caused by only one of the components (p_c). Then the relation: $\Delta_r G^o = - RT \ln (p_c / p_o)$ is valid. Oppermann et al. [64] measured total pressures with a 'membrane zero-manometer' in the partial system Bi_2O_3-Bi_2O_2Se-Bi_2Se_3-Se in the ternary system Bi/Se/O. The measured 'barograms', p/T, were used to construct the phase diagrams. The measurements revealed that the barogram of the ternary region $Bi_2Se_3/Bi_2O_2Se/Se$ can be attributed to the binary system Bi_2Se_3/Se, where the total pressure is predominantly that of Se.

5. THERMOGRAVIMETRY

5.1. Introduction

Thermogravimetry (TG) measures the loss or gain in mass of a sample as a function of temperature, time and also of the atmosphere (see Chapter 4 of Volume 1 of this Handbook). Information is obtainable about the thermal stability of materials in vacuum or in an inert atmosphere, as well as about reactions with the applied atmosphere such as air, hydrogen and, with special equipment, other reactive gases. Numerous measurements have been performed on the thermal degradation of polymers and other organic materials (see Volume 3 of this Handbook) and of samples of industrial interest (see other chapters of this Volume). TG results may be used for kinetic analyses of specified reaction steps (see Chapter 3 of Volume 1 of this Handbook).

Examples of applications of TG in inorganic chemistry include: calcination, purity determinations, sorption and desorption, gravimetric analysis, thermal stability, surface areas, desolvation, catalytic activity, oxidative and reductive stability, dehydration/hygroscopicity, sublimation and vaporisation, and solid-state reactions.

In the next section, decomposition reactions of simple inorganic substances and complex compounds are discussed. Hydrates are excluded because they are treated in another chapter of this Volume. Some solid-solid reactions and the uses of precursors are also covered.

5.2. Decomposition reactions

5.2.1. Experimental methods

For a decomposition reaction: $A(s) \rightleftarrows B(s) + C(g)$, the equilibrium pressure of the gaseous component, the saturation pressure, $p_s(c)$, is directly determined by the reaction temperature. Like all equilibrium quantities, its adjustment depends on the kinetics of the reaction.

In thermogravimetric experiments the conditions are usually far from equilibrium. The normal procedure is to heat a sample of about 10 mg in a gas

stream of 5 - 10 L h^{-1} with a heating rate of 2 - 10 K min^{-1}. A typical TG curve and its corresponding DTG curve are shown in Figure 9.

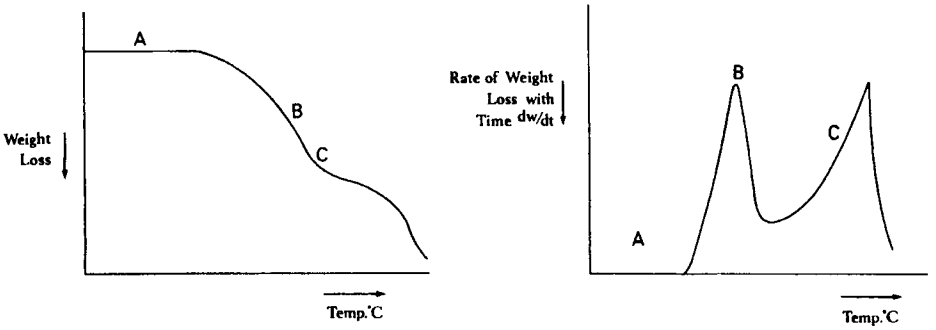


Figure 9. (a) A typical TG curve and (b) the corresponding DTG curve.

All modern TG instruments provide the rate of mass change, d*m*/d*t*, by numerical differentiation to give a DTG curve such as Figure 9 (b).(region A = plateau, dm/dt = 0; B = maximum rate of mass loss gives the 'peak temperature' in the DTG curve; C = the inflection point corresponding to a minimum in (-dm/dt) indicates an intermediate. This region may become a plateau at very low heating rates.

TG may be combined with DTA so that three curves are recorded simultaneously (see Figure 11). In general, the mass axis (ordinate) is much better defined than the temperature abcissa.

In a TG curve of a single-stage non-isothermal reaction, there are two characteristic temperatures; the initial temperature, T_i, and the 'peak temperature', T_p. T_i is defined as the lowest temperature at which the cumulative mass change reaches a magnitude that a particular thermobalance can detect. However, although a particular temperature may be the lowest temperature at which the start of a mass change can be observed with a certain apparatus under a given set of experimental conditions, it is by no means the absolute decomposition temperature, below which the reaction rate suddenly becomes zero. The 'peak temperature' is the temperature of the maximum reaction rate and is used by many authors as the decomposition temperature. It is, however, also determined by the given experimental conditions, such as the heating rate, the geometry of sample holder and furnace, the crucible size and shape, as well as by the amount, volume, particle size, packing density and thermal conductivity of the sample. The detailed experimental conditions are difficult to define and to reproduce. Especially at fast heating rates and with large sample masses, the characteristic temperatures shift to higher values.

The atmosphere around the sample has a strong influence on the reaction. Obviously heating in air may produce other reactions than occur on heating in an inert gas or vacuum, so it is of extreme importance that the applied inert gas must not contain small amounts of oxygen. Failure to take such precautions can lead to serious errors in the interpretation of the experimental results. Normally in TG the generated gaseous decomposition product is transported away by the applied gas-stream. Thus, the sample represents an open system, and the mass flow across the boundaries is continuously monitored by the balance. The TG curve is increasingly shifted to lower temperatures as the gas flow is increased, with a temperature minimum for vacuum conditions.

TG measurements are of great value for preparative inorganic chemistry. If, for the desired product, a long temperature plateau exists, it is no problem to apply a decomposition temperature at which the reaction will reach completion, i.e. all of the starting product is decomposed, but the further decomposition step, if it exists, has not yet begun. The situation is a very different if only an inflection exists between two decomposition steps. For this case, no distinct preparative temperature can be given and one has to take into account that this inflection temperature also depends on the experimental conditions, for instance preparation of the desired product in static air, in streaming gas or in vacuum.

A useful method for preparing intermediates was applied by Liptay [65] in his investigations on the stability of amine complexes of transition metal halides. In this 'freezing in' method, the desired intermediate could be easily separated with the aid of the DTG curve. At the temperature corresponding to its minimum the furnace temperature is quickly decreased. More accurately the temperature can be taken from the TG curve when the pre-calculated loss of mass is achieved.

To obtain several grams of the desired product, a 'preparative thermobalance' is required. For example, a thermogravimetric device for preparing about 100 g of sample has been developed [66]. This 'Macro STA 419' was constructed for simultaneous TG/DTA investigations with direct coupling for EGA (by MS/GC-MS).

The ideal way to get a uniform intermediate would be to work under equilibrium conditions, that is isothermal and reversible conditions, either by heating the system to the correct temperature in an atmosphere with the correct partial pressure of the evolved gas, or by working in a closed system. Progress towards equilibrium conditions was achieved with the derivatograph, as described in the monograph: F. Paulik "Special Trends in Thermal Analysis", Wiley, New York, 1995, using 'labyrinth crucibles'. These consist of six tightly-fitting lower and upper parts. The sample is placed in the innermost crucible and, when the parts are put together, a long and narrow channel system is established between the walls. The inert gas atmosphere is expelled by the liberated gaseous products so that the decomposition takes place in a 'self-

generated' atmosphere under quasi-isobaric conditions. Another step towards achieving quasi-equilibrium conditions is the establishment of quasi-isothermal conditions by automatically stopping the heating process when decomposition begins, that is, when the rate of mass loss, dm/dt, reaches a chosen value higher than zero. The heating programme is continued if the decomposition is complete, that is d*m*/d*t* becomes zero again. This procedure is called 'Q-TG' Figure 10 demonstrates the use of this method for the evaporation of water in different crucibles.

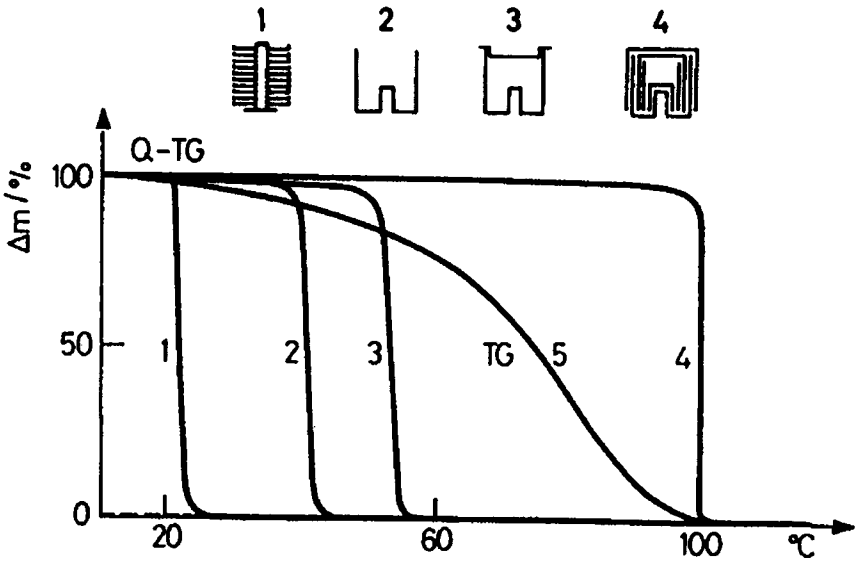


Figure 10. TG and Q-TG curves for the evaporation of H_2O in different sample crucibles (F. Paulik, Special Trends in Thermal Analysis, Wiley, New York, 1995.)

The most sophisticated development in solving the problem of resolving overlapping decomposition curves is the technique of 'controlled rate thermal analysis' (CRTA) introduced by Rouquerol (see Chapter 4 of Volume 1 of this Handbook). The sample is heated in such a way as to control, at any time, the flow of self -generated gas. Thus, the decomposition rate, -dm/dt, is held constant. In this technique, the gradients in the sample which originate from the rate of reaction, temperature, and partial pressure of evolved gases, are also controlled. This leads to an improved sensitivity and resolution. The technique was first described for mixtures of $CoSO_4.H_2O$ /$Ca(OH)_2$ or $Al(OH)_3$ / $Mg(OH)_2$ [67]. CRTA is also a powerful method for determination of the kinetics of

thermal decomposition [68]. A comparison of CRTA with similar methods, such as the Paulik-Paulik-Q-TG, 'rate controlled sintering' [69], and Sorensen's 'stepwise isothermal analysis' [70], is given by Rouquerol [71].

From a TG curve, the mass-loss stages can be used to determine the reaction stoichiometry. For instance, for the decomposition of dolomite: $CaMg(CO_3)_2(s) \rightarrow (CaCO_3 + MgO)(s) + CO_2(g) \rightarrow CaO(s) + MgO(s) + CO_2(g)$, one can calculate the mass losses caused by the evolution of CO_2, for each stage and compare the calculated with the experimental mass losses. Similarly, for the stepwise dehydration of a hydrate, $MX_n.mH_2O$, one can determine the value of m, provided that only H_2O is evolved, and that hydrolysis such as: $MCl_3.H_2O = MOCl + 2HCl$ does not occur. An automated system for thermogas-titrimetry has been described for the hydrolytic decomposition of $AlCl_3.6H_2O$ to the final products: Al_2O_3, H_2O and HCl by Petzold and Naumann [72]. This is a simple example of an extension to TG for 'evolved gas analysis' (EGA). More powerful techniques are gas chromatography (GC), mass spectroscopy (MS) and Fourier transform infrared spectroscopy (FTIR) (see Chapter 12 of Volume 1 of this Handbook). EGA is essential for complicated decompositions, including the reactions of the solid residue with the gas atmosphere, for instance with oxygen when using air, or secondary reactions with the initially evolved gases. Complete characterization of the reaction requires identification of the solid residue by XRD and/or IR-spectroscopy as well as microscopic examinations.

5.2.2. Selected examples of decompositions of simple inorganic compounds

Probably the most frequently analysed simple inorganic compounds are $CaCO_3$, $CaC_2O_4.2H_2O$ and $CuSO_4.5H_2O$, both qualitatively and semi-quantitatively and for kinetic evaluation. Other decompositions that have been intensively studied, include those of nitrates, hydroxides, formates, hydrides, sulfides and sulfates. Coordination compounds with volatile ligands have also been extensively studied. Results for 275 substances were collected by Liptay in the 'Atlas ofThermoanalytical Curves, Vol. 1-5, Akad. Kiado, Budapest, 1975. An example of such a curve, for $[Ni(NH_3)_6]Br_2$, is given in Figure 11. Another, very extensive collection of TG curves is found in the already mentioned monograph by Paulik (1995).

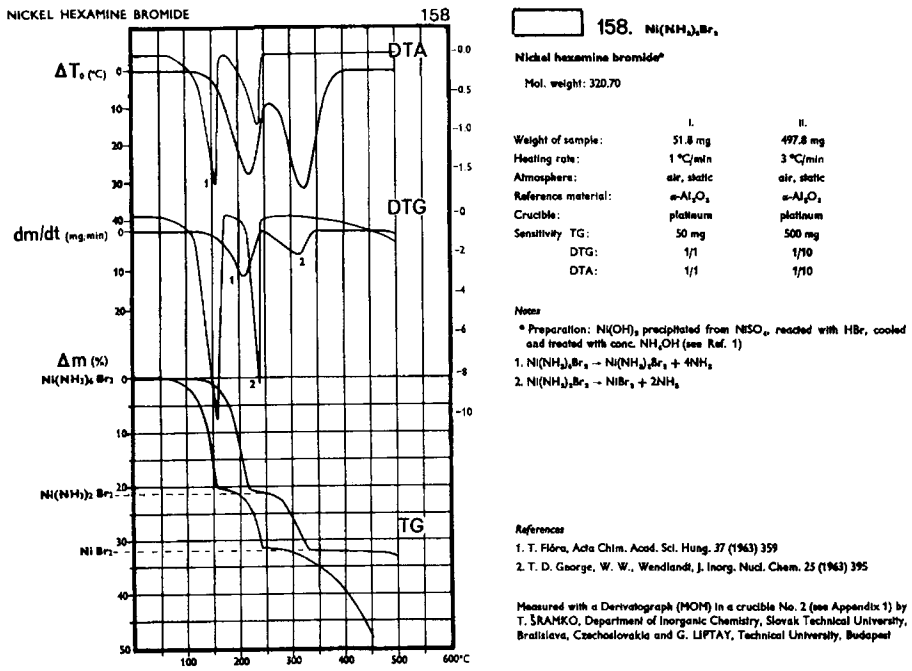


Figure 11. TG/DTG/DTA curves for $Ni(NH_3)_6Br_2$.

An example of a modern multi-method investigation of the decomposition of $CaC_2O_4.H_2O$, using TG, EGA(MS), DSC, modulated DSC, dilatometry and HT -XRD (isothermal with steps of 10°C), is that of Gallagher and Kociba [73]. They could confirm the known three-step decomposition, depicted in Figure 12. However, the focus of the work was on the order-disorder phase transition of $CaC_2O_4.H_2O$ from space group $P2_1/n$ to I2/m. This non-first-order transition begins at about 70 °C with a peak-maximum at 83 °C, found by MTDSC, while in conventional DSC, temperatures between 65 and 80 °C were found, depending on the heating rate. The onset of the dehydration is shifted from 100 °C to > 150 °C on going from open pans in dry N_2 to a covered pan in N_2 saturated with H_2O. The decomposition of Ca-oxalate is an example of the application of TG in analytical chemistry: $CaC_2O_4.H_2O$ is the best form for precipitation of calcium in gravimetry. The TG results show the temperatures to which the precipitate must be heated for weighing it as CaC_2O_4 or $CaCO_3$.

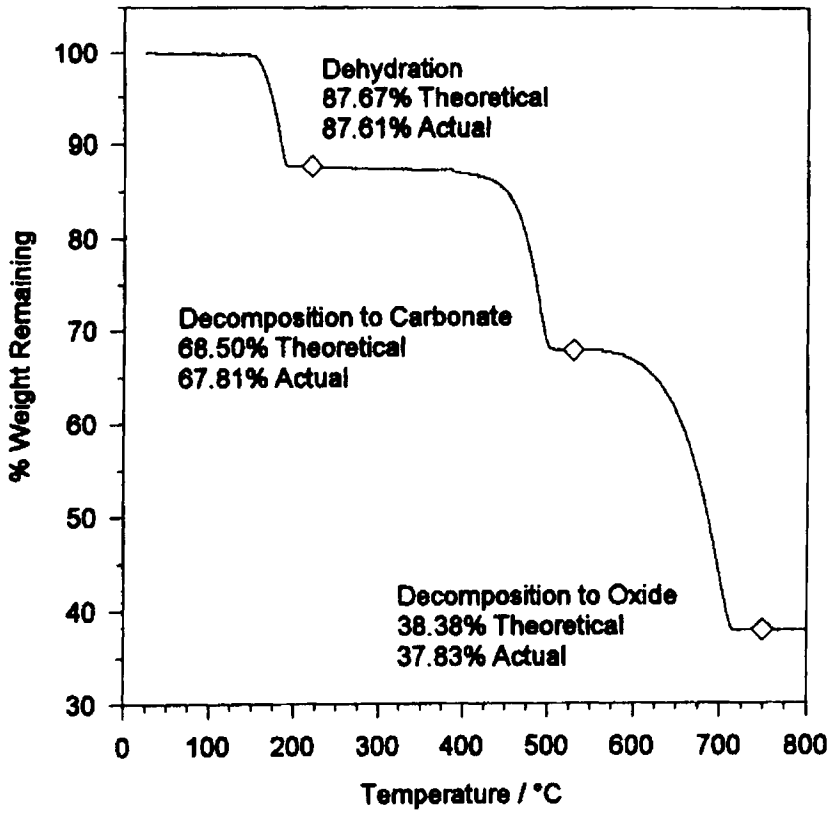


Figure 12. TG curve for Ca-oxalate-monohydrate [73].

For the heavier alkaline-earth compounds, $SrC_2O_4.H_2O$ [74] and $BaC_2O_4.H_2O$ [75], analogous decompositions occur. The decomposition temperatures were taken from EGA(MS) results because this technique allows the detection. of the first traces of evolved gases before any change can be seen in the TG/DTG curves. In an investigation of the decomposition of $BaC_2O_4.0.5H_2O$ by stepwise isothermal analysis Sørensen et al. [76] found that the intermediate $BaCO_3$ decomposes in three steps to BaO, forming two Ba-oxo-carbonates in the temperature range 960 to1020 °C, but without identifying the solid intermediates by XRD. Acid oxalates can also be prepared, which decompose similarly, however the anhydrous compounds produce formic acid besides (H_2O + CO + CO_2). All solid intermediates were identified by XRD. The behaviour of the oxalates of Mg [77] and Be[78] is different. After dehydration, the anhydrous

material decomposes directly to the oxide. For the hygroscopic hydrates of Be-oxalate the final step to the oxide probably starts from the monohydrate.

Complex oxalates, e.g. K-Ln-oxalates [78] decompose in a similar way: dehydration is followed by evolution of CO_2 (exothermic effect in air). Residues are (K_2CO_3 + oxo-carbonates, $Ln_2O_2CO_3$) for Ln = La - Ho or (K_2CO_3 + Ln_2O_3) for Er - Yb.

For the aims of basic inorganic chemistry, a thermogravimetric investigation consists of three parts: (1) the preparation and identification of the starting product; (2) the determination of the decomposition steps; and (3) the identification of evolved gases, solid intermediates and the final residue. For (2), in general, a combination TG/DTG/DTA (or DSC) is used. In simple cases, the reaction stoichiometries can be derived from the Δm-values alone; otherwise the evolved gases must be identified by EGA and the solid intermediates characterized by XRD, provided that they are crystalline. However, often amorphous intermediates or products are formed. For them, characterisation by IR spectroscopy is possible. The final residues can sometimes be treated to yield crystalline material.

5.2.3. Selected examples of decompositions of coordination compounds

The same conditions as for simple compounds hold for complexes too, however, the properties of the ligands must also be considered. They can react with the residue, as reductants in case of organic ligands, and with large organic ligands fragmentation can occur, often with different products in inert atmosphere or in air. It is thus necessary to investigate the thermal behaviour of the organic molecules themselves.

As an example, the work of Liptay and coworkers on the complexes of transition metals with substituted aromatic amines carried out since 1963 using the 'derivatograph' will be described. A first paper in 1963 [80] dealt with the thermal behaviour of metal anthranilates and pyridine complexes of metal thiocyanates from the point-of-view of their use as a weighing-form for gravimetric precipitates. TG/DTG/DTA measurements in air yielded the decomposition - intermediates for which probable compositions were postulated. In 1969/1970 intermediates of the decomposition of complexes, $M(py)_4X$ (M = Ni, Co and other bivalent metals, X = SCN^- and halides) [65,81] were isolated with the 'freezing-in' method, described before. Besides compounds like $M(py)_2X_2$, other intermediates like $Ni(py)Cl_2$ and $Ni(py)_{2/3}Cl_2$ were found and characterized by IR-, UV-spectra and magnetic measurements. The variation of decomposition temperatures for different metals is discussed in terms of ligand-field theory. From 1986, in papers together with Wadsten [82], intermediates were characterized by XRD on crystal powders, indexed with a trial-and-error program, but without intensity calculations. Together with others in 1992 [83],

a new solid-gas phase chemisorption method was described to prepare ternary mixed Co-picoline complexes, with intermediates prepared by the freezing-in method. From reaction of $[Co(\beta\text{-pic})_2]Cl_2$ in a vacuum desiccator with the vapour of α-picoline for a few days, the complex $[Co(\beta\text{-pic})_2(\alpha\text{-pic})_2]Cl_2$ was prepared. In 1993, for the first time a complete structure determination with single-crystal techniques on the chelate $[Zn[1,2\text{-ethanediol}]_2SO_4$ was performed [84]. One year later, the evaluation of powder patterns with the Rietveld method was applied for Co-lutidine-complexes $[CoL_4]X_2$ (X = Br) [85]. With molecular orbital (SINDO1) calculations bond lengths and angles were found in extremely good agreement with experimental data from X-ray analysis [86].

The most important task for further development is to find methods for the preparation of single crystals of intermediates. It would be of great interest to solve the structures of compounds like $Ni_3L_2Cl_6$ [87]).

For complexes with large organic or biochemical ligands, it is difficult to find papers where decomposition reactions are performed in an inert atmosphere. Characteristic for reactions in air are exothermic peaks where the organic matter is oxidized. Thus, Dranca et al. [88] found that Co(II)-*d*-tartrate-hydrate loses the crystal water in air and Ar at 99 °C. The main endothermic decomposition of the organic part in Ar occurs at 380 °C, leading finally to Co-metal, while in air at 395 °C the oxide Co_3O_4 is formed. But exothermic effects can also appear in inert atmospheres. For example, $Mg_2[Ti_2(O_2)_4].4H_2O$, is decomposed in a three-step reaction [89] to $Mg_2[Ti_2O_4(OH)_4] + 2O_2 + 4H_2O$ in the range 30-300 °C. The DSC curve reveals that the strong endothermic dehydration overlaps a smaller exothermic effect at 190 °C. The explanation is that the hydroxy-oxide is more stable than the dehydrated peroxide. Two other exotherms are found at 320 °C and 490 °C: 2) $\rightarrow Mg_2[Ti_2O_5(OH)_2] + H_2O$ and 3) $\rightarrow 2MgTiO_3 + H_2O$. For both reactions, the endothermic effect of separation of $2OH^-$ as water is overcompensated by the exothermic reconstruction of the oxide-bonds. Both intermediates are amorphous; crystalline $MgTiO_3$ is formed by annealing (2 h at 650 °C).

5.3. Precursors

In Section 4.6, the preparation of complex oxides with the ceramic method was described. A mixture of the binary oxides in the correct proportions is calcined at the reaction temperature, followed by several successive grinding and annealing sequences. Disadvantages of this conventional synthesis may be microscopic compositional inhomogeneities resulting in long calcination and sintering times, non-uniformity of particle size and shape and lack of reproducibility. Therefore, 'wet chemical methods' were developed. Starting systems are solutions with controlled content of the metals in question. Solid 'precursors' for the subsequent calcination are solid intermediates with the same

metal stoichiometry as the target oxides, prepared either by freeze-drying, spray-drying, sol-gel techniques or by coprecipitation of hydroxides, alkoxides, or double salts/complexes with thermally degradable ligands like carbonate, nitrate or organic anions or compounds.

Methods using dicarboxylates, such as oxalate, tartrate, etc., as ligands are described as examples. Inagaki et al. [90] found that for the synthesis of the spinel, $Li_2Mn_2O_4$, the complex Li-Mn-malonate was the most suitable precursor, because it has the lowest decomposition temperature in air, namely 260 °C. TG measurements were complemented by EGA, FTIR and XRD. Rojo et al. [91] likewise used double malonates, $M[Cu(mal)_2].nH_2O$ (M = Ca, Sr, Ba), for the preparation of oxocuprates(II), $MCuO_2$. By use of TG-DSC/DTA in air the thermal decomposition was found to involve three consecutive steps: endothermic dehydration; ligand pyrolysis giving mixtures of alkaline-earth carbonates and CuO; and decarbonation of these carbonates with increasing temperatures from Ca (660 °C) to Ba (>800 °C). The resulting $MCuO_2$ was identified by XRD and the final grain size was analysed by SEM. Mullens et al.[92] gave a comparison between coprecipitates and mechanical mixtures of Ca-Sr-oxalates having the same Ca/Sr ratio, based on XRD, SEM-EDX and TG measurements. The coprecipitates are solid solutions, $Ca_xSr_{1-x}C_2O_4.yH_2O$, formed by substitution of Sr^{2+} by Ca^{2+} in the $SrC_2O_4.2.5H_2O$ lattice as proved by XRD patterns. By use of TG/DTA and XRD it could be shown that the dehydrated coprecipitates decompose into a mixture of $CaCO_3$ and $SrCO_3$. The final decomposition to segregated oxides is the same as for the mechanical mixtures. With other systems, solid-solutions of precursors may give solid solutions of the final oxide phases.

For other chemical systems, precursors may also be of importance. An example was given in Section 4.3 of the preparation of orthorhombic $KMnCl_3$ from $KMnCl_3.2H_2O$. The ternary fluoride, $FeAlF_5$, can be obtained as a pure product from $FeAlF_5.7H_2O$ as precursor. By use of TG under quasi-isobaric conditions, it was found that a defined intermediate, $FeAlF_5.2H_2O$, is formed [93], isostructural with $Fe_2F_5.2H_2O$.

In Section 4 methods of monitoring the progress of the reaction between two metal oxides to form a ternary phase were described. If one of the reactants is a precursor, such as a carbonate or nitrate, then the progress can be detected using TG too, by measuring the mass-loss caused by the evolution of CO_2 or NO_x. There are, however, also reactions where one of the reactants may be volatile. Thus, the reaction: $ZrO_2 + 3TeO_2$ to form $ZrTe_3O_8$ occurs at 1000 °C. From TG it was found [94] that TeO_2 begins to volatilize at 800 °C, while the dissociation of TeO_2 from $ZrTe_3O_8$ started at higher temperatures. Using a heating rate of 2 K min^{-1}, it was found by DTA that the melting peak of TeO_2 at 732 °C was totally absent. Thus, an optimum method of synthesis at 900 °C could be

proposed and the purity of the $ZrTe_3O_8$ was confirmed by XRD. An analogous result was obtained for $HfFe_3O_8$. More complex is the situation in the system Nb-$NbBr_5$ (Figure 13) [95]. By use of DTA in a closed quartz vessel, it was found that, immediately after melting at 257 °C, $NbBr_5$ reacts exothermically with Nb to $NbBr_4$, followed by an endothermic, reversible disproportionation: $2NbBr_4 \rightarrow NbBr_3 + NbBr_5$. During a second heating in the opened vessel, the reaction takes place at 388 °C, also indicated in the TG-curve. From 578 – 700 °C, a monotonous mass loss was observed due to the formation of mixtures ($NbBr_{2.67} = Nb_6Br_{16}$ and $NbBr_3$). The final decomposition to unknown products occurs at about 700 °C. This reaction scheme was confirmed by tensimetric measurements of the total pressure.

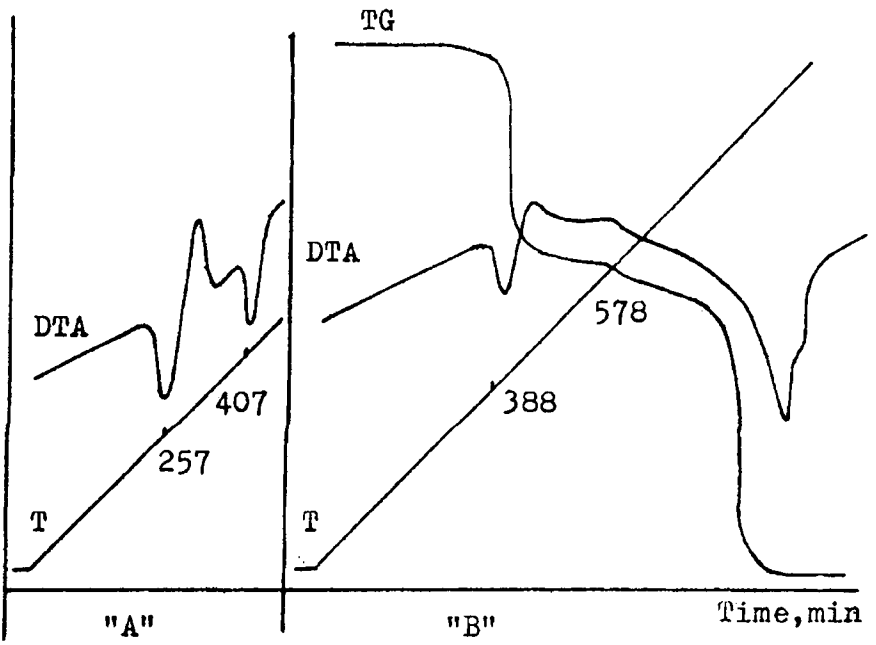


Figure 13. TG and DTA curves of reduction of $NbBr_5$ by Nb (molar ratio 1:4) [95].

Another group of reactions, which can be investigated by TG, are those with a reactive atmosphere, for instance where the sample is reduced by H_2 or CO, or oxidized by O_2. TG experiments in air belong to this group. One example is the reduction and re-oxidation of Nd_4PdO_7 with CO and air, respectively [96], monitored in a thermobalance. In a CO/He mixture the compound is reduced in one step from 380 to 600 °C (heating rate 10 °C min^{-1}) to Nd_2O_3 and Pd. Re-

oxidation in air occurs in two overlapping steps from 260 to 600 °C. At around 1185 °C, Nd_4PdO_7 starts to decompose to Nd_2O_3 and Pd. The growing solid phases where characterized by XRD, and their morphologies by scanning (SEM) and transmission (TEM) electron microscopy. Analogous reactions can be performed with hydrogen, however, often another detection method is used, described in the next Section.

5.4. Miscellaneous methods related to thermogravimetry

5.4.1. Temperature programmed reduction (TPR)

For reductions with H_2, the hydrogen consumed by the reaction can be measured by a thermal conductivity cell. The TPR patterns correspond with the mass loss of TG curves. Thus, the $AlVMoO_7$ phase was reduced with a 10% H_2 stream with a heating rate of 10 K min^{-1} up to 1100 °C [97]. The results were supplemented with XRD, IR spectra and SEM and compared with the reduction behaviour of V_2O_5 and MoO_3. A solid solution $(V_{1-x}Al_x)_2O_3$ was found to form at about 600 °C from an intermediate, $Al_2(MoO_4)_3$ which existed between 500 and 600°C.

5.4.2. Boiling-point determinations

Paulik et al. [98] used their quasi-isothermal, quasi-isobaric technique for measuring equilibrium temperatures of boiling with 100 to 1000 mg samples in labyrinth crucibles (see Figure 10). These sample-holders ensure that the air present in the crucible is expelled by the vapour at the very beginning of the experiment. Later, Goodrum and Siegel [99] used sealed holders with a laser-drilled aperture in a thermobalance under normal heating conditions. The onset temperature for the boiling process was constructed from the measured tangent. They applied controlled pressures from ambient down to 20 mmHg.

5.4.3. Transport balance [100]

In transport reactions, an otherwise nonvolatile solid migrates in a temperature gradient via a reactive gas phase, acting like a solvent. Best known is the situation in a halogen light bulb, where the simplified reaction: $W(s) + nI_2(g) \rightarrow WI_{2n}(g)$ takes place. Exothermic reactions cause migration into the region of higher temperature and endothermic reactions into the opposite direction. Because the formation of tungsten iodide is exothermic, the solid W is transported from cold to hot regions. Transport experiments are mostly carried out in closed silica tubes placed in the temperature gradient of a two-zone tubular furnace. After an experiment is terminated, the transport rate (provided that it is constant during the experiment) can be determined from the mass of the deposited solid recovered and the total time elapsed. In the 'transport balance'(see Figure 14), the mass flux can be measured in real time during the

crystal growth from the vapour phase. The sample ampoule lies on a horizontal support of a mass balance as shown, and the calculation of the mass change is done with the lever rule. Variations of the transport rate can used for evaluations of kinetics and reaction mechanisms, or with changing temperatures, for thermodynamic calculations, also for the determination of partial pressures and sublimations [101]..

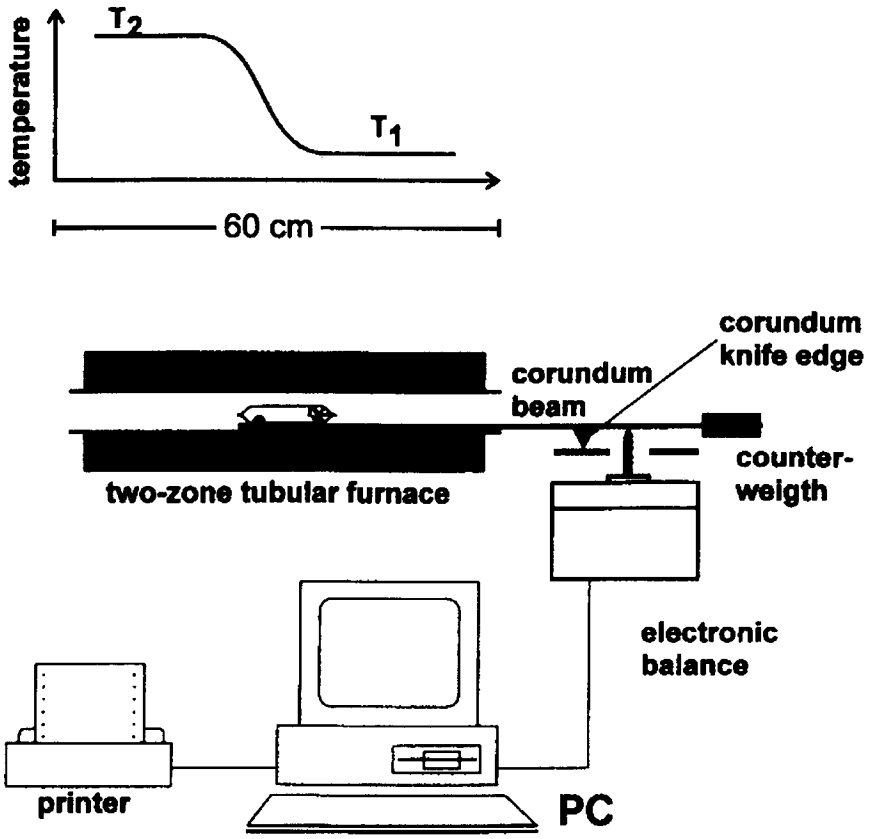


Figure 14. Schematic presentation of the transport balance [100].

6. THERMOMECHANICAL ANALYSIS

6.1. Introduction

The term thermomechanical analysis (TMA) is used for measurements of volume or length under torsion or load as a function of temperature. If the applied stress or the dimension of the substance varies as a function of time

during the measurements, the technique is called 'dynamic-mechanical analysis', usually abbreviated DMTA or DMA. The theory and equipment used for these techniques are described in detail in Chapter 6 of Volume 1 of this Handbook. An excellent introduction to DMTA is the book by K.P. Menard, "Dynamic Mechanical Analysis: A Practical Introduction", CRC Press, Boca Raton, USA, 1999. The importance of such measurements lies in the direct link of the experiment to the mechanical behaviour of the samples. The stress may be not only compression and tension, but also flexure or torsion, thus yielding the moduli of bulk, shear and tensile stresses. Thus DMTA is an extremely important method for checking the utility of macroscopic materials, for example, flexible, linear polymers. It is, in general, difficult to understand the measured macroscopic quantities in terms of their microscopic origin. This can be done sufficiently only if the stress goes to zero. Then only the dependence of the length (or volume) on temperature is measured, i.e. the thermal expansion. The TA technique is called 'thermodilatometry'. The measurement of thermal expansion applied to inorganic compounds is treated in the following Section.

6.2. Thermal expansion

All solid substances, when heated or cooled, undergo a reversible change in dimension known as thermal expansion or thermal dilatation. These effects are results of the thermal motion of the atoms or molecules of which the matter is composed. While in an ideal gas there are no interactions among the particles, in (crystalline) solids the atoms or ions occupy certain sites in the (lattice) structure with attractive and a repulsive forces in equilibrium. The particles vibrate about their equilibrium positions in dependence on T. Because the repulsive and attractive forces are not symmetrical, the centre of vibrations is displaced to increased interatomic distances with increasing temperature and the solid expands. This expansion is isotropic for cubic crystals, but anisotropic for all other crystal systems. It is also possible that deformations can be caused by a change in bond angle with temperature. The forces acting in certain directions in a complex solid may also be such that contraction may occur in certain directions in the crystal.

To describe the overall deformation at a given temperature thermal expansion coefficients (linear or bulk) are used: $(\alpha_L)_T = (dL/dT)/L$ and $(\alpha_V)_T = (dV/dT)/V$. Often the coefficients are approximately constant over large temperature ranges, then average coefficients with differences ΔL, ΔV and ΔT instead of differentials can be used. For isotropic materials, $(\alpha_V)_T = 3(\alpha_L)_T$. For anisotropic crystals, linear expansion coefficients for each lattice axis are required.

Correlations between thermal expansion, binding forces and geometry have been found for groups of inorganic compounds, but too many anomalies exist to allow the derivation of a general theory. A matter of special importance is the

influence of defects in the sample, either lattice defects or the porosity of aggregates, on the expansion of the sample. In the simplest case, that of an aggregate of isotropic crystals, each grain may expand equally in all directions without any differential movement among them. On cooling, the aggregate returns to its original site and shape and the thermal expansion curve does not show any hysteresis. In many other cases, however, during the thermal treatment the mutual grain orientations will change or the number of lattice defects will decrease. Then, either hysteresis or peaks in the thermal expansion curve will be observed. Differences between results from dilatometer curves and those from X-ray methods will also be obtained. Such effects may be understood by investigating the irreversibility over several heating-cooling cycles.

6.3. Experimental methods for measuring thermal expansion

The most basic method of measuring a variation of length is the direct observation of the sample with a microscope. If one face of a sample-block can be polished, then ΔL can be measured by interferometry using laser light. This is probably the method with the highest sensitivity. Electrical properties dependent on length variation can also be used. The most widely used dilatometers are, however, push-rod dilatometers. The length variation is transmitted by a push-rod to an amplifier device, such as a linear variable differential transformer (LVDT) outside the furnace. Such a system can also be used in differential dilatometry.

Among simultaneous methods including dilatometry, the combinations with DTA are of special importance. The most complete arrangement is that of Paulik and Paulik [102] who have incorporated a simple dilatometric device in the derivatograph. Another combination is that of an electrical conductivity device with a push-rod dilatometer by Duclot and Deportes [103]. An original apparatus was developed by Balek [104] including DTA, dilatometry and emanation thermal analysis [ETA]. (In ETA, an inert radioactive gas is incorporated in a solid. The rate of release of this gas when the sample is heated is measured. Thus variations of inner surfaces can be detected. More detail of ETA is given in Chapter 9 of Volume 1 of this Handbook.)

6.4. High-temperature X-ray diffraction (HT-XRD)

This technique is a branch of structure determination. One is solving the crystal structure of the sample (usually a powder) to obtain the dimensions of the unit cell at the given temperature. The material must be crystalline and the X-ray pattern must be able to be indexed. By recording X-ray patterns at different temperatures, one can calculate the thermal variation of the lattice parameters. The main problem is the time required to measure the pattern for a sufficiently

large diffraction angle. A direct comparison of the linear thermal expansion of calcite by X-ray and optical interferometer methods was described in 1940 by Austin et al. [105]. For the interferometry, small pieces cut from a single crystal were measured in four different directions. X-ray diffractometry was done on crystal powder. Temperature steps were 50 °C from 50 to 300 °C. The results of the two sets of measurements agreed within the limits of accuracy.

Bayer and Wiedemann [106] used a heating diffractometer (Philips, MRC furnace) and/or the Lenne-Guinier technique to study the thermal expansion of pseudo-brookites and the thermal features of metal oxides of the Pt group [107]. In the second paper, the thermal expansions of PdO, RuO_2, IrO_2 and their thermal dissociations were measured with an X-ray high temperature diffractometer isothermally at stepwise increased temperatures (Figure 15a), and the thermal behaviour continuously by TG/DTA. Expansion coefficients were calculated from the changing lattice parameters (Figure 15b).

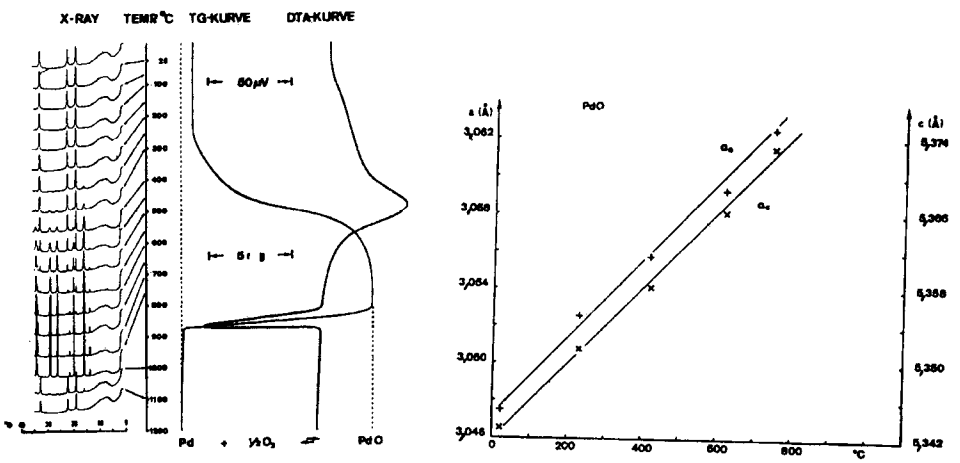


Figure 15.
(a) Oxidation and thermal dissociation of PdO in streaming air.
(b) Changes of lattice parameters of tetragonal PdO with temperature.

In the Lenne technique, the sample is compacted on the heating system, a platinum layer or net. If this is open to the surrounding atmosphere, there may be problems with hygroscopic substances. An improvement is the Simon-Guinier technique [108], where the samples are sealed in thin quartz ampoules. An example is the investigation of thermal expansion combined with a phase transition for Na_3GdCl_6 [109].

The introduction of position sensitive proportional counters in the seventies [110] lead to time and temperature resolved X-ray diffraction. This technique

allows measurement of about 200 angle dispersive diffraction patterns per day while the samples are heated continuously or stepwise, for the investigation of phase transitions or for kinetic evaluations. In Figure 16, the determination of the five phase transitions of NH_4NO_3 in the range -70 to 140 °C is shown as measured by Engel et al. [111]. The crystal structures of the different phases were evaluated with the Rietveld refinement. Other examples described in this and another paper [112] are the non-isothermal corrosion of nickel and iron, and the isothermal reaction of NH_4NO_3 with copper oxide.

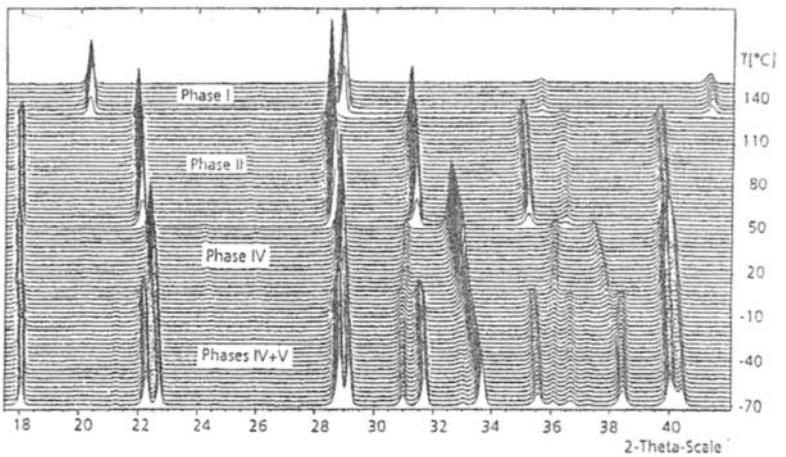


Figure 16. Selected diffraction patterns of ammonium nitrate measured at different temperatures.

More expensive than the use of normal X-rays are the use of neutrons or synchrotron radiation, which extend the investigation possibilities. A good survey with several examples, is given by Aranda [113], which also covers thermal expansion and its use for the Landau theory of second-order phase transitions, magnetic- transitions and texture determinations. A coupling of DSC and time-resolved synchrotron XRD has been described recently [114].

REFERENCES

1. J.A. Sommers and E.F. Westrum, J. Chem. Thermodyn., 8 (1976) 1115; 9 (1977) 1.
2. J.E. Callanan, R.D. Weir and E.F. Westrum, J. Chem. Thermodyn., 25 (1993) 209.
3. E. Palacios, R. Navarro, R. Burriel, J. Bartolomé and D. Gonzales, J. Chem. Thermodyn., 18 (1986) 1089.
4. T. Atake, K. Nomoto, B.K. Chaudhuri and H. Chihara, J. Chem. Thermodyn., 15 (1983) 339.
5. S.C. Mraw and D.F. Naas, J. Chem. Thermodyn., 11 (1979) 567.
6. F. Grønvold and E.F. Westrum, Inorg. Chem., 1 (1961) 36 ; J. Chem. Thermodyn., 8 (1976) 1039.
7. J.E. Callanan and S.A. Sullivan, Rev. Sci. Instr., 51 (1986) 2584.
8. S.M. Sarge, E. Gmelin, G.W.H. Höhne, H.K. Cammenga, W. Hemminger and W. Eysel, Thermochim. Acta, 247 (1974) 129.
9. M. Gaune-Escard, A. Bogacz, L. Rycerz and W. Szczepaniak, J. Alloys Comp., 235 (1996) 176.
10. R. Blachnik and C. Siethoff, Thermochim. Acta, 278 (1996) 39.
11. K. Adamkovicova, P. Fellner, L. Kosa, P. Lazor, I. Nerad and I. Proks, Thermochim. Acta, 191 (1991) 57.
12. C.M. Guttman and J.H. Flynn, Anal. Chem., 45 (1973) 408.
13. M. Chabin, F. Giletta and C. Ridou, Phys. Stat. Sol. (a), 48 (1978) 67.
14. P. Vanek, B. Brezina, M. Havrankova. and J. Biros, Phys. Stat. Sol. (a), 95 (1986) K 101.
15. J. Garcia, J. Bartolomé, D. Gonzales, R. Navarro and W.J. Crama, J. Chem. Thermodyn., 15 (1983) 1109.
16. J.C. Southard, J. Amer. Chem. Soc., 61 (1941) 3142.
17. J.L. Margrave and R.T. Grimley, J. Phys. Chem., 62 (1958) 1436.
18. A.S. Dworkin and M.A. Bredig, J. Phys. Chem., 64 (1960) 269 ; 67 (1963) 2499.
19. W.T. Thompson and S.N. Flengas, Canad. J. Chem., 42 (1971) 1550.
20. J.L. Holm, B.J. Holm and F. Grønvold, J. Chem. Thermodyn., 5 (1973) 97.
21. T. Hattori, K. Igarashi and J. Mochinaga, Bull. Chem. Soc. Japan., 54 (1981) 1883.
22. H. Kleykamp, Thermochim. Acta, 287 (1996) 191.
23. E. Gmelin, W. Hönle, C. Mensing, H.G. v. Schnering and K. Tentschev, J. Thermal Anal., 35 (1989) 2509.
24. R.T. Marano and E.R. Shuster, Thermochim. Acta, 1 (1970) 521.
25. A.S. Dworkin and M.A. Bredig, J. Chem. Eng. Data, 15 (1970) 505.
26. A.S. Dworkin, J. Chem. Eng. Data, 17 (1972) 289.

27. S. Cantor, D.P. McDermott and L.U. Gilpatrick, J. Chem. Phys., 52 (1970) 4600.
28. V.E. Gorbunov, K.S. Gavrichev, G.A. Totrova, L.N. Golushina, V.N. Plakhotnik, V.B. Tulchinskii and Y.B. Kovtun, Z. Neorg. Khim., 38 (1993) 217.
29. E.C. Reynhardt and J.A.J. Lourens, J. Chem. Phys., 80 (1984) 6240.
30. K.S. Gavrichev, G.A. Sharpataya and V.E. Gorbunov, Thermochim. Acta, 282/283 (1996) 225.
31. K.S. Gavrichev and V.E. Gorbunov, Z. Neorg. Khim., 41 (1996) 2105.
32. H. Hinode, Y. Ohira and M. Wakihara, Thermochim. Acta, 282/283 (1996) 331.
33. P.A.G. O'Hare and G.A. Hope, J. Chem. Thermodyn., 24 (1992) 639.
34. G.C. Fitzgibbon, C.E. Holley and I. Wadso, J. Phys. Chem., 69 (1965) 2464.
35. E.J. Huber and C.E. Holley, J. Amer. Chem. Soc., 75 (1953) 3594.
36. E.H.P. Cordfunke and A.S. Booij, J. Chem. Thermodyn., 21 (1995) 897.
37. H. Oppermann, A. Morgenstern and S. Ehrlich, Z. Naturforsch., 52b (1997) 1062.
38. F.H. Spedding, M.J. Pikal and B.O. Ayers, J. Phys. Chem., 70 (1960) 2440.
39. L.V. Vasilkova and I.L. Perfilova, Z. Neorg. Khim., 10 (1965) 1248.
40. D.V. Korolkov and V.O. Zakharzhevskaya, Z. Neorg. Khim., 12 (1967) 1561.
41. H.J. Seifert, J. Sandrock and J. Uebach, Z. anorg. allg. Chem., 555 (1987) 143.
42. G.N. Papatheodorou, J. Inorg. Nucl. Chem., 35 (1973) 465.
43. O.J. Kleppa, J. Phys. Chem., 64 (1960) 1937.
44. G.N. Papatheodorou and O.J. Kleppa, Inorg. Chem., 9 (1970) 406.
45. B. Cristol, J. Houriez and D. Balesdent, J. Chem. Thermodyn., 13 (1981) 937 ; 16 (1984) 1191.
46. Q. Guo and O.J. Kleppa, Thermochim. Acta, 288 (1996) 53.
47. J. Bartolomé and F. Bartolomé, Phase Trans., 64 (1997) 57.
48. A. Navrotsky, Phys. Chem. Miner., 24 (1997) 222.
49. R. Blachnik, J. Besser, P. Wallbrecht and K. Dreyer, Thermochim. Acta, 271(1996) 85.
50. Y. Jin and B. Wunderlich, J. Thermal Anal.,, 36 (1990) 765.
51. P.D. Kleinschmidt and K.M. Axler, High Temp. Sci., 28 (1990) 127.
52. G. Chattopadhyay, M.O. Karkhanavala and M.S. Chandrasekharaiah, J. Electrochem. Soc., 122 (1975) 325.
53. A. Gaumann, Chimica, 20 (1966) 82.
54. H .J. Seifert and G. Thiel, Thermochim. Acta, 100 (1986) 81.

55a. H.J. Seifert, H. Fink and J. Uebach, J. Thermal Anal.,, 33 (1988) 625.
55b. H.J. Seifert, H. Fink and G. Thiel, J. Less-Common Metals, 110 (1985) 139.
55c. H.J. Seifert, Thermochim. Acta, 114 (1987) 67.
56. A. Horowitz, M. Amit, J. Makovsky, L. Bendor and Z.H. Kalman, J. Solid State Chem., 43 (1982) 107.
57. H.J. Seifert and G. Thiel, J. Chem. Thermodyn., 14 (1982) 1159.
58. G. Friedrich and H.J. Seifert, J. Thermal Anal.,, 4l (1994) 725.
59. M. Gaune-Escard and J.P. Bros, Thermochim. Acta, 31 (1979) 323.
60. C.G.S. Pillai and P.V. Ravindran, Thermochim. Acta, 278 (1996) 109.
61. M.A. Eissa, M.A.A. Elmasry and S.S. Younis, Thermochim. Acta, 288 (1996) 169.
62. T. Petzel, F. Schneider and B. Hormann, Thermochim. Acta, 276 (1996) 1.
63. W. Weppner, Chen Li-Chuan and W. Piekarcyk, Z. Naturforsch., 35a (1980) 381.
64. H. Oppermann, H. Gobel and U. Petasch, J. Thermal Anal., 47 (1996) 595.
65. G. Liptay, K. Burger, E. Papp and S. Szebeni, J. Inorg. Nucl. Chem., 31 (1969) 2359.
66. A.G. Matuschek,H. Utschick, C. Namendorf, G. Brauer and A. Kettrup, J. Thermal Anal., 47 (1996) 623.
67. J. Rouquerol, Bull. Soc. Chim. Fr., (1964) 31.
68. A. Ortega, Thermochim. Acta, 22.8. (1997) 205.
69. H. Palmer and D.R. Johnson and G.C. Kuscynski, Sintering and Related Phenomena", Gordon and Breach, New York, 1967, p.779.
70. O.T. Sørensen, J. Thermal Anal., 13 (1978) 429.
71. J. Rouquerol, Thermochim. Acta, 144 (1989) 209.
72. D. Petzold and R. Naumann, J. Thermal Anal., 20. (1981) 71.
73. K. Kociba and P.K. Gallagher, Thermochim. Acta, 282/283 (1996) 277.
74. E. Knaepen, J. Mullens, J. Yperman and L.C. van Poucke, Thermochim. Acta, 284 (1996)213.
75. A.S. Bhatti and D. Dollimore, Thermochim. Acta, 78 (1984) 63.
76. F. Chen, O.T. Sørensen, G. Meng and D. Peng, J. Thermal Anal., 53 (1998) 397.
77. D. Dollimore, G.R. Heal and J. Mason, Thermochim. Acta, 30 (1978) 307.
78. D. Dollimore and J.L. Koniczay, Thermochim. Acta, 318 (1998) 155.
79. O. Gencova and J. Siftar, J. Thermal Anal., 48 (1997) 321, 877.
80. L. Erdey and G. Liptay, Period. Polytechn., 7 (1963) 185, 223.

81. G. Liptay, K. Burger, E. Moscari-Fulüp and J. Porubszky, J. Thermal Anal., 2 (1970) 25.
82. G. Liptay, T.Wadsten and A. Borbely-Kuszmann, J. Thermal Anal., 31 (1986) 845.
83. G.Liptay, G. Kennessey, L. Bihatsi, T. Wadsten and J. Mink, J. Thermal Anal., 38 (1992) 899.
84. I. Labadi, L. Parkanyi, G. Kenessey and G. Liptay, J. Cryst. Spectrosc. Res., 23 (1993) 333.
85. J.Kansikas, M. Leskela, G. Kennessey, P.E. Werner and G. Liptay, Acta. Chem. Scand., 48 (1994) 951.
86. L. Hiltunen, L. Niinistö, G. Kennessey, G.M. Keseru and G. Liptay, Acta Chem. Scand., 48 (1994) 456.
87. A.L. Nelwamondo, D.J. Eve, G.M. Watkins and M.E. Brown, Thermochim. Acta, 318 (1998) 165.
88. I. Dranca, T. Lupascu, V. Sofransky, V. Popa and M. Vass, J. Thermal Anal., 46 (1996) 1403.
89. V. Parvanova and M. Maneva, Thermochim. Acta, 279 (1996) 137.
90. T. Tsumura, S. Kishi, H. Konno, A. Shimizu and M. Inagaki, Thermochim. Acta, 218 (1996) 135.
91. M. Insausti, I.G. de Muro, L. Lorente, T. Rojo, E.H. Bocanegra and I.M. Arriortua, Thermochim. Acta, 287 (1996) 81.
92. E. Knaepen, M.K. Van Bael, I. Schildermans, R. Nouwen, J. D'Haen, M. D'Olieslager, C. Quaeyhaegens, D. Franco, J. Yperman, J. Mullens and L.C. Van Poucke, Thermochim. Acta, 318 (1998) 143.
93. U.Bentrup, Thermochim. Acta, 284 (1996) 397.
94. R. Mishra, M.S. Samant, A.S. Kerkar and S.R. Dharwadkar, Thermochim. Acta, 273 (1996) 85.
95. O.I. Vlaskiná, A.S. Ismailovich and V.I. Tsirelnikov, J. Thermal Anal., 46 (1996) 85.
96. M. Andersson, K. Jannson and M. Nygren, Thermochim. Acta, 318 (1998) 83.
97. I.L. Botto and M.B. Vasallo, Thermochim. Acta, 279 (1996) 205.
98. F. Paulik, S. Gal and K.M. Szeczenyi, J. Thermal Anal., 42 (1994) 425.
99. J.W. Goodrum and E.M. Siegel, J. Thermal Anal., 46 (1996) 1251.
100. M. Lenz and R. Gruehn, Chem. Rev., 97 (1997) 2967.
101. A. Hackert and V. Plies, Z. anorg. allg. Chem., 624 (1998) 74.
102. F. Paulik and J. Paulik, "Special Trends in Thermal Analysis", Wiley, New York, 1995, p28-39.
103. M. Duclot and C. Deportes, J. Thermal Anal., 1 (1969) 329.
104. V. Balek, J. Mater. Sci., 4 (1969) 919.

105. J.B. Austin, H. Saini, J.Weigle and R.H.H. Pierce, Phys. Rev., 57 (1940) 931.
106. G. Bayer, J. Less-common Metals, 24 (1971) 129.
107. G. Bayer and H.G. Wiedemann, Archiwum Hutnictwa, 22 (1977) 3..
108. A. Simon, J. Appl. Cryst., 3 (1970) 11.
109. G. Meyer, P. Ax, T. Schleid and M. Irmler, Z. anorg. allg. Chem., 554 (1987) 25.
110. S.K.. Byram and R.A. Sparks, Advances in X-ray Analysis, 20 (1977) 529.
111. W. Engel, N. Eisenreich, M. Herrmann and V. Kolarik, J. Thermal Anal., 49 (1997) 1025.
112. W. Engel, N. Eisenreich, M. Alonso and V. Kolarik, J. Thermal Anal., 40 (1993) 1017.
113. M.A.G. Aranda, Anal. Quimica, Int. Edn, 94 (1998) 107.
114. G. Keller, F. Lavigne, L. Forte, K. Andrieux, M. Dahim, C. Loisel, M. Ollivon, C. Borgaux and P. Lesieur, J. Thermal Anal., 51 (1998) 783.

Handbook of Thermal Analysis and Calorimetry. Vol. 2: Applications to Inorganic and Miscellaneous Materials
M.E. Brown and P.K. Gallagher, editors
© 2003 Elsevier B.V. All right reserved.

Chapter 11

APPLICATIONS OF THERMAL METHODS IN THE GEOSCIENCES

Werner Smykatz-Kloss[1], Klaus Heide[2] and Wolfgang Klinke[1]

[1] Institute for Mineralogy and Geochemistry, University of Karlsruhe, D-76128, Karlsruhe, Germany.

[2] Institute for Geosciences, University of Jena, Burgweg 11, D-07749, Jena, Germany.

1. INTRODUCTION

Geoscience is the cradle of thermal analysis as Le Chatelier stated in 1887 [1]. As outlined by R.C. Mackenzie [2] (Figure 1), Le Chatelier obtained heating rate traces for several clay minerals. During the following centuries, mainly *differential thermal analysis (DTA)* and - to a lesser degree -

This article is dedicated to Dr. R.C. Mackenzie, the great pioneer in thermal analysis and clay science.

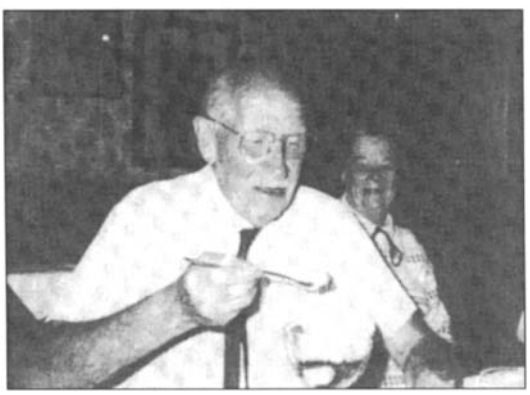


Figure 1: Robert Cameron and Hilda Mackenzie, (Berghausen / Karlsruhe 1990, photograph taken by A.M. Abdel Rehim).

thermogravimetry (TG) and thermodilatometry (TD) have been applied to mineralogical problems, using the changes of energy, mass or length, respectively, in dependence on temperature to determine minerals and mineral properties. The data obtained can be found in several handbooks, textbooks and review articles, e.g. [3 - 38], and in numerous special papers in thermoanalytical journals (TCA, JTAC) or proceedings of special meetings and workshops (e.g. ICTA, ICTAC, ESTAC, NATAS).

The peak time of thermal analysis research in the earth sciences was between 1950 and 1975. After that the application of thermal methods shifted more and more to physical and polymer chemistry, material sciences and metallurgy. Earth scientists "escaped" into combined techniques (high-pressure DTA, evolved gas analysis, mass-spectrometric TA, high-temperature microscopy, thermosonimetry) or into quantitatively improved methods (calorimetry, chromatography etc.). The reasons for this development are varied. The use of modern devices and equipment opened up new special fields of TA applications in the earth sciences, e.g. environmental studies, crystallographic and petrologic research and in applied and technical mineralogy.

The International Confederation for Thermal Analysis and Calorimetry, ICTAC, put a lot of effort into promoting new thermal techniques and their application in the geosciences, and improving the established methods for their use in the modern geoscientific fields. On the initiative of W. Smykatz-Kloss, in 1988 a *Geoscience Committee* was founded. This committee has tried to advance the application of thermal methods in the earth sciences, by holding several meetings and by the publication of two special books to characterise the state of the art [39, 40].

The most important section of thermal analysis in earth sciences is still the study of *clays*, that means minerals with a crystallite size < 0.002 mm. This is because many of the clay minerals and their complexes (e.g. the organo-clays), as well as hydroxides and carbonates, exhibit disturbed and disordered structures which are difficult to characterise by conventional solid-state methods (X-ray analysis and optical microscopy). In thermal studies the dehydration, dehydroxylation or phase transformation of clay minerals are frequently quite well characterised qualitatively and (semi-) quantitatively. The determination of the defect character or disorder of the clay mineral structures without special sample preparation and with a broad variation of sample mass (10 µg up to 1000 g) may be an additional advantage of the TA investigations.

Other important fields are the study of *phase transitions and phase relations* in petrology and applied mineralogy as well as those of *thermodynamics and kinetics*. These include the determination of melting temperatures, high-pressure and high-temperature mineral reactions in relation to gas fugacities, and of

thermal data, which depend on crystal chemical compositions of solid solutions or crystal chemical substitutions [41 – 50]. Among the "non-clays", hydrated or (OH)-bearing silicates, sulfates, vanadates, phosphates, borates and hydroxides may be characterised by their dehydration, dehydroxylation, or decomposition behaviour. Many minerals show characteristic reversible or irreversible phase transitions during the heating or cooling process. Further suitable criteria for mineral identification and quantitative determination of mineral contents are oxidation effects, especially those of Fe^{2+}, Mn^{2+}, Pb^{2+} or S^{2-} and carbon containing minerals, rocks or soils.

A special field of thermal study is the identification and quantification of carbonates in rocks and soils. The endothermic decomposition effects and the dependence of the decomposition rate on the partial pressure of CO_2 allow, in many cases, a differentiation and determination of carbonate minerals in quantities far below the detection limits of X-ray analysis. The latter effect has lead to some special techniques of mineral determination under strictly standardised conditions of analysis, e.g. ***PA-curves*** (**P**robenmengen-**A**bhängigkeit, [24, 25, 50 - 54]), the analysis in variable atmospheres [52, 55 - 57] and the study in high vacuum together with an oxygen source [58].

Particularly in soils and sediments, numerous minerals exhibit a high degree of structural disorder. Standardised DTA, EGA-MS or DSC often enable the characterisation of this degree of disorder and, through this, correlation to the milieu of formation and to paleo-climatologic conditions [59–62].

Last but not least, thermal methods have been widely applied in order to control technical processes or to characterise raw materials. In environmental sciences thermal methods have been used recently, mainly for characterising the decrease of the stability of (barrier) clays around waste disposals or in agricultural areas [63 – 65].

A special but intensively used device for the characterisation of organic matter in recent and palaeo sediments and soils is the Rock-Eval-Pyrolysis [66, 67]. In more recent research, the combination with a mass-spectrometric detection of evolved gases improved the method [68].

2. IDENTIFICATION AND DETERMINATION OF MINERALS

2.1. General: Effects, methods, calibration, standardisation

The thermal analysis of minerals, rocks and soils includes endothermic effects (dehydration, dehydroxylation, decomposition, melting, phase transition) and exothermic effects (oxidation, recrystallisation), which enable the identification and quantification of minerals in respect to their genesis, physical and technological properties and to their interaction with environmental factors.

For details about the methods, equipment, and general aspects of thermal analysis see the cited handbooks. The *theory* of thermal analysis is well summarised by Heide [29] and Cunningham and Wilburn [69]. The instrumentation and technique of the main method DTA is reviewed by Mackenzie and Mitchell [70, 71]. Redfern [72] gave a short but very clear overview of the "complementary methods "and the phenomena to be studied by the different thermal methods of analysis. In the *geosciences* mainly three methods have been applied, namely *differential thermal analysis (DTA), thermogravimetry (TG) and differential scanning calorimetry (DSC).* In technical mineralogy and material science (ceramics, glass technology), *thermodilatometry (TD)* is an important method as well [30]. All the other improved, combined and, to a degree, fairly sophisticated methods are normally only used in special investigations (see Sections 5 and 6).

For the *calibration* of thermal equipment a series of well-known reference materials and standards are available (metals, alloys, minerals and glasses [20, 29, 35, 73 – 79] or see Volume 1 of this Handbook).

The effects used for the identification and characterisation of minerals and their properties are mainly, dehydration and dehydroxylation, structural decomposition (decarbonatisation), solid-state phase transitions, melting and oxidation. In special cases additional effects may be applied (e.g. magnetic transformation, sublimation, sintering, devitrification, glass transition). To compare the data of different authors, to advance to more quantitative and reproducible results, all investigations (DTA, DSC, TG, TD etc. runs and the preparation) should be made under strictly standardised well-documented conditions of preparation and analysis [24, 80]. Some special types of materials demand special techniques of preparation and special design of the equipment (sample holder, thermocouples, furnace). In the field of geosciences, especially, samples containing S, P or halogenides should be analysed with care because of possible poisoning of metallic parts of the equipment. This applies particularly to some phosphates and sulfides.

2.2. Dehydration and dehydroxylation

2.2.1. Simple hydrates, chlorides, sulfates, phosphates, arsenates, vanadates, borates

The different type of water-bonding strength in minerals controls the dehydration behaviour of hydrated or OH-bearing structures. Water may be abundant simply by being *adsorbed* on the surface of the sample. The finer the material, the greater the adsorption. Water may be accommodated in four different ways:

- Either in the interlayer space of swelling clay minerals or of halloysite *(interlayer water)*.
- Or it may be abundant as *crystal water*, where it is incorporated in stoichiometric relations into the structure of minerals and occupies distinct sites of the structure (e.g. gypsum and other sulfates, water-rich chlorides).
- It may also be abundant in voluminous structures and filling some holes or vesicles *(zeolitic water)*.
- Last but not least, it may be present as *(OH)*, as is the case in all hydrolysates (e.g. hydroxides, micas, clay minerals), and other OH-bearing silicates like amphiboles or hydrogarnets.

Special thermal effects may result from dehydroxylation of hydrolysates that include polyvalent cations (Fe, Mn,...). and as an advantage (compared to X-ray analysis), H_2O-bearing amorphous minerals (e.g. allophanes, opals,...) show an exothermic effect when being transformed into a crystalline modification.

Chlorides

The salts which are rich in water, e.g. bischofite ($MgCl_2 \cdot 6\ H_2O$), carnallite ($KMgCl_3 \cdot 6\ H_2O$), tachyhydrite ($CaMg_2Cl_6 \cdot 12\ H_2O$) and kainite ($KMg[Cl/SO_4] \cdot 3\ H_2O$, show several endothermic reactions caused by complex dehydration, hydrolysis, decomposition, boiling and melting reactions (Table 1). During the hydrolytic reaction : >X-Cl + H_2O ==> >X-OH + HCl
the formation of inorganic acids occurs, e.g. HCl is evolved in the thermal decompositions of bischofite, carnallite and tachyhydrite [81]. The effect of admixtures generally lowers the endothermic temperatures [82]. Figure 2 shows the DTA curves of some additional halogenides (chlorides and fluorides).

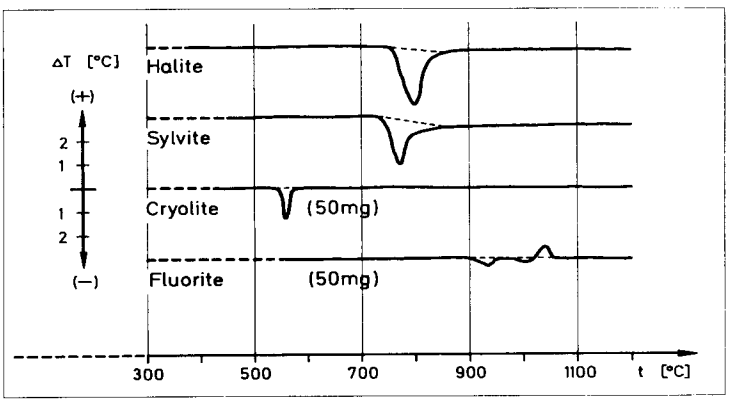


Figure 2. DTA curves of the halogenides: halite, sylvite, cryolite and fluorite.

Table 1
Thermal data of water-rich chlorides [81, 82]

formula mineral	endothermic reactions (°C, ± 1°)				
$MgCl_2 \cdot 6\ H_2O$ bischofite	118 (m)	130 (b)	155-185 (b, hy)	232 (deh)	298 (deh, hy)
$KMgCl_3 \cdot 6\ H_2O$ carnallite		160-165 (m)	190 (b)	230 (deh, hy)	425 (m)
$CaMg_2Cl_6 \cdot 12\ H_2O$ tachyhydrite	117 (tr)	190 250 302 391 (deh)			515 535 690 771 (dec)
$KMgSO_4Cl \cdot 3\ H_2O$ kainite		160 (deh)	277 (deh, hy)	425 (tr)	490-540 (dec)

m = melting; b = boiling; deh = dehydration; hy = hydrolysis; dec = decomposition; tr = structural transition

Sulfates

The thermal behaviour of hydrated sulfates is sometimes quite complex [13, 18, 82 – 87]. Heat changes may be caused by several endothermic processes like dissociation, dehydration, dehydroxylation, decomposition, structural transformation, melting, boiling, - as well as by exothermic effects, e.g. the transition from metastable (amorphous) to stable (intermediate) reaction products, recrystallisation or oxidation (Table 2) [24, 82, 85, 86]. The interpretation of these processes of sulfate dehydration, combined with the formation of intermediate reaction products impoverished in water, is not straightforward. Heide [85, 86] came to the conclusion that a phase analysis of hydrated sulfates by means of thermal methods is very informative in respect to structural changes.

In special cases, e.g. $Na_2SO_4 \cdot 10\ H_2O$, during heating the crystal hydrate-sulfate melts at 32.4 °C. The hydrate melt loses more and more water with increasing temperature by evaporation. This results in shifting the equilibrium and new sulfates (containing less water) will precipitate from oversaturated "solutions". Transformations and reorganisations of the frequently metastable components appear. Thus, the thermal effects occurring at higher temperatures cannot be traced back to the original substances, but only to intermediate metastable reaction products [83]. A typical example is the dehydration path of hydrated Mg-sulfates [18, 24, 86, 87],

$$\underset{\text{epsomite}}{MgSO_4 \cdot 7\ H_2O} \rightarrow (52\ °C) \rightarrow \underset{\text{hexahydrite}}{MgSO_4 \cdot 6\ H_2O} \rightarrow (94\ °C) \rightarrow$$

$$\underset{\text{pentahydrite}}{MgSO_4 \cdot 5\ H_2O} \rightarrow (106\ °C) \rightarrow \underset{\text{starkeyite (leonhardtite)}}{MgSO_4 \cdot 4\ H_2O} \rightarrow (117\ °C) \rightarrow$$

$MgSO_4 \cdot 3\ H_2O \rightarrow (138\ °C) \rightarrow MgSO_4 \cdot 2\ H_2O \rightarrow (164, 184\ °C) \rightarrow$
amorphous amorphous

$MgSO_4 \cdot 1½H_2O \rightarrow (340\ °C) \rightarrow MgSO_4$
amorphous crystalline

The DTA curve of epsomite thus shows eight endothermic effects which partly overlap (Figure 3). The amorphous phases with 3, 2, 1½ and ½ H_2O do not occur in nature. The sodium sulfate, mirabilite, shows similar behaviour. Under high vacuum conditions, the transformation into the crystalline anhydrite modification can be observed by an exothermic reaction.

Other examples for such "polythermic" dehydrations [86] are the minerals *pickeringite* $MgAl_2(SO_4)_4 \cdot 22\ H_2O$ [88, 89], *goslarite*, $ZnSO_4 \cdot 7\ H_2O$ [18, 24, 87], *melanterite*, $FeSO_4 \cdot 7\ H_2O$, which transforms to *rozenite*, $FeSO_4 \cdot 4\ H_2O$, and finally to *szomolnokite*, $FeSO_4 \cdot H_2O$ [18, 90], *chalkanthite*, $CuSO_4 \cdot 5\ H_2O$

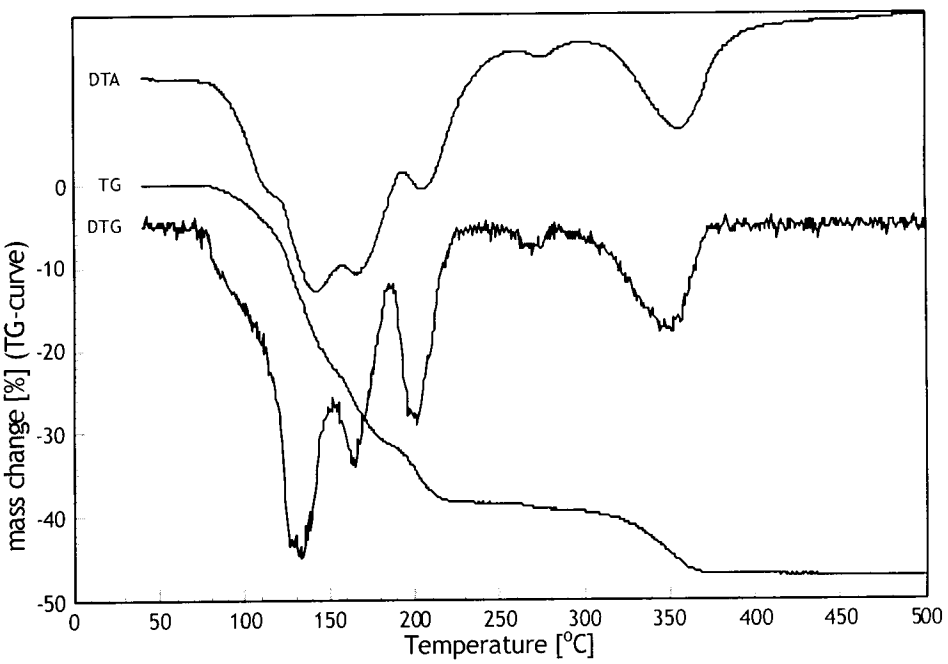


Figure 3. TG, DTG and DTA curves for the dehydration of epsomite, $MgSO_4 \cdot 7H_2O$, in the temperature range 40-500 °C.

[91], *bloedite* (astrakanite), $Na_2Mg(SO_4)_2 \cdot 4H_2O$ [18, 24, 92], *schoenite* (picromerite), $K_2Mg(SO_4)_2 \cdot 6\ H_2O$ [85], *kainite*, $KMg(Cl/SO_4) \cdot 3\ H_2O$ [18, 93], *mirabilite*, $Na_2SO_4 \cdot 10\ H_2O$ [82], *leonite*, $K_2Mg(SO_4)_2 \cdot 4\ H_2O$[85], *alunogen*, $Al_2(SO_4)_3 \cdot 18\ H_2O$ [84], *slavikite*, $MgFe_3[(SO_4)(OH)_3] \cdot 18\ H_2O$ [84], *loeweite*, $Na_{12}Mg_7(SO_4)_{13} \cdot 15\ H_2O$ [92, 94] and *copiapite*, $MgFe_4[OH/(SO_4)_3]_2 \cdot 18\ H_2O$ [84]. It is striking that most of the sulfates (and chlorides!) which show polythermic dehydration behaviour are *Mg* - bearing minerals (Table 2).

The Ca-bearing sulfate, *gypsum* $CaSO_4 \cdot 2\ H_2O$, dehydrates in two steps, including the intermediate product semi-hydrate (*bassanite*, $CaSO_4 \cdot \frac{1}{2}\ H_2O$), and transforms to an amorphous "soluble" γ-anhydrite, which further transforms with an exothermic effect at 380 °C into the crystalline anhydrite modification [24, 82]. Under atmospheric pressure, the decomposition of $CaSO_4$ to CaO and SO_3 occurs above 1000 °C. The dehydration of p*olyhalite*, $K_2MgCa_2(SO_4)_4 \cdot 2\ H_2O$ occurs in a one-step process with a maximum at 355 °C. The very common mineral gypsum has been studied by numerous thermal analysts [13, 46, 82, 86, 95]. Smykatz-Kloss [24, 51] determined traces of gypsum in sediments and soils (e.g. using the PA-curve method). Strydom and Potgieter [96] compared the dehydration behaviour of a natural gypsum and of a phospho-gypsum during milling.

The isotypic compounds free of crystal water *jarosite*, $KFe_3[(SO_4)_2(OH)_6]$, and *alunite*, $KAl_3[(SO_4)_2(OH)_6]$, and their solid solution products show dehydroxylation effects at 450 °C (jarosite, [82]) and around 540 °C [18, 24, 97]. Both the temperatures of dehydroxylation and of decomposition are lower in the Fe-end member jarosite. The exact composition of solid solutions in the jarosite - alunite series should be possible to be determined by the temperature of dehydroxylation (between the "end-member" temperatures of 550 °C and 450 °C) and by the maximum decomposition temperature. These temperatures of some (OH)-bearing sulfates vary between 710 °C (jarosite) and 850 °C (linarite), see Table 3.

The sulfate decomposition temperatures of dehydration products and the formation of oxy-sulfates depend on the crystal chemistry of the minerals, The comparison of the three isotypic heptahydrate sulfates (showing nearly the same size of the cations Fe^{2+}, Zn, Mg) shows that the sulfate decomposition of *melanterite* occurs at the lowest, and of the Mg-minerals at the highest temperature. This result is quite typical for several isotypic structures and solid solutions. The iron member (sulfate, smectite, chlorite, olivine) always proves to be less stable than the Mg member. This also applies to the pair Fe-III and Al (Table 4). The sulfate jarosite shows lower temperatures of dehydroxylation and decomposition compared with the isostructural alunite, whereas the

Table 2. Thermal data of hydrated sulfates (°C, ±1°) (*m = melting, dec = decomposition)*

mineral formula	endothermic reactions	exothermic	reference
$Na_2SO_4 \bullet 10\ H_2O$ mirabilite	32, 102, 240, 884 (m)		[82]
$CaSO_4 \bullet 2\ H_2O$ gypsum	120, 180, >1000 (dec), 1195 (m)	380	[18]
$FeSO_4 \bullet 7\ H_2O$ melanterite	83, 110, 130, 310, 735 (dec)		[24]
$MgSO_4 \bullet 7\ H_2O$ epsomite	46-93, 128-152, 258, 273, 800-1200 (dec)		[85]
$MgSO_4 \bullet 4\ H_2O$ starkeyite	340, 800-1200 (dec)		[18]
$MgSO_4 \bullet 1\ H_2O$ kiesente	350-380, 800-1200 (dec)		[93]
$ZnSO_4 \bullet 7\ H_2O$ goslarite	35-45, 80-120, 234-305, 700-1000 (dec)		[85]
$NiSO_4 \bullet 7\ H_2O$ morenosite	40, 87-106, 117, 123-143, 374, 407-472, 800, 870 (dec)		[85]
$CuSO_4 \bullet 5\ H_2O$ chalcantite	95, 120, 320, 820		[18]
$Al_2(SO_4)3 \bullet 18\ H_2O$ alunogen	130, 140, 320, 800, 820		[84]
$K_2Mg(SO_4)_2 \bullet 6\ H_2O$ picromerite	82, 129, 180-214, 560 (dec), 738 (m), 842 (m)	330	[85]
$K_2Mg(SO_4)_2 \bullet 4\ H_2O$ leonite	140, 180, 560 (dec), 738 (m), 842 (m)	330	[85]
$K_2MgCa_2(SO_4)_4 \bullet 2\ H_2O$ polyhalite	310-355, 890 (m)	510	[27]
$Na_2Mg(SO_4)_2 \bullet 2\ H_2O$ loeweite	269-280, 668 (m), 704 (m)		[85]
$Na_2Mg(SO_4)_2 \bullet 4\ H_2O$ bloedite	140, 260-290, 668 (m), 704 (m)		[85]

Table 3: Temperatures of dehydroxylation and of decomposition for some ((OH)-bearing sulfates (°C, ±1°)

formula mineral	mol SO_4/OH	dehydroxylation	exothermic	decomposition	reference
$PbCu[SO_4(OH)_2] \bullet 5\ H_2O$ linarite	1:2	360		800-850	[18]
$Al_2[SO_4(OH)_4] \bullet 7\ H_2O$ aluminite	1:4	250		800	[`18]
$KFe_3[(SO_4)_2(OH)_6]$ jarosite	1:3	215, 450		710	[577]
$KAl_3[(SO_4)_2(OH)_5]$ alunite	1:3	500-700 520-560 537	 725 715	700-900 720-760 795	[578] [579] [24]
$MgFe_3[(SO_4)_4(OH)_3] \bullet 18\ H_2O$ slavikite	4:3	450, 540		790	[84]
$Fe[SO_4OH] \bullet 5\ H_2O$ fibroferrite	1:1	530		750	[84]
$MgFe_4[(SO_4)_3OH]_2 \bullet 18\ H_2O$ copiapite	3:1	540, 740		810	[84]

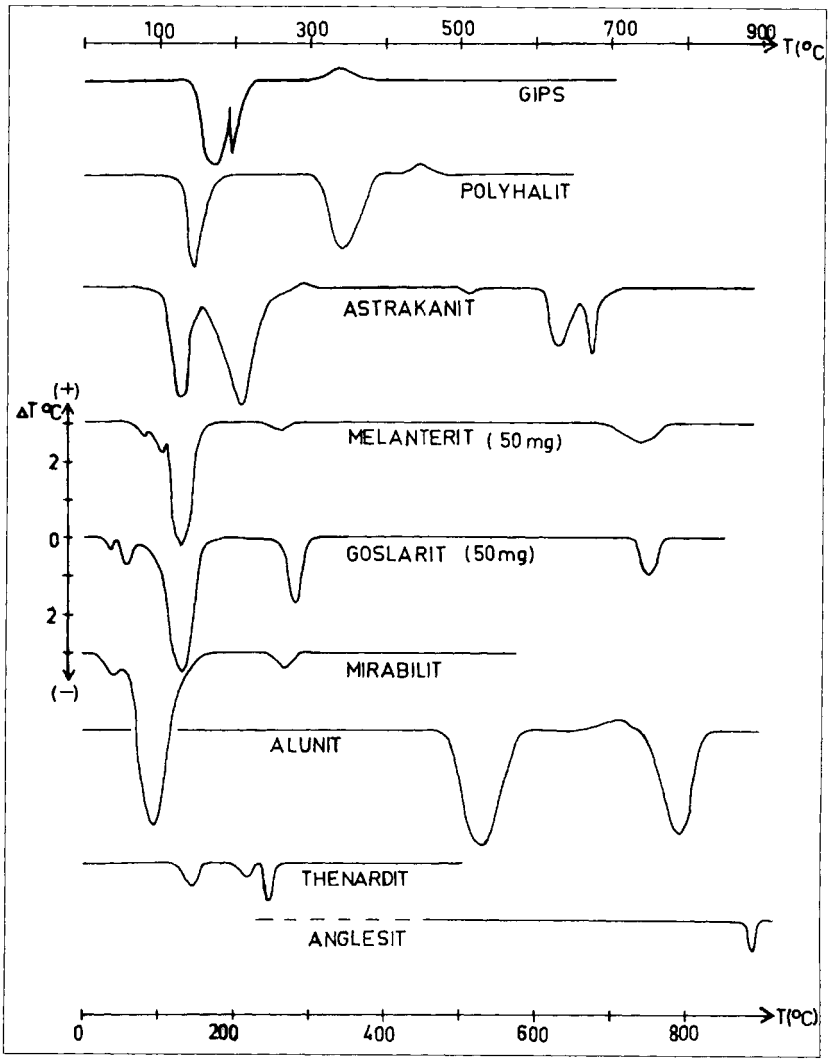


Figure 4. DTA curves of the sulfates (from above), gypsum, polyhalite, astrakanite, melanterite, goslarite, mirabilite, alunite, thenardite, and anglesite.

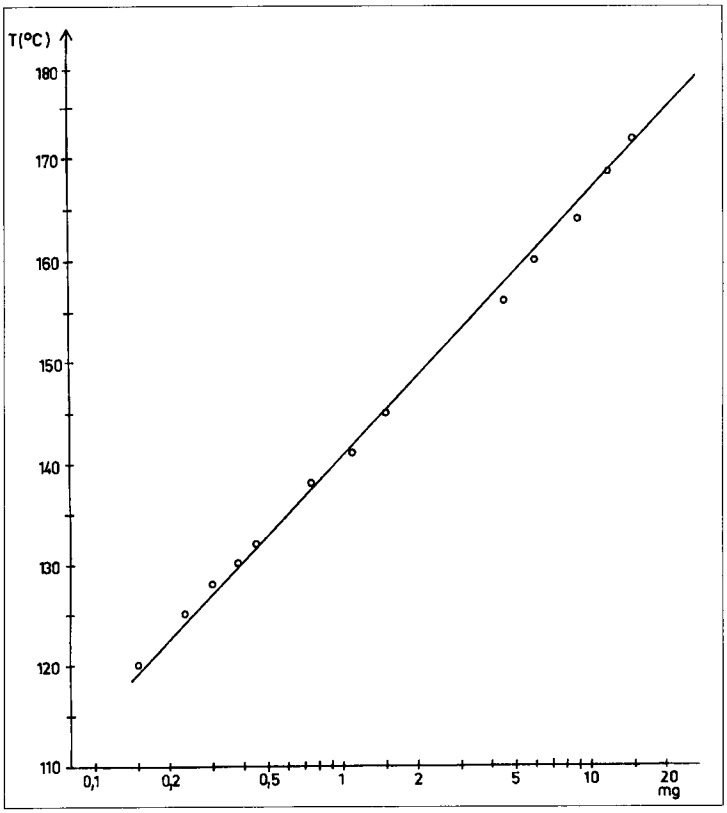


Figure 5. PA-curve of gypsum. The curve is obtained under strictly standardized conditions of preparation and analysis (as proposed in [24]). The sample amount was 100 mg (gypsum + inert material).

intensity of decomposition effects tends to be similar (compare the chapter on micas). Different amounts of water result in different dehydration effects (Table 2). The sulfate decomposition temperatures of dehydration products are not influenced by the original water content (Figures 4 and 5).

Phosphates and related minerals

The minerals of this group are commonly characterised by analogue crystal structures, e.g. tetrahedral anion groups (PO_4^{3-}, AsO_4^{3-}, VO_4^{3-}, MoO_4^{4-}, CrO_4^{2-}). Several phosphates, arsenates, etc., include hydroxyl groups as well, and many are rich in water (Table 4). Most of these minerals decompose or melt between 780 °C and 860 °C, and some (e.g. the phosphates, vivianite and struvite, and the arsenate, erythrite) exhibit exothermic effects, too. The Li-Al phosphate

Table 4: DTA data of water-rich phosphates, arsenates, vanadates (°C, ± 1°)

formula mineral	dehydration	OH	exothermic	decomposition melting	reference
$(Mn,Mg)_5(Mn,Fe)_8[(OH)_5(PO_4)_2] \cdot 15\ H_2O$ bermanite	120-250	350			[102]
$H_6(K,NH_4)_3(PO_4)_2 \cdot 18\ H_2O$ taranakite	130-200		530		[18]
$Ni_3[AsO_4]_2 \cdot 8\ H_2O$ annabergite	153, 195, 266		714	965 (d)	[18]
$Co_3[AsO_4]_2 \cdot 8\ H_2O$ erythrite	105, 235, 301		655, 690	877, 904 (d)	[18]
$Mg_3[AsO_4]_2 \cdot 8\ H_2O$ hoernesite	116, 258, 330			1030 (d)	[18]
$Cu[UO_2/PO_4] \cdot 12\ H_2O$ torbernite	100, 143, 175, 272				[18]
$NH_4Mg(PO_4) \cdot 6\ H_2O$ struvite	116, 182		332, 465, 665		[24]
$Fe_3[PO_4]_2 \cdot 8\ H_2O$ vivianite	230-260, 330, 400		560, 675, 810		[594]
$Cu_9Ca_2[(OH)_{10}(AsO_4)_4] \cdot 9\ H_2O$ tyrolite	110, 170, 350		599		[18]
$Na(Cu, Ca)_6[Cl/(AsO_4)_3] \cdot 5\ H_2O$ lavendulaite	160, 450, 530		302, 630		[18]
$Ca[UO_2/PO_4]_2 \cdot 15\ H_2O$ autunite	92, 141, 216				[18]
$FeAl_2[OH/PO_4]_2 \cdot 6\ H_2O$ paravauxite	190, 295		660		[18]
$(Fe^{II},Fe^{III})Al_2[(O,OH)/PO_4]_2 \cdot 8\ H_2O$ sigolite	185, 220, 255	293	840		[18]

Table 4: cont.

formula mineral	dehydration	OH	exothermic	decomposition melting	reference
$MnFe_2[OH/PO_4]_2 \cdot 8\ H_2O$ stewartite	130-150, 270-290	410	660, 750		[18]
$MnFe_2[OH/PO_4]_2 \cdot 8\ H_2O$ strunzite	180, 260, 305	407	680, 840		[18]
$Al_3[(OH)_3(PO_4)_2] \cdot 5\ H_2O$ wavellite	240, 305		650	802	[18]
$Al_3[(OH)_3(PO_4)_2] \cdot 9\ H_2O$ kingite	255		640		[18]

Table 5: DTA data of water-poor and –free phosphates, arsenates, vanadates (°C, ± 1°)

formula mineral	dehydration	(OH / CO_3)	exothermic	decomposition melting	reference
$MgH[PO_4] \cdot 3\ H_2O$ newberyite	130-200		600		[496]
$CaH[AsO_4] \cdot 1\ H_2O$ haidingerite	105-135, 207		671	856 (m)	[24]
$Cu[UO_2/PO_4]_2 \cdot 1\ H_2O$ meta-torbernite	143, 181, 263				[18]
$Ca_5[(F, CO_3)(PO_4)_3]$ phosphorite		700			[595]
$Ca_2Fe(PO_4)_2 \cdot 4\ H_2O$ anapaite	130		235, 269		[107]
$CaH[PO_4] \cdot 2\ H_2O$ brushite	180-400				[98]
$LiAl[(F,OH)/PO_4]$ amblygonite		733		802	[24]

Table 5: cont.

formula mineral	dehydration	(OH / CO_3)	exothermic	decomposition melting	reference
$Al[VO_4] \cdot 3\ H_2O$ steigerite	100, 290				[18]
$Fe_5[(OH)_9(VO_4)_2] \cdot 3\ H_2O$ russakovite	190, 280	500	535, 610	840	[18]
$CuAl_6[(OH)_8(PO_4)_4] \cdot 4\ H_2O$ turquoise	390		780		[18]
$Al_2[(OH)_3(PO_4)]$ augelite		730	960		[18]
$Fe[PO_4]$ meta-strengite			625, 850	740	[18]
$Fe[AsO_4] \cdot 2\ H_2O$ skorodite	320		110, 450, 550, 850		[18]
$Al[PO_4] \cdot 2\ H_2O$ variscite	150, 220		740		[105]
$Fe[PO_4] \cdot 2\ H_2O$ strengite	110, 290		625, 850	740	[18]
$Zn_2[OH/AsO_4]$ adamite		600	1000	1040	[18]
$Cu_2[OH/AsO_4]$ olivenite		630	670	980	[18]

amblygonite has to be heated very cautiously. At 800 °C melting starts, and the molten salt forms a very hard and compact product which can only be removed from the crucible with great difficulty [24]. DTA curves of common phosphates have been published by Kostov [18], Berennyi [98] (in urinary calculi, brushite and struvite), and Smykatz-Kloss [24] (including PA-curves of vivianite, struvite, annabergite, amblygonite and haidingerite). Kostov [18] reported the data of some rare minerals as well, e.g. of skorodite, turquoise, autunite, torbernite, meta-torbernite (see Table 5). The thermal data of some very rare minerals can be found in special papers, e.g. the vanadate schoderite [99], sanjuanite [100], beustite and bermanite [101, 102], the vanadate mounanaite [103], the OH-bearing Al-phosphate bolivarite [104], the Al-phosphate variscite [105], vivianite [106], and the Ca-Fe phosphate anapaite [107].

The Al-bearing phosphates, e.g. augelite, wavellite, turquoise, amblygonite and bolivarite, show similar thermal effects, e.g. dehydroxylation and decomposition at 200-1000 °C (Table 5). In their thermal behaviour they are quite similar to the Al-*sulfates* (alunogen, alunite, compare with Table 4). Frequently fluorine is incorporated in the structure, e.g. in wavellite. During the thermal treatment, fluorine and HF from hydrolytic reactions are evolved (Figure 6). The large number of minerals of this group (phosphates, arsenates, vanadates, molybdates, chromates) has to be the subject of further investigations. The DTA curves of some phosphates and arsenates are given in Figure 7.

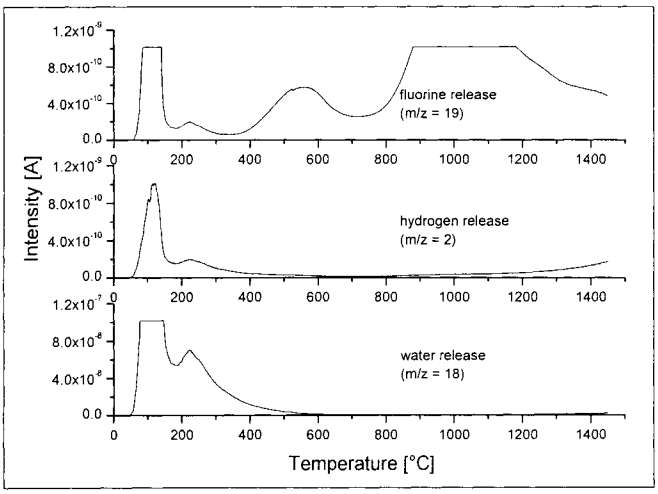


Figure 6. Vacuum decomposition of wavellite.

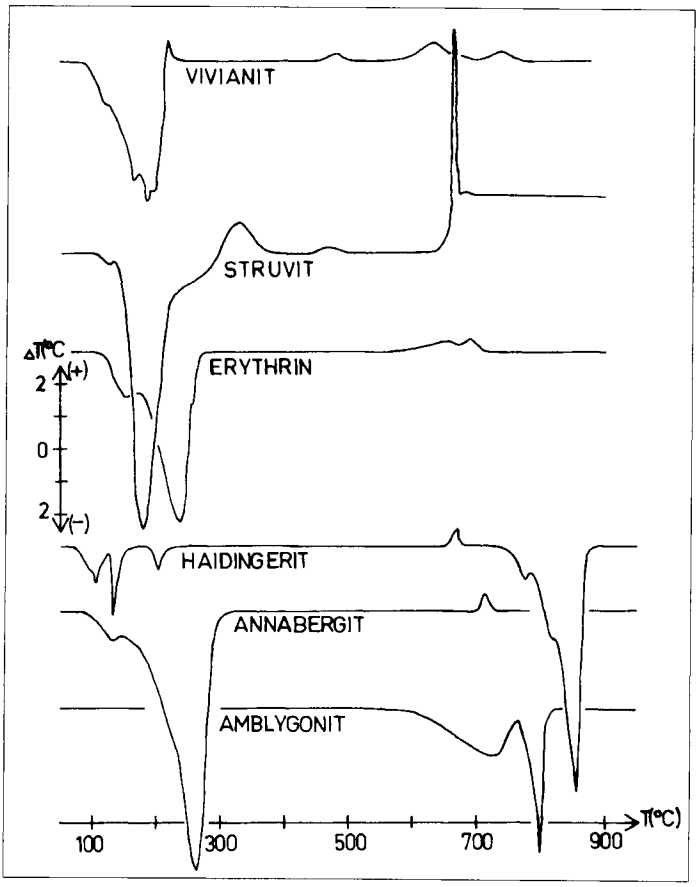


Figure 7. DTA curves of some phosphates and arsenates, e.g. of the minerals vivianite, struvite, erythrite, haidingerite, annabergite, and amblygonite.

Al- and *Fe-phosphates (arsenates)* include an exothermic effect (additional to the Fe^{2+} - Fe^{3+} oxidation) which mirrors the recrystallization of an anhydritic structure. Evidently, the temperature of this exothermic peak depends on the original amount of water (which has probably created some crystal structural disorder), but not on the incorporation of (OH). For Al-phosphates the peak temperatures decrease from 960 °C (free of water, augelite) to 530 °C (18 H_2O, taranakite), see Table 5. Figure 8 shows PA-curves of vivianite.

Borates

The borate minerals are very variable in their crystal structures and thus in their thermal behaviour (Figure 9) [24, 50, 82, 83, 102, 108 - 113]. In playa

deposits (e.g. in Andean salares or in the Mojave desert) a great variety of borates rich in water occur, the common minerals borax, kernite, colemanite or ulexite (Table 6) as well as a lot of rare minerals (e.g. rivadavite, ameghinite, ezcurrite, teruggite, macallisterite, inderite, inyoite, kaliborite, pandermite, pinnoite, see [82, 108 – 111]).

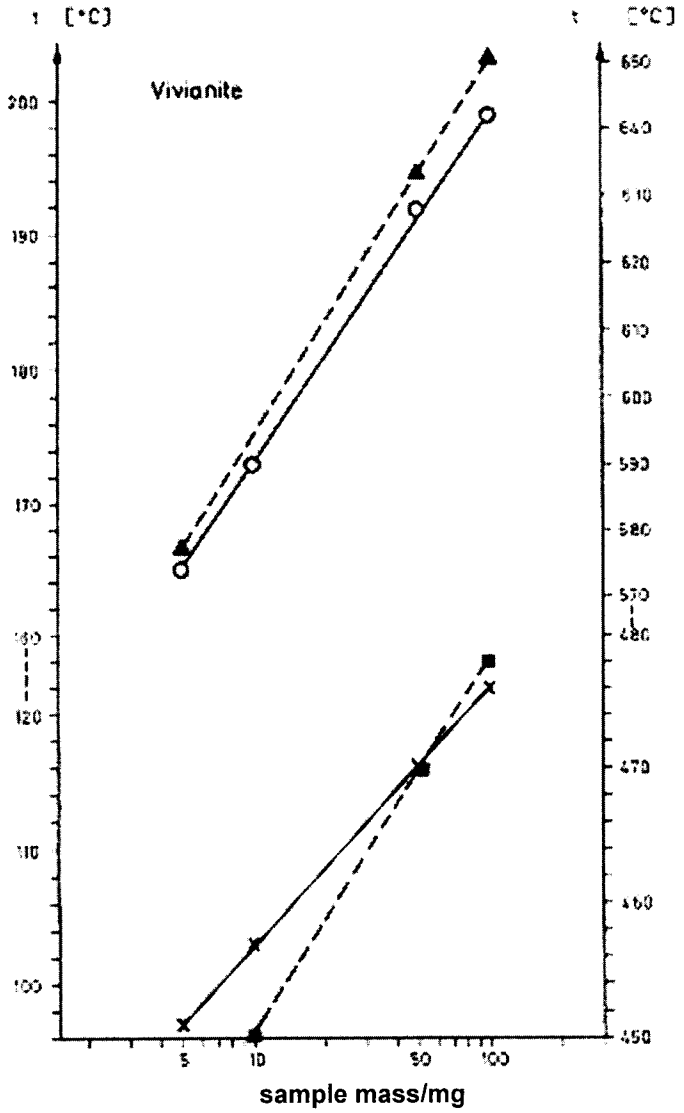


Figure 8. PA-curves of the iron-phosphate vivianite.

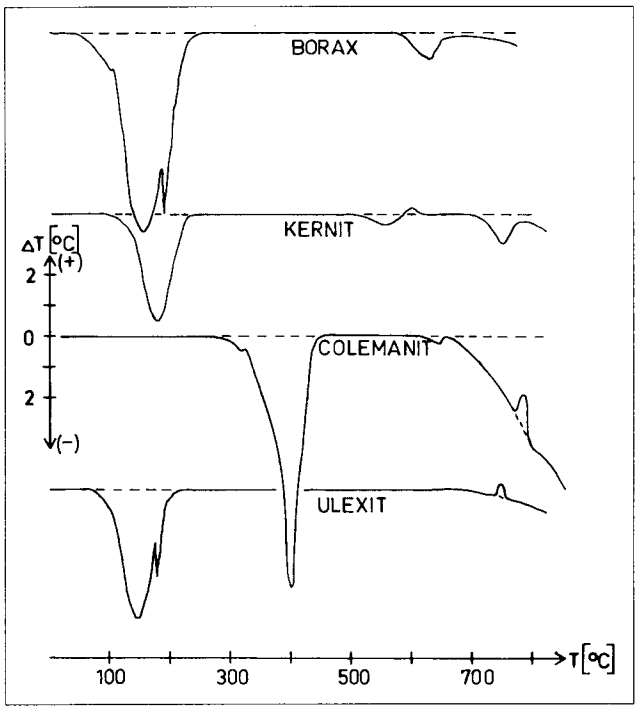


Figure 9. DTA curves of some borates, e.g. of the minerals borax, kernite, colemanite, and ulexite.

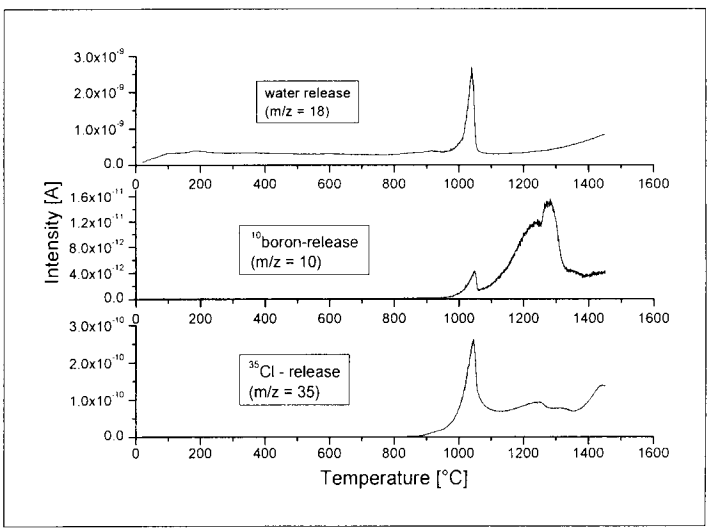


Figure 10. Vacuum decomposition of boracite.

Table 6: DTA data of borates (°C, ± 1°)

formula mineral	dehydration	phase transition	dehydrox.	exotherm.	decomposition melting	reference
$Na_2[B_4O_5(OH)_4] \cdot 8\ H_2O$ borax	75-135, 135-220			580	740 (m), 700-1300	[596]
$Na_2[B_4O_5(OH)_4] \cdot 3\ H_2O$ kernite	70-135, 135-220			580	740 (m), 700-1300	[596]
$Na_4[B_{10}O_{17}] \cdot 7\ H_2O$ ezcurrite	280, 575			680	790	[109]
$NaCa[B_5O_9] \cdot 5\ H_2O$ ulexite I	145, 182, 405			745		[109]
$NaCa[B_5O_9] \cdot 5\ H_2O$ ulexite II	45-150, 150-220		600	615-770		[24]
$Ca[B_2BO_4(OH)_3]$ colemanite I	315, 343, 371, 387		405	782	640	[24]
$Ca[B_2BO_4(OH)_3]$ colemanite II	320-380		410		710-770 (d)	[24]
$Ca_2[B_6O_{11}] \cdot 13\ H_2O$ inyoite	95, 100-130, 395				740 (d)	[82]
$Ca_5[B_{12}O_{23}] \cdot 9\ H_2O$ pandermite	270, 405				840	[82]
$CaMg[B_6O_{11}] \cdot 6\ H_2O$ hydroboracite	315-325			800-890	890	[93]
$Mg_3[Cl/B_7O_{13}]$ boracite		265		625	800-1000 (d)	[117]
$(Fe,Mg)_3[Cl/B_7O_{13}]$ ericaite		338			800 (d)	[117]
$Mg_2[B_6O_{11}] \cdot 15\ H_2O$ inderite	140				780	[82]
$Mg[B_2O_4] \cdot 4\ H_2O$ pinnoite	290-326			800	730-760	[82]
$KMg_2[B_{11}O_{19}] \cdot 9\ H_2O$ kaliborite	275			625-675	750, 815	[82]
$Mg[BO_2OH]$ ascharite			662	700		[83]

The DTA curve of ascharite has been published by Heide [83]. Recently, the dehydration kinetics of howlite, ulexite and tunellite have been studied using TG [114]. Chen Ruoyn et al. [115] reported some thermodynamic data for ulexite. The decomposition temperature mirrors the crystal structural properties and increases with increasing number of boron atoms per formula.

In respect to the thermal transformation, several hydrated borates show the formation of a very viscous glassy state during the heating process. In the DTA-curves the glass transition occurs as a small endothermic effect. The crystallization of the melt can be observed by one or several exothermic effects [113, 116]. The high-temperature behaviour of borates is controlled by the evaporation of boron. The decomposition of borax occurs in two steps: first $NaBO_3$ evolves and then B_2O_3 evaporates (Figure 10). The polymorphy and decomposition of borates with complex anions as boracite $Mg[Cl/B_7O_{13}]$ and the mixed crystals of Fe and Mn varieties (ericaite and cambersite) have been investigated simultaneously by DTA/TGA-MS and thermochromy [117].

2.2.2 Simple hydroxides

The dehydroxylation temperature of hydroxides occurs between 170 °C (sassolite) and 590 °C (portlandite [118]). Figure 11 contains some DTA curves of hydroxides and Figure 12 some PA-curves. For sassolite, $B(OH)_3$, the process of dehydroxylation is overlapped by the evaporation of ortho-boric acid (H_3BO_3) and the formation of meta-boric acid (HBO_2) [119]. With regard to the minerals that form the same type of crystal structure, it is striking that the dehydroxylation temperature seems to increase with *de*creasing size of the cation.

The cation Mg^{2+} forms several partly OH- and H_2O-bearing minerals, which exhibit intermediate decomposition temperatures, due to their amount of (OH) and water (see Table 8). The decomposition of brucite $Mg(OH)_2$ has been discussed in detail by Paulik and Paulik [120], who found newly formed hydrogen evolving in the final stage of decomposition. As shown in Figure 13, the decomposition under high vacuum conditions is complete around 800 °C. Figures 14 and 15 contain the mass-spectrometric/TG characterisation of *goethite*, FeOOH, and of soil *bauxite*, a mixture of the Al-hydroxides *gibbsite* and *diaspore*.

Table 7. DTA data of hydroxides (°C ± 1°)

formula mineral	endothermic reactions (ΔT)	exothermic reactions (ΔT)
α-FeOOH goethite	411 (5.4)	
α-(Fe,Al)OOH Al-goethite (30 mol-% Al; synthetic)	372 (3.4)	
γ-FeOOH lepidocrocite	345 (4.6)	470 (5.2)
γ-$Al(OH)_3$ gibbsite (hydrargillite)	340 (8.2)	
γ-AlOOH boehmite	545 (6.3)	
γ-AlOOH boehmite (from ageing of gibbsite)	526 (2.2)	
α-AlOOH diaspore	572 (6.2)	
α-$Al(OH)_3$ bayerite	325 (11.0)	
γ-MnOOH manganite	370 (4.4)	
$Mg(OH)_2$ brucite	98 (0.35) 135 (0.3) 374 (0.2) 493 (7.5)	
$B(OH)_3$ sassolite	102 (0.5) 172 190 (10.0)	
(Fe_2O_3 x H_2O) limonite	340 (3.7)	423 (5.0) 475 (5.5)

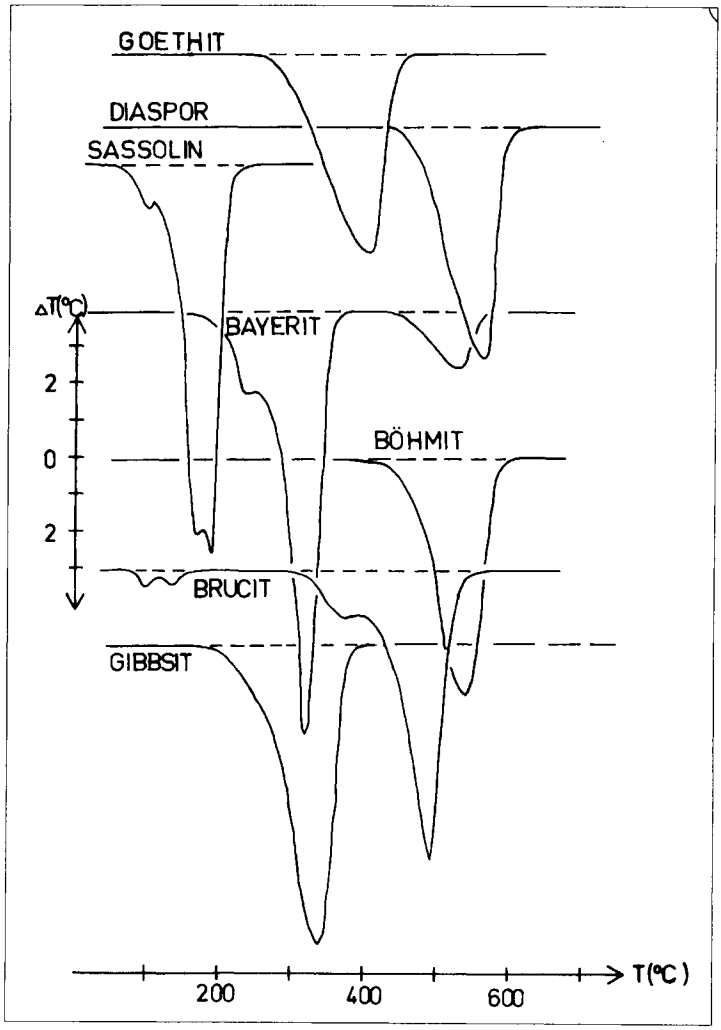


Figure 11. DTA curves of the hydroxides: goethite, diaspore, sassolite, bayerite, boehmite, brucite, and gibbsite.

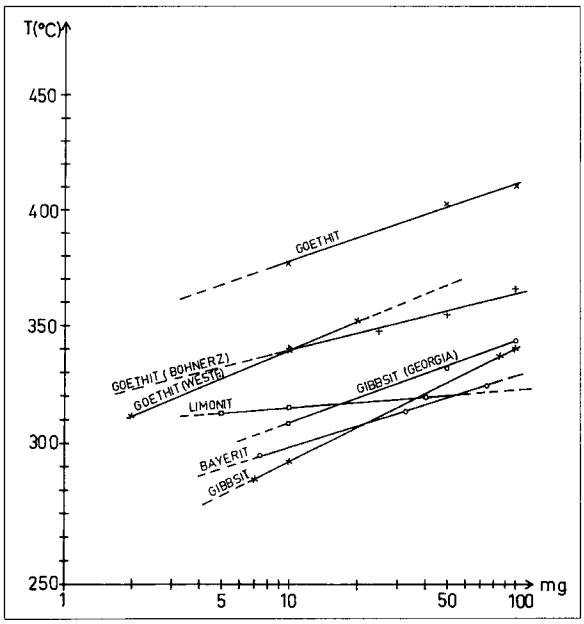


Figure 12. PA-curves of the hydroxides: goethite, limonite, gibbsite, and bayerite. Three different samples of goethite have been analyzed.

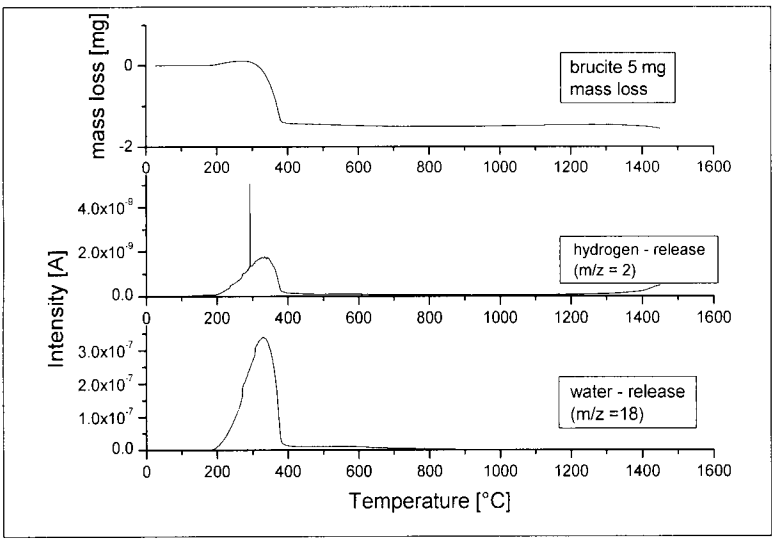


Figure 13. Vacuum decomposition of brucite.

Manganese (3^+, 4^+) forms the largest number of OH-bearing minerals (and of oxides), mainly in the exogenic cycle and caused by weathering and oxidation processes. Thus, many authors have dealt with the thermal behaviour of Mn-(hydr)oxides [10, 24, 91, 121 – 125]. Another reason for this is the fact that the extremely fine-grained and (normally) severely disordered sedimentary Mn-minerals (Mn-oxides, -hydroxides, manganomelanes) cannot be distinguished and identified easily by means of X-ray techniques.

Details on the thermal behaviour of iron hydroxides have been published by Mackenzie [10, 126], Kelly [127], Smykatz-Kloss [24], Keller [128], and Cornell and Schwertmann [129] (see Figure 14). Details on Al-hydroxides and bauxites have been published by Mackenzie [10], Smykatz-Kloss [24], Korneva et al. [130], Földvari [91], Bangoura [131] and Mendelovici [132] (see Figure 15). For manganates see Giovanoli [133] and Kim [134].

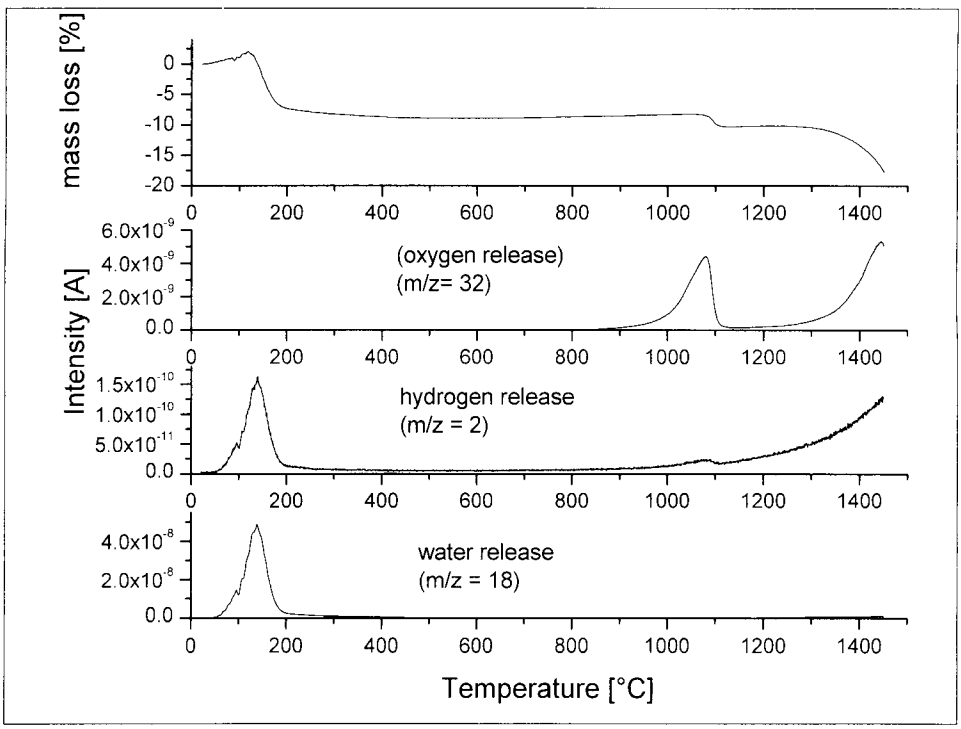


Figure 14. Vacuum decomposition of goethite.

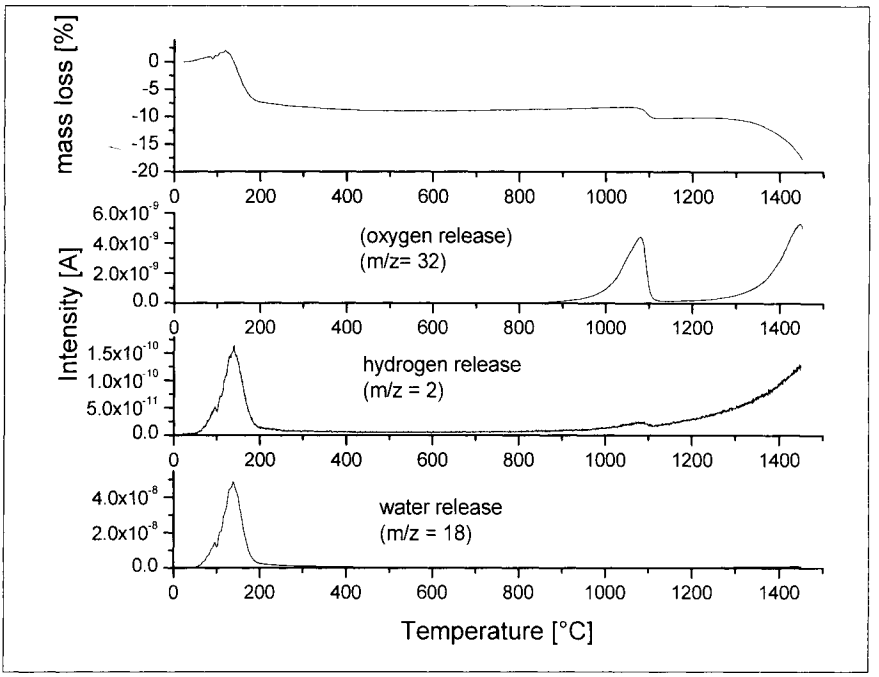


Figure 15. Vacuum decomposition of bauxite. The sample is a mixture of gibbsite and boehmite.

2.2.3. Clays and clay minerals

All clay minerals contain OH, that means they are true hydrolysates. Their particle size is generally < 2 μm in size. Many clay minerals contain H_2O as well. Clays are the most common sediments. Before the routine use of X-ray techniques, thermal methods of analysis were generally applied to identify and characterise clays and clay minerals [3, 4, 8, 17, 51, 135 - 174]. Later, the application of thermal analysis shifted more to special aspects of clay investigation, e.g. to the determination of crystal chemical or crystal physical properties [24, 28, 49, 54, 175 – 183], including kinetic and thermodynamic studies [184 - 186].

Thermal methods of investigations have been applied successfully mainly to *clay mineral mixtures* [24, 146, 187, 188], *sedimentary rocks* (e.g. shales [189, 190], lake sediments [144, 191], soils [8, 159], kaolin [24, 61, 165, 176], bentonites [136] and, impressively, to *amorphous or badly crystallised clay minerals* (e.g. allophanes [24, 192, 193], disordered kaolinites [24, 54, 61, 91], smectites [10, 24, 25, 91, 162, 177, 178, 180, 194, 195], regular mixed layers, corrensite, [24, 155, 171], rectorite [166], tosudite [171], and irregular interstratifications [24, 157, 171, 196]. Different groups of clay minerals have

been the main field of mineralogical TA studies, Mainly by means of DTA, numerous investigations have been carried out which gave insight into the crystal physical (including structural) and crystal chemical properties and which contributed to the geological and petrogenetic characterisation of clays and sediments and to their possible application as raw materials for several technologies and industries (see the section on "applied mineralogy").

Kaolin minerals free of molecular water show a strong endothermic deflection between 530 °C and 590 °C (dickites up to 700 °C) due to the dehydroxylation (Figure 16), and a smaller exothermic effect between 940 and 1000 °C, reflecting the crystallisation of a spinel phase [24, 25, 51, 54, 139 - 143, 198 - 204]. The decomposition of the crystal structure continues after the

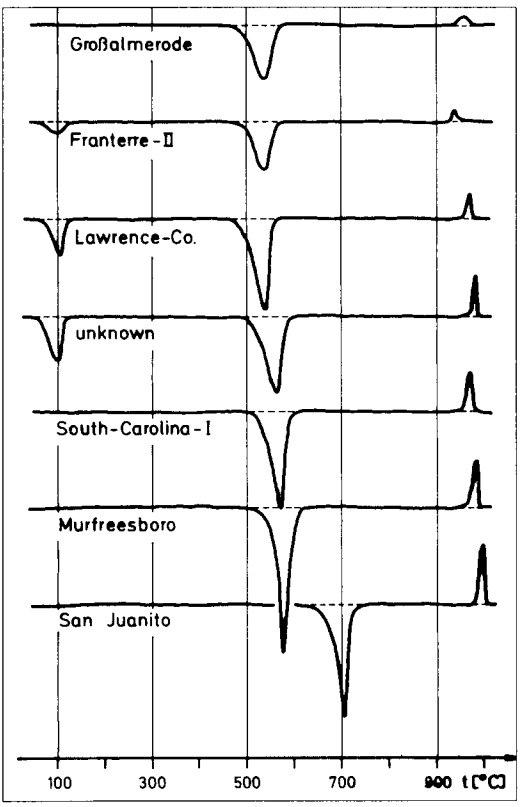


Figure 16. DTA curves of kaolin minerals. The lowest curve represents dickite. The degree of structural order improves from above.

dehydroxylation without a visible effect in the DTA curve. The peak temperature, the intensity and the shape of the endothermic effect are strongly dependent on the degree of disorder of the minerals. This is true for all hydrolysate minerals (hydroxides, OH-bearing silicates, see [24, 59, 61]), the less-defined and ordered the crystal structure, the lower are the peak temperature and intensity, but the broader the (dehydroxylation, decomposition) effect. Thus, a kaolinite which is strongly disordered with respect to the crystallographic b-axis ("fireclay mineral") dehydroxylates at 535 °C, while a well-ordered specimen from Murfreesboro, Arkansas, dehydroxylates at 580 °C (Table 8). In hydrothermal (very well-ordered) dickites this endothermic effect occurs at 700 °C. The dehydroxylation temperature of the famous kaolinite from Keokuk [165] appears between that of a well-ordered kaolinite and of a dickite, similar to some nacrites.

This interdependence of the dehydroxylation behaviour and the degree of disorder of kaolin minerals lead some authors to use it for obtaining a reliable method for the characterisation of structural disorder. Sand and Bates [199] and van der Marel [158] measured the peak area of the dehydroxylation effect, Carthew [200] used the ratio of the peak area to the peak width at half height, Smykatz-Kloss [61] used peak temperatures vs. peak intensity, Smykatz-Kloss [24] and Földvari [54] used PA curves (**PA** = "**P**robenmengen-**A**bhängigkeit"). On the basis of their standardised dehydroxylation temperatures, the kaolin minerals may be classified [24] as:

I	extremely disordered	(dehydroxylation temp. < 530 °C)
II	strongly disordered	(dehydroxylation temp. 530 – 555 °C)
III	slightly disordered	(dehydroxylation temp. 555 – 575 °C)
IV	well-ordered	(dehydroxylation temp. > 575 °C)

For a more detailed classification see [24, 61].

The tri-octahedral, two-layer silicates of the *serpentine* group have been studied by Caillère [137], Midgley [205], Caillère and Henin [206], Naumann and Dresher [207] (chrysotile), Pusztaszeri [208], Basta and Kader [209], Mackenzie [10], Saito et al. [210] (antigorite), and Smykatz-Kloss [24]. The different varieties of serpentine (e.g. antigorite, lizardite, chrysotile) do not differ strongly in their DTA curves (Figure 17). The thermal behaviour of these silicates is fairly similar to that of the Mg-chlorites [24]. The contents of Fe^{2+} lowers the dehydroxylation temperature of serpentines (chlorites, smectites, see [24]). The Fe-analogue to kaolinite and serpentine, e.g. the 2-layer silicate

berthierine, exhibits only the endothermic dehydroxylation effect (peak at 520 - 550 °C, see [10]), but no exothermic deflection.

The simplest 3-layer silicates are the tri-octahedral *talc*, $Mg_3(OH)_2Si_4O_{10}$, and the di-octahedral *pyrophyllite*, $Al_2(OH)_2Si_4O_{10}$ which only occur in metamorphic rocks. The dehydroxylation and decomposition of the Al-species (e.g. pyrophyllite) occurs more than hundred degrees lower than that of the tri-octahedral Mg-type (Figures 18 and 19). DTA curves of talc and pyrophyllite are to be found in publications of Grim and Rowland [141, 142], Schüller [170], Mackenzie [211] and Smykatz-Kloss [24]. In regard to the decomposition of *F*-bearing layer silicates the behaviour of *apophyllite* $KCa_4[F/(Si_4O_{10})_2] \times 8\ H_2O$ is of special interest. As shown in Figure 20 the dehydroxylation is a complex hydrolytic reaction with the formation of HF.

Table 8. DTA data of some kaolin minerals (°C, ± 1°)

mineral sample location	endothermic reactions (ΔT)	exothermic reactions (ΔT)
kaolinite Mesa Alta, N. Mexico	581 (3.9)	1005 (1.3)
kaolinite Mesa Alta, N. Mexico	580 (3.2)	983 (2.1)
kaolinite Murfreesboro, Arkansas	578 (6.1)	983 (2.0)
kaolinite South-Carolina	575 (4.1)	970 (1.5)
kaolinite South-Carolina	573 (3.5)	970 (1.6)
kaolinite Macon, Georgia	569 (4.0)	994 (1.2)
halloysite unknown	567 (3.3)	983 (1.8)
halloysite Djebel Debar, Algerie	555 (6.2)	990 (0.8)
fireclay-mineral Franterre, France	543 (2.0)	943 (0.5)
fireclay-mineral Franterre, France	550 (3.2)	963 (0.5)
fireclay-mineral North Germany	540 (2.3)	965 (0.3)
halloysite-clay Lawrence, Mo.	543 (3.7)	975 (1.0)
dickite San Juanito, Mexico	708 (4.6)	999 (2.5)

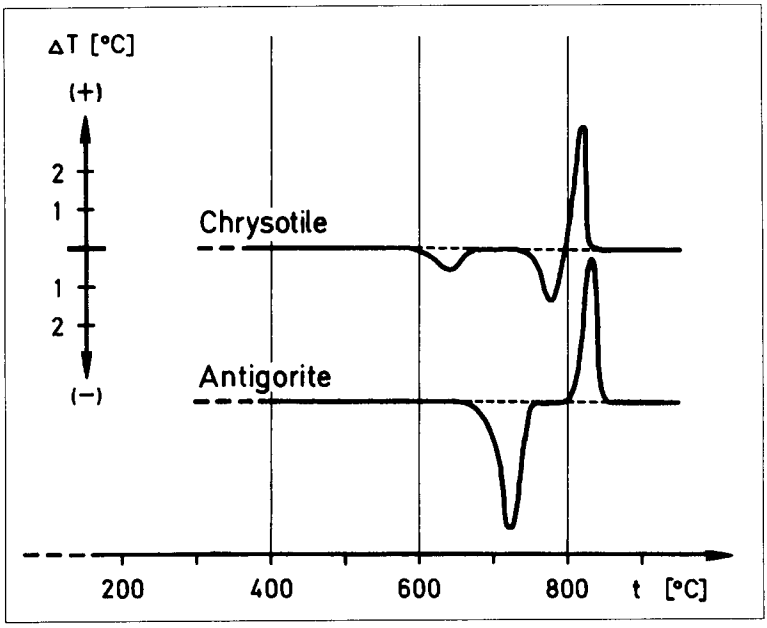


Figure 17. DTA curves of two serpentine minerals, e.g. the fibrous type chrysotile and the layer type antigorite

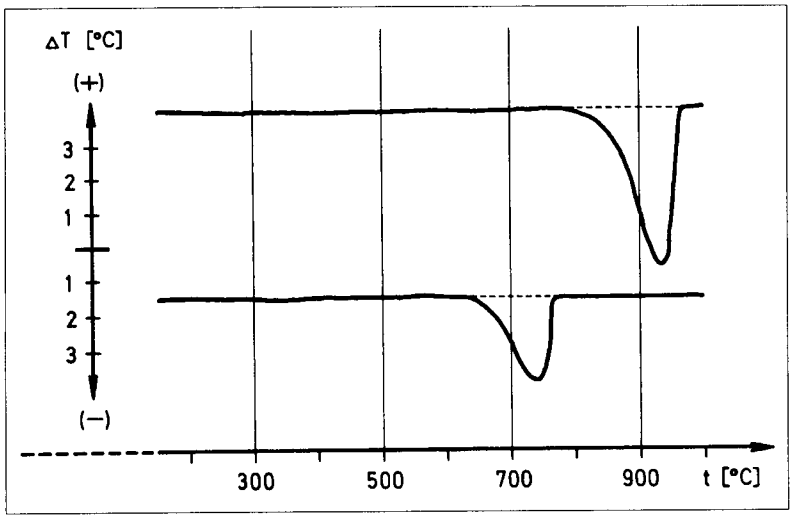


Figure 18. DTA curves of talc (top) and pyrophyllite.

Figure 21 shows the DTA curves of the different mica types, e.g. muscovite, biotite, zinnwaldite, glauconite, illites. The exothermic effect around 400 °C mirrors the content of some divalent iron (biotite, zinnwaldite, Fithian illite). *Micas* show a thermal behaviour strongly depending on their petrographic history. Micas from igneous or metamorphic rocks, which exhibit a high degree of order in their structures, dehydroxylate and decompose at higher temperatures than sedimentary or soil micas (e.g. illites, glauconites, see [24, 158, 179, 211, 212]). The dehydroxylation of micas occurs in the temperature range between 700 and 1050 °C. At temperatures > 1000 °C they start to sinter. As shown in the degassing experiments of biotite, water and fluorine escape first (Figure 22). This endothermic effect is shifted to higher temperatures with increasing titanium content [213] and is thus suitable for measuring the Ti content of biotites. Under the same conditions, the thermal decomposition of muscovite occurs with a maximum at 800 °C (Figure 23) and water and fluorine escape simultaneously. Table 9 gives the DTA data for some micas and other non-swelling 3-layer silicates.

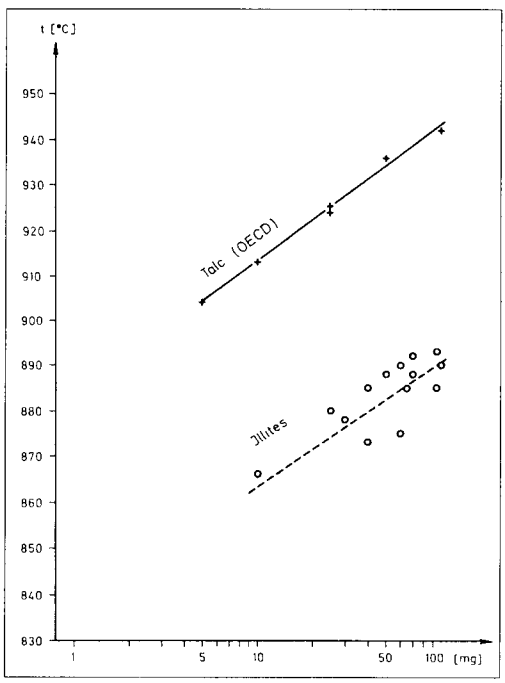


Figure 19. PA-curves of talc and illites. The scattering of the illites is due to crystal physical disorder and the slightly different chemical composition of the three analysed samples [24].

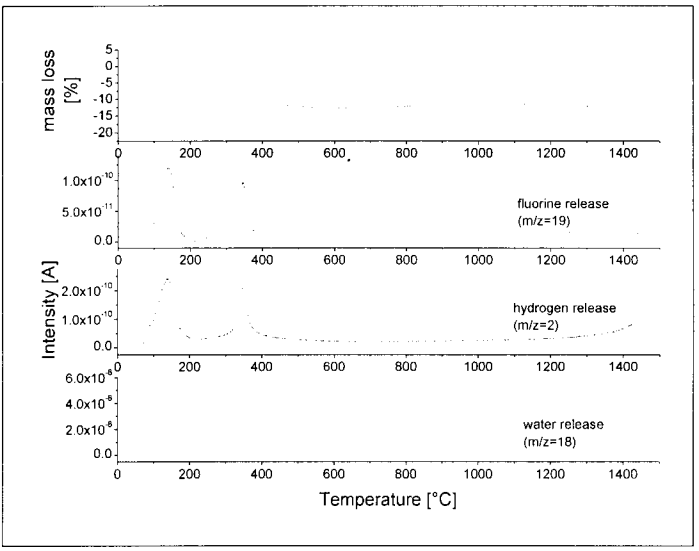


Figure 20. Vacuum decomposition of apophyllite.

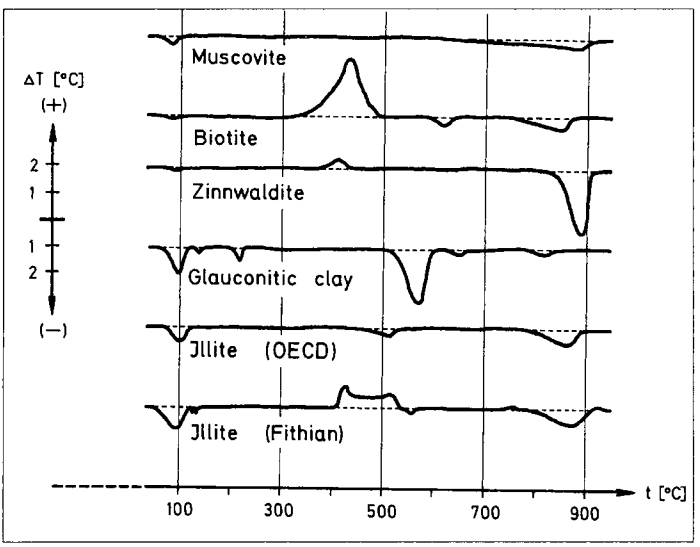


Figure 21. DTA curves of some micas.

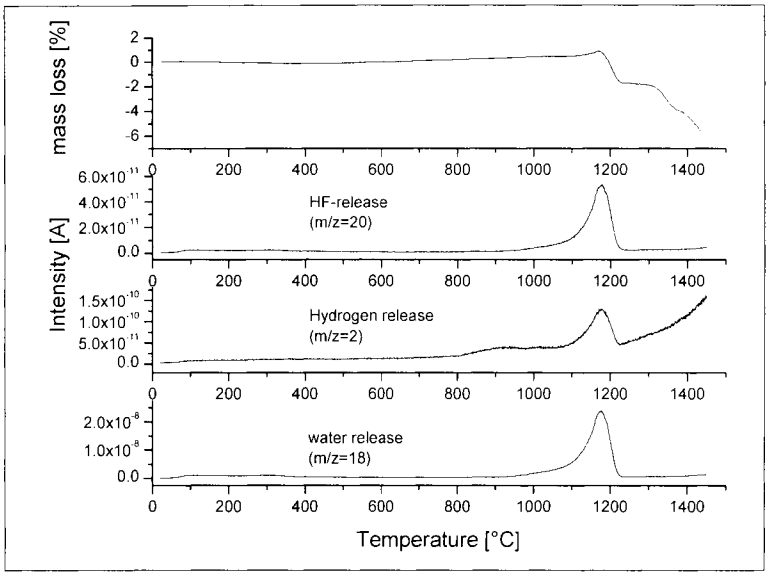


Figure 22. Vacuum decomposition of biotite.

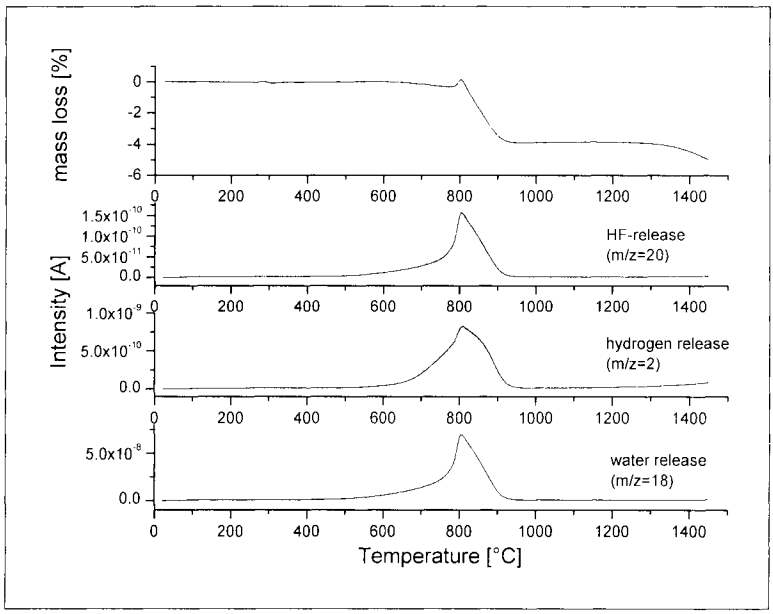


Figure 23. Vacuum decomposition of muscovite.

Table 9. DTA data of some non-swelling 3-layer silicates (°C, ± 1°)

formula mineral	dehydration	dehydroxy- lation (ΔT)	exothermic (ΔT)
$Al_2[(OH)_2Si_4O_{10}]$ pyrophyllite		745 (2.4)	
$Mg_3[(OH)_2Si_4O_{10}]$ talc, OECD		942 (3.0)	
$Mg_3[(OH)_2Si_4O_{10}]$ talc, Greiner / Tyrol		940 (4.6)	
$Mg_3[(OH)_2Si_4O_{10}]$ talc, white, Göpfersgrün		940 (2.7)	
$Mg_3[(OH)_2Si_4O_{10}]$ talc, speckstone		937 (2.8)	
$KAl_2[(OH)_2AlSi_3O_{10}]$ sericite	83	887 (broad)	
$K(Mg,Fe)_3[(OH)_2AlSi_3O_{10}]$ biotite	90	862 (0.4)	435 (2.2)
$K(Fe,Li,Al)_3[(OH)_2AlSi_3O_{10}]$ zinnwaldite	90	891 (2.5)	415 (0.4)
di-octahedral illite, OECD	107	864 (0.6)	
di-octahedral illite, Fithian (0.6-2 μm ∅)	100-150	870 (0.5)	426 (0.8)
di-octahedral illite, Fithian (<0.6 μm ∅)	98-135	878 (0.5)	510 (0.6) 925 (0.1)
di-tri-octahedral, Fe-bearing glauconite I	98-220	822 (0.2)	
di-tri-octahedral, Fe-bearing glauconite II	85-255	810 (0.2)	

Illites and glauconites, "incomplete" or hydro-micas, are richer in silica but poorer in tetrahedral aluminium and interlayer cations than muscovite or biotite, zinnwaldite, paragonite and phlogopite. DTA-curves of the igneous and metamorphic, well-ordered micas have been published by Hunziker [213], Schwander et al. [214], Mackenzie [211], Hansen [215] and Smykatz-Kloss [24] (see Table 9). Fe^{2+}-bearing micas (e.g. biotite, zinnwaldite, tri-octahedral illites and glauconites) show an additional exothermic effect between 400 and 500 °C (due to the oxidation of the Fe^{2+} [24]). DTA-curves of sedimentary micas can be found in publications of Grim and Rowland [141-143], Cuthbert [144], Grim and Bradley [148], Weaver [216], Kautz [217], Smykatz-Kloss [51], Ball [218], and Mackenzie [10]. Mackenzie and Milne [219] observed a strong decrease in the endothermic effects and temperatures after grinding. Smykatz-Kloss and Althaus [62] compared the DTA-curves with infrared and X-ray methods in

characterising the degree of structural disorder. They found the DTA method to be more sensitive than the widely used method of Kubler [220], who characterised the "illite crystallinity" by measuring the width at half-height of the basal XRD interferences. One reason for the differing thermal behaviour of the sedimentary micas (illite, glauconite) may be the fact that many of the sedimentary "micas" investigated have actually been mixed layers of mica and montmorillonite (smectite, bentonite) or chlorite [24].

During the decomposition of the quite complex fluorosilicate *charoite*, $K(Ca,Na)_2[(OH,F)/Si_4O_{10}]\cdot H_2O$, the formation of HF is observed (Figure 24). The release of CO_2 between 800 and 950 °C mirrors some substitution of carbonate anions for OH in the crystalline structure.

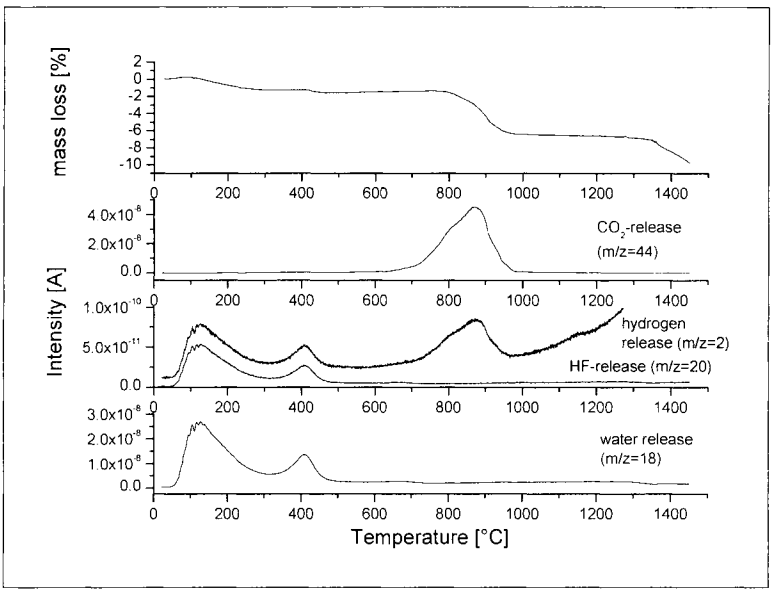


Figure 24. Vacuum decomposition of charoite.

Chlorites, three-layer silicates with another octahedral layer between the three-layer packets, vary strongly in their crystal chemical composition. All change-overs exist between the tri-octahedral talc-chlorite, $Mg_6[(OH)_8Si_4O_{10}]$, thuringite, $Fe_6^{2+}[(OH)_8Si_4O_{10}]$, and the di-octahedral Al-chlorite (sudoite), $Al_4[(OH)_8\ Si_4O_{10}]$, with additional substitutions in the octahedral layer (Zn, Li, Mn, Ni, Cr.) and the tetrahedral layer (Al, Cr, Fe^{3+}).

Table 10. DTA data of chlorites (°C, ± 1°)

mineral sample origin	dehydration (ΔT)	decomposition (ΔT)	exothermic (ΔT)
leuchtenbergite Sunk/Trieben, Austria	624 (1.1)	864 (2.6)	878 (0.2) 913 (0.15)
leuchtenbergite Kaintaleck, Styria, Austria	613 (1.5) 677 (0.3)	853 (0.7)	881 (0.6) 922 (0.1)
leuchtenbergite Ural, Russia	628 (1.0)	837 (0.5)	905 (0.1)
Mg-chlorite Neuberg, Austria	630 (5.5)	845 (0.6)	874 (1.8) 925 (0.1)
ripidolite Chaffee Co., USA	581 (0.2) 650 (0.2)	791 (1.0)	860 (0.3)
clinochlor Zillertal, Austria	580 (0.1)	847 (3.2)	872 (0.1) 900 (0.05)
Mg-prochlorite Kaareck, Austria	656 (0.8)	773 (1.9)	865 (0.3)
aphrosiderite Nassau, Germany	618 (1.2)	721 (0.3)	828 (0.8)
kaemmererite ($Cr^{[6]}$)	744 (1.0)	859 (0.9)	
kotschubeite ($Cr^{[4]}$)	604 (0.4) 639 (0.6)	801 (0.2)	828 (0.2)
pseudothuringite Carinthia, Austria		607 (2.2)	828 (1.2)
Fe-chlorite Canaglia, Alps		541 (2.0)	
Fe-chlorite (Lias) Czech Republic		526 (0.6)	
thuringite Schmiedefeld, Saxony, Germany		539 (1.9)	
chamosite (minette-ore) Lorraine, France		523 (0.6)	
Al-chlorite Cornberg, Hesse, Germany		498 (0.8)	898 (0.3)
prochlorite Marktredwitz, Bavaria, Germany	614 (2.1)	827 (0.5)	848 (0.8)
prochlorite, > 6 µm ∅ Marktredwitz, Bavaria, Germany	617 (2.2)	833 (0.9)	855 (0.8)
prochlorite, < 6 µm ∅ Marktredwitz, Bavaria, Germany	614 (2.2)	833 (1.2)	853 (1.0)
prochlorite, > 2 µm ∅ Marktredwitz, Bavaria, Germany	610 (1.7)	833 (0.8)	850 (0.7)
prochlorite, < 2 µm ∅ Marktredwitz, Bavaria, Germany	616 (1.75)	827 (0.5)	847 (0.7)

Table 11: Interdependence between chemical composition, decomposition temperatures and temperature of the exothermic peak of chlorites [24]

mineral origin	mass-% MgO	mass-% Fe_2O_3	dehydrox.	exotherm.	a-value	class
leuchtenbergite Ural, Russia	34.2	2.25	837			clinochlorite
leuchtenbergite Kärnten, Austria	33.6	2.54	864	881	17	clinochlorite
leuchtenbergite Sunk, Austria	33.5	2.4	856	878	22	clinochlorite
leuchtenbergite Neuberg, Austria	30.1	1.05	845	874	29	clinochlorite
grochauite Zillertal, Alps	25.7	10.2	847	872	25	clinochlorite
kaemmererite (8.7% Cr_2O_3)	35.12		858			$Cr^{[6]}$-chlorite
pennine Rimpfischwäng, Switzerland	28.4	5.6	820	836	16	pennine
pennine Rimpfischwäng, Switzerland	28.4	6.75	818	832	14	pennine
pennine Rimpfischwäng, Switzerland	26.6	8	809	827	18	pennine
pennine Rimpfischwäng, Switzerland	26.45	7.9	817	833	16	pennine
pennine Marktredwitz, Germany	27.1	5	832	852	20	pennine
pennine Marktredwitz, Germany	23.9	11.15	833	850	17	pennine
pennine Marktredwitz, Germany	23.5	11.95	827	847	20	pennine

Table 11: cont.

mineral origin	mass-% MgO	mass-% Fe_2O_3	dehydrox.	exotherm.	a-value	class
pennine Marktredwitz, Germany	22.6	12.7	833	853	20	pennine
pennine Marktredwitz, Germany	22.55	10.8	827	847	20	pennine
pennine Marktredwitz, Germany	21.3	14.7	833	855	22	pennine
kotschubeite (5.0% Cr_2O_3)	30.4	14.9	801	828	27	$Cr^{[4]}$-chlorite
prochlorite Chaffee Co., USA	20.25	11.6	791	860	69	ripidolite
prochlorite Kaareck, Austria	17.4	25.85	773	865	92	ripidolite
pseudothuringite Maltatal	14.35	28.6	731	828	97	Fe-Mg-chlorite
aphrosiderite Al-286	13.12	26.15	730	827	97	Fe-Mg-chlorite
aphrosiderite Al-288	12.8	26.7	725	828	103	Fe-Mg-chlorite
aphrosiderite Nassau, Germany	12.5	25.6	721	828	107	Fe-Mg-chlorite
thuringite Schmiedefeld, Germany	2.75	49.7	539			Fe-chlorite
Fe-chlorite Canaglia, Sardinia	2.84	41.5	541	805	264	Fe-chlorite
Lias-chlorite Czech Republic	3.7	9.5	526			Al-chlorite
cookeite Cornberg, Germany	1.6	2.3	511	898	387	Al-chlorite

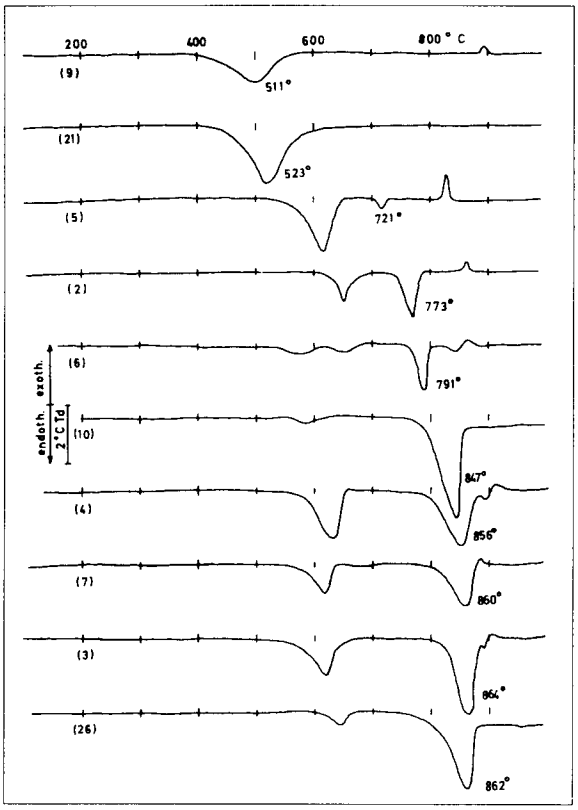


Figure 25. DTA curves of chlorites. The content of MgO increases from top to bottom.

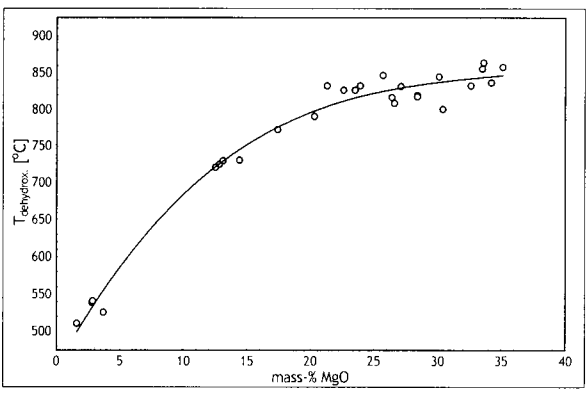


Figure 26. Dependence of the decomposition temperatures of chlorites on the MgO content.

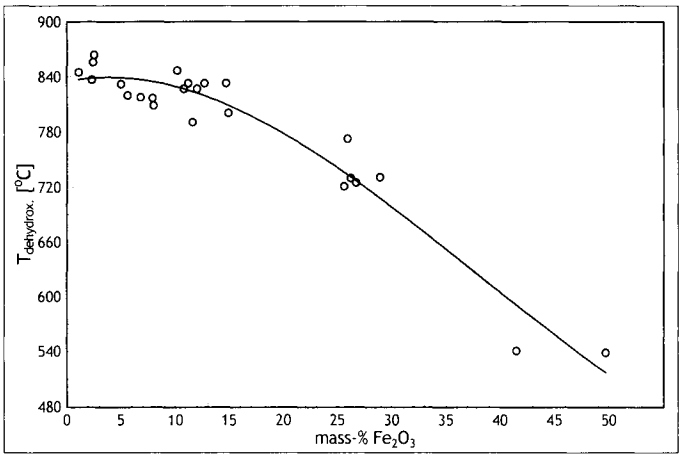


Figure 27. Dependence of decomposition temperature of chlorites on the Fe_2O_3 content.

DTA is very suitable for classifying the chlorite minerals [24]. The dehydroxylation and decomposition temperatures increase with increasing Mg-content, from nearly 500 °C for Mg-free species (e.g. the iron and the aluminium chlorites), to 860 °C for pure Mg-chlorites (Table 11, Figure 25). The exothermic effect decreases with increasing Fe-content, occurring at 920 °C (for pure Mg-chlorites) and at 810 °C for thuringites (= Fe-chlorites) (Figure 26). Pure (Mg-free) Fe-chlorites do not show an exothermic effect. DTA curves for chlorites have been published by Orcel et al. [151], Brindley [152], Phillips [156], Caillère and Henin [206], Lapham [223], Eckardt [224], Albee [163], Ross [226] and Chen [227], for Cr-thuringite by Borst and Katz [228], Mackenzie [10], and Černy et al. [174], and for cookeite by Smykatz-Kloss [24]. The decomposition of chlorites occurs in two steps,which are also related to hydrogen release. Carbon dioxide is obviously frequently incorporated in the structure. The highest dehydroxylation temperature is exhibited by the Cr-chlorite *kaemmererite* (858 °C, Figure 26, Table 11 and 12) and the lowest by Fe-chlorites (*thuringites*).

Lapham [223] showed that DTA was very suitable for the differentiation between both types of Cr-chlorites: *kotschubeite* and *kaemmererite*. Kotschubeite has the Cr incorporated into the $[SiO_4]$ tetrahedron and dehydroxylates and decomposes at a temperature more than a hundred degrees lower than kaemmererite (where the Cr is incorporated into the octahedral layer). With the exception of the $Cr^{[4]}$-chlorite kotschubeite, the dehydroxylation/decomposition temperatures of all the other (well-ordered) chlorites studied depend strongly on their MgO-content ([24], Figure 26, Table

11). One Cr-thuringite [227], with 0.22 mass % Cr_2O_3, 38.5 % Fe_2O_3 and 5.25 % MgO, shows a strong dehydroxylation/decomposition peak at 590 °C and fits very well to this interrelation (Figure 26). Table 12 contains the classification of chlorites on the basis of their thermal and chemical data.

Sedimentary chlorites dehydroxylate at a temperature 100 °C lower than igneous or metamorphic species of the same crystal chemical composition, due to their larger degree of structural disorder [24]. That means, this interrelation between the MgO content and the temperature of dehydroxylation is only valid for well-ordered chlorites, e.g. those from metamorphic and igneous rocks.

The "a-value" (= temperature interval between the last decomposition peak and the following exothermic peak, Table 11) has been introduced by Smykatz-Kloss [24]. A fairly reliable interdependence exists between this value and the content of MgO (see Figure 28). The larger the MgO content, the lower the a-value.

The *swelling* clay minerals of the *smectite* and *vermiculite* groups show similar thermal behaviour, endothermic reactions before 250 °C due to the dehydration of interlayer water, and between 450 °C (Fe-members) and 860 °C (Mg-members) due to the dehydroxylation, and an exothermic effect (which may be missing in the case of some Fe-rich minerals, e.g. nontronite, jefferisite) around 840 °C (vermiculite) and between 920 and 1000 °C (smectites). Some Mg-rich smectites and vermiculites exhibit a small endothermic effect shortly before the exothermic peak [24]. DTA curves of swelling clay minerals have been published by Orcel and Caillère [136], Grim and Rowland [141-143], Grim [146], Barshad [147], Kulp and Kerr [229, 230], Faust [153], sauconite, Earley et al. [154], Weiss et al. [231], saponite, Mackenzie [8, 160, 211], Bassett [161], Cu-vermiculite, Grim and Kulbicki [162], Nemecz [232], Takeuchi et al. [233], Boss [168], vermiculite, Wilson et al. [169], saponite, Smykatz-Kloss [24], Earnest [177, 178, 180], Stepkowska and Jefferies [181], Stepkowska et al. [182], Sun Kon et al. [184], Mekhamer et al. [186], thermodynamics.

The decomposition of bentonite (montmorillonitic alteration product of volcanic ash) is characterized by continuous dehydration with a maximum at 550 – 600 °C and simultaneous escape of hydrogen.

Table 12. Classification of chlorites [24]

class (number of specimen)	MgO [mass-%]	Fe_2O_3 [mass-%]	dehydroxyl. temp.[°C]	∅	exothermic effects [°C]	a-value [°C]
talc-chlorite (5)	35-30	< 2.5	864-837	852	881-874	17-29
$Cr^{[6]}$-chlorite (1)	35	-	858	858	-	-
pennine (10)	28.5-21	5-15	833-809	825	855-827	14-22
prochlorite (2)	20.5-17.5	12-26	790-770	782	865-860	69-92
Fe-Mg-chlorite (4)	14.5-12.5	26-29	730-720	727	828	97-107
Fe-chlorite (2)	< 3	> 40	541-539	540	805	264
Al-chlorite (2)	3.5-1.5	2.5-10	526-511	518	898	387

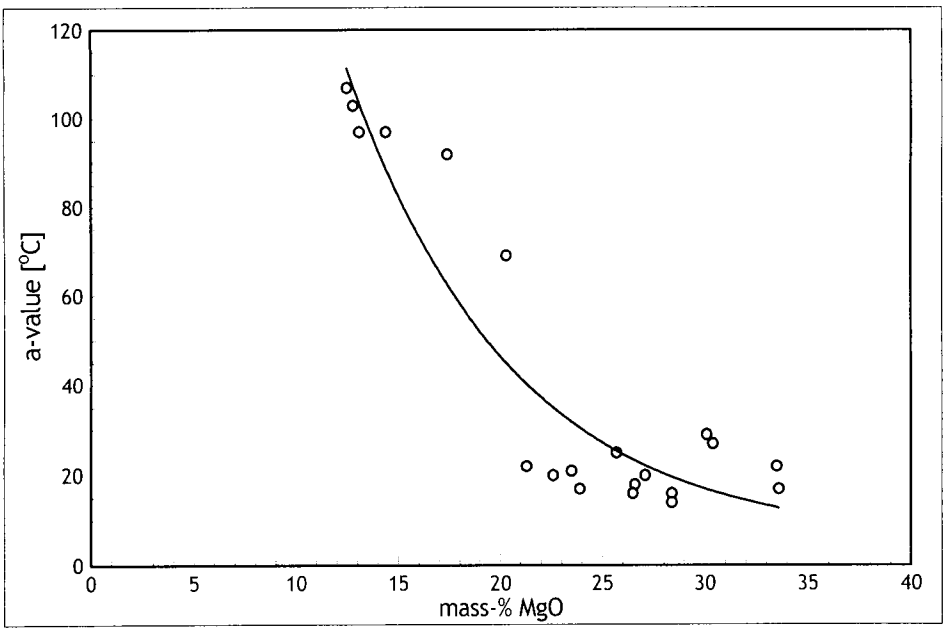


Figure 28. The "a-value" (= temperature interval between the last decomposition peak and the following exothermic peak, Table 11) versus MgO content of chlorites [24].

Similarly to the chlorites, the smectites show solid solutions between two di-octahedral Al-members (e.g. beidellite and montmorillonite), two Fe-members (nontronite, volkhonskoite, the latter incorporates some additional Cr) and tri-octahedral Mg-members (saponite, sauconite, hectorite etc.). The pure end-member minerals occur in nature, but most of the natural smectites are solid solutions. With regard to the vermiculites, the other group among the swelling clay minerals, more than 95% are tri-octahedral Mg-minerals. Only at special locations and in distinct environments do some types occur in which the Mg is substituted either by Fe^{2+} (jefferisite), Al (partly) or -rarely- by Cu [161].

DTA has proved to be very suitable for the characterisation of smectites and (to a lesser extent) of vermiculites [24, 177, 178, 180, 234]. The main smectite types exhibit very different dehydroxylation temperatures, e.g. 450-520 °C for Fe-smectites, 670-730 °C for Al-smectites, 770-860 °C for Mg-smectites (Table 13, Figure 29). This means that the types of octahedral cations determine the dehydroxylation temperatures. For two or more different octahedral cations, a further two or more dehydroxylation effects will appear in the DTA-curve. The temperature of the exothermic effect does not seem to be influenced by the crystal chemical composition of the smectite (except for some Fe-rich smectites, where it is missing).

Due to its dehydroxylation behaviour the smectite "*otayite*" from Otay (California) should not be characterised as "montmorillonite" (as is quite usual in the literature), but more clearly be placed in a separate group (tri-di-octahedral, [24]).

Vermiculites often undergo dehydration in several steps [24, 211, 234], which is caused by some orientated water layers at the contact to the inner surface *and* by the water of the central interlayer space.

The extremely large field of *pillared clays* and the importance of thermal analysis for this field is discussed below. One component of these organo-clays is a swelling layer-silicate (montmorillonite, hectorite, vermiculite). But the properties of these intercalation products are mainly determined by the type and the size of the organic molecules which, after having penetrated the space between the layers, may be partly removed, thus forming large cavities between remaining pillars. The application of swelling clay minerals, especially of organo-smectites (-vermiculites) and of pillared clays have been reported in many areas of chemical engineering (see [64, 434, 435]).

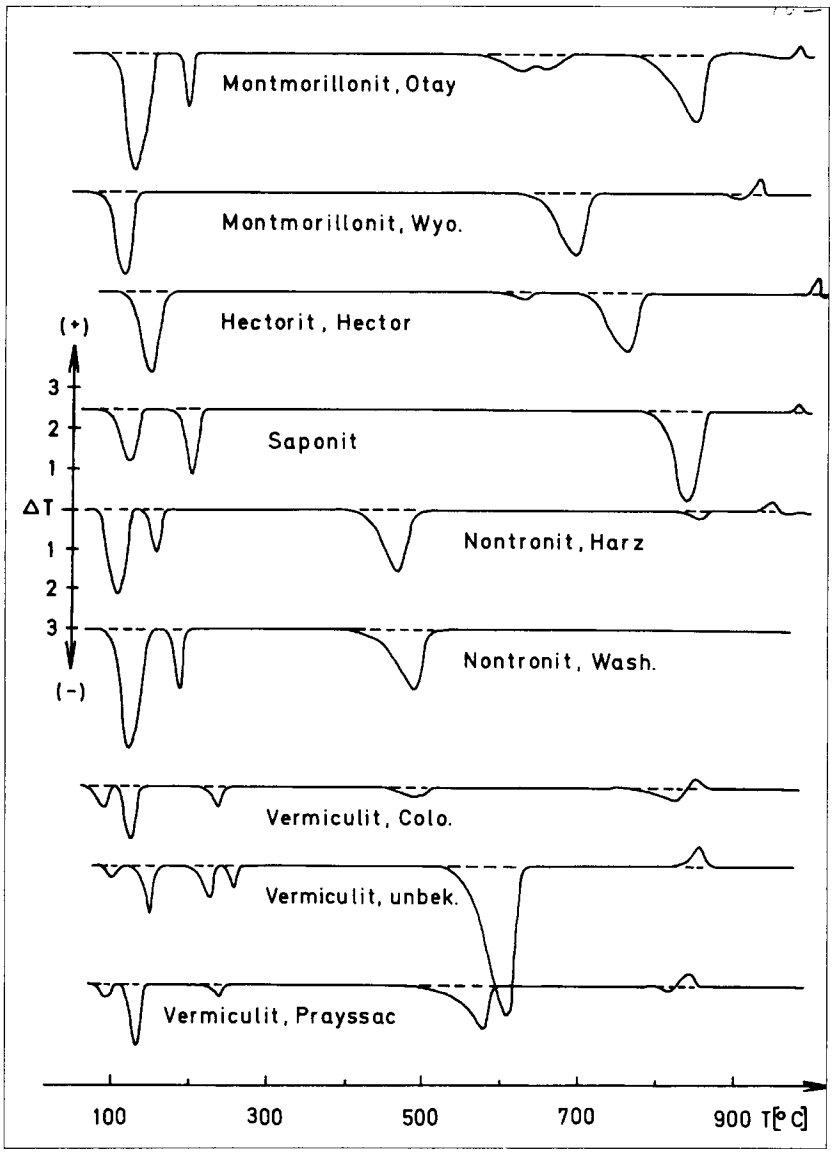


Figure 29. DTA curves of some swelling clay minerals.

Table 13: DTA of swelling clay minerals (°C, ± 1°)

mineral origin	octahedral cations	dehydration	dehydroxylation / decomp.	exothermic	reference
montmorillonite Upton	Al, Mg	118	702	936	[24]
montmorillonite OECD	Al, Mg	132, 190	674, 880	1000	[24]
montmorillonite Hesse / Germany	Al, Mg	145, 220	725	947	[24]
montmorillonite Chambers / Arizona	Al, Mg	160, 220	665, 860	990	[180]
otayite Otay	Al, Mg	135, 197	632, 653, 855	986	[24]
beidellite	Al	140, 205	560		[197]
nontronite Harz / Germany	Fe^{III}, Fe^{II}	110, 160	470, 860	950	[24]
nontronite Garfield	Fe^{III}, Fe^{II}	126, 188	493		[24]
nontronite Hoher Hagen / Germany	Fe^{III}, Fe^{II}	140	505, 780		[126]
volkhonskoite Ural	Fe^{III}, Cr^{III}	190, 220	480	810	
saponite Fichtelgebirge / Germany	Mg	127, 204	842	985	[24]
saponite II Fichtelgebirge / Germany	Mg, Fe^{II}	175, 266	600, 775, 818		[284]
saponite III Fichtelgebirge / Germany	Mg	136, 251	858		[284]

Table 13: cont.

mineral origin	octahedral cations	dehydration	dehydroxylation / decomp.	exothermic	reference
hectorite	Mg, Li	110, 162	728	828	[222]
hectorite S.Bernardino / California	Mg, Li	110	750, 835		[178]
sauconite	Mg, Zn, Al	178, 286	582, 734	833, 978	[153]
stevensite	Mg, Zn	152	628, 812, 862	429	[153]
vermiculite Colorado	Mg, Al	90, 125	503, 826	851	[24]
vermiculite II Colorado	Mg, Al	180, 280	585, 860	880	[24]
vermiculite Prayssac	Mg, Al	95, 133, 240	580, 816	845	[24]
vermiculite unknown		100, 151, 228, 263	610	865	[24]
corrensite Swabia / Germany	Mg, Al	140, 220	640, 810	825	[155]
corrensite Hesse / Germany	Mg, Al	110	600, 825	845	[24]
rectorite	Al, Mg	140, 220	600, 950	1030	[171]
tosudite	Al	130, 220	610, 860	920	[171]
irreg. chlorite / smectite	Mg, Al	115, 146	635, 665 830	875	[171]
irreg. chlorite / smectite	Al, Mg	98, 202	533, 557, 680, 763	808, 897	[171]

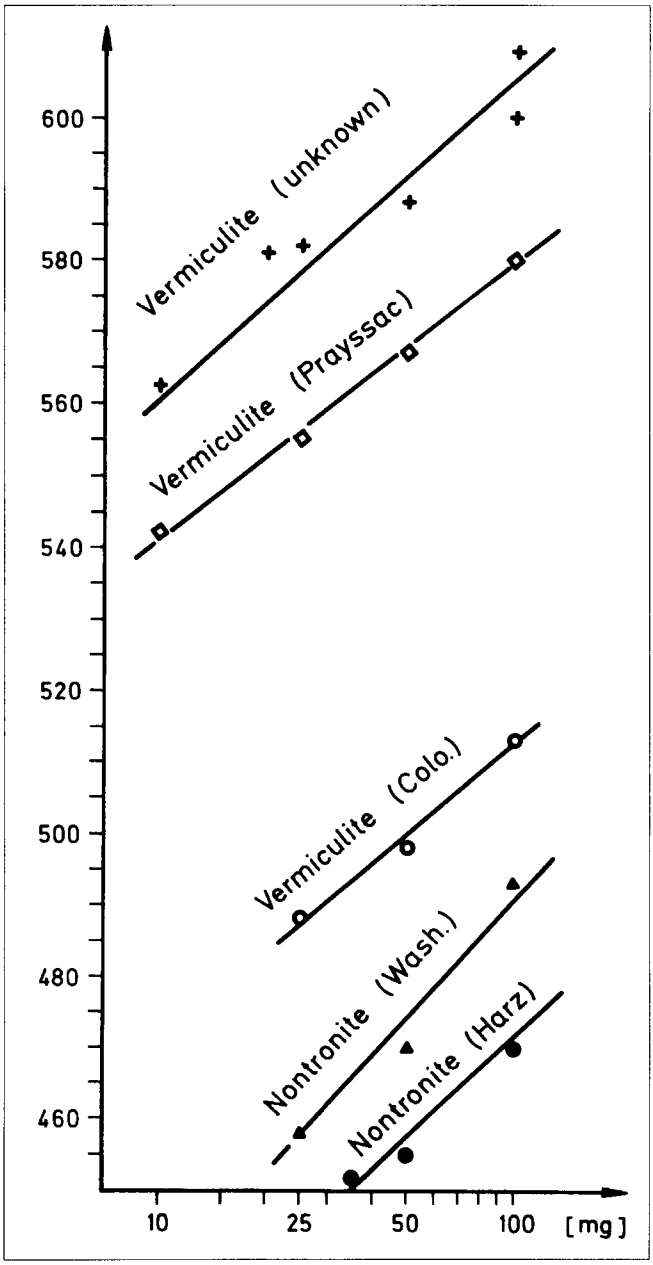


Figure 30. PA-curves of some swelling minerals.

Recently, compact and dense structures, like those of the two-layer silicates of the kaolinite group, have also been used for forming intercalation products [185, 453, 457]. The thermal behaviour of these products is quite similar to that of the organo-smectites.

The most common group of clay minerals in nature is that of *interstratified* minerals (mixed layers). Only a few *regular* interstratifications occur exhibiting a distinct ratio (1,1,2,1) of the components, e.g. *corrensite* (chlorite/vermiculite or chlorite/smectite, ratio 1,1), *rectorite* (illite/montmorillonite, 1,1), *kulkeite*, *tarasovite* or *tosudite* (sudoite/montmorillonite, 1,1). The thermal properties of these regular interstratifications are sometimes similar to those of the components (e.g. corrensite [24, 155], or rectorite [166]), but in other cases quite different [171].

Irregular mixed layers belong to the most frequent minerals of soils and young sediments, and their exact determination requires complex and combined methods of investigation. Thermal analysis may sometimes help significantly, but it will only be an additional method among others, e.g. X-ray diffraction of orientated (textured) specimen, infrared spectroscopy, swelling and heating techniques [24, 171]. DTA curves of mixed layers are shown in Figure 31.

The *amorphous* Al-(Fe-) silicates, *allophane* and *hisingerite,* dehydrate between 110 and 140 °C ([24, 192, 193, 235, 236]; Table 14). Like kaolin minerals, they show an exothermic effect between 880 and 1000 °C which mirrors the formation of an Al-spinel. The temperature of this effect is strongly dependent on the iron content of the mineral ([24]; Table 14). Some allophanes include a small endothermic (dehydroxylation) effect between 400 and 500 °C which shows the beginning of crystalline ordering, e.g. the beginning of formation of weakly ordered halloysite [235]. Well-crystallised *halloysite* shows a similar thermal behaviour (Table 14, Figures 16 and 33, e.g. see [24, 199, 204]).

There remains the discussion of some clay minerals which do not belong to the layer silicates, e.g. the Mg-silicates *palygorskite* (attapulgite), $(Mg, Al, Fe)_2[OH/Si_4O_{10}] \cdot 2\,H_2O + 2\,H_2O$, *sepiolite* ("Meerschaum") $(Mg,Fe)_4[(OH)_2 Si_6O_{15}] \cdot 2\,H_2O + 2\,H_2O$, and *loughlinite,* $Na_2Mg_3[(OH)_2Si_6O_{15}] \cdot 2\,H_2O + 2\,H_2O$. The two kinds of water are well differentiable in DTA [24]. The thermal behaviour of palygorskite is similar to that of vermiculites (Figure 17, Table 15). Fe^{2+} causes a strong exothermic effect in (Fe-) sepiolite (Figures 34 and 35). Figure 32 shows the PA-curves of chlorites and corrensite.

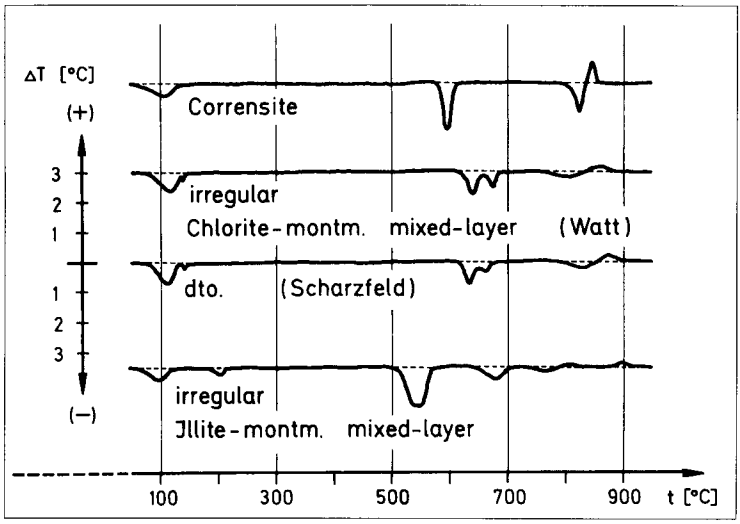


Figure 31. DTA curves of swelling clay minerals

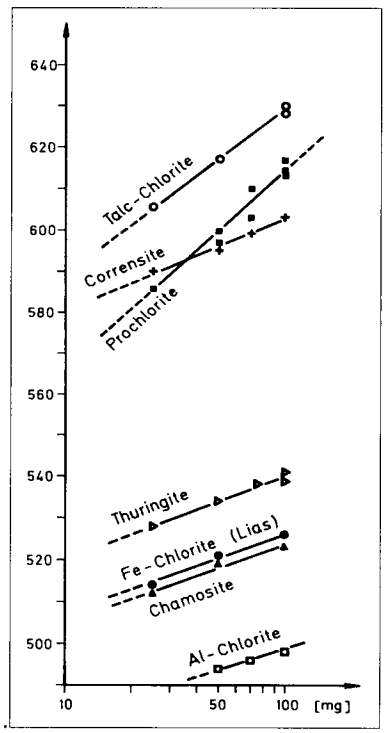


Figure 32. PA-curves of chlorites and corrensite.

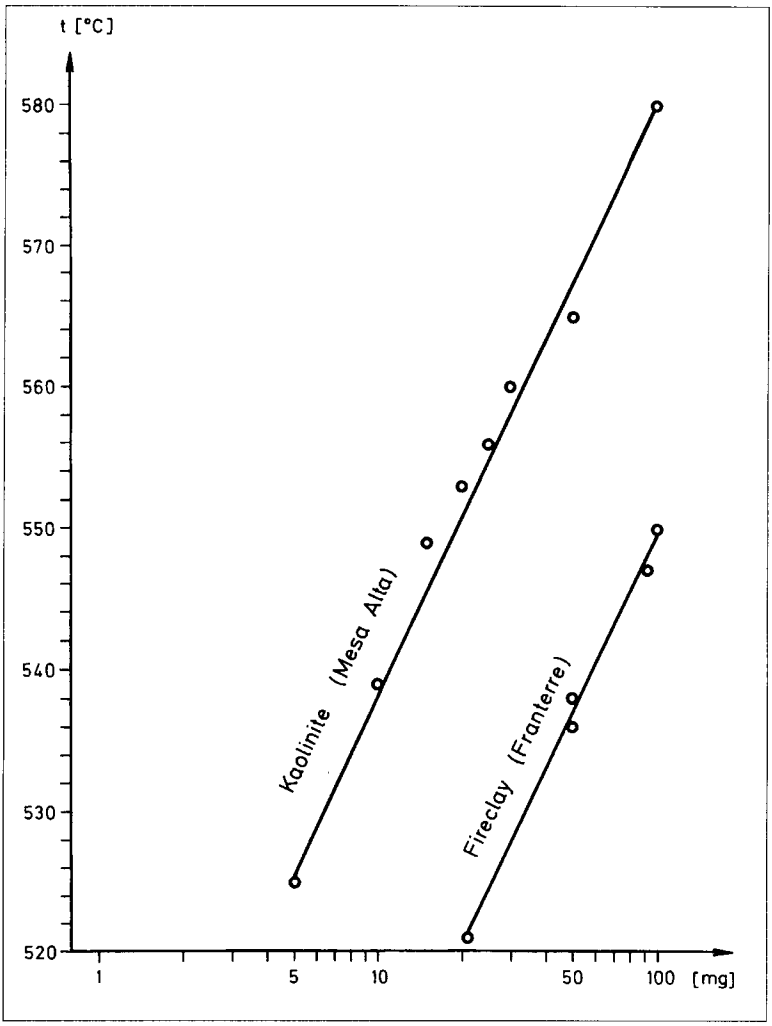


Figure 33. PA-curves of two kaolin minerals, e.g. one well ordered (Mesa Alta) and one strongly disordered (Franterre).

Table 14: DTA data for amorphous and disordered di-octahedral 2-layer silicates (from [24], except 1 & 2; °C, ± 1°; ΔT: °C, ± 0.1; Ni crucibles, 100 mg, 10 K/min)

mineral origin	composition / formula	dehydration temp.	ΔT	dehydroxylation temp.	ΔT	exothermic temp.	ΔT
allophane	SiO_2 / Al_2O_3 = 1 / 2	112	1.6			960	0.6
allophane, Fe-bearing	SiO_2 / Al_2O_3 / Fe_2O_3 = 1 / 1.5 / 0.2	116	1.8			923	0.2
hisingerite	SiO_2 / Al_2O_3 / Fe_2O_3 = 1 / 1.3 / 0.4	109	1.5			890	0.1
hisingerite, synthetic 1	SiO_2 / Al_2O_3 / Fe_2O_3 = 1 / 1.3 / 0.4	129		427		920	
kaolinite, disordered N-Germany	$Al_2[(OH)_4Si_2O_5]$			540	2.3	965	0.3
kaolinite, disordered Franterre	$Al_2[(OH)_4Si_2O_5]$			543	2.0	943	0.5
kaolinite, disordered Franterre II	$Al_2[(OH)_4Si_2O_5]$			550	3.2	963	0.5
halloysite Lawrence / Colorado	$Al_2[(OH)_4Si_2O_5] \cdot 2\ H_2O$	120	4.5	543	0.7	975	1.0
halloysite Djebel Debar / Algeria	$Al_2[(OH)_4Si_2O_5] \cdot 2\ H_2O$	125	4.0	555	6.2	990	0.8
halloysite Djebel Debar / Algeria II	$Al_2[(OH)_4Si_2O_5] \cdot 2\ H_2O$	122	4.0	567	3.3	983	1.8
kaolinite Georgia	$Al_2[(OH)_4Si_2O_5]$			569	3.3	994	1.2
kaolinite S-Carolina	$Al_2[(OH)_4Si_2O_5]$			573	3.5	970	1.6
kaolinite S-Carolina II	$Al_2[(OH)_4Si_2O_5]$			575	4.1	970	1.5

Table 14: cont.

mineral origin	composition / formula	dehydration temp.	ΔT	dehydroxylation temp.	ΔT	exothermic temp.	ΔT
kaolinite Murfreesboro	$Al_2[(OH)_4Si_2O_5]$			578	6.1	983	2.0
kaolinite Mesa Alta / N-Mexico	$Al_2[(OH)_4Si_2O_5]$			580	3.2	983	2.1
kaolinite Mesa Alta / N-Mexico	$Al_2[(OH)_4Si_2O_5]$			581	3.9	1005	1.3
kaolinite Keokuk	$Al_2[(OH)_4Si_2O_5]$			680		1000	
dickite Mexico	$Al_2[(OH)_4Si_2O_5]$			708	4.6	999	2.5

Table 15: DTA data of palygorskites and sepiolites ([24]; °C, ± 1°; ΔT: °C, ± 0.1)

mineral origin	dehydration (ΔT)	dehydroxylation (ΔT)	exothermic temp.	ΔT
palygorskite OECD	108 (1.0), 139 (0.3), 285 (0.2)	478 (2.5), 706 (0.4), 808 (0.1)	910	0.5
palygorskite Midway / Florida	160 (0.8), 285 (0.2), 316 (0.1)	482, 509 (3.0), 853 (0.2)	880	0.6
sepiolite Granada / Spain	99, 113 (1.0)	630 (0.2), 800 (0.6)	824	0.2
sepiolite Eskisehir / Turkey	100 (0.4, broad)	550 (0.4), 745 (0.2)	840	1.0
sepiolite Eskisehir / Turkey II	80 (0.2, broad)	577 (0.4), 756 (0.25)	835	0.8
sepiolite , Fe-bearing Eskisehir / Turkey	128 (1.6), 387 (0.5)	506 (3.0)	840	3.0

Table 16. Dehydroxylation/decomposition temperatures of some layer silicates (°C, ± 1°)

mineral	Fe – (OH)	Al – (OH)	Mg – (OH)
nontronite	480		
Fe-vermiculite	503		
berthierine	523		
pseudo-thuringite	540		
glauconite	550		
illite, di-octahedral		550	
kaolinite		580	
montmorillonite		675-710	
pyrophyllite		745	
serpentine			722-775
vermiculite			825
corrensite			826
biotite			862
talc-chlorite			864
talc			942

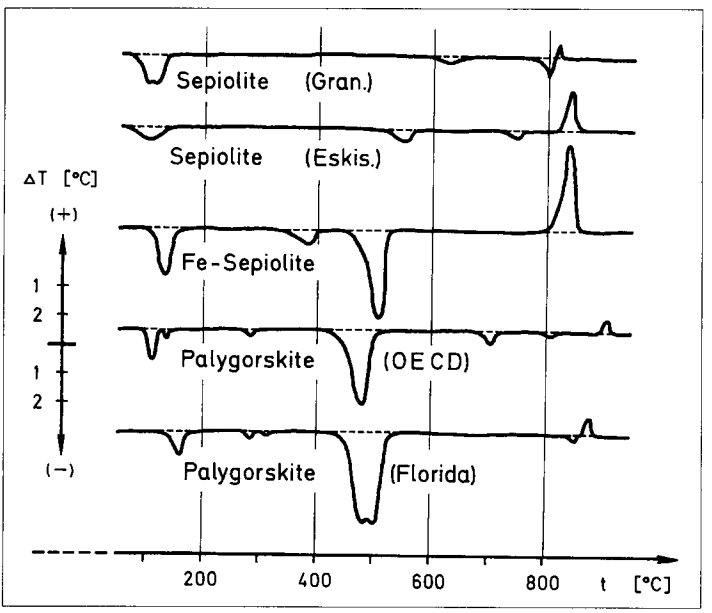


Figure 34. DTA curves of palygorskite and sepiolite.

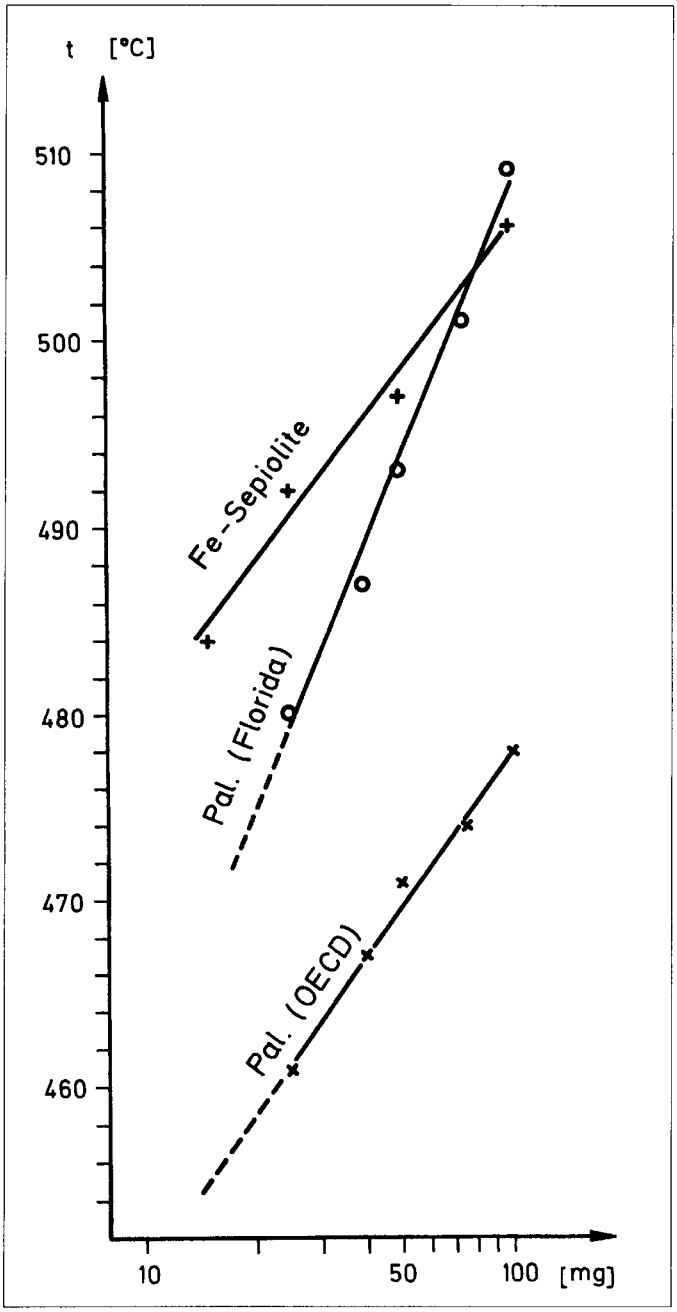


Figure 35. PA-curves of palygorskite and sepiolite.

DTA-curves of these minerals have been published by Kulp and Kerr [230], Kerr et al. [237], Caillère and Henin [206], Siddiqui [238], Echle [239], loughlinite, Hayashi et al. [240], Imai et al. [241], Müller-Vonmoos and Schindler [242], Smykatz-Kloss [24], Rouquerol et al. [49] (CRTA curves), and by Vivaldi and Hach-Ali [172].

The temperature of dehydroxylation mirrors the bonding strength between octahedral cations and (OH). Structural disorder lowers the bonding strength and thus the temperature of dehydroxylation. This may be the reason that the (OH) groups which are bound to iron escape at relatively low temperatures. The two iron cations (Fe^{2+}, Fe^{3+}) differ in size and physico-chemical properties and this influences the coordination geometry and increases the disorder inside the structure. Regarding the dehydroxylation temperatures of smectites, chlorites and other clay minerals (Table 16) the sequence: T_{max}(dehydrox.) (Fe^{2+}, Fe^{3+}) < T_{max}(dehydrox.) (Al) < T_{max}(dehydrox.) (Mg), seems quite evident.

The "a-values" (Tables 12 and 13) may be properly applied to characterise Mg- and Fe-minerals.

From more complex structures containing hydroxyl groups, the OH is partly released at temperatures > 700 °C, OH-bearing chain-, ring-or sorosilicates dehydroxylate at temperatures higher than 950 °C (e.g. amphiboles (Figure 36, 37), emerald (Figure 38), [24, 243]; or vesuvianite, [244]; see Section 2.2.5).

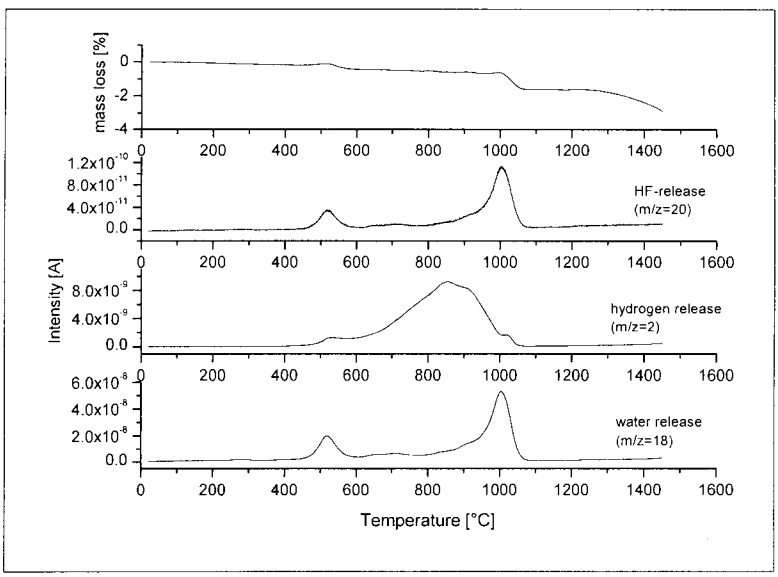


Figure 36. Vacuum degassing of hornblende.

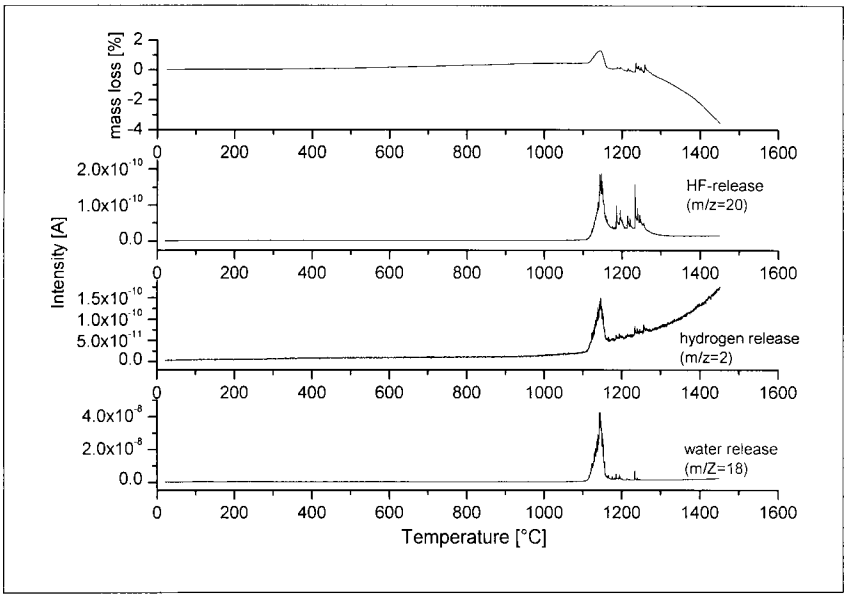


Figure 37. Vacuum degassing of basaltic hornblende.

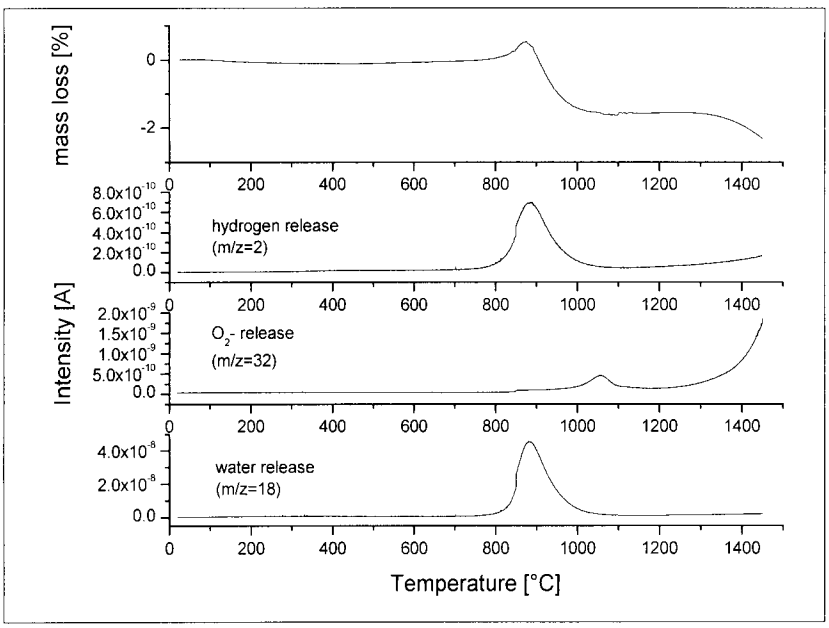


Figure 38. Vacuum degassing of emerald.

2.2.4. Zeolites

The minerals of this group form bulky framework structures with hollow channels which can be filled by water and some exchangeable cations (mainly Ca^{2+} and Na^{+}). The thermal behaviour of natural zeolites has been summarized by Gottardi and Galli [245]. The water can be released by heating without the structure being decomposed. Most of the zeolites lose their water below 400 °C (Table 17, Figure 39), with the exception of the natrolite group minerals (natrolite, scolezite, thomsonite), laumontite and chabazite, which dehydrate partly between 400 and 600 °C, so demonstrating that a part of the water has been structurally bound more effectively than the water of the channels. For details see Section 2.3.2.

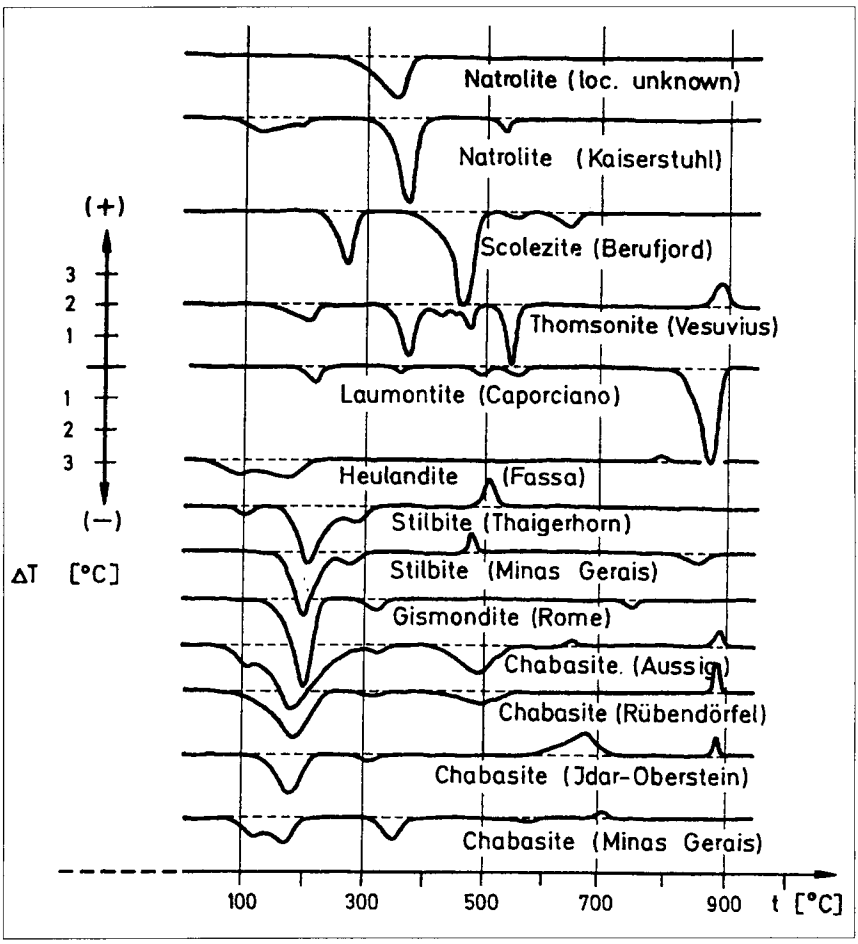


Figure 39. DTA curves of zeolites.

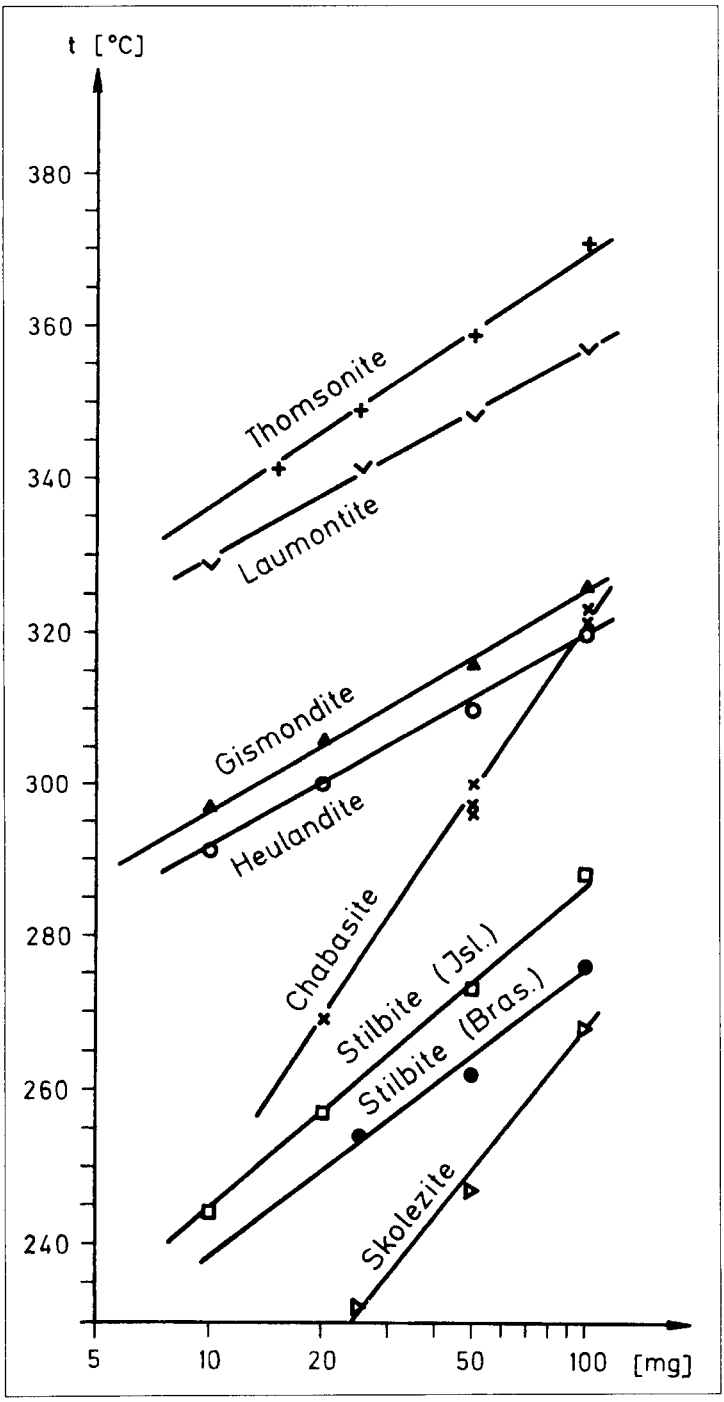


Figure 40. PA-curves of zeolites.

Table 17: DTA data of zeolites ([24], except 1 & 2; °C, ± 1°)

mineral origin	composition / formula	dehydration / decomposition	exothermic
natrolite unknown	$Na_2[Al_2Si_3O_{10}] \cdot 2\ H_2O$	350	
natrolite Kaiserstuhl / Germany	$Na_2[Al_2Si_3O_{10}] \cdot 2\ H_2O$	125, 190, 370, 531	
scolezite Berufjord / Iceland	$Ca[Al_2Si_3O_{10}] \cdot 3\ H_2O$	268, 465, 550, 645	
thomsonite Vesuvius / Italy	$NaCa_2[Al_2(Al,Si)Si_2O_{10}] \cdot 6\ H_2O$	208, 371, 425, 477, 544	889
laumontite Caporciano / Italy	$Ca[AlSi_2O_6]_2 \cdot 4\ H_2O$	215, 357, 493, 557, 870	
heulandite Fassa / Tyrol	$Ca[Al_2Si_7O_{18}] \cdot 6\ H_2O$	97, 176, 470	392, 787, 887
stilbite Theigerhorn / Iceland	$Ca[Al_2Si_7O_{18}] \cdot 7\ H_2O$	100, 204, 288	510
stilbite Minas Gerais / Brasil	$Ca[Al_2Si_7O_{18}] \cdot 7\ H_2O$	200, 276, 850	481
gismondite Rome / Italy	$Ca[Al_2Si_2O_8] \cdot 4\ H_2O$	201, 326, 745	
chabasite Aussig / Tchechia	$(Ca,Na_2)[Al_2Si_4O_{12}] \cdot 6\ H_2O$	108, 176, 321, 495, 520	650, 882
chabasite Silesia	$(Ca,Na_2)[Al_2Si_4O_{12}] \cdot 6\ H_2O$	183, 323, 495, 520	889
chabasite Idar-Oberstein / Germany	$(Ca,Na_2)[Al_2Si_4O_{12}] \cdot 6\ H_2O$	178, 312	673, 886
chabasite Minas Gerais / Brasil	$(Ca,Na_2)[Al_2Si_4O_{12}] \cdot 6\ H_2O$	120, 172, 350, 581	700

Zeolites, framework silicates with large structural channels, decompose between ~ 500°C (= the Na-containing species like natrolite, thomsonite or chabazite) and 900°C (= the Ca-zeolites, stilbite, heulandite, laumontite, compare with Table 17, Figure 39 and [24]). Some DTA curves of zeolites include exothermic effects at temperatures > 700°C which demonstrate that transformations (e.g. natrolite into nepheline, chabazite into plagioclase, [246]) are not phase transitions from one crystal structure into another, but reconstructions of crystal structures after the original structures have been decomposed. The dehydration behaviour, the decomposition and the exothermic reconstruction effects allow a good classification and determination of zeolite minerals [24]. Figure 40 shows the PA-curves of some zeolites.

The many contradictionary results in the numerous publications on zeolites are mainly due to crystal chemical variations within the same structural types, natrolite [247, 248], clinoptilolite [249, 250], Na-stilbite [251, 252], heulandite [253], zeolites from palagonite tuffs [254], fibrous zeolites from alpine veins [255], clinoptilolite [24, 25, 256], DSC-curves [204], combined methods [257], faujasite decomposition in nitrogen [258], and analcime [259]. Thus, the Na/Ca ratio may vary greatly for chabazites, thomsonites, stilbites etc.. The predominance of sodium will be mirrored by relatively low (endothermic) decomposition effects (e.g. < 500 °C), that of calcium by relatively high decomposition temperatures, e.g. > 500 °C [24].

2.2.5. Other Minerals

Many simple and complex salt minerals include structural water, chlorides like bischofite or carnallite, sulfates, phosphates, vanadates, arsenates and borates (2.2.1). The dehydration of the water-bearing salt minerals occurs at relatively low temperatures, e.g. < 200 °C. Detailed studies on evaporites will be found in [18, 82].

The amorphous alumosilicates of the *allophane* group (allophane, hisingerite), the altered silica gels of the *opal* group (opal A, opal CT), the extremely disordered water-bearing *Cu*-(chrysocolla) and *Zn-silicates* (hemimorphite) (Figure 41) dehydrate in a temperature range of some hundred degrees C [24].

Some silicate minerals, other than clays or zeolites, incorporate (OH) and some exhibit very high dehydroxylation temperatures (e.g. > 900 °C) due to high bonding energies. *Epidotes, vesuvianite, tourmalines* [24, 244, 260], and *amphiboles* dehydroxylate at temperatures above 950 °C (epidotes [213, 260, 261]; amphiboles (Figures 36 and 37), [24, 262 - 264]). DTA is quite applicable for the classification of these silicates. Freeman [243] found increasing dehydroxylation temperatures of amphiboles with increasing Mg-

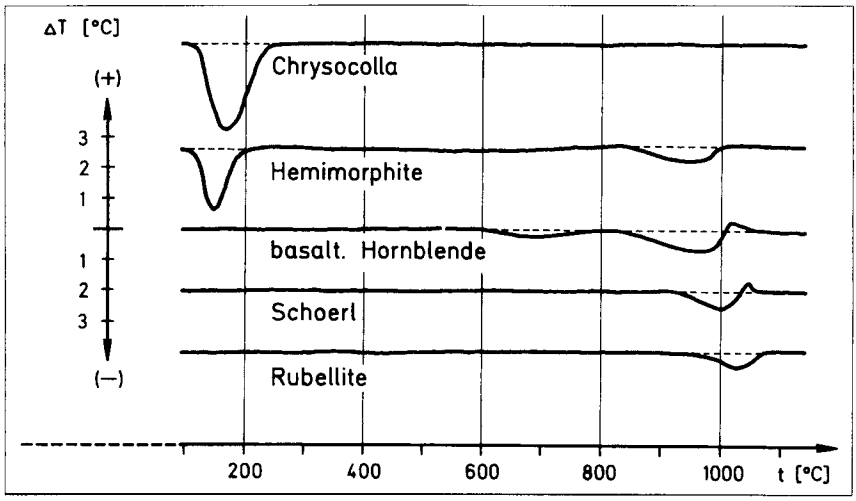


Figure 41. DTA curves of chrysocolla, hemimorphite, basaltic hornblende, schoerl and rubellite.

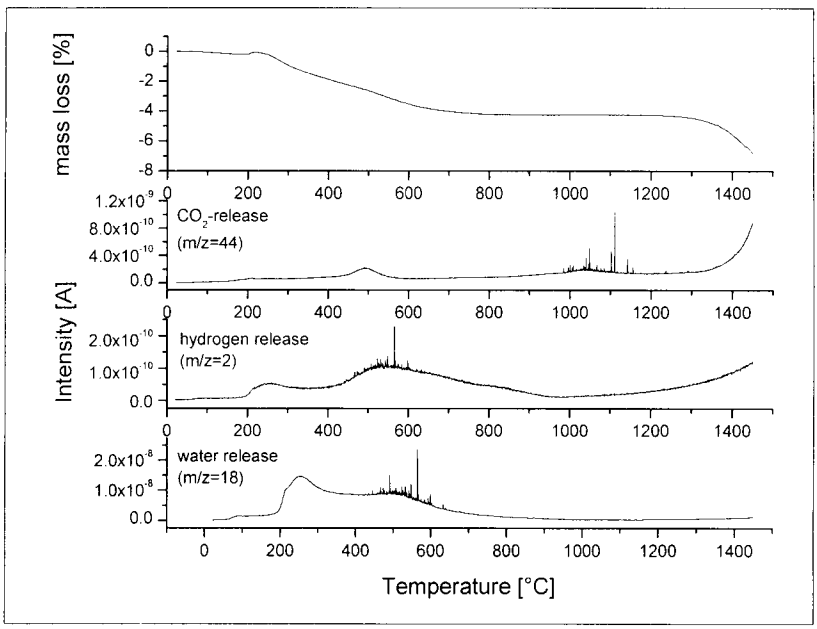


Figure 42. Vacuum decomposition of cordierite.

contents (950-1200 °C) - similar to the situation for chlorites, compare Section 2.2.3. Peters [264] correlated the release of (OH) with the iron content of epidotes. Heflik and Zabinski [265] studied OH-bearing garnets (hydrogrossulare). Geiger et al. [266] analyzed the content of volatiles in cordierites ($Mg_2Al_3[Al\ Si_5O_{18}]$ in dependence of the origin (Figure 42). In general it was shown by the evolved gas analysis, that the dehydroxylation is connected with the degassing of complex composed fluids or gases like HF, H_2, hydrocarbons etc..

2.3. Decomposition

2.3.1. Carbonates

Hydrolysates, e.g. clay minerals, aluminosilicates, decompose *after* their dehydroxylation. Normally this endothermic process covers a broad thermal region and is difficult to see in the DTA curve. In contrast to this slow and "soft" process, decomposition of *carbonate minerals* appears very spontaneously and strongly, exhibiting ΔT-values of more than 5 or 10 °C (100 mg, 10 °C/min; corundum crucibles). The decomposition reactions lead to the oxides + CO_2, and the decarbonation process is a very suitable criterion for the characterisation and determination of the mineral species.

As mentioned before, the decomposition reactions of carbonates are *strongly dependent on* p_{CO2} [24, 267]. Figure 43 demonstrates this interrelation for the mineral calcite, $CaCO_3$. As outlined by Smykatz-Kloss [24, 25, 51, 268] and later by Warne [52] and Földvari [54], the interdependence of the decomposition (peak) temperature of carbonates and the partial pressure of CO_2 may be used for (semi-) quantitative mineral determination provided that the DTA analyses are run under standardised conditions. The resulting *PA-curves* (published in [24, 25]), i.e. the temperature of decomposition vs the amount of the degassing mineral, may be helpful in determining the accurate amount of carbonates. This is mainly valid for low amounts of carbonates (e.g. < 30 mg in a standard sample of 100 mg). At higher amounts of carbonates (e.g. > 50 mg) the error increases.

It has to be stressed that this method of (semi-) quantitative carbonate determination by using PA-curves needs *strongly standardised conditions* of preparation and analysis [24, 269]. The lower the amount of a carbonate mineral in a sample (e.g. clay), the more closely the decomposition temperature approaches the true thermodynamic decomposition temperature, which is represented in the (DTA, DSC) curve by the *onset temperature* of the endothermic effect. Generally it is not possible to determine the onset temperature very exactly, but the *peak* temperature can be measured exactly.

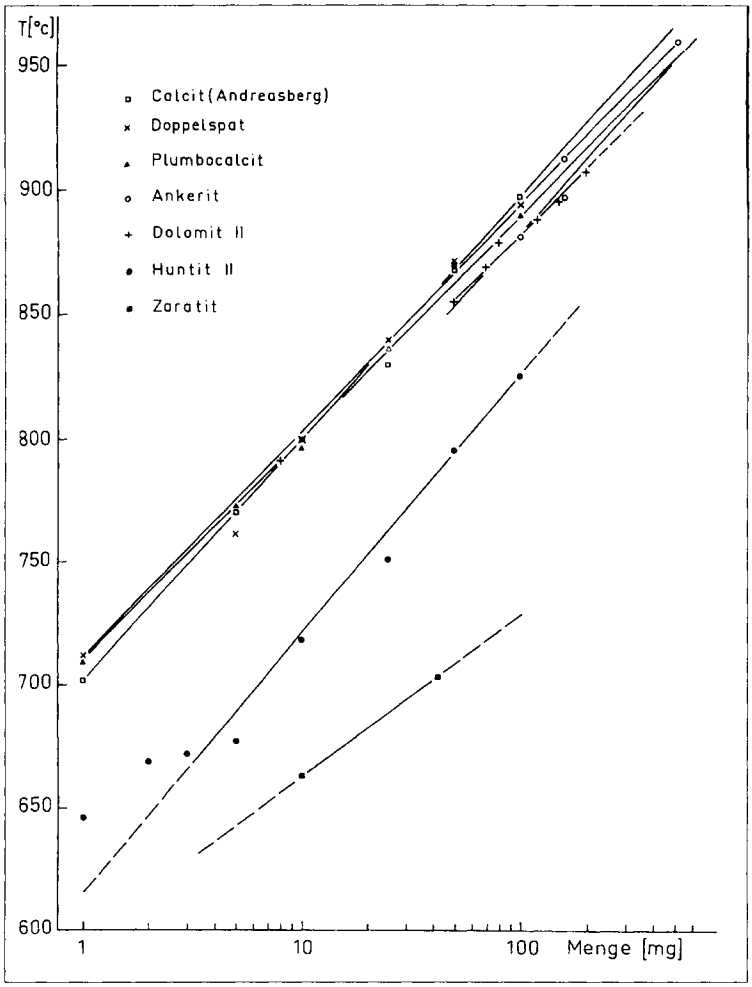


Figure 43. PA-curves of calcite, plumbocalcite, ankerite, dolomite, huntite, and zaratite.

Therefore, in practice, it seems much more reasonable to determine the peak temperature of the decomposition (dehydroxylation, phase transition, oxidation) effect under controlled and highly standardised conditions of analysis. Smykatz-Kloss [24] introduced the *"standard temperature"* of decomposition, that means the temperature of an amount of *1 mg carbonate* (in a 100 mg sample). The standard temperature of decomposition seems to be quite near to the thermodynamic decomposition temperature. Table 18 compares the decomposition of 100 mg with this "standard temperature" (1 mg) under standardised conditions of analysis for some carbonate minerals. The

connection line between both decomposition temperatures in the following diagrams (abscissa on a logarithmic scale) represents the PA-curve for the specific degassing reaction.

A quantitative determination of carbonate content in natural samples can also be done using thermogravimetry in combination with a gas detection system. The gas analysis is necessary for the separation of the CO_2 release from the release of water from minerals that decompose in the same temperature range. This method allows the determination from ppm up to 100% without any special sample preparation.

The decomposition temperatures of carbonates follow the order and size of cations:

$$Na < Pb, Cu < Ni, Zn < Ce, Ca/Ce, Ca/Mg_3 < Fe < Mg$$

$$< Na/Ca, Ca < Ca/Mg < Sr < Ba/Mg < Ba$$

The group of carbonate minerals has been among the main objects of thermal studies in mineralogy. Up to 1970 nearly 350 DTA studies on carbonates had been published [16, 270], since then some hundred additional papers have appeared. Surveys of the DTA behaviour of the most important carbonate minerals have been given by Cuthbert and Rowland [271], Beck [272], Spotts [273], Földvari-Vogl [12], Smykatz-Kloss [24, 25, 274], Kostov [18] and Webb and Krüger [270]. DTA data for individual carbonate minerals have been published by Caillère (hydromagnesite, [276]), Faust (huntite, [277]), Webb and Heystek (azurite, malachite, smithsonite, [118]), Warne and Bayliss (cerussite, [278]), Ross and Kodama (manasseite, [279]), and Chao (carletonite, [280]).

The most investigated carbonates are those exhibiting the *dolomite* structure (Ca-Mg-Fe-Mn carbonates, dolomite, ankerite, kutnahorite). *Dolomite* itself has been the object of numerous studies [24, 25, 46, 57, 270, 272, 274, 281 - 299]. Its thermal characteristics are strongly variable due to impurities, crystal chemical substitutions or disorder phenomena (e.g. proto-dolomite, [300]). Admixtures of NaCl lower the decomposition temperatures by nearly 30 °C [292, 301]. The incorporation of Fe^{2+} and Mn^{2+} causes additional endothermic effects [24, 25, 286, 302 - 304]. Different DTA data exist for the Mn-carbonates rhodochrosite, Mn-calcite, Mn-dolomite, Mn-ankerite, kutnahorite [24, 282, 305 – 310], but the greatest discrepancies have been described for the Fe^{2+} -carbonates *siderite* and *ankerite* [274, 282, 283, 307, 311 – 317]. DTA

Table 18. Decomposition temperatures of carbonates. Comparison of Tdec of 100 mg under standardized conditions of analysis [24] with the "standard temperature of decomposition", e.g. the T_{dec} of 1 mg (extrapolation from PA-curves, see text; °C, ± 1°)

mineral	formula	T_{dec} (100 mg)	T_{dec} (1 mg)
nahcolite	$NaHCO_3$	170	128
cerussite	$PbCO_3$	350, 427	298, 343
smithsonite	$ZnCO_3$	499	432
huntite	$CaMg_3(CO_3)_4$	568, 613, 826	489, 540, 647
magnesite (dense)	$MgCO_3$	625	527
magnesite (spaty)	$MgCO_3$	643	541
dolomite	$CaMg(CO_3)_2$	807, 901	753
plumbocalcite	$(Ca,Pb)CO_3$	890	710
calcite I	$CaCO_3$	895	712
calcite II	$CaCO_3$	898	702
strontianite I	$SrCO_3$	1148	905
strontianite II	$SrCO_3$	1151	910
strontianite III	$SrCO_3$	1151	910
norsethite	$BaMg(CO_3)_2$	810, 1174	925
witherite	$BaCO_3$	1195	940
malachite	$Cu_2[(OH)_2/CO_3]$	366	305
azurite	$Cu_3[(OH)_2/(CO_3)_2]$	390	336
hydrozincite I	$Zn_5[(OH)_3CO_3]_2$	267	254
hydrozincite II	$Zn_5[(OH)_3CO_3]_2$	278	262
aurichalcite	$(Zn,Cu)_5[(OH)_3CO_3]_2$	405	365
bastnaesite	$Ce[F/CO_3]$	500	459
parisite	$Ce_2Ca[F_2/(CO_3)_3]$	570	489
phosgenite	$Pb[Cl_2/CO_3]$	500	412
hydromagnesite	$Mg_5[OH(CO_3)_2]_2 \cdot 4\ H_2O$	521, 566	387, 504
artinite	$Mg_2[(OH)_2CO_3] \cdot 3\ H_2O$	538	240
brugnatellite	$Mg_6Fe[(OH)_{13}CO_3] \cdot 4\ H_2O$	447	337, 414
zaratite	$Ni_3[(OH)_4CO_3] \cdot 4\ H_2O$	728	426
hydrotalkite	$Mg_6Al_2[(OH)_{16}CO_3] \cdot 4\ H_2O$	464	210, 247
nesquehonite	$MgCO_3 \cdot 3\ H_2O$	530, 687	376, 392
soda	$Na_2CO_3 \cdot 10\ H_2O$	118, 126	95, 108
trona	$Na_3H(CO_3)_2 \cdot 2\ H_2O$	142	100, 126
gaylussite	$Na_2Ca(CO_3)_2 \cdot 5\ H_2O$	803	723

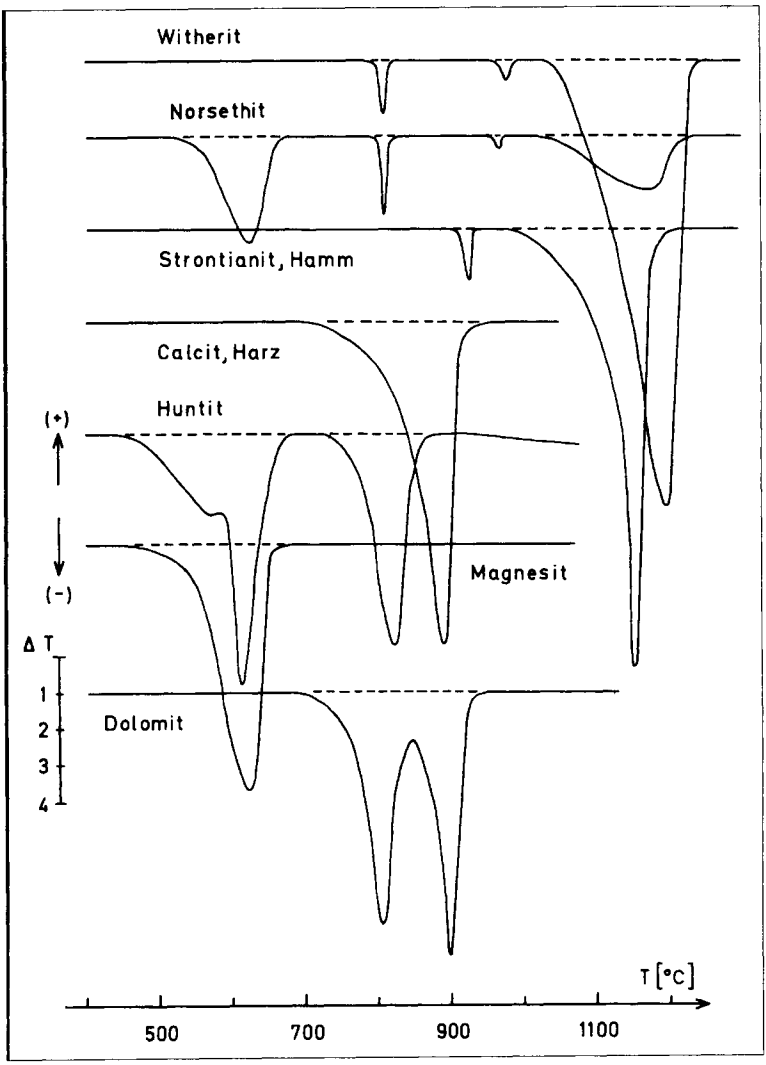


Figure 44. DTA curves of some carbonate minerals, e.g. witherite, norsethite, strontianite, calcite, huntite, magnesite, and dolomite.

curves showing only one endothermic or exothermic peak, or both peaks fairly separated or partly overlapping can be found. The authors' runs on a couple of siderites and ankerites proved that the cause of all these discrepancies is the *heating-rate* used. At low heating rates (e.g. < 10 K/min), only the exothermic process (oxidation of $Fe^{2+} \rightarrow Fe^{3+}$) appears [24, 318]. This is a striking example for the need for standardised conditions of analysis.

Among the large number of publications concerning the DTA/TG and MS of carbonates, some studies of very rare minerals may be mentioned, e.g. on alstonite, $BaCa(CO_3)_2$ [270], tarnowitzite, Pb-bearing aragonite [274], strontianite and witherite, $SrCO_3$ resp. $BaCO_3$ [24, 25, 268, 270, 271, 274, 289, 304], dundasite, $PbAl_2(CO_3)_2(OH)_4 \cdot 2\ H_2O$ [282], phosgenite, $Pb_2[Cl_2/CO_3]$ [24, 282], rutherfordine, UO_2CO_3 [24, 270], huntite, $CaMg_3(CO_3)_4$ [24, 270, 277], artinite, $Mg_2[(OH)_2CO_3] \cdot 3\ H_2O$ [24, 282, 319], hydromagnesite, brugnatellite and hydrotalcite, $Mg_5[OH/(CO_3)_2]_2 \cdot 4\ H_2O$, $Mg_6Fe^{3+}[(OH)_{13}CO_3] \cdot 4\ H_2O$, $Mg_6Al_2\ [(OH)_{16}CO_3] \cdot 4\ H_2O$ respectively [24, 275, 276, 282, 320], lansfordite and sjögrenite, $MgCO_3 \cdot 5\ H_2O$ and $Mg_6Fe_2[(OH)_{16}|CO_3)$ respectively [282], breunnerite $(Mg, Fe)(CO_3)$ [24, 270], zaratite, $Ni_3[(OH)_4|CO_3] \cdot 4\ H_2O$ [24],

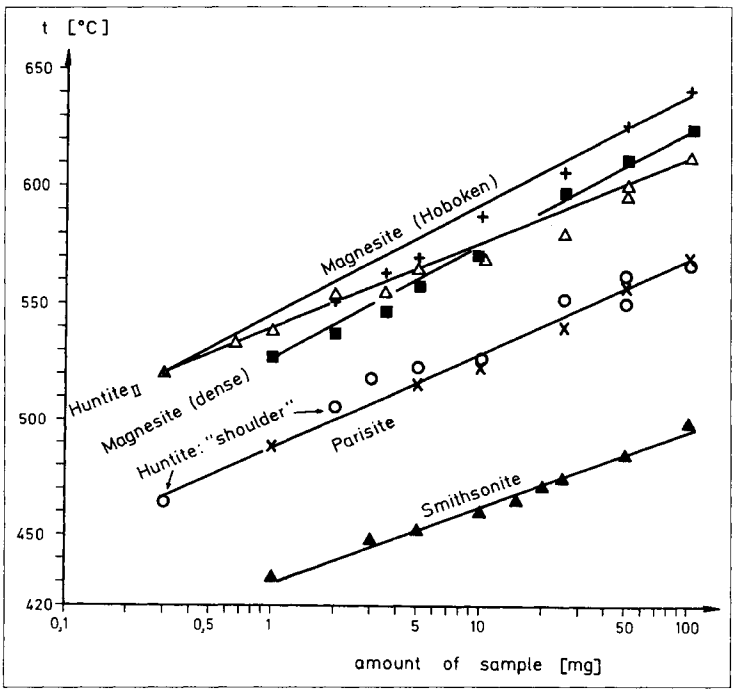


Figure 45. PA-curves of magnesite, huntite, parisite, and smithsonite.

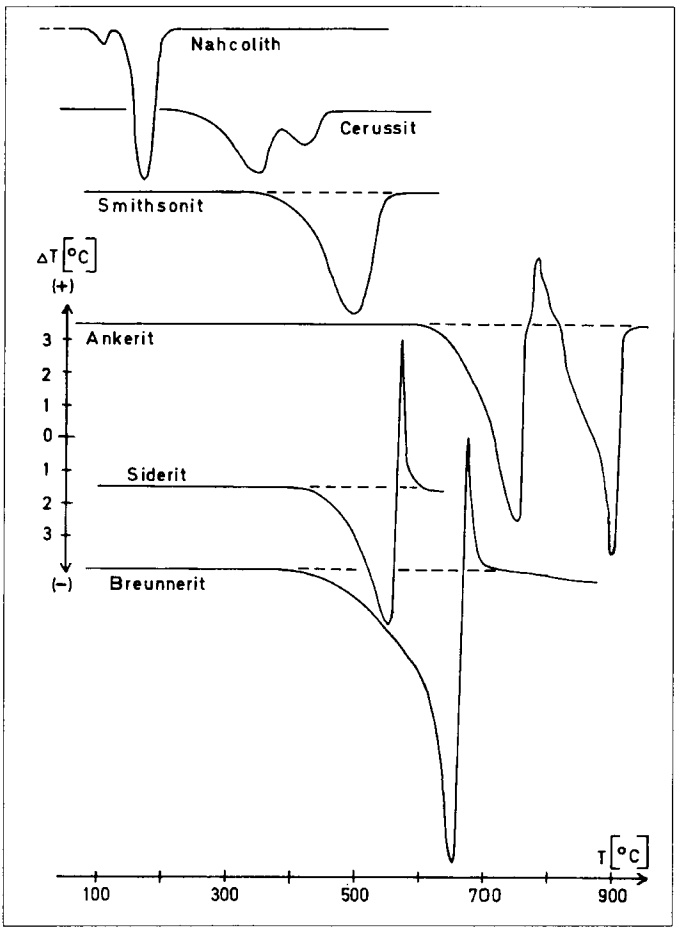


Figure 46. DTA curves of nahcolite, cerussite, smithsonite, ankerite, siderite, and breunnerite.

schröckingerite and voglite, $NaCa_3[UO_2|(CO_3)_3|SO_4|F] \cdot 10\ H_2O$ and $Ca_2Cu[(UO_2)_2(CO_3)_5]$, respectively [24, 270], dawsonite, $NaAl[(OH)_2|CO_3]$ [270], gaylussite and pirssonite, $CaNa_2[CO_3]_2 \cdot 5\ H_2O$ and $\sim 2\ H_2O$, respectively [24, 270], bastnaesite and parisite, $Ce[F|CO_3]$ and $Ce_2Ca[F_2|(CO_3)_3]$ [24], alumohydrocalcite, $CaAl_2[(OH)_4|(CO_3)_2] \cdot 3\ H_2O$ [274], hydrozincite, $Zn_5[(OH)_3|CO_3]_2$ [24], grimselite, and K-Ca-uranyl-carbonate [321]. Figures 43-49 contain DTA, PA and vacuum decomposition diagrams for several carbonates.

2.3.2. Silicates

During the last few years the interest in the volatile content of "water-free"-minerals increased remarkably. The quantities of such volatiles are low but the minerals with such low contents are very frequent. Garnets, olivine and pyroxenes, topaz as well as feldspars are potential minerals with volatiles in the structures. Furthermore the different valence states of iron are an important factor for the oxygen fugacity. By the reduction of the valence state from Fe^{3+} to Fe^{2+} the formation of volatile oxygen occurs as it is possible to observe in the high vacuum transformation of haematite:

$$3\ Fe_2O_3 \rightarrow 2\ Fe_3O_4 + \tfrac{1}{2}\ O_2$$

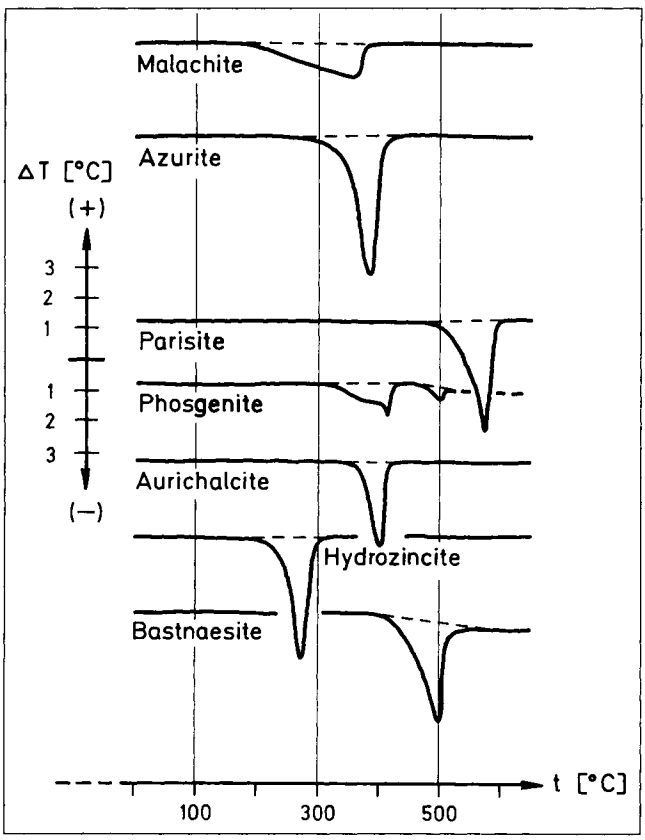


Figure 47. DTA curves of malachite, azurite, parisite, phosgenite, aurichalcite, hydrozincite, and bastnaesite.

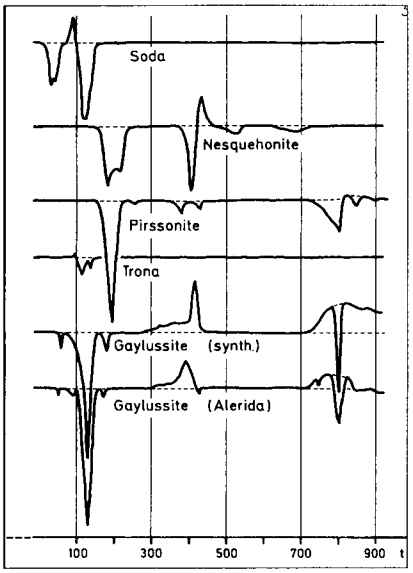


Figure 48. DTA curves of hydrated carbonates without other anions, e.g. soda, nesquehonite, pirssonite, trona, and gaylussite

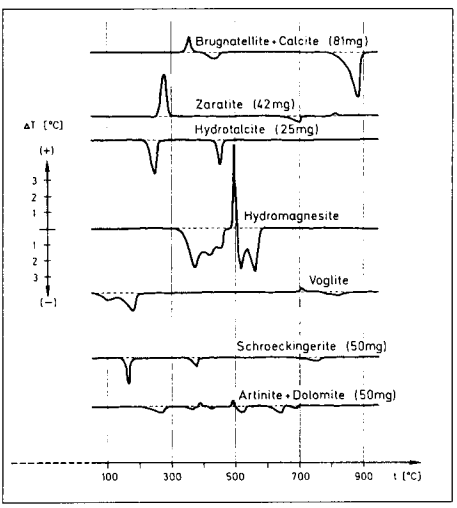


Figure 49. DTA curves of hydrated carbonates with other anions, e.g. brugnatelite, zaratite, hydrotalcite, hydromagnesite, voglite, schroeckingerlite, and artinite.

Clay minerals decompose after their dehydroxylation but, in general, decomposition is not spontaneous and is slow and difficult to detect. Thus, the dehydroxylated kaolinites still consist of *crystalline* (but badly disordered) *meta-kaolinites* which continuously transform to amorphous oxides of silica and alumina. This decomposition is not observable in DTA.

For the thermal behaviour of *zeolites* see Section 2.2.4.

2.4. Phase transitions

The changes of energy due to phase transitions of minerals ought to be much smaller than those occurring in dehydration or decomposition reactions. Thus, the ΔH of the low-high quartz inversion is 753 J/mol [322], that of the monotropic aragonite $\rightarrow$ calcite transition is 1632 J/mol [4], while the ΔH-values for the dehydration of hydrolysates are in the range 83 kJ/mol to 146 kJ/mol. The enthalpies of decomposition of carbonates are greater than 167 kJ/mol [4].

For the measurement of enthalpies of chemical reactions, DSC is recommended, rather than DTA, because of the larger errors in DTA ([323] and the cited handbooks). In spite of this, DTA is regularly used by geoscientists for the determination of phase transitions and, for example, for quick determinations of sulfidic phases (2.4.3), for petrogenetic information about SiO_2-bearing rocks (2.4.4), and for the estimation of crystal chemical compositions of minerals.

2.4.1. Melting

The melting of pure metals may be used as temperature standards. Silver (melting point at 961.78 °C) or gold (melting point at 1064.18 °C) are the most exact and reliable. Gallium (29.8 °C), indium (156.6 °C), tin (213.9 °C), bismuth (271.0 °C), lead (327.4 °C), zinc (419.5 °C), aluminium (660.3 °C), copper (1084.6 °C) may also be used [324].

Chlorides and (Na-) K-Ca-Mg sulfates show a broad range of melting temperatures [82, 83, 85, 87, 92]. Some borates, arsenates and phosphates (e.g. amblygonite, $LiAl(F,OH)PO_4$, [24]) exhibit melting temperatures above 700 °C.

Silicates melt generally at higher temperatures. Among the abundant common mineral systems: Na_2O-Al_2O_3-SiO_2, K_2O - (MgO,CaO) - SiO_2-Al_2O_3 the following minerals and their melting temperatures may be mentioned, together with their well-known behaviour of forming solid solutions, incongruent melting, or eutectic systems, described in mineralogical textbooks (e.g. [325]).

2.4.2. Sulfates and carbonates

Mainly alkali sulfates and carbonates show phase transitions. Berg [82] reported temperatures of phase transitions between 240 °C (thenardite,

Table 19. Melting temperatures of chlorides, fluorides and sulfates [82, 87]

mineral	formula	melting temperature [°C]
Mirabilite	$Na_2SO_4 \cdot 10\ H_2O$	32.4
Carnallite	$KMgCl_3 \cdot 6\ H_2O$	425
Loeweite	$Na_{12}Mg_7(SO_4)_{13} \cdot 15\ H_2O$	668 eutec.
Bloedite	$Na_2Mg(SO_4)_2 \cdot 4\ H_2O$	704 liqui.
Leonite	$K_2Mg(SO_4)_2 \cdot 4\ H_2O$	738 eutec.
Picromerite	$K_2Mg(SO_4)_2 \cdot 6\ H_2O$	842 liqui.
Sylvite	KCl	775
Halite	NaCl	800
Cryolite	Na_3AlF_6	1000
Vanthoffite	$Na_6Mg(SO_4)_4$	800
Syngenite	$K_2Ca(SO_4)_2 \cdot H_2O$	875
Polyhalite	$K_2MgCa(SO_4)_4 \cdot 2\ H_2O$	880
Thenardite	Na_2SO_4	884
Langbeinite	$K_2Mg_2(SO_4)_3$	945
Glaserite	$K_3Na(SO_4)_2$	940
Glauberite	$Na_2Ca(SO_4)_2$	944
Görgeyite	$K_2Ca_5(SO_4)_6 \cdot H_2O$	1044
Kieserite	$(MgSO_4 \cdot H_2O)$	1124
Epsomite	$(MgSO_4 \cdot 7\ H_2O)$	1124

mirabilite) and 580 °C (K-Mg-sulfates, Table 21). He states that there is no remarkable influence of admixtures. But there is a strong influence of substitution. That may be the reason for the differences in the data for the monotropic aragonite → calcite transformation, which is reported to occur between 387 °C and 488 °C. Passe-Coutrin [328] reported much lower transition temperatures for aragonites from *corals* (e.g. 290 °C, see Table 22) than for minerals of the inorganic aragonite matrix (450 °C). The reason for this very low transition temperature is not yet known, there may be some influence of the habit (fibrous, pisolitic) as well.

The pure sodium sulfates, mirabilite and thenardite, exhibit strong phase transitions which include five modifications ([329]; Table 23). Wiedemann and Smykatz-Kloss [330] correlated the DTA/TG data for these transitions with (hydro-) geochemical and crystal optical studies and found a distinct influence of the water content on the phase transition temperatures, e.g. of the amount of

Table 20. Melting temperatures of some silicates (1 hPa)

mineral	formula	melting temperature [°C]	remarks
Orthoclase	$K[AlSi_3O_8]$	1150	
Albite	$Na[AlSi_3O_8]$	1118	plagioclase
Anorthite	$Ca[Al_2Si_2O_8]$	1553	plagioclase
Diopside	$CaMg(Si_2O_6)$	1391.5	pyroxene
Spodumene	$LiAl[Si_2O_6]$	1410	pyroxene
Enstatite	$Mg_2[Si_2O_6]$	1557	pyroxene
Leucite	$KAl[Si_2O_6]$	1686	
Pseudowollastonite	$Ca_3[Si_3O_9]$	1540	
Carnegieite	$Na[AlSiO_4]$	1526	
Forsterite	$Mg_2[SiO_4]$	1890	olivine
Fayalite	$Fe_2[SiO_4]$	1205	olivine
Cuspidine	$Ca_4[(F,OH)_2/Si_2O_7]$	1405	[326]
Lazurite (Lapislazuli)	$(Na, Ca)_8[Al_6Si_6O_{24}]$	1320	[327]

Table 21. Phase transition temperatures of some sulfates and carbonates (heating; °C, ± 1°)

mineral	formula	transition temp.	reference
mirabilite	$Na_2[SO_4] \cdot 10\ H_2O$	240	[82]
kainite	$KMg[SO_4 \mid Cl] \cdot 3\ H_2O$	425	[82]
glaserite	$K_3Na[SO_4]_2$	437	[82]
syngenite	$K_2Ca[SO_4]_2 \cdot 1\ H_2O$	560	[82]
leonite	$K_2Mg[SO_4]_2 \cdot 4\ H_2O$	580	[82]
picromerite	$K_2Mg[SO_4]_2 \cdot 6\ H_2O$	580	[82]
anglesite	$Pb[SO_4]$	895	[17, 24]
trona	$Na_3H[CO_3]_2 \cdot 2\ H_2O$	170	[282]
soda	$Na_2[CO_3] \cdot 10\ H_2O$	355, 485	[270]
dawsonite	$NaAl[(OH)_2CO_3]$	436	[282]
vaterite → calcite	$CaCO_3$	470	[597]

Table 22. Phase transition temperatures of Ca-, Sr- and Ba-carbonates (heating; °C, ± 0.5°)

mineral origin, type	formula	transition temp.	reference
aragonite corals	$CaCO_3$	290	[328]
aragonite inorganic matrix between corals	$CaCO_3$	450	[328]
aragonite ten samples	$CaCO_3$	387-488	[598]
aragonite opalinus marl, Switzerland	$CaCO_3$	410	[187]
aragonite 8 clear twin crystals, Calaves / Aragon	$CaCO_3$	447-456	[24, 274]
aragonite pisolite, Carlsbad / Bohemia	$CaCO_3$	390	[24]
aragonite fibrous, Carlsbad / Bohemia	$CaCO_3$	387	[24]
aragonite unknown	$CaCO_3$	450	[270]
aragonite unknown	$CaCO_3$	430	[27]
tarnowitzite Tarnowitz / Poland	$(Ca,Pb)CO_3$	447	[274]
strontianite Loch Strontian / Scotland	$SrCO_3$	890-895, 912-930	[268]
strontianite unknown	$SrCO_3$	930	[282]
strontianite unknown	$SrCO_3$	900	[270]
strontianite unknown	$SrCO_3$	928.2-932.9 (± 0.2)	[599]
alstonite unknown	$BaCa(CO_3)_2$	900	[268]
norsethite unknown	$BaMg(CO_3)_2$	810-813, 980-982	[268]
witherite unknown	$BaCO_3$	981	[268]

relictic mirabilite ($Na_2SO_4 \cdot 10\ H_2O$) in thenardite samples (Na_2SO_4, water-free, Figure 50, [330, 304]).

2.4.3. Chalcogenides

The most striking thermal effect of chalcogenides (sulfides, arsenides, antimonides, bismuthides, tellurides...) is the very strong *oxidation* when heated in oxidising atmospheres (air, oxygen). But because of the danger of producing toxic gases reaction products (SO_2, SO_3...), this effect should only be studied if very low amounts of chalcogenides are present in the heated samples. Thus, impurities (< 1 % [304, 332, 333]) of pyrite or other sulfides may be determined in soils or ceramic raw materials) by means of DTA or DSC. This is possible, because the strong oxidation effect (the "roasting") occurs some hundred degrees later [24, 334]. The known interdependence between temperatures of phase transitions and the crystal chemical composition of sulfides enables the determination of substitutions or impurities [24, 304, 336].

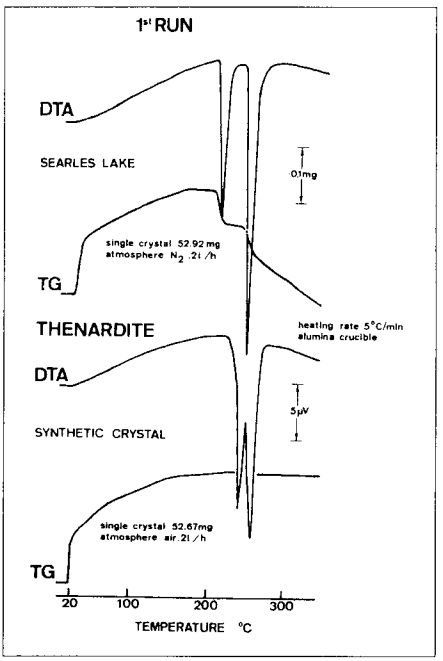


Figure 50. Phase transitions of sodium sulfate.

Table 23. Phase transition temperatures of thenardite, Na_2SO_4 (heating; °C, ± 1°)

transition temperatures		reference
212	236, 242-250	[477]
215	236-252	[330]
215	245	[27]
220, 230	235-255	[602]
227	243	[23]
	240	[82, 600]
	245	[24, 28, 601]
	270	[18]

Direct contact between metallic parts of the equipment (crucibles, sample holder, thermocouples) and the aggressive gaseous reaction products may be prevented by coating the crucibles and sample holders with thin cylinders of ceramic material or glass [336 - 339].

DTA curves of sulfides and arsenides have been published by Kracek [340], Hiller and Probsthain [337, 341], Sabatier [342], Kopp and Kerr [338, 343, 344], Asensio and Sabatier [345], Levy [346], Kullerud [347], Dunne and Kerr [339, 348], Paulik et al. [332], Maurel [349], Smykatz-Kloss [24, 25, 51], Cabri [350], Kostov [18], Bollin [351], Blazek [23], Wilson and Mikhail [352], Hurst et al. [353], Abdel Rehim [334], Schomburg [354], Balasz et al. [355, 356], Dunn [357, 358], and Chamberlain and Dunn [359].

The systems Cu-Fe-S and Ag-Cu-S have been extensively studied [336, 340, 350, 351, 361 - 369]. Table 24 contains the phase transition data of Cu-Ag sulfides given by Smykatz-Kloss and Hausmann [336].

Cabri [370], Yund and Kullerud [350] and Smykatz-Kloss and Hausmann [336] investigated Cu-Ag sulfides which had incorporated certain amounts of iron in their structures. The resulting phase-transition temperatures were remarkably lower than those of the Fe-free minerals. The transition temperatures of the high-low inversion of *chalcocite* (Cu_2S, 106 °C), *digenite* ($Cu_{1.78}S$, 74-90 °C), *stromeyerite* (CuAgS, 82-94 °C), *jalpaite* ($Cu_{0.5}Ag_{1.5}S$, 119 °C) and *acanthite* (Ag_2S, 176 °C) were *lowered* by crystal physical and, to a smaller degree, by crystal chemical defects. The intensities (ΔT) and enthalpies (ΔH) of the phase transitions decrease with increasing mechanical treatment (e.g. grinding, → physical disorder) and with increasing Fe incorporation in the structures (→ chemical disorder). An iron addition in the synthesis of Cu sul-

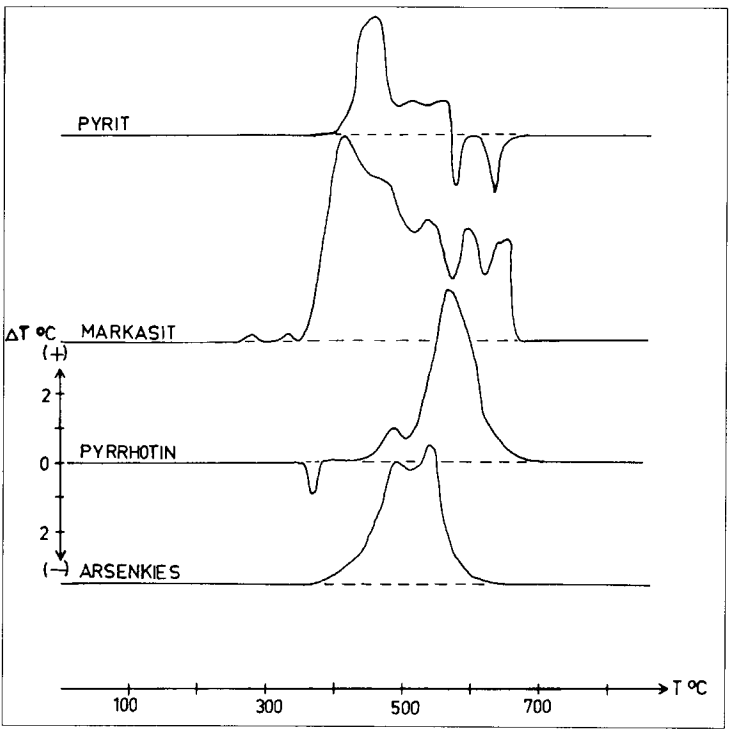


Figure 51. DTA curves of iron-sulfides, e.g. pyrite, marcasite, pyrrhotite, and arsenopyrite.

fides of more than 6.5 mass % leads to the formation of a new, until now unknown, phase ($Cu_{1.8\text{-}1.7}Fe_{0.2\text{-}0.3}S$) which differs strongly in its X-ray and thermal properties from the known Cu-Fe sulfides (Table 24, Figures 51 and 52 [336]).

Natural silver sulfides showed variations in their phase-transition temperatures between 174.5 ± 0.7 °C and 177.8 ± 0.7 °C [336, 340] which are mainly due to a surplus of Ag or S, Kracek [340] and Jensen [363] found 176.3 ± 0.5 °C for an *Ag*-rich sample, 177.8 ± 0.7 °C for a *S*-rich acanthite, and a remarkable hysteresis between heating and cooling curves. On cooling the transition temperatures were delayed by nearly 10 °C.

Phase transitions of synthetic Cu-(Fe-)S species (Table 24) showed a strong decrease in ΔT and ΔH with increasing incorporation of iron. The unknown phases $Cu_{2-x}Fe_xS$ (x = 0.3-0.2) differ from the chalcocite or digenite behaviour.

Table 24. Phase transition temperatures in Cu-(Fe-)Ag sulfides [336] (some pure Cu-, Ag-sulfides from [367]; heating)

composition	transition temp. (°C, ± 0.5°)	ΔH (kJ mol-1)	phase (XRD)
Cu_2S	91-106		chalcocite
Cu_2S	106	2.08	chalcocite
$Cu_{1.95}Fe_{0.05}S$	109	1.41	chalcocite
$Cu_{1.9}Fe_{0.1}S$	106, 115	0.83	chalcocite
$Cu_{1.85}Fe_{0.15}S$	105.5, 120	0.46	chalcocite
$Cu_{1.81}Fe_{0.19}S$	106, 116	0.38	chalcocite + unknown phase
$Cu_{1.8}Fe_{0.2}S$	126.5, 145	1.43	unknown phase
$Cu_{1.75}Fe_{0.25}S$	127, 144	0.99	unknown phase
$Cu_{1.7}Fe_{0.3}S$	127, 142	0.75	unknown phase
$Cu_{1.78}S$	74, 79.5, 90	1.52	digenite
$Cu_{1.68}Fe_{0.1}S$	79	0.92	digenite
$Cu_{1.58}Fe_{0.2}S$	79.5	0.08	digenite
Cu_5FeS_4	218	0.39	bornite
$Cu_{0.45}Ag_{1.55}S$	112-117		jalpaite
$Cu_{0.5}Ag_{1.5}S$	119	2.63	jalpaite
Ag_2S	174.5-176.5	1.9-3.15	acanthite / argentite

In the system Cu-Ag-S, the phase strohmeyerite, CuAgS, should be synthesised for a Cu/Ag ratio of 1:1 (Table 24). For higher ratios, e.g. in *Cu-rich* samples, digenite + strohmeyerite occurred. At lower ratios, e.g. in *Ag-rich* samples, strohmeyerite disappeared very quickly and mcinstryite ($Cu_{0.8}Ag_{1.2}S$) appears (Table 24, [336]). At very low Cu/Ag ratios, mcinstryite + jalpaite ($Cu_{0.45}Ag_{1.55}S$) occurs. Skinner [367] found only *one effect* for the transition from the orthorhombic (low) to the hexagonal (high) form of strohmeyerite. Smykatz-Kloss and Hausmann [336] showed that this transition occurs in *two* steps. The reported transition temperature of 93.3 ± 0.7 °C [367] coincides well with the second peak observed by Smykatz-Kloss and Hausmann [336] (e.g. 92.5 ± 1 °C). The first endothermic effect (specimen, $Cu_{1.25}Ag_{0.75}S$) seems to be caused by the transition of associated digenite (Table 24).

Smykatz-Kloss and Hausmann [336] reported data for samples of synthetic acanthites having small variations in the Ag/S ratio and small amounts of incorporated iron (Table 24). The resulting *double* effect for the homogeneous acanthite occurs in the *Fe-free* as well as the *Fe-bearing* specimen (Table 24).

This double effect has also been observed by Bollin [351], while Kracek [340] found only one spontaneous, intensive and reversible effect.

The results of Smykatz-Kloss and Hausmann [336] explain the controversial phase-transition data found in the literature for Cu-Fe- and Cu-Ag (Fe) sulfides. The differences in transition enthalpies and temperatures, ΔH and ΔT, were shown to be caused by crystal chemical disorder.

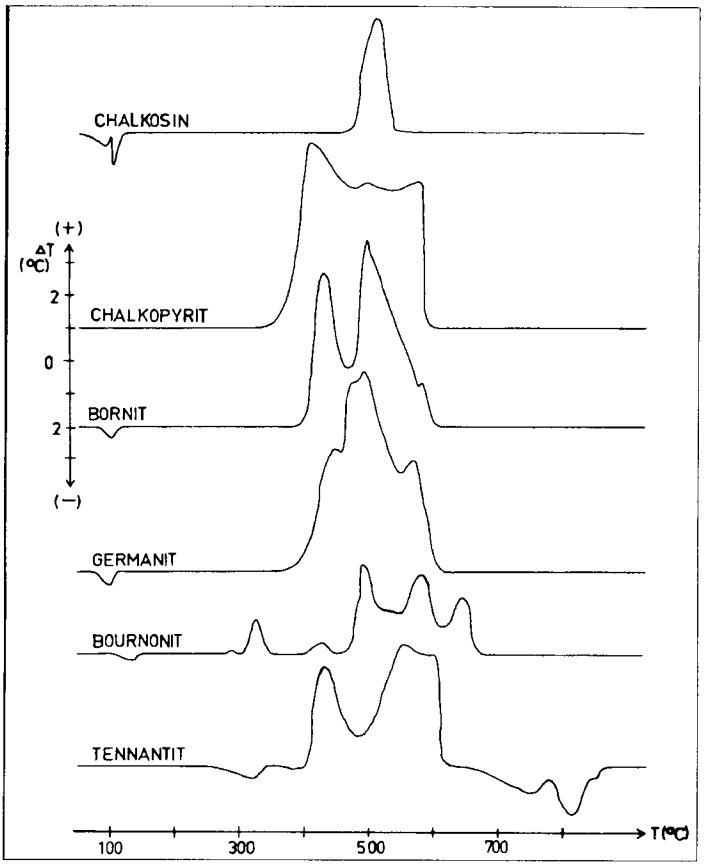


Figure 52. DTA curves of copper-sulfides, chalcocite, chalcopyrite, bornite, germanite, bournonite and tennantite.

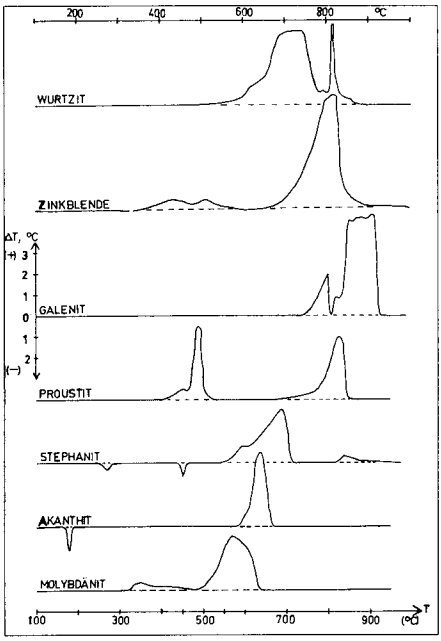


Figure 53. DTA curves of the sulfides: wurtzite, sphalerite, galenite, prousite, stephanite, acanthite and molybdenite.

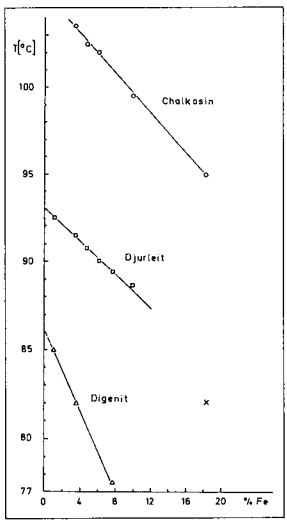


Figure 54. Dependence of the transformation temperatures of copper sulfides on the content of incorporated iron.

Iron is the most common substituent in (originally Fe-free) sulfides, as was shown by Smykatz-Kloss and Hausmann [336] and several other authors. Thus, the incorporation of Fe into the structure of copper sulfides causes a decrease in the phase-transition temperatures of these minerals (Figure 54).

Similar phase transitions to those for chalcocite, acanthite, digenite, strohmeyerite and jalpaite (Table 24) occur for many other chalcogenides. Table 25 contains the transition temperatures for sulfur and for some other sulfides, and includes the data for one telluride (hessite) and one selenide (penroseite).

The *oxidation* of chalcogenides occurs between 350 and 990 °C [18, 23, 24, 334, 352, 366]. Mostly a broad and very intensive "roasting effect" occurs (Figures 58 and 59). The iron and the Cu-Fe sulfides decompose below 700 °C, similar to the Ag sulfides [24, 25]. Only some *Pb-* and *Zn-* sulfides show their oxidation effects at very high temperatures, e.g. ~ 800 to 900 °C, wurtzite, sphalerite, galenite [24]. The oxidation behaviour of chalcogenides is quite sensitive to small variations of the apparatus and preparative conditions used for analysis. This means that the oxidation behaviour is not a very reliable parameter for mineralogical determinations, but results obtained on heating in an inert atmosphere, e.g. in nitrogen [357] (Table 26) are more reliable.

Table 25. Phase transition temperatures for some chalcogenides

mineral	composition	temperature [°C, ± 1 °C]	reference
bournonite	2 PbS x Cu_2S x Sb_2S_3	137	[24]
tennantite	$Cu_3AsS_{3.25}$	319	[24]
sulfur	S	96	[24]
heazlewoodite	Ni_3S_2	342	[24]
stephanite	$5Ag_2S$ x Sb_2S_3	270, 451	[24]
pyrrhotite	Fe_9S_8	348, 370	[24, 366]
hessite	Ag_2Te	160	[24, 366]
penroseite	Ni_3CuSe_8	380	[24, 366]
covellite	CuS	370	[349]
bornite	Cu_5FeS_4	228	[336]

Table 26. Decomposition temperatures for some Fe-bearing sulfides in nitrogen [357]

mineral	composition	decomposition temperature in N_2 [°C, ± 1°C]
pyrrhotite	Fe_9S_8	515
violarite	$(Ni,Fe)_3S_4$	545
pentlandite	$(Ni,Fe)_9S_8$	610
pyrite	FeS_2	645
chalcopyrite	$CuFeS_2$	800

2.4.4. SiO_2 minerals

The first thermal studies on SiO_2 minerals dealt with quartz, SiO_2 [1]. The high-low inversion of this very common mineral has concerned generations of mineralogists. When Tuttle [371] published his observation that the inversion can differ by up to 2 °C from the "textbook value" (573 °C, where the two modifications, high (α) quartz and low (β) quartz, are in thermodynamic equilibrium), and that this variable temperature may be used as a geological thermometer, he followed suggestions made by Fenner [372]. Keith and Tuttle [373] found this phase-transition temperature of 573 ± 1 °C to be true for ~95% of 260 samples studied, but the rest showed deviations of up to 160 °C. Fieldes [374] measured inversion temperatures between 550 and 560 °C for certain New Zealand samples. Nagasawa [375] observed remarkable differences in DTA curve shapes (and in transition temperatures as well). Faust [322] recommended the quartz inversion as a temperature standard. Well-ordered and crystallised specimens could indeed be used as a standard or reference material [24, 25]. Since 1970, the deviations from the "standard temperature" of 573 °C have been widely used for petrological or technical interpretations (see Section 4.2.2). For the period before 1970, a detailed bibliography will be found in Dawson and Wilburn [376]. Recently, Smykatz-Kloss and Klinke [377] updated the literature. The transformation of SiO_2-polymorphs is known as a reconstructive transformation, but the low high-transformation of quartz produced only small changes of atomic positions, without breaking any atomic bonds. Quite surprising, for the simple transformation mechanism, were the uncertainties about basic properties, such as the thermodynamic equations of state in the literature. Bachheimer [378] gave the first description of an intermediate phase in the transition region in the 1.4 K temperature range. This phase is characterized by a modulated structure with a period incommensurate with that of the quartz lattice. As Dolino [379] mentioned, "it is now clear that the principal cause of the change in the transition temperature comes from the

incorporation of chemical impurities, either substitutional or interstitial, in the quartz structure".

Fenner [372] found inversion temperatures for the $\alpha \leftrightarrow \beta_1 \leftrightarrow \beta_2$ transitions of *tridymite* at 117 °C (heat of transition, ΔH = 1.80 J/g) and 163 °C (ΔH = 0.96 J/g). For the $\alpha \leftrightarrow \beta$ transition of the other polymorph, *cristobalite,* between 200 and 260 °C (ΔH = 18.41 J/g).

The amorphous minerals, *opal-A* and *opal-C,* $SiO_2 \cdot n\ H_2O$, show dehydration temperatures between 65 and 300 °C [24, 380, 381], dependent on the state of alteration, e.g. on the water content of the opaline material.

According to Faust [322], the heat of transition of $\alpha \leftrightarrow \beta$ quartz is quite low (e.g. 13.0 J/g). Therefore, the quantitative determination of the amounts of quartz in unknown soil or sediment samples, as has been attempted by some authors (e.g. [382 – 384]) include large uncertainties and errors [376].

Recently, the inversion effects of silica polymorphs have been studied by some quite sophisticated TA methods, e.g. by a.c. calorimetry [323, 385] and by emanation thermal analysis (ETA, [386]), in order to measure the heats of transition, to study the effect of grinding, the influence of particle size (microsilica, [387]) or to characterise the firing process [388].

For a detailed review of the application of the high-low inversion of silica polymorphs to petrogenetic or technical problems see Section 4.2.2.

2.4.5. Other Minerals

The transition temperatures of some other (mostly rare) minerals have also been used as temperature standards. Thus, the α-β inversions of silica polymorphs (cristobalite, tridymite, quartz) have often been often calibrated against "normal standards" of added nitrates or sulfates, e.g. by use of the transition temperatures of KNO_3 (127.8 ± 0.3 °C), cryolite (Na_3AlF_6, 572.6 ± 0.5 °C) or K_2SO_4 (583.5 °C) [24, 25, 47, 267, 377, 389, 390]. Font and Muntasell [391] used KNO_3 in a thermobarometric study up to 150 MPa.

Kulp and Perfetti [121] and Mackenzie [8] studied the phase transitions of Fe-Al-Mn oxides. Pyrolusite, β-MnO_2, transforms at 690 °C, hausmannite, Mn_3O_4, at 750 °C. Pei Jane Huang et al. [392] investigated Ti-xerogels by means of Thermo-Raman spectroscopy combined with TGA/DTA and found two distinct phase transformations at 382 °C (amorphous → anatase) and at 573 °C (anatase → rutile).

The Lapis Lazuli mineral, lazurite, occurs in two polymorphs (e.g. orthorhombic and cubic) which exhibit a phase transition at 489 °C [327].

2.5. Magnetic transitions

2.5.1. Oxides

Magnetic properties of iron oxides are an important parameter in geosciences for the characterization of minerals and rocks. In order to quantify the magnetic properties, the magnetic moment (m) is used, which is obtained from the measured molar susceptibility χ,

$$\chi = \frac{Nm^2}{3kT} \rightarrow m = 2.83\sqrt{\chi T}$$

The temperature variance of χ is described by the Curie-Weiss law,

$$\chi_M = \frac{C_M}{T - T_C}$$

These properties were developed for palaeomagnetic studies in geology, geophysics and soil sciences, as well as for archaeometry, biology (biogenic magnetite extracted from magnetotactic bacteria) and material sciences [129].

C_M and T_C are the Curie constant and the Curie temperature, respectively and T is the actual temperature. As the temperature T rises, the susceptibility χ_M decreases and the iron oxide undergoes a phase transition. Numerous instruments have been described [393] for the direct measurement of magnetic susceptibility as a function of temperature.

Typical ferromagnetic iron oxides are magnetite (T_C = 850 K), maghemite (T_C 820 - 980 K) and feroxyhite (T_N 440 - 460 K) (T_N = Neel-temperature, the transition temperature for antiferromagnetic substances). The magnetization of magnetite decreases during the heating to a minimum at ≈580 °C (the Curie temperature of magnetite) and increases during the cooling back to the magnetization of the starting point [394].

The magnetic transition is connected with a so-called "λ-anomaly" in the c_p-T-function. The maximum in the c_p-curve characterizes the Curie temperature. This transformation was discussed as a reference material for the temperature calibration of thermobalances [395].

For goethite (α-FeOOH), a magnetic transition was determined in the temperature range between 80 °C and 120 °C. The magnetic transformation of maghemite (γ-Fe_2O_3) is difficult to determine because the transformation into haematite (α-Fe_2O_3) occurs above 400 °C. The magnetic transformation of maghemite should be above 580 °C. In the literature, temperatures up to 675 °C have been recorded [394]. A further complication results in case of the solid solution in the Fe-Ti-O system. At high temperatures haematite and ilmenite form a continuous solid solution. At low temperatures a large miscibility gap

exists [129]. A maximum exists in the magnetization between Fe_2O_3 and $FeTiO_3$ near 60% ilmenite and 40% haematite. The Curie temperatures decrease with increasing TiO_2-content [394].

Heating titanomagnetite in air above the Curie temperature ($T_C \approx 280$ °C) results in secondary phases with $T_C \approx 470$ °C (that is a titanomagnetite with composition near magnetite) [394].

The determination of the Curie temperature of magnetite ($Fe^{II}Fe_2^{III}O_4$) by differential thermal analysis has to be made under an inert atmosphere (N_2) [24, 396]. In air, the strong (exothermic) oxidation effect of Fe^{II} will mask the small endothermic magnetic transition, or it has to be measured in cooling curves. The Curie temperature of pure magnetite occurs at 580 °C ± 2 °C [397]. Substitution of Fe^{II} and/or Fe^{III} by Al^{3+}, Cr^{3+}, Ti^{4+}, Mg^{2+}, Ni^{2+}, Ca^{2+}, Mn^{2+}, and other ions which are common in natural magnetites, *lowers* the Curie temperature from 580 °C for 100 mass % Fe_3O_4 down to 450 °C for a magnetite containing 80 mass % Fe_3O_4, down to 300 - 350 °C for 60 mass % Fe_3O_4 (the remainder being TiO_2, Cr_2O_3, MgO, etc.) [24, 398].

Ferromagnetic minerals are the (titano-) magnetites, maghemite, pyrrhotite, some hematites and titanohematites. Hematites show a very weak change of magnetic properties reflected by a small endothermic DTA-peak at 680 °C. For titanohematites, the Curie temperature effect is lowered to 600 - 660 °C [399]. Neel temperatures (where antiferromagnetic substances lose their antiferromagnetism) occur generally below - 50 °C (wolframite solid solutions, e.g. [400]; olivines, e.g. [401]).

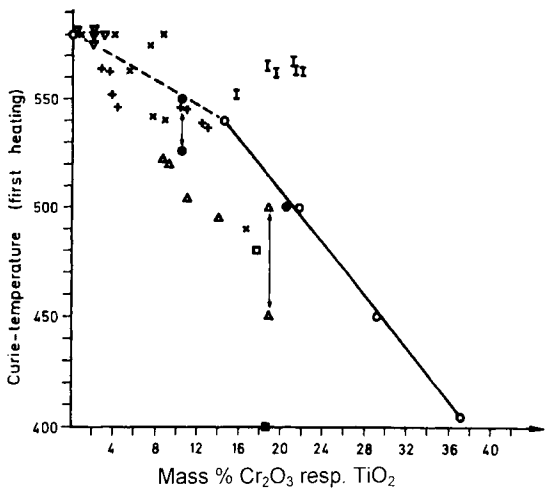


Figure 55. Dependence of the Curie-temperatures of magnetites on the amount of impurities.

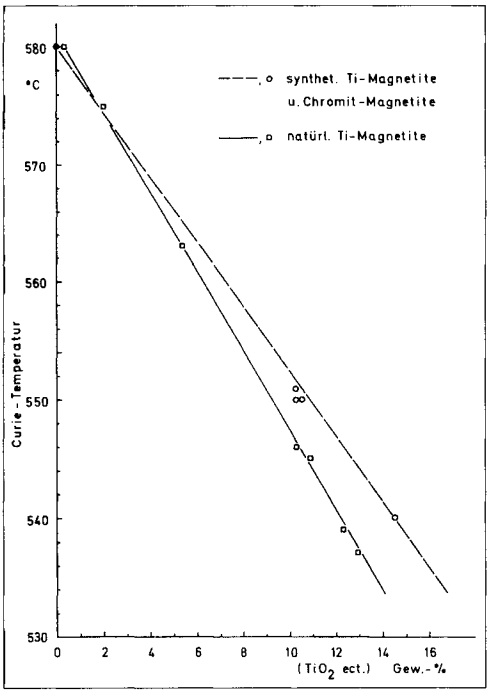


Figure 56. The Curie-temperatures of synthetic and natural ferromagnetic oxides in dependence on the amounts of incorporated Ti and Cr.

The Curie and the Neel temperatures are normally measured by methods other than DTA but, in case of magnetites, DTA measurements (in N_2) can help to classify and characterize natural (titano-) magnetites. The Curie temperatures of magnetites from Kiruna iron ores and from Tertiary basalts occurred between 490 and 580 °C [24].

Figure 55 contains the Curie temperatures of some magnetites vs their chemical composition. The data of Schmidt and Vermaas [397] and the data of Smykatz-Kloss [24] were obtained by DTA, the other mentioned Curie temperatures by different methods.

The scattering of the plot for natural titanomagnetites, which exceeds a value of 100 °C in places, and from which Lewis [402] drew his conclusion that the Curie temperatures of natural magnetites do not allow statements about their chemical composition, can be explained very simply. All values lying to the left of the marked line have only one part of the substituents incorporated into the magnetic structure. By supplementing the amount of TiO_2 (Cr_2O_3) with the amount of all those elements which substitute the iron, all values come to lie on the line or very close to it. The six values from Vincent [398] to the right of the

line represent natural intergrowths of magnetite and ulvite (Fe_2TiO_4). This means that the high TiO_2-contents (15-22 mass %) of these samples are not incorporated into the magnetite structure (and only in the case of substituents being incorporated in the magnetite structure would the Ti-content influence the Curie temperature!). In this case, the chemical analysis suggests an impure magnetite, but really the magnetite structure contains no, or only very few, TiO_2 units. The corrected values (those are the given values in Figure 56 minus the TiO_2-contents) all fall on the broken line in Figure 56. This correction is valid, as can be seen in the thermal behaviour (tempering) of these intergrowths. Vincent [398] obtained a homogenization of the intergrowths by heating the samples up to 950 °C. At this temperature only one phase had been recrystallized. During the slow heating process, a continous lowering of the Curie temperature occurred until 450-500 °C was reached for the completely homogenized phase, which was a titanomagnetite with 20-22 mass % of TiO_2 incorporated into its structure [398].

The investigation of one maghemite sample showed a Curie temperature of 640 ± 5 °C for this cubic Fe_2O_3, the value lying just between the Curie temperature of pure magnetites (580 °C) and that appearing weakly in the DTA curves of some hematites (680 °C). Thus it seems possible to use DTA to distinguish between the cubic forms of the iron oxides, magnetite and maghemite.

2.5.2. Sulfides

In petrological systems a further compound with magnetic properties is pyrrhotite Fe_7S_8, $Fe_{1-x}S$. The magnetic transition on heating was determined at 310 °C [394]. From the cooling curve, after heating pyrrhotites, decomposition of the pyrrothite and the formation of magnetite is observed. The cubic iron sulfide, greigite, has a magnetic transformation between 270 °C and 300 °C [394]. This mineral has been observed in tertiary and quaternary sediments in conjunction with special algae.

2.6. Exothermic effects, oxidation and pyrolysis

The *pyrolysis of organic material* has led to a large field of application in fuel technology and civil engineering (e.g. [403, 404]). In the earth sciences, the prospecting for, and exploration of, energy resources (e.g. crude oil, oil sand, oil shale, coal, bitumina), as well as the mining and quality control of such resources, has concerned mineralogists, geologists and geochemists for centuries, including the specialists of thermal analysis among them [405 - 421]. Warne [56, 422 – 429] and his co-worker Dubrawski [46, 430], using DTA, DSC and thermomagnetometry, published several studies on the regional petrography, characterization and possible applications of bitumina, coals and

oil shales. Lønvik et al. [566] applied thermosonimetry (TS) to oil shales and Balek [386] used emanation thermal analysis (ETA) for the characterization of two coals from Bohemia.

The study of the oxidation behaviour of organic material is - besides in coal and oil shale studies - of interest to clay scientists regarding the interrelationships of organic molecules and swelling clay minerals (smectites, vermiculites, mixed layers). Clay minerals swell in organic solvents [180, 431]. Organic molecules may be adsorbed on clay minerals [64, 432 – 448] or occupy the interlayer space between clay mineral sheets to form intercalation or organo-clay complexes [64, 449 – 452]. Hundreds of organo-clay complexes and intercalation compounds have been described, and the synthesis of pillared clays has led to a large and important interdisciplinary field of study and application in technical mineralogy, energy storage, catalysis, applied physical chemistry, chemical engineering and material sciences.

The swelling clay minerals mainly form these organo-clay complexes, but since the studies of Weiss [453], who described intercalations of non-swelling, water-free kaolinites with simple organic compounds, several authors have prepared organo-clay complexes of non-swelling minerals like kaolinite (with amino acids, [454 – 456]), talc and pyrophyllite (with stearic acid, [457]), sepiolite and palygorskite [172, 436, 452] and, recently, the water-bearing Mg-carbonate mineral hydrotalkite (with phenol, [458]).

All the authors mentioned used thermal methods to characterize the organo-clays. Several of the organo-clays described have been used as pharmaceutical drug-clay complexes, based on montmorillonites [452] or on sepiolite [459].

Thermoanalytical methods have also been used to characterize the biotic components in soil or sediments like cellulose or lignite. Differences in their pyrolysis allow a separation of such components.

Thermal analyses have also been applied in environmental studies to determine traces of sulfides, or other dangerous substances, in coals or raw materials [411, 422 – 429], in purity determination [304] and for controlling barriers around waste disposals, or for the detection of traces of pesticides or herbicides in soils [63 – 65, 444, 460, 461].

The oxidation of organic compounds takes place in two steps, showing two large exothermic effects between 300 °C and 400 °C and between 450 °C and 600 °C, respectively, due to the coking of hydrocarbons and finally to the pyrolysis of carbon (oxidation of C to CO_2) [64].

The main components of a plant framework, lignite and cellulose, are very well characterized by the fragments from the organic polymers (m/z= 39, 42, 43, 55, 97 114 for cellulose, from carbonyl-fragments, and 65, 77, 91, 151, 154,

164, 168 and 194 for lignite, from fragments of aromatic methoxyphenoles) by means of heat-controlled pyrolysis.

Balek [462] used emanation thermal analysis (ETA) for the characterization of morphological changes in bentonite during interaction with organic compounds. Yariv [444, 460] and Busnot [463] determined the origin of humic substances by DTA in the off-shore region of Normandy. Stout [464] identified Romanian amber and reconstructed its petrogenetic history, e.g. the alteration of former succinite.

The oxidation of chalcogenides (sulfides, arsenides, tellurides, etc.) occurs similarly, in two or more steps, resembling the roasting process and the sometimes complex formation process of intermediate compounds, see the section on chalcogenides and [18, 24, 357, 359, 465].

In geochemistry, the oxidation behaviour of Mn^{2+}, Pb^{2+} and (mainly) Fe^{2+} minerals, owing to changes in the redox conditions of soil or sedimentary environments, has concerned analysts of carbonates, oxides or hydroxides of manganese, lead and iron. Thus, the carbonate minerals, siderite, cerussite, rhodochrosite or ankerite, show spontaneous and large exothermic oxidation effects which partly overlap the endothermic decomposition effects and make the interpretation of the processes occurring quite complicated [18, 24, 52, 122, 125, 167, 283, 293, 295, 311, 312, 314 - 316, 424, 427, 467]. The heating rate used determines the shape and the exact decomposition/oxidation temperatures of Fe-bearing carbonates [318].

3. THERMODYNAMICS, KINETICS AND PHASE RELATIONS

3.1. Introduction

Dynamic thermoanalytical methods are frequently used for study of phase transitions (crystallization, melting) and non-isothermal kinetics during the transformation of natural compounds, minerals, rocks, and sludges [29, 471, 472]. The challenge is the deciphering of complex information from thermoanalytical signals. The situation differs considerably for the different thermoanalytical methods, e.g. the signal in a TG-trace is unambiguous with respect to the change of mass, but is ambiguous with respect to the chemical nature of the evolved volatiles. Dynamic thermoanalytical methods yield information about reaction temperatures of a mineral like a "fingerprinting", as well as data on changes of physical properties, e.g. sign and quantity of heat production, or changes of mass, of crystal structures, of dimensions, of colour etc [473]. This in turn provides data on the thermodynamic stability of a single or mixed compound under distinct physical and chemical conditions. Such studies also provide thermodynamic data for calculation of the equilibrium

conditions in heterogeneous phase systems, or cell-expansion parameters of rock-forming minerals, etc. [474 – 476].

3.2. Phase relation studies - phase diagrams

Measurement of physical parameters can be used to characterize phase relations that are dependent on temperature. By a combination of simultaneous X-ray diffraction, DTA/DSC/TG and thermo-optical microscopy, the influence of temperature can be determined for end-member-solids, binary or polynary systems. Certain aspects have to be taken into consideration during the analysis of natural minerals and rocks. Small quantities of other minerals or fluid inclusions may change the thermoanalytical results drastically. Phase transformations of the low-temperature modification of Na_2SO_4 (Type V), crystallized from aqueous solution above 32 °C under laboratory conditions, as well as under natural conditions (e.g. in the Wadi Natrun [330]), are different during the heating and the subsequent cooling processes [330, 477]:

$$\begin{array}{lcccc} & \overset{212\ °C}{\rightarrow} & & \overset{242\text{-}250°C}{\rightarrow} & \\ Na_2SO_4(V) & & Na_2SO_4(III) & & Na_2SO_4(I) \\ & & & \overset{215\text{ - }230\ °C}{\rightarrow} & \downarrow\ 236\ °C \\ & & Na_2SO_4(III) & \rightarrow & Na_2SO_4(II) \end{array}$$

This investigation showed, that phase (V) does not represent the equilibrium state in the heating and cooling programme. Sometimes a splitting of the III-I-transformation between 242 and 250 °C was observed. The reason of this splitting is not known at present. Furthermore, mass-loss curves for naturally occurring thenardite showed that small quantities of CO_2 and water escaped during the phase transition [330].

This example demonstrates the influence of trace compounds on the kinetics of phase transitions. The interpretation of phase transformation processes of natural materials has generally neglected such phenomena, but DTA/DSC and TG-MS experiments suggest the existence of kinetic barriers and assist in the the interpretation of X-ray or spectroscopic data on the structural relations of phase transitions. The influence of the sample preparation has also been observed in many cases by means of DTA/DSC and TG measurements, as demonstrated, for example, for crystal hydrates by Heide [85], or for the modifications of $CaCO_3$ by Bayer and Wiedemann [478].

The establishment of multi-compound phase relations in phase diagrams has been supported by thermoanalytical methods in many systems that are relevant for the geosciences. The possibility and difficulties of construction of polynary

phase diagrams have been discussed in detail, for example by Sestak [479] and for geosciences by Heide [29].

3.3. Determination of thermodynamic properties in petrological systems

A large number of heat capacity measurements, as functions of temperature, are now available for petrologically interesting phases. At temperatures above 298 K, heat capacities are derived by drop calorimetry [480] or by differential scanning calorimetry. Values are measured relative to a standard, such as corundum. For measuring the "high-temperature" $c_p(T)$ functions of minerals, dynamic temperature heat-flow calorimetry has become a frequently used technique. Measurements are possible with small quantities of samples (about 10 mg) without special preparation or special conditions. The accuracy of the c_p-data obtained by this technique is not better than ± 1%, however measurements can be made up to 1400 °C [481]. High-temperature heat capacites are often calculated by a polynominal: $c_p = a + bT + cT^{-2} + T^{1/2}$.

In petrological applications, the extrapolation of heat capacity data for high temperatures causes considerable problems. Therefore, high-temperature calorimetry by heat-flux calorimeters is useful, even if the accuracy is significantly lower than in the reaction calorimeter of the twin-microcalorimeter type [480].

Thermogravimetry is a valuable tool in the study of homogeneity of rock-forming minerals. A feldspar with a perfect alumino-silicate framework should not decompose when heated below the melting point. Mass losses of the order of 0.01 - 0.20 % have been reported on heating natural feldspars and explained by a loss of water from lattice defects [482]. Different loss patterns were observed for quartz and orthoclase when derived from magmatic or "post magmatic" rocks [483]. Microscopic and sub-microscopic fluid-inclusions may cause a decrepitation of the solid that is accompanied by a mass loss and degassing effect and frequently by an acoustic signal, e.g. it was detected in quartz or kaolinite [484, 485]. Alteration products of feldspars, like kaolinite or mica, can be determined quantitatively in very small amounts (< 0.1 %) from thermogravimetric data. Significant endotherms in the DTA-curves for albite and various plagioclases in the range of 700-900 °C indicate thermal effects of impurities. For the plagioclase, it might be possible to explain these effects in terms of structural changes in the feldspars [486, 487].

3.4. Kinetics

Many solid-state reactions are initiated at pre-existing defects by a heterogeneous nucleation process. Theories of heterogeneous nucleation in complex natural systems are not well developed. The rates of nucleation and of growth of nuclei depend upon the transformation mechanism [488].

In a *reconstructive* transformation, the rates are functions of temperature. Under isothermal conditions, the volume of the fraction transformed increases with time. Reconstructive transformations include changes in primary or secondary atomic coordination. For so-called "first-order" solid-solid transitions, the changes of thermodynamic parameters are similar to the changes accompanying phase transitions from gases or liquids. Polymorphic reconstructive transitions in minerals, such as aragonite to calcite, are generally very sluggish and, under laboratory conditions, such transitions are characterized by high metastability or considerable superheating or cooling [489]. On extensive-intensive variable plots (enthalpy, entropy volume and temperature), first-order transitions are discontinous at the transition temperature. Second-order transitions follow the thermodynamic classification by Ehrenfest [490]. Plots of H, S, and V have a cusp and plots of c_p (specific heat), α (expansion coefficient) or β (compression coefficient) are discontinuous. λ-transitions, or order-disorder transitions, show that problems arise if the rate of reaction is slow compared with the kinetics of transition. Some transitions are described as "mixed"-transitions. The classification of a phase-transition may sometimes depend on the technique of analysis used.

The rate of a *displacive transformation* is determined solely by a specific temperature with a specific transformed volume. That means that the volume does not increase with time under isothermal conditions. The polymorphism of quartz, one of the most abundant minerals of the earth's crust, is an example of the complexity of such apparently simple transformations (Section 2.4.4). The low-pressure phase transition of silica has been the subject of many investigations since its discovery by Le Chatelier [1] in attempts to determine its basic properties (such as the thermodynamic equation of state). Moreover, until 1980, the existence of an intermediate phase, with a temperature range of 1.4 K, between the α (high-temperature modification) and β (low-temperature modification) at 846 K was unknown [379].

The problem with the β-α transition results from the poor accuracy of the temperature control in previous experiments. This intermediate phase is characterized by a modulated structure with a period incommensurate to that of the quartz lattice [379].

A special case of a solid-solid transformation is rotational transformation. This transformation is controlled by a specific temperature, which transforms the libration of molecules into a free rotation.

Further mechanisms are order-disorder-transformations and spinodal-transformations (solid-solid or liquid-liquid phase separation) and the transformations of frozen-in metastable solid states (e.g. glass-transformation).

The process of crystallization in undercooled melts, or in the solid state, are considered in terms of the nucleation frequency (rate), J, and the (linear) nucleus growth rate, R. Nucleation theories presuppose a significant overstepping of the equilibrium boundary. The magnitude of the overstepping necessary for nucleation is, however, generally unknown. An analysis of nucleation kinetics shows that the processes generally have a non-steady state transition character [491]. If the system exists in a state (e.g. undercooled melt) in which nucleation, that means "crystallization", is possible, a time τ must elapse for a steady-state population of subcritical clusters to form. Kinetic equations of nucleation have been evaluated from theoretical and experimental results by various authors [491]. A basic relation proposed by Zeldovich [586] is as follows:

$$I(\mathrm{t}) = I_{\mathrm{ss}} \exp\left(\frac{\tau}{t}\right)$$

I_{ss} = steady state nucleation rate
τ = non-steady-state nucleation rate
t = time

The number of nuclei $N(t)$ (critical clusters) at a time t is given from the kinetic nucleation equation,

$$N(t) = \int_0^t I(t)dt$$

The experimental determination of the number of critical clusters ("nuclei", $N(t)$) is possible after nuclei have grown to microscopically visible size.

Nucleation kinetics are determined by two kinetic parameters: the non steady-state nucleation time, τ, and the steady-state nucleation rate I_{ss}. In general, experiments are carried out at a great distance from equilibrium. As Carlson [492] observed in the aragonite – calcite transformation at 1 bar, a large number of nuclei are formed in a very short time. When reacting to a large volume change, the reactant phase is strained during the growth of the product phase and fracturing of the product phase occurs [493].

In solid-state reactions, homogeneous nucleation, that is nucleation occurring without the advantage of a pre-existing internal surface, is subordinate to heterogeneous nucleation at the grain boundaries, dislocations, or other defects occurring in the bulk, or at the surface. This is caused by the energy that is associated with phase boundaries contributing to the energy required to form a critical nucleus. Homogeneous nucleation in the solid state is unlikely under natural conditions. For heterogeneous nucleation, the nucleation rate is determined by a function of the phase boundary $f(\Theta)$:

$$\frac{dN}{dt} = A' \exp\left(\frac{-\Delta G^* f(\Theta)}{kT}\right) \exp\left(\frac{-Q}{kT}\right)$$

$$\Delta G^* = \frac{16\pi}{3} \frac{\sigma^3}{(\Delta Go)^2} \text{ for a spherical nucleous} \approx \frac{1}{(Tm - T)^2}$$

Q = kinetic barrier to growth, "activation energy" of diffusion
σ = interfacial energy per unit area
ΔG_o = free energy change per unit volume of product
k = Boltzmann's constant
T = temperature
t = time
T_m = melting temperature.

The rate of nucleation in an allochemical solid-solid reaction is controlled both by the heat flow and the diffusion rate and/or by the change of the equilibrium constant of the chemical reaction.

After a nucleus is formed, the nucleus grows at a rate, R, controlled by the temperature and by the three slowest processes:
a) the thermal conductivity of the bulk which determines the local heat content resulting from the energy absorbed or released by the reaction,
b) the diffusion rate of nucleus forming ions to or from the growing nucleus,
c) the rate of dissolution or formation at an interface [494].

Dehydration and decarbonatisation reactions are typical allochemical processes relevant to the geosciences. The thermodynamics are described by the Gibbs energy change between the product phase and the pure reactant phase [495]. For geological examples, calculations are often only possible with several simplifying assumptions, because the thermodynamic data necessary for more accurate evaluation does not exist.

This is particularly true when surface nucleation and growth of the product are dominant. The results are then difficult to distinguish from grain boundary nucleation and growth in the bulk. Nucleation rates and growth rates on grain surfaces and on the grain boundaries may differ by orders of magnitude, because surface free energy and interfacial free energy are different. For solid-state transformations of geological interest, the volume change is often large, e.g. for the aragonite to calcite transformation the difference of volume at a pressure of 1 bar is + 8.15%, and for the transformation of quartz into cristobalite, ΔV= +13,7% [488]. The formation of calcite from aragonite develops a transformation strain which forms lamellar strain twins in the aragonite [493]. Additional factors, such as the particle size or the

microstructural development, may also control the reaction rate. For example, a polymorphic transformation may be different if nucleation occurs on grain boundaries or in intergranular defects [488]. Very high shear stresses may be produced by mechanical grinding and the reaction rate may be increased by several orders of magnitude. Under such tribo-chemical conditions, the transformation may occur during the preparation of the sample by grinding at room temperature. Furthermore, the addition of water to a dry system may accelerate reaction rates by 8-10 orders of magnitude and the contribution of the strain energy may be completely deleted.

The overall transformation may be described by empirical rate equations relating experimental observations of the amount of transformed material to temperature and time. These empirical rate equations may require substantial changes if the experimental configuration is changed. Thereby the model mechanism may be changed and the application cannot necessarily be applied with confidence to the geological process. These experiments do however illustrate the different possibilities of phase transitions. A characteristic phenomenon can be observed when the transformation rate is changed from a heat flow-controlled mechanism to a diffusion-controlled growth mechanism. This results for example in the change of the volume of sample. The volume or the packing-density of the sample may control the rate and mechanism of the phase transformation.

Examples relevant in geosciences are the transformation of gypsum or dolomite. The transformation of gypsum during heating leads to the formation of bassanite and finally to γ-anhydrite:

$$CaSO_4 \cdot 2\ H_2O(s) \rightarrow CaSO_4 \cdot \tfrac{1}{2}\ H_2O(s) + 1\tfrac{1}{2}\ H_2O(g)$$

Heide [496] demonstrated that the formation of the bassanite modification cannot be explained by the crystal-structure of gypsum, because the atomic positions of the two water molecules in the structure are completely equal. The decompositon should occur only in one or in two steps with an equal loss of H_2O to anhydrite. The dehydration is a one-step process if heat transfer is dominant over the diffusion-rate of water through the sample. If the diffusion rate of water decreases, a secondary hydration of the decomposition products is possible and the formation of bassanite occurs.

$$CaSO_4 \cdot 2\,H_2O(s) \rightarrow \gamma\text{-}CaSO_4(s) + 2H_2O(g)$$

$$\downarrow$$

$$CaSO_4 \cdot \tfrac{1}{2}\,H_2O(s) + 1\tfrac{1}{2}\,H_2O(g)$$

$$\downarrow$$

$$\gamma\text{-}CaSO_4(s) + \tfrac{1}{2}\,H_2O(g)$$

It is possible to control the formation of bassanite by the external conditions of the heat treatment. Oscillation of the rate of reaction results from a distinct relation between the volume and geometry of the sample and diffusion rate of the volatile compound in the decomposed solid [117]. It is possible to determine the conditions for a kinetic switch, in respect to the gain of a distinct phase, by experiments. This is important for the interpretation of the observed thermal behaviour both in industry and geoscience [29].

The same observation is made during the decomposition of dolomite. The double peak with maxima at about 800 °C and 900 °C is frequently used like a fingerprint for the detection of dolomite in carbonaceous rocks and argillaceous limestones [24, 25]. From the crystal structure alone, an explanation for the split in the decompositon rate is impossible. It is possible that the decomposition also occurs primarily in a one-step-reaction:

$$CaMg(CO_3)_2(s) \rightarrow CaMgO_2(s) + 2CO_2(g)$$

If the diffusion of CO_2 is hindered by the density of the reaction product, a secondary carbonization leads to the formation of calcite, which decomposes again at higher temperatures:

$$CaMg(CO_3)_2(s) \rightarrow CaOMgO(s) + CO_2(\text{trapped}) + CO_2(g)$$

$$\downarrow$$

$$CaCO_3(s) + MgO(s)$$

$$\downarrow$$

$$CaO(s) + CO_2(g) + MgO(s)$$

These observations lead to different aspects that should be considered in interpreting the results of experimental reaction kinetics:

- most important is the probability and possible reality of the physical model. A decision is generally impossible from one experiment alone. For the interpretation, aspects resulting from crystalline structure of the material must be taken into consideration, not only the analytical data of transformation e.g. a TGA or DSC run.
- furthermore, the numerical values of different possible models should be compared, especially in the context of single or coupled chemical reactions [497].

For crystal hydrates, multi-step decomposition is characterised by a consecutive first-order reaction:

$$A \rightarrow B + \text{volatile} \rightarrow C + \text{volatile}$$

Two maxima for the reaction rate are expected, determined by the stoichometry of the volatile formation and the formation of the intermediate (B), which is only formed under distinct experimental conditions. The process is controlled by the interrelation between the heating rate, the decomposition rate, the diffusion rate of the volatile in the decomposed solid, and by the volume of the sample.

Natural substances are characterised in dependence of their petrogenesis by their trace contents of volatiles, e.g. kaolinite contains traces of carbonates which decompose during the dehydroxylation. That means the TG curve is a superimposition of different chemical reactions in different ranges of temperatures. Such phenomena are detectable by TG with a step-by-step analyis of distinct reaction intervals [117], or by selective analysis of volatiles by means of specific gas detection, e.g. by mass spectrometry. Rate equations for reactions relevant to the geosciences are summarized in Table 27. They should be used and discussed under the aspects mentioned above.

4. THE INFLUENCE OF STRUCTURAL DISORDER ON THERMAL EFFECTS

4.1. Hydrolysates and carbonates

Crystal structural disorder may be caused by (a) chemical or (b) physical effects. Chemically substitutions and impurities may be the reason for changes in the thermal behaviour [304]. Physical disorder may be caused by any kind of lattice defects, which create deviations from the "normal" crystal geometry and structural order (Schottky and Frenkel type of defects) and lower the lattice energy. Grinding, or other types of mechanical treatment, causes physical

Table 27. Rate equations for nucleation and growth [488]

Rate equation	Theoretical source	Application in geological reactions
Homogenous nucleation $\frac{dN}{dt} = kN_0$	Stationary nucleation	at present no application in geological reactions
Heterogenous nucleation $\frac{dN}{dt} = A' \exp\left(\frac{-\Delta G^* f(\Theta)}{kT}\right) \exp\left(\frac{-E_{dif}}{kT}\right)$	nucleation on an interface, contact angle $f(\Theta)$ between 0° and 90°	
Crystal growth	n = 1 first order	aragonite ⇒ calcite
$\frac{d\alpha}{dt} = K_1 (1-\alpha)^n$	n = 1/3 , 1/2 interface controlled	olivine ⇒ spinel
$\frac{d\alpha}{dt} = K_2 \alpha^{-n}$	$n = 2/3, 1/2$ diffusion controlled	quartz + periclase ⇒ forsterite
$\frac{d\alpha}{dt} = K_3 [1-(1-\alpha)]^{1/3} (1-\alpha)^{2/3}$	powder reaction Jander-equ.	dehydration decarbonatisation
$\frac{d\alpha}{dt} = K_4 (1-\alpha)[-\ln(1-\alpha)]^n$	Avrami-Mehl-Johnson-equ. n = 3 ⇒ sphere n = 2 ⇒ plates n = 1 ⇒ needles	aragonite ⇒ calcite
$\frac{d\alpha}{dt} = K_5$	constant rate growth of planar layers	brucite ⇒ periclase + H_2O
$\frac{d\alpha}{dt} = K_6 \alpha$	empirical exponential equ.	

disorder in minerals [219, 286, 498, 499] which may eventually lead to complete amorphisation [113, 500]. Consequently, thermal effects decrease with increasing disorder. The decrease is manifested in peak temperature, intensity (ΔT) and peak area, until the effects have disappeared completely [499].

Mainly those minerals having formed authigenically in soils and sediments show large variations in chemical and physical disorder. Kelly [127] and Kühnel [59] described several goethites, α-FeOOH, which dehydroxylated between 450 °C and 350 °C due to different degrees of "crystallinity" (= disorder). Smykatz-Kloss [24] found a decrease of the dehydroxylation temperature from 410 °C to 370 °C (dependent on the amount of incorporated Al^{3+} for Fe^{3+}). Kulp and Trites [501], Mackenzie [59], Kelly [127] and Smykatz-Kloss [24] observed exothermic effects on heating goethites or lepidocrocites (γ-FeOOH). All these authors found the exotherms only in case of poorly ordered hydrolysates. The difference in temperature and shape of the dehydroxylation effects of goethites and of clay minerals are clearly seen in *PA-curves* [24, 25, 54, 61].

Different degrees of physical disorder can be estimated by X-ray diffractograms [220] or by DTA measurements [62]. The following results have been obtained from DTA curves for some kaolin minerals exhibiting different degrees of physical disorder (Figure 16). The analyses were conducted under strictly standardised conditions [24, 61].

With decreasing degree of disorder:

a) A shift in the peak temperature of the dehydroxylation effect occurs from 520 °C, for poorly crystallized "fireclay" types, to > 700 °C for well-ordered dickites,
b) The intensity of this effect (ΔT) increases continuously.
c) The peak temperature and ΔT of the exothermic effect (> 920 °C) increases as well.

Smykatz-Kloss [24] classified kaolin minerals according to their degree of disorder into four classes (Section 2.2.3).

Balek and Murat [502] measured the degree of disorder of kaolin minerals by ETA techniques. Frost [185] observed disordered kaolinite structures after de-intercalation from kaolinite/dimethylsulfoxide complexes by means of DTA/TG and Raman spectroscopy.

Other clay minerals (smectites, vermiculites, illites, chlorites...) show analoguous behaviour. Kubler [220] established the method of measuring the "illite crystallinity" (= disorder of sedimentary micas) by means of X-ray diffractometry. Smykatz-Kloss and Althaus [61] showed that DTA and IR techniques were more suitable than X-ray, because of interference of the X-ray data by grain size effects.

Chemical disorder occurs in numerous minerals. It is caused by substitutions, solid solutions and weathering. In clay minerals, the influence of tetrahedral and octahedral substition (Al for Si and Mg, Fe for Al) is remarkable. Smectites for instance, generally form solid solutions of the "end-members" beidellite ($Al^{[VI]}$), nontronite ($Fe^{2+,\,3+\,[VI]}$) and saponite ($Mg^{[VI]}$). The dehydroxylation temperatures decrease from the Mg-types (about 850 °C) to the Al-types (about 700 °C) and the Fe-types (about 500 °C), mirroring a constant decrease in the crystal structural order from saponite/hectorite to beidellite/montmorillonite and to nontronite. Whereas saponite/hectorite has the largest octahedral cation (Mg), beidellite/montmorillonite has the smaller cation Al^{3+} in the octahedral site. Nontronite includes two types of iron ions, namely Fe^{2+} and Fe^{3+}, thus creating additional disorder effects.

The DTA curve for a typical smectite sample includes four endothermic effects - one effect at 150-200 °C which reflects the dehydration of interlayer water and three effects near these mentioned temperatures - proves it to be a solid solution.

Chemical substitution can lower the decomposition temperatures of carbonates, phase transition temperatures of chalcogenides or the Curie temperatures of magnetites. In dolomites, $CaMg(CO_3)_2$, the partial substitution of Mg by Fe^{2+} and/or Mn^{2+} causes a third or fourth endothermic effect ($FeCO_3$ and $MnCO_3$ respectively). They occur at lower temperatures than those of the $Mg\text{-}CO_3$ decomposition. With increasing Fe and Mn incorporation into the dolomite structure, that means with increasing chemical disorder, the $Fe\text{-}CO_3$ decomposition occurs at lower temperatures [24] (Figure 57).

The incorporation of Mg for Ca in the calcite structure lowers the structural stability. Increasing Mg-incorporation causes decreasing decomposition temperatures of the Mg-calcites (Table 28) and a shift in the main X-ray reflection.

Table 28. MgO contents and decomposition temperature of Mg-calcites [24] (sample amount, 150 mg)

sample, locality	mol-% MgO	decomposition temp. [°C; ± 0.5 °C]	$d_{(1014)}$ [Å]
pure calcite, Harz/Germany	0.00	925	3.035
Mg-calcite, Bermudas	5.90	898	3.018
Calcite (Encrinus liliformis, Bermudas)	8.65	893	3.005
calcite algae, Gaybu	18.10	889	2.974
calcite, Sao Vicente	19.00	889	2.972
calcite, Fernando Poo	21.00	887	2.966

(The samples were kindly supplied by Prof. C.W. Correns, Göttingen)

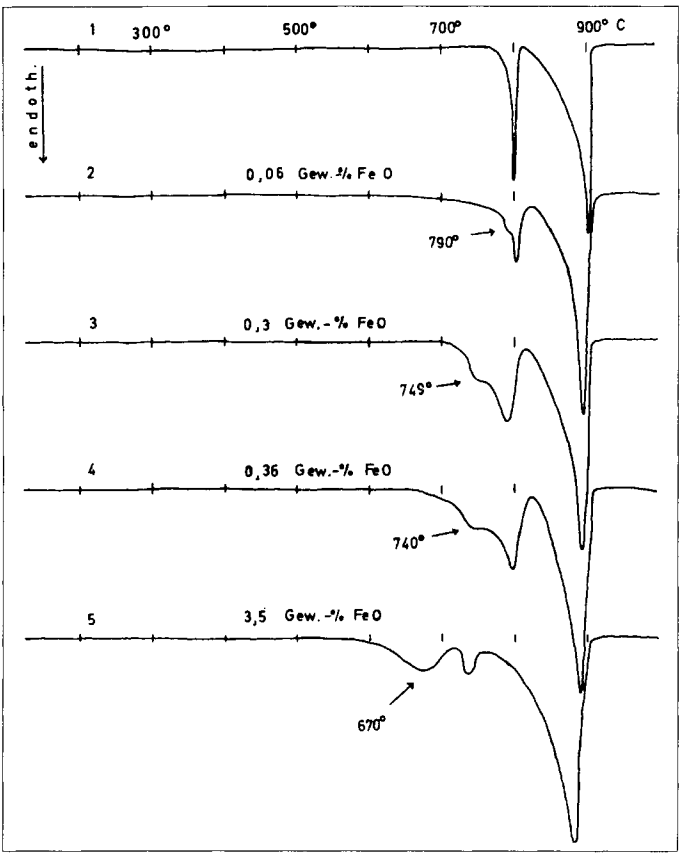


Figure 57. DTA curves of some Fe-bearing dolomites. The amount of incorporated FeO is (from the top) 0.06, 0.3, 0.36 and 3.5 mass %, respectively.

The structure of aragonite, the orthorhombic form of $CaCO_3$, can accommodate large divalent cations other than Ca^{2+} (ionic radius, 1.0 Å) in the Ca positions, e.g. Sr^{2+} (ionic radius, 1.27 Å), Ba^{2+} (1.43 Å), or Pb^{2+} (1.32 Å). More than 0.3% of these ions substituted for Ca causes a small endothermic shoulder *before* the $CaCO_3$ decomposition effect and one or two sharp little peaks *after* it (Figure 58) due to the decomposition of the Pb-, Sr- and Ba-CO_3 components of aragonite, respectively [24, 274].

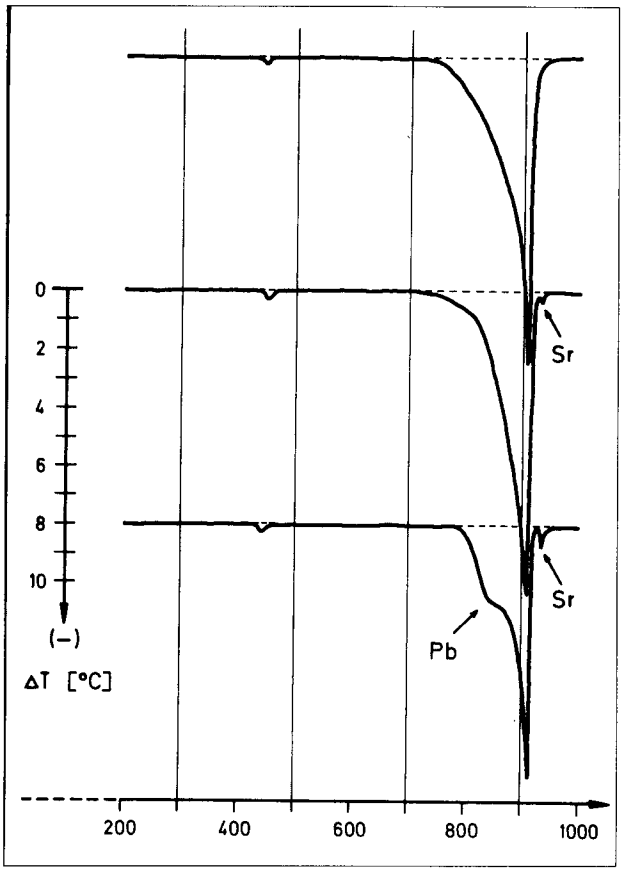


Figure 58. DTA curves of three aragonites. The small endothermic effect shortly after 400 °C represents the monotropic phase transformation aragonite -> calcite. The small endotherms before and after the $CaCO_3$ decomposition mirror small structural incorporations, e.g. of Pb ("lead aragonite", tarnowitzite) and Sr.

4.2. Silica minerals

The very common mineral *quartz*, SiO_2, occurs in two modifications which are in a thermodynamic equilibrium at 573°C (1 atm), e.g. low (β) and high (α) quartz (see also Section 2.4.4). At this temperature, a reversible inversion effect occurs causing a heat of reaction of 3.1 cal/g (=12.98 J/g, [322]) for this λ-transition. When Tuttle [371] published his observation that this inversion can differ by up to 2°C from the "textbook value", and that this slightly variable temperature may be used as a geologic thermometer, he followed suggestions

made by Fenner [372]. The high-low inversion of well-ordered and well-crystallised quartz crystals normally occurs at 573°C. Berkelhamer [382] found, that the effect differed in shape for coarse and fine fractions. Nagasawa [375] investigated 20 vein quartz crystals from Japan and reported remarkable shape variations for the inversion effect [377] and for the inversion temperature as well (see Table 29). Tuttle and Keith [504] found differences of nearly 40°C for

Table 29. Variation of quartz inversion temperatures (DTA-measurement, T_i, °C ± deviation)

(a) min	(b) max	samples		reference
"variation of 1.9 °C"				[371]
502 ± 3	572.2 ± 0.3	(a) cavity in Muschelkalk	(b) sandstone	[531][2]
518 ± 2	574 ± 1	(a) chrysoprase, silesia (microcrystalline quartz)	(b) agate, Pfalz	[390]
525 ± 5	545 ± 5	vein crystal, Scotland		[512][1]
532 ± 2	575 ± 0.5	(a) concretion in slates	(b) igneous	[389]
532 ± 3	575 ± 0.5	vein quartz crystals, Black Forest		[390]
538	575	(a) sediment	(b) granite	[504]
553 ± 2.5	573 ± 2.5	(a) meta-quartzite	(b) pegmatite	[509]
563	574	Japanese vein quartz		[375]
565 ± 2	574 ± 0.5	(a) authigenic in limestone	(b) hydrother-mal vein	[507]
567.6 ± 0.3	572.4 ± 0.3	(a) granite	(b) rock crystal	[525]
569.6 ± 0.35	572.4 ± 0.35	quartz from geothermal field, NZ		[527]
570	574.8	(a) geode in quartzite	(b) amphibolite	[508]
571.3 ± 0.2	574 ± 0.2	contact aureoles, granite	hornfels and	[510]

[1] – thermosonimetry measurement by Dr. K. Lønvik, Trondheim / Norway
[2] – DSC measurement

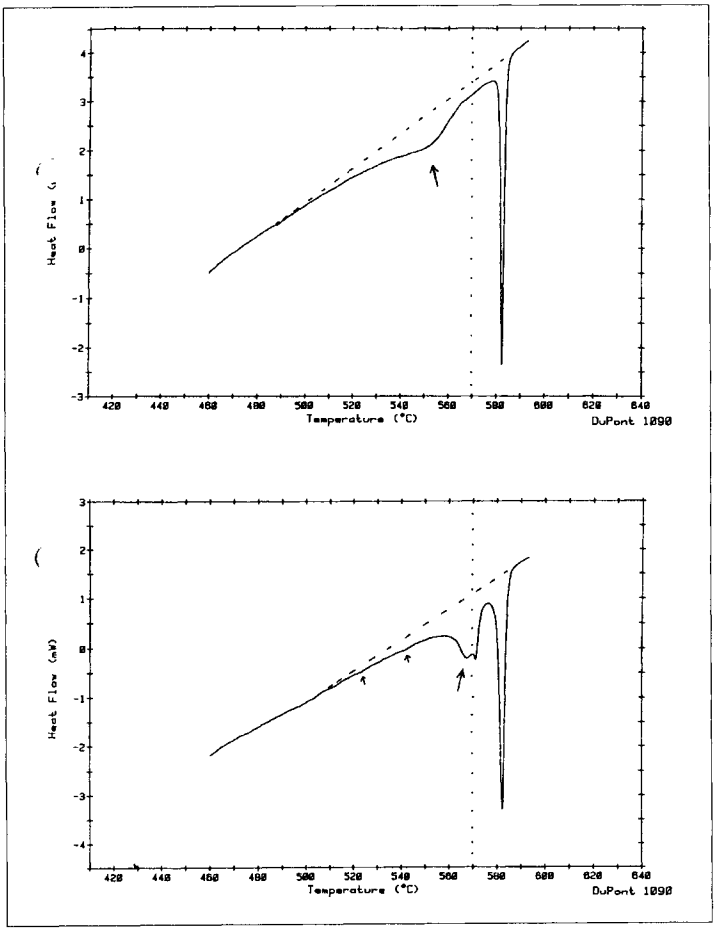


Figure 59. DSC curves of two microcrystalline quartz-crystals from limestones (top) and from sandstone plus internal standard (K_2SO_4, sharp endotherm).

the inversion temperature of sedimentary and igneous quartz crystals (Table 29). Fifteen years later (nearly simultaneously at several localities) geoscientists started to measure the inversion of some hundred quartz crystals from various rocks and soils, mostly by means of DTA [24, 389, 390, 505 – 512]. The most striking effects were found for microcrystalline and some authigenic quartz crystals from sediments and soils. They showed broad effects of low intensity and very often series of flat overlapping endotherms on heating, with corresponding exotherms on cooling, between ~500 and 570°C [205, 375, 382, 384, 389, 390, 513 – 515].

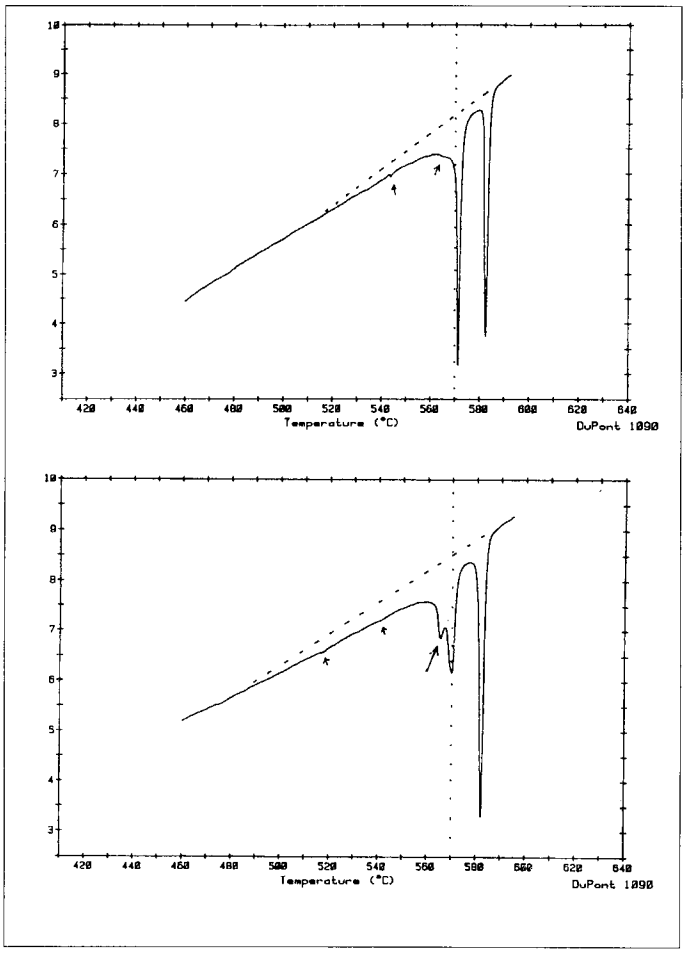


Figure 60. DSC curves of two quartz-crystals from cavities in limestones. The arrows point to disordered parts of the samples (from [531]).

Smykatz-Kloss and Klinke [377] reviewed the state-of-the-art of the research on the high-low quartz inversion and on its application to petrological problems. They discussed the main factors which influence the inversion effect. They had been found and described by several authors, e.g. the preparative and instrumental factors as well as the material-inherent factors. The requirements for optimal and reproducible measurements have been discussed. Besides the influence of grinding, sample and particle size, packing density, sample arrangement, reference material, gas adsorption, furnace atmosphere, thermocouples, crucibles or heating rate (e.g. mentioned in [24, 28, 219, 389, 390, 498, 499, 511, 516 – 523]), the reason for variable inversion temperatures

proved to be mainly the chemical composition and physical properties of the crystals [304, 371, 373, 389, 508 – 510, 524 – 527].

Quartz belongs to the very pure minerals, exhibiting not more than 0.3 mass-% of impurities in total [528]. The impurities consist of low amounts of water (fluid inclusions), some dissolved ions in the fluids (Na^+, Mg^{2+}, Ca^{2+}, Cl^-, SO_4^{2-}, HCO_3^-) and very low amounts of cations substituting the Si^{4+} (mainly Al^{3+}, Fe^{3+}, Na^+, Li^+, H^+, Ti^{4+}).

Crystal physical factors seem to be much more responsible than chemical impurities for the variation in quartz inversion behaviour [219, 304, 382, 390, 498, 499, 511, 517, 523, 525, 527, 529]. Mechanical treatment (e.g. crushing or grinding) weakens the bonding forces in a crystal lattice, lowering the energy necessary for structural transformations. Energy supply by mechanical treatment or by radiation (X-ray, γ-ray) creates structurally disordered parts in the (quartz) crystals, where the structural transformation (e.g. the high-low inversion) will occur somewhat earlier than in less-disordered parts. The result is a broadening and flattening of the inversion effect in the DTA (or DSC, TG) curve. This is observed for many disordered specimens as well as for artificially crushed crystals [60, 390, 499, 515, 516]. With increasing time (or intensity) of grinding, the inversion effects become smaller and smaller and finally disappear completely [219, 499]. The material has lost more and more of its crystallinity and a decrease in particle size implies an increase in disorder due to the larger surface [529].

Crystal physical disorder in natural crystals is caused by all processes which result in any kind of pressure (stress or strain). Stress may start with syngenetic processes during the transport of rocks or rock fragments and will be continued during diagenesis (e.g. pressure solution phenomena), weathering and metamorphism. The interdependence between metamorphism and structural disorder of (quartz) crystals, however, is more complex and complicated. Metamorphic processes may involve recrystallisation and retrograde transformation which may "overprint" and change the original (or at least, former) crystalline character and degree of disorder of quartz, - and its inversion characteristics. This has been broadly discussed, e.g. in [24, 389, 390, 508 - 510, 523, 527, 530].

A measure of the degree of disorder of minerals which involve a displacive transformation (a reversible high-low temperature inversion) is the *hysteresis* between the temperature of inversion on heating and that on cooling (Figure 62) [24, 60]. With increasing degree of disorder, the hysteresis effect becomes larger and larger. Smykatz-Kloss and Schultz [60] studied the inversion behaviour of synthetic cristobalites. Well-ordered *cristobalite* (tetragonal SiO_2) inverts at 270 ± 2°C into a high temperature modification. With increasing

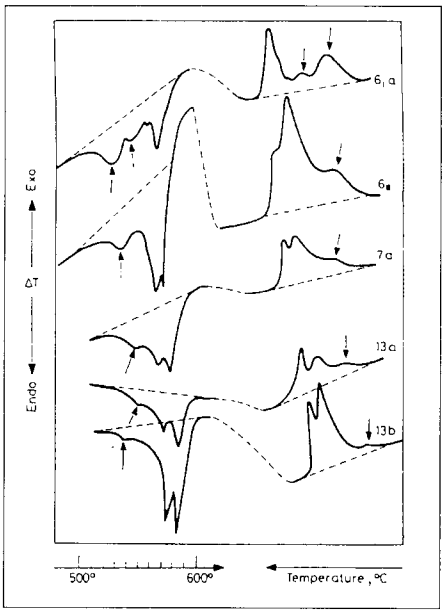


Figure 61. DTA traces of five microcrystalline quartz samples plus K_2SO_4 (internal standard, 584 °C); left, heating, right, cooling traces. The arrows point to the disordered parts.

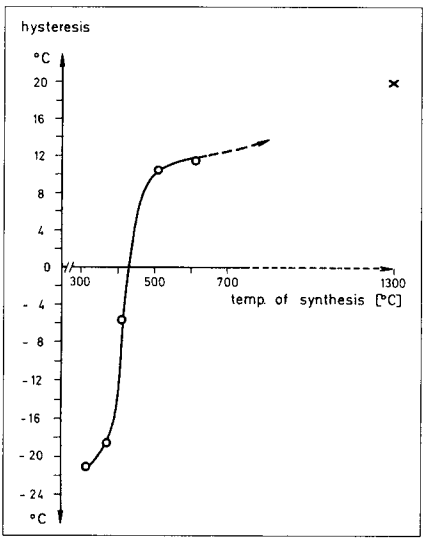


Figure 62. Interdependence between hysteresis and synthesis temperature of cristobalites.

temperatures of synthesis, the following changes in cristobalite inversion properties have been observed (Figure 62) [60]:

a) the character of the inversion effect changes from several, small, very broad and overlapping endotherms of low intensity ("domains") to one single and clear peak;
b) the effect becomes continuously clearer and sharper;
c) the temperature of inversion increases from ~100-150 °C (temperature of synthesis 300 °C) to 243.5 ± 0.5 °C (temperature of synthesis, 600 °C).

But the temperature of inversion for well-ordered cristobalites (e.g. 270 °C, see above) is not attained.

The accompanying X-ray diffractograms revealed that the degree of crystal structural order improved progressively. Low temperatures of synthesis and, consequently, low temperatures of formation, imply a higher degree of structural disorder for growing crystals. The lower the temperature of formation, the larger will be the defect character of quartz crystals. The growing crystals incorporate strange particles (solid inclusions), solutions and strange ions and thus, low temperature (i.e. low-energy) formations exhibit a high(er) degree of disorder than crystals formed in high-energy environments (e.g. igneous or metamorphic). Consequently, quartz crystals formed in low-energy environments (e.g. authigenic in sediments and soils; in some low-temperature veins) should exhibit less-intensive inversion effects (as compared with igneous crystals) and low inversion temperatures, (much) lower than 570 °C [24, 60, 373, 375, 377, 389, 390, 504, 510, 515, 530, 531].

The optimal determination of quartz inversion temperatures, that means the true characterisation of material inherent factors (= crystal chemical and, mainly, crystal physical disorder) demands that the conditions of preparation and analysis should be standardised as much as possible [24, 377, 389, 510, 523, 525, 527, 530, 531]. The intensive studies of Rodgers and Howett [525, 530] on the experimental procedures for determining precise inversion temperatures of quartz crystals culminated in the statement that "the present results emphasise, yet again, the need to standardise rigorously procedures used in TA, particularly where recorded data are to be compared between samples, operators, instruments and laboratories" [523] (Section 2.4.4).

In standardised DTA runs, the accuracy and reproducibility of the determination of the inversion temperature of well-ordered quartz-crystals have proved to be ± 0.3-0.5 °C [24, 389]. For badly-ordered (microcrystalline) crystals, the accuracy has been reported as ± 2–3 °C [390]. The values can be remarkably improved by using internal standards [24, 390, 510, 525]. Substances suitable for this are those where inversion effects and inversion temperatures occur in the same temperature range, e.g. the mineral cryolite,

Na_3AlF_6 (inversion temperature, 562.7 °C) and, especially, K_2SO_4 (inversion temperature, 583.5 °C, [77]). By applications of these internal standards, accuracies of ± 0.35 °C [523], ± 0.3 °C [24, 525, 531] and ± 0.2 °C [510] have been obtained.

Most of the inversion studies mentioned have used DTA. For special purposes, different methods, such as thermosonimetry (TS) or differential scanning calorimetry (DSC) may be suitable. Overlapping effects are better resolved in TS curves than by DTA, but the accuracy of temperature measurement may be lower [512, 532]. DSC has proved to be very accurate and sensitive and shows a good resolution of overlapping effects [531].

The method of quartz characterisation (measuring the inversion temperatures) can be used for petrogenetic purposes [24, 245, 373, 375, 377, 389, 390, 505 – 510, 523, 525, 527, 530, 531]. Some examples given below may illustrate the possibilities of the method's application.

a) The differentiation between quartz crystals of sedimentary and igneous origin,

Nagasawa [375] was the first geologist to mention differences between the inversion behaviour of "high-temperature deposits" and "low-temperature deposits". Studying 21 vein quartz crystals from Japan, he found that the DTA curves of these crystals exhibited considerable variations in the shape, which he attributed to the mixture of different quartz components, "Quartz from high-temperature deposits shows simple, and quartz from low-temperature deposits shows broad or flat curves". Some 15 years later, Smykatz-Kloss [507] studied authigenic quartz crystals from limestones in Germany and found the inversion temperatures of the quartz crystals from the limestone outcrop in Suttrop (Westfalia) to be above 571 °C, and those from the outcrop in Dietlingen (Badenia) to be below 571 °C. Additional optical investigations made it probable that the Suttrop crystals (exhibiting inclusions of anhydrite and some sulfides) had been formed from hydrothermal solutions, while the Dietlingen crystals were true authigenic formations from sedimentary pore solutions. From studies of more than 300 quartz crystals, it was suggested that the temperature of 571 °C (± 0.3 °C) was a "true borderline" between hydrothermal (igneous) and (some) sedimentary formations [24, 25, 390, 507]. Lisk [527] studied quartz crystals from the Broadlands-Ohaaki geothermal field in New Zealand and found similar relations, i.e. "slightly but consistently higher values for hydrothermal than for primary quartz". These differences were related to the permeability of the primary sediments for the thermal waters. "The data may reflect the differences in relative permeability with zones of higher primary permeability corresponding to zones whose quartz has higher inversion temperatures". Smykatz-Kloss and Klinke [377, 531] found broad inversion

effects at low temperatures, next to sharper effects and high temperatures in the DSC curves of the same sample, mirroring diagenetic alterations of primary (igneous) quartz.

b) Contact metamorphic aureoles

Giret [510] studied quartz crystals from granites and from the contact-metamorphic aureole around the granites. In their highly standardised differential thermal analysis (with K_2SO_4 as an internal standard), an accuracy of $\pm$ 0.2 °C was achieved, - the highest reported accuracy in all cited papers. They found that the hornfels (directly at the granite contact) exhibited higher quartz inversion temperatures than the host rock, which outcropped at a distance of some (few) metres. Evidently, the heat of the crystallising granite had lead to the recrystallisation of the surrounding rock by transforming it into contact-metamorphic hornfels, thus improving the quartz inversion temperatures.

c) Regional-metamorphic rocks

The quartz inversion behaviour of this group of highly recrystallised rocks seems to be much more complicated than the inversion behaviour of sedimentary or igneous rocks [24, 389, 506, 508, 509, 530]. The data show the complex pressure-temperature history of these rocks. Retrogressive processes may overprint older high-grade influences [24, 530]. A good account of these complex interrelations is offered by Rodgers and Howett [530]. They stated that "quartz crystals from progressively metamorphosed greenschist facies rocks show a slight decrease in their T_i with increasing mineralogical grade. But the pattern is confused by retrogressive metamorphism". They, additionally, investigated the quartz crystals from metamorphic rocks and always found lower inversion temperatures for the vein quartz crystals. Kresten [508, 509] found, in his studies of the metamorphic rocks in the Västervik area of Sweden, that the quartz inversion temperatures were directly proportional to the temperature of formation and to the partial pressure of the H_2O, and indirectly proportional to the total pressure. For migmatites and associated rocks, he reported inversion temperatures between 553 and 573 °C and observed a continuously increasing quartz inversion temperature with the metamorphic grade in the sequence: meta-sediment - metasediment + "granitic block" - schlieric neosome - homophanic neosome. He explained the increase in T_i with increasing migmatisation in terms of processes of recrystallisation.

d) Silcretes

Silcretes belong to the duricrusts and are (α) true soil formations formed from oscillating soil waters in situ on top of siliceous host rocks (autochthonous silcretes), or (β) allochthonous formations from sedimentary or weathering

solutions in alkaline playa lakes. Mineralogically, they consist of all kinds of microcrystalline silica minerals (opal-A, opal-CT, chalcedony = microcrystalline fibrous quartz). Table 30 shows the in-situ silcretes, the (sub-) recent types from the Cape Province and a Permian silcrete from the carneol horizon which shows low inversion temperatures (=badly disordered), but the two allochthonous samples show high inversion temperatures.

The suggestions of Tuttle [371], who expected to use the high-low quartz inversion as a geologic thermometer, and of Kresten [508, 509], who recommended the method for geologic thermometry and barometry, have been shown to be too optimistic. However, in many cases, the quartz inversion behaviour (e.g. the temperature of inversion, the hysteresis between heating and cooling values, the shape of the inversion effects) has been shown to be a suitable tool for petrologic interpretations and for petrogenetic characterisations. To achieve this, the DTA (DSC) runs have to be highly standardised in order to avoid any influence of preparative or instrumental factors on the inversion characteristics.

Table 30. Inversion data of microcrystalline quartz crystals from silcretes

sample, locality	type	inversion temp. (Ti) on heating	ΔT [°C]	hysteresis [Ti heat – Ti cool]
FG-4, Fort Grey / Cape Prov.	in-situ	500 ± 5	0.15	-55
Fe-bearing silcr., Makanaskop / Grahamstown	in-situ	547 ± 5	0.12	-6
PLK-II, Riversdale	allochthonous	571.5 ± 0.5	0.32	+2.5
Caura silcrete, W-Australia	allochthonous	571.0 ± 0.5	0.20	+1
Carneol, Schramberg, Black Forest / Germany	fossil duri-crust (Permian)	520 ± 5 540 ± 5	0.03 0.05	n.d.

5. TECHNICAL AND APPLIED MINERALOGY

Thermal analysts are involved in many fields of technical and applied mineralogy, such as testing raw materials for the cement, glass and ceramic industries, working in quality control and mineral processing, or in the synthesis of minerals, alloys and other technical compounds. More recently thermal methods have also been used in environmental studies.

5.1. Quality control

Clays as raw materials for bricks or ceramics have been the subject of thermal investigations for more than 50 years [136, 139, 143, 158, 159, 234, 533]. Later mainly kaolin and swelling clays (bentonites, vermiculitic clays) have been

studied extensively, e.g. for drilling mud, as barrier clay for waste disposals and many other purposes (see Section 2.3). Bangoura [131] applied DTA/TG to the quality characterization of Guinea's bauxite deposits. Piga [534] used TG in quality control of kaolinite - alunite ores.

Clays and coals frequentely contain small amounts of sulfides, mainly pyrite, which decrease the quality of the raw material and contaminate the air and the environment when burnt. Therefore many scientists have used thermal methods for controlling the quality and purity of raw materials, Warne [56, 422], Warne and French [167], Aylmer and Rowe [411], Warne and Dubrawski [296], Schomburg [354] and, recently, Bonamartini Corrado [333] have used DTA, DSC and variable atmosphere DTA for the determination of sulfidic and carbonatic impurities in oil shales, clays and coals. Gallagher and Warne [317] and Warne [424] used thermomagnetometry for the determination of iron minerals. Dunn [536] determined sulfatic impurities in cements. Dubrawski and Warne [57] investigated Fe-carbonates by DSC and by using a variable atmosphere method. Recently, Strydom and Potgieter [96] compared phosphogypsum with natural gypsum in order to evaluate possible use of this industrial by-product.

Many thermoanalytical studies cover the interactions of raw materials in the glass forming process, with respect to the optimisation of melting conditions [537, 538], evaporation [539], nucleation [540] or gas content [541].

5.2. Mineral processing and synthesis

The interactions of minerals, the gaseous reaction products of kaolinite/calcite mixtures [541, 542], and of clay minerals/NH_4F [334, 543] have been studied. A large field for the application of thermal methods in material control and in the processing of metals and ores is the roasting of sulfides [18, 24, 334, 351, 357, 359, 543]. Abdel Rehim [334] reviewed the thermal processes of oxidizing (roasting) of sulfides to obtain metal oxides. He describes the mechanism for roasting galena (PbS), sphalerite (ZnS), chalcopyrite ($CuFeS_2$), and molybdenite (MoS_2) in detail.

As early as 1951, Mackenzie [544] used DTA to characterize industrial dusts. Later Mackenzie and Meldau [545] reviewed the general application of DTA in industry, with special reference to dusts.

TG/DTA has been used in the calcination of zeolitic catalysts [258] and CWA for the determination of water in welding fluxes during the calcination of micas [546].

Charsley and Warrington [547] and Abdel Rehim [334,543] have illustrated the importance of thermal methods to various fields of mineral technology, including industrial chemical processing of minerals and the manufacturing of refractories, ceramics, glass, cement and metals. Abdel Rehim reported the

synthesis of cryptohalite, corundum, wulfenite, scheelite, mullite, baddeleyite and perovskite from slags and included examples of applications of DTA/DTG in the glass and ceramics industries. He stressed the applicability of sintering techniques and thermoanalytical control of the formation mechanism of topaz and corundum in industrial processes.

Eysel [47] applied DTA and DSC to phase relation studies of alkali-sulfate and Ca-silicate/germanate systems. Stoch [50] and Waclawska [113, 500] studied the amorphisation by grinding of the borate, colemanite, and the subsequent reconstruction process, by means of TG and DSC. Dubrawski [548] characterized the by-products of steel manufacturing, e.g. blast furnace slags, by DTA. Klimesh [549] synthesized hydrogarnets.

Kleykamp [550] and his co-workers used thermal methods (mainly DTA) for the characterization of alloys which may be used for the storage of radioactive waste, e.g. for the study of the phase systems Rh-Te, Pd-Te, Ru-Te and in the pseudobinary Li_2O-SiO_2 system [551 – 554].

Special applications for TA methods were found in characterizing ancient ceramic technologies [555] and in controlling the formation and the properties of high-temperature superconductors [556, 557].

5.3. Environmental studies

The contamination of the environment by aggressive liquids or gases damages buildings and flora and fauna. Thermal methods are suitable for characterizing the degree of weathering of rocks [300], corrosion of construction materials, salt-efflorescences on rock and building surfaces [558, 559], as well as detecting dangerous impurities in raw materials (see Section 5.1). The remnants of pesticides in soils can be detected by DTA, DSC, EGA or ETA [63, 461, 560]. Thermal methods may contribute to the analysis and control of municipal solid waste [561], red mud - the by-product of alumina production [562] - and gas development in waste disposals and sewage sludges [563].

6. SPECIAL THERMAL METHODS AND INVESTIGATIONS

For thermal studies in the geosciences, chemistry and material sciences, DTA, TG and DSC have proved to be the three main thermal methods used. Therefore handbooks on thermal analysis mostly deal with these methods (and there first derivatives, DDTA, DTG, DDSC) [3-17, 20, 23-27, 29, 34, 35, 43]. Calorimetric methods and methods using high-pressure equipment, such as the combination of DTA with a piston cylinder [564, 565], have been applied in physical (geo-) chemistry and in experimental petrology, where they are used

for example for the determination of thermodynamic and kinetic parameters [29, 35]. For the determination of true thermodynamic data refer to Saxena et al. [44], Chatterjee [481] or Navrotsky [593] and also Section 3.

The investigation of specific geoscientific problems requires special or combined thermal methods [72]. The Pauliks developed *derivatography*, a combination of TG and DTA, and Q-TG (*quasi-thermogravimetry*) [567 – 570]. Several Hungarian thermal analysts applied both methods to geoscientific problems [54, 91, 173, 571, 572]. The combination of *DTA and evolved gas analysis* (the gas being analysed by gas chromatography or mass spectroscopy) gained some importance for the determination of fluid and gaseous mineral inclusions [473, 573 – 575]. Recently, Carleer et al. [188] used thermogravimetry with mass spectrometry (*TG-MS*) for the investigation of clay mixtures. Starck [546] and Yariv [461] used *thermo-IR spectroscopy* (CWA, CSA) for the characterization of welding fluxes and organo-clay complexes, respectively.

Warne and co-workers applied *variable atmosphere DTA and DSC* in the study of carbonates, oil shales and clays [52, 56, 57, 167, 353, 425]. Cebulak et al. [576] measured kerogene by *oxyreactive thermal analysis* and Rouquerol et al. introduced *controlled rate thermal analysis* (CRTA) into geoscience, studying complex uranyl compounds [49, 587]. Balek et al. used radioactive tracers for the characterization of thermal processes and reaction products (ETA, *emanation thermal analysis,* [386, 462, 502, 560, 580]). In technical and applied mineralogy, *thermodilatometry* (TD, DTD) has been widely used for the determination of temperature-dependent volume or length changes [30, 175, 183, 354, 581]. *Thermooptical* methods (e.g. the combination of DTA and microscopy) have been used for the study of solid-state reactions [582, 583]. Wiedemann and Smykatz-Kloss [330] used this method for the observation of "phase transition fronts" in the study of Na_2SO_4 phase transitions. *Thermo-dielectric analysis* was introduced to clay mineralogy by Carrecas et al. and Alonso Perez et al. [584, 585]. *Thermoacoustimetry and thermosonimetry* (TS) have been used by Lønvik and co-workers [484, 532, 566]. This method is extremely useful for the resolution of overlapping effects (in DTA, DSC), e.g. in phase transition studies [532]. The method allowed the identification of a third modification of quartz, which occurs over the small temperature range of less than 1 °C ([379], see Section 3).

Gallagher, Warne and co-workers applied *thermomagnetometry* to the identification of Fe-bearing minerals [33, 317, 588]. The combination of thermal and luminescence techniques (*thermoluminescence*, TL) allows the determination of the age of sub-recent rocks [589- 591], - a welcome method for

the timespan up to 50 ka and for loose sediments free of organic carbon, e.g. for the dating of loess or desert soils [590].

Smykatz-Kloss and Heide [592] and Navrotsky [593] outlined the new directions in thermal analysis and in high-temperature calorimetry, respectively. The study of *phase transitions* of solid materials has become an important subject in earth sciences, in petrology as well as in crystallography. A special journal ("Phase Transitions") is concerned with these studies. Relevant for this review, e.g. for the thermal characterisation of minerals, rocks and geotechnical materials and processes, in addition to the already mentioned publications (Sections 2.4 and 2.5), are:

(1) Studies on the phase transition behaviour of alkaline-earth carbonates [597 – 599], sodium sulfates [600 – 602] and silicates (e.g. of pyroxenes [603 – 605] and framework silicates [606]). Recently, the Ba-Sr-Al silicates of the hexacelsian and related structures attracted an enormous amount of interest because of their possible use in technical mineralogy, e.g. as *superconductors* in high ceramic technology [607 – 611].

(2) For the iron, chromium and titanium oxides, the study of *(anti-) ferromagnetic* phase transitions has been widely established since the studies of Gallagher, Warne [33, 317, 588], Cremer [612], Vincent et al. [398] and Chevallier et al. [399]. Bocquet and co-workers measured the Néel temperatures of goethites and their dependence on their physical properties (e.g. particle size, [613, 614]). Schuette et al. characterized the magnetic properties of oxidised and reduced smectites [615].

(3) The phase transitions that have been most intensively studied are those for the several *phases of silica*. The importance of the high-low quartz inversion has been demonstrated in Section 2.4.4. In addition to the publications mentioned in Section 2.4.4, studies by Coe and Paterson and Dove et al. on the high-low quartz inversion [616, 617] and several papers on the thermochemical and thermophysical properties, including the high-low inversion of cristobalite and tridymite, have been published [618 – 621]. The studies were mainly done by means of quite modern techniques (e.g. high-temperature NMR). The inversion data of the two high-pressure polymorphs of SiO_2, coesite and stishovite, and the characterisation of the newly discovered phase moganite, have also been published recently [622, 623].

Another important field of application of thermal methods is to technical and applied mineralogy, including the characterisation of (mineral, clay, ore, rock) deposits [624 – 631], and the study of special clay mineral properties (mainly of swelling clays or intercalation structures [632, 633]). Thermal methods have also been applied to the control of the processing of limestone calcination [634]

and of industrial wastes [635 – 637]. A special field of technical application is found in "dangerous" environments, e.g. to study the explosion behaviour of solids [638], or in nuclear research and technology [639].

Kinetic and thermodynamic studies have increased enormously during the last decades [44, 481, 593]. In mineralogy, in addition to petrological applications, the studies of Criado et al., who mainly used the CRTA technique [640 – 643], and Heide and co-workers have to be mentioned [48, 81, 86, 319, 320, 539, 644 – 646].

Last but not least, thermal methods have been used for "fine arts", e.g. for art conservation [647], in archeometry [648], and to characterise precious stones, ambers or resins [649, 650].

7. FUTURE ASPECTS

As outlined earlier, future applications of thermal methods in the earth sciences are expected to be seen (I) in applied and technical geosciences and (II) in physical (geo-) chemistry [592]. (II) includes (a) the fields of crystallography (phase transitions, phase relations) and (b) the broad field of thermodynamics and kinetics. The latter (e.g. IIb) has developed into a very large field of petrological research, so that it cannot possibly be reviewed in its entirety in this paper. In this review, aspects of thermodynamics and kinetics are only mentioned very briefly. Special monographs and handbooks on petrologic calorimetry are sources of thermodynamic and kinetic data on minerals [44, 488, 481, 593].

In applied and technical mineralogy, thermal methods of analysis are also gaining importance for the characterization of raw materials such as clays, bauxites, carbonates, ores, salts, coals and other hydrocarbons for the pottery, ceramics, glass and cement industry. The properties and suitability of these materials can be analyzed for technical products, as well as for use as energy resources. The increasing research on organo-clay interactions leads to a strongly expanding number of products (clay-organic intercalations, pillared clays), which will be applied to more and more technological processes in many industrial fields.

The application of thermal methods in soil and environmental studies is also increasing. The necessary protection of our environment and of the living conditions for animals and mankind has to lead to an improvement and larger engagement in environmental research, to prevent soils, surfaces and soil waters, crops, forests and living beings from contamination with dangerous or toxic materials and to isolate sewage waters and gases from hazardous waste in

disposal processes, by testing the barrier materials (concrete, swelling clays, plastic liners), either by routine or special thermal methods.

ACKNOWLEDGEMENTS

We are grateful to Dr. W. Engel (Springer Co., Heidelberg / Germany) for his kind permission, to use some figures from the first author's monograph (Differential Thermal Analysis. Applications and Results in Mineralogy, Vol. 11 of "Minerals and Rocks", Springer, Heidelberg 1974) and we are grateful, too, to Nadine Smykatz-Kloss (Stroud, UK) for improving the authors' English.

REFERENCES

1. H. Le Chatelier, Bull. Soc. Franc. Minéral. Cryst., 10 (1887) 204-211.
2. R.C. Mackenzie in Thermal Analysis in the Geosciences, (Eds W. Smykatz-Kloss and S. St. J. Warne), Springer-Verlag, Berlin, 1991, pp. 2-15.
3. S. Speil, L.H. Berkelhamer, J. Pask and B. Davies, Differential thermal analysis of clays and aluminous minerals, US Bureau of Mines, Techn. Paper 664 (1945).
4. P.L. Arens, A study of the differential thermal analysis of clays and clay minerals, Diss. Univ. Wageningen, S´Gravenhage 1951.
5. H. Lehmann, S.S. Das and H.H. Paetsch, Die Differentialthermoanalyse, Tonind.–Ztg., Keram. Rundschau, 1. Beiheft, 1953.
6. P.D. Garn, Thermoanalytical Methods of Investigations, Academic Press, New York, 1965..
7. E. Deeg, Ber. Dt. Keram. Ges., 33 (1956) 321-329.
8. R.C. Mackenzie, (Ed.) The Differential Thermal Analysis of Clays, Mineralogical Society, London, 1957.
9. R.C. Mackenzie (Compiler) Scifax Differential Thermal Analysis Data Index, Macmillan, London, 1962.
10. R.C. Mackenzie (Ed.), Differential Thermal Analysis, Vol. 1, Fundamental Aspects, Academic Press, London, 1970.
11. R.C. Mackenzie (Ed.) Differential Thermal Analysis, Vol. 2, Application, Academic Press, London, 1972.
12. M. Földvari-Vogl, Acta Geol. Budapest 5 (1958) 3-102.
13. L.G. Berg, Introduction to Thermal Analysis, Akad. Nauk SSSR, Moscow, 1961, (in Russian).
14. C. Duval, Inorganic Thermogravimetric Analysis, 2nd edition, Elsevier, Amsterdam, 1963.

15. W.W. Wendlandt, Thermal Methods of Analysis, Wiley and Sons, New York, 1964.
16. W.J. Smothers and Y. Chiang, Handbook of Differential Thermal Analysis, Chemical Publ. Co., New York, 1966.
17. R.J.W. McLaughlin in Physical Methods in Determinative Mineralogy, (Ed. J. Zussman, Academic Press, London, 1967.
18. I. Kostov, Mineralogy, Oliver and Boyd, London, 1968.
19. C. Keattch, An Introduction to Thermogravimetry, Heyden and Sons, London, 1969.
20. D. Schultze, Differentialthermoanalyse, Verlag Chemie, Weinheim, 1969.
21. G. Liptay, (1971 / 1973 -1985), Atlas of Thermoanalytical Curves, Vol. 1-5, Akad. Kiado, Budapest.
22. Liptay, G. (1977 / 1973 -1985), Atlas of Thermoanalytical Curves, Vol. 1-5, Akad. Kiado, Budapest.
23. A. Blazek, Thermal Analysis, Van Nostrand Reinhold, London, 1972.
24. W. Smykatz-Kloss, Differential Thermal Analysis. Application and Results in Mineralogy, Springer-Verlag, Berlin, 1974.
25. W. Smykatz-Kloss, J. Therm. Anal., 23 (1982) 15-44.
26. C. Keattch and D. Dollimore, Introduction to Thermogravimetry, 2nd edn, Heyden and Sons, London, 1975.
27. D.N. Todor, Thermal Analysis of Minerals, Abacus Press, Tunbridge Wells, UK, 1976.
28. K. Heide, Dynamische thermische Analysenmethoden, VEB Dt. Verlag für Grundstoff-Ind., Leipzig, 1979.
29. K. Heide, Dynamische thermische Analysenmethoden, 2. Auflage, VEB Deutscher Verlag f. Grundstoff-Industrie, Leipzig, 1982.
30. J. Schomburg and M. Störr, Dilatometerkurvenatlas der Tonmineralrohstoffe, Akademie-Verlag, Berlin, 1984.
31. C.M. Earnest, Anal. Chem., 56 (1984) 1471 A.
32. C.M. Earnest (Ed.), Compositional Analysis by Thermogravimetry, ASTM Spec. Techn. Publ. 997, 1988.
33. S.St.J. Warne and P.K. Gallagher, Thermochim. Acta, 110 (1984) 269-279.
34. M.E. Brown, Introduction to Thermal Analysis, Chapman and Hall, London, 1988.
35. W. Hemminger and H.K. Cammenga, Methoden der thermischen Analyse, Springer-Verlag, Heidelberg, 1989.
36. E. Charsley, Advances in Thermal Analysis, Academic Press, London, 1990.

37. J.W. Stucki and D.L. Bish (Eds), Thermal Analysis in Clay Science, The Clay Minerals Group, Boulder/Colorado, 1990.
38. G.W. Brindley and J. Lemaitre in Chemistry of Clays and Clay Minerals. (Ed. A.C.D. Newnham), Mineral. Soc., London, 1987, pp. 319-370.
39. W. Smykatz-Kloss and S.St.J. Warne, (Eds), Thermal Analysis in the Geosciences, Lecture Notes in Earth Sciences, Vol. 38, Springer-Verlag, Berlin, 1991.
40. W. Smykatz-Kloss (Ed.), Special Issue in honour of the 75th birthday of R.C. Mackenzie, J. Therm. Anal., Vol. 48, number 1.
41. Y. Tsuzuki and K. Nagasawa, J. Earth Sci., Nagoya Univ. (Japan), 5 (1957) 153-182.
42. H.E. Kissinger, Anal.Chem., 29 (1957) 1702-1706.
43. D. Dollimore in The State and Art of Thermal Analysis (Eds O. Menis, H.L. Rook and P.D.Garn), Proc. Workshop NBS, Maryland, 1980, pp. 1-31
44. S.K. Saxena, N. Chatterjee, Y. Fei and G. Shen, Thermodynamic Data on Oxides and Silicates, Springer-Verlag, Berlin, 1993.
45. W. Smykatz-Kloss, G. Istrate, H. Hötzl, H. Kössl and S. Wohnlich, Chem. d. Erde, 44 (1985) 67-77.
46. J.V. Dubrawski in Thermal Analysis in the Geosciences, (Eds W. Smykatz-Kloss and S.St.J. Warne), Springer-Verlag, Berlin, 1991, pp. 16-59.
47. W. Eysel in Thermal Analysis in the Geosciences, (Eds W. Smykatz-Kloss and S.St.J. Warne), Springer-Verlag, Berlin, 1991, pp. 152-170.
48. K. Heide in Thermal Analysis in the Geosciences, (Eds W. Smykatz-Kloss and S.St.J. Warne), Springer-Verlag, Berlin, 1991, pp. 172-185.
49. J. Rouquerol, S. Bordère and F. Rouquerol in Thermal Analysis in the Geosciences, (Eds W. Smykatz-Kloss and S.St.J. Warne), Springer-Verlag, Berlin, 1991 pp. 134-151.
50. L. Stoch in Thermal Analysis in the Geosciences, (Eds W. Smykatz-Kloss and S.St.J. Warne), Springer-Verlag, Berlin, 1991, pp. 118-133.
51. W. Smykatz-Kloss, Contrib. Mineral. Petrol., 13 (1966) 207-231.
52. S.St.J. Warne, D.J. Morgan and A.E. Milodowski, Thermochim. Acta, 51 (1981) 105-111.
53. M. Palomba and R. Porcu, J. Therm. Anal., 34 (1988) 711-722.
54. M. Földvari, J. Therm. Anal., 48 (1997) 107-119.
55. S.St.J. Warne, Nature (London), 269 (1977) 678.

56. S.St.J. Warne in Thermal Analysis in the Geosciences, (Eds W. Smykatz-Kloss and S.St.J. Warne), Springer-Verlag, Berlin, 1991, pp. 62-83.
57. J.V. Dubrawski and S.St.J. Warne, Thermochim. Acta, 135 (1988) 225-230.
58. Th. Stelzner and K. Heide, Evolved gas-analysis, A technique to study cosmic alteration of chondrites, in M.E. Zolensky, A.N. Krot and E.R.D. Scott, LPI Tech. Rep. 97-02, 1, Lunar and Planetary Institute, Houston, 1997, p.71.
59. R.A. Kuehnel, D. van Hilten and H.J. Roorda, The crystallinity of minerals in alteration profiles, Delft Progress Report, Series E, Geoscience, Vol. 1 (1974) 1-32.
60. W. Smykatz-Kloss and R. Schultz, Contrib. Mineral. Petrol., 45 (1974) 15-25.
61. W. Smykatz-Kloss in Proc. Intern. Clay Conf. Mexico-City, (Ed. S.W. Bailey), 1975, pp. 429-438.
62. W. Smykatz-Kloss and E. Althaus, Bull. Group Franc. Argiles XXVI, (1975) 319-325.
63. W. Smykatz-Kloss, A. Heil, L. Kaeding and E. Roller in Thermal Analysis in the Geosciences, (Eds W. Smykatz-Kloss and S.St.J. Warne), Springer-Verlag, Berlin, 1991, pp. 352-367.
64. S. Yariv in Thermal Analysis in the Geosciences, (Eds W. Smykatz-Kloss and S.St.J. Warne), Springer-Verlag, Berlin, 1991, pp. 328-351.
65. E. Roller, Bodenmineralogische Untersuchungen und Herbizid-Bentonit-Kontaktversuche zum Erosionsverhalten des Löß und des Keupermergels im Weiherbachtal (Kraichgau), Diss. Fac. Bio-Geosciences, Univ. Karlsruhe, 1993.
66. S.D. Killops and V.J. Killops, An Introduction to Organic Geochemistry, Longman, London, 1993.
67. S.D. Killops and V.J. Killops, An Introduction to Organic Geochemistry, Longman, London, 1997.
68. C.M. Schmidt and K. Heide, J.Thermal. Anal. Cal., 64 (2001) 1297 – 1302.
69. A.D. Cunningham and F.W, Wilburn in Differential Thermal Analysis, (Ed. R.C. Mackenzie), Vol. 1 (1970) pp. 32-62.
70. R.C. Mackenzie and B.D. Mitchell in Differential Thermal Analysis, (Ed. R.C. Mackenzie), Vol. 1, Academic Press, London / New York, 1970, pp. 63-99 and 101-122.

71. R.C. Mackenzie and B.D. Mitchell in Differential Thermal Analysis, (Ed. R.C. Mackenzie), Vol. 2, Academic Press, London / New York, 1972, pp. 267-297.
72. J.P. Redfern in Differential Thermal Analysis, (Ed. R.C. Mackenzie), Vol. 1, Academic Press, London / New York, 1970, pp. 123-158.
73. W. Lugscheider, Ber. Bunsen-Ges., 71 (1960) 228-235.
74. H.G. Wiedemann and A. van Tets, Z. Anal. Chemie, 233 (1968) 161-175.
75. H.G. McAdie in Thermal analysis, Proceedings 3rd ICTA Davos 1971, (Ed. H.G. Wiedemann).
76. K.H. Breuer and W. Eysel, Thermochim. Acta, 57 (1982) 317-329.
77. W. Eysel and K.H. Breuer in Analytical Calorimetry, (Eds J.F. Johnson and P.S. Gill), Plenum, New York, 1984, pp. 67-80.
78. J.V. Dubrawsk and S.St.J. Warne, Thermochim. Acta, 104 (1986) 77-83.
79. H.K. Cammenga, W. Eysel, E. Gmelin, W. Hemminger, G.W.H. Höhne and S.M. Sarge, Die Temperaturkalibrierung dynamischer Kalorimeter. II Kalibriersubstanzen, PTB-Mitt., 102/1 (1992) 13-18.
80. G. Lombardi, For Better Thermal Analysis, ICTA – Publication, 1974
81. K. Heide and H.J. Eichhorn, J.Thermal. Anal., 7 (1975) 397 – 409.
82. L.G. Berg in Differential Thermal Analysis, (Ed. R.C. Mackenzie), Vol. 1, Academic Press, London / New York, 1970, pp.343-361.
83. K. Heide, Chemie der Erde, 22 (1962) 180-221.
84. Cz. August in Thermal Analysis in the Geosciences, (Eds W. Smykatz-Kloss and S.St.J. Warne), Springer-Verlag, Berlin, 1991, pp.102-114.
85. K. Heide, Chemie der Erde, 24 (1965) 94-111.
86. K. Heide, J. Therm. Anal., 1 (1969) 183-194.
87. K. Heide, Chemie der Erde, 24 (1965) 279-302.
88. R. Brousse and H. Guérin, Bull. Soc. Franç. Minéral. Cryst., 88 (1965) 704-705.
89. H.P. Jenni, Schweiz. Mineral. Petrogr. Mitt., 50 (1970) 276-290.
90. R. Brousse, G. Gasse-Fournier and F. Lebouteiller, Bull. Soc. Franc. Minéral. Cryst., 89 (1966) 348-352.
91. M. Földvari in Thermal Analysis in the Geosciences, (Eds W. Smykatz-Kloss and S.St.J. Warne), Springer-Verlag, Berlin, 1991, pp. 84-100.
92. K. Heide, Chemie der Erde, 25 (1966) 237-252.
93. I.N. Lepeshkov and N.K. Semendyaeva, Thermal Analysis, Proc. 4th ICTA, Budapest, (Ed. I. Buzas), Heyden & Son, London, Vol. 2 (1975) 677-683.
94. R. von Hodenberg, R. Kühn and F. Rosskopf, Kali und Steinsalz, 5 (1969) 178-189.
95. R. Piece, Schweiz. Mineral. Petrogr. Mitt., 41 (1961) 303-310.

96. C.A. Strydom and J.H. Potgieter, Thermochim. Acta, 332 (1999) 89-98.
97. G. Lombardi, Thermal Analysis, Proc. 2nd ICTA, Academic Press, New York, 1969, Vol. 2, pp.1269-1289.
98. M. Berennyi in Technik der Harnsteinanalyse, (Ed. H.J. Schneider), VEB G.Thieme Verlag, Leipzig, 1974, p. 46.
99. D.M. Hausen, Am. Mineralogist, 47 (1962) 637-648.
100. M. de Abeledo, V. Angelelli, M. de Benyacas and C. Gordillo, Am. Mineralogist, 53 (1968) 1-8.
101. C.S. Jr. Hurlbut and L.F. Aristarain, Am. Mineralogist, 53 (1968) 1799-1815.
102. C.S. Jr. Hurlbut and L.F. Aristarain, Am. Mineralogist, 53 (1968) 416-431.
103. F. Cesbron and J. Fritsche, Bull. Soc. Franc. Minéral. Cryst., 92 (1969) 196-202.
104. L. van Wambeke, Mineral. Mag., 38 (1971) 418-423.
105. H. Zwahr, J. Schomburg and D. Schmidt, Chem. der Erde, 37 (1978) 165-171.
106. R.L. Frost, M.L. Weier, W. Martens, J.Th. Kloprogge and Zheding, Thermochim. Acta, (2003) in press.
107. S.G. Eekhout, R. Vochta, N.M. Blaton, E. de Grave, J. Janssens and H. Desseyn, Thermochim. Acta, 320 (1998) 223-230.
108. C.S.Hurlbut, Jr. and L.F. Aristarain, Am. Mineralogist, 52 (1967) 326-335.
109. C.S.Hurlbut, Jr. and L.F. Aristarain, Am. Mineralogist, 52 (1967) 1048-1059.
110. L.F. Aristarain and C.S. Hurlbut, Jr., Am. Mineralogist, 52 (1967) 935-945.
111. L.F. Aristarain and C.S. Hurlbut, Jr., Am. Mineralogist, 52 (1967) 1776-1784.
112. L.F. Aristarain and C.S. Hurlbut, Jr., Am. Mineralogist, 53 (1968) 1815-1827.
113. I. Waclawska, J. Therm. Anal., 48 (1997) 145-154.
114. Y. Erdogan, Y. Zeybel and A. Demirbas, Thermochim. Acta, 326 (1999) 99-103.
115. Chen Ruoyu, Li Jun, Xia Shuping and Gao Shiyang, Thermochim. Acta, 306 (1997) 1-5.
116. E. Hartung and K. Heide, Krist. and Techn., 13 (1978) 57 – 60.
117. K. Heide, H. Franke and H.P. Brückner, Chemie der Erde, 39 (1980) 201 – 232.

118. T.L. Webb and H. Heystek, in Differential Thermal Investigation of Clays (Ed. R.C. Mackenzie), 1957, pp. 329-363.
119. K. Heide, E. Hartung and H.G. Schmidt, Glastechn. Ber., 59 (1986) 59 – 63.
120. J. Paulik and F. Paulik, Simultaneous thermoanalytical examination by means of the derivatograph, Wilson's Comprehensive Analyt. Chem., Vol.XII, (Ed. W.W. Wendlandt), Elsevier, Amsterdam, 1981, pp.277.
121. J.L. Kulp and J.N. Perfetti, Mineral. Mag., 29 (1950) 239-251.
122. J.V. Dubrawski and J. Ostwald, N. Jb. Mineral. Mh., 9 (1987) 406-418.
123. J. Ostwald and J.V. Dubrawski, N. Jb. Mineral. Abb., 157 (1987) 19-34.
124. J. Ostwald and J.V. Dubrawski, Mineral. Mag., 51 (1987) 463-466.
125. D.J. Morgan, A.E. Milodowski, S.St.J. Warne and S.B. Warrington, Thermochim. Acta, 135 (1988) 273-277.
126. R.C. Mackenzie in Problems of Clay and Laterite Genesis, Am. Inst. Mining Ing., New York, 1952, pp. 65-75.
127. W.C. Kelly, Am. Mineralogist, 41 (1956) 353-355.
128. P. Keller, N. Jb. Min. Mh., (1976) 115-127.
129. R.M. Cornell and U. Schwertmann, The Iron Oxides, VCH-Verlag, Weinheim, (1996) p.154ff.
130. T.A. Korneva, T.S. Yusupov, L.G. Lukjanova and G.M. Gusev, Thermal Analysis, Proc. 4th ICTA, Budapest, (Ed. I. Buzas), Heyden, London, 1975, Vol.2, 659-666.
131. M. Bangoura, Vergleichende mineralogisch-geochemische Untersuchungen an einigen Bauxit-Vorkommen Guineas, Diss. Fac. Bio-Geosciences, Univ. Karlsruhe, 1993.
132. E. Mendelovici, J. Therm. Anal., 49 (1997) 1385-1397.
133. R. Giovanoli, Chemie der Erde, 44 (1985) 227 – 244.
134. S.J. Kim, Fortschr. Miner., 52 (1975) 361 – 368.
135. J. Orcel, Bull. Soc. Franc. Minéral. Cryst., 50 (1927) 75-456.
136. J. Orcel and S. Caillère, Compt. Rend., (1933) 774-777.
137. S. Caillère, Bull. Soc. Franc. Minéral. Cryst., 59 (1936) 163-326.
138. S.B. Hendricks and L.T. Alexander, Soil Sci., 48 (1939) 257-271.
139. F.H. Norton, J. Am. Ceram. Soc., 22 (1939) 54-63.
140. M.H. Creer, J.B. Hardy, H.P. Roaksby and J.E. Still, Clay Minerals, 9 (1971)19-34.
141. R.E. Grim and R.A. Rowland, Am. Mineralogist, 27 (1942) 756-761.
142. R.E. Grim and R.A. Rowland, Am. Mineralogist, 27 (1942) 801-808.
143. R.E. Grim and R.A. Rowland, J. Am. Ceram. Soc. 27 (1944) 5-23.
144. F.L. Cuthbert, Am. Mineralogist, 29 (1944) 378-388.

145. C.S. Ross and S.B. Hendricks, Minerals of the montmorillonite group, US Geol. Survey Prof. Paper 205b, (1945) 23-79.
146. R.E. Grim, Am. Mineralogist, 32 (1947) 493-501.
147. I. Barshad, Am. Mineralogist, 33 (1948) 655-678.
148. R.E. Grim and W.F. Bradley, Am. Mineralogist, 33 (1948) 50-59.
149. R.E. Grim, R.S. Dick and W.F. Bradley, Bull. Geol. Soc. Am., 66 (1949) 1785.
150. P. Murray and J. White, Trans. Brit. Ceram. Soc., 48 (1949) 187-200.
151. J. Orcel, S. Caillère and S. Hénin, Mineral. Mag., 29 (1951) 329-340.
152. G.W. Brindley, Mineral. Mag., 29 (1951) 502-522.
153. G.T. Faust, Am. Mineralogist, 36 (1951) 795-822.
154. J.W. Earley, I.H. Milne and W.J. McVeagh, Am. Mineralogist, 38 (1953) 770-773.
155. F. Lippmann, Heidelberger Beitr. Mineral. Petrogr., 4 (1954) 130-134.
156. W.R. Phillips, Mineral. Mag., 33 (1954) 404-414.
157. W.F. Cole, Nature (London), 175 (1955) 384-385.
158. H.W. van der Marel, Am. Mineralogist, 41 (1956) 222-244.
159. R.C. Mackenzie, Agrochimica, 1 (1956) 1-22.
160. R.C. Mackenzie, Clay Miner. Bull., 3 (1958) 276-286.
161. W.A. Bassett, Am. Mineralogist, 43 (1958) 1112-1133.
162. R.E. Grim and G. Kulbicki, Am. Mineralogist, 46 (1961) 1329-1369.
163. A.L. Albee, Am. Mineralogist, 47 (1962) 851-870.
164. T. Sudo, S. Shimoda, S. Nishigaki and M. Aoki, Clay Minerals, 7 (1966) 33-42.
165. W.D. Keller, E.E. Pickett and A.L. Reesman, Proc. Intern. Clay Conf. Jerusalem, 1966, pp. 75-85.
166. H. Kodama, Am. Mineralogist, 51 (1966) 1035-1055.
167. S.St.J. Warne and D.H. French, Thermochim. Acta, 79 (1984) 131-137.
168. B.D. Boss, Am. Mineralogist, 52 (1967) 293-298.
169. M.J. Wilson, D.C. Bain and W.A. Mitchell, Clay Miner., 7 (1968) 343-349.
170. K.H. Schüller, N. Jb. Mineral. Mh., (1968) 363-376.
171. T. Sudo and S. Shimoda in Differential Thermal Analysis, (Ed. R.C. Mackenzie), Vol. 1, Academic Press, London / New York, 1970, pp. 539-551.
172. J.L.M. Vivaldi and P.F. Hach-Ali in Differential Thermal Analysis, (Ed. R.C. Mackenzie), Vol. 1, Academic Press, London / New York, 1970, pp. 553-573.
173. G. Bidlo, Period. Polytechn. Hung. Civil Eng., 15 (1971) 1-11.
174. P. Černy, P. Povondra and J. Stanek, Lithos, 4 (1971) 7-15.

175. J. Schomburg, Chemie der Erde, 35 (1976) 192-198.
176. L. Stoch, E. Rybicka and K. Gorniak, Mineralogia Polonica, 10 (1979) 63-77.
177. C.M. Earnest, Thermochim. Acta, 63 (1983) 277-289.
178. C.M. Earnest, Thermochim. Acta, 63 (1983) 291-296.
179. C.M. Earnest in Thermal Analysis in the Geosciences, (Eds W. Smykatz- Kloss and S.St.J. Warne), Springer-Verlag, Berlin, 1991, pp. 270-286.
180. C.M. Earnest in Thermal Analysis in the Geosciences, (Eds W. Smykatz-Kloss and S.St.J. Warne), Springer-Verlag, Berlin, 1991, pp. 288-312.
181. E.T. Stepkowska and S.A. Jefferies, Thermochim. Acta, 114 (1987) 179-186.
182. E.T. Stepkowska, Z. Sulek, J.L. Perez-Rodriguez, C. Maqueda and A. Justo in Thermal Analysis in the Geosciences, (Eds W. Smykatz-Kloss and S.St.J. Warne), Springer-Verlag, Berlin, 1991, pp. 246-269.
183. J. Schomburg and H. Zwahr, J. Therm. Anal., 48 (1997) 135-139.
184. M.R. Sun Kon, S. Mendioroz and M.I. Guijarro, Thermochim. Acta, 323 (1998) 145-157.
185. R.L. Frost, J. Kristof, E. Horvath and J.T. Kloprogge, Thermochim. Acta, 327 (1999) 155-166.
186. W.K. Mekhamer and F.F. Assaad, Thermochim. Acta, 334 (1999) 33-38.
187. Tj. Peters, Schweiz. Mineral. Petrogr. Mitt., 42 (1962) 359-380.
188. R. Carleer, G. Reggers, M. Ruysen and J. Mullens, Thermochim. Acta, 323 (1998) 169-178.
189. A. Langier-Kuzniarowa in Thermal Analysis in the Geosciences, (Eds W. Smykatz-Kloss and S.St.J. Warne), Springer-Verlag, Berlin, 1991, pp.314-326.
190. A. Langier-Kuzniarowa, J. Inczedy, J. Kristof, F. Paulik, J. Paulik and M. Arnold, J. Thermal Anal., 36 (1990) 67-84.
191. F. Stengele and W. Smykatz-Kloss, J. Thermal Anal., 51 (1998) 219-230.
192. T. Sudo and M. Nakamura, Am. Mineralogist, 37 (1952) 618.
193. J. White, Clay Minerals Bull., 2 (1953) 5-6.
194. W.F. Bradley and R.E. Grim, Am. Mineralogist, 36 (1951) 182-201.
195. R.C. Mackenzie, Acta Univ. Carol Geol., Suppl., 1 (1961) 11-21.
196. R. Greene-Kelly, Trans Faraday Soc., 51 (1955) 412-430.
197. A.H. Weir and R. Greene-Kelly, Am. Mineralogist, 47 (1962) 137.
198. P.F. Kerr and J.L. Kulp, Am. Mineralogist, 33 (1948) 387-419.
199. L.B. Sand and T.B. Bates, Am. Mineralogist, 38 (1953) 271-278.
200. A.R. Carthew, Am. Mineralogist, 40 (1955) 107-117.

201. F. Hofmann and Tj. Peters, Schweiz. Mineral. Petrogr. Mitt., 42 (1962) 349-358.
202. S. Caillère and I. Rodriguez, Bull. Soc. Franc. Minéral. Cryst., 90 (1967) 246-251.
203. A.M. Langer and P.F. Kerr, Am. Mineralogist, 52 (1967) 508-523.
204. H. Minato, Thermochim. Acta, 135 (1988) 279-283.
205. H.G. Midgley, Mineral. Mag. 29 (1951) 526-530.
206. S. Caillère and S. Henin in The Differential Thermal Investigation of Clays, (Ed. R.C. Mackenzie), 1957, pp.231-247.
207. A.W. Naumann and W.H. Dresher, Am. Mineralogist, 51 (1966) 1200-1211.
208. L. Pusztaszeri, Schweiz. Mineral. Petrogr. Mitt., 49 (1969) 425-466.
209. E.Z. Basta and Z.A. Kader, Mineral. Mag., 37 (1969) 394-408.
210. M. Saito, S. Kakitani and Y. Umegaki, J. Sci. Hiroshima Univ. Series C (Geology and Mineralogy), 6 (1972) 331-342.
211. R.C. Mackenzie in Differential Thermal Analysis, (Ed. R.C. Mackenzie), Vol. 1, Academic Press, London / New York, 1970, pp. 497-537.
212. J. Konta, Izv. Akad. Nauk SSSR, Ser. Geol., (1956) 109-113.
213. J.C. Hunziker, Schweiz. Mineral. Petrogr. Mitt., 46 (1966) 473-552.
214. H. Schwander, J. Hunziker and W. Stern, Schweiz. Mineral. Petrogr. Mitt., 48 (1968) 357-390.
215. J.W. Hansen, Schweiz. Mineral. Petrogr. Mitt., 52 (1972) 109-153.
216. Ch.E. Weaver, Am. Mineralogist, 38 (1953) 279-289.
217. K. Kautz, Beitr. Mineral. Petrogr., 9 (1964) 423-461.
218. D.F. Ball, Clay Minerals, 7 (1968) 363-366.
219. R.C. Mackenzie and A. Milne, Mineral. Mag., 30 (1953) 178-185.
220. B. Kubler in Coll. Et. Tectoniques, A la Baconnière, (1966) 105-122.
221. G.W. Brindley, Progr. Ceram. Sci., 3 (1963) 3-55.
222. G.T. Faust, J.C. Hathaway and G. Millo, Am. Mineralogist, 44 (1959) 342-370.
223. D.L. Lapham, Am. Mineralogist, 43 (1958) 921-956.
224. F.J. Eckardt, Geol. Jb., 75 (1958) 437-474.
225. A. Weiss, G. Koch and U. Hofmann, Ber. deut. Keram. Gesellschaft., 31 (1954) 301-305.
226. G.J. Ross, Can. Mineralogist, 9 (1968) 522-530.
227. P.Y. Chen,. Acta Geol. Taiwanica, 13 (1969) 9-19.
228. R.L. Borst and J.L. Katz, Am. Mineralogist, 55 (1970) 1359-1373.
229. J.L. Kulp and P.F. Kerr, Am. Mineralogist, 33 (1948) 387-420.
230. J.L. Kulp and P.F. Kerr, Am. Mineralogist, 34 (1949) 839-845.

231. A. Weiss, G. Koch and U. Hofmann, Ber. Dt. Keram. Ges., 32 (1955) 12-17.
232. E. Nemecz, Acta Geol. Hung., (1962) 365-388.
233. T. Takeuchi, I. Takahashi and H. Abe, Sci. Rep. Tohuku Univ., Sendai, Japan, 9 (1966) 371-484.
234. R.C. Mackenzie in The Differential Thermal Investigation of Clays, (Ed. R.C. Mackenzie), 1957, pp. 299-328.
235. F.V. Chukrov, S.I. Berkhin, L.P. Ermilova, V.A. Moleva and E.S. Rudnitskaya, Intern. Clay Conf. Stockholm, 1963, pp.19-28.
236. A.S. Campbell, B.D. Mitchell and J.M. Bracewell, Clay Minerals, 7 (1968) 451-454.
237. P.F. Kerr, J.L. Kulp and P.K. Hamilton, Differential thermal analysis of reference clay specimens, API Project 49, Columbia Univ. NY, 1949, p.40.
238. M.K.H. Siddiqui, Clay Minerals, 7 (1967) 120-123.
239. W. Echle, Contrib. Mineral. Petrol., 14 (1967) 86-101.
240. H. Hayashi, K. Korshi and H. Sakabe, Proc. Int. Clay Conf. Tokyo, Vol.1 (1969) 903-913.
241. N. Imai, R. Otsuka, H. Kashide and H. Hayashi, Proc. Int. Clay Conf. Tokyo, Vol.1 (1969) 99-108.
242. M. Müller-Vonmoos and C. Schindler, Schweiz. Mineral. Petrogr. Mitt., 53 (1973) 395-403.
243. A.G. Freeman, Mineral. Mag., 35 (1966) 953-957.
244. Tj. Peters, Schweiz. Mineral. Petrogr. Mitt., 41 (1961) 325-334.
245. G. Gottardi and E. Galli, Minerals and Rocks, Vol.18, Springer-Verlag, Heidelberg, 1985.
246. E. Pecsiné-Donath, Földt. Közl., Tonmin, 93 (1963) 32-39.
247. M. Koizumi, Mineral. J. (Japan), 1 (1953) 36-47.
248. C.J. Peng, Am. Mineralogist, 40 (1955) 834-856.
249. M. Koizumi and R. Roy, J. Geol., 68 (1960) 41-53.
250. B. Mason and L.B. Sand, Am. Mineralogist, 45 (1960) 341-350.
251. M.H. Grange, Compt. Rend., 259 (1964) 3277-3280.
252. K. Harada and K. Tomita, Am. Mineralogist, 52 (1967) 1438-1450.
253. A.B. Merkle and M. Slaughter, Am. Mineralogist, 53 (1968) 1120-1138.
254. A. Iijima and K. Harada, Am. Mineralogist, 54 (1969) 182-197.
255. H.R. Keusen and H. Bürki, Schweiz. Mineral. Petrogr. Mitt., 49 (1961) 577-584.
256. H. Minato, H. Namba and N. Ito, Jap.. Hyogo Univ. of Teacher Educ. Rep., (1984) 101-112.

257. B. Ullrich, P. Adolphi, J. Schomburg and H. Zwahr, Chemie der Erde, 48 (1988) 245-253.
258. V. Zholobenko, A. Garforth and J. Dwyer,. Thermochim. Acta, 294 (1997) 39-44.
259. M. De´Gennaro, P. Cappellotti, A. Langella, A. Perrotta and C. Scarpatti, Contrib. Mineral. Petrol., 139 (2000) 17-35.
260. F.P. Glaser in Differential Thermal Analysis, (Ed. R.C. Mackenzie), Vol. 1, Academic Press, London / New York, 1970, pp. 575-608.
261. A.F. Korschinskii, Izd. Akad. Nauk SSR, Moscow, (1958) 97-113 (in Russian).
262. M. Wittels, Am. Mineralogist, 37 (1952) 28-36.
263. L. van der Plas and Th. Hügi, Schweiz. Mineral. Petrogr. Mitt., 41 (1961) 371-393.
264. Tj. Peters, Schweiz. Mineral. Petrogr. Mitt., 43 (1963) 529-685.
265. W. Heflik and W. Zabinski, Mineral. Mag., 37 (1969) 241-243.
266. C.A. Geiger, N.S. Rahmoun and K. Heide, Eur. J. Mineralogy, 13 (2001) 60.
267. D. Dollimore in Differential Thermal Analysis, (Ed. R.C. Mackenzie), Vol. 1, Academic Press, London / New York, 1970, pp.396-426 and 427-446.
268. W. Smykatz-Kloss, Contrib. Mineral. Petrol., 16 (1967) 279-283.
269. Yong Wang and W.J. Thompson, Thermochim. Acta, 255 (1995) 383-390.
270. T.L. Webb and J.E. Krüger, in Differential Thermal Analysis, (Ed. R.C. Mackenzie), Vol. 1, Academic Press, London / New York, 1970, Vol. 1, pp.303-341.
271. F.L. Cuthbert and R.A. Rowland, Am. Mineralogist, 32 (1947) 111-116.
272. C.W. Beck, Am. Mineralogist, 35 (1950) 985-1013.
273. J.H. Spotts, X-ray studies and d.t.a. of some coastal limestones and associated carbonates of W-Australia, Thesis, Univ. of W-Australia, Perth, 1952.
274. W. Smykatz-Kloss, Beitr. Mineral. Petrogr., 9 (1964) 481-502.
275. S. Caillère, Bull. Soc. Franc. Minéral. Cryst., 60 (1943) 55-70.
276. S. Caillère, Bull. Soc. Franc. Minéral. Cryst., 66 (1943) 494-502.
277. G.T. Faust, Am. Mineralogist, 38 (1953) 4-24.
278. S.St.J. Warne and P. Bayliss, Am. Mineralogist, 47 (1962) 1011-1023.
279. G.J. Ross and H. Kodama, Am. Mineralogist, 52 (1967) 1036-1047.
280. G.Y. Chao, Am. Mineralogist, 56 (1971) 1855.
281. G.T. Faust, Econ. Geol., 39 (1944) 142-151.
282. C.W. Beck, Am. Mineralogist, 35 (1946) 508-524.

283. J.L. Kulp, P. Kent and P.F. Kerr, Am. Mineralogist, 36 (1951) 643.
284. R.C. Mackenzie, Mineral. Mag., 31 (1957) 672-680.
285. D.L. Graf, Am. Mineralogist, 37 (1952) 1-27.
286. W.F. Bradley, J.F. Burst and D.L. Graf, Am. Mineralogist, 38 (1953) 207-217.
287. M. Földvari-Vogl and V. Koblenc, Acta Geol. Ilung., 3 (1955) 15-25.
288. Y. Sanada and K. Miyazawa, Gypsum Lime, No. 17 (1955) 20-22.
289. T.L. Webb, Thesis, Univ. of Pretoria, South Africa, 1958.
290. P. de Souza Santos and P. Santini, Ceramica, Sao Paulo, 4 (1958) 9-25.
291. J.W. Smith, D.R. Johnson and M. Müller-Vonmoos, Thermochim. Acta, 8 (1974) 45-56.
292. K. Wieczorek-Ciurowa, J. Paulik and F. Paulik, Thermochim. Acta, 38 (1980) 157.
293. K. Iwafuchi, C. Watanabe and R. Otsuka, Thermochim. Acta, 60 (1983) 361-381.
294. R. Otsuka, Thermochim. Acta, 100 (1986) 69-80.
295. S.St.J. Warne and J.V. Dubrawski, Thermochim. Acta, 121 (1987) 39-49.
296. S.St.J. Warne and J.V. Dubrawski, J. Therm. Anal., 35 (1989) 219-242.
297. J.V. Dubrawski and S.St.J. Warne, Mineral. Mag., 52 (1988) 627-635.
298. A.E. Milodowski, D.J. Morgan and S.St.J. Warne, Thermochim. Acta, 152 (1989) 279-297.
299. R.M. McIntosh, J.H. Sharp and F.W. Wilburn, Thermochim. Acta, 165 (1990) 281-296.
300. W. Smykatz-Kloss and J. Goebelbecker in Progress in Hydrogeochemistry, (Eds G. Matthess, F. Frimmel, P. Hirsch, H.D. Schulz and E. Usdowski), 1992, pp.184-189.
301. D.L. Graf, Am. Mineralogist, 37 (1951) 1-27.
302. R.A. Rowland and C.W. Beck, Am. Mineralogist, 37 (1952) 76-82.
303. R.A.W. Haul and H. Heystek, Am. Mineralogist, 37 (1952) 166-179.
304. W. Smykatz-Kloss in Purity Determinations by Thermal Methods, ASTM STP 838, (Eds R.L. Blaine and C.K. Schoff), Am. Soc. for Testing and Materials, 1984, pp.121-137.
305. J.L. Kulp, H.D. Wright and R.J. Holmes, Am. Mineralogist, 34 (1949) 195-219.
306. C. Frondel and L.H. Bauer, Am. Mineralogist, 40 (1955) 748-760.
307. H.E. Kissinger, H.F. McMurdie and B.S. Simpson, J. Am. Ceram. Soc. 39 (1956) 168-172.
308. A. Otsuka, J. Chem. Soc. Japan, 60 (1957) 1507-1509.
309. Z. Trdlicka, Acta Univ. Carolina (Prag), Geologica, (1964) 159-167.

310. A. Tsuesue, Am. Mineralogist, 52 (1967) 1751-1761.
311. A.J. Frederickson, Am. Mineralogist, 33 (1948) 372-375.
312. R.A. Rowland and E.C. Jonas, Am. Mineralogist, 34 (1949) 550-558.
313. S. Guigné, Pupl. Serv. Carte Géol. Alger., 5 (1955) 43-56.
314. H.A. Stalder, Schweiz. Mineral. Petrogr. Mitt., 44 (1964) 187-399.
315. Z. Trdlicka, Acta Univ. Carolina (Prag), Geologica, (1966) 129-136.
316. D.R. Dasgupta, Mineral. Mag., 36 (1967) 138-141.
317. P.K. Gallagher and S.St.J. Warne, Thermochim. Acta, 43 (1981) 253-267.
318. K. Emmerich and W. Smykatz-Kloss, Clay Minerals, 37 (2002) 575-582.
319. K. Heide and W. Höland, Proc. 6. IBAUSIL Weimar, Vol. 3 (1976) 266 – 271
320. W. Höland and K. Heide, Thermochim. Acta, 15 (1976) 287-294
321. K. Walenta, Schweiz. Mineral. Petrogr. Mitt., 52 (1972) 93-108.
322. G.T. Faust, Am. Mineralogist, 33 (1948) 337-345.
323. I. Hatta, Thermochim. Acta, 305/306 (1997) 27-34.
324. L. Michalski, K. Eckersdorf, J. Kucharski and J. McGhee, Temperature Measurements, J.Wiley, New York, 2001.
325. C.W. Correns, Einführung in die Mineralogie, 2. Aufl., Springer-Verlag, Heidelberg, 1968.
326. A.van Valkenburg and G.F. Rynders, Am. Mineralogist, 43 (1958) 1197-1202.
327. I. Hassan, Am. Mineralogist, 85 (2000) 1383-1389.
328. N. Passe-Coutrin, Ph. N'Guyen, R. Pelmard, A. Ouensanga and C. Bouchon, Thermochim. Acta, 265 (1995) 135-140.
329. W. Eysel, Proc. 3rd ICTA, Vol. 2, Birkhauer – Basel, 1972, pp.179-192.
330. H.G. Wiedemann and W. Smykatz-Kloss, Thermochim. Acta, 50 (1981) 17-29.
331. K. Kobayashi and Y. Saito, Thermochim. Acta, 53 (1982) 299-307
332. F. Paulik, S. Gal and L. Erdey, Anal. Chim. Acta, 29 (1963) 381-394.
333. A. Bonamartini Corrado, C. Leonelli, T. Manfredini, L. Pennisi and M. Romagnioli, Thermochim. Acta, 287 (1996) 101-109.
334. A.M. Abdel Rehim in Thermal Analysis in the Geosciences, (Eds W. Smykatz- Kloss and S.St.J. Warne), Springer-Verlag, Berlin, 1991, pp. 188-222.
335. R. Sadanaga and S. Sueno, Mineral. J. (Japan), 5 (1967) 124-148.
336. W. Smykatz-Kloss and K. Hausmann, J. Therm. Anal., 39 (1993) 1209-1232.
337. J.E. Hiller and K. Probsthain, Erzmetall, 8 (1955) 257-267.
338. O.C. Kopp and P.F. Kerr, Am. Mineralogist, 42 (1957) 445-454.

339. J.A. Dunne and P.F. Kerr, Am. Mineralogist, 45 (1960) 881-883.
340. F.C. Kracek, Am. Geophys. Union Trans., 27 (1946) 364-373.
341. J.E. Hiller and K. Probsthain, Z. Kristallogr., 108 (1956) 108-129.
342. G. Sabatier, Bull. Soc. Franc. Minéral. Cryst., 79 (1956) 172-174.
343. O.C. Kopp and P.F. Kerr, Am. Mineralogist, 43 (1958) 732-748.
344. O.C. Kopp and P.F. Kerr, Am. Mineralogist, 43 (1958) 1079-1097.
345. J. Asensio and G. Sabatier, Bull. Soc. Franc. Minéral. Cryst., 81 (1958) 12-15.
346. C. Lévy, Bull. Soc. Franc. Minéral. Cryst., 81 (1958) 29-34.
347. G. Kullerud, Differential Thermal Analysis, Carnegie Inst. Wash. Yearbook 58 (1959) 161-163.
348. J.A. Dunne and P.F. Kerr, Am. Mineralogist, 46 (1961) 1-11.
349. C. Maurel, Bull. Soc. Franc. Minéral. Cryst., 87 (1964) 377-385.
350. L.J. Cabri, Econ. Geol., 62 (1967) 910-925.
351. E.M. Bollin in Differential Thermal Analysis, (Ed. R.C. Mackenzie), Vol. 1, Academic Press, London / New York, 1970, pp.193-234.
352. L.J. Wilson and S. Mikhail, Thermochim. Acta, 156 (1989) 107-115.
353. H.J. Hurst, J.H. Levy and S.St.J. Warne, Reactivity of Solids, 8 (1990) 159-168.
354. J. Schomburg in Thermal Analysis in the Geosciences, (Eds W. Smykatz- Kloss and S.St.J. Warne), Springer-Verlag, Berlin, 1991, pp. 224-232.
355. P. Balasz, H.J. Huhn and H. Heegn, Thermochim. Acta, 194 (1992) 189-195.
356. P. Balasz, E. Post and Z. Bastl, Thermochim. Acta, 200 (1992) 371-377.
357. J.G. Dunn, Thermochimica Acta, 300 (1997) 127-139.
358. J.G. Dunn, Thermochimica Acta, 324 (1998) 59-66.
359. A.C. Chamberlain and J.G. Dunn, Thermochim. Acta, 318 (1999) 101-113.
360. W.F. Cole and D.N. Crook, Am. Mineralogist, 51 (1966) 499-502.
361. E. Posnjak, E.T. Allen and H.E. Merwin, Econ. Geol., 10 (1915) 491-535.
362. M.J. Buerger and N.W. Buerger, Am. Mineralologist, 44 (1944) 55-65.
363. E. Jensen, Avh. norske Vidensk. Akad., Oslo, Math., Nat. Kl., 6 (1947) 1-14.
364. G. Kullerud, Carnegie Inst. Wash. Yearbook, 1958, pp.215ff.
365. S. Djurle, Acta Chem. Scand., 12 (1958) 1415-1426.
366. J.A. Dunne and P.F. Kerr, Am. Mineralogist, 46 (1961) 1-11.
367. B.J. Skinner, Econ. Geol., 61 (1966) 1-26.
368. E. Roseboom, Jr, Econ. Geol., 61 (1966) 641-672.
369. R.W. Potter, Econ. Geol., 72 (1977) 1524.

370. R.A. Yund and G. Kullerud, J. Petrol., 7 (1966) 454f.
371. O.F. Tuttle, Am. Mineralogist, 34 (1949) 723-730.
372. C.N. Fenner, Am. J. Sci. 4th Ser., 36 (1913) 331-384.
373. M.L. Keith and O.F. Tuttle, Bowen Vol., Am. J. Sci., (1952) 208-280.
374. M. Fieldes, Nature (London), 170 (1952) 366-367.
375. K. Nagasawa, J. Earth Sci., Nagoya Univ. (Japan), 1 (1953) 156-176.
376. J.B. Dawson and F.W. Wilburn in Differential Thermal Analysis, (Ed. R.C. Mackenzie), Vol. 1, Academic Press, London / New York, 1970, pp. 477-495.
377. W. Smykatz-Kloss and W. Klinke, J. Therm. Anal., 48 (1997) 19-38.
378. J.P. Bachheimer, J.Phys.Lett., 41L (1980) 342-348
379. G. Dolino in Adv.Phys.Geochem.,Vol 7, Structural and magnetic phase transitions in minerals, (Eds S. Ghose, J.M.D. Coey and E. Salje), Springer-Verlag, Berlin, 1988, pp.17 -38.
380. J. Konta, Sb. ustrd. Ust. geol., 19 (1952) 137-152.
381. T. Sudo, Sci. Rep. Tokyo Kyoiku Daig., C5 (1956) 39-55.
382. L.H. Berkelhamer, Rep. Invest. U.S. Bur. Mines, No. 3763, (1944).
383. R.W. Grimshaw, Clay Min. Bulletin, 2 (1953) 2-7.
384. O.W. Floerke, Schweiz. Mineral. Petrogr. Mitt., 41 (1961) 311-324.
385. H. Yao and I. Hatta, Thermochim. Acta, 266 (1995) 301-308.
386. V. Balek, J. Fusek, J. Kriz and M. Murat, Thermochim. Acta, 262 (1995) 209-214.
387. M. Bruno and J.L. Holm, Thermochim. Acta, 318 (1998) 125-129.
388. R.J. Hand, S.J. Stevens and J.H. Sharp, Thermochim. Acta, 318 (1998) 115-123.
389. W. Smykatz-Kloss, Contrib. Mineral. Petrol., 26 (1970) 20-41.
390. W. Smykatz-Kloss, Contrib. Mineral. Petrol., 36 (1972) 1-18.
391. J. Font and J. Muntasell, Thermochim. Acta, 293 (1997) 167-170.
392. Pei Jane Huang, Hua Chang, Chuin Tih Yeh and Ching Wen Tsai, Thermochim. Acta, 297 (1997) 85-92.
393. W.W. Wendlandt, Thermal Methods of Analysis, 2nd edition, Wiley and Sons, New York, 1974.
394. H.Ch. Soffel, Paläomagnetismus und Archäomagnetismus, Springer-Verlag, Heidelberg – Berlin, 1991.
395. P.D. Garn, O. Menis and H.G. Wiedemann, Thermal Analysis, Vol. 1, Proc. 6th ICTA, 1980, pp. 201-205.
396. S.L. Blum, A.E. Paladino and L.G. Rubin, Am. Ceram. Soc. Bull., 36 (1957) 175-176.
397. E.R. Schmidt and F.H.S. Vermaas, Am. Mineralogist, 40 (1955) 422-440.

398. E.A. Vincent, J.B. Wright, R. Chevallier and S. Mathieu, Mineral. Mag., 31 (1957) 624-655.
399. R. Chevallier, J. Bolfa and S. Mathieu, Bull. Soc. Franc. Minéral. Cryst., 78 (1955) 307-346.
400. H. Weitzel, N. Jb. Mineralogie, Abh., 113 (1970) 13-28.
401. E.J. Duff, J. Chem. Soc. A, (1968) 2072-2074.
402. J.F. Lewis, Am. Mineralogist, 55 (1970) 793-807.
403. A.A. Agroskin, E.I. Goncharev, L.A. Makeev and V.P. Yakunin, Coke and Chem. USSR, 5 (1970) 7-11.
404. G.J. Lawson in Differential Thermal Analysis, (Ed. R.C. Mackenzie), Vol.1, Academic Press, London / New York, 1970, pp.705-726.
405. O.P. Mahajan, A.Tomita and P.L. Walker, Jr., Fuel, 55 (1976) 63-69.
406. P.C. Crawford, D.L. Ornellas, R.C. Lum and P.L. Johnson, Thermochim. Acta, 34 (1979) 239-243.
407. P. Cardillo, Riv. Combast., 34 (1980) 129-137.
408. P.I. Gold, Thermochim. Acta, 42 (1980) 135-152.
409. R.J. Rosenvold, J.B. DuBow and K. Rajeshwar, Thermochim. Acta, 53 (1982) 321-332.
410. C.R. Phillips, R. Luymes and T.M. Halahel, Fuel, 61 (1982) 639-649.
411. D.M. Aylmer and M.W. Rowe, Thermochim. Acta, 78 (1984) 81-92.
412. C.M. Earnest in Analytical Calorimetry, (Eds J.F. Johnson and P.S. Gill), Plenum Press, New York, 1984, pp.343-359.
413. C.M. Earnest, Thermal Analysis of Clays, Minerals and Coal, Perkin-Elmer Corp., Norwalk, 1984.
414. J.P. Elder and M.B. Harris, Fuel, 63 (1984) 262-267.
415. R. Hefta, H. Schobert and W. Kube, Fuel, 65 (1986) 1196-1202.
416. J.W. Cumming and J. McLaughlin, Thermochim. Acta, 57 (1982) 253-272.
417. M. Levy and R. Kramer, Thermochim. Acta, 134 (1988) 327-331.
418. H.G. Wiedemann, R. Riesen, A. Boller and G. Bayer in Compositional Analysis by Thermogravimetry, (Ed. C.M. Earnest), ASTM STP 997, 1988, pp.227-244.
419. J.W. Cumming, Thermochim. Acta, 155 (1989) 151-161.
420. J.H. Patterson, Fuel, 73 (1994) 321-327.
421. M.V. Kök, Thermochim. Acta, 336 (1999) 121-125.
422. S.St.J. Warne in Analytical Methods for Coal and Coal Products. III, (Ed. C. Karr, Jr.), 1979, pp.447-477.
423. V. Balek, G. Matuschek, A. Kettrup and I. Sykorova, Thermochim. Acta, 263 (1995) 141-157.
424. S.St.J. Warne, Thermochim. Acta, 86 (1985) 337-342.

425. S.St.J. Warne, Thermochim. Acta, 109 (1986) 243-252.
426. S.St.J. Warne, Thermochim. Acta, 110 (1987) 501-511.
427. S.St.J. Warne and J.V. Dubrawski, J. Therm. Anal., 33 (1988) 435-400.
428. J.V. Dubrawski and S.St.J. Warne, Fuel, 66 (1987) 1733-1736.
429. S.St.J. Warne, Thermochim. Acta, 272 (1996) 1-9.
430. J.V. Dubrawski, Thermochim. Acta, 120 (1987) 257-260.
431. T.R. Jones, Clay Minerals, 18 (1983) 399-410.
432. W. Bodenheimer, L. Heller and S. Yariv, Clay Minerals, 6 (1966) 167 ff.
433. C. Chi Chou and J.L. McAtee, Jr., Clays and Clay Minerals, 17 (1969) 339.
434. B.K.G. Theng, The Chemistry of Clay Organic Reactions, A.Hilger, London, 1974.
435. G. Lagaly, Phil. Trans. R. Soc. London A 311, (1984) 315-332.
436. S. Yariv and L. Heller-Kallai, Chem. Geol., 45 (1984) 313-327.
437. S. Yariv, Thermochim. Acta, 88 (1985) 49-68.
438. S. Yariv, Int. J. Trop. Agric., 6 (1988) 1-19.
439. S.Yariv, D. Ovadyahu, A. Nasser, U. Shual and N. Lahav, Thermochim. Acta, 207 (1992) 103-113.
440. L. Heller-Kallai, S. Yariv and I. Friedman, J. Therm. Anal., 31 (1986) 95-106.
441. M. Störr and H.H. Murray, Clays and Clay Minerals, 34 (1986) 689.
442. U. Shuali, S.Yariv, M. Steinberg, M. Müller-Vonmoos, G. Kahr and A. Rub, Thermochim. Acta, 135 (1988) 291.
443. U. Shuali, M. Steinberg, S. Yariv, M. Müller-Vonmoos, G. Kahr and A. Rub, Clay Minerals, 25 (1990) 107-119.
444. S.Yariv, L. Heller-Kallai and Y. Deutsch, Chem. Geol., 68 (1988) 199ff.
445. S.Yariv, M. Müller-Vonmoos, G. Kahr and A. Rub, J. Therm. Anal., 35 (1989) 1997-2008.
446. A. Langier-Kuzniarowa, Thermochim. Acta, 148 (1989) 413.
447. F. Paulik, J. Paulik, M. Arnold, J. Inczedy, J. Kristof and A. Langier-Kuzniarowa, J. Thermal Anal., 35 (1989) 1849.
448. M.F. Brigatti, C. Lugli, S. Montorsi and L. Poppi, Clays and Clay Minerals, 47 (1999) 664-671.
449. M. Müller-Vonmoos, G. Kahr and A. Rub, Thermochim. Acta, 20 (1977) 387-393.
450. E. Morillo, J.L. Perez-Rodriguez and C. Maqueda, Clay Minerals, 26 (1991) 269-279.
451. W.T. Reichle, S.Y. Kang and D.S. Everhardt, J. Catal., 101 (1986) 352-359.

452. C. del Hoyo, V. Rives and M.A. Vicente, Thermochim. Acta, 286 (1996) 89-103.
453. A. Weiss, R. Thielepape, W. Göring, W. Ritter and H. Schaffer in Proc. Intern. Clay Conf. Stockholm, (Eds I. Rosenquist and P. Graaff-Peterson), Pergamon Press, Oxford, 1963, pp.287-305.
454. M. Gabor, L. Pöppl, U. Izvekov and H. Beyer, Thermochim. Acta, 148 (1989) 431-438.
455. M. Gabor, M. Toth, J. Kristof and G. Komaromi-Hills, Clays and Clay Minerals, 43 (1995) 223-228.
456. M. Sato, Clays and Clay Minerals, 47 (1999) 793-802.
457. C.H. Horte, Chr. Becker, G. Kranz, E. Schiller and J. Wiegmann, J. Therm. Anal., 33 (1988) 401-406.
458. J. Cornejo, R. Celis, I. Pavlovic, M.A. Ulibarri and M. Hermosiu, Clay Minerals, 35 (2000) 771-779.
459. C. del Hoyo, V. Rives and M.A. Vicente, Thermochim. Acta, 286 (1996) 89-103.
460. S. Yariv, L. Heller, Y. Deutsch and W. Bodenheimer, Thermal Analysis, Proc. 3rd ICTA, Davos, Birkhäuser-Verlag, Basel, Vol. 3, 1971, 663ff.
461. S. Yariv, Thermochim. Acta, 274 (1996) 1-35.
462. V. Balek, L. Kelnar, K. Györova and W. Smykatz-Kloss, Applied Clay Sci., 7 (1992) 179-184.
463. A. Busnot, F. Busnot, J.F. Le Querler and J. Yazbeck, Thermochim. Acta, 254 (1995) 319-330.
464. E.C. Stout, C.W. Beck and K.B. Anderson, Phys. Chem. Miner., 27 (2000) 666-678.
465. J.G. Dunn and V.L. Howes, Thermochim. Acta, 282 (1995) 305-316.
466. A.P. Dhupe and A.N. Gokaran, Int. J. Miner. Process., 20 (1990) 209-220.
467. P. Bayliss and S.St.J. Warne, Am. Mineralogist, 57 (1972) 960-966.
468. F. Rey, V. Forner and J.M. Rojo, J. Chem. Soc. Faraday Trans., 88 (1992) 2233-2238.
469. L. Stoch, J. Therm. Anal., 48 (1997) 121-133.
470. V. Balek, J. Therm. Anal., 35 (1989) 405-427.
471. Z. Chvoj, J. Sestak and A. Triska, Kinetic Phase Diagrams, Elsevier, Amsterdam, 1991.
472. E.T. Stepkowska, S. Yariv, J.L. Perez-Rodriquez, C. Maqueda, A. Justo, A. Ruiz-Condé and P. Sanchez-Soto, J. Therm. Anal., 49 (1997) 1449-1466.
473. K. Heide, K. Gerth, G. Büchel and E. Hartmann, J. Therm. Anal., 48 (1997) 73-81.

474. C.T. Prewitt, The Physics and Chemistry of Minerals and Rocks, Wiley and Sons, 1976, pp.433-442.
475. G.A. Merkel and J.G. Blencoe, Adv. Phys. Geochemistry 2, Springer-Verlag, 1982, p.247.
476. V.I. Babushkin, G.M. Matreyev and O.P. Mchedloy-Petrossyan, Thermodynamics of Silicates, Springer-Verlag, Berlin, 1985.
477. H.G. Wiedemann, W. Smykatz-Kloss and W. Eysel, Thermal Analysis, Proc. 6th ICTA, Vol.2, Birkhäuser, Basel, 1980, pp.347-352.
478. G. Bayer and H.G. Wiedemann, Angew. chem. Thermodynamik u. Thermoanalytik, Exper. Suppl., Vol. 37, Birkhäuser-Verlag, Basel, 1979, pp.9-22.
479. J. Sestak, V. Satava and W.W. Wendlandt, Thermochim. Acta, 7 (1973) 333-356.
480. O.J. Kleppa, The Physics and Chemistry of Minerals and Rocks, Wiley and Sons, 1974, p. 369-387.
481. N.D. Chatterjee, Applied Mineralogy Thermodynamics, Springer-Verlag, Berlin, 1991.
482. J.V. Smith, Feldspar Minerals, Vol. 1, Springer-Verlag, Berlin, 1974, p.591.
483. E. Nemecz, Acta Geol. Acad. Hungary, 6 (1959)119-151.
484. K. Lønvik, Thermal Analysis, Proc. 4th ICTA, Vol.3, Budapest, 1974, pp.1089-1105.
485. J. Binde, J.L. Holm, J. Lindemann and K. Lønvik, Thermal Analysis, Proc. 6th ICTA, Beyruth, 1980, Vol.2, Birkhäuser-Verlag, Basel, pp.313-318.
486. A. Köhler and P. Wieden, N. Jb. Mineral., Monat., 12 (1954) 249-252.
487. R.J. Kirkpatrick, Rev. Mineralogy, 8 (1981) 321-398.
488. D.C. Rubie and A.B.Thompson, Adv. Phys. Geochemistry, 4, Springer-Verlag, Berlin, 1985, pp.27-89.
489. A.B. Thompson and E.H. Perkins, Adv. Phys. Geochemisry, 1, Springer-Verlag, Berlin, 1981, pp.35-62.
490. P. Ehrenfest, Proc. Acad. Sci. Amsterdam, 36 (1933) 153 ff.
491. I. Gutzow and J. Schmelzer, The Vitreous State, Thermodynamics, Structure, Rheology and Crystallization, Springer-Verlag, Berlin, 1995.
492. W.D. Carlson, J. Geol., 91 (1983) 55-71.
493. W.D. Carlson and J.L. Rosenfeld, J. Geol., 89 (1981) 615-638.
494. J. Ridley and A.B. Thompson, Mineral. Mag., 50 (1986) 375-384.
495. T.J.B. Holland, Adv. in Phys. Geochemistry, 1 (1980) 19-34.
496. K. Heide in Der Harnstein, (Eds E. Hinzsch and H.J. Schneider), VEB Fischer-Verlag, Jena, 1973, pp.157-181.

497. G. Kluge, H. Eichhorn, K. Heide and M. Fritsche, Thermochim. Acta, 60 (1983) 303-318.
498. H. Hofmann and A. Rothe, Z. Anorg. Allgem. Chemie, 357 (1968) 196-201.
499. G.S.M. Moore, J. Therm. Anal., 40 (1993) 115-120.
500. I. Waclawska, J. Therm. Anal., 48 (1997) 155-161.
501. J.L. Kulp and A.F.Trites, Am. Mineralogist, 36 (1951) 23-44.
502. V. Balek and M. Murat, Thermochim. Acta, 282 (1995) 385-397.
503. G. Sabatier, Bull. Soc. Franc. Minéral. Cryst., 80 (1957) 444-449.
504. O.F. Tuttle and M.L. Keith, Geol. Magazine, 41 (1954) 61-72.
505. Ye. Panov, L.G. Muratov and B.K. Kasatov, Dokl. Akad. Nauk SSR, 175 (1967) 1359-1362.
506. J. Lameyre, C. Lévy and J. Mergoil, Bull. Soc. Franc. Mineral. Cryst., 91 (1968) 172-181.
507. W. Smykatz-Kloss, N. Jb. Mineral. Mh., (1969) 563-567.
508. P. Kresten, Stockh. Contrib. Geol., 23 (1971) 91-121.
509. P. Kresten, Linseis J., 1 (1971) 6-8.
510. A. Giret, J. Lameyre, C. Levy and C.R. Marion, C. R. Acad. Sci. Paris, f. 275 (1972) 161-164.
511. G.S. Moore and H.E. Rose, Nature (London), 242 (1973) 187-190.
512. R.H.S. Robertson, Scott. J. Sci., 1 (1973) 175-182.
513. W.A. Kneller, H.F. Kriege, E.L. Saxer, J.T. Wilbrand and T.J.Rohrbacher, Res. Found. Univ. Toledo / Ohio, Aggr. Res. Group Geol. Dept., (1968).
514. S.St.J. Warne, J. Inst. Fuel (Australia), (1970) 240-242.
515. P. Buurman and L. Van der Plas, Geol. Mijnbouw, 50 (1971) 9-28.
516. G.S. Moore, Phase Transitions, 7 (1986) 25f.
517. G.S. Moore, Thermochim. Acta, 126 (1988) 365f.
518. A.J. Gude, III$^{rd.}$ and R.A. Sheppard, Am. Mineralogist, 57 (1972) 1053-1065.
519. W.W. Wendlandt, Thermal Methods of Analysis, 3rd edition, Wiley and Sons, New York, 1984.
520. W. Klement, Jr. and L.H. Cohen, J. Geophys. Res., 73 (1968) 2249-2259.
521. U. Steinike, D.C. Uecker, K. Sigrist, W. Plötner and T. Köhler, Cryst. Res. Technol., 22 (1987) 1255f.
522. W. Dodd and K.H. Tonge, Thermal Methods, Wiley and Sons, Chichester, 1987.
523. M. Lisk, P.R.L. Browne and K.A. Rodgers, N. Jb. Mineral. Mh., (1991) 538 f.
524. G. Sabatier and J. Wyart, Compt. Rend., 239 (1954) 1053f.
525. K.A. Rodgers and N.M. Howett, Thermochim. Acta, 87 (1985) 363-655.

526. J.C. Newton-Howes and R.J. Fleming, Phys. Chem. Minerals, 17 (1990) 27-33.
527. M. Lisk, K.A. Rodgers and P.R.L. Browne, Thermochim. Acta, 175 (1991) 293 f.
528. H.U. Bambauer, Schweiz. Mineral. Petrogr. Mitt., 41 (1961) 335-369.
529. O.W. Flörke, Chemie der Erde, 22 (1962) 91-110.
530. K.A. Rodgers and N.M. Howett, N. Jb. Mineral. Abh., 159 (1988) 1-21.
531. W. Smykatz-Kloss and W. Klinke, J. Therm. Anal., 42 (1994) 85-97.
532. K. Lønvik and W. Smykatz-Kloss, Thermochim. Acta, 72 (1984) 159-163.
533. R.E. Grim and W.D. Johns, Jr., J. Am. Ceram. Soc., 34 (1951) 71-76.
534. L. Piga, Thermochim. Acta, 265 (1995) 177-187.
535. M.V. Kök, J. Therm. Anal., 49 (1997) 617-625.
536. J. Dunn, K. Oliver, G. Nguyen and L.D. Stills, Proc. 9th Austr. Symp. Anal. Chem. Sydney, 1 (1987) 88-91.
537. E. Hartung and K. Heide, Silikattechnik, 35 (1984) 343-345.
538. W. Höland and K. Heide, Silikattechnik, 32 (1981) 344–345.
539. K. Heide, J. Therm. Anal., 35 (1989) 305–318.
540. K. Heide, G. Völksch and Chr. Hanay, J. Therm. Anal., 40 (1993) 171-180.
541. L. Heller-Kallai and R.C. Mackenzie, Clay Minerals, 22 (1987) 349-350.
542. R.C. Mackenzie, L. Heller-Kallai, A.A. Rahman and H.M. Moir, Clay Minerals, 23 (1988) 191-203.
543. A.M. Abdel Rehim, J. Therm. Anal., 48 (1997) 177-202.
544. R.C. Mackenzie, Tonindustr. Zeitg., 75 (1951) 334-340.
545. R.C. Mackenzie and R. Meldau in Differential Thermal Analysis, (Ed. R.C. Mackenzie), Vol. 2, Academic Press, London, New York, 1972, pp.555-564.
546. S. Starck in Thermal Analysis in the Geosciences, (Eds W. Smykatz-Kloss and S.St.J. Warne), Springer-Verlag, Berlin, 1991, pp.234-242.
547. E.L. Charsley and S.B. Warrington in Compositional Analysis by Thermogravimetry, (Ed. C.M. Earnest), ASTM Spec. Techn. Publ. 997, (1988) 145-253.
548. J.V. Dubrawski, J. Therm. Anal., 48 (1997) 63-72.
549. D.S. Klimesh and A. Ray, Thermochim. Acta, 316 (1998) 149-154.
550. H. Kleykamp, J. Phase Equilibria, 16 (1995) 107-108.
551. M. Kelm, A. Görtzen, H. Kleykamp and H. Pentinghaus, J. Less Common Metals, 166 (1990) 125-133.
552. Zh. Ding, H. Kleykamp and F. Thümmler, J. Nucl. Materials, 171 (1990) 134-138.

553. S. Bernath, H. Kleykamp and W. Smykatz-Kloss, J. Nucl. Materials, 209 (1994) 128-131.
554. S. Claus, H. Kleykamp and W. Smykatz-Kloss, J. Nucl. Materials, 230 (1996) 8-11.
555. A. Moropoulou, A. Bakolas and K. Bisbikou, Thermochim. Acta, 269/270 (1995) 743-753.
556. J. Plewa, H. Altenburg and J. Hauck, Thermochim. Acta, 255 (1995) 177-190.
557. U. Wiesner, W. Bieger and G. Krabbes, Thermochim. Acta, 290 (1996) 115-121.
558. W. Smykatz-Kloss,Thermal Analysis, Proc. 6th ICTA, 1980, pp.301-306.
559. L. Die, M. Mauro and G. Bitossi, Thermochim. Acta, 317 (1998) 133-140.
560. V. Balek and J. Tölgyessy, Emanation Thermal Analysis, Elsevier, Amsterdam, 1984.
561. A.N. Garcia, A. Marcilla and R. Font, Thermochim. Acta, 254 (1995) 277-304.
562. L. Piga, F. Pochetti and L. Stoppa, Thermochim. Acta, 254 (1995) 337-345.
563. J.A. Conseca, A. Marcilla, R. Moral, J. Moreno-Casellas and A. Perez-Espinosa, Thermochim. Acta, 313 (1998) 63-73.
564. P.J. Wyllie and E.J. Raynor, Am. Mineralogist, 50 (1965) 2077-2082.
565. B. Turner, High Pressure, 5 (1973) 273-277.
566. K. Lønvik, K. Rajeshwar and J.B. Dubow, Thermochim. Acta, 42 (1980) 11-19.
567. F. Paulik, J. Paulik and L. Erdey, Talanta, 13 (1966) 1405-1430.
568. F. Paulik, J. Paulik and L. Erdey, Mikrochim. Acta, (Wien), (1966) 886-893.
569. F. Paulik, J. Paulik and L. Erdey, Mikrochim. Acta, (Wien), (1966) 893-902.
570. F. Paulik and J. Paulik, J. Therm. Anal., 5 (1973) 253-270.
571. J. Kristof, J. Inczedy, J. Paulik and F. Paulik, J. Therm. Anal., 37 (1991) 111-120.
572. M. Földvari, F. Paulik and J. Paulik, J. Therm. Anal., 33 (1988) 121-132.
573. C.B. Murphy, J.A. Hill and G.P. Schacher, Anal. Chem., 32 (1960) 1374.
574. H.G. Langer and R.S. Gohlke, Anal. Chem., 35 (1963) 1301-1302.
575. A.J. Parsons, S.D.J. Inglethorpe, D.J. Morgan and A.C. Dunham, J. Therm. Anal., 48 (1997) 49-62.
576. S. Cebulak, A. Karczewska, A. Mazurek and A. Langier-Kuzniarowa, J. Therm. Anal., 48 (1997) 163-175.

577. V. Karoleva, G. Georgiev and N. Spasov, Thermal Anal., Proc. 4th ICTA, Budapest, Vol. 2, 1975, pp.601-610.
578. E. Pekenc and J.H. Sharp, Thermal Anal., Proc. 4th ICTA, Budapest, Vol. 2, 1975, pp.585-600.
579. S. Tsutsumi and R. Otsuka, Thermal Anal., Proc 5th ICTA, Kyoto, 1977, pp.456-459.
580. Z. Malek, V. Balek, D. Garfunkel-Shweky and S. Yariv, J. Therm. Anal., 48 (1997) 83-92.
581. J. Schomburg and K.F. Landgraf, 7th Conf. Clay Min. and Petrology, Karlovy Vary Proc., 1976, pp.139-150
582. K. Heide, Thermal Analysis, Proc. 3rd ICTA, Vol 2, Birkhäuser Verlag, 1972 p.523 -536
583. H.J. Dichtl and F. Jeglitsch, Radex-Rundschau, H.3/4 (1967) 716-722.
584. M. Carreras, R. Roque-Malherbe and C. de las Pozas, J. Therm. Anal., 32 (1987) 1271-1276.
585. J.A. Alonso Perez, R. Roque-Malherbe, C.R. Gonzalez-Gonzalez and C. de las Pozas, J. Therm. Anal., 34 (1988) 865-870.
586. B. Zeldovrich, J. Exper. Theoret. Physik, 12 (1943) 525 (in Russian).
587. F.J. Gotor, M. Macias, A. Ortega and J.M. Criado, Int. J. Chem. Kinet. 30 (1998) 647-655.
588. S.St.J. Warne, H.J. Hurst and W.I. Stuart, Thermal Anal. Abstr., 17 (1988) 1-6.
589. M.J. Aitken, Thermoluminescence Dating, Academic Press, London, 1985.
590. L. Zöller, Catena, 41 (2000) 229-235.
591. S.St.J. Warne, J. Therm. Anal., 48 (1997) 39-47.
592. W. Smykatz-Kloss and K. Heide, J. Therm. Anal., 33 (1988) 1253-1257.
593. A. Navrotsky, Phys. Chem. Mineral., 24 (1997) 222-241.
594. W. Kleber, W. Wilde and M. Frenzel, Chemie der Erde, 24 (1965) 77-93.
595. R.O. Niedermeyer and J. Schomburg, Chemie der Erde, 43 (1984) 139-148.
596. E. Hartung, Grundlagenuntersuchungen zum Zersetzungs- und Verdampfungsverhalten in den Systemen Na_2O-B_2O_3 und Na_2O-B_2O_3-SiO_2, Diss. Univ. Jena, 1981.
597. J. Peric, M. Vucak, R. Krstulovic, J. Brecevic and D. Kralj, Thermochim. Acta, 277 (1996) 175-186.
598. G.T. Faust, Am. Mineralogist, 35 (1950) 207-225.
599. S.A. Robbins, R.G. Rupard, B.J. Weddle, T.R. Maull and P.K. Gallagher, Thermochim. Acta, 269/270 (1995) 43-49.
600. F.C. Kracek, J. Phys. Chem., 33 (1929) 1281-1308.

601. F.M. Nakhla and W. Smykatz-Kloss, FPME Journal, Tripoli (Libya), 1 (1978) 33-38.
602. W. Eysel, Amer. Mineralogist, 58 (1973) 736-747.
603. R.G. Schwab, Fortschr. Mineralogie, 46 (1969) 188-273.
604. R.G. Schwab and H. Jablonski, Fortschr. Mineral., 50 (1973) 223-263.
605. T. Arlt and R.J. Angel, Phys. Chem. Miner., 27 (2000) 719-731.
606. K.D. Hammonds, M.T. Dove, A.P. Giddy, V. Heine and B. Winkler, Am. Mineralogist, 81 (1996) 1057-1079.
607. W.F. Müller, Phys. Chem. Mineral., 1 (1977) 71-82.
608. A.T. Maiorova, S.N. Mudretsova, M.L. Kovba, Yu.Ya. Skolis, M.V. Gorbatcheva, G.N. Maso and L.A. Khramtsova, Thermochim. Acta, 269/270 (1995) 101-107.
609. A. Kremenovic, P. Norby, R. Dimitrijevic and V. Dondur, Phase transitions, 68 (1997) 587-605.
610. Y. Tabira, R.L. Withers, Y. Takéuchi and F. Marumo, Phys. Chem. Mineral., 27 (2000) 194-202.
611. R.L. Withers, Y. Tabira, J.A. Valgoma, M. Aroyo and M.T. Dove, Phys. Chem. Miner., 27 (2000) 747-756.
612. V. Cremer, N. Jb. Mineralogie Abh. 111 (1969) 184-205.
613. S. Bocquet and A.J. Hill, Phys. Chem. Mineral., 22 (1995) 524-528.
614. S. Bocquet and S.J. Kennedy, J. Magn. Mat., 109 (1992) 260-264.
615. R. Schuette, B.A. Goodman and J.W. Stucki, Phys. Chem. Mineral.. 27 (2000) 251-257.
616. R.S. Coe and M.S. Paterson, J. Geophys. Res., 74 (1969) 4921-4948.
617. M.T. Dove, M. Gambhir and V. Heine, Phys. Chem. Mineral., 26 (1999) 344-353.
618. D.R. Peacor, Z. Kristallogr., 138 (1973) 274-298.
619. D.M. Hatch and S. Ghose, Phys. Chem. Mineral., 17 (1991) 554-562.
620. D.R. Spearing, I. Farnan and J.F. Stebbins, Phys. Chem. Miner., 19 (1992) 307-321.
621. S.J. Stevens, R.J. Hand and J.H. Sharp, J. Therm. Anal., 49 (1997) 1409-1415.
622. J. Liu, L. Topor, J. Zhang, A. Navrotsky and R.C. Liebermann, Phys. Chem. Mineral., 23 (1996) 11-16.
623. I. Petrovic, P.J. Heaney and A. Navrotsky, Phys. Chem. Miner., 23 (1996) 119-126.
624. J.A. Bain and D.J. Morgan, Clay Minerals, 8 (1969) 171-192.
625. R.C. Mackenzie and S. Caillère in Soil Components, Vol. 2, (Ed. J.E. Gieseking), Springer, New York, 1975, pp.529-571.
626. D.M. Price, J. Therm. Anal., 49 (1997) 953-959.

627. K. Rajeshwar, Thermochim. Acta, 63 (1983) 97-112.
628. E. Bonaccorsi, P. Comodi and S. Merlino, Phys. Chem. Miner., 22 (1995) 367-374.
629. M.V. Kök and E. Okandan, J. Thermal. Anal., 46 (1996) 1657-1669.
630. M.V. Kök, Energy Sources, 24 (2002) 899-906.
631. W. Smykatz-Kloss and J. Goebelbecker in Ingenieurgeologische Probleme im Grenzbereich zwischen Locker-und Festgesteinen, (Ed. K.H. Heitfeld), Springer-Verlag, Heidelberg, 1985, pp.163-173.
632. K. Emmerich, F.T. Madsen and G. Kahr, Clays and Clay Minerals, 47 (1999) 591-604.
633. J. Kristof, M. Toth, M. Gabor, P. Szabo and R.L. Frost, J. Therm. Anal., 49 (1997) 1441-1448.
634. S. Felder-Casagrande, H.G. Wiedemann and A. Reller, J. Therm. Anal., 49 (1997) 971-978.
635. C.A. Strydom, E.M. Groenewald and J.H. Potgieter, J. Therm. Anal., 49 (1997) 1501-1510.
636. H. Li, X.Z. Shen, B. Sisk, W. Orndorff, D. Li, W.P. Pan and J.T. Riley, J. Therm. Anal., 49 (1997) 943-951.
637. E.T. Stepkowska, J.L. Perez-Rodriquez, A. Justo, P. Sanchez-Soto, A. Aviles and J.M. Bijen, Thermochim. Acta, 214 (1993) 97-102.
638. L. Stoch, J. Therm. Anal., 37 (1991) 1415-1429.
639. V. Venugopal, Proc. 12th Nat. Symp., "Thermans 2000", Indian Thermal Anal. Soc., Mumbay, India, 2000, pp.1-10.
640. J.M. Criado, J. Morales and V. Rives, J. Therm. Anal., 14 (1978) 221-228.
641. J.M. Criado, Thermochim. Acta, 28 (1979) 307-312.
642. J.M. Criado, F. Rouquerol and J. Rouquerol, Thermochim. Acta, 38 (1980) 109-115.
643. J.M. Criado and A. Ortega, Thermochim. Acta, 195 (1992) 163-167.
644. K. Heide, Chemie der Erde, 27 (1968) 353-368.
645. K. Heide, W. Höland, H. Gölker, K. Seyfarth, B. Müller and R. Sauer, Thermochim. Acta, 13 (1975) 365-378.
646. K. Heide, G. Kluge and V. Hlawatsch, Thermochim. Acta, 36 (1980) 151-160.
647. M. Odlyha, J.J. Boon, O. van den Brink and M. Bacci, J. Therm. Anal., 49 (1997) 1571-1584.
648. E. Franceschi, A. del Lucchese, D. Palazzi and G. Rossi, J. Therm. Anal., 49 (1997) 1593-1600.
649. I. Petrov and W. Berdesinski, Z. Dt. Gemmolog. Ges. 24, H. 2, (1975) 73-80.

650. K.A. Rodgers and S. Currie, Thermochim. Acta, 326 (1999) 143-149.

This Page Intentionally Left Blank

Handbook of Thermal Analysis and Calorimetry. Vol. 2: Applications to Inorganic and Miscellaneous Materials
M.E. Brown and P.K. Gallagher, editors
© 2003 Elsevier B.V. All right reserved.

Chapter 12

DEHYDRATION OF CRYSTALLINE HYDRATES

Andrew K. Galwey*

Department of Chemistry, Rhodes University, Grahamstown, 6140 South Africa

* NOW RETIRED : HOME ADDRESS : 18, Viewfort Park, Dunmurry, Belfast, BT17 9JY, Northern Ireland

1. INTRODUCTION

1.1. Crystalline hydrates

The distinguishing feature of crystalline hydrates, characterizing the range of reactant compounds surveyed in this review, is that water in these solids is accommodated as distinct H_2O molecules. The change most commonly observed on heating is dehydration, through the release of a proportion, or all, of the constituent H_2O. These reactions are widely studied by thermoanalytical methods. The water released is often volatilized immediately following liberation, though, when removal is prevented, the accumulation of liquid may be sufficient to dissolve the salt, an effect that resembles melting. Melting/decomposition temperatures are listed for some highly hydrated compounds. The literature concerned with the dehydrations of crystalline hydrates can be described (perhaps with oversimplification) as abundant and (as yet) uncoordinated. Hydrated salts are regarded as particularly attractive reactants for use in fundamental kinetic and mechanistic investigations of solid state reactions and the chemistry of these reactions has been the subject of many and numerous detailed studies. Many of these hydrates can be prepared fairly easily in the form of large single crystals containing relatively few imperfections. The flat surfaces exposed on crystal cleavage are particularly suitable for microscopic observations of the characteristic textural changes that often accompany the initiation and progress of dehydrations.

Investigations of the thermal dehydrations of many and diverse crystalline hydrates have notably contributed to the understanding of characteristic features of a wide range of decompositions and, indeed, these concepts and models have value in interpreting behaviour exhibited by other types of reactions that occur in the solid state [1,2]. However, problems remain in providing classification criteria that are capable of introducing systematic order into the extensive range of rate processes that are grouped within the scope of this relatively non-specific Chapter title: "Dehydration of Crystalline Hydrates." A recent review [3] addressed the difficulties of finding criteria for establishing systematic order amongst dehydrations. However, no detailed theory unifies the subject and, consequently, research reports tend to be concerned with individual or restricted groups of chemically comparable reactants. Conclusions reached for one salt may not be generally applicable to other substances.

This survey of dehydrations is predominantly concerned with fundamental studies of the chemistry of water elimination reactions from crystals, including characterization of the controls of reactivity together with the kinetics and mechanisms of the rate processes that participate. Coverage is conveniently introduced by consideration of the scope of the subject, through reference to the range of hydrate structures and types (Section 1.2.). This is followed by brief accounts of (Section 1.3.) the relevant theory as most usually employed in the recent literature [1,2], (Section 1.4.) the endothermic and reversible character of most dehydrations, (Section 1.5.) the relevant literature, the contents of this survey (Section 1.6.) and calorimetry (Section 1.7.). Section 2 reviews the experimental methods used in, and in association with, thermal analysis. The largest Section 3 is composed of individual accounts of a representative range of diverse dehydrations to illustrate the many different characteristic features of these reactions that have been reported in the literature. These synopses mention particularly aspects of kinetic behaviour and proposed reaction mechanisms, emphasis is on fundamental investigations directed towards extending theory and understanding the chemical foundations and controls of reactivity. Section 4 discusses some representative water evolution reactions that are generally related to the main group of dehydrations considered. A small number of specialist and unusual features of dehydrations are examined in Section 5. The review ends with Section 6, a short consideration of the present status of the subject and some directions for possible future progress.

1.2. Hydrate structures and types

Many, though not all, inorganic salts contain water of crystallization, the total range of hydrates includes suitable combinations of all anions and all cations. The water contents vary from mono, or even fractional numbers of H_2O molecules, e.g. $Li_2SO_4.H_2O$, $CaSO_3.½H_2O$, etc., to highly hydrated compounds such as the alums, $M^+M^{3+}(SO_4)_2.12H_2O$, $MgCl_2.12H_2O$, together with numerous sulfates, halides, nitrates, etc. Wells [4] notes that the inorganic hydrates "form an extremely large group of compounds." This and other, e.g. [5], compendiums of hydrate structures, to which the interested reader is referred, make further general points that are relevant here. In crystalline hydrates the H_2O molecule is a tetrahedral structural component that is retained in the solid by one or other of the following bonding situations. (i) Water may be coordinated to a cation as a ligand (thereby reducing the effective ionic charge) and hydrogen bonded to other crystal constituents. (ii) Alternatively, water may be present as a structure-stabilizing lattice component (packing), in which hydrogen bonding makes an important contribution. Molecules in both situations are present, for example, in nickel sulfate heptahydrate, which may be represented as $[Ni(OH_2)_6].H_2O.SO_4$. Loss of coordinated water can be accompanied by the generation of "replacement" bonds in which the cation links with the anion and/or ligands may become shared through the formation of binuclear complex salts.

The number of hydrates known is far larger than is indicated above because many cation/anion combinations can form two or more stable crystalline structures that contain different stoichiometric proportions of H_2O molecules. Sometimes these appear as a sequence of dehydration intermediates containing progressively lower proportions of water as the original hydrate is dehydrated. $MgSO_4.xH_2O$ is dehydrated [6] from x = 7, through x = 6, 4, 2, 1 and finally yields the x = 0, anhydrous, salt. There is the additional intervention of $MgSO_4.2.5H_2O$ when a sufficient pressure of water vapour is present. The dehydration of $NiSO_4.7H_2O$ depends on reaction conditions, several hydrates are known [7], in which x = 7, 6, 4, 2 and 1 (also 0). In dehydrations that occur through a sequence of stepwise water losses, fundamental kinetic and mechanistic studies must regard each successive reaction as a distinct rate process to be investigated separately and individually.

Water is also accommodated in many metal salts of organic acids, such as formates, acetates, oxalates, tartrates, etc., hydrated to various extents. Also a number of organic acids form crystalline hydrates e.g. $(COOH)_2.2H_2O$. More important for practical applications are the organic compounds, including metal salts, that exhibit pharmaceutical activity. The stabilities of these compounds,

in which water may influence the lengths of time during which each may be stored safely (the "shelf-life"), are of great importance. Loss of water from such hydrates may be followed by deterioration, perhaps by breakdown of the active substance when dissolved in liquid water, if H_2O is a product and remains in contact with the drug.

The accommodation of water in crystalline hydrates as cation ligands means that this set of substances can be classified as coordination compounds. Mixed complexes containing H_2O together with other ligands are well-known. "The hydrates undoubtedly constitute the most completely studied group of coordination compounds" quoted from [2] (p. 494), with reference to thermal reactions. Reactions resulting in ligand loss are chemically similar to other decompositions of coordination compounds which are, therefore, identified as including some dehydrations. Ligand removal may be followed by bond redistributions between the remaining ligands and the anions, usually including recrystallization.

Crystalline solids that evolve water on heating do not always, or necessarily, contain molecular H_2O, but water may be formed through thermal reactions between crystal components before subsequent release. Compounds that react in this way include metal hydroxides and many naturally-occurring minerals, such as the layered aluminosilicates, some of which contain extended planar anions in the form of hydroxyl-group arrays, e. g., muscovite, biotite, etc. Solids containing both water and hydroxyl ions are also known, e.g. $Ba(OH)_2.8H_2O$, montmorillonite clays, etc. Though strictly outside the scope of the present title, brief accounts of significant features of these dehydrations are given in Section 4, below. This is appropriate because the controls and mechanisms of water evolution may be similar to, or share features with the dehydrations of crystalline hydrates.

The above compilation of types of hydrated salts shows that the total number of potential reactants available is much greater than is likely to be investigated in the forseeable future. In initiating research in this field, therefore, the challenge is to select reactants that can be expected to yield results of the greatest interest and value. Many of the early studies were concerned with a relatively limited group of hydrates, most of which have featured in several published reports [1,2], e.g. $CuSO_4.5H_2O$, alums, etc.: some of these almost attaining the status of "model" reactants. More recently there has been an increase in the range of hydrated salts for which dehydration investigations have been published. A selection, intended to be representative, is presented below in Section 3.

Water elimination from crystalline hydrates cannot be recognised as a single identifiable reaction type: several different chemical steps may contribute to the

overall change and these may vary with reactant. H_2O molecules are accommodated in crystals in diverse bonding situations within a range of strengths and stereochemistries. The elimination of H_2O from these various environments often requires extensive redistribution of the intracrystalline structural links between neighbours, commonly resulting in the generation of a different product phase, recrystallization. Comparisons of dehydrations, from reactants already containing molecular H_2O and from those in which water is the product of an intracrystalline reaction, e.g. from hydroxyl groups, can provide information of mechanistic significance. This can be useful in classifying reaction types and in the formulation of reaction mechanisms. It follows, therefore, that dehydrations cannot be regarded as a single set of equivalent rate processes because they exhibit no obvious common mechanistic or, indeed, any other identifiable chemical features. Nevertheless, throughout the literature it has generally been found expedient to discuss dehydrations together in this "grouping of convenience", known to encompass a range of diverse rate processes.

Two other chemical features of dehydrations are of wide application and should be considered during the analysis and the interpretation of experimental measurements.

Hydrolysis. There is always the possibility that, on heating, H_2O released from a lattice site within the hydrate may react with other components of the solid: hydrolysis. For example, only half of the constituent water in $MgCl_2.2H_2O$ is released unchanged [8], the other molecule reacts to form 2HCl and the residual product, MgO.

Dehydration as a precursor reaction. Water release is often a precursor step in the preparation of a reactant to be used in the study of the breakdown of other crystal components, perhaps as another solid state decomposition. For example, the initial dehydration is rapidly completed before anion reaction in nickel oxalate: $NiC_2O_4.2H_2O$ (the prepared reactant) $\rightarrow$ NiC_2O_4 $\rightarrow$ Ni + $2CO_2$ [9]. In discussing and interpreting observations for a subsequent rate process, it must be remembered that, during the precursor H_2O evolution, the originally prepared solid has almost certainly undergone extensive reorganization. This includes the possibility of crystal structure changes, particle sizes and textures, imperfection numbers and distributions, etc.

1.3. Theory of dehydrations [1,2]

1.3.1. Nucleation and growth of nuclei

Many dehydrations are initiated at, or very close to, a crystal surface, by the formation of a particle of solid product: this is termed *nucleation.* Subsequent

reaction then occurs preferentially within a thin zone in the immediate vicinity of the reactant-product contact: the *active interface*, that, through the continued and facilitated chemical change at the nucleus boundary, moves forward into the unreacted crystal, *growth*. These advances result in increases in the sizes of the product phase crystallite assemblages, *nucleus growth*. The chemically active interfacial zone, within which reactant is transformed into product, progresses without transporting material (resembling, in this particular respect, an energy wave). Bond redistributions at the active interface may result in some displacements of the constituent atoms, ions or molecules of the residue, often including a recrystallization. The maintained advance of interfaces throughout each nucleated reactant particle finally results in the completed reaction.

Kinetic and mechanistic investigations of reactions proceeding by this nucleation and growth (n+g) model require consideration of two complementary aspects of behaviour: reaction geometry and interface chemistry. In formulating mechanistic explanations for observations obtained for a particular reaction, the overall conclusions relating to both of these features must be reconciled. The expression used to describe rate characteristics for an identified reaction will be referred to here as the *kinetic model*. The term *mechanism*, as used throughout this review, refers to the sequence of chemical steps, bond redistributions, through which the reactant is converted to product. [This nomenclature is strongly preferred to the alternative practice of using *mechanism* to describe the rate equation that best fits the data. This represents an inconsistency with terminology accepted throughout other branches of chemistry.]

1.3.2. Reaction geometry

Initiation of reaction at a set of active surface sites and subsequent growth of nuclei, by reactions that result in interface advance into unreacted material, means that the progressive changes in relative rates of an isothermal process, as reactions advance, are determined by area variations during changes of the dispositions of contact zones within the reactant crystallites [1,2]. It is generally accepted that the overall reaction rate is directly proportional to the area of the active interfaces participating. Thus the kinetic characteristics can be related quantitatively to systematic changes of interface geometry. This representation of kinetic behaviour, and formulation of product yield - time expressions, differs fundamentally from the derivation of rate equations based on concentration terms, that is familiar from homogeneous kinetics.

The n+g reaction model has been found to apply to many dehydrations but is not the only possibility. A more general account of the derivations of this set of

rate equations, applicable to solid state decompositions, has been given in Volume 1 of this Handbook [1], the monograph [2] and also in several other reviews [10-12] and need not be repeated here.

Several rate laws for the nucleation step have been experimentally established. These can then be combined with the usually constant rate of nucleus growth by interface advance to give equations that express quantitatively the yield-time relationships for isothermal n+g rate processes. In all geometry-based equations, the growth term must include allowance for the number of dimensions in which the interface advances and the shapes of nuclei. These expressions are widely applied in the kinetic analyses of decompositions of solids and provide a unifying feature of the subject. The demonstration that the yield-time data measured for a particular dehydration is well-represented by one of these rate equations is often accepted as evidence that the reaction proceeds by the geometric model from which that rate equation was derived. Often such conclusions can (and, if possible, always should) be confirmed by microscopic examinations of reactant samples that have been decomposed to various extents, wherein the growth characteristics of the participating nuclei can be directly observed. Those rate equations, $g(\alpha) = kt$, that have found most widespread and useful applications in kinetic studies of dehydrations in the solid state are summarized in Table 1, together with the designatory labels that have been widely accepted [1,2,10-12] and are used in the text below.

It appears [13] that the first use of the term *nucleus*, in the sense now generally accepted, was by Cumming [14] in 1910 to describe observations for $CuSO_4.5H_2O$ dehydration. Subsequent studies of water evolution reactions have contributed to the development and applications of the n+g model. Because suitable reactant crystals can be prepared and these rate processes are relatively easily studied, work on dehydrations of crystalline hydrates continue to further understanding of reactivity controls and mechanisms of these interface reactions. Recent research has, however, shown that chemical changes are not necessarily [15] completed within a thin advancing interface, as assumed in the above theory, upon which the kinetic model derivations are based. Water elimination and product phase recrystallization do not necessarily always coincide in space and time [16]. Furthermore, an initial loss of water from all crystal surfaces can contribute to reaction, particularly in the early stages. For this, and other reasons [3,17], yield-time measurements during the initial stages of dehydrations are not necessarily consistent with the predictions from the geometric model microscopically observed.

Table 1.
Kinetic expressions used in solid state kinetic analysis [1,2,10-12]
(Symbols from Table 2 of reference [1] and used in the text below.)

SYMBOLS	EQUATION NAME	kt =
A2, A3 or A4	Avrami-Erofeev (n = 2, 3 or 4)	$[-\ln(1-\alpha)]^{1/n}$
B2	Prout-Tompkins	$\ln[\alpha/(1-\alpha)]$
R2 or R3	Contracting Geometry (n = 2 or 3)	$1 - (1 - \alpha)^{1/n}$
D1 or D3	Diffusion Control (1 or 3 dimensions)	α^2 or $[1 - (1 - \alpha)^{1/3}]^2$
F0, F1 or F2	Reaction Order (zero, first or second)	constant, $-\ln(1-\alpha)$ or $(1 - \alpha)^{-1}$

where k is the rate constant, t is time and α is the fractional reaction.

In addition to the n+g models described above, Table 1, (A2, A3 and A4, also B1), other reactions are known in which there is a fast and dense nucleation process, completed soon after establishing reaction conditions. This results in the early appearance of product across all crystal faces. The subsequent inward advance of these reaction interfaces leads to a predominantly deceleratory reaction through a contracting geometry model, represented by the R3 or R2 equations or possibly as a first order process, F1 [18]. For those reactants that possess a stable, coherent and durable structure, the removal of water may not be accompanied by recrystallization and rate can then be controlled by the diffusive migration of H_2O molecules outwards from the crystal bulk, across a product that effectively forms a permeable barrier layer (D1 or D3) [19].

1.3.3. Interface chemistry

Discussions of the chemical changes that proceed within a reaction interface must include consideration of the invariably endothermic character of dehydrations, which are also frequently reversible [3,20]. Both properties can markedly influence the rates of reaction experimentally measured of and this

influence must be recognized and incorporated in the kinetic analysis and data interpretation.

Characterization of the mechanisms and controls of chemical changes proceeding within a thin, intercrystalline active interface poses great experimental difficulties. The preferred occurrence of reactions within these advancing zones indicates that reactivity is locally increased, but the reasons for this enhancement are not generally understood. Little is known, at the molecular level, about the interphase (i.e. reactant-product) contact textures or about the bond transformations that participate in reactions of this type. The total amounts of essential intermediates present within a layer of transformation material or disorganized structure, that may be only a few molecules thick, must be small. Mechanical separation of reactant and product crystals may destroy the intermediates and/or damage the structures or textures of interest. There are further problems in characterizing and measuring participants where a solid product, possibly poorly crystallized, metallic and/or opaque, inhibits the collection of analytical data by optical or resonance techniques. Furthermore, the kinetic controls operating within these intercrystalline specialized zones may be different from those recognized as being applicable during encounters between individual molecules in gas or in liquid phase reactions. For example, species confined between two crystalline phases may undergo a (virtually) infinite number of repeated collisional/vibrational encounters because they cannot diffuse apart (a 'supercage' effect). Furthermore, ter- or tetramolecular interactions may be capable of effectively contributing to product formation because these occur within groups of immobilized reactants disposed in close proximity.

In characterizing the sequence of bond changes, through which the reactant is transformed into product, sensitive techniques are required to probe the reaction zone. For dehydrations this may not involve rupture of primary valence forces but require redistributions of hydrogen bonds and/or coordination links. Microscopy can give information about textures, but not at a molecular level, though Atomic Force Microscopy may be capable of contributing to progress here. Diffraction techniques, by which crystal structures are determined at a sequence of small volumes traversing a reaction interface, appears to be a promising, though not widely available, approach [15]. The detection of topotactic relationships, between contiguous reactant and product crystals, again probed by diffraction and/or spectral methods, gives information that is valuable in determining interface properties, through examination of the order that is preserved across the reaction zone. Both techniques present considerable difficulties when products are finely divided and crystal structures are imperfect.

As a consequence of these experimental problems, the information most frequently used in discussing the mechanisms of interface reactions is the magnitudes of the Arrhenius parameters, the activation energy, E_a and the preexponential factor, A. It is usually assumed that these parameters possess the same significance for solid state reactions as in homogeneous kinetics and are interpreted as providing a measure of the energy barrier to and the frequency of occurrence of a rate limiting step. Objections to this theoretical approach have been based on the different energy distribution functions that are applicable to reactant participants immobilized in a crystal, which differ from those having the freedom to move in a gas or a liquid. This fundamental problem has been presented [21] and need not be repeated here. More recent articles discuss the significances of Arrhenius parameters reported in the literature where apparent magnitudes vary with the calculation method used and kinetic model [22-24]. To record the minimum information required to characterize the reactivity of a particular rate process of interest, it is essential to report the *kinetic triad*, A, E_a and $g(\alpha) = kt$.

1.3.4. The Polanyi-Wigner equation and interface reaction mechanisms

The Polanyi-Wigner (P-W) equation [20,25] was derived through application of the absolute reaction rate theory to solid state dehydrations. In this approach the rate of water release was identified with the activation of a vibration frequency at the reaction interface. The value of A calculated [26] for $CuSO_4.5H_2O$ dehydration approximately agreed with expectation predicted by this theory (about 10^{13} s^{-1}). From the calculated agreement, and other comparisons, it was concluded [20] that for this, and many other dehydrations, the magnitude of E_a was close to the reaction enthalpy and A values were related to a vibration frequency. Reactions fitting both criteria were said to be 'normal' whereas those giving significantly larger values of both A and E_a were 'abnormal' [20]. This value-judgemental terminology is based on the premiss that the P-W model is applicable to all such reactions. This cannot, however, be accepted generally, remembering the uncertainties concerning the mechanisms of interface reactions, including controls and with the recognition of the many instances of the so-called abnormal behaviour [27]. The recent literature, however, contains fewer comparisons with P-W predictions, perhaps because this approach has not always been successful and has provided few insights into the mechanisms and controls of interface reactions. There are also problems in establishing whether the experimentally determined Arrhenius

parameters can be identified with the rate of the chemical step resulting in product release chemical step: this point is discussed in greater detail below [22-24].

At least the first, and possibly all three, of the following types of chemical change participate in each dehydration reaction. (i) Water must be released by the breaking of hydrogen bonds within the reactant structure and/or the dissociation of a metal-OH_2 coordination link. (ii) Water must leave the reactant phase. This may occur immediately, if the liberated H_2O molecule is generated at a surface, perhaps in the vicinity of a crack, or release may be delayed during diffusive migration from the crystal bulk to a site from which desorption possible. Readsorption onto and/or reabsorbtion into the residual solid may occur if escape is impeded. (iii) The dehydrated, residual solid product(s), perhaps finely divided or zeolitic, may (or may not) recrystallize to form a different lattice structure.

It is possible that all three processes may occur concurrently within a monomolecular layer: this is one view of the P-W model. However, dehydrations of a number of solids do not involve a recrystallization step. Moreover, there is strong evidence [15,16,28] that in some other reactions the water elimination step, (i) above, and the structural reorganization, (iii), may be separated in space and time. Interface processes are more complicated than was accepted until recently and probably vary between different reactants.

The chemical processes initiating the earliest steps of dehydration (nucleation) may differ from those occurring subsequently within an advancing interface. Product formation may be difficult [2,10-12] within the reactant phase (germ nuclei) but becomes easier after the crystalline product has been formed.

1.3.5. The physical model for crystolysis reactions

Recognizing the theoretical limitations in applying the Arrhenius equation to explain the mechanisms of crystolysis reactions, L'vov developed an alternative physical model. This accounts for the exponential dependence on temperature of reaction rates through theory originally proposed by Hertz and by Langmuir.

The relevant background sources and the general applications of this approach to crystolysis reactions are given in [29]; the article of particular relevance to dehydrations is [30]. The uncertainties that exist in this subject, concerning identification of the chemical controls and factors that determine mechanisms of solid state dehydrations and, indeed, other crystolysis reactions, requires the fundamental consideration of alternative representations of all characteristics of these rate processes. The articles cited [29,30] apply classical models in a

novel perspective that has already been successful in identifying hitherto unrecognized patterns of reactivity and offers interesting prospects for future progress.

1.4. Dehydrations as endothermic and reversible reactions

1.4.1. Self-cooling

The effects of self-cooling of a reactant, reducing its temperature below that of the surroundings (and the value measured) due to the endothermic evolution of water, were incorporated into the data analysis in many of the early dehydration studies. More recent reports have, however, often placed less, or no, emphasis on this influence in rate control. Watelle and her co-workers [31] have made important contributions towards recognizing and understanding the influence on reaction rates of reactant cooling in the vicinity of the active interface. Other recent articles [30,32] discuss the significance of self-cooling on dehydrations and may reawaken perception of this often apparently ignored, or even forgotten, aspect of these, and indeed other, endothermic rate processes.

1.4.2. Reversibility

The magnitudes of the influences of product availability, represented as the prevailing water vapour pressure, $p(H_2O)$, in the immediate environment of the reaction on the (forward, measured) overall dissociation rates of reversible dehydrations are not always known. The contribution from the reverse, 'back', water uptake reaction, may have been seriously underestimated in many published kinetic studies. Furthermore, it is not known which, or how many, dehydrations are rate-sensitive to $p(H_2O)$ or the magnitudes of such effects.

Large kinetic influences, resulting from the presence of water, on the apparent measured magnitude of E_a for $NiC_2O_4.2H_2O$ dehydration were demonstrated by Flanagan et al. [33]. Their experimental technique was carefully designed to minimize $p(H_2O)$ within the reaction zone. Rates of water release were determined at low pressures during maintained product H_2O evacuation from small (always less than 3 mg) samples of fine, spread reactant between 358 to 397 K. Rates measured for a range of reactant masses, down to 0.2 mg, were extrapolated to zero mass to eliminate the influence of evolved water on reaction rates. From these data the calculated value of E_a was 130 kJ mol^{-1}. This is substantially greater than several of the values previously reported, and also the magnitude of A does not agree with predictions of the P-W equation: this is an 'abnormal' reaction [20]. It is significant that the dehydration rates at very low pressures were three orders of magnitude greater (x 10^3) than those estimated from previous higher temperature studies in air or N_2, which impede

the H_2O removal. Furthermore, the dehydration rate was substantially reduced (x 0.04 at 383 K), in the presence of the small $p(H_2O)$ = 5 Pa.

This is a most important result, that seems not to have gained the acceptance and recognition that it deserves. While there is the possibility that this particular dehydration could be atypical, this has not been demonstrated. There remains the worrying probability that this behaviour pattern, a strong dependence of the dehydration rate on $p(H_2O)$, could be widespread or even general. Perhaps surprisingly, little further effort appears to have been directed towards extending and/or establishing the generality of this work. Until similar observations for a representative selection of dehydrations become available, doubts must remain about the significance to be attached to the magnitudes of reported kinetic results (A, E_a and the rate equation, $g(\alpha) = kt$,) measured under conditions in which the reverse process is capable of contributing to an unknown extent. This remains an important and unresolved uncertainty in kinetic and mechanistic investigations of dehydrations.

Comparable uncertainties arise in rate measurements for other reversible (and endothermic) dissociations and a discussion, that may be equally applicable to dehydrations, has been given for $CaCO_3$ decomposition [34]. Again the value of E_a measured for the very low pressure reaction was significantly greater than the magnitudes measured for dissociation in the presence of some CO_2 or an inert gas that inhibits product CO_2 escape. Kinetic characteristics for this reaction vary with the procedural variables [35] [$p(CO_2)$, particle sizes, etc.] and compensation effects [36,37] have been found between $\ln A$ and E_a values for $CaCO_3$ decompositions under different prevailing conditions. These patterns of kinetic behaviour are mentioned here to emphasize the necessity to investigate the magnitudes and roles of *all* rate controls that participate in determining the kinetic characteristics of reversible reactions. It cannot be assumed, without suitable confirmatory (kinetic) evidence that measured magnitudes of A and E_a values relate directly to an interface step of the type envisaged in the transition state theory [34]. It is important, therefore, that dehydration rate studies should establish experimentally whether (i) the reaction is reversible and (ii) rates are sensitive to changes in prevailing reaction conditions, particularly $p(H_2O)$. Reaction conditions must always be comprehensively defined and reported.

1.4.3. Smith-Topley (S-T) behaviour

Many hydrates exhibit the characteristic S-T pattern of (isothermal) changes of dehydration rates with $p(H_2O)$ shown in Figure 1. In vacuum, the rate of water loss is fast. With an increase in $p(H_2O)$, the dehydration rate is rapidly

reduced to a minimum value, after which the rate rises, usually more slowly, to a maximum value. Finally, dehydration rates decrease in the approach to the equilibrium dissociation pressure. Garner [20] explained this behaviour pattern by suggesting that there is retention of adsorbed water on product surfaces at low $p(H_2O)$, which opposes escape through the fine channels in the largely unreorganized (perhaps zeolitic) product solid. At higher $p(H_2O)$ values, there is promotion of structural changes (recrystallization) in the residual material by retained water, which facilitates volatile product escape through the wider channels.

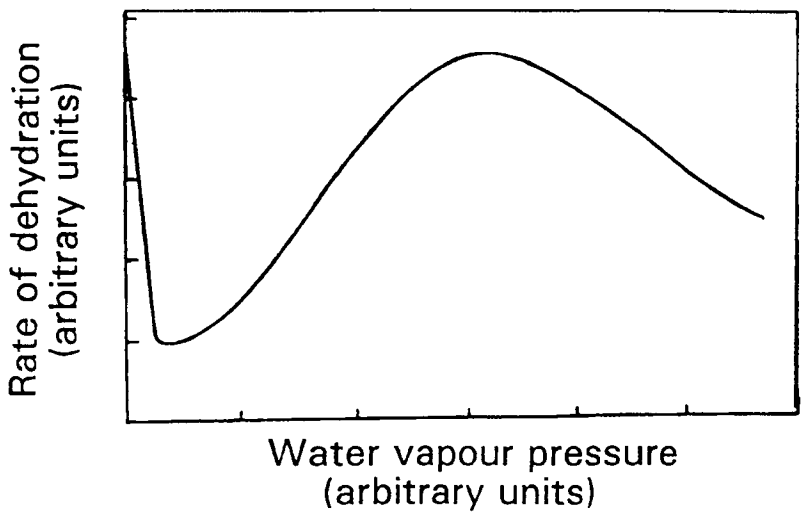


Figure 1. Schematic representation of the Smith-Topley effect ([12], p.125ff and [2], p. 224ff): the variation in rate of a reversible reaction (usually dehydration of a crystalline hydrate) with prevailing pressure of the volatile product [water vapour, $p(H_2O)$]. Reproduced from [1].

Bertrand et al. [31] made detailed comparative and quantitative examinations of the S-T behaviour exhibited by the dehydrations of a group of five selected reactants: $Li_2SO_4.H_2O$, $MgSO_4.4H_2O$, $CuSO_4.5H_2O$, $CuSO_4.3H_2O$ and $Na_2B_4O_5(OH)_4.8H_2O$. They believed that a reappraisal of previous explanations of S-T behaviour had become necessary. It was regarded as significant that the characteristic trends in S-T curves showed closely similar shapes for these chemically distinct reactants. The so-called abnormal dehydration rate decrease occurred within well-defined relative ranges of $p(H_2O)$ - temperature values. In addition, it was demonstrated [31] that a

comparable S-T type effect occurred during liquid evaporation. It was concluded, therefore, that the transfer of heat (reactant temperature) and the movements of product gas (H_2O) are interrelated. It follows that the S-T pattern (Figure 1) arises because thermal equilibrium is not maintained within the reaction interface during a heterogeneous, endothermic rate process. The patterns of reaction rate changes observed are a direct consequence of the development of irreversible conditions at the interface, where temperature and chemical potential distortions are coupled. It was further concluded [31] for endothermic decompositions that the apparent magnitude of E_a varies with departure from equilibrium and the presence of a thermal gradient.

Subsequently, L'vov pointed out [32] that the above study "did not receive much recognition". In a computer simulation of the layer-to-layer distribution of temperature and dehydration rate as functions of $p(H_2O)$ for $Li_2SO_4.H_2O$ dehydration, a substantial self-cooling of the sample was demonstrated [32]. This treatment accounts for the main features of the S-T effect.

Comment. It follows from the above results and discussion that it is *always* necessary in kinetic studies of a dehydration to define the prevailing atmosphere, including any inert gases that inhibit H_2O escape and to determine the sensitivity of reaction rates to the experimental conditions (reactant mass, particle sizes, etc.) [31-35]. At present such information is not invariably provided: a comment that applies equally to many of the papers cited in this review.

1.5. The literature of dehydration reactions

1.5.1. The scope of the literature

There is an extensive literature concerned with the dehydrations of crystalline hydrates. More original research articles continue to appear in this field and the total number that could be classified under the present Chapter heading is estimated to be more than one thousand. (A comprehensive citation list is expected to be longer than this review). A literature search and contents appraisal [38], for articles dated 1981, identified 34 directly concerned with dehydrations and about 100 discussed reactions involving water loss and/or other reactions of crystalline hydrates. More recently, the single journal, *Thermochimica Acta,* published more than 30 articles on dehydrations, bearing the dates 1994 or 1995. However, there have been remarkably few general reviews of this wealth of primary information. Potential reviewers may well be discouraged by the total number of articles to be considered in any comprehensive survey, the difficulties of locating them and the lack of any classification scheme or criteria for introducing order into the research material.

A book, enormously influential in developing the recognition of decompositions of solids (including dehydrations) as a distinctive subject area, or even as a discipline, was *Chemistry of the Solid State,* edited by W.E. Garner and published in 1955 [39]. This work contributed to the theory and identified behaviour patterns for diverse reactions of solids. Garner, in his own review articles, classified solid state decompositions as endothermic (Chapter 8, in which more than half is concerned with dehydrations [20]) or exothermic (Chapter 9). These are one of the few criteria that have been used to classify this subject. Chapter 8 [20] presents an account of the n+g reaction model, including excellent photomicrographs, together with consideration of the significance of the Arrhenius parameters. Chapter 7, by Jacobs and Tompkins [10], provides formal and detailed derivations of the geometry-based rate expressions, some of the kinetic models that remain generally used in the interpretation of rate data in thermal analysis. This book remains a classic contribution in the development of solid state chemistry, and which still retains importance as a literature source.

A selected set of dehydrations, mostly inorganic, were discussed individually by Young [11] with particular reference to the roles of the product phases in these reactions. Dehydrations form an important part of an account of solid state reactions by Brown et al. [12] (see also [1,2,40]). Makatun and Shchegrov [41] review the structures of water in hydrated salts and consider the steps that participate in its elimination. Lyakhov and Boldyrev [42] review kinetic, theoretical and mechanistic aspects of solid dehydrations, including the roles of self-cooling, atmosphere including $p(H_2O)$, impedance of H_2O escape by residual products and the formation of labile or liquid intermediates. Hydrates are included in an account of thermal analysis and the kinetics of solid state reactions by Tanaka [43].

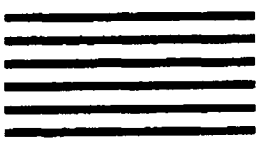
Further comparative discussions of often limited groups of dehydrations are to be found in the literature. However, the subject lacks recent, authoritative, comprehensive and critically comparative reviews from which trends of behaviour might be discerned that could be used to classify reaction characteristics. In this absence of criteria that can be used as a basis for the systematic ordering of the information available, results for each salt must be presented individually. Consequently, there is no perspective to enable relationships with other dehydrations to be identified. This absence of any general theory of reactivity must be regarded as a factor that tends to retard the advance of the subject, see, however, [29].

1.5.2. Classification of Dehydrations

The superficial appearance of similarities in the removal of H_2O molecules from diverse hydrates suggests that these reactions might be considered as a group. Within this set of apparently related rate processes, it is possible that common features and/or trends may be identified leading to insights into the controls of reactivity and factors determining reaction mechanisms. Such advances would be particularly valuable in encouraging development of theory possibly applicable to a much wider range of crystolysis reactions. Progress in this direction has, however, been slow.

Although some dehydrations are correctly regarded as a sub-set of decompositions of complex salts, reactions involving water loss from hydrates are often presented together as a group, e.g., [2,11,12]. Garner, in 1955 [20], compared kinetic results from a selected, but limited, set of dehydrations for which careful rate measurements were then available. Continued studies have now resulted in the accumulation of kinetic data for an ever widening range of hydrates. In the absence of a theoretical framework for the subject, many of these appear as individual reports, unrelated to each other and not contributing to the organic growth of the subject. To address this problem of order, the present author proposed a classification scheme [3], to distinguish different reaction types, based on the varied textural properties of the reaction interface. The original paper presents the criteria in detail, including discussions of many specific reactions, with appropriate examples cited. Here only brief descriptions of the six main differentiated reaction types (Water Evolution Types: WET, 1-6) are given.

WET 1: Crystal structure unchanged by dehydration



Kinetic rate controls: Intracrystalline diffusion or desorption. No geometric factor.

Examples: Dehydrations of zeolites, $UO_2(NO_3)_2.6H_2O$.

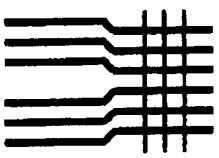
WET 2: Topotactic reaction, dehydration results in reduction of crystal spacing but without cracking



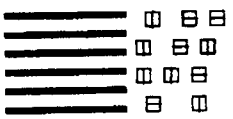
Kinetic rate controls: Diffusion and (sometimes) (without geometric factor.
Examples: Dehydrations of vermiculite, muscovite, illite, etc.

WET 3: Interface reaction in which a crystalline product may, or may not, be topotactically related to the reactant structure but cracking ensures release of water at the advancing interface. Alternatively, the immediate product may not recrystallize, or only form crystalline products after a delay, perhaps in a zone remote from the active, advancing reaction interface. These are the most frequently encountered dehydration mechanisms, for crystalline hydrates.

Kinetic rate controls: Interface reactions and geometric rate controls (not diffusion).
Examples: Dehydrations of $Li_2SO_4.H_2O$, $CuSO_4.5H_2O$, alums and many others.



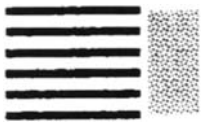
Topotactic reaction with cracking



Product recrystallization



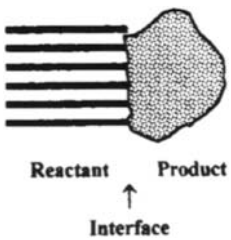
Product crystallization delayed



Product does not crystallize

WET 4: Homogeneous intracrystalline dehydration.
Kinetic rate controls: Varies with reaction.
Examples: Dehydrations of colemanite (explosive), barium hydrogen oxalate hydrate, $Ca(OH)_2$.

WET 5: Water loss is accompanied by melting and the formation of impervious layers.



Kinetic rate controls: Little is known about reactions in which solid and melt both contribute.
Examples: 2-Aminopyrimidium $[CuCl_3(H_2O)]$, trehalose dihydrate.

WET 6: Dehydration of a completely melted reactant.
Kinetic rate controls: Not adequately investigated, but presumably proceeds as a homogeneous reaction or by evaporation from liquid surface.
Examples: Lithium potassium tartrate hydrates.

Cited sources, with discussions, are given in [3]. In addition a number of dehydrations are accompanied by secondary reactions (perhaps influenced by reaction conditions) and some include hydrolysis.

Crystolysis. The author believes that the use of an agreed specific index term (key-word, topic label, etc.) would be an invaluable aid towards reducing the labour of literature searches by providing an unambiguous route towards locating articles concerned with solid state decompositions. The extent of this subject area is well-known to its practitioners but the relevant publications are not always easily or comprehensively located by the usual search methods. The words 'dehydration', 'decomposition' and 'solid' do not appear in the titles of many articles cited here and such labels are highly non-specific. Accordingly, it is recommended that the term *crystolysis* is always used to label specifically and exclusively all decompositions (including dehydrations) that proceed in *solid* reactants [2,38]. This terminology could also encourage researchers to establish unambiguously, and to state definitely, whether the reaction of interest proceeds in the solid state or if melt formation is a significant feature of the mechanism.

1.6. The present review

The title of this Handbook, 'Thermal Analysis', has been interpreted widely here, for dehydrations, to consider all thermoanalytical research directed towards increasing understanding of the mechanisms and controls of the chemical changes that occur on heating crystalline hydrates. However, for reactions of solids generally, apart from [3], there has been little recent progress towards establishing criteria and providing theories that are useful in classifying observed reactivity patterns. Consequently, few common features have been found, so that references to [3], WET 1-6, are used as a basis for the systematic presentation of results. Other generalizations are the concept of the reaction interface and the set of characteristic kinetic models used in rate analyses, Table 1 and [1,2] do not provide suitable criteria for the classification of behaviours observed. The representative dehydrations described below have been selected to illustrate both diversity, through the range of different reaction types that have been recognized, and progress, by accounts of the reactions for which mechanisms have been investigated in greatest detail. Because different workers have used alternative experimental methods and reaction conditions, and have focussed attention on diverse aspects of these chemical changes, overall coverage of the different types of known hydrates tends to be uneven.

On heating, many highly hydrated compounds apparently melt with dissolution of the hydrophilic salt in the liquid H_2O liberated on disintegration of the crystal structure. For example, for several alums ($M^+M^{3+}(SO_4)_2.12H_2O$) melting points are listed, together with the number of water molecules lost when a lower hydrate is formed. The changes occurring, water loss and/or melting, depends on the conditions prevailing. In a vacuum, water product is immediately vaporized and such reactions appear as typical nucleation and growth processes. (It is believed, however, that water temporarily retained in alum growth nuclei [44] participates in the reaction by promoting product phase recrystallization). In contrast, on heating large reactant samples under conditions that prevent or restrict escape of the H_2O released, there may be salt melting/dissolution, perhaps followed by the crystallization of a lower hydrate, if the solvent can escape only slowly. A variety of types of intermediate behaviour are possible, including the development of inhomogeneities, such as local melting, or of high (and possibly locally inhomogeneous) $p(H_2O)$ values within the fine powder aggregates of reactant crystallites. There is also the ability of even small values of $p(H_2O)$ to influence significantly the rates of a least some dehydrations (e.g., [33]). Other types of behaviour include the completion of melting before dehydration, see [45,46]. This type of rate process (water loss from a liquid/melt containing no added solvent) has been the subject of only a small number of detailed kinetic studies and such behaviour will not be emphasized here. However, the possibility of the intervention of a liquid phase must not be forgotten in interpreting thermal reactions of hydrates, particularly where the sample is large, in a closed or confined container and/or the presence of air or other inert gas that restricts H_2O escape.

Representative dehydrations selected for mention below are intended to include some of the most detailed and reliable kinetic and mechanistic investigations in which the contributions from the reverse process (water uptake) are minimized. However, this has not always been demonstrated for the examples described. Comprehensive topic coverage within an account of reasonable length is not practicable. The reports cited here and in [3] are intended to provide insights into reaction chemistry for a range of diverse dehydrations. Identifications of the bond changes that control the rate of water release from a particular reactant are often not known with certainty and usually must be inferred from indirect evidence. The sensitivity of kinetic properties to prevailing conditions is sometimes unexpectedly large, a point not always readily apparent for this set of rate processes that superficially appear to be so straightforward. For this reason it is essential that useful reported observations should mention reaction conditions in detail and should include a positive

investigation of whether kinetic data are influenced by the procedural variables [35]. Dehydrations are invariably endothermic and are frequently reversible [20]. Consequently rates are often influenced by diffusion of heat and/or water (see the S-T effect above and [31,32]) resulting from the non-equilibrium conditions that may be developed within the reaction interface.

1.7. Calorimetry

The wide use of thermoanalytical methods that measure enthalpy changes during the progress of reaction, most notably DTA and DSC, has increased the accuracy and convenience of obtaining calorimetric data during dehydrations (and, indeed, other reactions). However, this opportunity has not been widely exploited and, with occasional exceptions [47,48], the measurement and interpretations of enthalpy change measurements have predominantly been directed towards the characterization of kinetic behaviour. This is an unfortunate limitation because there are uncertainties in the methods of interpretation and analysis of rate data [23,24], which do not apply in the determination of calorimetric values. Moreover, the two approaches can be complementary in describing the chemical change of interest.

A particular application of calorimetry in the study of dehydrations has been through determinations of entropy of recrystallization of primary product of dehydration. Residual phases formed by water removal in vacuum may be disorganized and finely divided and the enthalpy change resulting from structural reorganization may give information about the texture and crystal properties of the material constituting the product side of the active reaction interface. Reports of some such studies from the older literature are cited by Young [49], including the work by G. B. Frost.

2. EXPERIMENTAL

2.1. General

Thermoanalytical and kinetic investigations of crystalline hydrates, for reactants that have not previously been studied, are conveniently commenced by non-isothermal measurements to determine the sequences of reactions and temperature interval in which each change occurs. Thermoanalytical measurements are particularly valuable in the detection of stepwise sequences of water losses [6] and (using enthalpy measurements) also phase changes, including melting. It is particularly important to demonstrate that any reaction for which kinetic data are to be obtained refers to a only *single* rate process. Overlapping rate processes should not be treated as a pseudo-single reaction in

kinetic analysis. The conclusions from such an interpretation are meaningless and misleading. The present account mentions briefly the thermoanalytical methods, with which this Handbook is primarily concerned, that are frequently used to study reaction kinetics. Further information can be found in Volume 1, *Principles and Practice* [50] and [51] and also about other experimental techniques, some of which have been useful in elucidating dehydration chemistry.

2.2. Reaction stoichiometry

Studies of crystolysis reactions should include confirmation of both the composition and the structure of the original reactant and of the final product. The stoichiometry of each chemical process of interest should be characterized fully. Assumptions based on limited analytical evidence (e.g. only a mass loss) can be unreliable and diminish the value of results. The possibility that there are concurrent or secondary processes, involving the participation of species other than water, and including hydrolysis [8], always requires adequate investigation.

2.3. Reaction kinetics

2.3.1. Introduction

Kinetic data may be obtained from measurements of the changes with time [at known temperature(s)] of any parameter that can be quantitatively related to the extent of a particular dehydration step (usually expressed as the fractional reaction, α, Table 1 and [1,2]). The parameters used most frequently include mass loss, $p(H_2O)$ evolved (see, however, [52]) and heat absorbed. The geometric form of the interface advance process, deduced from kinetic data, is often interpreted with support from microscopic observations, that can additionally give information about the individual rates of the nucleation and of the growth processes. Information about the structural characteristics of interface phenomena can be obtained from diffraction measurements [15], particularly where there is topotaxy [53-55]. The greatest insights into the controls and mechanisms of solid state reactions are made through the imaginative and complementary use of several different experimental techniques.

Kinetic data can be obtained both from measurements during which the reactant temperature is held constant or is varied according to a prespecified programme, most usually a constant rate of increase. The principles used to analyse such sets of measured (temperature, time, α) values are to be found in many publications (such as [1,2,12,51]) and need not be repeated here. To

specify adequately the results of a kinetic study, including reactivity, it is necessary to report both Arrhenius parameters and the kinetic model [A, E_a and $g(\alpha) = kt$].

It has been concluded [56] that the most accurate values of A and E_a are obtained from isothermal measurements whereas the kinetic model is more reliably deduced from rising temperature experiments. Kinetic analyses of non-isothermal data have traditionally relied on approximations [23,24] that simplify the intractable integrations of combinations of kinetic model and Arrhenius equations. It is now possible, however, as Flynn [57] has pointed out, to avoid the use of imprecise approximations for the temperature integrals because values can be calculated to accuracies that can be as precise as we wish them to be.

2.3.2. Thermogravimetry (TG and DTG)

Mass-loss measurements have been widely used in kinetic studies of dehydrations, both under isothermal and rising temperature conditions [51,58,59]. An important experimental consideration is that dehydrations can be completed either in a vacuum maintained throughout [33,59,60], or at a selected constant $p(H_2O)$ value [31,61]. Combinations of TG and DSC have also been used successfully [62]. This method cannot detect changes that do not involve a mass-loss/gain, e.g., there is no response on reactant melting.

2.3.3. Evolved gas pressure measurements

Isothermal dehydration kinetics have been measured by changes in the evolved $p(H_2O)$ with time in a constant volume apparatus, e.g. for alums [17] and for $Li_2SO_4.H_2O$ [18]. Rates of alum dehydrations appeared to be largely independent of $p(H_2O)$ below about 0.3 p_e (the equilibrium dissociation pressure) and above this value became proportional to $[p_e - p(H_2O)]$ [17]. Final values of $p(H_2O)$ from such reactions were proportional to the H_2O yield, though there may be significant adsorption on the walls of a glass apparatus [52].

2.3.4. Differential scanning calorimetry (DSC)

This experimental technique is based on the assumption that the rate of heat absorption during an endothermic rate process is directly proportional to the rate of chemical change. This requirement for kinetic measurements is not always confirmed. From determinations of the amount of heat required to maintain the sample at a constant, or at a programmed (usually rising) temperature, the kinetic characteristics of the reaction can be measured [50,51].

In DSC, the heat required to eliminate any temperature difference between the sample and a similarly heated inert standard is used to measure the reaction rate. A problem in the application of this technique to endothermic reactions, including dehydrations, is that, at low pressures, temperature inhomogeneities (including self-cooling) are developed within reactants that are poor heat conductors. The presence of a gas will increase thermal conductivity but may also influence observed kinetic behaviour by impeding H_2O escape. DSC combined with TG can be used to extend the information available, for example, there is the ability to discriminate between free and bound water in solids [63]. It may be more difficult to differentiate between water of crystallization and water absorbed within either a zeolite or a clathrate system.

2.4. Diffraction

A powerful, but not widely available, experimental method, capable of investigating intracrystalline changes during reactions, is through the use of diffraction data obtained from short but powerful bursts of synchrotron radiation [15]. Structure changes in the vicinity of the reaction interface can be detected from measurements of lattice spacings in small reactant volumes at a serial sequence of sites that traverse the active reactant-product interface. Observations for $Li_2SO_4.H_2O$ dehydration have shown that here the thickness of the reaction zone was about 150 μm.

X-ray, or other diffraction measurements, can be used to confirm the structure of an original reactant and to identify the phases present in the residual products [64]. Measurements may be made at reaction temperature to avoid the possibility that further phase changes had occurred during sample cooling [65].

This technique can also be used to detect topotactic relationships between reactants and products [53-55]. Such information, including the number of dimensions in which structural features are conserved [53,54], is useful in the formulation of reaction mechanisms and interface properties.

2.5. Microscopy

Direct observations of the visible textural changes that accompany dehydration were originally used [13,20,66] to establish the geometric principles that are the foundation for the kinetic models widely employed in the rate analyses of crystolysis reactions [1,2,10-12]. Garner [20] profitably exploited observations from the optical microscope in the development of the nucleation and growth reaction model. This experimental approach still maintains its importance in confirming interpretations of kinetic data, although

it is not always applied. Direct inspection, together with measurements of textural modifications for partially reacted surfaces, are effectively the most satisfactory methods for obtaining the fundamental kinetic data: nucleation rates, dispositions and shapes of nuclei, rates of interface advance, etc. Microscopy has also recognized the occurrence of surface retexturing ('orange peel') developed on exposure of partially dehydrated material to water vapour [44,67].

Scanning electron microscopy provides much higher magnifications and, therefore, reveals greater textural detail and perspectives. However, this technique can only be directly applied to reactants that are sufficiently stable to withstand the heating by the electron beam in the vacuum chamber. For some reactants these problems can be circumvented by the preparation of replicas [68] that retain textural features of surfaces, crack structures and can even enable interfacial sections to be viewed [69]. Transmission electron microscopy [70] is generally of less value in the examination of most solids.

Atomic force microscopy, operating under conditions that impose relatively little stress on the sample, may be capable of revealing reaction zone structures in greater detail than has been possible hitherto. The potential value of this instrument in crystolysis studies has yet to be demonstrated and explored.

Specimens for microscopic examinations are often cooled following a thermal reaction but before examination. The effects of temperature change, including possible recrystallization and the solidification of any melted constituents, must be considered in the interpretation of the textures observed.

2.6. Comment

The above paragraphs provide only the briefest outline to some of the principal techniques that are usually used to study dehydrations, see [1,51]. More detailed information is given in many of the references cited, including experimental modifications that may be required in investigations of particular reactants or specific aspects of these reactions. Many specialized methods have been employed, often in combination with those mentioned above, including spectra (which can provide information about bonding and/or constituents present), surface area (textural properties), evolved gas analysis (mass spectrometry, glc, etc.), photoacoustic spectra (hydration in superficial layers [17]) and others.

Through the exploitation of the highly automated data collection and analysis (TG, DSC, etc.) instruments, now available, some recent articles report the fit of α-time data to each of a list of rate equations, together with calculated apparent values of A and E_a (which show surprisingly large ranges of variation).

This approach measures only the effective level of reactivity for the selected reactant. In the absence of confirming and complementary observations, that were so much a part of earlier work, such 'kinetic-analysis-only' studies contribute little towards increasing our understanding of the detailed chemistry, controls or mechanisms of dehydrations [23,24].

3. DEHYDRATIONS OF CRYSTALLINE HYDRATES

3.1. General

In these short accounts of representative dehydrations some E_a values have been averaged and magnitudes are given to accuracies of ±1 kJ mol^{-1}. This is probably better than that which can be achieved in reproducibility studies. Similarly some reaction temperature ranges have been averaged and values are reported to ±1 K. Under some of the substance headings below, selected related reactions are mentioned to extend subject coverage.

Loss of constituent water from a crystalline hydrate, the primary interest in this survey, usually occurs at an advancing active interface, from which the H_2O product is directly volatilized. Such dehydrations have been classified [3] as WET 3 and are so assigned in the treatment below unless otherwise described. For some reported reactions, there is insufficient information available to enable the mechanism or the interface texture to be adequately characterized.

The reaction model, WET 3 (etc.) was originally derived from an earlier set of distinctions of nucleus functions based on observed variations of product textures, proposed for crystolysis reactions generally, in which two types [71] referred to dehydrations: *Flux-fluid nuclei,* proposed for alums [44,71] and *Flux-filigree nuclei,* for lithium sulfate monohydrate [71,72]. The recent review [73] by Koga and Tanaka: 'A physico-geometric approach to the kinetics of solid state reactions as exemplified by the thermal dehydration and decompositions of solids' provides a most valuable and up-to-date survey of the literature. The current relationships of observations on interface development, functions and textures (microscopic examinations) with kinetic developments is surveyed with authority and discernment. The current achievements of the title subject are admirably summarized and unresolved problems described, much theory that is relevant to the present account is included in this significant publication.

3.2. Lithium sulfate monohydrate

$Li_2SO_4.H_2O$ is dehydrated in a single endothermic step. Kinetic measurements are usually completed between 340 and 400 K [18] and rates are influenced by reaction conditions, including particle size, $p(H_2O)$, etc., attributable to (at least partial) reversibility. Measured α-time data fit the R2, R3 and F1 equations. Reported magnitudes of E_a vary mainly between 60 to 120 kJ mol^{-1} with $\ln(A/s)$ between 10 to 30 (together with a few higher values) in which a compensation effect was found [18,36]. Although there have been several kinetic studies of this reaction, the high vacuum conditions required to eliminate the water reuptake process [33] have rarely been applied. However, one such study [74], using the quartz crystal microbalance in a good vacuum (about 10^{-4}Pa), measured the constant rate of H_2O evolution from single crystals at low α between 333 to 363 K. It appears from the rates reported that E_a was 106 kJ mol^{-1}.

A proposal [75] to use the dehydration of $Li_2SO_4.H_2O$ as a standard reaction, enabling quantitative comparisons to be made between kinetic results measured by different laboratories, remains uncompleted. This reactant was initially regarded as suitable because both reactant and reaction are well-defined, can be easily prepared and studied, dehydration proceeds at a low temperature, etc. However, it later became apparent that the kinetic results reported by different workers, and those obtained by different techniques, were inconsistent and irreproducible. Nevertheless, the initiative may have been responsible for several published kinetic studies, e.g., [18].

For this reaction Boldyrev et al. [15] demonstrated the value of using diffraction methods to elucidate mechanisms. It was shown that dehydration was not completed within a monomolecular interface layer but that there was a systematic change in water concentration across a layer of about 150 μm thickness.

An interesting comparison of reaction mechanisms was made [76] between the dehydrations of $Li_2SO_4.H_2O$ and of $HCOOLi.H_2O$. Although both reactants contain equivalent H_2O sublattices, the dehydrations show significant differences, values of E_a for the reactions of the sulfate and the formate being 87 and 146 kJ mol^{-1}, respectively. Diffraction data, again using synchrotron radiation, showed that both reactions proceeded with the intervention of a metastable intermediate phase. For $Li_2SO_4.H_2O$ the crystallographic differences were small. In contrast, marked structural modifications were found between the $HCOOLi.H_2O$ reactant, the metastable intermediate and the anhydrous product phase, in which the second transformation was slow. The

important conclusion is that the kinetic characteristics of reactions proceeding in a crystal may be controlled by structural reorganizations.

Tanaka and Koga have reported several studies of $Li_2SO_4.H_2O$ dehydration [72,77]. Microscopic examinations of cleaved sections of partly reacted crystals showed that dehydration was initiated by rapid and dense surface nucleation at, or near, the crystal surface. This was followed by the early establishment of a coherent well-defined interface, covering all original surfaces, that thereafter progressed inwards. This is consistent with the isothermal yield-time kinetic measurements where, following a brief early acceleratory stage, the overall reaction is predominantly deceleratory. Measured sets of α-time data initially fitted the A2 and A3 equations. However, the greater proportion of the reaction was most satisfactorily represented by the deceleratory R2 and R3 expressions. Reported magnitudes of E_a depended on reaction conditions and were usually between 80 and 130 kJ mol^{-1}.

Huang and Gallagher [78] compared the dehydrations of crystal, powder and pellet forms of $Li_2SO_4.H_2O$ using rising temperature TG and DSC in N_2, dry or with water vapour. The TG observations showed that the presence of H_2O influenced reaction rates, particularly for powders at low α, ascribed to diffusion effects. Arrhenius parameters measured by the two alternative experimental methods were of similar magnitudes and values of E_a were little changed by the presence of H_2O. Apparent values of E_a diminished with increase in α and there was compensation behaviour.

Further comparative kinetic studies, based on measurements of $p(H_2O)$, TG and DSC were reported by Brown et al. [18], who also found a compensation effect. In agreement with previous work, there was evidence of initial rapid and dense nucleation across all crystal faces. Thereafter, the reaction was predominantly deceleratory during the inwards advance of interfaces. However, no agreed magnitude of E_a, characteristic of this reaction, was identified from these data and the best estimate was 'probably between 80 and 100 kJ mol^{-1}'. This uncertainty is ascribed to a dependence of rate on prevailing conditions, thus confirming the difficulties of using this salt as a kinetic standard [75].

In a comprehensive survey of kinetic parameters published for this dehydration, L'vov [30] explains the pattern of reported variation by the mechanism of dissociative evaporation. This reconciliation of conclusions includes consideration of the effects of water vapour on the measured dehydration rates.

3.3. Magnesium sulfate hydrates

Lallemant and Watelle-Marion [6] have characterized the several distinct rate processes that participate in the stepwise dehydration of $MgSO_4.7H_2O$. In a controlled $p(H_2O)$, powdered samples (15 mg and particle sizes 20 to 30 μm) were investigated by X-ray diffraction, DTA and TG during slow heating (less than 7 K h^{-1}). Between 280 and 400 K, with $p(H_2O)$ values from 0.1 to 5 kPa, dehydration proceeded through the successive phases $MgSO_4.xH_2O$ with x = 7,6,4,2 and 1 and to anhydrous $MgSO_4$ above 500 K. When $p(H_2O)$ was greater than 7 kPa, the same sequence of hydrates was again identified but with the additional intervention of $MgSO_4.2.5\ H_2O$, which has a structure (β) different from that of the dihydrate. Phase diagrams showing the stability ranges of these hydrates are given. The reactions are not, however, entirely reversible because, on cooling in water vapour, the hexahydrate reforms without the appearance of the lower hydrates.

Boldyrev [79] made a comparative study of dehydration rates of $MgSO_4.7H_2O$ from different crystal faces in air at 323 K. Five crystals of different habit were examined in which the relative areas of the {111} and {110} faces varied systematically. The inward rate of interface advance was significantly greater from the {111} face than from the {110} face.

$MgSO_4.7H_2O$ dehydrates to $MgSO_4$ in a single step when irradiated by an infrared laser [80].

The dehydration of $MgSeO_4.6H_2O$ is a stepwise process [81] : (363 K) → $MgSeO_4.5H_2O$ (403 K) → $MgSeO_4.2H_2O$ (528 K) → $MgSeO_4.H_2O$ (603 K) → $MgSeO_4$.

3.4. Calcium sulfate dihydrate

Ball et al. [82,83] have reported several studies of the dehydration and allied reactions of $CaSO_4.2H_2O$, for which the reaction products can be summarized:

$$\begin{array}{ccccc} & & CaSO_4.\tfrac{1}{2}H_2O & & \\ & & \downarrow\uparrow \quad\quad \uparrow\downarrow & & \\ CaSO_4.2H_2O & \rightarrow & CaSO_4\ (\text{hexagonal}) & \rightarrow & CaSO_4\ (\text{orthorhombic}) \end{array}$$

(the α and β forms of the hemihydrate are now distinguished as different hydrates [60] with α-$0.67H_2O$ and β-$0.5H_2O$). The kinetics and mechanisms of these reactions are complicated and depend on reaction conditions. For example, below 383 K, $CaSO_4.2H_2O$ dehydration proceeds by nucleation and boundary control reaction (WET 3) whereas above this temperature the rate is

determined by diffusion (probably WET 2). Similarly, dehydration of the α-hemihydrate depended on reaction conditions below 383 K. Above about 388 K, water losses from both α and β hemihydrates were diffusion controlled. The calculated magnitudes of E_a extended from about 40 to 120 kJ mol^{-1} so that the behaviour pattern is not concisely summarized [82,83] and includes an influence from $p(H_2O)$. Some rehydrations were also investigated, together with measurements of the surface areas and pore size distributions of the solid products. Rehydration of the hemihydrate is of considerable commercial importance and has been studied in detail [84,85].

$CaSO_4.2H_2O$ dehydration below 425 K and at low pressure yields γ-$CaSO_4$. This deceleratory reaction was studied [60] between 324 and 371 K, using single crystals that have a layered structure. The rate of interface advance in the (010) crystallographic direction is controlled by the diffusive migration of H_2O across the solid product layer. In contrast, advance in the (001) direction is determined by the chemical step (E_a = 82 kJ mol^{-1}).

Paulik et al. [86] draw attention to the variations in rate of water evolution that result from changes in reaction conditions. The literature concerned with $CaSO_4.2H_2O$ dehydrations is reviewed and it was concluded that not all inconsistencies had yet been resolved. There is no evidence for the occurrence of possible melting at 311 or at 366 K, predicted thermodynamically, but water loss yields the hemihydrate at about 400 K and anhydrous $CaSO_4$ above 440 K.

$Na_2SO_4.5CaSO_4.3H_2O$ dehydrated in a single rate process (-$3H_2O$). The deceleratory reaction, studied [87] between 450 and 490 K, fitted the parabolic law, ascribed to a one-dimensional diffusion process. In vacuum the value of E_a was 75 kJ mol^{-1} and this increased systematically with water pressure to 159 kJ mol^{-1} when $p(H_2O)$ = 2.6 kPa.

3.5. Zirconium sulfate hydrate ($5.5H_2O$)

The dehydration of $Zr(SO_4)_2.5.5H_2O$ is described [88] as proceeding to completion in four steps through the stepwise losses of 0.5, 3, 1 and 1 H_2O. The authors stress the importance of ensuring that the rate data used in kinetic analyses refer to a single rate process only. It is also pointed out that enthalpy values could include contributions from phase transformations and that care is required in the handling of hygroscopic reactants.

3.6. Copper sulfate hydrates

The dehydration of $CuSO_4.5H_2O$ probably has the longest investigative history of any nucleation and growth reaction [13,14,20]. Early work stressed the importance of using very low pressure conditions for kinetic measurements

of the rates of water loss from single crystals on which all surfaces had been nucleated by abrasion with $CuSO_4.H_2O$. (Initial establishment of an active interface across all crystal faces reduced the uncertainties in this early kinetic interpretation of an acceleratory process). It was regarded as surprising that the rate of H_2O evolution was comparatively insensitive to the thickness of the superficial layer of dehydrated product. A useful review of the early research has been given by Young (pages 79 to 89 of [11]).

On relatively perfect crystal faces, the numbers of nuclei present during the onset of dehydration increased linearly with time. The different shapes of nuclei, distinguished on nine different crystallographic faces, were ascribed to the preferred advance of reaction interfaces orientated in a limited number of index directions [89]. The P-W model [25] was regarded [26] as providing an acceptable theoretical representation of reaction rates [20]. The magnitude of A calculated from dehydration rates agreed with the predicted expectation within an order of magnitude.

Zagray et al. [90] concluded that, for $p(H_2O)$ values less than 1 Pa, dehydration nuclei are star- or X-shaped and composed of monohydrate that is amorphous to X-rays. When $p(H_2O)$ is greater than about 100 Pa at 323 K nuclei are elliptical, probably composed of crystalline trihydrate. At the same $p(H_2O)$ the X-shaped nuclei become rounded and are identified as crystalline monohydrate. When heated in vacuum at 373 K, the product was the normal monohydrate.

Ng et al. [91] report isothermal studies of $CuSO_4.5H_2O$ dehydration to the trihydrate between 320 and 336 K. The sigmoid curves were satisfactorily represented by the A1.5 equation and E_a = 104 kJ mol^{-1}. Dehydration of the trihydrate to the monohydrate fitted the A2 equation with E_a = 134 kJ mol^{-1}. Both values of E_a were close to the reaction enthalpies, which is probably (see [34]) evidence of significant participation by the reverse process in kinetic measurements that used relatively very large sample masses (about 2 g).

Boldyrev et al. [15], from diffraction data obtained using a synchrotron source, identify a metastable intermediate phase, a distorted reactant structure, at the interface during $CuSO_4.5H_2O$ dehydration (-4 H_2O). Okhotnikov and Lyakhov [59] selected the same reaction to investigate the response characteristics of a quartz crystal microbalance. Dehydration at low pressures between 260.6 to 286.2 K proceeded at a constant rate of weight loss during dehydration at an established interface. The value of E_a determined, 74 kJ mol^{-1}, was in substantial agreement with a previous value, 76 kJ mol^{-1}[92].

In a dynamic apparatus, developed to characterize sequential dehydration steps, evidence was obtained [93] that $CuSO_4.5H_2O$ evolves $1.0H_2O$ (331 to 338 K), $1.5H_2O$ (348 K), $0.5H_2O$ (358 K) and $1.0H_2O$ (488 to 513 K). (It appears that one water molecule is not accounted for in these conclusions.)

Comparative studies of $CuSO_4.H_2O$ dehydration rates [94] in a gas flow at about 500 K show that isothermal measurements fit the D3 equation but, under non-isothermal conditions, rate data are consistent with the n+g model. The apparent value of E_a was about 200 kJ mol^{-1}. These different rate characteristics are ascribed to the water uptake reaction, which exerts less influence under dynamic conditions because the pressure of water vapour corresponding to equilibrium rises as the temperature is increased. It is stressed that, to obtain reliable results, it is necessary to use small reactant samples in an open chamber with a flowing atmosphere.

3.7. Nickel sulfate hexahydrate

Microscopic observations of the (00l) faces of $NiSO_4.6H_2O$ large crystals, dehydrated at low pressures (less than 0.1 Pa) ($\rightarrow$ $NiSO_4.H_2O$), showed [95] that the numbers of dehydration patches did not increase during the early stages of reaction (Instantaneous Nucleation [12]). It was not possible to decide, from comparisons of slightly reacted and lightly etched matched pairs of cleavage faces, whether or not nucleation occurred *exclusively* at dislocations or whether other imperfections such as point defects or impurities were involved. From vacuum TG and microscopic measurements for single crystals and for powder samples, the value of E_a was found to be about 70 kJ mol^{-1} between 300 to 316 K. This is consistent with the view that proton motion controlled the interface advance rate. α-time data for dehydrations of single crystals fitted the A2 equation over almost the complete reaction. The dehydration rate of the powder was about eight times that of the single crystal.

Guarini [16] confirmed this general pattern of kinetic behaviour and concluded that dehydration is not a simple n+g process. He distinguished three steps that together contribute to water release: reaction, water migration and product recrystallization. The last of these was the slowest. Crystal dehydration in N_2 showed significant differences, including the remarkable development of large bubbles [96] due to the retention of H_2O (steam) beneath a surface layer of partially dehydrated salt that was elastic and relatively impermeable (?WET 5). Photoacoustic measurements [97] confirmed the view that there was an initial water loss from reactant surfaces.

Comparative studies of $NiSO_4.6H_2O$ dehydrations under a range of selected reaction conditions were made by Koga and Tanaka [7]. TG-DSC or TG-DTA measurements were complemented by X-ray diffraction, FTIR and microscopic observations. In vacuum, dehydration proceeded directly ($-5H_2O$) to the monohydrate. Yield-time data fitted the A2 equation and values of E_a increased from about 94 to 110 kJ mol^{-1} with a decrease in particle sizes of powdered reactants. The reaction in static air is more complicated, with H_2O losses proceeding through the tetrahydrate and dihydrate intermediates, involving the inward advances of two interfaces. The participation of self-generated water in the reactant atmosphere is consistent with the appearance of a liquid phase at the onset of some non-isothermal reactions. This study demonstrates the value of complementary observations, obtained both by isothermal and by non-isothermal measurements, for the interpretation of kinetics and in formulating mechanisms for solid state reactions. This can be particularly useful where alternative pathways are possible and where reactions occurring depend on conditions locally prevailing.

The above pattern of behaviour may be compared and contrasted with earlier isothermal and non-isothermal (5 K min^{-1}) measurements by Sinha et al. [98], again for $NiSO_4.6H_2O$ dehydration. In this work, however, neither the prevailing atmosphere nor the sample masses are specified. Reaction stoichiometries and temperatures are summarized here conveniently by referring (only) to the numbers of H_2O molecules in the hydrates presumed to be present:

Isothermal (453 K): $6H_2O \rightarrow 4H_2O \rightarrow H_2O$
Isothermal (583 K): $6H_2O \rightarrow H_2O \rightarrow$ anhydrous
Dynamic: $6H_2O$(416 K) $\rightarrow$ $5H_2O$(453 K) $\rightarrow$ $3H_2O$(503 K) $\rightarrow$ H_2O(613 K) $\rightarrow$ anhydrous
[Also (from [99]) dynamic : $7H_2O$(403 K) $\rightarrow$ $6H_2O$(463 K) $\rightarrow$ $3H_2O$(483 K) $\rightarrow$ H_2O(653 K) $\rightarrow$ anhydrous].

These reaction temperatures and stoichiometries are quite different from those reported for the vacuum study [95], where the hexahydrate is directly dehydrated to the monohydrate (at 0.1 Pa between 308 to 323 K; below this range there is some water retention approximating to $NiSO_4.1.5H_2O$). This has been confirmed by low pressure TG [7]. However, during dehydration in static air (which may approximate to the conditions used in the above studies [98,99]), heating at 8 K min^{-1}, three mass loss steps were distinguished, corresponding to the evolution of $2H_2O$(390 K), $3H_2O$(440 K) and H_2O(615 K).

The hydrates were positively identified [7], by X-ray diffraction, as being present in the residue included the following mixtures (after the onset of reaction there were always two, or more, hydrates present.):

420 K	$4H_2O + 2H_2O + 6H_2O$
470 K	$4H_2O + 2H_2O + H_2O$
520 K	$2H_2O + H_2O$

The higher temperature reactions [98], therefore, presumably refer to chemical changes resulting from displacement of water vapour equilibria in large samples: volatilization, water removal, occurs when sufficiently large values of $p(H_2O)$ have been achieved. It follows, therefore, that in the absence of specific characterization of the phases present (e.g. by X-ray diffraction), evidence from TG and/or DSC/DTA cannot be reliably used to establish the stoichiometry of dehydrations. These difficulties are increased when considering research reports that do not specify reaction conditions such as gases present, reactant mass, etc. [The references listed in [98] also include studies of the dehydrations of $MnSO_4.4H_2O$ and $CoSO_4.7H_2O$, which might similarly be expected to involve equilibrium displacement and water removal processes, though positive confirmation would require further and more detailed data examination.]

3.8. Alums

Early studies of alum dehydrations by Garner and his coworkers [20,66,100,101], not only provided insights into the chemistry of these reactions, but also contributed to the wider development of the n+g interface reaction mechanism. The concepts proposed became essential foundations [10] for the derivation of those geometry-based kinetic rate equations (Table 1 above and [1,2]) that provide a (perhaps *the*) unifying feature in the kinetic studies of crystolysis reactions. Microscopic observations, extended to the limits of the optical instruments then available, characterized the shapes and textures of nuclei in alums and, with supporting X-ray diffraction studies, determined product structures to investigate the role of zeolitic phases in dehydrations [20]. Water vapour was identified as promoting product recrystallization and the consequent crack development that reduced the influence of the residual solids in impeding H_2O escape.

It was also shown [20] that the kinetics of nucleation varied between different reactants, or even sometimes on different faces of a single crystal, and with $p(H_2O)$. During $KAl(SO_4)_2.12H_2O$ dehydration all nuclei became active from

the start of reaction [100] and no more appeared subsequently (Instantaneous Nucleation [12]). In contrast, nuclei were formed at a constant rate during the early stages of $KCr(SO_4)_2.12H_2O$ dehydration [20] (Linear Nucleation). Growth nuclei [13], once formed, developed thereafter at a constant rate of interface advance [10].

These results were replicated in a kinetic study [44] based on microscopic measurements for nucleus growth in these alums between 290 and 305 K below 10^{-2} Pa. The values of E_a for the linear interface advance during dehydrations of $KAl(SO_4)_2.12H_2O$ (-$10H_2O$) and of $KCr(SO_4)_2.12H_2O$ (-$6H_2O$) were 108 and 70 kJ mol^{-1}, respectively. Initial growth rates of individual nuclei were sometimes less than, and sometimes greater than, the constant rate of growth, subsequently attained that later became equal for all nuclei on a crystal face [44].

Microscopic examinations showed [44] that flat cleavage faces of $KAl(SO_4)_2.12H_2O$, after evacuation followed by exposure to water vapour, underwent superficial modification, descriptively termed the "orange peel texture". No similar change was found after this treatment of $KCr(SO_4)_2.12H_2O$ but, on re-evacuation, there was [101] a rapid and large increase in nucleation rate. These alternative behaviour patterns were ascribed [44] to initial water losses across *all* crystal faces in vacuum but such dehydration was restricted to a thin superficial layer. Subsequent exposure to water vapour results in retexturing and/or strain generation within this layer which was identified as the first step in the recrystallization required to enable the reaction to proceed inwards below the surface layer. Initial, superficial water loss is facile, but continued reaction is more difficult and requires recrystallization with cracking of the water depleted material to form a particle of the product phase. Dehydration is facilitated at the product contact surfaces with the reactant phase [102].

The preferred occurrence of dehydrations at intracrystalline reactant-product contact interfaces, during nucleus growth (in an n+g reaction), is an inherently unexpected behaviour pattern. It appears (intuitively) that water losses from a nucleus interior should be less rapid than from an outer surface. However, water-promoted recrystallization of the initial water-depleted material appears to be an essential feature in enabling reaction to continue and this generates water-escape channels [44]. Thus the nucleus function here can be recognized as a specific structure that is admirably capable of promoting reaction by retaining sufficient water to facilitate product recrystallization at the active interface and thus diminish the impeding effect of a barrier layer of accumulated dehydrated material. This accounts for the unexpected features of the n+g reaction model.

Subsequently evidence was obtained [17] to confirm that the residual (intranuclear) solids retain (at least temporarily) appreciable quantities of water. This study of alum dehydration under accumulatory conditions showed that the magnitudes of Arrhenius parameters were similar to those previously determined in vacuum [17]. This is consistent with the essential participation of temporarily retained intranuclear water (including vapour) in promoting dehydration. However, the rate characteristics of these H_2O accumulatory experiments were inconsistent with expectation for the kinetic behaviour based on the geometry of the (three dimensional) n+g reaction observed microscopically, because data fit the A2 equation. The differences may be reconciled by considering the contributions from the initial water losses from all surfaces, together with some H_2O retention by adsorption on the product. (See also, [3] p. 207-208.) Dehydration in an appreciable $p(H_2O)$ fitted a 'first order' approach to the establishment of equilibrium between H_2O vapour and the reactant-product solids.

3.9. Calcium sulfite hemihydrate

The crystal structure of the anhydrous product given by $CaSO_3.½H_2O$ dehydration depends [103] on the nature of the hemihydrate and the reaction conditions, including $p(H_2O)$. An accumulatory kinetic study of this reaction [104] showed sigmoid curves that fitted the A2 equation with E_a = 173 kJ mol^{-1} [ln(A/s) = 24.9] between 573 and 673 K. This is a relatively high temperature for a reaction releasing water of crystallization. There were unusually close agreements between reactivities and kinetic parameters for the dehydrations of this salt and of $Ca(OH)_2$ [105]. There is the possibility that similar chemical changes control the rates of water release from both reactants, perhaps involving an interaction of H_2O with a Ca^{2+} ion or the participation of hydroxyl ions.

3.10. Sodium thiosulfate pentahydrate

Dehydrations at cleaved {010}, {001} and {111} faces of $Na_2S_2O_3.5H_2O$ were studied by microscopic and by kinetic methods [106]. It was concluded that recrystallizations proceeded within already dehydrated material and were influenced by crystal perfection. Under strongly dehydrating conditions it appeared that initially a thin superficial anhydrous layer was formed. Subsequently, at the $Na_2S_2O_3/Na_2S_2O_3.5H_2O$ interface, the dihydrate intermediate was formed and this generated active interfaces with both $Na_2S_2O_3$ and with the pentahydrate which advanced outwards and inwards, respectively. When all the outer surface had been partially rehydrated, to $Na_2S_2O_3.2H_2O$, the

anhydrous phase was again nucleated and the $Na_2S_2O_3/Na_2S_2O_3.2H_2O$ contact progressed inwards. Isothermal kinetic measurements, using thermal analysis, showed that the pentahydrate to dihydrate dehydration fitted the R2 equation and the subsequent reaction of the anhydrous salt was well represented by the A2 expression. No reliable Arrhenius parameters could, however, be determined.

3.11. Barium chloride dihydrate

$BaCl_2.2H_2O$ dehydration has been the subject of several kinetic studies. Guarini and Spinicci [107] have shown that, in a flow of dry N_2, water is lost in two consecutive reactions at about 335 and 370 K with the intermediate formation of $BaCl_2.H_2O$. Both reactions showed an initial acceleratory stage, after which the processes became deceleratory, and were then satisfactorily represented by the R2 equation. Microscopic observations confirmed the early occurrence of an n+g reaction. Values of E_a, calculated from rising temperature DSC measurements, 97 kJ mol^{-1}, were greater than isothermal values (about 70 kJ mol^{-1}) for both rate processes in both crystal and powder reactants.

From microscopic measurements of the rates of interface advance during $BaCl_2.2H_2O \rightarrow BaCl_2.H_2O$, Osterheld and Bloom [108] find that, below 334 K, E_a was 145 kJ mol^{-1} and was less above this temperature. There were some indications of topotaxy and the crystallographic changes that accompany reaction were discussed.

Lumpkin and Perlmutter [109] identify $BaCl_2.2H_2O$ dehydration as an n+g process. The rate of reaction was very sensitive to $p(H_2O)$ and its transient variations, which may be due to water vapour pressure gradients developed during product H_2O diffusion between small reactant particles. Apparent magnitudes of E_a, 92 to 150 kJ mol^{-1}, vary with both sample mass and α.

3.12. Other hydrated halides

Dehydrations of hydrated halides have been studied less extensively, and in less detail, than the sulfates. Some representative examples from the literature are mentioned here to illustrate further characteristics of these reactions.

The stoichiometry of $MgCl_2.2H_2O$ dehydration, N_2 atmospheric pressure, is [8]:

$$MgCl_2.2H_2O \rightarrow MgO + 2HCl + H_2O$$

This rate process is well represented by equation R2 and values of E_a for reactions in dry N_2 or in 1 kPa of H_2O are 110 and 75 kJ mol^{-1}, respectively, between 623 and 803 K.

The lanthanide chlorides form hexa- or heptahydrates. Stoichiometries of dehydration have been determined from measurements using a fluidized bed, in the presence of sufficient HCl to suppress hydrolysis. The results obtained are reported and discussed [110] in the context of published information concerning the individual sequences of dehydration steps.

From X-ray diffraction measurements, Günter et al. [111] showed that the structure of $Rb_2MnF_5.H_2O$ included infinite chains of coordinated $[MnF_6]$ octahedra, sharing corners, between which the Rb^+ ions and water molecules were accommodated. Dehydration was shown to be topotactic and, following water loss, parallel cracking of the crystals was detected by scanning electron microscopy.

The dehydration of $CuCl_2.2H_2O$ proceeds directly to the anhydrous salt at about 360 K in N_2 [112]. The dehydration of $K_2CuCl_4.2H_2O$ [113], studied by rising temperature TG in N_2, fitted a contracting geometry kinetic model. Microscopic examinations of crystals sectioned after partial reaction revealed the inward advance of reaction interfaces, in which three stages could be recognized. (i) Surface nucleation followed by inward advance of reaction fronts. (ii) Random nucleation and growth at sites within the reactant crystal but close to the reaction front. (iii) Product recrystallization that facilitates escape of the water released. Apparent magnitudes of E_a were usually between 80 and 130 kJ mol^{-1} and varied with heating rate, particle size and α.

3.13. Sodium perchlorate monohydrate and magnesium perchlorate hexahydrate

The dehydration of $NaClO_4.H_2O$ proceeds through two irreversible steps [114] with the losses of 0.2 H_2O at 333 K and 0.8 H_2O at 420 K. These fractional values are attributed to different water-accommodating structures in the complicated unit cell of the monohydrate that contains eight formulae weights.

The steps in $Mg(ClO_4)_2.6H_2O$ dehydration are accompanied by melting [114] (WET 5 or 6). The loss of two molecules of water above 420 K occurs with partial melting and is complete by 463 K. The second step, again with $-2H_2O$, but with some partial intervention of the trihydrate, yields the dihydrate between 520 and 550 K and there is melting. Dehydration was completed by 670 K.

3.14. Sodium carbonate monohydrate

The dehydration of $Na_2CO_3.H_2O$ was studied [115] by TG in flowing N_2 between 336 and 400 K. The sigmoid α-time curves were shown by microscopic observations to be due to a n+g process. Nucleation was identified as occurring at crystal imperfections, possibly at sites of occluded solution. The rate data fitted the A2 equation with E_a = 71.5 kJ mol^{-1} in dry N_2. Dehydration rates decreased with increase in $p(H_2O)$, a trend that was relatively greater at low temperatures. Acceptable allowances for these rate reductions were made by including the contribution from the reverse process with an enthalpy change of 13.8 kJ mol^{-1}. Calculated rate constants, k_i/s, that satisfactorily represent the observations, were given by :

$$k_i/s = [2.2 \times 10^7 \exp(-71500/RT)] - [3.1 \times 10^{-6}.p(H_2O).\exp(-13800/RT)]$$

3.15. Calcium nitrate tetrahydrate

Steps in the dehydration of $Ca(NO_3)_2.4H_2O$ [116] are not due to consecutive reactions but, in air, result from physical processes, including incongruent melting, followed by boiling of the water, leading to crust formation with drying.

3.16. Uranyl nitrate hexahydrate

This dehydration is unusual, perhaps unique, but this is not known with certainty because few such low temperature reactions have been reported. The kinetics of water loss ($-3H_2O$) from $UO_2(NO_3)_2.6H_2O$ were studied [117] isothermally between 213 and 243 K in vacuum. The rate of water evolution remained constant throughout almost the complete reaction and, from the zero-order rate constants, E_a was 46 kJ mol^{-1}. The residual product was crystalline (but non-zeolitic) and reaction did not involve the generation of an advancing interface. The dependence of the dehydration rate on $p(H_2O)$ was linear. These exceptional kinetic characteristics were explained by H_2O evaporation from the existing crystal faces and the vacancies concurrently generated were highly mobile within the partially dehydrated crystal, that remained pseudomorphic with that of the reactant. The self-diffusion coefficient of H_2O within this structure was shown [117] to be unusually large. This appears to be the only known example of an immobile interface in reactions of this type, though the absence of a crystallographic change following water loss is less unusual.

3.17. Barium nitrite monohydrate

The dehydration of $Ba(NO_2)_2.H_2O$ is stepwise [118] reacting at 373 K to the hemihydrate (425 K) $\rightarrow$ $Ba(NO_2)_2.1/3H_2O$ and the anhydrous salt above 457 K.

3.18. Some hydrated permanganates (Sr, Cd and Ca)

These three relatively unstable hydrated permanganates (Sr, Cd and Ca) lose water just above ambient temperature [119]. The kinetic characteristics of single crystal dehydrations tended to be irreproducible so that rate measurements, TG in N_2, used powders.

$Sr(MnO_4)_2.3H_2O$ lost $2H_2O$ in the first dehydration step, E_a = 27 kJ mol^{-1} between 323 and 373 K. The anhydrous salt was given ($-H_2O$) by the second, slower process with E_a = 57 kJ mol^{-1}.

$Cd(MnO_4)_2.6H_2O$ lost water in two equal ($-3H_2O$) steps that were studied between 303 and 333 K and the values of E_a were low, 5 and 60 kJ mol^{-1}.

The dehydration of $Ca(MnO_4)_2.6H_2O$ was found to be too irreproducible to permit kinetic studies. There was some evidence that water was evolved in two steps, $-2H_2O$ and $-4H_2O$.

3.19. Sodium tungstate dihydrate

Below 373 K, $Na_2WO_4.2H_2O$ dehydrated directly to the anhydrous salt and DSC rate measurements were complemented with microscopic observations [120]. Reaction commenced at separated nuclei, randomly distributed, that are believed to arise through recrystallization of an already dehydrated surface layer and this enables H_2O to escape. Initially the inward interface advance process was rapidly established, by about α = 0.03, and reaction thereafter was predominantly deceleratory, fitting the R2 equation. Kinetic characteristics, including the Arrhenius parameters, varied appreciably for different preparations.

3.20. Some alkali and alkaline earth hydrated phosphates

Sodium and potassium triphosphate hydrates. Through consideration of previously published kinetic studies of the dehydrations of $Na_5P_3O_{10}.6H_2O$ and of $K_5P_3O_{10}.4H_2O$, Prodan and Lesnikovich [121] proposed a 'zonary' model for the propagation of interfaces in crystals and in powder reactant particles. According to this model, a section cut across the reacting zones would reveal a sequence of hydrates, the H_2O content of each decreasing outwards from the particle centre. Each contact between successive neighbouring phases is an active advancing interface. The value of this model and its applications in

representing multistage reactions is discussed. Dehydration of the sodium salt proceeds through four steps.

Magnesium hydrogen phosphate trihydrate. The changes of infrared spectra that occur on heating $MgHPO_4.3H_2O$ to 435 K are ascribed [122] to increased proton mobility that leads to hydrogen bond dissociations, proton tunnelling and orientation of acceptor sites. Water loss was accompanied by increasing disorder of the hydrate structure, including distortion of the symmetry of the PO_4^{3-} ion. Dehydration, studied by rising temperature DSC between 393 and 523 K, occurred in a single step ($-3H_2O$) and the value of E_a was about 146 kJ mol^{-1}.

Calcium hydrogen phosphate dihydrate. Dehydration of $CaHPO_4.2H_2O$, with loss of one water molecule, was studied by isothermal TG in N_2 between 409 and 537 K and was diffusion controlled [123]. Below 478 K, E_a was 190 kJ mol^{-1} and the rate was independent of $p(H_2O)$. Above 478 K, however, the magnitude of E_a depended on $p(H_2O)$. The formation of the monohydrate is consistent with the presence, in the reactant dihydrate, of two forms of H_2O that differ in their strengths of bonding.

Calcium dihydrogen phosphate hydrates. Dehydration of the equimolar mixture, $Ca(H_2PO_4)_2.2H_2O$ + $Ca(H_2PO_4)_2.H_2O$, proceeded with loss of crystalline and zeolitic water between 363 and 433 K: values of E_a were about 83 kJ mol^{-1}[124]. Apparent magnitudes of the Arrhenius parameters varied with the calculation methods. Above 540 K further water is released following anion condensation.

A series of dehydrations have been studied [125] for the mixed hydrogen phosphates containing two cations, including $Zn_{0.5}Mg_{0.5}(H_2PO_4)_2.2H_2O$ and further similar mixtures with the cation pairs: Zn + Ca; Co + Mg and Mn + Mg.

3.21. Hydrated metal formates and acetates

The dehydrations of hydrated salts of simple organic acids, including the extensively studied carboxylates, are apparently kinetically and mechanistically similar to the comparable reactions of inorganic hydrated salts. No features distinguishing these two groups of reactants appear to have been identified. A representative selection of these reactions are, therefore, given here to extend coverage across the range of substances that are often considered together under the present Chapter title.

Manganese formate dihydrate. Microscopic observations showed [126] that in vacuum the reactant-product interface advanced inwards from the {011} faces at constant rate during dehydration. Similar values of E_a, 77 kJ mol^{-1}, were

obtained by isothermal TG and microscopic measurements. This is consistent with proton motion as the rate determining step in interface advance.

Copper formate tetrahydrate. The anhydrous solid, $Cu(HCOO)_2$, given on dehydration of the tetrahydrate is a different crystallographic modification from that obtained by a direct preparation route [127]. Because this dehydration is topotactic, the orientation relationships between reactant and product were used to identify the crystal structure of the anhydrous product. Water removal left the two-dimensional structural elements in the copper formate layers substantially unaltered, but the mode of stacking was modified. Loss of H_2O resulted in pronounced crystal splitting parallel to the basal plane.

Zinc formate dihydrate. The anhydrous product from the dehydration of $Zn(HCOO)_2.2H_2O$ was amorphous, when obtained from the reaction in vacuum, but in water vapour it was crystalline [128]. The value of $p(H_2O)$ required for the formation of the crystalline product decreased linearly, from 80 to 13 Pa, with temperature increase from 370 to 400 K. At first the dehydration rate increased with a rise in $p(H_2O)$ and at higher values decreased. This is ascribed to the greater ease of H_2O escape, through the wider channels formed by product recrystallization. This was then followed by a diminution of the dehydration rate at high $p(H_2O)$ values due to the onset of the reverse reaction. (This is in accordance with one explanation for Smith-Topley behaviour [129]).

A TG kinetic study of the reaction in air containing 1.6 kPa H_2O identified a two-dimensional contracting interface process (R2) with $E_a = 99$ kJ mol^{-1}.

Rare earth formate dihydrates. The dehydrations of Dy, Ho, Er, Tm, Yb and Lu formate dihydrates, studied [130] in TG-DTA rising temperature experiments, proceeded by an advancing interface reaction with E_a values in the range 108 to 142 kJ mol^{-1}. The reaction enthalpy increased linearly with the reciprocal of ionic radius, ascribed to the strength of electrostatic attraction at the Ln-OH_2 bonds.

Copper acetate monohydrate. The dehydration of $Cu(CH_3COO)_2.H_2O$ was studied [131] by TG in flowing N_2 between 353 and 406 K. Below 371 K, reaction proceeded by a nucleation and growth process, fitting the A2 equation with $E_a = 154$ kJ mol^{-1} and $A = 8.5 \times 10^{17}$ s^{-1}. Above this temperature the contracting interface equation (R2) applied, with $E_a = 76$ kJ mol^{-1} and $A = 1.6 \times 10^7$ s^{-1}. Microscopic observations confirmed that there were different textural changes within the two temperature intervals. (See also [73].) The dehydration of $CaCu(CH_3COO)_4.6H_2O$ is also complicated [132] and again the controlling processes change with temperature.

Zinc acetate dihydrate. The anhydrous salt is formed in a single step (-$2H_2O$), studied [58,73] isothermally by TG in flowing N_2 between 333 and 361 K.

Reaction was initiated at the edges of the thin reactant crystals and subsequently formed an interface that progressively advanced inwards. Apparent values of E_a decreased from 165 kJ mol^{-1} for single crystals to 75 kJ mol^{-1} for fine powder.

3.22. Hydrated metal oxalates

Reference has already been made [33] to the sensitivity to reaction conditions of the kinetic parameters calculated for $NiC_2O_4.2H_2O$ dehydration.

The dominant process in water loss from *magnesium oxalate dihydrate* [133], studied by TG between 420 and 495 K in flowing N_2, was a two-dimensional advancing interface (R2), rapidly established initially, with E_a = 111 kJ mol^{-1}. Careful analysis of the brief acceleratory process, during the earliest stages of reaction at the lowest temperatures, enabled the kinetics of the nucleation step to be measured, for which E_a was reported as 430 kJ mol^{-1}.

The dehydrations of *Co, Ni and Fe(II) oxalate dihydrates* and the *hydrates of the mixed Fe-Cu, Co-Cu and Ni-Cu oxalates* have been studied by TG in N_2 [134]. The deceleratory reactions, usually occurring between 400 and 450 K, for both simple and mixed oxalates, were generally similar and fitted the R2, R3 or F1 equations. Most values of E_a were between 80 and 90 kJ mol^{-1}.

Phase diagrams for the system *barium hydrogen oxalate dihydrate* - water vapour were determined in detail by Mutin et al. [135] using complementary measurements that included TG, DTA, X-ray diffraction and microscopy. Water is accommodated in the dihydrate within linear intracrystalline channels between the stable Ba^{2+} and $C_2O_4^{2-}$ ionic arrays that maintain crystal coherence. Dehydration follows intracrystalline diffusive H_2O migration to surfaces, without crystal restructuring (WET 4B [3]).

3.23. Sodium citrate dihydrate

Tanaka et al. [136] found that between 420 and 440 K single crystals of sodium citrate dihydrate (unexpectedly) dehydrated more rapidly than the relatively more stable powder. This is ascribed to enhanced nucleation, leading to strain within the larger crystals, together with some retention of water that promotes reaction. For single crystal dehydrations E_a was 203 kJ mol^{-1}, $A = 1.0 \times 10^{22}$ s^{-1} and rate data fitted the A3 or A4 equations, while for powder E_a was 294 kJ mol^{-1}, $A = 1.3 \times 10^{32}$ s^{-1} and reaction was satisfactorily expressed by the F1 equation.

3.24. Lithium potassium tartrate hydrates

Comparative studies [45,46,102] were made of the dehydrations of $LiKC_4H_4O_6$ crystalline hydrates which contained the *d, dl* and *meso* forms of the tartrate anion. These three salts are composed of identical ionic constituents disposed in different stereochemical arrangements. Dehydrations of the racemic (*dl*) monohydrate [45] and the *meso* dihydrate [46] were accompanied by melting and used in kinetic studies of the release of water from a molten reactant to which no additional solvent (H_2O) had been added. Both salts are classified as WET 5 [3].

Water loss from *d*-$LiKC_4H_4O_6.H_2O$ [102] single crystals proceeded predominantly by a nucleation and growth reaction (WET 3 [3]). Initial dehydration from all crystal outer surfaces was diffusion controlled and limited in extent, prior to the appearance of growth nuclei. The induction period to nucleation was almost completely eliminated by the contiguous presence of anhydrous product, which was identified as providing seed crystals for the recrystallization of water-depleted reactant to form the anhydrous product. This method of promoting product formation appears to be maintained at the interface during nucleus growth. [Water retention and adsorption, as a recrystallization promoter, is expected to be less favoured (than e.g., [44]) at these reaction temperatures, about 400 K]. It was concluded [102] that diffusive water losses from hydrate surfaces are restricted in extent until nucleation generates the crystalline, anhydrous product that continually seeds recrystallization at advancing dehydration nucleus boundaries. Channels permitting H_2O escape then become available. Interface advance is controlled by diffusive water loss from the hydrated reactant surfaces, at an active nucleus boundary, coupled with restructuring facilitated by continual reseeding promoted at the contact with the intranuclear product.

3.25. Coordination compounds containing both H_2O and other ligands

Hydrates, in which water forms ligands by dative coordination bonding to a cation (usually a transition metal ion) are correctly regarded as coordination compounds. There is also the additional propensity for such H_2O ligands to form hydrogen bonds with other crystal constituents, so increasing stability. Examples of dehydrations of salts of this type have been included above, e.g., the alums. There are further types of coordination compound in which there is one, or more, H_2O ligand present (per cation), together with other groups that complete the coordination sphere. Thermal reactions of these compounds is a larger topic than can be comprehensively reviewed here, but the examples given below include representative types of chemical changes in which water is

eliminated. These can be regarded as 'dehydrations of crystalline hydrates'. Particular interest appears to have been directed towards those reactants which contain a single H_2O ligand on each cation.

On heating, some of these coordination compounds eliminate H_2O to form binuclear species, as shown by the following examples from [137,138]:

$$[Co(NH_3)_5H_2O][Co(CN)_5Cl]\ (8\ h\ at\ 400\ K) \rightarrow [(NH_3)_5CoNCCo(CN)_4Cl]$$

$$[Co(NH_3)_5H_2O][Fe(CN)_6](380\ K) \rightarrow [(NH_3)_3Co(NH_2)_2(NC)Fe(CN)_3]$$

In one of the few mechanistic discussions concerned with this particular type of solid state reaction, House [139] identified the transition state during such intracrystalline interactions as the generation of a point defect. From consideration of the magnitude of E_a and the reaction entropy, it is concluded that reactions of the type:

$$[Cr(NH_3)_5H_2O]X_3 \rightarrow [Cr(NH_3)_5X]X_2 + H_2O$$

(X representing a halide ion) proceed through the intervention of a Frenkel-type defect and dissociate by an S_N1 mechanism with the elimination of the H_2O molecule.

Later LeMay and Babich [140] pointed out that the magnitudes of the activation parameters measured for these reactions may not be reliable due to unsatisfactory control of conditions within the reaction chamber. The controls resulting from influences through the procedural variables may be greater than the effects of structure in determining the reaction rates. For some of these reactions isokinetic behaviour [36,37] has been found.

This proposed mechanism [139] has been applied to the reactions of many coordination compounds that contain some water, by Ribas et al. [141,142], and also to the dehydration of $CoCl_2.6H_2O$ [143]. In an S_N1, process E_a is determined by the crystal field as well as the lattice components [137]. For reactions of this general type, the "unit cell free space" has been identified as an important parameter in controlling the ease of the chemical steps contributing to water elimination. If space is available at the reaction site, the H_2O molecules eliminated from the coordination shell may be accommodated with minimum lattice distortion and E_a will be low.

3.26. Reproducibility of measured kinetic characteristics

House et al. [144,145] emphasize the necessity of making several complementary sets of rate measurements across a range of varied reaction conditions. Reliable conclusions are based on reproducible kinetic analyses from several replicated experiments, as illustrated by the two following examples.

At least four sets of measurements were made for each of a series of dehydrations of $(NH_4)_2C_2O_4.H_2O$ [144], with varied reaction conditions, using TG in N_2 for both isothermal and rising temperature experiments. From rate determinations between 328 to 348 K, it was concluded that the data were most satisfactorily represented (22 out of 28 experiments) by the R2 equation, with the A1.5 or A2 equations giving the 'next best fit'. It is concluded that there are difficulties in deducing the mechanism from the precise correspondence of data with the kinetic models. The value of E_a was 73 kJ mol^{-1}, which differs significantly from 138 kJ mol^{-1} obtained by kinetic analysis of non-isothermal measurements.

From similar sets of multiply replicated kinetic measurements for the dehydration of $K_4[Ni(NO_2)_6].0.75H_2O$ at about 375 K [145], it was shown that the most frequent 'best fit' of data was by the A1.5 or A2 equations.

4. OTHER DEHYDRATIONS

4.1. General

Diverse crystalline solids, including metal hydroxides, layer silicates, acid phosphates and many others, contain constituents (hydroxyl, acid groups, etc.) that react to form H_2O molecules and evolve water on heating. While such reactants cannot be regarded as crystalline hydrates, the mechanisms of some of these reactions show points of similarity with the dehydrations discussed in Section 3, above. A short account of these related processes is, therefore, included here to complement the main theme because recognition of parallels may contribute generally towards increasing chemical understanding of *all* dehydrations. Some of these (possibly) related reactions are briefly described here; this topic would benefit from a more comprehensive review.

4.2. Metal hydroxides

The dehydration of *magnesium hydroxide* has been identified [146] as a nucleation and growth process in which interfacial strain, due to the large reduction in volume ($\times$ 0.45) that occurs on forming the MgO product, results in crystal cracking. There is some evidence of topotaxy. The hexagonal close-

packed anions in $Mg(OH)_2$ are converted to the cubic close-packed MgO, initially distorted so that the (111) product spacing matches the (0001) spacing of the reactant. Reactions of samples composed of small crystals fitted the F1 equation with $E_a = 125$ kJ mol^{-1}.

An important review, describing dehydrations of metal hydroxides, has been given by Brett et al. [147], including some discussions of reaction models. According to the *homogeneous* mechanism, neighbouring hydroxyl groups, throughout each particle bulk, generate H_2O by proton transfer which is released after diffusion to a crystal surface. The *inhomogeneous* mechanism exhibits features in common with those of the nucleation and growth representation [146]. Acceptor regions are those to which Mg^{2+} ions migrate, and are subsequently converted to MgO, while the donor regions lose cations and H_2O is formed. This is accompanied by the development of strain and particle disintegration. NMR studies using ^{25}Mg [148] detected the early generation of small MgO particles that grow within the reactant structure and later coalesce to form the larger MgO crystallites that can be identified by X-ray diffraction.

Kinetic studies [105] of the deceleratory dehydration of *calcium hydroxide* showed that reaction rates were sensitive to procedural variables, particularly reactant packing and disposition. The magnitudes of apparent Arrhenius parameters varied with reaction conditions and exhibited a compensation effect. It was concluded that the water elimination reaction and the product recrystallization steps were separated in space and time. Chaix-Pluchery and Niepce [149] identify the occurrence of precursor, pre-reaction second-order transitions that convert the reactant to a form in which dehydration can occur.

Water elimination from the various aluminium hydroxides which yield the several Al_2O_3 structures have also been described [147]. Similarly there are many reports of studies of iron hydroxides dehydrations, at least some of which may be topotactic [150]. The loss of water from $Cd(OH)_2$ is a nucleation and growth process, but (unusually) does not always proceed to completion [151]. Rao [152] has recognized a new class of materials formed by dehydroxylation accompanied by intergrowths of structurally related but different oxides. There have also been studies [153-155] of the thermal reactions of a selection of the many possible mixed hydroxides (basic salts) such as Cu(OH)F, etc.

4.3. Layer minerals containing hydroxide

These reactants are mentioned here to draw attention to some similarities of the dehydrations of layer-structured hydroxide-containing minerals with the topotactic dehydrations of such crystalline hydrates as copper formate

tetrahydrate [127] and calcium sulfate dihydrate [60]. Dehydrations of many layer-type minerals proceed through diffusion controlled loss of H_2O that may be already present, or generated, within extended and relatively stable ionic or covalent structures (classified [3] as WET 2). If the product solid is resilient and insufficiently stressed during water loss, there will be no recrystallization step or cracking at the advancing interface. The product, little modified from the reactant, may then retain coherent and comprehensive contact, including a close topotactic relationship, with the phase from which it was derived. Dehydrations of some naturally occurring silicates, including highly condensed anionic structures composed of strong covalent bonds, have been shown to lose H_2O by diffusion-controlled escape between the layers. This occurs, for example, during the dehydroxylation of muscovite, for which E_a = 225 kJ mol^{-1} in vacuum [19]. The theory has been discussed by Okhotnikov et al. [156].

5. SOME OTHER FEATURES OF DEHYDRATIONS

5.1. Explosive dehydrations

This rare reaction type, reviewed by Stoch [157], may be regarded as the consequence of a considerable three-dimensional stability of the reactant (WET 4A). Within a strongly cohesive confining structure the diffusive escape of water is prevented because nucleation and/or cracking does not occur and there are no intracrystalline channels or planes for facile H_2O movement between extended structural units, as described in Section 4.2. In the very few solids that possess these specialized crystal characteristics, the molecular H_2O or water formed by hydroxyl group interactions is retained within the crystal, with relatively minor losses. At a characteristic temperature, the pressure of this confined water becomes sufficiently large for the retentive structure to be disintegrated vigorously. For example, colemanite, $Ca_2B_6O_8(OH)_2.2H_2O$ violently releases H_2O at 648 K, leaving a residue that is amorphous to X-rays and retains a proportion of water that is released only at higher temperatures. Rapid heating of the mineral vermiculite results [157] in exfoliation of the structure to give an expanded material, having useful insulating properties.

5.2. Glass formation and polymorphism

Reference has been made above to the possibility that an anhydrous, or lower hydrate, product may not recrystallize in the immediate vicinity of the dehydration interface. In many salts structural ordering may be delayed or not occur at all: moreover, such behaviour may be influenced by prevailing conditions. An additional possibility in some dehydrations is that the product

may be generated, and remain, in one, or more, vitreous states. This is of considerable practical importance in pharmaceutical formulations where the properties of prepared mixtures can be sensitive to the precise form, structures and textures, of the particles or crystallites. The dehydration of trehalose dihydrate has attracted particular attention in this respect, because dehydrations have been shown to yield several different anhydrous polymorphs, glassy and crystalline [158]. Progress is undoubtedly being made towards characterizing the complicated and conditions-dependent chemistry of anhydrous product formation. In addition to contributing to the understanding of this system, the report by Descamps and co-workers [158] reviews some of the problems identified and provides access to the literature. This active topic is mentioned here to encourage assessment of the relevance of these developing ideas in investigating interface properties and product structures, including the possibly of intervention of different amorphous phases, across a much wider range of dehydrations of crystalline hydrates.

5.3. Topotaxy

A reaction exhibits topotaxy if the solid product is formed in one, or more, crystallographically equivalent orientations relative to the reactant and if this reaction can proceed through the complete bulk of the reactant crystal [53-55,159]. At least some of the order and lattice orientation characteristics of the reactant are preserved across the interface discontinuity and are retained in the product. Structure conservation indicates that a proportion of the reactant components have undergone only minor displacements during passage of the reaction zone. Consideration of the structural features that remain apparently undisturbed can, in principle, provide mechanistic information about aspects of the chemical steps involved, and may be used to exclude processes that introduce disorder. Types of topotaxy have been discussed by Oswald [53,54,159] and examples include the dehydrations of $MoO_3.2H_2O$ ($\rightarrow$ $MoO_3.H_2O$ $\rightarrow$ MoO_3), of $Mg_2(OH)_2CO_3.3H_2O$, of $KVO_3.H_2O$ and of $Co_3(OH)_2(SO_4)_2.2H_2O$.

5.4. Surface reactions

Microscopic observations have shown that the surfaces of some crystalline hydrates, such as $KAl(SO_4)_2.12H_2O$, after having been subjected to dehydration conditions and subsequently exposed to water vapour, underwent superficial modifications to develop the 'orange peel' texture [44,47]. Chrome alum did not similarly retexture but surface reactivity was enhanced, as shown by the massive rise in numbers of nuclei formed on restoration of dehydration

conditions [20,44]. These behaviour patterns were ascribed to initial water losses, later followed by some rehydration, within a limited thickness of probably strained material at crystal surfaces. Recrystallization, to generate the product phase, was identified as the difficult step in initiating and maintaining reaction, dehydration by a nucleation and growth process [102]. An ability of water to promote the retexturing of partially dehydrated salt explains the enhanced reactivity at active and advancing nucleus boundaries [44]. Guarini and Dei [67] have subsequently demonstrated the more general occurrence of 'orange peel' texture formation, for eleven different hydrated salts. Thermal methods were used to study these reactions [47] and later work [160] was concerned with the changes that occur on ageing.

Surface dehydrations that produce a coherent, semi-permeable, or impermeable but flexible, boundary layer may prevent the escape of water released. This accounts for the bubble-like swellings formed during $NiSO_4.6H_2O$ dehydration under appropriate conditions [96]. Somewhat different behaviour was observed during the dehydrations of two coordination compounds of copper [161]. Water was lost smoothly from the powdered pyrimidinium complex salt below 413 K. In contrast, the onset of reaction in crystals is sharp when the temperature rises towards 373 K, with the sudden appearance of liquid bursting from the reactant particle before re-solidification at 393 K (WET 5 [3]). This is ascribed to the breaching of an almost impermeable superficial skin and differs from the comprehensive and coherent intracrystalline retentive structure that is maintained up to the vigorous disruption of colemanite [157].

Modifications, including the development of strain, within the surface layer during the onset of dehydrations (and other crystolysis reactions) may be the reason for the difficulties that have been experienced in correlating the positions of dislocations with those of growth nuclei (developed under dehydration conditions) in microscopic comparisons of matched pairs of cleavage faces [95]. It remains a priority for this subject to extend research to characterize in greater detail the chemistry of the initial reactions of surfaces, if we are to provide an adequate theoretical representation of nucleation phenomena.

5.5. Reactant dehydration

Studies of high temperature crystolysis reactions, including anion breakdown or other thermal processes, often use reactants prepared originally as hydrates. On heating, the constituent water is usually lost rapidly during an initial step, that may be completed before the attainment of reaction temperature. This may

not be detected (or even considered) when using an apparatus that incorporates a refrigerant trap. TG experiments have shown that the initial loss of water of crystallization is sometimes so rapidly completed that it does not overlap with the reaction to be studied (except, perhaps, by extending slightly the heat-up time).

It must be remembered that the structural and textural changes that accompany many dehydrations can transform the reactant in important respects. The crystal lattice, particle sizes, surface area and texture, crystal faces exposed, strain, types, concentrations and distributions of imperfections (etc.) all may be profoundly modified. A high reaction temperature may enable a proportion of the crystal imperfections introduced during restructuring to be removed by annealing. However, the overall effects of dehydration and/or recrystallization on the newly-formed reactant cannot be ignored.

This topic is beyond the scope of the present review, except to emphasize that, for hydrates, changes of the types described above are precursor steps in the preparation of the (usually anhydrous) reactant of interest. Two examples are given to illustrate the importance of these steps.

(i) The kinetic characteristics of cobalt oxalate decomposition [162] varied significantly with the temperature of the previous dehydration. Removal of water at 420 K gave a porous reactant, whereas at 470 K the anhydrous salt formed has a lower surface area.

(ii) The dehydration of nickel squarate dihydrate [163] occurs in a similar temperature range to that of anion ($C_4O_4^{2-}$) breakdown, 470 to 540 K. Considerable difficulties were experienced in obtaining reliable kinetic data for the decomposition step.

6. COMMENTS AND CONCLUSIONS

The recent literature provides considerable evidence that interest in dehydration chemistry has been maintained and continues. The large, relatively perfect crystals of many hydrated inorganic salts, that are easily prepared, have been selected as attractive reactants for the investigation of dehydrations in addition to other aspects of solid state chemistry. Complementary kinetic and microscopic studies for this type of thermal reaction have contributed notably to the development of the nucleation and growth and, indeed, all interface reaction models [1-3,10-12,51,73]. Recognition that bond redistributions occur preferentially within an advancing zone of chemical change, at or near the

reactant-product interface, has lead to the development [10] of the well-known [1,2,10-12,51] set of geometry-based kinetic expressions. These are accepted and appear as an important unifying feature of this field.

However, the early optimism, based on the initial (apparently rapid) progress in developing theoretical explanations of solid state reaction controls and mechanisms (e.g., the P-W model), has not been entirely realized. It now appears that dehydrations of crystalline hydrates may not be controlled by a single chemical step, as originally assumed or described by theory based on perceived parallels with the then successfully advancing theoretical concepts applicable to homogeneous processes. It has since become evident that the chemistries of crystolysis reactions are more difficult to characterize than was at first appreciated. Reaction reversibility and/or endothermicity can be rate controlling or, at least, rate influencing under some of the reaction conditions used for kinetic measurements. These properties, sensitive to the procedural variables [35], have been identified [31,32] as reasons for Smith-Topley behaviour. Again, probably due to reversibility, the overall kinetic characteristics are not always in accordance with expectation from the known rates of nucleation and of growth [3,17]. It further appears that the Polanyi-Wigner equation [11,20,25-27] is no longer generally acceptable as quantitative representation of interface reaction rates, where mechanisms are probably more complicated than the simple, one-step model on which this treatment was based. Recognition of the difficulties inherent in characterizing interface chemistry and the shortcomings of the available theory is, nevertheless, a type of progress. The present survey confirms that much is already known about dehydrations, though gaps and weaknesses are evident in the theory available, but advances still continue to be made in our understanding of these reactions.

For many dehydrations, the reliability of the magnitudes of reported Arrhenius parameters, and their significances, have not been established. Without a knowledge of the sensitivity of A and E_a to reaction conditions, their values cannot be taken as a measure of the rate of a postulated determining step [33-36]. Further work is required to establish how sensitive each dehydration is to the experimental environment because of the marked variations of the influence of the local availability of water vapour. For example, the rate of $NiC_2O_4.2H_2O$ dehydration is strongly influenced by $p(H_2O)$ [33], whereas alum dehydrations appear to be much less sensitive to the availability of water outside the crystal [17,44]. The dehydration of $NiSO_4.6H_2O$ is changed considerably by reaction conditions [7,95-99]. The necessity for making complementary and replicable measurements to obtain reproducible data has

been stressed [144,145] though not usually implemented. In addition to these effects of reversibility, self-cooling/(heating) also may exert a significant influence upon dehydration rates [31,32].

The interpretation of kinetic data, for measurements that have been positively related to a specific process, must proceed using theoretically acceptable reaction models and calculation methods [23,24]. An adequate description of rate characteristics requires specification of the 'kinetic triad', the kinetic model [$g(\alpha) = kt$] together with both Arrhenius parameters, A, E. The form of the kinetic model should express rate constants with the unit $(\text{time})^{-1}$ together with consistent usages of terms that conform to generally accepted chemical definitions. Moreover, kinetic analysis requires that data are required from multiple isothermal kinetic experiments, covering an adequate temperature range, and/or, when the non-isothermal approach is used, measurements must include a sufficient range of different heating rates. A single experiment of either type is insufficient to characterize the rate process [164].

Kinetic results obtained empirically, sometimes for a reaction under precisely specified conditions (which are not always reported), often have considerable practical value, perhaps for preparative or manufacturing purposes. However, data used to obtain insights into reaction chemistry, including mechanism, the reactivity controls or the influences of individual procedural variables [35], require much more comprehensive measurements and confirmatory observations than are sometimes completed. In the personal opinion of the author, progress in this field, and, indeed, for all crystolysis reactions, is impaired by the absence of accepted criteria capable of classifying different types of behaviour and in recognizing systematic trends of reactivity variations between related types of reactants. This lack of order [3] can be identified with limitations inherent in the theory that is currently available. One consequence is that observations for each reactant tend to be interpreted individually, so that chemical relationships between diverse rate processes are not always comprehensively, comparatively and critically explored. It is not clear whether this situation is a reason for, or the result of, the remarkable (and perhaps surprising) scarcity of critical reviews relating to these well-studied reactions.

Reasons for the wide diversity of dehydration behaviour patterns and kinetic characteristics observed for the numerous different hydrated salts are not hard to find. The problem is to systemize these differences and to represent the behaviour patterns reported into generally applicable theories [3,73,165]. Water is accommodated as H_2O within crystalline hydrates in diverse different retaining structures, having a range different of bonding strengths, involving several types and combinations of links, that include coordination as ligands,

through hydrogen bonds and/or as 'space fillers'. Water evolved on heating solids may, (from suitable reactants) alternatively be derived from hydroxyl and/or acid groups. Thus, the dehydrations of crystalline hydrates have been studied from below ambient temperature, 213 K [117] to above 650 K [104]. Also, as illustrated by several of the above examples, water evolution may proceed stepwise through a sequence of successive and distinct, stoichiometric dehydrations. Product recrystallization, which is a possible consequence of each step, may occur concurrently with water elimination, be delayed or not occur at all. The role of lattice reorganization in formulating reaction mechanisms for dehydrations, and other solid state processes, has been discussed in detail by Petit and Coquerel [165]. This article presents an Organization Chart that interrelates structural, physical and chemical features that control the changes that occur during and as a consequence of water elimination from crystalline hydrates. The Unified Model described provides a perspective useful for comparing and contrasting possible dehydration mechanisms for molecular crystals.

In conclusion, the author would stress the importance of applying complementary measurements to supplement and to confirm conclusions from the interpretation of rate studies (only) concerned with the dehydrations of crystalline hydrates (and, indeed, all crystolysis reactions). Indispensable contributions to all fundamental kinetic studies are the confirmation of reaction stoichiometry and the demonstration that each chemical change of interest is a *single* rate process. Conclusions concerning the geometry of interface advance, deduced through interpretation of kinetic data, may be confirmed (and, perhaps, sometimes obtained more directly and reliably) by microscopic observations. Derived kinetic parameters, A and E_a, may be capable of providing insights into interface chemistry, including indications of reactivity controls and the mechanism of the target reaction. The reliability of kinetic conclusions is increased by reconciling consistent information obtained from the widest range of relevant complementary experiments using diverse techniques: microscopy, X-ray diffraction, spectra, etc.

It the considered opinion of the author that critical and comparative surveys of the abundant literature are an essential 'next step' in developing the scientific foundation and theoretical framework that this topic now lacks. General progress is more likely through ordering of the knowledge already available than from additional kinetic investigations for novel reactants. The study of crystolysis reactions can be recognized as a separate discipline that presents greater intellectual challenges in chemical and mechanistic interpretations than has perhaps been generally appreciated. Nevertheless, there remains ample scope for the imaginative work that is required to build on, to extend and (most

importantly) to systematize the information that constitutes the substantial foundations that are already in place.

ACKNOWLEDGEMENT

I thank Professor Michael Brown for stimulating and illuminating discussions on the topics covered in this review, during the many years that we have worked together [166], and for his kind, constructive and generous help in preparing this paper for publication.

REFERENCES

1. A.K. Galwey and M.E. Brown, Handbook of Thermal Analysis and Calorimetry, Vol.1, (Ed. M.E. Brown), Elsevier, Amsterdam, 1998, Chap.3.
2. A.K. Galwey and M.E. Brown, Thermal Decomposition of Solids, Elsevier, Amsterdam, 1999.
3. A.K. Galwey, Thermochim. Acta, 355 (2000) 181.
4. A.F. Wells, Structural Inorganic Chemistry, 4th Edn, Clarendon, Oxford, 1975, p. 537-569.
5. R.W.G. Wyckoff, Crystal Structures, 2nd Edn, Vol. 3, Interscience, New York, 1965, p. 529-926.
6. M. Lallemant and G. Watelle-Marion, C. R. Acad. Sci. Paris, C264 (1967) 2030; C265 (1967) 627; C272 (1971) 642.
7. N. Koga and H. Tanaka, J. Phys. Chem., 98 (1994) 10521.
8. A.K. Galwey and G.M. Laverty, Thermochim. Acta, 138 (1989) 115.
9. P.W.M. Jacobs and A.R. Tariq Kureishy, Trans. Faraday Soc., 58 (1962) 551; React. Solids, Elsevier, Amsterdam, 1961, p. 353.
10. P.W.M. Jacobs and F.C. Tompkins, Chemistry of the Solid State, (Ed. W.E. Garner), Butterworths, London, 1955, Chap.7.
11. D.A. Young, Decomposition of Solids, Pergamon, Oxford, 1966.
12. M.E. Brown, D. Dollimore and A.K. Galwey, Comprehensive Chemical Kinetics, Vol.22, Elsevier, Amsterdam, 1980.
13. A.K. Galwey and G.M. Laverty, Solid State Ionics, 38 (1990) 155.
14. A.C. Cumming, J. Chem. Soc., 97 (1910) 593.
15. V.V. Boldyrev, Y.A. Gaponov, N.Z. Lyakhov, A.A. Politov, B.P. Tolochko, T.P. Shakhtshneider and M.A. Sheromov, Nucl. Inst. Methods Phys. Res., A261 (1987) 192.
16. G.G.T. Guarini, J. Thermal Anal., 41 (1994) 287.

17. A.K. Galwey and G.G.T. Guarini, Proc. R. Soc. (London), A441 (1993) 313.
18. M.E. Brown, A.K. Galwey and A. Li Wan Po, Thermochim. Acta, 203 (1992) 221; 220 (1993) 131.
19. H. Kodama and J.E. Brydon, Trans. Faraday Soc., 64 (1968) 3112.
20. W.E. Garner, Chemistry of the Solid State, (Ed. W.E. Garner), Butterworths, London, 1955, Chap.8.
21. A.K. Galwey and M.E. Brown, Proc. R. Soc. (London), A450 (1995) 501.
22. M.E. Brown and A.K. Galwey, Thermochim. Acta, 387 (2002) 173.
23. A.K. Galwey, Thermochim. Acta, 397 (2003) 249.
24. A.K. Galwey, Thermochim. Acta, 399 (2003) 1.
25. M. Polanyi and E. Wigner, Z. Phys. Chem., A139 (1928) 439.
26. B. Topley, Proc. R. Soc. (London), A136 (1932) 413.
27. A.K. Galwey, Thermochim. Acta, 242 (1994) 259.
28. M.E. Brown, A.K. Galwey and G.G.T. Guarini, J. Thermal Anal., 49 (1997) 1135.
29. B.V. L'vov, Thermochim. Acta, 373 (2001) 97.
30. B.V. L'vov, Thermochim. Acta, 315 (1998) 145.
31. G. Bertrand, M. Lallemant, A. Mokhlisse and G. Watelle-Marion, J. Inorg. Nucl. Chem., 36 (1974) 1303; 40 (1978) 819; see also : Phys. Chem. Liq., 6 (1977) 215; J. Thermal Anal., 13 (1978) 525; Thermochim.Acta, 38 (1980) 67.
32. B.V. L'vov, A.V. Novichikhin and A.O. Dyakov, Thermochim. Acta, 315 (1998) 169.
33. T.B. Flanagan, J.W. Simons and P.M. Fichte, Chem. Commun., (1971) 370.
34. D. Beruto and A.W. Searcy, J. Chem. Soc., Faraday Trans. I, 70 (1974) 2145.
35. F.H. Wilburn, J.H. Sharp, D.M. Tinsley and R.M. McIntosh, J.Thermal Anal., 37 (1991) 2003, 2021.
36. A.K. Galwey and M.E. Brown, Thermochim. Acta, 300 (1997) 107.
37. A.K. Galwey, Adv. Catal., 26 (1977) 247.
38. N.J. Carr and A.K. Galwey, Thermochim. Acta, 79 (1984) 323.
39. W.E. Garner (Ed.), Chemistry of the Solid State, Butterworths, London, 1955.
40. A.K. Galwey, J. Thermal Anal., 38 (1992) 99.
41. V.N. Makatun and L.N. Shchegrov, Russ. Chem. Rev., 41 (1972) 905.
42. N.Z. Lyakhov and V.V. Boldyrev, Russ. Chem. Rev., 41 (1972) 919.
43. H. Tanaka, Thermochim. Acta, 267 (1995) 29.

44. A.K. Galwey, R. Spinicci and G.G.T. Guarini, Proc. R. Soc. (London), A378 (1981) 477.
45. S.D. Bhattamisra, G.M. Laverty, N.A. Baranov, V.B. Okhotnikov and A.K. Galwey, Phil. Trans. R. Soc. (London), A341 (1992) 479.
46. A.K. Galwey, G.M. Laverty, V.B. Okhotnikov and J. O'Neill, J. Thermal Anal., 38 (1992) 421.
47. L. Dei, G.G.T. Guarini and S. Piccini, J. Thermal Anal., 29 (1984) 755.
48. M.A. Mohamed, A.K. Galwey and S. Halawy, Thermochim. Acta, 323 (1998) 27.
49. D.A. Young, Decomposition of Solids, Pergamon, Oxford, 1966, Chap. 3.
50. M.E. Brown, (Ed.), Handbook of Thermal Analysis and Calorimetry, Vol.1, Elsevier, Amsterdam, 1998.
51. M.E. Brown, Introduction to Thermal Analysis, Chapman and Hall, London, 1988; 2nd Ed., Kluwer, Dordrecht, 2001.
52. M.G. Burnett, A.K. Galwey and C. Lawther, J. Chem. Soc., Faraday Trans., 92 (1996) 4301.
53. H.R. Oswald, Proc. 6th Int. Conf. on Thermal Analysis, (Ed. W. Hemminger), Birkhaüser, Basel, 1 (1981) 1.
54. J.R. Günter and H.R. Oswald, Bull. Inst. Res. Koyoto Univ., 53 (1975) 249.
55. V.V. Boldyrev, React. Solids, 8 (1990) 231.
56. S.V. Vyazovkin and A.I. Lesnikovich, J. Thermal Anal., 35 (1989) 2169.
57. J.H. Flynn, Thermochim. Acta, 300 (1997) 83.
58. N. Koga and H. Tanaka, Thermochim. Acta, 303 (1997) 69.
59. V.B. Okhotnikov and N.Z. Lyakhov, J. Solid State Chem., 53 (1984) 161.
60. V.B. Okhotnikov, S.E. Petrov, B.I. Yakobson and N.Z. Lyakhov, React. Solids, 2 (1987) 359.
61. M.C. Ball, Thermochim. Acta, 24 (1978) 190.
62. H. Tanaka and N. Koga, J. Phys. Chem., 92 (1988) 7023.
63. D.E. Brown and M.J. Hardy, Thermochim. Acta, 90 (1985) 149.
64. E. Dubler and H.R. Oswald, Helv. Chim. Acta, 54 (1971) 1621, 1628.
65. N. Gérard, Bull. Soc. Chim. Fr., (1970) 103.
66. J.A. Couper and W.E. Garner, Proc. R. Soc. (London), A174 (1940) 487.
67. G.G.T. Guarini and L. Dei, J. Chem. Soc., Faraday Trans. I, 79 (1983) 1599.
68. A.K. Galwey, R.Reed and G.G.T. Guarini, Nature, London, 283 (1980) 52.
69. A.K. Galwey and M.A. Mohamed, Thermochim. Acta, 121 (1987) 97.

70. M.E. Brown, B. Delmon, A.K. Galwey and M.J. McGinn, J. Chim. Phys., 75 (1978) 147.
71. A.K. Galwey, Thermochim. Acta, 96 (1985) 259.
72. A.K. Galwey, N. Koga and H. Tanaka, J. Chem. Soc., Faraday Trans., 86 (1990) 531.
73. N. Koga and H. Tanaka, Thermochim. Acta, 388 (2002) 41.
74. V.B. Okhotnikov, N.A. Simakova and B.I. Kidyarov, React. Kinet. Catal. Lett., 39 (1989) 345.
75. M.E. Brown, R.M. Flynn and J.H. Flynn, Thermochim. Acta, 256 (1995) 477.
76. Yu. A. Gapanov, B.I. Kidyarov, N.A. Kirdyashkina and N.Z. Lyakhov, J. Thermal Anal., 33 (1988) 547.
77. H. Tanaka and N. Koga, J. Phys. Chem., 93 (1989) 7793; J. Thermal Anal., 36 (1990) 2601; Thermochim. Acta, 183 (1991) 125.
78. J. Huang and P.K. Gallagher, Thermochim. Acta, 192 (1991) 35.
79. V.V. Boldyrev, Bull. Soc. Chim. Fr., (1969) 1054.
80. C. Popescu, V. Jianu, R. Alexandrescu, I.N. Mihalescu, I. Morjan and M.L. Pascu, Thermochim. Acta, 129 (1988) 269.
81. D. Stoilova and V. Koleva, Thermochim. Acta, 255 (1995) 33.
82. M.C. Ball and L.S. Norwood, J. Chem. Soc. A, (1969) 1633; (1970) 1476; J. Chem. Soc., Faraday Trans. I, 69 (1973) 169; 73 (1977) 932; 74 (1978) 1477; React. of Solids, Chapman and Hall, London, 1972, p.717.
83. M.C. Ball and R.G. Urie, J. Chem. Soc. A, (1970) 528.
84. K. Fugii and W. Kondo, J. Chem. Soc., Dalton Trans., (1986) 729.
85. I.V. Melikhov, V.N. Rudin and L.I. Vorob'eva, Mendeleev Commun., (1991) 33.
86. F. Paulik, J. Paulik and M. Arnold, Thermochim. Acta, 200 (1992) 195.
87. M.C. Ball, Thermochim. Acta, 24 (1978) 190.
88. C.A. Strydom and G. Pretorius, Thermochim. Acta, 223 (1993) 223.
89. W.E. Garner and M.G. Tanner, J. Chem. Soc., (1930) 47; N.F.H. Bright and W.E. Garner, J. Chem. Soc., (1934) 1872; W.E. Garner and H.V. Pike, J. Chem. Soc., (1937) 1565.
90. A.I. Zagray, V.V. Zyryanov, N.Z. Lyakhov, A.P. Chupakhin and V.V. Boldyrev, Thermochim. Acta, 29 (1979) 115.
91. W-L. Ng, C-C. Ho and S-K. Ng, J. Inorg. Nucl. Chem., 34 (1978) 459.
92. M.L. Smith and B. Topley, Proc. R. Soc. (London), A134 (1932) 224.
93. S. El-Houte, M. El-Sayed and O.T. Sorensen, Thermochim. Acta, 138 (1989) 107.
94. P.V. Ravindran, J. Rangarajan and A.K. Sundaram, Thermochim. Acta, 147 (1989) 331.

95. J.M. Thomas and G.D. Renshaw, J. Chem. Soc. A, (1969) 2749, 2753, 2756.
96. G.G.T. Guarini and M. Rustici, React. Solids, 2 (1987) 381.
97. G.G.T. Guarini and A. Magnani, React. Solids, 6 (1988) 277.
98. S.G. Sinha, N.D. Deshpande and D.A. Deshpande, Thermochim. Acta, 113 (1987) 95; 144 (1989) 83; 156 (1989) 1.
99. P.N. Nandi, D.A. Deshpande and V.G. Kher, Thermochim. Acta, 32 (1979) 143.
100. G.P. Acock, W.E. Garner, J. Milsted and H.J. Willavoys, Proc. R. Soc. (London), A189 (1947) 508.
101. W.E. Garner and T.J. Jennings, Proc. R. Soc. (London), A224 (1954) 460.
102. A.K. Galwey, G.M. Laverty, N.A. Baranov and V.B. Okhotnikov, Phil. Trans. R. Soc. (London), A347 (1994) 139, 157.
103. A. Cohen and M. Zangen, Thermochim. Acta, 133 (1988) 251.
104. D.C. Anderson and A.K. Galwey, Canad. J. Chem., 70 (1992) 2468.
105. A.K. Galwey and G.M. Laverty, Thermochim. Acta, 228 (1993) 359.
106. G.G.T. Guarini and S. Piccini, J. Chem. Soc., Faraday Trans. I, 84 (1988) 331.
107. G.G.T. Guarini and R. Spinicci, J. Thermal Anal., 4 (1972) 435.
108. R.K.Osterheld and P.R. Bloom, J. Phys. Chem., 82 (1978) 1591.
109. J.A. Lumpkin and D.D. Perlmutter, Thermochim. Acta, 249 (1995) 335; 202 (1992) 151.
110. Vu Van Hong and J. Sundström, Thermochim. Acta, 307 (1997) 37.
111. J.R. Günter, J-P. Matthieu and H.R. Oswald, Helv. Chim. Acta, 61 (1978) 328, 336.
112. M.A. Mohamed and S.A. Halawy, J. Thermal Anal., 41 (1994) 147.
113. H. Tanaka and N. Koga, J. Phys. Chem., 92 (1988) 7023; Thermochim. Acta, 163 (1990) 295.
114. D.J. Devlin and P.J. Herley, Thermochim. Acta, 104 (1986) 159; React. Solids, 3 (1987) 75.
115. M.C. Ball, C.M. Snelling and A.N. Strachan, J. Chem. Soc., Faraday Trans. I, 81 (1985) 1761.
116. J. Paulik, F. Paulik and M. Arnold, J. Thermal Anal., 27 (1983) 409, 419.
117. M.L. Franklin and T.B. Flanagan, J. Phys. Chem., 75 (1971) 1272; J. Chem. Soc., Dalton Trans., (1972) 192.
118. H. Kawaji, K. Saito, T. Atake and Y. Saito, Thermochim. Acta, 127 (1988) 201.
119. K.R. Sakurai, D.A. Schaeffer and P.J. Herley, Thermochim. Acta, 26 (1978) 311.

120. G.G.T. Guarini and L. Dei, Thermochim. Acta, 250 (1995) 85.
121. E.A. Prodan and L.A. Lesnikovich, Thermochim. Acta, 203 (1992) 269.
122. N. Petranovic, U. Mioc and D. Minic, Thermochim. Acta, 116 (1987) 131, 137.
123. M.C. Ball and M.J. Casson, J. Chem. Soc., Dalton Trans., (1973) 34.
124. T.C. Viamakis, P.J. Pomonis and A.T. Sdoukos, Thermochim. Acta, 173 (1990) 101.
125. M. Trojan and D. Brandova, Thermochim. Acta, 157 (1990) 1, 11; 159 (1990) 1, 13; 161 (1990) 11.
126. T.A. Clarke and J.M. Thomas, J. Chem. Soc. A, (1969) 2227, 2230.
127. J.R. Günter, J. Solid State Chem., 35 (1980) 43.
128. Y. Masuda and K. Nagagata, Thermochim. Acta, 155 (1989) 255; 161 (1990) 55.
129. Y. Masuda and Y. Ito, J. Thermal Anal., 38 (1992) 1793.
130. Y. Masuda, Thermochim. Acta, 60 (1983) 203.
131. M.C. Ball and L. Portwood, J. Thermal Anal., 41 (1994) 347.
132. Y. Masuda, S. Shirotori, K. Minigawa, P.K. Gallagher and Z. Zhong, Thermochim. Acta, 282/283 (1996) 43.
133. Y. Masuda, K. Iwata, R. Ito and Y. Ito, J. Phys. Chem., 91 (1987) 6543.
134. A. Coetzee, M.E. Brown, D.J. Eve and C.A. Strydom, J. Thermal Anal., 41 (1994) 357.
135. J-C. Mutin, G. Watelle-Marion, Y. Dusausoy and J. Protas, Bull. Soc. Chim. Fr., (1972) 4498 (see also : (1969) 58).
136. H. Tanaka, Y. Yabuta and N. Koga, React. Solids, 2 (1986) 169.
137. J. Casabo, T. Flor, F. Texidor and J. Ribas, Inorg. Chem., 25 (1986) 3166.
138. J.E. House and F.M. Tahir, Polyhedron, 10 (1987) 1929.
139. J.E. House, Thermochim. Acta, 38 (1980) 59.
140. H.E. LeMay and M.W. Babich, Thermochim. Acta, 48 (1981) 147.
141. M. Corbella and J. Ribas, Inorg. Chem., 25 (1986) 4390; 26 (1987) 3589; (see also : 23 (1984) 2236).
142. J. Ribas, A. Escuer and M. Monfort, Thermochim. Acta, 76 (1984) 201; 103 (1986) 353.
143. J. Ribas, A. Escuer, M. Serra and R. Vicente, Thermochim. Acta, 102 (1986) 125.
144. J.E. House and R.P. Ralston, Thermochim. Acta, 214 (1993) 255.
145. J.E. House, J.K. Muehling and C.C. Williams, Thermochim. Acta, 222 (1993) 53.
146. R.S. Gordon and W.D. Kingery, J. Amer. Ceram. Soc., 49 (1966) 654; 50 (1967) 8.

147. N.H. Brett, K.J.D. MacKenzie and J.H. Sharp, Q. Rev. Chem. Soc., 24 (1970) 185.
148. K.J.D. MacKenzie and R.H. Meinhold, Thermochim. Acta, 230 (1993) 339.
149. O. Chaix-Pluchery and J.C. Niepce, React. Solids, 5 (1988) 69.
150. R.M. Cornell, S. Mann and A.J. Skarnulis, J. Chem. Soc., Faraday Trans. I, 79 (1983) 2679.
151. J.C. Niepce and G. Watelle-Marion, C. R. Acad. Sci. Paris, C269 (1969) 683; C270 (1970) 298.
152. C.N.R. Rao, Proc. Indian Nat. Sci. Acad., A52 (1986) 699.
153. M.C. Ball and R.F.M. Coultard, J. Chem. Soc. A, (1968) 1417.
154. P. Ramamurthy and E.A. Secco, Canad. J. Chem., 47 (1969) 2181, 3915; 48 (1970) 1619, 2617, 3510.
155. K. Beckenkamp and H.D. Lutz, Thermochim. Acta, 258 (1995) 189.
156. B. Okhotnikov, I.P. Babicheva. A.V. Musicantov and T.N. Aleksandrova, React. Solids, 7 (1989) 273.
157. L. Stoch, J. Thermal Anal., 37 (1991) 1415.
158. J.F. Willart, A. De Gusseme, S. Hemon, M. Descamps, F. Leveiller and A. Rameau, J. Phys. Chem. B, 106 (2002) 3365; Solid State Commun., 119 (2001) 501.
159. H.R. Oswald and J.R. Günter, React. Solids, Proc. 10th Int. Conf., (1984) 101.
160. G.G.T. Guarini and L. Dei, Thermochim. Acta, 269/270 (1995) 79.
161. T. Manfredi, G.G. Pellicani, A.B. Corradi, L.P. Battaglia, G.G.T. Guarini, J.G. Giusti, G. Pon, R.D. Willett and D.X. West, Inorg. Chem., 29 (1990) 2221.
162. D. Broadbent, D. Dollimore and J. Dollimore, J. Chem. Soc. A, (1966) 1491.
163. A.K. Galwey and M.E. Brown, J. Chem. Soc., Faraday Trans. I, 78 (1982) 411.
164. F. J. Gotor, J.M. Criado, J. Malek and N. Koga, J. Phys. Chem. A, 104 (2000) 10777.
165. S. Petit and G. Coquerel, Chem. Mater., 8 (1996) 2247.
166. S. Vyazovkin and T. Ozawa (Eds), Thermochim. Acta, 388 (2002) 1-460.

Handbook of Thermal Analysis and Calorimetry. Vol. 2: Applications to Inorganic and Miscellaneous Materials
M.E. Brown and P.K. Gallagher, editors
© 2003 Elsevier B.V. All right reserved.

Chapter 13

THERMAL ANALYSIS IN METALLURGY

Shaheer A. Mikhail* and A. Hubert Webster**

Formerly: CANMET, Department of Natural Resources Canada, Ottawa, Ontario, Canada

1. INTRODUCTION

The application of thermal analysis in different fields of science and engineering is an extensive topic which has been the subject of significant interest particularly since the beginning of the modern era of thermal analysis in the early 1960s. With the continuous development of new techniques and the rapid improvements in data acquisition, manipulation and presentation using modern computers, more and more applications are constantly being explored and reported. In the last several years, applications in the fields of cement chemistry [1], clays and minerals [2], polymeric materials [3,4], pharmaceuticals [5] and other general applications [6,7], have been discussed in detail. Thermal analysis techniques have also been used extensively in the field of metallurgy and a large number of publications (several thousands in the last four decades) on this subject have been identified in the literature. These cover topics such as corrosion, solidification/microstructure, extractive metallurgy, sintering, roasting, catalysis, powder metallurgy, thin films, composite materials and others. For obvious practical reasons, however, only a select number of publications, in which thermal analyses were used as primary techniques or important supplementary techniques, were chosen to address metallurgical topics that have received most attention in the recent past. From the many thermal analysis techniques that have been used in a wide variety of applications, thermogravimetry (TG), differential thermal analysis (DTA) and differential scanning calorimetry (DSC) were found to be the most commonly used in metallurgy. The principles, operation and commercial availability of these and other techniques are discussed in detail in Volume 1 of this Handbook.

---

* Current address: 14 Meadowbank Drive, Ottawa, Ontario K2G-0N9, Canada
** Current address: 1198 Checkers Road, Ottawa, Ontario K2C-2S7, Canada

Consequently, only specific features like sample or container geometry, unusual instrument configurations or exceptional experimental conditions will be referred to in this chapter.

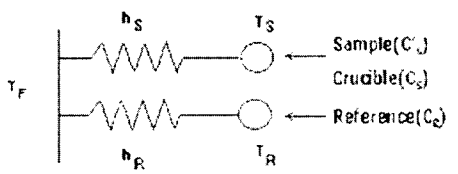
2. EQUILIBRIUM PHASE DIAGRAMS

2.1. General

Equilibrium relationships between substances in different states, or between reactants and reaction products, have been traditionally expressed as phase diagrams correlating temperature and composition. Conventional cooling and heating curves, where the sample temperature is recorded as a function of time, have been, and in some cases still are, used to determine equilibrium phase boundary changes and ultimately to construct phase diagrams, predominantly in unary and binary metallurgical systems. During the 50's and 60's, thermal analysis techniques, such as DTA, have, to a large extent, replaced cooling / heating curves, due to their superior sensitivity, accuracy, versatility and convenience. The general principles and approaches for the determination of simple and complex phase diagrams using thermal analysis as principle techniques were adequately discussed by Gutt and Majumdar [8], Wunderlich [in 1] and Brown [9].

2.2. Phase transitions, eutectics and equilibrium lines and surfaces

Methods for the evaluation of types and temperatures of phase transitions were developed by Shull [10] using DTA, together with transmission electron microscopy, optical microscopy and XRD. First-order transitions, e.g., melting, boiling and allotropic structural changes, are characterized by discontinuities in the first derivative of the free energy with respect to temperature, $\partial G/\partial T$, and in the enthalpy, H, as functions of temperature. In second-order transitions, the second derivative of the free energy is discontinuous and the heat capacity, C_p, has a maximum at the transition temperature. Different stages on the DTA curve (ΔT vs T), before, during and after the transition, were treated on the basis of a heat transfer model:



T_F, T_s, T_R = temperatures of furnace, sample, reference; C_s, C_s', C_R = heat capacities of crucible, sample, reference; h_s = thermal conductance between furnace and sample crucible; h_R = thermal conductance between furnace and reference; $T_R = T_0 + \beta t$ (β= rate of heating).

An "ideal" case with no thermal lag between the sample and crucible and a "non-ideal" case with finite thermal conductance between the sample and crucible were discussed. For the ideal case, the first deviation of the peak from the baseline should be the equilibrium transition temperature for diffusionless transitions with no kinetic barrier. For the case with finite heat conductance between sample and crucible, there will be a lag before peak starts. It was suggested that the transition be studied at different heating rates and peak starting temperatures be extrapolated to zero heating rate. It is best to approach a transition from a single phase region, whether this be by heating or cooling, when the transition involves changes in composition.

The Ti-Al system was treated as example. The stability range of the α-Ti phase, previously accepted as 25 at.% Al, was revised to 45 at.% Al. DTA curves for selected alloys in this system are shown in Figure 1. The two apparent endothermic effects in the low-aluminium alloys $Ti_{81}Al_{19}$, $Ti_{77}Al_{23}$ and $Ti_{75}Al_{25}$ were attributed to the $\alpha \rightarrow Ti_3Al$ and $\alpha \rightarrow$ ß transformations (known for pure titanium). In addition, a eutectoid reaction: $\alpha \rightarrow Ti_3Al + \gamma$, was reported to take place around 45 at.% Al at about 1125 °C.

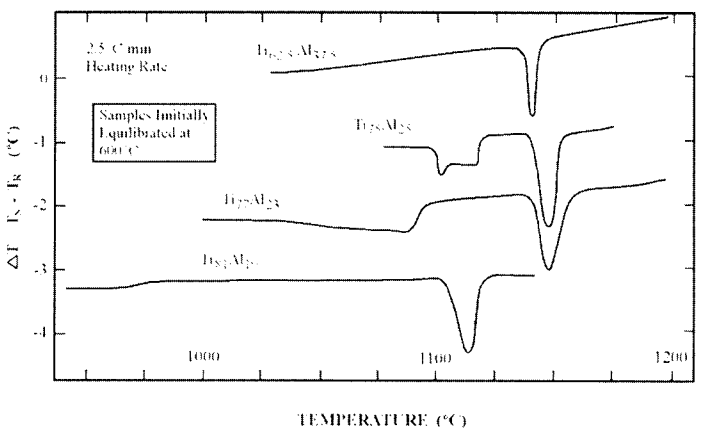


Figure 1. Temperature difference (<T) between the sample and reference as a function of reference temperature for several Ti-Al samples containing less than 40 at % Al, initially equilibrated at 600 °C for 3 weeks, measured using a heating rate of 2.5 °C min^{-1}. From R.D. Shull, reference 10.

The author remarked that, under proper conditions, DTA is a powerful technique that can be used to determine the presence and temperature of first and second-order transformations, while the nature of transformations can best be

determined by supplementary techniques such as transmission electron microscopy, optical microscopy and XRD, which were used in this study.

Titanium aluminides are considered good candidates for aerospace and automobile applications due to their low density and superior high-temperature strength, creep properties and corrosion resistance. Alloying with Mn, V, and Cr in the proper ratios was found to modify their microstructure, resulting in a substantial improvement in their poor room-temperature ductility which is restricting their application. Butler and McCartney [11] studied the phase diagram of the ternary system Ti-Al-Mn using DTA at 10 K min^{-1} heating and cooling rates in flowing ultra-high purity argon. Scanning electron microscopy was used to examine the microstructures of the different alloys. Four alloys Ti:Al = 1.14 with Mn (5, 10, 20 30 at.%) were examined. The results indicated the presence of γ-TiAl, α_2-Ti_3Al and a Laves phase (Mn_2Ti) and evidence for a eutectic valley which separates Liq. + Laves phase region from Liq. + α, Liq. + β, and Liq + γ-TiAl regions in the ternary system. High-temperature DTA was recognized as a useful tool in the determination of the solid state phase transitions and melting reactions.

Reliable equilibrium solid-solid transition temperatures usually are difficult to obtain directly from DTA due to superheating or undercooling. Zhu et al. [12] have developed a DTA procedure to deal with this aspect in the determination of phase region boundaries in phase diagrams. In the procedure, the onset transformation temperature is determined by using different heating rates and followed by extrapolation to calculate the equilibrium transition temperature, T_o, using the following formulae [13,14]:

$$T = C[\beta T.\exp(Q_b/RT)]^{1/3} + T_o \qquad (1)$$

where Q_b = lattice diffusion activation energy
β = heating rate (K min^{-1})
C = constant
T = onset temperature during heating.

Equation (1) was simplified because Q_b needed to be estimated.

$$T = C'\beta^{1/3} + T_o \qquad (2)$$

where C' is a constant.

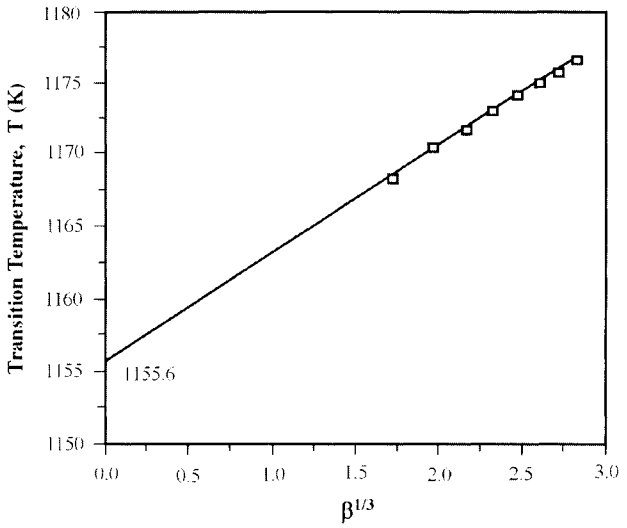


Figure 2. Determination of the equilibrium α / β transition temperature for pure Ti using equation 2. From Y.T. Zhu et al., reference 12.

The formulae were used to determine the α/β transition of pure titanium metal. Equation (1) gave 1155.3 K and equation (2) gave 1155.6 K, for T_o, indicating the validity and accuracy of the simplified equation (2). The extrapolation using equation (2) is illustrated in Figure 2. The roles of grain boundary diffusion, nucleation, strain energy, surface energy of the new phase and temperature non-uniformity of metallic specimens were also discussed.

The FeO-K_2O section of the K-Fe-O ternary system was investigated by Seetharaman et al. [15] using DTA and EMF measurements at low oxygen potentials. The ternary system is of particular interest in conjunction with the circulation of alkali metals, and their interaction with iron oxides, in the iron-making blast furnace. The thermal stability of the K/Fe/O ternary compounds is also of major significance due to their role in corrosion by the liquid metal coolant. In the DTA measurements the liquidus temperatures were generally determined on cooling and the solidus on heating. The samples were contained in Pt-Pt10%Rh crucibles which were sealed to avoid the loss of sample by volatilisation. The solubility of potassium in wüstite was found negligible, which was attributed to the large difference between the ionic sizes of K^+, 1.33, and Fe^{2+}, 0.76 Å. The phase transformation of metallic iron ($\alpha \rightarrow \gamma$) at 914 °C was identified. Other transition points at 577 and 720 °C were attributed to phase transformations of the compound $K_2Fe_2O_4$. Another possible phase transformation for this compound around 1145 °C, detected only on heating, was

also reported. The presence of a eutectic around the ratio K/(K+Fe)=0.255 and 1170 °C was suggested.

The increasing interest in the Cu-In-Pb system may be attributed to the superior properties exhibited by the lead-indium solders and the potential for these solders to replace conventional lead-tin solders used in microelectronics packaging. These desirable properties include a higher thermo-mechanical fatigue resistance and a lower liquidus (flow) temperature. Together with the Pb/In solder, copper is normally used as a metallization agent in joint pads and circuit tracks. DSC up to 400 °C and DTA for higher temperatures, together with electron probe microanalysis (EPMA), were used by Bolcavage et al. [16] to determine isotherms and isopleths of importance in this ternary system and to explain the kinetics of intermetallic interaction at the interface, which affect the strength and reliability of the joint. A better sensitivity of the DSC at lower temperature was evident. An example of a DSC heating curve for a ternary alloy (15at.%Cu-75at.%In-10at.%Pb) is shown in Figure 3. Two reactions or phase transitions can be seen for this alloy. DTA heating curves for the same alloy, Figure 4, indicated that the liquidus for this composition is situated at about 543 °C. The authors found no evidence of ternary intermetallic compounds and little solubility of copper in the lead-indium solutions at low temperatures. The latter finding was expected, because copper is virtually insoluble in either lead or indium.

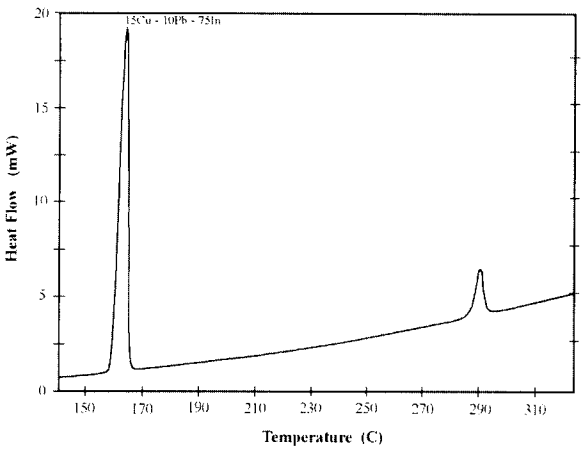


Figure 3. DSC heating curve for an alloy with composition 15Cu-75In-10Pb. From A. Bolcavage et al., reference 16.

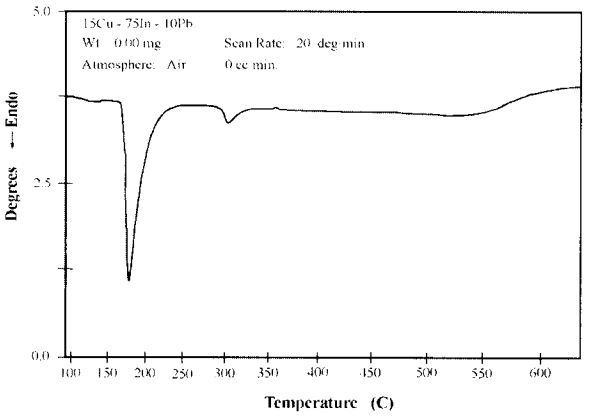


Figure 4. DTA heating curve for an alloy with composition 15Cu-75In-10Pb. From A. Bolcavage et al., reference 16.

Transition metal carbides represent a series of materials of particular importance in the production of high-hardness specialty steels and alloys with superior abrasion resistance. Iron alloys with carbide-forming elements such as vanadium, within the Fe-C-V system, were the subject of investigation by Kesri and Durand-Charre [17]. Relative to iron, vanadium is one of several elements with much higher affinity to carbon and, consequently, during solidification, vanadium carbide would form in preference to Fe_3C. Solid-liquid equilibria in the iron-rich corner of the ternary system were determined and the mechanisms of transformations that occur during cooling were analyzed using differential thermal analysis with optical and transmission electron microscopy and electron microprobe analysis as supplementary techniques. Quenched interrupted DTA, a modified DTA technique developed earlier by Durand-Charre et al. [18], was used. In this technique, the solidification is monitored under controlled conditions in the differential thermal analyzer, then the sample is quenched at a certain moment to arrest the microstructure for further examination. A DTA cooling curve for an iron-rich alloy containing 2.25% C and 5.85% V (alloy A) is shown in Figure 5. The different endothermic peaks were related to: 1. Primary austenite formation, 2. VC-A eutectic, 3. An order-disorder transition of $VC_{0.89}$ to V_6C_5, 4. A phase transition from $VC_{0.89}$ to V_8C_7 and 5. Pearlitic reaction. The solidification phases and transformation temperatures were identified for several other compositions. Two invariant points were found in the iron-rich corner of the system: a pseudo-peritectic point involving δ-ferrite, austenite, VC carbides and the liquid, and a ternary eutectic point involving austenite, VC, V_3C carbides and the liquid. The effect of additional elements, such as Si, Ni, Mo and Cr, to the Fe-C-V system was also investigated.

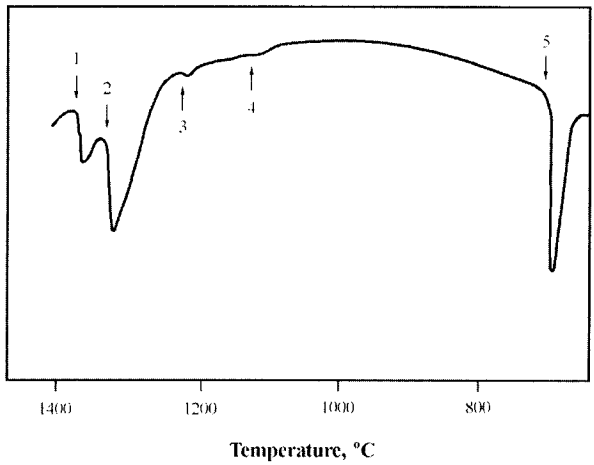


Figure 5. DTA curve for alloy A (2.25%C, 5.85%V, balance Fe), during cooling. From R. Kesri and M. Durand-Charre, reference 17.

An attempt to determine the phase relations in the Pt - Se system for the first time and to construct the complete binary phase diagram was made by Richter and Ipser [19], using DTA, metallography and XRD. In the DTA experiments, samples of different compositions were vacuum sealed in fused silica containers and heated at relatively slow rates (0.2 - 2 K min^{-1}). The liquidus curve was determined between 35 and 42 and between 45 and 66.7 at.%Se, Figure 6. Dashed lines are used to designate the speculative segments. As can be seen from Figure 6, the authors were able to characterize and verify the presence of the two phases Pt_5Se_4 and $PtSe_2$, which were earlier reported in the literature.

The Sn-Pb phase diagram, and the liquidus line in particular, are of major importance in the electronics and other industries due to the common use of the Sn-Pb alloys in small connections soldering. The phase diagram was reconstructed by Kuck [20] using DSC measurements of selected compositions of the alloy. The samples were melted in a nitrogen atmosphere and then slowly cooled at 5 °C min^{-1}. The liquidus temperature, T_L, was determined as the beginning of crystallization on cooling, (T_C), and end of fusion on heating (T_M). The solidus was determined as the temperature at which melting commenced on heating, T_O. The solvus was more difficult to determine experimentally and, therefore, the solid-solution limit at the eutectic temperature was determined by extrapolating the eutectic heat of fusion, plotted against the alloy composition. The liquidus temperature was used to determine the alloy composition. The hypereutectic alloy was distinguished from the hypoeutectic alloy by the ratio of ΔH (solid solution) / ΔH (eutectic). Figure 7 represents DSC curves of two Sn-

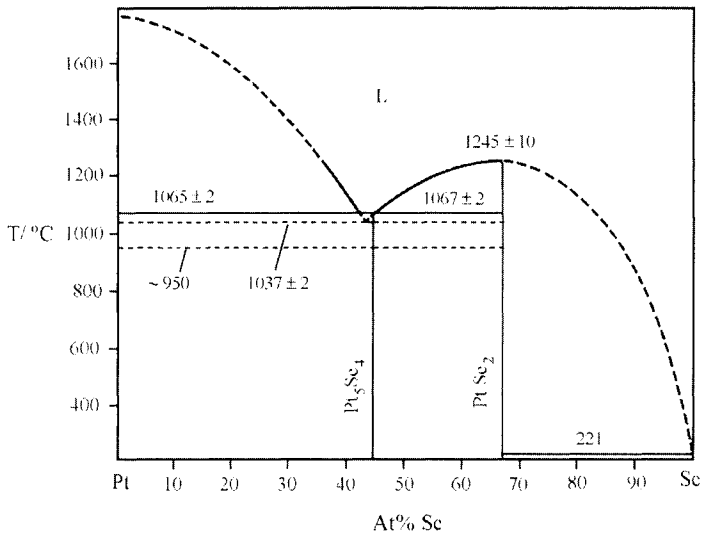


Figure 6. Platinum-selenium phase diagram according to the results of Richter and Isper. From K.W. Richter and H. Isper, reference 19.

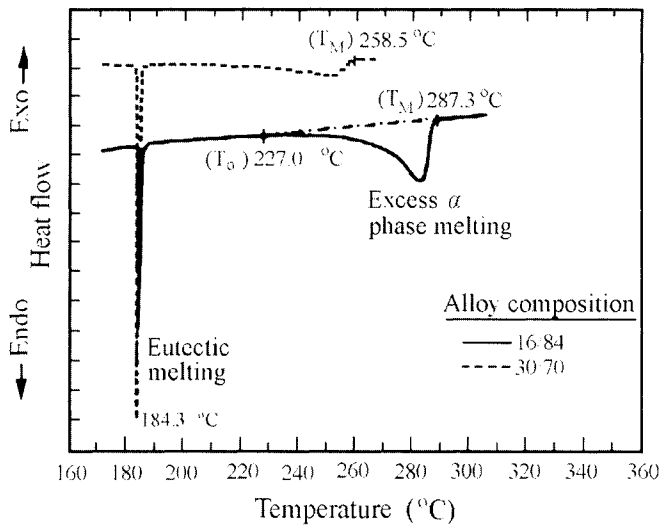


Figure 7. DSC curves comparing the melting of a 16/84 Sn/Pb alloy with that of a 30/70 Sn/Pb alloy. From V.J. Kuck, reference 20.

Pb alloys in the system. The Pb/Sn phase diagram was constructed with an eutectic at 182.5 °C and 62 mass % Sn. The author maintained that thermal analysis was more reliable and practical than conventional wet chemical analysis, atomic absorption or X-ray fluorescence techniques for the determination of alloy compositions.

Welding tests, DTA, and microscopy were employed by Lienert et al. [21] to examine the solidification behaviours of Hastelloy B-2 (Ni + 27.7 mass% Mo, 1.0 Fe ..) and Hastelloy W (Ni + 23.6 Mo, 6.3 Fe, 5.3 Cr ..). These corrosion-resistant alloys are used in aerospace and chemical processing industries. DTA, in argon atmosphere, was used to identify high-temperature phase transformations and solidification events in these alloys. Tungsten was used as reference material. On heating, the solidus and liquidus were detected at 1376 and 1431 °C for Hastelloy B-2 and 1333 and 1396 °C for Hastelloy W. On cooling, B-2 showed a very small peak at 1277 °C and Hastelloy W showed two minor peaks at 1290 °C and 1250 °C related to the solidification of minor constituents. Welding tests showed longer fusion-zone cracks for W than for B-2. Microstructure examinations showed more minor interdendritic material in Hastelloy W welds. Hot cracking associated with interdendritic material rich in Mo and depleted in Ni was found to correlate with low-temperature DTA peaks detected on cooling.

Due to the high cost of precious metals, copper/phosphorus-based brazing filler metals are gradually replacing silver-based ones. For practical reasons, however, small amounts of silver or tin (sometimes both) are still added to the brazing alloy in order to lower its operating (melting) temperature. In this context, Takemoto et al. [22] explored the ternary systems Cu-Ag-P and Cu-Sn-P using DTA (on cooling), optical microscopy, electron probe microanalysis and XRD. In the Cu-Ag-P system, the liquidus temperature of the copper primary phase surface decreased with the increase in the silver content. The effect of small changes in the silver content was evident; an alloy with 1% Ag was found to solidify in a binary eutectic structure, namely, Cu + Cu_3P while that with 2% Ag solidified in a ternary eutectic structure; Cu + Ag +Cu_3P. In the Cu-Sn-P system, at low phosphorus content, the addition of tin changed the primary phase surface from copper solid solution to Cu_3P, indicating that tin has a similar effect to that of phosphorous in that region with respect to the kind of primary phase precipitation.

Since the sixties, the ternary system Pb-Sn-Se in general and the (Pb,Sn)Se solid solution in particular have attracted the attention of researchers in the field of semiconductors and optics, especially as related to infrared detection. In this study, DTA, DSC, optical and electron microscopy and XRD were used by Dal Corso et al. [23] to explore the subternary system PbSe-SnSe-Se. Several ternary alloys were made by mixing, melting and annealing for extended periods

of time the binary compounds PbSe, SnSe and $SnSe_2$. The binary system PbSe-SnSe was determined, Figure 8, and was found to contain two solid solutions, α (rich in PbSe) and γ (rich in SnSe) and a γ_1-γ_2 SnSe phase transition. The suggested solubility limits were 59 mol% and 76 mol% SnSe, respectively, at the invariant line (870 °C). The isoplethal PbSe-$SnSe_2$ was also determined and was found to contain five two-phase fields and six three-phase fields and was characterized by the presence of horizontal lines at 220 °C (eutectic), 540 °C (monotectic) and 589 °C (peritectic). Finally, the planes related to the eutectic, monotectic and peritectic reactions in the subternary system PbSe-SnSe-Se were identified, a eutectic at 75 mol% SnSe was confirmed and a new interpretation was offered.

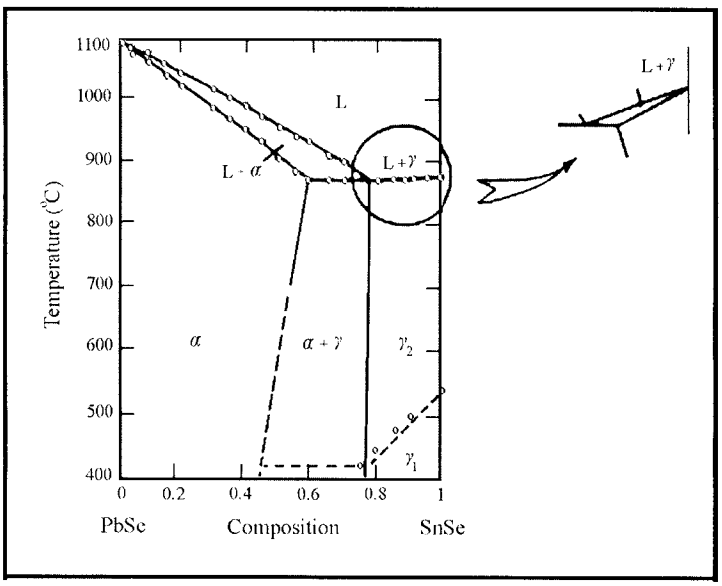


Figure 8. PbSe-SnSe phase diagram. From S. Dal Corso et al., reference 23.

In connection with the development of advanced magnetic materials, the Fe-Co-Gd system is one of several transition metal / rare earth systems with significant importance. Atiq et al. [24] used XRD and electron probe microanalysis to investigate compositions and crystal structures, and DTA to determine phase transformations, in this system up to 33at.%Gd. Several ternary alloys were prepared in sealed, evacuated silica tubes and annealed at 1323 K for 14 days before examination. Three sets of ternary compounds, namely, $(Fe_{1-x}Co_x)_{17}Gd_2$, $(Fe_{1-x}Co_x)_3Gd$ and $(Fe_{1-x}Co_x)_2Gd$, where $0<x<1$, with complete mutual solid solubility, and three binary compounds, namely, $Fe_{23}Gd_6$,

Co_5Gd and Co_7Gd_2, with limited solid solubility for cobalt and iron, were determined in the ternary system.

2.3. Determination of phase diagrams

As discussed in the previous section, DTA and DSC are very useful in the determination of phase transitions, eutectic temperatures, liquidus temperatures and other features that are required in the determination of equilibrium phase diagrams. A selection of recent phase diagram determinations that have involved thermoanalytical methods will be considered in this section to illustrate the applications of these methods for binary and ternary systems.

The increasing interest in rare-earth alloying is attributed to their significant effect, in small concentrations, on the characteristics of metallic matrices. The Pr-Mn system was determined by Saccone et al. [25] using DTA (heating and cooling at 8 - 10 °C min^{-1}), XRD, metallography and electron probe microanalysis. In the DTA experiments, tantalum or molybdenum crucibles were used to contain the sample and reference materials due to the reactivity of the samples with alumina. The resulting Pr-Mn phase diagram is shown in Figure 9. A eutectic at 25 at. % Mn and 660 °C was detected. Pr_6Mn_{23} with a low limit of stability (650 °C), a peritectic decomposition at 790 °C and $PrMn_2$, which formed metastably but decomposed on annealing, were also identified. According to points plotted on the phase diagram, the peritectic for Pr_6Mn_{23} produced a thermal effect mainly on heating. Thermal effects observed at 600 °C near the Mn side of diagram and detectable only on cooling were attributed to a sluggish $\alpha = \beta$ transition in Mn [equilibrium 710 °C]. The peritectic decomposition of metastable $PrMn_2$ generated a thermal effect at 740 °C on heating; this disappeared on annealing the sample just below 740 °C.

The phase diagram of the V-Te system was constructed by Terzieff and Ipsen [26] using DTA, XRD and magnetic susceptibility measurements. This system has attracted much attention due to the attractive magnetic properties of the vanadium tellurides. For the DTA measurements, the samples were sealed under vacuum in specially designed quartz containers. The magnetic susceptibility measurements were conducted on the stoichiometric composition V_3Te_4 in the temperature range 1150-1350 K. Based on clear thermal effects and obvious discontinuity in the magnetic susceptibility measurements in the composition range 56-63 at.% Te, the presence of a high-temperature modification of monoclinic V_3Te_4 around 1180 K was suggested by the authors.

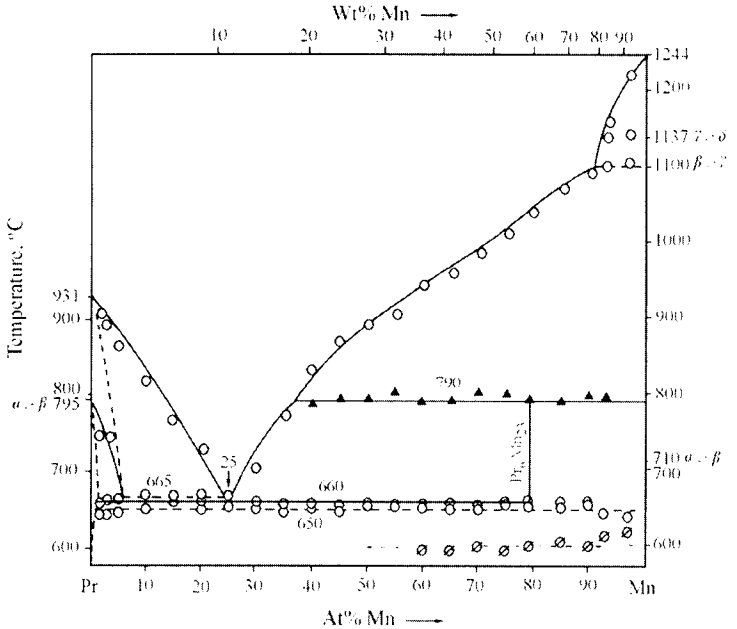


Figure 9. Phase diagram of the Pr-Mn system: ▲- thermal effects observed mainly on heating; o - thermal effects observed on both heating and cooling (averaged values); ⇔ - thermal effects observed only on cooling (these may be related to the sluggish rate of the α/β Mn transformation. From A. Saccone et al, reference 25.

The vanadium-tritium phase diagram was determined by Lässer and Schober [27], using differential thermal analysis as a principal technique and autoradiology as a supplementary one. Vanadium-based alloys are of significant interest in many high-temperature applications and were reported as possible construction materials in fusion reactors. The system was studied within the composition range $0 \leq x \leq 0.8$ ($x = [T]/[V]$) and the temperature range $100 < T < 473$ K. The samples were sealed in aluminium crucibles under sub-atmospheric pressure to minimize the risk of leakage of tritium. The transition temperatures were all determined on heating and the resulting V-T phase diagram was constructed and compared with previously determined phase diagrams of V-D and V-H.

The binary phase diagrams of Cr-Se and Fe-Se were studied by Katsuyama et al. [28] in the compositional regions $CrSe_x$ and $FeSe_x$, where $1.0 \leq x \leq 1.4$ and in the temperature range ambient to 1000 °C using DTA. The samples were sealed under vacuum in quartz ampoules and a heating (or cooling) rate of 20-30 °C min^{-1} was employed. XRD was also used to identify the materials at different

stages. The two systems were found to be very similar in the range of composition studied. In the above-mentioned region of both systems, the phase transformation: $M_7Se_4 \rightarrow M_3Se_4 \rightarrow CdI_2$-type structure (M is Cr or Fe) was evident. The process was interpreted on the basis of an order-disorder transition of metal vacancies that occurs on heating.

Differential thermal analysis, optical microscopy, SEM and XRD were used by Dubost et al. [29] to determine the ternary phase diagram Al-Li-Mg. In this system, the magnesium-rich region is of particular importance in foundry applications, the lithium-rich region, in electrochemical applications and the aluminium-rich region, in aeronautic applications. Equilibrium, intermetallic phases in this ternary system were identified as follows:

1. δ-AlLi, cubic, melts congruently,
2. Al_2LiMg, cubic, melts incongruently,
3. $Mg_{17}Al_{12}$, cubic, and
4. Al_3Mg_2, cubic, melts congruently.

The following invariant reactions were identified in the Al-rich side of the ternary diagram:

Liq.+ δ-AlLi $\rightarrow$ α-Al + Al_2LiMg	peritectic reaction at 528 °C,
Liq.+ $Al_2LiMg \rightarrow$ α-Al + $Mg_{17}Al_{12}$	peritectic reaction at 485 °C, and
Liq. $\rightarrow$ α-Al + Al_3Mg_2 + $Mg_{17}Al_{12}$	eutectic reaction at 447 °C.

Theoretical calculations based on available data of the binary systems were also carried out, taking into consideration the interaction between different phases. A good agreement with the experimentally determined monovariant lines in the ternary system was found.

The tin- and lead-rich sides (>30%) of the binary systems Sc-Sn and Sc-Pb were investigated by Palenzona and Manfrinetti [30] using DTA, metallography, XRD and electron microscopy. Scandium is a reactive rare earth element with a relatively high melting point (1541 °C). In the DTA experiments, molybdenum sample containers were used and heating / cooling rates of 10 or 20 °C min^{-1} were applied. The similarity between the two systems was evident, Figures 10 and 11, with the phases Sc_5Sn_3 and Sc_5Pb_3 melting congruently at 1800 °C and 1700 °C, respectively, and the phases Sc_6Sn_5 and Sc_6Pb_5 forming by peritectic reactions at 1455 °C and 1290 °C, respectively. In the Sc-Sn system, however, two more intermediate phases, namely, $ScSn_2$ and ScSn, were identified, both forming by peritectic reactions at 895 °C and 945 °C, respectively. Sc_5Sn_3 and Sc_5Pb_3 were the only phases known for these systems before this study.

Isoperibolic calorimetry, DSC and DTA were used by Hassam et al. [31] to determine the equilibrium surfaces in the Ag-Au-Ge system. Several alloys were examined and both the binary and ternary phase diagrams were determined. The equilibrium temperatures and thermodynamic functions of the three constituent binary systems were also used to calculate the ternary system. A satisfactory agreement between the experimental and the calculated values was limited only to the liquidus surface.

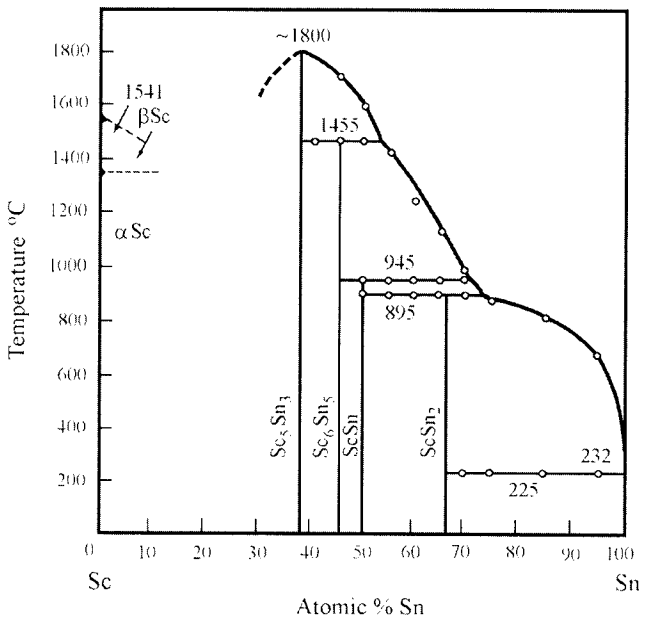


Figure 10. Scandium-tin phase diagram. From A. Palenzona and P. Manfrinetti, reference 30.

The phase diagram of Y-Tl was determined by Saccone et al. [32] for the first time using DTA, metallography, electron probe microanalysis and XRD. In the DTA, the samples were contained in tantalum crucibles sealed under argon and heating/cooling rates of 2-10 °C min^{-1} were used. Eutectic reactions at 1085 °C and 20 at.%Tl and at 303 °C and >99.5 at.%Tl were detected. Five intermetallic phases, namely, Y_5Tl_3, Y_5Tl_{3+x}, YTl, Y_3Tl_5 and YTl_3 were identified. The first melts congruently at 1470 °C and the second was presumed to form by a peritectic-type or a peritectoid reaction and decomposes at 1180 °C. The last three phases were found to melt incongruently at 1220 °C, 980 °C and 880 °C, respectively. An α/ß transformation of Tl at 235 °C was also determined. The

authors found it difficult to determine, with any degree of accuracy, the narrow regions of solid solubility with DTA.

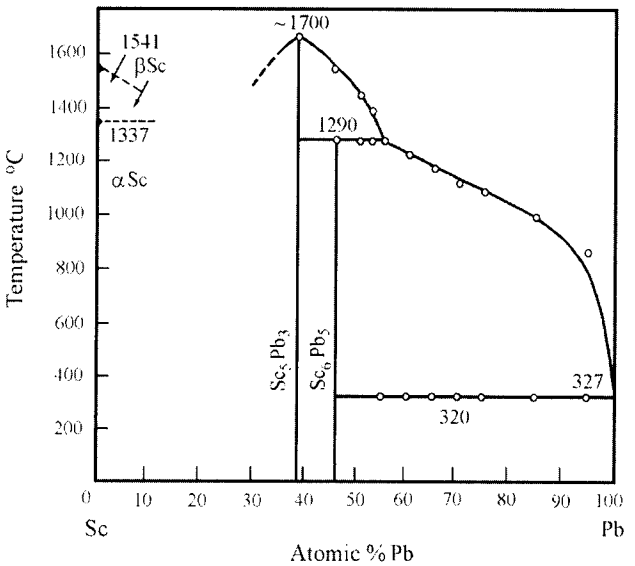


Figure 11. Scandium-lead phase diagram. From A. Palenzona and P. Manfrinetti, reference 30.

Significant progress has been made in the last few years in the production of permanent magnets using transition-metals rare-earth alloys such as CoSm and FeNdB. To acquire more knowledge on the latter system, Faudot et al. [33] used DTA, metallography and XRD to examine the constituent binary system Fe-Nd. One incongruently melting compound, $Fe_{17}Nd_2$, was identified. A peritectic reaction: $Fe_{17}Nd_2 \rightarrow$ liquid + Fe_γ, was found to take place at about 1210 °C and a eutectic reaction: $Fe_{17}Nd_2$ + α-Nd → liquid, was found to occur at 684 ±0.5 °C and 76.5 at.%Nd. A very limited solid solubility of Fe in Nd (about 0.12 at.%) was detected. The α/ß polymorphic transformation of pure neodymium was found to occur at 856 °C. A DTA curve for pure neodymium is shown in Figure 12 and the proposed binary phase diagram in Figure 13.

The ternary system Zn-Ga-Hg was studied by Nosek et al. [34] for the first time using DTA, at a heating / cooling rate of 2 °C min^{-1}. XRD at room temperature was also used to identify different products. Ternary alloys, prepared in special glass ampoules sealed under an argon atmosphere, were examined by DTA in the temperature range 70 to 450 °C. Due to the

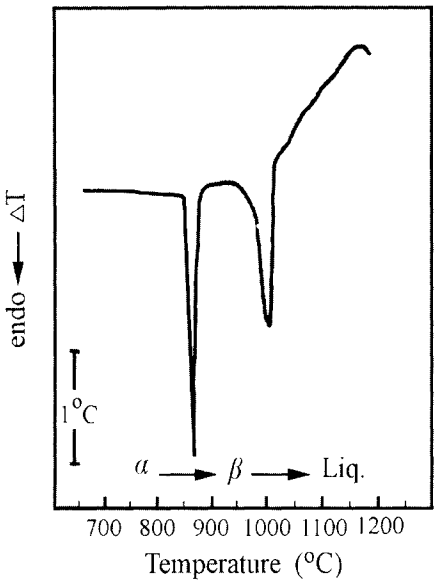


Figure 12. DTA curve for pure neodymium heated in a stream of argon after preliminary degassing in vacuum at about 300 °C. From F. Faudot et al., reference 33.

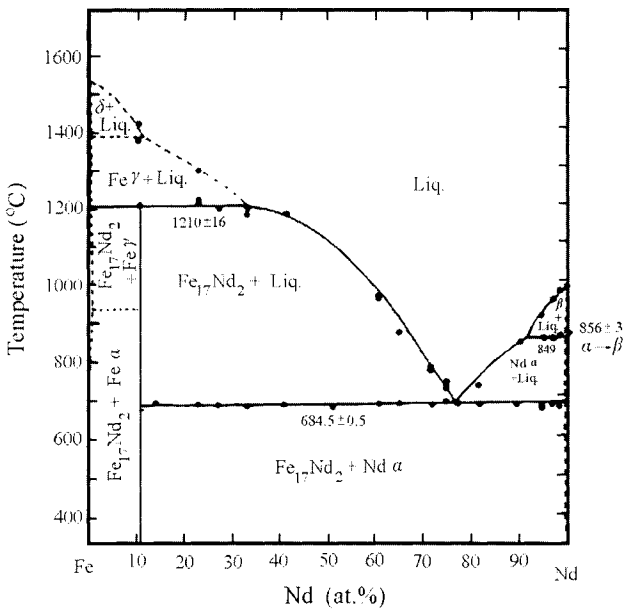


Figure 13. Proposed phase diagram for iron-neodymium. From F. Faudot et al., reference 33.

susceptibility of gallium-containing alloys to supercooling, the thermal data were collected on both heating and cooling. The proposed ternary diagram contained no ternary intermetallic compounds. It contained, however, a limited solid solubility region as well as the following four nonvariant equilibria:

$L1 \rightarrow L2 + Zn + Ga$ at 21 °C, monotectic
$Zn + L \rightarrow \gamma + Ga$ at 1 °C, peritectic
$\gamma + L \rightarrow \beta + Ga$ at –10 °C, peritectic
$Ga + L \rightarrow \beta + Hg$ at –41 °C, peritectic

where γ and β are intermediate phases in the Hg-rich field of the system.

2.4. Verification and assessment of phase diagrams

Well documented thermoanalytical results can be used in subsequent work for the critical assessment of phase diagrams; a few examples of this will be considered in the present section. Additional thermoanalytical experimental investigation may be required to clarify the results of previous phase diagram work.

The Ni-Pr diagram was assessed by Pan and Nash [35], essentially on the basis of earlier work by Vogel [36] and Pan and Cheng [37] who used DTA and XRD. The presence of seven intermetallic compounds, namely, Pr_3Ni, Pr_7Ni_3, PrNi, $PrNi_2$, $PrNi_3$, Pr_2Ni_7 and $PrNi_5$ was established. Besides the melting points of Ni and Pr and the allotropic transformation of the latter, the system also exhibited five eutectic and three peritectic reactions and four congruent meltings.

The chromium-osmium phase diagram was assessed by Venkatraman and Neumann [38], primarily on the basis of an earlier work by Svechnikov et al. [39], who used DTA and XRD. This system is of notable importance due to the interesting magnetic and electrical properties of the CrOs alloys. The results indicated an extensive terminal solid solubility and two intermediate phases, namely, Cr_3Os and Cr_2Os, occurring at about 25 and 33 at.% Os. The former phase, Cr_3Os, was earlier identified as a superconductor [40,41].

Foltyn and Peterson [42] conducted a critical review of earlier work [43-45] carried out on the system Pb-Pu using DTA as principal technique and metallography, XRD and electron microprobe analysis as supplementary techniques. The binary phase diagram of this system was reconstructed by the authors and the presence of six metallic compounds, namely, Pu_3Pb, Pu_5Pb_3, Pu_5Pb_4, Pu_4Pb_5 (tentative), $PuPb_2$ and $PuPb_3$ was affirmed. The presence of a eutectic at 68.8 at.% Pb and 1129 °C, and four peritectic decompositions of Pu_3Pb at 896 °C, of Pu_5Pb_3 at >1300 °C, of Pu_4Pb_5 at 1185 °C, and of $PuPb_2$ at 1129 °C were also indicated. Six allotropes were verified for plutonium between ambient and the melting point (640 °C).

Kim et al. [46] reinvestigated the complex Pd-Te binary system using DTA, XRD, electron probe microanalysis and reflected-light microscopy. For the DTA measurements, mixtures of the starting materials were sealed under vacuum in silica containers and heated at 6 or 12 °C min^{-1} to the desired temperature. All transitions were determined on heating. Eight phases were detected and verified: $Pd_{17}Te_4$ (or "Pd_4Te"), $Pd_{20}Te_7$, Pd_8Te_3, Pd_7Te_3, Pd_9Te_4, Pd_3Te_2, PdTe and $PdTe_2$. The solid solubility of Te in Pd was found to be about 13.5 at.% at 700 °C, 14.8 at.% at 800 °C and 10.8 at.% at 1000 °C. The peritectic decomposition of $Pd_{17}Te_4$ at 770 °C and a eutectic between $Pd_{17}Te_4$ and $Pd_{20}Te_7$ at 23.5 at.%Te and 720 °C were identified. The phase Pd_8Te_3 was found to melt congruently at 900 °C and to have polymorphic transformations at 270 and 680 °C. Pd_7Te_3 (a newly reported phase) showed thermal effects at 470, 595 and 830 °C attributable to two polymorphic transformations and melting, respectively. Pd_9Te_4 was found to melt incongruently at 605 °C with a possible phase transformation at 462 °C. Pd_3Te_2 showed endothermic effects at 462 °C (polymorphic transformation) and 504 °C. A eutectic between Pd_9Te_4 and Pd_3Te_2 was detected at 39 at.%Te and 498 °C. The existence of the phases PdTe and $PdTe_2$ was also confirmed and no solid solubility of Pd in Te was reported. DTA was found to be invaluable in determining this complex system and in clarifying earlier conflicting data in the literature.

3. TRANSFORMATIONS INVOLVING NON-EQUILIBRIUM PHASES

3.1. Introduction

Some significant applications of DSC to metallurgical studies pertaining to advanced solidification processing were reviewed by Cantor [47]:

Solid fraction vs. temperature: A DSC curve obtained on cooling through solidification can be integrated to give the latent heat of solidification. The fraction of metal solidified as a function of temperature also can be estimated from the DSC curve. This data can be used in modelling spray-forming processes in which metal atomized into a gas stream is deposited onto a collector. Results for particle velocity, temperature of particles and solid fraction were presented as functions of axial distance from the atomizer. Heat loss and solidification for a squeeze casting process were also modelled [48].

Heterogeneous nucleation: An alloy consisting of 10-100 nm droplets embedded in a solid matrix can be cooled and the nucleation of the droplets followed by DSC. Results for In particles in an Al matrix showed about 56 °C of supercooling. A model for heterogeneous nucleation was discussed. The effects of agents added to promote nucleation and hence achieve grain refinement (smaller grain size) can be investigated [49].

Crystallization of amorphous alloys: Crystallization of melt-spun amorphous alloys can be investigated by DSC. A Fe-Si-B amorphous alloy, used for low-loss transformer cores, was heated at a series of rates, and exothermic crystallization peaks were recorded. Crystallization peaks from isothermal DSC scans were also determined. The results could be treated using the Johnson-Mehl-Avrami equation,

$$f = 1 - \exp[-(kt)^n],$$

where f is the crystalline fraction after an annealing time t, and k is a rate coefficient. The exponent n for the Fe-Si-B alloy was about 4, corresponding to bulk nucleation and linear 3-dimensional growth. For an Fe-Cr-Mo-B alloy, n = 3, corresponding to linear 3-dimensional growth on pre-existing nuclei [50].

A number of thermal analysis applications dealing with transformations in non-equilibrium phases may be roughly grouped under the following four titles. Many other relevant topics are found in the literature and the present grouping is only intended to provide a demonstration of the breadth of the subject and the versatility of the TA techniques in this field.

3.2. Rapid diffusionless transformation - martensite

When certain alloy phases, such as the austenite phase of steels, are very rapidly cooled into a temperature region where the austenite becomes metastable, the alloy may undergo a diffusionless transformation to a new phase, martensite; this transformation involves displacement of the atoms in the crystal structure and distortion of the crystal lattice. The process is reversible on heating, and the alloy returns exactly to the microstructure and crystal structure that it had before the transformation to the martensite phase (provided that the alloy does not undergo decomposition to a more stable phase assemblage). More recently, it has been demonstrated that for certain alloys that undergo a martensite transformation, such as NiTi, the martensite platelets can be induced under mechanical stress to align the orientation of the distortion so that a macroscopic change in shape occurs. On heating through the temperature at which the reverse transformation back to austenite occurs, the alloy specimen will return to its original microstructure and the macroscopically distorted specimen will return to its original shape. This phenomenon, the shape memory effect, has been the subject of much recent research. Because the formation of martensite and the reverse transformation involve considerable changes in enthalpy, the heat effects can be readily detected by DTA or DSC.

The rapid solidification of shape memory alloys with special mechanical properties leads to the formation of different microstructures, depending on the cooling rate. Donner [51] used DSC and other techniques to determine the

starting temperature and the mechanism of the martensitic transformation during cooling of Fe-Mn-Si and Cu-Al-Ni alloys that had been rapidly solidified by the melt spinning technique. In the Fe-Mn-Si alloy, the transformation starting temperature, M_s, and Néel temperature decrease with the increase in cooling rate. The change in the transformation behaviour and, consequently, the shape memory effect and mechanical properties of the alloy, were attributed to internal stresses and defect densities preserved by the fast cooling rates. The content of residual austenite (incomplete martensitic transformation) also increased with the increase in cooling rate. In the Cu-Al-Ni alloy, the cooling rate did not have a significant effect on the homogeneous microstructure consistently obtained.

DSC played an important role in the production of controlled transformation Ni-Ti alloys which are very difficult to manufacture commercially. Johnson et al. [52] used DSC to determine and compare the martensite/austenite transformation temperatures of nickel-titanium powders prepared by vacuum arc remelting / atomization and high-temperature annealing. Mixtures of the Ni and Ti powders were hot isostatically processed at 900 °C and subjected to the thermal measurements. Figure 14 shows the heating and cooling profiles of a $Ni_{55}Ti_{45}$. A_s and A_f signify the austenite start and finish, respectively, on heating, and M_s and M_f, the martensite start and finish, respectively, on cooling. Powder metallurgical processing, after quenching and blending different compositions, was found to result in the elimination of macrosegregation and a drastic reduction of microsegregation, both of which are inherent characteristics of 'normal' solidification processes. Macrosegregation results in a sluggish completion of the transformation reaction and microsegregation in a larger $\Delta T_{As\text{-}Af}$. The relationship between the transformation temperature and the blend ratio was found to be linear. Thermal arrest DSC experiments, involving the cooling of the samples below M_f and reheating, were also carried out and were found to cause splitting in the transformation endotherm. The authors reported that DSC has played a significant role in the production of controlled-transformation NiTi.

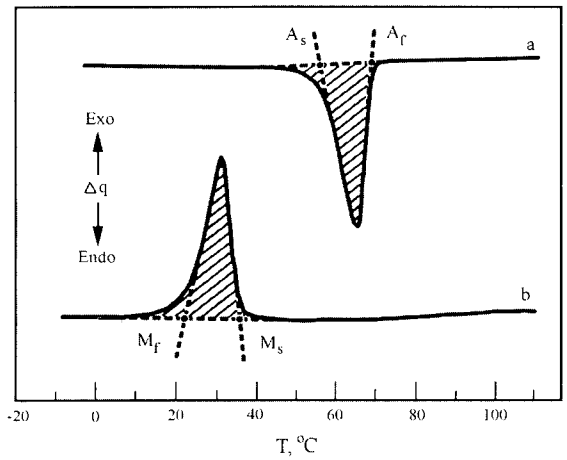


Figure 14. Typical DSC curve for NiTi; (a) heating, (b) cooling. From W.A. Johnson et al., reference 52.

NiTi with excess titanium was also prepared by hot pressing with added TiC and the austenitic/martensitic transformations were studied by Mari and Dunand [53] using DSC on cooling and on heating. Thermal cycling was done between -10 and 170 °C and cooling/heating curves for the first and the 100th cycles were determined. Two subsidiary peaks, one on cooling and one on heating, were detected. The transformation, temperatures, M_s, M_f, A_s, A_f, all decreased with cycling; all but M_s decreased with the added second phase, TiC. The heat of transformation also decreased with cycling and in the presence of the second phase. Figure 15 shows the influence of the TiC addition on the transformation temperature after one thermal cycle, at a heating/cooling rate of 3 °C min^{-1}. The results were interpreted in terms of the formation of some rhombohedral R phase from fcc B_2 phase on cooling, which transforms to two somewhat different martensite phases (M_1 and M_2); on heating, these transform to the B_2 phase in slightly different temperature regions. The presence of TiC suppresses the formation of the R phase. The effects of cycling and of the second phase were attributed to internal misfit stresses. Changes in enthalpies of transformation were attributed to elastic stored energy and to some untransformed B_2 austenite phase.

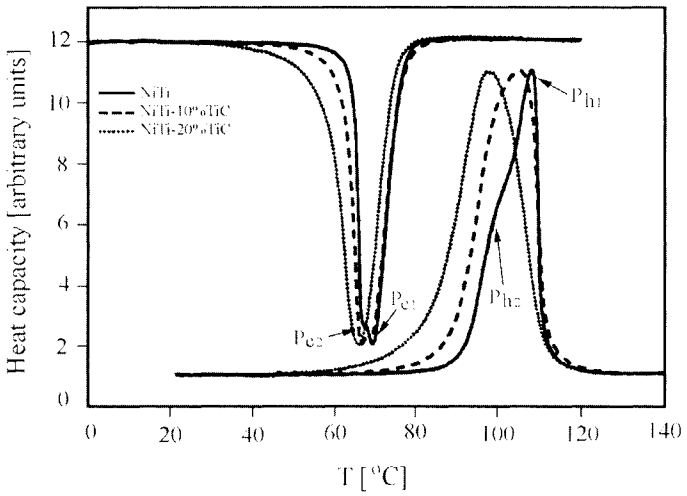


Figure 15. DSC curves for NiTi with and without TiC; first cooling-heating cycle, with a scanning rate of 3 K/min. From D. Mari and D.C. Dunand, reference 53.

3.3. Common transformations in metals and alloys

In alloy systems in which there is limited solid solubility of an alloying metal in the major constituent, the solubility of the alloying metal generally decreases with decreasing temperature. If a homogeneous solid solution is formed by annealing at high temperature and then rapidly quenched, the homogeneous solid solution may be retained in a metastable supersaturated condition at the lower temperature. In some alloy systems the metastable solid solution may begin to transform toward a more stable condition on annealing, or aging, at an intermediate temperature. During this transformation the mechanical strength of the alloy often will increase considerably before finally decreasing as the system approaches equilibrium. This phenomenon of age hardening is of great practical importance, especially for aluminum alloys used for structural applications. The heat effects that occur during the aging process may be followed by DSC.

The precipitation in Al-Cu alloys takes place through the sequence: solid solution → Guinier-Preston(I) zones → θ"→ θ'→ θ, where the θ phase is $CuAl_2$ (tetragonal). The formation of the GP(I) zones decreases the electrical conductivity (σ) compared to the super-cooled solid solution, while the formation of θ' and θ phases increases σ. The precipitation hardening in the alloy AA-2011 (Cu 5.4 mass %, Fe 0.31%, Si 0.12%, Pb 0.35%, Bi 0.44%, bal. Al) was studied by García Cordovilla and Louis [54] using DSC, in dry N_2, with pure Al as reference. Electrical conductivity and Vickers hardness (VH) were measured on samples quenched from the appropriate temperatures. All samples

were solution heat treated at 525 °C for 5 hours and water quenched before ageing heat-treatment at various temperatures from 25 °C to 420 °C. DSC peaks were attributed to:

A: formation of GP zones, exothermic, below 100 °C
B: dissolution of GP zones, endothermic, about 190 °C
C: reversion of θ" phase, endothermic, about 220 °C
D: formation of θ' phase, exothermic, about 300 °C
E: precipitation of θ phase, exothermic, about 420 °C
F: dissolution of θ phase, endothermic, increasing to 500 °C

Some peaks varied with the heating rate, and some peaks did not appear, depending on the ageing heat treatment. Overlap of peaks was suspected, because more than one reaction could be proceeding at a given time. A sample annealed at 400 °C for 6 h and cooled, being close to equilibrium, showed only the dissolution of the θ phase (F). Only the as-quenched sample showed peak A, followed by peaks B, D, E and F. In samples aged at 170 °C the first endotherm was attributed to dissolution of θ" (C), whereas in samples aged at 25° and 100 °C the first endotherm was attributed to dissolution of GP zones (B), Figure 16. Samples aged at these temperatures showed similar behaviours above 300 °C, i.e., at peaks (D), (E) and (F). A sample aged at 250 °C for 5 hours showed only peaks (E) and (F), with perhaps some indication of dissolution of the θ' phase.

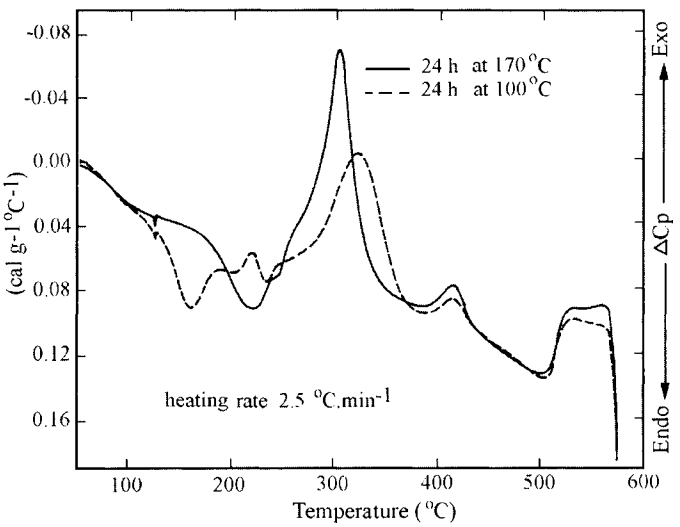


Figure 16. DSC curves for samples of aluminum alloy AA-2011 aged for 24 hours at two different temperatures; heating rate of 2.5 °C min^{-1}. From C. García Cordovilla and E. Louis, reference 54.

Activation energies for reactions (E) and (D) were estimated using Kissinger's method from the results of a series of experiments at different heating rates. Changes in the electrical conductivity and hardness were correlated with the DSC results and were used to identify the nature of the process associated with each peak. Dissolution of Cu-containing phases into the α solid-solution decreased the electrical conductivity, while precipitation increased it. The formation of coherent phases (GP zones, θ", θ') increased hardness, and dissolution of these phases decreased it. Cold work on the alloy accelerated the formation of the θ' phase during DSC, and decreased the temperature of peak (C). A very small sharp endotherm was observed at about 125 °C, which corresponded to the Pb-Bi eutectic; these elements are added to the alloy to improve machinability.

Shenoy and Howe [55] used DSC to study a Weldalite™ type alloy, RX 818. Al-Li alloys of the Weldalite type are candidates for use in airframes. Alloy RX-818 (3.6 mass % Cu, 0.9 % Li, 0.4% Mg, 0.4% Ag, 0.13 % Zr, balance Al) has $T_1(Al_2CuLi)$ as the principal strengthening phase, with small amounts of $S'(Al_2CuMg)$ and $\delta'(Al_3Li)$; $\theta'(CuAl_2)$ also occurs but may not be involved in strengthening. The alloy was treated to T8 temper (solution anneal, cold work, aging at 160 °C for 16 h). Further exposures were for up to 2500 h at 107, 135 and 163 °C. DSC was done in nitrogen at heating rates of 5, 10 and 20 °C min^{-1}, with Al as reference. TEM studies on samples quenched from various temperatures had identified the following peaks:

90 °C - endotherm, dissolution of δ'
135 °C - endotherm, dissolution of Guinier-Preston zones
160-280 °C - endotherm, dissolution of T_1
280-300 °C - exotherm, precipitation of θ' (may overlap with the dissolution of T_1)
300-400 °C - precipitation and/or dissolution of θ and Ag/Mg phases

The size and temperature of the T_1 peak depended on the exposure treatment of the sample. Estimates of the relative T_1 volume fraction were made from the area of the T_1 peak; this fraction increased with exposure temperature to 135 °C and then dropped. Relative size distributions were estimated from the ΔC_p - T shape of the T_1 peak, on the basis that smaller T_1 particles dissolved at lower temperatures. Coarsening of the T_1 particles occurred during all exposures. Changes in tensile strength were rationalized in light of the effects of T_1 volume fraction and size distribution, and θ' precipitation. Activation energies for T_1 dissolution were estimated using Kissinger plots.

The characterization of the metallurgical behaviour of commercial borated stainless steels in the temperature range associated with their fusion welding was

carried out by Robino and Cieslak [56]. Certain borated alloy steels are being considered as good candidates for structural use (in addition to their current use in thermal neutron shielding) in the nuclear industry due to their desirable mechanical properties and neutron absorption ability. DTA in inert atmosphere was the main technique used to identify solidus and liquidus temperatures as a function of the boron concentration. Solidification microstructures and mechanical properties were also examined and correlated to the thermal behaviour.

Figure 17 depicts the DTA heating/cooling curves of a commercial type stainless steel (304B2A) with an intermediate boron content of 0.68%. The first deviation from the base line (point 1) corresponds to the initial melting and the reaction of the boride contained with the surrounding austenite to form an eutectic-like liquid. Temperature 2 corresponds to the exhaustion and complete melting of the boride. Temperatures 3 and 4 correspond to the initial and complete melting of austenite, respectively. During the cooling cycle, temperature 5 signifies an initial supercooled solidification of primary austenite,

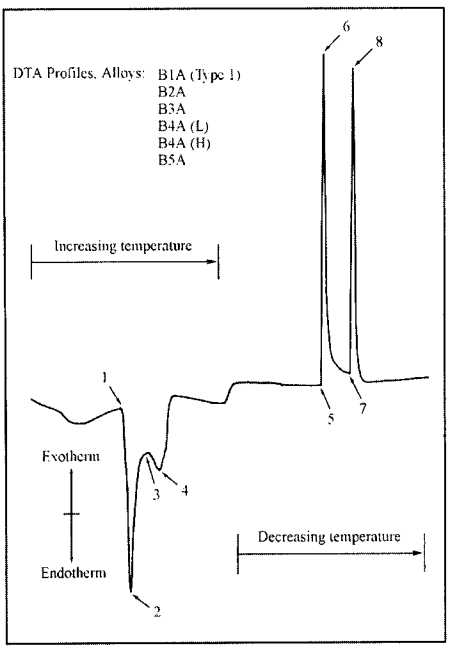


Figure 17. DTA curve for the borated stainless steel alloy 304B2A. The curve is representative of the behavior of alloys B1A through B5A. From C.V. Robino and M.J. Cieslak, reference 56.

ending at temperature 6, and the initial and complete solidification of the eutectic-like boride/austenite constituent are represented by temperatures 7 and 8, respectively. Temperatures 1 and 4 were considered the on-heating solidus and liquidus, respectively, while temperatures 5 and 8 the on-cooling liquidus and solidus, respectively. The presence of a eutectic was supported by microstructure examination. On annealing, the impact energy absorption was found to decrease and the boride particle size to increase moderately.

DTA was also used by Fischmeister et al. [57] to study the solidification and microstructure of high-speed steels alloyed with niobium. High-speed steels are characterized by wide solidification intervals and by the presence of blocky, or primary, carbides of the types MC or M_6C in the microstructure. The solidification process was distinguished by three temperatures: the onset of the eutectic crystallization, the temperature of the maximum rate of the eutectic formation and the solidus temperature. Reactions occurring during the solidification process of a large group of high-speed steels with carbon content of 0.8-1.2% were depicted as follows: (1) primary crystallization of delta ferrite; (2) peritectic transformation of ferrite plus liquid to austenite; (3) solidification of the residual interdendritic melt by crystallization of ledeburite eutectic (γ + M_2C, M_6C and/or MC); and (4) transformation of residual ferrite in the dendrite cores to austenite and carbide. The knowledge gained by using DTA on the solidification reactions and resulting structures was used to develop a processing philosophy for niobium-containing high-speed steels.

Cieslak and Savage [58] used DTA in the determination of compositional variables which influence fusion-zone hot-cracking in weldments of an austenitic stainless steel casting alloy (CN-7M). Like other wholly austenitic and nickel-based alloys, CN-7M was found to be particularly susceptible to hot-cracking during casting and welding. Liquidus and solidus temperatures and the solidification temperature range for each composition were determined by heating the sample in helium to about 50 °C above the liquidus then cooling at 6 °C min^{-1} through the solidification temperature range. Reactions involving less than 1% of the bulk materials were very difficult to detect and therefore the formation of thin-film eutectics could be missed. The solidification temperature range of the alloy was found to be narrow, relative to readily weldable stainless steels. The reason for hot cracking was related, however, to the segregation of elements such as S, P and Si at grain boundaries during solidification.

The solidification path of wear-resistant high-chromium white cast iron was determined by Laird and Doğan [59], using DTA together with electron microscopy. Solidification paths greatly influence the carbide phase size and morphology and, hence, the mechanical properties of the alloy. Three compositions, namely, hypoeutectic, eutectic and hypereutectic were examined. The samples were heated in argon to about 50 °C above the liquidus temperature

at 5 °C min^{-1}, allowed to equilibrate for 5 minutes and then cooled at 5 °C min^{-1} to 700 °C. Reactions occurring during solidification may be expressed as:

$L \rightarrow M_7C_3 + \gamma Fe$	eutectic
$L \rightarrow \gamma Fe$, then $L \rightarrow M_7C_3 + \gamma Fe$	hypoeutectic
$L \rightarrow M_7C_3$, then $L \rightarrow M_7C_3 + \gamma Fe$	hypereutectic

The solidification paths are presented as DTA cooling curves in Figure 18 for a 26 mass % chromium alloy. The hypereutectic alloy is the first to start solidification (1287 °C), followed by the hypoeutectic (1278 °C) and the eutectic (1264 °C) alloys. It also starts and finishes the eutectic solidification at a lower temperature than the two other alloys and shows a much wider solidification interval, allowing more time for the nucleation and growth of the carbide phase (M_7C_3). Solidification mechanisms were proposed in order to explain the formation of macro- and micro-structures as a function of the solidification rate and alloy composition. Correlations between the structures and the mechanical properties were also suggested.

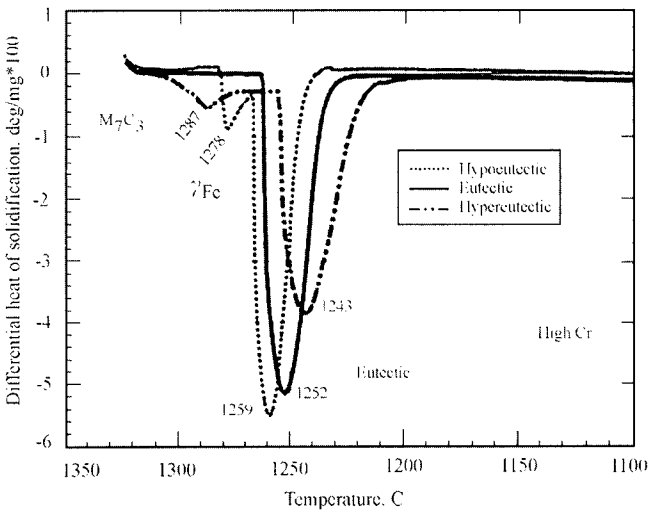


Figure 18. DTA curves for high-chromium (26%) white cast iron samples with three different carbon contents; cooling rate 5 °C min^{-1}. From G. Laird II and Ö. N. Doğan, reference 59.

Hui et al. [60] investigated the use of DTA in the determination and examination of thermal effects occurring during the solidification of five different types of cast iron, namely, compacted graphite (CG), grey, boron, high phosphorus, and boron-phosphorous cast iron. The mode of eutectic solidification was identified and ultimately linked to resulting mechanical

properties. The results were discussed in terms of various parameters, read from the cooling curves and DTA curves, which correlated with properties such as microstructures, tensile strength and chemical composition. In the DTA experiments, large sample containers of up to 40 mm in diameter and 100 mm high were used. For CG cast iron, the parameters ΔT_E [the difference between the maximum temperature of eutectic arrest and the lowest temperature of eutectic undercooling] and dT_2/dt [the maximum rate of temperature increase during eutectic solidification after undercooling] increased with the ratio of compact graphite to the spheroidal graphite in the microstructure. Larger values of both these parameters are indicative of rapid eutectic solidification. For gray cast iron, the ratio of t_4 (time from the start of eutectic solidification to point of maximum temperature rise] to t_1 (total time for eutectic solidification] was found to increase with the increase in the amount of inoculant added (FeSi, CaSi or BaSiCa). Inoculants are added to induce nucleation and minimize undercooling. For boron cast iron, which has a uniform distribution of boron carbide in the microstructure, there was a thermal effect at the austenite/boron carbide eutectic. For high-phosphorus cast iron thermal effects were evident at the Fe_3P - αFe - Fe_3C ternary eutectic and the Fe_3P- αFe binary eutectic after the austenite-graphite eutectic. For boron-phosphorus cast iron, thermal effects, related to the boron carbide and the iron phosphide eutectics, were also observed and correlated to mechanical properties. The authors concluded that DTA could be used to predict and control the graphite morphology in compact graphite cast iron, for fast evaluation of the effectiveness of inoculation and prediction of tensile strength in grey cast iron, and for the prediction of the carbide content in the microstructure of boron or high phosphorous cast irons.

DSC was used by Lendvai et al. [61] to explore and compare the solidification behaviour of chill-cast ingots of Al-Fe alloys under equilibrium conditions and with fast cooling rates. Alloys with iron content of up to 1.8 mass % were examined. Alloys prepared under equilibrium solidification conditions (slow cooling) exhibited two endothermic peaks; the first, around 655 °C, corresponding to the melting of the Al(Fe)-Al_3 Fe eutectic, and the second, below 660 °C, corresponding to the melting of the Al-Fe solid solution (≤ 0.05 mass % Fe). The eutectic point was determined as 1.7 mass % Fe and 654.7 °C. The melting peaks were also used to determine the heat of fusion of different Al/Fe mixtures and, by extrapolation, that of pure Al was determined and compared favourably with literature values. For samples prepared under various fast cooling rates, an additional endothermic peak appeared around 652 °C and was attributed to the melting of a metastable eutectic, namely, Al(Fe)-Al_6Fe. By annealing above 600 °C for short periods of time, the metastable phase, Al_6Fe, almost completely disappeared and was replaced with the equilibrium phase Al_3Fe.

Heats of solidification are required for the design of gating and risering for casting metals, and for the design of continuous casting processes. DTA was used by Sarangi et al. [62] to determine the heats of fusion (solidification) of Pb-Bi, Zn-Al and Pb-Te eutectics. The system was calibrated by melting pure metals (Sn, Bi, Pb, Zn, Al, Ag, Cu) to determine values of k in $A = k.\Delta H$, where A is the DTA peak area and ΔH is the enthalpy change. The constant k was considered as equal to $M/2K_m$, where M is the sample mass and K_m is the thermal conductivity of the medium between the sample and the thermocouple. The plots of k vs. T (temperature) fell on two straight lines, one for the three lower-melting metals and another for the higher-melting metals. The discontinuity at about 400 °C was attributed to the onset of heat loss by radiation. Experimental values were compared to values calculated from thermodynamic data in the literature for Pb-Bi and Zn-Al with agreement to about 8% and 3% respectively.

3.4. Very rapidly cooled metals and alloys

Since its recognition in the early seventies, this field of metallurgy has accelerated significantly and expanded to deal with various topics related to very rapidly cooled (quenched) metals and alloys. These topics include solidification processing techniques, structure characterization, property measurements, applications of amorphous and micro-crystalline materials, and others [63].

Rapid quenching of a metallic melt to an amorphous (glass) nano-crystalline or micro-crystalline structure allowed the incorporation of larger amounts of intermetallic phases, with strong beneficial influence on the final properties of the alloy. These phases would, otherwise, precipitate out in the conventional, relatively slow solidification processing. The quenching process allows the production of alloys with superior properties and desirable characteristics (for specific applications) such as high specific strength, low density, high-temperature performance, high corrosion and stress-corrosion cracking resistance and toughness [64,65].

A comparison of the main properties of metals, dielectric glasses and metallic glasses produced by rapid quenching was reported by Güntherodt [66]. He also pointed out some applications related to the relevant property. For instance, superior magnetic properties of metallic glasses allow their use in distribution transformers, electric motors, low-voltage power supplies, flexible magnetic shielding, sensors, transducers, etc. Their mechanical properties allow their use in reinforcing filaments in plastics, rubber, cement, etc., their electrical properties allow their use in electrical resistors, heating wires, resistance thermometers, etc., and their chemical properties allow their use in corrosion resistant alloys, catalysis, etc. The superior magnetic, mechanical and chemical properties of nano- and micro-crystalline alloys emanate from their soft- and

hard- magnetic behaviour, fine grain size, enhanced elastic modulus, high strength, superelasticity, and high catalytic reactivity, allowing their use in soft-magnetic material with little core losses, permanent magnets leading to lighter electrical devices, etc.

Several rapid quenching techniques, normally characterized by cooling rates of more than 10^4 K s^{-1}, as compared to quenching rates of 10^2 K s^{-1} in conventional metallurgy, were developed and used to synthesize products of different shapes and sizes for different applications. Melt spinning, splatting and atomization are some the main techniques used [66,67].

By definition, this field of research involves, in most part, metastable systems in non-equilibrium situations with a large free energy difference that may be released by the substance during its transition to a more stable state. In addition, drastic changes in the properties of the amorphous metals and alloys usually take place when the material is heated to or above the crystallization temperature. A clear understanding of the crystallization process is, therefore, imperative for the interpretation of the influence of crystallization on the material properties. Thermal analysis techniques in general, and differential scanning calorimetry in particular, have proven to be extremely valuable, and sometimes essential, in the study of these systems by detecting and quantifying metastable/stable transitions, magnetic transitions, activation energies, heat capacities, etc., significantly contributing to the understanding of the structure, behaviours and properties of the rapidly quenched metals and alloys.

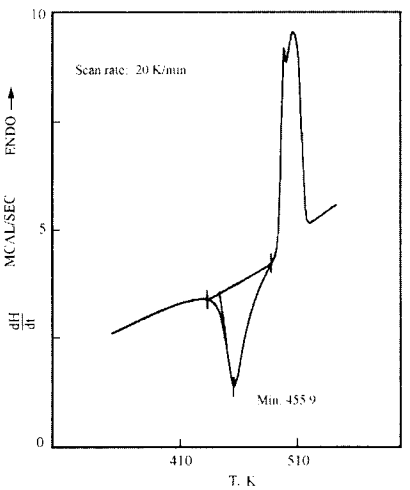


Figure 19. DSC curve for amorphous selenium. From W. Jingtang et al., reference 68.

Jingtang et al. [68] studied the change in properties and structure of rapidly quenched amorphous alloys (in the form of ribbons), namely Fe-Si-B and Ni-P, and selenium metal, with the change in quenching rate, using differential scanning calorimetry, XRD, scanning electron microscopy and Curie-temperature measurements. The critical cooling rates below which micro-crystallization takes place were determined for the three materials. Crystallization temperatures and enthalpies of crystallization were determined by DSC. For amorphous selenium, the crystallization temperature was manifested by an exothermic peak with a maximum at 455.9 K, Figure 19. The subsequent melting was found to occur in two stages, which was interpreted on the basis the existence of two stable phases in the selenium crystal. The authors concluded that the physical properties of amorphous metals / alloys are influenced by the chemical and topological short-range order related to the metastable structure while the mechanical properties are strongly related to structural defects.

Hertz and Notin [69] demonstrated that DSC can often be used to detect irreversible processes and help understand their mechanisms. Examples were given of the cooling/solidification of Mg_5Ga_2 liquid to form an amorphous alloy, and the heating of the amorphous alloys Ni-P, Cr-Si steel, Fe-Al, Pb-Ca and Au-Cu. Exothermal effects detected during heating were related to such phenomena as crystallization, elimination of quenched vacancies and structural hardening. The effect of pre-annealing an amorphous alloy on the intensity of the thermal effect was found to be significant. The longer the annealing time at a certain temperature, the smaller the thermal effect on heating.

Structural relaxation is a phenomenon that takes place when an amorphous alloy is heat treated resulting in an enthalpy release and a change in the alloy's physical, mechanical, magnetic, electrical and other properties. Noh et al. [70] investigated this phenomenon by monitoring the enthalpy relaxation of two amorphous alloys, a metal-metalloid, $(Fe_{0.5}Co_{0.5})_{83}P_{17}$ and a metal-metal $(Fe_{0.5}Co_{0.5})_{90}Zr_{10}$ using differential scanning calorimetry. The alloys were prepared by melt spinning in the form of thin ribbons (20 μm thick) and, for the DSC experiments, the alloy samples were annealed for different periods of time at various temperatures below the crystallization temperature. No significant influence of the annealing temperature on the enthalpy relaxation temperature was detected. A linear relationship was found, however, between the natural logarithm of the annealing time and the enthalpy change (ΔH) for both alloys. The magnitude of ΔH was found to be much higher for the metal-metalloid, indicating that the enthalpy relaxation occurs much more easily for this alloy.

For the metal-metal alloy, a smaller enthalpy relaxation and a higher activation energy were attributed to the atomic structure with a higher atomic packing density for this type of alloy.

The structural relaxations in quenched metallic glasses affect many of physical and mechanical properties. Fouquet et al. [71] produced ribbons of different thicknesses of the metallic glass $Fe_{75}Cr_4C_{10.5}P_{8.5}Si_2$ by melt spinning at different quench rates, and examined their structural relaxation in argon using differential scanning calorimetry.

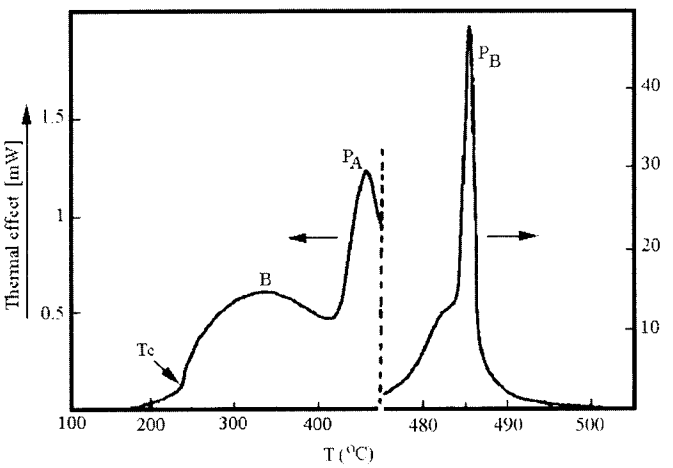


Figure 20. DSC curve of an as-quenched ribbon sample of the alloy $Fe_{75}Cr_4C_{10.5}P_{8.5}Si_2$; heating rate 5 °C min^{-1}. From F.J. Fouquet et al., reference 71.

The Curie temperature, Young's modulus and bending (embrittlement) properties were also determined. The DSC curve for a ribbon sample of 27.5 μm thickness depicted the structural relaxation effect as a broad exothermic peak in the temperature range 250-400 °C followed by two sharp crystallization (exothermic) peaks at 454 and 485 °C, Figure 20. The crystallization enthalpy was determined as 3.8 ± 0.3 kJ mol^{-1}. The quenching rate was found to influence the degree of relaxation but not the crystallization enthalpy. From the DSC and other measurements, the authors proposed that the "defects" concept can be used to explain the behaviour of a metallic glass during structural relaxation. Two stages are involved. The first involves the elimination of "non-equilibrium" defects in the structure leading to local equilibrium, and the second, a redistribution of equilibrium defects with atomic rearrangements and short-range ordering in the whole amorphous matrix.

Iron-based amorphous alloys were found to be susceptible to embrittlement. Yamasaki et al. [72] investigated the effect of alloy composition on temper embrittlement of two master alloys, namely, Fe-B-Si and Fe-B-Si-X (X=Cr and Ti) using DSC, XRD and ductility bend test. The amorphous alloys were prepared by melting under argon followed by melt spinning on a steel wheel. The embrittlement susceptibility of Fe-B-Si was found to increase significantly with the increase in the metalloid (B and Si) content and that of Fe-B-Si-X increases with the increase in the Ti or Cr content. The DSC measurements, Figure 21, indicated that the embrittlement time decreases as the crystallization peak temperature increases, pointing to different kinetics for the embrittlement and the crystallization. The alloys were found to remain ductile until crystallization at compositions close to the eutectic.

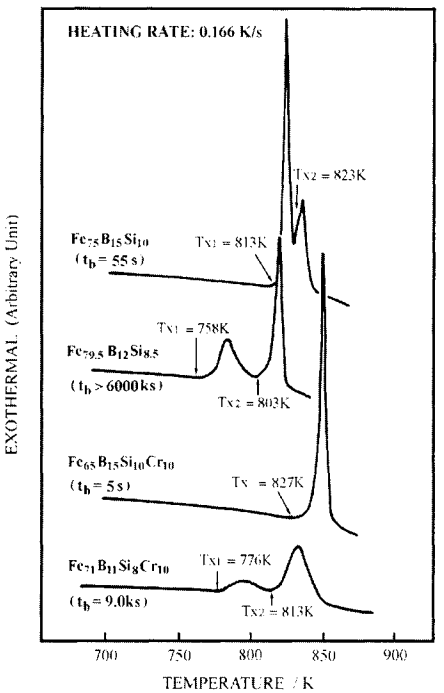


Figure 21. DSC curves for some Fe-B-Si and Fe-B-Si-Cr alloys; t_b indicates the embrittlement time at 623 K. From T. Yamasaki et al., reference 72.

The structural relaxation of amorphous alloys may, in may instances, lead to a significant loss in ductility. This behaviour was noticed in alloys with a major metallic constituent which has a body-centered cubic structure in its pure crystalline form or with a high metalloid content. Wu and Spaepen [73]

examined the ductile to brittle transition of $Fe_{79.3}B_{16.4}Si_{4.0}C_{0.3}$ amorphous alloy by measuring the enthalpy of the structural relaxation transition using differential scanning calorimetry. The annealing temperature and time were both found to retard the onset temperature of the ductile to brittle transition (T_{BD}). T_{BD} was found to characterize the embrittlement of the metallic glass very satisfactorily. A gradual shift in T_{BD} with annealing, Figure 22, indicated the continuous nature of the embrittlement, similar to other physical properties, due to structural relaxation.

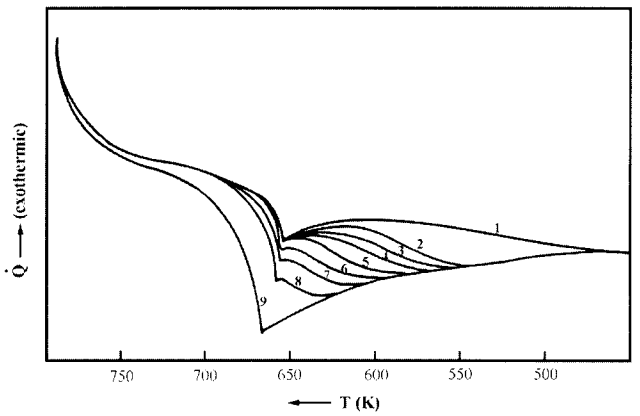


Figure 22. DSC curves for $Fe_{79.3}B_{16.4}Si_{4.0}C_{0.3}$ amorphous alloy annealed for increasing lengths of time at 281°C; heating rate 40 °C min^{-1}. Trace 1 corresponds to the as-quenched glass. From T-W. Wu and F. Spaepen, reference 73.

Graydon et al. [74] studied the effect of composition on the formation and thermal stability of metallic glasses using differential scanning calorimetry. The effect of molybdenum and cobalt additions on the structure, thermal stability, glass transition and crystallization behaviour of a Ni-B amorphous alloy was examined. Such a metal-metalloid amorphous alloy was found to possess certain properties desirable for the manufacture of electrodes used in water electrolysis. The alloy system $Ni_{72}Mo_xCo_{8-x}B_{20}$ ($0 < x < 8$) was found to be of considerable promise in the production of stable, corrosion-resistant glasses, with the molybdenum contributing to further enhancing the electro-catalytic properties. The alloys were prepared by vacuum-induction melting followed by vacuum melt spinning in the form of ribbons. The thermal characteristics were determined using DSC in argon atmosphere and the enthalpy of crystallization was obtained by integrating the DSC crystallization-peak area. The glass transition was identified by a discontinuity in the slope of the baseline prior to the crystallization peak. XRD was used to verify the crystallinity or amorphous

nature of the alloy. The DSC results indicated that the crystallization temperature, enthalpy and activation energy increase with the increase in the molybdenum content, indicating an increase in the thermal stability of this quaternary glass. The mechanisms of nucleation and crystal growth were elucidated on the basis of the DSC curves and the Johnson-Mehl-Avrami equation:

$$f = 1 - \exp[-(kt)^n]$$

where f is the fraction transformed as a function of time (t), k is a rate coefficient and n is the Avrami exponent which reflects the nature of the nucleation rate and growth morphology. Among other findings based on the DSC measurement, the authors suggested that amorphous ribbons from the alloy $Ni_{72}(MoCo)_8B_{20}$ may only be produced in the presence of molybdenum.

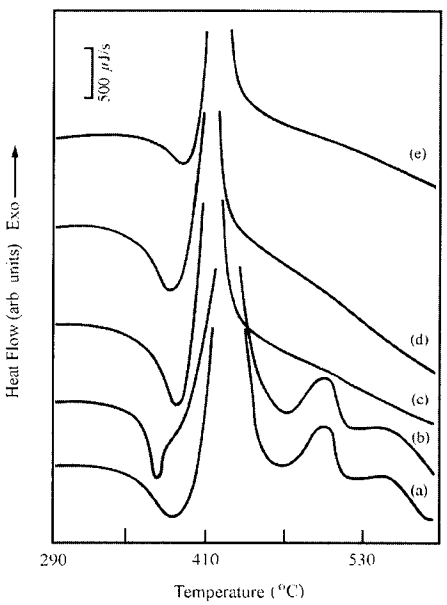


Figure 23. DSC curves for WC- amorphous-$Pd_{77.5}Cu_6Si_{16.5}$ metal matrix composites; heating rate 10 °C min^{-1}. (a) - 0% WC, non-preannealed, and (b) 0% WC, (c) 2% WC, (d) 6% WC, (e) 8% WC in $Pd_{77.5}Cu_6Si_{16.5}$ composites preannealed at 330 °C for 10 min. From W-N. Myung et al., reference 75.

The crystallization behaviour of the amorphous alloy $Pd_{77.5}Cu_6Si_{16.5}$, with and without the addition of tungsten carbide as a nucleation material, was explored by Myung et al. [75] using DSC, transmission electron microscopy and XRD.

The metal matrix composites were produced by induction stirring and melt spinning. Micron-size WC particles were dispersed in the alloy during synthesis. As-quenched samples were pre-annealed for different periods of time at 230 and 330 °C before examination by DSC. The activation energy for crystallization was found to decrease with the increase in the WC addition. Tungsten carbide also enhanced the reaction kinetics and the rate of crystallization. This was reflected in the differences in the exothermic DSC peaks of pre-annealed and non pre-annealed composites containing different ratios of WC, Figure 23. It was maintained that the WC dispersed particles (embryos) shift the crystallization mechanism at the early stages from nucleation to growth and, hence, hasten the transition.

Myung et al. [76] also investigated the influence of dispersed tungsten carbide particles on the crystallization characteristics and viscous flow properties of amorphous $Ni_{73}Si_{10}B_{17}$ metal matrix composites using DSC, XRD and thermomechanical analysis. The latter technique was used for the viscosity measurements under different conditions, such as applied stress, heating rate and pre-annealing. The samples of WC/amorphous $Ni_{73}Si_{10}B_{17}$ alloy were prepared by induction stirring and melt spinning. The authors found that the dispersed carbide caused a higher rate of crystallization relative to that detected in the amorphous alloy alone. With the increase in the volume fraction of WC in the composite, the enthalpy of crystallization decreased (as demonstrated by the DSC exotherms), the activation energy (of non-annealed samples) increased linearly, and the viscosity decreased.

Radinski and Calka [77] studied the effect of picosecond laser annealing on Pd-Si amorphous metallic ribbons using DSC, XRD, laser-pulse crystallization and metallography. Picosecond laser annealing, which induces quenching rates of 10^{11} K s^{-1}, was found to remove the surface nuclei of crystallization (crystallites) and drastically decrease the bulk nuclei of crystallization. DSC was used to measure the enthalpy of crystallization which is proportional to the rate of crystallization. The rate of crystallization was also calculated using the Johnson-Mehl-Avrami relationship. The experimental and the calculated data, presented in terms of the temperature dependence of the rate of crystallization were found to compare favorably. The authors suggested that picosecond annealing causes a significant heating of the metal surface, leading to a 'boiling off' of the surface crystallites. The subsequent rapid quenching sustains the amorphous nature of the surface. This treatment results in a significant improvement in the stability of the metallic glass against devitrification as compared to metallic glasses produced by conventional quenching techniques.

Intermetallic alloys with Fe_3Al as a base were found to have desirable high-temperature properties like corrosion resistance (particularly in oxidizing and sulphidizing environments), strength and ductility. The low-temperature

ductility, however, is poor. This was thought to be due to the interaction between the atmospheric moisture and Al to form Al_2O_3 and atomic hydrogen, leading to hydrogen embrittlement. The room-temperature ordered bcc structure of Fe_3Al, which becomes less ordered at high temperatures, seems to facilitate the hydrogen diffusion and, therefore, to promote the low ductility. The influence of alloying elements Cr, Mo, Nb, Zr, Ti, Si, Mn and B on the order-disorder transformation temperature and, hence on the ductility, was explored by Johansson et al. [78] using differential scanning calorimetry. The alloys were prepared by atomizing the powdered mixtures at high temperatures in argon. The transformation temperatures were determined both on heating and on cooling. Tensile properties and hot hardness were also examined. The results indicated that the influence of Ti and Si on the transformation temperatures was significant, while that of Nb and Mo was moderate and that of Cr, Zr and Mn was negligible. The formation of a highly elongated structure, with minimum transverse grain boundaries as well as the suppression of the bcc ordered structure minimize the hydrogen diffusion, which causes the alloy's inferior ductility.

Nano-crystalline alloys of the type Fe-Cu-Nb-Si-B, were found to have excellent soft magnetic properties with high saturation magnetization, high permeability, little magnetostriction and low core loss. Leu et al. [79] studied the magnetic phase transition of the alloy $Fe_{73.5}Cu_1Nb_3Si_{13.5}B_9$ using differential scanning calorimetry, thermomagnetometry (TM), XRD and transmission electron microscopy. DSC detects the Curie temperature as a change in enthalpy, while TM shows an apparent mass change at the ferromagnetic/paramagnetic transition. The alloy was prepared by melt spinning to a ribbon with an amorphous structure, prior to annealing at 550 °C for one hour to a nano-crystalline structure. The DSC trace of the as-quenched amorphous alloy, Figure 24, identified the Curie temperature as a weak endothermic peak and the nucleation of the nano-crystalline structure and the formation of intermetallic Fe-Nb-B phases as two major exotherms. It was not possible, however, to determine the Curie transition of the nano-crystalline structure as it partially overlaps the large nucleation peak. TM, on the other hand, Figure 25, detected a sharp and significant apparent weight loss at the Curie transition of the amorphous alloy, an apparent weight gain during the formation of the nano-crystalline ferromagnetic structure followed by another weight loss at the Curie transition of the nano-crystalline structure and, finally,

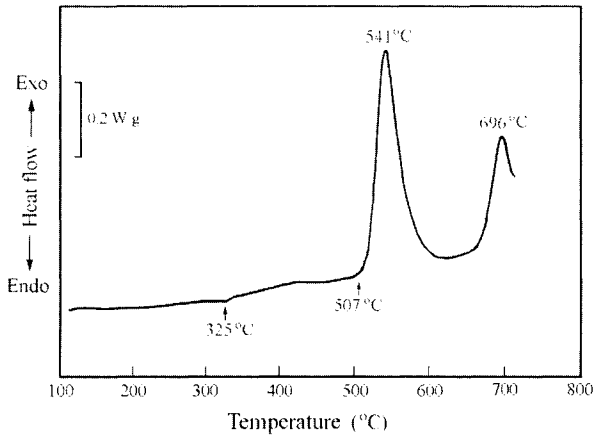


Figure 24. DSC curve of an amorphous $Fe_{73.5}Cu_1Nb_3Si_{13.5}B_9$ alloy. From M.S. Leu et al., reference 79.

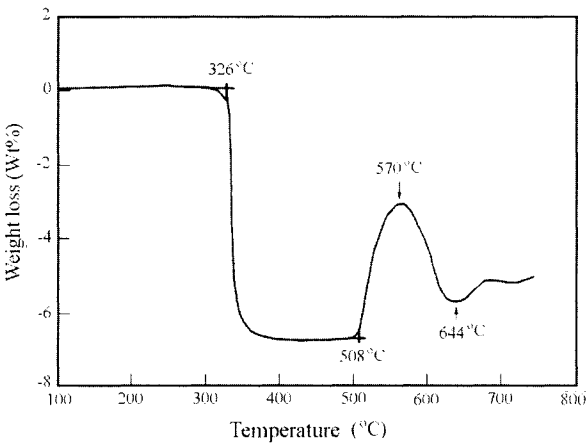


Figure 25. TGA curve under a magnetic field (thermomagnetometry) for an amorphous $Fe_{73.5}Cu_1Nb_3Si_{13.5}B_9$ alloy. From M.S. Leu et al., reference 79.

a weight gain due to the formation of the ferromagnetic intermetallic phases. The TM was also performed on the annealed material and it was found that the Curie transition of the amorphous material and the transformation to nano-crystalline material had disappeared.

The crystallization behaviour and specific heat of $Cu_{60}Zr_{40}$ amorphous alloy were investigated by Ladiwala et al. [80] using DSC at different heating rates. The work aimed at gaining more understanding of the crystallization phenomena which impact drastically on certain properties, e.g. specific heat, of metallic

glasses. The Cu/Zr alloy was prepared by melt spinning at a cooling rate of about 10^6 K s^{-1}. DSC identified a double glass-transition phenomenon and a two-stage crystallization. The temperature of the first glass-transition increased with the heating rate, while that of the second glass-transition was independent of the heating rate. The first crystallization peak was related to a partial crystallization of the amorphous glass and was found to occur at higher temperatures at higher heating rates. The second exothermic reaction (crystallization) was related to the crystallization of the remaining amorphous matrix to form an equilibrium crystalline phase. This transition almost disappeared at higher heating rates. The measured enthalpy of crystallization was found to increase, while the specific heat was found to decrease, with the increase in heating rate.

Amiya et al. [81] studied the thermal behaviour of Ti-based amorphous alloys using differential scanning calorimetry and XRD. These amorphous alloys were found to have superior properties in engineering applications compared to those of crystalline ones having the same chemical compositions. The amorphous alloys, $Ti_{50}Zr_{10}Cu_{40}$ and $Ti_{50}Zr_{10}Ni_{20}Cu_{20}$ were prepared by arc melting, followed by high-pressure argon atomization. The heat of crystallization and the effect of particle size on the crystallization of the amorphous alloys were also measured by DSC. The presence of Zr (>10%) was found to be very effective in suppressing (delaying) the crystallization, and results in the formation of a single amorphous phase and, hence, the glass-forming tendency. Within the Ti-Zr-Ni-Cu system, the ternary alloy $Ti_{50}Zr_{10}Cu_{40}$ had the greatest glass-forming ability in addition to an extensive supercooling temperature region before crystallization. This was attributed to the difficulty in the long-range redistribution of the constituent elements for the precipitation of crystalline phases and the large difference in atomic sizes of these elements.

Merry and Reiss [82] selected differential thermal analysis as a reliable method to study of the mechanism and rate of nucleation in liquid metals. Metallic tin was prepared by a method developed earlier by Rasmussen and Loper [83] and Perepezko et al. [84,85] in the form of liquid droplets suspended in oil. Cooling curves were determined by DTA and an elaborate theoretical equation, based on 13 different parameters simulating and describing the DTA curve, was developed. By substituting different values for the various parameters in the theoretical equation, the authors were able to determine the influence of each of these parameters on the shape of the solidification peak. They found that higher cooling rates shift the peak slightly to a lower temperature, while the liquid droplet size distribution, a temperature fluctuation of up to 0.1K during cooling, and nucleation mechanisms (homogeneous, heterogeneous-surface or heterogeneous-volume) have only a small influence on the shape of the DTA trace. The authors concluded that it is possible to describe the nucleation

phenomena in supercooled melts by a mathematical equation and a theoretically derived DTA peak simulating and matching the actual solidification peak. This study was based on earlier work by Rasmussen and Loper [86] on the use of DTA and DSC in the determination of the supercooling range (Figure 26), and nucleation rates, respectively, in the tin/bismuth system. Rasmussen and Loper demonstrated the possibility of determining the temperature dependence of the nucleation rate from a single constant cooling-rate DSC experiment.

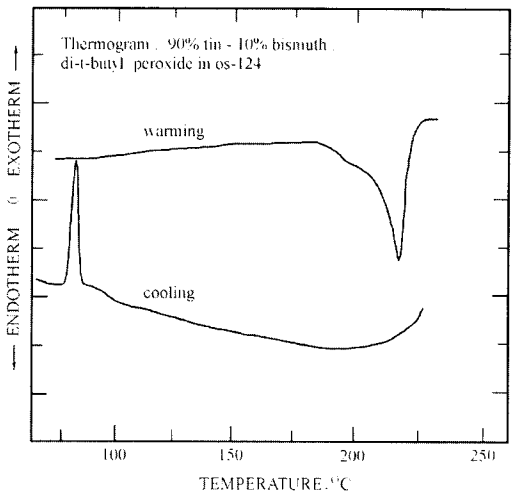


Figure 26. DTA curves for a 90% tin - 10% bismuth alloy. Emulsion was formed by di-t-butyl peroxidation in the presence of isophthalic acid in OS-124. Solidus reaction begins at 183 °C on heating; melting point is 219 °C. The crystallization temperature on cooling is 83 °C; supercooling to the peak is 136 degrees; supercooling range is 11 degrees. From D.H. Rasmussen and C.R. Loper, reference 86.

Ultrafine-grained Cu, Ag, AgCu, AgAu and Pd were prepared by Kumpmann et al. [87] by evaporation under reduced pressure of He, followed by condensation on a liquid nitrogen cooled container and consolidation. Materials were examined by DSC and transmission electron microscopy. DSC of Cu just after preparation showed an exothermic peak at about 100 °C; this peak disappeared after 5 days storage at room temperature, but not after storage at -20 °C. Ag, just after preparation, showed two peaks at 125 and 225 °C; after 1 month storage the lower temperature peak had disappeared. TEM indicated that the process occurring was abnormal grain growth, which could take place at room temperature. Oxidation of the Ag particle surface increased the thermal stability, but grain growth was still abnormal at about 250 °C, the decomposition

temperature of Ag_2O. Activation energies were determined by Kissinger's method. The enthalpy of reaction, per unit area of powder, appeared to be about 0.5 J m^{-2}. For Ag-Cu alloy, the exothermic reaction started at about 70 °C and reached a peak at 320 °C; Ag and Cu separated as separate phases, and only normal grain growth was observed.

3.5. Mechanically-milled alloys

As mentioned earlier, amorphous alloys have traditionally been produced in the form of ribbons, flakes, filaments, etc., by different rapid quenching techniques. Due to the nature of these techniques, however, the production of these materials in large amounts was costly and time consuming. In addition, the production of very fine amorphous metallic powders for use in certain applications, like pigments and composite materials with superior properties, was mostly done by cutting, grinding or attrition of materials produced by melt-spinning or splat quenching. In the search for alternative, more convenient and economical methods for the production of amorphous materials in general and powders in particular, it was realized that prolonged mechanical milling of metals and alloys gradually decreases the particle size to the micro and nano-crystallite range and ultimately, in many cases, renders them amorphous. It was also realized that by mixing elemental powders or alloys, binary, ternary and more complex phases can be synthesized. This mechanical alloying process is normally done in high-energy ball mills under inert atmosphere to avoid overheating and oxidation of the material leading to unintended chemical and physical changes. To characterize and examine the behaviour of these amorphous, micro- and nano-crystalline powders, thermal analysis techniques, and particularly differential scanning calorimetry, were found most useful as complementary techniques, together with microscopy and X-ray diffraction. The material-specific, irreversible amorphous/crystalline transition, manifested as an exothermic effect on a DSC curve, is an easily determined characteristic that can be monitored as a function of different experimental factors and, hence, can be used to study the material as well as the synthesis process.

The effect of transition elements, namely, Cr, Mo and Co, on the amorphization of metal-metalloid materials (Fe-C) by mechanical alloying was studied by Omuro et al. [88] using DSC, XRD and electrical resistivity measurements. Pure crystalline elemental powders with a particle-size range of 63-149 μm were used as starting materials to prepare mixtures of $Fe_{83-x}M_xC_{17}$ (M = Cr, Mo or Co and $0 < x < 35$). The mechanical milling/alloying was performed under argon in a ball mill. The results indicated that amorphization did not take place to any great extent with the $Fe_{83}C_{17}$ powder alone, even after 720 ks of milling. With the addition of the high-carbide forming elements, Cr or Mo, however, amorphization and alloying was strongly enhanced. This effect

was detectable even at relatively small Mo concentrations (x = 3), and, for both elements, the effect increased with the increase in concentration. The effect of Co, a low-carbide forming element, after 720 ks of milling, was not apparent. The DSC measurements indicated a strong exothermic effect at 788 and 912 K, Figure 27, for the crystallization of the amorphous mechanical milling products $Fe_{48}Cr_{35}C_{17}$ and $Fe_{48}Mo_{35}C_{17}$, respectively, verifying the process effectiveness.

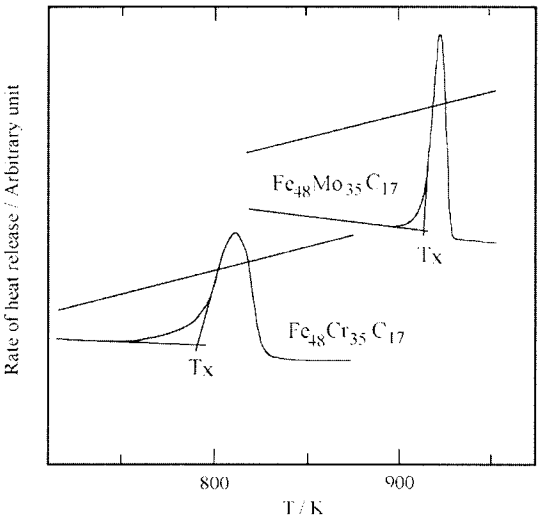


Figure 27. DSC curves of $Fe_{48}Cr_{35}C_{17}$ and $Fe_{48}Mo_{35}C_{17}$, alloy samples after mechanical alloying for 200 h.; heating rate 4.8 K min^{-1}. From A.K. Omuro et al., reference 88.

The synthesis of amorphous powders for the fabrication of high-temperature Zr-based alloys by mechanical milling (alloying) was explored by Hellstern and Schultz [89]. In this work, amorphous transition-metal Zr alloys, namely, $Ni_{68}Zr_{32}$, $Co_{55}Zr_{45}$, $Fe_{40}Zr_{60}$ and $Cu_{60}Zr_{40}$ were prepared from pure crystalline elemental powders in a ball mill. The products were examined periodically using optical and scanning electron microscopy and XRD, and their crystallization temperatures were determined by DSC. The crystallization temperatures were found to be 820, 825, 790 and 804 K, for the above-mentioned alloys, respectively. Mechanical alloying seems to take place via a mechanism that involves a structural refinement within the powder particles accompanied by a solid-state reaction. The authors suggested that mechanical alloying may be a more convenient alternative to melt spinning, evaporation or sputtering techniques used for the preparation of amorphous powders, provided that the two starting elements are sufficiently ductile.

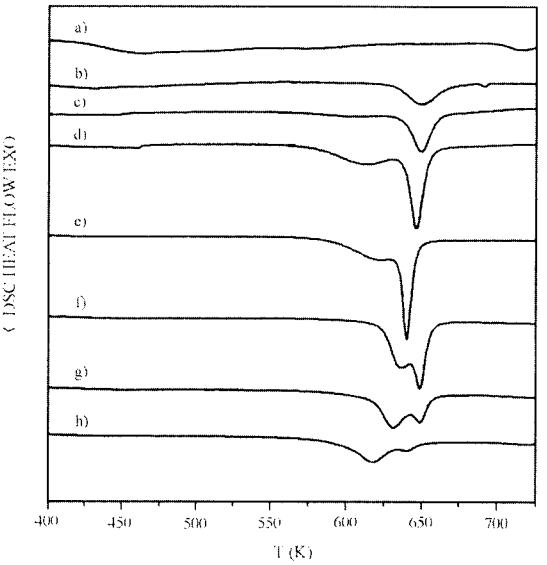


Figure 28. DSC scans for $Fe_{40}Ni_{40}B_6P_{14}$ powders prepared from the elements as precursors by mechanical alloying for (a) 3 h, (b) 10 h, (c) 20 h, (d) 30 h, (e) 35 h, (f) 92 h, (g) 132 h, and (h) 156 h; heating rate 40 K min^{-1}. From S. Suriñach et al., reference 90.

Fe-based amorphous alloys are known to have attractive soft-magnetic properties. Suriñach et al. [90] prepared the two metal-metalloid alloys $Fe_{40}Ni_{40}B_6P_{14}$ and $Fe_{40}Ni_{40}Si_6P_{14}$ by high-energy ball milling in argon and examined the different factors affecting the amorphization process using DSC, XRD and scanning electron microscopy. Polycrystalline elemental Fe, Ni, P, B and Si as well as Fe-B and Fe-P were used as precursors in the preparations. Another batch of the alloys was also prepared by melt spinning in ribbon form. The enthalpy of crystallization as determined from DSC scans of powders examined after different milling times, Figure 28, revealed that a complete amorphization of the two materials is achieved after 35 hours of milling when the elements are used as precursors. Powders prepared from compound precursors showed some crystallinity after milling for the same number of hours. Further milling for several more hours seems to induce partial crystallization of the alloys. The DSC scans also showed that the crystallization takes place in two stages with nonreversible exothermic effects. The amount of amorphous metastable phase formed during milling could also be calculated from the DSC scans by determining the total enthalpy generated. The temperature, enthalpy and activation energy of crystallization were found to be lower for the

amorphous powders than for the liquid-quenched ribbon of the same alloy. Besides the milling time, the starting precursors and the milling conditions were found to influence amorphization, i.e., the mechanical alloying results.

Mechanical milling was used by Oleszak et al. [91] to synthesize Fe-Ni and Fe-W alloys from pure crystalline Fe (-100 mesh), Ni (-100 mesh) and W (-250 mesh) metal powders. The binary compositions Fe-60 at.%Ni and Fe-33.3 at.%W were targeted. XRD and DSC were used to study the process which was carried out in a ball mill in a dynamic argon flow. The milling process was stopped periodically and the product was examined to determine the extent of alloying. For the Fe-60 at.%Ni powder, the results indicated that the average powder crystallite size diminishes with increasing milling time, reaching 10nm after 100 hours. The formation of a nanocrystalline γ(Fe,Ni) solid solution was also evident after this milling time. DSC was used to monitor the transition temperature, as well as the heat evolved during the interaction between the two powders and the dissolution of Fe in Ni to form the solid solution. For the Fe-33.3 at.%W powder, the formation of Fe(W) and W(Fe) extended solid solutions was evident with milling. After 100 hours of milling time, the equilibrium intermetallic compound Fe_2W started to form and, after 220 hours, the three phases, Fe_2W, Fe(W) and W(Fe), were still present.

Mechanical alloying of aluminum powder and the metal oxides CuO, Fe_2O_3, SiO_2 and MgO, was carried out by Kaneko et al. [92] to examine the thermite reaction in which Al_2O_3 is formed. The reaction was claimed to increase the mechanical strength of the aluminum-based powder metallurgical materials. The mechanical milling of mixtures of Al (~20 μm) and oxide (~30 μm) powders (Al, 10 at.% oxide) was done in a high-energy ball mill under argon in the presence of methanol, and the powders were subsequently cold pressed, vacuum degassed and hot extruded. DSC, supplemented by XRD and SEM, was used to study the solid state reactions induced by the mechanical milling process. DSC curves of processed mixtures, Figure 29, showed no peaks up to the melting point of aluminum, except for the CuO-containing mixture for which a second endothermic peak appeared at the melting temperature of the Al-$CuAl_2$ eutectic. The results indicated that the thermite reaction occurred with copper and iron oxides forming $CuAl_2$ and $FeAl_3$, respectively. In both cases, amorphous Al_2O_3 was also formed. No thermite reaction took place, however, with SiO_2 or MgO. It was also confirmed, from tensile strength measurements, that the thermite reaction led to an increase in the mechanical strength of the powder metallurgical materials examined.

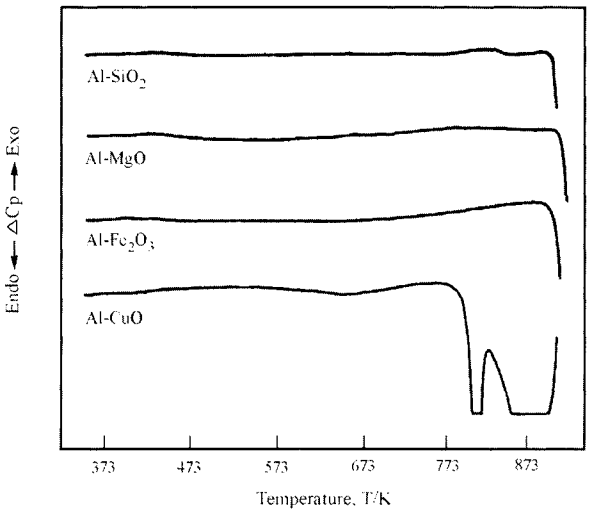


Figure 29. DSC curves for aluminum metal - metal oxide powder mixtures; heating rate 10.2 K min^{-1}. From J. Kaneko et al., reference 92.

Tsai [93] investigated the thermal and magnetic behaviours of the amorphous metal-metalloid powder, $Fe_{87}Cr_2P_{13}B_7$, by dynamic and isothermal DSC and thermomagnetometry. The powder was prepared by high-energy ball milling of the amorphous alloy, originally obtained by quenching using melt spinning. The as-quenched alloy was also examined before milling. The results obtained by dynamic DSC of the as-quenched alloy indicated only one crystallization peak. The powder, however, exhibited an additional crystallization peak at a lower temperature, indicating the formation of a new phase on milling. Figure 30 shows the dynamic DSC curves for the as-quenched alloy and the powder. The crystallization enthalpies, as measured by DSC, were the same (100 J g^{-1}) for both materials. The intensity of the high-temperature peak diminished, and that of the low-temperature peak increased, as the milling time (mechanical deformation) increased. The latter peak also appeared at lower temperatures as the milling time increased. The results implied that the as-quenched material transforms gradually into a new material on milling. This was verified by XRD, which indicated that the new phase is also amorphous. In addition to the lower crystallization temperature, the new metastable material was found to have a lower activation energy for crystallization and is, therefore, less thermally stable. Isothermal DSC confirmed the thermal behaviour of the two materials. The author suggested that the crystallization of the new material takes place by direct grain growth with a pre-existing nucleation mechanism, while that of the as-

quenched material occurs essentially by a nucleation and grain-growth mechanism. Ball milling was thought to induce deformation and introduce defects in the as-quenched material. Thermomagnetometry results revealed an increase in the Curie temperature by ball milling, which was attributed to a higher Fe-Fe association in the new metastable material.

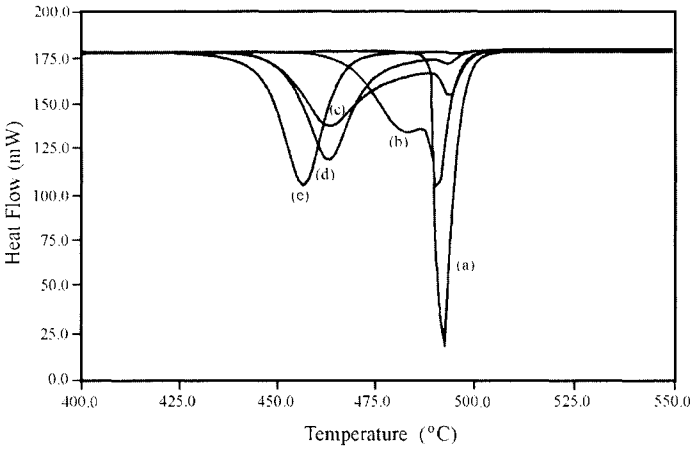


Figure 30. DSC curves for $Fe_{87}Cr_2P_{13}B_7$ alloy; (a) as quenched, (b) milled for 30 min, (c) milled for 60 min, (d) milled for 120 min, and (e) milled for 180 min. From C-L Tsai, reference 93.

DSC was also very valuable in the study of the formation of disordered nano-crystalline Ni-Al and Ni-Ge intermetallics by mechanical alloying (milling). Aoki et al. [94] prepared disordered nano-crystalline Ni_3Al and Ni_3Ge from the elemental powders in argon atmosphere using a high-energy planetary ball mill. The formation and ordering of these alloys, after different milling times, was monitored by DSC and XRD. For powders milled for shorter times, the DSC traces depicted three exothermic peaks corresponding to the formation of disordered Ni_3Al from the elemental components (alloying), the ordering of this phase and the formation of NiAl phase. Only one peak corresponding to the ordering of Ni_3Al, appeared for powders milled for longer times, indicating that the alloying took place during milling. The enthalpy change of the Ni_3Al ordering transition (including grain growth), as calculated from the DSC peak area, was found to be 5.4 kJ mol^{-1}. The activation energy was calculated to be 160 kJ mol^{-1}. Similar formation and ordering transitions were found for Ni_3Ge. The enthalpy change and activation energy of the Ni_3Ge ordering transition were found to be 7.9 kJ mol^{-1} and 140 kJ mol^{-1}, respectively.

Kasai et al. [95] studied the effect of mixed grinding (mechanical milling) on the reduction of hematite by graphite and of iron ore by metallurgical coke. Mixed grinding was done using planetary and tumbling ball mills. TG/DTA measurements (in argon) under different conditions, XRD and surface area measurements were used in the study. The results indicated that the reduction of hematite by graphite was significantly enhanced by mixed grinding. The metallic iron generated during reduction reaction seems to act as a catalyst for the reaction of graphite with CO_2 to produce CO, which effects the reduction according to the following solid-gas reaction:

$$Fe_xO_y + CO \rightarrow Fe_xO_{y-1} + CO_2$$

The TG/DTA results, Figure 31, indicated that the mass loss and associated endothermic peak, corresponding to the reduction of iron oxide, occurred at lower temperatures for samples prepared using longer mixing-grinding times. The reduction of iron ore by metallurgical coke, on the other hand, was not affected by mixed grinding, which was attributed to the presence of gangue minerals and impurities in both powders.

Differential scanning calorimetry, together with XRD and transmission electron microscopy, were used by Yang and Bakker [96,97] to examine phase transformations that occur in σ-phases of the transition metal couples FeV, CrFe, CoCr and NiV which were prepared by mechanical milling. The σ-phase is described as a partially disordered body-centered-cubic structure. For σ-FeV, after milling for 120 hours, the DSC curve exhibited two exothermic peaks. The first was related to overlapping effects of grain growth and the recovery of atomic order, and the second to the restoration of the b.c.c. structure to the original σ-phase. For σ-NiV, after milling for 240 hours, two exothermic peaks corresponding to crystallization (820 ^{o}C, 3.34 kJ mol^{-1}) and grain growth (928 ^{o}C, 0.17 kJ mol^{-1}) were recorded. The authors suggested that mechanical milling induces three types of metastable phases: a distorted b.c.c. solid solution (FeV and CrFe), a nano-crystalline σ-phase (CoCr) and an amorphous material (NiV).

While the Fe-C and Fe-C-Si systems are most fundamental in ferrous metallurgy, high-carbon alloys are considered difficult to study because of the problems encountered in their preparation by direct melting. Tanaka et al. [98], therefore, used mechanical milling to prepare these alloys and DSC, XRD, TEM and Mossbauer spectroscopy to study them. DSC was particularly useful because it identifies the crystallization of amorphous phases and determines the effect of the different compositions on the formation and behaviour of these phases. Exothermic reactions attributable to the crystallization of amorphous silicide and carbide phases formed during milling were determined, Figure 32. The formation of a high-carbon iron phase, Fe_7C_3, was confirmed and the

suppression of carbide formation with the addition of Si and the formation of a single amorphous ternary phase in the high-silicon region were verified.

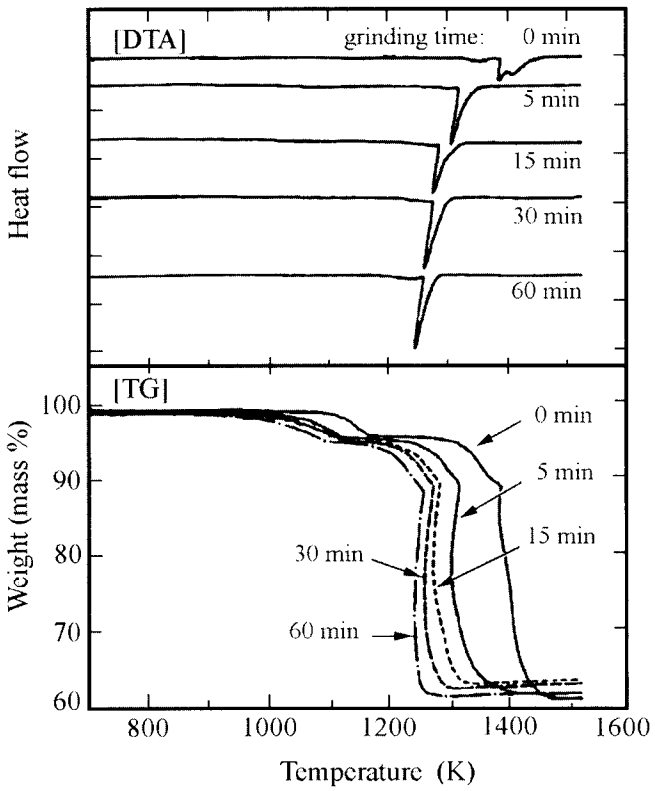


Figure 31. DTA and TG curves for hematite - graphite mixtures ground in a planetary ball mill for different lengths of time. From E. Kasai et al., reference 95.

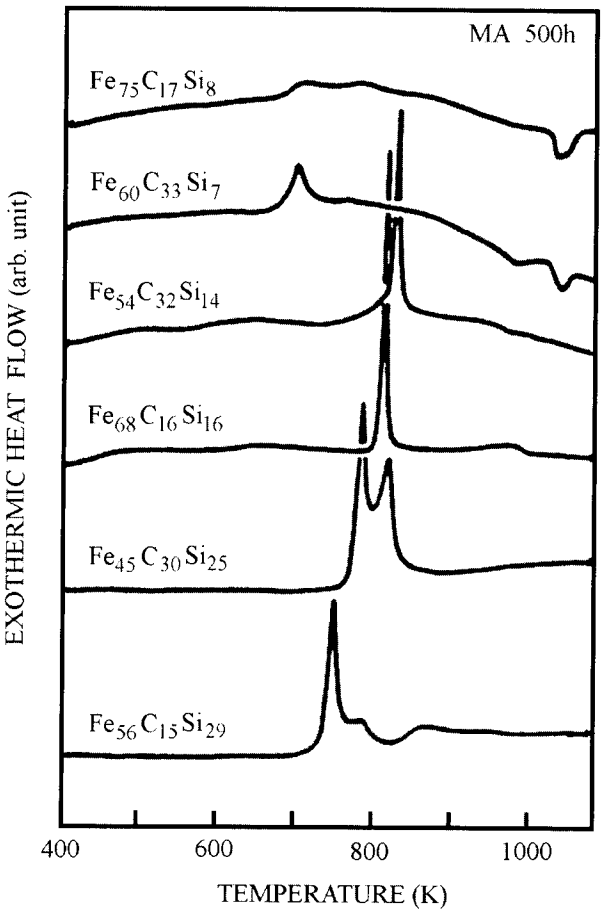


Figure 32. DSC curves for Fe-C-Si powders with various compositions after 500 h mechanical alloying. From T. Tanaka et al., reference 98.

4. OXIDATION AND CORROSION

4.1. Introduction

Thermogravimetry is one of the principal techniques used in investigations of the oxidation of metals and alloys by gaseous atmospheres containing oxygen. Studies of the resistance of metals and alloys to oxidation in air are particularly important in determining their suitability for high-temperature applications and for the development of alloys for use at elevated temperatures. The thermogravimetric technique (see Chapter 4 of Volume 1 of this Handbook) is used also in the study of the resistance of metals and alloys to more aggressive atmospheres, such as those containing sulfur oxides, chlorine or hydrogen sulfide. These gases are often found in the products of combustion in power plant boilers burning coal that contains significant amounts of sulfur impurities, and in the gases handled in various types of chemical plants.

For the most part, isothermal thermogravimetry, rather than thermogravimetry with continuous heating, is used in studies of high-temperature oxidation and corrosion of metals, since this technique is generally more amenable to interpretation in terms of the kinetics and mechanism of the reactions involved, and because many of the applications in which alloys undergo high-temperature attack involve exposure over extended periods of time. The particular techniques and precautions required for investigations in high-temperature corrosion of metals have been reviewed in an article by Grabke [99].

The sample of the material to be investigated is generally in the form of a thin flat coupon, rectangular [100,101] or circular [102,103], about 1 or 2 mm thick and 10 to 20 mm on a side or in diameter. For metals and alloys, such shapes usually are relatively easy to fabricate and the area of the reacting interface will be well defined and will remain approximately constant. However, the decrease in interfacial area may need to be considered in some cases [104]. Any surface layers on the sample should be removed by polishing with abrasives, such as silicon carbide, followed by removal of any residual abrasive powder, by ultrasonic cleaning for example. Any organic film on the surface of the sample should be removed by washing with an organic solvent, such as acetone or alcohol, that is free of non-volatile impurities [99,101,105]. The nature of the investigation may require the application or avoidance of certain treatments; for example, a cold-worked sample may give different results from an annealed sample, because grain-boundary diffusion of alloying elements that partake in the formation of an oxide surface layer may be affected by the condition of the alloy.

The changes in mass of the sample are most often determined by a sensitive recording microbalance, with the sample suspended from the balance by a platinum or silica filament. At high temperatures, silica filaments should be

avoided under strongly reducing conditions, because of the formation of volatile SiO, and platinum may lose mass in oxidizing atmospheres above 1450 °C.

When a quantitative treatment of the results of oxidation experiments is to be made to determine the kinetics of the surface reaction, it is necessary to minimize the uncertainty in the time at which the reaction starts. Grabke [99] discusses four methods for starting an experiment: (a) A furnace that can be moved vertically is heated with the reaction tube in place and the sample outside the hot zone of the furnace; to start the reaction the furnace is raised so that the sample is in the hot zone. (b) The furnace is heated with the sample above the furnace in the reaction tube; the sample is lowered into the hot zone of the furnace to start the reaction. (c) The sample is heated in the furnace with a vacuum or inert atmosphere in the reaction tube; the atmosphere being used for the study is introduced after the sample has reached the required temperature. (d) The sample is heated in place surrounded by the furnace; the furnace is heated as rapidly as possible. Grabke recommended methods (a) or (b) for quantitative studies. If method (c) is used, it should be ascertained that low concentrations of impurities in the inert atmosphere do not react to form a significant amount surface layer on the sample.

When corrosive atmospheres are used, for example gaseous mixtures containing chlorine, the metallic parts in the balance mechanism should be protected. This may be done with a current of inert gas flowing through the balance and out the aperture for the filament that suspends the sample, so that the corrosive gases do not enter the balance chamber. If the reactant gas is flowing upward from the sample, the mixed gas stream can be made to exit near the top of the reaction tube. If the reactant gas enters the reaction tube near the top and flows downward, corrections to the concentrations of constituents in the reactant gas mixture will need to be made on the basis of the rate of flow of the inert protective gas.

The general procedures and precautions that are applicable to thermogravimetry are covered in Chapter 4 of Volume 1 of this Handbook.

Whereas thermogravimetric studies provide data on changes in mass as a function of time or temperature, other supplementary techniques are required to elucidate fully the nature of the products of oxidation and corrosion reactions. These techniques include X-ray diffraction (XRD) studies to determine the different crystallographic phases in the product layer, optical microscopy and scanning electron microscopy (SEM) to determine the morphology of the product layer, and in-situ instrumental analysis by energy-dispersive analysis by X-rays (EDAX), or electron probe microanalysis, to determine the distribution of the various elements in the surface product layer.

4.2. Kinetics of oxidation reactions

Before considering particular examples of oxidation and corrosion reactions, it will be useful to review briefly the most generally applicable types of reaction kinetics that may be encountered. Indeed, the principal application of isothermal thermogravimetric investigations of oxidation and corrosion reactions is to furnish quantitative data for kinetic analysis.

One simple form of kinetics for the oxidation of metals arises when a compact and adherent product layer is formed on the surface of the metal or alloy and the rate of reaction is governed by diffusion through this layer. By Fick's first law:

$$J = - D\,(dc/dx)$$

where J = flux of the diffusing species through the product layer
D = diffusion coefficient
c = concentration of the diffusing species
x = distance into the product layer.

For a reaction taking place on a flat surface, the flux J, per unit area, will be constant, and assuming D is constant also:

$$J.x = -D.\Delta c$$

where x is now the thickness of the product layer and Δc is the difference between the concentration of the diffusing species at the gas/layer interface and at the layer/substrate interface. Δc may be assumed to be constant if the concentration of the reactive diffusing species is constant at the gas/layer interface and at the substrate/layer interface; that is, equilibrium is attained at these two interfaces and there are no significant concentration gradients outside the product layer. The rate of growth of the product layer is then proportional to the absolute value of the flux of the reactive diffusing species:

$$|J| = k_1.\,(dx/dt)$$

Hence:

$$k_1.(dx/dt).x = D.\Delta c$$

$$x.dx = (D.\,\Delta c/k_1).dt$$

Integrating:

$$x^2 = (2D.\ \Delta c/k_1).t\ =\ k_p.t$$

since it is assumed that $x = 0$ when time, $t = 0$.

Because of the form of this equation, it is known as the 'parabolic rate law' and k_p is often referred to as the parabolic rate constant. It should be noted that this 'law' is a function of not only the diffusion mechanism of the product layer growth, but also of the plane geometry of the samples used in this type of study. Edge effects will introduce small but usually negligible deviations.

No assumptions have been made in the derivation of the parabolic equation about the nature of the diffusing species, other than it must be involved in the reaction forming the product layer. In some cases it is a cation diffusing through a compact oxide layer from the metal/layer interface, accompanied by conduction of the compensating electrical charge, to the gas/layer interface, where oxygen gas is reduced to oxide ion which, with the cation, forms more oxide. A theoretical treatment for this type of oxidation reaction has been developed by Wagner [106]. Another simple case is that in which the rate of reaction between the gaseous reactant and the metal controls the consumption of the metal and the rate of production of reaction products. It is assumed that there is no impediment to the supply of reactants. Then the rate of reaction on a planar surface whose area does not change is:

$$-(dm/dt)\ = k_2$$

where m = mass of metal per unit area, and k_2 = a constant, which may depend on the concentration of the reactive gas. Integrating:

$$\Delta m = -k_2.t$$

If the product of reaction is volatile, the change in mass of the sample will be given by this equation. If a very porous product layer is formed, which offers no impediment to rapid diffusion, the net increase in mass will be proportional to Δm, so that a linear rate law is obtained:

$$\Delta m = K_2.t$$

where Δm = the net mass increase of the sample and K_2 is a constant.

A logarithmic form of reaction kinetics also has been used to treat the results of oxidation and corrosion studies:

$dx/dt = k_4 \exp\{-k_3 x\}$

which gives on integration:

$x = K_3 \ln (K_4 t + K_5)$

where $K_3 = 1/k_3$ and $K_4 = k_3 k_4$. The logarithmic form has been used mainly for treating the results from the initial stages of oxidation, when a very thin film of oxide is formed on a metal surface. Indeed, parabolic kinetics would not be expected to apply strictly at the very beginning of reaction because the reaction rate would be infinite at time zero when the film thickness is zero.

An inverse logarithmic form has also been used for the formation of thin oxide films:

$1/x = K_6 - K_7 . \ln t.$

Experimental data may often be fitted empirically to a power law:

$\Delta m = a . t^{n}.$

When the exponent $n = 0.5$, this form becomes equivalent to the parabolic law.

The two rate 'laws', parabolic and linear, represent ideal cases. Often intermediate cases are observed, or the kinetics are complicated by other factors, such as spalling of the product layer, formation of liquid phases, or the partial volatilization of products of reaction. In many instances the processes are so complex that mathematical analysis of the thermogravimetric results is not possible. The different mechanisms of oxidation and corrosion of metals and alloys and related theory have been discussed in books by Kofstad [107], Hauffe [108] and Fromhold [109].

4.3. Oxidation of unalloyed metals

The reaction of unalloyed metals with oxygen gas at high temperatures probably represents the simplest type of system, but even here there are many factors that can contribute to complexity in the interpretation of the results of isothermal thermogravimetric studies. Parabolic kinetics are generally considered to represent the 'normal' course of oxidation, and have been observed for the reaction of copper [110] and of nickel [111].

In a study of the oxidation of copper in oxygen in the temperature range 900° to 1050 °C, at oxygen pressures from $5x10^{-3}$ to 0.8 atm, Mrowec and Stokłosa [112] used a helical tungsten spring microbalance in a system that could be pumped out before the introduction of oxygen at the required pressure. The effect of changing gas flow rate was examined, and the experiments were conducted in the region where the flow rate was sufficient so that it did not affect the results. The authors made corrections for changes in the effective surface area of their specimens. When the oxygen pressure was below the dissociation pressure of CuO, compact adherent films of Cu_2O were formed for oxide film thicknesses up to 0.17 mm. The kinetic results could be plotted according to the equation:

$$(\Delta m/A)^2 = k''_p.t + C$$

where Δm = increase in mass of the specimen, A = surface area, and t = time, as shown in Figure 33. The parabolic rate constant, k''_p, could then be determined. From the results at different oxygen pressures, Po_2, the relationship:

$$k''_p = \text{const.}\ (Po_2)^{1/3.9}$$

was determined. From plots of log k''_p against 1/T, an activation energy for the formation of the monophase Cu_2O layer was obtained. In contrast, when the oxygen pressure was higher than the dissociation pressure of CuO, k''_p was found to be independent of oxygen pressure. In this case there was a duplex film with a thicker inner Cu_2O layer and a thinner CuO outer layer. The oxygen potential across the Cu_2O layer was controlled by the Cu/Cu_2O and the Cu_2O/CuO equilibria, and since the film growth was controlled by diffusion through the thicker Cu_2O layer, the rate of film growth became independent of the external oxygen pressure.

The kinetics of the oxidation of cobalt in the temperature range 600 to 800 °C, in $Ar-O_2$ mixtures corresponding to oxygen partial pressures from 0.001 to 1 atm, were investigated by Hsu and Yurek [113] by thermogravimetry using an electrobalance. The kinetics followed the parabolic law after a short initial non-parabolic stage, as illustrated by plots of $(\Delta m/A)^2$ against time, from which values of K_p, the gravimetric parabolic rate constant, were obtained with excellent reproducibility. Two different sources of zone-refined cobalt were used. A two-phase adherent layered scale was formed, with a CoO layer next to the metal and an outer layer of Co_3O_4. Theoretical treatment of the kinetic results, together with microstructural examinations of the oxide layers, indicated that the oxidation rate was controlled by cation diffusion, with lattice diffusion

predominating in the larger grained CoO but with significant grain boundary diffusion in the finer grained Co_3O_4.

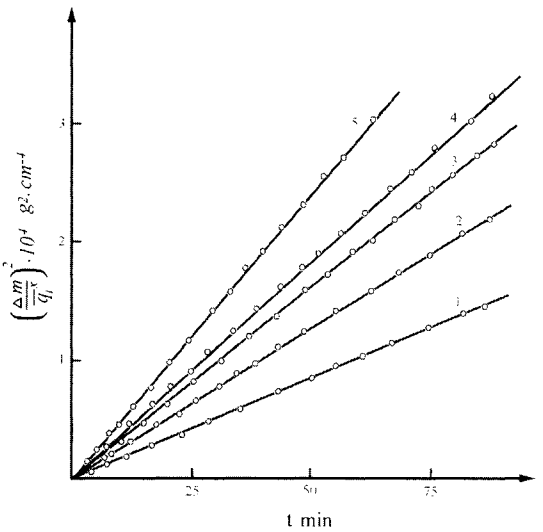


Figure 33. Plots showing parabolic kinetics for copper oxidation at Po_2 = $2.6x10^{-2}$ atm for several temperatures. Curves 1-5 correspond, respectively, to 900, 950, 980, 1000 and 1050 °C. From S.Mrowec and A. Stokłosa, reference 112.

The rate of oxidation on different crystal faces of nickel was investigated by Herchl et al. [114] in the temperature range 500° to 800 °C at an oxygen pressure of 400 torr, using a Cahn RG continuously recording microbalance. Oxidation rates were found to differ on different crystal faces of the face-centered cubic nickel, the rates decreasing in the order (100) > (110) > (111). Discontinuities in approximately parabolic plots were attributed to blistering and cracking of the polycrystalline oxide product layer.

If the oxidation of copper or nickel was interrupted by a period of annealing in argon, the oxidation rates, as determined by thermogravimetry, were slower when oxidation was recommenced [115]; this decrease was attributed to a decreased cation vacancy gradient across the oxide scale due to a decrease in oxygen partial pressure at the oxide-gas interface during the annealing period. This indicates that phenomena other than simple layer thickening can affect the rate of oxidation, even in fairly simple cases where protective oxide scales are formed.

The oxidation of unalloyed iron at 10 to 760 torr oxygen pressure at 500 °C was studied by Caplan et al. [116]. Considerable differences were observed between the behaviour of cold-worked specimens and annealed specimens. With the annealed specimens, the rate of mass increase due to oxidation was slower; this was attributed to the formation of voids, which formed between the oxide scale and the metal surface due to vacancy diffusion from the outer surface. The oxide scale consisted of Fe_3O_4 (inner) and α-Fe_2O_3 (outer) layers. The faster rate of oxidation of the cold-worked specimens was attributed to better contact between the metal substrate and the scale, but the rate of oxidation decreased as the exposure time increased. This was attributed to grain growth and recrystallization in the cold-worked specimens. The authors presented apparent parabolic rate constants, calculated as $2m.dm/dt$, as functions of time. The rate of oxidation was dependent on the impurities present in the iron [117]. Jansson and Vanneberg [118] also found that the rate of iron oxidation was significantly affected by the method of specimen preparation. At 625 °C the oxide scale included a layer of wustite, $Fe_{1-x}O$, between the metal and Fe_3O_4 (wustite is not stable below 560 °C).

In a thermogravimetric investigation of the oxidation of iron at a still higher temperature, 800 °C, and with lower oxygen pressures, $2.5x10^{-3}$ to $3.0x10^{-1}$ torr, Goursat and Smeltzer [119] observed a different pattern of behaviour. Oxidation typically started with a period of increasing rate of mass gain during which grains of wustite nucleated on the iron surface and grew until a layer of uniform thickness covered the surface. This was followed by a period of linear oxidation, for which the rate was directly proportional to the oxygen pressure. The rate controlling mechanism for this stage appeared to be non-dissociative adsorption of oxygen on the surface of the wustite. Finally a period of parabolic kinetics was reached for which k_p was independent of oxygen pressure. A thin layer of magnetite was present on the outer surface of the wustite, and so the flux of iron for growth of the scale was directly related to the iron vacancy concentration established by the oxygen activities at the $Fe/Fe_{1-x}O$ and $Fe_{1-x}O/Fe_3O_4$ interfaces. These studies on the oxidation of iron illustrate the complexities that may arise in what might have been expected to be a fairly simple system.

The effect of impurities on the high-temperature oxidation of zirconium was studied by Voitovich et al. [120], who found that technical grade Zr, in the temperature range 900 to1300 °C, oxidized faster than more pure Zr refined by the iodide process. The kinetics of the oxidation were studied by thermogravimetry, and some of the results are shown in Figure 34. At the higher temperatures, at first the parabolic rate law was followed, but this later changed to linear kinetics as "breakaway" corrosion began. Above the α-β transition temperature of 862 °C, the β-Zr phase is normally present, but diffusion of

oxygen into the metal substrate stabilized wedges of the α-phase. At lower temperatures, in the range 600 to 700 °C, no transition from parabolic to linear kinetics was observed in the thermogravimetric studies.

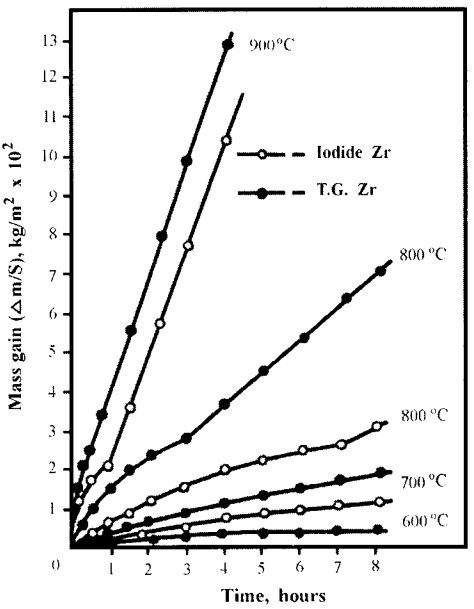


Figure 34. Thermogravimetric curves for the oxidation of iodide zirconium and technical grade zirconium at temperatures from 600 °C to 900 °C. From V.B. Voitovich et al., reference 120.

A thermogravimetric investigation of the oxidation of titanium in oxygen at 1 atm pressure, over the temperature range 600 to 800 °C, indicated that at first there was a period during which pseudo-parabolic kinetics were followed, but with periodic discontinuities in the slopes of the mass gain - time plots [121]. Subsequently linear kinetics were observed. Examination of the oxide scale indicated the presence of layers separated by short cracks that impeded the diffusion of oxygen and titanium and altered the oxidation rates. The final linear period commenced after the formation of continuous cracks between the oxide scale and the metal and the development of porosity in the oxide scale. In another investigation of the oxidation of titanium using thermogravimetry, Bertrand et al. [122] found a series of parabolic-like steps in the oxidation curves obtained at 695 °C and Po_2 = 105 torr. At higher temperatures, 840 °C and 965 °C they found that the slopes of the oxidation curves at first decreased, but then as the oxidation proceeded the oxidation rates began to increase. They

also found a complex layer structure with lamellar voids in the oxide scale. The formation of disrupted, non-compact oxide scales resulted in the complex kinetics observed during oxidation of titanium.

Vanadium oxidation by air, in the temperature range 700° to 1000 °C, was investigated by Keller and Douglass [123] by thermogravimetry, using a porcelain crucible suspended under the specimen to collect any liquid oxide that might drop off. Molten V_2O_5 (melting point 670 °C) did form as expected, but the correct total mass increase could still be measured. The increase in mass was linear with time, consistent with an interface reaction that could proceed unhindered by a protective product layer. However, under different conditions, in particular with lower oxygen pressures of 13.3 and 133 Pa, so that the vanadium would oxidize only to VO_2 rather than to V_2O_5, Yamawaki et al. [124] found that the parabolic rate law was followed.

The oxidation of rhodium in air, over the temperature range 600 °C to 1000 °C, was investigated by thermogravimetry in connection with studies on the degradation of rhodium catalysts in automobile catalytic converters [125]. Logarithmic kinetics were observed for the mass gain in the lower part of the temperature range. Then, as the temperature was increased through a transition range, the kinetics changed to follow a power law:

$$\Delta m = k_p.t^n$$

where Δm is the mass gain, t = time, and k_p and n were constants for the conditions used. At 1000 °C, however, it was found that, after an initial mass gain, the sample lost mass and then dropped below its original mass. This was attributed to volatilization of rhodium oxide and, when the specimen was examined after completion of the experiment, there was no oxide layer such as had been formed at lower oxidation temperatures.

4.4. Oxidation of alloys

The oxidation of alloys can involve several complicating factors that are not present in the oxidation of unalloyed metals. These factors include the selective oxidation of the less-noble alloy constituents, the formation of composite scales that involve oxides of the different constituents, and the formation of complex oxide phases that involve two or more of the alloy constituents. The kinetics of the oxidation reactions generally will be affected by these factors, and so the interpretation of thermogravimetric experiments requires the examination of the oxide scales by metallography, X-ray diffraction, and methods for *in situ* microanalysis. Of particular importance for many alloys is the presence of constituents that can form protective oxide layers, such as Cr_2O_3 and Al_2O_3.

The oxidation of binary alloys of cobalt and manganese was investigated using thermogravimetry by Narita et al. [126] over the temperature range 1000 to 1200 °C, in oxygen-helium mixtures chosen to give oxygen partial pressures from 10 to 10^5 Pa. The parabolic rate law was followed, except during the early stage of the reaction, as indicated by plots of $(\Delta m)^2$ against t, where Δm = mass change and t = time, as illustrated in Figure 35. For low Mn content in the alloy (0.23 or 3.2% Mn), values of k_p, as determined from the slopes of these plots, increased with increasing Mn content, and the oxide scale consisted of only the monoxide, (Co,Mn)O. With more than about 6% Mn, the values of k_p passed through a maximum and then decreased, as the manganese content of the alloy increased further, and a spinel phase, $(Co,Mn)_3O_4$, was found in the scale as well as the monoxide phase.

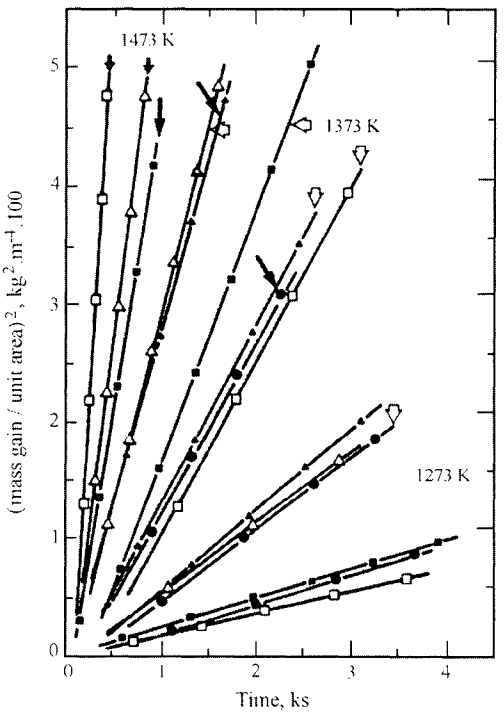


Figure 35. Plots showing parabolic kinetics for the oxidation of cobalt-manganese alloys at temperatures of 1273 K, 1373 K (open arrow), and 1473 K (closed arrow) at $Po_2 = 10^5$Pa. Results are shown for alloys with 23.0% Mn (open squares), 17.0%Mn (filled squares), 6.0% Mn (open triangles), 3.2% Mn (filled triangles) and unalloyed Co (filled circles). From T. Narita et al., reference 126.

A thermogravimetric study of the oxidation of alloy compositions corresponding to CoFe and $CoFe_3$ was made by Cabrera and Maple [127] over the temperature range 800 to 1000 °C in oxygen at 1 atm pressure. The alloy samples were in the form of 50 mg spheres held in a small quartz cup suspended from a microbalance, rather than foil or coupon samples as generally used for investigating the oxidation of metals. The CoFe composition was reported to show parabolic kinetics, whereas the oxidation of the $CoFe_3$ composition was better described by a direct logarithmic law.

A low-alloy steel, 2.5%Cr - 1%Mo, was studied by Raman et al. [128] to determine the effect of grain size on the oxidation resistance of this material at 550 °C in air. In the thermogravimetric investigations, parabolic kinetics were followed for all specimens. Various grain sizes had been obtained by grain growth during annealing samples in the temperature range 950 to 1250 °C. The oxidation rate decreased with increasing grain size; this was attributed to the smaller grain boundary area, which led to a decreased short-circuit grain-boundary diffusion path.

A phenomenon that is observed in certain alloy systems is internal oxidation. This may occur when an element that forms a very stable oxide is alloyed with a more -noble metal, through which oxygen can diffuse rapidly in comparison to the rate of diffusion of the oxidizable alloy constituent. Under these circumstances, the dissolved oxygen can react with the oxidizable constituent to form a dispersed oxide precipitate within the alloy phase. The oxidation of dilute alloys of magnesium (about 0.5% Mg) in silver at temperatures below 600 °C was investigated gravimetrically by Charrin et al. [129]. At first there was a short initial period during which the parabolic law was not followed; this was followed by a period of parabolic kinetics. Finally the oxygen/magnesium ratio passed through a maximum which in some cases might rise as high as 1.5, well above the ratio of 1.0 expected for stoichiometric MgO. It was postulated that clusters of Mg and O formed with excess oxygen, and that these clusters finally coalesced into particles of MgO, with the release of oxygen as was indicated by a mass loss. The oxidation of Ag-2.2%Al alloys was studied thermogravimetrically in the temperature range 500 to 900 °C by Takada et al. [130] using powder samples. In this system also, it was found that the O/Al ratio could rise above the stoichiometric value of 1.5. At the higher temperatures, the ratio would drop back to 1.5, but at lower temperatures, the ratio could remain above 1.5.

Stainless steels form one of the most important types of oxidation-resistant alloys, and, consequently, thermogravimetric investigations are of great importance in characterizing their resistance to oxidation. Botella et al. [131] studied the oxidation of AISI type 304 stainless steel (18%Cr - 8%Ni) at 700 °C, in comparison with a low-nickel steel in which manganese was used to replace

much of the nickel (17% Cr - 2.6% Ni - 11.5% Mn). Specimens, in the form of 20 x 10 mm plates, were oxidized in synthetic air at 700 °C, using a thermobalance. The results were expressed in the form of a power-law equation. The values of n (0.65 for AISI 304 and 0.31 for the low-Ni alloy) were such that the thermogravimetric plots, as shown in Figure 36, roughly resembled those for parabolic kinetics (n = 0.5). Coherent oxide scales grew on both alloys; Cr_2O_3 was the principal scale constituent on the 304 stainless steel, whereas $(Cr,Mn)_2O_3$ was found on the low-Ni, high-Mn alloy. Some nodules, rich in iron, were found on the outer surface of the oxide scale over spots where there appeared to be oxidation penetrating into the metallic phase. These nodules were more numerous on the low-Ni alloy, and the authors suggested that this might indicate lesser oxidation resistance over extended exposure to an oxidizing atmosphere, even though the themogravimetric results indicated roughly comparable oxidation after about 80 h exposure.

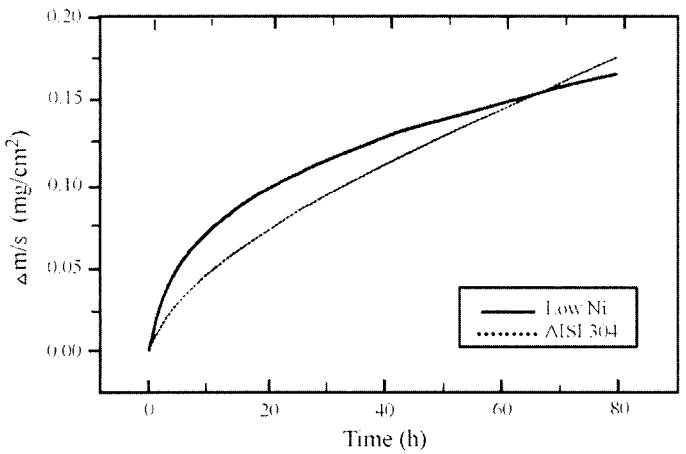


Figure 36. Thermogravimetic curves for the oxidation of AISI 304 stainless steel and a low-nickel alloy in air at 973 K. From J. Botella et al., reference 131.

The oxidation of a series of iron-chromium-nickel alloys, with chromium contents up to 30%, was investigated at 1000 °C in static oxygen at 200 torr pressure by Croll and Wallwork [132] using an electrobalance. The thermogravimetric results were presented as plots of log [mass gain ($mg.cm^{-2}$)] against log [oxidation time (h)] for times up to 100 h. These plots had slopes that were close to 0.5, so the kinetics were approximately parabolic. Alloys with the lowest Cr content (<1%) showed the highest oxidation rates. For alloys with less than 10% Cr, internal oxidation took place, with precipitation of Cr_2O_3 at

the grain boundaries in the alloy phase under the oxide scale. Alloys with the highest chromium content (20 to 30%) showed the lowest oxidation rates, and Cr_2O_3 was the major oxide phase in the scale. With the highest chromium contents, negative deviations from parabolic kinetics were observed; this was attributed to volatilization of chromium as CrO_3.

The oxidation of a Fe-19.6%Cr-15.1%Mn stainless steel in air over the temperature range 700 to 1000 °C was investigated by Douglass and Rizzo-Assuncao [133], who found that the general shape of the mass gain - time curves was parabolic, but with some deviations. Under certain conditions there was initially a slight mass loss that was attributed to volatilization of manganese. There was considerable spinel phase $(Fe,Cr,Mn)_3O_4$ present in all the oxide scales, as well as Cr_2O_3. The rate of oxidation was found to be much slower than for a Fe-9.5%Cr-17%Mn alloy, which had a significantly lower chromium content and did not form Cr_2O_3 in the oxide scale.

The formation of an aluminum oxide layer on aluminum metal provides remarkable oxidation resistance to what would otherwise be a very reactive metal. This property of Al_2O_3 can be used to improve the oxidation resistance of alloys by the addition of aluminum. Lambertin and Beranger [102] have investigated the high temperature oxidation of iron-chromium alloys with additions of up to 6 mass % aluminum. Fe - 20%Cr alloy with about 4% aluminum showed parabolic kinetics during reaction with oxygen at atmospheric pressure in the temperature range 800 to 1100°C, as illustrated by plots of mass gain against time$^{1/2}$ in Figure 37. The oxidation product layer was α-Al_2O_3 on this alloy. But with only 2% aluminum in the alloy, three sub-scales were observed: an external Fe_2O_3 layer, an intermediate layer of Cr_2O_3 and an inner layer of Al_2O_3. Thermogravimetric results for this latter alloy showed rapid initial oxidation followed by a much reduced rate. These observations taken together indicated initial rapid formation of iron and chromium oxides followed by precipitation of Al_2O_3 at the internal interface.

Brazing alloys for making metal to ceramic joints must be able to withstand oxidizing conditions at elevated temperatures, because ceramic materials often are chosen for use under such conditions. Silver-copper alloys with a Ag/Cu ratio of 60/40, near the eutectic composition in this system, have been used as brazing material, usually with the addition of a few percent of titanium to improve wetting, and hence adhesion, on oxide ceramics. Xian and coworkers [134,135] found, by thermogravimetry in air at 873 K, that the eutectic alloy showed parabolic oxidation kinetics both with and without 5 at.% Ti. The addition of small amounts of Cr, Ni or Y had only minor effects on the parabolic rate constant, but the addition of 5 at.% of aluminum produced an alloy for which the oxidation rate became negligible after about 20 hours. The oxidized

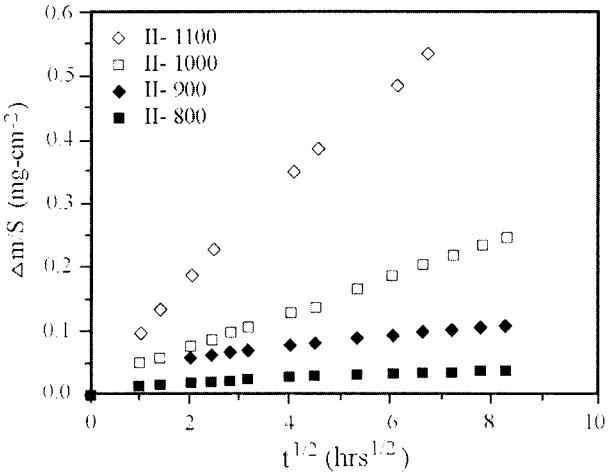


Figure 37. Plots showing parabolic kinetics for the oxidation of an Fe - 20% Cr - 4% Al alloy at temperatures from 800 °C to 1100 °C under 1 atm Po_2. From M. Lambertin and G. Beranger, reference 102.

film on alloys without aluminum consisted of an outer layer of CuO and a thinner inner layer of Cu_2O, as determined by XRD and EDAX examinations. With aluminum present in the alloy, an inner adherent protective layer of $CuAl_2O_4$ was formed. The melting temperatures for these alloys, an important property for brazing alloys, were determined by DTA. The oxidation behaviour of Ag-Cu-Ti brazing alloy layers applied to ceramic substrates has also been studied [136]. Parabolic kinetics were observed in Ar-O_2 mixtures in the temperature range of 400 to 700 °C. A particular observation was that the oxidation rates of an alloy applied to partially stabilized zirconia were higher than the rates for the same alloy applied to alumina. This difference was attributed to oxygen transport through the zirconia; the observation of a layer of TiO between the alloy and the zirconia substrate was consistent with this explanation.

Alloys consisting of hard, tungsten carbide particles embedded in a metallic matrix are used extensively in cutting tools. During use, these alloys, or cermets, become quite hot. Isothermal thermogravimetric studies on the oxidation of WC-16% Co, WC-8% Co-8% Ni and WC-16% Ni in air in the temperature range 500 to 800 °C have been reported by Voitovich et al. [137]. For these alloys, there is the possibility of the formation of gaseous products, CO and CO_2, with consequent loss of mass by the material being examined and, indeed, at 500 and 600 °C loss of mass was observed and attributed to reactions such as: $WC + 0.5\ O_2 = 1/2\ W_2C + 0.5\ CO_2$ and $WC + O_2 = W + CO_2$. At

800 °C the rate of mass gain was essentially constant, whereas at intermediate temperatures more complex kinetics were observed. Examination of the oxidation products by scanning electron microscopy and X-ray diffraction indicated the formation of $CoWO_4$ on WC-Co, and WO_3 and lesser amounts of NiO and $NiWO_4$ on the less oxidation-resistant WC-Ni. The thermogravimetric results demonstrated also that the alloys were more oxidation resistant than tungsten carbide alone.

The surface hardness and wear resistance of steels may be increased by "case hardening", which involves treatment in ammonia gas and hydrogen to form a nitrided surface. Coates et al. [138] have conducted thermogravimetric studies on the oxidation of nitrided Fe-2.3%Cr and Fe-5%Mo alloys. The iron nitride particles in the treated alloy seemed to provide nucleation sites for the formation of a more adherent fine-grained oxide structure, but this did not always appear to correlate with increased oxidation resistance.

4.5. Oxidation by gases other than molecular oxygen

Metals and alloys can be oxidized by oxygen-containing gases such as water vapor or carbon dioxide, with the formation of surface oxide layers. If metal oxides are the only reaction products, then thermogravimetic results may be interpreted in the same way as results from oxidation by molecular oxygen. For example, the oxidation of titanium metal in atmospheres of water vapor plus hydrogen has been studied in the temperature range 750 to 1010 °C [139]. When changes in mass were plotted against time, the initial portions of the plots were parabolic but later became linear. Measurements of the thicknesses of the oxide layers were made by optical microscopy and these measurements were correlated with the changes in mass. These correlations indicated that some oxygen went into solid solution in the α-Ti by diffusion and this apparently gave rise to the initial parabolic kinetics. As reaction proceeded, a layer of TiO_x formed by precipitation from the Ti-O solid solution, together with an outer layer of TiO_2. The linear reaction kinetics appeared to arise from the formation of TiO_2 at the TiO_x-TiO_2 interface. A series of experiments at 950 °C showed that the rate of oxidation of the titanium increased as the water vapor content of the gas mixture was raised from 3% to 57%.

The reaction of unalloyed iron with gas mixtures that covered a range of CO_2/CO ratios has been investigated by Bredesen and Kofstad [140-142] at temperatures from 1000 to 1200 °C and at total pressures of 0.1 to 1 atm. Experiments were conducted to ensure that gas flow rates were fast enough so that they did not affect the thermogravimetric results. Under mild oxidation conditions (low temperature, low total pressure and low mole fraction of CO_2 in the gas phase), a period of slow reaction, involving nucleation and initial film formation, was observed. This period was followed by linear film-growth

during which the rate was assumed to be governed by surface reaction, with the number of adsorption and growth sites remaining constant. Diffusion through the wustite film was relatively rapid and was not rate controlling. Under more severe conditions (at 1200 °C), the initial period of film formation was too short to be observed, but there was a period of linear scale-growth during which the rate was not dependent on the scale thickness, but did increase with Pco_2. This indicated that adsorption of CO_2 was rate controlling. The linear scale- growth was followed by a period of parabolic scale-growth, which indicated that diffusion had become rate controlling as the scale became thicker. However, the form of the dependence on Pco_2 and composition of the gas mixture indicated that the surface of the wustite was not in equilibrium with the gas phase. No magnetite (Fe_3O_4) was found in the scales, even though it would have been stable under equilibrium conditions.

The kinetics of oxide-scale formation on a series of iron-manganese alloys were investigated thermogravimetrically by Mayer and Smeltzer using CO_2/CO atmospheres at 1000 °C [143]. The plots of (mass gain / unit area)^2 against time were generally linear after an initial non-linear period. The parabolic rate constants derived from these plots were found to increase with the CO_2/CO ratio in the gas phase and to decrease with increasing Mn content in the alloy. X-ray diffraction of the compact scales showed that they were (Fe,Mn)O.

A simulated combustion atmosphere, composed of a mixture of nitrogen with 6.55% CO_2, 18.84% H_2O, and 3.75% O_2, was used in an investigation of the oxidation of low alloy steels containing small amounts of silicon and aluminum [105]. The thermogravimetric tests were conducted at 1050 °C for 3 h on duplicate specimens so that the significance of the effects of changes in alloy composition could be more clearly discerned. The kinetics of the oxidation reaction were essentially parabolic, although at the commencement of reaction there was a short period of linear kinetics. The oxidation products, identified by electron microprobe analysis and XRD, were reported as FeO, Fe_3O_4, Fe_2O_3 and $FeSiO_4$, with $FeAl_2O_4$ occasionally present when the alloy contained aluminum.

4.6. Oxidation and corrosion in aggressive atmospheres

The high temperature corrosion rate for metals and alloys is often accelerated greatly in the presence of compounds of sulfur or chlorine. It is not surprising, therefore, that there have been many studies to determine the resistance of structural alloys to service in atmospheres similar to those encountered in chemical processing plants and in power plants burning sulfur-bearing fuels. In atmospheres containing such gases as SO_2, SO_3, Cl_2 or HCl, the products of reaction on the metal surface may well include sulfates, sulfides or chlorides in addition to various metal oxides.

The high temperature corrosion of iron has been investigated by thermogravimetry using a gas mixture of oxygen plus 4% SO_2 in the temperature range 500 to 800 °C by Holt and Kofstad [100]. The specimens in the thermobalance were surrounded by an inverted bucket of platinum cloth, used as a catalyst to ensure the equilibrium ratio of SO_2/SO_3. Changes in mass followed essentially parabolic kinetics. The parabolic rate constant increased with temperature to 640 °C, whereupon the rate constant suddenly dropped by an order of magnitude before continuing to increase again as the temperature was raised further, as indicated in Figure 38. Examination of the surface scales by X-ray photoelectron spectroscopy, X-ray diffraction and scanning electron microscopy indicated that, below 640 °C, iron(III) sulfate was formed and, with Fe_2O_3, constituted the outer layer of the scale. The layer next to the metal consisted of wustite ($Fe_{1-y}O$) and $Fe_{1-x}S$ with some magnetite. At higher temperatures, the scale consisted of $Fe_{1-y}O$/ Fe_3O_4/ Fe_2O_3, similar to the surface scale formed by the reaction of iron with oxygen alone. The predominant phase was wustite, with only a very minor amount of $Fe_{1-x}S$ present near the scale-metal interface. Above 640 °C, no iron(III) sulfate was found. The abrupt change in reaction rate at 640 °C was attributed the higher diffusion rate of iron in $Fe_{1-x}S$ compared to $Fe_{1-y}O$.

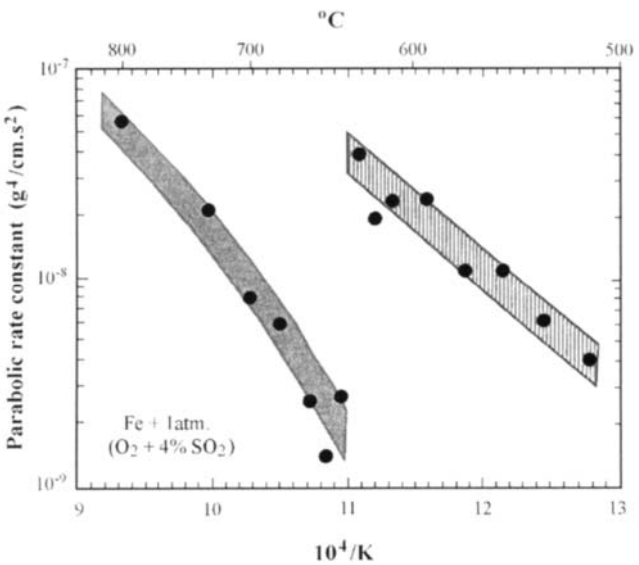


Figure 38. The parabolic rate constant for the corrosion of iron in O_2 + 4% SO_2 as a function of reciprocal absolute temperature; note the discontinuity at about 640 °C. From A. Holt and P. Kofstad, reference 100.

When chlorine or compounds of chlorine are present in the atmosphere at high temperatures, there is the possibility of the formation of volatile metal chlorides; this will lead to losses in mass and will complicate the interpretation of the results of thermogravimatric experiments. The oxidation of cobalt metal in an atmosphere of 50% O_2 with up to 6% Cl_2 was investigated at 1200 K by Maloney and McNallan [103], who found that volatilization of $CoCl_2$ was an important process in the reaction mechanism. The results of their thermogravimetric studies were interpreted on the basis of the formation of a CoO surface layer by reaction with O_2 following parabolic kinetics, and the simultaneous removal of CoO by the reaction:

$$CoO(s) + Cl_{2(g)} = CoCl_2(g) + 0.5\ O_2(g).$$

This suggested a rate equation of the form:

$$dx/dt = K_p/2x - K_s$$

where K_s is the linear rate constant for the decrease in thickness of the oxide layer. The value of K_p was determined from the rate of oxidation of Co in the absence of chlorine, and K_s was determined from the rate of reaction of Cl_2 with Co samples that had been completely oxidized to CoO. The value of K_s was dependent on the gas flow rate and partial pressure of Cl_2. The calculated and experimental results in O_2 + y% Cl_2 + Ar agreed fairly well for y > 0.1% to y = 3%, for which latter composition an almost linear decrease of mass with time was observed. At lower temperatures, in the range 900 to 1100 K, the results were more complex, and at 1000 K much higher rates of mass increase were observed than would be expected on the basis of the mechanism suggested above.

Further complexity is introduced if an alloy, rather than a pure metal, is involved in the reactions with an atmosphere containing chlorine. The high temperature corrosion of iron-chromium alloys in atmospheres of 50% O_2 with 0.25% and 1% Cl_2 was investigated by Kim and McNallan [144] and found to be quite complex. With 1% Cl_2 at 1000 K, the three alloys studied, 1%, 5% and 20% Cr, all showed mass loss over the two hour period of the thermogravimetric experiments due to volatilization of metal chlorides or oxychlorides. Under other conditions, thermogravimetry showed mass increases, but often the shape of the mass-time plot would be complex and probably was the result of competing gains and losses in mass. The corrosion products were characterized by optical microscopy and scanning electron microscopy. Typically, it was found that porous oxide layers were formed in the chlorine environments, except for the 20% Cr alloy with 0.25% Cl_2, for which compact, fairly protective oxide

layers were formed at temperatures other than 1000 K. At the lower temperatures, 900 and 1000 K, $FeCl_2$ was found between the porous oxide layer and the metal. The oxide scale generally had an inner layer of Cr-Fe oxide and an outer layer of iron oxide and, at 1000 K and above, the scale was quite porous, leading to accelerated corrosion.

In order to approach even more closely to conditions found in engineering practice, investigations have been made, for example by Spiegel and Grabke [145], using an atmosphere containing 5% O_2 with 500 ppm HCl and 250-1000 ppm SO_2, in He as carrier gas, to simulate a waste incineration atmosphere. Samples of a boiler tube steel with 2.25% Cr - 1% Mo, after initial pre-oxidation treatment, were used for thermogravimetric studies at 500 °C. HCl greatly accelerated the rate of mass increase over that in 5% oxygen alone, but SO_2 appeared to have little effect on the rate. The presence of SO_2 in addition to HCl actually decreased the rate of mass gain from that observed with HCl alone. With HCl alone, $FeCl_2$ was found under a defective Fe_3O_4/Fe_2O_3 layer, but with SO_2 alone, no phase containing sulfur was found. With both HCl and SO_2, $FeCl_2$ and FeS_2 were formed under the oxide scale. The authors proposed a mechanism to account for the different rates of attack on the steel.

4.7. Corrosion in the presence of salt deposits

During the combustion of coal or other fuels containing sulfur or chlorine in power plants, sulfate or chloride salts of calcium, sodium or potassium may be formed. The ash containing these salts may then deposit in boiler tubes, and, with sulfur oxides or chlorine in the gaseous combustion products, very severe corrosion conditions can result. Thermogravimetry has been a useful technique for investigating the complex reactions the take place under such conditions. A horizontal microbalance can be used, with the solid, such as a loose fly ash, applied to the upper surface of the metallic coupon [146], or a vertical furnace configuration may be used, with a salt applied as a saturated aqueous solution to a heated metal surface [147] to form an adherent deposit.

The oxidation of a 2.25%Cr-1%Mo steel, in contact with surface deposits of sodium chloride and deposits of a fly ash from a waste incineration plant, was investigated by Grabke et al. [146] by thermogravimetry at 500 °C in atmospheres of 5% or 13.3% O_2 in He. Chloride in the deposits reacted with the iron oxide surface scale on the pre-oxidized steel to form $FeCl_2$ at the scale/metal interface, probably by a mechanism involving a reaction such as:

$$2NaCl + Fe_2O_3 + 0.5\ O_2 = Na_2Fe_2O_4 + Cl_2.$$

The chlorine apparently penetrated the scale, and then reacted with iron at the metal/scale interface to form $FeCl_2$, some of which volatilized sufficiently to

diffuse out to the scale/atmosphere interface, where oxidation occurred with the formation of porous iron oxide:

$2FeCl_2(g) + 1.5\ O_2 = Fe_2O_3 + 2Cl_2$.

Application of a surface deposit of the fly ash, which contained mixed sodium and potassium chlorides as well as sulfates, also produced accelerated corrosion, as indicate in Figure 39. The effect of adding SO_2 to the atmosphere was investigated using the fly ash deposited on a sample of the steel and also using fly ash alone. The fly ash alone showed an increase in mass due to the formation of pyrosulfate, and the resulting thermogravimetric plot could be used, with the plot for the steel sample plus fly ash, to estimate the net mass changes due to corrosion of the steel. Similar experiments with HCl added to the atmosphere indicated a mass loss due to reactions such as:

$(K,Na)_2Ca_2(SO_4)_3 + 2HCl = 2(K,Na)Cl + 2CaSO_4 + SO_2 + H_2O + 0.5\ O_2$.

The corrosion produced by 500 ppm HCl was much greater than that produced by 500 ppm SO_2. However, the presence of SO_2 mitigated the enhancing effect of HCl on the corrosion rate.

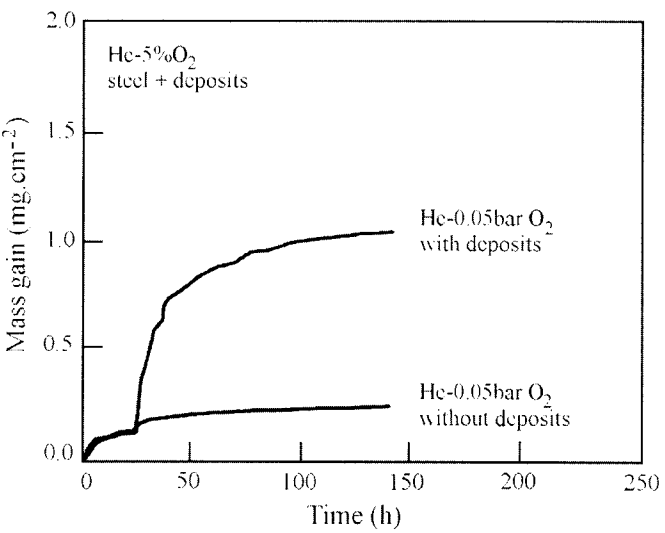


Figure 39. Thermogravimetric curves for the reaction of 2¼%Cr - 1%Mo steel in He-5%O_2 at 500 °C, without fly ash deposits and with fly ash deposited at 24 h. From H.J. Grabke et al., reference 146.

The hot corrosion of 2.25%Cr-1%Mo steel was studied also by Ahila et al. [147], with a mixture of K_2SO_4 and KCl applied to the surfaces of the steel samples. The results for the temperature range 550 to 750 °C corroborate the enhancement of the corrosion rate by surface deposits of chloride and sulfate salts. A particular feature of this investigation was the use of alloy samples that were cut from joints welded by different techniques.

Nickel alloys are often chosen for use because of their good high-temperature mechanical properties and resistance to corrosion. The nickel-based alloy designated as IN-738 has been used in gas turbines and, in view of this application, an extensive investigation was undertaken [148] on pre-oxidized alloy samples with surface deposits of Na_2SO_4 exposed to air at 975 °C. IN-738 is a nickel-based alloy with 16.0%Cr, 8.5%Co, 3.4%Al 3.4%Ti and lesser amounts of Mo, W, Ta, Nb, Zr and C. Pre-oxidation of the alloy in O_2, without Na_2SO_4, showed parabolic kinetics with the formation of a Cr_2O_3-TiO_2 surface layer. Thermogravimetric study of the pre-oxidized alloy, coated with Na_2SO_4, showed an induction period of about 55 h, followed by catastrophic oxidation with increase in mass until about 75 h, and then a deceleration period to the end of the experiment at 100 h., as shown in Figure 40. The nature of the reactions involved were investigated by monitoring the evolved SO_2, chemical analysis of soluble compounds in the surface coating, and electron microprobe analysis of sections though the product layers. Several reactions that were involved in the complex corrosion process were studied individually by thermogravimetry as well as by the other analytical methods. These reactions included the vaporization of Na_2SO_4 and Na_2CrO_4 and the reactions:

$$Cr_2O_3 + 2Na_2SO_4(l) + 1.5\ O_2 = 2Na_2CrO_4(l) + 2SO_3(g),$$

$$nTiO_2 + Na_2SO_4(l) = Na_2O(TiO_2)_n + SO_3(g).$$

These reactions, together with continuing oxidation of the alloy, contributed to competing mass gains and losses during the induction period. The rapid corrosion period apparently involved the formation of molten molybdates and tungstates that acted as fluxes.

As discussed in the section on the oxidation of alloys, the presence of aluminum in an alloy may enhance resistance to oxidation by the formation of an aluminum oxide layer. There has been interest, therefore, in the hot corrosion resistance of aluminum-containing alloys in the presence of salt deposits. The corrosion of Fe, Fe-5% Al and Fe-10% Al, with a surface deposit of Na_2SO_4, has been studied by thermogravimetry in atmospheres of O_2 plus 0.5% or 1% SO_2/SO_3 at 650 °C [101]. The SO_2/SO_3 equilibrium was established by passing an O_2-SO_2 gas mixture over a honeycomb ceramic containing Pt and/or Rh. The

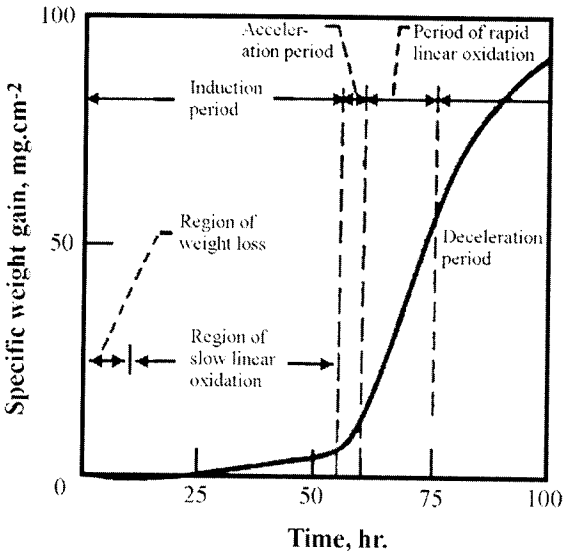


Figure 40. Thermogravimetric curve for the corrosion of pre-oxidized IN-738 alloy at 975°C in flowing oxygen, with 3 mg cm^{-2} Na_2SO_4 applied to the surface. The effect of rapid catastrophic oxidation is evident. From G.C. Fryburg et al., reference 148.

Na_2SO_4 deposits accelerated the corrosion of both the iron and the iron-aluminum alloys. Corrosion rates decreased with higher aluminum concentration in the alloy and increased with SO_2/SO_3 concentration in the atmosphere. Examination of the corrosion products by X-ray diffraction, scanning electron microscopy and electron probe microanalysis indicated that on iron, in the presence of Na_2SO_4, the scale consisted of three layers: a loose outer layer of Fe_2O_3, a layer of Na and Fe sulfates, and an inner compact layer of Fe oxides and sulfide. On the Fe-Al alloys, the outer two layers were similar to those formed on iron, but the inner compact layer consisted of two sub-layers, a top sub-layer of iron oxides and an inner sub-layer of oxides and sulfides rich in aluminum. The suggested mechanism involved the inward diffusion of oxygen (probably as $S_2O_7^{2-}$) through the molten Na-Fe sulfate flux, and the outward diffusion of Fe^{2+} which oxidized to Fe_2O_3 at the gas/melt interface. The formation of the sulfides was attributed to the low oxygen potential at the metal/corrosion product interface.

Alloys based on iron aluminide (Fe_3Al) have been suggested for applications in fluidized-bed combustion systems, gas turbines and coal gasification processes. Corrosion resistance in the presence of SO_2 and molten salts such as alkali sulfates is important for these applications. The alloys Fe_3Al-2%Cr and Fe_3Al-

5%Cr were examined by thermogravimetry in air containing 1% SO_2, with and without a surface deposit of Na_2SO_4-Li_2SO_4 eutectic mixture [149]. Without a salt deposit, the rates of mass increase were relatively slow for up to 24 h in the temperature range 605 to1000 °C. With the salt deposit, the rates increased greatly, and, for Fe_3Al-2%Cr at 1000 °C, catastrophic corrosion took place after about 7 h. For Fe_3Al-5%Cr at 1000 °C, however, the rate of mass increase was less than at 605 and 800 °C. It was concluded that these alloys were not suitable for use in environments where salt deposition may take place, and some comparison tests indicated that stainless steels 310 (18 at.%Cr) and 321 (23 at.%Cr) had better corrosion resistance.

4.8. Formation of sulfides in reducing atmospheres

For most of the systems considered in previous sections, the atmospheres have been oxidizing, with significant partial pressures of oxygen. However, systems involving reducing atmospheres with significant partial pressures of hydrogen sulfide are important in some applications such as coal gasification, for which corrosion-resistant materials of construction need to be selected. In general, surface layers of metal sulfides are not expected to provide as much protection against further reaction as metal oxide layers because of the higher diffusion rates of metal cations in sulfides as compared to oxides.

Alloys based on Fe_3Al, with 28 at.% Al and various levels of Cr, have been examined by thermogravimetry using atmospheres of H_2S-H_2-H_2O-Ar in the temperature range of 700 to 800 °C [150]. The Fe-28at.% Al material was much more corrosion resistant than the alloys Fe-25%Cr-20%Ni and Fe-18%Cr-6%Al. The scale formed on the Fe-Al alloy was γ-Al_2O_3, which provided protection from further attack. Chromium is added to the Fe_3Al alloy to increase its ductility, but the addition of more than 2at.% Cr to the alloy adversely affected its resistance to the sulfidizing atmosphere, as indicated in Figure 41. With 4 and 10 at.% Cr in the Fe_3Al alloy, the scale was composed of Fe and Cr sulfides, with some Al_2S_3 at the metal/scale interface. The presence of Nb or Zr in the alloy reduced the corrosion rate. It was found that the adverse effect of 4% Cr could be offset also by increasing the Al content to 40%. A pre-oxidation treatment reduced the rate of corrosion in the sulfidizing atmosphere, by a factor of about 4, for the 5% Cr alloy, and a pre-oxidized 2% Cr alloy showed no detectable mass increase at 800 °C [151]. A protective Al_2O_3 layer was formed by pre-oxidation, as opposed to the non-protective Fe and Cr sulfide scales formed when there was no pre-oxidation.

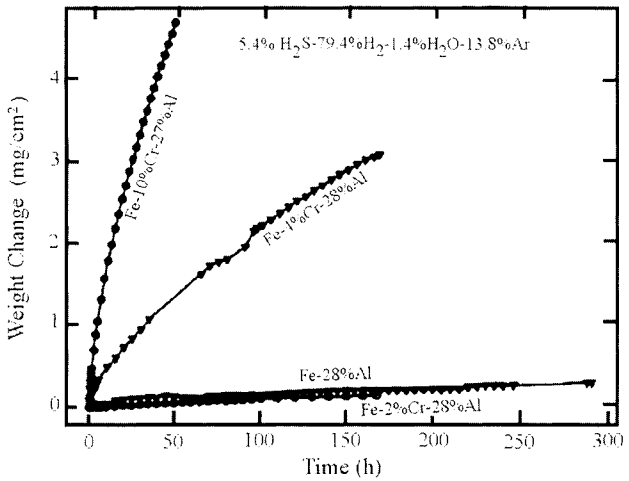


Figure 41. Thermogravimetric curves for the reaction of Fe_3Al alloys with a corrosive H_2S-H_2-H_2O atmosphere at 800 °C; these curves show the adverse effect of more than 2% Cr. From J.H. DeVan, reference 150.

The reactions of iron and of the alloy Fe-41% Ni with H_2S-H_2-N_2 atmospheres have been studied thermogravimetrically in the temperature range 520 to 800 °C [152]. Under some conditions significant deviations from parabolic kinetics were observed during the initial part of the reaction. Using partial pressures of S_2 calculated for the equilibrium:

$$H_2S(g) = H_2 + \tfrac{1}{2} S_2$$

it was found that the rate of reaction increased with P_{H_2S} at constant P_{S_2}, and so it was concluded that equilibrium among the gaseous reactants was not attained at the gas/metal sulfide interface. It was postulated that slow adsorption and surface dissociation of the H_2S was affecting the overall reaction rate and causing deviations from the parabolic kinetics that would be expected if diffusion through the product layer were the only process affecting the overall rate. The rate of sulfidization of the Fe-Ni alloy was faster than that for iron under similar conditions. Whisker growth was observed during reaction of the alloy and was attributed to catalysis of H_2S dissociation at the tips of the whiskers.

For the interpretation of the mechanisms of high-temperature corrosion reactions, it is often useful to have knowledge of the equilibria that can exist between the atmosphere and the solid sulfide, even though full equilibrium between the solid and gas phases has not been attained. In favorable cases,

where diffusion through the products of the gas-solid reactions is sufficiently rapid, isothermal thermogravimetric measurements can be used. Iron-nickel alloy samples of known composition were equilibrated with H_2-H_2S-Ar gas mixtures, and the sulfur contents of the equilibrated specimens were determined from the mass changes and the original masses of the specimens [153]. Both sulfurizing and desulfurizing experiments were carried out in order to approach equilibrium from different directions. Isothermal sections of the ternary phase diagram Fe-Ni-S were constructed at temperatures from 700 to 850 °C from the thermogravimetric results.

4.9. Surface treatments to increase corrosion resistance

The high-temperature corrosion resistance of a metal may be increased by coating the surface with a thin layer of material that is more resistant to the ambient atmosphere than the metal substrate. To be effective, however, the applied surface layer must be adherent and resistant to spallation.

A thin layer of aluminum can be deposited on stainless steels by electrodeposition from an organic electrolyte and subsequently oxidized at 600 °C to provide a protective coating of alumina [154]. Isothermal thermogravimetric oxidation tests performed in air in the temperature range 1000 to 1100 °C showed that the alumina coated samples oxidized more slowly than the uncoated samples. In thermal cycling tests (15 min at 1000 °C and 5 min at room temperature), samples of coated type 446 stainless steel could withstand up to 1000 cycles, but a sample of coated type 321 stainless steel failed after 700 cycles, as indicated by catastrophic mass loss due to spallation. A sample of 304 stainless steel failed even sooner, after 200 cycles. The inferior resistance of the austenitic stainless steels (304 and 321) under thermal cycling, compared to the ferritic stainless steel (446), was attributed to a larger difference in thermal-expansion coefficient between the alloy and the alumina coating.

Another method for applying aluminum to the surface of a steel is by pack cementation. In this process the steel is packed in a mixture of aluminum powder and NH_4Cl and heated to 500-800 °C; during this treatment a layer of $(Fe,Cr)Al_3$ will form on a Fe-17%Cr steel. Isothermal thermogravimetric oxidation tests at 800-1000 °C indicated an initial relatively rapid mass increase, followed by much slower oxidation [102]. The surface product layer was α-Al_2O_3. Also, pack aluminizing was found to increase the corrosion resistance of a sample of Fe-28at.%Al-5at.%Cr in an atmosphere of H_2S-H_2-H_2O-Ar during thermogravimetric tests [155].

Zirconia coatings have been applied to metals in attempts to increase their oxidation resistance. A film of CaO-stabilized zirconia was deposited onto iron by rf magnetron sputtering [156]. Thermogravimetric tests in air at 500 °C showed that the rate of mass increase was much slower for the coated samples

than for the untreated iron. The ZrO_2 layers were examined by X-ray diffraction, scanning electron microscopy and Auger electron spectroscopy. These examinations indicated the formation of Fe_2O_3 and Fe_3O_4 at the interface between the zirconia layer and the Fe substrate. Coatings of CeO_2-stabilized zirconia could be applied on iron and 304 stainless steel by thermal decomposition in vacuum of organic solutions containing Zr and Ce [157]. Thermogravimetric studies of these materials showed that the oxidation rates in air were significantly lower for the coated materials compared to untreated metal samples.

4.10. Non-isothermal studies

In addition to the isothermal thermogravimetric studies on metals and alloys, there have been some investigations that have used continuous heating. With this technique, it would be expected that the results will depend on the rate of heating, and this has been found to be so. The oxidation reactions of nickel powder, tantalum foil and zirconium sponge were studied by Kitheri et al. [158] in air at a series of different heating rates (β) from 1 to 20 K min^{-1}. For a given degree of reaction (α) for a given metal, the results could be fitted to an equation suggested by Urbanovici and Segal:

$$1/T_r = A + B \log \beta$$

where T_r is the reaction temperature at which conversion α has been reached, and A and B are constants found by fitting the data. As the values found for B were always negative, the temperature at which a given degree of reaction was reached increased with increasing rate of heating.

Non-isothermal thermogravimetry was used by Bereznai and Würtz [159] to study the oxidation of zircalloy with regard to the possibility of pyrophoricity of fine particles of this alloy in air during the processing zircalloy-clad nuclear reactor fuel elements. These authors found very rapid oxidation at the temperature at which the α (hcp) solid solution began to transform to β (bcc) at about 850 °C. This sudden and temporary increase in reaction rate was attributed to a state of disorder in the alloy during the phase transition. This phenomenon would have been difficult, if not impossible to detect by isothermal gravimetric studies.

For relatively quick studies, when quantitative results are not needed, non-isothermal investigations can be useful. Wakasa and Yamaki [160] examined nickel, chromium, copper and Ni-Cr and Ni-Cu alloy powders by DTA and TG in air. The DTA results gave some indication of the temperature region in which significant oxidation began, but the non-isothermal gravimetric results on heating to 900 °C were needed to show the relative oxidation rates. The authors

found increases of mass for Ni (29%), Cu (28%) and Cr (11%), but no detectable increase for the Ni-14.5% Cr alloy and only 1.5% mass increase for the Ni-7.7% Cu alloy powder. The use of powdered metals provides high, but generally not accurately known, specific surface areas, and hence relatively large changes in mass are observed. Quantitative treatment of the results, however, is difficult.

Non-isothermal methods have been applied in a study of the hot corrosion reactions between metals and calcium sulfate. Limestone may be added in fluidized-bed combustion systems to capture sulfur dioxide, formed by combustion of sulfur-containing coal, and so prevent emission of this pollutant. Reactions between $CaSO_4$ and Cr, Ni, Co, Fe and some commercial alloys, in powder form, were investigated in argon by differential thermal analysis and thermogravimetry [161] to determine the susceptibility of these materials to attack by $CaSO_4$ deposits. Chromium reacted endothermally from about 800 to 1200 °C with a loss of mass. X-ray diffraction showed the reaction products to be $CaCr_2O_4$, Cr_2O_3, and CaO, but gave no indication of chromium sulfide. Co, Ni and Fe showed DTA peaks that were characteristic of the presence of metal sulfides. These results indicated that Cr appeared to be the metal that would show the most resistance to $CaSO_4$. Of the commercial alloys investigated, 304 stainless steel (18% Cr, 8% Ni) showed the best resistance to $CaSO_4$.

The reaction between lanthanum nitrate and chromium oxide, which may form on the surface of Cr-containing stainless steels, has been investigated by thermogravimetry [162]. This reaction was of interest because the presence of rare earth elements may improve the protective properties of the oxide scales formed on the steel surfaces. Derivative (DTG) curves were plotted to show the temperature regions of maximum rates of mass loss. The phases formed were identified by X-ray diffraction. It was shown that $La(NO_3)_3.6H_2O$ decomposed in three main stages and finally formed a perovskite, $LaCrO_3$, with the chromium oxide.

4.11. Investigations of corrosion of metals by liquids

Although thermoanalytical methods are almost indispensable for the study of the high temperature corrosion of metals and alloys by gases, their applicability to the study of corrosion by liquid phases is much more limited. However, there are a few examples of applications in this area.

Charles [163] has applied thermomagnetometry to the investigation of the corrosion of metals and alloys by liquids. One example was the corrosion of iron by aqueous solutions of ethylenediammine tetraacetic acid (EDTA). The iron foil sample, sealed in a non-ferromagnetic container with the solution, was placed, at the desired temperature, in an inhomogeneous magnetic field and the force on the container was measured by a recording microbalance as a function

of time. As the ferromagnetic iron was corroded away by the solution, this force decreased. It was found that, in a 5% ammoniated EDTA solution, in the temperature range 90 to 150 °C, the corrosion of the iron followed linear kinetics after an initial induction period. Another example of the application of thermomagnetometry was the study of the corrosion of type 304 stainless steel (an austenitic steel, and hence non-ferromagnetic; composition Fe-18% Cr-8% Ni) by oxygen-saturated liquid sodium. This system was investigated non-isothermally in a series of heating and cooling cycles to 620 °C. The increase in magnetization of the sample indicated the formation of an Fe-Ni magnetic alloy as chromium was removed by the formation of $NaCrO_2$. The value of the Curie temperature, above which the magnetization disappeared, indicated that the magnetic phase was an alloy rather than unalloyed iron or nickel.

In an investigation of the corrosion of platinum by liquid sodium, it was desired to determine the solubility of platinum in sodium [164]. This was done by differential thermal analysis on mixtures of platinum powder (5 to 20 at.%) and sodium sealed in stainless steel capsules. Liquidus temperatures were determined; the residue in the capsule, after removal of the sodium by vacuum distillation, consisted of platinum and the compound $NaPt_2$.

5. EXTRACTIVE METALLURGY

5.1. General

Extractive metallurgy is a large branch of the field of metallurgy that deals with the treatment of minerals and concentrates for the recovery of contained metallic values. These materials are normally thermally active and were therefore the subject of major studies by thermal analysis in the last 50 years [165]. In the same context, studies on thermal reactions of metal carbonates, oxides, hydroxides, chlorates and oxysalts were also documented by Mackenzie [166]. Advances in conventional thermal analysis techniques, the development of new ones and the use of separate and combined supplementary techniques resulted in an even more extensive use. Applications of DTA in the study of oxidation reduction reactions, blast-furnace slags, sulfur in sulfides and sulfates, grading of coals and raw material standardization and control were reported by Ray and Wilburn [167].

Mosia et al. [168] used simultaneous TG/DTA (Derivatograph) to study physico-chemical transformations in the manganese oxides during the extraction of manganese by pyrometallurgical processing of manganese concentrates. In air, at 700 °C, MnO_2 dissociates to form β-Mn_2O_3 which undergoes a crystal transformation at 990 °C. In argon, these activities were found to take place at lower temperatures and, in oxygen, at somewhat higher temperatures. Another type of manganese concentrate exhibited the decomposition of MnO(OH) to α-

Mn_2O_3 at 370 °C and the dissociation of the latter at 990 °C. In a mixed-carbonate concentrate, $MnCO_3$ and $CaCO_3$ were found to decompose at 600 and 850 °C, respectively. The study of the reaction of manganese ores with bituminous coals and coke breeze was also carried out in connection with the ferroalloy process. Following the decomposition of MnO(OH) at 360 °C, MnO_2 dissociates and the oxidation of coal takes place. The decomposition of psilomane, the reduction of Mn_3O_4 and the gasification of coal take place at around 820 °C. The authors found that thermal analysis, conducted in different atmospheres, were very helpful in the determination of the thermal behaviour of the concentrates and their reaction products and, hence, in the determination of optimum parameters for the processing of these concentrates.

Kaolinitic clay minerals have been considered as possible substitutes for bauxite as sources of alumina for the production of Al metal. One of the methods proposed in the literature [169,170] involves the high-temperature treatment of the clay minerals with ammonium sulfate for the extraction of aluminium as sulfate which is later converted to hydroxide and then to alumina by calcination. Bayer et al. [171] examined the reaction of kaolinite, and other minerals, with $(NH_4)_2SO_4$ in air using simultaneous TG and DTA. The reaction with kaolinite was found to commence at about 230 °C with the formation of $(NH_4)_3Al(SO_4)_3$ which decomposes at above 250 °C to $(NH_4)Al(SO_4)_2$. The latter double salt changes gradually to $Al_2(SO_4)_3$ which, in turn, decomposes at about 650 °C to Al_2O_3. Other Fe-, Mg- and Ti-containing silicate and oxide minerals also were found to react with the sulfate. The reaction extent and product depend on the reaction temperature and the amount of sulfate added.

Differential thermal analysis, with other techniques, was used by Sen et al. [172] to identify processes for the treatment of low-grade complex non-sulfide ores, namely, laterites to produce metal concentrates. The lateritic ore examined was composed mainly of goethite, chromite, hematite, magnetite, pyrite and chalcopyrite, with non-metallic minerals like quartz, lizardite and chlorite. DTA was performed in air atmosphere. The dehydroxylation of the material took place with an endothermic peak around 600 °C. At higher temperatures, an exothermic peak indicated the crystallization of disordered, metal-containing goethites. More understanding of the nature of the complex ore was achieved by applying thermal and mineralogical techniques allowing an insight to means of treatment for metal extraction.

Weissenborn et al. [173] studied the selective adsorption of starch on hematite and kaolinite using thermogravimetry. In the last several years, starch has been used successfully as a selective flocculant for hematite. The authors developed a method-based thermogravimetry for the determination of the amount of polysaccharide adsorbed on the surface of the mineral particles. The mass loss at 250-375 °C caused by the pyrolysis of the adsorbed polysaccharide was

compared with that of prepared standard mixtures of starch and hematite or kaolinite to determine the amount of adsorbed polysaccharide. Saturation adsorption densities of starch on hematite and kaolinite were calculated and the results indicated that hematite has a larger capacity for adsorption of starch, which was attributed to the higher concentration of adsorption sites on the hematite particles.

Significant efforts have continuously been made to find alternatives to the roasting process of sulfide ores for the extraction of non-ferrous metals due to the negative environmental impact of the process caused by SO_2 emissions. The chlorination of galena (PbS) to extract lead in the form of lead chloride was examined by Mikhail and Webster [174] using dynamic and isothermal thermogravimetry and differential thermal analysis. A reaction assembly specially designed to handle corrosive atmospheres was used in the study. The reaction of chlorine gas with galena can be expressed as follows:

$$PbS + Cl_2 \rightarrow PbCl_2 + S$$

The reaction was found to start at a relatively low temperature and terminate below 500 °C. In the isothermal studies, the dependence of the rate of reaction on the Cl_2 flow rate and partial pressure, sample particle size and temperature was determined. The reaction was found to be governed by the rate of solid-state diffusion through a $PbCl_2$ product layer that forms at the initial stage of reaction on the surface of the individual sulfide particles (shrinking-core model kinetics). Figure 42 shows the correlation between the fraction reacted (R), expressed in terms of the diffusion model, and time, at different temperatures. The activation energy of the reaction was found to be 113 kJ mol^{-1}. Figure 43 shows photomicrographs of galena particles, partially reacted with chlorine.

5.2. Reduction

Metal oxide reduction is the basis for the production of metals in many pyrometallurgical processes. Ryzhonkov [175] used non-isothermal thermogravimetry together with gas analysis to investigate the solid-state reduction of iron/nickel oxide and iron/chromium oxide mixtures by carbon. By determining the rate and extent of reduction of the individual oxides, FeO, NiO, Fe_2O_3 and Cr_2O_3 and the mixtures FeO+NiO and Fe_2O_3+Cr_2O_3 by carbon, using the change in mass and the $CO/CO+CO_2$ ratio, it was found that the relative amounts of the oxides in the mixture and the interaction between the oxides play a significant role in enhancing or retarding the reduction process. In the Fe_2O_3/Cr_2O_3 system, the reduction process is hampered by the formation of Fe/Cr spinel.

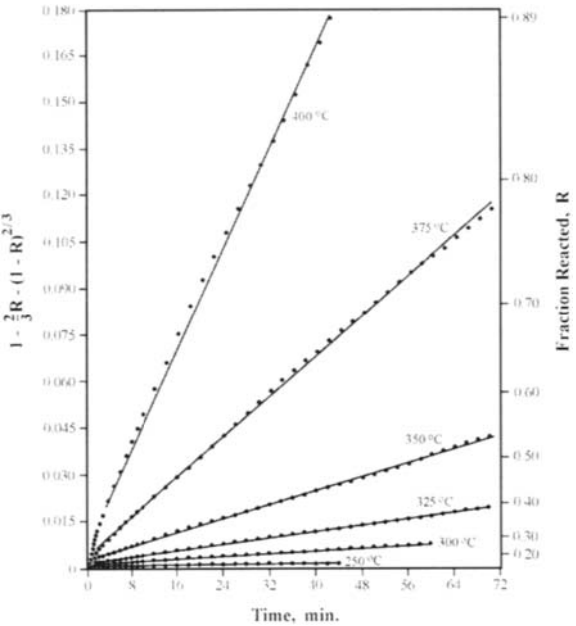


Figure 42. TG results for the kinetics of chlorination of galena according to the diffusion model. From S.A. Mikhail and A.H. Webster, reference 174.

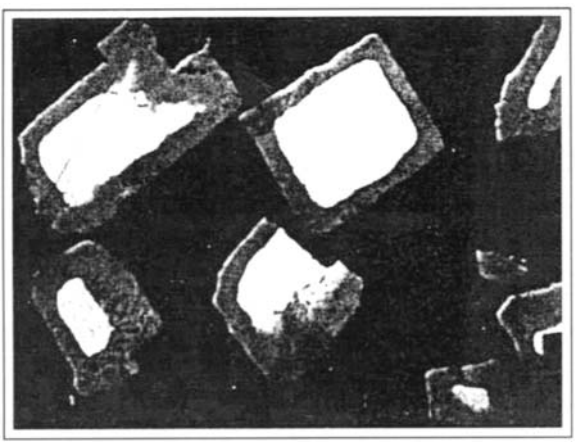


Figure 43. Photomicrograph of a polished section for a galena sample at 60% chlorination. From S.A. Mikhail and A.H. Webster, reference 174.

The reactivity of carbons used in the production of zinc and lead by pyrometallurgical processes was evaluated using thermogravimetry and differential thermal analysis. Carter et al. [176] studied the oxidation behaviour of graphitising and non-graphitising carbons, coke and coal char under different experimental conditions using a heating rate of 5 °C min^{-1}. A coke sample with a fairly coarse particle-size was found to oxidize in static air in the temperature range 600 to 900 °C with a broad doublet exothermic peak. In flowing air, the oxidation occurred in a somewhat lower temperature range, but generated a similar type exotherm. This split-peak behaviour was found to relate to the particle size of the coke and was interpreted as a change in the oxidation kinetics which may become diffusion controlled at high temperature.

Thermogravimetry was also used by Igiehon et al. [177] to investigate the carbothermic reduction of PbS in presence of lime in relation to the production of metallic lead. Both graphite and coal were used. The authors had earlier investigated a series of metal sulfides and the general reaction was expressed as follows:

$$MS + C + CaO = M + CaS + CO$$

X-ray diffraction and electron microscopy were used to identify reaction products and, especially, intermediate phases. It was thought that the reaction may take place in two stages. The first is an exchange reaction between PbS and CaO followed by the reduction of the PbO product with carbon. It was found, however, that the first reaction takes place according to the following scheme:

$$7PbS(s) + 6CaO(s) = PbSO_4.2PbO(s) + 4Pb(l) + 6CaS(s)$$

$$PbSO_4.2PbO(s) + 2PbS(s) = 5Pb(l) + 3SO_2(g)$$

The reduction of PbS by carbon was suggested to proceed also with the formation of basic lead sulfate as intermediate product. The authors concluded that metallic lead can readily be produced by the reduction of PbS by coal in the presence of CaO above 800 °C, with the formation of $PbSO_4.2PbO(s)$ as intermediate product. Carrying out the reaction at a relatively low temperature (800 °C) was found to minimize the loss of PbS by volatilization.

A method to recover lead from PbS without the evolution of SO_2 was also investigated by Rao and El-Rahaiby [178] using thermogravimetry. Mixtures of PbS:4CaO:4C were reacted isothermally under nitrogen atmosphere in alumina crucibles in a TG apparatus consisting of a vertical furnace and an Ainsworth balance. Gas analysis was done using a gas chromatograph/mass spectrometer. The following materials were investigated as catalysts at 2.5 wt% addition:

Li_2CO_3, Na_2CO_3, K_2CO_3, Rb_2CO_3, Na_2SO_4, NaF, and the ternary eutectic of $(Li,Na,K)_2CO_3$.

Plots of α (degree of reaction) vs. time showed a constant slope (rate) from α = 0.2 to 0.8. The rate coefficients, K_u and K_c, were determined in this region for the uncatalyzed and catalyzed reactions. For the uncatalyzed reaction from 1068 to 1255 K, E_a = 295 kJ mol^{-1}. All the catalysts increased the rate of the reaction and were effective in the order: Li_2CO_3 > Rb_2CO_3 > ternary = NaF = K_2CO_3 > Na_2CO_3 > Na_2SO_4. For the ternary mixture, E_a = 237 kJ mol^{-1}. Only CO and CO_2, but no SO_2, were detected in the effluent gas. Chemical determinations of the S from CaS in the reaction product were in agreement with calculated values. The amounts of elemental lead recovered were in some cases slightly low. The uncatalyzed reaction appeared to proceed through gaseous intermediates:

$PbS + CO = Pb + COS$
$COS + CaO = CaS + CO_2$
$C + CO_2 = 2\ CO$ (Boudouard reaction)

The reduction mechanism of tin and iron oxides in connection with the production of tin in reverberatory furnaces at pre-slag forming temperatures, 973-1273 K, was examined by Mitchell and Parker [179]. Thermogravimetry in nitrogen atmosphere was used as the main technique with a specially designed apparatus using a flexed-beam thermobalance. The reduction rate of SnO_2 with C increased with the increase in temperature and with the increase in the C/SnO_2 molar ratio up to 3/1. The reduction reaction occurs with the generation of CO gas which, in turn, reacts with SnO_2 to generate liquid metal and CO_2. The reduction of iron oxide, Fe_2O_3, was also studied and was found to be significantly slower than that of SnO_2. The reduction rate of Fe_2O_3 also increased with the increase in the C/Fe_2O_3 molar ratio up to 5/1. With both metal oxides, the carbon oxidation was found to be the rate controlling step and the higher the amount of carbon present, up to certain limits, the higher the reduction rate.

The electric smelting of non-ferrous calcines for the extraction of copper and nickel is influenced by the degree sulfur elimination in the preceding roasting stage, the coke additions, the gas atmosphere and the lime additions. Thermogravimetry and gas chromatography were used by Celmer et al. [180] to investigate the effect of these variables on a Ni-Cu calcine pre-roasted to different degrees of sulfur elimination. The experiments were done in nitrogen or air at 5 °C min^{-1}. Solid-solid and solid-gas reactions occurred below 900 °C. Above this temperature, solid, liquid and gas phases are present. In nitrogen, a rapid increase in mass loss with the increase in coke additions, due to the

decomposition/reduction of sulfates, was observed above 700 °C. Large mass losses, accompanied by the evolution of CO and CO_2 were attributed to the main reduction reactions.

In air, substantial mass loss and SO_2 evolution occurred in the temperature range 350 to 900 °C, sulfate decomposition took place at 700-830 °C and little reduction occurred because of the depletion of coke before the reduction temperatures. The addition of lime enhanced the reduction reactions by capturing the evolving sulfur oxides to form $CaSO_4$ which, in presence of coke is converted to CaS. Possible reactions in presence of lime were reported as follows:

$$MeS + CaO + ½C = Me + CaS + ½CO_2$$

$$MeS + CaO + CO = Me + CaS + CO_2$$

It was suggested that experiments in nitrogen atmosphere closely represent the electric smelting conditions, the high-temperature smelting reactions are limited by coke supply and that high sulfur elimination in the pre-roasting stage is environmentally beneficial.

In the last three decades, large oil-sand deposits have been treated for the extraction of bitumen. The process generates tailing streams containing significant amounts of valuable heavy minerals like TiO_2 and ZrO_2. Mikhail et al. [181] studied the thermal and thermomagnetic behaviour of the tailings using TG/DTA/FTIR and thermomagnetometry in inert, oxidizing and reducing atmospheres to determine the optimum conditions for the removal of bitumen as part of the heavy minerals extraction process. Figure 44 shows the TG/DTA/FTIR curves obtained on heating the concentrate in air. The main mass loss (TG) takes place in the temperature range 350 to 650 °C, accompanied by exothermic activity (DTA) and the evolution of SO_2, CO_2, CO and H_2O (FTIR). These activities were attributed to the combustion of bitumen, the decomposition of siderite and the oxidation of pyrite present in the material. The results of thermomagnetometry indicated that, in a reducing atmosphere, the concentrate is rendered magnetic due the formation of metallic iron or magnetite, which suggested the possibility of a subsequent treatment of the concentrate by magnetic separation.

5.3. Roasting

Roasting, together with drying and calcination, is often a component of the metallurgical pre-treatment of ores and concentrates in metal extraction processes. It is the process of oxidation of metal sulfides at high temperatures, but below the melting point of the powders, as a preparatory treatment for metal

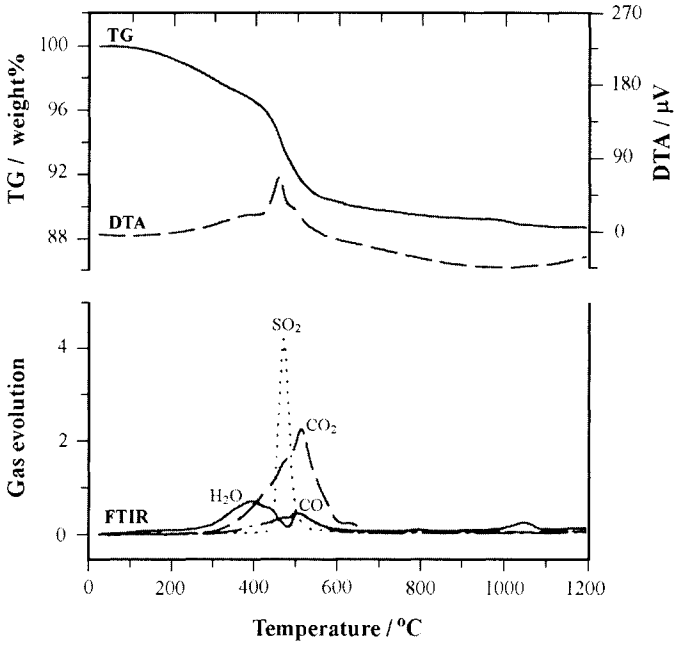


Figure 44. TG, DTA and Fourier transform infrared (FTIR) spectroscopy results from heating oil sands tailings flotation concentrate in air. From S.A. Mikhail et al., reference 181.

extraction. While other types of roasting such as reducing, chlorinating and sulfatizing are in practice, the most common is the oxidizing roast, which is highly exothermic. Drying is the removal of physically adsorbed water from substances by evaporation, while calcination refers to the removal by heating of chemically bound water, CO_2 or other gases, present in the form of hydrates, carbonates, etc. Both processes are highly endothermic. Since roasting, drying and calcination processes involve various degrees of enthalpy and mass changes, they, traditionally, were good candidates for study by thermal analysis.

The reduction roasting of chalcopyrite ($CuFeS_2$) using carbon, CO or H_2 as a reductant and calcium oxide or sodium carbonate as a desulfurizer was discussed in a series of reports by Udupa et al. [182-184] in an attempt to assist non-ferrous smelters in their search for new metal extraction processes with potential for reducing SO_2 emissions. Thermogravimetry, together with optical and scanning electron microscopy, electron microprobe analysis and XRD, was used in the study. The results implied that, on heating to 1000 °C, a complete reduction of the chalcopyrite with full metallization to Cu and Fe is achievable in H_2 in presence of either desulfurizer. Figure 45 shows TG curves of

chalcopyrite in different reducing atmospheres with the two different desulfurizers. The copper produced contained about 2% iron and the iron contained about 3% Cu. Both metals were free from sulfides after one hour of reduction roasting. With carbon, or in CO, full metallization to Cu, with only partial reduction of iron oxide, was reported. It was also pointed out that sulfur fixation took place in the form of calcium sulfide or sodium sulfide, depending on the desulfurizer. The proposed reactions for chalcopyrite were as follows:

$$CuFeS_2 + 2\,CaO + 2\,H_2 = Cu + Fe + 2\,CaS + 2\,H_2O$$
$$CuFeS_2 + 2\,CaO + CO = Cu + FeO + 2\,CaS + CO_2$$
$$CuFeS_2 + 2\,CaO + C = Cu + FeO + 2\,CaS + CO$$
$$CuFeS_2 + 2\,Na_2CO_3 + 2\,H_2 = Cu + Fe + 2\,Na_2S + 2\,CO_2 + 2\,H_2O$$
$$CuFeS_2 + 2\,Na_2CO_3 + CO = Cu + FeO + 2\,Na_2S + 3\,CO_2$$
$$CuFeS_2 + 2\,Na_2CO_3 + C = Cu + FeO + 2\,Na_2S + 2\,CO_2 + CO$$

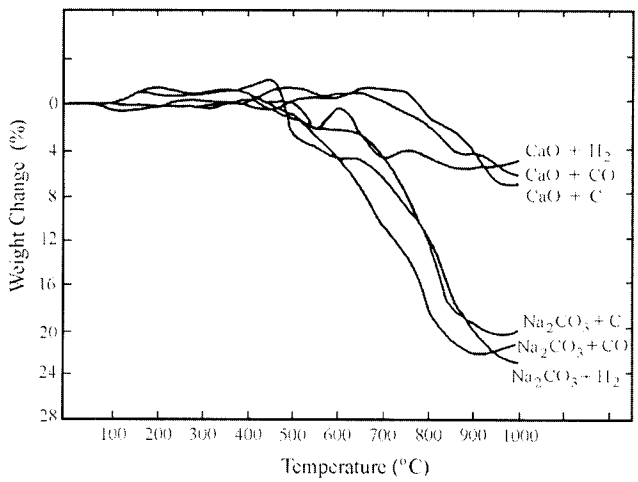


Figure 45. TG curves for the reduction of chalcopyrite in the presence of three different reducing agents and two different desulfurizers. From A.R. Udupa et al., reference 183.

Chalcocite, pyrrhotite and pentlandite were also examined using the same combinations of reductants and desulfurizing agents. Similar results were obtained and all examined minerals were found to be readily reducible to their metallic constituents. The most effective combinations of reductant and desulfurizing agent were found to be CO and CaO for chalcopyrite (above 1000 °C) and H_2 and CaO for chalcocite, pyrrhotite and pentlandite. The authors

maintained that thermogravimetry provided a fast and efficient technique for assessing reduction-roasting reactions.

Dimitrov and Boyanov [185] used thermogravimetry, together with XRD, chemical and gas analysis, Mössbauer spectrometry and electrical resistivity techniques to study the oxidative roasting of sulfide minerals, namely, sphalerite (ZnS), marmatite (Zn(Fe)S), chalcocite (Cu_2S), chalcopyrite ($CuFeS_2$) and pyrite (FeS_2) and concentrates of zinc, copper, copper/zinc and iron sulfides. The temperature regions where extensive roasting takes place and the temperature above which partial melting may occur - which is critical for the operation of a fluidized bed reactor - were determined for the different materials. The temperature region for the roasting of iron and copper sulfides was found to be significantly lower than that for the lead and zinc.

Further detailed investigations were carried out by Dimitrov and Boyanov [186] on the oxidation (roasting) of sulfide minerals and concentrates using thermogravimetry, differential thermal analysis, XRD, Mössbauer spectrometry, fluid-bed resistivity measurements, gas analysis and electron microprobe analysis. The TG and DTA measurements were done in air at a heating rate of 8 °C min^{-1} using 20-50 μg- samples. Based on the DTA peaks, SO_2 evolution and fluid-bed resistivity measurements, the onset temperatures of several characteristic events, namely, the initial oxidation and intensive oxidation of a metal sulfide, the oxidation of the most easily oxidized sulfide in a concentrate and the initial oxidation and intensive oxidation of the main sulfide in a concentrate were defined and determined for the sulfide minerals and concentrates. In addition, the minimum temperature for complete desulfurization, the maximum acceptable temperature for roasting in a fluid bed and the lowest temperature at which partial melting and particle agglomeration interfere with fluidization were also defined and determined. Differences in the characteristic temperatures of the different materials were explained and their significance in the roasting process was clarified.

In the pyrometallurgical extraction of Cu, Zn and Pb from sulfide ores, the pretreatment of the concentrate involves a high-temperature roasting process to remove most of the sulfur and convert the material into sulfates or oxides for further processing. Isothermal thermogravimetry was used by Ajersch and Benlyamani [187] to elucidate the different reactions and the reaction sequence involved in the removal of sulfur from liquid or solid sulfides. In the case of liquid sulfides, different reaction sequences were reported for Cu_2S and FeS. For Cu_2S, a mass loss due to removal of sulfur and a subsequent mass gain due to the oxidation of the Cu metal were evident, Figure 46. For FeS, an increase in mass due to the oxidation of the sulfide and the formation of Fe-S-O solution, preceded a mass loss due to the oxidation of sulfur and the evolution of SO_2.

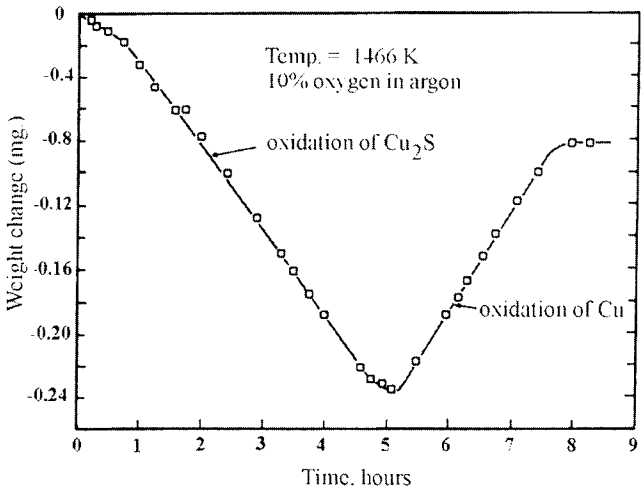


Figure 46. Isothermal TG results for the oxidation of liquid Cu_2S at 1466 K with 10% O_2 in the reaction gas. From F. Ajersch and Benlyamani, reference 187.

A general oxidation reaction in which a solid sulfide reacts with O_2 to generate an oxide, an oxysulfide or a sulfate was expressed as:

$$MS(s) + kO_2(g) \rightarrow Product(s) + SO_2(g)$$

where k is a stoichiometric factor. In the oxidation of ZnS, a gradual decrease in the reaction rate with temperature was attributed to the an increased sintering of the sulfide particles. XRD analysis indicated the ZnO was the final product. The oxidation of solid FeS followed a similar trend to that of liquid FeS. The reaction product was Fe_3O_4 during the mass gain stage and Fe_2O_3 during the mass loss stage. In the oxidation of PbS, a mass gain due to the formation of the sulfate or oxysulfate was observed. The oxidation temperature of PbS was found to be significantly lower than that of the other sulfides.

The reactions of ammonium chloride with non-ferrous sulfide minerals, namely, chalcopyrite, sphalerite and galena, in air have been explored by Penev *et al.* [188] using non-isothermal thermogravimetry and differential thermal analysis. Ammonium chloride was used in the chlorination roasting of complex sulfide ores for the extraction of non-ferrous and precious metals from these ores. With chalcopyrite, the main products formed above 400 °C are CuCl and Fe_2O_3. CuCl reacts with oxygen to form CuO at 500 °C, and copper ferrite started to form above 700 °C. In the lower temperature range, $ZnCl_2$ and $PbCl_2$ were found to be the major components of the interaction of sphalerite and

galena, respectively, with NH_4Cl. The gaseous products in the three cases are mainly NH_3, SO_2 and H_2O.

5.4. Reactions of metal compounds

Numerous examples are found in the literature on the use of thermal techniques in the study of reactions directly or indirectly related to metallurgy. Solid-solid and solid gas reactions in oxidizing, reducing or inert atmospheres, reactions involving catalytic agents, decomposition reactions, synthesis reactions, etc., have been reported.

Donald and Pickles [189] used inert-atmosphere thermogravimetry to examine the reduction of synthetic zinc ferrite, $ZnFe_2O_4$, in the form of briquettes with iron powder. Reactions involving zinc ferrite, particularly in a reducing environment, is of major interest in the secondary steelmaking industry. During the production of steel, a significant amount of hazardous electric arc furnace dust containing up to 30% zinc is collected. One quarter to one half of this zinc is present as a very stable ferrite spinel which complicates its treatment and recycle. The mixture, in the form of a cylindrical briquette, was contained in a chromel strip basket and suspended in the thermobalance. The overall reaction is expressed as follows:

$$ZnO.Fe_2O_3(s) + 2\ Fe(s) = Zn(g) + 4\ FeO(s)$$

This reaction is thermodynamically favorable above 888 °C, while, in absence of iron, the decomposition of zinc ferrite occurs at 1227 °C. Higher iron additions, temperature, smaller zinc ferrite particle size and the addition of lime and sodium chloride enhanced the reduction reaction. At the initial stages, the reaction was found to be chemically controlled with an activation energy of 178.1 kJ mol^{-1}. At the advanced stages, a reaction product formed at the outer surface of the briquette and further reaction occurred by the diffusion of zinc vapour through the product layer.

Based on the results of their earlier work on the reduction of synthetic zinc ferrite with iron [189], Donald and Pickles [190] proceeded to examine the reduction of an industrial electric arc furnace dust with iron powder in argon using the same technique, procedure and sample geometry. The dust contained about 25% zinc ferrite, 21% zinc oxide and 6% metallic zinc. High iron additions, temperature and fine particle size promoted the reduction reaction as had been shown with the synthetic ferrite. Above 1000 °C, the EAF briquettes were found to sinter, causing a delay in the reaction due to a build up of the zinc partial pressure. The addition of CaO was found to prevent sintering and, hence, promote the reduction, by raising the melting temperature of the dust. The addition of NaCl also enhanced the reduction by disrupting the dense product

layer formed on the reaction interface. A reaction mechanism identical to that of the synthetic ferrite was proposed.

Metal-hydrogen reaction mechanisms for the preparation of metal hydrides were studied by Schur et al. [191] using isothermal thermogravimetry. Reaction-rate limiting factors of surface and diffusion processes were eliminated by utilizing atomic hydrogen and thin foil samples of 25-30 μm thickness. The hydrogenation reaction was carried out in a plasmochemical chamber of a quartz-helix microbalance. Monitoring of the hydrogen intake of Ti, Zr and Nb foils under isothermal conditions by thermogravimetry allowed the determination of kinetic curves, elucidating various structural transformations induced by hydrogen saturation of the specific metal.

The reduction of synthetic ilmenite ($FeTiO_3$) by hydrogen in the temperature range 923 to 1573 K was explored by Kapilashrami et al. [192] using isothermal thermogravimetry. Titanium metal is normally extracted as the oxide from ilmenite ore after an initial treatment for the separation of iron. The results indicated that, below 1186 K, ilmenite is reduced directly to iron and TiO_2 according to the following reaction:

$$FeTiO_3(s) + H_2(g) = Fe(s) + TiO_2(s) + H_2O(g)$$

with an activation energy of 108 kJ mol^{-1}, based on reaction rates at the initial stages of reduction. It was suggested that the diffusion of iron through a TiO_2 product layer becomes rate controlling at the later stages of the reaction. Above 1186 K, the reaction proceeds further with the reduction of TiO_2 to Ti_3O_5 and H_2O. Based on these results, a pretreatment of ilmenite ore by hydrogen at about 1073 K was recommended for the separation of metallic iron from TiO_2.

The catalytic effect of alkali carbonates on the reduction of ilmenite ($FeTiO_3$) was examined by Barnes and Pickles using thermogravimetry [193]. Crushed ilmenite ore was briquetted and sintered in air, with some resulting oxidation of ilmenite:

$$2\ FeTiO_3 + 0.5\ O_2 = Fe_2TiO_5 + TiO_2$$

The sintered briquettes were reduced in CO in a vertical furnace with the sample suspended from a mechanism attached to a transducer which provided continuous mass measurement. Additions of alkali carbonates to the ilmentite increased the rate of reduction to iron, but also increased the rate of carbon deposition by the reverse Boudouard reaction:

$$2CO \rightarrow C + CO_2,$$

so that the mass loss - time curves went through a maximum. The carbon deposition was more pronounced at lower temperatures in the range 800 to 950 °C. Increasing the sintering temperature in the range 700 to 880 °C increased the rate of reduction (with 5 mass % K_2CO_3) at 950 °C. The increased sintering temperature disrupts the ilmenite grains due to oxidation. The effects of the alkali carbonates on the reduction rate were in the order: K_2CO_3 > Na_2CO_3 > Li_2CO_3.

The reaction of fine titanium and aluminum powders for the synthesis of $TiAl_3$ is a typical self-propagating high-temperature synthesis (SHS) reaction. Wang et al. [194] demonstrated the use of differential scanning calorimetry in the study of the influence of various parameters on the kinetics of this highly exothermic reaction above the melting point of aluminum. The powders were pressed into thin pellets and examined in argon atmosphere. Isothermal DSC was used to determine the reaction kinetics in the temperature range 690 to 740 °C and non-isothermal DSC, Figure 47, was used at the higher temperatures. Two mechanisms were proposed. At the lower temperature range, the reaction proceeds at a measurable rate with an activation energy of 149 kJ mol^{-1}. At 740-900 °C, a reaction rate of second-order with respect to the fraction of reactant available, with an activation energy of 517 kJ mol^{-1}, was determined. The influences of pellet thickness and green density, as well as that of the heating rate, were studied.

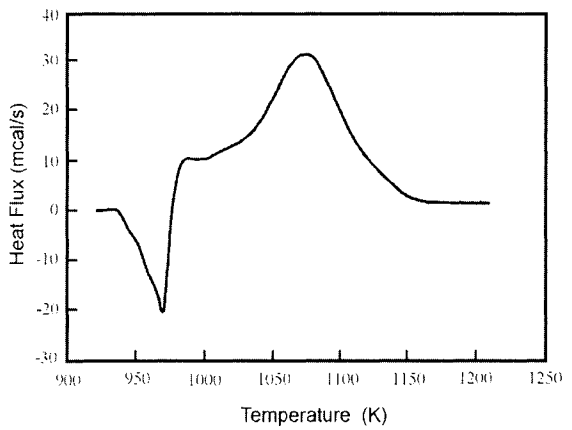


Figure 47. Non-isothermal DSC curve for the formation of $TiAl_3$ from titanium and aluminum powders; heating rate 30 K min^{-1}, particle size < 45 μm. From X. Wang et al., reference 194.

The phenomena and mechanism of re-oxidation of direct reduced iron (DRI) pellets were examined by Upadhya [195] using simultaneous TG/DTA. DRI is the product of direct or solid-state reduction of iron concentrate. In an air flow

above the critical value where the mass transport in the gas boundary layer is rate controlling, the results indicated that negligible oxidation occurs below 220 °C. An oxidation runaway reaction (auto-ignition), with a significant non-linear mass gain was found to occur around 230 °C. Scanning electron microscopy and XRD indicated the presence of both Fe_2O_3 and Fe_3O_4 in the outer scale and FeO in the inner scale of the DRI pellet. The presence of moisture was found to affect the rate of oxidation substantially. In moisture-saturated air atmosphere, the percentage oxidation was approximately 50% higher than that in dry air. A kinetic model involving the closure of internal pores between the grains by the oxide products was proposed. The mechanism describes the oxidation of a highly porous solid where the initial rate of reaction is controlled by the available surface areas (on the pore walls) and later by diffusion.

The nitridation reactions of magnesium and aluminum metals and their alloy in presence of MgO and Al_2O_3 were investigated by Szabó et al. [196], using primarily thermogravimetry and differential thermal analysis. Samples in the form of metal (or alloy) filings were heated to the completion of the nitridation reactions at 10 °C min^{-1} in nitrogen. The reaction of magnesium with N_2 starts below the melting point (645 °C), aluminium at the melting point (660 °C) and the alloy, appreciably above the melting point (445 °C). The addition of MgO to the individual metals and to the alloy promoted the nitridation significantly, as verified by the lowering of the initiation and completion temperatures. This phenomena was most pronounced in the alloy where the reaction temperature was lowered by >350 °C. The catalytic effect of MgO was attributed to the disruption of the Mg_3N_2 protective layer and, hence, the increase in the accessibility of nitrogen to the reactant surface.

An extensive literature review (106 references) on the study of the decomposition of metal oxalates in different environments using thermal analysis was done by Dollimore [197]. Following an initial dehydration (endothermic) step, four main general routes for the decomposition of simple oxalates (endothermic) were suggested. The first route is the decomposition to oxide, as follows (Figure 48):

$$ZnC_2O_4 = ZnO + CO + CO_2$$

In air, CO, catalyzed by ZnO, reacts exothermally to produce CO_2. This category includes Mg, Al, Cr (III), Mn(II), Fe(III) and Fe(II). With Fe(II), metal may also form depending on the conditions.

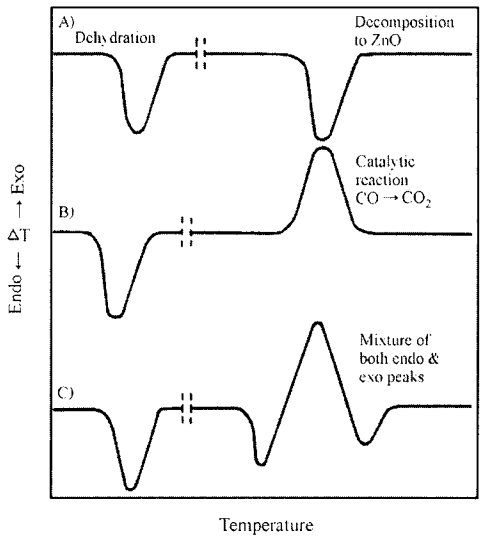


Figure 48. DTA curves for the decomposition of zinc oxalate dihydrate in various atmospheres (schematic and not to scale). (A) in nitrogen, (B) in oxygen or air, (C) in oxygen or air where the DTA pattern is more complex. From D. Dollimore, reference 197.

The second route is the decomposition directly to the metal as follows (Figure 49):

$$NiC_2O_4 = Ni + 2CO_2$$

In air, Ni reacts (strongly exothermic) vigorously to form NiO. This category includes metals such as Co, Cd, Sb, Pb, Sn, Bi and Ag. Sn and Bi give a mixture of metal and oxide.

The third route is the decomposition to carbonate as follows:

$$CaC_2O_4 = CaCO_3 + CO$$

In air, CO, catalyzed by CaO, reacts exothermally to produce CO_2. This category includes Li, Na, K, Sr and Ba.

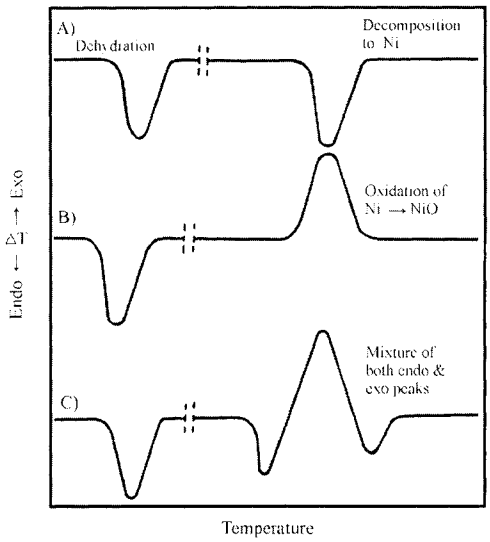


Figure 49. DTA curves for the decomposition of nickel oxalate dihydrate in various atmospheres (schematic and not to scale). (A) in nitrogen, (B) in oxygen or air, (C) in oxygen or air where the DTA pattern is more complex. From D. Dollimore, reference 197.

The fourth route is the decomposition (in inert atmosphere) to oxide and some carbon, particularly reported with rare earth oxalates Ce(III), Th(IV), Pr and La. The author cautioned that the reported list of metals was by no means complete and that experimental conditions and material history could result in different reaction routes. For the interpretation of the different decomposition behaviours, mechanisms involving the rupture of carbon/oxygen and metal/oxygen bonds and other kinetic and thermodynamic considerations were presented.

Thermal analysis techniques were also used by Dollimore [198] to demonstrate the production of highly active metals and alloys (very high surface area) far below their melting temperatures by the decomposition of the oxysalts, e.g., formates, acetates, citrates, stearates, etc., in addition to oxalates. Nickel catalysts, for instance, can be prepared in an inert atmosphere by the formate decomposition in two concurrent reactions as follows:

$Ni(COOH)_2 = Ni + H_2O + CO + CO_2$ and
$Ni(COOH)_2 = Ni + H_2 + 2\ CO_2$

In air, Ni metal would oxidize readily to form the oxide. Potential reactions in inert atmosphere for the formate decomposition may generally be expressed as follows:

$M(COOH)_2 = M + H_2O + CO + CO_2$,
$M(COOH)_2 = M + H_2 + 2\ CO_2$,
$M(COOH)_2 = MO + H_2O + 2\ CO$, and
$M(COOH)_2 = MO + CO + CO_2 + H_2$

For the decomposition of acetates, the reactions may be as follows:

$M(CH_3COO)_2 = M + CH_3COOH + CO_2 + C + H_2$, and
$M(CH_3COO)_2 = MO + (CH_3)_2CO + CO_2$

Textural and surface chemistry considerations indicated that a highly active metal powder with an apparent increase in the surface area is produced by the decomposition. On heating, or holding isothermally for extended periods of time at a specific temperature, the powder undergoes sintering which involves an increase (growth) in the particle size with a decrease in the surface area. These considerations relate directly to the kinetic factors affecting the production of the metal powders from their oxysalts.

In metallurgical and ceramic industries, the formation of ferrites is of significant interest. The reaction of alkali metal carbonates with iron oxide to form ferrites was investigated by Riga et al. [199] to simulate high temperature reactions of oxidized iron metal surfaces. Thermogravimetry in inert atmosphere was the principal technique used and the results indicated that ferrite is more likely to form with carbonates which undergo melting prior to decomposition, e.g., Li_2CO_3 and Na_2CO_3. Carbonates of calcium and magnesium were found to be less reactive and the product of reaction was predominantly magnetite. Among the examined carbonates, the order of reactivity with iron oxide was reported as $Li_2CO_3 > Na_2CO_3 > BaCO_3 > CaCO_3 > MgCO_3$. On the basis of the TG results, proposed mechanisms for the reactions were developed.

DTA, TG and high temperature XRD were used to study reactions in the thermal decomposition of precipitated ammonium molybdate to produce MoO_3 for use in the reduction synthesis of Mo metal [200]. DTA and TG were carried out in air at 5 °C min^{-1}. Endotherms and mass losses were detected at various temperatures and were related to the following reactions:

$110\ °C - (NH_4)_6Mo_7O_{24}.4H_2O \rightarrow (NH_4)_4Mo_5O_{17} + NH_3 + H_2O$

220 °C - $(NH_4)_4Mo_5O_{17} \rightarrow (NH_4)_2Mo_4O_{13} + NH_3 + H_2O$

290 °C - $(NH_4)_2Mo_4O_{13} \rightarrow (NH_4)_2Mo_{14}O_{43} + NH_3 + H_2O$
$(NH_4)_2Mo_{14}O_{43} \rightarrow (NH_4)_2Mo_{22}O_{67} + NH_3 + H_2O$
$(NH_4)_2Mo_{22}O_{67} \rightarrow MoO_3 + NH_3 + H_2O.$

From the first two stages of mass loss, the amounts of the compounds $(NH_4)_6Mo_7O_{24}.4H_2O$, $(NH_4)_4Mo_5O_{17}$ and $(NH_4)_2Mo_4O_{13}$ in a precipitated mixture could be determined, assuming that only these compounds were originally present. XRD showed that $(NH_4)_2Mo_4O_{13}$ was present in two crystalline forms.

A boiler fly ash containing 7.8% Ni from a power station in Egypt was leached with water and with HCl/HNO_3 to recover the nickel [201]. With increasing temperature, the water leach efficiency went through a maximum, but the efficiency of the acid leach increased with temperature. After solution purification, the nickel could be recovered as oxalate or acetate. Kaolinite was impregnated in stages with slurries and catalysts were formed by thermal decomposition of this material in hydrogen. Differential thermal analysis was used and the decomposition temperatures were given as 653 K for the acetate, 693 K for the oxalate, 1173 K for the Ni hydroxide. Catalytic activity in cracking natural gas + steam showed a maximum for a catalyst reduction temperature of 573 K.

6. MISCELLANEOUS APPLICATIONS

Numerous "other" fields of applications of thermal analysis can be found in the literature. Some of the more popular ones are metal-matrix composites, powder metallurgy and thin films. In this section, only a few studies in each of the three fields are discussed.

6.1. Metal-matrix composites

Metal-matrix composites is a relatively new field of metallurgy that is growing very rapidly. The development of metal-based amorphous and crystalline composite materials with special physical, mechanical, electrical, magnetic and chemical characteristics has attracted a large number of scientists and engineers in industry and academia in the last two decades. This field of metallurgy has a much wider scope and greater opportunities than that of traditional alloys because it utilizes techniques such as rapid quenching, solution treatment and aging to allow the inclusion of minor metallic and non-metallic components into the metal lattice and, therefore, induce specific properties such as hardness, ductility, corrosion resistance and machinability, required for certain

applications. Metal-matrix composites that have generated most interest include those based on aluminum, copper, titanium, nickel and iron. Additions of Cu, Al, Si, Mn, Cr, Mg, Ni, P, Co, Ti, Fe, C, Be, and others, in the elemental, oxide or carbide form are common. Thermal analysis techniques have been extensively used to explore the stability and behaviour of these materials at high temperatures and to design heat treatment schemes for property development. Differential scanning calorimetry and dynamic mechanical analysis are the most common thermal analysis techniques used in this field.

Friend et al. [202] used dynamic mechanical analysis (DMA) to differentiate between the interfacial bond strengths of different metal-matrix composites and to study the effect of annealing (550 °C for 5 hours in inert atmosphere) on the interfacial bonding in these composites. Three composite materials were examined: boron-aluminum, which has a very strong interfacial bond but for which exposure to elevated temperatures causes degradation in tensile strength; borsic-aluminum, which incorporates SiC-coated boron fibers to maintain high-temperature strength; and SiC-aluminum with a carbon-rich coating which has a week interfacial bond. DMA was carried out at different frequencies, strains and temperatures by applying a sinusoidal shear strain to the sample. The results indicated that DMA is an appropriate and sensitive technique for the detection of interfacial bond strengths as well as small changes in composite damping on annealing. Damping is the process of energy dissipation during viscoelastic or anelastic changes. Changes in composite damping were attributed to the formation of an "interphase", a fibre-matrix inhomogeneous interfacial region, on annealing. This interphase greatly influences the structural integrity of the composite.

Aluminum-based metal-matrix composites continue to be of major interest to the aerospace industry due to their low density and excellent thermal and mechanical properties. DSC, TG and XRD were used by Hébert and Karmazsin [203] to characterize a SiC-reinforced Al/Cu/Mg alloy. The mixed billet was prepared by powder metallurgy followed by an elaborate heat treatment procedure. An endothermic interaction between the SiC whiskers and the metal matrix composite was detected by DSC at 412 °C, Figure 50. No change in mass was observed. The amplitude of the endothermic peak was taken as an indicator of the extent of cohesion at the interface between the SiC and the composite. The use of DSC was suggested for the evaluation of the degree of reinforcement of the composite in the fabrication process.

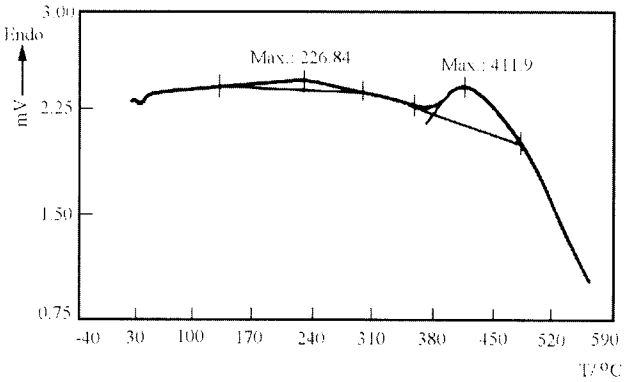


Figure 50. DSC curve for a normalized Al/SiC sample; heating rate 20 deg min^{-1}. From J.P. Hébert and E. Karmazsin, reference 203.

The precipitation characteristics and age-hardening behaviour of SiC-reinforced Al-Cu alloys, processed by powder metallurgical techniques, were also studied by Kim et al. [204] using differential scanning calorimetry together with macrohardness measurements and TEM. Al-4 mass % Cu alloys, unreinforced and reinforced with 5-15% SiC whiskers, were examined. Age hardening of this metal-matrix composite is induced by the precipitation of metastable phases, θ" and θ', and is detected by DSC as exothermic effects at 458 and 523 K. The DSC measurements indicated that the precipitation of these phases and, hence age hardening, is significantly retarded by the addition of SiC whiskers. The magnitude of age hardening also diminished in the presence of the whiskers.

Like SiC whiskers, particulate SiC is being used to reinforce aluminum matrix composites to achieve a superior strength. The SiC particles seem to enhance the precipitation and dispersion of a fine phase responsible for the strength development throughout the matrix. Das et al. [205] used DSC and DMA to study the microstructure and physical characteristics of a series of particulate-reinforced aluminum metal- matrix composites (PMMC) based on the 6061 aluminum alloy. Samples of as-prepared and heat-treated material were examined. Exothermic reactions responsible for the fine-phase precipitation were found by DSC to occur at higher temperatures in the SiC reinforced materials. DMA results indicated that the reinforced composite, 20 vol.% SiC/6061, has the highest storage modulus at all temperatures, in contrast with 6061 alone which was found to have the lowest modulus among all samples examined. DSC and DMA together allowed the identification of phases and

changes responsible for the maximum damping characteristics of all the materials examined.

Elomari et al. [206] investigated the effect of prestraining on the elastic modulus and the damping capacity of the Al_2O_3/Al metal matrix composite as a function of temperature, using dynamic mechanical analysis. This type of ceramic particulate-reinforced composite was found to possess excellent properties like high strength, stiffness, wear resistance, low coefficient of thermal expansion and high thermal conductivity compared to those of conventional unreinforced aluminum alloys. Under high stress during cold deformation processing, however, the mechanical properties of these reinforced materials may deteriorate. The investigators found that the elastic modulus decreases substantially (particularly in the composite with 20 vol.% Al_2O_3) with increasing prestrain, Figure 51. This was attributed to the presence of voids at particle fracture sites, reducing the reinforcing effect of the Al_2O_3 particulates and, at the same time, creating a defect structure with deleterious effect on the elastic modulus. The damping capacity was found to increase with the increase in the Al_2O_3-particulate content. At 20 vol.% Al_2O_3, the damping capacity was also found to increase with the increase in plastic strain. Image analysis was used as a complementary technique in this study.

White et al. [207] studied solid-state amorphization reactions in multi-layered metallic composites. Conditions conducive to the formation of amorphous metallic phases were discussed by the authors. Interlayered foils of Ni and Ti or Zr were passed through a rolling mill, folded and re-rolled to desired degree of reduction (deformation), forming diffusion couples. The rolled materials were examined by DSC, XRD and electron diffraction. To follow amorphization reactions in the DSC, the samples were sealed in aluminum pans and heated at a constant rate to determine the heat flow as a function of temperature. Exothermic activities were detected up to 850 K. Those below about 620 K were taken to be due to formation of the amorphous alloy. The first peak above about 620 K was taken to be the crystallization of the amorphous phase, followed by reaction of remaining unalloyed metals. Zr was found to form amorphous alloy much more readily than Ti; this was attributed to the more rapid diffusion of Ni in Zr than in Ti.

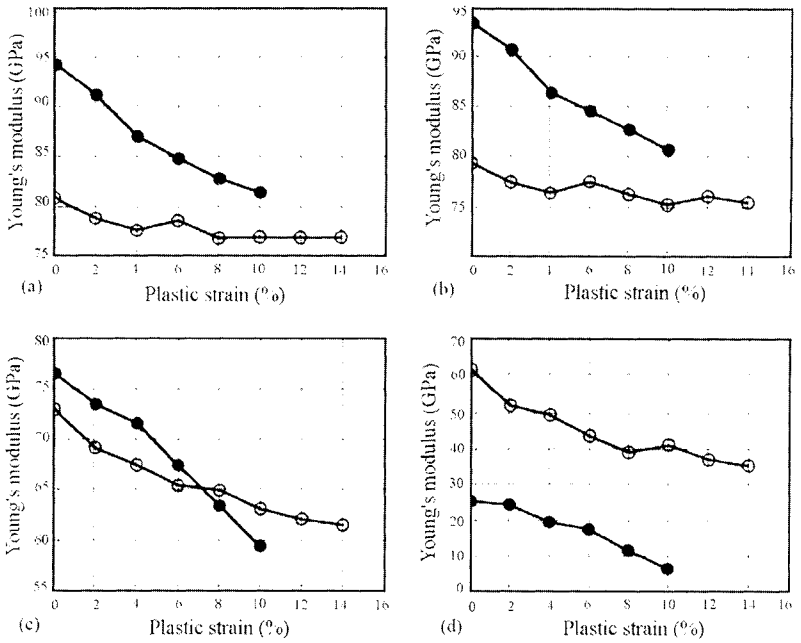


Figure 51. Young's modulus for composites of (O) 10 vol % and (●) 20 vol % Al_2O_3 in aluminum alloy 6061 as a function of plastic strain at various temperatures: (a) 25 °C, (b) 50 °C, (c) 250 °C, and (d) 450 °C. From S. Elomari et al., reference 206.

A Pd-Cu-Si alloy (7.5 at.% Pd, 6 at.% Cu, 16.5 at.% Si), with WC micron-sized particles (2 - 12%), was prepared, melted and quenched by chill-block melt spinning [75] to form an amorphous metal-matrix composite. Crystallization characteristics, such as the activation energy and Avrami exponent, were determined as a function of WC volume fraction by using DSC, TEM and XRD. DSC showed a glass-transition endothermic peak at about 380 °C and a large exothermic crystallization peak at 410-420 °C. Two smaller exotherms at higher temperature occurred with 0% and 2% WC. XRD showed crystalline WC, and progressive crystallization of the amorphous alloy by annealing for over 5 h at 330 °C. Activation energies for crystallization were estimated by Kissinger's method [208], and values of n, the Avrami exponent, were estimated from Ozawa's equation [209]:

$$[d\{\log(-\ln(1-x))\}/d \log \beta\,]_T = -n$$

where β = the heating rate and x = the fraction crystallized. E_a and n were plotted as functions of %WC and annealing time at 330 °C. With an increase in the WC

volume fraction, the activation energy for crystallization was found to decrease, while n was found to increase. The authors speculated that WC-particle dispersions caused the rate-determining crystallization mechanism to change from nucleation to growth by preannealing the WC-amorphous-$Pd_{77.5}Cu_6Si_{16.5}$ metal-matrix composite. Figure 23 shows DSC curves with exothermic crystallization peaks of the composite (preannealed and non-preannealed), with different ratios of WC.

Myung et al. [76] have also studied the crystallization and viscous behaviours of WC-amorphous $Ni_{73}Si_{10}B_{17}$ metal-matrix composite under continuous heating conditions using DSC, TMA and XRD. DSC results, obtained at a heating rate of 10 K min^{-1}, showed that the glass-transition temperature decreased with the increase in the WC volume fraction, the exothermic crystallization peak moved to slightly lower temperatures for 6% and 10% WC materials (791-789 K), and the enthalpy of crystallization decreased with increasing WC content. Values of activation energies (E_a) and the Avrami exponent (n) were estimated from results at different heating rates. Unlike the earlier system investigated by the authors [75], E_a increased and n decreased with increasing volume fraction of WC for the non-annealed samples. Plots of crystalline fraction vs. temperature were developed using the DSC peaks. The viscosity of the metal-matrix composite appeared to decrease with the presence of WC.

Solidification rates for the alloy $Cu_{90}Pb_5Ti_5$, with and without the addition of graphite, were determined by Konopka and Braszcznski [210] using cooling curves. The graphite/Cu-Pb-Ti composite is used as a bearing material and can be formed by casting. The solidification of the composite was done in a thin-walled metal mould and the temperature was monitored as $T = f(t)$ and $dT/dt = f'(t)$. The solidification equation was taken as:

$$-(\alpha.\theta/R\rho c) + (\beta/c) = d\theta/dt \qquad \text{or} \qquad U_{TG} + U_{TZ} = U_T$$

where α = overall heat transfer coefficient, R = characteristic dimension of the casting, c = specific heat, ρ = density, $\theta = T - T_o$, and T_o = temperature of the heat sink. U_T (dT/dt) was determined as the slope of the cooling curve and U_{TG} was estimated by calculation as a function of θ; U_{TZ} was then found by difference to give $\beta = dL/dt$, where L is latent heat of solidification. β was plotted against time to give a graphic representation of the solidification kinetics. The fraction solidified ($c/L \int U_{TZ} dt$) versus time t was also plotted. Somewhat more rapid initial crystallization of the composite, compared to that of the alloy, was attributed to nucleation effects of the graphite.

6.2. Powder metallurgy

Sintering, the basis of the field of powder metallurgy, is essentially a process in which fine powders are heated to incipient melting at temperatures significantly below the melting point of the whole powder to form a dense compact or agglomerate for further processing or a finished product. It is a physical phenomenon, except for reactive sintering, in which the free energy of the powder decreases, usually resulting in a measurable thermal effect. Like roasting, drying and calcination, sintering involves an enthalpy change and, therefore is a good candidate for study by thermal analysis.

Powder-metallurgy processing is used in different industries to produce materials for tools, electronics, automotive applications and others. Kieback et al. [211] studied the sintering process of starting powders, mixed with lubricants or binders, using thermogravimetry, differential thermal analysis and dilatometry to examine the chemical, microstructural and dimensional changes taking place during sintering and material transport. Two powder mixtures, namely WC-Co and Fe-Si (or Fe-FeSi) were studied. In the former system, the thermoanalytical results indicated that sintering takes place above the eutectic temperature (in presence of a persistent liquid phase) leading to an enhancement in the compaction of the powder mixture. In the latter system, the formation of intermetallic compounds was confirmed, together with a transient liquid-phase sintering above 1250 °C. Figure 52 shows the thermal events occurring during heating/sintering of the Fe-Si and Fe-FeSi powders as determined by differential thermal analysis. The thermal techniques were very useful in the interpretation of the mechanisms governing the material transport and in the determination of the optimum conditions for sintering.

During the production of certain high-temperature materials using powder metallurgical techniques, a significant volume change occurs during the sintering process. Hädrich et al. [212] used dilatometry, a conventional thermal analysis technique, to monitor the dimensional change on heating. The first derivative of the dimensional change with time (or temperature) helps in detecting small changes and increases the resolution of overlapping transitions, Figure 53. An example of the usefulness of dilatometry in the industrial manufacture of magnets was quoted. The calcination of barium and strontium ferrite compacts for the production of magnets involved the placing of the raw compacts in the kiln in such a manner that they touch each other. With this configuration, it was found that the number of rejected magnets was noticeably high despite the significant final shrinkage. Dilatometry revealed that the compacts exhibited a low-temperature expansion prior to the high-temperature contraction causing the damage. By spacing the compacts in the kiln, the problem was eliminated. The same authors [213] found simultaneous TG/DTA

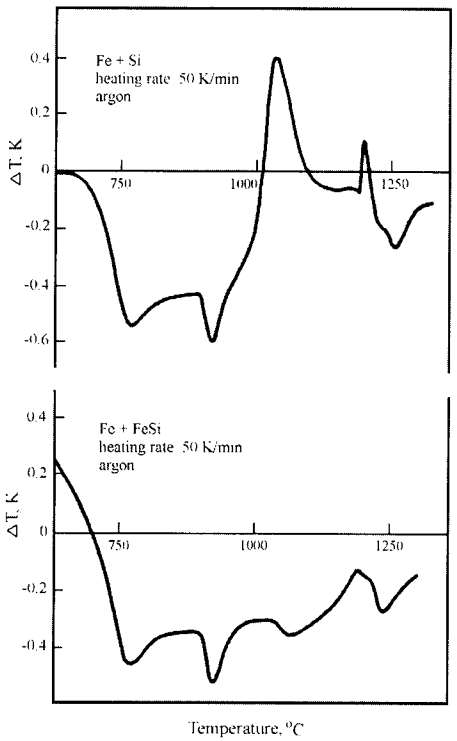


Figure 52. DTA curves showing thermal effects during heating of Fe + Si and Fe + FeSi powder mixtures. From B.F. Kieback et al., reference 211.

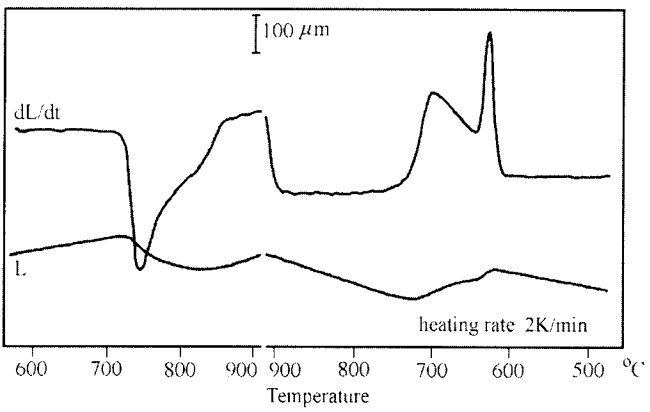


Figure 53. Dilatometer measurements on the sintering of a steel powder sample. From W. Hädrich et al., reference 212.

very useful in determining the temperature and rate of the release of the paraffin binder in pre-sintered, extruded metal-powder compacts. Cracking during the sintering process often occurs if the binder is released too rapidly (with the degassing) or above a certain temperature.

Minor additions of certain elements to metallic powders were found to affect their sintering behaviour and ultimately their mechanical properties, corrosion resistance and high-temperature oxidation. In this study, Wang [214] explored the microstructural changes occurring during the sintering of 304L stainless steel powder with silicon additions using differential thermal analysis (in H_2) and metallography. In the preliminary work, the eutectic melting of 70% Ni-30% Si powder (965 °C) was verified experimentally. The eutectic melting of the stainless steel powder with silicon additions (3 and 4%) was found to take place at 960 °C, with an endothermic melting peak which increased in intensity with the increase in the silicon additions. The peak temperature was found to be very close that of the Ni-Si mixture, indicating a diffusion of the nickel from the steel matrix into the silicon particles. This was also verified by metallography. The volume change during sintering in hydrogen, argon and vacuum also was determined using dilatometry and the results indicated different sintering behaviour in the different atmospheres. Sintering in vacuum was found to be the most effective, resulting in the highest volume shrinkage of 24%.

German [215] studied the combustion synthesis of intermetallic compounds formed during the fabrication of high-temperature materials using reactive sintering. In this process, elemental powders (generally metallic) are mixed together and heated to high temperatures to initiate the sintering process which, in turn, releases a large amount of heat due to the formation of intermetallic compounds. The released heat is sufficient to increase the rate of reaction and leads to the formation of a transient liquid phase, which diffuses very quickly to fill the voids between the solid particles, resulting in the sintering and densification of the powder compacts. The author used DTA and dilatometry to study the reactive sintering of green compacts of nickel aluminide powders. A significant exothermic effect, Figure 54, was evident at 880 K on the DTA diagrams, signifying the formation of Ni_3Al from the starting powders. The corresponding densification of the compact was detected at the same temperature by dilatometry (about 12% shrinkage). The completeness of this synthesis was verified by reheating the sintered compact. Only an endothermic melting peak of Ni_3Al above 1600 K appeared on the DTA curve. DTA was also very useful in determining the effect of pre-annealing of the compacts at temperatures far below the sintering temperature. Several other parameters such as powder composition and homogeneity, heating rate, particle size, particle-size ratio, green density, degassing procedures, were examined to determine their influence on the reactive sintering process.

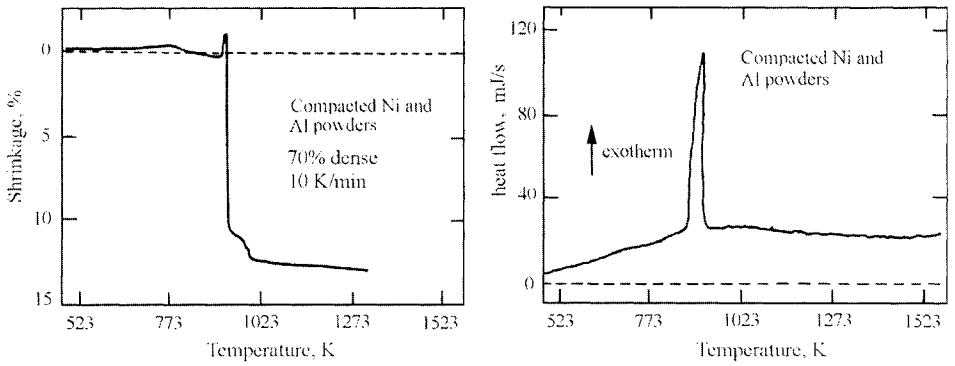


Figure 54. Dilatometry and DTA of compacted mixed nickel and aluminum powders heated at a constant rate. The rapid densification corresponds to the exothermic reaction temperature. From R.M. German, reference 215.

High-speed tool steels made by powder metallurgy (PM) were compared with cast steels. DTA was carried out by Pumpyanskaya et al. [216] using a high-temperature (1600 °C) DTA apparatus. The results showed that PM steels and cast steels had identical Curie temperatures and $T(\alpha \rightarrow \gamma)$, but the temperature ranges for dissolution of carbides during austenizing were significantly lower for PM steels than for cast steels. $M_{23}C_6$ carbide dissolution occurred in the range 950-1050 °C for PM steel and 970-1100 °C for cast steel. For the M_6C and MC carbides, dissolution started at 1140 °C (PM) and 1190 °C (cast). The lower temperatures for carbide dissolution were attributed to the finer particle-sizes of the carbides in the PM steels.

The authors showed that annealing temperatures prior to quenching could be lower for PM steels than for cast steels. Impact strength, bending strength and hardness were determined on quenched and annealed samples.

6.3. Thin films

Thermal analysis is also very valuable in the area of metallic and ceramic thin film research and technology since the sample required to generate a measurable signal may be in the milligram (or less) size range. Homogeneous thin films, normally a few micrometers thick, are usually produced by Physical Vapour Deposition (PVD) techniques, e.g., sputtering, in a low-pressure inert atmosphere on a metallic or a ceramic substrate. This technology has been used in many fields of applications such as the fabrication of optical and electronic devices, oxygen sensors, buffer layers for integrated circuits and protective films. It was also shown that DSC can be used to generate both thermodynamic and kinetic data on the amorphization reactions in thin films. For instance,

Highmore et al. [217] studied solid-state amorphization and subsequent crystallization in multi-layer Ni/Zr thin films, using constant heating rate DSC. The films were prepared by magnetron sputtering. Figure 55 shows two major exothermic peaks for a sample with an average composition of $Ni_{67}Zr_{33}$ heated in argon at 40°C min^{-1}. The broad first peak was attributed to the reaction of the two polycrystalline elements to form a homogenous amorphous alloy, and the second peak to the crystallization of the amorphous alloy. The activation energy and pre-exponential factor for the interdiffusion of Ni and Zr during the amorphization reaction, and the activation energy of crystallization were determined. The results suggested that amorphization may occur by the motion of one element only, while crystallization may require the motion of both elements.

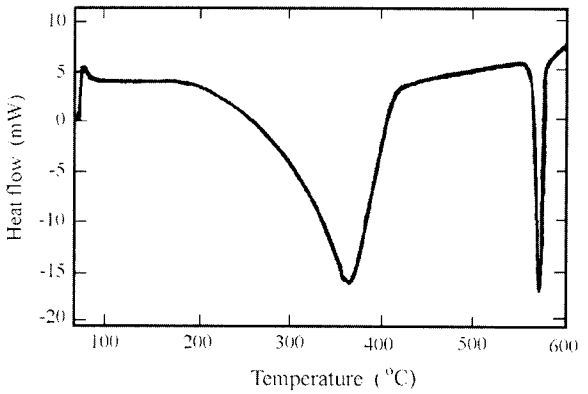


Figure 55. DSC curve for heating a $Ni_{67}Zr_{33}$ multilayer with a modulation wave length of 63 nm from 70 to 600 °C at 40 °C min^{-1}. From R.J. Highmore et al., reference 217.

Spaepen and Thompson [218] reviewed several examples of the application of DSC in the study of the epitaxial regrowth of ion-implanted amorphous silicon, the formation of amorphous metals (e.g. Ni-Zr) by solid-state reaction, the formation of intermetallic compounds in metallic multi-layered films (e.g., $NbAl_3$ in Nb/Al system), the transformations in Ni/amorphous Si multi-layers and the identification of microcrystalline structures by the observation of grain growth (e.g. in Al-Mn and Al-Fe systems). In the last example, it was shown that isothermal DSC could be used to differentiate between "truly amorphous" materials and microcrystalline ones on the basis of the fact that the first material undergoes both nucleation and grain growth, while the latter undergoes only grain growth, generating different DSC traces. In the studies examined, different sample geometries were used in acquiring the DSC measurement and in

enhancing the DSC signal. In some cases, the thin film was examined on the substrate, on several substrates stacked together or as deposited on both sides of the substrate.

The use of Al or Al-Cu alloys interlayered with transition metals shows considerable promise as thin films for fine device interconnections. The temperature and sequence of phase formation, as well as the activation energy for intermetallic thin film couples of transition metal aluminides, were determined by Ball and Todd [219] using DSC and XRD. Couples of Al/Cr, Al-4 mass % Cu/Cr, Al/Ti, Al-4 mass % Cu/Ti, Al/Zr, Al-4 mass % Cu/Zr, Al/Nb and Al-4 mass % Cu/Nb were examined. The results indicated that the formation of intermetallic compounds (aluminides) commenced above 300 °C, with the first intermetallic phases formed being the aluminum-rich ones. The DSC peak temperature signifying the formation of intermetallics increased with the addition of copper and with the increase in heating rate. Activation energy data also indicated that the addition of copper retards the growth of the intermetallics and minimizes the void propagation in the thin stripe. This improves the electromigration resistance in the multi-layer structure by preventing void coalescence from severing the interconnection. Zr and Ti were found to be most effective in enhancing the electromigration resistance in multi-layer conductors of Al-Cu thin films.

Solid-state reactions in multi-layered thin-film diffusion couples of elemental Ni and Zr metals were studied by Cotts et al. [220] using DSC, with XRD as a supplementary technique. A solid-state reaction between the starting, crystalline metals in a sputtered, multilayered thin film takes place with the formation of an amorphous alloy, in this case $Ni_{68}Zr_{32}$, generating a large heat of mixing, easily detected by a large exothermic DSC effect. A subsequent exothermic DSC peak signified the crystallization of the alloy. The amorphous thin-film alloy seems to have a high degree of homogeneity comparable to that of a bulk liquid-quenched alloy. It was suggested that the enthalpy released during the amorphization, 35 kJ mol^{-1}, as measured by DSC, represents the enthalpy of formation of the $Ni_{68}Zr_{32}$ amorphous phase. This was essentially independent of the layer thickness, as can be seen in Figure 56, and, hence, of the intermixing geometry of the two metals. DSC measurements yielded detailed information on the nature and kinetics of amorphous alloy formation in multi-layered thin-film structures.

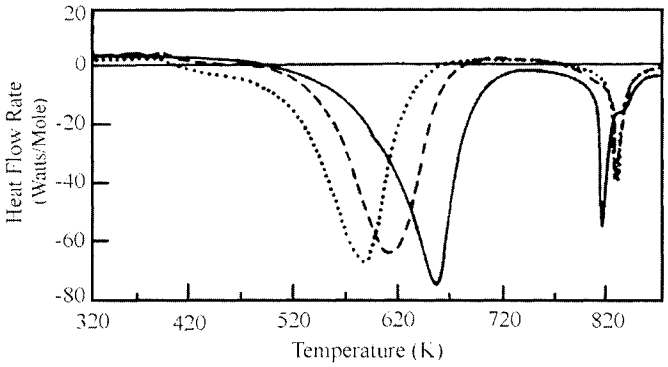


Figure 56. DSC curves for sputtered, multilayered thin films of equal-thickness layers of Ni and Zr (average stoichiometry $Ni_{68}Zr_{32}$) with different layer thicknesses: dotted line, 300 Å; dashed line, 450 Å; solid line, 1000 Å; heating rate 10 K min^{-1}. From E.J. Cotts et al., reference 220.

REFERENCES

1. V.S. Ramachandran, Differential Thermal Analysis in Cement Chemistry, Chemical Publishing Company, Inc., New York, 1969.
2. R.C. Mackenzie, Differential Thermal Analysis, Academic Press, London and New York, Vol 1, 1970 and Vol. 2, 1972.
3. E.I. Turi, Thermal Characterization of Polymeric Materials, Academic Press, New York, 2nd Edn, 1997.
4. B. Wunderlich, Thermal Analysis, Academic Press, Inc., New York, 1990.
5. J.L. Ford and P. Timmins, Pharmaceutical Thermal Analysis, Ellis Harwood, Chichester UK, 1989.
6. W. Wendlandt, Thermal Methods of Analysis, Second Edition, John Wiley & Sons, New York, 1974.
7. W.W. Wendlandt, Thermal Analysis, Third Edition, John Wiley & Sons, New York, 1986
8. W. Gutt and A.J. Majumdar, in R.C. Mackenzie (ed), Differential Thermal Analysis, Academic Press, London and New York, Vol. 2, 1972; pp.79-117.
9. M.E. Brown, Introduction to Thermal Analysis, Kluwer, Dordrecht, 2nd Edn, 2001.
10. R.D. Shull, in R. D. Shull and A. Joshi (eds), Thermal Analysis in Metallurgy, The Minerals, Metals & Materials Society, Warrendale PA, 1992, pp.95-119.

11. C.J.Butler and D.G. McCartney, in Y-W Kim, R. Wagner and M. Yamaguchi (eds), Gamma Titanium Aluminides, The Minerals, Metals & Materials Society, Warrendale PA, 1995, pp. 491-497.
12. Y.T. Zhu, J.H. Devletian and A. Manthiram, J. Phase Equilibria, 15 (1994) 37.
13. Y.T. Zhu and J.H. Devletian, Metall. Trans.A, 22 (1991) 1993.
14. Y.T. Zhu and J.H. Devletian, Metall. Trans.A, 23 (1992) 451.
15. S. Seetharaman, R. Eichler and A. Hultin, Scand. J. Metall., 21 (1992) 86.
16. A. Bolcavage, C.R. Kao, Y.A. Chang and A.D. Romig,jr., in J.E. Morral, R.S. Schiffman, S.M. Merchant (eds), Experimental Methods of Phase Diagram Determination, The Minerals, Metals & Materials Society, Warrendale PA, 1994, pp. 21-30.
17. R. Kesri and M. Durand-Charre, Mater. Sci. Tech., 4 (1988) 692.
18. M. Durand-Charre, N. Valignat and F. Durand, Mém. Étud. Sci. Rev. Métall., 76 (1979) 51.
19. K.W. Richter and H. Isper, J. Phase Equilib., 15 (1994) 165.
20. V.J. Kuck, Thermochim. Acta 99 (1986) 233.
21. T.J. Lienert, C.V. Robino, C.R. Hills and M.J. Cieslak, in R.A. Patterson and K.W. Mahin (eds), Weldability of Materials. Proceedings of the Materials Weldability Symposium, Detroit, Michigan, October 1990, ASM, Materials Park, OH, pp.159-165.
22. T. Takemoto, I. Okamoto and J. Matsumura, Report II, Transactions of JWRI (Japan Welding Research Institute), 16 (1987) 73.
23. S. Dal Corso, B. Liautard and J.C. Tedenac, J. Phase Equilib., 16 (1995) 308.
24. S. Atiq, R.D. Rawlings and D.R.F. West, J. Mater. Sci. Lett., 9 (1990) 518.
25. A. Saccone, S. Delfino and R.Ferro, J. Less-Common Met., 108 (1985) 89.
26. P. Terzieff and H. Ipsen, J. Less-Common Met., 119 (1986) 1.
27. R. Lässer and T. Schober, J. Less-Common Met., 130 (1987) 453.
28. S. Katsuyama, Y. Ueda and K. Kosuge, Mater. Res. Bull., 25 (1990) 913.
29. B. Dubost, Ph. Bompard and I. Ansara, Mém. Étud. Sci. Rev. Métall., 83 (1986) 437.
30. A. Palenzona and P. Manfrinetti, J. Alloys Compd., 220 (1995) 157.
31. S. Hassam, M. Gambino, M. Gaune-Ecard, J.P. Bros and J. Ågren, Metall. Trans. A, 19A (1988) 409.
32. A. Saccone, S. Delfino, G. Cacciamani and R. Ferro, J. Less-Common Met.,
154 (1989) 99.
33. F. Faudot, M. Harmelin and J. Bigot, Thermochim. Acta, 147 (1989) 205.
34. M.V. Nosek, N.M. Atomanova and Z.D. Abisheva, Izvestiya Akademii Nauk SSSR. Metally, No.4, (1987) 198.

35. Y.Y. Pan and P. Nash, Bull. Alloy Phase Diagrams, 10 (1989) 253.
36. R. Vogel, Z. Metallkd., 38 (1947) 97.
37. Y.Y. Pan and C.S. Cheng, Chinese Nat. Symp. Phase Diagrams, Kumming, Sept. 21-23; 1984.
38. M. Venkatraman and J.P. Neumann, Bull. Alloy Phase Diagrams, 11 (1990) 8.
39. V.N. Svechnikov, G.P. Dmitrieva, G.F. Kobzenko and A.K. Shurin, Dokl. Akad. Nauk SSSR, 158 (1964) 668.
40. R.D. Blaugher, R.E. Hein, J.E. Cox and R.M. Waterstrat, J. Low Temp. Phys., 1 (1969) 539.
41. R. Fluekiger, A. Paoli and J. Muller, Solid State Commun., 14 (1974) 443.
42. E.M. Foltyn and D.E. Peterson, Bull. Alloy Phase Diagrams, 9 (1988) 267.
43. D.H. Wood, E.M. Cramer, P.L. Wallace and W.J. Ramsay, J. Nucl. Mater., 32 (1969) 193.
44. R.F. Nikerson, USAEC (US. Atomic Energy Commission) Rep. UCRL-50509, 1968.
45. R.F. Nickerson, J. Nucl. Mater., 32 (1969) 208.
46. W.S. Kim, G.Y. Chao and L.J. Cabri, J. Less-Common Met., 162 (1990) 61.
47. B. Cantor, J. Therm. Anal., 42 (1994) 647.
48. P.S. Grant, P.P. Maher and B. Cantor, Mater. Sci. Eng., A179/A180 (1994) 72.
49. D.L. Zhang, K. Chattopadhyay and B. Cantor, J. Mater. Sci., 26 (1991) 1531.
50. W. Gao and B. Cantor, Acta Metall., 36 (1988) 2293.
51. P. Donner, J. Physique IV, 1 (1991), Colloque C4, C4-355.
52. W.A. Johnson, J.A. Domingue and S.H. Reichman, J. Physique, 43 (1982), Colloque C4, C4-285.
53. D. Mari and D.C. Dunand, Metall. Mater. Trans. A., 26A (1995) 2833.
54. C. García Cordovilla and E. Louis, J. Mater. Sci., 19 (1984) 279.
55. R.N. Shenoy and J.M. Howe, Scripta Metall. Mater., 33 (1995) 651.
56. C.V. Robino and M.J. Cieslak, Metall. Mater. Trans., 26A (1995) 1673.
57. H.F. Fischmeister, R. Riedl and S. Karagöz, Metall. Trans., 20A (1989) 2133.
58. M.J. Cieslak and W.F. Savage, Weld. J., 64 [5] (1985) 119-s.
59. G. Laird II and Ö.N. Doğan, Int. J. Cast Metals Res., 9 (1996) 83.
60. D. Hui, Y. Jingxiang, K.G. Davis, Trans. Amer. Foundrymen's Society, 39 (1985) 917.
61. J. Lendvai, G. Honyek, Zs. Rajkovits, T. Ungár, I. Kovács and T. Túrmezey, Aluminium (Duesseldorf), 62 (1986) 363.

62. B. Sarangi, A. Sarangi, S. Misra and H.S. Ray, Thermochim. Acta, 196 (1992) 45.
63. H. Warlimont, in S.Steeb and H. Warlimont (eds), Rapidly Quenched Metals, Elsevier Science Publishers B.V., Vol.1, 1985, p. xlv.
64. N.J. Grant, in S.Steeb and H. Warlimont (eds), Rapidly Quenched Metals, Elsevier Science Publishers B.V., Vol. 1, 1985, pp. 3-24.
65. R. Pickens, in S.Steeb and H. Warlimont (eds), Rapidly Quenched Metals, Elsevier Science Publishers B.V., Vol. 2, 1985, pp. 1711-1714 (and 4 pages in the Errata Section).
66. H.J. Güntherodt, in S.Steeb and H. Warlimont (eds), Rapidly Quenched Metals, Elsevier Science Publishers B.V., Vol. 2, 1985, pp. 1591-1598.
67. W.A. Heinemann, in S.Steeb and H. Warlimont (eds), Rapidly Quenched Metals, Elsevier Science Publishers B.V., Vol. 1, 1985, pp. 27-34.
68. W. Jingtang, P. Dexing, S. Qihong and D. Bingzhe, Mater. Sci. Eng., 98 (1988) 535.
69. J. Hertz and M. Notin, Thermochim. Acta, 133 (1988) 311.
70. T.H. Noh, A. Inoue, H. Fujimori, T. Masumoto and I.K. Kang, J. Non-Crystalline Solids, 110 (1989) 190.
71. F.J. Fouquet, J.P. Allemand, J. Perez and B. de Guillebon, Z. Phys. Chem. Neue Folge, 157 (1988) 295.
72. T. Yamasaki, M. Takahashi and Y. Ogino, in S.Steeb and H. Warlimont (eds), Rapidly Quenched Metals, Elsevier Science Publishers B.V., Vol.2, 1985, 1381.
73. T-W. Wu and F. Spaepen, Phil. Mag. B, 61 (1990) 739.
74. J.W. Graydon, S.J. Thorpe and D.W. Kirk, Acta Metall. Mater., 43 (1995) 1363.
75. W-N. Myung, S-J. Yang, H. Kimura and T. Masumoto, Mater. Sci. Eng., 97 (1988) 259.
76. N. Myung, S-J. Yang, H-G. Kim, J-B. Lee and T. Masumoto, Mater. Sci. Eng. A, 133 (1991) 513.
77. A.P. Radinski and A. Calka, Phys. Rev. Lett., 57 (1986) 3081.
78. P. Johansson, B. Uhrenius, A. Wilson and U. Stalberg, Powder Metall., 39 (1996) 53.
79. M.S. Leu, W.K. Wang and S.C. Jang, Mater. Sci. Eng., A181/A182 (1994) 997.
80. G.D. Ladiwala, N.S. Saxena, S.R. Joshi, A. Pratap and M.P. Saksena, Mater. Sci. Eng., A181/A182 (1994) 1427.
81. K. Amiya, N. Nishiyama, A. Inoue and T. Masumoto, Mater. Sci. Eng., A179/A180 (1994) 692.
82. G.A. Merry and H. Reiss, Acta Metall., 32 (1984) 1447.
83. D.H. Rasmussen and C.R. Loper, Acta Metall., 23 (1975) 1215.

84. J.H. Perepezko and D.H. Rasmussen, A.I.A.A. Papers, No. 79-0030, 1979, 9 pp.
85. J.H. Perepezko, C. Gallop and D.H. Rasmussen, in Proc. 3rd. Eur., Symp. on Material Sciences in Space, ESA SP-142, 1979, pp. 375-383.
86. D.H. Rasmussen and C.R. Loper, Acta Metall., 24 (1976) 117.
87. A. Kumpmann, B. Günther, H.-D. Kunze, Mater. Sci. Eng., A168 (1993)165.
88. A K. Omuro, H. Miura and H. Ogawa, Mater. Sci. Eng., A181/A182 (1994) 1281.
89. E. Hellstern and L. Schultz, Appl. Phys. Lett., 48 (1986) 124.
90. S. Suriñach, J.J. Suñol and M.D.Baró, Mater. Sci. Eng., A181/A182 (1994) 1285.
91. D. Oleszak, M. Jachimowicz and H. Matyja, Mater. Sci. Forum, 179-181 (1995) 215.
92. J. Kaneko, D.G. Kim and M. Sugamata, in J.J. de Barbadillo, F.H. Froes, and R. Schwarz (eds), Proceedings of the 2nd International Conference on Structural Applications of Mechanical Alloying, Vancouver BC, Canada, 20-22 September, 1993, ASM International, Materials Park OH, c1993, pp. 261-268.
93. C-L. Tsai, Mater. Sci. Eng., A181/A182 (1994) 986.
94. K. Aoki, X.-M. Wang, A. Memezawa and T. Masumoto, Mater. Sci. Eng., A181/A182 (1994) 390.
95. E. Kasai, K. Mae and F. Saito, ISIJ International, 35 (1995) 1444.
96. H. Yang and H. Bakker, Mater. Sci. Forum, 150/151 (1994) 109.
97. H. Yang and H. Bakker, Mater. Sci. Eng., A181/A182 (1994) 1207.
98. T. Tanaka, S. Nasu, K. Nakagawa, K.N. Ishihara and P.H. Shingu, Mater. Sci. Forum, 88/90 (1992) 269.
99. H.J. Grabke, in H.J. Grabke and D.B. Meadowcroft (eds), A Working Party Report on Guidelines for Methods of Testing and Research in High Temperature Corrosion, European Federation of Corrosion Publications Number 14, The Institute of Materials, London, 1995, pp.52-61.
100. A. Holt and P. Kofstad, Mater. Sci. Eng., A120 (1989) 101.
101. L. Shi, Y. Zhang and S. Shih, Corros. Sci., 33 (1992) 1427.
102. M. Lambertin and G. Beranger, in J.D. Embury (ed), High-Temperature Oxidation and Sulphidation Processes, Proceedings of Symposium, Hamilton ON, Canada, August 1990, Pergamon Press, New York, 1990, pp. 93-100.
103. M.J. Maloney and M.J. McNallan, Metall. Trans. B, 16B (1985) 751.
104. S. Mrowec and S. Stokłosa, Oxid. Met., 8 (1974) 379.
105. Y.-N. Chang, Brit. Corros. J., 30 (1995) 320.

106. C. Wagner, in Atom Movements, American Society for Metals, Cleveland, Ohio, 1951, pp. 153-173.
107. P. Kofstad, High-Temperature Oxidation of Metals, Wiley, New York, 1966.
108. K. Hauffe, Oxidation of Metals, Plenum Press, New York, 1965.
109. A. T. Fromhold, Theory of Metal Oxidation, North-Holland, Amsterdam, 1975.
110. C. Zhou and W.W. Smeltzer, in J.D. Embury (ed.), International Symposium on High Temperature Oxidation and Sulfidation Processes, Metallurgical Society of the CIM, Pergamon Press, New York, 1990, pp. 43-54.
111. E.A. Gulbransen and E.F. Andrew, J. Electrochem. Soc., 104 (1957) 451.
112. S.Mrowec and A. Stokłosa, Oxid. Met., 3 (1971) 291.
113. H.S. Hsu and G.J. Yurek, Oxid. Met., 17 (1982) 55.
114. R. Herchl, N.N. Khoi, T. Homma and W.W. Smeltzer, Oxid. Met., 4 (1972) 35.
115. G.C. Wood and F.H. Scott, Oxid. Met., 14 (1980) 187.
116. D. Caplan, M.J. Graham and M. Cohen, Corros. Sci., 10 (1970) 1.
117. D. Caplan, G.I. Sproule and R.J. Hussey, Corros. Sci., 10 (1970) 9.
118. L. Jansson and N.-G. Vanneberg, Oxid. Met., 3 (1971) 453.
119. A.G. Goursat and W.W. Smeltzer, J. Electrochem. Soc., 120 (1973) 390.
120. V.B. Voitovich, V.A. Lavrenko, R.F. Voitovich and E.I. Golovko, Oxid. Met., 42 (1994) 223.
121. T.E. Lopes Gomes and A.M. Huntz, Oxid. Met., 14 (1980) 249.
122. G. Bertrand, K. Jarraya and J.M. Chaix, Oxid. Met., 21 (1983) 1
123. J.G. Keller and D.L. Douglass, Oxid. Met., 36 (1991) 439.
124. M. Yamawaki, T. Igarashi, T. Yoneoka and M. Kanno, J. Jap. Inst. Met., 44 (1980) 425.
125. L.A. Carol and G.S. Mann, Oxid. Met., 34 (1990) 1.
126. T. Narita, I. Ishikawa, S. Karasawa and K. Nishida, Oxid. Met., 27 (1987) 267.
127. A.L. Cabrera and M.B. Maple, Oxid. Met., 32 (1989) 207.
128. R.K. Singh Raman, A.S. Khanna, R.K. Tiwari and J.B. Gnanamoorthy, Oxid. Metal., 37 (1992) 1.
129. L. Charrin, A. Combe and J. Cabane, Oxid. Met., 37 (1992) 65.
130. T. Takada, Y. Tomii, N. Yoshida, M. Sasaki and M. Koiwa, Oxid. Met., 37 (1992) 13.
131. J. Botella, C. Merino and E. Otero, Oxid. Met., 49 (1998) 297.
132. J.E. Croll and G.R. Wallwork, Oxid. Met., 4 (1972) 121.
133. D.L. Douglass and F. Rizzo-Assuncao, Oxid. Met., 29 (1988) 271.

134. Xian Aiping, Si Zhongyao, Zhou Longjiang, Shen Jianian and Li Tiefan, in Corrosion Control - Proceedings of 7th APCCC, Vol. 1, Academic Publishers, Beijing, 1991, pp. 160-165.
135. A.P. Xian, Z.Y. Si, L.J. Zhou, J.N. Shen and T.F. Li, Mater. Lett., 12 (1991) 84.
136. A.J. Moorhead and H.-E. Kim, J. Mater. Sci., 26 (1991) 4067.
137. V.B. Voitovich, V.V. Sverdel, R.F. Voitovich and E.I. Golovko, Int. J. Refract. Met. Hard Mater., 14 (1996) 289.
138. D.J. Coates, B. Mortimer and A. Hendry, Corros. Sci., 22 (1982) 951.
139. F. Nardou, P. Raynaud and M. Billy, J. chim. phys., 81 (1984) 271.
140. R. Bredesen and P. Kofstad, Oxid. Met., 34 (1990) 361.
141. R. Bredesen and P. Kofstad, Oxid. Met., 35 (1991) 107
142. R. Bredesen and P. Kofstad, Oxid. Met., 36 (1991) 27.
143. P. Mayer and W.W. Smeltzer, J. Electrochem. Soc., 119 (1972) 626.
144. A.S. Kim and M.J. McNallan, Corrosion, 46 (1990) 746.
145. M. Spiegel and H.J. Grabke, in J.M. Costa and A.D. Mercer (eds), Progress in the Understanding and Prevention of Corrosion, Vol. 1, The Institute of Materials, London, 1993, pp. 758-764.
146. H.J. Grabke, E. Reese and M. Spiegel, Corros. Sci., 37 (1995) 1023.
147. S. Ahila, S.R. Iyer and V.M. Radhakrishnan, Trans. Indian Inst. Met., 47 (1994) 169.
148. G.C. Fryburg, K.J. Kohl and C.A. Stearns, J. Electrochem. Soc., 131 (1984) 2985.
149. W.H. Lee and R.Y. Lin, in R.R. Judkins and D.N. Braski (eds), Proceedings of the 4th Annual Conference on Fossil Energy Materials, (DE91 001158) NTIS, Springfield VA, 1990, pp. 475-487.
150. J.H. DeVan, in T.Grobstein and J. Doychak (eds), Oxidation of High-Temperature Intermetallics, The Minerals, Metals & Materials Society, 1989, pp. 107-115.
151. J.H. DeVan, in R.R. Judkins and D.N. Braski (eds), Proceedings of the 4th Annual Conference on Fossil Energy Materials, (DE91 001158) NTIS, Springfield VA, 1990, pp. 299-310.
152. D.J. Young and J.P. Orchard, Can. Metall. Quart., 30 (1991) 227.
153. K.-C. Hsieh, M.-Y. Kao and Y.A. Chang, Oxid. Met., 27 (1987) 123.
154. G.A. Capuano, A. Dang, U. Bernabai and F. Felli, Oxid. Met., 39 (1993) 263.
155. J.H. DeVan, Environmental effects on iron aluminides, Oak Ridge National Laboratory Report No. CONF-9105184-9; NITIS Accession No. DE91014576/XAB. Paper presented at the 5th Annual Conference on Fossil Energy Materials, Oak Ridge TN, USA, May 1991, 10 pp.

156. A. Tomasi, P. Scardi and F. Marchetti, in M.J. Hampden-Smith, W. G. Klemperer and C.J. Brinker (eds), Better ceramics through chemistry V, Proceedings of Symposium held April 27-May 1, 1992, San Francisco CA, Materials Research Society Symposium Proceedings, Vol. 271, Materials Research Society, Pittsburgh PA, 1992, pp.477-483.
157. R. di Maggio, P. Scardi and A. Tomasi, in B.J.J. Zelinski, C.J. Brinker, D.E. Clark and D.R. Ulrich (eds), Better Ceramics Through Chemistry IV, Proceedings of Symposium held in San Francisco CA, April 1990, Materials Research Society Symposium Proceedings Vol. 180, Materials Research Society, Pittsburgh PA, 1990, pp. 481-484.
158. M.U. Kitheri, P.S. Murti and G. Seenivasan, Thermochim. Acta, 232 (1994) 129.
159. T. Bereznai and R. Würtz, J. Nucl. Mater., 152 (1988) 323.
160. K. Wakasa and M. Yamaki, J. Mater. Sci., 23 (1988) 1459.
161. P.J. Ficalora, Hot-corrosion reactions of calcium sulfate with Cr, Ni, Co, Fe and several alloys, Oak Ridge National Laboratory, Tennessee, Report No. ORNL/TM-8735, DE83 013715, 1983, 39 pp.
162. M.I. Ruiz, A. Heredia, J. Botella and J.A. Odriozola, J. Mater. Sci., 30 (1995) 5146.
163. R.G. Charles, in R. D. Shull and A. Joshi (eds), Thermal Analysis in Metallurgy, The Minerals, Metals & Materials Society, Warrendale PA, 1992, pp. 27-46.
164. H.U. Borgstedt and N.P. Bhat, J. Less-Common Met., 161 (1990) L1.
165. R.C. Mackenzie (ed.), Differential Thermal Analysis, Vol. 2: Applications, Academic Press, London, 1972.
166. R.C. Mackenzie (ed.), Differential Thermal Analysis, Vol. 1: Fundamental Aspects, Academic Press, London, 1970.
167. H.S. Ray and F.W. Wilburn, Trans. Indian Inst. Met., 35 (1982) 537.
168. D.V. Moisa, L.K. Svanidze, T.N. Zagu and T.I. Sigua, in B. Miller (ed.), Proceedings of the 7th International Conference on Thermal Analysis, Kingston ON, Canada, Vol. 2, Wiley, New York, 1982, pp.1419-1425.
169. R.E. Grim, Applied Clay Mineralogy, McGraw-Hill, New York, 1962, pp. 335-345.
170. Ullmanns Encyklopädie der technischen Chemie, Bd. 3, Urban & Schwarzenberg, München & Berlin, 1969, 3.Auflage, pp. 400-406.
171. G. Bayer, G. Kahr and M. Muller-Vonmoos, Clay Minerals, 17 (1982) 271.
172. R. Sen, B. Yarer, D.J. Spottiswood and F.D. Schowengerdt, in W.C. Park, D.M. Hausen and R.D. Hagni (eds), Procedings of the Second International Congress on Applied Mineralogy in the Minerals Industry, Metallurgical Society of AIME, Warrendale, PA, c1985, pp. 441-466.

173. P.K. Weissenborn, L.J. Warren and J.G. Dunn, Colloids Surfaces A: Physicochem. Eng. Aspects, 99 (1995) 29.
174. S.A. Mikhail and A.H. Webster, Can. Metall. Quart., 21 (1982) 261.
175. D.I. Ryzhonkov, Scand. J. Metall., 11 (1982) 135.
176. M.A. Carter, D.R. Glasson and S.A.A. Jayaweera, Thermochim. Acta, 51 (1981) 25.
177. U.O. Igiehon, S. Heathcote, B.S. Terry and P. Grieveson, Trans. Inst. Min. Metall. C, 101 (1992) C159.
178. Y.K. Rao and S.K. El-Rahaiby, Metall. Trans. B, 16B (1985) 465.
179. A.R. Mitchell and R.H. Parker, Miner. Eng. 1 (1988) 53.
180. R.S. Celmer, G.H. Kaiura and J.M. Toguri, Can. Metall. Quart., 26 (1987) 277.
181. S.A. Mikhail, A.M. Turcotte and C.A. Hamer, Thermochim. Acta, 273 (1966) 103.
182. A.R. Udupa, K.A. Smith and J.J. Moore, in W.C. Park, D.M. Hausen and R.D. Hagni (eds), Proceedings of the Second International Congress on Applied Mineralogy in the Minerals Industry, Metallurgical Society of AIME, Warrendale, PA, c1985, pp. 757-770.
183. A.R. Udupa, K.A. Smith and J.J. Moore, in H.Y. Sohn, D.B. George and A.D. Zunkel (eds), Advances in Sulfide Smelting, Proceedings of the 1983 International Sulfide Smelting Symposium and the 1983 Extractive and Process Metallurgy Meeting of the Metallurgical Society of AIME, San Francisco, California, November 6-9, 1983, Vol. 1, pp. 317-328.
184. A.R. Udupa, K.A. Smith and J.J. Moore, Trans. Inst. Min. Metall. C, 93 (1984) C99.
185. R. Dimitrov and B. Boyanov, in D. Dollimore (ed.), Proceedings of the 2nd European Symposium on Thermal Analysis, Heyden, London, 1981, pp. 340-343.
186. R. Dimitrov and B. Boyanov, Thermochim. Acta, 64 (1983) 27.
187. F. Ajersch and M. Benlyamani, Thermochim. Acta, 143 (1989) 221.
188. P. Penev, A. Boteva and V. Angelova, Fizykochemiczne Problemy Mineralurgii, 22 (1990) 173.
189. J.R. Donald and C.A. Pickles, in P.B. Queneau and R.D. Peterson (eds), Proceedings of The Third International Symposium on Recycling of Metals and Engineering Materials, Minerals, Metals and Materials Society, Warrendale, PA, 1995, pp. 603-621.
190. J.R. Donald and C.A. Pickles, Can. Metall. Quart., 35 (1996) 255.
191. D.V. Schur, V.A. Lavrenko, V.M. Adejev and I.E. Kirjakova, Int. J. Hydrogen Energy, 19 (1994) 265
192. A. Kapilashrami, I. Arvanitidis and D. Sichen, High Temp. Mater. Processes, 15 (1996) 73.

193. C. Barnes and C.A. Pickles, High Temp. Technol., 6 (1988) 196.
194. X. Wang, H.Y. Sohn and M.E. Schlesinger, Mater. Sci. Eng., A186 (1994) 151.
195. K. Upadhya, J. Metals, 36[10] (1984) 39.
196. Z.G. Szabó, S. Perczel and M. G bor, Thermochim. Acta, 64 (1983) 167.
197. D. Dollimore, Thermochim. Acta, 117 (1987) 331.
198. D. Dollimore, Thermochim. Acta, 177 (1991) 59.
199. A. Riga, G. Patterson and R. Kornbrekke, Thermochim. Acta, 226 (1993) 353.
200. Z. Yin, X. Li, Q. Zhao, S. Chen, G. Liu and S. Wang, Trans. Nonferrous Metall. Soc. China, 4 (1994) 46.
201. M.A. Rabah and M.A. Barakat, Hydrometallurgy, 32 (1993) 99.
202. R.D. Friend, J.M. Kennedy and D.D. Edie, in R. B. Bhagat (ed.), Proceedings of the Damping of Multiphase Inorganic Materials Symposium, ASM Materials Week, Chicago IL, 2-5 November 1992, ASM International, Materials Park OH, c1993, pp. 123-135.
203. J.P. Hébert and E. Karmazsin, J. Therm. Anal., 36 (1992) 989.
204. T.S. Kim, T.H. Kim, K.H. Oh and H.I. Lee, J. Mater. Sci., 27 (1992) 2599.
205. T. Das, S. Bandyopadhyay and S. Blairs, J. Mater. Sci., 29 (1994) 5680.
206. S. Elomari, R. Boukhili, M.D. Skibo and J. Masounave, J. Mater. Sci., 30 (1995) 3037.
207. B.E. White, Jr., M.E. Patt and E.J. Cotts, Phys. Rev. B, 42 (1990) 11,017.
208. H. E. Kissinger, J. Res. Nat. Bur. Stand., 57 (1956) 217.
209. T. Ozawa, J. Therm. Anal. 2 (1970) 301.
210. Z. Konopka and J. Braszcznski, in R. Pichoir and P. Costa (eds), The 3rd European Conference on Advanced Materials and Processes, Paris, June 1993, J. Physique IV, Colloque C7, Suppl,ment au J. Physique II, Vol. 3, 1993, pp. 1825-1828.
211. B.F. Kieback, G. Leitner and K. Pischang, J. Therm. Anal. 33 (1988) 559.
212. W. Hädrich, E. Kaiserberger and W.-D. Emmerich, Ceram. Forum Int. (CFI), 63 (1986) 413.
213. W. Hädrich, E. Kaiserberger and W.-D. Emmerich, Ceram. Forum Int. (CFI), 63 (1986) 494.
214. W.F. Wang, Powder Metall., 35 (1992) 281.
215. R.M. German, in R.D. Shull and A. Joshi (eds), Thermal Analysis in Metallurgy, The Minerals, Metals and Materials Society, Warrendale, PA 1992, pp.205-231.
216. T.A. Pumpyanskaya, N.I. Sel'minskikh, D.A. Pumpyanskii, L.N. Andreyanova and V.I. Deryabina, Met. Sci. Heat Treatment (Russia), 33 (1991) 608.

217. R.J. Highmore, J.E. Evetts, A.L. Greer and R.E. Somekh, Appl. Phys. Lett., 50 (1987) 566.
218. F. Spaepen and C.V. Thompson, Appl. Surf. Sci., 38 (1989) 1.
219. R.K. Ball and A.G. Todd, Thin Solid Films, 149 (1987) 269.
220. E.J. Cotts, W.J. Meng and W.L. Johnson, Phys. Rev. Lett., 57 (1986) 2295.

This Page Intentionally Left Blank

Handbook of Thermal Analysis and Calorimetry. Vol. 2: Applications to Inorganic and Miscellaneous Materials
M.E. Brown and P.K. Gallagher, editors
© 2003 Elsevier B.V. All right reserved.

Chapter 14

PYROTECHNICS

E.L Charsley[a], P.G. Laye[a], and M.E. Brown[b]

[a] Centre for Thermal Studies, School of Applied Sciences, University of Huddersfield, Huddersfield HD1 3DH, UK
[b] Chemistry Department, Rhodes University, Grahamstown, 6140 South Africa

1. INTRODUCTION

Pyrotechnics find many applications in a wide variety of civilian and military systems although they are probably best known as fireworks - a descriptor which in no way does justice to their versatility*. Rather surprisingly it is difficult to offer a concise definition of pyrotechnics. In some definitions reference is made to the use of pyrotechnics in timing devices, or in the production of smoke or light, or as sources of heat. In the context of this chapter we shall define a *pyrotechnic* as a mixture of a solid fuel and an oxidant which is capable of self-sustaining combustion even in the absence of air. This definition has the advantage of focusing attention on the combustion itself which is the key chemical process in pyrotechnics. It is this process which has been central to thermal analysis studies. Although such studies have contributed greatly to our understanding, the thermal analysis of pyrotechnics remains a relatively small and specialised area of application.

Pyrotechnics, together with explosives and propellants, make up the trio of high-energy materials. The distinction between these materials is associated with the nature of the combustion process. In pyrotechnics it occurs by deflagration, i.e. layer-to-layer propagation, in contrast to explosives where combustion leads to detonation and the establishment of a shock wave. Less obvious is the distinction between solid propellants and those pyrotechnics which also generate gaseous combustion products. Here the difference is more a matter of degree and how they are used: it is the particularly powerful evolution of gas in propellants which is the basis for their application in propulsion devices.

*See for example, A.P. Hardt, 'Pyrotechnics, Pyrotechnica Publications', Post Falls ID, USA, 2001, and in 'Kirk-Othmer Encyclopaedia of Chemical Technology', Vol 19, 3rd Edn, (Eds M. Grayson and D. Eckroth), Wiley, New York, USA, 1982, pp. 484 – 499.

Traditionally pyrotechnics have been made from the fuel and oxidant in the form of finely-divided powders. Fuels have ranged from metals, such as aluminium, magnesium and iron, to non-metals, such as silicon, carbon, sulfur and some organic compounds. Oxidants have included oxides, peroxides and oxysalts. Various additives may be included to promote particular properties important to the manufacture or application of the pyrotechnics. Of more recent origin has been the development of bimetallic alloying pyrotechnics and the use of resin-bonded and polymeric materials.

Thermal analysis studies have as their ultimate goal an understanding of the combustion process. Techniques which have been used include: differential thermal analysis (DTA), differential scanning calorimetry (DSC), modulated temperature DSC (MTDSC), thermogravimetry (TG), evolved gas analysis (EGA), thermomicroscopy and a variety of simultaneous techniques. Of these techniques DTA and DSC have proved the most valuable in their breadth of application. In addition to their role in the study of pyrotechnic reactions, they find further application in the measurement of thermal properties of pyrotechnic mixtures. In the present context TG has been applied mostly to the study of the aerial oxidation of metallic fuels and the thermal decomposition of oxidants. With highly reactive fuels there is a risk of ignition which may be minimised by the use of sample-controlled TG* in which a pre-set rate of mass change is maintained by controlling the temperature programme. Other thermal techniques which have found application are combustion calorimetry, microcalorimetry and temperature profile analysis.

The wide variety of fuels and oxidants means that during combustion some components remain as solids while others melt, vaporise or decompose to yield gaseous products. Mechanisms encountered may thus cover the wide field of solid-solid, solid-liquid, solid-gas and possibly even liquid-gas and liquid-liquid reactions. A specialised application of pyrotechnic combustion has been the self-propagating synthesis of high-temperature materials where the focus of interest is the solid product itself**. Whilst this technology has prompted notable contributions to the theory of the propagation process it has not generated an independent body of innovative thermal analysis.

Thermal analysis has probably had the greatest impact on our understanding of the chemistry of gasless pyrotechnics. The term *gasless* is usually taken to mean

---

* Sample controlled techniques have been reviewed by M. Reading in 'Handbook of Thermal Analysis and Calorimetry , Vol. 1, Principles and Practice', (Ed. M.E. Brown), Elsevier, Netherlands, 1998, pp.423-443.

** See for example, A.G. Merzhanov in 'Combustion and Plasma Synthesis of High-Temperature Materials', (Eds Z.A. Munir and J.B. Holt), VCH Publishers, New York, 1990, pp.1-53.

the evolution of less that 10 cm^3 of gas during the combustion of one gram of pyrotechnic mixture. Gasless pyrotechnics can be designed to have reproducible burn-times and in this way can be used as timing or delay devices. By their very nature they lend themselves to investigation by temperature profile analysis where the theory can only be applied in its entirety to non-gaseous systems.

A comprehensive review of the thermal analysis of pyrotechnics which included reference to earlier summaries was published by Laye and Charsley [1] in 1987. More recently Charsley et al. [2] have provided an overview of how thermal analysis and calorimetry can be used to study reactivity, reaction mechanisms and ageing. Charsley et al. [3] have also evaluated the role of MTDSC in the study of pyrotechnic systems. Brown [4] has provided an up-to-date review of the applications of thermal analysis and temperature profile analysis to a variety of binary pyrotechnics where the aim was to identify the factors which influence the burning properties. Specific to the use of the Calvet-type DSC is the discussion by Le Parlouer and Chan [5] on the characterisation of explosives, propellants and pyrotechnics. The application of thermal techniques to hazard evaluation of pyrotechnics has been the subject of a comprehensive review by Lightfoot et al. [6]. The topic is discussed further under the heading 'Thermal hazard evaluation, compatibility testing and life-time prediction' in Section 4 of this chapter.

2. EXPERIMENTAL TECHNIQUE

Much of the experimental protocol in current use in the thermal analysis of pyrotechnics can be traced to the early work carried out in Japan [7] and USA [8,9]. It includes the separate investigation of the thermal behaviour of individual components and their various mixtures. The concern here is with the thermal analysis of pyrotechnics themselves, not with that of the components, notwithstanding the vital role that such experiments play in the interpretation of results. The identification of the nature of the products of pyrotechnic reactions forms an important part of thermal analysis studies. Optical and scanning electron microscopy, infrared spectroscopy, X-ray diffraction and mass spectrometry have all been used to this end.

There are a number of factors to be considered when designing thermal analysis experiments for pyrotechnics. Experiments should be carried out with the sample in an inert atmosphere to eliminate aerial oxidation of the fuel. It may be desirable to determine the effect of air on the reaction mechanism, but such investigations should be preceded by experiments in an inert atmosphere. Studies where the sample has been investigated only in air have proved to be much less satisfactory. Often the reality is that the results from such

experiments are predominantly a description of the aerial oxidation of the fuel. Nitrogen and argon are most frequently used to maintain an inert atmosphere, but care should be taken when selecting nitrogen because it will react with some fuels at high temperatures. Gas scrubbers may be used to remove moisture and oxygen from the gas stream. Traces of oxygen remaining may be removed using zirconium or titanium powder in small crucibles placed near the sample.

A distinction should be made between experiments carried out under ignition and non-ignition conditions. In the former, the sample undergoes a combustion reaction and the DTA/DSC curve shows a sharp exothem. Experiments allow the various factors affecting ignition to be investigated. Under non-ignition conditions, the exotherm may be resolved into several peaks. It is here that DTA and DSC are at their most powerful, providing the means of identifying the individual reaction stages. Often intermediate products may be isolated and separate experiments carried out to confirm the nature of the reaction stages. However, the very different thermal environments need to be taken into account when assigning results from non-ignition experiments to the combustion process. Non-ignition experiments are usually carried out with small samples ($\leq$10 mg) and slow heating rates ($\leq$5 $^{\circ}$C min^{-1}), but the precise conditions will depend on the properties of the pyrotechnic mixture and the design of the equipment. It follows that it is essential for the full experimental conditions to be given when reporting results.

The highly reactive nature of pyrotechnics means that care must be taken in the design of experiments. Mention has already been made of the need for experiments to be carried out with the sample in an inert atmosphere. The choice of material for the crucible is important in order to minimise reaction between the pyrotechnic sample and its reaction products and the crucible. Pyrex glass, quartz and platinum have been most widely used, depending on the reactivity of the pyrotechnic and the temperature range of the investigation. Platinum is attacked at high temperatures by boron, a number of metallic fuels including molten magnesium and aluminium, and a variety of reaction products. Tall-form crucibles are necessary to retain samples such as those containing nitrates, nitrites and dichromates which tend to foam or creep when heated.

Adequate precautions must be taken during the preparation and handling of pyrotechnic mixtures. There is the obvious danger of accidental ignition, with some mixtures being sensitive to friction or electrical discharge. Equally, there is a danger of inhalation of finely-divided materials which may be toxic. Small samples of pyrotechnics can often be prepared by brush mixing the components through a fine sieve. Thermal analysis experiments with 'gassy' pyrotechnics under ignition conditions may lead to products being widely dispersed, possibly resulting in damage to equipment. The likelihood of such damage still exists

with modern equipment, but the use of small samples, made possible by high instrumental sensitivity, has decreased the hazard potential.

3. SPECIALISED INSTRUMENTATION AND EXPERIMENTATION

3.1. Introduction

For the most part, thermal analysis studies have made use of commercial equipment. This section is concerned with a discussion of a number of specialised instruments and techniques which have been developed to meet the particular demands imposed by pyrotechnics. Also included is a brief account of other thermal techniques, which although not specialised, have played an important role in pyrotechnic research.

The celebrated DTA apparatus developed by Gordon and Campbell [8,9] was described in the earlier review [1]. It was used extensively in the early work at Picatinny Arsenal and was unusual by present-day standards in using large samples (1–5 g). Reference was also made in the earlier review to a DTA apparatus developed by Campbell and Beardell [10], in which samples were maintained at a constant volume, and an apparatus in which very small samples (50–200 μg) could be heated to give rates of temperature rise up to 10^6 °C min^{-1}, similar to the temperature rise in ignited samples [11].

3.2. High-temperature DSC measurements

A high temperature DSC apparatus (Figure 1) has been described by Charsley et al. [12]. It was developed from an earlier DTA apparatus, designed to avoid damage to the DTA head, which allowed routine measurement of ignition temperatures of pyrotechnics to be made without the need for frequent calibration [13]. The DSC head incorporates a nisil heat-flux plate. Contamination of the plate is minimised by using tall-form, quartz crucibles to contain the sample and by fitting the DSC head with a lid. A photocell is used to detect ignition for those pyrotechnics which on ignition eject material from the crucible, giving rise to a poorly defined temperature rise.

Measurements can be made at faster heating rates than are available using conventional DSC by lowering the pre-heated furnace over the sample [12]. The resulting temperature-time trace yields the time-to-ignition, the ignition temperature and the heating rate at ignition. Figure 2 shows an example of ignition measurements on the pyrotechnic: Mg-$NaNO_3$-Alloprene. Ignition is identified by the rapid rise in the heating-rate curve (HR) at 477 °C and the stepwise increase in the signal from the photocell detection system (PDS). The heating-rate curve also shows the presence of a pre-ignition exotherm at about 370 °C. Increasing the sample mass caused ignition to coincide with the lower

temperature exotherm, which was found to be due to the reaction of the sodium nitrate with the Alloprene binder.

Boddington et al. [14] have described the use of a DTA apparatus to measure times-to-ignition with a view to obtaining chemical activation energies. The experimental procedure was similar to that described above. The DTA head was pre-heated and the furnace raised to allow the sample to be introduced and then immediately lowered. The authors discussed the theory of the approach and presented results for the binary mixtures: B-MoO_3, Mg-$KClO_4$ and C-KNO_3.

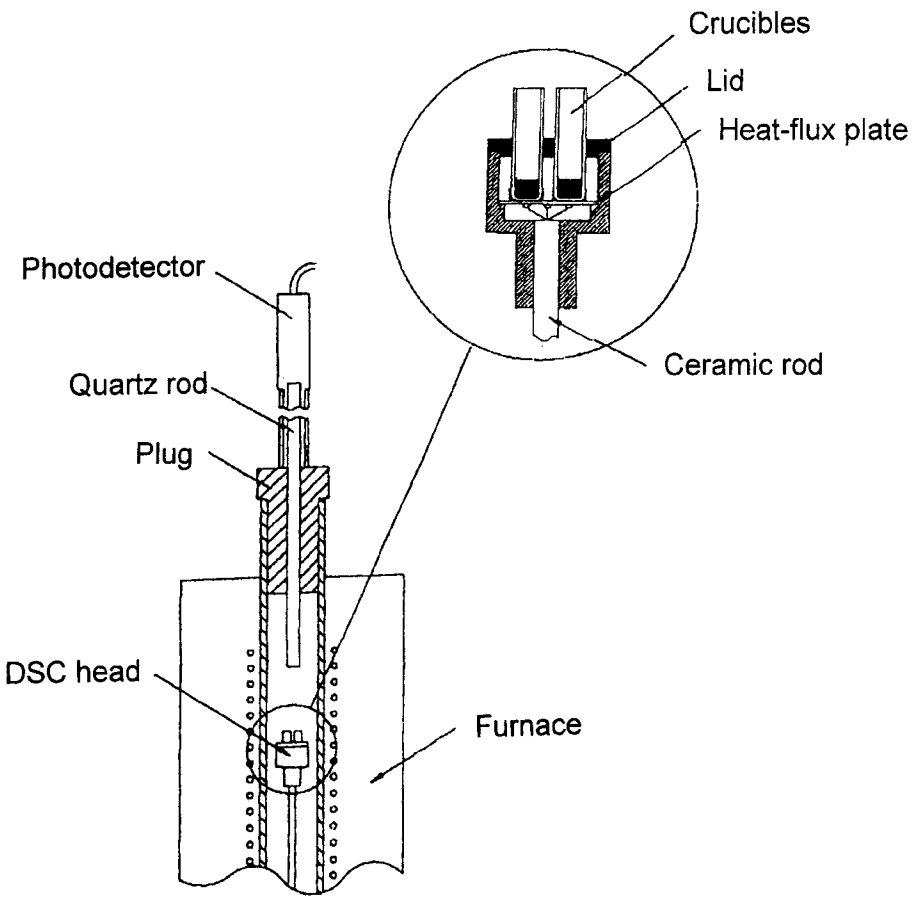


Figure 1. Cross-section of a high-temperature DSC apparatus [12].

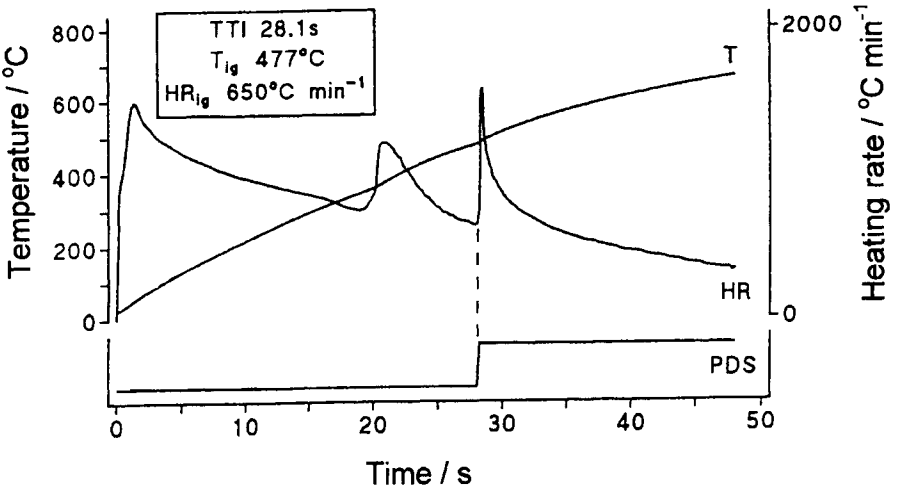


Figure 2. Time-to-ignition measurements for a 44% Mg-44% $NaNO_3$-12% alloprene composition. (sample mass 15 mg; temperature 800 °C; atmosphere argon) [12].

3.3. Thermal diffusivity measurements

An apparatus for the measurement of the thermal diffusivity of pyrotechnics has been described by Boddington et al. [15]. Figure 3 shows the modified DTA head. The sample was in the form of a cylinder, 15 mm in diameter, with thermocouples pressed in the centre and just within the surface of the cylinder. The cylinder was supported by fine quartz-needles which could be adjusted to accommodate cylinders of different lengths. The temperature difference between the two thermocouples was measured when the ambient temperature was increased either linearly with time, or suddenly from one constant value to another. The theory of the method was developed and results were reported for binary mixtures of W and $K_2Cr_2O_7$.

Brassy et al. [16] have made similar measurements using an apparatus, shown in Figure 4, based on the design of Miller [17]. These authors extended the temperature range of the experiments to the onset of the reaction exotherm and were able to derive the associated kinetic parameters (chemical activation energy and pre-exponential factor), in addition to the thermal diffusivity. Results were reported for a ternary mixture of W, $K_2Cr_2O_7$ and $KClO_4$ [16] and more recently for binary mixtures of Zr and $PbCrO_4$ [18], both in an oxidising atmosphere. Miller [17] reported the kinetic parameters for the thermite reaction $3Cu_2O + 2Al = 6Cu + Al_2O_3$. Brassy et al. [19] have also discussed the

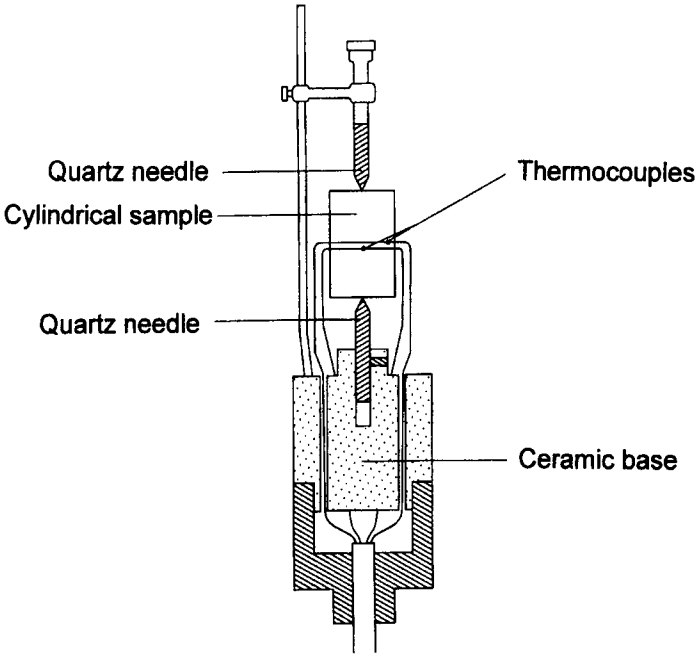


Figure 3. Modified DTA head for measuring thermal diffusivities of pyrotechnic mixtures [15].

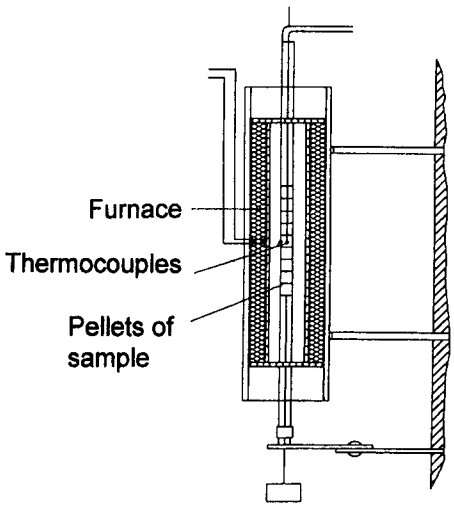


Figure 4. Apparatus for the measurement of thermal diffusivity and kinetic parameters of pyrotechnic mixtures [16].

ignition mechanism of the Zr-$PbCrO_4$ reaction. Gillard et al. [20] have investigated the thermal properties of Mg-$NaNO_3$ and, by means of an iterative procedure, obtained kinetic parameters from which it was possible to obtain the auto-ignition temperature.

3.4. Thermal conductivity measurements

The practical disadvantage of the methods for measuring thermal diffusivity lies in the use of large samples which poses a potential hazard with some pyrotechnic mixtures. Boddington et al. [21] have described a modified DSC head for the measurement of thermal conductivity, using small samples in the form of cylinders 5 mm in diameter and 5 – 8 mm long. The apparatus was based on that originally designed by Brennan et al. [22]. The measurement of thermal conductivity provides an alternative route to thermal diffusivity because the two are linked by the relationship, $D = \kappa/\rho c$, where D is the thermal diffusivity and κ, ρ and c are the thermal conductivity, density and heat capacity respectively. The theory of the method was discussed in a later publication [23]. Results were reported for a range of W-$K_2Cr_2O_7$ mixtures. A similar approach was adopted by Hindle [24] who measured the thermal conductivity of Mg-$Sr(NO_3)_2$-chlorinated rubber binder and combined the results with heat capacity values, also obtained by differential scanning calorimetry, to give the thermal diffusivity

3.5. Thermomicroscopy

The development and application of hot-stage microscopy and ciné photography to pyrotechnics were described by Charsley and co-workers [25,26]. Since then the apparatus has been extensively modified [27] to enable both reflected-light intensity measurements and video recordings to be made with a continuous display of temperature. The use of thermomicroscopy is not widespread, but this is a reflection of the small field of study rather than the significance of the results obtained. The particular value of thermomicroscopy lies in the additional information provided for the interpretation of results from other thermal techniques.

3.6. Thermomagnetometry

Perhaps the most unusual piece of recent work has been the thermomagnetometry study of iron-containing pyrotechnics [28]. It provides a direct link with the pioneering work of Spice and Staveley [29] who identified the pre-ignition exotherm between Fe and BaO_2. The recent work illustrates how thermomagnetometry, TG and DTA may be used in combination to show

that the mechanism of the reaction between Fe and the oxidants BaO_2, SrO_2 and $KMnO_4$ is predominantly between solid and gas.

3.7. Modulated-temperature DSC (MTDSC)

This technique is included here because its application to pyrotechnics remains specialised, with few publications. Charsley et al. [2,3] have explored its potential. Preliminary experiments were carried out on a number of pyrotechnics, including B-$K_2Cr_2O_7$, potassium benzoate-$KClO_4$, Zr-$KClO_4$-nitrocellulose and Zr/Ni alloy-$KClO_4$-nitrocellulose. The results suggest that MTDSC holds significant promise for distinguishing those fusion processes which, in conventional DSC, are masked by strongly exothermic reactions. Figure 5 shows the total and reversing heat-flow curves for Zr/Ni alloy-$KClO_4$-nitrocellulose. The reversing signal shows an endotherm which corresponds to melting of the eutectic formed from unreacted $KClO_4$ and the reaction product KCl. The authors have discussed the selection of the control parameters which, because of the sharp nature of the transitions, may not conform to the instrument manufacturer's recommendations.

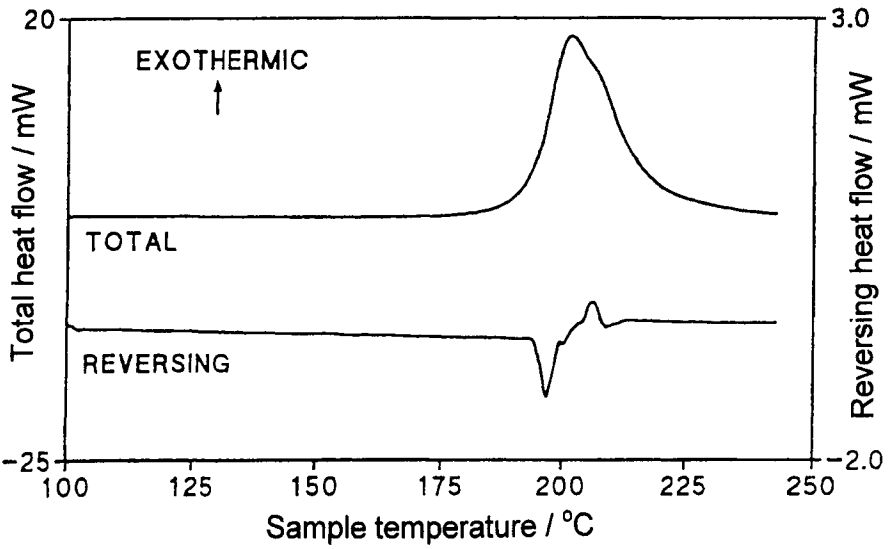


Figure 5. MTDSC curves for 50% Zr/Ni alloy-49% $KClO_4$-1% nitrocellulose. (sample mass 5 mg; heating rate 3 °C min^{-1}; amplitude 0.1 °C; period 30 s; atmosphere helium) [3].

3.8. Temperature profile analysis

Although not strictly a thermal analysis technique, temperature profile analysis has played a significant role in complementing DTA and DSC in the study of the kinetics of pyrotechnic reactions. The information gained from temperature profile analysis is difficult if not impossible to obtain by other means. In principle the experiment is simple: the pyrotechnic in the form of a cylinder is ignited at one end and the temperature-time profile across the combustion zone recorded using a fine thermocouple. The method was developed by Hill and co-workers [30,31] and the theory expounded by Boddington et al. [32,33]. It has been used by Brown and co-workers [34-41] to study an extensive range of pyrotechnics with the aim of obtaining information on the combustion kinetics. Earlier Nakahara and Hikita [42] recorded the temperature profiles for the combustion of Fe/Si–Pb_3O_4 as a function of the pressing density and particle size of the Fe/Si. A detailed study of the combustion kinetics of Si–Pb_3O_4 has been carried out by Jakubko [43]. Analysis of the temperature profiles is based on the theory of layer-to-layer combustion and ignores mass transport. It is for this reason that the technique is fully applicable only to gasless pyrotechnics. The results will be discussed under the heading 'kinetics' in the next section of this chapter.

Pyrometry has been considered as a possible means of extending the temperature range beyond that accessible by thermocouples [44-46], but has a number of practical limitations. Changes in the emissivity of the sample during combustion, together with the inadequate response time and spatial resolution of equipment available, present considerable problems. A complete analysis of the temperature profiles requires a knowledge of the thermal diffusivity. It is this, together with its importance in the theoretical prediction of burning velocity, which has prompted the attempts to measure thermal diffusivity already discussed.

3.9. Combustion calorimetry

The use of combustion calorimetry to measure the exothermicity of pyrotechnic reactions is routine, but important nevertheless in view of the significance of exothermicity as a design parameter for pyrotechnic systems. Many of the qualifications associated with thermal analysis experiments are equally applicable to combustion calorimetry. Measurements should be carried out with the sample in an inert atmosphere unless the intention is to investigate the effect of air on the exothermicity. The variation of exothermicity with composition is used to obtain information on the stoichiometry of the combustion reaction. The use of combustion calorimetry provides a link with the early classification of pyrotechnics as Class 1 or 2 depending on the

stoichiometry of their combustion reaction [47]. Combustion calorimeters with adiabatic operation are available commercially and these are finding widespread application because of the simplicity and the rapidity with which measurements can be made. In principle only two measurements of temperature need to be made, one before and the other after ignition of the sample. For feebly burning mixtures it may be necessary to ignite the sample by using a more reactive mixture.

3.10. Microcalorimetry

The term 'microcalorimetry' is used here to indicate a technique for the measurement of very small quantities of heat. No attempt will be made to differentiate between different types of equipment which are almost entirely of commercial design. The application of microcalorimetry to pyrotechnics has been far less comprehensive than the application of thermal analysis. From the stand-point of sample through-put, the technique is less convenient than thermal analysis, with experiments lasting many days or even months. However, microcalorimetry has the advantage over thermal analysis of its much higher sensitivity. It is an established technique for investigating the thermal hazard potential of a wide variety of materials. Microcalorimetry plays an important role in the prediction of the storage-life of materials. It has been used to study the corrosion of fuels and the efficacy of protective coatings. Its high sensitivity allows slow changes in samples to be monitored under conditions approaching those in practical storage situations. The primary concern of this chapter is the application of thermal analysis rather than microcalorimetry. However, passing reference will be made to the microcalorimetry of pyrotechnics in Section 4 under the heading 'Thermal hazard evaluation, compatibility testing and life-time prediction'.

4. SELECTED APPLICATIONS

4.1. Introduction

Table 1 lists many of the pyrotechnics which have been studied by thermal analysis. It is an up-date of the Table given in reference [1], but it is not intended to be an exhaustive list. It includes examples of the major categories of pyrotechnics: flares, smokes, igniters, heat sources and delays. In the present discussion, attention is focussed on examples published since the previous review, but reference will be made to earlier work where this is of particular significance.

Many of the pyrotechnics discussed in the previous review have continued to be studied because of their complex chemistry or commercial importance.

Areas of application which have become increasingly important in recent years are thermal hazard evaluation, compatibility testing, life-time prediction and the design of less-sensitive and environmentally-friendly pyrotechnic systems. Thermal analysis provides useful information in experiments taking only a short time. In thermal hazard evaluation thermal analysis is often used as a quick screening technique, before undertaking more sensitive but more time-consuming microcalorimetric experiments.

4.2. Thermal hazard evaluation, compatibility testing and life-time prediction

The review by Lightfoot et al. [6] on the application of thermal techniques to hazard evaluation includes accounts of DSC, TG, accelerated rate calorimetry (ARC*), microcalorimetry and TG-DTA. For each technique there is guidance on experimental aspects and an indication of the information that may be obtained. The authors comment that no single technique is without its limitations and that a combination is often the best approach.

Thermal analysis: There have been a number of other publications with varying degrees of generality. Johnson [48] discussed the application of DTA and DSC to the investigation of the effect of storage on thermal degradation, reliability and safety, focussing attention on a flare device containing four pyrotechnics, of which three were identified: red phosphorus-varnish-adhesive, B-PbO_2-binder and $KClO_4$-charcoal-dextrin-binder. An investigation into the spontaneous ignition of fireworks was reported by Miyake et al. [49] who used three pyrotechnic mixtures, Al-$KClO_4$, Al-KNO_3-S and $KClO_4$-S-$CuSO_4.5H_2O$ as 'model' fireworks. Miyake et al. [50] also reported on the combustion and safety evaluation of Mg-PTFE. Not surprisingly there have been a number of publications on the development and safety of gas-generating pyrotechnics used in automobile air bags: a comparison between the application of different thermal techniques including MTDSC was published by Mendenhall and Reid [51] but the identity of the pyrotechnic was not revealed. Neutz et al. [52] have

* In this chapter the abbreviation 'ARC' is used for 'accelerated rate calorimetry' but it is also the name of a commercial automated adiabatic calorimeter used for thermal hazard evaluation.

Table 1
Some pyrotechnics studied by thermal analysis

Pyrotechnic	Ref	Pyrotechnic	Ref	Pyrotechnic	Ref
Al:-		**B(cont):-**		**Mg (cont):-**	
$KClO_3$, $KClO_4$	114	KNO_3,binder	123	$NaNO_3$	68,69,126
$KClO_4$, $Ba(NO_3)_2$	115	$KClO_4$, nitrocellulose	124	$NaNO_3$, fluorides	116
$KClO_4$, AlF_3	98			PTFE	50,117,131
Nitrates, fluorides	65-67,116	**Fe:-**			
PTFE	117	MoO_3	80	**Mn:-**	
Al/Mg, PTFE	117	Fe/Si, Pb_3O_4	7	$KClO_4$, $BaCrO_4$	132
		Fe/Si, MnO_2	78	BaO_2, SrO_2	35,36,83
B:-		$KMnO_4$, BaO_2, SrO_2	28		
Bi_2O_3	118			**Mo:-**	
PbO,Pb_3O_4	112,119	**Mg:-**		BaO_2,SrO_2	35,36,83,133
Pb_3O_4, Cr_2O_3	111	BaO_2, acaroid resin	13,86	$KClO_4$, $BiCrO_4$	134
KNO_3	111,120	BaO_2, calcium resinate	125		
Si, KNO_3	13	$LiNO_3$, $NaNO_3$	126		
MoO_3	79	$NaNO_3$, $Sr(NO_3)_2$, binders	127-129	**Ni:-**	
$K_2Cr_2O_7$, $Na_2Cr_2O_7$	104,121	$KClO_3$, fluorides	130	$KClO_4$, HTPB	135
Si, $K_2Cr_2O_7$	105,121	$KClO_4$, dopants	97		
$NaNO_3$, fluorides	116	KNO_3	63	**Sb:-**	
KNO_3, additives	122	KNO_3, phenolic resin	96	$KMnO_4$	10,136

Si:-		**Ti(cont):-**			
PbO, Pb_3O_4	7,73-77	$NaNO_3$,$Sr(NO_3)_2$,binders	127,149,150	**Zr(cont):-**	
$K_2Cr_2O_7$	121			$KClO_4$	155
KNO_3	137	**V:-**		Fe_2O_3, SiO_2	10
Sb_2O_3, Fe_2O_3,KNO_3,SnO_2	37-39,84, 138	MoO_3	80	MoO_3	81,82
Pb_3O_4, Fe_2O_3	139			$KClO_4$,nitrocellulose,	87-89, 91
Ta:-		**W:-**		Zr/Ni,$KClO_4$, nitrocellulose	90
PbO, Pb_3O_4	140	$K_2Cr_2O_7$	106	$Bi(OH)CrO_4$	156
$PbCrO_4$	141	$KClO_4$, $BaCrO_4$	10,151,152		
$KClO_4$	142				
$K_2Cr_2O_7$	143				
		Zn:-		Miscellaneous:-	
Ti:-		$KClO_4$, hexa-chlorobenzene	8	ZnO, $CaSi_3$, hexa-chloroethane	95
MoO_3	80	TNT, hexa-		K benzoate, $KClO_4$	157,158
TiN, BaO_2	144	chloroethane	153	$KClO_3$, lactose,	
$KClO_4$, $BaCrO_4$	145	Pb,Ba,Sr oxides,$KMnO_4$	41,85	dyes	92,94
$KClO_4$, $KClO_3$,KIO_4,$RbCrO_4$	99			$Ba(ClO_3)_2$, $KClO_4$, acaroid resin	153
KNO_3	64,146	**Zr:-**		Silumin,	
$NaNO_3$, $Sr(NO_3)_2$,		KNO_3	64,146	hexachloroethane	159
Alloprene	147,148	chromates	154	C, S, KNO_3	72,159-162

investigated the potential of a complex amine as a new gas generator fuel. The DSC and TG data were used in commercial software to derive a decomposition model from which the kinetic parameters of the reaction steps were obtained.

Yoshida et al. [53] have applied 'sealed cell' DSC to the investigation of the reactivity of 36 combustible mixtures of chlorates, perchlorates, nitrites and nitrates with metal and non-metal fuels. The use of sealed cells (crucibles) avoided the loss of material through sublimation or vaporisation which may give rise to uncertainty in the interpretation of results. The composition of the mixtures corresponded to the theoretical oxygen balance. The authors evaluated the onset temperature and heat of reaction and used the derivative of the DSC signal $(d^2\Delta q/dt^2)_{max}$ as a measure of the rate of acceleration of the reactions. These parameters were correlated with ignitability and shock sensitivity. Ohtsuka et al. [54] reported on the evaluation of energetic materials using sealed cell-DSC, micro-DSC and ARC. The larger sample-size and higher sensitivity of micro-DSC, compared with more conventional DSC, made it a useful technique for the measurement of 'self-accelerating' decomposition temperatures. Arai et al. [55] also used the sealed-cell DSC approach to investigate the use of NH_4NO_3 in gas generating pyrotechnics.

A novel application of thermal analysis is in the prediction of shock response. Lee and Finnegan [56] used TG-DTA to investigate the equivalence between auto-ignition enthalpy and the energy required for shock initiation. The auto-ignition enthalpy was obtained from the auto-ignition temperature and the heat capacity measured by DSC. The auto-ignition temperature was identified as the temperature at which significant exothermic reaction was observed. The pyrotechnics investigated were $KClO_4$-Mg/Al alloy-Ca resinate, Ti-Teflon and Fe_2O_3-Al-Teflon. The authors concluded that for $KClO_4$-Mg/Al alloy-Ca resinate and Ti-Teflon there was reasonable correspondence between the auto-ignition enthalpy and the energy required for shock initiation, but the prevailing message was one of the need for extreme care to be taken when making such comparisons.

Microcalorimetry: The application of microcalorimetry to pyrotechnics has become more prominent over the last 10 years. The following are examples chosen to illustrate its distinctive role. Its application to stability and compatibility testing is exemplified by the work of Paulsson [57] and Li et al. [58]. Paulsson investigated the use of B-KNO_3 as an igniter in a propellant system and showed that the increased consumption of propellant stabiliser was due to the instability of the igniter giving rise to oxides of nitrogen. Figure 6 shows the heat-flow curves for B-KNO_3 and B-KNO_3-0.1% diphenylamine. The addition of the stabiliser to the mixture delays the maximum heat-flow by

about 3.5 days. Li et al. [58] found that B-KNO_3 was incompatible with Cr/Mo steel, a result not revealed by the traditional vacuum storage test. On this basis it was concluded that microcalorimetry had proved to be more reliable than the traditional test. Berger et al. [59] also investigated the stability of B-KNO_3, using a combination of DSC, TG-DSC and microcalorimetry. The authors derived a kinetic model from which it was possible to calculate the times of accelerated ageing at 60 °C to simulate storage at 10 °C.

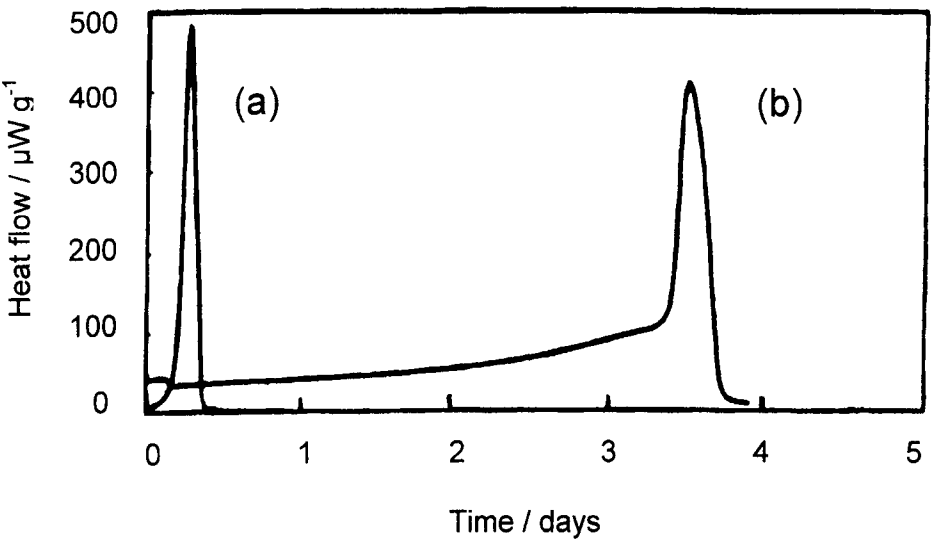


Figure 6. Heat-flow curves for (a) B-KNO_3 and (b) B-KNO_3-0.1% diphenylamine at 77 °C [57].

Other examples are the microcalorimetric investigations of the ageing of Si and Zr in pyrotechnic mixtures. Shortridge and Hubble [60] reported the results for the two ternary pyrotechnics Si-KNO_3-viton binder and Si-Pb_3O_4-viton. Si-KNO_3-viton was shown to be prone to a significant ageing reaction with moist air over the temperature range 35 to 70 °C, whereas Si-Pb_3O_4-viton binder appeared to be largely unaffected. Si-KNO_3-viton binder was to be preferred on environmental grounds, but careful control of manufacture and storage wascritical if degradation was to be avoided. Lagerkvist and Elmqvist [61] investigated the ageing of Zr pyrotechnics and concluded that microcalorimetry is well adapted to quality inspection and to the estimation of the storage-life of pyrotechnics - a role already proved of value in its application to propellants. Cournil and Ramangalahy [62] investigated ageing of the pyrotechnic Zr-

$PbCrO_4$, using a wide range of techniques which included thermoluminescence and also electron spectroscopy for chemical analysis (ESCA) for surface characterisation (an approach which complements the macroscopic scale of thermal analysis). The authors concluded that the formation of an oxide layer on the surface of the Zr was responsible for ageing.

One final example illustrates the combined use of microcalorimetry and DSC to show that low temperature ageing reactions in pyrotechnics can have a direct influence on high temperature exotherms. Charsley et al. [63] aged samples of Mg-KNO_3 in a microcalorimeter for periods from 4 to 28 days. MTDSC was used to establish that the pre-ignition reaction, which started at about the melting temperature of KNO_3 in the unaged sample, was absent in the aged sample. The ignition temperature of the aged sample, measured by high temperature DSC, was higher than that of the unaged sample.

4.3. Reaction mechanisms

This is undoubtedly the most extensive area of application of thermal analysis. The term *'reaction mechanism'* is used here to mean the reaction stages which occur in the pyrotechnic reaction. A number of examples will be used to illustrate the application of thermal analysis and to demonstrate the advantages to be gained by combining different thermal analysis techniques with chemical analysis of the products. It is important to bear in mind the point already made that it is under non-ignition conditions that information is gained about the separate reaction stages. The grouping of published work into the topic areas 'Reaction mechanisms', 'Ignition' and 'Kinetics' is somewhat arbitrary because most investigations incorporate elements from more than one area. Similarly the headings below are intended only to highlight particular aspects of experimental techniques.

TG, DTA, DSC: These techniques are central to virtually all thermal analysis investigations. The work of Miyata and Kubota [64] into the reactions in Ti-KNO_3 and Zr-KNO_3 provides an illustration of the utility of the approach. It continues a long line of investigative research by many authors, which reflects the extensive use of alkali and alkaline-earth nitrates as oxidants in igniters, flares and heat sources. Much of the early work was described in the previous review [1], including the extensive study by Rosina and Pelhan [65,66] on the ternary heat sources Al-KNO_3-NaF, Al-KNO_3-CaF_2, Al-$NaNO_3$-NaF and Al-$NaNO_3$-CaF_2, where considerable use was made of X-ray diffraction to analyse intermediate and final products. The study was a continuation of an earlier wide-ranging investigation of binary and ternary mixtures of Al with $NaNO_3$, $Ba(NO_3)_2$, NaF, CaF_2 and Na_3AlF_6 [67].

The combined use of TG and DTA by Miyata and Kubota [64] revealed differences between the Ti-KNO_3 and Zr-KNO_3 systems which impacted on their ignition and combustion characteristics. Figure 7 shows the TG and DTA curves for KNO_3 and the two pyrotechnic mixtures.

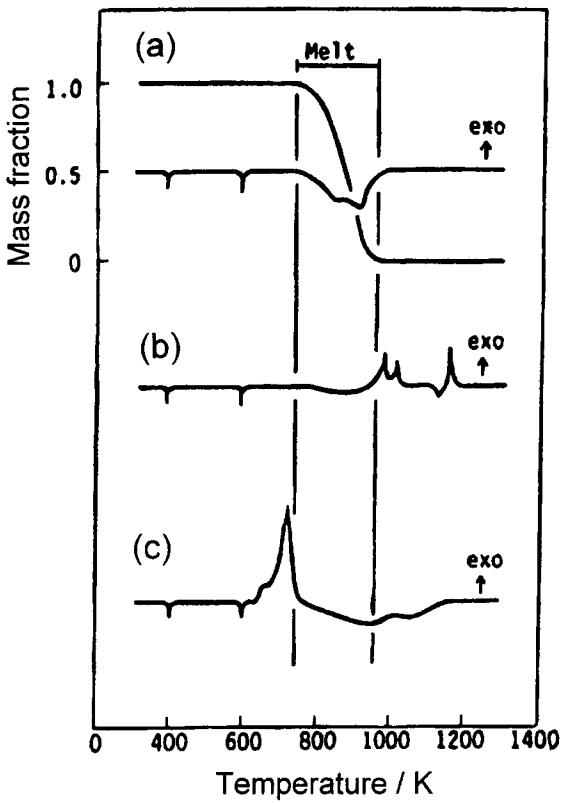


Figure 7. The TG and DTA curves for (a) KNO_3 and the pyrotechnic mixtures (b) Ti-KNO_3 and (c) Zr-KNO_3 (sample mass 5 mg; atmosphere argon) [64].

The authors concluded that decomposition of the oxidant:
$2KNO_3 = 2KNO_2 + O_2$
$4KNO_2 = 2K_2O + 4NO + O_2$
occurred at 447 – 697 °C following melting at 339 °C. A comparison between the TG and DTA curves for the two pyrotechnics showed that, in the Ti-KNO_3system, the reaction was between Ti and the gaseous products of decomposition of the KNO_3, whereas with Zr-KNO_3 the reaction was with liquid KNO_3. This difference in mechanism accounted for the variation in

burning characteristics: the burning rate of Ti-KNO_3 was strongly dependent on pressure, whereas for Zr-KNO_3 it was much less so. The activation energies derived from the DTA curves were quite different for the two pyrotechnics: 200 kJ mol^{-1} for Ti-KNO_3 and 105 kJ mol^{-1} for Zr-KNO_3.

DTA has been used by Singh and Rao [68] to study the influence of particle size on the combustion behaviour of the pyrotechnic Mg-$NaNO_3$. Previously Bond and Jacobs [69] had concluded from self-heating studies that the critical stage in ignition was the decomposition of $NaNO_3$ to $NaNO_2$ and the simultaneous oxidation of Mg. In the work by Singh and Rao [68] a detailed analysis of the shape of the DTA curves pointed to a more complex situation. Decomposition products from KNO_3 containing finely ground oxidant (50 μm) reacted in the condensed phase with Mg, whereas with coarser KNO_3 the reaction was shifted to the vapour phase. These differences were reflected in the ignition and burning characteristics, with low pressure sensitivity being associated with decomposition of the oxidant in the condensed phase.

The part played by thermal analysis in the development of novel components is illustrated by the work of Dawe and Cliff [70]. They evaluated the oxidants sodium dinitramide (NaDN) and potassium dinitramide KDN) as replacements for metal nitrate and ammonium salts in flare compositions with boron. The TG-DTA curves for NaDN are shown in Figure 8. A melting endotherm is evident at 97 °C, followed by a large exotherm at 156 °C, a small broad exotherm at about 210 °C and a total mass loss of 38.1%. The authors drew attention to the close match between the mass loss and that expected for the loss of N_2O and the formation of $NaNO_3$. X-ray diffraction was used to confirm that the only crystalline phase was $NaNO_3$. The pattern of decomposition for KDN was more complex than that of NaDN.

Earlier Tompa et al. [71] investigated the thermal properties of the dinitramide salts of ammonia, hexamethylenetetramine, sodium and potassium using TG, DSC, MTDSC and dielectric analysis (DEA). Using MTDSC the authors identified the presence of low-temperature transitions in the salts and reported a linear relationship between the DEA tan δ value at the temperature of the transition and the rate of decomposition at the DSC peak maximum. The decomposition temperature appeared to increase with the increasing cation basicity, while the reaction rate at the peak maximum and the enthalpy of decomposition decreased.

Two further examples, which continue the themes established in earlier work, are investigations into black powder and pyrotechnics containing Pb_3O_4. Black powder has long been the focus for investigation by thermal analysis. A matter of contention has been the precise nature of the pre-ignition reaction. Brown [72] has reported a study which underlines the importance of experimental

design. In a conventional DTA experiment, no significant reaction was observed between sulfur and KNO_3, as a consequence of the loss of sulfur through vaporisation. This occurred between the temperature of the liquid-liquid transition in sulfur and the melting temperature of KNO_3. However, by the use of a pre-heated furnace, or high heating rates, the loss of sulfur was sufficiently decreased for a reaction to be observed with molten KNO_3. This reaction is regarded as the pre-ignition reaction which leads to a high-temperature reaction between charcoal and molten KNO_3 responsible for propagating the combustion.

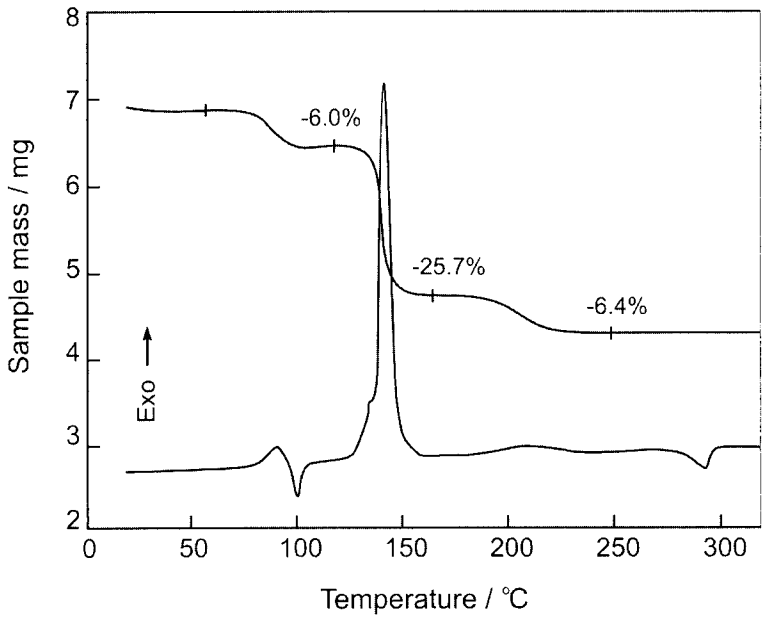


Figure 8. The TG and DTA curves for Na dinitramide [70].

Pyrotechnics containing lead oxides were among the earliest studied by thermal analysis. Mixtures of Si and Fe/Si with Pb_3O_4 were the object of the study by Nakahara [7]. Investigations by Rees and co-workers [73-75] and Matsumoto et al. [76] followed, with the aim of clarifying the mechanism of the pyrotechnic reaction. DTA was used by Jakubko and Černošková [77] in a study in which samples of Si-Pb_3O_4 were sealed into quartz crucibles under vacuum. Figure 9 shows the DTA curves for a range of compositions. All of the curves show three exotherms. The authors concluded that the first peak corresponded to oxidation of Si by diffusion of oxygen ions from Pb_3O_4 to the surface of the Si. The process was retarded by the accumulation of SiO_2 on the

surface. The second peak, starting at about 480 °C, was the largest of the three exotherms (with the exception of the 5% Si mixture) and was attributed to the main reaction. The authors agreed with the conclusion of Al-Kazraji and Rees [73] that this was the decomposition of Pb_3O_4 and the simultaneous oxidation of Si predominantly through the reaction with PbO. The final peak was ascribed to the formation of silicates. Sulacsik [78] used thermal analysis to investigate the reaction between Fe/Si and MnO_2.

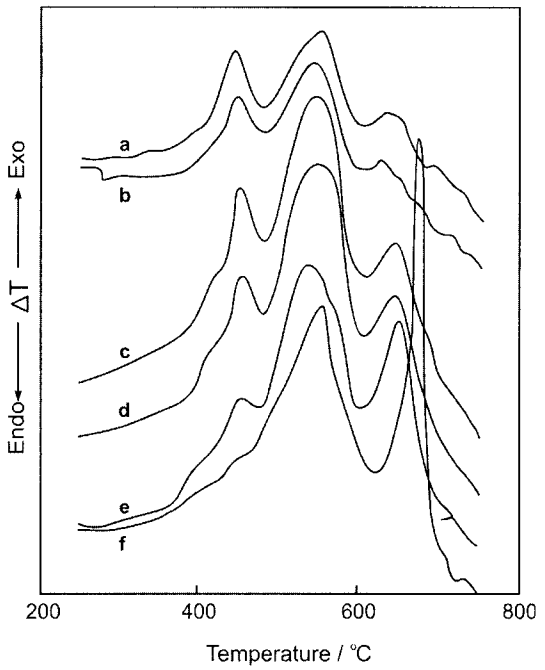


Figure 9. The DTA curves for a range of mixtures of Si (a: 55%, b: 45%, c: 35%, d: 25%, e: 15%, f: 5 %) and Pb_3O_4 (sample mass 20 mg; heating rate 20 °C min^{-1}) [77].

TG, DTA, X-ray diffraction: X-ray diffraction has proved to be a powerful means of identifying solid reaction intermediates and final products from thermal analysis experiments. Mention has already been made of its use in connection with the studies of Rosina and Pelhan [65-67] of ternary heat sources. It has been used with great success in comprehending the reaction between MoO_3 and B, where the DTA curve shows five rather poorly defined overlapping exotherms [79]. Analysis by X-ray diffraction of intermediate products at various stages through the reaction indicated the following reaction scheme:

$2B + 3MoO_3 = B_2O_3 + 3MoO_2$
$2B + 12MoO_3 = B_2O_3 + 3Mo_4O_{11}$
$2B + Mo_4O_{11} = B_2O_3 + 4MoO_2$
$4B + 3MoO_2 = 2B_2O_3 + 3Mo.$

The pattern of successive reduction of MoO_3 to Mo was similar to that observed earlier by Kirshenbaum and Beardell [80] in an investigation of binary mixtures of MoO_3 with Ti, Zr, V and Fe, using simultaneous TG-DTA supported by X-ray diffraction studies. The DTA curve for Zr-MoO_3 showed two overlapping exotherms corresponding to the reduction of MoO_3 to MoO_2 and finally to elemental Mo. The authors [81] investigated the kinetics of the reactions using a number of approaches and concluded that the Freeman and Carroll [82] equation gave the most consistent results. An ingenious strategy was adopted to resolve the overlapping peaks: the first peak was obtained by subtracting the second peak recorded separately for the reaction between Zr and MoO_2. An activation energy of 272 kJ mol^{-1} was obtained for both reaction stages.

Brown and his co-workers have reported a comprehensive programme of research into binary and ternary pyrotechnics. For the most part these were of the gasless variety and X-ray diffraction and infrared spectroscopy were used extensively for the identification of intermediate and final products of the pyrotechnic reactions. Three groups of pyrotechnics constituted the major part of this programme: Mn and/or Mo with BaO_2 and/or SrO_2 [35,36,83]; Si with Fe_2O_3, SnO_2, Sb_2O_3 and KNO_3 [37-39,84] ; Zn with PbO, PbO_2, Pb_3O_4, BaO_2, SrO_2, and $KMnO_4$ [41,85]. TG, DTA and DSC were used to study the thermal decomposition of the oxidants and the pyrotechnic reactions under non-ignition conditions. Combustion calorimetry was used to measure the exothermicity of the pyrotechnic reactions.

The review by Brown [2] summarises much of this work. The point was made that oxidation of the fuels occurred at temperatures well below their melting temperatures and also below the empirical Tamman temperatures which mark the onset of considerable mobility of the constituents of the crystal lattice. The different mechanisms that may arise were discussed in the context of the thermal and chemical properties of the fuels and oxidants. The authors explored relationships between combustion properties (burning rate, exothermicity, maximum temperature rise) and thermal properties (thermal conductivity, thermal diffusivity and heat capacity). Thermal analysis, together with temperature profile analysis, were used to obtain activation energies and pre-exponential factors. This aspect will be discussed under the heading of 'Kinetics' (Section 4.5).

TG, DTA, mass spectrometry: For gassy pyrotechnics, the analysis of evolved gases provides a parallel to X-ray diffraction studies of solid products. The use of mass spectrometry with TG-DTA is exemplified by investigations into the role of binders in pyrotechnics. Binders are naturally-occurring organic materials or synthesised polymers which are added as an aid to the manufacturing process. Frequently they have been shown to have a marked effect on the ignition and combustion of pyrotechnics. Barton et al. [86] investigated the factors affecting the ignition temperature of pyrotechnics using high temperature DTA. The authors reported that the addition of 6% linseed oil to 50% Ti-50% $NaNO_3$ decreased the ignition temperature by 400 °C.

The pyrotechnics Zr-$KClO_4$ and Zr/Ni alloy-$KClO_4$ have been the subject of an extended programme of research using simultaneous TG-DTA-mass spectrometry, DSC, MTDSC and thermomicroscopy [87-91]. The pyrotechnics are used as initiators, with nitrocellulose added to improve the handling characteristics. The DTA curve for the binary mixtures of Zr and $KClO_4$ showed a broad exotherm following an endotherm at 306°C due to the solid-state phase transition in $KClO_4$. The exotherm was attributed to the reaction:

$2Zr + KClO_4 = 2ZrO_2 + KCl$

which occurred mainly in the solid-state. A second endotherm was evident at 506 °C which was due to melting of a mixture of $KClO_4$ and KCl. Decomposition of un-reacted $KClO_4$ was catalysed by both KCl and ZrO_2.

The addition of nitrocellulose was found to modify the shape of the DTA curve. Simultaneous TG-DTA-mass spectrometry and thermomicroscopy showed that nitrocellulose both melted and decomposed exothermically at 200 °C with the evolution of CO, CO_2, H_2O and NO. In the ternary mixture, the exotherm corresponding to the decomposition at 200 °C was scarcely visible, but the expected evolution of CO_2 was detected. The main reaction increased at a faster rate than in mixtures without nitrocellulose. Figure 10 shows the TG, DTA and EGA curves for O_2 and CO_2 for the ternary mixture. The curve for O_2 shows the decomposition of unreacted $KClO_4$ at later stages of the reaction. Ion-specific electrodes were used to follow quantitatively the consumption of $KClO_4$ and the production of KCl in both Zr-$KClO_4$-nitrocellulose and Zr/Ni alloy-$KClO_4$-nitrocellulose. The results were compared with the area of the endotherm recorded by DSC corresponding to the solid-state transition of $KClO_4$. Figure 11 shows the agreement between the results as measured by the two techniques for Zr/Ni alloy-$KClO_4$-nitrocellulose, demonstrating the use of DSC measurements to obtain extents of reaction.

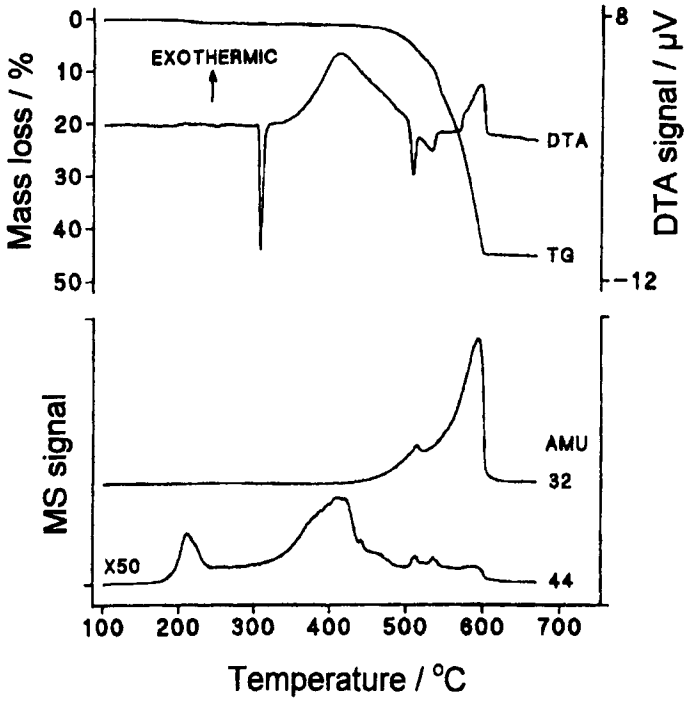


Figure 10. TG, DTA and EGA curves for 10% Zr-89% $KClO_4$-1% nitrocellulose (sample mass 10 mg; heating rate 10°C min^{-1}; atmosphere helium) [87].

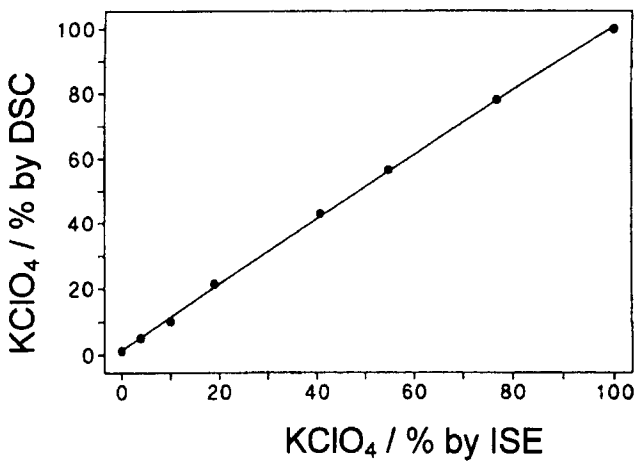


Figure 11. Percentage $KClO_4$ reacted measured by DSC and an ion-specific electrode for 50% Zr/Ni alloy-49% $KClO_4$-1% nitrocellulose [90].

TG, DTA, FTIR, mass spectrometry: The study of pyrotechnic smokes represents another area in which EGA has played a major part. Smokes are largely organic-based and, in one category – vaporising smokes - the smoke is formed from a dye which is vaporised by the heat from the reaction between a suitable mixture of fuel and oxidant. One such mixture is lactose and $KClO_3$ which was investigated by Scanes [92], using DTA complemented by TG and mass spectrometry. Krein [93] investigated the thermochemistry of a range of dyes with a view to quantifying the energetics of smoke production. The aim is to disperse the dye without appreciable decomposition.

In a recent publication, Abdel-Qader et al. [94] have investigated the thermal characteristics of a smoke-producing pyrotechnic based on lactose and $KClO_3$ and containing an anthraquinone orange dye, a binder and $NaHCO_3$ as a cooling agent. The authors employed thermal analysis supported by analytical techniques: DSC, TG, simultaneous TG-DTA-FTIR-mass spectrometry and ARC. DTA results for the pyrotechnic smoke, with the sample in helium, showed two exotherms with onset temperatures of 190 °C and 300 °C. The exotherm at 190 °C was related to the rapid reaction of some $KClO_3$ with lactose, which was probably initiated by partial solution of the oxidant in the liquid phase. The heat from this reaction was responsible for vaporisation of the dye. The second exotherm was similar to that obtained with lactose-$KClO_3$ and arose largely from oxidation of carbonaceous residues formed from decomposition of lactose, residual dye or decomposition of the binder.

Figure 12 shows the results from FTIR for the evolution of CO, CO_2 and H_2O which were identified as the main gaseous products. Above about 700 °C the formation of CO is favoured over that of CO_2. Acetic acid, formic acid, HNO_3 and NH_3 were also formed in small quantities above 500 °C. The presence of nitrogen-containing species indicated that some decomposition of the dye had occurred. In air the decomposition pattern was more complex. The authors referred to the difficulty of obtaining representative samples and it is interesting that, in a study of a white smoke, Jarvis [95] in 1970 reported that he chose to add the components separately to the crucible in order to obtain a more representative sample.

4.4. Ignition

The concern here is with the role of thermal analysis in the investigation of the factors which influence the ignition process. This represents a crucial area of research linked to the practical utilisation of pyrotechnics. Most investigations of reaction mechanisms are concerned ultimately with gaining an understanding of the ignition process. Reference has already been made to the integral part

of the ignition process. Reference has already been made to the integral part played by binders in pyrotechnic reactions and the substantial decrease in the ignition temperature which often accompanies the addition of a binder. DTA has been used by Redkar et al. [96] to investigate the role of the binder in the combustion of Mg-KNO_3–phenolic resin. The investigation formed part of a detailed comparative study of Mg-KNO_3-phenolic binder and black powder. The authors reported that the addition of the binder to Mg-KNO_3 decreased the ignition temperature by 43°C as the result of an exothermic reaction between the binder and oxidant.

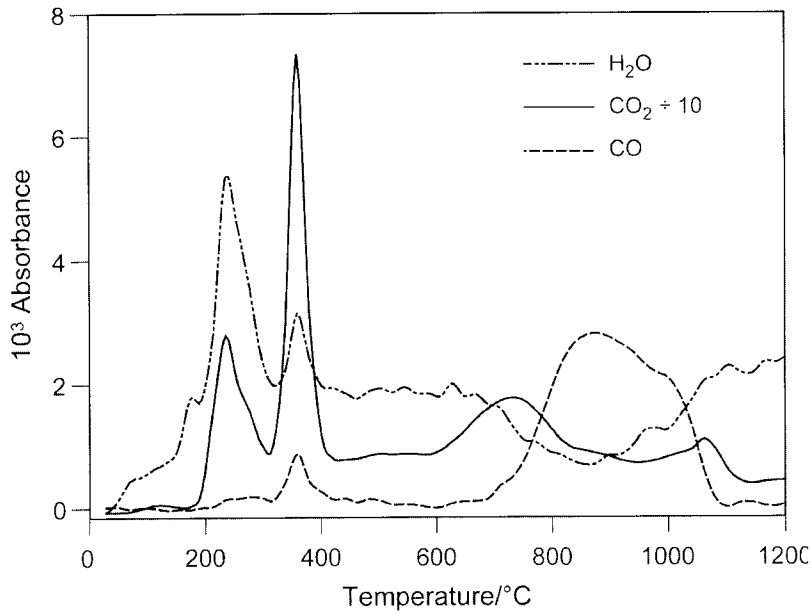


Figure 12. FTIR results for a smoke pyrotechnic based on lactose and $KClO_3$ (sample mass 1.0 g; heating rate 20 °C min^{-1}; atmosphere helium) [94].

DTA and TG were used by Freeman et al. [97] to investigate the ignition of Mg-$KClO_4$. Two features which emerged were the need for a sufficiently high heating rate and the susceptibility of the ignition temperature to the presence of small amounts of dopants in the oxidant. The effect of the addition of AlF_3 on the combustion of Al and $KClO_4$ was investigated by Freeman and Anderson [98]. The authors concluded that $KClO_4$ and AlF_3 formed a complex fluoride AlF_3KF with the evolution of O_2 and Cl_2. An ingenious experiment was designed to show the role played by the gases in promoting ignition. A mixture of $KClO_4$ and AlF_3 was placed in a sample tube, followed by a layer of Al_2O_3

mixture and another in the Al. The thermocouples revealed that ignition of the Al occurred during an endotherm at 500 °C, corresponding to the formation of the complex fluoride in the mixture. Ignition was not observed in the absence of AlF_3.

DTA was used in a notable study by Collins [99] into the ignition of the subhydride $TiH_{0.15}$ with the oxidants $KClO_4$, $RbClO_4$, KIO_4 and $KClO_3$. The DTA curves for the mixtures all showed ignition at 550 °C. The study was extended using TG and DSC. $TiH_{0.15}$-$KClO_4$ was heated to 450 °C and held isothermally. The oxidation exotherm established during heating returned to the base line, but was re-established when the temperature of the sample was further raised. This suggested that the decelerating rate of oxidation was due to depletion of reactive Ti at the surface, rather than completion of the bulk reaction. The thermal analysis experiments were complemented by examination of the surface reaction using Auger spectroscopy. The study is of particular interest because it led, full-circle, to attempts to predict the response of a thermal analyser to the ignition of a pyrotechnic [100-102].

The ignition of Ti-based pyrotechnics was investigated by Erickson et al. [100]. Auger spectroscopy was used to examine depth profiles from isothermally oxidised single crystals of Ti. Under the conditions of the thermal analysis experiments, the growth of a TiO_2 layer adjacent to the gas-solid interface was thought to lead to ignition. A theoretical model of the response of a thermal analyser was developed which incorporated the kinetic scheme for the growth of TiO_2. Heat losses from the sample were evaluated using an electrical heating element in contact with the thermocouple platform.

More recently, Beck and Brown [103] developed a finite-element simulation of the DTA response to the ignition of a pyrotechnic. The parameters required for the simulation were related to those of the actual equipment used by comparing the simulation with the results of calibration experiments.

The relationship between peaks recorded by DTA and ignition is shown to advantage in a study of B-K_2CrO_7 [104,105]. Mixtures containing more than 4% B showed two exotherms, the first corresponding to the reduction of $K_2Cr_2O_7$ to K_2CrO_4 and the second to the reaction of excess B with the K_2CrO_4. In the absence of this second exothermic reaction, the mixtures failed to propagate combustion. Addition of Si was shown not to influence the first exotherm but to introduce a higher temperature exotherm. As a result, ternary mixtures containing 4% B were able to propagate combustion. A two-stage reaction scheme also exists with W and $K_2Cr_2O_7$ [106] and it is the melting of $K_2Cr_2O_7$ which seems to trigger the ignition process. Boddington et al. [107] attempted to use DTA and DSC to study the influence of the heating rate on

thermal runaway. A simple analytical model accounted for the general shape of the results, but led to unacceptable values for the kinetic parameters.

4.5. Kinetics

Since the previous review [1] there has been a steady increase in the number of publications reporting chemical kinetic measurements using thermal analysis. The methods of Kissinger [108], Ozawa [109] and Borchardt and Daniels [110] have proved to be the most popular methods of analysis. More background to methods of kinetic analysis is given in Chapter 3 of Volume 1 of this Handbook. The precise significance of the kinetic results in mechanistic terms is seldom obvious. The aim is rather to obtain a formal description of the rate of the reaction. Even so comparison between results can produce useful insights. Whelan et al. [111,112] have reported the kinetic results for B-KNO_3, B-Pb_3O_4, B-PbO and B-Pb_3O_4-Cr_2O_3. The authors drew attention to the similarity between the activation energies for B-Pb_3O_4 (434 kJ mol^{-1}) and B-PbO (435 kJ mol^{-1}) with the implication of a common reaction step. The exothermicity values derived from peak area measurements were also reported.

It must be remembered that the experimental data used in the analysis are from experiments under non-ignition conditions and the relevance of the kinetic parameters to the propagation of the pyrotechnic reaction is not self-evident. In their discussion of the reaction mechanism of Zr-$PbCrO_4$, Brassy et al. [19] introduced a diffusion term in addition to a first-order decomposition term with an Arrhenius temperature dependence. Yu Snegirev and Taylor [113] have discussed the determination of kinetic parameters for pyrotechnic mixtures using 45% Si-55% Pb_3O_4 as an example. The authors obtained an activation energy of 200 kJ mol^{-1} from experiments in which a sample was ignited by a heated surface at a constant temperature.

In sharp contrast to the magnitudes of the activation energies obtained by thermal analysis, temperature profile analysis has yielded results an order of magnitude smaller. Boddington et al. [33] reported activation energies of 9.4 to 15.1 kJ mol^{-1} and 7.2 to 13.3 kJ mol^{-1} for mixtures of W-$K_2Cr_2O_7$ and W-$K_2Cr_2O_7$-Cr_2O_3, respectively. The scale of these values is similar to the earlier results obtained by Hill [31] for Fe-$KMnO_4$. Jakubko [43] obtained a value of 9.7 kJ mol^{-1} for 45% Si-55% Pb_3O_4 (using the method of analysis in references [32,33]). The kinetic parameters were utilised in a simple combustion model to predict the effect of composition, exothermicity and ambient temperature on the burning rate.

Reference has already been made to the extensive publications by Brown and his co-workers [35-39,41,83-85]. The authors applied both thermal analysis and temperature profile analysis, using as a starting point the assumption of a simple

rate law: $d\alpha/dt = k(1 - \alpha)^n$, where $k = A \exp(-E/RT)$. α is the fractional extent of reaction, n the order of the reaction, A the pre-exponential factor and E the activation energy. The authors used the approach of Borchardt and Daniels [110] to analyse the thermal analysis curves. Only for a few pyrotechnics were the kinetic parameters obtained from both thermal analysis and temperature profile analysis. Two such pyrotechnics were 40% Si-60% Sb_2O_3 and 40% Mn-60% SrO_2. For the former, thermal analysis gave 339 kJ mol^{-1} and temperature profile analysis 13.3 kJ mol^{-1}. For 40% Mn-60% SrO_2 the difference between the results was even more marked: 434 kJ mol^{-1} from thermal analysis and 13.9 kJ mol^{-1} from temperature profile analysis.

The disparity between the results from thermal analysis and temperature profile analysis have been reconciled in a more complex kinetic model in which the results from the two techniques are combined. This is illustrated in Figure 13 which shows the rate constants from (a) thermal analysis, (b) temperature profile analysis and (c) the combined rate constant for the pyrotechnic 40% Mn-60% SrO_2. At high temperatures, the low activation energy obtained from temperature profile analysis was consistent with the low temperature dependence of the burning rate. In combination, thermal analysis and temperature profile analysis have provided a description of the kinetics which may be used to model combustion both in the steady-state and the low-temperature transient behaviour.

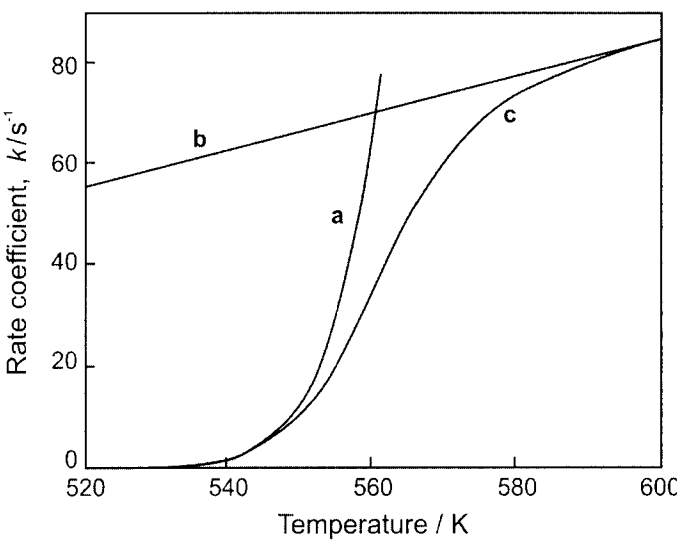


Figure 13. Temperature dependence of the rate constant for the 40% Mn-60% SrO_2 composition. (a) kinetic data from thermal analysis; (b) kinetic data from temperature profile analysis; (c) combined rate constant [36].

5. CONCLUSIONS

Thermal techniques have proved to be amongst the most productive of the various approaches to the investigation of pyrotechnic systems. An earlier review [1] provided a summary of literature published up to 1987. Although the present chapter has highlighted more recent research, it has not been the intention to provide an update to the previous review, but rather to indicate the variety of applications of thermal analysis and the information that can be obtained from thermal studies. Thermal analysis in recent years has come to play an increasingly important role in hazard evaluation, compatibility testing and life-time predictions. Here thermal analysis offers the means for a rapid preliminary survey, with microcalorimetry playing the predominant role in more detailed investigations.

Thermal analysis techniques are routinely applied in pyrotechnic research. The most extensive area of application is to the study of reaction mechanisms in order to gain an insight into the component reactions which contribute to the overall pyrotechnic process. In this context the interpretation of thermal analysis experiments owes much to the use of complementary analytical techniques including X-ray diffraction, mass spectrometry and infrared spectroscopy. Patterns of behaviour have been identified, with the most obvious being reaction at a surface, followed by bulk-phase reaction and the successive reduction of the oxidant by the fuel. Contributions to the understanding of mechanisms at the microscopic level have been made through investigations using surface spectroscopic techniques.

The combustion process itself is fundamental to the application of pyrotechnic mixtures in practical devices. Thermal analysis has been used to measure ignition temperatures and to investigate the factors which influence the ignition process. For many pyrotechnics, thermal analysis has shown that it is the melting or vaporisation of a component which is critical to the onset of propagative combustion. One of the few methods by which information on the chemical kinetics of the combustion process can be obtained directly is temperature profile analysis. Comparison between the results obtained using this technique and those from thermal analysis has led to a more complete description of the kinetics which may be used to model the combustion process.

Combustion calorimetry is the standard technique for the measurement of the exothermicity of pyrotechnic reactions. The results can be used to explore the reaction stoichiometry and to calculate the adiabatic combustion temperature. The alternative route to exothermicity, using DTA and DSC peak areas, is limited to gasless systems and is seldom used, although these measurements provide a means of estimating the contributions of the separate reaction stages.

The measurement of peak areas associated with phase changes has been used to follow the consumption of a particular component.

Nearly all thermal analysis is carried out using commercial equipment, but a small number of purpose-built adaptations continue to make a useful contribution. Although the application of thermal techniques is routine, it should not be inferred that problems of interpretation have been universally resolved. It is in the design of experimental procedures with the various mixtures of components and their intermediate products that the craft of the practitioner still comes into its own.

REFERENCES

1. P.G. Laye and E.L. Charsley, Thermochim. Acta, 120 (1987) 325.
2. E.L. Charsley, T.T. Griffiths and B. Berger, Proc. 24th Int. Pyrotech. Seminar, IIT Research Institute, Chicago, USA, 1998, p.133.
3. E.L. Charsley, J.J. Rooney, H.A. Walker, T.T. Griffiths, T.A. Vine and B. Berger, Proc. 24th Int. Pyrotech. Seminar, IIT Research Institute, Chicago, USA, 1998, p.147.
4. M.E. Brown, J. Therm. Anal. Cal., 65 (2001) 323.
5. P. Le Parlouer and I Chan, Proc. 29th NATAS Conf. on Thermal Analysis, St. Louis, Missouri, USA, 2001, p.710.
6. P.D. Lightfoot, R.C. Fouchard, A.-M. Turcotte, Q.S.M. Kwok and D.E.G. Jones, J. Pyrotechnics, No. 14 (2001) 15.
7. S. Nakahara, Kogyo Kayaku Kyokai-Shi, 22 (1961) 259.
8. S. Gordon and C. Campbell, Proc 5th Symp. on Combustion, Reinhold, New York, USA, 1955, p.277.
9. S. Gordon and C. Campbell, Anal. Chem., 27 (1955) 1102.
10. C. Campbell and A.J. Beardell, Thermochim. Acta, 8 (1974) 27.
11. A.J. Beardell, J. Staley and C. Campbell, Thermochim. Acta, 14 (1976) 169.
12. E.L. Charsley, S.B. Warrington, T.T. Griffiths, A.J. Brammer and J.J. Rooney, Proc. 26th Int. ICT Conf., Fraunhofer-Institut für Chemische Technologie, Karlsruhe, Germany, 1995, p.23/1.
13. E.L. Charsley, C.T. Cox, M.R. Ottaway, T.J. Barton and J.M. Jenkins, Thermochim. Acta, 52 (1982) 321.
14. T. Boddington, A. Cottrell, P.G. Laye and M. Singh, Thermochim. Acta, 106 (1986) 253.
15. T. Boddington, P.G. Laye and J. Tipping, Combust. Flame, 50 (1983) 139.

16. C. Brassy, M. Rejman, M. Roux and A. Espagnacq, Proc. 12th Int. Pyrotech. Seminar, Groupe de Travail de Pyrotechnie Spatiale, France, 1987, p.351.
17. G. D. Miller, Thermochim. Acta, 34 (1979) 357.
18. F. Marlin, M. Roux, C. Brassy and A. Espagnacq, Propellants, Explosives, Pyrotechnics, 19 (1994) 113.
19. C. Brassy, F. Marlin and M. Roux, Propellants, Explosives, Pyrotechnics, 19 (1994) 165.
20. P. Gillard, M. Roux, B. Bayard and M. Regis, Proc. 5th Congrès International de Pyrotechnie du Groupe de Travail, France, 1993, p.525.
21. T. Boddington, P.G. Laye, J. Tipping and J.F. Griffiths, Proc. 6th Symp. Chem. Problems connected with Stabil. of Explos., Sektionen för Detonik och Förbränning, Sweden, 1982, p.149.
22. W.P. Brennan, B. Miller and J.C. Whitwell, J. Appl. Polym. Sci., 12 (1968) 1800.
23. T. Boddington and P.G. Laye, Thermochim. Acta, 115 (1987) 345.
24. M.R Hindle, Proc. 14th Int. Pyrotech. Seminar, RARDE, UK, 1989, p.251.
25. E.L. Charsley and A.C.F. Kamp in 'Thermal Analysis, Vol.1' (Ed. H.G. Wiedemann), Birkhauser Verlag, Basel, Switzerland, 1972, p.499.
26. E.L. Charsley and D.E. Tolhurst, The Microscope, 23 (1975) 227.
27. B. Berger, A.J. Brammer and E.L. Charsley, Thermochim. Acta, 269/270 (1995) 639.
28. M.E. Brown, M.J. Tribelhorn and M.G. Blenkinsop, J. Therm. Anal., 40 (1993) 1123.
29. J.E. Spice and L.A.K. Staveley, J. Soc. Chem. Ind., 68 (1949) 313.
30. R.A.W. Hill, L.E. Sutton, R.B. Temple and A. White, Research, 3 (1950) 569.
31. R.A.W. Hill, Proc. Roy. Soc. (London), A 226 (1954) 455.
32. T. Boddington, P.G. Laye, J. R. G. Pude and J. Tipping, Combust. Flame, 47 (1982) 235.
33. T. Boddington, P.G. Laye, J. Tipping and D. Whalley, Combust. Flame, 63 (1986) 359.
34. M.W. Beck and M.E. Brown, Combust. Flame, 65 (1986) 263.
35. R.L. Drennan and M.E. Brown, Thermochim. Acta, 208 (1992) 223.
36. R.L. Drennan and M.E. Brown, Thermochim. Acta, 208 (1992) 247.
37. R.A. Rugunanan and M.E. Brown, Combust. Sci. Technol., 95 (1994) 61.
38. R.A. Rugunanan and M.E. Brown, Combust. Sci. Technol., 95 (1994) 85.
39. R.A. Rugunanan and M.E. Brown, Combust. Sci. Technol., 95 (1994) 117.

40. M.J. Tribelhorn, M.G. Blenkinsop and M.E. Brown, Thermochim. Acta, 256 (1995) 291.
41. M.J. Tribelhorn, D.S. Venables and M.E. Brown, Thermochim. Acta, 256 (1995) 309.
42. S.Nakahara and T. Hikita, Kogyo Kayaku Kyokai-Shi, 20 (1959) 275.
43. J. Jakubko, Combust. Sci. Technol., 146 (1999) 37.
44. T. Boddington, A. Cottrell and P.G. Laye, Combust. Flame, 79 (1990) 234.
45. R.A. Rugunanan and M.E. Brown, J. Therm. Anal., 37 (1991) 2125.
46. J.A.C. Goodfield and G.J. Rees, Fuel, 60 (1981) 151.
47. J.E. Spice and L.A.K. Staveley, J. Soc. Chem. Ind., 68 (1949) 348.
48. D.C. Johnson, Proc. 22nd Int. Pyrotech. Seminar, IIT Research Institute, Chicago, USA,1996, p.227.
49. A. Miyake, T. Aochi, N. Oshino and T. Ogawa, Proc. 22nd Int. Pyrotech. Seminar, IIT Research Institute, Chicago, USA, 1996, p.325.
50. A. Miyake, K. Kitoh, T. Ogawa, M. Watanabe, N. Kazama and S.Tsuji, Proc. 19th Int. Pyrotech. Seminar, IIT Research Institute, Chicago, USA, 1994, p.124.
51. I.V. Mendenhall and S.F. Reid, Thermochim. Acta, 272 (1996) 221.
52. J. Neutz, J. Kerth, H. Ebeling and H. Schuppler, Proc. 33rd Int. ICT Conf., Fraunhofer-Institut für Chemische Technologie, Karlsruhe, Germany, 2002, p.152/1
53. T. Yoshida, T. Akiba, H. Endow, K. Aoki, K. Hara and J. Peng, Proc. 9th Symp. Chem. Problems connected with Stabil. of Explos., Sektionen för Detonik och Förbränning, Sweden, 1992, p.87.
54. Y. Ohtsuka, M. Matsuo, S. Kaneko and T. Yoshida, Proc. 20th Int. Pyrotech. Seminar, IIT Research Institute, Chicago, USA, 1994, p.779.
55. M. Arai, N. Nakazato, Y. Wada, T. Harada and M. Tamura, Proc. 28th Int. Pyrotech. Seminar, Weapons Systems Division, DESTO, Australia, 2001, p.25.
56. I. Lee and S.A. Finnegan, J. Therm. Anal., 50 (1997) 707.
57. L-E Paulsson, Proc. 10th Symp. Chem. Probl. Connected Stabil. Explos., Sektionen för Detonik och Förbränning, Sweden, 1995, p.211.
58. Qinglian Li, Pu Yao, Liuxia Wang and Weidong Zhang, Thermochim. Acta, 253 (1995) 213.
59. B. Berger, H Brechbühl and W. de Klerk, Proc. 29th Int. Pyrotech. Seminar, IIT Research Institute, Chicago, USA, 2002, p.443.
60. R.G. Shortridge and B.R. Hubble, Proc. 18th Int. Pyrotech. Seminar, IIT Research Institute, Chicago, USA, 1992, p.847.

61. P.E. Lagerkvist and C.J. Elmqvist, Proc. 9th Int. Pyrotech. Seminar, IIT Research Institute, Chicago, USA, 1984, p.323.
62. M. Cournil and J. Ramangalahy, J. Therm. Anal., 35 (1989) 175.
63. E.L. Charsley, T.T. Griffiths, S.J. Goodall, P.G. Laye and J.J. Rooney, Proc. 29th NATAS , St. Louis, USA, 2001, p.697.
64. K. Miyata and N. Kubota, Propellants Explosives, Pyrotechnics, 21 (1996) 29.
65. A. Rosina and C. Pelhan, J.Therm. Anal., 11 (1977) 29.
66. A. Rosina and C. Pelhan, J.Therm. Anal., 17 (1979) 371.
67. C. Pelhan and N. Majcen, Giesserei-Forschung, 23 (1971) 29.
68. H. Singh and R. B. Rao, Combust. Sci. Technol., 81 (1992) 233.
69. B.D. Bond and P.W.M. Jacobs, Combust. Flame, 10 (1966) 349.
70. J.R. Dawe and M.D. Cliff, Proc. 24th Int. Pyrotech. Seminar, IPS, USA, 1998, p.789.
71. A.S. Tompa, R.F. Boswell, P.Skahan and C. Gotzmer, J. Therm. Anal., 49 (1997) 1161.
72. M.E. Brown and R.A. Rugunanan, Thermochim. Acta, 134 (1988) 413.
73. S.S. Al-Kazraji and G.J. Rees, Combust. Flame, 31 (1978) 105.
74. S.S. Al-Kazraji and G.J. Rees, J. Therm. Anal., 16 (1979) 35.
75. A.Z. Moghaddan and G.J. Rees, Fuel, 60 (1981) 629.
76. M. Matsumoto, J. Yoshimura, T. Nagaishi and S. Yoshinaga, Kogyo Kayaku Kyokai-Shi, 40 (1979) 283.
77. J. Jakubko and E. Černošková, J. Therm. Anal., 50 (1997) 511.
78. L. Sulacsik, J. Therm. Anal., 5 (1973) 33.
79. E.L. Charsley and M.R. Ottaway in Proc. 8th Int. Symp. on Reactivity of Solids (Eds J. Wood, O. Lindqvist and N.G. Vannerberg), Plenum, New York, USA, 1977, p.737.
80. A.D. Kirshenbaum and A.J. Beardell, Thermochim. Acta, 4 (1972) 239.
81. A.J. Beardell and A.D. Kirshenbaum, Thermochim. Acta, 8 (1974) 35.
82. E.S. Freeman and B. Carroll, J. Phys. Chem., 62 (1958) 394.
83. R.L. Drennan and M.E. Brown, Thermochim. Acta, 208 (1992) 201.
84. R.A. Rugunanan and M.E. Brown, Combust. Sci. Technol., 95 (1994) 101.
85. M.J. Tribelhorn, D.S. Venables and M.E. Brown, Thermochim. Acta, 269/270 (1995) 649.
86. T.J. Barton, N. Williams, E.L. Charsley, J.A. Rumsey and M.R. Ottaway, Proc. 8th Int. Pyrotech. Seminar, IIT Research Institute, Chicago, USA, 1982, p.99.
87. B. Berger, E.L. Charsley and S.B. Warrington, Propellants, Explosives. Pyrotechnics, 20 (1995) 266.

88. B. Berger, E.L. Charsley, J.J. Rooney and S.B. Warrington, Thermochim. Acta, 255 (1995) 227.
89. B. Berger, A.J. Brammer and E.L. Charsley, Thermochim. Acta, 269/270 (1995) 639.
90. B. Berger, E.L. Charsley, J.J. Rooney and S.B. Warrington, Thermochim. Acta, 269/270 (1995) 687.
91. B. Berger, E.L. Charsley, J.J. Rooney and S.B. Warrington, Proc. 26th Int. ICT Conf., Fraunhofer-Institut für Chemische Technologie, Karlsruhe, Germany, 1995, p.80/1.
92. F.S. Scanes, Combust. Flame, 23 (1974) 363.
93. G. Krein, Thermochim. Acta, 81 (1984) 29.
94. Z. Abdel-Qader, Q.S.M. Kwok, R.C. Fouchard, P.D. Lightfoot and D.E.G. Jones, J. Pyrotechnics, in press, 2003.
95. A. Jarvis, Combust. Flame, 14 (1970) 313.
96. A.S. Redkar, V.A. Mujumdar and S.N. Singh, Defence Sci. J., 46 (1996) 41.
97. E.S. Freeman, V.D. Hogan and D.A. Anderson, Combust. Flame, 9 (1965) 19.
98. E.S. Freeman and D.A. Anderson, Combust. Flame, 10 (1966) 337.
99. L.W. Collins, Combust. Flame, 41 (1981) 325.
100. K. L. Erickson, J.W. Rogers and S.J. Ward, Proc. 11th Int. Pyrotech. Seminar, IIT Research Institute, Chicago, USA, 1986, p.679.
101. J.W. Rogers, Jr and K.L. Erickson, Proc. 12th Int. Pyrotech. Seminar, Groupe de Travail de Pyrotechnie Spatiale, France, 1987, p.407.
102. K.L. Erickson, J.W. Rogers Jr and R.D. Skocypec, Proc. 12th Int. Pyrotech. Seminar, Groupe de Travail de Pyrotechnie Spatiale, France, 1987, p.49.
103. M.W. Beck and M.E. Brown, J. Chem. Soc., Faraday Trans., 87 (1991) 711.
104. E.L. Charsley, T. Boddington, J.R. Gentle and P.G. Laye, Thermochim. Acta, 22 (1987) 175.
105. E.L. Charsley, Chieh-Hua Chen, T. Boddington, P.G. Laye and J.R.G. Pude, Thermochim Acta, 35 (1980) 141.
106. E.L. Charsley, M.C. Ford, D.E. Tolhurst, S Baird-Parker, T. Boddington and P.G. Laye, Thermochim. Acta, 25 (1978) 131.
107. T. Boddington, Feng Hongtu, P.G. Laye, M. Nawaz and D.C. Nelson, Thermochim. Acta, 170 (1990) 81.
108. H.E. Kissinger, J. Res. Nat. Bur. Stand., 57 (1956) 217.
109. T. Ozawa, Bull. Chem. Soc. (Japan), 38 (1965) 1881.
110. H.J. Borchardt and F. Daniels, J. Amer. Chem. Soc., 79 (1957) 41.

111. D.J. Whelan, M. Maksacheff and L.V. de Yong, Proc. 16th Int. ICT Conf., Fraunhofer-Institut für Chemische Technologie, Karlsruhe, Germany, 1985, p.55/1
112. D.J. Whelan, M. Maksacheff and L.V. de Yong, Proc. 11th Int. Pyrotech. Seminar, IIT Research Institute, Chicago, USA, 1986, p.595.
113. A.Yu Snegirev and V.A. Taylor, Fizika Goreniyai Vzryva, 27 (1999) 79.
114. N. Nakamura, Y. Hara and H. Osada, Kogyo Kayaku Kyokai-Shi, 44 (1983) 15.
115. V.D. Hogan, S. Gordon and C. Campbell, Anal. Chem., 29 (1957) 306.
116. V.E. Zarko, V.N. Simonenko, A.B. Kiskin, S.V. Larionov and Z.A. Savelyeva, Proc. 32nd Int. ICT Conf., Fraunhofer-Institut für Chemische Technologie, Karlsruhe, Germany, 2001, p.57/1.
117. S. Cudzilo and W.A. Trzcinski, , Proc. 29th Int. ICT Conf., Fraunhofer-Institut für Chemische Technologie, Karlsruhe, Germany, 1998, p.151/1.
118. N. Davies, T.T. Griffiths, E.L. Charsley and J.A. Rumsey, Proc. 16th Int. ICT Conf., Fraunhofer-Institut für Chemische Technologie, Karlsruhe, Germany, 1985, p.15/1.
119. J.A.C. Goodfield and G.J. Rees, Fuel 61 (1982) 843.
120. P. Barnes, T.T. Griffiths, E.L. Charsley, J.A. Hider and S.B. Warrington, Proc. 11th Int. Pyrotech. Seminar, IIT Research Institute, Chicago, USA, 1986, p.27.
121. S.L. Howlett and F.G.J. May, Thermochim. Acta, 9 (1974) 213.
122. M.A. Benmahamed, A Mouloud and N.Ikene, Proc. 21st Int. ICT Conf., Fraunhofer-Institut für Chemische Technologie, Karlsruhe, Germany, 2000, p.85/1.
123. V.S. Bhingarkar, P.P. Sane and R.G. Sarawadekar, Defence Sci. J., 47 (1997) 365.
124. B. Berger, A.J. Brammer, E.L. Charsley, J.J. Rooney and S.B. Warrington. J. Therm. Anal., 49 (1997) 1327.
125. V.D. Hogan and S. Gordon, J. Phys. Chem., 61 (1957) 1401.
126. E.S. Freeman and S. Gordon, J. Phys. Chem., 60 (1956) 867.
127. T.J. Barton, T.T. Griffiths, E.L. Charsley and J.A. Rumsey, Proc. 8th Int. Pyrotech. Seminar, IIT Research Institute, Chicago, USA, 1982, p.83.
128. T.J. Barton, T.T. Griffiths, E.L. Charsley and J.A. Rumsey, Proc. 9th Int. Pyrotech. Seminar, IIT Research Institute, Chicago, USA, 1984, p.743.
129. T.T. Griffiths, E.L. Charsley and J.A. Hider, Proc. 13th Int. Pyrotech. Seminar, IIT Research Institute, Chicago, USA, 1988, p.393.
130. C. Campbell and F.R. Taylor in 'Thermal analysis, Vol. 2, Inorganic Materials and Physical Chemistry',(Eds. R.F. Schwenker and P.D. Garn), Academic Press, New York, USA,1969, p.811.

131. T.T. Griffiths, J. Robertson, P.G. Hall and R.T. Williams, Proc. 16th Int. ICT Conf., Fraunhofer-Institut für Chemische Technologie, Karlsruhe, Germany, 1985, p.19/1.
132. T. Nagaishi, F. Shinchi, M. Matsumoto and S. Yoshinaga, Kogyo Kayaku Kyokai-Shi, 44 (1983) 21.
133. S. Yoshinaga, K. Watanabe, M. Matsumoto and T. Nagaishi, Kyushu Sangyo Daigaku Kogakubu Kenkyu Hokoku, 21 (1984) 47.
134. R.G. Sarawadekar, R. Daniel and S. Jayaraman, Proc. 26th Int. ICT Conf., Fraunhofer-Institut für Chemische Technologie, Karlsruhe, Germany, 1995, p.56/1.
135. R. Daniel and H. Singh, Proc. 23rd Int. Pyrotech. Seminar, IIT Research Institute, Chicago, USA, 1997, p.131.
136. M.W. Beck and M.E. Brown, Thermochim. Acta, 65 (1983) 197.
137. G. Krishnamoham, E.M. Kurian and K.R.K. Rao, Proc. 8th Int. Pyrotech. Seminar, IIT Research Institute, Chicago, USA, 1982, p.404.
138. R.A. Rugunanan and M.E. Brown, J. Therm. Anal., 37 (1991) 1193.
139. S.R. Yoganarasimhan and O.S. Josyulu, Defence Sci. J., 37 (1987) 73.
140. S.R. Yoganarasimhan, N.S. Bankar, S.B. Kulkarni and R.G. Sarawadekar, J. Therm. Anal., 21 (1981) 283.
141. R.G. Sarawadekar, A.R. Menon and N.S. Bankar, Thermochim. Acta., 70 (1983) 133.
142. R.G. Sarawadekar and N.S. Bankar, Proc. 8th Int. Pyrotech. Seminar, IIT Research Institute, Chicago, USA, 1982, p.574.
143. U.C. Durgapal and A.R. Menon, Proc. 15th Int. Pyrotech Seminar, IIT Research Institute, Chicago, USA, 1990, p.221.
144. M. Matsumoto, F. Shinchi, T. Nagaishi and S. Yoshinaga, Kogyo Kayaku Kyokai-Shi, 44 (1983) 218.
145. T. Nagaishi, S. Okamoto, M. Matsumoto and S. Yoshinaga, Kogyo Kayaku Kyokai-Shi, 38 (1977) 271.
146. K. Miyata and N. Kubota, Proc. 20th Int. Pyrotech Seminar, IIT Research Institute, Chicago, USA, 1994, p.729.
147. E.L. Charsley, S.B. Warrington, P. Emmott, T.T. Griffiths and J. Queay, J. Therm. Anal., 38 (1992) 641.
148. P. Emmott, T.T. Griffiths, J. Queay E.L. Charsley and S.B. Warrington, Proc. 16th Int. Pyrotech Seminar, IIT Research Institute, Chicago, USA, 1991, p.937.
149. T.J. Barton, T.T. Griffiths, E.L. Charsley and J.A. Rumsey, Proc. 16th Int. ICT Conf., Fraunhofer-Institut für Chemische Technologie, Karlsruhe, Germany, 1985, p.20/1.

150. T.J. Barton, T.T. Griffiths, E.L. Charsley and J.A. Rumsey, Proc. 9th Int. Pyrotech. Seminar, IIT Research Institute, Chicago, USA, 1984, p.723.
151. T. Nagaishi, S. Okamoto, T. Kaneda, M. Matsumoto and S. Yoshinaga, Kogyo Kayaku Kyokai-Shi, 38 (1977) 65.
152. H. Nakamura, T. Yamato, Y. Hara and Osada, Kogyo Kayaku Kyokai-Shi, 40 (1979) 31.
153. G. Krien, Explosivstoffe, 13 (1965) 205.
154. R.Daniels, R.G. Sarawadekar and U.C. Durgapal, Proc. 26th Int. ICT Conf., Fraunhofer-Institut für Chemische Technologie, Karlsruhe, Germany, 1995, p.48/1.
155. U.C. Durgapal, A.S. Dixit and R.G. Sarawadekar, Proc. 13th Int. Pyrotech Seminar, IIT Research Institute, Chicago, USA, 1988, p.209.
156. R.G. Sarawadekar, N.B. Swarge, B.K. Athawale, S. Jayaraman and J.P. Agrawal, Proc. 27th Int. Pyrotech Seminar, IPSUSA Inc., Chicago, USA, 2000, p.151.
157. E.L. Charsley, J.J. Rooney and S.B. Warrington, T.T. Griffiths and T.A. Vine, Proc. 27th Int. Pyrotech Seminar, IPSUSA Inc., Chicago, USA, 2000, p.382.
158. K. Ishikawa, M. Koga, M. Matsumoto, T. Tsuru and S. Yoshinaga, Proc. 4th Int. Seminar on Propellants, Explosives and Pyrotechnics, (Eds. Chen, Lang and Feng, Changen) China Science and Technology Press, Beijing, China, 2001, p.629.
159. F.R. Hartley, S.G. Murray and M.R. Williams, Propellants Explosives Pyrotechnics, 9 (1984) 205.
160. C. Campbell and G. Weingarten, Trans. Faraday Soc., 55 (1959) 2221.
161. A.D. Kirshenbaum, Thermochim. Acta, 18 (1977) 113.
162. E.L. Charsley, S.B. Warrington, J. Robertson and P.N.A. Seth, Proc. 9th Int. Pyrotech Seminar, IIT Research Institute, Chicago, USA, 1984, p.759.

This Page Intentionally Left Blank

Handbook of Thermal Analysis and Calorimetry. Vol. 2: Applications to Inorganic and Miscellaneous Materials
M.E. Brown and P.K. Gallagher, editors
© 2003 Elsevier B.V. All right reserved.

Chapter 15

THERMAL ANALYSIS IN STUDIES OF HIGH-T_c SUPERCONDUCTORS

J. Valo and M. Leskelä

Laboratory of Inorganic Chemistry, Department of Chemistry,
P.O.Box 55, FIN-00014 University of Helsinki, FINLAND

1. INTRODUCTION

After the discovery of high temperature superconductivity in the La-Ba-Cu-O system in 1986 [1] there was an explosion of interest in oxide superconductors. This quickly led to the discovery of superconductivity above liquid nitrogen temperature in $YBa_2Cu_3O_{7-\delta}$ (Y-123; n(Y):n(Ba):n(Cu) = 1:2:3) [2] and later above 100 K in Bi-Sr-Ca-Cu-O [3], Tl-Ba-Ca-Cu-O [4,5] and Hg-Ba-Ca-Cu-O [6,7] systems. These oxide systems have been extensively studied and the variations in the structures are now relatively well characterised.

Studies on high-T_c superconductors (HTSC) (T_c = critical temperature) have focused on the search for new phases and characterisation of the properties of already known phases as a means of understanding the superconductivity phenomenon and where it is likely to exist. Fabrication of high-quality thin films and processing the bulk materials for practical application has assumed continually growing importance during recent years.

This chapter is devoted to thermoanalytical (TA) studies of HTSC. Studies on bulk samples are described first, and then investigations of the volatile precursors used in the preparation of thin films.

The most important topics covered with regard to bulk HTSC are the thermal decomposition of precursors used in the synthesis, the formation of superconducting phases, the thermal stability of prepared samples and the analysis of oxygen stoichiometry. The examples come mainly from Y-Ba-Cu-O and Bi-Sr-Ca-Cu-O systems, with a few pertaining to Tl- and Hg-based superconductors. Also discussed is the oxygen non-stoichiometry in La-Sr-Cu-O, Pb-Sr-Y-Ca-Cu-O, Ru-Sr-Gd-Cu-O and Nd-Ce-Cu-O systems. Since TA methods can even be employed in the determination of the superconducting transition temperature, this is briefly mentioned as a curiosity.

The precursors that we describe for chemical vapour deposition (CVD) of HTSC thin films are mostly β-diketonates and special attention is given to Y, Ba and Cu precursors. Because the precursors of alkaline-earth metals are difficult to work with due to problems of volatilisation, considerable attention is devoted to these. The use of TA methods in studies of thermal stability, volatility and species in the gas phase is described.

This chapter deals only with investigations made by TA techniques [8]. Studies on the thermochemistry and thermodynamics of HTSC made by acid solution calorimetry [9–11] or oxide-melt solution calorimetry [12] are not included.

2. THERMOANALYTICAL TECHNIQUES

TA techniques offer wide scope for the investigation of cuprate superconductors, and a great many different techniques have been applied (Table 1). HTSC are synthesised by many routes, in the form of powders, single crystals and thin films. TA techniques such as thermogravimetry (TG), differential thermal analysis (DTA) and evolved gas analysis (EGA) provide highly useful information for both the synthesis and characterisation of bulk HTSC [13]. Formation processes and crystallisation can be investigated, for example, through gas evolution and changes in mass and heat. High-temperature X-ray diffraction (XRD) can be applied *in situ* in the determination of phases formed during annealing, while thermodilatometry (TD) can be used to investigate sintering and crack formation. The formation kinetics of HTSC materials is yet another field where thermal analysis can be applied. In the early stage of the research on cuprate superconductors, DTA was found to be a good tool in the study of phase diagrams used in growing single crystals [14]. Melting accompanied by decomposition and glass formation has also been studied by DTA. Thermodynamics of cuprate superconductors have been followed by differential scanning calorimetry (DSC) [11,15], but such studies are few, owing to problems associated with measurements at high temperatures.

Vapour pressure measurement by TG and evolved gas analysis or detection (EGD) have been important in the development of fabrication for superconducting thin films, especially in the growth of films by chemical vapour deposition (CVD) methods [13,16]. TD, in turn, has been helpful in investigating the difference in thermal expansion between the film and the substrate [14].

Studies on oxygen stoichiometry are among the most important applications of thermal analysis, because the oxygen content is closely related to superconductivity [17]. Oxidation–reduction reactions are responsible for the oxygen content of a superconductor [18,19]. The non-stoichiometry of oxide superconductors was first discovered by thermogravimetry, and temperature-programmed reduction has been applied in the determination of oxygen content

[14,20]. DSC can be applied to confirm the existence of bulk superconductivity if the calorimeter is suitable for measurements at a low temperature [13,21]. Superconducting transition temperatures (T_c^{onset}) can also be determined by thermomagnetometry (TM) [22,23].

A reversible exchange of oxygen between a superconducting oxide and its surrounding atmosphere occurs at temperatures above 300 °C [18]. The reactions with ambient gases, which produce undesired products on the surface or at grain boundaries, are important limiting factors for the values of critical temperature. Many superconductors react deleteriously with CO_2 and H_2O, with the formation of insulating phases which undermine the superconducting properties. The interactions of superconductors with their gaseous environment are conveniently studied by thermal analysis.

Table 1.
Thermoanalytical techniques used in research on HTSC [modified after 13].

Application targets	Techniques
Formation process and kinetics	TG, DTA, EGA, ETA, XRD, MO
Crystalline transition	DTA, DSC, TD
Melting and glass formation	DTA, DSC, MO
Sintering and crack formation	TD
Thin film formation (expansion matching)	TD
Volatility and vapour pressure (MOCVD)	TG, EGA
Melting of CVD precursors	DSC
Phase diagram	DTA, XRD
Crystal growth	DTA
Oxygen content	TG (TPR), EGA
Non-stoichiometry	TG, EGA, (TD)
Critical temperature	TE, TM, DSC
Thermodynamics	(DSC)

TG, thermogravimetry; DTA, differential thermal analysis; EGA, evolved gas analysis; ETA, emanation thermal analysis; XRD, X-ray diffraction; MO, microscopic observation; DSC, differential scanning calorimetry; TD, thermodilatometry; TPR, temperature programmed reduction; TE, thermoelectrometry; TM, thermomagnetometry; MOCVD, metal organic chemical vapour deposition.

3. HIGH-T_c SUPERCONDUCTORS

Figure 1A is a schematic representation of the structure of a layered cuprate, while Figure 2 shows the structures of selected HTSC and related cuprates in more detail. In the cuprate structure, 2-dimensional Cu-O_2 planes alternate with (i) bare alkaline-earth (AE) or rare-earth (RE) atom sheets (or alternatively, fluorite-type RE-O_2 layers, not shown in Figure 1A), (ii) rock-salt-type AE-O or RE-O planes and (iii) charge reservoir layers built up by *e.g.* Cu-O, Pb-O, Ru-O_2, Bi-O, Tl-O or Hg-O_δ planes [24–26]. Up to now more than one hundred different HTSC cuprates have been discovered [27]. Superconductivity in cuprate superconductors is believed to be associated with charge transfer from the charge reservoir layers to superconducting Cu-O_2 planes [24,25]. Most HTSC are *p*-type superconductors, where the carriers are positive holes. Within a homologous series of cuprate phases, T_c varies with the number n of consecutively stacked Cu-O_2 planes in the infinite-layer unit, and it depends crucially on the carrier concentration, *i.e.* the amount of excess charge on the Cu-O_2 planes (Figure 1B).

$La_{2-x}Ba_xCuO_{4+\delta}$ was the first reported superconductor among the HTSC [1]. $La_{2-x}Ba_xCuO_{4+\delta}$ (La-214 or 0201; see details of the four-integer naming system below Table 2) consists of double La-O layers and Cu-O_2 planes [27]. The [La-O] layers possess positive charge and act as hole donors for the [La-O-Cu-O_2] blocks [28,29]. Partial replacement of La^{3+} ions by Ba^{2+} ions increases the oxidation state of Cu in the Cu-O_2 planes, causing the material to become superconducting. Similarly, in the case of $Pb_2Sr_2(Y,Ca)Cu_3O_{8+\delta}$ (Pb-2213 or Pb,Cu-3212), superconductivity is achieved when Ca^{2+} ions are substituted for some Y^{3+} ions in the bare-cation-containing planes in the infinite-layer blocks. Another way to obtain suitable conditions for superconductivity is by increase of the oxygen content, as in the tri-perovskite, $YBa_2Cu_3O_{7-\delta}$ (Y-123 or Cu-1212), where oxygen occupancy in the Cu-O chains in the charge reservoir layers determines the phenomenon. Two other superconducting phases (l = 1,2), in addition to Y-123 (l = 0), exist in the $Y_2Ba_4Cu_{6+l}O_{14+l}$ family. The basic building blocks in these are pyramidal Cu-O_2 layers and single or double Cu-O chains. Between the two Cu-O_2 planes are located bare Y atom sheets, and Ba-O planes exist between the Cu-O chains and Cu-O_2 planes. Rutheno-cuprate, $RuSr_2GdCu_2O_{8-\delta}$ (Ru-1212) is isostructural with Y-123, where Y, Ba, and Cu-O chains in the charge reservoir layer, are replaced by Gd, Sr and Ru-O_2 sheets, respectively [30–34]. Ru atoms form an octahedral coordination with oxygen atoms. At first, bulk superconductivity was not unambiguously attributed to the Ru-1212 phase [30]. Recently, coexistence of superconductivity and magnetsim was found in Ru-1212 [35]. Ru-1212 exhibits magnetic transition, T_M (T_M = magnetic transition temperature) at about 133 K, but its T_c depends strongly on the synthesis

procedure, being in the range of 15–40 K [35].

In Bi-based superconductors, $Bi_2Sr_2Ca_{n-1}Cu_nO_{2n+4+\delta}$ (n = 1–3), double Bi-O layers are the charge reservoir layers [25,28]. Between the consecutively stacked Cu-O_2 planes are located bare Ca atom sheets. Tl-based superconductors, which are denoted by $TlBa_2Ca_{n-1}Cu_nO_{2n+3+\delta}$ and $Tl_2Ba_2Ca_{n-1}Cu_nO_{2n+4+\delta}$ (n = 1–3), have both single and double Tl-O layers as charge reservoir layers. In the homologous series $HgBa_2Ca_{n-1}Cu_nO_{2n+2+\delta}$ (n = 1–3), the oxygen stoichiometry on Hg-O_δ planes plays an essential role in the superconductivity. At present, $HgBa_2Ca_2Cu_3O_{8+\delta}$ has the highest known T_c (135 K) of the superconducting cuprate phases under ambient pressure (Table 2) [36].

$Nd_{2-x}Ce_xCuO_{4+\delta}$ (Nd-214 or 0021) is an example of an electron-doped system where the carriers are electrons. The structure consists of [(Nd,Ce-O_2)-Nd,Ce] fluorite-type blocks and Cu-O_2 planes [27]. [Nd,Ce-O_2] layers possess negative charge and act as electron donors for positively charged [Nd,Ce-Cu-O_2] blocks [28,29]. This is called an n-type superconductor.

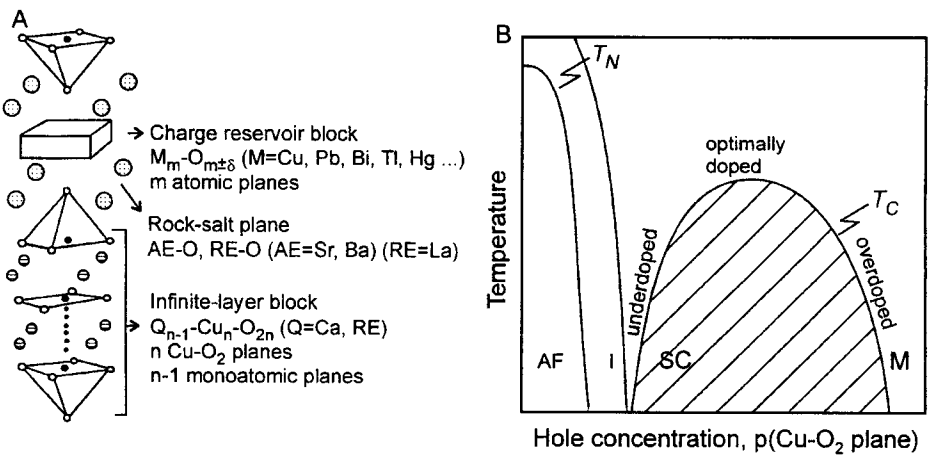


Figure 1. (A) Schematic crystal structure of a layered cuprate phase [modified after 37,38] and (B) schematic phase diagram for superconducting p-type cuprates [modified after 39]. SC = superconducting, AF = antiferromagnetic, I = insulating, M = metallic, T_c = superconducting transition temperature and T_N = Néel temperature.

Table 2.
Approximate transition temperatures of selected high-T_c superconductors.

Compound		T_c /K
$(La,Sr)_2CuO_4$	La-214 or 0201	35
$(Nd,Ce)_2CuO_4$	Nd-214 or 0021	20
$YBa_2Cu_3O_{7-\delta}$	Y-123 or Cu-1212	90
$YBa_2Cu_4O_8$	Y-124 or Cu-2212	80
$Y_2Ba_4Cu_7O_{15-\delta}$	Y-247	90
$RuSr_2GdCu_2O_{8-\delta}$	Ru-1212	35
$Pb_2Sr_2(Y,Ca)Cu_3O_8$	Pb-2213 or Pb,Cu-3212	80
$Bi_2Sr_2CuO_6$	Bi-2201	10
$Bi_2Sr_2CaCu_2O_8$	Bi-2212	80
$Bi_2Sr_2Ca_2Cu_3O_{10}$	Bi-2223	105
$Tl_2Ba_2CuO_6$	Tl-2201	80
$Tl_2Ba_2CaCu_2O_8$	Tl-2212	105
$Tl_2Ba_2Ca_2Cu_3O_{10}$	Tl-2223	125
$Tl_2Ba_2Ca_3Cu_4O_{12}$	Tl-2234	100
$TlBa_2CuO_5$	Tl-1201	10
$TlBa_2CaCu_2O_7$	Tl-1212	80
$TlBa_2Ca_2Cu_3O_9$	Tl-1223	110
$TlBa_2Ca_3Cu_4O_{11}$	Tl-1234	120
$HgBa_2CuO_4$	Hg-1201	90
$HgBa_2CaCu_2O_6$	Hg-1212	120
$HgBa_2Ca_2Cu_3O_8$	Hg-1223	135

Examples of the four-integer naming system of HTSC [after 25,28].
La-214: 0201, where number (no.) of charge reservoir layers = 0, no. of rock-salt-type RE-O planes = 2, no. of bare RE atom sheets = 0, no. of Cu-O_2 planes =1.
Y-123: Cu-1212 = $CuBa_2YCu_2O_{7-\delta}$, where no. of charge reservoir layers = 1, Cu-$O_{1-\delta}$, which is perovskite-type, no. of rock-salt-type AE-O planes = 2, no. of bare RE atom sheets = 1, no. of Cu-O_2 planes = 2.
Pb-2213: Pb,Cu-3212 = $Pb_2CuSr_2(Y,Ca)Cu_2O_8$, where no. of charge reservoir layers = 3, Pb-O, Cu-O_δ, and Pb-O, which all are perovskite-type, no. of rock-salt-type AE-O planes = 2, no. of bare RE atom sheets = 1, no. of Cu-O_2 planes = 2.
Nd-214: 0021, where no. of charge reservoir layers = 0, no. of rock-salt-type AE-O planes = 0, no. of fluorite-type planes = 2, no. of Cu-O_2 planes = 1.
In this chapter the naming system is based on the mole ratios of elements, not their location in the crystal lattice of HTSC.

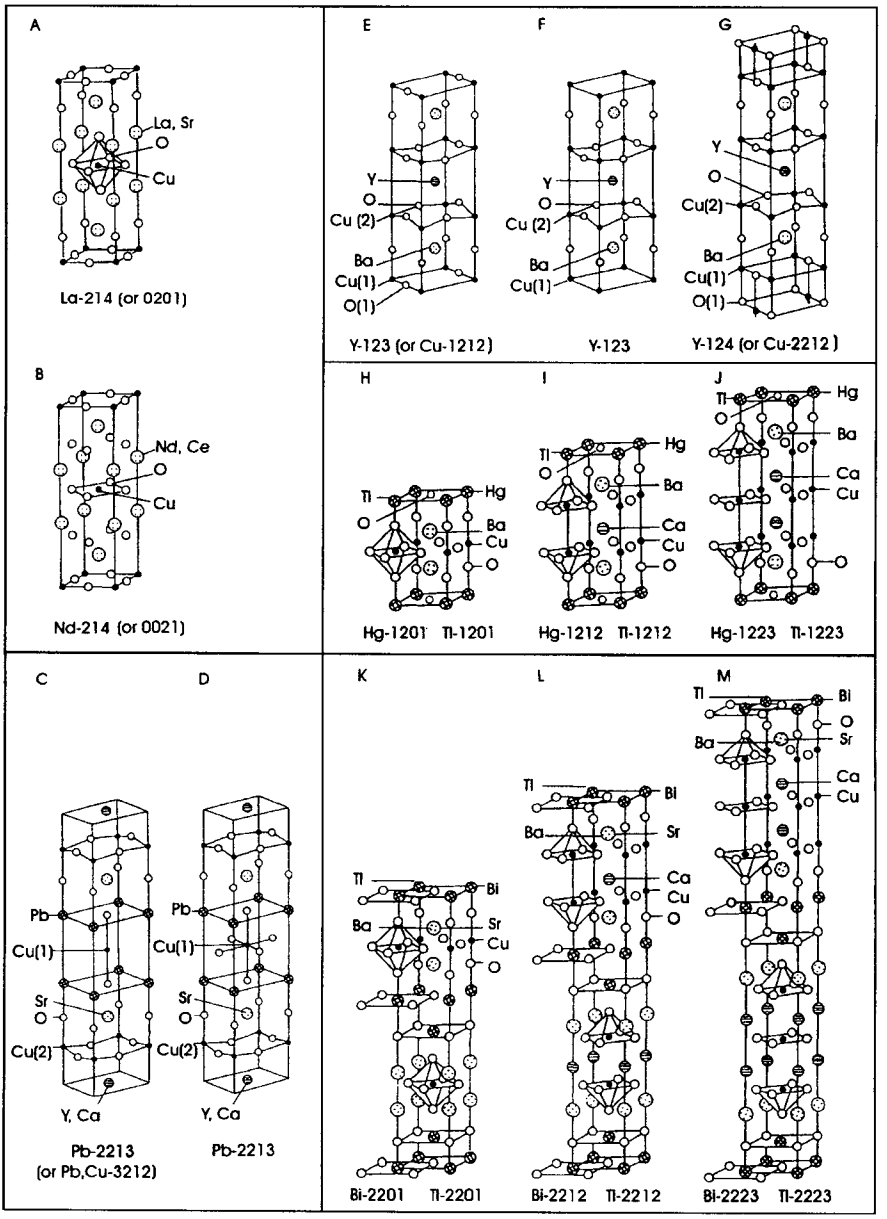


Figure 2. Ideal crystal structures of selected HTSC and related cuprates [after 24,40]. (A) $(La,Sr)_2CuO_4$, (B) $(Nd,Ce)_2CuO_4$, (C) $Pb_2Sr_2(Y,Ca)Cu_3O_8$, (D) $Pb_2Sr_2(Y,Ca)Cu_3O_{10}$, (E) $YBa_2Cu_3O_7$, (F) $YBa_2Cu_3O_6$, (G) $YBa_2Cu_4O_8$ (~ half of the structure), (H)-(J) $HgBa_2Ca_{n-1}Cu_nO_{2n+2}$; n = 1-3 or $TlBa_2Ca_{n-1}Cu_nO_{2n+3}$; n = 1-3 and (K)-(M) $Bi_2Sr_2Ca_{n-1}Cu_nO_{2n+4}$; n = 1-3 or $Tl_2Ba_2Ca_{n-1}Cu_nO_{2n+4}$; n = 1-3. Original structures of (C)-(F), (H)-(M): © Institute of Physics Publishing, see details in Acknowledgements.

4. THERMOANALYTICAL STUDIES ON PROPERTIES RELATED TO SUPERCONDUCTIVITY

4.1. Specific heat anomaly at T_c

The entire superconductivity transition process, and thus T_c, can be analysed more precisely by AC calorimetry than by electrical resistivity and AC susceptibility measurements [41]. The phase transition from a normal to superconducting state brings about an anomaly in the specific heat, and the magnitude of the anomaly, $\Delta C_p/T_c$, reflects the electron density that contributes to the superconductivity. This heat jump can also be measured by DSC, when an apparatus suitable for low temperature measurements is available [42]. The specific heat curve also provides information about the quality of the sample [41]. For a good quality $YBa_2Cu_3O_{7-\delta}$ (Y-123) superconductor the specific heat *vs.* temperature curve exhibits a distinct jump, and $\Delta C_p/T_c$ is greater than 40 mJ mol^{-1} K^{-2}. The specific heat discontinuity near T_c can also be measured by DTA [43]. In this case the anomaly becomes sharper when a low heating rate is employed (0.1 °C min^{-1}).

4.2. Determination of T_c^{onset}

Even though T_cs are usually measured by SQUID (superconducting quantum interference device), it is also possible to determine the T_c^{onset} values by thermomagnetometry [22,23]. The measurement is carried out by varying the magnetic field between zero and some constant value as a function of increasing temperature. The weight of the sample in the magnetic field increases rapidly to a constant value because the sample is no longer entirely diamagnetic but slightly paramagnetic above T_c. The paramagnetic impurities present in the sample can easily be observed by thermomagnetometry.

5. DETERMINATION OF SYNTHESIS CONDITIONS OF BULK HTSC

5.1. Introduction

Thermoanalytical studies on the synthesis of HTSC materials have been carried out to clarify the optimal temperature conditions for syntheses proceeding by various routes and to characterise the processes involved in different types of synthesis in various atmospheres [13,21]. TA methods have also been used to study the relation between the characteristics of the starting materials and the synthesised superconductors, and to monitor the progress of the target reaction during synthesis. Finally, thermal analysis of oxygen desorption and absorption has an important role in determining the conditions of the thermal treatment needed after synthesis to obtain a desired oxygen stoichiometry [13,21,44].

Most TA investigations have dealt with RE-123 compounds (RE = rare-earth element), because these were the first compounds to be discovered with critical temperatures above liquid nitrogen temperature. Y-123 is a suitable material for study of the reaction kinetics, because the reactions leading to the formation of Y-123 from different starting materials can be observed from beginning to end by TA techniques [13]. In the case of Bi-, Tl- or Hg-based superconductors, reactions cannot be followed to completion by thermal analysis at the usual heating rates due to the low melting temperatures of these compounds and the relatively slow reaction kinetics. The conditions used in preparing HTSC materials influence the oxygen content obtained, and in many cases the preparations also involve volatile oxides: Tl_2O_3, PbO_2, and HgO [45]. As a consequence, to monitor the stoichiometry of the HTSC material by TG-DTA implies systematic measurements.

5.2. Synthesis of $YBa_2Cu_3O_{7-\delta}$ by solid-state reactions

Synthesis of bulk HTSC by solid-state reactions involves mixing, calcining, compacting and sintering of component oxides or carbonates. Though many other synthesis routes have been developed as well, this is the most widely used method for the preparation of Y-123. A stoichiometric powder mixture of Y_2O_3, $BaCO_3$ and CuO is calcined in order to decompose $BaCO_3$ [46]. The mixture is reacted at temperatures slightly below the incongruent melting point of Y-123. The decomposition reaction of $BaCO_3$ appears to be the rate-limiting step in the synthesis, and a relatively high calcination temperature (930 °C) is needed for total decomposition. According to TG-DTA data reported for this process, mass loss begins gradually at about 750 °C [13]. The mass loss is mostly due to evolution of CO_2 from $BaCO_3$ during perovskite formation and partly due to oxygen loss from the synthesised superconductor. The endothermic peak at 810 °C, caused by a γ-β transition of $BaCO_3$, can be used to evaluate the quality of the synthesised sample, because DTA measurements are sensitive enough to detect carbon contents exceeding 1% in the Y-123 product [13,47,48]. The reaction mechanism in the preparation of Y-123 by solid-state reaction from Y_2O_3, $BaCO_3$ and CuO has been studied non-isothermally by TG-DTA [49]. The synthesis of Y-123 proceeds *via* formation of various intermediate products, *viz.* $Y_2Cu_2O_5$, $BaCuO_2$ and Y_2BaCuO_5. The endotherm related to the formation of Y-123 occurs around 940–960 °C. The Y-123 formation was proposed to be controlled by diffusion [50].

$LaBa_2Cu_3O_{7-\delta}$ is difficult to prepare as a stoichiometric and orthorhombic compound in air, but according to TG-EGA (evolved gas analysis) measurements it can be obtained at 950 °C under decreased $p(O_2)$ by the decomposition of $BaCO_3$ [51].

5.3. Synthesis of Y-123 and Y-124 by coprecipitation and sol–gel methods

5.3.1. Introduction

If very pure and chemically homogeneous powders are to be obtained at relatively low temperatures, the synthesis procedure needs to be carried out by wet chemical routes. These methods include coprecipitation of metal ions as carbonates, oxalates or citrates; pyrolysis of organic acid salts; and sol–gel methods [46]. Whilst pure Y-123 is easily synthesised by solid-state reaction from oxides and carbonates, synthesis of $YBa_2Cu_4O_8$ (Y-124) by this route is not possible without fluxing agents [23]. Y-124 has been widely prepared by wet chemical routes [52]. The superconducting Y-124 phase is obtained under a flowing oxygen atmosphere at 800 °C.

5.3.2. Preparation of Y-123 and Y-124 from coprecipitated oxalates

Thermal decomposition reactions of oxalates are exothermic owing to the combustion of volatilised CO to CO_2 [13]. The TG curve is a sum of the decomposition curves of the individual oxalates [46]. The activation energy (E_a) for Y-123 perovskite formation from oxalates was proposed to be 263 kJ mol^{-1} on the basis of the so-called Ozawa plot [14]. An Ozawa plot is obtained when the logarithm of the heating rate β (log β) is plotted against the reciprocal temperature ($1/T$) at a given mass loss (m%) [53]. The plots obtained for different mass losses are linear and the activation energy can be estimated from the slope of the straight line.

In air, CuC_2O_4 decomposes to CuO around 230–260 °C [46,54]. Yttrium oxalate decomposition to Y_2O_3 occurs *via* $Y_2(CO_3)_3$ in the temperature range 300–550 °C. Barium oxalate transforms to $BaCO_3$ at about 500 °C, and $BaCO_3$ starts to decompose to BaO at 750–800 °C. In an oxygen atmosphere, where the Y-124 synthesis is carried out, the oxalate precursor decomposes in one step at around 300 °C [55]. $BaCO_3$ is formed during the synthesis and starts to decompose at about 700 °C [56]. A study by mass spectrometric EGA showed the final stage of perovskite formation reaction from $BaCO_3$ to be CO_2 evolution [14].

5.3.3. Preparation of Y-124 from acetate–tartrate precursors

Decomposition of the individual acetate and tartrate precursors employed in the preparation of Y-124 by coprecipitation was studied in an oxygen atmosphere [57]. On the basis of TG data for the individual metal-containing acetate and tartrate precipitate, the precursor gel was concluded to consist of $Y_3(OH)(C_4H_4O_6)_4(H_2O)_x$ or $Y_3(CH_3COO)(C_4H_4O_6)_4(H_2O)_x$ (x = 4–8), $Ba(C_4H_4O_6)$ and $Cu_2(C_4H_4O_6)(H_2O)_4$ or $Cu_2(OH)_2(C_4H_4O_6)(H_2O)_2$. In the case of Y-Ba-Cu ternary gels, the tartrate ligands tend to form complexes with copper, and barium possibly forms a gelatinous product, and thus the situation may be different. The final

decomposition of the acetate–tartrate precursor occurred above 200 °C *via* intermediate species, *e.g.* $BaCO_3$.

5.3.4. Preparation of Y-123 by sol–gel methods

A homogeneous Y-Ba-Cu alkoxide solution is fairly difficult to prepare because copper alkoxides are only sparingly soluble in common organic solvents [46]. Obtaining single-phase Y-123 products requires the partial hydrolysis of a homogenous alcoholic solution of Y, Ba and Cu alkoxides to control the condensation processes in the preparation. Two exothermic peaks seen in TG-DTA curves at 200–300 °C and 400–500 °C in air were due to the decomposition and oxidation of organic groups of as-prepared gel powders obtained by the partial hydrolysis of Y, Ba and Cu alkoxides [46]. $Cu(OC_2H_4OC_2H_5)_2$, which is soluble in 2-ethoxyethanol, was used as the Cu source. A gradual mass loss was seen between 200 and 500 °C and another, minor mass loss occurred above 600 °C. In a specimen prepared without water addition, a large mass loss was observed above 800 °C owing to decomposition of the $BaCO_3$ formed during pyrolysis.

5.4. Melt-processing of RE-123

The peritectic melting of pure Y-123 occurs at 1020 °C (equation (1)), as shown by TG-DTA (Figures 3 and 4). The existence of secondary phases shifts the endotherm towards lower temperatures and causes additional effects at temperatures ranging from 900 to 990 °C [48,58]. The impurities or additives react with Y-123 as described in equations (2)–(4) [59,60]. The univariant reactions can be classified into three types on the basis of liquid phase formation: (*m*) congruent or incongruent melting reactions of a single compound, (*e*) eutectic reactions, where several components react to produce a homogeneous melt, and (*p*) peritectic reactions, where several compounds react to produce another solid phase and melt [59].

$$YBa_2Cu_3O_{7-\delta} \rightleftarrows Y_2BaCuO_5 + \text{liquid} + O_2 \qquad (1020\ ^\circ C) \qquad (1)$$

$$YBa_2Cu_3O_{7-\delta} + BaCuO_2 + CuO \rightleftarrows \text{liquid} + O_2 \qquad (899\ ^\circ C) \qquad (2)$$

$$YBa_2Cu_3O_{7-\delta} + CuO \rightleftarrows Y_2BaCuO_5 + \text{liquid} + O_2 \qquad (940\ ^\circ C) \qquad (3)$$

$$YBa_2Cu_3O_{7-\delta} + BaCuO_2 \rightleftarrows YBa_4Cu_3O_{8.5} + \text{liquid} + O_2 \qquad (991\ ^\circ C) \qquad (4)$$

The DTA and DSC curves should look the same when the run is repeated for the same sample under identical conditions [61]. If this is not the case, then the measurements themselves must be affecting the results and, for example, the proposed phase diagrams are based on states that have not yet reached equilibrium.

In the $YBa_{2-y}Sr_yCu_3O_{7-\delta}$ series (y = 0–0.4) the peritectic temperature, T_p (equation (1)) was found to increase with increasing Sr doping level [62]. In thermodilatometry (TD) runs an increase in the densification rate was observed at 930–950 °C. The densification was assigned to the formation of a liquid phase as indicated by endotherm in the DTA runs (equation (3)). After T_p the thickness of the pellets continued to decrease.

The $Nd_{1+x}Ba_{2-x}Cu_3O_{7-\delta}$ system has been of great interest, because Nd can substitute at the Ba sites over a large range, *i.e.* x = 0.0–0.6 or up to 0.9 [63,64]. Nd-123 also represents an interesting alternative to Y-123 in practical application, because of its wider solidification range and higher peritectic decomposition temperature (Table 3) [63,65]. An increase in the ionic radius of the RE element increases the onset melting temperature [47,66]. According to XRD and DTA measurements, the solid solution limits of $Nd_{1+x}Ba_{2-x}Cu_3O_\sigma$ lie between x = 0.0 and x = 0.9 [64]. Maximum variation in the solid solution was found in an O_2 atmosphere at 950–1050 °C. A temperature decrease caused an abrupt narrowing of the solid solution range to x = 0.1 at 800 °C. When the Nd substitution at the Ba sites increases in $Nd_{1+x}Ba_{2-x}Cu_3O_\sigma$, also the oxygen content increases above seven [67]. The variation in the oxygen content, however, decreases with increasing x.

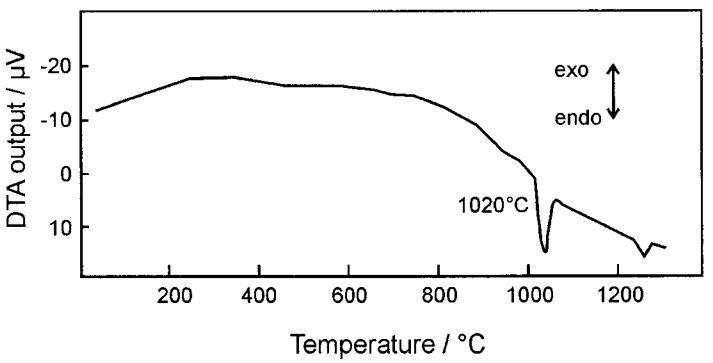


Figure 3. DTA curve of $YBa_2Cu_3O_{7-\delta}$ in air, heating rate 10 °C min^{-1} [after 58]. At T = 1020 °C reaction after equation (1) and at T = 1247 °C: Y_2BaCuO_5 + liquid $\rightleftarrows$ Y_2O_3 + liquid.

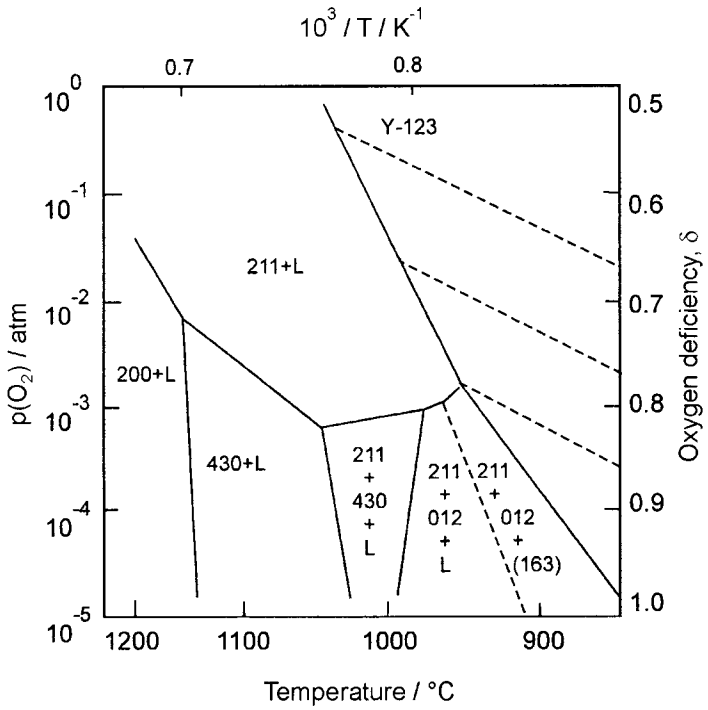


Figure 4. Stability field of $YBa_2Cu_3O_{7-\delta}$ and its dependence on T and $p(O_2)$, and subsequent reactions observed by TG-DTA with slow heating rates [modified after 59]. Y-123 = $YBa_2Cu_3O_{7-\delta}$, 211 = Y_2BaCuO_5, 012 = $BaCu_2O_2$, 430 = $Y_4Ba_3O_9$, 200 = Y_2O_3, 163 = $YBa_6Cu_3O_{10.5}$ and L = liquid.

Melt-processing yields the best superconducting properties in bulk Y-123 [48]. Melt processing of Y-123 consists of two steps, which can be described by the following scheme [48]: Y-123 precursors + additives $^{(i)} \rightarrow Y_2BaCuO_5$ + liquid $^{(ii)} \rightarrow$ Y-123 + other phases. The scheme is based on the peritectic decomposition or formation reaction of Y-123 (equation (1)) [59]. A powder mixture of Y-123 precursor is heated to 1000–1100 °C and the peritectic Y_2BaCuO_5 (Y-211) phase and a liquid phase are formed [48]. Next the solid–liquid mixture is cooled in a temperature gradient, which drives the peritectic growth of Y-123 grains and eventually the formation of other phases. Owing to the incompleteness of the peritectic reaction, which is very time-consuming, some of the Y-211 particles are usually trapped within the Y-123 phase. The melt-growth processes include MTG (melt-textured growth), QMG (quench and melt growth) and MPMG (melt powder melt growth) methods [68].

Purity, composition and grain-size of the precursor influence the properties of the material obtained in melt processing [48]. Thus carbon present as an impurity

alters the reactivity of the mixtures and increases the porosity of samples. The heating rate has an influence on the phases formed during heating. Prevention of Y-123 formation during heating may have a positive impact on the melt-processing. When no Y-123 forms during heating *via* the solid-state reaction, there are no peritectically grown Y-211 crystals after processing. The Y-211 particles that are generated after the peritectic melting of the Y-123 phase tend to be larger than those originating from the solid-state reaction. There are also fewer Y-211 crystals when they have been grown peritectically. The use of Y_2O_3, $BaCuO_2$ and CuO as Y-123 precursors yields a homogeneous distribution of Y-211 inclusions in the melt-processed Y-123 samples [48].

A composite material consists of several phases. DTA has been used to measure decomposition temperatures in the processing of melt-textured Y-, Sm- and Nd-123 composites. The temperatures increase systematically with the content of substituted Sm or Nd for Y (Table 3) [63]. The non-superconducting phases may act as pinning centres, which can enhance the critical current density, J_c, of the material. (For magnetic fields, H, where $H_{c1}<H<H_{c2}$, (H_{c1} and H_{c2} are the lower and upper critical magnetic field) the superconductor is in a mixed state and tubes of normal-state material occur in the superconductor [69]. These tubes are called vortices. The vortices can be pinned in their positions by pinning centres.)

Table 3.
Processed Y-, Sm- and Nd-123 composites [modified after 63].

Powder composition	Addition mol/mol 123	T_c /K powder	T_p /°C	Melt textured composition	T_c /K melt textured
Y-123		92 ($\Delta T = 1$)	1020	$Y_{0.98}Ba_{1.95}Cu_{3.0}O_\sigma$	92 ($\Delta T = 2$)
$Y_{0.5}Sm_{0.5}$-123	0.40 Y_2O_3 + 0.40 Sm_2O_3			$Y_{0.42}Sm_{0.56}Ba_{1.89}Cu_{3.0}O_\sigma$	91 ($\Delta T = 2.4$)
Sm-123			1061		
$Y_{0.5}Nd_{0.5}$-123		91 ($\Delta T = 5$)	1049	$Y_{0.44}Nd_{0.63}Ba_{1.90}Cu_{3.0}O_\sigma$	92 ($\Delta T = 1$)
$Y_{0.5}Nd_{0.5}$-123	0.25 Y_2O_3 + 0.125 Nd-422			$Y_{0.36}Nd_{0.71}Ba_{1.90}Cu_{3.0}O_\sigma$	92 ($\Delta T = 1.5$)
$Nd_{1+x}Ba_{2-x}$-123, $x<0.05$		89 ($\Delta T = 6$)	1086	$Nd_{1.12}Ba_{1.78}Cu_{3.0}O_\sigma$	88 ($\Delta T = 2$)

The following peritectic reactions occur at the peritectic temperature, T_p [63,68]:
$YBa_2Cu_3O_{7-\delta} \rightleftarrows$ Y-211 + liquid + O_2; $SmBa_2Cu_3O_{7-\delta} \rightleftarrows$ Sm-211 + liquid + O_2 and
$NdBa_2Cu_3O_{7-\delta} \rightleftarrows Nd_4Ba_2Cu_2O_{10}$ + liquid + O_2.
$Nd_4Ba_2Cu_2O_{10}$ (Nd-422) has a tetragonal crystal structure, while Y-211 is orthorhombic [68].

5.5. Growth of RE-123 single crystals

The fabrication of large Y-123 single crystals is made difficult by the very low solubility of Y in the Ba-Cu-O melt at growth temperature and a steep liquidus slope near the Y-123 peritectic temperature [70]. The primary crystallisation area of Y-123 (Figure 5) is bounded by the melt compositions of the reactions (2)–(4). Reaction (2) is eutectic, while reactions (3) and (4) are peritectic [59].

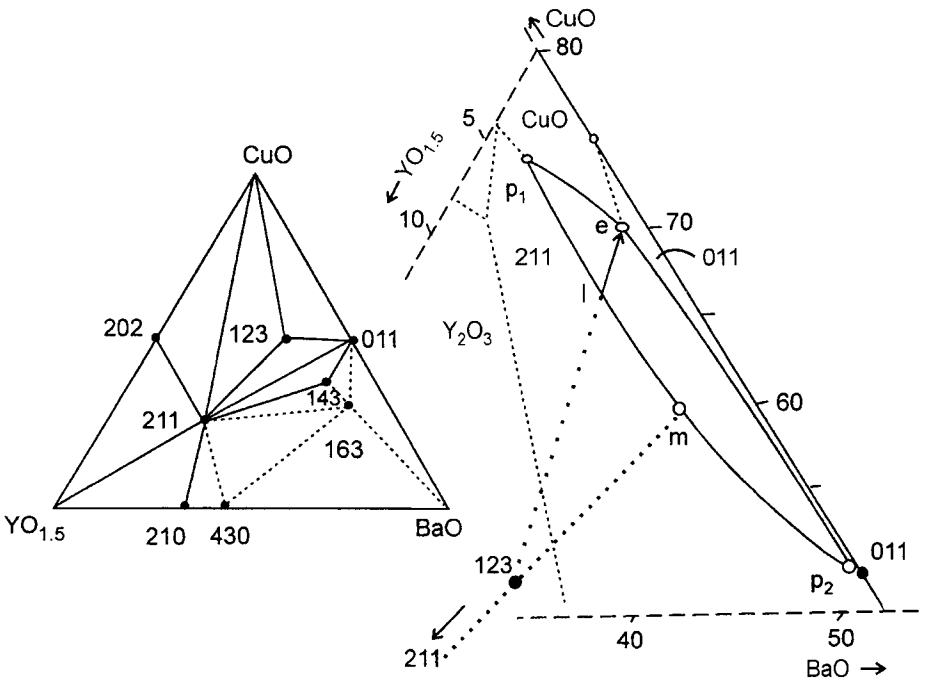


Figure 5. The primary crystallisation field of Y-123 [after 59]. The path *l*–*e* is the most suitable for crystal growth. p = peritectic reaction, e = eutectic reaction, m = melting reaction, p_1 = equation (3), p_2 = equation (4), e = equation (2) and m = equation (1). The inset shows phases existing in the pseudo-ternary phase diagram of $YO_{1.5}$-BaO-CuO at 890 °C in air [after 59]. 202 = $Y_2Cu_2O_5$, 011 = $BaCuO_2$, 430 = $Y_4Ba_3O_9$, which is stable only above 977 °C, 210 = Y_2BaO_4, 211 = Y_2BaCuO_5, 123 = $YBa_2Cu_3O_{6+\delta}$, 143 = $YBa_4Cu_3O_{8.5}$ and 163 = $YBa_6Cu_3O_{10.5}$.

It is difficult to obtain large Y-123 single crystals by a flux method, and a special solute-rich-liquid–crystal-pulling (SRL-CP) method has been developed [70]. In this method the $3BaCuO_2 \cdot 2CuO$ solution is maintained in a temperature gradient so that Y-211 can exist at the bottom of the crucible as an Y source for solute. The means for increasing crystal growth rate are: (i) use of high oxygen partial pressure, (ii) selection of RE elements with higher solubility in the solution and (iii) growth of RE-123 crystals containing several RE elements. Sm and Nd have

maximum solubility and minimum liquidus slope near the peritectic temperature, T_p. The oxygen-controlled melt growth method (OCMG) has been found to be good for the production of high-T_c Nd-123 and Sm-123 bulk superconductors, suggesting that low $p(O_2)$ is an effective T_c-controlling parameter for producing RE-123 superconductors [70]. With the use of low $p(O_2)$, Nd-123 single crystals have also been grown by top-seeded solution-growth (TSSG), traveling-solvent floating-zone (TSFZ) and flux-grown (FG) methods [71]. Growth by the TSSG method of Nd-123 single crystals with a sharp superconducting transition at about 95 K ($\Delta T = 0.5$ K) has been reported [71].

The standard annealing procedure for single crystals consists of treatment under $p(O_2) = 1$ atm at around 500 °C for 100–200 h, followed by quenching to room temperature [72]. Such crystals show T_cs above 90 K. The same oxygen content can be achieved by annealing at higher temperatures under increased $p(O_2)$. At high pressures, the oxygen diffusion constants are larger and the time needed for the oxygenation of the crystals decreases. Oxygen-deficient $YBa_2Cu_3O_6$ crystals have been obtained after annealing Y-123 crystals at 840 °C in an Ar atmosphere [73]. This annealing temperature was selected from the results of DTA, which showed that $YBa_2Cu_3O_6$ decomposes under an Ar atmosphere at 864 °C.

5.6. Formation of Bi,Pb-Sr-Ca-Cu-O superconductors

Bi_2O_3, PbO, $SrCO_3$, $CaCO_3$ and CuO have been used as starting materials in solid-state reactions to obtain Bi-based materials [13,74]. Bi and Pb oxides volatilise close to the calcination temperature [75]. Carefully selected precursor systems are required in the synthesis to lower the calcination temperatures and shorten the reaction times. Bi-based HTSC can be stabilised only in a narrow temperature range, owing to their complicated many-body composition. TG-DTA shows that phase formation and decomposition reactions occur at temperatures above 780 °C [75,76]. The formation reactions, as well as, melting and decomposition processes occur at lower temperatures in an N_2 atmosphere than in an O_2 atmosphere [76,77]. An increase in the Ca content of the Bi material lowers the melting point. Bismuth and thallium superconductors are formed by the decomposition of the primary phase [13]. Thus, $Bi_2Sr_2CaCu_2O_{8+\delta}$ (Bi-2212) is formed first and then decomposes to $(Bi,Pb)_2Sr_2Ca_2Cu_3O_{10+\delta}$ (Bi,Pb-2223). Bi(Pb)-2212 is transformed to Bi,Pb-2223 by relatively lengthy annealing procedures [75].

The Bi-2212 phase is thermodynamically stable over a wide temperature range and in the presence of most of the oxides existing in the Bi_2O_3-SrO-CaO-CuO system [78]. The Bi-2223 phase is stable only in a narrow temperature range and exhibits phase equilibrium with fewer components. Even small variations in the stoichiometry or temperature result in different phase compositions and dramatically affect the volume fraction of Bi-2223 in the prepared material. This

behaviour must be taken into account in the processing of wires and tapes. Considering that the Bi,Pb-2223 phase, in turn, is in equilibrium with Bi(Pb)-2212, Ca_2CuO_3, $Sr_{14}Cu_{24}O_{41}$, CuO, Ca_2PbO_4, $Pb_4Sr_5CuO_{10}$ and a liquid existing in the Bi_2O_3-PbO-SrO-CaO-CuO system, there may be as many as 40 phase regions, with very narrow ranges in stoichiometry, surrounding Bi,Pb-2223 [78]. Phase characterisation can be made by high-temperature XRD, equipped with an optical microscope for a direct observation of melting and solidification, and TG-DTA or DSC measurements can be applied to determine the phase transformation temperatures [79–83]. A schematic representation of the single-phase region of the Bi,Pb-2223 phase at 850 °C in air is presented in Figure 6.

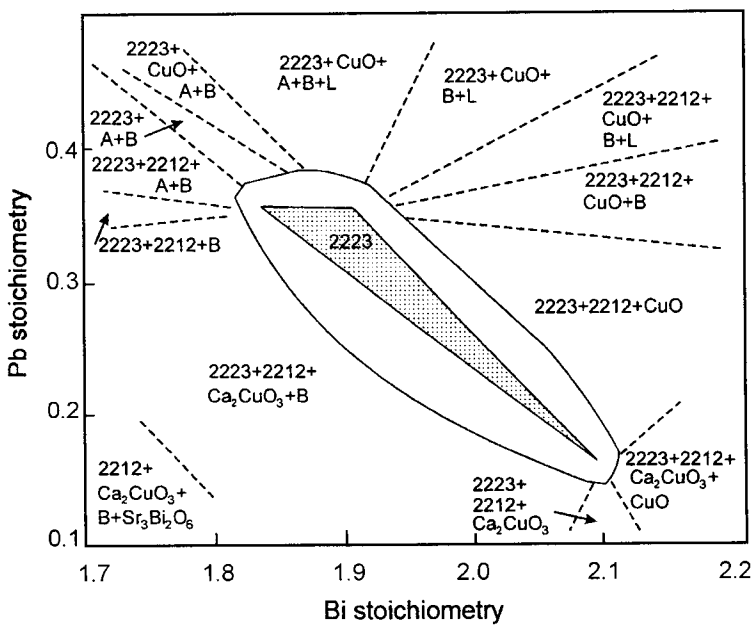


Figure 6. Schematic section through the single-phase region of the Bi,Pb-2223 phase at 850 °C including part of the surrounding phase regions [after 78]. The two- and three-phase equilibria which exist in the oval area around the single-phase region are not presented here. 2223 = Bi,Pb-2223, 2212 = Bi(Pb)-2212, A = $Pb_4Sr_5CuO_o$, B = $Sr_{14}Cu_{24}O_{41-\delta}$ and L = liquid.

In studies of the formation of Bi,Pb-2223 from mixed metal oxide and carbonate powders, according to TG-DTA curves, after the decomposition of $CuCO_3$ by 400 °C, the decomposition of $CaCO_3$ and $SrCO_3$ continued up to 820 °C, where the superconducting phase started to form [84]. When the Bi,Pb-2223 phase formation was studied with different lead contents, the endotherms seen between 700 and 880 °C shifted to lower temperatures when the lead content was increased [85].

Between the lowest and highest lead content (from 0 to 0.6 mol per formula unit) the downward shift in temperature of the last endothermic peak was 15 °C.

The DTA result for the calcined powder of Bi,Pb-2223 showed a clear endotherm around 850 °C, which is believed to indicate the transformation of Bi(Pb)-2212 to Bi,Pb-2223 [74,86]. It is suggested that the endotherm arises from two reactions: (i) a eutectic-like partial melting of the Bi(Pb)-2212, Ca_2PbO_4 and CuO phases and (ii) a formation of Bi,Pb-2223 from Bi(Pb)-2212 and a liquid phase. It has been shown that Ca_2PbO_4 promotes the formation of Bi,Pb-2223. Large amounts of Ca_2PbO_4 result in more liquid and the diffusion rate is then enhanced. DSC curves of Bi,Pb-2223 samples during cooling demonstrate that the solidification temperature varies in different atmospheres [81]. Crystallisation takes place at higher temperatures in an oxygen atmosphere than in air or an argon atmosphere. The exothermic peaks move to lower temperatures as the cooling rates increase.

A serious problem in Ag-sheathed Bi-2212 wires is oxygen release from the material during processing [87]. According to TG measurements of calcined $Bi_2Sr_2CaCu_2Ag_xO_\sigma$ samples, the release of oxygen can be suppressed by Ag doping [87]. The melting point of Ag-doped Bi-2212 material decreases with decreasing $p(O_2)$ and increasing Ag doping. As the $p(O_2)$ decreased from 0.2 to 0.0 atm, the melting point of $Bi_2Sr_2CaCu_2Ag_{0.2}O_\sigma$ fell by 40 °C from 880 °C. The powders released less oxygen when they were calcined at temperatures close to the melting point. A DTA study has given information about the optimal synthesis temperature for the preparation of Bi,Pb-2223/Ag tapes [74]. The ideal sintering temperature for obtaining high critical current densities has been experimentally found to be 3–4 degrees above the onset temperature of the first endotherm in the DTA curve. The formation of Bi,Pb-2223 inside Ag-sheathed tapes from Bi,Pb-2212 was confirmed by *in situ* neutron diffraction (ND) measurements in air [88]. Pb diffused out from Bi,Pb-2212 up to 800 °C, and Pb-rich phases, such as Ca_2PbO_4 and $Pb_3(Bi,Sr)_3Ca_2CuO_\sigma$, were formed. Above 800 °C Pb diffused into Bi-2212, and Bi,Pb-2212 started to transform to Bi,Pb-2223 between 820 and 835 °C.

In the DTA curve of lead-free Bi-2223, two endotherms only 10 °C apart appeared, one on either side of the favourable sintering temperature range of 870–880 °C [89]. The decomposition temperatures of Bi-2212 and Bi-2223 are so close to each other, that it is difficult to produce large amounts of liquid from Bi-2212 inside the stability region of Bi-2223 [90].

5.7. Synthesis of Bi,Pb-Sr-Ca-Cu-O superconductors by coprecipitation methods

Several TA investigations have been reported relevant to the synthesis of bismuth-based superconductors by, in addition to solid-state reactions, coprecipitation and sol–gel methods [13].

A TG curve of metal oxalates, used as starting materials in the synthesis of Bi,Pb-based materials by coprecipitation, shows that first copper oxalate decomposes to copper oxide, and then bismuth and lead oxalates decompose to oxides, and calcium and strontium oxalates to carbonates (Figure 7) [91]. Above 400 °C, calcium and strontium carbonates decompose to oxides, and calcium oxide and lead oxide react to produce Ca_2PbO_4. In the DTA curve (inset Figure 7) the decomposition of oxalates is seen as exotherms where the oxidation occurs. The exotherm at around 400 °C is due to the pyrolysis of residual metal oxalates into carbonates and oxides [92]. The occurrence of complex endothermic reactions at higher temperatures is possibly related to the formation of intermediate products or phase transitions [93]. Melt formation starts in a Pb-free material at around 860 °C.

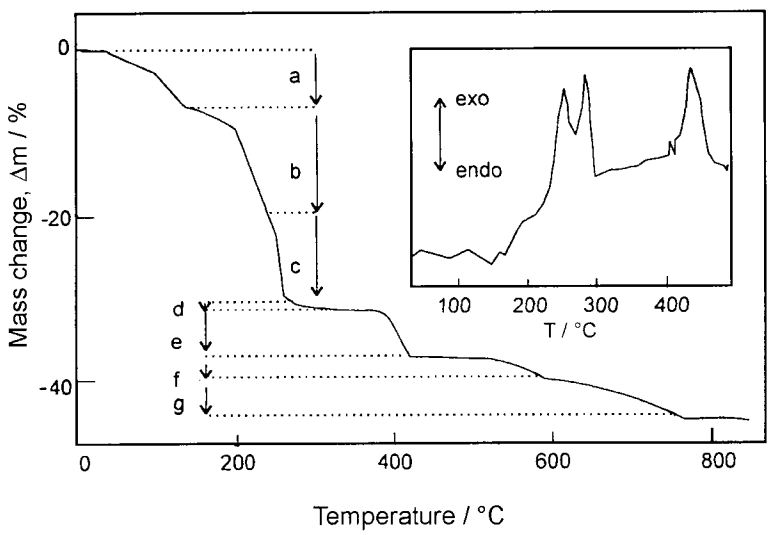


Figure 7. TG curve of coprecipitated oxalates in the preparation of Bi,Pb-2223 in air, heating rate 0.2 °C min^{-1} [after 91]. a: dehydration, b: $CuC_2O_4 + 0.5O_2 \rightarrow CuO + 2CO_2$, c: $Bi_2(C_2O_4)_3 + 1.5O_2 \rightarrow Bi_2O_3 + 6CO_2$, d: $PbC_2O_4 + 0.5O_2 \rightarrow PbO + 2CO_2$, e: $CaC_2O_4 \rightarrow CaCO_3 + CO$ and $SrC_2O_4 \rightarrow SrCO_3 + CO$, f: $CaCO_3 \rightarrow CaO + CO_2$ and $2CaO + PbO + 0.5O_2 \rightarrow Ca_2PbO_4$ and g: $SrCO_3 \rightarrow SrO + CO_2$. The inset shows a DTA curve, heating rate 2 °C min^{-1}.

In a TG study of the formation of the Bi,Pb-2223 phase from metal acetates in air, the TG curve first showed a gradual mass loss, and then two abrupt losses in the temperature region 200–550 °C [94,95]. The first abrupt loss was seen in the DTA curve as an endotherm at 230 °C and a sharp exotherm at about 250 °C, indicating, respectively, the dehydration and decomposition of polymerised acetates and other metal organic compounds present in the gel. The two endotherms at about 370 and 490 °C, near the second loss, corresponded to the decomposition of residual organic compounds and carbonates formed during pyrolysis. The crystallisation of the $Bi_2Sr_2CuO_{6+\delta}$ phase (Bi-2201) occurred between 470 and 590 °C, as seen in the TG curve as a gradual loss in mass. Ca_2PbO_4 was formed before 750 °C, and the endotherm in the DTA curve around 790 °C was attributable to the formation of Bi-2212. The endotherm at about 840 °C may be associated with the formation of Bi,Pb-2223, and the compound that melts at about 860 °C may also be Bi,Pb-2223.

5.8. Synthesis of Bi,Pb-Sr-Ca-Cu-O glass ceramics

The conventional solid-state method for preparing Bi,Pb-Sr-Ca-Cu-O ceramics produces poorly sintered materials of low density [96]. Processing *via* the glass-ceramic [97] route offers advantages such as improvement in homogeneity, reduced phase segregation, extended solid solubility and flexibility for moulding into various shapes [96]. Attention in the preparation of glass ceramics has been focused on optimising the starting compositions and processing conditions to obtain the desired material properties for particular applications. The most common method of preparation is to mix the starting powders of Bi_2O_3, Pb_3O_4 or PbO, $SrCO_3$, $CaCO_3$ and CuO, bring the mixture to a temperature above melting (1100–1400 °C) and stir. The glass can be formed in a twin-roller apparatus and is then subjected to metal-plate quenching [96]. Because an amorphous material is thermodynamically metastable, crystallisation occurs only at elevated temperatures [98]. The crystallisation is polymorphous when the amorphous material crystallises into only one phase with no changes in stoichiometry. In many cases, however, crystallisation occurs through complicated decomposition reactions and several phases precipitate at the same time (eutectic crystallisation) [98].

DSC and TG-DTA play an important role in the characterisation of the crystallisation [96]. From the various thermal and mass loss events, the glass transition temperature and crystallisation temperature can be determined [96]. From the information obtained by different thermal analysis techniques, the optimal heat-treatment conditions can be selected.

The first phase in the Bi-(Pb)-Sr-Ca-Cu-O series to crystallise upon heating of the amorphous powder is Bi-2201 (Figure 8A), and the last is Bi,Pb-2223 [96]. The crystallisation of Bi-2201 begins around 430 °C and is completed below

750 °C in air (Figure 8B). The formation of the Bi,Pb-2223 phase takes place around 830–850 °C. Between these two regions, Bi-2212 crystallises.

The endotherm in the DTA curve of melt-quenched Bi-2212 is due to the glass transition (T_g = 435 °C) and the exotherm is due to the crystallisation of $Bi_2Sr_2CuO_\sigma$ (Bi-2201) (T_x = 486 °C) [99]. Bi-2201 forms until Cu(II) is consumed [96]. After this, $Bi_2Sr_{3-y}Ca_yO_\sigma$ ($y \approx 1$) and Cu_2O are formed in the residual glass. At 780 °C a liquid is formed in an amount related to the amount of Cu_2O present. The oxidation of Cu(I) to Cu(II) yields Bi-2212. The DTA curve of the cooling Bi-2212 sample shows exothermic peaks at 920, 862 and 735 °C [100]. The peaks at about 860 and 735 °C are assigned to the crystallisation of Bi-2212 and Bi-2201, respectively.

The formation of the Bi-2212 and Bi,Pb-2223 phases is enhanced by the presence of partially melted phases containing Ca_2PbO_4 [96]. The glass transition temperature, T_g, has been reported to be as low as 400 °C for the Pb-containing Bi-2223 (Figure 8). Pb extends the glass-working range. The volume fraction of the Bi,Pb-2223 phase increases with the Pb content, but an excess of Pb lowers the formation temperature of intermediate products, and Sr_2PbO_4 forms as a result.

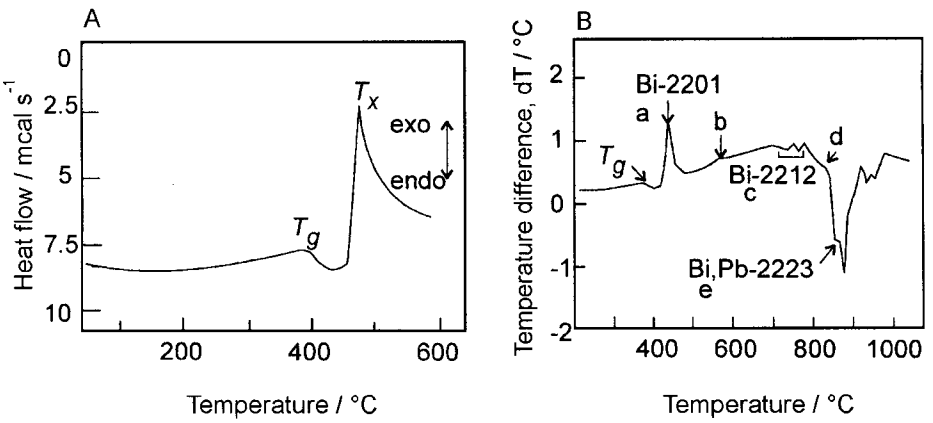


Figure 8. (A) DSC curve of $Bi_{1.5}Pb_{0.5}Sr_2Ca_2Cu_3O_\sigma$ glass in an Ar atmosphere, heating rate 40 °C min^{-1} [after 101]. T_g = glass transition temperature, 392 °C and T_x = crystallisation temperature, 473 °C, and (B) DTA curve of $Bi_{1.84}Pb_{0.34}Sr_{1.91}Ca_{2.03}Cu_{3.06}O_\sigma$ glass in air [after 96]. a: CaO, Cu_2O and Bi-2201 begin to crystallise, b: Ca_2PbO_4, CuO form, c: Bi-2201 + CaO + CuO → Bi-2212, d: Ca_2PbO_4 → CaO + PbO + liquid and e: Bi(Pb)-2212 + CaO + CuO → Bi,Pb-2223.

A modified Avrami or Kissinger analysis has been applied to determine E_a of the crystallisation of Bi-(Pb)-Sr-Ca-Cu-O glasses at the crystallisation temperature, T_x, by non-isothermal DSC [101,102]. In these modified analyses, ln (T_t^2/β) was plotted against $1/T_t$, where β is the heating rate and T_t the temperature at the top of the DSC peak at the crystallisation temperature [101], or ln $(\beta/(T_t - T_0))$ was plotted against $1/T_t$, where T_0 is the starting temperature in DSC measurements [102,103]. The temperature at the top of the peak has been selected on the assumption that the rate of the crystallisation reaction is maximum at T_t. E_a is calculated from the slope of the plot. E_a was about 395 kJ mol^{-1} for the crystallisation of a Bi-2212 glass [102] and about 292 kJ mol^{-1} of a $Bi_{1.5}Pb_{0.5}Sr_2Ca_2Cu_3O_\sigma$ glass [101].

5.9. Preparation of Tl-based superconductors

Tl-based HTSC have been prepared using pelletised Tl_2O_3 and Ba-Ca-Cu-O precursors as starting materials [104,105]. Use of a precursor matrix decreases the reaction time, lowers the synthesis temperature and thus minimises the evaporation of thallium(I) oxide (equations (5)–(7)) [106]. The pellets can be wrapped in Au foil [104]. The synthesis is carried out in a flowing oxygen atmosphere or in a sealed quartz tube at about 900 °C. A high pressure process has been developed to avoid thallium loss [107]. At high pressures, reaction temperatures can be raised.

$$Tl_2O_3(s) \rightarrow 0.5Tl_4O_3(s,l) + 0.75O_2(g) \quad p(O_2) = 1 \text{ atm}, T = 800 \text{ °C} \tag{5}$$

$$Tl_2O_3(s) \rightarrow Tl_2O(g) + O_2(g) \tag{6}$$

$$Tl_4O_3(s) \rightarrow 2Tl_2O(g) + 0.5O_2(g) \tag{7}$$

According to DTA measurements $Tl_2Ba_2O_5$ has a congruent melting point at 1100 °C, and has thus been used as a precursor material in the synthesis of both orthorhombic and tetragonal $Tl_2Ba_2CuO_{6+\delta}$ (Tl-2201) [45,107].

One method to prepare materials containing volatile components is through oxidation of alloys at moderate temperatures [45]. Heating $TlBa_2Ca_3Cu_4$ alloy in an oxygen atmosphere resulted in exothermic formation of oxides at temperatures as low as 300 °C [45]. Although the superconducting phase was not completely formed during the TG-DTA run, the experiment indicated a continuing oxidation reaction at 600 °C. The exothermic oxidation of $Tl_2Ba_2CaCu_2$ alloy in an O_2 atmosphere had started already at room temperature, and continued up to 350 °C where an endothermic reaction began due to oxygen release, followed again by an exothermic oxidation reaction [108]. Around 780 °C, thallium oxide evaporated.

The formation of (Tl,Bi,Pb)(Ba,Sr)$_2$Ca$_2$Cu$_3$O$_{9-\delta}$ (Tl,Bi,Pb-1223) competes with (Tl,Pb)(Ba,Sr)$_2$CaCu$_2$O$_o$, which acts as a diffusion barrier [45]. A TG-DTA study showed that heating up to 900 °C facilitated the crossing of this barrier, but also at $p(O_2)$ = 1 atm the Tl,Bi,Pb-1223 phase decomposed [45].

5.10. Preparation of Hg-based superconductors

Hg-based materials are typically prepared from HgO and Ba-Ca-Cu-O precursors, which are mixed and pressed into pellets [109,110]. The synthesis is carried out in a quartz tube, which is evacuated, sealed and encapsuled, for instance in steel tubing before heating to the reaction temperature (800 °C). The crucial problems in the synthesis are the decomposition of HgO above 500 °C (equation (8)) and the high vapour pressure of Hg. Also, $CaHgO_2$ is easily formed at about 550 °C.

$$2HgO(s) \rightarrow 2Hg(g) + O_2(g) \qquad (8)$$

Hg-based superconductors can also be prepared by a high-pressure, high-temperature technique [111]. $HgBa_2Ca_{n-1}Cu_nO_{2n+2+\delta}$ compounds melt peritectically, but under ambient pressure they decompose before melting [112]. When single crystals are grown, decomposition before peritectic melting can be avoided by encapsulation of the sample with a high hydrostatic Ar gas pressure until the melting temperature is reached. The peritectic decomposition temperature can be lowered with use of a PbO or $BaCuO_2 \cdot CuO$ flux. The crystallisation occurs at 1020–1070 °C at an Ar pressure of about 10 000 atm.

The formation of $HgBa_2CaCu_2O_{6+\delta}$ (Hg-1212) was investigated with precursor gels annealed under various atmospheres (flowing oxygen, air, vacuum) [113]. The gels were prepared from solutions of Ba, Ca and Cu acetates to which tartaric acid was added. The gel is highly sensitive to both moisture and CO_2, and the best Hg-1212 material was obtained with a vacuum-treated precursor. Cu must have been in oxidation state +I in this precursor, because the mass gain began around 350 °C in the TG curve recorded in air.

A BaO-CaO-CuO precursor used in the high-pressure synthesis of $HgBa_2Ca_2Cu_3O_{8+\delta}$ (Hg-1223) has been studied by DTA [114]. The DTA curve of a powder with a nominal composition of $Ba_2Ca_2Cu_3O_{7+\delta}$ exhibited two endotherms, one at about 850 and the other at about 910 °C. The Hg-1223 sample prepared from the precursor powder after calcination at 865 °C under a flowing oxygen atmosphere was nearly pure. The main phases present in the well-calcined precursor were $BaCuO_2$ and Ca_2CuO_3.

The preparation of Hg-1201 was studied by a static weight technique (SWT) in order to determine the mass of Hg(g) in the vapour phase [115]. Hg-1201 was

synthesised from $Ba_2CuO_{3+\delta}$ and HgO in sealed silica tubes. The vapour mass increased up to 600 °C under heating the starting mixture to 800 °C. Above 600 °C this mass decreased because Hg-1201 was formed from Hg(g) or HgO(g) and $Ba_2CuO_{3+\delta}$. The vapour mass was measured at constant $p(O_2)$ in heating or cooling regimes, and at constant T in increasing or decreasing $p(O_2)$. The p(Hg) and p(HgO) values were calculated from the total vapour mass applying the ideal gas law and the equilibrium constant of a formation reaction of HgO(g) from Hg(g) and O_2(g). The stability fields of both Hg-1201 and $BaHgO_2$ depend strongly on $p(O_2)$ [116]. At $p(O_2) = 0.2$ atm only Hg-1201 is stable when p(Hg) = 7 atm and $T = 850$ °C. At $p(O_2) = 0.8$ atm in addition to Hg-1201 also $BaHgO_2$ is stable and in equilibrium with the gaseous phase. At a lower $p(O_2)$ the synthesis of Hg-1201 is possible under a larger temperature range.

Thermobaric analysis (TBA) has been used in the measurement of total pressure of gases in the quartz tubes during syntheses of Hg-1223 and $CaHgO_2$ [117,118]. The TBA showed a temperature region where the synthesis pressure of the Hg-1223 phase is lower than that of $CaHgO_2$ and thus the synthesis of the superconducting phase is favoured. A simultaneous monitoring of temperature and pressure at high temperatures has been employed in the synthesis of Hg-1223, for example, in studies of the influence of heating and cooling rates, Re doping, and the oxygen content in the precursor [119,120].

6. THERMOANALYTICAL CHARACTERISATION OF BULK HTSC

6.1. Introduction

$REBa_2Cu_3O_{7-\delta}$ and $Pb_2Sr_2RE_{1-x}AE_xCu_3O_{8+\delta}$ (AE = Ca) display variations in the oxygen content that strongly influence their superconducting properties [121,122]. Also in the case of Bi-, Tl- and Hg-based systems [*e.g.* $Bi_2Sr_2CaCu_2O_{8+\delta}$ (Bi-2212), $Tl_2Ba_2CuO_{6+\delta}$ (Tl-2201) and $HgBa_2CuO_{4+\delta}$ (Hg-1201)], the T_cs change abruptly in response to even small variations in oxygen content [45,123,124].

6.2. $La_{2-x}Sr_xCuO_{4-\delta}$

Anomalies in the conductivity were first observed in the $La_{2-x}Sr_xCuO_{4-\delta}$ system: under ambient pressure, the conductivity first decreased drastically during heating from room temperature up to 150 °C and then increased again between 150 and 380 °C [125]. The TG curves characterised by a mass loss and gain clearly showed that this phenomenon was due to desintercalation and intercalation of oxygen.

Superconductivity in $La_{2-x}AE_xCuO_{4-\delta}$ (AE = Ca, Sr, Ba) compounds is observed only within a narrow range of alkaline-earth metal substitution [126]. The highest T_c of 37 K has been observed for $La_{1.85}Sr_{0.15}CuO_{3.98}$. Variations in oxygen stoichiometry with Sr in $La_2CuO_{4-\delta}$, measured by TG, are shown in Figure 9.

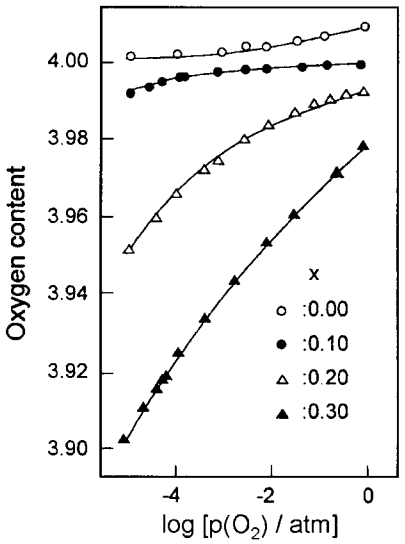


Figure 9. Oxygen content of $La_{2-x}Sr_xCuO_{4-\delta}$ as a function of $p(O_2)$ and Sr content (x) at 900 °C [after 127].

6.3. $YBa_2Cu_3O_{7-\delta}$

6.3.1. Oxygen stoichiometry in Y-123

The oxygen stoichiometry of $YBa_2Cu_3O_{7-\delta}$ varies widely ($0<\delta<1$) with the conditions of synthesis [128]. During high-temperature synthesis the tetragonal, non-superconducting form of the Y-123 phase is formed. When the cooling is performed in air, oxygen passes into the structure and a superconducting phase (T_c = 90 K) with orthorhombic structure results. The highest oxygen content obtained by annealing in a flowing oxygen atmosphere around 440 °C has been $\delta = 0.04$, *i.e.* slightly below the stoichiometric value [121].

The oxygenation and deoxygenation processes of Y-123, as well as the oxygen diffusion coefficients (D), have been studied by TG. D is largely independent of $p(O_2)$ but depends on the oxygen non-stoichiometry [129–131]. Oxygen diffusion occurs faster in the orthorhombic than the tetragonal phase [129]. The oxygen uptake in Y-123 is an activated process, and an E_a value of 74 kJ mol^{-1} has been determined for orthorhombic Y-123 in air, and a value of only 31 kJ mol^{-1} for tetragonal [129]. The oxygen desorption activation energy of orthorhombic Y-123 increased from 184 to 290 kJ mol^{-1} when the temperature increased from 500 to 650 °C [132]. A minor increase in E_a was observed in the tetragonal phase in the temperature range of 650–800 °C. The E_a values were obtained by DTG (derivative thermogravimetry). The chemical diffusion coefficient of Y-123 ($\delta \approx 0.1$) was calculated to be $\sim 1 \cdot 10^{-10}$ cm^2 s^{-1} in a powder sample at 500 °C [133].

The value of the coefficient is two or three orders of magnitude greater for sintered than for non-sintered samples [134]. The chemical diffusion coefficients reported in the literature range rather widely and their temperature dependencies in Arrhenius plots are only approximately linear [134,135].

In samples that were highly textured due to preparation by a zone-melting method, the mechanism for oxygen absorption could be divided into chemical reaction and diffusion parts, with E_a values in an oxygen atmosphere of 105 kJ mol^{-1} and 68 kJ mol^{-1}, respectively [136]. Pure oxygen is the best atmosphere for oxygen absorption of Y-123 crystals. The oxygen content reaches the maximum value fastest at 450 °C (Figure 10).

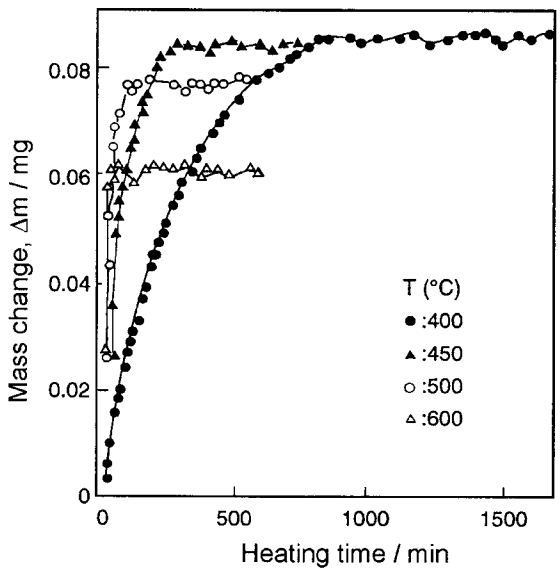


Figure 10. Mass change, Δm, *vs.* heating time in the oxygen absorption process at various temperatures at $p(O_2) = 1$ atm in highly aligned Y-123 samples [after 136].

The oxygen diffusion into an orthorhombic Y-123 has been observed to be faster than its diffusion out from Y-123 [44]. The observed differences in oxygen in- and out-diffusion in O_2 and $1\%O_2/Ar$ atmospheres at 400 °C were assumed to be connected to the experimental conditions. At lower temperatures (<325 °C) the so called moving boundary mechanism was used to explain the differences between in- and out-diffusion. According to the moving boundary mechanism, the oxygen out-diffusion from a crystallite interior can be slowed down due to a barrier created by an oxygen depleted surface layer.

As seen in Figure 11A, oxygen release and uptake of a nearly stoichiometric Y-123 material in an O_2 atmosphere are reversible if the heating and cooling cycles are carried out under the same conditions [121]. In the case of an oxygen-deficient Y-123 with $\delta = 0.82$ (determined by iodometric titration) heated in oxygen (Figure 11B), a mass gain starts at about 200 °C, whereafter O_2 incorporates in the structure until a balance between O_2 gain and loss is achieved at 360 °C ($\delta = 0.12$) [121]. After this, a continuous mass loss occurs. The overall mass loss is due to the loss of oxygen [47]. The final composition of the oxygen-deficient Y-123 phase has the δ value 0.89 at 900 °C [121]. The oxygen stoichiometry is recovered on cooling, and at the end point the δ value is 0.14. DSC measurements have shown that the oxygen release process is endothermic, while the oxygen incorporation into the lattice is an exothermic reaction [15,137]. Somewhat different results have been reported for other experiments in an O_2 atmosphere: mass gain was registered up to 530 °C, and loss of oxygen occurred above 630 °C [75].

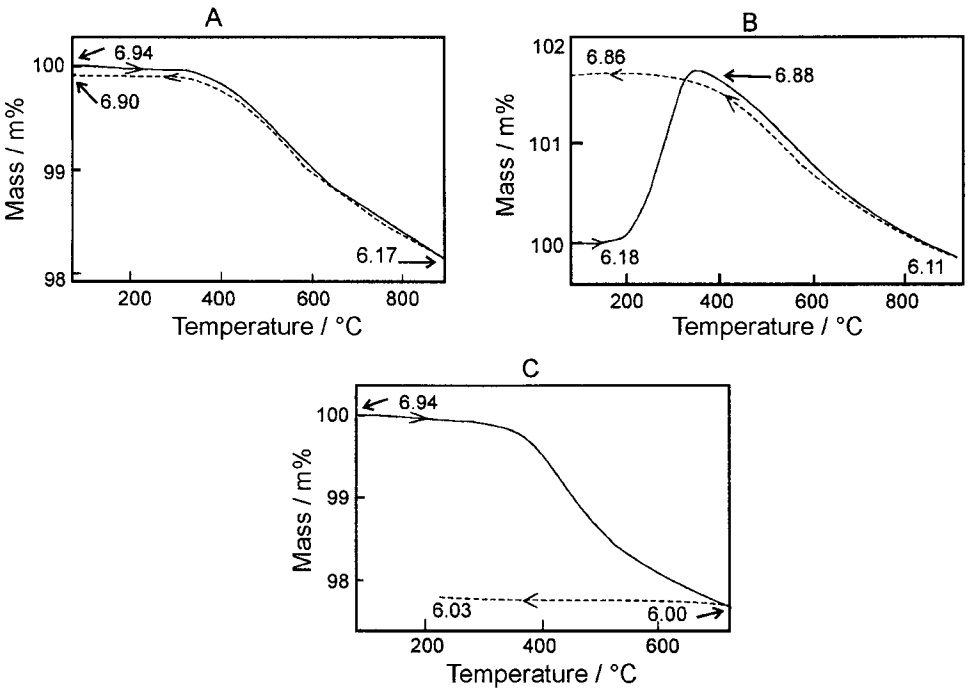


Figure 11. Oxygen uptake and release in Y-123 materials under different atmospheres [after 121]. (A) Nearly stoichiometric $YBa_2Cu_3O_{7-\delta}$ in an O_2 atmosphere, heating and cooling rates 2 °C min^{-1}, (B) oxygen-deficient Y-123 in an O_2 atmosphere, heating and cooling rates 1 °C min^{-1} and (C) nearly stoichiometric Y-123 in an N_2 atmosphere, heating rate 2 °C min^{-1} and cooling rate 20 °C min^{-1}.

In an N_2 atmosphere, as in an O_2 atmosphere, a rapid mass loss was found to begin at 350 °C, but the composition with $\delta = 1.0$ was already reached at about 750 °C (Figure 11C) [121]. The step from $\delta = 0$ to $\delta = 1$ implies a mass loss of 2.4% in TG [45]. The composition is maintained during cooling [121]. The oxygen stoichiometry of a sample heated in an N_2 atmosphere can be increased again during cooling in an oxygen-rich atmosphere [128].

van't Hoff plots (Figure 12) can be applied to determine enthalpies for the oxidation processes of HTSC materials [138]. A van't Hoff plot is a diagram of the logarithm of oxygen partial pressure (log $p(O_2)$) versus the reciprocal temperature ($1/T$) [12,138]. Straight lines obtained from van't Hoff plots of R ln $p(O_2)$ *vs.* $1/T$ (R is the gas constant) for a given oxygen deficiency value, δ, give $\Delta H_{O2}(\delta)$, and RT ln $p(O_2)$ *vs.* T give $\Delta S_{O2}(\delta)$ [12,139,140]. $\Delta H_{O2}(\delta)$ and $\Delta S_{O2}(\delta)$ represent the enthalpy and entropy change, respectively, when 1 mol of $O_2(g)$ is dissolved in material with an oxygen deficiency [140]. The enthalpies for the oxidation processes of Y-123, evaluated from the slopes of isocompositional lines in van't Hoff diagrams were, for orthorhombic and tetragonal modifications of Y-123, -225 and -200 kJ mol^{-1} per O_2, respectively [15,141]. Applying the so called oxygen vacancy model, the dependence of ΔH and ΔS on $p(O_2)$ for the reaction of the oxygen vacancies formation during the oxygen release from Y-123 can be calculated [44]. The equation combines the oxygen content in Y-123 with the temperature and $p(O_2)$.

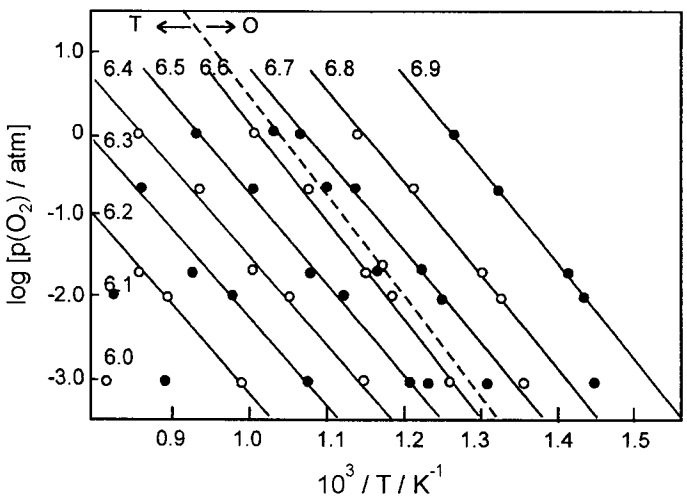


Figure 12. Isocompositional plots of $YBa_2Cu_3O_{7-\delta}$, log $p(O_2)$ *vs.* reciprocal T [after 15]. The dashed line shows the O-T transition.

6.3.2. O-T transition in Y-123

TG analyses of Y-123 show no discontinuity in the δ value in the orthorhombic (O) to tetragonal (T) phase transition area when $p(O_2)$ varies in the range 10^{-4}–1 atm [142]. This is an indication that the O-T transition is higher than first-order. The TG scans convey more information than simply the mass changes: even though the system is not necessarily at equilibrium, changes in the slope are indicative of phase changes [143]. The O-T transition is seen as a distinct inflection point or a change in slope of the TG curve (Figure 11A), or as a minimum or maximum in the DTG curve [47,144]. The point at which the structure transforms from an orthorhombic to a tetragonal structure can be induced thermally, but it depends on $p(O_2)$ as well (Figure 12) [138,145], as has been revealed by *in situ* XRD measurements [146]. The heating or cooling rates also affect the transformation point. According to TG studies, the O-T transition of Y-123 is not located at any constant δ value, but the phase boundary has a slope of $d\delta/dT \approx -4.7 \cdot 10^{-4}$ K^{-1} [144] and δ can be expressed between 550 and 700 °C by a linear approximation: $\delta_{O\text{-}T} = 0.848 - 4.83 \cdot 10^{-4}T$ [134,147]. The high-temperature XRD data showed that heating of a fully oxidised sample in air results in a smooth O-T transition near 600 °C [145,148]. *In situ* powder neutron diffraction (PND) measurements showed that the O-T transition occurs near 700 °C in pure oxygen, and O atoms are lost from the 1-dimensional Cu-O chains during heating [149,150]. The oxygen deficiency value, δ, was close to 0.5 at the transformation point [149]. The transformation into a tetragonal structure is the combined result of thermally induced deoxygenation and disorder in the remaining fraction of the oxygen atoms in the Cu-O chains [134,149]. During heating, a tetragonal, oxygen-deficient Y-123 material (δ = 0.74) transformed to orthorhombic at about 390 °C in a pure oxygen atmosphere [151].

The change in length or volume of Y-123 due to the T-O transition can be followed by isothermal dilatometry [138]. A change in length occurs as the atmosphere is changed at constant temperature. A volume change in a dense polycrystalline sample leads to microcracking, which provides increased surface for gases to penetrate into the sample and, as a result, there is a significant increase in the rate of oxidation. The cracks are detrimental for the superconductivity, however.

When a tetragonal sample of Y-123 with δ = 0.8 was heated or cooled in an N_2 atmosphere, a nearly constant change was observed in thermal expansion [152]. The coefficient of thermal expansion (CTE) was $10.7 \cdot 10^{-6}$ $°C^{-1}$. The initial CTE when an orthorhombic sample ($\delta \approx 0$) was heated in air was $12.9 \cdot 10^{-6}$ $°C^{-1}$, but a larger value was obtained for the expansion between 450 and 650 °C.

6.3.3. O-T transition in the RE-123 series

As can be seen from the DSC and TG results in Table 4, in the RE-123 series the transformation temperature tends to increase with the decreasing ionic radius of the RE element, and the oxygen deficiency at the transformation point increases with the transformation temperature [153]. For La-123 the temperature of the T-O transition was measured by DSC, while for all other RE-123 compounds the O-T transformation point was measured by TG. In the case of La-123, the endothermic signal corresponding to deoxygenation was much larger than the discontinuous change in the specific heat in the O-T transition area and, for this reason, the transition temperature was determined from the anomalies observed in the DSC curve during cooling [154].

Table 4.
O-T transition temperatures in the RE-123 series in an oxygen atmosphere [153,154].

RE element	Transition temperature /°C	Oxygen deficiency, δ
La	485	
Nd	566	0.140
Sm	615	0.157
Eu	633	0.178
Gd	641	0.171
Dy	672	0.284
Ho	691	0.255
Y	686	0.318
Er	699	0.201
Tm	706	0.300
Yb	681	0.193

La-123: DSC measurements during cooling; Nd-123–Yb-123: TG measurements; the initial δ values were not determined, Yb-123 contained impurities.

6.3.4. Evolved gases

O_2 and CO_2 release from Y-123 during heating has been determined by mass spectrometric evolved gas analysis [51]. CO_2 originates from the unreacted $BaCO_3$, which has either been used as starting material or formed during synthesis. The mass loss around 350 °C in the TG or DTG measurements was due to release of O_2 from the sample, because the EGA curve of a sample heated in an Ar atmosphere showed that O_2 is released from 350 °C, followed by CO_2 at around 540 °C. The maximum release was detected at 530 °C for O_2 and 800 °C for CO_2.

6.3.5. Microstructural changes in Y-123

Emanation thermal analysis (ETA) can be applied to obtain information on the microstructural changes occurring at the nanometre level during heating of a superconductor under oxygen or hydrogen atmospheres [155].

^{220}Rn atoms were incorporated to a depth of about 80 nm from the surface of Y-123 powder particles, locating in structural defects which served as paths or traps for their diffusion [155]. The onset temperature value in the ETA curve, recorded in an oxygen atmosphere, was located at 385 °C, indicating a change in the microstructure of the Y-123 sample. A rapid increase in the release rate of the radon atoms indicated the creation of many new paths for the diffusion of Rn. Around 700 °C, where the O-T transition took place, a sharp decrease occurred in the release rate of radon atoms. In the ETA curve recorded in a hydrogen atmosphere, the decrease in the rate of ^{220}Rn release was detected around 500 °C. On the basis of TG data ($\delta = 1$), this was concluded to mark a decomposition point of the structure. The peak in the ETA curve around 400 °C was associated with the O-T transition.

6.3.6. Oxygen isotope exchange

It was first shown by the isotope effect that the molar mass is related to the superconducting transition temperature [156]. Because the properties of HTSC are affected by the oxygen isotope in only a minor way, it is important that samples be well-characterised [128]. Y-123 samples containing high ^{18}O content can be prepared by oxidising appropriate metals in an $^{18}O_2$ atmosphere [44,157]. The resulting oxygen isotope ratio in the sample can be determined by a TG measurement. In a natural oxygen atmosphere the isotope exchange takes place in the temperature range 300–470 °C.

The interaction between the ^{16}O-containing solid oxide and the gas phase enriched in ^{18}O isotope has been investigated in Nd-123 by dynamic thermal heating in decreased $p(O_2)$ [158]. Adsorbed H_2O and CO_2 molecules, which disturb the oxygen isotope exchange measurements, were removed from the sample surface by heating the sample to 300 °C. The isotopic composition of the sample changed in the studied temperature range through diffusion and oxygen exchange processes, with the highest exchange rate observed from 400 to 500 °C. In the dominating exchange reaction, which was classified as partially heterogeneous, some of the ^{16}O atoms (in the solid) on the phase boundary reacted with $^{18}O_2$(g) molecules producing $^{16}O^{18}O$(g) and ^{18}O(in the solid). As determined by quadrupole mass spectrometry, some of the $^{16}O^{18}O$(g) molecules so formed reacted with ^{16}O(in the solid) and liberated $^{16}O_2$(g).

6.3.7. Sensitivity to moisture or CO_2

The thermochemical reactivity of HTSC with CO_2 and moisture works against their long-term stability [75]. Y-123 reacts with water and liberates oxygen [138]. A long-time exposure of the material to high humidity degrades its electrical properties, presumably as a result of both reduction and the formation of insulating hydroxides [18]. The moisture present in the material results during heating in a mass gain because of hydroxide formation, but when the hydroxides become unstable a mass loss is observed in a TG curve [138].

Even small amounts of CO_2 (0.01%) in the atmosphere alter the normal TG curve of Y-123 samples [18]. CO_2 is soluble in the Y-123 lattice to some extent and, as a result, non-superconducting $YBa_2Cu_{3-z}(CO_3)_zO_{6-3z/2+\delta}$ oxide carbonates ($z \approx 0.2$) are formed [134]. The TG curves recorded under higher concentrations of CO_2 indicate a total decomposition of Y-123 at elevated temperatures and $BaCO_3$ is regenerated [18]. If $p(CO_2)$ is lowered, $BaCO_3$ will react again, to reform the Y-123 material. The mass gains indicate that, in a pure CO_2 atmosphere, the total decomposition of Y-123 to form $BaCO_3$ occurs by 800 °C [138].

6.4. Thermal stability of $YBa_2Cu_4O_8$

TG measurements have been applied to check the purity of the $YBa_2Cu_4O_8$ (Y-124) product, to determine whether it contains Y-123 or $Y_2Ba_4Cu_7O_{15-\delta}$ (Y-247) as an impurity. In a pure oxygen atmosphere, Y-123 loses oxygen beginning at about 400 °C and Y-247 beginning at about 500 °C, while Y-124 decomposes to $YBa_2Cu_3O_{6+\delta}$ and CuO above 800 °C [159,160]. According to DTA studies at $p(O_2) = 1$ atm the decomposition of Y-124 to Y-123 proceeds *via* the Y-247 phase [161]. Oxygen atoms are more tightly bound in the double Cu-O chains of the Y-124 structure than in the single Cu-O chains of Y-123 [52] and thus in an inert atmosphere Y-124 is stable even up to 670 °C (Figure 13) [23].

6.5. $Pb_2Sr_2(Y,Ca)Cu_3O_{8+\delta}$

The greatest variation in the oxygen content of a HTSC material occurs in the $Pb_2Sr_2RE_{1-x}AE_xCu_3O_{8+\delta}$ (AE = alkaline-earth metal) system [18]. $Pb_2Sr_2Y_{1-x}Ca_xCu_3O_{8+\delta}$ (Pb-2213) becomes superconducting at about 80 K when Ca^{2+} ions are substituted for some of the Y^{3+} ions [122,162]. In this case, the extra positive charge oxidises the Cu^{2+} ions in the $Cu\text{-}O_2$ planes, but not Pb^{2+} to Pb^{4+} or Cu^+ to Cu^{2+} in the [(Pb-O)-(Cu-O_δ)-(Pb-O)] blocks, as might be expected. The optimum in the superconductivity is reached when the oxygen content is essentially 8.0 mol per formula unit. The structure is orthorhombic at that point. When the material is annealed, it takes up large quantities of oxygen to the [(Pb-O)-(Cu-O_δ)-(Pb-O)] blocks and transforms to a semiconducting tetragonal modification.

When Pb-2213 is heat-treated at 450 °C in an O_2 atmosphere it takes up oxygen, and after about 20 h the mass gain, as determined by isothermal TG measurements, corresponds to $\delta = 1.9$ [122]. Conversely, if the same product is heat-treated at 500 °C in an N_2 atmosphere it loses oxygen and goes back to $\delta \sim 0.0$. The oxygen uptake suppresses the superconducting transition, which is re-established by heating the sample at the same temperature in an N_2 atmosphere. Under O_2-containing atmospheres the oxygen-deficient material is reversibly oxidised at 300–600 °C (Figure 14A) [162]. The oxygen content saturates at only these two limit values [27]. Above 630 °C the compound undergoes an oxidative decomposition, which depends on $p(O_2)$ and the substituents [162]. Pb is oxidised and a second phase is formed also having a perovskite structure. At low $p(O_2)$ the structure undergoes an O-T transition near 750 °C.

In an O_2 atmosphere, anomalously great expansion in Pb-2213 begins at 300 °C [138,152]. Two maxima of about 1.4% are observed in the expansion near 550 and 700 °C. Inspection of the dilatometer data against the TG curve shows that a gain or loss of oxygen is accompanied by an increase or decrease in length. When the oxygen content of the atmosphere is increased isothermally at 550 °C, expansion is found for Pb-2213 but shrinkage for Y-123 (Figure 14B).

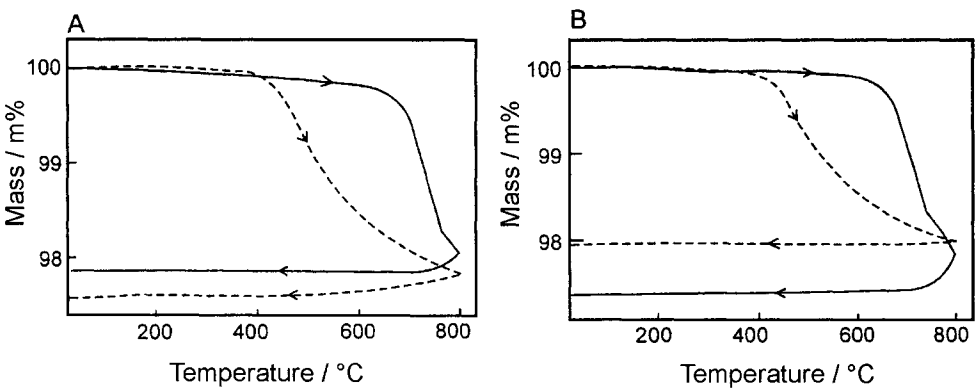


Figure 13. TG curves recorded in a flowing N_2 atmosphere, heating and cooling rates 5 °C min^{-1}, for (A) $Y_{0.5}Sm_{0.5}$-124 (–) compared to that of $Y_{0.5}Sm_{0.5}$-123 (- - -) and (B) $Y_{0.5}Nd_{0.5}$-124 (–) compared to that of $Y_{0.5}Nd_{0.5}$-123 (- - -) [163,164].

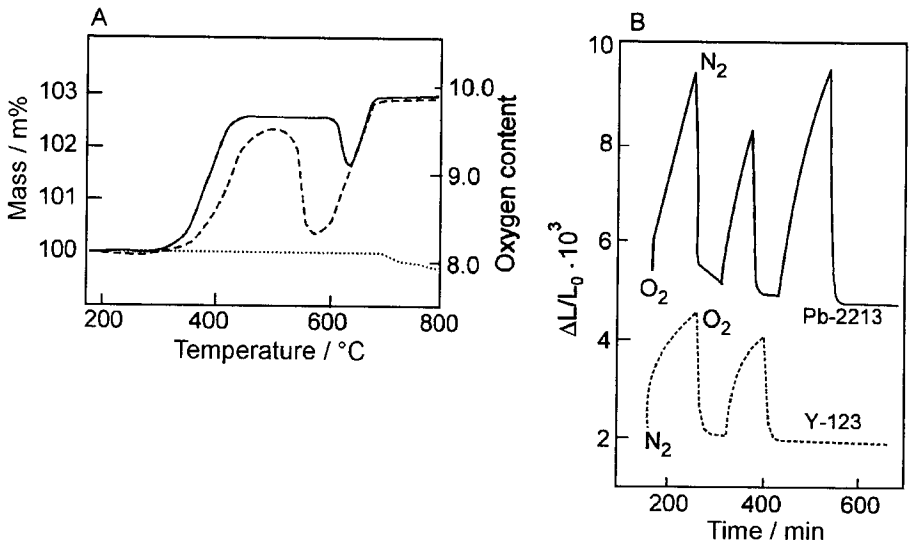


Figure 14. (A) TG curves of $Pb_2Sr_2Y_{0.60}Ca_{0.40}Cu_3O_{8.08}$ in an O_2 atmosphere (–), air (- - -) and at $p(O_2) = 60$ ppm, in an N_2 atmosphere (·····), heating rate 2 °C min^{-1} [after 162], and (B) isothermal expansion of $Pb_2Sr_2YCu_3O_8$ (–) compared to $YBa_2Cu_3O_{7-\delta}$ (- - -) in O_2 and N_2 atmospheres at 550 °C [after 152].

6.6. Bi-, Tl- and Hg-based superconductors

6.6.1. Bi-based systems

The oxygen loss is less in single phase Bi-, Tl- and Hg-containing HTSC than in Y-123 and thus the low temperature mass loss is also much smaller. The oxygen non-stoichiometry in Bi-based materials depends on the oxygen vacancies existing in double Bi-O layers [76]. Thermal treatment of these materials leads to a loss of small amounts of oxygen when the temperature is close to the melting point. The process is reversible if the heating is performed in the presence of oxygen.

In as-prepared Bi-2212 material the mass loss upon heating the sample in air to 850 °C was 0.17%, which corresponds to 0.1 mol oxygen per formula unit [22]. During cooling back to room temperature only 0.07% mass was regained. As a result of this thermal cycle, the T_c^{onset} increased from 68 to 77 K. When the Bi-2212 sample was cooled in an Ar atmosphere the mass loss was 0.16% and the corresponding T_c^{onset} was 95 K. This experiment shows how the critical temperature can be varied by changing the annealing conditions. Annealing in a low $p(O_2)$ atmosphere raises the T_c of a Bi-2212 sample [165]. Bi-2212 shows a parabolic (bell-shaped) change in T_c as a function of the oxygen content [123]. *In situ* high temperature XRD measurements have shown that the Bi-2212 material with a high T_c value (89 K) undergoes a T-O transition at about 600 °C in an Ar

atmosphere [166].

Knudsen cell mass spectrometric measurements showed oxygen loss from $Bi_{1.9}Pb_{0.35}Sr_{2.0}Ca_{2.2}Cu_{3.0}O_{10.2}$ in vacuum to occur between 650 and 700 °C [167]. The oxygen release corresponded to 1.6 mol per formula unit. Bi(g) was also observed as a vapour species. The optimal δ values to achieve the highest transition temperatures in $(Bi,Pb)_2Sr_2Ca_2Cu_3O_{10+\delta}$ are in the range 0.14–0.29 [168].

6.6.2. Tl-based systems

The structure of $Tl_2Ba_2CuO_{6+\delta}$ (Tl-2201) has both orthorhombic and tetragonal modifications, both of which may be superconducting [107]. The critical temperature varies between 0 and 90 K. The T-O transition can be achieved by annealing a tetragonal Tl-2201 sample in an oxygen atmosphere [45,169]. The oxygen content is increased by 0.15, resulting from a mass increase of 0.3%. This process is thermally activated with E_a = 78 kJ mol^{-1}. Thallium release begins already at 480 °C in a low $p(O_2)$ atmosphere [45,170].

Thallium oxide losses begin in $TlBa_2Ca_2Cu_3O_\sigma$ at about 900 °C [171]. In the DTA curve of $Tl_{0.6}Pb_{0.4}Ba_{0.4}Sr_{1.6}Ca_2Cu_3O_\sigma$ recorded in an oxygen atmosphere a large endothermic peak seen at 991 °C is due to the peritectic decomposition of $(Tl,Pb)(Ba,Sr)_2Ca_2Cu_3O_\sigma$ into (Tl,Pb)(Ba,Sr)-1212 and a mixture of Ba-Sr-Ca-Cu oxides (Figure 15). As seen in the TG curve (Figure 15), thallium oxide loss begins before the peritectic decomposition.

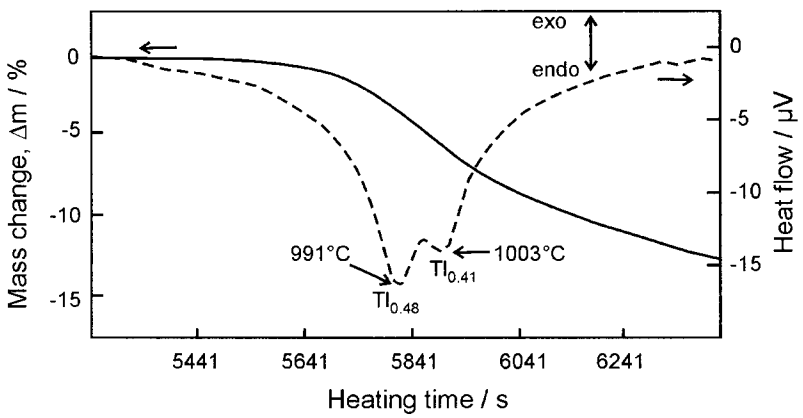


Figure 15. TG-DTA curves of $Tl_{0.6}Pb_{0.4}Ba_{0.4}Sr_{1.6}Ca_2Cu_3O_\sigma$ recorded in an O_2 atmosphere [after 171].

6.6.3 Hg-based systems

The Hg content in $HgBa_2CuO_{4+\delta}$ (Hg-1201) is lower than the stoichiometric value at commonly used synthesis conditions in a sealed tube at 800 °C [172]. A three-temperature static weight technique (SWT) was used in the determination of the Hg content in $Hg_{1-x}Ba_2CuO_{4+\delta}$ at a given $p(O_2)$ and $p(Hg)$. A CoO/Co_3O_4 or a Mn_2O_3/MnO_2 pair was used to adjust $p(O_2)$ inside the closed silica tubes. At fixed $p(O_2)$ a Hg-1201/$Ba_2CuO_{3+\delta}$ pair was used to control $p(Hg)$. From the computed $p(O_2)$–$p(Hg)$ and $p(Hg)$–T cross sections of the $p(O_2)$–$p(Hg)$–T phase diagram the maximum value of the Hg content was determined to be 0.84 in Hg-1201 when $p(O_2)$ = 0.42 atm, $p(Hg)$ = 4.5 atm and T = 800 °C. At a lower temperature under the same $p(O_2)$ and $p(Hg)$ values the Hg content can be increased close to the stoichiometric value (0.94 at 650 °C).

Hg-1201 and its precursor $Ba_2CuO_{3+\delta}$, have been studied in an oxygen atmosphere by TG-DTA in the temperature interval 20–1100 °C [173]. $Hg_\gamma O_\delta$ was released between 240 and 706 °C and metallic mercury and oxygen were released between 706 and 822 °C. After this the TG curve coincided with the curve of $Ba_2CuO_{3+\delta}$ and the resulting product was assumed to be $Ba_2CuO_{3.1}$ [173]. A parabolic (bell-shaped) variation of T_c with δ has been found in Hg-1201 [174]. The oxygen non-stoichiometry in these Hg-1201 samples was determined by TG measurements.

The oxygen release from $HgBa_2CaCu_2O_{6+\delta}$ (Hg-1212) in an inert atmosphere starts above 350 °C [109]. As confirmed by mass spectrometry the mass loss seen in TG curves below that temperature (Figure 16) is due to the evaporation of metallic mercury from grain boundaries. The endothermic peaks in the DTA curve above 600 °C are already associated with the decomposition of the material.

If oxygen-deficient $HgBa_2Ca_{n-1}Cu_nO_\sigma$ samples are post-annealed, the temperature corresponding to the maximum oxygen incorporation depends on both n and $p(O_2)$ [175]. The starting temperature of oxygen in-loading increases from about 220 °C to about 290 °C at $p(O_2)$ = 1 atm when going from n = 1 phase to n = 3 phase. A decrease in $p(O_2)$ seems to increase the optimum temperature for O_2 loading. When the $p(O_2)$ decreases the amount of incorporated oxygen also decreases. Irreversible reactions due to Hg loss occurred at $p(O_2)$ = 1 atm above about 420, 480 and 510 °C in Hg-1201, Hg-1212 and Hg-1223 samples, respectively [175]. Somewhat different results were obtained in a TG study where the equilibrium conditions of decomposition of Hg-1201 and Hg-1223 were determined in various $p(O_2)$ using van't Hoff plots [176]. The calculated decomposition temperatures at $p(O_2)$ = 1 atm were 376, 396 and 440 °C for Hg-1201, Hg-1212 and Hg-1223, respectively [176]. The decomposition temperature of Hg-1223 at $p(O_2)$ = 0.2 atm was measured to be only 406 °C. Judging from the TG data the oxygen content varied in $Hg_{0.92}Ba_{2.05}Cu_{1.03}O_\sigma$ from 4.04 to 4.11 and in $Hg_{0.75}Ba_{2.07}Ca_{2.07}Cu_{3.11}O_\sigma$

from 8.13 to 8.21 depending on $p(O_2)$.

The T_c^{onset} of an as-sintered Hg-1223 powder sample was increased from 117 to 133 K by oxygen annealing at 300 °C [177]. A similar kind of increase was achieved in single crystals of Hg-1223: TG measurements showed the crystals to be thermally stable when annealed under a flowing oxygen atmosphere at 300 °C for 72 h, while the T_c increased from 115 to 135 K [178]. At 550 °C a linear decrease in mass was recorded, possibly due to the decomposition of Hg-1223 [179]. Thallium substitution was found to improve the thermal stability of the Hg-1223 phase: a $Hg_{0.5}Tl_{0.5}Ba_2(Ca_{1-y}Sr_y)_2Cu_3O_{8+\delta}$ (Hg,Tl-1223) powder sample was stable under oxygen and argon atmospheres up to about 550 °C [180].

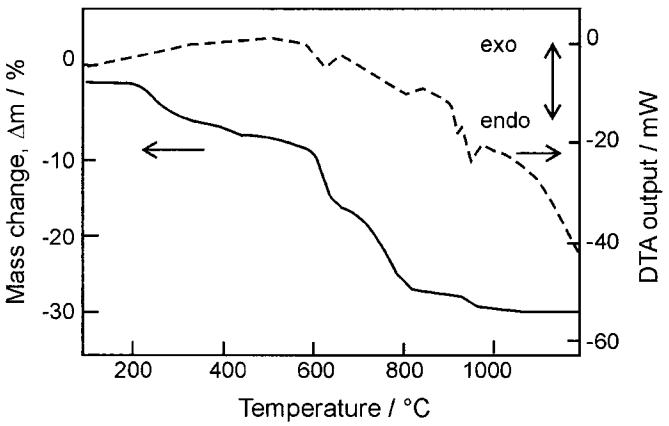


Figure 16. TG-DTA curves of $HgBa_2CaCu_2O_{6+\delta}$ recorded in an Ar atmosphere, heating rate 5 °C min^{-1} [after 109].

6.7. $RuSr_2GdCu_2O_{8-\delta}$

It seems that superconductivity in $RuSr_2GdCu_2O_{8-\delta}$ (Ru-1212) is in a great deal affected by the preparation process [32]. Contradictory experimental results have been reported about the nature of magnetism and the appearance of superconductivity. The diamagnetic transition is seen only in the zero-field cooled (ZFC) branch of magnetic susceptibility data, due to the coexistence of superconductivity and magnetism [181]. The Ru-1212 samples are prepared from oxides and carbonates through high-temperature solid-state reaction above 1000 °C and also annealed above 1000 °C in a flowing oxygen atmosphere [32]. A typical impurity in the Ru-1212 samples is $SrRuO_3$, which itself is a ferromagnetic material [181, 182]. In order to minimize the amount of $SrRuO_3$ in the product, Ru-1212 has been prepared using Sr_2GdRuO_6 as a precursor [183]. The reaction kinetics of Ru-1212 from Sr_2GdRuO_6 and CuO in a flowing O_2

atmosphere has been a subject of a DTA study [183]. Comparing the E_a values obtained from the XRD data analysis to that estimated from the DTA measurements, based on the first endotherm at about 1000–1100 °C, it was concluded that the formation reaction of Ru-1212 is associated with the diffusion mechanism.

The mass loss seen in TG curves of Ru-1212 is small, about 0.5% up to 1000 °C in a flowing oxygen atmosphere [184]. According to a high-temperature XRD measurement Ru-1212 starts to decompose in an O_2 around 1050 °C [184]. Two endotherms were located in the DTA curve at 1050 °C (maximum) and 1118 °C (onset). The first, minor one, was connected to the decomposition of Ru-1212 and the other to incongruent melting of compounds.

The oxygen content of the as-synthetised Ru-1212 material is slightly below the stoichiometric value [34]. The oxygen release, observed as a mass loss during heating Ru-1212 samples ($\delta = 0.07$) in an argon atmosphere up to 750 °C, lowered the oxygen content to 7.80.

6.8. $Nd_{2-x}Ce_xCuO_{4-\delta}$

Superconductivity in $RE_{2-x}Ce_xCuO_{4-\delta}$ (RE = Nd, Sm, Pr, Eu) is observed in a small range of RE doping (0.14–0.18) [185]. As-prepared samples are not superconducting until after an additional heat-treatment at high temperatures (reduction step) under slightly decreased $p(O_2)$ (10^{-6}–10^{-3} atm). A small amount of oxygen is removed during the reduction step and the oxygen deficiency after this varies between 0.01 and 0.05 per formula unit. However, the reduction and oxidation are not entirely reversible and some decomposition of the material is necessary to obtain a sufficiently reduced state for superconductivity [18]. $Nd_{2-x}Ce_xCuO_{4-\delta}$ often contains free, unreacted CuO as an impurity phase, and this can be detected by TG as a reduction of CuO to Cu_2O at about 1000 °C in air [186]. The Cu_2O-$Nd_2CuO_{4-\delta}$ mixture melts near 1030 °C.

7. USE OF TG TO CONTROL THE AMOUNT OF OXYGEN

After establishing the oxygen content in Y-123 the changes in the oxygen stoichiometry produced by a variation of T and $p(O_2)$ can be detected in a TG run [18]. The most accurate data are obtained by isothermal TG, in which the sample is allowed to come to constant mass after each step. When both heating and cooling patterns are recorded, it is possible to establish that the same mass is achieved from both directions. van't Hoff plots can be used to predict the conditions, needed to obtain a particular oxygen content in HTSC (Figure 12) [138]. One of the main difficulties with this method is that the equilibrium must be established. The knowledge about oxidation kinetics of Y-123 can be used to

predict the conditions needed to obtain samples with desired oxygen content and homogeneous oxygen distribution [44].

The amount of incorporated oxygen into $Pb_2Ba_2EuCu_3O_{8+\delta}$ was determined by performing the annealing in a thermobalance in a flowing oxygen atmosphere [128]. The best temperature region for oxygen-loading was around 350 °C. The oxygen stoichiometry of the as-prepared material was established as $\delta = 0.16$ (coulometric titration). After oxygen-annealing, the oxygen stoichiometry corresponded to the value 9.79. The same method has been used to prepare $Pb_2Sr_2Eu_{0.75}Ca_{0.25}Cu_3O_{8+\delta}$ samples [187]. For the oxygen incorporation, E_a was only 50 kJ mol^{-1}, but for the oxygen removal it was 150 kJ mol^{-1}.

If an oxygen-deficient material is desired, then an oxygen-saturated material is post-annealed in a flowing inert atmosphere at a known equilibrium temperature [128]. Oxygen-deficient $Yb_{1-x}Ca_x(Ba_{0.8}Sr_{0.2})_2Cu_3O_{7-\delta}$ samples ($x = 0$–0.35, $\delta = \sim 0$–1) were obtained by the temperature-controlled oxygen depletion (TCOD) method from the fully-oxygenated samples by annealing in an Ar atmosphere at various fixed temperatures (Figure 17) [188–190]. An isothermal heating period was used in order to establish equilibrium. TCOD method has been used also in the preparation of oxygen-deficient $Yb(Ba_{1-y}Sr_y)_2Cu_3O_{7-\delta}$ samples ($y = 0$–0.4, $\delta \approx 0.4$) [191].

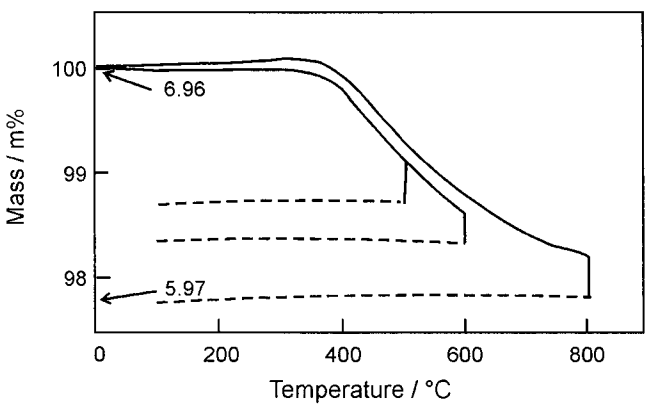


Figure 17. TG curves of $Yb_{1-x}Ca_x(Ba_{0.8}Sr_{0.2})_2Cu_3O_{7-\delta}$ samples recorded in a flowing Ar atmosphere [after 188].

8. DETERMINATION OF ABSOLUTE OXYGEN CONTENT BY TG

8.1. TG reduction method

With the TG reduction method, the amount of oxygen in a sample can be calculated by monitoring the total mass loss during thermal treatment under a reducing atmosphere [18,143]. Because the mass losses in TG are not large, it is necessary to subtract background curves obtained under identical conditions in order to minimise the effects of buoyancy and the aerodynamic or convective forces [18]. The accuracy of the results also depends very much on the absence of even relatively small amounts of second phases and volatile impurities. A limitation on the method is also the volatility of metals. The accuracy may suffer from difficulties incurred in defining the resulting products or the end point of the reduction [44,192].

8.2. Oxygen content in $YBa_2Cu_3O_{7-\delta}$ and $YBa_2Cu_4O_{8-\delta}$

The absolute oxygen content in Y-123 can be determined by measuring the mass loss in a synthesis starting from a known mixture of Y_2O_3, $BaCO_3$ and CuO or by following through the total reduction of Y-123 in an H_2 atmosphere to a mixture of Y_2O_3, BaO and metallic Cu [193]. If a standard reference sample with identical metal composition to the sample and with known oxygen stoichiometry is available, the unknown oxygen content in the sample can also be calculated from the difference in the mass loss of the sample and the standard detected by TG in an inert atmosphere [128]. From these possibilities the reduction method is preferred.

Hydrogen is the most frequently used reductant. In a hydrogen atmosphere Y-123 (and RE-123) may form metastable hydrogen-containing phases at low temperatures (equation (9)) [194,195], but at higher temperatures the compounds decompose to stable reaction products and metallic copper and alkaline-earth and rare-earth oxides are formed [195].

$$YBa_2Cu_3O_{7-\delta} + \gamma H_2 \rightarrow YBa_2Cu_3O_{7-\delta}H_{2\gamma} \qquad (9)$$

Heating of the Y-123 sample in a reducing H_2/Ar atmosphere results in a selective reduction of copper to a metallic state by 950 °C (equation (10)) [196]. Yttrium and barium are maintained in the process as binary oxides at least up to 1000 °C [197]. The mass loss must be determined at 950 °C because, during cooling, the mass of the sample gradually increases due to the reaction of BaO with moisture or CO_2 to form $Ba(OH)_2$ or $BaCO_3$ [196,198]. The overall mass loss may vary between 6.15 and 8.41%, corresponding to δ values from 1.0 to 0.0 [128]. In the oxygen deficiency value, δ the total experimental error has been evaluated at 0.01–0.02.

$$2YBa_2Cu_3O_{7-\delta} + (7-2\delta)H_2 \rightarrow Y_2O_3 + 4BaO + 6Cu + (7-2\delta)H_2O \quad (10)$$

The mass loss in the reduction of Y-123 is stepwise (Figure 18A) [128,196]. The reduction is believed to start with a loss of oxygen atoms from the Cu-O chains [128]. The mass loss around the temperature range 350–500 °C correlates well with the initial oxygen non-stoichiometry (= oxygen content above six) while the changes at temperatures higher than 500 °C are largely independent of the oxygen non-stoichiometry. The last plateau in the TG curve of Y-123 around 800 °C corresponds to Cu_2O and 2Cu [128]. The TG reduction method has sometimes given somewhat higher values of oxygen content than the various titration methods that have been employed [196,198]. The discrepancy in the results may be due to the presence of unreacted $BaCO_3$, which decomposes in the reduction process and increases the mass loss [196].

The hydrogen reduction method has also been applied in the determination of oxygen content in $YBa_2Cu_4O_{8-\delta}$ (Y-124) [55,199]. The reduction of Y-124 also occurs in steps (Figure 18B). The oxygen stoichiometry was calculated at 950 °C applying equation (11):

$$2YBa_2Cu_4O_{8-\delta} + (9-2\delta)H_2 \rightarrow Y_2O_3 + 4BaO + 8Cu + (9-2\delta)H_2O \quad (11)$$

The hydrogen reduction method gave a slightly higher oxygen content value in the studied Y-124 samples (7.98) than iodometric (7.95) or coulometric titrations (7.93) [199].

8.3. Oxygen content in other cuprates

The reduction process has also been used in the evaluation of the oxygen content of $La_2CuO_{4-\delta}$, $RuSr_2GdCu_2O_{8-\delta}$ and $Nd_2CuO_{4-\delta}$ [34,126,185,200]. The reduction products of $La_{2-x}AE_xCuO_{4-\delta}$ (AE = Ba, Sr, Ca) at 900 °C, used in the determination, were alkaline-earth oxides, La_2O_3 and Cu [126]. The oxygen content in $RuSr_2GdCu_2O_{8-\delta}$ samples was calculated on the basis of TG reduction curves, which showed the decomposition to occur by 550 °C [34]. The products were supposed to be Ru, Cu, SrO and Gd_2O_3. Those of $Nd_{2-x}Ce_xCuO_{4-\delta}$ in a dry H_2 atmosphere at 1100 °C were assumed to be Nd_2O_3, Ce_2O_3 and Cu [185]. Samples of $Nd_{2-x}Ce_xCuO_{4-\delta}$ with a particular oxygen content were prepared, at a given value of decreased $p(O_2)$, by subsequently quenching samples from the synthesis temperature.

The determination of the oxygen content when metals are easily volatilised is more complicated. The reduction method has been applied also to the determination of oxygen content in cuprates containing Bi or Pb [*e.g.* $Bi_2Sr_2CaCu_2O_{8+\delta}$ and $Pb_2Sr_2YCu_3O_{8+\delta}$], by taking care to avoid loss of the metals

during the thermal treatment [162,201,202]. The one step reduction of Bi- and Pb-based cuprates, which produces metallic bismuth, lead and copper, is completed at 400–600 °C, varying with the heating rate [162,202]. The additional mass losses seen in the TG curves beyond these temperatures are due to the evaporation of Bi or Pb [128,162].

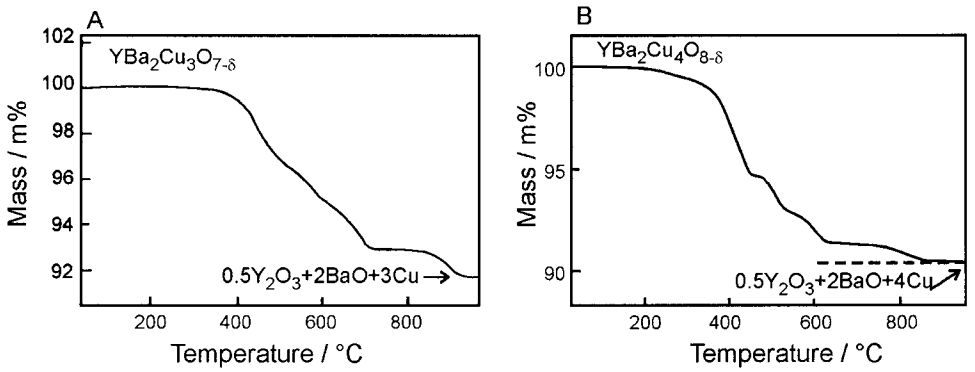


Figure 18. Hydrogen reduction curves of (A) $YBa_2Cu_3O_{7-\delta}$ [after 196] and (B) $YBa_2Cu_4O_{8-\delta}$ [199] heating rate 5 °C min^{-1}.

9. VOLATILE PRECURSORS FOR HTSC THIN FILM DEPOSITION

9.1. HTSC thin films

It was recognised very early in the studies of HTSC that the first applications would be in the field of electronics (SQUIDs, Josephson devices, microwave devices, interconnection wires) and in the form of thin films. Accordingly, the deposition of HTSC thin films has been extensively studied [203]. Physical vapour deposition (PVD) techniques, *viz.* sputtering, evaporation and laser ablation, were the methods used most extensively in the late 1980s, while chemical methods such as chemical vapour deposition (CVD) and thermal decomposition of painted films became available somewhat later [13,204–206]. Excellent HTSC thin films can be grown by PVD methods, especially from Y-123 material. However, PVD methods have the drawbacks of requiring high vacuum, being limited to line-of-sight deposition and not allowing for large-scale deposition. Chemical methods offer a means to overcome these limitations. CVD is a suitable method for the deposition of HTSC films for several other reasons as well: it is effective over a wide range of oxygen partial pressures [207], the deposition temperature can be low because chemical instead of thermal activation is used and, finally, it allows the deposition on substrates of complex shapes.

9.2. Chemical vapour deposition

In CVD, volatile precursors of the film components are introduced to a reactor either simultaneously or in successive pulses (the pulsed CVD method is called Atomic Layer Deposition (ALD) [208]). A film is formed on the substrate as a result of chemical reaction, thermal decomposition or photodecomposition [209]. The key requirement in CVD is a volatile precursor, with the following properties: (i) vapour pressure high enough to allow volatilisation, (ii) adequate thermal stability and not subject to decomposition before reaching the substrate surface, (iii) reaction and formation of the desired solid film material under the conditions chosen and (iv) reaction side-products that are gaseous and easily removed from the reactor. CVD requires a stable constant flow of the precursor gas to guarantee the homogeneous growth of the film, and precursors that are gaseous or liquid at room temperature are therefore preferred.

Because of the difficulties in precursor chemistry the studies of CVD of HTSC materials have mainly been focused on Y-Ba-Cu oxides. It is difficult to find volatile, thermally stable and sufficiently reacting precursors for Bi, Pb, Tl and Hg.

9.3. TA studies of CVD β-diketonate precursors

9.3.1. Precursors

For CVD growth of HTSC films, sufficiently volatile compounds of Cu, AE and RE as well as Bi, Tl, Pb and Hg must be available. Volatility is a problem for rare-earth and alkaline-earth metals, which are electropositive and do not form simple inorganic compounds volatile at reasonable temperatures (<400 °C). An extensive search has thus been made among organometallic compounds for volatile precursors of these metals [210–212]. The compounds most studied are the β-diketonates, and in particular, thd (thd = 2,2,6,6-tetramethyl-3,5-heptanedione or 2,2,6,6-tetramethyl-heptane-3,5-dione) complexes [204], which were earlier used in the gas chromatographic separation of metals [213,214]. $Cu(thd)_2$ has recently received attention as a precursor for Cu metal films [215].

Another type of a ligand system has also been developed for alkaline-earth metals. In those complexes polyethylene glycol units are covalently appended to non-fluorinated β-ketoiminate backbone [216,217]. Complexes are mono-molecular and applicable in CVD although their thermal stability is not perfect. During 1990s the precursors have been further developed, and recently five new encapsulating ligands have been published. Good volatility and stability was observed for example for 2,2,5,25,28,28-hexamethyl-9,12,15,18,21-pentaoxa-4,25-diene-6,24-diimino-3,27-pentacosadionato barium(II), $Ba[(dhd)_2CAP\text{-}5]$ (where dhd comes from 2,2-dimethyl-3,5-hexanedionate) [218].

Alkaline-earth alkoxides are usually thermally unstable [219–221]. Among simple Ba alkoxides only *tert*-butoxide has shown some volatility under drastic conditions

(270 °C; $<10^{-5}$ Torr) [222]. Better results have been obtained with aryloxides $[AE_2(O\text{-}2,4,6\text{-}{}^tBu_3C_6H_2)_4]$ (240 °C; 10^{-4} Torr) and donor functionalised alkoxides $[AE_2\{OC(CH_2O^iPr)_2{}^tBu\}_4]$ (150–185 °C; 10^{-2} Torr) [221,223]. A further group of AE complexes showing some volatility is formed by alkyl silyl amides. They form easily dimers but monomeric complexes are formed with Lewis bases [224,225]. The η^2-coordinated pyrazolato ligands form volatile complexes with calcium [226].

Recently, the cyclopentadienyl (Cp) compounds of alkaline-earth metals have gained attention as volatile compounds. Several differently substituted compounds have been synthesised and characterised structurally [227–230]. Various Cp compounds (pentamethyl, tri-isopropyl, tri-*tert*-butyl, different N- and O-functionalised compounds) have been characterised and studied especially as precursors for ALD [231,232]. Pyrrolyl complexes are another example of volatile η^5-bonded AE complexes [233].

Yet other precursors studied are organometallics such as triphenylbismuth, cyclopentadienylthallium, tetramethyllead, and various alkoxides, both mono- and bimetallic. A major problem with the alkoxides is their limited thermal stability [219–221]. Mixed metal complexes, bi- or trimetallic, would be attractive and they have been studied in some extent. Their volatility and thermal stability are, however, often limited. The best results, *i.e.* volatilities in the range 150–170 °C (10^{-3} Torr), have been obtained in Y-Ba, Ba-Cu, Y-Cu systems when mixed ligand complexes of 1,1,1,3,3,3-hexafluoro-2-propoxide and thd have been used [234]. Other interesting bimetallic mixed ligand complexes are those of copper and rare-earths with thd and salen ligands [235].

9.3.2. Thermogravimetry

Thermal stability is a problem, even with the β-diketonato complexes, and TG measurements have been used to determine whether, and to what extent, partial thermal decomposition occurs during volatilisation. When heated in vacuum or in a nitrogen atmosphere, Cu and RE β-diketonato complexes often volatilise completely in a narrow temperature range, but AE complexes, particularly those of Ba complexes, tend to decompose (Figure 19) [236].

The sublimation temperature may be influenced by the substitutions in the β-diketonato ligand. The effect of hydrocarbon groups on the volatility is, in order: *i*-butyl>*t*-butyl>cyclopentyl = hydrogen>cyclohexyl>phenyl. In the case of copper β-diketonates, the sublimation temperature of copper 1-phenyl-4,4-dimethylpentane-1,3-dionate is thus about 150 °C higher than that of copper 2,2,6-trimethylheptane-3,5-dionate [236]. Fluorine substitution, in turn, lowers the sublimation temperature markedly and also affects the completeness of the reaction. Copper 1,1,1-trifluoropentane-2,4-dionate, for example, begins to sublime at 120 °C (Figure 20) [237].

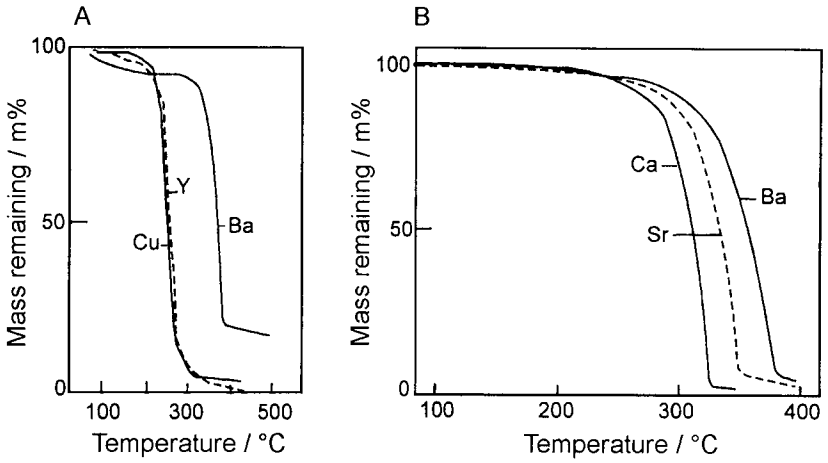


Figure 19. TG curves for (A) Cu, Y and Ba thd complexes measured in a flowing He atmosphere, heating rate 20 °C min^{-1} [after 238] and (B) Ca, Sr and Ba thd complexes determined in a He atmosphere, heating rate 10 °C min^{-1} [after 213].

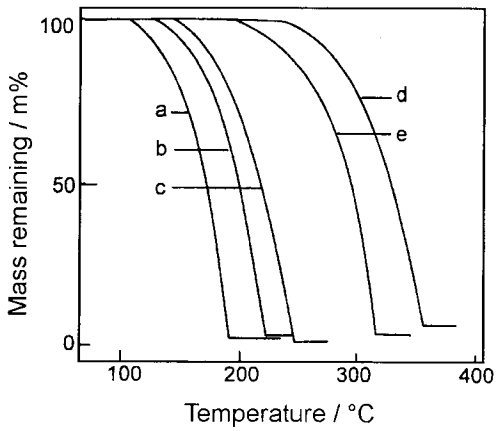


Figure 20. TG curves for selected Cu β-diketonates: (a) 1,1,1-trifluoropentane-2,4-dionate, (b) 2,2-dimethylhexane-3,5-dionate, (c) 2,2,6,6-tetramethylheptane-3,5-dionate (thd), (d) 2,2-dimethyl-5-phenylpentane-3,5-dionate and (e) 2,2-dimethyl-5-cyclohexylpentane-3,5-dionate [after 236].

The sublimation can also be enhanced by introducing free β-diketonate ligand into the sublimation atmosphere, for example to the carrier gas. This effect has been realised in several β-diketonato complexes of metals needed in HTSC films [236]. The sublimation temperature is also dependent on the atmosphere and is much lower in vacuum than in 1 atm pressure of nitrogen or argon. TG studies in vacuum are preferred if the CVD growth, where the precursors are used, takes place in vacuum [239].

The volatility of RE β-diketonato complexes is generally good, increasing with the decrease in ionic radius of the RE ion. Volatility is also inversely proportional to the molar mass of the subliming molecule, but in the case of rare-earths, the prediction of volatility is not straightforward, because the structure of the β-diketonato complexes often changes from dimeric to monomeric as the ionic radius decreases and this is reflected in the volatility. The effects on the sublimation of the presence of free ligand and substitution in the β-diketonate ligand, noted above for copper complexes, also hold for the RE complexes.

In the alkaline-earth metal series, the volatility of β-diketonato complexes decreases towards the end of the series, with Ba complexes being the least volatile. TG measurements in a dynamic argon atmosphere showed that the amount of decomposition residue is greatest for Ba complexes and least for Ca complexes [240]. In the case of "$Ba(thd)_2$", residues are as much as 15–20% (Figures 19 and 21) [241].

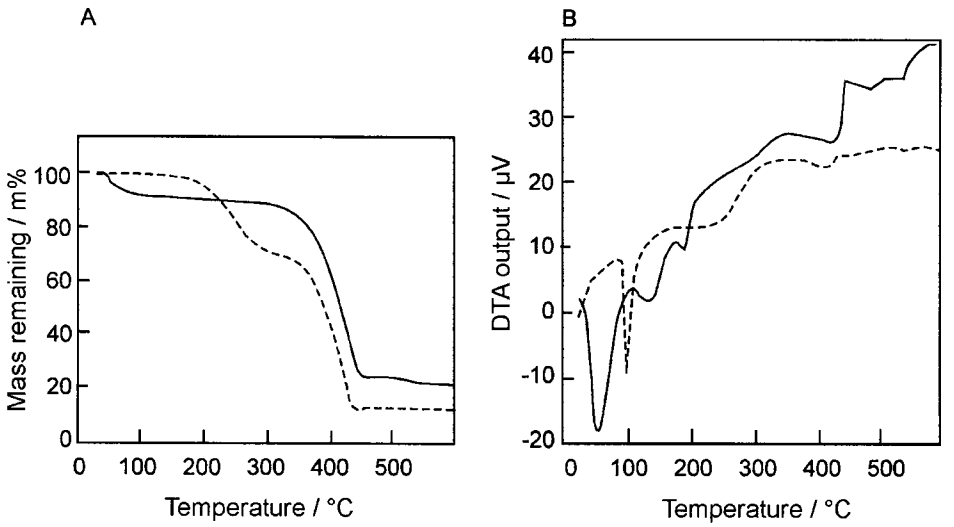


Figure 21. (A) TG and (B) DTA curves recorded in a flowing Ar atmosphere, heating rate 10 °C min^{-1}, for ten-week-old commercial samples of "$Ba(thd)_2$" (–) and [$Ba(thd)_2$(tetraglyme)] (- - -) [after 241].

Owing to the coordinative unsaturation (AEL_2), the complexes of Sr and Ba are highly sensitive to the conditions of synthesis. If moisture is present, aqua or hydroxo ligands are easily coordinated (*e.g.* $[Ba_5(thd)_9(H_2O)(OH)]$ [238]). In dry conditions the coordination unsaturation is removed by coordination of the solvent (*e.g.* $[Ba(thd)_2Et_2O]_2$ [242]) and, if a non-polar solvent is used, by oligomerisation (*e.g.* $[Ba_4(thd)_8]$ [243]). The oligomeric complexes tend to exhibit limited volatility and monomeric complexes are therefore preferred. The Sr and Ba β-diketonato complexes can be monomerised through the use of adduct ligands, such as polyethers (tetraglyme [241,244]) or amines [245,246]. Besides the better volatility, the adducts stabilise the complexes, allowing for better storage and handling. The degradation of the complexes in air at room temperature is a problem [247]. However, TG curves of the adducted complexes have shown that, upon heating, the neutral ligand does not stay intact but is usually removed first and the volatilisation of the β-diketonato complex occurs separately (Figure 21) [205,241,248,249].

The volatility of Ba β-diketonato complexes can be improved by fluorine substitution [205,210,250]. Fluorine increases the volatility more than the length of the hydrocarbon substituent in the ligand. In TG measurements the fluorine-containing complexes show excellent volatility, especially if they contain a neutral ligand [251]. The TG curve of $[Ba(hfa)_2(tetraglyme)]$ (hfa = 1,1,1,5,5,5-hexafluoropentane-2,4-dione), for example, shows a single volatilisation step with nearly 100% mass change between 160 and 350 °C [252]. One problem with the fluorine-containing precursors is the formation of BaF_2 in the film growth [250]. Fluorine traces in HTSC may be detrimental for the superconducting properties. Part of the fluorine can be removed by a high-temperature, water-vapour treatment [253].

Studies of encapsulated bis(β-ketoiminato) polyether Ba complexes showed that for example $Ba[(dhd)_2CAP\text{-}5]$ sublimes at 100 °C (10^{-5} Torr) with a neglible residue [218]. In TG the same complex showed a mass loss more than 80 % before 220 °C, which is the starting temperature for decomposition. Substituents in the Cp ring strongly affect the thermal behaviour of the Sr and Ba compounds. Complete sublimation at 110–220 °C and high volatility (residual less than 20%) in TG in a flowing nitrogen atmosphere were observed for tri-isopropyl and tri-*tert*-butyl substituted Cp compounds. All the other compounds decomposed in TG measurements [232].

9.3.3. Differential scanning calorimetry

The melting temperatures of volatile precursors have usually been determined by DSC. The melting point of $Cu(thd)_2$ is 198 °C, while the melting points of the rare-earth thd complexes vary between 160 and 230 °C [212]. Very different

melting points have been reported for "$Ba(thd)_2$" and "$Sr(thd)_2$", no doubt because the different methods of preparation produce oligomers with different melting points. $Ca(thd)_2$ seems to be easier to synthesise reproducibly and its reported melting points converge at 223–225 °C [212,213]. The melting points of the AE precursors cannot be lowered by fluorine substitution in the ligand framework, but those of the RE complexes can. A substantial decrease in the melting points of alkaline-earth β-diketonato complexes can be obtained through the addition of neutral ligands. For example, [$Ba(thd)_2$(triglyme)] melts at 77–79 °C [254] and [$Ba(hfa)_2$(pentaethyleneglycol methyl ethyl ether)] at 40 °C [255]. The low melting points make these complexes attractive liquid precursors for CVD.

Sublimation enthalpies have been estimated from the DSC curves, but more often the enthalpy values have been derived from vapour pressure evaporation studies [236,256]. The values given in the literature vary from 30 to 60%, however [257].

9.3.4. Measurements of vapour pressure and evaporation rate

Vapour pressures have been measured for numerous β-diketonato complexes of metals, including those used in HTSC materials. The techniques applied are conventional ones relying on direct vapour pressure determination with a Bourdon gauge, or a mercury manometer [256], or by the Knudsen cell method [258], but also a TG method has been used [16]. The Knudsen cell method is also applicable in TG and has been used for β-diketonato complexes (Figure 22) [259]. In this method, the complex is volatilised by effusion through the orifice of the cell and a steady rate of mass loss is recorded by a thermobalance kept at a constant temperature. The vapour pressure is estimated from the rate of mass loss, the radius of the orifice and the temperature. A stepwise heating system and helium gas flow have also been used in the measurements [260]. Vapour pressures for several complexes could be calculated from the mass loss, carrier gas flow rate and heating time when the vapour of the sample was saturated in the He carrier gas stream.

The decomposition of precursors and any volatile impurities present will affect the vapour pressure measurement of β-diketonates considerably and, in the case of $Ba(thd)_2$, the vapour pressure can be measured only from a high-quality product [261]. The thd chelates of Y, Ba and Cu have vapour pressures high enough for MOCVD growth of HTSC films, however [262].

The evaporation rate of the precursors can be studied thermogravimetrically by determining the mass loss rate at constant temperature below the melting point. It has been shown that the evaporation rate of thd complexes decreases with decreasing effective surface area and increasing diffusion distance in the region above the sample [263]. Evaporation rates are higher for complexes containing a neutral ligand than for non-adducted complexes (Figure 23) [264].

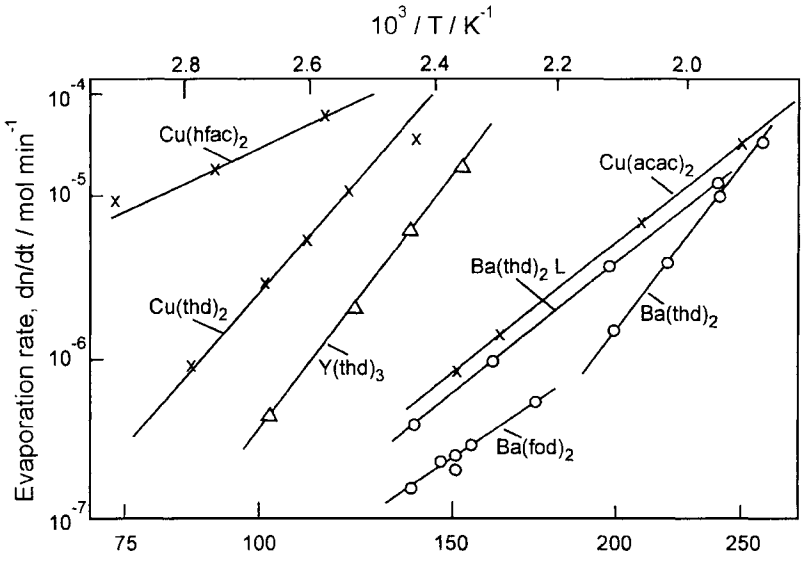


Figure 22. Molar evaporation rates of selected CVD precursors [after 265]. hfa = 1,1,1,5,5,5-hexafluoropentane-2,4-dione, thd = 2,2,6,6-tetramethylheptane-3,5-dione, fod = 1,1,1,2,2,3,3-hepta-fluoro-7,7-dimethyloctane-4,6-dione and acac = pentane-2,4-dione.

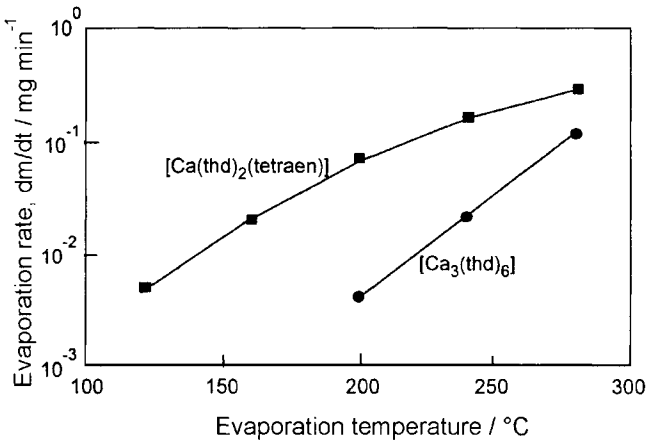


Figure 23. Evaporation rates of $[Ca_3(thd)_6]$ and $[Ca(thd)_2(tetraen)]$ as a function of temperature [after 264]. thd = 2,2,6,6-tetramethylheptane-3,5-dione, tetraen = tetraethylenepentamine.

9.3.5. Mass spectrometry in combination with TG

The species of β-diketonato complexes existing in the gas phase have been studied by TG with detection by mass spectrometry (MS). In the MS studies, however, the instruments used were usually conventional high-resolution mass spectrometers with electron ionisation and a sample heating system.

The positive-ion mass spectra of Cu and RE complexes that are monomeric in the crystalline state usually reveal the presence of monomeric species like $Cu(thd)_2$, $Cu(thd)$, $Y(thd)_3$, $Y(thd)_2$, metal species containing partially decomposed thd ligands and, of course, fragments of the ligands [238,240,266,267]. Oligomers relatively often appear in the spectra, but they are presumably caused by ion-molecule interactions in the mass spectrometer source and are recognisable by the variation in peak intensity with pressure. The positive-ion spectra show more oligomers than the negative-ion spectra, and it is believed that the oligomers in the negative-ion spectra are real and not formed *via* ion-molecule reactions [238].

The positive-ion mass spectra of alkaline-earth β-diketonates also give evidence of oligomers, the strongest peak in the spectra often being that of $AE_2L_3^+$ [213,240], but larger oligomers have been detected in the case of Ba. The negative-ion spectra show barium tetramers and pentamers as well [238]. The mass spectra of complexes with neutral ligands show that the adduct ligand may remain intact to some extent [248,249,251].

Mass spectrometric studies on barium β-ketoiminato and Cp complexes are in line with the sublimation and TG studies. Monomolecular complexes which showed complete sublimation and high volatility in TG, showed a molecular peak in MS [218,232]. The release of solvent molecules present in solid alkaline-earth Cp compounds, seen in TG curves, could be verified with MS.

9.4. CVD growth

The preference in CVD of HTSC thin films is for *in situ* processes where the as-deposited films are superconducting. The advantages of CVD over the PVD method can then be fully exploited. The most common CVD methods rely on the continuous flow of precursors into the deposition zone. The vaporisation temperatures of the precursors vary with the experimental set-up (*e.g.*, in the case of $Cu(thd)_2$ between 80 and 150 °C, in the case of $Y(thd)_3$ 90–170 °C, and in the case of "$Ba(thd)_2$" 180–280 °C). The optimum film properties are obtained when the oxygen partial pressure is matched to the deposition temperature according to the stability criteria of the HTSC phase desired. The substrate temperatures vary between 300 and 850 °C and, at temperatures above 500 °C, the poor thermal stability of the β-diketonato complexes may be a limitation. In most examples reported in the literature, the as-deposited films have not been superconducting but post-depositional annealing is required and, during cooling, films must be exposed

to a much higher oxygen pressure than used in deposition. The preferred orientation in the thin films is that where the *c*-axis is perpendicular to the substrate surface, and that requires the use of particular single crystalline substrates (*e.g.* (100)-oriented MgO, $SrTiO_3$) [204,205]. The difference in the thermal expansion coefficients of the substrate and thin film material is also an important factor because it determines the possible crack formation. The thermal expansion coefficients of HTSC are larger than those of the ceramics conventionally used as substrates [268]. Therefore, the use of substrates that have a relatively large thermal expansion coefficient (*viz.* in addition to MgO and $SrTiO_3$, YSZ, RE aluminates and gallates) is recommended for film deposition [268,269]

The properties of CVD HTSC thin films are comparable to those of PVD deposited films. Most of the work on CVD HTSC thin films has been carried out with Y-123, but good results have also been obtained with Bi- and Tl-based materials [204], although their preparation is more difficult than that of Y-123. Ideal precursors for alkaline-earth metals have not yet been found and more research is required. More research is also needed to understand better the surface reactions of the precursors on the substrate in the growth processes of thin films.

Thermodynamic calculations have been used in searching for suitable deposition conditions, optimising process parameters and characterising on-going reactions in the CVD growth of Y-123 and Bi-2212 thin films [270]. The calculations are based on the minimisation of Gibbs energy, ΔG [270,271]. The input parameters consist of the temperature, total pressure, amounts of starting materials and thermodynamic data reported for the substances, while the output consists of the equilibrium composition of the system and various thermodynamic quantities, *e.g.* ΔG. The results are in the form of CVD stability diagrams, which show, qualitatively, the influence of critical deposition parameters on the stability region in the growth processes by MOCVD.

Because CVD of HTSC materials has turned out to be rather difficult the new alkaline-earth precursors are usually tested in deposition of Sr or Ba titanates. The deposition of these perovskites is easier but achieving of a right stoichiometry and good crystallinity is challenging. Good results have been reported for CVD of $BaTiO_3$ grown from $Ba[(dhd)_2CAP\text{-}5]$ and $Ti(thd)_2(O^iPr)_2$ at a susceptor temperature of 825 °C [218]. A barium pentamethyl Cp compound has been examined in CVD for an oxide formation [272]. In these experiments oxygen was too reactive but with N_2O a controlled growth of oxide film could be achieved. In ALD where the precursors are introduced one at a time into the reactor, Cp compounds can be used together with water to form an oxide. Crystalline Sr and Ba titanate films have been deposited at as low temperature as 325 °C [273].

10. SUMMARY

Thermoanalytical techniques provide an important and effective tool in the research on high-T_c superconductors. In the case of bulk superconductors, they provide invaluable information at every stage of the preparation process. For thin film growth by chemical vapour deposition methods, the information provided on the thermal behaviour of the volatile precursors is valuable both for understanding and for controlling film growth processes.

In the case of bulk materials, the most important TA studies pertain to (i) the decomposition reactions of precursors used in synthesis, (ii) the processes by which high-T_c phases are formed, (iii) the thermal stability of these phases in the surrounding atmosphere, and (iv) the effect of thermal cycles on oxygen stoichiometry, affecting the superconducting properties, or (v) non-stoichiometry in metal cations because of volatilisation. The most important TA techniques employed in these studies are TG and DTA. In studies of the thermal behaviour and possible decomposition of the volatile precursors used as source materials in CVD growth, the typical TA techniques used in addition to TG are DSC and EGA.

TA methods could offer even wider possibilities to study the formation of HTSC and characterise superconducting properties. High-temperature XRD, which is now rarely used in studies of phases formed *in situ* in either bulk-processing or the growth of thin films, could give information about the formation reactions, and thus could help in selecting optimal conditions for the synthesis of a particular compound. Improved high-temperature DSC would be a straightforward method to obtain thermodynamic data at high temperatures. A DSC equipped with a cooling system could in turn provide an alternative way to determine the superconducting phase transition at low temperatures. Since no ideal volatile Ba precursor for thin films has been found, studies must continue. For their part, improved TG-EGA methods would be an important step in the reliable detection of species present in the gas phase and participating in surface reactions.

ACKNOWLEDGEMENTS

We are grateful to Dr. K. Ahonen for revising the language and Mrs. R. Sassi for drawing the figures. In addition, we acknowledge Prof. M. Karppinen, Materials and Structures Laboratory, Tokyo Institute of Technology, Yokohama, Japan, for cooperation. Mr. T. Hänninen, Ph. Lic., is thanked for useful discussions.

We thank the Institute of Physics Publishing, Dirac House, Temple Back, Bristol BS1 6BE, United Kingdom, for kind permission to reproduce the structures (C)–(F) and (H)–(M) in Figure 2 of HTSC and related cuprates. The structures have been reprinted from Superconductor Science and Technology 8 (1995);

M. Karppinen, A. Fukuoka, L. Niinistö and H. Yamauchi, Determination of oxygen content and metal valences in oxide superconductors by chemical methods, 1–15.

REFERENCES

1. J.G. Bednorz and K.A. Müller, Z. Phys. B, 64 (1986) 189.
2. M.K. Wu, J.R. Ashburn, C.J. Torng, P.H. Hor, R.L. Meng, L. Gao, Z.J. Huang, Y.Q. Wang and C.W. Chu, Phys. Rev. Lett., 58 (1987) 908.
3. H. Maeda, Y. Tanaka, M. Fukutomi and T. Asano, Jpn. J. Appl. Phys., 27 (1988) L209.
4. Z.Z. Sheng and A.M. Hermann, Nature, 332 (1988) 55.
5. Z.Z. Sheng and A.M. Hermann, Nature, 332 (1988) 138.
6. S.N. Putilin, E.V. Antipov, O. Chmaissem and M. Marezio, Nature 362, (1993) 226.
7. S.N. Putilin, E.V. Antipov and M. Marezio, Physica C, 212 (1993) 266.
8. For better Thermal Analysis and Calorimetry, 3rd Ed., J.O. Hill (ed.), International Confederation for Thermal Analysis, 1991, p. 7, 11.
9. V.B. Lazarev, K.S. Gavrichev, V.E. Gorbunov, J.H. Greenberg, P.Z. Slutskii, Ju.G. Nadtochii and I.S. Shaplygin, Thermochim. Acta, 174 (1991) 27.
10. L.R. Morss, D.C. Sonnenberger and R.J. Thorn, Inorg. Chem., 27 (1988) 2106.
11. V.A. Alyoshin, D.A. Mikhailova, E.V. Antipov, A.S. Monayenkova, A.A. Popova, L.A. Tiphlova and J. Karpinski, J. Alloys Compd., 284 (1999) 108, and references therein.
12. Z. Zhou and A. Navrotsky, J. Mater. Res., 7 (1992) 2920.
13. M. Kamimoto, Thermochim. Acta, 174 (1991) 153.
14. T. Ozawa, Thermochim. Acta, 133 (1988) 11.
15. P.K. Gallagher, Adv. Ceram. Mater., 2 (1987) 632.
16. A. Niskanen, T. Hatanpää, M. Ritala and M. Leskelä, J. Therm. Anal. Cal., 64 (2001) 955.
17. P. Strobel, J.J. Capponi, C. Chaillout, M. Marezio and J.L. Tholence, Nature, 327 (1987) 306.
18. P.K. Gallagher, Thermochim. Acta, 174 (1991) 85.
19. M. Marezio, Acta Cryst. A, 47 (1991) 640.
20. W.J. Weber, L.R. Pederson, J.M. Prince, K.C. Davis, G.J. Exarhos, G.D. Maupin, J.T. Prater, W.S. Frydrych, I.A. Aksay, B.L. Thiel and M. Sarikaya, Adv. Ceram. Mater., 2 (1987) 471.
21. W.P. Brennan, M.P. DiVito, R.F. Culmo and C.J. Williams, Nature, 330 (1987) 89.
22. J. Zhao and M.S. Seehra, Physica C, 159 (1989) 639.
23. J. Valo, R. Matero, M. Leskelä, M. Karppinen, L. Niinistö and J. Lindén, J. Mater. Chem., 5 (1995) 875.

24. M. Karppinen, A. Fukuoka, L. Niinistö and H. Yamauchi, Supercond. Sci. Technol., 8 (1995) 1.
25. C. Park and R.L. Snyder, J. Am. Ceram. Soc., 78 (1995) 3171.
26. F. Izumi and E. Takayama-Muromachi, in D. Shi (ed.), High-Temperature Superconducting Materials Science and Engineering, Elsevier Science Ltd, Oxford (1995) p. 81.
27. M. Karppinen and H. Yamauchi, Mater. Sci. Eng., 26 (1999) 51.
28. H. Yamauchi and M. Karppinen, Superlattices Microstruct. A, 21 (1997) 127.
29. T. Wada, A. Ichinose, H. Yamauchi and S. Tanaka, J. Ceram. Soc. Jpn., Int. Ed., 99 (1991) 420.
30. L. Bauernfeind, W. Widder and H.F. Braun, Physica C, 254 (1995) 151.
31. K.B. Tang, Y.T. Qian, L. Yang, Y.D. Zhao and Y.H. Zhang, Physica C, 282–287 (1997) 947.
32. C. Artini, M.M. Carnasciali, G.A. Costa, M. Ferretti, M.R. Cimberle, M. Putti and R. Masini, Physica C, 377 (2002) 431.
33. O. Chmaissem, J.D. Jorgensen, H. Shaked, P. Dollar and J.L. Tallon, Phys. Rev. B, 61 (2000) 6401.
34. M. Matvejeff, V.P.S. Awana, L.-Y. Jang, R.S. Liu, H. Yamauchi and M. Karppinen, submitted to Physica C (2002), Los Alamos National Laboratory, Preprint Archive, Condensed Matter (2002), 1-15, arXiv:cond-mat/0211100.
35. C. Bernhard, J.L. Tallon, C. Niedermayer, Th. Blasius, A. Golnik, E. Brücher, R.K. Kremer, D.R. Noakes, C.E. Stronach and E.J. Ansaldo, Phys. Rev. B, 59 (1999) 14099, and references therein.
36. K. Izawa, A. Tokiwa-Yamamoto, M. Itoh, S. Adachi and H. Yamauchi, Physica C, 222 (1994) 33.
37. H. Yamauchi, T. Tamura, X.-J. Wu, S. Adachi and S. Tanaka, Jpn. J. Appl. Phys., 34 (1995) L349.
38. H. Yamauchi, M. Karppinen and S. Tanaka, Physica C, 263 (1996) 146.
39. M. Cyrot and D. Pavuna, Introduction to Superconductivity and High-T_c Materials, World Scientific Publishing Co. Pte. Ltd., Singapore, 1992, p. 172.
40. Structures (A) and (B): Y. Tokura, Solid State Physics (Kotai Butsuri) 25 (1990) 618 (in Japanese).
41. A. Kishi, R. Kato, T. Azumi, H. Okamoto, A. Maesono, M. Ishikawa, I. Hatta and A. Ikushima, Thermochim. Acta, 133 (1988) 39.
42. A. Dworkin and H. Szwarc, High Temp. High Pressures, 21 (1989) 195.
43. A. Schilling and O. Jeandupeux, Phys. Rev. B, 52 (1995) 9714.
44. K. Conder, Mater. Sci. Eng. R32 (2001) 41.
45. J.L. Jorda, J. Therm. Anal., 48 (1997) 585.
46. S.-I. Hirano and T. Hayashi, Thermochim. Acta, 174 (1991) 169.
47. D. Noël and L. Parent, Thermochim. Acta, 147 (1989) 109.
48. J. Plewa, A. DiBenedetto, H. Altenburg, G. Eβer, O. Kugeler and G.J. Schmitz, J. Therm. Anal., 48 (1997) 1011.
49. N.-L. Wu and Y.-C. Chang, Thermochim. Acta, 203 (1992) 339.

50. A.M. Gadalla and T. Hegg, Thermochim. Acta, 145 (1989) 149.
51. T. Wada, H. Yamauchi and S. Tanaka, J. Am. Ceram. Soc., 75 (1992) 1705.
52. J. Valo and M. Leskelä, in A. Narlikar (ed.), Stud. High Temp. Supercond., Vol. 25, Nova Science Publishers, Inc., New York 1997, p. 135.
53. A. Negishi, Y. Takahashi, R. Sakamoto, M. Kamimoto and T. Ozawa, Thermochim. Acta, 132 (1988) 15.
54. P. Kumar, V. Pillai and D.O. Shah, Solid State Commun., 85 (1993) 373.
55. J. Mullens, A. Vos, A. De Backer, D. Franco, J. Yperman and L.C. Van Poucke, J. Therm. Anal., 40 (1993) 303.
56. A. Vos, J. Mullens, R. Carleer, J. Yperman, J. Vanhees and L.C. Van Poucke, Bull. Soc. Chim. Belg., 101 (1992) 187.
57. A. Kareiva, M. Karppinen and L. Niinistö, J. Mater. Chem., 4 (1994) 1267.
58. J. Plewa, H. Altenburg and J. Hauck, Thermochim. Acta, 255 (1995) 177.
59. G. Krabbes, W. Bieger, P. Schätzle and U. Wiesner, Curr. Top. Cryst. Growth Res., 2 (1995) 359.
60. T. Aselage and K. Keefer, J. Mater. Res., 3 (1988) 1279.
61. A. Erb, T. Biernath and G. Müller-Vogt, J. Cryst. Growth, 132 (1993) 389.
62. E.A. Oliber, E.R. Benavidez, G. Requena, J.E. Fiscina, C.J.R. González Oliver, Physica C, 384 (2003) 247.
63. P. Schätzle, W. Bieger, U. Wiesner, P. Verges and G. Krabbes, Supercond. Sci. Technol., 9 (1996) 869, and references therein.
64. E.A. Goodilin, N.N. Oleynikov, E.V. Antipov, R.V. Shpanchenko, G.Yu. Popov, V.G. Balakirev and Yu.D. Tretyakov, Physica C, 272 (1996) 65.
65. L. Dimesso, M. Marchetta, G. Calestani, A. Migliori and R. Masini, Supercond. Sci. Technol., 10 (1997) 347, and references therein.
66. M. Muralidhar, H.S. Chauhan, T. Saitoh, K. Kamada, K. Segawa and M. Murakami, Supercond. Sci. Technol., 10 (1997) 663.
67. E. Goodilin, M. Limonov, A. Panfilov, N. Khasanova, A. Oka, S. Tajima and Y. Shiohara, Physica C, 300 (1998) 250.
68. X. Yao, K. Furuya, Y. Nakamura, J. Wen, A. Endoh, M. Sumida and Y. Shiohara, J. Mater. Res., 10 (1995) 3003, and references therein.
69. G. Burns, High Temperature Superconductivity, Academic Press, Inc., San Diego, CA 1992, p. 160–164.
70. X. Yao and Y. Shiohara, Supercond. Sci. Technol., 10 (1997) 249.
71. X. Yao, M. Kambara, T. Umeda and Y. Shiohara, Jpn. J. Appl. Phys., 36 (1997) L400, and references therein.
72. A. Erb, J.-Y. Genoud, F. Marti, M. Däumling, E. Walker and R. Flükiger, J. Low Temp. Phys., 105 (1996) 1033.
73. W.-J. Jang, H. Mori, M. Watahiki, S. Tajima, N. Koshizuka and S. Tanaka, J. Solid State Chem., 130 (1997) 42.
74. A. Jeremie, G. Grasso and R. Flükiger, J. Therm. Anal., 48 (1997) 635.
75. A. Reller, J. Therm. Anal., 36 (1990) 1989.
76. A. Reller, Pure Appl. Chem., 61 (1989) 1331.

77. A.J. Bourdillon, N.X. Tan and C.L. Ong, J. Mater. Sci. Lett., 15 (1996) 439.
78. P. Majewski, Supercond. Sci. Technol., 10 (1997) 453.
79. A. Sebaoun, P. Satre, M. Mansori and A. L'Honore, J. Therm. Anal., 48 (1997) 971.
80. G.M. Zorn, R. Hornung, H.E. Göbel, B. Seebacher, H.W. Neumüller and G. Tomandl, Supercond. Sci. Technol., 8 (1995) 234.
81. H. Zhang, F. Ritter, T. Frieling, B. Kindler and W. Assmus, J. Appl. Phys., 77 (1995) 3704.
82. T. Suzuki, K. Yumoto, M. Mamiya, M. Hasegawa and H. Takei, Physica C, 301 (1998) 173.
83. T. Suzuki, K. Yumoto, M. Mamiya, M. Hasegawa and H. Takei, Physica C, 307 (1998) 1.
84. M.M.A. Sekkina and K.M. Elsabawy, Physica C, 377 (2002) 254.
85. M. Mizuno, H. Endo, J. Tsuchiya, N. Kijima, A. Sumiyama and Y. Oguri, Jpn. J. Appl. Phys., 27 (1988) L1225.
86. Y.T. Huang, C.Y. Shei, W.N. Wang, C.K. Chiang and W.H. Lee, Physica C, 169 (1990) 76, and references therein.
87. T. Kanai and T. Kamo, Supercond. Sci. Technol., 6 (1993) 510.
88. E. Giannini, E. Bellingeri, R. Passerini and R. Flükiger, Physica C, 315 (1999) 185.
89. T. Hatano, K. Aota, S. Ikeda, K. Nakamura and K. Ogawa, Jpn. J. Appl. Phys., 27 (1988) L2055.
90. J.-C. Grivel and R. Flükiger, Supercond. Sci. Technol., 11 (1998) 288.
91. J.-C. Grivel, F. Kubel and I. Flükiger, J. Therm. Anal., 48 (1997) 665.
92. F.H. Chen, H.S. Koo and T.Y. Tseng, J. Mater. Sci., 25 (1990) 3338.
93. G. Marbach, S. Stotz, M. Klee and J.W.C. De Vries, Physica C, 161 (1989) 111.
94. Q. Xu, L. Bi, D. Peng, G. Meng, G. Zhou, Z. Mao, C. Fan and Y. Zhang, Supercond. Sci. Technol., 3 (1990) 564.
95. G.V. Rama Rao, U.V. Varadaraju, S. Venkadesan and S.L. Mannan, J. Solid State Chem., 126 (1996) 55.
96. W. Wong-Ng and S.W. Freiman, Appl. Supercond., 2 (1994) 163.
97. T. Komatsu, R. Sato, K. Imai, K. Matusita and T. Yamashita, Jpn. J. Appl. Phys., 27 (1988) L550.
98. D. Shi, M. Tang, M.S. Boley, M. Hash, K. Vandervoort, H. Claus and Y.N. Lwin, Phys. Rev. B, 40 (1989) 2247.
99. T. Komatsu and K. Matusita, Thermochim. Acta, 174 (1991) 131.
100. Y. Oka, N. Yamamoto, H. Kitaguchi, K. Oda and J. Takada, Jpn. J. Appl. Phys., 28 (1989) L213.
101. N.P. Bansal, J. Appl. Phys., 68 (1990) 1143.
102. D.P. Matheis, S.T. Misture and R.L. Snyder, Physica C, 207 (1993) 134.
103. T. Komatsu, R. Sato, Y. Kuken and K. Matusita, J. Am. Ceram. Soc., 76 (1993) 2795.

104. R.S. Liu, J.M. Liang, S.F. Wu, Y.T. Huang, P.T. Wu and L.J. Chen, Physica C, 159 (1989) 385.
105. A. Iyo, Y. Ishiura, Y. Tanaka, P. Badica, K. Tokiwa, T. Watanabe and H. Ihara, Physica C, 370 (2002) 205.
106. W.L. Holstein, J. Phys. Chem., 97 (1993) 4224.
107. C. Opagiste, G. Triscone, M. Couach, T.K. Jondo, J.-L. Jorda, A. Junod, A.F. Khoder and J. Muller, Physica C, 213 (1993) 17.
108. H.-U. Schuster and J. Wittrock, J. Therm. Anal., 39 (1993) 1397.
109. Q. Xu, T.B. Tang and Z. Chen, Supercond. Sci. Technol., 7 (1994) 828.
110. C.W. Chu, J. Supercond., 7 (1994) 1.
111. J.J. Capponi, J.L. Tholence, C. Chaillout, M. Marezio, P. Bordet, J. Chenavas, S.M. Loureiro, E.V. Antipov, E. Kopnine, M.F. Gorius, M. Nunez-Regueiro, B. Souletie, P. Radaelli and F. Gerhards, Physica C, 235–240 (1994) 146.
112. J. Karpinski, H. Schwer, K. Conser, J. Löhle, R. Molinski, A. Morawski, Ch. Rossel, D. Zech and J. Hofer, in P. Klamut and B.W. Veal (eds.), Lecture Notes in Physics Ser., Vol. 475, Springer-Verlag GmbH, Germany 1996, p. 83.
113. A. Kareiva and I. Bryntse, J. Mater. Chem., 5 (1995) 885.
114. Q.M. Lin, Z.H. He, Y.Y. Sun, L. Gao, Y.Y. Xue and C.W. Chu, Physica C, 254 (1995) 207.
115. V.A. Alyoshin, D.A. Mikhailova and E.V. Antipov, Physica C, 271 (1996) 197.
116. D.A. Mikhailova, V.A. Alyoshin, E.V. Antipov and J. Karpinski, J. Solid State Chem., 146 (1999) 151.
117. A.G. Cunha, M.T.D. Orlando, F.G. Emmerich and E. Baggio-Saitovitch, Physica C, 341–348 (2000) 2469.
118. A.G. Cunha, A. Sin, X. Granados, A. Calleja, M.T.D. Orlando, S. Piñol, X. Obradors, F.G. Emmerich and E. Baggio-Saitovitch, Supercond. Sci. Technol., 13 (2000) 1549.
119. A. Sin, A.G. Cunha, A. Calleja, M.T.D. Orlando, F.G. Emmerich, E. Baggio-Saitovich, S. Piñol, J.M. Chimenos and X. Obradors, Physica C, 306 (1998) 34.
120. A.G. Cunha, M.T.D. Orlando, K.M.B. Alves, L.G. Martinez, F.G. Emmerich and E. Baggio-Saitovitch, Physica C, 356 (2001) 97.
121. A. Manthiram, J.S. Swinnea, Z.T. Sui, H. Steinfink and J.B. Goodenough, J. Am. Chem. Soc., 109 (1987) 6667.
122. M. Marezio, A. Santoro, J.J. Capponi, E.A. Hewat, R.J. Cava and F. Beech, Physica C, 169 (1990) 401.
123. C. Namgung, J.T.S. Irvine, J.H. Binks, E.E. Lachowski and A.R. West, Supercond. Sci. Technol., 2 (1989) 181.
124. A. Fukuoka, A. Tokiwa-Yamamoto, M. Itoh, R. Usami, S. Adachi, H. Yamauchi and K. Tanabe, Physica C, 265 (1996) 13.
125. C. Michel and B. Raveau, Rev. Chim. Miner., 21 (1984) 407.

126. K. Oh-ishi, M. Kikuchi, Y. Syono, N. Kobayashi, T. Sasaoka, T. Matsuhira, Y. Muto and H. Yamauchi, Jpn. J. Appl. Phys., 27 (1988) L1449.
127. H. Kanai, J. Mizusaki, H. Tagawa, S. Hoshiyama, K. Hirano, K. Fujita, M. Tezuka and T. Hashimoto, J. Solid State Chem., 131 (1997) 150.
128. M. Karppinen, L. Niinistö and H. Yamauchi, J. Therm. Anal., 48 (1997) 1123.
129. S. Chernyaev, L. Rudnitsky and A. Mozhaev, J. Therm. Anal., 48 (1997) 941.
130. J.L. Routbort and S.J. Rothman, J. Appl. Phys., 76 (1994) 5615.
131. K. Kishio, K. Suzuki, T. Hasegawa, T. Yamamoto, K. Kitazawa and K. Fueki, J. Solid State Chem., 82 (1989) 192.
132. Z. Zhu, D. Yang, Y. Guo, Q. Liu, Z. Gao and X. Hu, Physica C, 383 (2002) 169.
133. T.B. Tang and W. Lo, Physica C, 174 (1991) 463.
134. P. Karen and A. Kjekshus, J. Therm. Anal., 48 (1997) 1143.
135. J.-S. Lee and H.-I. Yoo, J. Electrochem. Soc., 142 (1995) 1169.
136. Z.-G. Fan, Y.-X. Zhuang, G. Yang, R. Shao and G.-F. Zhang, J. Alloys Compd., 200 (1993) 33.
137. S.T. Lin, J.Y. Jih and K.F. Pai, J. Mater. Sci., 25 (1990) 1037.
138. P.K. Gallagher, Thermochim. Acta, 148 (1989) 229.
139. H. Ishizuka, Y. Idemoto and K. Fueki, Physica C, 204 (1992) 55.
140. K. Fueki, Y. Idemoto and H. Ishizuka, Physica C, 166 (1990) 261.
141. T.B. Lindemer, J.F. Hunley, J.E. Gates, A.L. Sutton, Jr., J. Brynestad, C. R. Hubbard and P.K. Gallagher, J. Am. Ceram. Soc., 72 (1989) 1775.
142. K. Kishio, J. Shimoyama, T. Hasegawa, K. Kitazawa and K. Fueki, Jpn. J. Appl. Phys., 26 (1987) L1228.
143. A.J. Jacobson, J.M. Newsam, D.C. Johnston, J.P. Stokes, S. Bhattacharya, J.T. Lewandowski, D.P. Goshorn, M.J. Higgins and M.S. Alvarez, in C.N.R. Rao (ed.), Chemistry of Oxide Superconductors, the Alden Press, Oxford 1988, p. 43.
144. Y. Kubo, Y. Nakabayashi, J. Tabuchi, T. Yoshitake, A. Ochi, K. Utsumi, H. Igarashi and M. Yonezawa, Jpn. J. Appl. Phys., 26 (1987) L1888.
145. M.O. Eatough, D.S. Ginley, B. Morosin and E.L. Venturini, Appl. Phys. Lett., 51 (1987) 367.
146. J. Mizusaki, H. Tagawa, K. Hayakawa and K. Hirano, J. Am. Ceram. Soc., 78 (1995) 1781.
147. P. Meuffels, R. Naeven and H. Wenzl, Physica C, 161 (1989) 539.
148. H.M. O'Bryan and P.K. Gallagher, Adv. Ceram. Mater., 2 (1987) 640.
149. J.D. Jorgensen, M.A. Beno, D.G. Hinks, L. Soderholm, K.J. Volin, R.L. Hitterman, J.D. Grace, I.K. Schuller, C.U. Segre, K. Zhang and M.S. Kleefisch, Phys. Rev. B, 36 (1987) 3608.
150. A.W. Hewat, J.J. Capponi, C. Chaillout, M. Marezio and E.A. Hewat, Solid State Commun., 64 (1987) 301.
151. A. Kulpa, A.C.D. Chaklader, G. Roemer, D.L.I. Williams and W.N. Hardy, Supercond. Sci. Technol., 3 (1990) 483.

152. H.M. O'Bryan, Thermochim. Acta, 174 (1991) 223.
153. Y. Nakabayashi, Y. Kubo, T. Manako, J. Tabuchi, A. Ochi, K. Utsumi, H. Igarashi and M. Yonezawa, Jpn. J. Appl. Phys., 27 (1988) L64.
154. T. Wada, N. Suzuki, A. Maeda, T. Yabe, K. Uchinokura, S. Uchida and S. Tanaka, Phys. Rev. B, 39 (1989) 9126.
155. V. Balek and P.K. Gallagher, Thermochim. Acta, 186 (1991) 63.
156. Reference 69, p. 135.
157. K. Conder, Ch. Krüger, E. Kaldis, G. Burri and L. Rinderer, Mater. Res. Bull., 30 (1995) 491.
158. E. Kemnitz, A.A. Galkin, T. Olesch, S. Scheurell, A.P. Mozhaev and G.N. Mazo, J. Therm. Anal., 48 (1997) 997.
159. D.E. Morris, N.G. Asmar, J.H. Nickel, R.L. Sid, J.Y.T. Wei and J.E. Post, Physica C, 159 (1989)
160. J. Karpinski, S. Rusiecki, E. Kaldis, B. Bucher and E. Jilek, Physica C, 160 (1989) 449.
161. T. Wada, N. Suzuki, A. Ichinose, Y. Yaegashi, H. Yamauchi and S. Tanaka, Appl. Phys. Lett., 57 (1990) 81.
162. P.K. Gallagher, H.M. O'Bryan, R.J. Cava, A.C.W.P. James, D.W. Murphy, W.W. Rhodes, J.J. Krajewski, W.F. Peck and J.V. Waszczak, Chem. Mater., 1 (1989) 277.
163. J. Valo and M. Leskelä, unpublished material.
164. J. Valo, M. Leskelä, B.C. Hauback, H. Fjellvåg, S.-M. Koo and K.V. Rao, Int. J. Inorg. Mater., 2 (2000) 269.
165. H.M. O'Bryan, W.W. Rhodes and P.K. Gallagher, Chem. Mater., 2 (1990) 421.
166. H. Zhang, Q.R. Feng, Y. Zhao, F. Ritter, W. Sun, T. Frieling and W. Assmus, Solid State Commun. 95 (1995) 601.
167. P.G. Wahlbeck, D.L. Myers and K.V. Salazar, Physica C, 252 (1995) 147.
168. Z.X. Zhao and G.C. Che, Appl. Supercond., 2 (1994) 227.
169. J.L. Jorda, T.K. Jondo, R. Abraham, M.T. Cohen-Adad, C. Opagiste, M. Couach, A.F. Khoder and G. Triscone, J. Alloys Compd, 215 (1994) 135.
170. J.L. Jorda, T.K. Jondo, R. Abraham, M.T. Cohen-Adad, C. Opagiste, M. Couach, A. Khoder and F. Sibieude, Physica C, 205 (1993) 177.
171. K. Lebbou, S. Trosset, R. Abraham, M.T. Cohen-Adad, M. Ciszek and W.Y. Liang, Physica C, 304 (1998) 21.
172. V.A. Alyoshin, D.A. Mikhailova, E.B. Rudnyi and E.V. Antipov, Physica C, 383 (2002) 59.
173. A.F. Maiorova, S.N. Mudretsova, M.L. Kovba, Yu.Ya. Skolis, M.V. Gorbatcheva, G.N. Maso and L.A. Khramtsova, Thermochim. Acta, 269–270 (1995) 101.
174. Q. Xiong, Y.Y. Xue, Y. Cao, F. Chen, Y.Y. Sun, J. Gibson, C.W. Chu, L.M. Liu and A. Jacobson, Phys. Rev. B, 50 (1994) 10346.
175. A. Tokiwa-Yamamoto, A. Fukuoka, M. Itoh, S. Adachi, H. Yamauchi and K. Tanabe, Physica C, 269 (1996) 354.

176. T. Tsuchiya, K. Fueki and T. Koyama, Physica C, 298 (1998) 49.
177. A. Schilling, M. Cantoni, J.D. Guo and H.R. Ott, Nature, 363 (1993) 56.
178. A. Bertinotti, D. Colson, J. Hammann, J.-F. Marucco, D. Luzet, A. Pinatel and V. Viallet, Physica C, 250 (1995) 213.
179. D. Colson, A. Bertinotti, J. Hammann, J.F. Marucco and A. Pinatel, Physica C, 233 (1994) 231.
180. N.H. Hur, N.H. Kim, K.W. Lee, Y.K. Park and J.C. Park, Mater. Res. Bull., 29 (1994) 959.
181. V.P.S. Awana, S. Ichihara, M. Karppinen and H. Yamuchi, Physica C, 378–381 (2002) 249.
182. G. Gao, S. McCall, M. Shepard, J.E. Crow and R.P. Guertin, Phys. Rev. B, 56 (1997) 321.
183. C. Shaou, H.F. Braun and T.P. Papageorgiou, J. Alloys Compd., 351 (2003) 7.
184. N.D. Zhigadlo, P. Odier, J.C. Marty, P. Bordet and A. Sulpice, Physica C, (2003), in press.
185. F. Prado, A. Caneiro and A. Serquis, J. Therm. Anal., 48 (1997) 1027, and references therein.
186. H.R. Amrani Idrissi, G. Peraudeau, R. Berjoan, S. Piñol, J. Fontcuberta and X. Obradors, Supercond. Sci. Technol., 9 (1996) 805.
187. T. Karlemo, M. Karppinen, L. Niinistö, J. Lindén and M. Lippmaa, Physica C, 292 (1997) 225.
188. K. Fujinami, M. Karppinen and H. Yamauchi, Physica C, 300 (1998) 17.
189. T. Nakane, K. Fujinami, M. Karppinen and H. Yamauchi, Supercond. Sci. Technol., 12 (1999) 242.
190. M. Karppinen and H. Yamauchi, in A. Narlikar (ed.), Stud. High Temp. Supercond., Vol. 37, Nova Science Publishers, Inc., New York 2001, p. 109.
191. T. Nakane, Y. Yasukawa, E.S. Otabe, T. Matsushita, M. Karppinen and H. Yamauchi, Physica C, 338 (2000) 25.
192. A.Q. Pham, A. Maignan, M. Hervieu, C. Michel, J. Provost and B. Raveau, Physica C, 191 (1992) 77.
193. H. Vlaeminck, H.H. Goossens, R. Mouton, S. Hoste and G. Van der Kelen, J. Mater. Chem., 1 (1991) 863.
194. H. Lütgemeier, S. Schmenn, H. Schone, Yu. Baikov, I. Felner, S. Goren and C. Korn, J. Alloys Compd., 219 (1995) 29.
195. J. Hauck, B. Bischof, K. Mika, E. Janning, H. Libutzki and J. Plewa, Physica C, 212 (1993) 435.
196. M. Karppinen and L. Niinistö, Supercond. Sci. Technol., 4 (1991) 334.
197. P.K. Gallagher, H.M. O'Bryan, S.A. Sunshine and D.W. Murphy, Mater. Res. Bull., 22 (1987) 995.
198. D.C. Harris and T.A. Hewston, J. Solid State Chem., 69 (1987) 182.
199. J. Valo, Studies on preparation and substitution of $YBa_2Cu_4O_8$, PhD thesis, University of Helsinki, Yliopistopaino, Helsinki (1999).

200. N. Nguyen, J. Choisnet, M. Hervieu and B. Raveau, J. Solid State Chem., 39 (1981) 120.
201. P. Krihnaraj, M. Lelovic, N.G. Eror and U. Balachandran, Physica C, 234 (1994) 318.
202. M. Karppinen, O. Antson, P. Baulés, T. Karlemo, T. Katila, J. Lindén, M. Lippmaa, L. Niinistö, C. Roucau, I. Tittonen and K. Ullakko, Supercond. Sci. Technol., 5 (1992) 476.
203. M. Leskelä, J.K. Truman, C.H. Mueller and P.H. Holloway, J. Vac. Sci. Technol. A, 7 (1989) 3147.
204. M. Leskelä, H. Mölsä and L. Niinistö, Supercond. Sci. Technol., 6 (1993) 627.
205. I.M. Watson, Chem. Vap. Deposition, 3 (1997) 9.
206. D.L. Schulz and T.J. Marks, in W.S. Rees (ed.), CVD of Nonmetals, VCH Verlafsgesellschaft, Weinheim 1996, p. 39.
207. J. Zhao, C.S. Chern, Y.Q. Li, D.W. Noh, P.E. Norris, P. Zawadski, B. Kear and B. Gallois, J. Cryst. Growth,107 (1991) 699.
208. M. Leskelä and L. Niinistö, in T. Suntola and M. Simpson (eds.), Atomic Layer Epitaxy, Blackie and Sons, Glasgow 1990, p. 1.
209. H.O. Pierson, Handbook of Chemical Vapor Deposition. Principles, Technology and Applications, Noyes Publications, Park Ridge, N.J. 1992, p. 26.
210. S.C. Thompson, D.J. Cole-Hamilton, D.D. Gilliland, M.L. Hitchman and J.C. Barnes, Adv. Mater. Opt. Electron., 1 (1992) 81.
211. D.J. Otway, B. Obi and W.S. Rees, J. Alloys Compd., 251 (1997) 254.
212. M. Tiitta and L. Niinistö, Chem. Vap. Deposition, 3 (1997) 167.
213. J.E. Schwarberg, R.E. Sievers and R.W. Moshier, Anal. Chem., 42 (1970) 1828.
214. G. Guiochon and C. Pommier, Gas Chromatography in Inorganics and Organometallics, Ann Arbor Science Publishers, Ann Arbor 1978, p. 205.
215. G.S. Girolami, P.M. Jeffries and L.H. Dubois, J. Am. Chem. Soc., 115 (1993) 1015.
216. D.L. Schulz, B.J. Hinds, D.A. Neumayer, C.L. Stern and T.J. Marks, Chem. Mater., 5 (1993) 1605.
217. D.L. Schulz, B.J. Hinds, C.L. Stern and T.J. Marks, Inorg. Chem., 32 (1993) 249.
218. D.B. Studebaker, D.A. Neumayer, B.J. Hinds, C.L. Stern and T.J. Marks, Inorg. Chem, 39 (2000) 3148.
219. L.G. Hubert-Pfalzgraf, New J. Chem., 19 (1995) 727.
220. F. Labrize, L.G. Hubert-Pfalzgraf, J.-C. Daran, S. Halut and P. Tobaly, Polyhedron, 15 (1996) 2707.
221. W.A. Herrmann, N.W. Huber and O. Runte, Angew. Chem. Int. Ed. Engl., 34 (1995) 2187.
222. A.P. Purdy, C.F. George and J.H. Callahan, Inorg. Chem., 30 (1991) 2812.

223. S.R. Drake, D.J. Otway, M.B. Hursthouse and K.M.A. Malik, Polyhedron, 11 (1992) 1995.
224. M. Westerhause, Inorg. Chem., 30 (1991) 96.
225. B.A. Vaarstra, J.C. Huffman, W.E. Streib and K.G. Caulton, Inorg. Chem., 30 (1991) 21.
226. D. Pfeiffer, M.J. Heeg and C.H. Winter, Inorg. Chem., 39 (2000) 2377.
227. D.J. Burkey, R.A. Williams and T.P. Hanusa, Organometallics, 12 (1993) 1331.
228. T.P. Hanusa, Polyhedron, 9 (1990) 1345.
229. H. Sizmann, T. Dezember and M. Ruck, Angew. Chem. Int. Ed., 37 (1998) 3114.
230. F. Weber, H. Sitzmann, M. Schultz, C.D. Sofield and R.A. Andersen, Organometallics, 21 (2002) 3139.
231. J. Ihanus, T. Hänninen, T. Hatanpää, T. Aaltonen, I. Mutikainen, T. Sajavaara, J. Keinonen, M. Ritala and M. Leskelä, Chem. Mater., 14 (2002) 1937.
232. T. Hatanpää, T. Hänninen, J. Ihanus, J. Kansikas, I. Mutikainen, M. Vehkamäki, M. Ritala and M. Leskelä, Proceed. Electrochem. Soc., (2003), in press.
233. H. Schumann, J. Gottfriedsen and J. Demtschuk, Chem. Comm., (1999) 2091.
234. F. Labrize, L.G. Hubert-Pfalzgraf, J.-C. Daran, S. Halut and P. Tobaly, Polyhedron, 15 (1996) 2707.
235. A.N. Gleizes, F. Senocq, M. Julve, J.L. Sanz, N. Kuzmina, S. Troyanov, I. Malkerova, A. Alikhanyan, M. Ryazanov, A. Rogachev and E. Deblovskaya, J. Phys. IV Fr., 9 (1999) Pr8-943.
236. T. Ozawa, Thermochim. Acta, 174 (1991) 185.
237. E.W. Berg and N.M. Herrera, Anal. Chim. Acta., 60 (1972) 117.
238. S.B. Turnipseed, R.M. Barkley and R.E. Sievers, Inorg. Chem., 30 (1991) 1164.
239. B.J. Hinds, D.B. Studebaker, J. Chen, R.J. McNeely, B. Han, J.L. Schindler, T.P. Hogan, C.R. Kannewurf and T.J. Marks, J. Phys., IV, (1995) C5-391.
240. M. Leskelä, L. Niinistö, E. Nykänen, P. Soininen and M. Tiitta, Thermochim. Acta, 175 (1991) 91.
241. I.M. Watson, M.P. Atwood and S. Haq, Supercond. Sci. Technol., 7 (1994) 672.
242. G. Rossetto, A. Polo, F. Benetollo, M. Porchia and P. Zanella, Polyhedron, 11 (1992) 979.
243. S.R. Drake, M.B. Hursthouse, K.M.A. Malik and D.J. Otway, J. Chem. Soc., Dalton Trans., (1993) 2883.
244. R. Gardiner, D.W. Brown, P.S. Kirlin and A.L. Rheingold, Chem. Mater., 3 (1991) 1053.
245. T. Kimura, H. Yamauchi, H. Machida, H. Kokubun and M. Yamada, Jpn. J. Appl. Phys., 33 (1994) 5119.
246. T. Hänninen, M. Leskelä, I. Mutikainen, G. Härkönen and K. Vasama, Chem. Mater., to be published.

247. T. Hashimoto, H. Koinuma, M. Nakabayashi, T. Shiraishi, Y. Suemune and T. Yamamoto, J. Mater. Res., 7 (1992) 1336.
248. S.R. Drake, M.B. Hursthouse, K.M. Abdul Malik and S.A.S. Miller, Inorg. Chem., 32 (1993) 4653.
249. S.R. Drake, S.A.S. Miller, M.B. Hursthouse and K.M. Abdul Malik, Polyhedron, 12 (1993) 1621.
250. H. Sato and S. Sugawara, Inorg. Chem., 32 (1993) 1941.
251. K. Timmer, K.I.M.A. Spee, A. Mackor, H.A. Meinema, A.L. Spek and P. van der Sluis, Inorg. Chim. Acta, 190 (1991) 109.
252. G. Maladrino, F. Castelli and I.L. Fragala, Inorg. Chim. Acta, 224 (1994) 203.
253. J. Zhao, K.-H. Dahmen, H.O. Marcy, L.M. Tonge, T.J. Marks, B.W. Wessels and C.R. Kannewurf, Appl. Phys. Lett., 53 (1988) 1750.
254. S.R. Drake, S.A.S. Miller and D.J. Williams, Inorg. Chem., 32 (1993) 3227.
255. T.J. Marks, J.A. Belot, C.J. Reedy, R.J. McNeely, D.B. Studebaker, D.A. Neumayer and C.L. Stern, J. Alloys Compd., 251 (1997) 243.
256. W.R. Wolf, R.E. Sievers and G.H. Brown, Inorg. Chem., 11 (1972) 1995.
257. S.H. Shamlian, M.L. Hitchman, S.L. Cook and B.C. Richards, J. Mater. Chem., 4 (1994) 81.
258. R. Amano, A. Sato and S. Suzuki, Bull. Chem. Soc. Jpn., 54 (1981) 1368.
259. H.R. Brunner and B.J. Curtis, J. Therm. Anal., 15 (1973) 1111.
260. N. Matsubara and T. Kuwamoto, Inorg. Chem., 24 (1985) 2697.
261. P. Tobaly and G. Lanchec, J. Chem. Thermodyn., 25 (1993) 503.
262. E. Waffenschmidt, J. Musolf, M. Heuken and K. Heime, J. Supercond., 5 (1992) 119.
263. K. Chou and G. Tsai, Thermochim. Acta, 240 (1994) 129.
264. T. Hänninen, I. Mutikainen, V. Saanila, M. Ritala, M. Leskelä and J.C. Hanson, Chem. Mater., 9 (1997) 1234.
265. E. Schmaderer, R. Huber, H. Oetzmann and G. Wahl, Appl. Surf. Sci., 46 (1990) 53.
266. A.F. Bykov, P.P. Semyannikov and K.I. Igumenov, Thermochim. Acta, 38 (1992) 1463.
267. A.F. Bykov, P.P. Semyannikov and K.I. Igumenov, Thermochim. Acta, 38 (1992) 1477.
268. T. Hashimoto, K. Fueki, A. Kishi, T. Azumi and H. Koinuma, Jpn. J. Appl. Phys., 27 (1988) L214.
269. H.M. O'Bryan, P.K. Gallagher, G.W. Berkstresser and C.D. Brandle, J. Mater. Res, 5 (1990) 183.
270. A. Hårsta, J. Therm. Anal., 48 (1997) 1093.
271. C. Vahlas and T.M. Besmann, J. Am. Ceram. Soc., 75 (1992) 2679.
272. Y. Tasaki, R. Sakamoto, Y. Ogawa, S. Yoshizawa, J. Ishiai and S. Akase, Jpn. J. Appl. Phys., 33 (1994) 5400.
273. M. Vehkamäki, T. Hänninen, M. Ritala, M. Leskelä, T. Sajavaara, E. Rauhala and J. Keinonen, Chem. Vap. Deposition, 7 (2001) 75.

This Page Intentionally Left Blank

INDEX

α (see also fractional reaction) 602,617
A
Abel test for explosives 355
'abnormal' reactions 605,607
acanthite 526,527,530
AC calorimetry 533,824
accelerated ageing 52,63,77,81
accelerating rate calorimetry (ARC) 354,362,789,792
accessory minerals 266,276,282,293,302
acetates 597,636,751,826,836
acetic acid 71,72
acid solution calorimetry of HTSC 818
acoustic signal 541
acrylamide 146
acrylic paint 72
acrylonitrile hydration 146
AC susceptibility 824
activated carbon 97,98,106
activation energy (E_a) 22, 98,99,102,110,114,120,132,136,147, 157,169,178,329,335,352,358,366, 371,374,375,377,379,381,385,390,391, 420,421,603,660,681,687,689,692,698, 700,702,703,712,748,757,758,763, 782,796,805,826,838,841,842,854
active interface 600
adiabatic calorimetry 22,402
adiabatic explosion model 358
adsorbate interactions 27,28,41
adsorbate phase changes 24,37,38
adsorbed water 274,296,302
adsorbents 244
adsorption 1-46,120,129,132,164,223
adsorption calorimetry 1,22
adsorption isotherms 28,29
adsorption manometry 27
adsorption upgrading 345
AFM (see atomic force microscopy)
Ag-Al alloys 718
Ag-Au alloy 697
Ag-Au-Ge system 671
Ag-Cu alloy 697,698,764
Ag-Cu-Ti alloys 721
age hardening 679,755
ageing of art materials 48,62,66,74,75,83
ageing of pyrotechnics 793,794
age of rocks 564
Ag-Mg alloys 718
Ag_2O 698
Ag_2S 409
Ainsworth balance 739
air bags 789
albite 262
Al-Cr system 764
Al-Cu system 679,701,755,764
Al-Cu-Cr system 764
Al-Cu-Mg alloy 754
Al-Cu-Nb system 764
Al-Cu-Ti system 764
Al-Cu-Zr system 764
AlF_3 803
Al-Fe alloys 685,693,701,763
AlH_3 decomposition 230,231
Al-In system 675
alkali-metal tetrafluoroborates 411
alkane aromatization 179
Al-$KClO_4$ pyrotechnic system 789,803
alkene metathesis 143
Al-KNO_3 pyrotechnic system 781
Al-KNO_3-CaF_2 pyrotechnic system 794
Al-KNO_3-NaF pyrotechnic system 794
alkoxides 827,859
alkylammonium tetrachlorozincates 406
alkyldiphenyl 331
alkyldiphenylethane 326,327,331
Al-Li alloys 681
Al-Li-Mg system 670
allophanes 476,498,510
alloys 19,208,209,426,563, 664,666,672,676,679,688,704,707,716,728
alloys oxidation 716,838
Al-Mn system 763
Al-$NaNO_3$-CaF_2 pyrotechnic system 794
Al-$NaNO_3$-NaF pyrotechnic system 794
Al-Nb system 764
AlN oxidation 225
$Al_2(MoO_4)_3$ 424
Al_2O_3-Al composite 756
Al-SiC composites 754,755
Al-Ti system 764

alumina 217,237,408,426
alumina coating 732
aluminides 764
aluminium alloy AA-2011 680
aluminium alloy 6061 757
aluminium and metal oxides 701,702
aluminium corrosion 728
aluminium hydroxide 475,642
aluminium nitridation 749
aluminium oxidation 720
aluminium production 736
aluminophosphates 21,36,38,39,41
aluminosilicates 512,598
alums 597,598,612,615,621,629-631,639,647
alunite 458
alunogen 458
$AlVMoO_7$ 424
Al-Zr system 764
amber 539,566
amblygonite 466
amersooite 278
amine complexes 431,436
amino acid analysis 78,88
amino acids 538
ammonia adsorption/desorption 176,177
ammonium dinitramide (ADN) 355
ammonium molybdate 122
ammonium nitrate (AN) 351,354,360,445,792
ammonium nitrate emulsion 360
ammonium oxalate monohydrate 641
ammonium salts 796
ammonium sulfate 736
amorphization 549,756,762,763
amorphous alloys 676,688
amorphous carbon 97
amorphous materials 274,686,689,690,698,699,763
amphibole 66,68,505
AN (see ammonium nitrate)
anatase 293
ANFO (ammonium nitrate fuel oil) 351
anhydrite 458,545
anhydrous reactants, preparation 646
ankerite 513,514,518,539
annealing 422,427,679,688,691,693,707,713,714,754,757,832,839,866
anorthite 290
anthracite 376,378
anthranilates 436
antigorite 480
antimonides 525
apophyllite 479,482
aragonite 521,522,542,551,552
ARC (see accelerating rate calorimetry)
archaeology 47-96,566
Arrhenius parameters (E_a and A) 123,132,240,362,374,386,603,610,622,642,647,648
arsenates 454,463-465,510
arsenides 525,526
arsenopyrite 527
artinite 520
art preservation 47-96,566
aryloxides 860
ascharite 471
ash content of coal 204,380
asphaltenes 384,385
asphaltite 376,380,381
ASTM E698-79 kinetics method 359,360
ASTM-Fisher analysis of coals 205
Atlas of Thermoanalytical Curves 433
atmosphere control 376,377,431,723,726,746
atmosphere effects 51
atomic force microscopy (AFM) 54,603,620
atomization 687,696
attapulgite 34
Au-Cu system 688
Auger electron spectroscopy 733,804
aureoles 560
aurichalcite 519
austentite 663,676,678,682,683
autocatalysis 358,361
auto-ignition 749
automobile catalytic converter 716
autoradiology 669
a-value 491,492,505
Avrami-Erofeev equation 155-159,602,676,692,693,757,838
azurite 619

B
baddeleyite 565
$Ba_xLa_{1-x}CoO_3$ 151
ball clays 292-295,298,299,303
ball milling 286,700,701
$BaPtO_{3-x}$ 196,197
$BaPt(OH)_6$ 197
barium carbonate 400,401,524,825, 826,857
barium chloride dihydrate 632
barium compounds 400
barium hydrogen oxalate dihydrate 613,638
barium hydroxide octahydrate 613
barium nitrite monohydrate 635
barium oxalate hemihydrate 435
barium oxalate monohydrate 435
Barrett, Joyner and Halenda method 19
base-exchange capacity 268,278,293-295
baseline determination 362
basic magnesium carbonate trihydrate 644
basic calcium sulfate dihydrate 644
bassanite 458,545,546
bastnaesite 519
$BaTiO_3$ 194,195,250
$BaTiO(C_2O_4)_2.4H_2O$ 252
batteries 309,346
bauxite 471,476,486
bayerite 473,474
beeswax 60
beidellite 272,274,275
bentonites 292,295,299,303,476,491,539
berthierine 479
beryllium oxalate 435
beryllium silicate 222
BET area 5,8,165,223
BET equation 28,129,137
Beypazari lignite 373
Bi-based superconductors 850
binary compounds 397
binary systems 399,418,419
binders 232-234,759,761
binders in paintings 52,53,63
binders, pyrotechnic 800,803
biomass 375,380
biotite 278,279,481,483,598
Bi-Pb,Sr-Ca-Cu-O glass ceramics 836
Bi-Pb,Sr-Ca-Cu-O HTSC system 851
bischofite 455,456
bismuthides 525
bismuth nitrate 122
bismuth oxalate 835
Bi-Sr-Ca-Cu-Ag-O HTSC system 834
Bi-Sr-Ca-Cu-O HTSC system 817, 821-823,832,863
bitumen 382,537,741
bituminous coals 374-376
$B\text{-}K_2Cr_2O_7$ pyrotechnic system 786,804
$B\text{-}KNO_3$ pyrotechnic system 792,793,805
black powder 796,797,803
bloedite 458
BN 241,243
$B\text{-}MoO_3$ pyrotechnic system 782,798,799
boetimite 473,476
boiling-point 440
bomb calorimetry 411
bond character 397
bond energy 352
bookbindings 76,83
boracite 469
borated alloy steels 681
borates 453,454,467-471,510,563
borax 469,471
Borchardt and Daniels kinetic method 359,360,805,806
boric acids 471
bornite 529
boron-aluminium composite 754
borsic-aluminium composite 754
Boudouard reaction 740,747
bournonite 529
$B\text{-}PbO_2$-binder pyrotechnic system 789
$B\text{-}Pb_3O_4$ pyrotechnic system 805
$B\text{-}Pb_3O_4\text{-}Cr_2O_3$ pyrotechnic system 805
B-PbO pyrotechnic system 805
brammalite 278
Brayton cycle 312,313
brazing alloys 720,721
brazing filler metals 666
breunnerite 518
brick clays 292,295,303
bricks 200,201,261,561
bronzes 50,69,70

Brownian motion 265
brucite 272,282-284,302,471-474
brugnatelite 520
buckminsterfullerene 100
buoyancy effects 198-200
burning profiles of coals 375,380

C
cadmium hydroxide 642
cadmium permanganate hydrate 635
cadmium titanyl oxalate 178
calcination 429,437,742,759,832
calcite 68, 291,297,512,513,516,542
calcium carbonate 53,69,72,76,78,123, 433,524,540,607,833,835
calcium copper acetate hexahydrate 637
calcium hydroxide 123,245,613,642
calcium nitrate tetrahydrate 74,634
calcium oxalate 750
calcium oxalate monohydrate 57,433-435
calcium oxide catalysts 123-125
calcium permanganate hydrate 635
calcium phosphate hydrate 636
calcium sulfate dihydrate 624,642
calcium sulfate hemihydrate 624
calcium sulfite hemihydrate 597,633
calibration 405,406,454
Caloria HT 332,333
calorific values of coals 380
calorimeter, drop 408
calorimeter, Tian-Calvet 411,779
calorimetry 311,362,397-399,596,616,671
canvas 48,51,53,63,69,78-84,91
capillary condensation 42
carbides 663,683,698,754,762
carbon 7,22,31,32,97-117,318,664
carbonaceous matter 291,298
carbonate content 512-514
carbonates 376,390,452,453,512-524,539, 735,748,752,826
carbon black 97,102,113
carbon black, oxidation 101-104,109
carbon dioxide pressure 512,607
carbon fibres 110
carbon, fixed 372
carbon in polymers 113
carbonization 372,375,546
carbothermic reduction 225
carnallite 455,456
casein 74
$CaSiO_3$ 408
$CaSr_2F_6$ 404
casting of metals 686
cast iron 683-685
cast steels 762
catalysis 119-190,196,657
catalysts 107,119-190,739,740
catalytic reactions 119,375,381,389,427, 687,740
cation absorption 268,272
cation exchange 286,287,302
cellulose 62,78,105,538
cement 245-248,261,561
cementation 732
ceramic fibres 217
ceramics 50,191-260,261,561,563, 721,756,762,836
cerium hydroxide 127
cerium oxide 126,160,161
cermets 721
cerussite 518,539
chalcocite 526,529,743,744
chalcogenides 525-532,539,550
chalcopyrite 529,562,742-745
chalkanthite 457
channel black 98
characteristic temperatures 430
charcoal 8,99,105
charoite 485
chemical energy storage materials 344
chemical reactivity test for explosives 350
chemical vapour deposition (CVD) 98, 241,242,818,858,859,866,868
chemisorption 163,165
"Chemistry of the Solid State" (W.E. Garner) 610
china clays 292,293,296,303
chlorides 454,456,510,522
chlorine 707,723,725,737
chlorites 263,282-284,295,302,478, 485-492
chromates 466
chrome alum 630,644
chromia-alumina catalysts 173

chromium oxidation 733
chrysocolla 511
chrysotile 480
citrates 751,826
C-KNO_3 pyrotechnic system 782
clathrate compounds 327
clathrate system 619
Clausius-Clapeyron equation 138
clay analysis 300
clay deposits 276,290-292,296,97,303
clay minerals 261-306,386,390,
451,476,494,497,549,565
clays 33, 67,70,200,261-
306,380,382,384,386,452,476,538,598,
657,736
cleaning of coal 379
cleaning of paintings 54,56,69,78,80,91
clinkering 246
coal blends 380
coal char 372,375,377
coal combustion 374,378
coal dust 378
coal, gaseous products of pyrolysis 379
coal, maceral composition 376
coal, rank 372,374,376,378
coals 97,102,204,371-381,537,538,
735,736,739
Coats-Redfern kinetic method 386,390
cobalt chloride hexahydrate 640
cobalt oxalate dihydrate 638,646
cobalt oxidation 712,725
cobalt oxide pigments 64,74
cobalt oxide precursors 142
cobalt sulfate heptahydrate 629
cobalt tartrate hydrate 437
cobalt thin film 244
Co-Cr alloy 704
coesite 565
Co-Fe alloys 718
CO hydrogenation 142
coke 105,114,374,704,736,739,741
coke combustion 385
coke formation 137,171-174,374,375,382
cold work 707,714,756
colemanite 469,563
collagen-based materials
56,63,77,82,85,86,90
Co-Mn alloys 719
colemanite 613,643,645
colloidal character of oils 385
colloidal clays 264
combustion calorimetry 399,411,
778,787,788,807
combustion of explosives 349
combustion of fuels 372,374,381
combustion synthesis 761
compatibility testing of pyrotechnics 789
compensation effect 102,377,607,622,642
competitive adsorption 140
complexes (see also coordination
compounds) 398,429,436
complex oxalates 436
complex reactions 647
composite explosives 352
composites 318,341,657,753,757,830
composite superconductors 830
compositional analysis 195
congruent composition 206,220
Co-Ni alloys 211
consecutive reactions 647
conservation science 47-96
contracting geometry models 602,633,737
controlled rate evolved gas detection
15,20,21
controlled rate thermal analysis (CrRTA or
CRTA) 432,564,566
controlled rate thermodesorption 1
cookeite 490
cook-off tests for explosives 354,356
coordination compounds 436,598,639,
640,645
coordination number 398
copiapite 458
copper acetate monohydrate 637
copper alkoxides 827
copper carbonate 833
copper(II) chloride dihydrate 633
copper formate tetrahydrate 637,642
copper metal 202,203,697
copper oxalate 826,835
copper oxidation 711-713,733
copper production 740
copper sulfate hydrates 625

copper sulfate pentahydrate 433, 598,601,608,612,625
copper sulfides 529,530
coprecipitation synthesis of HTSC 826,834
cordierite 275,511,512
corrensite 476,498
corrosion 70,71,73,89,202,203,228,229, 445,563,657,686,713,723,734
corrosion by salts 726
corrosion resistance 732,753,761
corrosive atmosphere 707,708,723,737
corundum 280,563
Co-Sm alloy 672
counterions 398
Co-Zr alloys 699
crack formation 83,818
cracking (crystal) 612,629,630,845
cracking (of organic molecules) 374,377,381,382
Cr-Fe system 704
cristobalite 219,268,274,275,297, 533,556,557
critical dimensions of explosives 352
critical temperature for explosives 352,364,366
critical temperature for HTSC (T_c) 817,850
Cr_2O_3 426
cross-linking density 377
cross-linking reactions 65,317,332,377
Cr-Os system 674
Cr-Se system 669
Cr-Si steel 688
CRTA (see constant rate thermal analysis)
crucibles 431,432,440,780
crude oil 381
crude oil-sand mixtures 385
cryolite 533,558
cryptohalite 563
crystal defects 443,541,547,599,627,646
crystal faces 624,626,629,631
crystal fracture (see cracking)
crystal growth 558,831,832
crystal imperfections (see crystal defects)
crystallinity 65,82,83,485
crystallization 194,213, 126,132,137, 147,156,160,543,612,613,676,688,689, 700,714
crystal structure 599
crystal textures 599,621
crystal water 455
crystolysis 605,614,621,629,645,648
$CsBF_4$ 410
$CsCaCl_3$ 417
$CsCrCl_3$ 407
$Cs_2NaLaCl_6$ 426
Cs_2NdCl_5 420,422
Cs_3NiCl_5 416
$CsNiCl_3$ 416
Cu-Ag-P system 666
Cu-Al-Ni system 677
Cu-Ge-O system 426
Cu-In-Pb system 662,663
cultural heritage, preservation of 47-96
cumene 137-139
cuneiform tablets 53,66-69
CuO/kieselguhr catalysts 146
Cu-Pb-Ti system 758
cuprates 196,197,857
cuprate structure 820,821,823
Curie constant 534
Curie temperature 207,211,223, 534-537,550,688,689,694,762
Curie-Weiss law 534
Cu_2S 745
Cu-Sn-P system 666
Cu-Zr system 695,696,699
cyanides as precursors 252

D

damping 754,756
DEA (see dielectric analysis)
de-acidification 78,81
Dead Sea scrolls 56,80
decarbonatisation 454,544
decomposition 429,454,490,510,512
defects 689,756
deflagration 777
deflocculants 265,294
degradation 47,52,62,65
dehydration 120,126,429,433, 452,454,510,544,595-656
dehydration, classification 611
dehydration, explosive 613,643

dehydroxylation 120,126,
268,269,274,278,279,286,289,298,301,
303,452,454,478,490,505,510,549,550
delay, pyrotechnic 788
delta transition 100
denaturation 52,63,84
densification 238
dental materials 261
derivative thermogravimetry (see DTG)
Derivatograph 14,15,77,436,564,735
desalination 66
desilication 290
desolvation 429
desorption 120,132,223,429
desorption energy profiles 17
desulfurizing 742-744
detonation 349,352,353,777
devitrification 454
devolatilisation of coals 372,374
diamond 97,98
diamond films 98
diamond oxidation 98,99
diaspore 471,473
diathermal calorimetry 22,23
dickite 266,267,270,281,286,288,477,539
dielectric analysis (DEA) 50,74,564,796
dielectric glasses 686
dielectric properties 262,295
differential enthalpy of adsorption 28,29
differential scanning calorimetry (see DSC)
differential thermal analysis (see DTA)
diffraction techniques (see also X-ray
diffraction) 603,617,619,621,622
diffusion 21,238,389,534,624,642,
709,723,737,738,839,842,854
diffusion coefficient 41,226,634,709,
841,842
diffusionless transitions 659,676
diffusion models 602
digenite 452
β-diketonates 818,859-866
dilatometry (see also TD)
261,268,269,299,303,434,443,759-762,
845
dimethylsulfoxide 545
dinitramide salts 796,797
dinnerware 261
dioctahedral illite 280,281
dioctahedral micas 278
diphenyl ether 408
direct reduced iron (DRI) 748
direct temperature resolved mass
spectroscopy (DTMS) 55,60
displacive expansion 300
displacive transformation 542
disproportionation 439
dissociative evaporation 605,623
distillation of crude oil 381,385
distribution coefficient 207
DMA (dynamic mechanical analysis see
also DMTA and DTMA) 754,755
DMTA (dynamic mechanical thermal
analysis) 51,54,80-82,85,91
dolomite 264,291,297,433,513-
516,545,546,550,551
dosimeters 52,62,91
double carbonates 427
double compounds 398
drilling mud 561
drop calorimetry 408,417,541
drying of oil shale 390
DSC (differential scanning calorimetry) 11,
51,53,56,65,74,91,100,120,192,210,215,
311,320,326,353,358,372,375,377,
398,399,405-407,417,434,455,
453.559,563,616,618,657,675,687,
778,794,818,819,824,836,868
DSC apparatus for pyrotechnics 781,782
DTA (differential thermal analysis) 53,57,
120,261,269,270,274-290,297,299,300,
303,372,398,418,422,425,430,454,
451,453,461,467,473,490,499,505,506,
516,549,559,563,616,657,778,794,
818,819,824,828,835,868
DTA apparatus for pyrotechnics 781
DTG (derivative thermogravimetry)
77,79,91,430
DTMA (dynamic thermomechanical
analysis) 51,52,65,91,442
DTMS (see direct temperature resolved
mass spectroscopy)
Dubinin-Raduschkevitch equation 130,131
ductile to brittle transition 691
ductility 690,691,693,699,753

dusts 562
dynamic mechanical analysis (see DMA)
dynamic mechanical thermal analysis (see DMTA)
dynamic thermomechanical analysis (see DTMA)

E
earth sciences 451-593
EDAX (energy dispersive analysis by X-rays) 708,721
efflorescence 72,563
EGA (evolved gas analysis) 18,174-177, 196,200-202,225,226,354,355,359,380, 431-434,453,547,564,728,739,741, 778,802,658,659,665,686,708
EGD (evolved gas detection) 818,819
egg tempera paintings 56,58
Egyptian blue pigment 50
Egyptian copper alloys 69-72
Egyptian limestone 72
elastic modulus 687,756
elastomers 113
electrical conductivity 243,679
electrical insulators 261
electrical properties 223,418,744,848
electrical resistivity 824
electro-catalytic properties 691
electroceramics 295
electrochemical cells 309
electron diffraction 756
electronegativity 397
electronic materials 191-260
electron microscopy 440
electron probe microanalysis (EPMA) 211,212,662,708,728,744
electron spectroscopy for chemical analysis (see ESCA)
electro-optical properties 205
Elovich equation 132,135-139,168,169
emanation thermal analysis (see ETA)
embrittlement 690,691
emerald 505,506
emissivity 787
endothermic processes 610,647
energy conservation 307
energy dispersive analysis by X-rays (see EDAX)
energy outputs of fuels and explosives 351
energy storage 307-348
enstatite 285
enthalpy function 398,399,402
enthalpy of crystallization 700
enthalpy of evaporation 385
enthalpy of formation 402,411
enthalpy of fusion (melting) 406
enthalpy of liquefaction 32
enthalpy of oxidation 844
enthalpy of solution 416
entropy of reaction 425
entropy of recrystallization 616
environmental aspects 51,52,371, 453,538,561,563
epidotes 510,511
epitaxial growth 763
epsomite 456,457
equilibrium constant 402
ESCA (electron spectroscopy for chemical analysis) 794
ESR 252
ETA (emanation thermal analysis) 239, 443,533,538,539,549,564,819,847
ethylenediamine tetra-acetic acid (edta) 734
ethylene dimerization 179
ethylene glycol 323,324,331
eutectic formation 193,298,300,302, 314,330,336,338,340,426,658,663, 683,684,827
eutectic temperature 399
evaporation 838,858,864,865
evaporites 510
evolved gas analysis (see EGA)
evolved gas detection (see EGD)
evolved gas measurement 618,846
exergy 313
exfoliation 283
exothermic processes 610
expansion coefficient linear 218,262, 442
expansion coefficient volume 442
experimental conditions 430,555
explosives 349-369,566,777

extent of reaction (see also fractional reaction α)
extractive metallurgy 657,735

F
Fe-Al system 688,693,729-731
Fe-BaO_2 pyrotechnic system 785,786
Fe-B-Si system 690
Fe-B-Si-C system 691
Fe-B-Si-Cr system 690
Fe-C system 704,705
Fe-Co-Gd system 667
Fe-Co-P system 688
Fe-Co-Zr 688
Fe-Cr alloys 720
Fe-Cr-Al alloys 721
Fe-Cr-C system 699
Fe-Cr-C-P-Si system 689
Fe-Cr-Mn alloys 720
Fe-Cr-Mo-B system 676
Fe-Cr-Ni alloys 719
Fe-Cr-P-B system 702,703
Fe-C-Si system 704,706
Fe-Cu-Nb-Si-B system 694,695
Fe-C-V system 663,664
Fe-FeSi system 759,760
Fe-$KMnO_4$ pyrotechnic system 786,805
feldspar 262,264,290,293,519,541
Fe-Mn alloys 723
Fe-Mn-Si system 677
Fe-Mo-C system 699
Fe-MoO_3 pyrotechnic system 799
Fe-Nd system 672,673
Fe-Nd-B alloy 672
Fe-Ni system 701,731,732
Fe-Ni-B-P system 700
Fe-Ni-Si-P system 700
Fe_2O_3-Al-Teflon pyrotechnic system 792
Fe_2O_3 synthesis 251
Fe_2O_3-Al-Teflon pyrotechnic system 792
Fe_3O_4 oxidation 231
feroxyhite 534
ferrites 197,250,663,752,759
ferroalloy process 736
ferroelectric materials 194,205
ferromagnetic phase transitions 565
Fe-Se system 669
Fe-Si system 759,760
Fe-Si-B system 676,688
Fe/Si-MnO_2 pyrotechnic system 798
Fe/Si-Pb_3O_4 pyrotechnic system 787,797
Fe-SrO_2 pyrotechnic system 786
Fe-V system 704
Fe-W system 701
Fe-Zr system 699
fibre optics 219
fibres 64
fibrous ceramics 217
Fick's first law 709
films 18
fire clays 292,295,303,549
fire damage 53,63
fireworks 777,789
firing temperatures 66,69,262
first-order kinetics 361,377,387,389-391
first-order phase transitions 399,407,542, 658
Fischer-Tropsch catalysts 179
fixed bed reactor 390
fixed carbon content of coal 204,380
flares 788,789,796
flint 262
flocculants 736
fluorides 340,342,343,417,522
fluorine bomb calorimetry 411
fluxes 270,272,296,298,300-303,826,839
fly ash 378,726,727,753
Flynn and Wall kinetic method 98, 329,330,335
formates 433,597,636,751
formation reaction 402
forsterite 284
fossil fuels 371-395
Fourier transform infrared spectroscopy (see FTIR)
four-integer naming system for HTSC 820,822
fractional reaction (α) 602,617
Frank-Kamenetskii model 365
Freeman-Carroll kinetic method 386
freezing point depression 13
frequency factor (A) 603
Freundlich adsorption model 137-141

FTIR (Fourier transform infrared spectroscopy) 63,174,175,201,202,234, 252,379,433,627,741,742,802
fuel cells 309
fuel deposition (FD) 381,386
fuels (see fossil fuels)
fullerenes 35,97,100
Fuller's Earth 295
fusion (see melting)

G
Ga-As-based semiconductors 241,242
galena 562,737-739,795
galenite 530
gallium reduction 179
gallophosphates 36
galvanic cells 423,424
garnets 512,519
gas chromatography (GC) 74,79,174,363, 433
gas clathrate compounds 327,328
gas flow 142
gas generating pyrotechnics 789,792
gasless pyrotechnics 778,779,807
gas scrubbers 780
gas titrimetry 433
gaylussite 520
Ga/ZSM-5 catalysts 179
$GdFeO_3$ 423
gelatin 56,77,86
gels 839
geologic thermometer 552,553,561
geometric models 602,610,646,649
Geoscience Committee (ICTAC) 452
geosciences 451-593
Gibbs energy 418,423
Gibbs energy of formation 402
Gibbs energy of reaction 425
Gibbs-Helmholtz equation 402,423
gibbsite 266,270,302,471-476
glass 191-260,561
glass ceramics 191-260,836
glasses 262,686
glass formation 194,214, 262,562,643
glass, toughened 227
glass transition 50,85,194,221,454,542, 691,837
glass transition temperature T_g 50,54,55,62,79,384
glassy state 262,274,686
glauconite 278,484
glazes 55,60,296
goethite 471-475,534,549,736
gold sample pan 341
goslarite 457
grain growth 703,714,718
grain size 675,687,697,718
granite 560
graphite 26,35,97,99,685,704,705,739,758
graphite oxidation 99
graphitization 111
graphon 6
gravimetric analysis 429
green ceramics 235
green strength 294,295
greigite 537
grinding 286-288,302,545,547,556
grog 296
ground layers of paintings 74
growth of crystals 839
growth of nuclei 599
Guinier-Preston (I) zones 679-681
gypsum 57,72,291,458,462,545,562

H
haematite 519
halides 408,416
halloysite 266,270,281,289,290,297,498
hardening 679,688
Harkins and Jura surface area method 1-6
Hastelloy B-2 666
Hastelloy W 666
hausmannite 533
hazard evaluation 789
heat capacity 215,311,339,398-400, 403-405,531,687
heat capacity measurement 326,405,541
heat exchangers 316-326
heat-flux calorimeters 541
heat-flux DSC 342
heating rate effect 51,380,516
heat of adsorption 132,137
heat of fusion 327,342
heat of immersion 3

heat of solidification 686
heat source pyrotechnics 788,798
heat transfer 422,658
heat transfer fluids 331,332,335
hectorite 272,275,301
Hedvall effect 230,231
hematite 198,704,705,736,737
hemicellulose 70,78
hemimorphite 511
Henkin/McGill time-to-explosion test 355
herbicides 538
Hertz-Langmuir theory 605
Hg-Ba-Ca-Cu-O HTSC system 817, 821-823
Hg-based superconductors 839,850,852
high-carbon alloys 704
high-pressure DTA 563
high-pressure synthesis of HTSC 839
high-pressure thermogravimetry 377
high-speed steels 683,762
high-T_c superconductors (see HTSC)
high-temperature oxidation(HTO) 381,386,389
high-temperature superconductors (HTSC) 817-879
hisingerite 498
HMTD 352
HMX 350,355
hornblende 290,505,506,511
hot cracking 683
hotel china 262
hot-wire thermal conductivity measurements 216
howlite 471
HPLC 76,85
HTSC, four-integer naming system 820,822
HTSC (high-T_c superconductors) 817-879
HTSC synthesis 824,825
HTSC tapes 834
HTSC wires 834
humic acid 291
humidification 78-80,83
huntite 513,516,517
humidity 47,50,51,54
hydrates 327,328,429,454,540, 547,595-656
hydrates, structures 596,597,648
hydrates, types 596,597
hydration 290
hydration of cement 247,248
hydrides 311,345,433,747
hydrodesulfurization 143
hydroelectricity 308,309
hydrogarnets 563
hydrogasification of coal 372
hydrogen 225,311,376,730,747,856,857
hydrogen chloride 726
hydrogen fluoride 201,202
hydrogen sulfide 707
hydrogenation 142,143
hydrogen reduction 225
hydrolysates 455,476,478,512,521,547,549
hydrolysis 433,455,479,599,614
hydromagnesite 520
hydromuscovite 278
hydrotalcite 175,520,538
hydrothermal decomposition 290
hydrous micas 278
hydrous pyrolysis 387
hydroxides 314,336,433,452,453, 471-476,598,735
hydroxyapatite 22
hydrozincate 519
hygroscopicity 74,429
hypereutectic alloy 208,664,683,684
hypoeutectic alloy 664,683,684
hysteresis 420,422,443,556

I

ice 311
ICTAC (see International Confederation for Thermal Analysis)
igniter 788,792
ignition 780,794,802,807
ignition conditions 780
ignition temperature 378,785,792,800
illites 69,263,276,278,281,293,295,302, 481,484,612
ilmenite 534,747
imino acids 82
immersion calorimetry 1,2,6,8
impurities 142,829,830
incongruent melting 420

induction period 362
induction stirring 693
inertinite 378
infrared spectroscopy (see also FTIR) 74, 142,377,436,564,779
inoculation 685
InP 240,241
instrumental effects 286
intercalation 498,538,565
interface chemistry 600,602,621,646
interferometry 443,444
interlayer water 455
intermetallic phases 397,686,761
internal oxidation 718
International Confederation for Thermal Analysis (ICTAC) 452
interstratified minerals 498
ion chromatography 72,355
ion implantation 763
ion-specific electrodes 800,801
iron alloy corrosion 725
iron alloys 663,693
iron-bearing dolomites 551
iron carbide 663,704
iron compounds 224
iron content of coal 204
iron corrosion 724,734,735
iron hydroxides 475,642
iron ore 704
iron(II) oxalate dihydrate 638
iron oxidation 229,230,714,722
iron oxide 66,79,295,534
iron oxide catalysts 179
iron phase transitions 661
iron salts 251
iron sulfides 527,532
irradiation 556,624
irreversible processes 688
isocompositional plots 199
isokinetic effect 377
isosteresis 132
isosteric method 26
isothermal conditions 361,363,501

J
jalpaite 526
jarosite 458
JMAEK equation (*see* Avrami-Erofeev equation)
Josephson devices 858

K
kaemmererite 490
kainite 456,458
kaolinite 33,70,262,265,269,274,281, 293-297,301,538,549,736,737
kaolins 263,266,270,274,279,292, 298,299,302, 476-479,500
KBF_4 410
$KCdCl_3$ 416
KCl 409
$KClO_3$-lactose pyrotechnic system 802,803
$KClO_4$-charcoal-dextrin-binder pyrotechnic system 789
$KClO_4$-Mg/Al alloy-Ca resinate pyrotechnic system 792
$KClO_4$-S-$CuSO_4.5H_2O$ pyrotechnic system 789
Kelvin equation 17,19
kernite 469
kerogen 386,387,390,391
K-Fe-O system 661
kieselguhr-supported catalysts 146
kiln 69
kinetic models 600,602,614
kinetics 63,120,154,158,167,170, 178,329,330,335,359,364,372,376, 377,385,386,390,391,429,539,596, 679,702,703,707,709,748,783,784, 794,805,808,818,825,850
kinetic standard 622
kinetic triad 604,607,618,647
Kissinger kinetic method 359,360, 680,698,757,805,838
$KMgCl_3$ 409
K_2MgCl_4 409
$KMnCl_3$ 423
KNO_3 795
Knudsen cell 417,864
Knudsen conditions 410
Knudsen method 100
Koenen test for explosives 354
KOH 338
kottschubeite 490

K_2PrCl_5 415
K_2SO_4 559
KSr_2Br_5 420
$KTiOAsO_4$ 221,222

L
La-Ba-Cu-O HTSC system 817,820,825
labyrinth crucibles 15,18,431,440
$LaCl_3$ 403,404,406,414
$LaCoO_3$ 142,146,170,171
$LaCrO_3$ 132-134,167,170,171
La_2CuO_4 153
$LaFeO_3$ 148-150,167,215
$LaGaO_3$ 221
lamda (λ)-transitions 100,400
$LaMeO_3$ oxides 171
$La_{1-x}M_xMnO_3$ catalysts 181
$LaMn_{1-x}Cu_xO_3$ 153
$LaMnO_3$ 148,150,158,160,167-171
$LaMO_3$ oxides 148
lampblack 97
La_2O_3 126,414
Langmuir adsorption model 138,141
$LaNiO_3$ 142,148,150,158,167
lanthanide chloride hydrates 633
lanthanide chlorides 403,404,406,413,419
lanthanide formate hydrates 637
lanthanide sesquioxides 127
$LaRhO_3$ 146
laser annealing 693
laser-flash technique 216,217
laser irradiation 624
La-Sr-Cu-O HTSC system 817,822,823,840,841
La-Sr-Mn-O system 226,227
latent thermal energy storage 310, 313-316,327
laterites 736
$LaTi_{1-x}Cu_xO_3$ 151-153
lattice enthalpy 415
lattice parameters 444
Laves phase 660
layer minerals 642
lead 224
lead carbonate 74,81
lead-indium solders 662
lead oxalate 835
lead pigments 60,63,72,79,80
lead production 739,740
lead salts 63
lead-tin solders 662
leather 52,56,57,63,76,77
leonite 458
lepidocrocite 549
lepidolite 278
leucite 280
$LiBF_4$ 410,411
Li_2CO_3 250,251
$LiFeO_2$ 250
life-time prediction for pyrotechnics 789
ligands, monodentate 398
lignite 204,264,291,294,296,373, 374,376,378,384,538
limestone 565
Li-Mn/MgO catalysts 144,145
limonite 264,291,474
linarite 458
linear rate equation 710,715,722,723,735
linear variable differential transformer (LVDT) 443
linen 62,72,79,84
linseed oil 72
liquid chromatography 363
liquidus curves 399,420,426
liquidus temperatures 420
$LiTaO_3$ 322
literature, dehydrations 609
lithium fluoride 314,318,323,340,342,343
lithium formate hydrate 622
lithium niobate 205-207,220,250,252
lithium potassium tartrate hydrate 613,638
lithium sulfate monohydrate 178,409, 597,608,612,619,622
lithographs 77
livesite 268
loeweite 458
logarithmic rate equation 711
loughlinite 498
low temperature oxidation (LTO) 381,386,389
low-temperature oxygen chemisorption (LTOC) 163,164
lubricants 759
lutidine complexes 437

L'vov physical model 605,623

M
machinability 753
maghemite 534
magnesite 297,516,517
magnesium calcites 550
magnesium carbonate 80
magnesium chloride dihydrate 599,632
magnesium chloride dodecahydrate 597
magnesium hydroxide 641
magnesium-nickel oxide catalysts 125
magnesium nitridation 749
magnesium oxalate dihydrate 435,638
magnesium perchlorate hexahydrate 633
magnesium phosphate hydrates 636
magnesium selenate hexahydrate 624
magnesium sulfate heptahydrate 597,623
magnesium sulfate lower hydrates 597,608,623
magnetic materials 667,687
magnetic measurements 436,454,534, 734,735
magnetic properties 534,694
magnetic susceptibility 142,223,534,873
magnetic transitions 454,534,687,820,853
magnetite 534,535,550,714,723,724,752
magnets 672,687,759
malachite 519
maltene 385
manganates 475
manganese formate dihydrate 636
manganese ores 736
manganese oxides 735
manganese sulfate tetrahydrate 629
manuscripts 76,83
marcasite 293,527
margarite 278
marmatite 744
martensitic transformations 676,677
mass spectrometry (MS) 63,74,174,175, 433,453,547,779,800,802,866
mass transfer 133
MCFC (see molten carbonate fuel cell)
MCM-41 42
mechanical alloying 698-700
mechanical milling 698-701
mechanical properties 262
mechanisms 596,600,778,794,807
megilp 55,60,79,80
melanterite 457,458
melt-growth processes 829,832
melting 454,521,522,613,615
melt processing of HTSC 827,829
melt spinning 687-690,693,700
Mengen oil shale 386,388
mercury compounds (see under Hg)
mercury porosimetry 10,18
mesoporous solids 11,29,42
meta-halloysite 270
meta-kaolinite 268,302
metal hydroxides, dehydration 641,642
metallic glasses 686,689,691,696
metallic threads 87,88
metallography 418,664,761
metallurgy 657-775
metal-matrix composites 753,757
metal powders 752,761
metals 50,657-775,778,780
metastable phases 192,194,198,422,542, 687,702
methanation 377
methane reforming 142
methanol synthesis 146
$Mg_5(CO_3)_4(OH)_2.4H_2O$ 125
Mg_5Ga_2 liquid 688
Mg-$KClO_4$ pyrotechnic system 782,803
Mg-KNO_3 pyrotechnic system 794,796,803
Mg_6MnO_8 144,145
Mg-$NaNO_3$ pyrotechnic system 785,796
Mg-$NaNO_3$-alloprene pyrotechnic system 781,783
Mg-PTFE pyrotechnic system 789
Mg-$Sr(NO_3)_2$-binder pyrotechnic system 785
$Mg_2[Ti_2(O_2)_4].4H_2O$ 437
$MgTiO_3$ 437
$MgWO_4$ 416
micas 263,276,278,279,293, 302,481-484,541
microbalance 119,184,707
microcalorimetry 778,789,792
microclimate 48,52,64
microcrystalline material 686,698,763

micro-DSC 55,792
microhardness 418
microporosity 7,9,32
microscopy 88,91,177,452,
595,601,617,619,621,627,629,632,
645,646,649,658,708,779,819,833
microstructure 657,660,663,847
micro-TA 54,64,83-90
microwave devices 858
mineral inclusions 564
mineral matrix of oil shales 389
mineral processing 562
minerals 451-593,598,657,735,741,744
mineral synthesis 562,563
mirabilite 457,458,522
mixed crystals 426
mixed hydroxides 642
mixed oxalates 436
mixed oxalate hydrates 638
mixed oxide catalysts 122,176
mixed sulfate hydrates 625
Mn-BaO_2 pyrotechnic system 799
$MnFe_2O_4$ 225
Mn_3O_4 180
Mn-SrO_2 pyrotechnic system 799,806
Mo/Al_2O_3 catalysts 143,144
Mo-BaO_2 pyrotechnic system 799
Mo-Bi-P-O systems 176
MOCVD (metal organic chemical vapour deposition) 819,864
modelling of heat transfer 319,322
modelling of oil shale pyrolysis 387
modelling of pyrotechnic ignition 804
modulated temperature DSC (see MTDSC)
modulus, loss 54,80-82
modulus, mechanical 54
moganite 565
moisture analysis 225
moisture content of coal 380
moisture content of wood 69
moisture damage 74
moisture loss 53,76
moisture sorption 53,81
molecular crystals, dehydration 649
molten carbonate fuel cell (MCFC) 312,324-326
molten salt latent thermal storage 312,325
molybdates 143,466
molybdenite 530,562
molybdenum metal 752
molybdenum(VI) oxide dihydrate 644
montmorillonites 263,270-276,293,
301,302,538,598
MoO_2 175
MoO_3 143,154,164
MoO_2/SiO_2 catalysts 166
MoO_3/SiO_2 catalysts 161
Mo-Pr-Bi-oxides 176,177
Mo-Pr-O catalysts 156
mortars 245
Mo-SrO_2 pyrotechnic system 799
Mössbauer spectroscopy 214,215,744
MTDSC (modulated temperature DSC) 216,417,434,778,779,786,796
mullites 262,268,274,275,280,563
mummy coffins 53,69
muscovite 276,277,279,481,483,
598,612,643

N

$NaBF_4$ 410
Na_2CO_3-$CaCO_3$ system 230,231
$NaFeO_2$ 408
Na_3FSO_4 406
Na_3GdCl_6 442
nahcolite 518
nanocrystalline materials 698,701,703
nanotubes 35,100
NaOH 340
NaOH-KOH system 337
NaOH-$NaNO_2$ system 314,318,321,323
NaOH-$NaNO_3$ system 339
$NbBr_5$ 439
Nd-Ba-Sr-Cu-O HTSC system 828
Nd-Ce-Cu-O HTSC system 817,
821-823,857
$NdCl_3$ 403
Nd-Cu-O HTSC system 857
$NdMO_3$ perovskites 417
Nd_4PdO_7 440
Néel temperature 215,223,534,536,821
neodymium 672,673
nesquehonite 520
neutron diffraction 41,845

neutron irradiation 445
NH_4CdCl_3 423
NH_4MgF_3 404
Ni-Al system 703,761,762
Ni-B system 691
Ni-Cr alloys 733
nickel 224
nickel alloy corrosion 728
nickel catalysts 751
nickel oxalate 750
nickel oxalate dihydrate 599,606, 640,649,751
nickel oxidation 711
nickel production 740,753
nickel squarate dihydrate 644
nickel sulfate heptahydrate 597
nickel sulfate hexahydrate 627,645,647
nickel sulfate lower hydrates 597
nickel zinc ferrites 197,198
Ni-Cu alloys 733
$NiFe_2O_4$ 253
Ni-Ge system 703
Ni-Mo-Co-B system 691,692
$[Ni(NH_3)_6]Br_2$ 433,434
niobium oxidation 411
NiO reduction 230
$NiO-ZrO_2$ catalysts 179,180
Ni-P system 688
Ni-Pr system 674
NiS inclusions in glass 227,228
Ni-Si alloys 661,663
Ni-Si-B system 695
Ni-Ti alloy 676-679
nitramines 350
nitrate esters 350
nitrate precursors 254
nitrates 433
nitridation 749
nitrided alloys 722,749
nitroalkanes 350
nitrocellulose 350,800,801
nitrogen physisorption 18
nitroglycerine 350
nitromethane 350
Ni-Zr system 699,763-765
NMR 88,565,642
non-ignition conditions 780
non-isothermal conditions 733
non-isothermal kinetics (NIK) 618, 733
non-stoichiometry 196,205,220
nontronite 272,274,275,301
'normal' reactions 604
norsehite 511
n-type semiconductor 821
nucleation 12, 148,154,159,194, 198,541,599,627,675,693,696,697,702,758
nucleation and growth models 154,378, 541,548,600,601,610,617,629,634,641, 642,647,692
nucleation kinetics 543,544,548,601
nucleus 601,621,626,629
nucleus growth 600,626,629,632

O

ODTX (one-dimensional time to explosion) 354,356
oil (see also crude oil)
oil composite 382
oil generation from coal 381
oil sands 741,742
oil shales 200-202,375,376,386,387,538
oil viscosity 382
olivine 284,290,519,535
onset temperature 430,512
opals 510,533
order-disorder transitions 542,670,694
order-of-reaction models 602
ordering transitions 703
organo-clays 452,538,564
organometallics 860
organophosphorus compounds 100
orthoclase 290,541
orthorhombic-to-tetragonal (O-T) transitions 844-846,849
oscillating reaction 546
oscillatory catalytic reactions 182,183
overlapping processes 616
oxalates 436,597,749,750
oxalates as precursors 178,252,826,835
oxalic acid dihydrate 597
oxidation 146,429,437,440,444, 453,537,707
oxidation by CO_2 722,723
oxidation by H_2O 722,723

oxidation, internal 718
oxidation of alloys 716,838
oxidation of crude oil 381
oxidative degradation 58-61,65,76
oxide-melt solution calorimetry of HTSC 818
oxides 99,225,735,778
oxygen adsorption 842
oxygen chemisorption 163-167
oxygen content of HTSC 840,841,843,848,849,854
oxygen desorption 843
oxygen diffusion coefficients 843
oxygen exchange 819
oxygen isotope exchange 847
oxygen stoichiometry 817,818,821,824, 840,841,850,852,854
oxygen vacancy model 844
oxysalts 735,751,752,778
Ozawa kinetic method 329,330,335, 757,805,826

P

PA-curves (Probenmengen-Abhängigkeit) 453,462,468,474,478,481,497,499,500, 504,508,510,512,513,517,549
paintings, conservation 47,53,54, 56-60,74,78,80
paints 53,55,90
palladium metal 697
palladium oxidation 183
palygorskite 66,69,498,502-504,538
paper 77,261
papyri 50,53,54
parabolic rate equation 710-713,717, 720-725,731
paragonite 278
parchment 49,51,53,55,56,63, 76,77,80,82,85,86,90
parisite 517,519
particle size effects 378,380,599,622
Pb-Ba-Eu-Cu-O HTSC system 855
Pb-Bi-Sr-Ca-Cu-O HTSC system 836,837
Pb-Bi system 686
Pb-Ca system 688
Pb_2MoO_5 437
$PbMoO_4$ 437
PbS 745
Pb-Sn system 666
Pb-Sn-Se system 666,667
Pb-Sr-Ca-Cu-O HTSC system 832
Pb-Sr-Eu-Ca-Cu-O HTSC system 855
Pb-Sr-Y-Ca-Cu-O HTSC system 817,820,822,823,848
Pb-Sr-Y-Cu-O HTSC system 857
Pb-Te system 686
$PbTiO_3$ 427
Pb-Zr-Ti-O system 253
Pd-Cu-Si system 692,757
Pd-Te system 675
Pd/TiO_2 183
peak temperature 430,512
pearlitic reaction 663
peat 376,379
penninite 282
pentaerythritol 314-322,333,334
pentaerythritol trinitrate (see PETN)
pentlandite 743
periclase 275
peritectics 193,426,827,829,830
peritectic temperature 399,828
perovskites 143,146,149-151,167,196, 417, 563
perovskite structure 849
peroxides 351,352,778
pesticides 538,563
PETN 350
petrochemicals 371
petrogenesis 547
petrographic analysis 378
petroleum coke 374
petrological systems 541
pharmaceuticals 657
phase diagrams 192,193,398,399,418,425,426,540,541, 658,668,674
phase equilibria 192,193
phase rule 418
phase transitions 100,194,221,261, 402,406,434,452,521,531,540,565, 616,658
phenol 538
phlogopite 278
phosgenite 519

phosphates 453,454,462-465,510
phospho-gypsum 458,562
photoacoustic spectroscopy 627
photodetection of ignition 781
photoionization mass spectroscopy 379
'physical model' (L'vov) 605,623
physical vapour deposition (PVD) 762,858
pickeringite 457
picoline complexes 437
picric acid 350
pigments 51,57,60,64,69,80
pillared clays 493,538
pinning centres 830
pirssonite 520
pitches 374
pitch resins 107
pitch resin oxidation 107
plagioclase 541
plastic ice model 12
plasticity 278,294,295,297,300,303
plasticizers 79
plastic state of coal 374,375
platinum 708
platinum corrosion 735
platinum doping 181,182
plumbocalcite 513
Polanyi-Wigner equation 109,110, 604,626,647
polutant gases 47,64,71,91
polyacrylonitrile (PAN) 111,112
polyacrylonitrile fibre oxidation 112
polyethylene 314,317,323,324,331,332
polyhalite 458
polymers 18,50,380,657
polymorphism 643
polyphosphides 410
polypropylene 389
porcelain 261,262,300,313
pore curvature 42
pore size 13,17-21
porosity 1,3, 120,129,172,223,443,830
potassium alum 630,644
potassium benzoate-$KClO_4$ pyrotechnic system 786
potassium copper chloride hydrates 633
potassium metavanadate monohydrate 644
potassium phosphate hydrates 635
pottery 69
powder metallurgy 657,752,753,759
power law 711,716
praseodymium nitrate 122
$PrCl_3$ 403,415
$PrCoO_3$ catalysts 142-146
precursors 134,135,178,248-254,437
precursors for HTSC 817,818,832,838,839,858,859,868
pre-exponential factor (*see* frequency factor)
preparative chemistry 431,437
preparative thermobalance 431
pressure DSC 382,384,389
principal component analysis 76
printed-circuit boards 207
Pr-Mn system 668,669
Pr_6O_{11} 154-157
Probenmengen-Abhängigkeit (see PA-curves)
propane dehydrogenation 171
propellants 777,792
propylene oxidation 176
proton magnetic resonance thermal analysis (PMRTA) 377
proton motion 627,642
prousite 530
Prout-Tompkins equation 602
proximate analysis of coals 204,205, 374,375,380
pseudo-binary systems 398,420, 421,425,426
pseudo-mullite 268
pseudo-parabolic kinetics 715
pseudo-peritectic point 363
psilomane 736
PTFE cell 337,338
Pt-Se system 664,665
p-type semiconductor 820
pulse thermal analysis 202,203,244,245
Pu-Pb system 674
purge gas 708
purity 429,538
pyridine complexes 436
pyrite 203,204,293,405,525,527,744
pyrolusite 533
pyrolysis of coals 371

pyrolysis of minerals 537
pyrolysis of oils 371
pyrometry 787
pyrophillite 270,271,276,282,302, 479,480,538
pyrophoricity 733
pyrotechnic additives 778,803
pyrotechnic fuels 778
pyrotechnic oxidants 778
pyrotechnics 777-816
pyrotechnics, special instruments 781-784
pyrotechnic systems, table 790,791
pyroxene 290,519
pyrrhotite 527,537,743

Q

Q-TG 432
quartz 68, 209,262,264,293,295, 297,298,300,412,532,533,541,542, 552-561,707
quartz content 211,219
quartz crystal balance 622,626
quartz inversion 209-213,219, 532,533,552-561,565
quasi-isobaric methods 432,440
quasi-isothermal methods 15,16,22, 432,440
quenching 679,686-689,693,753, 832,836

R

rabbit-skin glue 72,85
Raman crude oil 381,383
Raman spectroscopy 533,549
rank of coals (see coal, rank)
rare-earth (RE) based HTSC 846
rare earth elements 734
rare earth oxalates 751
rare minerals 517
rate coefficient 363,648
rate constant (*see* rate coefficient)
rate controlled sintering (RCS) 236,237
rate equations 548,603
rate equations, table 602
rate jump method 21
$RbBF_4$ 410
$RbCaF_3$ 407
Rb_2CoCl_4 407
$RbCrCl_3$ 407
$RbLa_2Cl_7$ 420
Rb_3LaCl_6 420-424
$RbMgCl_4$ 409
Rb_2ZnCl_4 405
RCS (see rate controlled sintering)
RDX 350,351,362
reaction calorimetry 411
reaction conditions 615,622,625,627,631,647
reaction geometry 600
reaction intermediates 431
reaction kinetics 617
reaction mechanism (see also mechanism) 619
reaction order (RO) 372,602
reaction stoichiometry 617,649
reaction zone 603
reactive atmospheres 142
reactivity of HTSC with CO_2 and H_2O 848
reactor geometry 133
recarbonation 71
reconstruction 510,542
recrystallization 598-601,608,615,620, 629,630,644-648
rectorite 476,498
reducing atmosphere 730,731
reduction 142,154,172,225,429,439,440, 704,730,735,737,742,856,858
reduction-oxidation cycles 146
reflectance of coals 378,380
refractories 215,234,235,261,295
refractoriness 278,295
rehydration 53
relative humidity (RH) (see also humidity) 51,64,69,81,83,91
re-oxidation 748
replicas 620
reproducibility of kinetic parameters 640,641
reservoir rock composition 384
resolution 192
reverse configuration DMTA 83,91
reversible processes 606,626,646
RH (see relative humidity)
rheological properties 264,377

rhodium oxidation 716
rhodochrosite 539
roasting 657,737,741
Rock-Eval-Pyrolysis 453
rocks 453
Rogers and Morris kinetic method 360
rosasite 173
rotary disintegrator 294
rotational transformation 542
rubber 113,261
rubellite 511
rubidium manganese fluoride hydrate 633
Ru-Sr-Gd-Cu-O HTSC system 817,820,822,853,857

S
safety in studying pyrotechnics 780
salt corrosion 726,730,734
sample controlled thermal analysis (SCTA) 14,17,20,778
sample environment 286
sample preparation 286
sample size 51,84,142,286
sanitaryware 261
saponite 272,275
sapphire standard 215,405
sassolite 471,472
scanning electron microscopy (SEM) 75, 620
SCB (small-scale cook-off bomb) test for explosives 354,356
scheelite 563
schoenite 458
schoerl 511
schroekingerlite 520
Sc_2O_3 126,139,140
$Sc(OH)_3$ xerogel 128
Sc-Pb system 670
Sc-Sn system 670,671
SCTA (see sample controlled thermal analysis)
sculpture 74
sealed-cell DSC 792
second-order phase transitions 407,542, 658
sedimentary clays 292,303
sedimentary micas 278,295
selenium 687
self-cooling 606,619
self-heating 647
self-propagating high-temperature synthesis (SHS) 748.778
Semenov model 365
semiconductors 240
sensible thermal energy storage 310
sensitivity 192
sepiolite 34,498,502-504,538
serecites 278
serpentine 478,480
shales (see also oil shales) 476
shape memory alloys 676
shelf-life 598
shock initiation 792
shrinkage 56,84,235,236,293-298,303
shrinking-core kinetic model 737
SiC-Al composites 754,755
SiC-reinforced materials 318,341,343,755
siderite 514,518,539
sigmoid models 602
Si-KNO_3-viton pyrotechnic system 793
silica 7,10,31,209,218,408
silica-alumina surface 137
silica-gel 16,30,31,238,239
silicalite 25,36-38
silica minerals 552
silica-supported catalysts 163,164
silicate glass 280
silicates 453,478,484,501-503, 519-523,563,565
silicates, dehydration 643
silicone oil 331
silks 50,51,53,64,65,74,83,88
silver metal 697
silver metal 88.89
simplex optimization 380
simulation of coal processing 378
simulation of firing of cuneiform tablets 67
simulation of heat transfer 319,322-324
simulation of pyrotechnic ignition 804
single crystals of HTSC 831,832,839
sintering 146,216,232,235,236,262, 300,303,433,454,657,746,748, 759-761, 818
Si-oxidant pyrotechnic system 799

Si-Pb_3O_4 pyrotechnic system 787,797,798,805
Si-Pb_3O_4-viton pyrotechnic system 793
Si-Sb_2O_3 pyrotechnic system 806
slags 735
slavikite 458
slip casting 265
small angle X-ray scattering (SAXS) 65
smalt pigments 74
smectites 272,476,478,491,493,538,550
SMES (see superconducting magnetic energy storage)
smithsonite 517,518
Smith-Topley effect 607,608,647
smoke-generating pyrotechnics 788.802
Sn-Bi system 697
Sn-Pb system 664-666
soda 520
soda-lime-silica glass 214,249
sodium carbonate monohydrate 634
sodium citrate dihydrate 638
sodium copper acetate carbonate 71
sodium dinitramide 796,797
sodium, liquid 735
sodium perchlorate monohydrate 633
sodium phosphate hydrates 635
sodium sulfate 525,526,540
sodium tetraborate 608
sodium thiosulfate pentahydrate 632
sodium tungstate dihydrate 635
softening temperature 54,78-80,87-90
soils 386,453,538
solar energy 307
solder 207,208,662
sol-gel synthesis 252
sol-gel synthesis of HTSC 826
solid electrolytes 417,423
solid-gas reactions 707,746
solidification 12,657,675,685
solidification equation 758
solid-liquid transitions 399,419
solid-solid reactions 429,746,764
solid-solid transitions 333,334,399,420,660
solid solutions 550
solid-state reactions, displacive 420
solid-state reactions, reconstructive 420,421
solid-state reactivity 225
solid-state synthesis of HTSC 825,826
solidus curves 426
solution calorimetry 399,411,412,425
solvent extraction of coal 106,379
solvent swelling ratio 377
SO_2 adsorption 245
SO_2 poisoning 181,182
specific-heat anomaly 824
specific heat capacity (see heat capacity)
specific heat of coals 375,377
specific heat of oils 384
specific surface areas 5
spectroscopy 63,213,605,649
spermaceti wax 55,60
sphalerite 530,562,744,745
spheron 99,108
spinel formation 289
spinodal transformations 542
splatting 687
spontaneous combustion 371
spray-forming processes 675
sputtering 762.763
SQUID (superconducting quantum interference device) 824
$SrBr_2$ 409
$SrRuO_3$ 853
stainless steels 681,682,718-720,732,761
standard entropy 402
standard temperature of decomposition 513
starch 736,737
steam accumulator 308
stearic acid 530
steels 228,229,676,683,718-720,746,759
stephanite 530
stepwise isothermal analysis 433
stishovite 565
stoichiometry 120,149,151,433,619
stoneware clays 296
storage of pyrotechnics 789
stromeyerite 526
strontianite 516
strontium carbonate 524,833,835
strontium oxalate monohydrate 435
strontium permanganate hydrate 635
structural changes 646
structural relaxation 688-690

sub-bituminous coals 375,376
sublimation 429,454,866
substitution in minerals 550
substrate 142
succinite 539
sulfated-zirconia catalysts 178
sulfates 178,203,433,475,481, 453,454,456,459-461,510, 521-523,526-533,537,562, 563,565
sulfides 433,525-528,731,735,737,781,784
sulfur 707,723,735
sulfur dioxide 203
sulfur oxides 525,707,723,724,734
superconducting magnetic energy storage (SMES) 309
superconducting properties 824
superconducting transition temperature 817,819,822,824,849
superconductivity 817-878
superconductors 563,565,817-878
supercooling 192,334,542,834,857
supercritical extraction of oils 385
surface area 1,3,5,142,163,165,166,172, 223,429,713
surface chemistry 1-46
surface reactions 644,645,708,723
surface-to-volume ratio 364,365
swelling 18,54,274,278,283,295,377,379
synchrotron radiation 445,619,622,626
synthesis of inorganic compounds 248-254

T

tachyhydrite 455,456
talc 272,273,278,280,282,302,479-481,538
Taliani test for explosives 355
tan δ 54,80-82
Ta_2O_5 detector 225
tapestries 51,55,64,83,87-89
tar 377
tarnowitzite 552
tartrates 597,826
$TaSi_2$ films 242,243
TATB 350
TATP 352
TBA (thermobarometric analysis) 840
TD (thermodilatometry) 209,218,236, 442, 452,564,818,819,828
TD-DSC 194,195
TE (thermoelectrometry) 819
TeF_6 412
tellurides 525
temperature integral ($p(x)$) 618
temperature jump method 101
temperature profile analysis 778,779,787,806,807
temperature programmed desorption (see TPD)
temperature programmed reduction (see TPR)
tennantite 529
ternary systems 398,418,426
terracotta sculptures 54
tetragonal-to-orthorhombic transition in HTSC 845,850,851
tetrapropylammonium (TPA) 178
textural changes 619,620,630,644,646
T_g (see glass-transition temperature)
TG (thermogravimetry) 50,53,68,71,74, 99,120,142,195,261,269,276,281,311,329, 335,353,358,372,382,389,429,452,541, 563,618,657,707,778,794,818,819,835, 845,854,856,868
TGA (thermogravimetric analysis – see TG)
TG-DSC 627
TG-DTA 74,338,430,431,475, 481,627,836
TG-EGA 825
TG-FTIR 234
TG reduction method 856,857
thallium oxide loss from HTSC 851
thallium substitution in HTSC 853
thecotrichite 72
thenardite 522,525,526,540
thermal conductivity 55,88,216,320, 321, 785
thermal conductivity detector 225
thermal diffusivity 216,783,784,787
thermal energy storage 310
thermal equilibrium 609
thermal expansion 86,218-222,442

thermal expansion coefficient 845
thermal hazard evaluation 789
thermal insulation 283
thermal runaway 358,364,805
thermal shock resistance 262
thermal stability 353,354,429
thermite reaction 701,783
thermoacoustimetry 564
thermobalance 431
thermobarometric analysis (see TBA)
thermochemical energy storage 310,311
Thermochimica Acta 609
thermodesorption 1,14
thermodilatometry (see TD)
thermodynamic cycle 415
thermodynamic data 400,401,539,564
thermoelectrometry (see TE)
thermogravimetric analysis (TGA) (see TG)
thermogravimetry (see TG)
thermoluminescence 564,794
thermomagnetometry (see TM)
thermomechanical analysis (see TMA)
thermomicroscopy (see also microscopy) 52,55,56,85,540,564,778,785,800
thermomolecular effects 133
thermophysical properties 320
thermoporometry 1,11-14
thermosonimetry (see TS)
thick films 253,254
thin film HTSC 817,818,858,867,868
thin films 191,199,200,239,657,753, 762-765
third law of thermodynamics 402
three-component systems 426
thuringites 490,491
Ti-Al system 659,660,748
Ti-Al-Mn system 660
Tian-Calvet calorimeter 23
TiC 678,679
$TiH_{0.15}$-oxidant pyrotechnic systems 804
Ti-KNO_3 pyrotechnic system 794,795
tiles 261,296
time-to-event tests for explosives 355,358
time-to-ignition of pyrotechnics 782
Ti-MoO_3 pyrotechnic system 799
tin 696,740
Ti-$NaNO_3$ pyrotechnic system 800
tin-lead system 208,209
TiO_2 741
TiO_2 photo-anodes 252
titania 6,291
titania-supported Pd catalysts 182
titania xerogel 253
titanium butoxide 252
titanium hydrogenation 747
titanium metal transitions 661
titanium oxidation 715,722
titanohematite 535
titanomagnetite 535,537
Ti-teflon pyrotechnic system 792
Ti-Zr-Cu system 696
Ti-Zr-Ni-Cu system 696
Tl-Ba-Ca-Cu-O HTSC system 817, 821-823,851
Tl-based HTSC 838,850,851
$TlCdF_3$ 407
TM (thermomagnetometry) 195,204,211,223,224,229,244,377, 562,564,694,695,734,735,739,785,819,824
TMA (thermomechanical analysis) 50,51,53,74,78-80,87,377,441,693
TM-DTA 224
TNAZ 350
TNT 350,351
TNT equivalence 352
topaz 519,563
topography 85,86
topotactic reactions 612,617,619,641-644
tosudite 476
toughened glass 227
tourmalines 510
TPD (temperature programmed desorption) 15,120,176
TPR (temperature programmed reduction) 120,142-144,174,440,818,819
transition enthalpies 399
transition entropies 399,400
transition state theory 607
transport measurements 440
trehalose dihydrate 613,644
triangular phase diagrams 426
tridymite 300,533
trinitrotoluene (see TNT)

trioctahedral illites 280,281
trioctahedral micas 278
tritium 669
trona 520
TS (thermosonimetry) 213,553,559,564
tunellite 471
tungsten carbide 692,693,721,722,757
tungsten iodide 440
twin microcalorimeter 541
two-zone furnace 437,438
tyres 113

U
ulexite 469,471
ulvite 537
unsupported catalysts 164
UO_2 216
uranyl nitrate hexahydrate 611
urea 327,329
UV irradiation 230,231
UV spectroscopy 436

V
vacuum stability test for explosives 355
vanadates 453,454,463-465,510
vanadium carbide 663
vanadium catalysts 120,121
vanadium oxidation 716
vanadium oxides 122
vanadium-tritium system 669
vanadyl oxalate 121
van't Hoff plots 844,852,854
vaporization 429,728
vapour-pressure measurement 100, 818,840,864
VCl_3 415
Vegard's line 426
vermiculites 263,282-287,302, 491,493,538,612,643
vesuvianite 505,510
Vickers hardness test 679
vis-breaking 381,385
vitreous state (see glassy state)
vitrifying range 294
vitrinite 374,378
vivianite 468
V-MoO_3 pyrotechnic system 799
voglite 520
volatile content of coals 380
volatile ligands 859,860
volatility 859,868
volcanic ash 295
volcanic glass 295
vortices 830
V_2O_5/SiO_2 catalysts 161
V-Te system 668

W
Washburn equation 11
waste lubricating oils 385
waste disposal 453,562,563,566
waste products 371,385
water adsorption 129,130,278,289
water as a ligand 597,598,639,648
water of crystallization 597,619
water evolution types (WET) 611,614,621
water-gas shift 146
water in minerals 455
water removal 126
water softeners 262
water vapour pressure 289,560, 606,608,615,618,622,626,628, 629,631,634,647,749
wavellite 466
waxes 55,291
WC-amorphous Ni-Si-B composite 758
WC-amorphous Pd-Cu-Si composite 758
WC-Co system 211,212,722,759
WC-Ni system 722
weathering of clays 294,295
weathering of coal 379
weathering of rocks 563
Weldalite RX818 681
welding fluxes 564
welding tests 666,682
WF_6 412
whitewares 295,303
wind energy 307
witherite 516
W-$KClO_4$ pyrotechnic system 783
W-$K_2Cr_2O_7$ pyrotechnic system 783,785,804,805
W-$K_2Cr_2O_7$-Cr_2O_3 pyrotechnic system 805
wolframite 535

wollastonite ($CaSiO_3$) 408
Wollaston thermal probe 54,84
wood 54,72
wood bark 379
wood chips 379
wood degradation 105
wool 51,64,65,74,75,83,87,88
WTe_2 414
wulfenite 563
wurtzite 530
wustite 714,722,724

X
xerogel 253,533
X-ray diffraction (XRD) 36, 64,72,74,82, 142,149,177,210,213,214,230,252,268, 386,399,404,411,418,423,425,434,436, 437,443-445,452,540,549,627,629,642, 649,658,708,716,779,798,818,819,833, 845,850,868
X-ray lithography 241
X-ray photoelectron spectroscopy (XPS) (see ESCA) 78

Y
Y-Ba-Cu-O HTSC system 828,829,841,843,848,856
Y-Ba-O HTSC system 817,820,822-825
Y-based HTSC 847,849
Y-Ba-Sr-Cu-O HTSC system 828,855
$Yb(OH)_3$ 127
Young's modulus 689,757
Y-Tl system 671
yttrium oxalate 826

Z
zaratite 513,520
zeolites 19,21,36-41,129-131,178,180,507-510,611,619
zeolitic catalysts 562
zeolitic residue 605,608,629
zeolitic water 455
zero-order reaction 358,360,363,634
zinc 224
zinc acetate dihydrate 637
zinc ferrite 746
zinc formate dihydrate 637
zinc oxalate 750
zinc production 739
zinc titanyl oxalate 178
zinnwaldite 278,279
Zintl phases 397
zircalloy 733
zirconia coating 732,733
zirconium alloys 699
zirconium hydrogenation 747
zirconium oxidation 714,715
zirconium sulfate hydrates 625
Zn-Al system 686
Zn-Ga-Hg system 672
ZnO 216
Zn-oxidant pyrotechnic systems 799
ZnS 745
'zonary' model 635
zone melting 842
Zr-$KClO_4$ pyrotechnic system 800,801
Zr-$KClO_4$-nitrocellulose pyrotechnic system 786
Zr-KNO_3 pyrotechnic system 794,795
Zr-MoO_3 pyrotechnic system 799
Zr/Ni alloy-$KClO_4$ pyrotechnic system 800,801
Zr/Ni alloy-$KClO_4$-nitrocellulose pyrotechnic system 786
ZrO_2 741
Zr-$PbCrO_4$ pyrotechnic system 783,785
$ZrTe_3O_8$ 439

This Page Intentionally Left Blank